KARADENIZ
TECHNICAL UNIVERSITY

AES 2021

Proceedings of the 5th International Anatolian Energy Symposium

24-25 March 2021

Editors

Burhan ÇUHADAROĞLU
Ömer Necati CORA

proceedings of the

5th International Anatolian Energy Symposium

AES2021

24-25 March 2021

Trabzon/TURKEY

editors

Burhan ÇUHADAROĞLU, Karadeniz Technical University, Turkey

Ömer Necati CORA, Karadeniz Technical University, Turkey

organized by

Karadeniz Technical University,

School of Engineering,

Department of Mechanical Engineering

ISBN : 978-605-2271-33-9

AES-2021

Karadeniz Technical University

Trabzon/TURKEY

Honorary Chairmen

Prof. Hamdullah ÇUVALCI	Rector of Karadeniz Technical University
Prof. Gençağa PÜRÇEK	Dean of Karadeniz Technical University Engineering Faculty

Honorary Committee

İsmail USTAOĞLU	Governor of Trabzon
Murat ZORLUOĞLU	Mayor of Trabzon

Organizing Committee

Prof. Burhan ÇUHADAROĞLU	(Chairman)	Karadeniz Technical University
Assoc. Prof. Ömer Necati CORA	(Co-Chairman)	Karadeniz Technical University
Prof. Kadir BİLEN		Atatürk University
Prof. Nevin ÇELİK		Fırat University
Lecturer Kaan ÖZEL		Trakya University
Res. Assist. Furkan Erman KAN		Karadeniz Technical University
Res. Assist. Aleyna AĞIRMAN		Karadeniz Technical University
Res. Assist. Ayşe CANDAN		Karadeniz Technical University
Res. Assist. Mehmet SAĞLAM		Karadeniz Technical University
Res. Assist. Mustafa Yavuz COŞKUN		Karadeniz Technical University
Res. Assist. Soner BİRİNCİ		Karadeniz Technical University
Res. Assist. Cansu AY		Karadeniz Technical University

Supporting Institutions and Organizations

Scientific Committee

Prof. Ünal AKDAĞ	Aksaray University
Prof. Mehmet Emin ARICI	Karadeniz Technical University
Prof. Kamil ARSLAN	Karabük University
Assist. Prof. Cemalettin AYGÜN	Karadeniz Technical University
Prof. Tülin BALİ	Karadeniz Technical University
Prof. Tanmay BASAK	Indian Institute of Technology Madras, India
Prof. Şenol BAŞKAYA	Gazi University
Assoc. Prof. Hakan BAYRAKTAR	Karadeniz Technical University
Prof. Kadir BİLEN	Atatürk University
Prof. Atilla BİLGİN	Karadeniz Technical University
Prof. Şefik BİLİR	Konya Technical University
Prof. Ertan BUYRUK	Cumhuriyet University
Assoc. Prof. Ömer Necati CORA	Karadeniz Technical University
Prof. Selin ARADAĞ ÇELEBİOĞLU	TED University
Prof. Yunus A. ÇENGEL	Adnan Menderes University
Prof. Burhan ÇUHADAROĞLU	Karadeniz Technical University
Prof. Can Özgür ÇOLPAN	Dokuz Eylül University
Prof. İhsan DAĞTEKİN	Fırat University
Prof. Alican DALOĞLU	Karadeniz Technical University
Prof. Yaşar DEMİREL	University of Nebraska-Lincoln, USA
Assist. Prof. Cevdet DEMİRTAŞ	Karadeniz Technical University
Assoc. Prof. Muhammad Ghaffar DOGGAR	Energy Research Center Comsats University, Pakistan
Prof. Orhan DURGUN	Avrasya University
Assist. Prof. Mustafa EYRİBOYUN	Bülent Ecevit University
Prof. Ali GÜNGÖR	Ege University
Prof. Oktay HACIHAFIZOĞLU	Trakya University
Prof. Arif HEPBAŞLI	Yaşar University
Prof. Muhammad Azhar IQBAL	School of Science University of Management&Tech., Pakistan
Assist. Prof. Erdem IŞIK	Munzur University
Prof. Kamil KAHVECİ	Trakya University
Prof. Kamil KAYGUSUZ	Karadeniz Technical University
Assoc. Prof. Ali KEÇEBAŞ	Muğla Sıtkı Koçman University
Prof. Birol KILKIŞ	Başkent University
Prof. Muammer KOÇ	Hamad bin Khalifa University, Qatar
Prof. Günnur KOÇAR	Ege University
Prof. Ramazan KÖSE	Dumlupınar University
Prof. Ümit KÖYLÜ	Missouri University of Science and Technology
Prof. İrfan KURTBAŞ	Hitit University
Prof. Haydar KÜÇÜK	Recep Tayyip Erdoğan University
Assoc. Prof. Lütfü NAMLI	Ondokuz Mayıs University
Assoc. Prof. Mustafa ÖZBEY	Ondokuz Mayıs University
Assoc. Prof. Hakan ÖZCAN	Ondokuz Mayıs University
Prof. Yücel ÖZMEN	Karadeniz Technical University
Prof. Djamila REKIOUA	University of Bejaia, Algeria
Prof. Hasan SADIKOĞLU	Yıldız Technical University
Assoc. Prof. Mustafa SARIOĞLU	Karadeniz Technical University
Prof. Mohammad Taghi Shervani-Tabar	University of Tabriz, Iran
Assoc. Prof. Youcef SOUFI	University Larbi Tebessi, Algeria
Prof. Arzu ŞENCAN ŞAHİN	Süleyman Demirel University
Prof. Beşir ŞAHİN	Çukurova University
Prof. Zehra ŞAHİN	Karadeniz Technical University
Assist. Prof. Mustafa Ergin ŞAHİN	Recep Tayyip Erdoğan University
Prof. Haşmet TÜRKOĞLU	Çankaya University
Prof. Ahmet ÜNAL	Karadeniz Technical University
Prof. Mortaza YARİ	University of Tabriz, Iran
Prof. Tahir YAVUZ	Başkent University
Prof. Cengiz YILDIZ	Fırat University
Prof. Abdulvahap YİĞİT	Uludağ University

Keynote Speakers

Assoc. Prof. Hafiz Muhammad ALI
Topic: "Surface Condenser: Heat Transfer"

Dr. Hafiz Muhammad Ali, an associate professor of Mechanical Engineering at King Fahd University of Petroleum and Minerals, Saudi Arabia, received his Ph.D degree from Mechanical Engineering, Queen Mary, University of London, United Kingdom in 2011. He was a post-doc at Water and Energy Laboratory, University of California at Merced, United States during 2015-16 period. Dr. Ali is a noted faculty member having thermal sciences, heat transfer and solar energy as areas of interest. Over the years, he has supervised several undergraduate and postgraduate students and his work, more than 230 papers (h-index: 40, citations: +5000 according to Google Scholar), have been featured in various reputed international journals. Dr Ali has also represented his institution and Pakistan at several international and national conferences as an invited speaker and delivered numerous keynote talks. His other research interests include electronics cooling, condensation, nanofluids, heat transfer devices, thermal management. He is the recipient of the 'Best Young Research Scholar Award' for 2017 in the Engineering category. He was conferred the honor at the 7th HEC Outstanding Research Award Ceremony held the other day. The award is of immense value to scholars competing for the honor as there is only one award reserved in the Engineering Category for 'Best Young Research Scholar' across all of Pakistan. Dr Ali has also had the honor of receiving HEC's Best Research Paper Award (2013/2014) and Research Productivity Award by Pakistan Council of Science and Technology (2016-17).

Prof. Frede BLAABJERG
Topic: "Wind Power – A Technology Enabled by Power Electronics"

Frede Blaabjerg (S'86–M'88–SM'97–F'03) was with ABB-Scandia, Randers, Denmark, from 1987 to 1988. From 1988 to 1992, he got the PhD degree in Electrical Engineering at Aalborg University in 1995. He became an Assistant Professor in 1992, an Associate Professor in 1996, and a Full Professor of power electronics and drives in 1998. From 2017 he became a Villum Investigator. He is honoris causa at University Politehnica Timisoara (UPT), Romania and Tallinn Technical University (TTU) in Estonia. His current research interests include power electronics and its applications such as in wind turbines, PV systems, reliability, harmonics and adjustable speed drives. He has published more than 600 journal papers in the fields of power electronics and its applications. He is the co-author of four monographs and editor of ten books in power electronics and its applications. He has received 33 IEEE Prize Paper Awards, the IEEE PELS Distinguished Service Award in 2009, the EPE-PEMC Council Award in 2010, the IEEE William E. Newell Power Electronics Award 2014, the Villum Kann Rasmussen Research Award 2014, the Global Energy Prize in 2019 and the 2020 IEEE Edison Medal. He was the Editor-in-Chief of the IEEE TRANSACTIONS ON POWER ELECTRONICS from 2006 to 2012. He has been distinguished Lecturer for the IEEE Power Electronics Society from 2005 to 2007 and for the IEEE Industry Applications Society from 2010 to 2011 as well as 2017 to 2018. In 2019-2020 he served as a President of IEEE Power Electronics Society. He has been Vice-President of the Danish Academy of Technical Sciences. He is nominated in 2014-2020 by Thomson Reuters to be between the most 250 cited researchers in Engineering in the world.

Assoc. Prof. Barbaros ÇETİN
Topic: "Grooved Heat Pipes: Modeling, Experimentation and Applications"

Dr. Barbaros Çetin received his B.S. (2002) and M.S. (2005) in Mechanical Engineering at Middle East Technical University, Ankara, Turkey. He received his PhD (2009) in the Department of Mechanical Engineering at Vanderbilt University where he focused on electrokinetic transport and particle manipulation in lab-on-a-chip devices for biomedical applications. Following his PhD, he became a faculty member in Middle East Technical University-Northern Cyprus Campus Mechanical Engineering Program. In 2011, he became a faculty member in the Mechanical Engineering Department at I.D. Bilkent University, Ankara, Turkey. His current research interests include particle manipulation for microfluidic application, modeling of particle motion using boundary element method, and modeling, fabrication and experimentation of flat-grooved heat pipes. Dr. Çetin is the recipient of the 2015 Bilkent University Distinguished Teacher Award, 2017 Outstanding Young Scientist Award of the Turkish Academy of Sciences (TÜBA-GEBİP), 2017 METU Prof. Dr. Mustafa N. Parlar Research Incentive Award and 2018 Science Academy Distinguished Young Scientist Award (BAGEP).

Prof. Orhan DURGUN
Topic: "Recent Situation of Energy on the World and Turkey and some Solution Proposals"

Professor DURGUN obtained his combined B.Sc. and M.Sc degree from İstanbul Technical University (ITU), Department Mechanical Engineering in 1973. After working as an operation and maintenance engineer at TEK Seydişehir Gas Turbine Power Plant for a year, he had started working as research assistant at the Department of Mechanical Engineering in Karadeniz Technical University (KTU). He completed his Ph.D. study in 1983 at ITU Faculty of Naval Architecture and Marine Sciences. Then, he worked as an assistant professor, associate professor and professor in KTU Mechanical Engineering Department. Since 2014, he is at the Department of Mechanical Engineering of Avrasya University. Prof. Orhan DURGUN served as chairman of the department of KTU Marine Engineering, head of the Energy, Automotive branches of KTU Department of Mechanical Engineering. He is currently the chairman of the Department of Mechanical Engineering at Avrasya University, Trabzon. His research expertise focuses on internal combustion engines, fuels, engine design, combustion modeling, and ship hydrodynamics. Prof. Orhan DURGUN has about 100 scientific articles published in national and international journals, symposium proceedings. He also authored two book on internal combustion engines, and supervised +13 M.Sc. and Ph.D theses. Besides his technical expertise, Prof. Orhan DURGUN is an active folk dancer, trainer and has publications on Trabzon and Turkish Folklore, Trabzon folk dance and music.

Prof. Birol KILKIS
Topic: "Exergy Solutions in Energy and Global Warming Dilemma"

Dr. Kilkis received his Ph.D. degree in Mechanical Engineering with high honors from Middle East Technical University. He graduated in 1972 with honors degree from von Karman Institute for Fluid Dynamics in Belgium. Since then, Kilkis has been working on heat transfer, unified heat transfer theory, high-performance buildings, quantum mechanics, fluid dynamics, heat pumps, energy strategies, aerodynamics, exergy analysis, combined heat and power, tri-generation, hybrid solar PV systems, simulation, and computer aided design of green buildings. He is also active in wind, solar, and geothermal energy, global warming issues and solutions, innovative HVAC systems, low-exergy and waste heat utilization, district energy systems, and energy strategies. He revised Chapter 6 in ASHRAE Handbook on Radiant Panel Heating and Cooling and four other chapters at a capacity of principal reviewer. He is the co-author of a most recent book on cogeneration with renewables. He taught graduate and undergraduate courses at several universities like Gannon University (full time, Director of Computer Graphics), University of Missouri Rolla (adjunct), Middle East Technical University (full time, Assistant Dean, Assistant Director of the Graduate School), Baskent University (full time, Head of Energy Engineering Graduate Program), and Atılım University (Adjunct) between 1972 until 2019. In 1981 he received the Science Encouragement Award from TUBİTAK. He is the author of more than 500 papers in several journals and proceedings. ASHRAE has elevated him to Fellow Grade and has been named distinguished lecturer. In 2008, he received Distinguished Service and Exceptional Service awards from ASHRAE. Kilkis was always charged with the most challenging sustainable building design and radiant projects and has worked on more than 250 unique projects. One of them is the LEED Platinum ESER Building in Ankara Turkey. Kilkis has been appointed to the Executive Committee membership of the European Union Solar Thermal Technologies Platform in 2015. After the commencement of this duty in 2018, he became the Vice Chair of Renewable Heating and Cooling Committee (RHC).

Foreword

The 5th Anatolian Energy Symposium, which has been held in March 24-25, 2021 in Trabzon, is the latest one of the Anatolian Energy Symposium series. Since the first symposium hosted by Fırat University in Elazığ, each one was organized in different parts of Anatolia including Diyarbakır, Muğla and Edirne which each has a great cultural heritage.

With the civilization, the human being is highly motivated by at least two things of elapse of time, and the infinity of space. Although we dare to discover Mars and Titan, we sometimes dismiss the universe's infinite limits. During the last few decades, it has been increasingly important to minimize our footprints on the earth while trying our best in our professions. Specifically, in our opinion, we have to control the post-term of catalyzer and chemical reaction in our universe, which is made of chemical compounds. In other words, "the energy conversion process by burning" is not a contemporary approach for humankind anymore. "Energy conversion without burning" is regarded as an essential indicator in today's civilization.

Fire and its energy have been a close friend of humankind during our journey of civilization. The limit of our knowledge and skills have been increasing, yet chemical reactions through firing have still been an important energy source. The concept of "sustainable development" defined by Gro Harlem Brundtland, one of the former prime ministers of Norway, suggest to replace this conventional energy generation. This new concept has been transformed our world into a new era focusing on sustainability even though we have a lot to do on our way ahead.

Energy, which represents life and health, has a significant role in all economic activities and scientific endeavors. Moreover, developing a financial perspective on energy is an essential issue for governmental politics. International Energy Agency-IEA has provided medium-to long-term energy projections using the World Energy Model. The model is a large-scale simulation model designed to replicate how energy markets function and is the principal tool used to generate detailed sector-by-sector and region-by-region projections for the World Energy Outlook scenarios. The model consists of three main modules: final energy consumption; energy transformation including power generation and heat, refinery and other transformation – such as coal to liquids or hydrogen production; and energy supply [1].

Today, many countries develop different energy policies based on their domestic circumstances with varying natural resources and socioeconomic systems. This diversity of energy sources leads simply to no single golden path for the successful energy transition. Instead, each country will need to determine its unique energy policy pathway considering its situation and priorities. This means that direct comparisons between countries' rankings and scores can be less informative, but instead, it helps to provide a conversation opener. Nevertheless, governments can and should learn from each other by learning which policies work better and why such policies might be successful within some contexts but not in others. The Energy Trilemma Index can help countries and energy stakeholders in an ongoing dialogue to determine which areas of energy policies need to improved and examples from other countries that may help decide which options might be more appropriate [2]. Trilemma Index has the following dimensions of 1) energy security, 2) energy equity, and finally, environmental sustainability. Trilemma scores of countries reveal that scientific and technical infrastructure has a significant role in affordable, abundant energy and environmental harm mitigation.

These are the policies and resulted from increasing energy demand, depletion and lack of conservation of natural resources along with unrestrained greed of human being. We believe that each of us has responsibility and should act accordingly by remembering one single self-check question in our every action "How can we make the world a better place to live?"

We are now carrying out our mission by providing a scientific medium to scientists and energy researchers to exchange ideas and share recent works and applications on various aspects of energy and related technologies. The symposium has a broad perspective from Heat and Mass Transfer to Fluid Mechanics and Thermodynamics, Computational Heat Transfer and Fluid Dynamics, HVAC Systems, Solar Energy, Wind Energy, Fuel Cells, Hydrogen Energy, Energy Technologies, Cooling Technologies, Fuels and Combustion, Heat Insulation, Exergy, Energy Management, Power Plants and Power Generation, Nanofluids, Global Warming and Environmental Pollution, Energy Policies, Occupational Health and Safety in Energy Sector, Energy Transmission Lines, and so on.

The symposium would not be realized without the support and efforts of too many individuals. We would like first to thank Karadeniz Technical University president, Professor Hamdullah ÇUVALCI and our former president, Professor Süleyman BAYKAL, for their sincere support. Thanks to the Trabzon Chamber of Commerce and Industry for their financial support. We express our gratitude to the invited speakers and all participants for their valuable contributions. We especially thank our colleagues Furkan, Ayşe, Aleyna, Mustafa Yavuz, Mehmet, Soner and Cansu, for their devoted efforts.

Karadeniz Technical University, Trabzon, TURKEY

March 2021

Burhan ÇUHADAROĞLU

Ömer Necati CORA

[1] World Energy Model Documentation, 2020 version (19.02.2021), International Energy Agency, Available at: https://iea.blob.core.windows.net/assets/dd88335f-91ab-4dbd-8de7-d2dc4fee90e0/WEM_Documentation_WEO2020.pdf, Last access date: 29.03.2021.

[2] 2021 World Energy Issues Monitor, World Energy Council, Available at: https://www.worldenergy.org/assets/downloads/Issues_Monitor_2021-final.pdf , Last access date: 29.03.2021.

Symposium Program

24.03.2021 (DAY 1)

Start	End	Welcome Remarks
09:30	09:40	Prof. Burhan ÇUHADAROĞLU (Conference Chairman)
09:40	09:50	Prof. Hamdullah ÇUVALCI (President of KTU)
09:50	10:00	Prof. Gençağa PÜRÇEK (Dean of School of Engineering)
10:00	10:10	Dr. M. Suat HACISALİHOĞLU (Chairman of the Trabzon Chamber of Commerce and Industry)
10:10	10:40	**Keynote Speaker-1 : Professor Frede Blaabjerg | *"Wind Power – A technology enabled by power electronics"***
10:40	10:45	Break

Parallel Session-1

		ROOM 1: Heat and Mass Transfer-I	ROOM 2: Energy Technologies-I	ROOM 3: HVAC Systems
		Session Chair: *M.E. ARICI*	Session Chair: *C. TURHAN*	Session Chair: *A. DALOĞLU*
10:45	11:05	**A comparative Analysis on Heat Pipe Heat Exchangers and Rotary Regenerative Heat Exchangers** *K.ÖZDEMİR, E. BÜYÜK ÖĞÜT*	**Electrochemical Characterization of Temperature Dependence of a Lithium-Ion Battery** *O. B. SABAN, E. GÜZEL, M. F. SERİNCAN, M. A. ARSLAN*	**Effect of Vertical Skirt on Airflow and Particle Distributions in an Operating Room A Numerical Study** *A. AGIRMAN, Y. E. CETIN, M. AVCI, O. AYDIN*
11:05	11:25	**Numerical Investigation of Flow and Heat Transfer in an Open Cavity** *E. ÖZGİRGİN YAPICI, E. AYLİ, A. DENİZ*	**Smart Thermos Design Integrated with Thermoelectric Module** *E. ÖZTÜRK, A. HİNDİSTAN, K.YILDIZLI*	**Investigation of BIM (Building Information Modeling) System in Terms of Pressure Energy Losses in Ventilation Systems** *F. DEMİRTAŞ, C. DEMİRTAŞ*
11:25	11:45	**An Experimental Study on Overall Heat Transfer Coefficient of Some Wall Brick Models** *A. RAHMANPARAST, B. ÇUHADAROĞLU, F. E. KAN*	**Calibration of a Low-Cost Globe Thermometer with Linear Comparative Calibration Method** *M. F. ÖZBEY, C. TURHAN*	**On the Use of Natural Ventilation System for Suction of Inhaled Gases in Production Lines for Improved Indoor Air Quality** *O. KAYAPINAR, O. ARSLAN*
11:45	12:05	**The Effect of the Various Arrangements of the Lithium-ion Battery Pack on the Cooling Performance** *A. AKTÜRK, M. E. ARICI, F. E. KAN*	**Development of a Novel Temperature and Relative Humidity Data Logger** *A.Y. BAYHAN, C. TURHAN*	**Air Conditioning System Design of a Archives Storage Facility in the Warm Climate Region** *M. SUNMAN, Ö. AĞRA*
12:05	12:10	Break		

Parallel Session-2

		ROOM 1: Heat and Mass Transfer-II	ROOM 2: Energy Technologies-II	ROOM 3: Wind Energy
		Session Chair: *O.AYDIN*	Session Chair: *K. BİLEN*	Session Chair: *M. E. ŞAHİN*
12:10	12:30	**Mixed Convection in a Vertical Parallel-Plate Microchannel with Viscous Dissipation Effect** *A. N. ALTUNKAYA, M. AVCI, O.AYDIN*	**Energy Efficiency Analysis of Turbocharges with Wastegate** *K. BİLEN, T. TOPCU, D.HAYDARGİL*	**Investigation of Vertical Axis Wind Turbines and Their Components Design** *A. BOZTAŞ, O. DEMİRBAŞ, M. E. ŞAHİN*
12:30	12:50	**Artificial Neural Networks For Drying Characteristics Determination An Application In Fluidized Bed Drying** *A. YILDIRIM, H.ERGÖK, Ö. AĞRA*	**Influences of Vanisperse in Negative Active Material on the Performance of Lead-Acid Battery** *Y. ŞİRİN, Y. EYDEMİR, Ç. AYHAN, E. DEMİRYÜREK, E. KOÇ*	**Design of the Deformable Wind Turbine Blade to Keep Efficiency High** *Y. GÜLTEKİN, E. KOÇ, T. YAVUZ*
12:50	13:10	**Experimental Investigation Jet Flow with Different Aluminium Foam Receivers** *B. ÖZŞAHİN, S. ÇALIŞKAN, K. BİLEN, F. GÜLER*	**Turkey's Pumped Hydro Storage Status: Current Scheme and Potential** *S.C. TOKER, G. SOYTÜRK, Ö. KIZILKAN*	**Design and Aerodynamic Performance Analysis of Micro Wind Turbine Blade** *K. KAYA, E. KOÇ*
13:10	13:30	**Experimental Investigation of the Effects of Foam Heat Sinks on Heat Transfer in Cross Flow** *S. ÇALIŞKAN, U. R. ŞAHİN, F. GÜLER, O. ÖZENÇ*	**The Thermal Decomposition of the Liquid Hot Water & Alkali Pretreated Cotton Fiber** *S. ÖZGÜL, G. KOÇAR*	**The State of Energy in World and Turkey – Wind Energy** *K. KAYA, E. KOÇ*
13:30	13:35	Break		

Parallel Session-3

		ROOM 1: Heat and Mass Transfer - Nanofluids	ROOM 2: Comput. Heat Transfer &Fluid Dynamics - I	ROOM 3: Heat Insulation - Power Plants and Power Generation
		Session Chair: *İ. KURTBAŞ*	Session Chair: *T. BALİ*	Session Chair: *H.K. ÖZTÜRK*
13:35	13:55	**Mixed Convection in a Square Cavity Filled with Hybrid Nanofluid** *B. ŞAHİN*	**Numerical Investigation of the Effect of Obstacles Configuration in the Flow Channel on Heat Transfer** *İ. KURTBAŞ, M. SENER, S. KIZILCAOĞLU, H. DURAN*	**Optimization of Insulation Thickness for Pipes in a Low Temperature District Heating Network** *M. TERHAN*
13:55	14:15	**Investigation of Boiling Instability in Rectangular Spiral Mini Channel** *M. SENER,İ. KURTBAŞ, S. KIZILCAOĞLU*	**Effect of Magnetic Field on Flow and Heat Transfer in Hydrodynamically and Thermally Developing Couette-Poiseuille Flow Between Paralel Plates** *E. YAĞCI, O. AYDIN, T. BALİ*	**Thermal Comfort Analysis of Historical Mosques. Case Study: The Ulu Mosque, Manisa, Turkey** *Y. DİLER, C. TURHAN, Z. D. ASLAN, G. G. AKKURT*
14:15	14:35	**A Review of the Effects of Micro Fin Geometry and Alignment on Flow Boiling Characteristics in Microchannel Heat Sinks** *B. MARKAL, B.KUL*	**Numerical Investigation of Naturally Ventilated Facade with PCM Located in Mediterranean Region** *S. BIRINCI, M.SAGLAM, B. SARPER, M. Y. YAZICI, O. AYDIN*	**Auxiliary Power Generation Design for Power Plants with Using Thermoelectric Generators** *Ş. K. YENER, B. AKBOĞA, B. ÇETİN*
14:35	14:55	**Adaptation of the Touhami *et al.* Correlation for Pool Boiling Outside a Horizontal Tube at Subatmospheric Pressures** *T. BAKI, D. NEHARI*	**Numerical Investigation of the Effect of Air Velocity on Heat Transfer to Heat Sink in Thermoelectric Modules** *S. ÖZBEKTAŞ, B. TOPAL, B. SUNGUR*	**Comparative Thermodynamic Analysis of Organic Rankine Cycle with Different Working Fluids** *O. ARSLAN, İ. CEYLAN*
14:55	15:00	Break		
15:00	15:30	**Keynote Speaker-2 : Professor Birol KILKIS | *"Exergy Solutions in Energy and Global Warming Dilemma"***		
15:30	15:35	Break		

Parallel Session-4

		ROOM 1: Thermodynamics-I	ROOM 2: Comput. Heat Transfer and Fluid Dynamics II	ROOM 3: Global Warming and Environmental Pollution
		Session Chair: *A. GÜNGÖR*	Session Chair: *T.YAVUZ*	Session Chair: *B. ÇUHADAROĞLU*
15:35	15:55	**The Performing of Thermodynamic Analysis of R134a Refrigerant and Alternative Refrigerants on Their Application Areas** *Ö. F. SEL, O. HACIHAFIZOĞLU, Ü. AYBEK, A. CİHAN*	**Numerical Analysis of Aerodynamic and Aeroacoustic Characteristics of Subsonic Rectangular Cavity with Different Aspect Ratios** *E. KOCAK, E. AYLİ, H.TURKOGLU*	**Geopolymer Cement Production in the Struggle to Global Warming** *S. OZEN*
15:55	16:15	**Development and Thermodynamic Analysis of a Hybrid Evaporative Evaporator Air Cooling System** *F. ÖZDEMİR, A. GÜNGÖR*	**A New Vortex Preventing Element Design for Francis Turbines and Comparison of Different Geometric Shapes** *D. S. SEMERCİ, T. YAVUZ*	**Sustainable Phytoremediation with Energy Crops in Turkey** *B. BAŞTABAK, E. GÖDEKMERDAN, G. KOÇAR*
16:15	16:35	**Performance Prediction of a Two-Bed Adsorption Chiller Using the Silica Gel Water Working Pair Considering the Effect of Hot and Cold Water Temperatures** *T. Ü. ERKEK, A. M. S. SHAKIR, M. W. K. JABER, A. GÜNGÖR*	**Design and Prototyping of Air-to-Ground Smart Fire Extinguisher Ammunition** *M. TOPTAŞ, M. YILMAZ*	**Türkiye Şartlarında Fitoremediasyon Tekniğinde Kullanılan veya Kullanılma Potansiyeli Olan Bazı Bitkiler** *E. YILMAZ, Ö. KILIÇ, M. ZAFAR, M. AHMAD*
16:35	16:55	**Termodynamic Investigation of Flat Plate Collector** *A. B. GÜNDÜZ ALTIOKKA, A. MAVİ, O. ARSLAN*	**Modelling and Performance of a Thermoelectric Refrigerator** *H. KEPEKÇİ, E. KOSA , C. EZGI*	**Nanoakışkan Kullanılan Parabolik Oluk Tipi Güneş Kolektörlü Organik Rankine Çevriminin Teorik Modellenmesi ve Sistem Parametrelerinin İncelenmesi** E. KIRTEPE, O. E.TURGUT
16:55	17:00	Break		

Parallel Session-5

		ROOM 1: Thermodynamics-II	ROOM 2: Comput. Heat Transfer & Fluid Dynamics-III	ROOM 3: Cooling Technologies
		Session Chair: *Z. YUMURTACI*	Session Chair: *E. BUYRUK*	Session Chair: *M. AVCI*
17:00	17:20	**Performance Analysis of Solar and Geothermal Energy Powered Kalina Cycle** *M. Ş. ACAR, O. ARSLAN*	**Effects of Injection and Suction Through a Perforated Circular Cylinder on Some Thermo-Fluid Parameters** *M. E. VAKHSHOURI, B. ÇUHADAROĞLU*	**Experimental Investigation of the Pulsating Heat Pipes Having Larger Flow Sections in the Evaporator Region** *A. CANDERE, B. MARKAL, O. AYDIN, M. AVCI*
17:20	17:40	**Comparative Techno-economic-environmental Assessment of Biomass Fuelled Integrated Energy Systems** *P. HEIDARNEJAD, H. GENCELİ, Z. YUMURTACİ*	**A Numerical Study on Phase Change Material Integrated Borehole Heat Exchanger** *N. Y. ÇAM, M. A. EZAN, L. BİLİR*	**Heat Transfer and Thermal Management of Lithium-Ion Battery Pack System with Forced Air Convection** *İ. HOŞ, G. TÜRKAKAR*
17:40	18:00	**Thermodynamic Analysis of Automobile Brake System** *A. MAVİ, A. B. GÜNDÜZ ALTIOKKA, O. ARSLAN*	**Validaton Study of a Naturally Ventilated Solar Facade** *B. SARPER, S. BIRINCI, M. SAGLAM,O. AYDIN*	**Superelastic Properties of NiTi for new generation cooling technologies** *S. ÖZKAN, E. DEMİRTAŞ, G. DURAK YÜZÜAK, E. YÜZÜAK*
18:00	18:20	**ORC Sistemlerinde Kullanılan n-Pentane Akışkanının Pompada Sıkıştırma Oranının Termodinamik Verimlere ve Ekserji Yıkımına Etkisi** *M. ALTINKAYNAK*	**CFD Analysis of Fluid Passing Through Venturimeter** *C. KISTAK, F. ÖZGEN*	**Elastocaloric Properties of the Optimized Ni-Ti Alloy** *G. DURAK YÜZÜAK, E. YÜZÜAK*

End of Day 1

Symposium Program

25.03.2021 (DAY 2)

Start	End			
09:00	09:10	**Second Day Welcome** | *Assoc. Prof. Ömer Necati CORA (Co-Chairman)*		
09:10	09:40	**Keynote Speaker-3 : Professor Orhan DURGUN | *"Dünya'da ve Türkiye'de Enerji Üretiminin Güncel Durumu ve Türkiye için Çözüm Önerileri"***		
09:40	09:45	Break		
		Parallel Session-6		
		ROOM 1: Fuels and Combustion - Exergy	**ROOM 2: Solar Energy-I**	**ROOM 3: Fuel Cells - Wind Energy - Solar Energy**
		Session Chair: *Z. ŞAHİN*	Session Chair: *N. ÇELİK*	Session Chair: *M. ÖZBEY*
09:45	10:05	**Second Law Analysis of Novel Fractal Structure Heat Exchanger** *A. B. ÇOLAK , İ. KOTCİOĞLU, O. ARSLAN*	**Dynamic Simulation of a Flat Plate Solar Collector System under Hot and Humid Climatic Conditions** A. YUMUŞAK, H. GENCELİ, M. ASKER	**Development of a Dynamic System-Level Thermodynamic Model of Solid Oxide Fuel Cell (Sofc) Integrated Gas Turbine (Gt) Power Plant** *M. B. KAYA , A. C. İNCE, F. BEDİR, M. F. SERİNCAN*
10:05	10:25	**Engine Performance and Exhaust Emissions of a Spark Ignition Engine Operating on 2.5 % N-Butanol/Gasoline Blend and 2.5 % N-Butanol/Gasoline Blend with 9 % Water Injection to Intake Air** *Z. ŞAHİN, O. N. AKSU, C. BAYRAM*	**Exergy Analysis of a Solar Power Plant and Comparison of Production Values with Software** *B. GÜLMEZ, R. KÖSE, O. O. YOLCAN*	**Thermal Expansion, Porosity, and Microhardness Properties of Solid Oxide Fuel Cell Metallic Interconnects Manufactured by Powder Metallurgy Approach** *A. TOPCU , Ö. F. YALÇIN, B. ÖZTÜRK, Ö. N.CORA*
10:25	10:45	**Theoretical Investigation of Engine Performance and Exhaust Emissions in Ethanol-fueled Dual-plug SI Engine** *İ. ALTIN , A. BİLGİN, İ. SEZER*		**Wind Energy Potential Assessment of Susurluk Region in Balıkesir** *A. DÜZCAN , Y. A. KARA*
10:45	11:05	**Sesame Harvesting Waste: Thermal Characterization and Conversion for Biofuel and Biochar Production** *E. GÖDEKMERDAN , B. BAŞTABAK, G. KOÇAR*		**Potential for the Use of Solar Energy in the Food Industry** *D. BAYANA , F. İÇİER*
11:05	11:10	Break		
11:10	11:40	**Keynote speaker-4 : Assoc. Prof. Barbaros ÇETİN | *"Grooved Heat Pipes: Modeling, Experimentation and Applications"***		
11:40	11:45	Break		
		Parallel Session-7		
		ROOM 1: Solar Energy-II	**ROOM 2: Energy Management - Occupational Health and Safety in Energy Sector**	**ROOM 3: Fluid Mechanics-I - Cooling Technologies**
		Session Chair: *K. KAYGUSUZ*	Session Chair: *M. YILMAZ*	Session Chair: *O.TURAN*
11:45	12:05	**Artificial Neural Network Modeling of Parabolic Trough Type Solar Thermal Power Plant** *D. KILIÇ, O. ARSLAN*	**Effect of Collection Tank Level on Energy Consumption of Lifting Pumps in Drinking Water Distribution Systems** *U. SEKMEN , M. YILMAZ, Ö. ÖZDEMİR, A. İNCE*	**Numerical and Experimental Investigation of Air Injection Process with Venturi Pipe Part** *Ö. F. CAN, T. BAĞATUR, N. ÇELİK*
12:05	12:25	**Analysis and Design of a Cooling Channel for a Photovoltaic Panel** *Z.ÖZCAN , M.GÜLGÜN , E. ŞEN, N. Y. ÇAM, L. BİLİR*	**Lead Acid Batteries for Micro Hybrid Electrical Vehicles – Influence of Different Type Expanders on the Performance of the Negative Plates** *Y. ŞİRİN , Y. EYDEMİR, Ç. AYHAN, E. DEMİRYÜREK, E. KOÇ*	**An Energy Efficient Mixed Flow Submersible Pump Design and Computational Fluid Dynamic Processes in a Case Study 7" 110 m3h** *M. AKDEMİR , M. C. ÇAKMUR*
12:25	12:45	**Collaborating Sharing Decentralized Solar EnergySystem in Pakistan** *S. M. K. SHAH , R. TANZEEL*	**Ship Energy Efficiency Analysing Approaches: A Case Study** *O. YILMAZ , T. UYANIK, Y. ARSLANGOĞLU*	**Analysis and Design of an Air to Air Heat Exchanger Used in Energy Recovery Systems** *H. Ü. ELMACIOĞLU , İ. ÖZSEVGİ, C. KOCABIYIK, N. Y. ÇAM, L. BİLİR*
12:45	13:05	**Design and Analysis of Evacuated Tube Solar Collector Integrated Supercritical Brayton Cycle for Low-Temperature Applications** *G. SOYTÜRK , S.Ç. TOKER, Ö. KIZILKAN*	**Rüzgar Enerji Santrallerinde İş Sağlığı ve Güvenliği** *S. ŞİMŞEK, F. DOĞAN*	**Magnetic Refrigeration Technology and Applications** *A. ZAİM , H. ARAS*
13:05	13:10	Break		
		Parallel Session-8		
		ROOM 1: Solar Energy-III	**ROOM 2: Energy Management - Hydrogen Energy**	**ROOM 3: Fluid Mechanics-II - Comp. Heat and Mass Trans.**
		Session Chair: *Y. ARSLANOĞLU*	Session Chair: *E. F. KENT*	Session Chair: *L. NAMLI*
13:10	13:30	**Experimental Investigation of Thermal Gain in PV Panels** *H. DUMRUL , S.YILMAZ*	**Parametric Analysis of a Plate, Finned and Cross Flow Heat Exchanger for Heat Recovery in Buildings** *S. TEKİN, G. TÜRKAKAR*	**Investigation of Flow Field Characteristics of Synthetic Jet Driven by Half Sinusoidal Signal** *M. Y. BAYAT , M. SARIOĞLU, Y. E. AKANSU*
13:30	13:50	**Following the Balloon Temperature of a Solar Water Heater Installed in Oran, Algeria** *T. BAKI , M. TEBBAL, H. BERREBAH*	**An Ore Enrichment Plant, The Effect of Operation Optimization of Operators on Production and Energy Efficiency** *E. BULAT , C. AYGÜN*	**Bubble Pump Design and Performance Analysis** *A. DALLOUL , M. ÖZBEY*
13:50	14:10	**Bidirectional Flyback Based Differential Power Processing Converter for Photovoltaic Applications** *E. KARAKAŞ , Y. ÖNER, S. KESLER*	**Exergy and Thermoeconomic Analyses of Solar Hydrogen Production and Liquefaction Process** *T. KOYUN, E. F. KENT*	**Numerical Investigation and Optimization of the Effect of Heat Transfer and Pressure Drop on the Circuit in Finned Tube Heat Exchangers** *A. YILDIRIM , Ş.Ö. ATAYILMAZ*
14:10	14:30	**A Machine Learning Approach for Solar Power Plant Electrical Power Estimation** *T.UYANIK, O. YILMAZ , Y. ARSLANOĞLU*	**Hidrojen Tedarik Zinciri ve Türkiye Örneği** **A. ERDOĞAN, E. GEÇİCİ, M. G. GÜLER**	**Investigation of Air Flow Inside an Airplane Passenger Cabin** *L. BİLİR , H. ÇELİK, M. B. ÖZERDEM*
14:30	14:35	Break		
14:35	15:05	**Keynote speaker-5 : Assoc. Prof. Hafız Ali | *"Surface condenser: Heat transfer"***		
15:05	15:10	Break		
		Parallel Session-9		
		ROOM 1: Solar Energy-VI	**ROOM 2: POSTER SESSION**	**ROOM 3: Energy Technologies-III**
		Session Chair: *C. DEMİRTAŞ*	Session Chair: *F.E. KAN*	Session Chair: *Ö.N. CORA*
15:10	15:30	**State of the Art Review on the Cu(InGa)Se2 Thin-film Solar Cells** *M. A.OMID , Ö. N. CORA*		**Thermoelectric Thin Film Modules** *S. ÖZKAN , G. DURAK YÜZÜAK, E. YÜZÜAK*
15:30	15:50	**A Study of the Effect of Baffles Inside Solar Collector** *B. GÜLMEZ , A. B. AKSOY*	**Sensorless Flow Rate and Total Head Measurement of Centrifugal Pumps Operating with Variable Frequency Drive** *E. KARAKAŞ , Y. ÖNER, S. KESLER*	**Indigenous Oil Yielding Plants as Energy Sources in Pakistan** *M. ZAFAR, M. AHMAD, Ö. KILIÇ , S. SULTANA, J. ZAHOOR, E. YILMAZ*
15:50	16:10	**Analysis of 100 kW Solar Photovoltaic Power Plant Which Can Be Installed In Trabzon** R. KÖSE, A. B. AKSOY, B. GÜLMEZ, O. O. YOLCAN	**Thermal Power Plant Emissions and Emission Prevention Studies in Turkey** *H. ERGÖK , A. YILDIRIM*	**RF Sputtered TiO2 Thin Films with Various Deposition Conditions for Triboelectric Friction Layer** *G. DURAK YÜZÜAK , S. ÖZKAN, E. YÜZÜAK*
16:10	16:30	**Important Parameters in Solar Power Plant Installation and Analytical Hierarchy Process** B. GÜLMEZ, R.KÖSE, O. O. YOLCAN	**Solar Powered Cooler Design** *H. KORKMAZ , M. E. GAZI, Ö. N. CORA*	**Comparative Environmental Sustainability of Two Different Sizes of Wind Turbines** *B. A. TÜRKMEN*
		Closing Remarks & Farewell		

CONTENTS

Page No

HEAT AND MASS TRANSFER

FLUID MECHANICS

THERMODYNAMICS

COMPUTATIONAL HEAT TRANSFER AND FLUID DYNAMICS

HVAC SYSTEMS

SOLAR ENERGY

WIND ENERGY

FUEL CELLS

HYDROGEN ENERGY

ENERGY TECHNOLOGIES

COOLING TECHNOLOGIES

FUELS AND COMBUSTION

HEAT INSULATION

ENERGY MANAGEMENT

GLOBAL WARMING AND ENVIRONMENTAL POLLUTION

OCCUPATIONAL HEALTH AND SAFETY IN ENERGY SECTOR

POWER PLANTS AND POWER GENERATION

EXERGY

NANOFLUIDS

POSTER PRESENTATIONS

HEAT AND MASS TRANSFER

INVESTIGATION OF BOILING INSTABILITY IN RECTANGULAR SPIRAL MINI CHANNEL

Mehmet ŞENER*, Irfan KURTBAŞ, Selçuk KIZILCAOĞLU****
*Hitit University, Scientific Technical Application, and Research Centre, Çorum/Turkey
Email: mehmetsener45@gmail.com
**Hitit University, Department of Mechanical Engineering, Çorum/Turkey
Email: ikurtbas@gmail.com, selcukkizilcaoglu@gmail.com

ABSTRACT

Boiling behavior in two-phase flow studies is significant in terms of the operational performance of nuclear reactors, heat exchangers, and electronic systems. Boiling instabilities indicate dynamic changes that occur on the system against sudden changes of flow on the systems. Boiling instabilities have a significant effect on boiling instabilities with the channel's elongation and mixing of the flow.

In this study, density, pressure, and temperature oscillations were investigated experimentally in a spiral mini channel with a rectangular cross-section. The spiral mini channel has a rectangular cross-section of 3 mm x 2 mm, a spiral width of 16 mm, and a diameter of 60 mm. System working pressure was examined at 0.4 MPa values. A refrigerant of R-134a is used as a working fluid in the experimental setup. Experiments were carried out at 100 kg/m^{2}s and 300 kg/m^{2}s mass flow rates. The vapor quality was between 0-0.99. Stainless steel foil was used to provide homogeneous heat flux from the bottom surface of the duct. In order to measure the temperature oscillations (TO) in the spiral mini channel, T-type thermocouples are placed at the channel inlet and outlet. Coriolis flowmeter was used for the measurement of density wave oscillations (DWO). Pressure difference oscillations (PDO) were also obtained using absolute pressure gauges at the inlet and outlet of the test section.

According to the experimental results, stable-unstable regions were determined. Accordingly, the region where density change oscillations are effective was obtained. It is determined that the characteristic curve is "S" shaped. Also, The pressure change oscillations decrease with the increasing heat flux and the oscillation formation period decreases.

Keywords: Two-phase flow, boiling, pressure oscillation, R-134a

1. INTRODUCTION

Two-phase flows; In industrial areas such as a steam generators, heat exchangers, reactors, and seawater distillation, instability is considered in their design and application. Curved channels are frequently used in heat exchanger applications. For instabilities within the system, there are changes according to the flow conditions of different flow regimes. In applications, density change oscillations are examined as pressure differences and thermal oscillations.

Rahman and Singh [1] examined the flow travel and pressure drop oscillations caused by boiling in 2019 two-phase flow conditions. These oscillations are Ledinegg instability (flow rides), pressure change oscillations (BDO) and flow rides that occur with the compressible flow. Internal, and external pressure drops and curves were obtained. They defined pressure drop oscillations and Ledinegg oscillations using the Bifurcation theory. By making numerical simulations, they dynamically examined the system at different points. These simulations presented the development of variables over time. Liu et al. [2], instability properties for forced two-phase flow in a horizontal channel Lyapunov stability theory and numerical analysis for dynamic analysis were performed. The system model consists of two first-order nonlinear ordinary differential equations. An initial limit (IB) has

been established with several key eigenvectors in the phase pressure and pressure drop phase of the mass flux. Numerical simulation shows the results obtained from Lyapunov stability analysis.

S. Kakaç [3], in his general research, classified the two flow instabilities. It revealed dynamic instability events and their causes from three oscillations. He explained what could be the variations of the overcooling degree, the fluid inlet flow rate, the heat fluxes affecting these instabilities. He presented models with appropriate results in estimating steady-state limits by evaluating biphasic flow events used for forced convection boiling systems in an upstream and single channel. Evaluate the suitability of the mathematical connections used in this modeling Lee et al. [4] emphasized the determination and suppression of the dominant instabilities for the boiling of R134a in a micro-channel cooler with a 609.6-mm length and a 203.2-mm width base area and 100 channels of 1x1 mm^2. They defined a dominant charge transition imbalance (CTI) as causing significant oscillations for mass velocity and pressure drop. They discussed how PID control could be used to suppress CTI. However,It also takes relatively small amplitude, high-frequency oscillations, becoming common in individual CTI oscillation cycles.

In the literature, there are many researchers are working on the boiling instability in R-134a and flat mini-micro channels. However, there is no study on boiling instabilities and boiling characteristic curves in the spiral mini channels. Inlet and outlet pressure oscillations, density change oscillations, and inlet-outlet temperature oscillations are examined under different heating conditions and mass fluxes. Besides, Ledinegg instability, which is the result of mass flux-pressure difference change, has also been studied. Accordingly, relatively stable and unstable regions have been identified in working conditions.

2. MATERIAL AND METHOD

In order to measure two-phase flow instabilities, an experimental setup is used in Figure 1. Two-phase flow system; gear pump, body tube heat exchanger, DC power supply, plate heat exchanger, water baths, Coriolis type flow meter, storage tank, check valve, sight glasses, and filter. In the study, R-134a is used as a refrigerant. The refrigerant is stored in the tank in the system.

The refrigerant is turned on the system using a gear pump. In the system, the body tube heat exchanger is used to provide the conditions for entering the test section of the refrigerant. The body tube heat exchanger works depending on the water bath. In this way, entrance prerequisites are provided. Coriolis type flowmeter is used to provide the mass flow determined in the test section. Stainless steel foil is used in the fluid test section, which passes the flow meter, to provide different heating conditions. It is conditioned with the help of stainless steel foil stretching plates and the DC power unit. Also, the foil is 0.02 mm thick, and its thermal resistance is minimal due to its thickness. This foil is used to provide homogeneous heating conditions. The fluid heated in the test section is directed towards the tank in liquid/vapor or vapor form. A plate heat exchanger is used to liquefy the fluid after tank exit. A water bath was also connected to condition the plate heat exchanger. Thus, the fluid in the vapor phase is converted into a liquid phase. One-way valve is used in the system for flow to flow in one direction. Besides, sight glasses are used to observe liquid-vapor changes in the flow using sight glasses. The test section includes spiral mini channel and measuring elements.

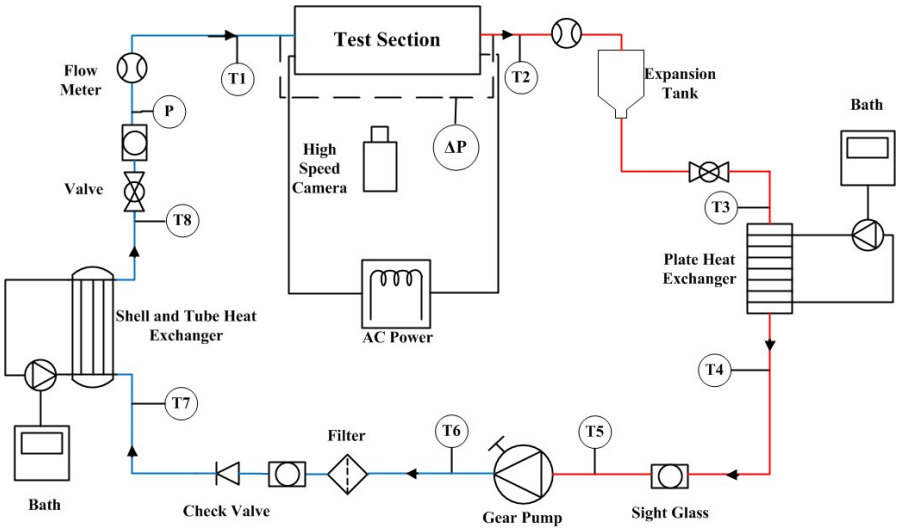

Figure 1. Experimental Setup

The spiral mini channel consists of four parts (Figure 2). These consist of the spiral mini channel; lower thermocouple plate, glass, and upper plate. Mini channels and plates are manufactured using 7075-T6 aluminum block pieces. These parts are machined on a high-speed precision CNC machine. Under the spiral mini channel, stainless steel foil was used as a heater. Heating was provided from the bottom surface of the steel foil channel. In this way, the heat is transferred directly to the fluid. Under the steel foil, there is a thermocouple plate for measuring surface temperatures. This plate was used to measure surface temperature values. It is connected to the Sorensen brand DC power supply with the help of steel foil stretching plates. In this way, different heating conditions are provided.

On the spiral mini channel top surface, glass and upper glass support plates are used. The images of boiling regimes occurring in the spiral mini channel were obtained from the front surface of the glass. Phantom brand high- speed camera is used for regime images. The obtained pictures were recorded in picture and video format using the PCC (Phantom Camera Control Program) program. The speed camera has a resolution of 1380 fps (frame/ second). Flowmeters and temperature values were recorded in the National Instrument brand (NI 9203) data collection unit.

Film sealing and liquid sealing are used to ensure tightness in the spiral mini channel. Also, tightness tests were carried out before each experiment. Nitrogen gas was used for tightness tests. It was kept under the pressure of 6 bar in the channel. The experimental setup was vacuumed for 5 hours with the help of a Value brand vacuum pump before the experiment started. Then the whole system was rechecked for leakage again with the help of nitrogen gas.

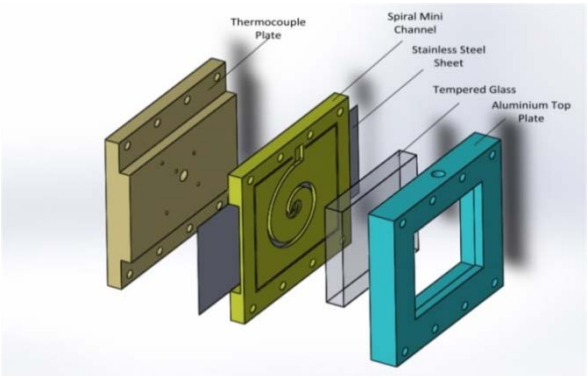

Figure 2. Spiral mini channel parts

2.1. Experimental Procedure

In the boiling instability study for two-phase flow, the parameters of pressure, mass flux, inlet overcooling were taken into account during the experiment. These parameters are fixed at the beginning of the experiment process. The heat flux is applied to the system when the system reaches the extreme cooling level. Then, when the system reached a steady state, data was recorded. The oscillations obtained were recorded in the data collection unit. The collection unit receives 100 data (Hz) per second. The data obtained was created by using the Fast Fourier Transform 8th order equation.

Another instability process in the experimental process was made for Ledineeg instability. Under high flow, the system has been kept in excessive cooling degrees. The flow rate was gradually reduced at small intervals. With the start of boiling, the experiment process continued until the lowest flow rate. The resulting mass flux-pressure difference graph is the S-N characteristic curve. S-N stands for S or N-shaped graphical change. Therefore, these graphs in which stable-unstable regions are expressed are called S-N. In these experimental conditions, system pressure and heat flux were kept constant.

Table 1. The ranges of experimental parameters

Parameters	**Value**	**Unit**
P_{sys}	0.4	MPa
G	100 and 300	kg/m^2s
q	0-60	kW/m^2
α	0 and 90	Degree

3. EXPERIMENTAL RESULTS

3.1. Static Instability

Static instability is a type of instability where the characteristic curve occurs and leds by Ledinegg. Later, its name was called Ledineeg instability. Vapor-liquid two-phase instability occurs with flow vibrations that occur at boiling, which causes different steam quality. Also, mass flux, pressure drop, and steam quality affect flow instabilities. The oscillation caused by biphasic flow under boiling conditions is essential for the hydrodynamic characteristics of the system. The hydrodynamic characteristic of the system is extremely important for understanding the instability mechanism.

Variations of different parameters should be examined to achieve the types of instability. [5] These parameters have two-phase flow instability effects, including system performance, operating conditions, and boundary conditions. Boundary conditions and parameter conditions should be examined for safe working conditions.
Oscillations are located in different regions on the static hydrodynamic characteristic curve [6-7]. The period and amplitude density can be shown by the system hydrodynamic characteristic curve. The required reflux of the pressure drop oscillation can also be indicated by the curve. Changing the slope of the hydrodynamic characteristic curve by optimizing the boiling structure can prevent pressure drop.

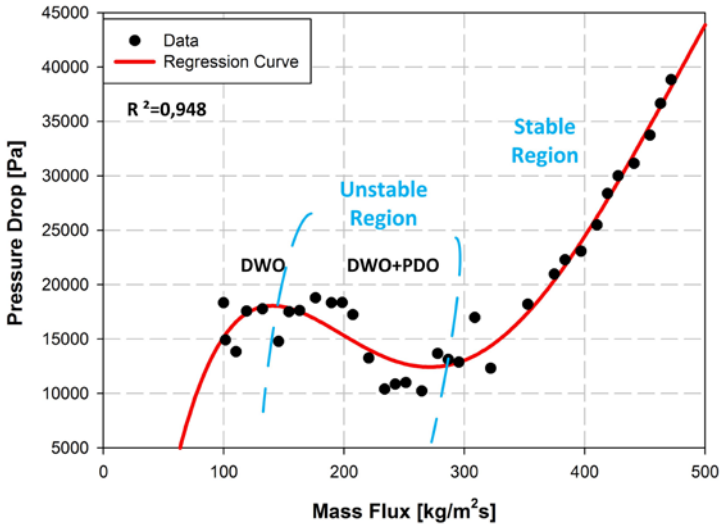

Figure 3. Stable-unstable regions on the spiral mini channel (P/W = 0.33, Psys = 0.4MPa, α = 90 °, q=8.3 kW/m^2)

The flow corresponding to the higher mass flow rate on the right side of the characteristic curve of the stable state is only the liquid phase. The slope of the curve is positive in this region. In the two-phase region, the first bubbles are observed at the local minimum of this characteristic curve. The slope of the curve from this local minimum point to the maximum point of the characteristic curve is negative. As the mass flux decreases, the pressure drop increases. Beyond the local minimum point of the characteristic curve, the flow is in the single-phase vapor zone. Pressure drop begins to decrease with decreasing mass flow rate.

3.2. Dynamic Instabilities

In Figure 4, the instabilities of the inlet and outlet temperatures that occur over time are given. Figure 4a and d plot change according to heat flux. With increasing heat flux, instability in the inlet and outlet temperatures increased. Periodic increase changes in the outlet temperature of 23.3 kW/m^2 heat flux were observed. Also, the amplitudes increase at the inlet temperature. Period width decreased with increasing heat flux in Figure 4d. It was observed that the oscillations caused by the increase of vapor density and bubbles size increased.

Pressure exchange oscillations for G=100 kg/m^{2}s are given in Figure 5. In these graphs, the pressure change oscillation, which changes according to the increasing heat flux, is examined. The vapor phase increases with increasing heat flux accordingly, the pressure difference increases. However, an effect for pressure amplitudes with increasing heat flux is not observed. Also, changes were determined on periods with increasing heat flux.

Accordingly, period times decrease with increasing heat flux. Besides, each data process was examined as 120 seconds. Accordingly, the frequency of oscillation formation is gradually increasing. In Figure 5a, periodic changes occur with less frequency in more extended period. However, short-term changes are obtained with increasing frequency in high heat flux. This situation is explained as the effect of increasing vapor density on volumetric change.

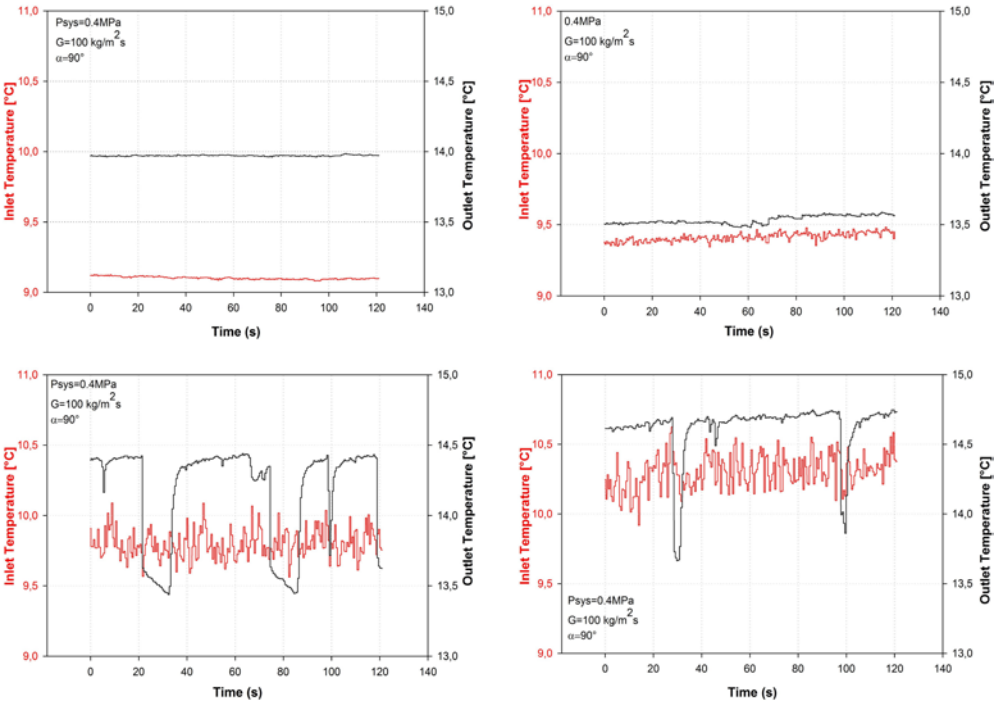

Figure 4. Inlet and Outlet Temperature Oscillations a.8.3 kW/m^2 b. 13.8 kW/m^2 c. 23.3 kW/m^2 d. 30.5 kW/m^2 (G=100 kg/m^{2}s, Psys = 0.4MPa, α = 90°)

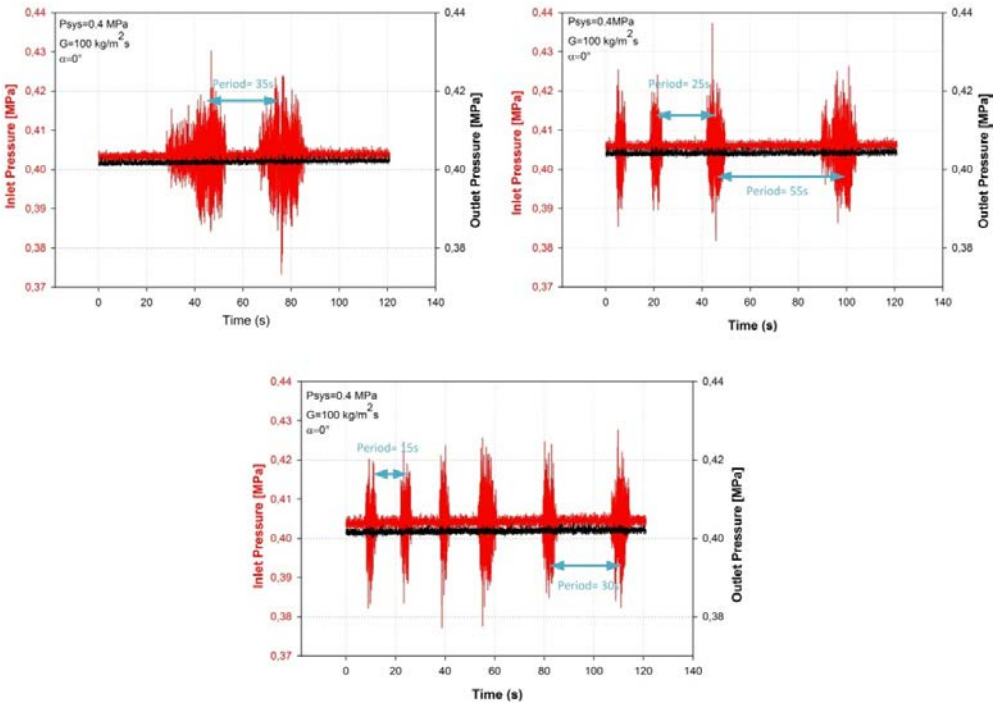

Figure 5. Pressure Difference Oscillations a. 8.3 kW/m^2 b. 13.8 kW/m^2 c. 30.5 kW/m^2(G=100 kg/m^{2}s, P_{sys} = 0.4MPa, α = 0°)

In Figure 6, the change of pressure change oscillations for G = 300 kg / m^{2}s is given. These graphs are similar to the results obtained in Figure 5. It is observed that period formation times decrease with increasing heat flux.

Besides, the effect of heat flux on amplitude remains low. For this, when Figure 6a is examined, the average formation period for 2.7 kW/m^2 is ~ 100 seconds, while the period of formation time is obtained as ~ 20 seconds at 47.2 kW / m^2. This results supports the projected projection for low mass flux in Figure 5. However, it is observed that the heat flux increases at 47.2 kW/m^2 and the local vibrations increase, and the amplitude amount increases. When Figure 5 and Figure 6 are examined, the amount of amplitude decreases with increasing mass flux.

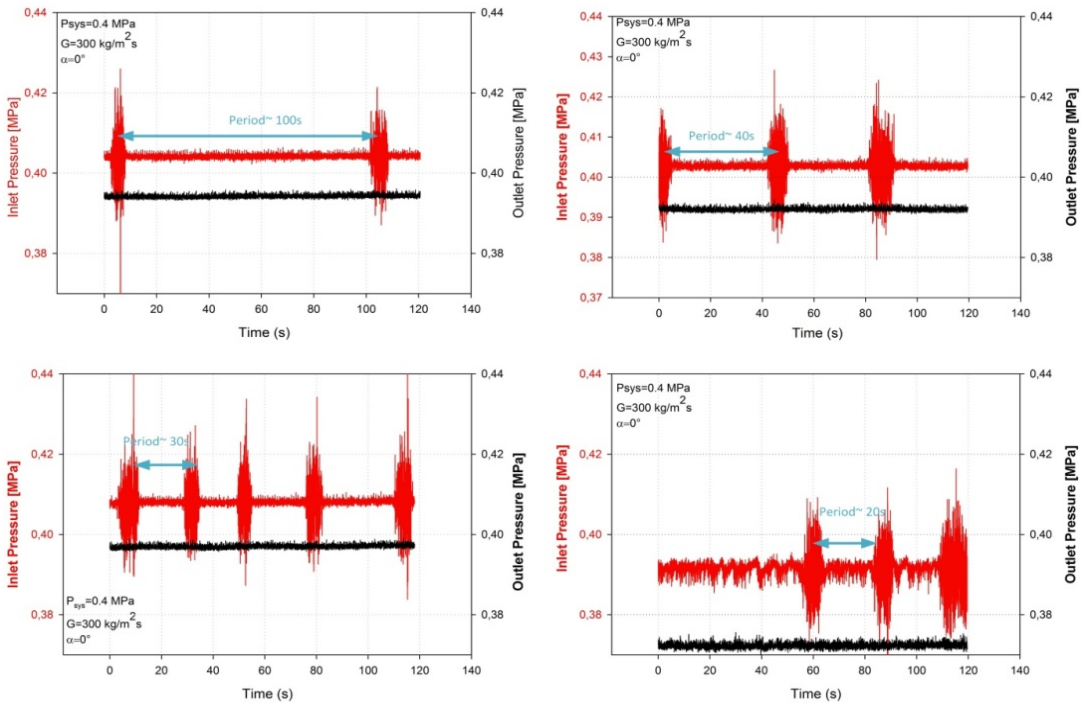

Figure 6. Pressure Difference Oscillations (G=300 kg/m^{2}s, Psys = 0.4MPa, α = 0°)

In Figure 7, density change oscillations are given for different mass and heat fluxes. It was observed that the increased heat flux did not affect the oscillation amplitude. It was obtained that the period did not change with increasing heat flux at two different mass flow rates. However, it is observed that the graph increases the amplitude (Figure 7a-b). With the increase in the flow, the amplitude also increases. It was determined that amplitude is released in high amounts in high heat flux and mass flow.

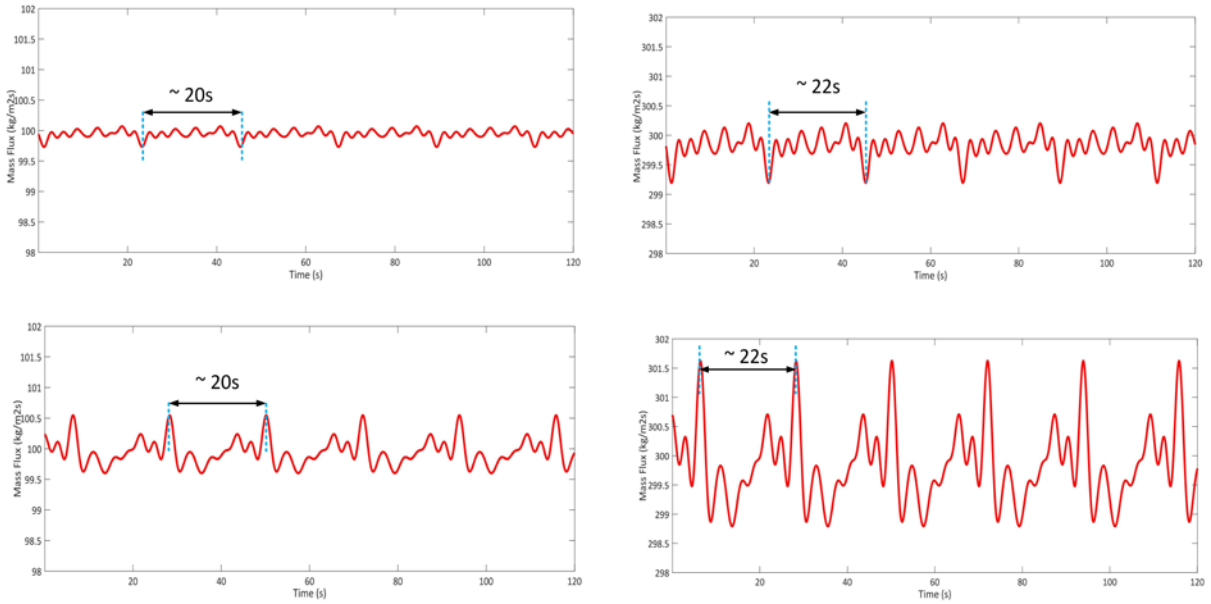

Figure 7. Density Wave Oscillation a. G=100 kg/m^{2}s, q= 8.3 kW/m^2 b. G=300 kg/m^{2}s, q= 8.3 kW/m^2 c. G=100 kg/m^{2}s, q=30.5 kW/m^2 d. G=300 kg/m^{2}s, q=30.5 kW/m^2

4. CONCLUSION

The formation of static and dynamic instabilities on two-phase flow instability in a spiral mini channel was investigated in this study. System pressure was used as 0.4 MPa in the study. In the channel flow, measurements were taken in the range of 0-55 kW/m^2 of heat flux in the mass flows of G = 100 kg/m^{2}s and 300 kg/m^{2}s. Accordingly, pressure change oscillations, flow rate oscillations, and temperature change oscillations were examined. Also, a study for Leedineg instability was carried out on the spiral mini channel. The general results obtained in this study are given below.

- S-N characteristic curve was achieved in the spiral mini channel. Accordingly, stable-unstable regions were determined. Accordingly, the region where density change oscillations are effective was obtained. It is determined that the characteristic curve is "S" shaped.

- Temperature variation oscillations for the inlet and temperature of the spiral duct were examined. It was observed that periodic oscillations occur at outlet temperature with increasing heat flux. While the frequency of periodic changes does not change in high heat fluxes, the period duration is shortened.

- It has been obtained that the effect of increasing heat flux on amplitude is low for temperature change oscillations. However, it was concluded that the amplitude increased slightly in high heat fluxes. The reason for this is that the vapor density increases within the channel.

- The pressure change oscillations decrease with the increasing heat flux and the oscillation formation period decreases. However, with increasing heat flux, changes in amplitude are relatively low.

- The amplitude amount increases when the mass flux and heat transfer increase in density change oscillations. However, the period duration does not change significantly.

ACKNOWLEDGEMENTS

This work was supported by The Scientific and Technological Research Council of Turkey (TUBITAK) with grant number 315M173. We also acknowledge the support of the Hitit University BAP, project number MUH19001.16.001

REFERENCES

[1] Rahman M.E., Singh S., Flow excursions and pressure drop oscillations in boiling two-phase channel, *International Journal of Heat and Mass Transfer*, 138 ,647-658, 2019.

[2] Liu F, Zhang B, Zhuqiang Y., Lyapunov stability and numerical analysis of excursive instablity for forced two-phase boiling flow in a horizontal channel, *Applied Thermal Engineering*, 159, 113664, 2019

[3] Kakac, S.,. A review of two-phase flow instabilities. *Advances in Two-Phase Flow on Heat Transfer, Martinus, Nijhoff, Boston*. 2, 577-668, 1994.

[4] Lee S, Devahdhanush V.S., Mudawar I., Experimental and analytical investigation of flow loop induced instabilities in micro-channel heat sinks, *International Journal of Heat and Mass Transfer*, 140, 303-330, 2019.

[5] Ruspini L.C, Dorao C.A., Fernandino M, Dynamic simulation of Ledinegg instability, *J.Natl. Gas Sci.Eng.* 2, 211-216, 2010.

[6] Ruspini L.C, Inertia and compressibility effects on density waves and Ledinegg phenomena in two-phase flow systems, *Nucleer Engineering and Design*, 250, 19-22, 2012.

[7] Yuan W.B., Li L.Y., Nonlineer instability of angle section beams subjected to static and dynamic sudden step loads, J. Constr. Steel Res. 77, 19-22, 2012.

EXPERIMENTAL INVESTIGATION OF THE EFFECTS OF FOAM HEAT SINKS ON HEAT TRANSFER

Sinan ÇALIŞKAN*, Uğur Recep ŞAHİN*, Furkan GÜLER*, Osman ÖZENÇ*
*Hitit University, Department of Mechanical Engineering, Çorum/Turkey
Email: sbycaliskan@gmail.com, ugurrecepsahin@hitit.edu.tr, furkanguler1919@gmail.com, ozencosman19@gmail.com

ABSTRACT

This study aimed to improve the heat transfer increase in the channel with the crossflow and different parameters. Different Reynolds values (4000-20553) were used in the experimental study, and local Nusselt changes in the channel were examined. Air is used as a working fluid. It is placed 50 mm inside the aluminum foam channel entrance with different PPI values (5, 10, and 20) inside the test section. The reason for this situation is that when the increase in heat transfer is examined, it is seen that this model is the most efficient. In the study conducted based on different heat flux values, the temperature distributions formed on the surface were obtained thanks to the thermal imaging technique. In the results obtained from the experiments, it was observed that 20 PPI aluminum foam used according to the smooth channel had a positive and significant effect on the heat transfer increase. In addition, it is lighter than the fin form used today and is likely to be used in machinery and / or equipment in the future.

Keywords: Heat transfer, Cross flow, Aluminum foam

Nomenclature

A	Sectional area of the channel (mm^2)
b	Lenght of aluminum foam (mm)
c	Lenght of Heater surface (mm)
D_h	Hydraulic diameter (mm)
e	Lenght of channel (mm)
h	Conduction factor ($\frac{W}{m^2 K}$)
k	Convection factor ($\frac{W}{mK}$)
Nu	Nusselt Number
Nu_x	Local Nusselt Number
Pr	Prandtl Number
Re	Reynolds Number
T	Temperature (K)
U	Velocity ($\frac{m}{s}$)
W	The inlet and outlet width of the channel(mm)
x/D_h	Longitudinal dimensionless distance
Q	Heat Transfer (W)
ε	Emissivity value
σ	Stefan Boltzmann constant ($\frac{W}{m^2 K^4}$)
μ	Dynamic viscosity (Pa.s)
ρ	Density ($\frac{m}{V}$)
PPI	Pixels Per Inch

1. INTRODUCTION

The development of technology leads to some negative situations on the devices produced besides the positive effects. The electronic systems, which are becoming more common every day, increase the amount of heat per unit volume for the devices. For these reasons, the studies carried out have become essential for the cooling of the electronic devices and their correct operation by increasing the thermal efficiency.

Heat transfer increase is provided in different ways. Passive methods aim to change the flow form by placing vortex generators or different types of obstacles used to increase the contact surface area within the area where the flow passes. Thus, by creating turbulence in the flow form, an increase in heat and mass transfer by convection will be achieved.

In the studies, different types of obstacles have been used to increase the heat transfer rate. In addition to the location of the channel's obstacles and its geometric optimization, it was also studied to direct the fluid into the channel. In the numerical, theoretical, and experimental studies, the air jet's effects applied to the channel, and the geometric surfaces on the fluid's heat transfer rate were examined [1-3]. In another study, the fins' effect on the fluid's contact surface, such as rectangular, triangular, square, etc., on the heat transfer rate together with the air was investigated [4,5]. Also, with the type of geometries created in the determined Reynolds value ranges, the channel's eddy formation was examined depending on the fluid's different welcome angles, and it was seen that the highest flow separation occurred at $\alpha = 34^{o}$ [6].

In recent studies, aluminum foams with different PPI values are used as a type of obstacle. The fact that aluminum foams have a high surface area per unit volume increases the channel's heat transfer [7]. In the experimental studies in this context, it was observed that 30% to 70% more heat transfer was provided depending on the position of the aluminum foams with different PPI (5,10,20,40, etc.) placed in the channel, the speed of the fluid, etc. according to the smooth channel [8-10].

2. METHOD

In this study, the effect of aluminum foam with three different PPI values are used in the channel on heat transfer in a certain Reynolds value range was investigated experimentally. A 277 mm long rectangular channel with a cross-section of 20 mm x 50 mm was used as the channel. Also, as a result of the experimental study, the temperature values for Reynolds values determined were investigated, and the effect of 20 mm x 50 mm x 90 mm aluminum foams with different PPI values at the single Reynolds value was examined according to the channel where the heat transfer and friction coefficient were found.

2.1 Theoretical Principle

The heat transfer rate between a solid surface and the fluid per unit area and per unit temperature difference is called the convection heat transfer coefficient and is showed by h. The local heat transfer coefficient and Nusselt number are shown below.

$$h_x = \frac{q_c}{(T - T_{b,x})} \tag{1}$$

$$Nu_x = \frac{h_x D_h}{k} \tag{2}$$

Here T is the heating surface, $T_{b,z}$ is the local temperature value of the fluid. Also, h_x local heat transfer coefficient shown in Nusselt number, D_h hydraulic diameter and k is the thermal conductivity coefficient of the fluid.

Convection heat flux is defined as shown in Equation 3.

$$Q_c = \frac{Q_{inlet} - Q_{outlet}}{A} \tag{3}$$

Q_{inlet} is the input power value to the heater. Radiation is considered as the transport and conduction heat loss on the bottom surface.

Radiation heat flux for the top and bottom surfaces of the plate,

$$q_{r,top} = \varepsilon_t \sigma (T^4 - T_b^4) \quad (4)$$

$$q_{r,bottom} = \varepsilon_b \sigma (T^4 - T_\infty^4) \quad (5)$$

ε_t and ε_b are emissivity values for unpainted and painted surfaces, respectively. σ is the Stefan Boltzmann constant and 5.67 x 10^{-8} W/(m^2 K^4) has a value.

Free convection heat flux for the bottom surface of the plate is shown in Equation 6.

$$q_f = h_f (T-T_\infty) \quad (6)$$

The free convection coefficient is h_f 1.1 W/ (m^2 K) for the air velocity of 0.1 m/s [12].

The transmission value is as in Equation 7.

$$Q_c = k\frac{\Delta T}{x} \quad (7)$$

k is the heat transfer coefficient for the layer, T is the temperature difference across the layer, and x is the layer thickness.

Equation 8 based on the hydraulic diameter of the channel calculates the Reynolds number.

$$Re = \frac{\rho U D_h}{\mu} \quad (8)$$

3. EXPERIMENTAL STUDY

In the test section shown in Figure 1, the air is passed through a rectangular channel with a length of 50 mm x 20 mm and a rectangular channel with a length of 277 mm. The heating plate made of stainless steel foil used in the experiment is 100 mm wide, 277 mm long, and 0.02 mm thick.

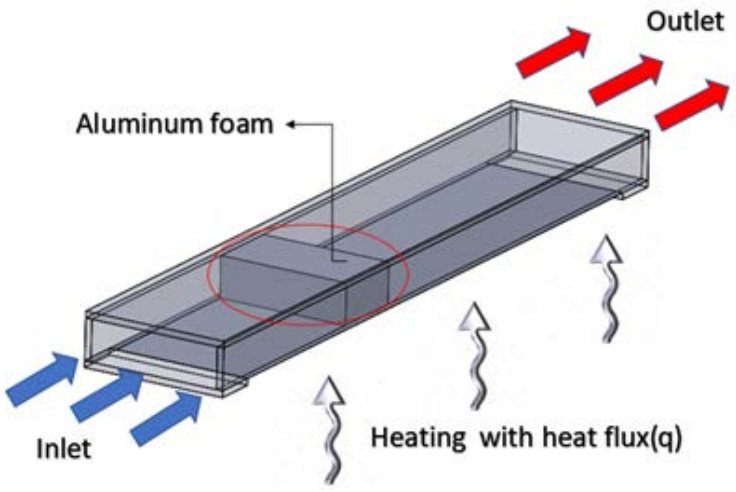

Figure 1. General view of the rectangular profile channel

The stainless steel foil was heated with a high current DC power supply to create a constant heat flux surface. The rectangular channel is fixed on stainless steel foil, and aluminum foams with three different PPI values are placed in the channel, as shown in Figure 1. FLIR branded thermal camera was placed under the heater assembly vertically in the Z direction so that it can take the thermal images in the channel. Infrared thermography system with a PC with Researcher software can measure temperature values between -20 0C and 1200 0C with an accuracy of ± 2%. The speed of the air passed through the channel with the help of a fan was measured with the help of an anemometer. In addition, a thermocouple and pressure meter were used to measure the inlet and outlet temperature and pressure values. As a result of the experiment, the images showing the change in the temperature values taken by the thermal camera were arranged and recorded with the help of a computer.
The bottom surface of the stainless steel foil layer is covered with black paint.

The emissivity value was measured as 0.82 for the painted plate and 0.13 for the unpainted plate [14].

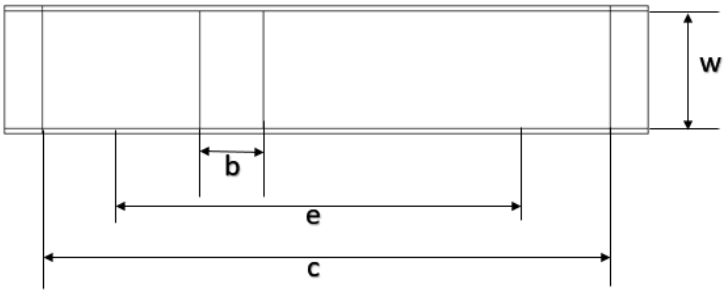

Figure 2. Rectangular profile channel interior dimensions

Firstly, experiments were done for the location of the aluminum foam, and the most efficient value was found in terms of heat transfer. This value was seen to be compatible with the literature. As shown in Figure 2 of the aluminum foam inside the channel, the rectangular foam section is positioned at a distance from the entrance of the channel. In the study, it was studied in the range of 4111-28774 Reynolds value, and its effect on Nu value was investigated. Images showing temperature value for the Reynolds number of 20553 were examined.

4. RESULTS

In this study, it was experimentally studied for the smooth channel under forced transport conditions, and friction factor and Nusselt number were calculated according to the obtained values. These values were compared with the data obtained by Dittus-Boelter.

Dittus-Boelter correlation,

$$Nu = 0.023Re^{0.8}Pr^{0.4} \quad (9)$$

The friction coefficient and Nusselt number obtained as a result of the experimental study for the smooth channel was found to be in harmony in the literature as seen in Figure 3.

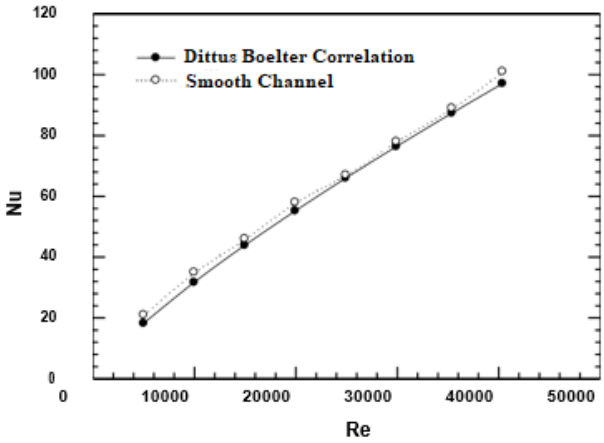

Figure 3. Comparison of Nusselt number for smooth channel

4.1. Temperature Distributions

In the experimental study, the channel's temperature distribution was recorded according to certain air velocity values, and Reynolds values obtained according to the thermal camera in the test section and transferred to the computer environment with the FLIR Quick Report program. In the experiment results, the distribution in the channel for the 20553 Reynolds value is as shown in Figure 4.

In the experimental results, the distributions within the channel for the 20553 Reynolds value are as shown in Figure 4. As can be seen from the temperature contours, a significant cooling performance has been obtained with aluminum foams' effect compared to the flat channel. As aluminum foams' PPI value increases, the fluid contact surface area increases, thus increasing the cooling performance.

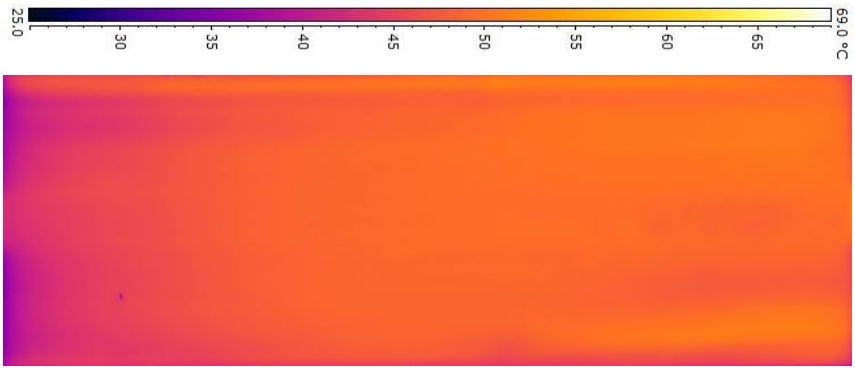

(a)

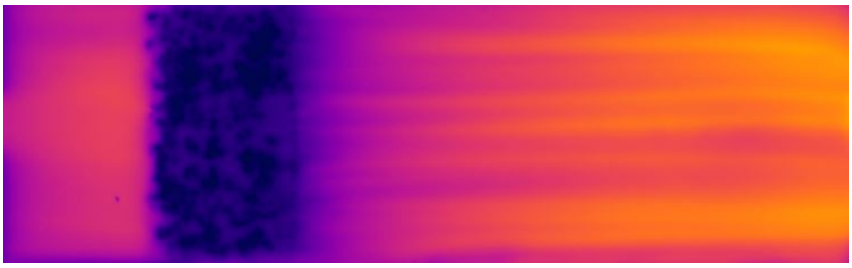

(b)

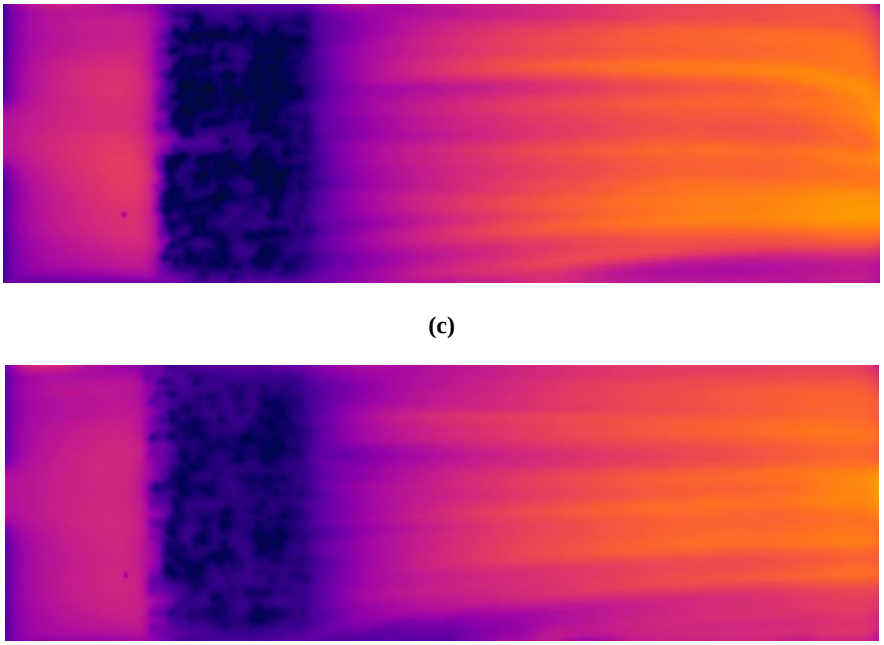

(c)

(d)

Figure 4. Temperature distributions within the rectangular section channel; (a) Smooth channel (b) 5 PPI channel (c) 10 PPI channel (d) 20 PPI channel

4.2. Heat Transfer Analysis

In the experimental study, the effects of parameters such as Reynolds number, PPI values of aluminum foams on heat transfer, and local Nusselt number were investigated. As shown in Figure 5, a significant increase in heat transfer has been achieved in the channel where all the PPI aluminum foams are used compared to the smooth channel. When the highest heat transfer increase compared to the smooth channel is 20 PPI, an increase of approximately 85% has been achieved. Also, when examined for PPI values, it was observed that 20 PPI aluminum foam had an increase in heat transfer of approximately 26% compared to 10 PPI aluminum foam and 42% compared to 5 PPI. This situation can be explained by increasing the surface area with which the fluid comes into contact. In addition to these, it was seen that 10 PPI foam had a better performance in terms of heat transfer when the x/D_h value was 0.7 in the channel.

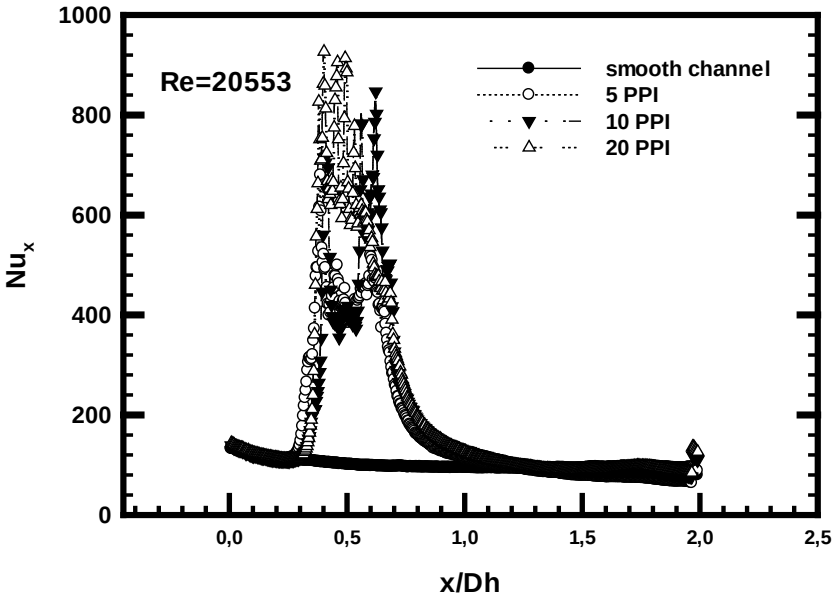

Figure 5. Temperature changes obtained depending on temperature sections

5. CONCLUSIONS

In this experimental study, it has been observed how the aluminum foam with three different PPI values used in the rectangular channel affects heat transfer in the channel according to the different Reynolds value range, and the following results have been obtained.

- A significant increase in heat transfer has been achieved in the channel where all the PPI aluminum foams are used compared to the smooth channel.

- When the highest heat transfer increase compared to the smooth channel is 20 PPI, an increase of approximately 85% has been achieved.

- When examined for PPI values, it was observed that 20 PPI aluminum foam had an increase in heat transfer of approximately 26% compared to 10 PPI aluminum foam and 42% compared to 5 PPI.

REFERENCES

[1] Yan, W.M., Liu, H.C., Soong, C.Y., Yang, W.J., Experimental study of impinging heat transfer along rib-roughened walls by using transient liquid crystal technique, *Heat and Mass Transfer*, 48, 2420-2428, 2005.

[2] Arguis, E., Rady, M.A., Nada, S.A, A numerical investigation and parametric study of cooling an array of multiple protruding heta sources by a laminar slot air jet, *International Journal of Heat And Fluid Flow*, 28, 787-805, 2006.

[3] Nishimura, M., Kimura, N., URANS computations for an oscillatory non-isothermal triple-jet using the *k–ε* and second moment closure turbulence models, *International Journal for Numerical Methods in Fluids*, 43, 1019-1044, 2003.

[4] Gau, C., Lee, C.C., Impingement cooling flow structure and heat transfer along rib-roughened walls, *International Journal of Heat and Mass Transfer*, 35 (11), 3009-3020, 1992.

[5] Gau, C., Lee, I.C., Flow and impingement cooling heat transfer along triangular rib-roughened walls, *International Journal of Heat and Mass Transfer*, 43 (24), 4405-4418, 2000.

[6] Ng Z.Y., Vo T., Hussam W.K., Sheard G.J., Two dimensional wake dynamics behind cylinders with triangular cross-section under incidence angle variation, *Journal of Fluids Structures*, 63, 302-324, 2016.

[7] Chumpia, A., Hooman, K., Performance of tubular aluminum foam heat exchangers in multiple row bundles, *Journal of Thermal Analysis and Calorimetry*, 135, 1813-1822, 2019.

[8] Doğan, A., Öney, B., Alüminyum köpük isi alicilardan taşinimla isi transferinin deneysel olarak incelenmesi, *Journal of the Faculty of Engineering and Architecture of Gazi University*, 29 (1), 71-78, 2014.

[9] Hamadouche, A., Nebbali, R., Benahmed, H., Kouidri, A., Bousri, A., Experimental investigation of convective heat transfer in an open-cell aluminum foams, *Experimental Thermal and Fluid Science*, 71, 86-94, 2016.

[10] Mancin, S., Zilio, C., Rossetto, L., Cavallini, A., Foam height effects on heat transfer performance of 20 ppi aluminum foams, *Applied Thermal Engineering*, 49, 55-60, 2012.

[11] Çengel Y.A. ve Ghajar, A.J., *Isı ve Kütle Transferi* (Ankara: Palme Yayınevi, 2019), 375.

[12] Janssen, L.P.B.M., Warmoeskerken M.M.C.G., *Transport Phenomena Data Companıon*, DUM, Delft, 2.

[13] Lytle, D., Webb, B.W., Air Jet Impingement Heat Transfer at Low Nozzle Plate Spacings, *International Journal of Heat and Mass Transfer*, 37, 1687-1697, 1994.

[14] Çalışkan, S., Farklı Jet ve Çarpma Plakası Özelliklerinde Çarpmalı Akışkan Jetlerinin Isı Transferi ve Akışının Deneysel ve Sayısal Olarak İncelenmesi, *Doktora Tezi*, Gazi Üniversitesi Fen Bilimleri Enstitüsü, Ankara, 2012.

A COMPARATIVE ANALYSIS ON HEAT PIPE HEAT EXCHANGERS AND ROTARY REGENERATIVE HEAT EXCHANGERS

Koray ÖZDEMİR*, Elif ÖĞÜT**
*Kocaeli University, Department of Mechanical Engineering, Kocaeli/Turkey
Email: 176109004@kocaeli.edu.tr
** Kocaeli University, Vocational School of Hereke, Kocaeli/Turkey
Email: elif.ogut@ kocaeli.edu.tr

ABSTRACT

In this study, a mathematical modeling study of a heat pipe heat exchanger (THEX) was performed. Then, the rotary type regenerative heat exchanger (RHEX), which is widely used in heat recovery applications, is also analytically modeled. Using these models confirmed by experimental data from the literature, a regenerative heat exchanger design with the same volume as the heat pipe heat exchanger has been designed. Using the proposed designs, heat pipe heat exchanger and rotary type regenerative heat exchanger with the same mass flow and air inlet temperatures were compared in terms of air outlet temperatures, total effectiveness value, total fan power requirements, mass and material cost. In this context, the effects of heat pipe heat exchanger fin spacing and hot air inlet velocity were investigated. Under the same operating conditions, the total effectiveness value of THEX is found to be 34.60% higher than RHEX, the total fan power requirement at RHEX is approximately 151 times higher than THEX, the total mass of RHEX is approximately 16 times higher than THEX, RHEX total material cost is approximately 4 times higher than THEX. In general, the heat pipe heat exchanger stands out in terms of effectiveness, total fan power requirement, and cost.

Keywords: Heat pipe heat exchanger, rotary type regenerative heat exchanger, heat recovery, mathematical modelling

1. INTRODUCTION

Rotary type regenerator is a gas-gas heat exchanger frequently used in coal-fired thermal power plants. Generally, it is called REGAVO when it is used in Flue Gas Sulfur Treatment (FGD) systems and LUVO when used as an air preheater. LUVO is used to heat the air required for combustion in the boiler by the heat of gases after combustion from the boiler. REGAVO, on the other hand, heats the exhaust flue gas with a portion of the heat of the flue gas sent to the scrubber. This heat exchanger takes the heat of the gas coming from the dirty side to the scrubber in the desulfurization system and stores it in the rotating metal plate elements. As REGAVO turns from the untreated side to the treated side, it transfers the stored heat to the clean gas coming from the scrubber of the desulfurization system and raises the temperature of treated gas above the saturation temperature.

Heat pipes are heat transfer devices in which a liquid evaporates and condenses between the evaporator and the condenser, and there is a circulation between these two phases. Due to their evaporation and condensation mechanisms, they have high effective thermal conductivity. Due to its high heat-carrying capacity, the heat pipe heat exchanger has become much smaller than conventional heat exchangers due to its ability to operate in high heat fluxes. With the working fluid in a heat pipe, heat can be absorbed in the evaporator zone and moved to the condenser zone, where the steam releases the heat to the cooling medium.
Recently, researchers have developed advances in heat pipe technology for heat recovery. Studies have generally analyzed the application, design, construction, and thermal performance of heat pipes. Here, some studies on practice will be mentioned.

Noie-Baghban and Majideian [1] examined waste heat recovery using CHPs (conventional heat pipe) for operating rooms in hospitals. CHPs are designed for use with low-temperature sources (15-55 ° C). In the study, it was found

that the effectiveness of CHP was 0.16, although it depends on the diameter and fin spacing. This value is very low since the CHP is designed for low-temperature operating conditions. Abd El-Baky and Mohamed [2] applied the CHP to heat recovery between two fresh and rotating air streams in an air-conditioning system where fresh air can be cooled. The ratios of mass flows (1, 1.5 and 2.3) between return and fresh air were tested to verify heat transfer and temperature change of fresh air. The results showed that as the inlet temperature of the fresh air increased, the temperature changes of the fresh and returning air increased. When the inlet fresh air temperature is increased to 40 °C, heat transfer for both evaporator and condenser sections increases and the efficiency value rises to approximately 48%. The effect of the mass flow rate on the efficiency is positive for the evaporator side and negative for the condenser side. Martinez et al. [3] designed a mixed energy recovery system for air conditioning, consisting of a CHP heat exchanger and indirect steam collectors. As a main result, it has been reported that with the application of a mixed energy recovery system in air conditioning plants consisting of two CHP and indirect evaporative systems, some of the energy from the return air stream can be recovered, thereby increasing energy efficiency and reducing environmental impacts. In two-phase closed thermospyhon (TPCT) applications, Lukitobudi et al. [4] designed, installed, and tested several different heat pipes for a medium temperature heat recovery in furnaces. TPCT has been reported to be very efficient (65%). It has been reported that the preferred finned steel water heat exchanger is stronger and is able to recover the waste heat from the furnace flue gas. It is stated that the efficiency of the bare copper heat pipe heat exchanger is very low, but since the production cost is also low and less maintenance is required, this heat exchanger may be an alternative assessment. Yang et al. [5] examined the possible application of heat recovery from the exhaust gas of a large bus engine with a heat exchanger with TPCT. The study determined that TPCTs can be used effectively as a tool for heat recovery. Riffat and Gan [6] investigated the effectiveness of TPCT heat exchangers for naturally ventilated buildings. In this research, the performance of three types of TPCT heat recovery units was tested in a two-chamber room with a horizontal chamber. With the study, it was suggested that the designed air velocity should be less than 1 m / s in the naturally ventilated low buildings without wind effect. For the application of the oscillating heat pipe (OHP) as a heat exchanger, Rittidech et al. [7] used a closed-end shaker heat pipe air preheater for drying. The study found that it can save energy by using a heat pipe heat exchanger for air preheating in the drying system. Bertrand et al. [8] investigated the application of a heat pipe heat exchanger to improve the energy efficiency of industrial processes. To this end, they aimed at reducing the potential heat recovery and fuel consumption by addressing the state of the ceramic industry. With the theoretical and numerical model they developed based on experimental data, the application of the heat pipe heat exchanger to the cooling chimney of the ceramic furnace has been shown to be able to recover more than 863 MWh of thermal energy, which can be used to heat the hot air-flow of the furnace pre-dryer. Thus, they emphasized that approximately 110,600 Sm^3 natural gas per year can be saved from burners that power the dryer, and 164 tons of carbon dioxide emissions can be prevented annually. In addition, it has been reported that the amount saved due to the reduction in fuel consumption is more than 22,000 Euros per year. These data support the improvement of energy efficiency and environmental impacts as well as the application of heat recovery based on heat pipes to the ceramic process in terms of economic investments. Zhang et al. [9] proposed a heat pipe heat exchanger used to cool the communication base station to replace the traditional air conditioning system during the winter and transition seasons. They conducted experiments in a commercially available heat exchanger to examine the effects of air-flow rate and temperature on the cooling capacity, heat transfer unit (NTU) and cooling efficiency of the heat pipe heat exchanger. The results show that as the air-flow rate increases, the NTU shrinks and the cooling capacity increases. Based on the analysis of experimental data, they proved that the heat pipe heat exchanger can reduce the system operating time and the operating cost of the air conditioning system. Tian et al. [10] designed and implemented a new type of waste heat recovery heat pipe heat exchanger to recover thermal energy from the high-temperature exhaust gas emitted from the adjustment machine in the paint and printing industry. The quarterly continuous operation of recovering dirty exhaust gas waste heat shows that the new type of heat pipe heat exchanger can save 15% natural gas without any blockage in the gas side channel. In order to evaluate and compare the regenerator of the liquid desiccant dehumidification system (LDDS) with and without heat pipe heat exchanger, Shen and his team [11] performed performance analysis with hybrid heat transfer, mass transfer, and heat recovery models and verified the simulation results with experimental results. In the study, the effects of air mass flow on regeneration and heat recovery performance are also discussed. It is stated that regeneration performance is generally improved with the heat pipe heat exchanger. With the predicted results from the model, they found that the maximum net heat recovery rates were 25% and 26.5%, which contributed to 27% maximum energy savings compared to regeneration without HPHE. Mahajan et al. [12] have investigated the use of finned-sFin heat pipes (OHPs) for the heat exchange between counter-floFin air currents in HVAC air systems and the feasibility of relevant cost savings in typical

North American climates. For this purpose, they developed a model with the ε-NTU method. The results showed that heat pipe heat exchangers can have a reasonable pressure drop (<200 Pa) and are capable of achieving a heat recovery rate of> 5 kW. In general, this study has shown that the heat pipe heat exchanger has the potential to effectively reduce energy consumption and operating cost of air handling units in buildings. Jouhara et al. [13] described the manufacture and testing of an innovative heat recovery system based on a straight heat pipe heat exchanger (FHP). Considering that the heat pipe heat exchanger used is 1 m long and the production line is 70 m long, it is stated that in a full-scale system, approximately three quarters of 1 megawatt can be recovered. From the results, it was concluded that FHP is an innovative and highly efficient technology for waste heat recovery from such industrial applications. Yağbasan [14] compared different types of heat exchangers used in energy recovery applications in his master's thesis. Consequently, when the comparison of the heat pipe with other heat exchangers is examined, the pressure loss of the heat pipe is low compared to other heat exchangers, the heat transfer coefficient is high, it does not require maintenance, it does not cost much, there is no need for auxiliary power, the transfer area for the unit volume is high and the fluids It is stated to be extremely advantageous in terms of preventing interference.

The studies described above show that heat pipe heat exchangers are prominent in heat recovery applications. Thus, in this study, the performances of rotary regenerative heat exchangers and heat pipe heat exchangers, which are widely used in heat recovery, were compared.

2. METHOD

In the first part of this section, an analytical modeling study of a heat pipe heat exchanger has been performed. This model was compared with the experimental data obtained from the literature. In the second part, the rotary type regenerative heat exchanger, which is widely used in heat recovery applications, is again analytically modeled and compared with the experimental data obtained from the literature. In the last part, a regenerative heat exchanger design with the same volume as the heat pipe heat exchanger was designed using the models obtained. Using the proposed designs, the heat pipe heat exchanger and rotary type regenerative heat exchanger for the same mass flow and air inlet temperatures were compared in terms of air outlet temperatures, total effectiveness value, total fan power requirements, mass and material cost.

2.1. Heat Pipe Heat Exchanger Model

In this section, an empirical modeling study of a thermospyhon and plate type heat exchanger studied in the literature will be explained. In this context, the experimental and ε-NTU method heat exchanger was chosen by Noie [15] as the reference heat exchanger (Figure 1-left). The same heat exchanger is also Yonghua et. get. [16] (Figure 1-left) and Leong et. Get. It was also modeled by [17]. This study was carried out using the three modeling studies mentioned above.

The geometrical properties and other details of the reference heat exchanger are given in Figure 1-left and Table 1, respectively.

Table 1. Heat pipe heat exchanger features

Feature	Unit	Value
Fin type		Flat plate
Fin material		Aluminum
Fin material cost	$/kg	1.8
Fin thickness	mm	0.4
Fin spacing	mm	10
Heat pipe type		Thermosyphon
Tube material		Copper
Pipe material cost	$/kg	6.18
Working fluid		Water
Transverse row number		15
Number of longitudinal rows		6
Total number of water heaters		90
Thermosyphon outer diameter	mm	15
Thermosyphon inner diameter	mm	14

Figure 1-shows a typical thermospyhon consisting of a right condenser, an evaporator, and an adiabatic section, partially filled with working fluid. The fluid and steam in the thermospyhon are assumed to be in equilibrium, and the saturation temperature is relatively the same. In addition, the thermal resistances of the liquid-vapor interfaces and the axial resistance of the pipe shell can be neglected. Thus, all heat transfer resistance from hot to cold fluid consists of six parts, namely R1, R2, R3, R4, R5, and R6, shown on the right side of Figure 1. Thermal resistance related to the evaporator, an external convection ($R_1 = \frac{1}{\pi d_{ext} L_e h_{ext,e}}$), a radial conduction ($R_2 = \frac{\ln (d_{ext}/d_{int})}{2\pi L_e k_t}$) and an evaporation contains ($R_3 = \frac{1}{\pi d_{int} L_e h_{int,e}}$). R4, R5, and R6 represent capacitors-related thermal resistors and take forms similar to R1, R2, and R3, respectively. Except for radial resistors, the above heat transfer resistors are determined by empirical correlations as shown below:

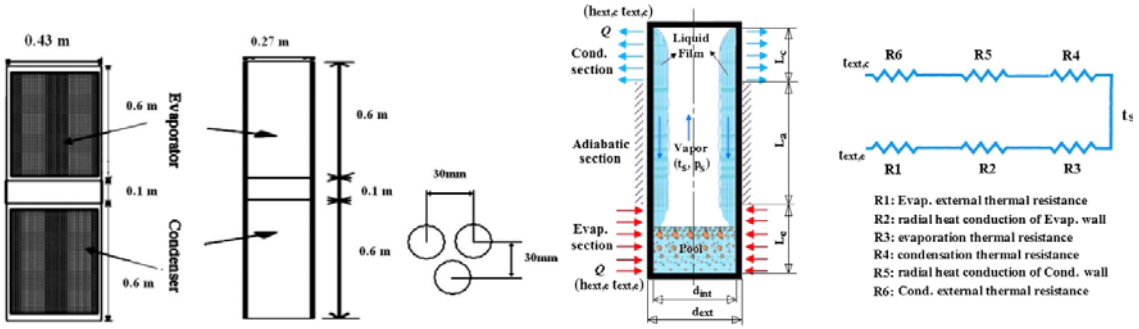

Figure 1. Heat pipe heat exchanger dimensions and thermospyhon placement [15] (left), Thermosyphon schematic and thermal resistance network (right) [16]

2.1.1. Condensation Heat Transfer Correlation

Nusselt's film-type condensation theory is generally accepted for the heat transfer coefficient in the condenser region, and it is calculated as shown in Eq. (1):

$$h_{Nu} = 0.943 \left[\frac{\rho_l g h_{fg} (\rho_l - \rho_v) {k_l}^3}{\mu_l L_c (T_s - T_w)} \right]^{1/4} \quad (1)$$

However, experiments show that the above equation can exceed the condensation heat transfer coefficient of the thermospyhon [16]. This is explained by the fact that the liquid stream is exposed to large viscous stress from the rising steam and the accumulation of important droplets dragged by the steam in the condenser wall. As the condensation heat transfer coefficient, the relation proposed by Jouhara and Robinson [18] (Eq. (2)) has been shown to meet experimental data well [16].

$$h_c = 0.85 {Re_{fill}}^{0.1} e^{(-0.000067 \frac{\rho_l}{\rho_v - 0.14})} h_{Nu} \quad (2)$$

Here Reynolds Re_{fill} is the Reynolds number of the condensing film, which is as follows:

$$Re_{fill} = \frac{4Q_e}{\pi d_{ext} h_{fg} \mu_l} \quad (3)$$

2.1.2. Evaporation Heat Transfer Correlation

Evaporation heat transfer here is complicated since the evaporator consists of both the liquid pool and the liquid film, depending on the fluid rate and heat flux. Eq. (4), which includes natural convection, combined convection, and bubbling boiling, has been found to well overlap with experimental data [16] and was accepted in this study.

$$h_{int,e}^{pool} = 0.32 {q_e}^{0.4} \left(\frac{{\rho_l}^{0.65} {k_l}^{0.3} {c_{p,l}}^{0.7} g^{0.2}}{{\rho_v}^{0.25} {h_{fg}}^{0.4} {\mu_l}^{0.1}} \right) \left(\frac{p}{p_a} \right)^{0.3} \quad (4)$$

Since the thin film in the evaporator is short, Nusselt's theory is reasonable, and the film heat transfer coefficient is calculated as follows.

$$h_{int,e}^{film} = 1.333 h_{Nu} \tag{5}$$

The average heat transfer coefficient of the evaporator is equal to the average of the pool heat transfer coefficient given above and the film heat transfer coefficient [16].

$$h_{int,e} = 0.5(h_{int,e}^{film} + h_{int,e}^{pool}) \tag{6}$$

2.1.3. Coefficient of Heat Transfer by Convection Around the Thermospyhon

The heat transfer coefficient by convection around the thermospyhon is calculated as follows [17]:

$$h_{ext,e} = \frac{j \rho_{h,air} V_{h,max} c_{p,h,air}}{{Pr_{h,air}}^{2/3}} \tag{7}$$

Here, j is the Colburn factor and Eq. It is given in (8).

$$\begin{aligned} j_4 &= 0.14 {Re_{D,h,max}}^{-0.328} \left(\frac{s_t}{s_l}\right)^{-0.502} \left(\frac{f_s}{d_{ext}}\right)^{0.031} \\ \frac{j_{N_R}}{j4} &= 0.991 \times \left[2.24 {Re_{D,h,max}}^{-0.092} \left(\frac{N_R}{4}\right)^{-0.031}\right]^{0.607 \times (4 - N_R)} \end{aligned} \tag{8}$$

Eq. $V_{h,max}$ in (7) is calculated as follows for the staggered sequence:

$$V_{h,max} = \begin{cases} 2(s_d - d_{ext}) < (s_t - d_{ext}) & \frac{s_t}{2(s_d - d_{ext})} V_{h,max} \\ 2(s_d - d_{ext}) > (s_t - d_{ext}) & \frac{s_t}{(s_t - d_{ext})} V_{h,max} \end{cases} \tag{9}$$

Eq. $Re_{D,h,max}$in (8) is calculated as follows:

$$Re_{D,h,max} = \frac{\rho_{h,air} V_{h,max} d_{ext}}{\mu_{h,air}} \tag{10}$$

While calculating the combined heat transfer coefficient, the heat transfer coefficient around the thermospyhon is multiplied by the total surface efficiency coefficient (Eq. (11)) associated with the fins.

$$\eta_0 = 1 - (1 - \eta_f) \frac{A_f}{A_{t,ext}} \tag{11}$$

Here η_f is the fin efficiency which is as follows:

$$\eta_f = \frac{2 r_{ext}}{m({r_{eq,f}}^2 - {r_{ext}}^2)} \left[\frac{K_1(mr_{ext}) I_1(mr_{eq,f}) - K_1(mr_{eq,f}) I_1(mr_{ext})}{K_1(mr_{eq,f}) I_0(mr_{ext}) + K_0(mr_{ext}) I_1(mr_{eq,f})}\right] \tag{12}$$

Here, I_n and K_n are modified first and second Bessel functions, respectively.
The m given in Eq. (12) is calculated as in Eq. (13).

$$m = \sqrt{\frac{2 h_{ext,e}}{k_{fin} t}} \tag{13}$$

$r_{eq,f}$ given in Eq. (12) is the equivalent circular fin radius for the hexagonal fin form resulting from the staggered array, calculated as in Eq. (14) [19]:

$$r_{eq,f} = 1.28 s_t \sqrt{\frac{s_l}{s_t} - 0.2} \tag{14}$$

2.1.4. ε-NTU Method

The effectiveness value of the evaporator for a single row is as follows [15]:

$$\varepsilon_{h1} = 1 - e^{-NTU_h} \tag{15}$$

Here NTU_h is the number of transfer units and Eq. (16) is found with:

$$NTU_h = \frac{(UA)_h}{C_h} \tag{16}$$

$(UA)_h$ and C_h are calculated as in Eq. (17) and (18), respectively.

$$\frac{1}{(UA)_h} = \frac{1}{\pi d_{int} L_e h_{int,e}} + \frac{1}{\eta_0 A_{t,ext} h_{ext,e}} + \frac{\ln(d_{ext}/d_{int})}{2\pi L_e k_t}), \tag{17}$$

$$C_h = \dot{m}_h c_{p,h} \tag{18}$$

The efficiency value for n rows in the evaporator is as in Eq. (19).

$$\varepsilon_{hn} = 1 - (1 - \varepsilon_{h1})^n \tag{19}$$

When Eq. (15) - (19) is repeated for the condenser side, the total effectiveness value of the heat pipe heat exchanger is calculated as follows.

$$\varepsilon_t = \begin{cases} C_h > C_c & \varepsilon_t = \left(\frac{1}{\varepsilon_{cn}} + \frac{C_c/C_h}{\varepsilon_{hn}}\right)^{-1} \\ C_c > C_h & \varepsilon_t = \left(\frac{1}{\varepsilon_{hn}} + \frac{C_h/C_c}{\varepsilon_{cn}}\right)^{-1} \end{cases} \tag{20}$$

After the total effectiveness value is found, the hot air and cold air outlet temperatures are calculated in Eq. (21) and (22), respectively.

$$T_{h,o} = T_{h,i} - \varepsilon_t \frac{C_{min}}{C_h}\left(T_{h,i} - T_{c,i}\right) \tag{21}$$

$$T_{c,o} = T_{c,i} + \varepsilon_t \frac{C_{min}}{C_c}\left(T_{h,i} - T_{c,i}\right) \tag{22}$$

2.1.5. Total Fan Power Requirement

Fan power requirements for the evaporator and condenser parts are as follows.

$$PP_t = \dot{V}\Delta P \tag{23}$$

Here $\dot{V}$ is the volume flow and ΔP is the pressure drop and is found with Eq. (24) [20].

$$\Delta P = \frac{G^2}{2\rho_i}\left[f\frac{A_t}{A_{min}}\frac{\rho_i}{\rho} + (1+\sigma^2)(\frac{\rho_i}{\rho_o} - 1)\right] \tag{24}$$

$$G = \frac{\rho V}{\sigma} \tag{25}$$

$$\frac{A_t}{A_{min}} = \frac{4L}{D_h} = \frac{total\ heat\ transfer\ aera}{\min flow\ area} \tag{26}$$

$$\sigma = \frac{A_{min}}{A_{fr}} = \frac{\min free\ surface\ area}{frtontal\ flow\ area} \tag{27}$$

f friction coefficient in Eq (24) is as follows [21]:

$$f = f_F \frac{A_f}{A_t} + f_T(1 - \frac{A_f}{A_t})(1 - \frac{t}{f_s}) \tag{28}$$

f_F in Eq. (28) expresses the friction coefficient for the fins and with Eq. (29); f_T expresses the friction coefficient for the pipes and is calculated by Eq (30).

$$f_F = 1.455 {Re_D}^{-0.656} \left(\frac{f_s}{d_{ext}}\right)^{-0.134} \left(\frac{s_t}{d_{ext}}\right)^{1.23} \left(\frac{s_t}{s_l}\right)^{-0.347} \tag{29}$$

$$f_T = \frac{\pi}{4}\left\{0.25 + \frac{0.188}{(s_t/d_{ext} - 1)^{1.08}} {Re_D}^{-0.16}\right\} \cdot \left(\frac{s_t}{d_{ext}} - 1\right) \tag{30}$$

2.1.6. Heat Pipe Heat Exchanger Model Verification

Yonghua et al. [16] presented the experimental data carried out by Noie [15] as graphs of the type of hot air outlet temperature varying depending on the hot air outlet temperature for the heat pipe heat exchanger modeled in its study, where the hot air inlet speed is 2.5 m/s and 4 m/s. The model created by using the graphic values for the hot air outlet temperature, the cold air outlet temperature and the value calculated according to the hot air outlet temperature in the following sections were compared with the experimental data.

In the case where the hot air inlet speed is 4 m/s, the comparison of the hot air outlet temperature with the values calculated with the model is shown in Figure 2. According to the model values, lower hot air outlet temperature and accordingly higher cold air outlet temperature are estimated.

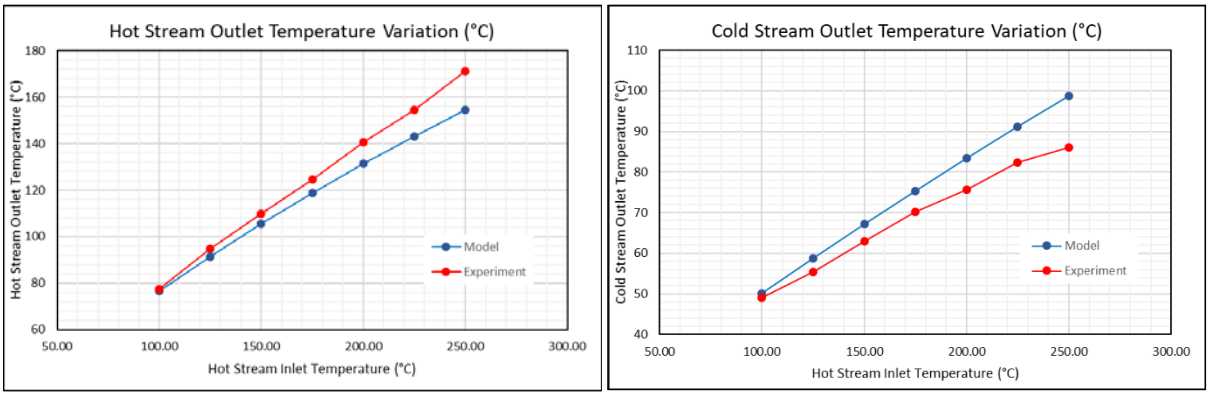

Figure 2. Hot air outlet temperature variation (left), hot air outlet temperature variation (right) ($V_{h,\,i}$= 4 m / s)

Accordingly, experimental data at low hot air inlet values and the results calculated by the model give very close results, while the hot air inlet temperature is noticeable as the temperature increases but remains within acceptable

limits. As a result, it has been revealed that the empirical model created can be used to model the heat pipe heat exchanger operating conditions.

2.2. Rotary Type Heat Exchanger Models

Rotary type regenerative heat exchanger is the most commonly used heat exchanger type in heat recovery applications, especially coal-fired thermal power plants.

In this section, an empirical modeling study of a rotary type heat exchanger studied in the literature will be explained. In this context, experimental and numerical heat exchangers were chosen by Zhang [22] as the reference heat exchanger (Figure 3). This study was carried out using the modeling study described by Shah and Sekulic [23].

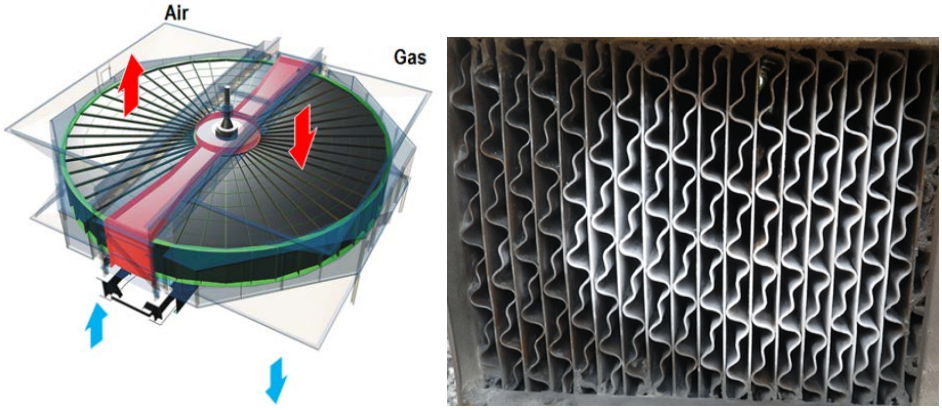

Figure 3. Rotary type heat exchanger model (left) and matrix channels (right)

Characteristic features of the modeled rotary heat exchanger are given in Table 2.

Table 2. Reference rotary type heat exchanger features

Feature			
Angular velocity	N_{rpm}	rpm	0.75
Outer diameter	D_w	m	14.80
Inner diameter	D_s	m	3.10
Channel length	L_w	m	1.60
Void ratio	σ		0.75
Percentage of sealing	S_c	%	10.00
Packaging density	β	m^2/m^3	391.15
Total matrix surface area	A_{surf}	m2	92646.72
Hot air inlet temperature	$T_{h,i}$	°C	311.00
Hot air mass flow	m_c	kg/s	384.00
Hot air heat transfer coefficient	h_h	W/m^2K	64.41
Cold air inlet temperature	$T_{c,i}$	°C	38.79
Cold air mass flow	m_c	kg/s	276.00
Cold air heat transfer coefficient	h_c	W/m^2K	57.31
Matrix material			Carbon steel (0.5%)
Matrix material cost		$/kg	0.5

2.2.1. Heat Transfer

Hot and cold air outlet temperatures are calculated as follows:

$$T_{h,o} = T_{h,i} - \varepsilon_t \frac{C_{min}}{C_h}\left(T_{h,i} - T_{c,i}\right) \tag{31}$$

$$T_{c,o} = T_{c,i} + \varepsilon_t \frac{C_{min}}{C_c}\left(T_{h,i} - T_{c,i}\right) \tag{32}$$

Total effectiveness value for the rotary heat exchanger is calculated with ε_t Eq (33).

$$\varepsilon_t = \varepsilon_{cf}\left[1 - \frac{1}{9C_r^{*1.93}}\right] \tag{33}$$

Here ε_{cf} is given by Eq (34).

$$\varepsilon_{cf} = \frac{1 - e^{[-NTU_0(1-C^*)]}}{1 - C^* e^{[-NTU_0(1-C^*)]}} \tag{34}$$

Here NTU_0 , is given by Eq. (35) and C^* is expressed by Eq. (35).

$$NTU_0 = \frac{1}{C_{min}} \frac{1}{1/(hA)_h + 1/(hA)_c} \tag{35}$$

$$C^* = \frac{C_{min}}{C_{max}} \tag{36}$$

The C_r^* in Eq. (33) is as follows.

$$C_r^* = \frac{C_r}{C_{min}} \tag{37}$$

Here C_r is the heat capacity ratio and is given as in Eq. (38).

$$C_r = M_w c_{p,w} N \tag{38}$$

Here, $c_{p,w}$ matrix material specific heat, N rotational speed and M_w total matrix mass are calculated as follows:

$$M_w = \frac{\pi}{4}\left({D_o}^2 - {D_i}^2\right) L_w \rho_w (1 - \sigma) \tag{39}$$

Here D_o is the matrix outer diameter, D_i, matrix inner diameter, L_w, matrix length, ρ_w matrix density, and σ is the matrix void ratio.

The heat transfer coefficient in Eq. (35) was calculated as 1.5 times the number of Nusselt given by h_c and h_h Niu and Zhang [24] for a channel with sinusoid (a/b = 1.52) and hydraulic radius $d_h = 2.35\ mm$. Because the channel geometry in the reference study contains a full and a half sinusoidal curve. Therefore, the heat transfer coefficients are as follows.

$$h_c = \frac{k_c Nu}{d_h} = \frac{k_c 1.5 \times 2.545}{d_h} \tag{40}$$

$$h_h = \frac{k_c Nu}{d_h} = \frac{k_h 1.5 \times 2.545}{d_h} \tag{41}$$

Here k is the thermal conductivity of air.

2.2.2. Total Fan Power Requirement

The total fan power requirement of the rotary heat exchanger is calculated in Eq. (23). The pressure drop is as follows:

$$\Delta P = 4f\frac{L_w}{d_h}\frac{\rho V^2}{2} \tag{42}$$

The friction coefficient here is determined as follows using the same reference and method as the heat transfer coefficient:

$$f = 1.5 \times 14.023 \tag{43}$$

2.2.3. Rotary Type Heat Exchanger Model Verification

Table 3 shows the comparison of the model with the experimentally given hot and cold air outlet temperatures. The model created accordingly can be used to model the rotary heat exchanger.

Table 3. Rotary heat exchanger model values and experimental values

	$\mathbf{T}_{h,o}$ (°C)	$\mathbf{T}_{c,o}$ (°C)
Experiment	143.50	281.84
Model	140.03	279.46
Difference	-2.42%	-0.84%

3. RESULTS AND DISCUSSION

3.1. Comparison of Heat Pipe Heat Exchanger and Rotary Type Heat Exchanger

In this section, a regenerative heat exchanger design with the same volume as the heat pipe heat exchanger was designed using the models obtained above. Using the proposed designs, the heat pipe heat exchanger and rotary type regenerative heat exchanger for the same mass flow and air inlet temperatures were compared in terms of air outlet temperatures, total effectiveness value, total fan power requirements, mass and material cost.

In this context, the effects of heat pipe heat pipe heat exchanger blade spacing and hot air inlet speed have been examined.

3.1.1. Hot Air Inlet Velocity Effect

In this section, the heat pipe heat exchanger and rotary heat exchanger with the same volume, the same air inlet temperatures and speeds are modeled with different hot air inlet speeds, 2 and 6 m/s, and the results are compared in graphs.

3.1.1.1. Hot Air Inlet Velocity $V_{h,i}$=2 m/s

In the case where the hot air inlet speed is 2 m/s, the total effectiveness values and total fan power requirements obtained depending on the hot air inlet temperature for THEX and RHEX are shown in Figure 4 and Table 4.

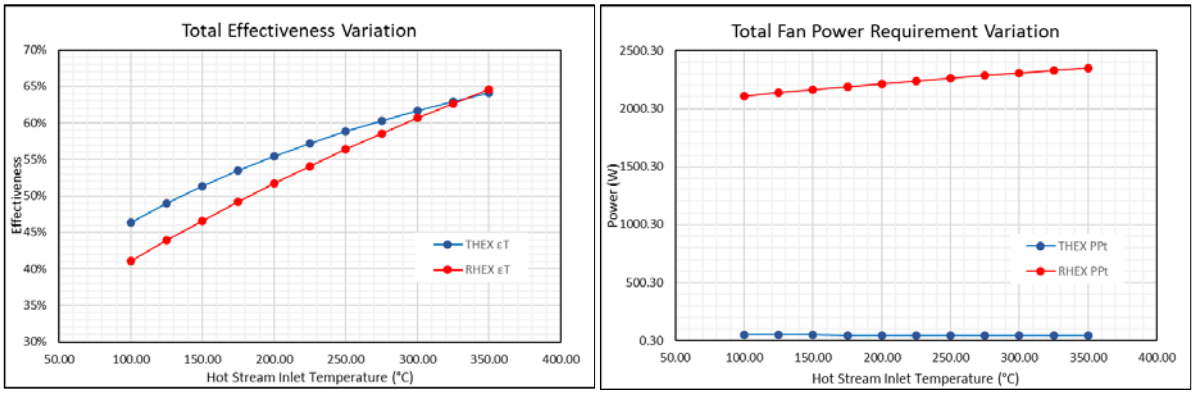

Figure 4. Total effectiveness change (left), Total fan power requirement change (left) ($V_{h,\,i}$ = 2 m / s)

3.1.1.2. Hot Air Inlet Velocity $V_{h,i}$=6 m/s

In the case where the hot air inlet speed is 6 m/s, the total effectiveness values and total fan power requirements obtained depending on the hot air inlet temperature for THEX and RHEX are shown in Figure 5 and Table 4.

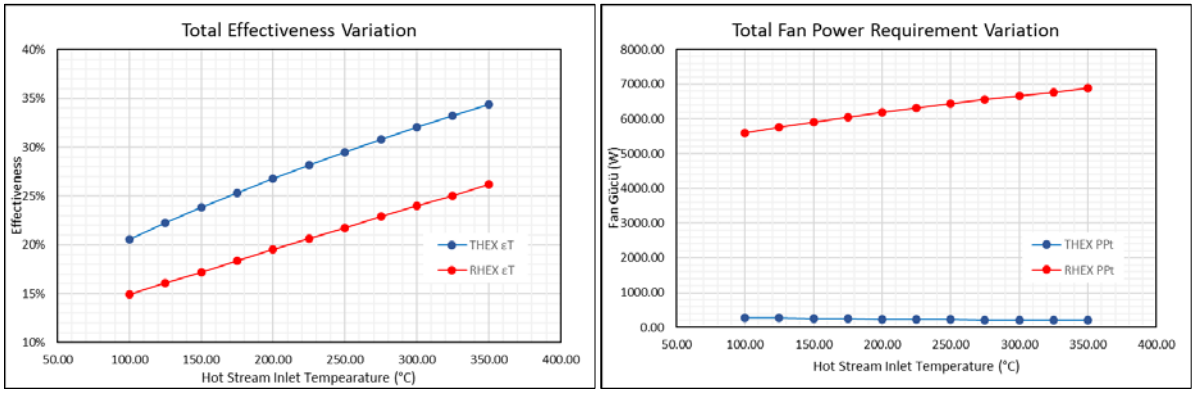

Figure 5. Total effectiveness change (left), Total fan power requirement change (right) ($V_{h,\,i}$ = 6 m / s)

As the hot air inlet temperature increases, the cold air outlet speed increases for both heat exchangers due to the improved heat transfer due to the increase in temperature gradients. However, RHEX becomes advantageous in terms of hot air outlet temperature with increasing hot air inlet temperature. As the hot air inlet temperature increases, the mass flow decreases as the hot air inlet density decreases. As the hot air inlet temperature increases for both heat exchangers, friction factors increase and Reynolds numbers decrease. Since the rate of increase in temperature related to friction factor for THEX is lower than the increase in average density, the total fan power requirement decreases due to increasing hot air inlet temperature and pressure drop. For RHEX, since the rate of increase in friction factor related to temperature is higher than the rate of increase in average density, total fan power requirement increases due to increasing hot air inlet temperature and pressure drop. The rotary type heat exchanger, which has a narrow and long metal circumferential duct in terms of total fan power requirement, is quite disadvantageous compared to the heat pipe heat exchanger.

Table 4. General comparison of rotary heat exchanger and heat pipe heat exchanger

			$V_{h,i}$=2 m/s			**$V_{h,i}$=6 m/s**		
	$T_{h,i}$	°C	150.00	250.00	350.00	150.00	250.00	350.00
	$T_{c,i}$	°C	25	25	25	25	25	25
THEX	$T_{h,o}$	°C	85.85	117.70	141.51	120.19	183.62	238.29
RHEX	$T_{h,o}$	°C	91.76	123.15	140.17	128.49	201.03	264.77

Dif.			-6.88%	-4.63%	0.94%	-6.91%	-9.48%	-11.11%
THEX	$T_{c,o}$	°C	55.36	76.11	93.28	67.44	102.45	136.08
RHEX	$T_{c,o}$	°C	52.56	74.00	93.72	55.55	81.76	108.74
Dif.			5.05%	2.77%	-0.47%	17.63%	20.20%	20.09%
THEX	ε_T		51%	59%	64%	24%	30%	34%
RHEX	ε_T		47%	56%	65%	17%	22%	26%
Dif.			9.21%	4.12%	-0.64%	27.84%	26.22%	23.70%
THEX	PP_t		48.28	46.95	45.96	254.61	223.39	202.11
RHEX	PP_t		2164.91	2263.07	2347.89	5906.08	6437.99	6882.71
Dif.			-4383.62%	-4720.35%	-5008.56%	-2219.63%	-2781.90%	-3305.40%
THEX	Mass	kg	11.67	11.67	11.67	11.67	11.67	11.67
RHEX	Mass	kg	184.15	184.15	184.15	184.15	184.15	184.15
Dif.			-1478.49%	-1478.49%	-1478.49%	-1478.49%	-1478.49%	-1478.49%
THEX	Cost	$	22.16	22.16	22.16	22.16	22.16	22.16
RHEX	Cost	$	92.08	92.08	92.08	92.08	92.08	92.08
Dif.			-315.53%	-315.53%	-315.53%	-315.53%	-315.53%	-315.53%

When Table 4 is examined, a better efficiency value is obtained for both types of heat exchangers at low inlet velocity, ie flow rate, under the same hot air inlet temperature condition. Due to the increase in inlet temperatures, the difference between RHEX and THEX total effectiveness decreases and RHEX can have more effectiveness value at low speeds. Total fan power requirement increases as the temperature rises. At low speeds, THEX stands out with serious differences in terms of total fan power requirement. Heat exchanger mass and cost are approximately 16 and 4 times higher in RHEX than THEX respectively.

4. CONCLUSION

In the first part of this study, examples regarding the use of heat pipe heat exchangers for heat recovery are given. In the second part, mathematical modeling study of a heat pipe heat exchanger has been done. This model is compared with the experimental data obtained from the literature. Then, the rotary type regenerative heat exchanger, which is widely used in heat recovery applications, was again analytically modeled and compared with the experimental data obtained from the literature. In the last part, a regenerative heat exchanger design with the same volume as the heat pipe heat exchanger was designed using the models obtained. Using the proposed designs, the heat pipe heat exchanger and rotary type regenerative heat exchanger for the same mass flow and air inlet temperatures were compared in terms of air outlet temperatures, total effectiveness value, total fan power requirements, mass and material cost. Both models of heat exchangers overlap with experimental data. In general, heat pipe heat exchanger effectiveness stands out in terms of total fan power requirement and cost.

ACKNOWLEDGMENTS

The authors would like to thank for the financial support received from Kocaeli University BAP Project No. FDK-2020-2098.

REFERENCES

[1] S.H. Noie-Baghban, G.R. Majideian, Waste heat recovery using heat pipe heat exchanger (HPHE) for surgery rooms in hospitals, Appl. Therm. Eng. 20 (2000) 1271–1282. doi:10.1016/S1359-4311(99)00092-7.

[2] M.A. Abd El-Baky, M.M. Mohamed, Heat pipe heat exchanger for heat recovery in air conditioning, Appl. Therm. Eng. 27 (2007) 795–801. doi:10.1016/j.applthermaleng.2006.10.020.

[3] R.H.M. F.J.R. Martinez, M.A.A. Plasencia, E.V. Gomez, F.V. Diez, Design and experimental study of mixed energy recovery system, heat pipe and indirect evaporative equipment for air conditioning, Energy Build. 35 (2003) 1021–1030.

[4] A.R. Lukitobudi, A. Akbarzadeh, P.W. Johnson, P. Hendy, Design, construction and testing of a thermosyphon heat exchanger for medium temperature heat recovery in bakeries, Heat Recover. Syst. CHP. 15 (1995) 481–491. doi:10.1016/0890-4332(95)90057-8.

[5] F. Yang, X. Yuan, G. Lin, Waste heat recovery using heat pipe heat exchanger for heating automobile using exhaust gas, Appl. Therm. Eng. 23 (2003) 367–372. doi:10.1016/S1359-4311(02)00190-4.

[6] G.G. S.B. Riffat, Determination of effectiveness of heat pipe heat recovery for naturally ventilated buildings, Appl. Therm. Eng. 18 (1998) 121–130.

[7] S.S. S. Rittidech, W. Dangeton, Closed-ended oscillating heat-pipe (CEOHP) air-preheater for energy thrift in a dryer, Appl. Energy. 81 (2005).

[8] B. Delpech, M. Milani, L. Montorsi, D. Boscardin, A. Chauhan, S. Almahmoud, B. Axcell, H. Jouhara, Energy efficiency enhancement and waste heat recovery in industrial processes by means of the heat pipe technology: Case of the ceramic industry, Energy. 158 (2018) 656–665. doi:10.1016/j.energy.2018.06.041.

[9] L.Y. Zhang, Y.Y. Liu, X. Guo, X.Z. Meng, L.W. Jin, Q.L. Zhang, W.J. Hu, Experimental investigation and economic analysis of gravity heat pipe exchanger applied in communication base station, Appl. Energy. 194 (2016) 499–507. doi:10.1016/j.apenergy.2016.06.023.

[10] E. Tian, Y.L. He, W.Q. Tao, Research on a new type waste heat recovery gravity heat pipe exchanger, Appl. Energy. 188 (2017) 586–594. doi:10.1016/j.apenergy.2016.12.029.

[11] S. Shen, W. Cai, X. Wang, Q. Wu, H. Yon, Investigation of liquid desiccant regenerator with heat recovery heat pipe system, Energy Build. 146 (2017) 353–363. doi:10.1016/j.enbuild.2017.04.057.

[12] G. Mahajan, S.M. Thompson, H. Cho, Energy and cost savings potential of oscillating heat pipes for waste heat recovery ventilation, Energy Reports. 3 (2017) 46–53. doi:10.1016/j.egyr.2016.12.002.

[13] H. Jouhara, S. Almahmoud, A. Chauhan, B. Delpech, G. Bianchi, S.A. Tassou, R. Llera, F. Lago, J.J. Arribas, Experimental and theoretical investigation of a flat heat pipe heat exchanger for waste heat recovery in the steel industry, Energy. 141 (2017) 1928–1939. doi:10.1016/j.energy.2017.10.142.

[14] A.K. Yağbasan, Isi Borularinin Dizayn Teknolojisi ve Isi Borulu Isi Degistiricilerinin Incelenmesi, Eskişehir Osmangazi Üniversitesi, 2009. http://www.albayan.ae.
[15] S.H. Noie, Investigation of thermal performance of an air-to-air thermosyphon heat exchanger using ε-NTU method, Appl. Therm. Eng. 26 (2006) 559–567. doi:10.1016/j.applthermaleng.2005.07.012.

[16] Y. You, T. Zhao, Z. Wu, P. Chen, X. Xu, Comprehensive thermal model of thermosyphon heat exchanger integrated with thermal resistances of phase changes, Appl. Therm. Eng. 128 (2018) 471–479. doi:10.1016/j.applthermaleng.2017.09.056.

[17] K.Y. Leong, R. Saidur, T.M.I. Mahlia, Y.H. Yau, Performance investigation of nanofluids as working fluid in a thermosyphon air preheater, Int. Commun. Heat Mass Transf. 39 (2012) 523–529. doi:10.1016/j.icheatmasstransfer.2012.01.014.

[18] H. Jouhara, A.J. Robinson, Experimental Investigation of Small Diameter Two-Phase Closed Thermosyphons Charged with Water , FC-84 , FC-77 and FC-3283, Appl. Therm. Eng. 30 (2010) 201–211.

[19] T. Perrotin, D. Clodic, Fin efficiency calculation in enhanced fin-and-tube heat exchangers in dry conditions, in: Int. Congr. Refrig., 2003: pp. 1–8. http://www.ces.mines-paristech.fr/francais/visite/chapitre5/pdf/ICR0026Hex.pdf.

[20] S. Kakaç, H. Liu, A. Pramuanjaroenkij, Heat Exchangers Selection, Rating, and Thermal Design, Third Edit, CRC Press, 2012.

[21] T.A. Tahseen, M. Ishak, M.M. Rahman, An overview on thermal and fluid flow characteristics in a plain plate finned and un-finned tube banks heat exchanger, Renew. Sustain. Energy Rev. 43 (2015) 363–380. doi:10.1016/j.rser.2014.10.070.

[22] Q. Zhang, F. Sun, C. Chen, Research on the three-dimensional wall temperature distribution and low-temperature corrosion of quad-sectional air preheater in larger power plant boilers, Int. J. Heat Mass Transf. 128 (2019) 739–747. doi:10.1016/j.ijheatmasstransfer.2018.09.006.

[23] R.K. Shah, D.P. Sekulic, Fundamentals of Heat Exchanger Design, John Wiley & Sons Inc., 2003.

[24] J.L. Niu, L.Z. Zhang, Heat transfer and friction coefficients in corrugated ducts confined by sinusoidal and arc curves, Int. J. Heat Mass Transf. 45 (2002) 571–578. doi:10.1016/S0017-9310(01)00177-6.

AN EXPERIMENTAL STUDY ON OVERALL HEAT TRANSFER COEFFICIENT OF SOME WALL BRICK MODELS

Amir RAHMANPARAST*, Burhan ÇUHADAROĞLU*, Furkan Erman KAN*
*Karadeniz Technical University, Department of Mechanical Engineering, Trabzon/Turkey
Email: rahmanparast@ktu.edu.tr, burhan@ktu.edu.tr, fekan@ktu.edu.tr

ABSTRACT

It is known well that the majority of the heat losses of buildings occur at outer walls, which are made of a few layers such as plaster, wall bricks, insulation material, etc. It is expected that the wall bricks having a low overall heat transfer coefficient to reduce heat losses through buildings in order to increase building heating performance. To achieve this expectation, the wall bricks are produced with materials with low thermal conductivity and cavity (hole), which weakens the thermal transport mechanism. This study, it is aimed to decrease the overall heat transfer coefficient of wall brick models with various cavities, which affect the natural convection mechanism. For this purpose, some changes are made to the cavity geometry of a single cell of the hollow wall brick model. The proposed geometries' heat transfer experiments were repeated under three different (7, 9, 12 W) thermal powers. The building is simulated as an insulated chamber made of styrofoam with 300 mm x 300 mm x 300 mm. The wall brick models are produced from PVC (decota) material in 160 mm x 160 mm x 50 mm and mounted to a wall of the insulated chamber. The experiments are carried out on the brick models having the cavity geometries of regular symmetrical I profile and asymmetrical Z profile. The temperatures are measured at 3 points on both sides of the brick models. It has been measured that the overall heat transfer coefficient of the Z model is lower than that of the regular I profile at 7.1%, depending on the heat transfer direction.

Keywords: Hollow wall brick, Inclined cavity, Thermal insulation, Heat transfer direction, Energy saving.

1. INTRODUCTION

The bricks are building elements that are used frequently in building constructions. In addition to creating independent sections in buildings, the bricks also have an important role in buildings' thermal performance. Heat losses through buildings should be calculated carefully, as well as energy performance analysis of buildings. Heat losses occur through the floor, ceiling, window, etc., as well as walls. It is expected that building walls should have a low overall heat transfer coefficient to save energy. Therefore, the lower overall heat transfer coefficient of bricks forming walls in buildings means that buildings' energy performance is high. When the heat transfer mechanism in building bricks is examined, it is seen that it has a periodic structure such as conduction in solid walls and convection in air space following it. It is well known that to reduce the overall heat transfer in this kind of structure, materials having a low heat conduction coefficient should be used, or some specific cavity geometry should be designed to reduce heat conduction. It is clear that a combination of these concepts may obtain the best thermal performance of bricks. Fourier's law defines the heat transfer through multi-layered and spaced materials as:

$$\dot{Q} = UA\Delta T \tag{1}$$

Here $\dot{Q}$ (W) represents transferred heat, ΔT (˚C) refers to the temperature difference in the direction of heat transfer and U (W/m^{2}K) refers to the overall heat transfer coefficient. The overall thermal resistance R_{equ} (m^{2}K/W) is defined as follows:

$$U = \frac{1}{R_{equ}} \tag{2}$$

$$R_{equ} = [\frac{L_1}{k} + \frac{1}{h_1} + \frac{L_2}{k} + \frac{1}{h_2} + \cdots + \frac{1}{h_n} + \frac{L_n}{k}] \quad (3)$$

Here the L_n (1, 2,.., n) is the inner part thicknesses of the brick separating the spaces, and k is heat conduction coefficient of the brick material. The h_n_(1,2,…, n) which varies depending on the natural convection in the spaces, refer to heat conduction coefficients on solid surfaces of the space cells.

The majority of the studies on the subject are performed as numerical modeling and experimental in the literature. In the numerical study by Al-Hazmy [1], the heat transfer was studied on three different bricks' configurations. The study was conducted locally at the summer climatic data of the city of Jeddah, Saudi Arabia. He revealed that the heart rate through hollow building blocks could be reduced 36% when polystyrene bras filled inside the cavities. Ait-Taleb et al. [2] studied heat transfer in brick with two vertical and three horizontal cavities under the condition of constant heat flux from the lower or upper surface. They used different distributions of spaces as parameters and obtained that the hollow block with two air cells deep in a vertical direction reduces heat transfer from inside to the outside of the building roofs. Arici et al. [3] performed a thermal analysis on building bricks with unequally ordered holes experimentally and numerically. They obtained that the most suitable configuration to increase thermal resistance is to configure the expansion of the gaps in the heat transfer direction. The worst one is to configure an arrangement just opposite of it. Gossard and Lartigue [4] developed a three-dimensional numerical model for coupled heat transfer in building components with air-filled vertical cavities and verified the model's validity with the experiments.

The numerical studies should be verified and validated by the experimental studies, which have an important role in the literature. Vivancos et al. [5] studied heat transfer on different types of clay and concrete bricks using a common measurement method and developed a model based on experimental data. The study presented by Morales et al. [6] gives some information on geometrical arrangements of the partitions of bricks. According to the results of this study, thermal bridges must be avoided in the brick. A small gap in the brick assembly also notably improves the brick's conductivity; the greater the number of rows, the greater this improvement.

The present study, it is aimed to increase the thermal resistance by reducing the heat transfer in the cavities. The study was carried out experimentally, considering a single cavity of the brick. The brick cavity was examined with two models divided by a diagonal plate, and the other one is a standard model, which was considered for comparison.

2. EXPERIMENTAL SETUP

Two types of brick models with different internal geometries were designed by SolidWorks code. One of them is a regular model with asymmetrical cavity geometry and referred to as Type I and used for comparison. The brick model has asymmetrical cavity geometry referred to as Type Z, divided diagonally, as seen in Figure 1. Both types of bricks used in the experiments are produced PVC-foam material using laser cutting and bonding techniques on ready-made plates. Firstly, the bricks models' mainframe is constructed, then the inner cavity has been divided with a plate. Type I model has two equal rectangular partitions, while Type Z has two equal triangle partitions. The images of the models produced in this study are seen in Figure 2.

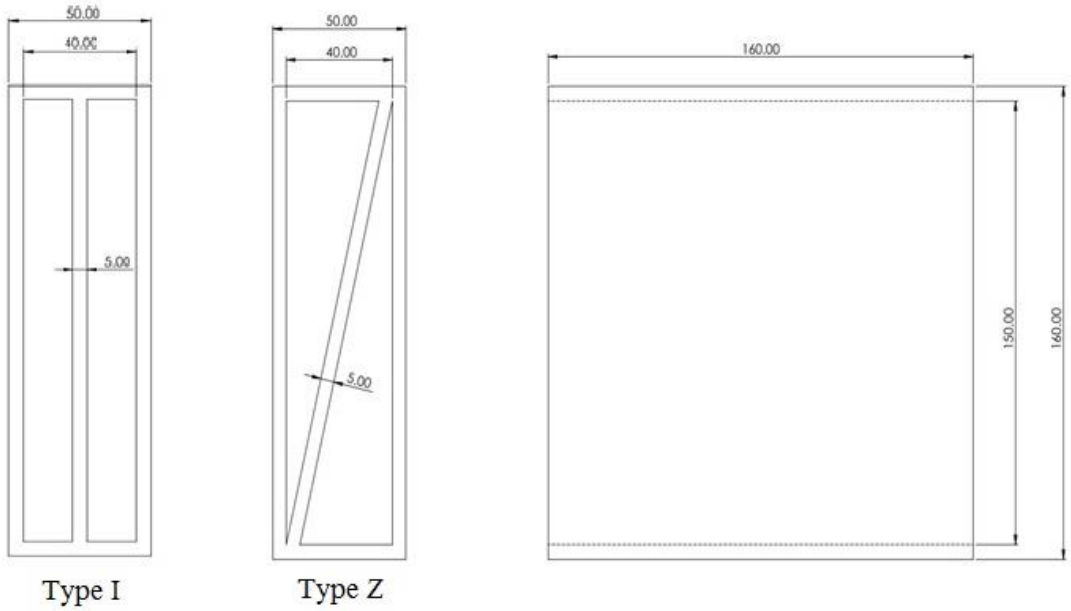

Figure 1. SolidWorks design of the models

Figure 2. The Brick models

The experimental chamber with dimensions of 400x400x400 mm has been designed to simulate the building and keep the thermal power passing through the brick constant. Technical drawings and views of the designed room are presented in Figures 3 and 4. The all chamber is made of thermal insulation material to maintain all thermal power to pass through the brick model in the wall. It is aimed to provide absolute insulation on other surfaces by covering with plaster material except for the part of the room where the brick is placed. Thus, it is accepted that all thermal power coming from the heater placed in the chamber volume center passes over the brick by neglecting the cable losses.

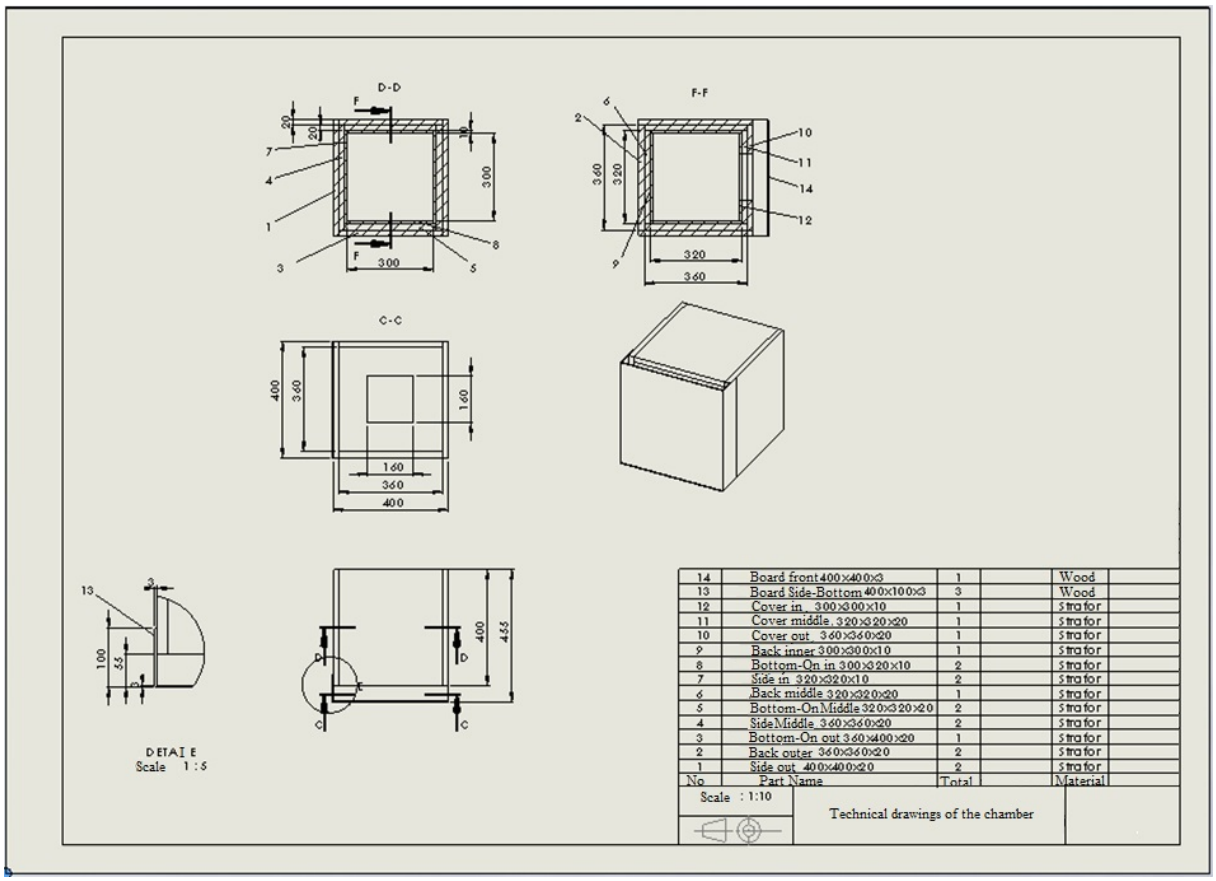

No	Part Name	Total		Material
14	Board front 400×400×3	1		Wood
13	Board Side-Bottom 400×100×3	3		Wood
12	Cover in 300×300×10	1		Strafor
11	Cover middle 320×320×20	1		Strafor
10	Cover out 360×360×20	1		Strafor
9	Back inner 300×300×10	1		Strafor
8	Bottom-On in 300×320×10	2		Strafor
7	Side in 320×320×10	2		Strafor
6	Back middle 320×320×20	1		Strafor
5	Bottom-On Middle 320×320×20	2		Strafor
4	Side Middle 360×360×20	2		Strafor
3	Bottom-On out 360×400×20	1		Strafor
2	Back outer 360×360×20	2		Strafor
1	Side out 400×400×20	2		Strafor

Figure 3. Technical drawings of the chamber

Figure 4. Insulated chamber and the wall which brick model is mounted

The heater cartridge to provide constant heat input to the system is connected to a power source that can be adjusted for voltage. The heater cartridge is placed in the chamber's volume center through the circular section that opened in dimensions suitable for insulation on the upper surface of the chamber. The brick models with different cavity geometries that have been created were placed in the chamber where the thermal power was kept constant, in a square section space prepared in 160x160x50 mm dimensions on a wall, so that it has been modeled as the wall of the room. To prevent the incorrect temperature measurements on the outer surface of the brick model, which is affected by the outer air circulation, a guarded plate is mounted on the surface. The schematic and image of the experimental setup are shown in Figures 5 and 6.

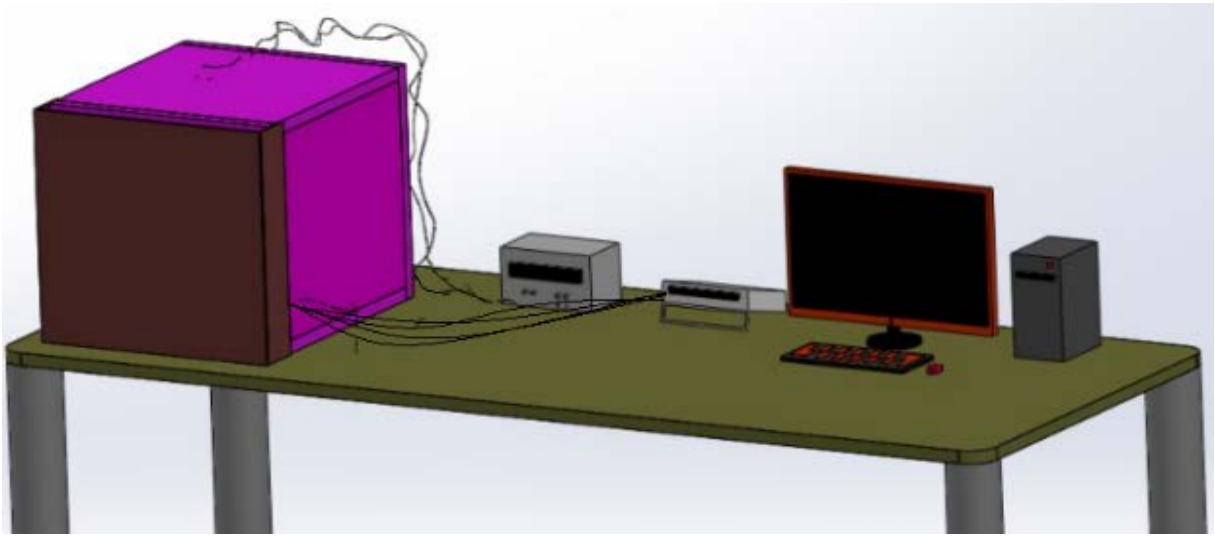

Figure 5. The schematic of the experimental setup

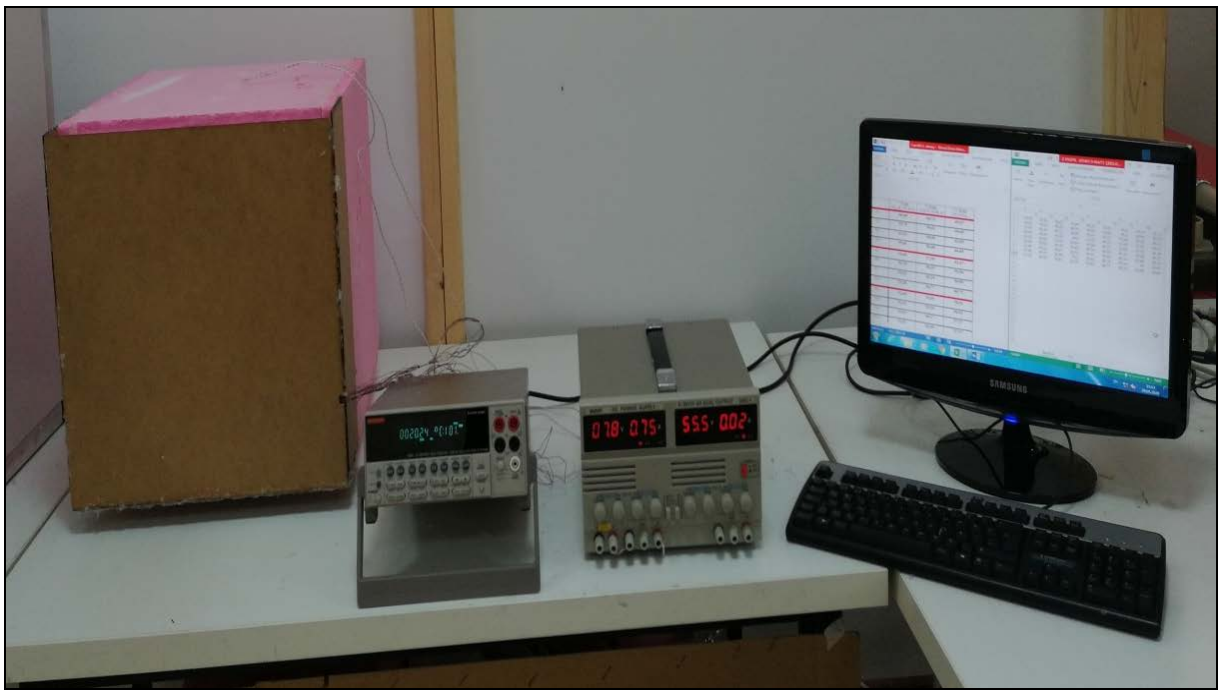

Figure 6. A view of experimental setup

Temperature measurements were taken from the brick surfaces to determine the overall heat transfer coefficient in equation 1. The K-type thermocouples are used for temperature measurements at 6 points and logged as data onto a computer for acquisition. The thermocouples are positioned on the surfaces' vertical mid-axis, which is one at the center, and the others are 40 mm above and below this point. The average surface temperatures were determined from the three surface temperatures. The locations of the temperature measurements are seen in Figure 7.

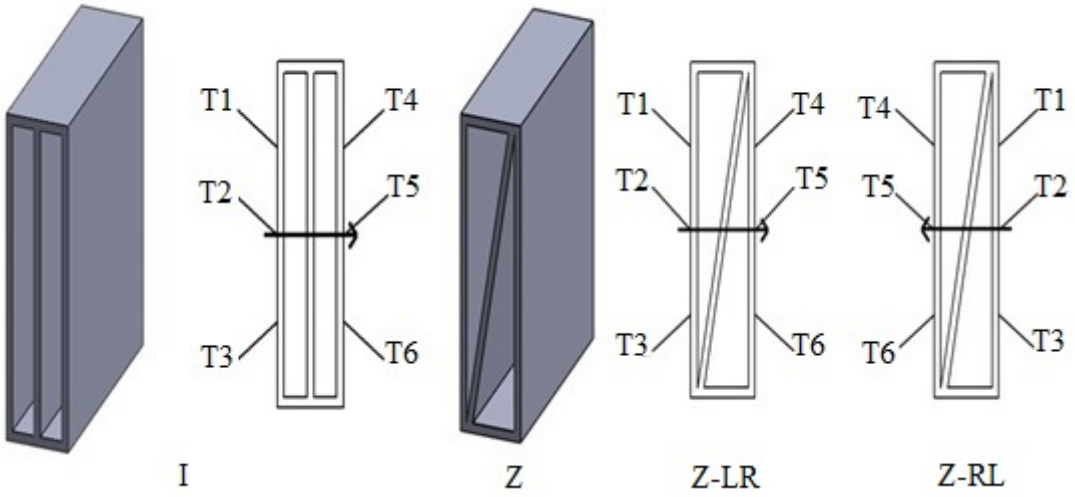

Figure 7. Thermocouple locations

3. RESULTS AND DISCUSSION

The brick models surface temperatures were measured at three heat power of 7, 9 and 12 W, which is generated by a heater in the insulated chamber. The overall heat transfer coefficient was calculated with the difference of the average temperatures of the surfaces. It can be obtained from equation (1) as $U = \dot{Q}/(A\Delta T)$ depending on the surface area A of the brick model and heat power $\dot{Q}$ and temperature difference ΔT. The surface area of the brick models is A = 0.16 m x 0.16 m = 0.0256 m^2.

The overall heat transfer coefficients of the models have been determined for three different configurations and three different heat power conditions as it is known well that the U value is used as an important parameter for the analysis of the thermal performance of a building. A certain level of U directly results in positive effects on heat energy savings and environmental issues. In this context, it has been experimentally determined the overall heat transfer coefficients of the symmetrical and asymmetrical models have been in Figure 7. The present study hypothesizes that the U depends on heat transfer direction for asymmetrical brick configurations such as the Type Z model. To confirm this hypothesis, the brick model of Type Z has been tested for heat powers in two different directions a right to left and left to right. The U variations, which are seen in Figure 8, reveal that the Z models' overall heat transfer coefficients are lower than the regular I profile for all heat powers. Also, it is seen that the lowest U values are obtained for the heat power right to left (Z-RL). This result confirms the hypothesis of the U depends on heat transfer direction in asymmetrical hollow bricks.

Figure 9 shows that there is about a 7 % decrease of the U value for the Z-RL configuration compared to the regular I profile, which means heat saving in buildings and economy at heating systems directly. According to the U and T, the sequential diagram representation of the brick models is presented in Figure 10. Comparing the U variations of the brick models with different internal structure geometries considered in this study, it is seen that the overall heat transfer coefficient U decreases with chancing internal structure geometry from symmetrical (regular) to asymmetrical (diagonal).

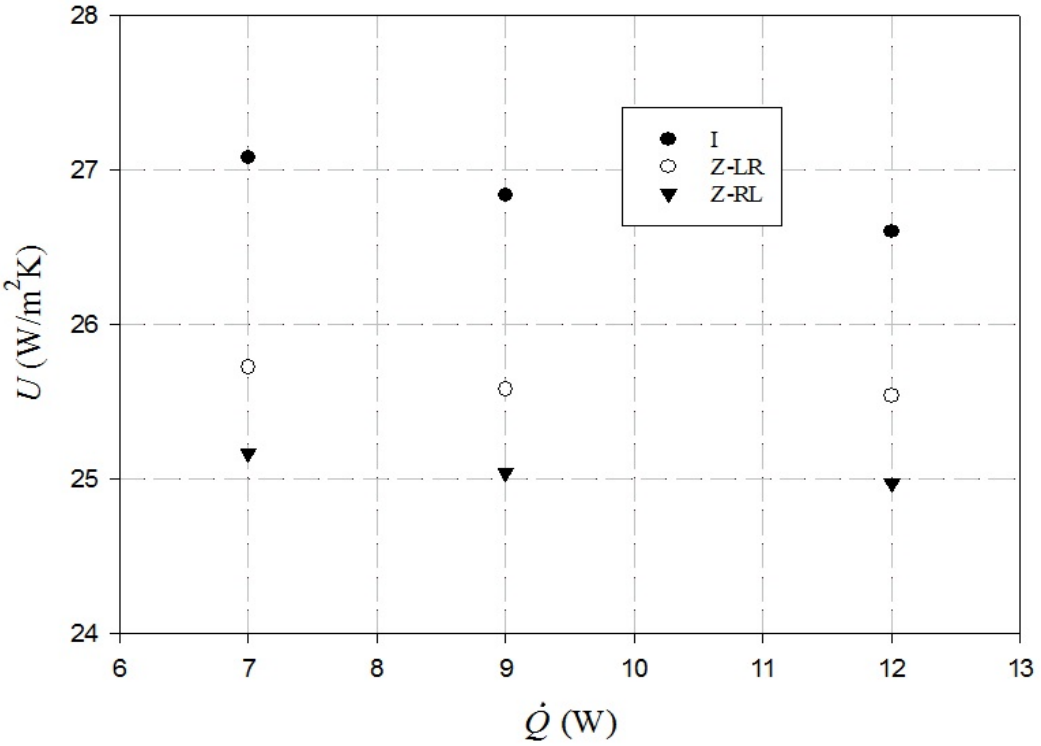

Figure 8. The normalized U variations versus the rate of heat transfer

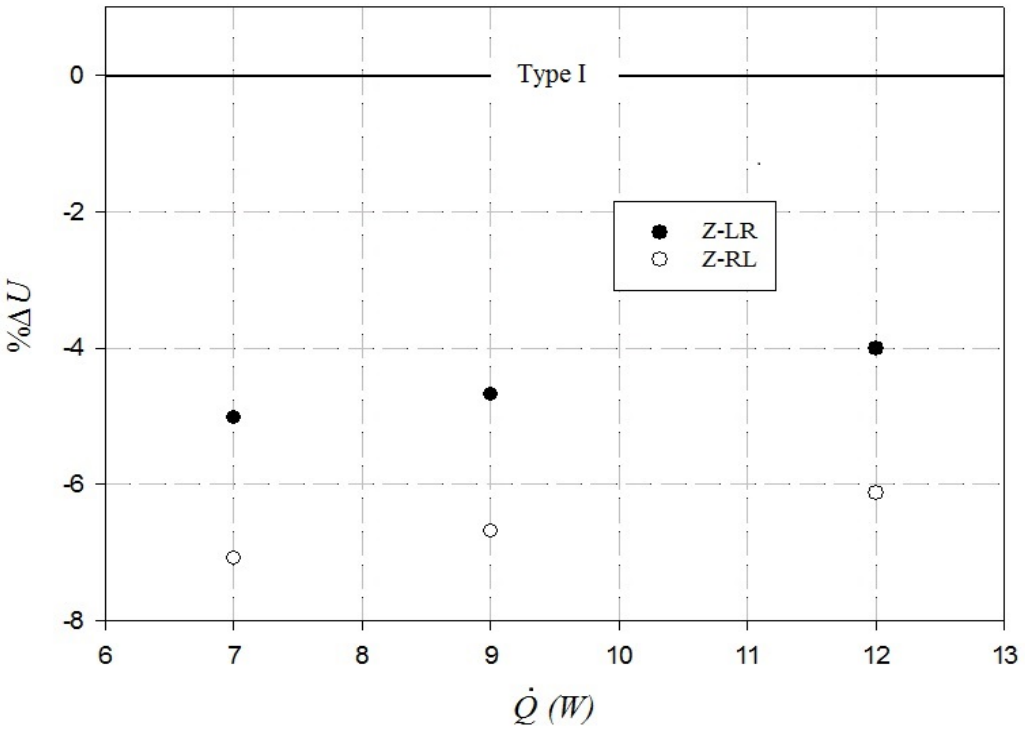

Figure 9. The normalized U variations versus the rate of heat transfer

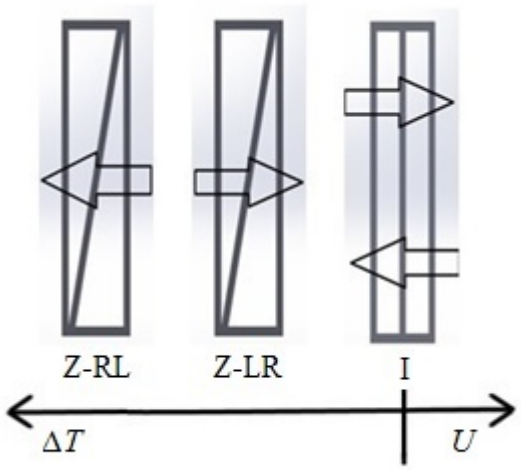

Figure 10. Sequential view of the brick models

The findings obtained from the study can be summarized as follows:

- The overall heat transfer coefficients of bricks models considered in the study decreases with increasing heat power.
- The overall heat transfer coefficient of the asymmetrical brick model is lower than the regular symmetrical brick model.
- The overall heat transfer coefficient of the asymmetrical brick model depends on heat transfer direction.
- The bricks having asymmetrical internal structure may provide heat saving in buildings.

REFERENCES

[1] Al-Hazmy, M. M., Analysis of Coupled Natural Convection-Conduction Effects on The Heat Transport Through Hollow Building Blocks, *Energy and Buildings*, **38** (5), 515-521, 2006.

[2] Ait-Taleb, T., Abdelbaki, A. & Zrikem, Z., Simulation of Coupled Heat Transfers in a Hollow Tile with Two Vertical and Three Horizontal Uniform Rectangular Cavities Heated from Below or Above, *Energy and Buildings*, **84**, 628-632, 2014.

[3] Arıcı, M. E., Kan, F. E., Candemir, A. E. & Özkan, E. Eşit Boyutlu Olmayan Ardışık Boşluklara Sahip Bir Tuğlada Isı Transferi, *22th Congress on Thermal Science and Technology*, Kocaeli-Turkey, 2019

[4] Gossard, D. & Lartigue, B., Three-Dimensional Conjugate Heat Transfer in Partitioned Enclosures: Determination of Geometrical and Thermal Properties by Inverse Method, *Applied Thermal Engineering*, **54** (2), 549-558, 2013.

[5] Vivancos, J., Soto, J., Perez, I., Ros-Lis, J. V. & Martinez-Manez, R., A New Model Based on Experimental Results for The Thermal Characterization of Bricks, *Building and Environment*, **44** (5), 1047-1052, 2009.

[6] Morales, M. P., Juarez, M. C., Lopez-Ochoa, L. M. & Domenech, J., Study of The Geometry of a Voided Clay Brick Using Rectangular Perforations to Optimize its Thermal Properties, *Applied Thermal Engineering*, **31**, 2063-2065, 2011.

THE EFFECT OF THE VARIOUS ARRANGEMENTS OF THE LITHIUM-ION BATTERY PACK ON THE COOLING PERFORMANCE

Ahmet AKTÜRK*, Mehmet Emin ARICI, Furkan Erman KAN****
*Iğdır University, Department of Mechanical Engineering, Iğdır/Turkey
Email: aakturk@igdir.edu.tr
**Karadeniz Technical University, Department of Mechanical Engineering, Trabzon/Turkey
Email: arici@ktu.edu.tr, fekan@ktu.edu.tr

ABSTRACT

There is a growing interest in high-efficiency, long-lasting, and safe energy storage systems used in various applications such as transportation, aviation, and grid energy storage. Batteries, which are electrochemical energy storage devices, play a vital role in meeting this interest. The operation temperature directly affects the efficiency, lifetime, and safety of the battery pack. Thus, heat removal from the battery surfaces is of great importance to eliminate the harmful effects of over temperature and to keep the battery pack in the desired temperature range during the operation. In this study, the cooling problem of a lithium-ion battery pack was numerically investigated using the air as the coolant in a rectangular duct. Two different staggered arrangements and the in-line arrangement of the battery pack were applied separately. Heat removal from the cell surfaces was compared for the prescribed arrangements under the same hydrodynamic condition. The finite control volume-based numerical solution was used to solve the forced convection heat transfer for the cross-flow through the battery pack in a three-dimensional domain. Solutions of the governing and the auxiliary equations were carried out by using the ANSYS/Fluent software. In ANSYS/Fluent, a constant heat generation of 52000 W/m^3 was assigned for each cell in the pack. The results showed that the battery packs using two different staggered arrangements had further improvement in heat transfer up to 12.07% compared to the in-line arrangement.

Keywords: Lithium-ion battery, heat transfer enhancement, thermal management, cooling, CFD

1. INTRODUCTION

The growing human population and increasing human comfort demands lead to an increase in energy needs. Fossil fuels are among the most widely used sources to compensate for this need. However, the use of fossil fuels pollutes the environment by increasing emissions of pollutants. Besides, the rapid depletion of fossil fuels poses a severe energy crisis threat. The oil used in transportation corresponds to approximately two-thirds of oil consumed in the world today [1]. For years, the interest in clean energy resources has been gaining momentum in the transportation sector to reduce environmental pollution and to eliminate the possible energy crisis. Electric vehicles (EV), plug-in hybrid electric vehicles (PHEV), and hybrid electric vehicles (HEV) are more environmentally friendly and higher energy-efficient compared to internal combustion engine vehicles [2]. The primary step of creating such electric and clean energy vehicles is to determine and implement the appropriate energy storage system. Although various battery systems such as lead-acid (Pb-acid), nickel-metal hydride (Ni-MH), sodium-based and, lithium-ion (Li-ion) have been proposed as power sources for this task [3], Li-ion batteries are the most prominent candidate due to their higher energy and power densities, longer cycle life and lower self-discharge rates [4]. Because of these superior features, lithium-ion batteries are used quite frequently not only in electric vehicles but also in almost all portable electronics, aerospace applications and, energy storage areas as well [5]. Despite its widespread use and outstanding features, the undesirable operating temperature can adversely affect the performance, safety and, calendar life of Li-ion batteries. To clarify, the risk of thermal runaway increases in lithium-ion batteries operating at elevated temperatures, and severe power losses and performance deterioration occur in Li-ion batteries that operate below 0 ◦C [6]. Maintaining the thermal stability of the battery pack with the fluctuating temperature values is one of the essential elements that is taken into account when creating the pack.

High temperatures cause safety concerns and shorten the calendar life of the battery packs to a considerable extent and therefore it is incredibly essential to remove the heat produced by the battery packs from the system. Otherwise, heat accumulates in the pack and causes excess temperature [5,6]. In the literature, some studies have been conducted on the operating temperature of the single-cell and battery pack, and some restrictions have been proposed due to these studies. Väyrynen et al. [7] stated that current Li-ion batteries operate between -20 ◦C to 60 ◦C in practice. Pesaran et al. [8] underlined that Li-ion batteries maintain their optimum performance in a narrower temperature range of 15 ◦C -35 ◦C. Molotch et al. [9] examined the calendar life of Li-ion batteries in the 30 ◦C - 40 ◦C range and found that 1 ◦C increase in the operating temperature reduced the battery life by two months. Pesaran [10] proposed in another study that the temperature difference between the modules of the battery pack should be less than 5 ◦C. Moreover, uniform temperature distribution between cells in the pack is vital in reaching the maximum cycle life [11]. Besides, Yang et al. [12] found that the capacity loss rate increases with the non-uniform temperature distribution between the cells.

Researchers studied different types of cooling systems in order to ensure more uniform temperature distribution and to keep the battery pack under thermal control as desired. These can be listed as air-cooled systems, liquid-cooled systems, heat pipe systems, phase change applications, or hybrid medium systems. Air-cooled systems have a relatively simple structure, easy maintenance and, low-cost advantage compared to other systems. Because of these advantages, the air-cooled systems have a relatively wide range of application fields in battery pack cooling techniques. The air-cooled system may apply as natural convection cooling or as forced convection cooling. Pack configuration, the distance between cells, connection type of cells, air inlet speed, air inlet temperature and, discharge rate are the parameters to be considered in the design of air-cooled thermal management systems [13]. Utilizing forced air convection, Tong et al. [14] created a lithium-ion battery pack with an active thermal management system. They showed that the maximum temperature variation in the pack is reduced by regulating the cells with a staggered design. Li et al. [15] worked out on an air-cooled battery pack model. They found that the air at a velocity of 5 m/s reduces the maximum temperature increment in the package up to 8.4 °C and decreases the temperature difference between the cells up to 3 °C for the velocity of 1 m/s. Park [16] simulated the forced flow of air through the several shaped channels to compare cooling effects. He found that the tapered manifold adopted geometry is the best among the others. Fan et al. [17] examined the effects of the gap spacing between the cells and the effect of flow rate on the cooling performance of the thermal management system for a forced flow of air. They displayed that the model that cells were placed at an even gap spacing of 3 mm and two-sided cooling was applied with a volume flow of 40.8 m^3/h provides excellent cooling.

In this study, it was aimed to find out an efficient geometric arrangement for thermal management of battery packs cooling by placing the cells in different positions. The effect of the in-line arrangement, the zigzag-staggered arrangement, and the extended-staggered arrangement on the cooling performance were numerically investigated by using the air as the coolant. A 3D-CFD model was developed for the numerical solution. All arrangements were examined for air velocity of 1.5 m/s, 2 m/s and 2.5 m/s. In addition to the literature, thermal conductivity values were defined for the x, y, and z directions using the orthotropic thermal conductivity option for all the batteries placed in the in-line arrangement, novel zigzag-staggered arrangement, and the extended-staggered arrangement.

2. DESIGN OF THE BATTERY PACKS

The intended thermal management problem cases of this study are illustrated in Figure 1, Figure 2, and Figure 3. An in-line arrangement and two different staggered arrangements were considered as the study cases. ANSYS / Fluent CFD package was used to model a 3D conjugate heat transfer mechanism. All cells shown in Figure 1, Figure 2, and Figure 3 are cylindrical Li-ion cells consisting of LiFePO4/C cathode and anode. The diameter of each cell is D = 18 mm, and height is 65 mm.

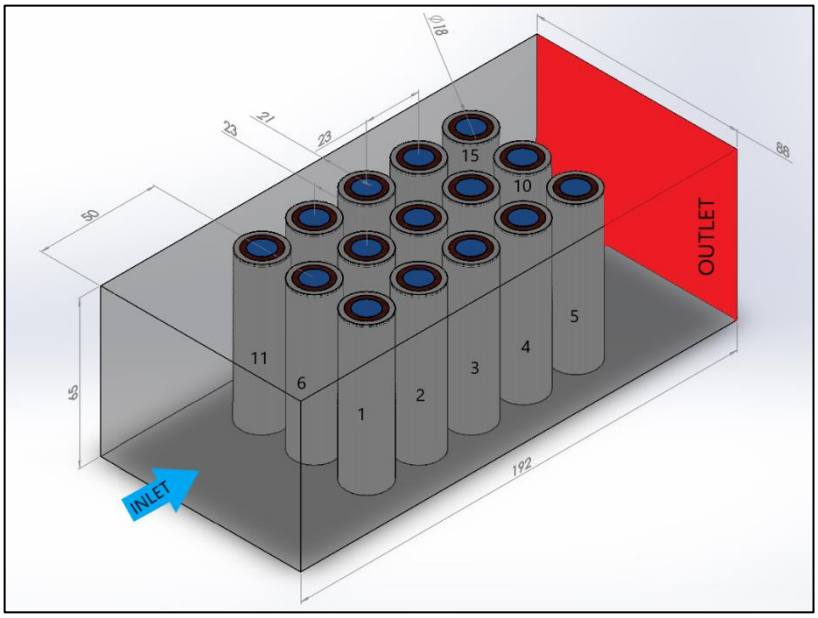

Figure 1. The test section of in-line arrangement, dimensions in mm.

Each battery pack consists of 15 commercial Lithium Iron Phosphate (LFP) cells with 5P3S electrical configuration (5 cells in parallel and 3 cells in series) for the current operation. The cell group created by connecting 5 cells in parallel is assumed to form a module.

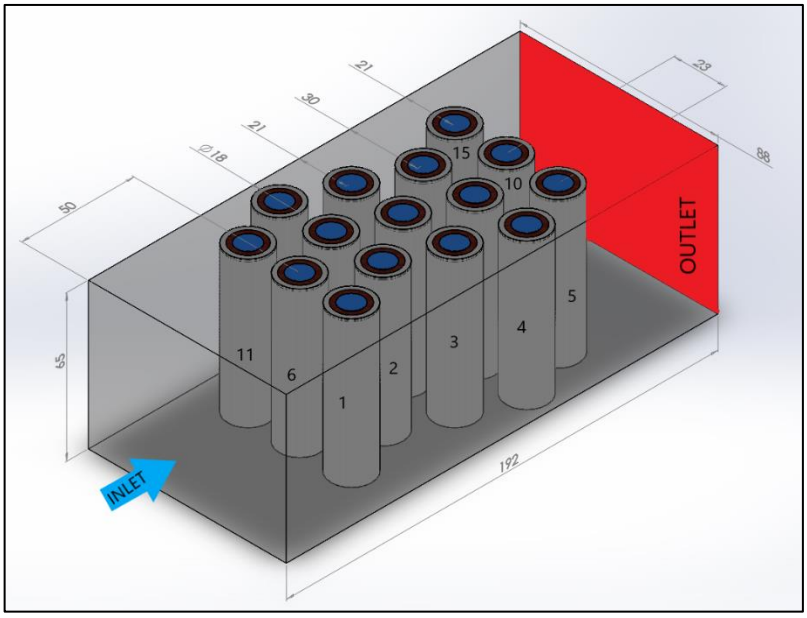

Figure 2. The test section of the zigzag-staggered arrangement, dimensions in mm.

The rated voltage and capacity of the battery pack were 9.6 V and 6 Ah, respectively. As in Reference [6], the average density, the average specific heat, and the heat transfer rate for the battery electricity core can be calculated. Because of the small size and low heat generation rate of negative and positive terminals compared to the electricity core, they were excluded in the simulation for simplicity.

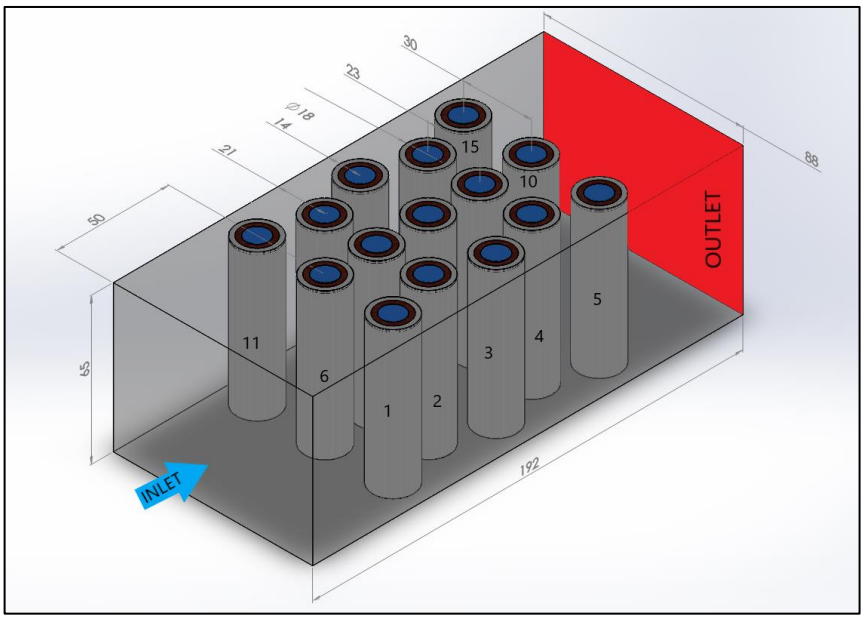

Figure 3. The test section of the extended-staggered arrangement, dimensions in mm.

In Table 1, the thermophysical properties of the electricity core at 298 K and heat generation rate at 3C discharge are given [6]. In this numerical study, cylindrical cells were considered to consist of a single material of electricity core. Each cell in the pack was assumed to produce 52000 W/m^3 of heat at 298 K and the discharge rate of 3C. Additionally, the directional dependence of thermal conductivity is indicated in the table.

Table 1. Thermophysical properties and heat generation rate of the selected material at 298 K temperature and 3C discharge rate.

Material	**Density ρ $(\frac{kg}{m^3})$**	**Specific Heat c $(\frac{J}{kg.K})$**	**Thermal Conductivity k $(\frac{W}{m.K})$**	**Heat Generation $\dot{q}(\frac{W}{m^3})$**
Electricity core	2000	900	$k_X = k_Z = 1.6$ $k_y = 3$	52000

In the first three figures, it is shown that 15 cells are placed with various arrangements in the rectangular duct having 192 mm length, 88 mm width, and 65mm height.

3. NUMERICAL MODEL

3.1. Boundary Conditions and Mesh Structure

The numerical study was carried out under adiabatic and no-slip channel wall, velocity inlet, and outflow boundary conditions. The mesh size was selected to sustain that the obtained temperature field is independent of the size. The quadrilateral mesh structure option was used for both core and edge regions. Also, 10-layer inflation with a maximum thickness of 1mm was applied around all cells and walls using the inflation option. Figure 4 shows that the inflation option was applied on duct walls and around cells. The reason for using the inflation option around the cells was to model the flow boundary layers and to keep the y^+ values in the acceptable range on battery surfaces.

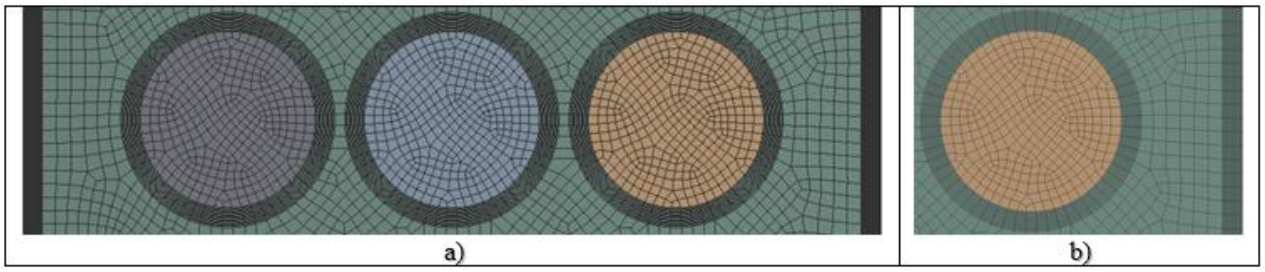

Figure 4. a) View of cells and walls with inflation from In-line arranged pack. **b)** Detailed mesh structure of cell with inflation.

For a Realizable k-ε turbulent model with an enhanced wall treatment option, y^+ values were found to be lower than 5. The value of y^+ <5 indicated that the mesh structure was fine and velocity, and pressure gradients were correctly estimated in the boundary layers [18].

3.2. Mathematical Model

The continuity, the momentum, and the energy equations under steady-state conditions for the forced flow of air are as follows:

Continuity Equation;

$$\nabla \cdot \left(\rho \vec{V}\right) = 0 \tag{1}$$

Momentum Equation;

$$\rho \nabla \cdot \left(\vec{V}\vec{V}\right) = -\nabla P + \nabla \cdot \left[(\mu + \mu_t)\left(\nabla \vec{V} + \nabla \vec{V}^T\right)\right] \tag{2}$$

Energy Equation;

$$\nabla \cdot (\rho c_p \vec{V} T) = \nabla \cdot \left[(k + k_t)\nabla T + \left(\bar{\bar{\tau}}_{eff} \cdot \vec{V}\right)\right] + q_g \tag{3}$$

where $\vec{V}$ is the velocity vector, μ_t is the eddy viscosity, k_t is the turbulent thermal conductivity, and q_g is the heat generation rate of the cell. The second term on the right-hand side of the momentum equation represents the stress tensor and the second term on the right-hand side of energy equation represents energy transfer due to viscous dissipation [19,20].Due to the its excellent performance to numerically solve flows involving rotation, separation, recirculation, and reverse pressure gradients, the Realizable k-ϵ model with enhanced wall treatment was chosen as the turbulence model to determine μ_t and k_t model for this particular problem [18].

4. RESULTS AND DISCUSSIONS

The x-z plane temperature contours at y = 0.0325 m for velocity of 1.5 m/s, 2 m/s, and 2.5 m/s are illustrated in figures 5, 6, and 7, respectively. Under all prescribed hydrodynamic conditions, the highest temperature of the battery pack occurs across the midline of the duct. For visual convenience, temperature variations are given in a single scale for arrangements with the same airflow rate.

Figure 5 shows that with 298 K air inlet temperature, zigzag-staggered arrangement and extended-staggered arrangement have a better cooling performance than the in-line arrangement at the velocity of 1.5 m/s. In in-line arrangement and extended-staggered arrangement, the middle row batteries show a blocking effect. Therefore, the cells with the highest temperature in these packs are in the cells along the middle part. The cell-numbered 10 in the in-line arrangement and the cell-numbered 8 cells in the extended-staggered arrangement have the highest temperature values considering the area-weighted average. In the zigzag-staggered arrangement, unlike the other arrangements, the temperature values of two cells numbered 10 and numbered 14, are close to each other. These cells have the highest temperature values. Although, for all arrangements, considering the air inlet temperature 298 K and the maximum temperature points, the maximum temperature difference in the battery packs are 7.311 K for in-line arrangement, 6.707 K for zigzag-staggered arrangement, and 6.428 K for extended-staggered

arrangement. It is found that the average temperature difference between the cells is less than 5 K for all arrangements according to the contour distribution and temperature scale of the packs, and is therefore within the acceptable range.

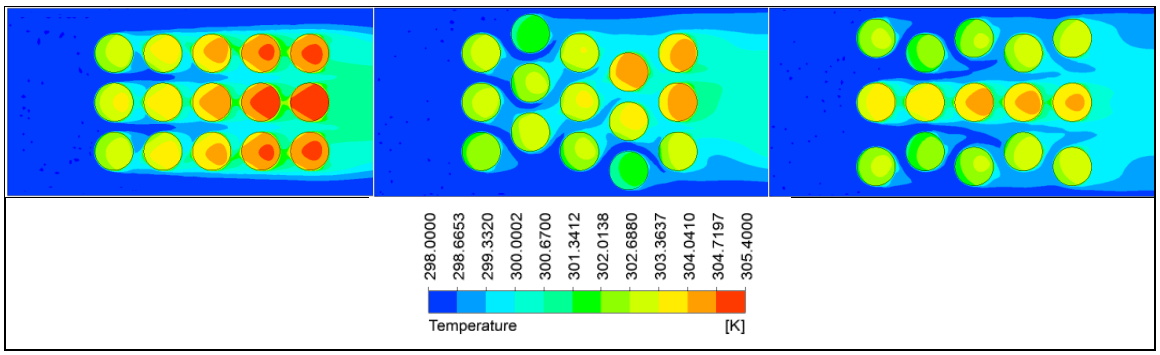

Figure 5. Temperature contours of Lithium-ion Battery Pack for V=1,5 m/s, a) The in-line arrangement, (b) The zigzag-staggered arrangement, (c) The extended-staggered arrangement.

Similar to the velocity of 1.5 m/s, it can be seen in Figure 6 that both staggered arrangements show better cooling performance than the in-line arrangement for the velocity of 2 m/s. By observing, the area-weighted average, it can be seen that the same numbered cells have maximum temperatures for packs with the same arrangement as in the airflow rate of 1,5 m/s. The maximum temperature difference in the battery packs is 6.042 K for in-line arrangement, 5.597 K for zigzag-staggered arrangement, and 5.476 K for extended-staggered arrangement. In addition, temperature contours and temperature scale are examined, and it is clear that the temperature difference between cells does not exceed 3.5 K.

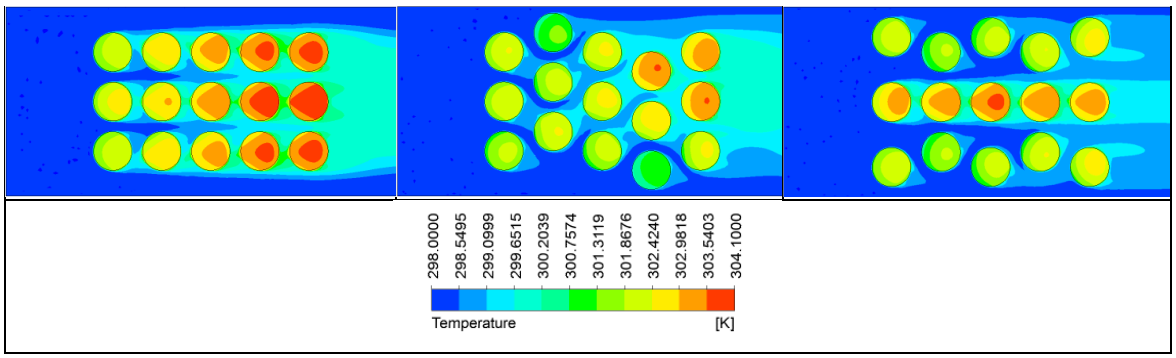

Figure 6. Temperature contours of Lithium-ion Battery Pack for V=2 m/s, a) The in-line arrangement, (b) The zigzag-staggered arrangement, (c) The extended-staggered arrangement.

The results in Figure 7 have a trend similar to those in Figure 5 and Figure 6. Since this is the case with the highest air flow rate, the heat removed from the cell surfaces is higher than in the other cases. Therefore, the temperature differences in the packs also decreased significantly. The maximum temperature difference in the battery packs is 5.428 K for in-line arrangement, 5.016 K for zigzag-staggered arrangement, and 4.911 K for extended-staggered arrangement. Besides, considering all the arrangements, it can be stated that the maximum temperature difference between the cells is less than 3 K. Therefore, increasing air velocity tends to the uniformity of the temperature in all arrangements.

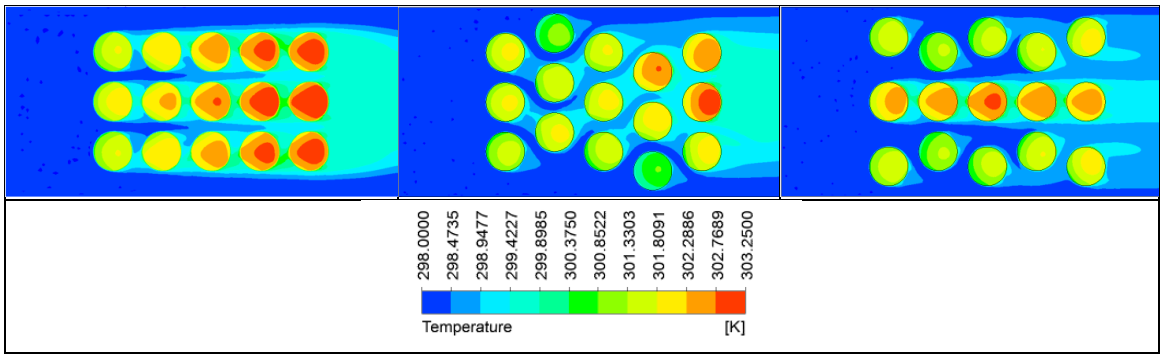

Figure 7. Temperature contours of Lithium-ion Battery Pack for V=2,5 m/s, a) The in-line arrangement, (b) The zigzag-staggered arrangement, (c) The extended-staggered arrangement.

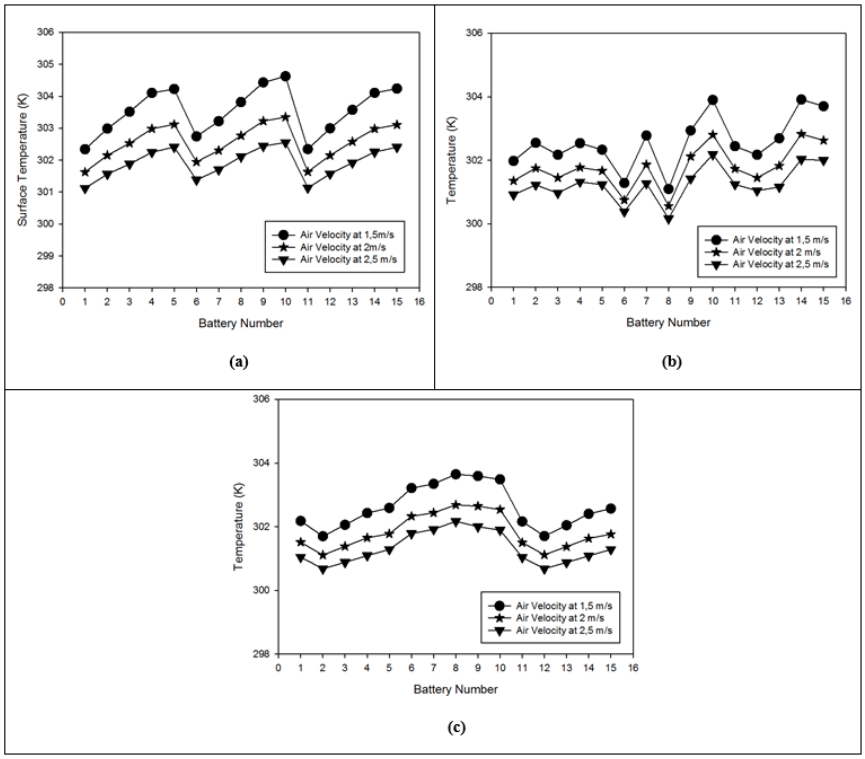

Figure 8. The area-weighted average surface temperature of each cell; (**a)** The in-line arrangement, (**b)** The zigzag-staggered arrangement, and (**c)** The extended-staggered arrangement.

Illustrations in Figure 8 show the area-weighted average temperature values of cell surfaces versus the battery numbers marked in Figure 1, Figure 2, and Figure 3. Figure 8 indicates the best uniformity among the arrangements is the extended-staggered arrangement. Besides, the surface temperature for the symmetrically placed cells in the in-line staggered arrangement and the extended-staggered arrangement (1 and 11, 2 and 12, 3 and 13, 4 and 14 and 5 and 15) are almost the same. Unlike in-line and extended-arrangements, the zigzag-staggered arrangement is not symmetrical, so the symmetry in temperature does not exist. The in-line arrangement has the worst performance for all velocities. Comparing the zigzag-staggered arrangement and the extended-staggered arrangement, many cells in the zigzag- staggered arrangement are better cooled than the extended- staggered arrangement, but the maximum temperature difference in the pack is greater for the zigzag-staggered arrangement since the cells 10, 14, and 15 cannot be cooled as the other cells.

5. CONCLUSIONS

The effect of three arrangements on heat removal from the battery pack was examined under the same boundary conditions and the same geometric dimensions. A numerical study was repeated for the velocity of 1,5m/s, 2m/s, and 2.5 m/s. The results were concluded as follows.

1. The extended-staggered arrangement showed the best uniformity in temperature distribution for the prescribed velocities.

2. The obtained working temperature ranges from 300 K to 305.4 K were within the optimum performance temperature range given by Reference [8].

3. The obtained temperature difference between the modules for the prescribed velocities and the arrangements was less than 5 K, within the acceptable range given by Reference [10].

4. Compared to the in-line arrangement, the heat transfer enhancement was 12.07% for the extended-staggered arrangement and 8.2% for the zigzag-staggered arrangement.

5. From a geometrical point of view, the extended staggered followed by the zigzag staggered and the in-line staggered arrangements showed the best cooling performance. However, in the hydrodynamic aspect, the velocity effect on the cooling performance was more pronounceable in the in-line arrangement; the zigzag arrangement and the extended-staggered arrangement follow it.

REFERENCES

[1] Liu, H., Wei, Z., He, W., and Zhao, J., Thermal issues about Li-ion batteries and recent progress in battery thermal management systems: A review, *Energy Conversion and Management*, **150**, 304–330, 2017.

[2] Wada, M., Research and development of electric vehicles for clean transportation, *Journal of Environmental Sciences*, **21**(6), 745–749, 2009.

[3] Budde-Meiwes, H., Drillkens, J., Lunz, B., Muennix, J., Rothgang, S., Kowal, J., and Sauer, D. U., A review of current automotive battery technology and future prospects, *Proceedings of the Institution of Mechanical Engineers, Part D: Journal of Automobile Engineering*, **227**(5), 761–776, 2013.

[4] Gwon, H., Hong, J., Kim, H., Seo, D.-H., Jeon, S., and Kang, K., Recent Progress on Flexible Lithium Rechargeable Batteries, *Energy Environ. Sci*., **7**(2), 538–551, 2014.

[5] Akturk, A., and Turk, S., Comparison of an interval type-2 fuzzy sets and AHP Methods for material selection problem on Lithium Ion Batteries, *The International Conference of Materials and Engineering Technologies (TICMET'19)*, Gaziantep-Turkey, 2019.

[6] Wang, Z., Ma, J., and Zhang, L., Finite element model and simulation for a cylindrical Li-Ion battery, *IEEE Access: Specıal Sectıon on Battery Energy Storage and Management Systems*, **5**, 15372–15379, 2017.

[7] Väyrynen, A., and Salminen, J., Lithium ion battery production, *The Journal of Chemical Thermodynamics*, **46**, 80–85, 2012.

[8] Pesaran, A., Santhanagopalan, S. & Kim, G. H., Addressing the impact of temperature extremes on large format Li-Ion batteries for vehicle applications, 30*th international battery seminar*, Ft. Lauderdale-Florida-USA, 2013.

[9] Motloch, C. G., Christophersen, J. P., Belt, J. R., Wright, R. B., Hunt, G. L., Sutula, R. A., Duong, T., Tartamella, T. J., Haskins, H. J., and Miller, T. J., High-Power battery testing procedures and analytical methodologies for HEVs, *SAE 2002 Transactions Journal of Passenger Cars - Electronic and Electrical Systems*, **111**, 797-802, 2002.

[10] Pesaran, A. A., Battery thermal models for hybrid vehicle simulations, *Journal of Power Sources*, **110**(2), 377–382, 2002.

[11] Rao, Z., and Wang, S., A review of power battery thermal energy management, *Renewable and Sustainable Energy. Reviews*, **15**(9), 4554–4571, 2011.

[12] Yang, N., Zhang, X., Shang, B. B., and Li, G., Unbalanced discharging and aging due to temperature differences among the cells in a lithium-ion battery pack with parallel combination, *Journal of Power Sources*, **306**, 733–741, 2016.

[13] An, Z., Jia , L., Ding, Y., Dang, C., and Li, X., A review on lithium-ion power battery thermal management technologies and thermal safety, *Journal of Thermal Science*, **26**(5), 391–412, 2017.

[14] Tong, W., Somasundaram, K., Birgersson, E., Mujumdar, A. S., and Christopher Y., Thermo-electrochemical model for forced convection air cooling of a lithium-ion battery module, *Applied Thermal Engineering*, **99**, 672–682, 2016.

[15] Li, X., He F., Ma L., Thermal management of cylindrical batteries investigated using wind tunnel testing and computational fluid dynamics simulation, *Journal of Power Sources* ,**238**, 395–402, 2013.

[16] Park, H., A design of air flow configuration for cooling lithium ion battery in hybrid electric vehicles, *Journal Power Sources*, **239**, 30–36, 2013.

[17] Fan, L., Khodadadi, JM., Pesaran, AA., A parametric study on thermal management of an air-cooled lithium-ion battery module for plug-in hybrid electric vehicles, Journal of Power Sources, **238**, 301–312, 2013.

[18] Fluent 6.3 User's Guide, Fluent Corporation, Lebanon, New Hampshire, 2006.

[19] Hoffman, J. D., Numerical Methods for Engineers and Scientists, Second Edition, Marcel Dekker, New York, 2001.

[20] White, F. M., Viscous Fluid Flow, Second Edition, McGraw-Hill, 1991.

ARTIFICIAL NEURAL NETWORKS FOR DRYING CHARACTERISTICS DETERMINATION: AN APPLICATION IN FLUIDIZED BED DRYING

Atalay YILDIRIM* , Hamdi ERGÖK**
*Yıldız Technical University, Department of Mechanical Engineering, Istanbul/Turkey
Email: atalayy@yildiz.edu.tr
** Yıldız Technical University, Department of Mechanical Engineering, Istanbul/Turkey
Email: hamdi.ergok@std.yildiz.edu.tr

ABSTRACT

Drying has several usages of purpose, which are extending the shelf life of food products, reducing packaging costs and shipping weights, protecting original flavors and nutritional values. In recent years, with increased interest in organic foods, dried vegetables and fruits are in great demand. In this study, the drying characteristics of button mushrooms have been investigated in a fluidized bed dryer. Button mushrooms (Agaricus Bisporus) are a rich protein source and covers 37,7% of the world's fungal production. An experimental study was carried out in fluidized bed dryer at air temperatures of 45-50-55-60 °C at a constant air velocity of 6,5 m/s and constant 50 °C drying air temperature of 5.5-6.5-7.5 m/s. Mushrooms cut like a slab with a thickness of 5 mm and experimental drying times have been examined. Experimental data were used as inputs of an artificial neural network and then a network was trained. With the help of the trained network, the best experimental conditions were selected by calculating the error rates between the inputs and outputs. Thus, test costs, equipment usage rates and energy consumption were reduced.

Keywords: Mushroom, Drying, Fluidized bed dryer, Drying characteristic, Artificial Neural Networks.

SYMBOLS

D_{eff}	Diffusion coefficient of the product (m^2/s)
E	Slope that provides the diffusion coefficient
h	Experimental sample thickness (m)
M	Dimensionless moisture content (water vapor per dry amount) (g_{sb}/g_{km})
M_e	Dimensionless moisture content (water vapor per dry amount) (g_{sb}/g_{km})
M_i	Dimensionless moisture content (water vapor per dry amount) (g_{sb}/g_{km})
m_k	Dry weight of the sample (g)
m_{ky}	Total weight of the sample (g)
MR	Dimensionless moisture ratio
m_y	Moisture content in the sample (g)
R^2	Number of definitions
t	Time (s)

1. INTRODUCTION

Controlled heating of food products to evaporate the initial moisture in foods is known as drying or dehydration. Drying of the selected food products is necessary to reduce the weight of the product for ease of transportation and to extend the shelf life of the product for a long time without loss of quality. Drying requires simultaneous removal of both heat and moisture from food. The main parameters controlling the drying rate of food, vegetables and fruits are temperature, air humidity and air velocity, which vary depending on the food temperature and the specific dryer design (Sharada, 2013).

Mushroom cultivation has excellent potential for producing protein-rich, high-quality food and recycling cellulose agricultural residues. It is consumed because of its delicious taste, low-calorie content, high protein content, and B group vitamins. Mushrooms contain 20-40% of their dry weight, protein, cholesterol-free and almost lean (FOA, 1970). Among the 38000 known mushroom varieties, the most consumed ones are Button mushrooms (Agaricus Bisporus), shitake or Japanese mushrooms (Lentinus Edodes) and oyster mushrooms (Pleurotus ostreatus) (Singh et al. 1999). Button mushrooms constitute 37.7% of world mushroom production and oyster mushrooms constitute 24.1% (Singh et al. 1995). The mushroom starts to deteriorate within one day after harvest. Mushroom needs to be processed to extend its off-season usage and shelf life. Canning is the most accepted method. Mushrooms can also be processed in many other ways, such as drying, pickling. Drying is known to be a relatively inexpensive method (Rama and Jacob, 2000). For these reasons, the drying characteristic of the Button mushroom was investigated.

Various hot air-drying methods include fluid bed drying; It offers important advantages such as high heat and mass transfer, less drying time, uniform moisture reduction and high drying speed (Kassem et al. 2011). Fluid bed dryers increase the efficiency of this process by acting as a fluid and mixing solid materials with air efficiently. They provide uniform bed temperature and constant drying rate during drying. However, stratified flow and hot spot formation in fluid bed dryers can cause high moisture change damage to the product with loss of quality. Special additives are used to dry very wet adhesive materials and adhesive hygroscopic products in fluid bed dryers (Patil and Dattaatreya 2012).

Studies in the literature have focused on researching drying kinetics for different products, different drying methods, different types of dryers, CFD analysis of airflow and heat transfer in the drying oven, reducing energy used for drying. The general purpose of these studies is to determine the drying character of the product to be dried by providing the desired quality product characteristics after drying and to make the optimization and design of the drying systems that will provide these conditions in terms of cost and energy (Kaya, 2008). Walde et al. conducted experimental studies to find the drying characteristics of Button mushrooms for different pretreatments. In these experimental studies, the fluidized bed dryer was compared at different temperatures (60 ˚C) for different pretreatments (bleaching, whey soaking) and derivatives of these pretreatments (Walde et al., 2005). In this study, mushrooms of a certain degree of dryness were studied and fresh mushrooms were not used.

Silva et al. Agaricus Blazei examined the drying characteristics of sliced mushrooms at different air temperatures (45-60-75-80 ˚C) and airspeeds (1-1.2-1.75-2.3-2.5 m / s) in the fixed bed dryer. As a result of these studies, it was determined that high drying temperatures and high drying speeds increased the diffusion coefficient. It calculated the diffusion coefficients between 4.084E-10 and 17.8E-10 (Silva, 2009). The diffusion coefficients were calculated larger because the experimental studies conducted were at higher speeds.

2. METHOD

2.1 Material

Button mushrooms were bought from a specific brand so that the results were not affected. The mushrooms were washed and cleaned of dirt, then separated from the stems. Mushroom diameters were chosen between 60 mm and 45 mm. Mushrooms were cut into slices with a thickness of 5 ± 1 mm. The oval cork pieces left in the corners after cutting were not included in the experiment.

2.2 Experimental Setup

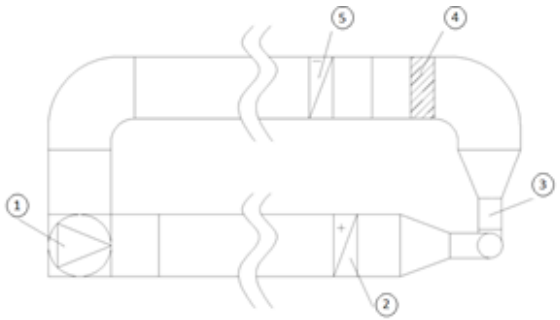

Numbers on the test system:
1) Centrifugal Fan
2) Heater Battery
3) Experiment Pane
4) Filter
5) Cooler Battery

Figure 1. Schematic representation of the fluid bed dryer

2.3 Experimental Study

Firstly, the temperature in the test chamber of the dryer was expected to reach the drying temperature. Samples were prepared after temperature and speed balance was achieved. The weight of the prepared samples was measured and put into the drying oven and the experiment was started. The weight of the samples was measured every 15 minutes. The experiment was completed when the samples dropped below approximately 10% of their initial weight. During the experiment, temperature and humidity data from the data loggers were continuously monitored and temperature fluctuations did not exceed ± 2 ˚C. According to the results of the experiment, the moisture content time graphs were drawn.

2.4 Diffusion Coefficient Calculation

To find the dry mass percentage of the mushrooms, a batch of mushrooms was kept at 60˚C until the water in the oven was completely removed (24 hours). As a result of this experiment, 6,15% of the Button mushroom mass was observed to be a solid mass. Equation(1) was obtained as a result of this experiment.

$$0,0615 m_{ky} = m_k \tag{1}$$

$$m_{ky} = m_y + m_k \tag{2}$$

$$M = \frac{m_y}{m_k} \tag{3}$$

$$MR = \frac{M(t) - M_e}{M_i - M_e} \tag{4}$$

The change of the moisture content of the product frequently appears in the literature in the form of Eq. (4) (Rezagah et al., 2010). M_e value was taken approximately 0.06 depending on relative humidity. (Cemeroglu and Acar, 1986)

Diffusion coefficients of drying of samples were found with the model proposed by Crank (Crank, 1975). In Eq. (5), n = 0 represents the equation used for drying of flat objects.

$$MR = \frac{M(t) - M_e}{M_i - M_e} = \frac{8}{\pi^2} \sum_{n=0}^{\infty} \frac{1}{(2n+1)} \exp\left(-\frac{(2n+1)^2 \pi^2 D_{eff} t}{4h^2}\right) \tag{5}$$

It is sufficient to open the first term of Equation(5) in long drying.

$$MR = \frac{M(t) - M_e}{M_i - M_e} = \frac{8}{\pi^2} \exp(-\frac{\pi^2 D_{eff} t}{4h^2}) \tag{6}$$

If the natural logarithm of both sides is taken;

$$\ln(MR) = \ln(\frac{8}{\pi^2}) - (\frac{\pi^2 D_{eff} t}{4h^2}) \tag{7}$$

D_{eff} is found from the slope of the graph of $-\ln(MR)$ by time, found in Eq. (7).

$$E = \frac{\pi^2}{4} \frac{D_{eff}}{h^2} \tag{8}$$

The values of the experiments are found by substituting the values in Equation (8).

2.4 Artificial Neural Networks for Drying Characteristics Determination

2.4.1 Artificial Neural Networks

ANNs began as an attempt to exploit the architecture of the human brain to perform tasks that conventional algorithms had little success with. They soon reoriented towards improving empirical results, mostly abandoning attempts to remain true to their biological precursors. Neurons are connected to each other in various patterns to allow the output of some neurons to become the input of others. The network forms a directed, weighted graph.

An artificial neural network consists of a collection of simulated neurons. Each neuron is a node that is connected to other nodes via links that correspond to biological axon-synapse-dendrite connections. Each link has a weight, which determines the strength of one node's influence on another.

2.4.2 ANN Application

Artificial neural networks have been preferred in recent years and they are used to obtain new results by training networks in multi-data systems. For the drying device, analysis has been done with many mathematical models in the literature. In this study, artificial neural networks were used to compare experimental results with theoretical results. Thus, MR values can be reached in a short time.

In this experimental setup, the MR values in seconds determined under a specific temperature and a certain speed are measured. With these data, either mathematical models or algorithms should be used for the desired temperature, speed and MR values per second.

The study manager used the speed, time and temperature data obtained as a result of his observations in his previous experiments as inputs of the artificial neural network. MR values obtained as a result of the experiment were defined as the output. These data are divided into train data and test data. Thus, test data is used to calculate error values after the system is trained.
Before the system is created in the data, the processes are completed, normalization can be given as an example. In the Matlab program, the system establishment process for artificial neural networks training is initiated. Then, neural networks are trained with the specified function types or learning rates by using the neural networks toolbox or by coding the Matlab interface. The study giving the lowest error rate is calculated by calculating the error rates with the reserved test data. Then estimation is made depending on this study.

Table 1. Artificial Neural Networks Data Sample

INPUT			OUTPUT
T(°C)	**V(m/s)**	**t(sn)**	**MR**
45	5,5	3600	0,190501681
45	6,5	1800	0,402575882
50	6,5	900	0,57750116
50	7,5	6300	0,016785822
55	5,5	5400	0,076189236
55	6,5	0	1
55	6,5	4500	0,080583269
60	5,5	1800	0,322138895
60	6,5	900	0,52844023

3. RESULTS

The moisture content created as a result of the experiments was compared with time graphs, air velocity and temperature.

In the fluid bed dryer, the airspeed was adjusted to be 5.5 m / s and experiments were carried out such that the temperature was 45, 50, 55, 60 ˚C.

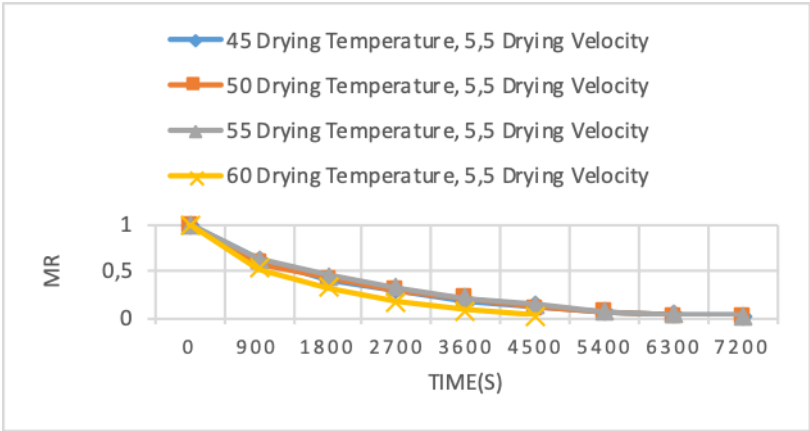

Figure 2. Temperature comparison in fluid bed dryer.

As seen in Figure 2, increasing the temperature increased the drying speed of the button mushrooms.

In the fluid bed dryer, the temperature was set at 55 ˚C and experiments were carried out with the airspeed of 5.5, 6.5, 7.5 m /s.

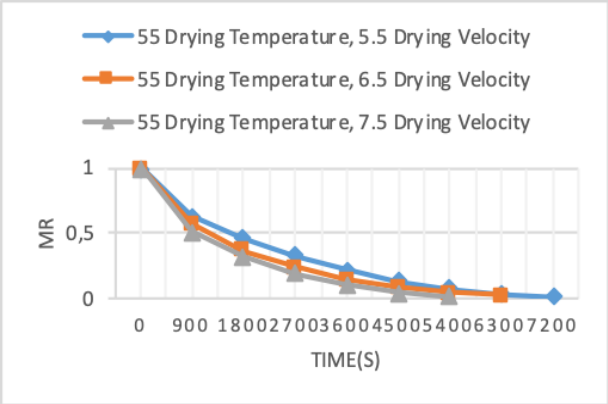

Figure 3. Air velocity comparison in fluid bed dryer.

As shown in Figure 3, increasing the airspeed increased the drying rate of the mushroom.

3.1 Calculation of moisture ratio with Artificial Neural Networks

The data shown in Table 1, which was formed as a result of the experiments, were divided into train and test data. Train data were created in the "MATLAB" program with artificial neural networks as in Figure 4. The network training were repeated and it was checked whether the network was memorizing or not.

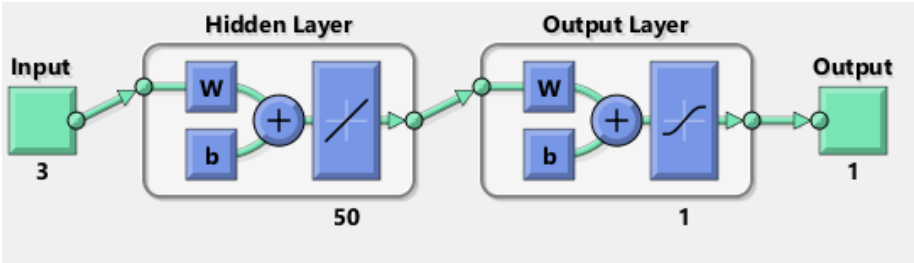

Figure 4. An artificial neural network system to find moisture ratio

After this stage, the test data we separated at the beginning was introduced into the system with the trained network and moisture ratio outputs were created. You can examine the MR values in Table 2. After this process was completed, R^2 was calculated between experimental observations and artificial neural network estimation.

Table 2. Moisture Ratio and R^2 values calculated according to artificial neural networks

Type	Sıcaklık (˚C)	Hız (m/s)	t (sn)	MR	R^2
Fluid	45	5,5	3000	0,1505051621	0,99646
Fluid	50	6,5	800	0,7575	0,99819
Fluid	55	6,5	100	0,94	0,99190
Fluid	60	6,5	1000	0,4783	0,99737
Fluid	50	5,5	1900	0,403694	0,99996
Fluid	50	7,5	4000	0,07032	0,99856

4.DISCUSSION

According to the data obtained from the experimental studies, increasing the drying temperature or increasing the drying speed shortened the drying times and increased the diffusion coefficients. It was observed that the fungi lost their fluid form after a specific second. With the help of artificial neural networks, the trained network saves material and great time.

REFERENCES

[1] Aktaş, M. ve Ceyhan, İ., (2009). "Determination of drying characteristics of apples in a heat pump and solar dryer desalination", 239:266-275.

[2] Cemeroglu, B., Acar, J., 1986. Meyve ve sebze isleme teknolojisi. Gıda Teknolojisi Derneği Yayın No: 6, Ankara

[3] Crank, J., (1975). The Mathematics of Diffusion, Second Edition, Oxford University Press, Londra.

[4] FAO (1970). Amino acid contents of foods and biological data on proteins. Nutritional Studies No. 24.

[5] Henderson, S.M. ve Pabis, S., (1961). "Grain drying theory. II. Temperature effects on drying coefficients", Journal of Agricultural Engineering Research, 6:169-174.

[6] Kassem AS, Shokr AZ, Mahdy ARE, Aboukarima AM, Hamed EY. Comparison of drying characteristics of Thompson seedless grapes using a combined microwave oven and hot air drying. J Saudi Soc Agric Sci 2011; 10:33–40

[7] Kaya, A., (2008). Kurutmada Isı ve Kütle Transferinin Teorik ve Deneysel Olarak İncelenmesi, Doktora Tezi, Karadeniz Teknik Üniversitesi Fen Bilimleri Enstitüsü, Trabzon.

[8] Page, G., (1949). Factors influencing the maximum rates of air-drying shelled corn in thin layer, Yüksek Lisans Tezi, Makine Mühendisliği, Purdue Üniversitesi, Doğu Lafayette, Amerika

[9] Sacilik, K., Elicin, A.K. ve Unal, G., (2006). "Drying kinetics of Üryani plum in a convective hot-air dryer", Journal of Food Engineering, 76(3):362-368.

[10] Sharada S. Studies on the effect of various operating parameters & foaming agents – drying of fruits and vegetables. Int J Mod Eng Res 2013; 3:1512–9.

[11] Singh, A. K., Sharma, H. K., Kumar, P., & Singh, B. (1999). Physicochemical changes in white button mushroom (Agaricus bisporus) at
different drying temperatures. Mushroom Research, 8(2), 27–30.

[12] Silva, C.K., Silva, Z.E., Mariani, V.C., (2009). Determination of the diffusion coefficient of dry mushrooms using the inverse method. Journal of Food Engineering 95 (2009),1-10

[13] Beale, Hagan Demuth, Howard B. Demuth, and M. T. Hagan. "Neural network design." Pws, Boston (1996).

MIXED CONVECTION IN A VERTICAL PARALLEL-PLATE MICROCHANNEL WITH VISCOUS DISSIPATION EFFECT

Ayse Nur ALTUNKAYA*, Mete AVCI*, Orhan AYDIN**
* Recep Tayyip Erdogan University, Department of Mechanical Engineering, Rize/Turkey
Email: aysenur.altunkaya@erdogan.edu.tr , mete.avci@erdogan.edu.tr,
** Karadeniz Technical University, Department of Mechanical Engineering, Trabzon/Turkey
Email: oydin@ktu.edu.tr

ABSTRACT

In the present study, fully developed mixed convection flow in an open-ended vertical parallel plate microchannel is theoretically analyzed by using a perturbation series method. The viscous dissipation in the fluid as well as the velocity slip and the temperature jump at the wall are included in the analysis. The microchannel is considered as asymmetrically or symmetrically heated with uniform wall temperatures. The effects of mixed convection parameter, Knudsen number, Brinkman number and ratio of wall temperature difference on the Nusselt number as well as the velocity and temperature profiles are examined. It is disclosed that the value of *Nu* decreases with the increase of *Kn*. A singularity is observed for some specific values of Brinkman number.

Keywords: microchannel, vertical parallel plate, mixed convection, rarefaction, viscous dissipation.

Symbols

A	constant $= dp/dx$
a_n	dimensionless coefficient, equation (30)
Br	Brinkman number, equation (7)
c_p	specific heat at constant pressure [Jkg^{-1} K^{-1}]
D	hydraulic diameter [m]
F	tangential momentum accommodation coefficient
F_t	thermal accommodation coefficient
g	gravitational acceleration
Gr	Grashof number, equation (7)
h_-	convective heat transfer coefficient (at $y=-L/2$)
h_+	convective heat transfer coefficient (at $y=L/2$)
k	thermal conductivity [Wm^{-1} K^{-1}]
Kn	Knudsen number, equation (7)
L	channel width [m]
$Nu\|_{-L/2}$	Nusselt number (at $y=-L/2$), equation (31)
$Nu\|_{L/2}$	Nusselt number (at $y=L/2$), equation. (32)
p	pressure [Pa]
Pr	Prandtl number $=\nu/\alpha$
Re	Reynolds number, equation (7)
r_T	ratio of wall temperature differences, equation (7)
T	temperature [K]
T_0	reference temperature [K], equation (9)
u	axial velocity [m/s]
u_0	reference velocity [m/s], equation (9)

U dimensionless axial velocity, equation (7)
x, y axial and transverse coordinate [m]
Y dimensionless transverse coordinate, equation (7)

Greek symbols

α thermal diffusivity $= k/\left(\rho_0 c_p\right)$
β thermal expansion coefficient
β_v, β_t dimensionless variables, equation (7)
γ specific heat ratio
ΔT reference temperature difference, equation (8)
ε dimensionless parameter $= Br\left(Gr/\mathrm{Re}\right)$
θ dimensionless temperature, equation (7)
λ molecular mean free path
μ dynamic viscosity
ν kinematic viscosity $= \mu/\rho_0$
ρ_0 density [kg/m^3]

Subscripts

1 value on cold wall (i.e., at $y = -L/2$)
2 value on hot wall (i.e., at $y = L/2$)
b bulk
m mean
s fluid properties on walls
s_1 fluid properties on cold wall
s_2 fluid properties on hot wall
w wall

1. INTRODUCTION

Fluid flow and heat transfer in micro-geometries have attracted a great deal of research interest in recent years due to the rapid growth of novel techniques applied in MEMS (microelectromechanical systems) and biomedical applications such as drug delivery, DNA sequencing, and bio-MEMS.

Reduced geometrical dimensions at microscale geometries leads to different heat and fluid characteristics than those observed at macroscale. Based on the value of the Knudsen number, defined as the ratio of the molecular mean free path to the characteristic length, different flow regime classifications are made. The slip regime is one of them. This regime has been studied extensively since most microfluid devices operate in this regime at the standard atmospheric conditions.

Many of the studies appeared in the literature on forced convection. Comparatively, much fewer studies are available for free or mixed convection at microscale. Chen and Weng [1] analytically studied natural convection in an open-ended vertical parallel plate microchannel with asymmetric wall temperature distributions. The effects of rarefaction and fluid-wall interaction were shown to increase the volume flow and to decrease the heat transfer rate. Chen and Weng extended their analysis by considering thermal creep [2-3], a second-order slip condition and variable working temperature [4-5]. Chen and Weng [6] also considered natural convection in an open-ended vertical annular microchannel. They showed that it is possible to obtain both reduced flow drag and enhance heat transfer by decreasing the value of the curvature ratio. Biswall et al. [7] numerically investigated natural convection in vertical microchannels by considering the entrance effect. Khadrawi et al. [8] analytically investigated the transient hydrodynamics and thermal behaviors of fluid flow in an open-ended vertical parallel-

plate microchannel under the effect of the hyperbolic heat conduction model. Chakraborty et al. [9] numerically investigated heat transfer characteristics of natural convection gas flows in vertical microchannels using a boundary layer integral analysis. Buonomo and Manca [10] numerically examined natural convection in a vertical parallel-plate microchannel. Karimipour et al. [11] studied gravity effects on the mixed convection heat transfer in a microchannel using the lattice Boltzman method. They concluded that the effects of buoyancy forces are important for $Kn < 0.05$ while they could be ignored $Kn > 0.05$. Jian and Weng [12] investigated mixed convection flow in an asymmetrically heated long vertical microchannel using a second-order slip. They disclosed that the second-order slip had an appreciable effect on the flow but a negligible effect on the heat transfer. Rahimi and Niazmand [13] numerically studied natural convection in an open-ended vertical parallel-plate microchannel including a second-order slip model, thermal creep effect and variable thermophysical properties. Wang and Ng [14] numerically studied natural convection in vertical parallel-plate microchannel by taking the velocity slip and temperature jump at one wall only. Jha and Aina [15] studied natural convection problem of fully developed laminar flow in a vertical parallel plate microchannel by considering the viscous dissipation effect.

Our research group did pioneering studies on mixed convection in some microgeometries, in a vertical parallel plate microchannel [16-17] and a vertical micro-annulus between two concentric microtubes [18]. All these articles have neglected the effect of viscous dissipation. In our recent article [19], we included this effect for the same problem of mixed convection problem in a vertical parallel plate microchannel with constant heat flux boundary condition. The perturbation method based on series expansion was used to solve momentum and energy equations.

The cited literature review shows that the mixed convection problem inside a vertical parallel plate microchannel under constant wall temperature has not been solved yet. The aim of this study is to analytically investigate the laminar mixed convection problem in the fully developed region of a parallel plate microchannel subjected to constant wall temperature. The combined effects of the rarefaction and viscous dissipation on the temperature profiles and, in the following, on the Nusselt number, are determined and discussed.

2. METHOD

Fully developed steady flow of an incompressible fluid in a vertical microchannel between two parallel plates held at different uniform temperatures is considered (see Fig. 1). Thermophysical properties of the fluid are assumed to be constant and the axial heat conduction in the fluid and the wall is assumed to be negligible.

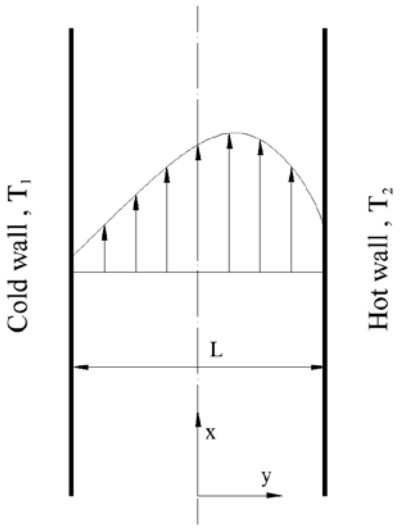

Figure 1. Schematic of the problem geometry.

In a sufficiently long channel, the velocity and temperature profiles will cease to change with distance along the channel ($\partial u / \partial x = 0$ and $\partial T / \partial x = 0$), i.e., a fully developed flow will exist [20]. Except that, in fully developed flow of mixed convection in a vertical channel with constant temperature boundaries, the longitudinal pressure gradient is also constant ($dp / dx = A = const.$).

Under the usual Boussinesq approximation and above considerations, the momentum and energy equations for fully developed flow can be written in the following form:

$$0 = -\frac{dp}{dx} + \mu \frac{d^2u}{dy^2} + \beta g \rho_0 (T - T_0) \tag{1}$$

$$0 = \left(\frac{k}{\rho_0 c_p} \right) \frac{d^2T}{dy^2} + \frac{\nu}{c_p} \left(\frac{du}{dy} \right)^2 \tag{2}$$

where the second term in the right hand side of equation (2) is the viscous dissipation term.

In the analysis, the usual continuum approach is integrated with the two main characteristics of the microscale phenomena: the velocity slip and the temperature jump [21]

$$u_s = -\frac{2 - F}{F} \lambda \left. \frac{\partial u}{\partial y} \right|_{y=L/2} \tag{3}$$

$$T_s - T_w = -\frac{2 - F_t}{F_t} \frac{2\gamma}{\gamma + 1} \frac{\lambda}{\mathrm{Pr}} \left. \frac{\partial T}{\partial y} \right|_{y=L/2} \tag{4}$$

where F is the tangential momentum accommodation coefficient and F_t is the thermal accommodation coefficient. Particularly for air, the accommodation coefficients assume typical values near unity. Therefore, for the rest of our analysis F and F_t are assumed to be 1.

The boundary conditions describing velocity slip and temperature jump conditions at the fluid-wall interface are given as:

$$\begin{aligned} u &= u_{s1} && \text{at } y = -L/2 \\ u &= u_{s2} && \text{at } y = L/2 \\ T &= T_{s1} && \text{at } y = -L/2 \\ T &= T_{s2} && \text{at } y = L/2 \end{aligned} \tag{5}$$

By differentiating twice both sides of equation (1) with respect to y and substituting equation (2) into equation (1) one can obtain a fourth-order nonlinear differential equation for u, as in the following form:

$$\frac{d^4u}{dy^4} = \frac{\beta g}{\alpha c_p} \left(\frac{du}{dy} \right)^2 \tag{6}$$

Substituting the following non-dimensional quantities into equations (6) and (2),

$$Y=\frac{y}{D},\quad \theta=\frac{T-T_0}{\Delta T},\quad U=\frac{u}{u_0},\quad Kn=\frac{\lambda}{D},\quad \beta_v=\frac{2-F}{F},\ r_T=\frac{T_2-T_1}{\Delta T}$$

$$\beta_t=\frac{2-F_t}{F_t}\frac{2\gamma}{\gamma+1}\frac{1}{\mathrm{Pr}},\ Gr=\frac{\beta g\Delta T D^3}{\nu^2},\ \mathrm{Re}=\frac{u_0 D}{\nu},\quad Br=\frac{\mu u_0^2}{k\Delta T} \tag{7}$$

where $D(=2L)$ is the hydraulic diameter, ΔT is the reference temperature difference and u_0 and T_0 are the reference velocity and temperature given, respectively, as:

$$\Delta T=T_2-T_1 \qquad \text{for} \quad T_1<T_2 \tag{8a}$$

$$\Delta T=\nu^2\ /c_p D^2 \qquad \text{for} \quad T_1=T_2 \tag{8b}$$

$$u_0=-\frac{AD^2}{48\mu},\qquad T_0=\frac{T_1+T_2}{2} \tag{9}$$

one can obtain a 4th order differential equation for U, which is given in the following form

$$\frac{d^4U}{dY^4}=\frac{Gr}{\mathrm{Re}}Br\left(\frac{dU}{dY}\right)^2 \tag{10}$$

By using equations (1) and (2) and the non-dimensional quantities introduced in equation (7), the boundary conditions can be written as:

$$U=\beta_v Kn\frac{dU}{dY} \qquad \text{at}\ \ Y=-1/4 \tag{11a}$$

$$U=-\beta_v Kn\frac{dU}{dY} \qquad \text{at}\ \ Y=1/4 \tag{11b}$$

$$\frac{d^2U}{dY^2}=-48+\frac{Gr}{\mathrm{Re}}\frac{r_T}{2}+\beta_t Kn\frac{d^3U}{dY^3} \qquad \text{at}\ \ Y=-1/4 \tag{12a}$$

$$\frac{d^2U}{dY^2}=-48-\frac{Gr}{\mathrm{Re}}\frac{r_T}{2}-\beta_t Kn\frac{d^3U}{dY^3} \qquad \text{at}\ \ Y=1/4 \tag{12b}$$

Here, r_T represents the temperature difference ratio and the case of $r_T=0$ and $r_T=1$ correspond to symmetric and asymmetric heating [22].

Applying the same procedure, the energy equation and the corresponding boundary conditions can be written as:

$$\frac{d^2\theta}{dY^2}+Br\left(\frac{dU}{dY}\right)^2=0 \quad \text{or} \quad \theta=-\frac{1}{Gr/\mathrm{Re}}\left[48+\frac{d^2U}{dY^2}\right] \tag{13}$$

$$\theta=-\frac{r_T}{2}+\beta_t Kn\frac{d\theta}{dY} \qquad \text{at}\ \ Y=-1/4 \tag{14a}$$

$$\theta=\frac{r_T}{2}-\beta_t Kn\frac{d\theta}{dY} \qquad \text{at}\ \ Y=1/4 \tag{14b}$$

In the absence of viscous dissipation ($Br = 0$),equations (10) and (13) indicate that the dimensionless velocity and the dimensionless temperature are uncoupled and can be solved analytically. In this case, without going into detail, it can be shown that the solutions of equations (10) and (13) subject to equations (11) and (12) can be obtained as follows:

$$U(Y) = \frac{Gr}{\mathrm{Re}} \frac{r_T}{\left(3+12\beta_t Kn\right)} \left[-Y^3 + Y \frac{\left(1+12\beta_v Kn\right)}{\left(16+64\beta_v Kn\right)} \right] + 24 \left[-Y^2 + \frac{\left(1+8\beta_v Kn\right)}{16} \right] \tag{15}$$

$$\theta(Y) = \frac{2r_T}{\left(1+4\beta_t Kn\right)} Y \tag{16}$$

Barletta [22] studied the similar problem using the same method for the macroscale case (*Kn* = 0). For *Kn* = 0.0, it can be shown that the velocity and temperature distributions are exactly the same as those given in Ref. [22]:

$$U(Y) = \left(\frac{Gr}{3\mathrm{Re}} r_T Y + 24 \right) \left(\frac{1}{16} - Y^2 \right) \tag{17}$$

$$\theta(Y) = 2r_T Y \tag{18}$$

But, in the presence of viscous dissipation ($Br \neq 0$) with the case of $Gr / \mathrm{Re} \neq 0$, the problem represented by equations (10-13) is a coupled nonlinear boundary value problem and does not possess an exact solution. However, approximate analytical solutions can be obtained using the perturbation method. As in Ref. [22], by considering $Br\left(Gr / \mathrm{Re}\right)$ as the perturbation parameter, ε , the perturbation solution of equation (10) in the form of the asymptotic expansion can be expressed as follows:

$$U(Y) = U_0(Y) + \varepsilon U_1(Y) + \varepsilon^2 U_2(Y) + \cdots = \sum_{n=0}^{\infty} \varepsilon^n U_n(Y) \tag{19}$$

By substituting equation (19) into equations (10-12) and equating terms of identical powers of ε , one obtains the sets of ordinary differential equations that can be solved in succession and yield unknown functions of $U_n(Y)$. This sequential solution procedure begins with the zero-order problem, $n = 0$, and progresses to $n = 1, 2, \ldots$ etc.

According to the above considerations, the zero order problem ($n = 0$) yields

$$\frac{d^4 U_0}{dY^4} = 0 \tag{20}$$

$$U_0\left(-1/4\right) = \beta_v Kn \left. \frac{dU_0}{dY} \right|_{Y=-1/4} \tag{21a}$$

$$U_0\left(1/4\right) = -\beta_v Kn \left. \frac{dU_0}{dY} \right|_{Y=1/4} \tag{21b}$$

$$\left. \frac{d^2 U_0}{dY^2} \right|_{Y=-1/4} = -48 + \frac{Gr}{\mathrm{Re}} \frac{r_T}{2} + \beta_t Kn \left. \frac{d^3 U_0}{dY^3} \right|_{Y=-1/4} \tag{22a}$$

$$\left.\frac{d^2U_0}{dY^2}\right|_{Y=1/4} = -48 - \frac{Gr}{\mathrm{Re}}\frac{r_T}{2} - \beta_t Kn \left.\frac{d^3U_0}{dY^3}\right|_{Y=1/4} \tag{22b}$$

By solving equation (20) under the corresponding boundary conditions given in equations (21) and (22), we obtain

$$U_0(Y) = \frac{Gr}{\mathrm{Re}}\frac{r_T}{\left(3+12\beta_t Kn\right)}\left[-Y^3 + Y\frac{\left(1+12\beta_v Kn\right)}{\left(16+64\beta_v Kn\right)}\right] + 24\left[-Y^2 + \frac{\left(1+8\beta_v Kn\right)}{16}\right] \tag{23}$$

Note that the zero order problem described by equations (20-22) represents the case without the effect of viscous dissipation. This fact can be clearly seen when the solution of equation (20) compared with the solution of equation (10) in the case of negligible viscous dissipation, $Br = 0$.

For every integer $n > 0$, the n-order boundary value problem is given as:

$$\frac{d^4U_n}{dY^4} = \sum_{j=0}^{n-1}\frac{dU_j}{dY}\frac{dU_{n-j-1}}{dY} \tag{24}$$

$$U_n(-1/4) = \beta_v Kn \left.\frac{dU_n}{dY}\right|_{Y=-1/4} \tag{25a}$$

$$U_n(1/4) = -\beta_v Kn \left.\frac{dU_n}{dY}\right|_{Y=1/4} \tag{25b}$$

$$\left.\frac{d^2U_n}{dY^2}\right|_{Y=-1/4} = \beta_t Kn \left.\frac{d^3U_n}{dY^3}\right|_{Y=-1/4} \tag{26a}$$

$$\left.\frac{d^2U_n}{dY^2}\right|_{Y=1/4} = -\beta_t Kn \left.\frac{d^3U_n}{dY^3}\right|_{Y=1/4} \tag{26b}$$

Since $U_0(Y)$ is the known function, an iterative solution of equations (24-26) is possible and yields the function of $U_n(Y)$ for $n > 0$. In a similar way, by using equations (13), (19) and (23), the perturbation solution of dimensionless temperature can be expressed as follows:

$$\theta(Y) = \frac{2r_T}{\left(1+4\beta_t Kn\right)}Y - \frac{1}{Gr/\mathrm{Re}}\sum_{n=1}^{\infty}\varepsilon^n\frac{d^2U_n}{dY^2} \tag{27}$$

At any cross section in the channel, the dimensionless mean velocity U_m and the dimensionless bulk temperature θ_b can, respectively, be written as:

$$U_m = \frac{u_m}{u_0} = \int_{-1/4}^{1/4} U dY \Big/ \int_{-1/4}^{1/4} dY = 1 + \sum_{n=1}^{\infty}\left(2\int_{-1/4}^{1/4} U_n dY\right)\varepsilon^n \tag{28}$$

$$\theta_b = \frac{T_b - T_0}{\Delta T} = \int_{-1/4}^{1/4} U\theta dY \Big/ \int_{-1/4}^{1/4} U dY$$
$$= \frac{48}{Gr/\mathrm{Re}}\left(\frac{1+12Kn\beta_v}{U_m} - 1\right) + \frac{r_T^{\,2}\, Gr/\mathrm{Re}\left(1+24Kn\beta_v\right)}{2880U_m\left(1+4Kn\beta_T\right)^2\left(1+4Kn\beta_v\right)} - \frac{1}{U_m}\sum_{n=1}^{\infty} a_n \varepsilon^n \tag{29}$$

where the coefficient a_n is given by

$$a_n = \frac{2}{Gr/\mathrm{Re}} \sum_{j=0}^{n} \int_{-1/4}^{1/4} \frac{dU_j(Y)}{dY} \frac{dU_{n-j}(Y)}{dY} dY \tag{30}$$

The Nusselt number based on the difference between the wall and the bulk temperature for the left and right wall can, respectively, be expressed as follows:

$$Nu\big|_{-L/2} = \frac{h_- D}{k} = \frac{2}{r_T + 2\theta_b}\left[\frac{2r_T}{1+4\beta_t Kn} - \frac{1}{Gr/\mathrm{Re}}\sum_{n=1}^{\infty}\varepsilon^n \frac{d^3U_n}{dY^3}\bigg|_{Y=-1/4}\right] \tag{31}$$

$$Nu\big|_{L/2} = \frac{h_+ D}{k} = \frac{2}{r_T - 2\theta_b}\left[\frac{2r_T}{1+4\beta_t Kn} - \frac{1}{Gr/\mathrm{Re}}\sum_{n=1}^{\infty}\varepsilon^n \frac{d^3U_n}{dY^3}\bigg|_{Y=1/4}\right] \tag{32}$$

For all the cases considered, the above sequential solution procedure is continued until the change in *Nu* values between two successive steps is negligible. The obtained results showed that including the first 30 terms is sufficient to obtain the desired results.

3. RESULTS AND DISCUSSIONS

In this study, mixed convection for fully developed laminar flow in a vertical microchannel between two parallel plates held at different uniform wall temperatures is investigated considering rarefaction and viscous dissipation effects. The interactive effects of mixed convection parameter, *Gr/Re*, rarefaction, *Kn*, and viscous dissipation, *Br*, on convective heat transfer are examined.

For the asymmetric heating case (r_T = 1), the dimensionless velocity and temperature variation with the mixed convection parameter, *Gr/Re*, are given in Fig. 2. As seen from the figure, for the forced convection case (*Gr/Re* = 0), the dimensionless velocity profile is symmetric with respect to the line *Y* = 0. However, as the mixed convection parameter increases, the axisymmetric structure distorts with an increase in the velocity by the buoyancy forces and the peak velocity point moves towards the hot wall (Fig. 2a). This fact can be explained by the aiding effect of buoyancy force on forced convection, which establishes an upward free convection flow near the hot wall. However, as seen from Fig. 2b, the effect of mixed convection parameter is nearly negligible on the dimensionless temperature profiles when the degree of viscous dissipation is small, *Br* = 0.01.

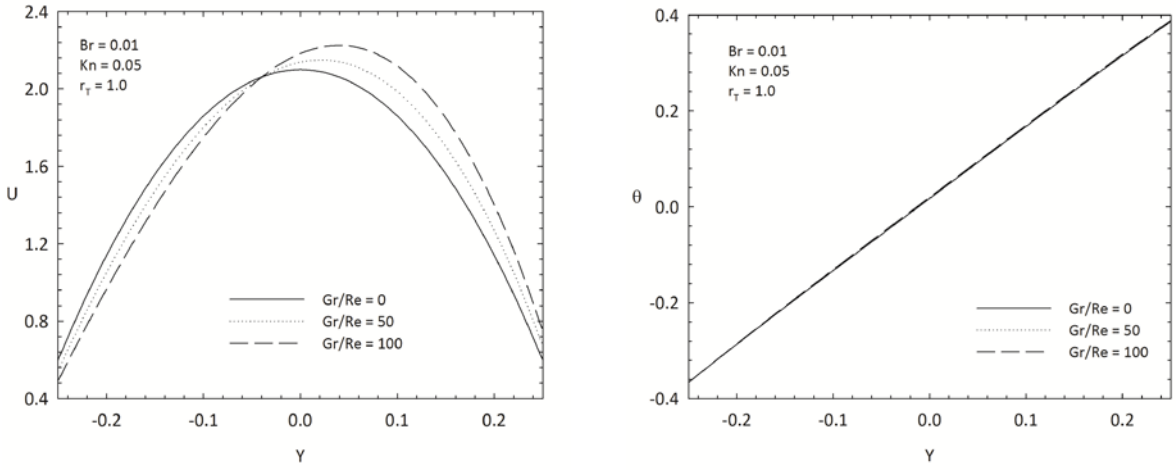

(a) (b)

Figure 2. Dimensionless velocity and temperature profiles for varying values of *Gr/Re* at *Br* = 0.01, *Kn* = 0.05 and r_T = 1.

The variation of dimensionless velocity for different values of Brinkman numbers are depicted in Fig. 3a. An increase in the Brinkman number leads to higher velocities in the channel. Actually this is an expected result when the equation (13) closely examined. In the presence of viscous dissipation ($Br \neq 0$), the thermal energy generated by viscous dissipation will increase the overall temperature of the fluid (see Fig. 3b), which consequently, results in greater buoyancy forces, and ultimately, in higher velocities in the channel. Similar trends are observed by Barletta [22].

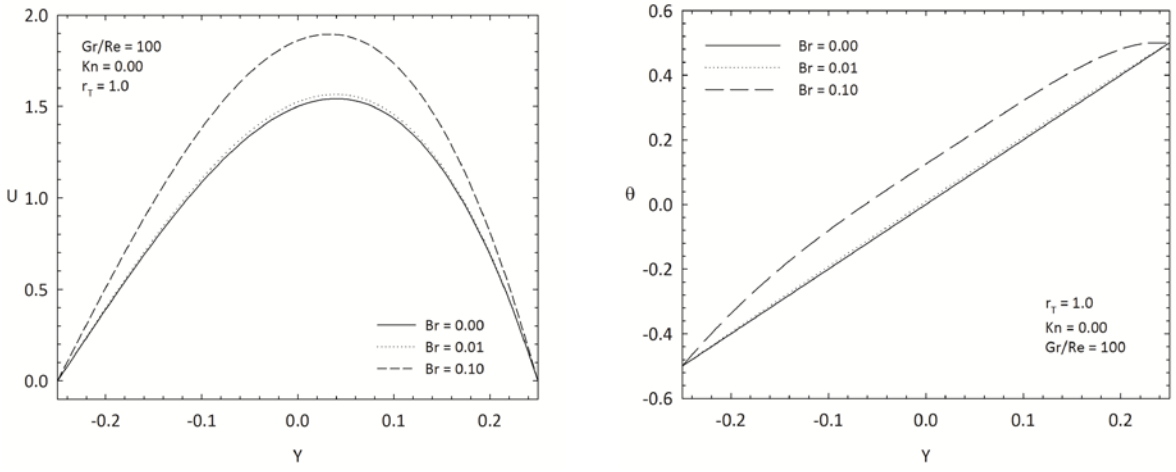

(a) (b)

Figure 3. Dimensionless velocity and temperature profiles for varying values of *Br* at *Gr/Re* = 100, *Kn* = 0.0 and r_T = 1.

In order to see the combined effect of rarefaction and viscous dissipation on heat transfer, the variation of Nusselt number with *Br* for various values of *Kn* and *Gr/Re* are illustrated in Fig. 4. As seen from the Fig 4a and 4b, for the forced convection case (*Gr/Re* = 0), the Nusselt number increases with increasing *Br* at the left wall (cold wall) while an opposite trend is observed at the right wall (hot wall) for a given value of *Kn*. This is expected because an increase in *Br* increases the temperature difference between the left wall and the bulk (see Fig. 3b), which reinforces the driving potential for the heat transfer from fluid to the left wall. But at the right wall, it decreases the temperature difference between the wall and the bulk, leading to a decrease in the Nusselt number (Fig. 4b). Fig 4a and 4b also show the significant role of rarefaction on the Nusselt number. As seen

from the figure, the value of *Nu* decreases with the increase of *Kn*. The reason is because of the decrease in the wall temperature gradient as the temperature jump effect becomes stronger.

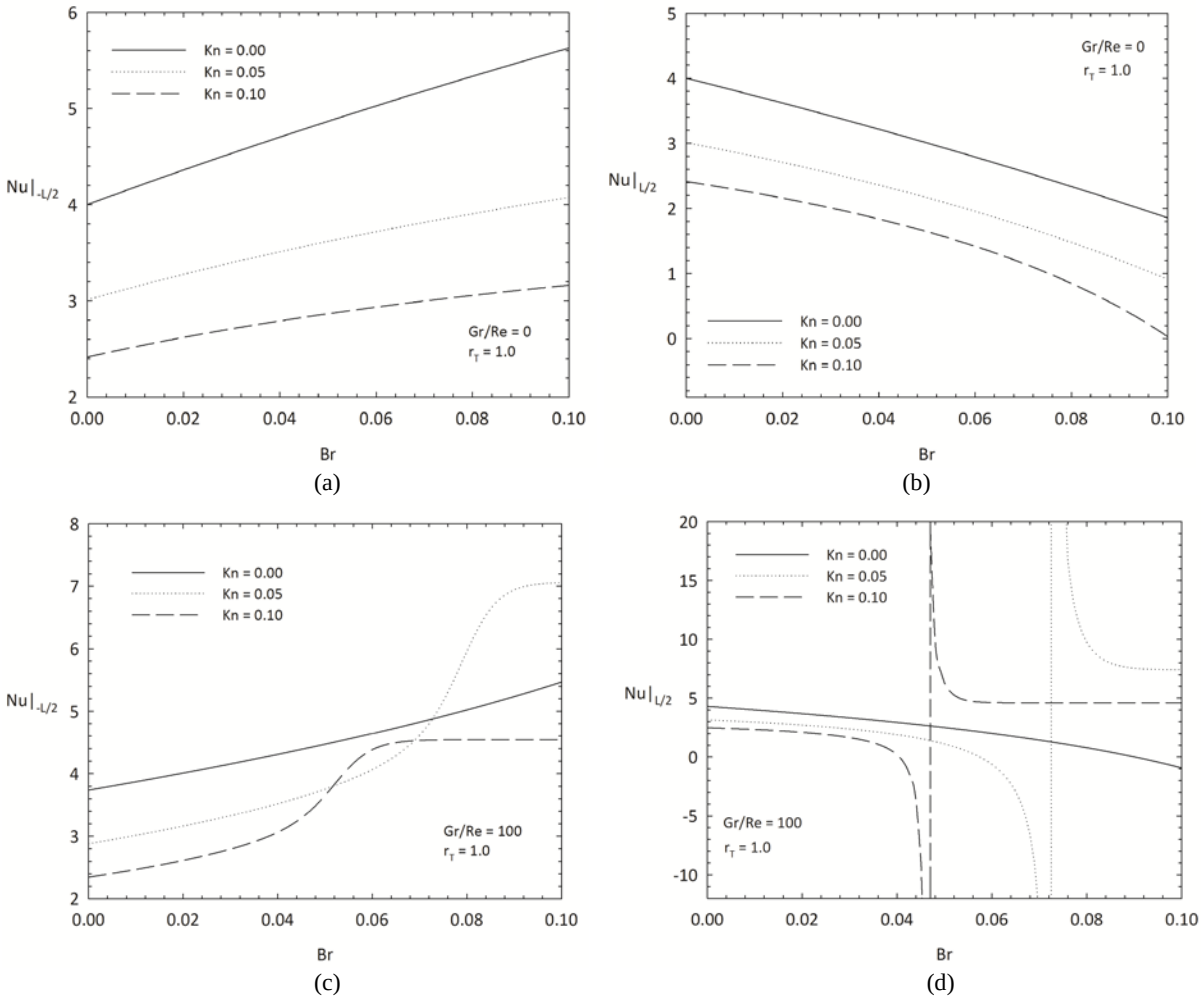

Figure 4. The variation of the *Nu* with *Br* for different values of *Gr/Re* and *Br*.

For the mixed convection case (*Gr/Re* = 100), an interesting behavior is observed (Fig. 4c,d). At *Kn* = 0, with an increase in *Br*, the left-side *Nu* increases while the right-side *Nu* decreases, as expected. However, at *Kn* = 0.1, the left-side *Nu* increases nearly linearly with an increase in *Br* up to $Br \approx 0.045$, then this increase accelerates up to $Br \approx 0.055$ and finally an asymptotic variation in *Nu* is observed (Fig. 4c). Interestingly, *Nu* receives an asymptotic value about $Br \approx 0.065$, beyond which *Br* has no influence on *Nu*. A similar behavior is detected at *Kn* = 0.05. Very surprisingly, after following the similar periods with *Kn* = 0.1, which are nearly-linear increase, accelerated nearly-linear increase and asymptotic, with increasing *Br*, *Nu* reaches a higher value than that at *Kn* = 0. This clearly proves interactive and complicated effects of *Gr/Re*, *Br* and *Kn*. The right-side *Nu*-*Br* variation for varying values *Kn* also presents an interesting character for the case of slip regime ($Kn \neq 0$). A singularity is observed. Up to this singular value of *Br*, *Nu* decreases and, in follows, it becomes constant beyond this value. The value of *Br* at which this singularity is observed increases with an increase in *Kn*.

4. CONCLUSIONS

As an original attempt, the mixed convective heat transfer in an open-ended vertical parallel plate microchannel has been studied for the fully developed flow condition. The slip regime has been examined by including

velocity slip and the temperature jump conditions in the analysis. The viscous dissipation was taken into account, too. A perturbation series method has been used in the analysis. The working parameters were the mixed convection parameter, *Gr/Re*, the Knudsen number, *Kn*, the Brinkman number, *Br*, and the ratio of wall temperature difference, r_T. Their interactive effects on the Nusselt number as well as the velocity and temperature profiles have been determined. The major findings of the present study can be summarized as follows:

1. Results obtained show excellent agreements with those available for the same problem at macroscale and those without the viscous dissipation at microscale.
2. Introducing buoyancy increases the forced convection velocity by moving the peak velocity location towards the hot wall.
3. Including viscous dissipation ($Br \neq 0$), results in an increase in the temperature of the fluid and, in follows, in the velocity.
4. For the forced convection case ($Gr/Re = 0$), the Nusselt number is found to increase with an increase in *Br* at the left wall (cold wall) while the opposite is true for the right wall (hot wall) for a given value of *Kn*. An increase in *Kn* results in a decrease in *Nu* due to the rarefaction effect, as expected. However, for the mixed convection case, and interesting and interactive dependence of *Nu* on *Br* and *Kn* is observed.

5.REFERENCES

[1] Chen, C.K. & Weng, H.C. Natural convection in a vertical microchannel. *Journal of Heat Transfer*, **127**, 1053-1056, 2005.

[2] Chen, C.K. & Weng, H.C. Developing natural convection with thermal creep in a vertical microchannel. *Journal of Physics D: Applied Physics*, **39**, 3107-3118, 2006.

[3] Chen, C.K. & Weng, H.C. On the importance of thermal creep in natural convective gas microflow with wall heat fluxes. *Journal of Physics D: Applied Physics*, **41**, 115501, 2008.

[4] Weng, H.C. & Chen, C.K. A challenge in Navier-Stokes-based continuum modeling: Maxwell-Burnett slip law. *Physics of Fluid*, **20**, 106101, 2008.

[5] Weng, H.C. & Chen, C.K. Variable physical properties in natural convective gas microflow. *Journal of Heat Transfer*, **130**, 082401, 2008.

[6] Chen, C.K. & Weng, H.C. Drag reduction and heat transfer enhancement over a heated wall of a vertical annular microchannel. *International Journal of Heat and Mass Transfer*, **52**, 1075-1079, 2009.

[7] Biswal, L., Som, S.K. & Chakraborty, S. Effects of entrance region transport processes on free convection slip flow in vertical microchannels with isothermally heated walls. *International Journal of Heat and Mass Transfer*, **50**, 1248-1254, 2007.

[8] Khadrawi, A.F., Othman, A. & Al-Nimr, M.A. Transient free convection fluid flow in a vertical microchannel as described by the hyperbolic heat conduction model. *International Journal of Thermophysics*, **26**, 905-918, 2005.

[9] Chakraborty, S., Som, S.K. & Rahul. A boundary layer analysis for entrance region heat transfer in vertical microchannels within the slip flow regime. *International Journal of Heat and Mass Transfer*, **51**, 3245-3250, 2008.

[10] Buonomo, B. & Manca, O. Natural convection slip flow in a vertical microchannel heated at uniform heat flux. *International Journal of Thermal Science*, **49,** 1333-1344, 2010.

[11] Karimipour, A., Nezhad, A.H., D'Orazio, A. & Shirani, E. Investigation of the gravity effects on the mixed convection heat transfer in a microchannel using the lattice Boltzmann method. *International Journal of Thermal Science*, **54,** 142-152, 2012.

[12] Jian, S.J. & Weng, H.C. Second-order mixed convective flow in a long vertical microchannel. *Journal of Heat Transfer*, **135**, 022506, 2013.
[13] Rahimi, B. & Niazmand, H. Effects of high-order slip/jump, thermal creep, and variable thermophysical properties on natural convection in microchannels with constant wall heat fluxes. *Heat Transfer Engineering*, **35,** 1528-1538, 2014.

[14] Wang, C.Y. & Ng, C.O. Natural convection in a vertical slit microchannel with superhydrophobic slip and temperature jump. *Journal of Heat Transfer*, **136**, 034502, 2014.

[15] Jha, B.K. & Aina, B. Impact of viscous dissipation on fully developed natural convection flow in a vertical microchannel. *Journal of Heat Transfer*, **140**, 094502, 2018.

[16] Avci, M. & Aydin, O. Mixed convection in a vertical parallel plate microchannel. *Journal of Heat Transfer*, **129**, 162-166, 2007.

[17] Avci, M. & Aydin, O. Mixed convection in a vertical parallel plate microchannel with asymmetric wall heat fluxes. *Journal of Heat Transfer*, **129**, 1091-1095, 2008.

[18] Avci, M. & Aydin, O. Mixed convection in a vertical microannulus between two concentric microtubes *Journal of Heat Transfer*, **131**, 014502, 2007.

[19] Altunkaya, A.N., Avci, M. & Aydin, O. Effects of viscous dissipation on mixed convection in a vertical parallel-plate microchannel with asymmetric uniform wall heat fluxes: The slip regime. *International Journal of Heat and Mass Transfer*, **111**, 495-499, 2017.

[20] Aung, W. & Worku, G. Theory of fully developed, combined convection including flow reversal. *Journal of Heat Transfer*, **108**, 485-488, 1986.

[21] Gad-el-Hak, M. The MEMS Handbook. ed. New York: CRC Press; 2001.

[22] Barletta, A. Laminar mixed convection with viscous dissipation in a vertical channel. *International Journal of Heat and Mass Transfer*, **41**, 3501-3513, 1998.

ADAPTATION OF THE TOUHAMI *et al.* CORRELATION FOR POOL BOILING OUTSIDE A HORIZONTAL TUBE AT SUB-ATMOSPHERIC PRESSURES

Touhami BAKI*, Driss NEHARI**
*USTO-MB, Faculté de Mécanique, Laboratoire de Carburants Gazeux et Environnement, Oran, Algérie.
Email: touhami.baki@univ-usto.dz
** Laboratory of Intelligent Structures, University, Belhadj Bouchaïb Center, Ain Témouchent, Sidi Bel Abbes Road - BP 284- (46000). Email: nehari2746@gmail.com

ABSTRACT

Boiling at pressures below atmospheric pressure finds its application in the evaporators of absorption refrigeration machines. The design and sizing of these pieces of equipment require the determination of the heat transfer coefficient with correlations taken from the literature under these operating conditions; we review the correlations giving the heat transfer coefficient during pool boiling. Likewise, a review of the experiments of boiling outside a horizontal tube carried out at sub-atmospheric pressures for three kinds of substances namely, water, hydrocarbons, and refrigerants were studied; a comparison of the data collected from the experiment and those calculated with five chosen correlations showed a deviation with relatively high margins; the modification and adaptation of the correlation of Touhami *et al.* to the case of low-pressure boiling have given convincing results.

Keywords: Boiling, Horizontal tube, Heat transfer coefficient, Pressure, Sub-atmospheric.

Symbols

a	Thermal diffusivity (m^2/s)
B	Correlation coefficient [11]
c_p	Heat capacity ($J/kg.K$)
D	Diameter of the tube (m)
F_p	Pressure function [07]
g	Gravity acceleration (m/s^2)
h	Heat transfer Coefficient ($W/m^2.K$)
K	Correlation coefficient [10]
l_c	Capillary length (m)
L	Latent heat of vaporization (J/kg)
Nu	Nusselt Number
P	Pressure (N/m^2)
Pr	Prandtl Number
q	Heat flux (W/m^2)
r	Correlation coefficient
r_o	Radius of the nucleation site (m)
R_a	Arithmetic roughness (nm)
Re	Reynolds Number
R_i	Individual perfect gas constant ($J/kg.K$)
R_q	Quadratic roughness (nm)
T	Temperature (K)

Greek symbols

β	Angle contact ($degree$)
Δ	Difference
ε	Quadratic roughness (μm)
λ	Thermal conductivity ($W/m.K$)

μ	Dynamic viscosity ($Pa.s$)
v	Kinematic viscosity (m^2/s)
ρ	Density (Kg/m^3)
σ	Surface tension (N/m)

Subscripts

c	Critic
cal	Calculated
d	Departure
exp	experimental
l	Liquid
v	Vapor
w	Wall
r	Reduced
sat	Saturated

1. INTRODUCTION

Boiling is a physical phenomenon that allows releasing of a large amount of heat for low-temperature gradients. It occurs outside of horizontal tubes in two-phase equipment such as smoke tube steam boilers and evaporators, and finds its application in various fields such as energy, food, chemicals, industrial heating, and refrigeration.

Vapor compression machines provides refrigeration and air conditioning, where the common application is industrial and domestic sector; another type of machine, absorption refrigeration machines, have appeared and are used more and more, they meet the new directives and regulations for the protection of the environment. These refrigeration machines involve two fluids, a refrigerant, and a transport fluid; the most widely used couple is the ammonia-water system (NH_3-H_2O), where ammonia is the refrigerant and water takes on the role of transport means, cold is produced at the evaporator where the pressure involved is lower than atmospheric pressure. The design of the evaporator requires better knowledge of the boiling phenomenon at sub-atmospheric pressures; modeling of the correlations during pool boiling is relatively well framed, but at low pressures, new phenomena appear, and the valid correlations for pool boiling should be checked.

Boiling at low pressure shows completely different characteristics to known boiling regimes such as nucleate or film boiling; it is characterized by more significant bubble volumes at the detachment, higher bubble growth rates, longer waiting times between bubbles; as pointed out by Florence Giraud *et al.* [01], also, besides in their experiments they noted the non-homogeneity of the pressure and the temperature of saturation, and the influence of the height of the liquid on the experimental conditions; they detected a new boiling regime. Baki and Aris [02] carried out the experimental study of the boiling of R141b on a horizontal tube, and the results are compared with three known correlations, Baki *et al.* [03] studied the impact of the outside diameter of a horizontal tube during pool boiling and proposed a correlation which could give the heat transfer coefficient as a function of the diameter and the thermophysical characteristics of the fluid, Baki [04,05] compared the experimental data of boiling of fluids outside a horizontal tube with known correlations.

The objective of this article is the evaluation of five correlations drawn from the literature with experimental data, for the case of pool boiling outside a horizontal tube at pressures below atmospheric pressure, for this, a review of the correlations giving the heat transfer coefficient was made and compared with experimental results; the adaptation of the correlation of Touhami *et al.* which was initially developed for the determination of the heat transfer coefficient during pool boiling outside of a horizontal tube at pressures higher than atmospheric pressure.

2. REVIEW OF CORRELATIONS AND EXPERIMENTAL DATA

There exist in the literature a multitude of correlations developed, being able to determine the heat transfer coefficient during pool boiling on a hot surface, we have chosen five correlations [06, 10] set out chronologically in Table 1. These correlations allow the heat transfer coefficient to be calculated directly or indirectly through the heat flow; the predicted values are determined as a function of the heat flow, the thermophysical characteristics of the fluid, and the pressure.

The correlation (1) of Mc Nelly [06] determines the heat transfer coefficient from the heat flow, the density ratio, some thermophysical parameters, and the working pressure; the correlation (2) of Mostinski [07] gives the heat transfer coefficient as a function of critical pressure, heat flux and a function of reduced pressure; the correlation (3) of Labuntsov [08] determines the heat transfer coefficient as a function of the thermophysical parameters, of the saturation temperature and the heat flux, that of Yagov [09] makes it possible to calculate the heat flux in the function of the temperature difference between the wall and that of the fluid, the saturation temperature, and the thermophysical parameters. Correlation (5) of Touhami *et al.* [10] predicts the value of the heat transfer coefficient as a function of thermophysical parameters, reduced pressure, heat flow, capillary length, and a geometric parameter, which is the diameter of the tube.

A set of experimental data was retrieved from the literature, totaling 447 points; they are classified in time in Table 2 and relate to the pool boiling of fluids outside a horizontal tube at sub-atmospheric pressures. In this case, the diameter varies from 10 to 70 mm and the absolute pressure from 1.8 to 100.07 kN/m²; The heat flow covers a range from 3 to 115 kW/m², the heat transfer coefficient is between 0.2 and 8.5 kW/m².K; the tube grades are mild steel, stainless steel, brass and copper, the roughness was only available for specific experiments [12,14,15], the substances used are grouped into three categories, water, hydrocarbons, and refrigerants.

Table 1. Correlation prediction of the heat transfer coefficient

Author, Reference / Year	Correlation
Mc Nelly, [06] / 1953	$h = 0.225\left(\frac{qc_p}{L}\right)^{0.69}\left(\frac{P\lambda}{\sigma}\right)^{0.31}\left(\frac{\rho_l}{\rho_v}-1\right)^{0.32}$ (1)
Mostinski, [07] / 1963	$h = 0.106P_{cr}^{0.69}q^{2/3}F_p$ and $F_p = 1.8(p_r)^{0.17} + 4(p_r)^{1.2} + 10(p_r)^{10}$ (2)
Labuntsov, [08] / 1972	$h = 0.075\left[1 + 10\left(\frac{\rho_v}{\rho_l-\rho_v}\right)^{0.67}\right]\left(\frac{\lambda^2}{\nu\sigma T_{sat}}\right)^{0.33} q^{0.67}$ (3)
Yagov, [09] / 2009	$q = 3.43\times10^{-4}\frac{\lambda^2\Delta T^3}{\nu\sigma T_{sat}}\left(1+\frac{L\Delta T}{2R_iT_{sat}^2}\right)\left(1+\sqrt{1+800B}+400B\right)$ and $B = \frac{L(\rho_v\nu)^{3/2}}{\sigma(\lambda T_{sat})^{1/2}}$ (4)
Touhami *et al*, [10] / 2014	$\frac{hD}{\lambda} = 0.5\left(\frac{qD}{\mu L}\right)^{0.67}\left(\frac{\mu c_P}{\lambda}\right)^{0.4}\left(\frac{P}{P_c}\right)^{-0.1}\left(\frac{\varepsilon}{D}\right)^{0.07}\left(\frac{l_c}{D}\right)^{-0.2}$ (5)

Table 2. Experimental data of boiling outside a horizontal tube at sub-atmospheric pressure

Reference	Fluid	Tube: grade, diameter, longer mm	Roughness Ra µm	Flux kW/m²	h kW/m².K	Pressure kN/m²	Points
Varma *et al.* [11] / 1994	Water	Stainless steel /14,05/240		25-83	3-7	6.67	10
Bhaumik *et al.* [12] / 2004	Water Benzene Toluene	Ss /32 / 150		16-42 16-43 16-43	1.1-3.5 1-2.9 1-1.5	20.01-97.39 23.75-97.13 23.35-96.72	36 36 36
Jabardo *et al.* [13] / 2004	R-11, R-123	Copper 19/210	0.16- 2.3 0.16-3.3	5-115 5-115	0.3-8.5 0.3-7.4	48.5 40.3	50 45
Prasad *et al.* [14] / 2007	Methanol	Mild steel 32/145 copper coated 32/145		15-43 15-43	1.4-3.8 1.7-5.2	27.95-97.23 27.72-97.56	30 30
Saiz Jabardo [15] / 2009	R-123	Brass 19/210 Copper 19/210	0.16 0.16	3-77 3-115	0.2-3.2 0.3-4.1	40.3 40.3	17 17
Cieśliński *et al.* [16] / 2011	Water	Stainless steel 10/100	0.06	13-90	2.9-7.7	10	9
Yu *et al.* [17] /2015	Water	Copper 20.8/190		4-10	0.7-5.3	1.8-3.5	77
Kumar *et al.* [18] /2019	Water Benzene	Stainless steel 70/179		13-34 5-25	1.4-3.9 0.5-2.5	35.36-100.07 39.29-98.07	29 25

3. COMPARISON OF CORRELATIONS

A comparison of the experimental and predicted data by each of the chosen correlations, are presented in the following figures; in order to make a comparative assessment, a definition of the error was retained, as follows:

$$Error = \left|\frac{h_{cal}-h_{exp}}{h_{cal}}\right| \quad (6)$$

$$Mean\ Error = \sum_{i=1}^{n} \frac{Erreur_i}{n} \quad (7)$$

$$Standard\ Deviation = \sqrt{\sum_{i=1}^{n} \frac{(Error_i - Mean\ Error)^2}{n}} \quad (8)$$

$$r = \frac{covariance_{h_{exp}h_{cal}}}{variance_{h_{exp}}.variance_{h_{cal}}} \quad (9)$$

Equations from (6) to (9) make it possible to evaluate the mean error and its standard deviation of the heat transfer coefficient calculated, and compare the calculated and the experimental values; the correlation coefficient measures the affinity between the values of the abscises and those of the coordinates, the more the coefficient tends towards the unit value and the more the values calculated with the corresponding correlation approach the experimental values and give small average errors.

3.1 Mc Nelly Correlation [06]

Figure 1 shows the comparison of the experimental data to that calculated with the Mac Nelly correlation [06], the points are mostly below the median line, the calculated values are superior to those experimental, a series of data relating to the water is above the set, the mean error is 44%, and the correlation coefficient is 0.72.

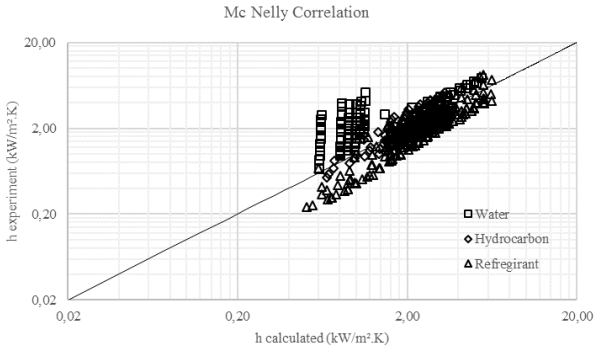

Figure 1. Validation of experimental data with Mc Nelly correlation [06]

3.2 Mostinski Correlation [07]

Figure 2 shows a comparison of the heat transfer coefficients of the experimental data with those calculated with the Mostinski correlation [07], a set of points focus along the centerline another group of points is above, the mean error is around 84%, and the correlation coefficient which indicates the affinity of the two types of values is determined and is worth 0.71.

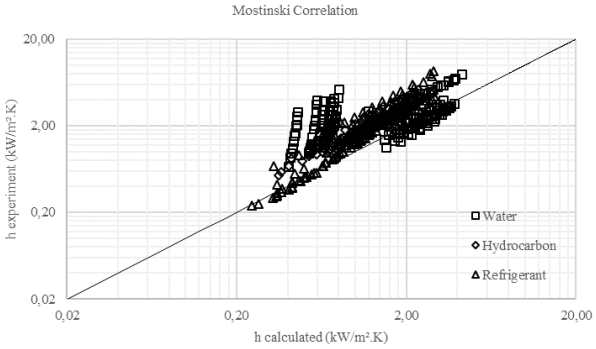

Figure 2. Validation of experimental data with Mostinski correlation [07]

3.3 Labuntsov Correlation [08]

The Labuntsov correlation [08] gives results with an error of around 63% and a correlation coefficient of 0.74, just as for the other correlations, two sets of points detach from the line middle and another above at right, see Figure 3.

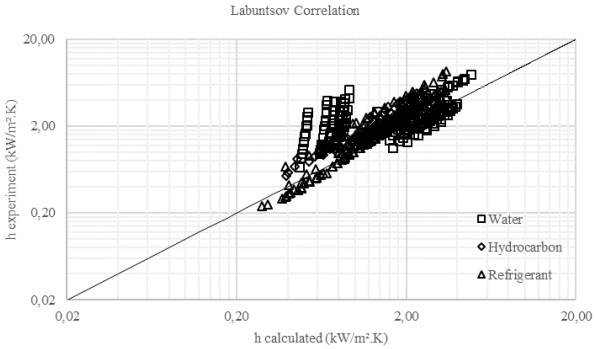

Figure 3. Validation of experimental data with Labuntsov correlation [08]

3.4 Yagov Correlation [09]

The Yagov correlation [09] gives a large dispersion of the points calculated with the correlation in Figure 4, particularly for the water data, with an error of 396% and the coefficient r = 0.13; this correlation is not valid for the case studied.

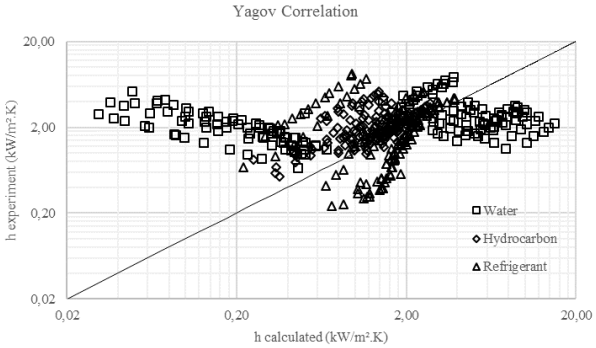

Figure 4. Validation of experimental data with Yagov correlation [09]

3.5 Touhami *et al.* Correlation [10]

The points of the calculated values, presented in Figure 5, concentrates in the area above the median line, which indicates that the calculated values are underestimated compared to the experimental values. The mean of error is 121%, and the correlation coefficient is 0.76.

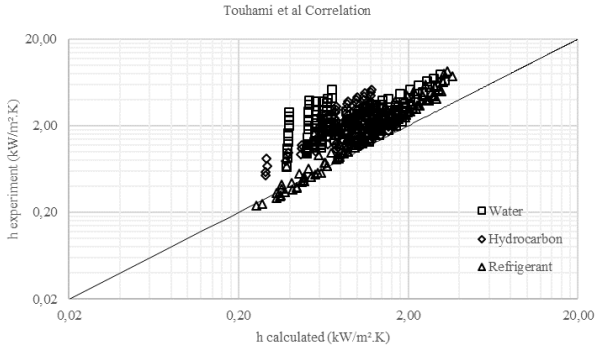

Figure 5. Validation of experimental data with Touhami *et al.* correlation [10]

4. ADAPTATION OF THE TOUHAMI *et al.* CORRELATION [10]

Figure 5 presents the data from the validation of Touhami *et al.* [10], which gives convincing results; by adapting this same correlation to boiling at low-pressure, we can further improve the calculated data and minimize the error.

4.1 Influence of pressure

By plotting the Nusselt as a function of the reduced pressure of all the experimental data collected, see Figure 6, we found a relationship using the least-squares method. The relationship is of the form:

$$Nu = 2688{,}9\left(\frac{P}{Pc}\right)^{0.42} \tag{10}$$

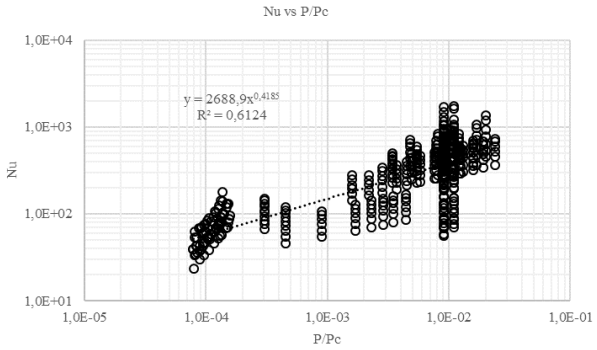

Figure 6. The relation between Nu and reduced pressure

4.2 Proposal for a new correlation

Correlation (5) is presented in the form of equality between the Nusselt and a product of dimensionless numbers;

This correlation is a product of the first two groups of dimensionless numbers $\left(\frac{qD}{\mu L}\right)^{0.67}$, $\left(\frac{\mu c_P}{\lambda}\right)^{0.4}$ and cannot be changed; the group $\left(\frac{P}{P_c}\right)^{-0.1}$ will replace by $\left(\frac{P}{P_c}\right)^{0.42}$, the group $\left(\frac{\varepsilon}{D}\right)^{0.07}$ is deleted, since the roughness data are not always available, in addition the exponent 0.07 shows that there is little influence of roughness on the result; we added another dimensionless number which is the density ratio $\left(\frac{\rho_v}{\rho_l - \rho_v}\right)$ for better smoothing; we obtain a new correlation presented below:

$$\frac{hD}{\lambda} = 5.5\left(\frac{qD}{\mu L}\right)^{0.67}\left(\frac{\mu c_P}{\lambda}\right)^{0.4}\left(\frac{P}{P_c}\right)^{0.42}\left(\frac{l_c}{D}\right)^{-0.2}\left(\frac{\rho_v}{\rho_l - \rho_v}\right)^{-0.6} \quad (11)$$

The data calculated with the newly adapted correlation (11), are presented in Figure 7. The points concentrates around the centerline with a margin of error of 39% and a correlation coefficient of 0.78; the results of the adapted correlation are very significant.

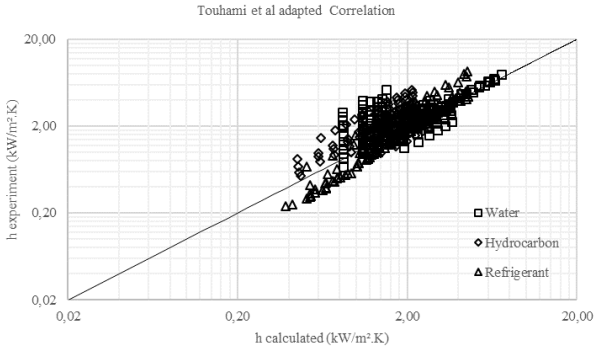

Figure 7. Validation of experimental data with the adapted Touhami *et al.* correlation (11)

5. CONCLUSION

- A review of the correlations giving the heat transfer coefficient during the pool boiling for pressures higher than atmospheric pressure was carried out.
- A review of experimental data relating to the pool boiling outside of a horizontal tube for pressures below atmospheric pressure was made.
- The validation of the correlations with the experimental data gave medium to low results with margins of error from 44 to 400%
- The correlation of Touhami *et al.* [10] adapts to the case studied, namely pool boiling at low-pressure, and a new correlation is presented.
- The validation of the newly adapted correlation presented in equation (11) gave very noticeable results with an error of 39% and a correlation coefficient of 0.78.

ACKNOWLEDGMENTS

The author address the most sincere thanks to the directorate-general for scientific research and technological development for its financial support under the FNRSDT/DGRSDT within the framework of ERANETMED3 (Project ERANETMED3-166 EXTRASEA).

REFERENCES

[1] Giraud, F., Rullière, R., Toublanc, C., Clausse, M., & Bonjour, J., Experimental evidence of a new regime for boiling of water at subatmospheric pressure. *Experimental Thermal and Fluid Science*, *60*, 45-53, 2015.

[2] BAKI Touhami, ARIS Abdelkader, étude expérimentale du transfert de chaleur lors de l'ébullition en vase du R141b, *Communication Science & technologie, COST*, N° 11. Juillet, 2012.

[3] Baki Touhami, Aris Abdelkader, Guessab Ahmed, Impact du diamètre extérieur d'un tube horizontal lors de l'ébullition en vase, *12ème Congrès de Mécanique*, Casablanca - Maroc, 21-24 Avril 2015.

[4] Baki Touhami (2018). Ebullition à l'Extérieur d'un Tube Horizontal, Comparaison de Corrélations, *Congrès National sur les Energies et Matériaux (CNEM),* Naâma - Algeria, 17-18 Décembre 2018.

[5] Touhami BAKI, Ebullition à l'extérieur d'un Tube Horizontal à des Pressions sous Atmosphérique, Comparaison de Corrélations, *1st International Symposium on Materials, Energy and Environment MEE'2020*, El Oued, ALGERIA, January 20-21st; 2020.,

[6] Mc Nelly, M. J., A correlation of rates of heat transfer to nucleate boiling of liquids. J. *Imperial College Chem. Eng. Soc*, 7, 18-34. 1953.

[7] Mostinski, I.L., Application of the rule of corresponding states for calculation of heat transfer and critical heat flux, *Teploenergetika*, 1963.

[8] Labuntsov, D.A., Heat transfer problems with nucleate boiling of liquids, *Therm. Eng*. 19 (9) 21–28, 1972.

[9] Yagov, V. V., Nucleate boiling heat transfer: Possibilities and limitations of theoretical analysis, *in: Heat Mass Transf. Und Stoffuebertragung*, 2009.

[10] Touhami, B., Abdelkader, A., & Mohamed, T., Proposal for a correlation raising the impact of the external diameter of a horizontal tube during pool boiling. *International Journal of Thermal Sciences*, 84, 293-299, 2014.

[11] Varma, H. K., Mehrotra, R. K., Agrawal, K. N., & Singh, S., Heat transfer during pool boiling of LiBr-water solutions at sub atmospheric pressures. *International communications in heat and mass transfer*, 21(4), 539-548, 1994.

[12] Bhaumik, S., Agarwal, V. K., & Gupta, S. C., A generalized correlation of nucleate pool boiling of liquids, *Indian journal of chemical technology* Vol. 11, pp. 719-725, 2004.

[13] Jabardo, J. M., Silva, E., Ribatski, G., & de Barros, S. F., Evaluation of the Rohsenow correlation through experimental pool boiling of halocarbon refrigerants on cylindrical surfaces. *Journal of the Brazilian Society of Mechanical Sciences and Engineering*, 26(2), 218-230, 2004.

[14] Prasad, L., Siraj Alam, M., Gupta, S. C., & Agarwal, V. K., Enhanced boiling of methanol on copper coated surface. *Chemical Engineering & Technology: Industrial Chemistry-Plant Equipment-Process Engineering-Biotechnology*, 30(7), 901-906, 2007.

[15] Saiz, J., Nucleate boiling heat transfer, *ECI International Conference on Boiling Heat Transfer*, Florianópolis-SC-Brazil, 3-7 May 2009.

[16] Cieśliński, J., & Kaczmarczyk, T., The effect of pressure on heat transfer during pool boiling of water-Al2O3 and water-Cu nanofluids on stainless steel smooth tube. *Chemical and Process Engineering*, 32(4), 321-332, 2011.

[17] Yu, L. H., Xu, S. X., Ma, G. Y., & Wang, J., Experimental research on water boiling heat transfer on horizontal copper rod surface at sub-atmospheric pressure. *Energies*, 8(9), 10141-10152, 2015.

[18] Tarun Kumar, C. H. Tyagi, Varun Tyagi, Effect of heat flux and pressure on heat transfer coefficient during the boiling of distilled water and benzene, *International Research Journal of Engineering and Technology (IRJET)*, Volume: 03 Issue: 09 | Sep -2016.

NUMERICAL INVESTIGATION OF FLOW AND HEAT TRANSFER IN AN OPEN CAVITY

Ekin Özgirgin Yapici, Ece Aylı, Eyup Kocak, Ahmet Deniz
Çankaya University, Department of Mechanical Engineering, 06790, Ankara, Turkey

ABSTRACT

In this study, buoyancy-driven cavity flow for mixed convection regime is investigated. A parametric study is carried out to investigate the effect of the heated wall, Richardson number, Reynolds number, heat flux value, and cavity geometric parameters numerically for turbulent flow. The working fluid is assumed as air with Pr=0.71 The problem is modeled as 2D incompressible flow with solving Navier-Stokes equations using Fluent software with Boussinesq approximation. Length to depth ratio and height to depth ratio of the cavity is varied between $0.25<L/H<5$, $0.25<D/H<3$, respectively. Reynolds number is changed between $24000<Re<96000$ Firstly, numerical parameters effect like turbulence model, dimension effect, mesh effect are carried out to obtain results that are independent of the numerical errors. After developing a numerical methodology, a parametric study is carried out. Results indicate that the D/H and L/D ratio has a direct effect on the thermal performance of the enclosure. It is observed that when $Ri<1$, buoyancy effects are negligible, and when $Ri>1$, buoyancy effects are dominant; thus, increasing the Richardson number raises the Nusselt number. This parametric study also depicts that the turbulent diffusion mechanism has a critical role in heat transfer. It is demonstrated that, for an aspect ratio lower than 1, a single elongated eddy is formed in the cavity region.

Keywords: cavity, mixed convection, heat transfer, Richardson number

1. INTRODUCTION

Convective flow and heat transfer in a square cavity have been extensively investigated for decades as it has an extensive range of applicability, such as nuclear reactors, geothermal energy systems, heat exchangers, and air conditioning (HVAC) systems. In these systems, heat transfer occurs in natural, combined, or mixed convection methods. In the literature, several studies are affected to investigate the interaction of free stream flow and buoyancy flow inside the cavity, both numerically and experimentally. The main aim of those studies is to enhance the heat transfer rate, provide the durability and reliability of the systems [1, 2]. In an experimental study of Manca et al. [3], mixed convection in an open cavity with the heat-ed wall is examined experimentally. The left wall of the cavity is heated, while other walls are adiabatic. The flow and heat transfer within the cavity is controlled by Reynolds number, Richardson number, and the buoyancy parameter. The results were reported for Reynolds numbers between 100 and 1000. Richardson number is taken between 30-110 for Reynolds number 1000, and Richardson number is taken between 2800-8700 for Reynolds number 100. The length to the height and height to depth ratio is varied between $0.5<L/D<1.5$ and $0.5<H/D<1$, respectively. Researchers found that, for Re=1000, there were two different fluid motions, which were a parallel forced flow and recirculation flow within the cavity. For Re=100, the buoyancy effects were stronger and determined the penetration of thermal starting from the plate wall (heated) into the upper channel. Bilgen and Oztop [4] examined the natural convection heat transfer numerically in the partially open and inclined square cavity, and this study shows that the inclination angle does not affect the Nusselt number linearly.

Chaves et al. [5] performed numerical analysis for mixed convection heat transfer for a semi-porous open cavity. Studied geometry comprises two vertical walls where one is a porous wall and one bottom wall. The study aims to observe the effect of natural convection, which can improve the forced convection inside the cavity. According to the obtained results, it is shown that for cooling purposes, the forced convection inside the semi-porous open cavity studied may be significantly enhanced by natural convection effects.

Manca et al. [6] studied the effect of the heated wall position in the open cavity numerically. The maximum temperature occurred when the cavity is heated from the below, while minimum temperature distribution is observed in the case that the cavity is heated from the right wall. Timuralp and Altaç [7] numerically investigated the effect of duct height to cavity height and cavity width to cavity height. They verify their numerical results with the experimental study of Leong et al. [8]. They observed that increasing the H/D ratio also increases the Nusselt number. Showole and Tarasuk [9] investigate the natural convection in inclined cavities numerically. They performed their analysis 2-dimensionally for incompressible, steady-state, viscous flow. They used k-ε turbulence model to solve the Reynolds stress term. They showed their results in the form of velocity and temperature profiles and local and average heat transfer rates. Insight of their results, inclination creates better mixing in the flow and causes a higher heat transfer coefficient. Carozza [10] carried out a numerical study to examine the effect of aspect ratios of the cavity on mixed convection for two-dimensional flow. Decreasing the L/D ratio increases the temperature values as the cavity zone gets tighter. Mulaweh et al. [11] studied buoyancy-opposing, two-dimensional (2D), laminar airflow over a vertical forward-facing step under the mixed convection condition. They found that the local Nusselt number decreases with increasing the opposing buoyancy force, and in the assisting flow opposite situation is observed. Koufi et al. [12] have examined the heat transfer by mixed convection within ventilated cavities with exhaust and supply slots, and loaded with air under turbulent and constant flow regimes numerically. The lowest part of the cavity's temperature is held in TH, and others are held in constant temperature as TC. The cavity has two slots, which are an outlet slot for extracting hot air and an inlet slot for letting in the fresh air. Due to their results, configuration D provides higher Nusselt number distribution when it is compared with the other configurations.

In the literature, most previous studies considered only natural convection or forced convection. On the other hand, sometimes natural convection is insufficient for thermal management and control of such systems, so forced convection is required. Especially for electronics cooling problems, mixed convection is necessary to increase the effectiveness and reliability [10]. Faure et al. [11] conducted experimental studies for different L / D ratios and Reynolds numbers. In their study, they have shown the dynamics of cavity flow. In the cavity region, there are 3 vortex formations whose sizes vary depending on the geometric properties. These structures are the main vortex, the corner vortex, and the secondary vortex which is formed near the front wall. Ayli [12], studied the heat transfer characteristics of laminar combined forced convection through a horizontal duct with numerical methods. According to results, increasing the L/D ratio of the cavity also rises the Nusselt number and heat transfer. Also increasing the Reynolds number 4 times increases the Nusselt number 1.75 times. Ajmera and Mathur [13] studied numerically the free and forced convection in an enclosure for different ventilation arrangements as a cooling strategy for the heater in a cavity. They proposed that increasing the Richardson number enhance heat transfer in forced convection regime while it does not affect natural convection.

Faure et al. [14] conducted experimental studies for different L / D ratios and Reynolds numbers. In their study, they have shown the dynamics of cavity flow. In the cavity region, there are 3 vortex formations whose sizes vary depending on the geometric properties. These structures are the main vortex, the corner vortex, and the secondary vortex which is formed near the front wall. Ayli [15], studied the heat transfer characteristics of laminar combined forced convection through a horizontal duct with numerical methods. According to results, increasing the L/D ratio of the cavity also rises the Nusselt number and heat transfer. Also increasing the Reynolds number 4 times increases the Nusselt number 1.75 times. Ajmera and Mathur [16] studied numerically the free and forced convection in an enclosure for different ventilation arrangements as a cooling strategy for the heater in a cavity. They proposed that increasing the Richardson number enhance heat transfer in forced convection regime while it does not affect natural convection. Heat transfer in a cavity geometry is great of an interest in engineering applications as low heat transfer rates will cause high-temperature gradients that decrease the durability, lifetime, and reliability. Therefore as it is seen in the previous research several studies are performed to optimize the cavity parameters to enhance the heat transfer. For this purpose in this study, combined forced and natural convection heat transfer and fluid flow are examined in an open cavity. The effect of cavity geometries like cavity depth, cavity length, on heat transfer rate is investigated. As a flow parameter, Reynolds number, heat flux, heated wall position, and Richardson num-ber effect on the heat transfer are investigated. The left wall of the cavity is heated with constant heat flux, and other walls are assumed as adiabatic. A comprehensive investigation regarding investigate the heat transfer rates in different cavity configurations is performed with Computational Fluid Dynamics (CFD) techniques.

2. PROBLEM DEFINITION AND NUMERICAL METHODOLOGY

The considered geometry is illustrated in Figure 1. The cavity bottom and right wall are taken adiabatic while the right wall is heated with constant heat flux. The fluid enters the channel at the uniform velocity U_0 on the left and at a temperature of T_0 = 300 K. The upper wall of the free stream domain is considered as a pressure far field. For the outlet, the pressure outlet boundary condition is utilized. The bottom surface of the cavity is exposed to constant heat flux. To examine the effect of the heated wall, the wall which subjects to constant heat flux is changed. Flow is considered as laminar, incompressible, and steady. The flow is Newtonian with constant thermal properties.

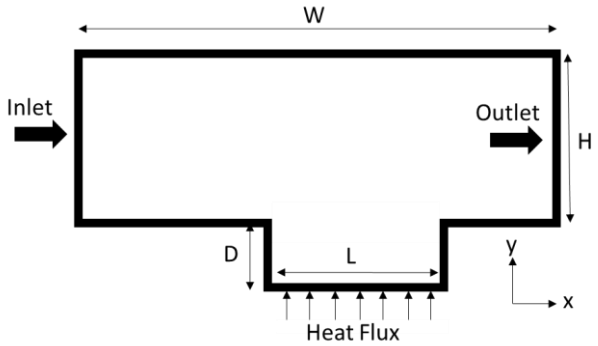

Figure 1. Schematic view of the geometry.

The Navier-Stokes equations define the motion of a viscous fluid conforming to Newton's law. Under the assumptions for this problem governing equations can be stated as:

$$\frac{\partial u}{\partial x}+\frac{\partial v}{\partial y}=0 \tag{1}$$

$$u\frac{\partial u}{\partial x}+v\frac{\partial v}{\partial y}=-\frac{1}{\rho}\frac{\partial P}{\partial x}+\upsilon\left(\frac{\partial^2 u}{\partial x^2}+\frac{\partial^2 u}{\partial y^2}\right) \tag{2}$$

$$u\frac{\partial u}{\partial x}+v\frac{\partial v}{\partial y}=-\frac{1}{\rho}\frac{\partial P}{\partial y}+\upsilon\left(\frac{\partial^2 u}{\partial x^2}+\frac{\partial^2 u}{\partial y^2}\right)+\beta g(T-T_0) \tag{3}$$

$$u\frac{\partial T}{\partial x}+v\frac{\partial T}{\partial y}=\alpha\left(\frac{\partial^2 T}{\partial x^2}+\frac{\partial^2 T}{\partial y^2}\right) \tag{4}$$

Where ρ is the density, β is the thermal expansion coefficient, T is the temperature, and g is the gravity. Eq (1)-Eq (4) are valid for this problem. The Boussinesq approximation is employed to convert the problem to a steady-state. The non-dimensional numbers encountered for this problem are given below.

$$\mathrm{Re}=\frac{u_0 H}{\nu}, Gr=\frac{g\beta(T_H-T_c)H^3}{\nu^2},\ \mathrm{Pr}=\frac{\nu}{\alpha}, Ri=\frac{g\beta(\mathrm{T}_{hot}-\mathrm{T}_{ref})\mathrm{L}}{V^2} \tag{5}$$

The Prandtl number set to Pr=0.7; Re ranges from 24000 to 96000 and Ri from 0.1 to 100. The ranges are wide enough to explore the development of the unsteady regime in the problem of mixed convection.The Nusselt number is computed by the following equation:

$$Nu = \frac{1}{L}\int_0^L Nu(y)dy = \frac{1}{L}\int_0^L \frac{h(y)y}{k}dy \tag{6}$$

where

$$h(y) = \frac{q}{T(y) - T_0} \tag{7}$$

The boundary conditions are stated as given below:

$$u = u_0, \mathrm{v} = 0, T = T_0 \;\; at\ inlet$$
$$u' = v' = 0, T' = 0 \;\; at\ duct\ outlet$$
$$\frac{\partial T}{\partial n} = 0, u = v = 0 \;\; at\ adiabatic\ walls$$
$$k\frac{dT}{dy}\bigg|_{y=D} = q_w \;\; heated\ cavity\ wall$$

The convergence criterion is defined in Equation (8).

$$\frac{\sum\left|\theta^{n+1} - \theta^n\right|}{\Delta\tau\sum\theta^n} \le 10^{-4} \tag{8}$$

where θ is the dependent variable and n is the iteration index. A segregated finite volume solver is chosen for analysis. ANSYS Fluent software is used to perform analysis. The convective terms are computed using the UPWIND second-order accurate differencing scheme based on the SIMPLE method. In the study, 36 different cases are analyzed to observe the effect of the geometrical parameters, Reynolds number, heat flux, and heated wall effect. A test matrix is given in Table 1.

Table 1. Test Matrix

Test Case	L/H	H/D	Re	Heat Flux
Case 1-4	0.25<L/H<5	1	24000	100
Case 5-9	1	0.25<H/D<3	24000	100
Case 10-13	0.25<L/H<5	1	48000	100
Case 14-17	1	0.25<H/D<3	48000	100
Case 19-22	0.25<L/H<5	1	96000	100
Case 23-26	1	0.25<H/D<3	96000	100
Case27-30	.1	1	48000	100<Q<300
Case 31-33	1	1	96000	Heated wall effect (100)

3.VALIDATION AND VERIFICATION

To determine the accuracy of the numerical study, and to obtain independent results from numerical parameters, the numerical solutions are compared with the experiment of Manca et al. [2]. Results that are not independent of

time and mesh structure are not very accurate in Computational Fluid Dynamics; therefore, mesh independency study should be carried out, and analysis should be started after minimizing numerical errors. Prior to examining the effect of the parameters that are mentioned on heat transfer, the results that are independent of the mesh and turbulence model are ensured. Several mesh structures are put up with quadrilateral elements. The result of each grid and comparison are shown in Table 2. In the previous study [13], the details about mesh independency and turbulence model are given. From the obtained, it is seen that the $6x10^5$ element grid provides satisfactory results with a maximum deviation of 0.088 compared to the $1x10^6$ element grid. For the chosen mesh number of grid nodes inside the thermal boundary layer is 45. The y+ value is smaller than 5 for all of the prepared mesh cases.

Table 2. Mesh Independency Test Results

Number of Mesh Element	T_w-T_0 [K]	Relative Error [%]
100000	8.7	-
300000	8.8	11.364
600000	8.99	2.113
1000000	8.998	0.088
1200000	8.999	0.011

The turbulence model study is performed by comparing the temperature distributions for L/D=1, Re=1000, and 50 W/m2 heat flux flow conditions. All of the models' temperature distributions are compared with the experimental study that is performed by Manca et al. [2]. Figure 2 depicts the comparison of temperature distribution obtained using different turbulence models. In Table 3, tried turbulence models and RMSE values are given when the results are compared with the experimental study. According to the results, using the k-ω SST turbulence model gives the best approach.

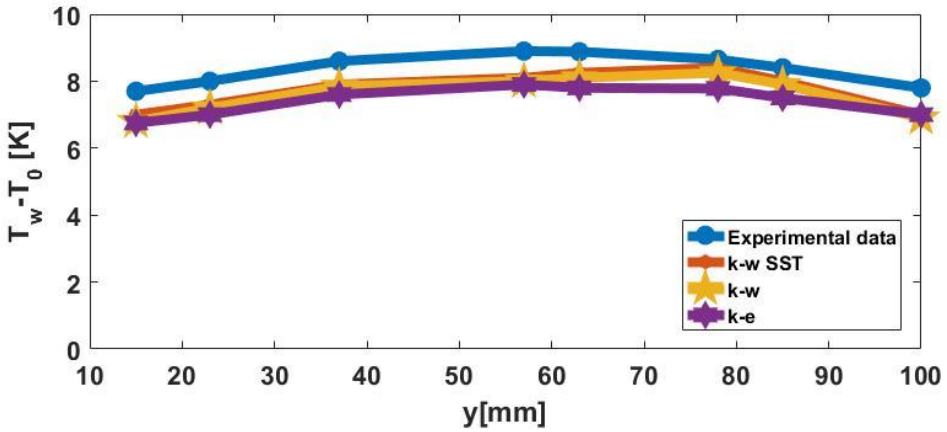

Figure 2. Turbulence model study

Table 3. Turbulence Model Test Results

Turbulence Model	RMSE [%]
Spallart-Allmaras	9.425
k-ε	7.529
k-ω	6.445
k-ω SST	5.06

Also, to reduce the computational cost analysis is performed 2-D. Therefore, firstly 2-D and 3-D analyses are compared with each other for case 1 which has L/D=0.25, D/H=1, Re=24000, q=100 W/m2. To make an accurate comparison, firstly, for both 3D and 2D geometries, meshes are refined until results are not varied with the mesh quality. In Figure 3, temperature contours for 3-dimensional flow are shown for different planes. Although 3D simulations are more realistic and capture the gradients along the z-axis, in all of the planes, flow behavior is similar to each other. This similar temperature flow distribution shows that there is a periodic behavior in the flow in the z-direction. Also, in Figure 4, the temperature distribution is depicted for 2-D and 3-D flow. Therefore making a 2D analysis is enough to model the problem accurately. In the literature, several researchers have also performed cavity analysis with two-dimensional assumption [14,15].

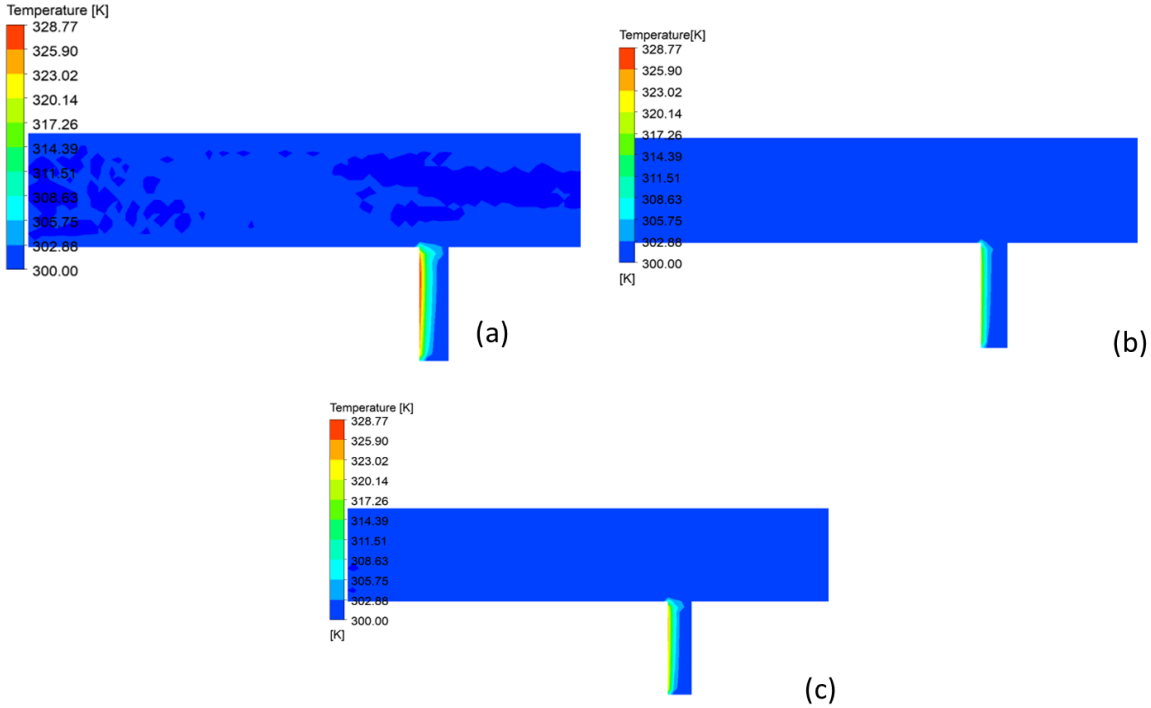

Figure 3. Temperature distribution for (a) y=0 m (b) y=0.05 m (c) y=0.01 m

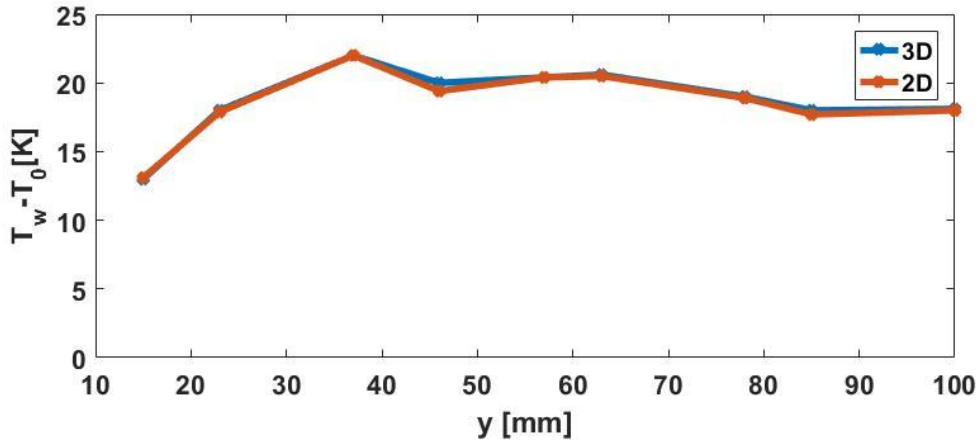

Figure 4. Temperature distribution for 2-D and 3-D simulation

When the viscous effects due to the shear stress between the fluid particles and the pipe wall create a fully

developed velocity profile, it is known as fully developed flow. To reach a fully developed flow, 2-dimensional flow through a straight pipe is solved for all of the Reynolds numbers that are used in this study. In the inlet of the cavity, the obtained velocity profile is given, so flow is fully developed before entering the test section. In Figure 5, a developed boundary layer profile is given for all of the Reynolds numbers. A parabolic shape velocity profile is obtained for all of the velocity values. The obtained fully developed velocity profile is given to the inlet of the cavity due to the reduced computational cost.

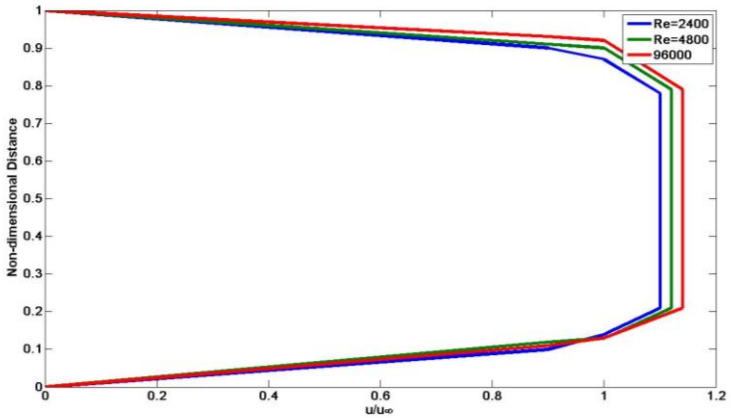

Figure 5. Velocity distribution graphic for channel flow

After obtaining the results independent from the mesh and fully developed validation is performed with the experimental study of Manca et al. [2]. For the case with L/D=0.5 and 2, H/D=1, q=100 w/m2, and Re=1000; the temperature distribution is compared with the numerical value as it is depicted in Table 4. The temperature distribution trend is observed similar to the experiment and in the numerical study. It is seen that in the middle of the cavity temperature difference reaches its maximum value for both in the numerical and experimental study. The details of the verification study can be found in our previous study [13]. For case 1 maximum difference is calculated as 6.4%, while for case 2 maximum error is 7.76%.

Table 4. Comparison of numerical and experimental temperature distribution results

	Case 1				Case 2			
Tw-T0 [K]	Experimental Value	y [mm]	Numerical Value	Error [%]	Experimental Value	y [mm]	Numerical Value	Error [%]
	14,6	18	14,02	3,97	13,02	18	12,01	7,76
	15,6	23	14,7	5,77	13,78	23	13	5,66
	16,3	37	15,3	6,13	14,3	37	13,76	3,78
	16,98	53	16,89	0,53	14,78	53	14	5,28
	16,92	62	16,91	0,06	14,62	62	13,97	4,45
	16,89	73	16,87	0,12	14,01	73	13,96	0,36
	16,23	84	16,02	1,29	13,76	84	12,98	5,67
	14,97	96	14,01	6,41	12,98	96	12,4	4,47

4.RESULTS

4.1. Richardson Number Effect: To investigate the effect of Richardson number, it is varied between 0.1<Ri<10 for a square cavity with different Reynolds numbers. When Ri<1, a small recirculating cell is observed in the cavity region. Conduction is dominant in the cavity zone. As the buoyancy effect is small, then

the mechanical effect of the induced flow. Nusselt number is small in the smallest Richardson number. When the Richardson number is larger than the unity, the buoyancy effect is dominant, and the Nusselt number increases. The vortex structures grow up and fill the entire closure and plume formation becomes dominant. For Ri<1, the Nusselt number increment is small when it is compared with the cases Ri>1 as shown in Figure 6. This trend can be observed in the highest Reynolds number case. Also, Burgos et al. [16] observed a similar pattern for laminar mixed convection.

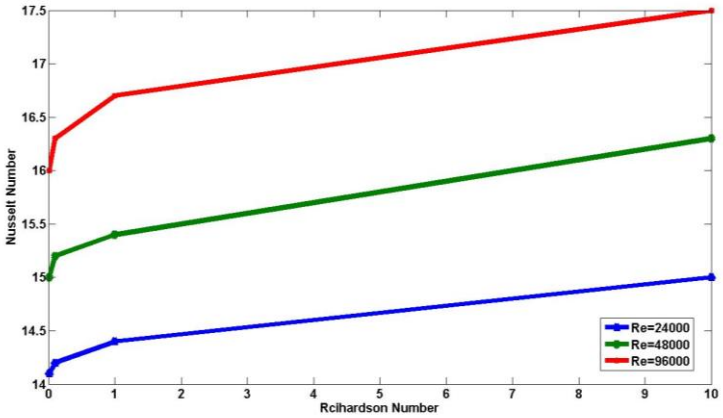

Figure 6. Average Nusselt number distribution as a function of Richardson number for different Reynolds numbers

3.2. Position of the Heated Wall Effect: To investigate the effect of the heated wall effect in the flow field and the heat transfer, three different cases are prepared. In the first case, the right wall is heated, which is called assisting flow. In the second case, the left wall is heated and called an opposing flow, and in the last case bottom wall is heated. Heating one wall with uniform heat flux and keeping other walls in constant temperature causes an interaction between a buoyancy induced flow and a forced flow. In Figure 7, Nusselt number distribution is presented for different heating location cases. Due to the results, the best heat transfer enhancement is achieved when the opposing wall is heated. As incoming air hits the warm air which moves in the spanwise direction and mixing occurs efficiently in this case. When assisting the wall is heated, the maximum temperature difference and minimum Nusselt number is attained.

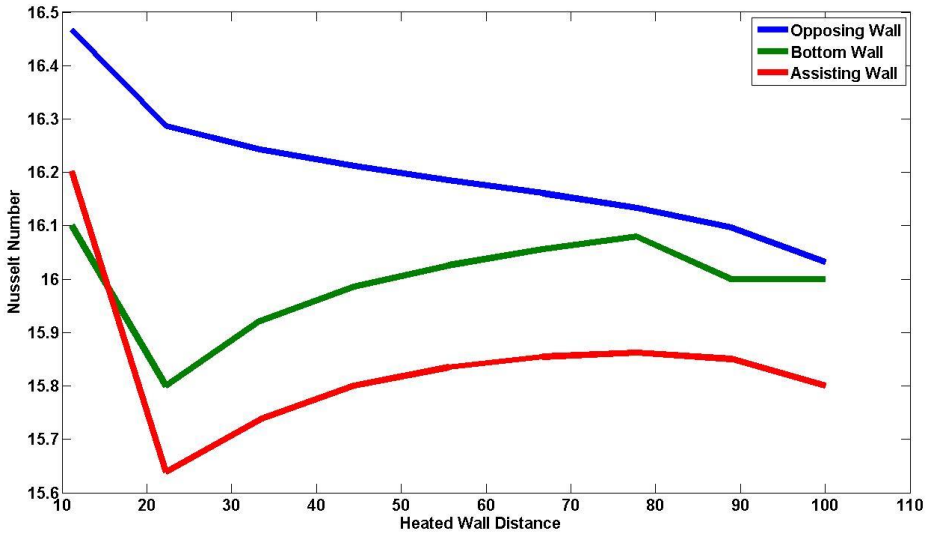

Figure 7. Average Nusselt number distribution for different heating positions

In Figure 8, flow behavior is shown for different heating walls. When the cavity is heated from the bottom

wall, a single low-speed vortex exists in the zone. In the opposing flow condition, incoming warmer air penetrates the cavity, exiting adjacent to the upper corner of the heat source.

Figure 8. The behavior of the flow inside the cavity for different heating wall modes (colored by temperature)

3.3. Heat Flux Effect on Heat Transfer Characteristics: To observe the heat flux effect, geometry and Reynolds Number were kept constant, and heat flux values were changed to 100,200 and 300 W/m2. As it is given in Figure 9, the temperature difference increases with increasing the heat flux value, which means that heat flux and temperature difference are directly proportional. The time to reach a steady-state is lower when heat flux is 100 W/m2. When heat flux values increase, the time to reach steady-state also rises.

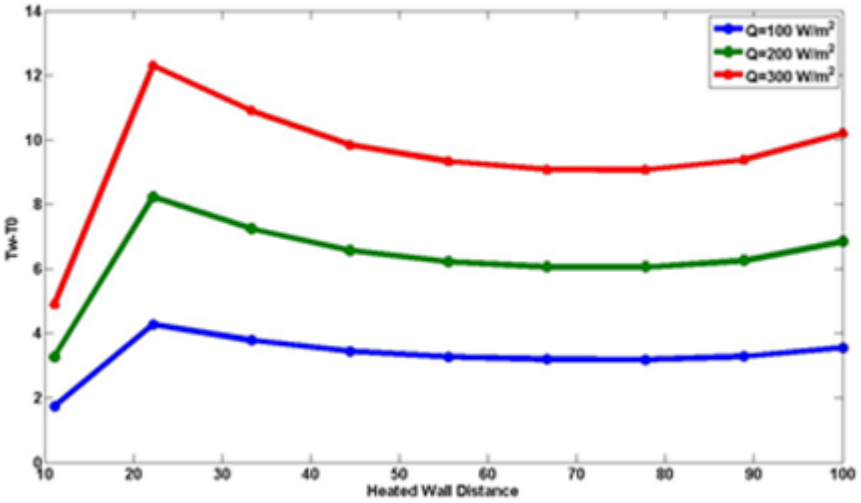

Figure 9. Temperature distribution for different heat flux

3.4. Aspect Ratio Effect on Heat Transfer Characteristics: The L/D ratio is varied between 0.25<L/D<5 to observe the effect of cavity length on heat transfer. When thermal buoyancy dominates the flow, multiple cells are observed in the flow field as shown in Figure 10. When L/D=5, multiple cells are observed in the flow zone while only one cell appeared in the channel with L/D=1. When L/D<1, warm air cannot penetrate with the hot air which causes high-temperature values inside the cavity. With increasing the cavity length, especially when L/D>1, hot air mix with the warm air. The more vortices inside the cavity cause higher turbulence inside the zone and better mixing. From those observations, it can be claimed that the cavity aspect ratio has a dominant role in the flow pattern and stability. Increasing the aspect ratio causes higher heat transfer rates when Reynolds and Grashof number varies.

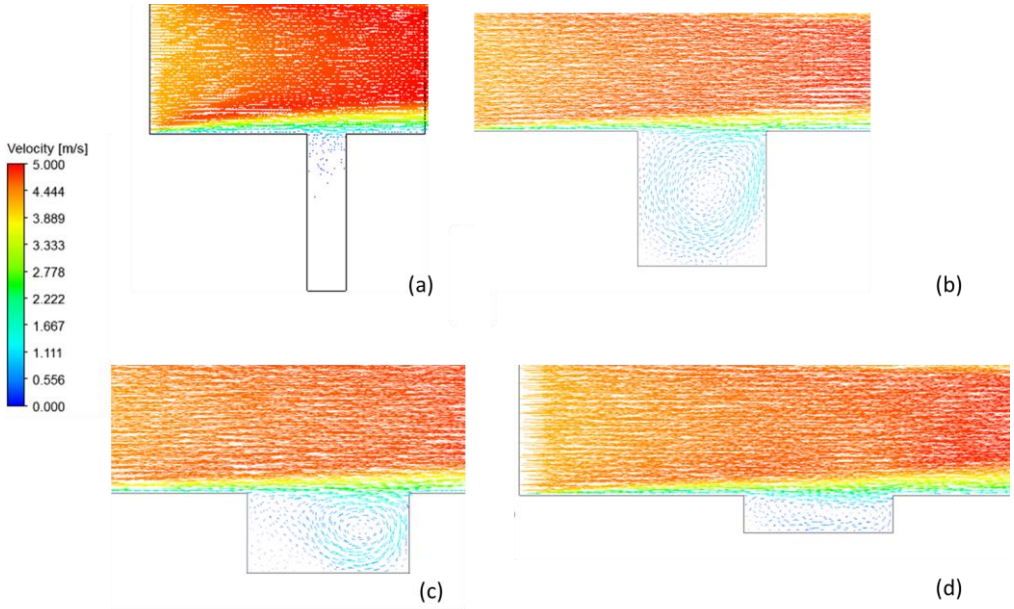

Figure 10. Velocity vectors for (a)L/D=0.25 (b)L/D=1 (c)L/D=2 (d)L/D=5 for Ri=10 (only the cavity region is shown)

In Figure 11, the mean Nusselt number distribution with the Reynolds number is shown for different D/H values. For all Reynolds numbers, increasing the D/H decreases the Nusselt number. Because of the thermal boundary layer formation on the cavity walls due to the vortices inside the cavity, increasing the Reynolds number 4 times (Re=24000 to Re=96000) increases the Nusselt number 1.2 times only (For D/H=0.25). This pattern is similarly observed in the research of Timuralp and Altac [7]. At high Reynolds numbers, temperature gradients are parallel to the hot wall which indicates that forced convection is dominant in the flow region.

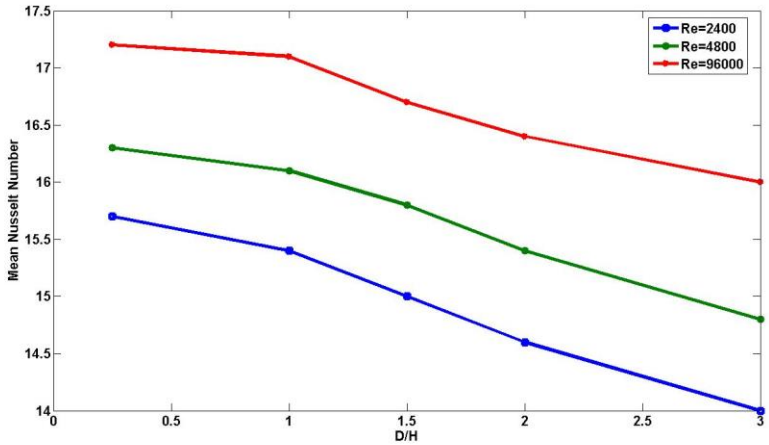

Figure 11. The variation of mean Nusselt Number with Reynolds Number and H/D for Ri=10

When D/H<1, the vortex structure can fill the enclosure and creates turbulence inside the cavity. When D/H>1, the separated flow from the leading edge cannot reach the bottom of the cavity; thus, warmer air cannot penetrate the hot air. That is why heat transfer enhancement is better for the cases D/H<1.

3.5. Reynolds Number Effect: The effect of velocity on flow and temperature was examined by taking Reynolds number 24000, 48000, 96000. In the cavity zone, a vortex structure is observed for all of the cases. Almost 83% of the cavity volume is filled with the vortex structure. Although the flow topology is the same for all of the cases, velocity values increased with rising the Reynolds number. When Reynolds number is reached to the highest value, free stream velocity value also reached its maximum value which causes more forced convection effect on the cavity zone. Therefore, the Nusselt number and heat transfer coefficient are the highest when Re=1600. In Figure 12, the temperature contour is shown for an open cavity with different Reynolds numbers. It is seen that the flow regime is almost the same for whole cases on the other hand, as Reynolds number is varied, maximum temperature changes due to the velocity variation. When Reynolds number is 24000, the maximum temperature reaches to the 312 K, when Reynolds number increased to the 96000, maximum temperature drops to 303 K. Temperature distribution trend is observed same for three cases, but maximum temperature value changes. According to the results; temperature decreases when the Reynolds number increases. The reason for this situation is increasing the Reynolds number rises the kinetic energy inside the cavity. Also, the cold air penetrates to the warm air better when Reynolds number increases.

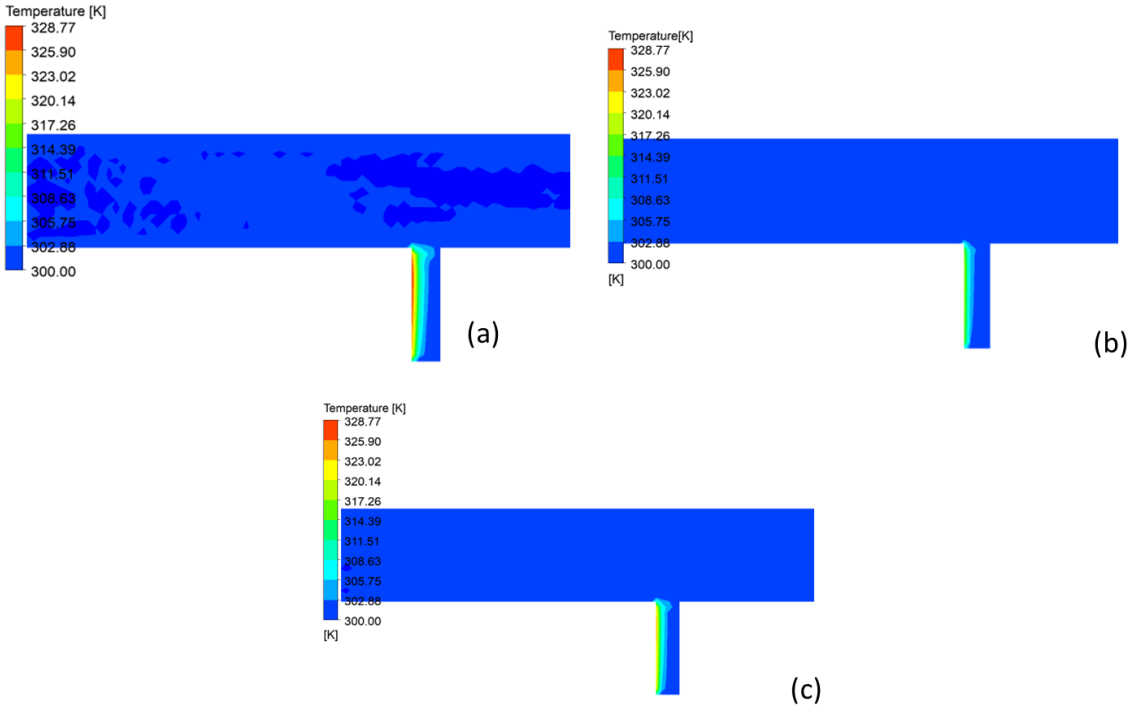

Figure 12. Temperature distribution for (a) Re=24000 (b) Re=48000 (c) Re=96000

As the Reynolds number is one of the most crucial parameters in the flow field in Figure 13, the average Nusselt number distribution for different Reynolds number is depicted. With increasing the Reynolds number, the heat transfer coefficient and Nusselt number rise which means better heat transfer enhancement.

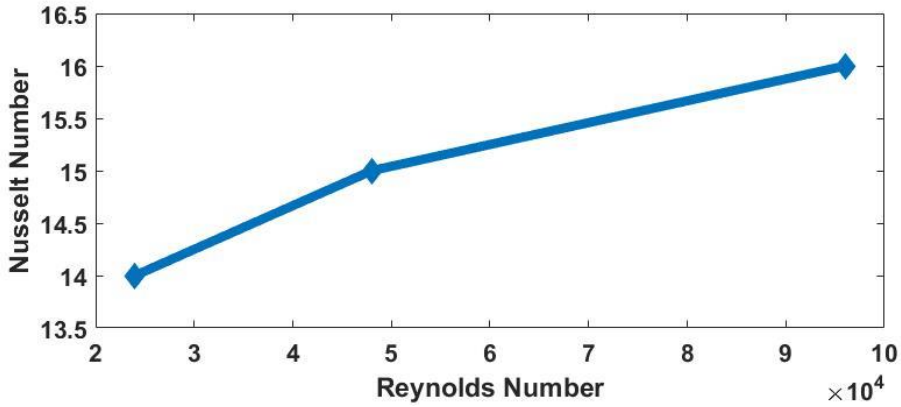

Figure 13. Nusselt number distribution versus Reynolds number

5. CONCLUSION

The present study shows the several parameters effect on heat transfer performance of the open cavity with mixed convection. Numerical parameters effect are investigated, and validation study is performed using ANSYS Fluent Software. Results of the analysis are shown with the help of the Nusselt, Richardson, and Reynolds number distribution. Also, temperature contours and velocity streamlines are used to visualize the flow and to better understanding the flow behavior inside the enclosure. This study yields the following conclusions:
i) Cavity depth and cavity length have a direct effect on the flow and heat transfer characteristics. For the geometries with D/H<1 (Figure 14 (a)) vortex structure fills the enclosure which causes higher turbulence and better mixing. When D/H>1, which means cavity depth is larger than cavity height vortex structure, cannot reach the bottom wall; thus, thermal performance reduces.
ii) The geometry with L/D>1, secondary vortices are observed in the cavity zone which results in a higher heat transfer coefficient and Nusselt number (Figure 14(b)).

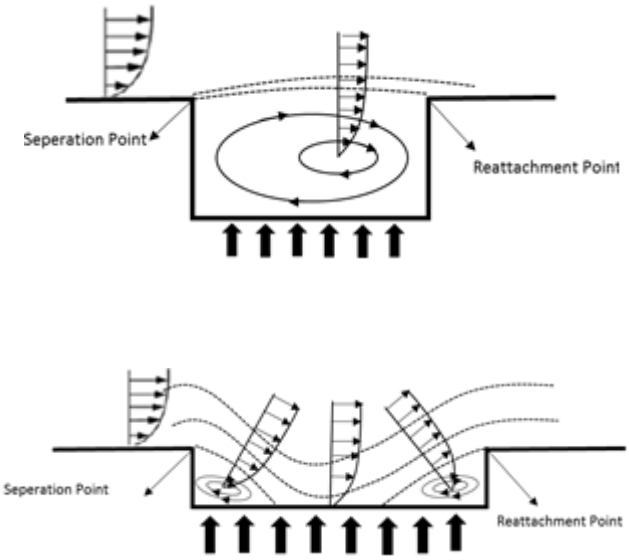

Figure 14. (a) Schematic view of an open cavity with D/H<1 (b) Schematic view of an open cavity with L/D>1

iii) Richardson number has a direct effect on heat transfer. When Ri<1 buoyancy effects are negligible when

Ri>1 buoyancy effects are dominant. Increasing the Richardson number rises the Nusselt number.
iv) When the Reynolds number is increased, the circulation is observed in the cavity, which causes higher Nusselt numbers. At high Reynolds numbers, mixed convection becomes more dominant.
v) The results show that the opposing flow configuration has higher thermal performance when compared with the assisting flow and bottom wall heated configurations.

REFERENCES

[1] N. Brown, F. Lai, Correlations for combined heat and mass transfer from an open cavity in a horizontal channel, International Communications in Heat and Mass Transfer, 32 (2005) 1000-1008.

[2] O. Manca, S. Nardini, K. Vafai, Experimental investigation of mixed convection in a channel with an open cavity, Experimental Heat Transfer, 19 (2009) 53-68.

[3] Manca, O., Nardini, S., Vafai, S., Experimental Investigation of Mixed Convection in a Channel With an Open Cavity, Experimental Heat Transfer, 19 (2006) pp:53-68.

[4] E. Bilgen, H. Oztop, Natural convection heat transfer in partially open inclined square cavities, International Journal of Heat and Mass Transfer. 48 (2005) 1470–1479.

[5] C.A., Chaves, J.R. Camargo, V.A. Correa, Combined forced and free convection heat transfer in a semiporous open cavity, Scientific Research and Essay, 3(8) (2008), 333-337.

[6] O. Manca, S.Nardini, K.Khanafer, K.Vafai, Effect of Heated Wall Position on Mixed Convection in a Channel with an Open Cavity., Numerical Heat Transfer, 43 (2003) 259-282.

[7] C., Timuralp, Z.Altac, Investigation of Fluid Flow and Heat Transfer in a Channel with an Open Cavity Heated From Bottom Side, Mugla Journal of Science and Technology, 2(1) (2016), 55-59.

[8] J.C. Leong, N.M. Brown, F.C., Lai, Mixed Convection From an Open Cavity In a Horizontal Channel, International Communications in Heat and Mass Transfer,32 (2005), 583-592.

[9] A. P. Ortiz, J. Hinojosa, V. Maytorena, Test of turbulence models for natural convection in an open cubic tilted cavity, International Communications in Heat and Mass Transfer, 57 (2014) 264–273.

[10] A. Carozza, Numerical Study on Mixed Convection in Ventilated Cavities with Different Aspect Ratios, Fluids, 3 (11) (2018), 1-18.

[11] H.I. Abu-Mulaweh, B.F. Armaly, T.S. Chen, Measurements in buoyancy-opposing laminar flow over a vertical forward-facing step, International Journal of Heat and Mass Transfer, 39 (9) (1996) 1805-1813.

[12] L. Koufi, Y. Zohir, N. Hasanne, Numerical investigation of turbulent double-diffusive mixed convection in a slot ventilated enclosure with supply airflow ports, 23 ème Congrès Français de Mécanique.

[13] A. Deniz, E. Aylı, Numerical Analysis of Mixed Convection in a Channel wıth Open Cavity, 5th International Conference on Advances In Mechanical Engineering, (2019), Istanbul, Turkey.

[14] Faure, T.M., Adrianos, P., Lusseyran, F., Pastur, L., Visualizations of the Flow Inside an Open Cavity at Medium Range Reynolds Number, Experiments in Fluids, 42:169-184, 2007.

[15]Ayli,E., Modeling of Mixed Convection in an Enclosure with using Multiple Regression, ANN and ANFIS Models,Proceedings of the Institutions of Mechanical Engineers, Part C: Journal of Mechanical Engineering Science, 2020.

[16] Ajmera, S.K., Mathur, A.N., Combined Free and Forced Convection in an Enclosure with Different Ventilation Arrangements, Procedia Engineering, vol: 127, pp: 1173-1180, 2015.

[15] A. K. Chenak, M. Mbaye, P. Vasseur, E. Bilgen, Mixed Convection and conduction heat transfer in open cavities, Heat and Mass Transfer, 30 (1995) 229-235.

[16] J. Burgos, I.Cuesta, C. Saluena, Numerical study of laminar mixed convection in a square open cavity, International Journal of Heat and Mass Transfer, 99 (2016)I 599-612

A REVIEW OF THE EFFECTS OF MICRO FIN GEOMETRY AND ALIGNMENT ON FLOW BOILING CHARACTERISTICS IN MICROCHANNEL HEAT SINKS

Burak MARKAL*, Beyzanur KUL**
*Recep Tayyip Erdogan University, Department of Mechanical Engineering, Rize/Turkey
Email: burak.markal@erdogan.edu.tr
** Recep Tayyip Erdogan University, Department of Energy Systems Engineering, Rize/Turkey
Email: beyzanurkul00@gmail.com

ABSTRACT

In parallel with the reduction in the size of electronic devices, the amount of heat released per unit surface area of the device components increases. To ensure system security and sustainable performance, the high heat fluxes must remove from the relevant surfaces. In this context, one of the most effective thermal management methods that can be used is the flow boiling in heat sinks with micro fins. The role of phase change in heat transfer, the nearly constant surface temperatures during the relevant process, and the increase of surface area per unit volume due to the micro fins make this method effective.

In flow boiling, the bubble dynamics and the heat transfer have a close and complex relation. In micro-scale flow passages, the continuously variable characteristics of the bubble dynamics and/or the strong interaction between the liquid and vapor phases lead to a much more complex physical mechanism. Therefore, by means of the advancing manufacturing technologies, the novel heat sinks consisting of micro fins with different geometric configurations are developed instead of conventional parallel microchannel ones. In the present paper, the studies investigating flow boiling characteristics in heat sinks having different geometric configurations and alignments are reviewed, and detailed information regarding the effects of geometry on heat and flow behavior is presented. This study considering the fin configuration will contribute to the development of novel heat sink designs for the enhancement of heat transfer performance.

Keywords: Micro Fin, Microchannel, Flow boiling, Heat Transfer, Bubble Dynamic.

1. INTRODUCTION

Although single-phase flow studies in microchannels began in the 1980s, two-phase flow studies date back to the 2000s. Today, it is commonly used in many emerging technological fields such as electronic, electro-mechanical devices, space industry and defense industry. Microchannel heat sinks containing two-phase flow boiling are prefer due to being a highly efficient thermal control method to overcome the high heat generation problem occurring in the devices. By means of boiling, more heat is absorbed throughout the channel, and an almost uniform temperature is provided. Thus, exposure of the device to thermal stresses is prevented, the device is safely under thermal control, and its performance increases. Despite the small dimensions, the power consumption is continuously getting increased, and the necessity of removal of the high heat fluxes from these kinds of surfaces increases the interest in micro-scale channels of which the hydraulic diameter range of 0.2 – 1 mm. [1]. During the phase change, very much heat is transferred from or to the fluid without changing the temperature of the pure fluid. Due to the high heat transfer coefficients in spite of small flow rates and providing almost uniform wall temperatures, flow boiling in microchannels offers many advantages over other cooling methods.

In recent years, unlike conventional parallel microchannels, micro fins are manufactured on the channel surfaces to increase the thermal performance via increasing the heating surface area, enhancing the mixing or supporting the unidirectional flow. In the scope of the present paper, micro-finned microchannel heat sinks with different

geometrical shapes and alignments are compiled, and regarding the flow boiling characteristics, their roles are presented.

2. CLASSIFICATION OF MICRO FINNED HEAT SINKS

Manufacturing techniques having progress in recent years enable more advanced microchannel heat sinks to produce. In this way, depending on the geometrical design, microchannel heat sinks may provide many advantages such as enhancement of heat transfer, raising of the critical heat flux (CHF) to higher values, decrement of the pressure drop, and reduction of the two-phase flow instabilities, etc. From the literature review, it is observed that fin geometry and alignment in microchannel heat sinks are two important criteria for flow boiling in microchannels. Therefore, a classification performed based on these two criteria (including their effects) is presented in the following sections.

2.1 Fin Geometry

Under this title, the microchannel heat sinks made of conductive or semiconductor materials are chronologically examined based on three subtitles: (1) micro pin fins (fin geometries as square, circle, conical, diamond, streamline, cuboid, smooth, porous, etc.), (2) oblique fins and (3) reentrant fins.

a) Micro pin fin geometry

Micro-pin-fin microchannels are generally compared in the literature with conventional parallel microchannels. Studies are handled depending on different parameters such as type of refrigerant, different mass fluxes, heat fluxes, amount of subcooling, etc. Micro-pin-fin geometries offer some advantages such as increasing heat transfer, decreasing pressure drop, increasing active bubble nucleation areas, increasing critical heat flux, preventing partial dry-out, providing early bubble generation, reducing two-phase flow instabilities.

Lie et al. [2] performed experimental studies to research flow boiling characteristics (including bubble behavior). They studied with the silicon microchannels including micro pin fins with different lengths and widths, and they used FC-72 as fluid. The addition of the micro pin fins increased the active bubble density, and thus, the thermal performance. It is observed that the average outlet diameters of the bubbles decreased with increasing mass flux, while they were slightly smaller for micro pin fin surfaces. In the micro pin fin heat sink, the frequencies of the bubbles leaving from the surface increased with the mass velocity and the applied heat load. Ma et al. [3] conducted an experimental study by using FC 72 in three different silicon heat sinks. One of the heat sinks was a smooth type, while the other two included various fin heights (60 μm and 120 μm). The fin thickness was common for both of them as 30 μm. Heat transfer improved due to the micro pin fin surfaces, and it also increased with the increasing fin height. On the other hand, the smooth one was the poorest one in term of thermal performance. At the same time, as the fin height raised, the boiling curve slope increased, and the CHF was postponed. The values of the CHF increased with subcooling for all channel types. It was concluded that subcooling level and fluid velocity were the two important parameters affecting the critical heat flux. They also underlined the dominance of convective boiling. Zhuan and Wang [4] carried out experimental studies on flow boiling (working fluid: R134a) in a microchannel heat sink with cuboid fins. Bubbly and/or slug flow was seen as dominant flow patterns in the convective boiling and evaporation region. In these conditions, the heat flux positively played a dominant role on the heat transfer coefficients, while mass velocity slightly increased the heat transfer coefficients. On the other hand, an increasing amount of subcooling enhanced the heat transfer. In the evaporation region, there were two different dominant flow patterns (annular and semi-annular). In the relevant region, heat flux did not play any role in the thermal behavior, while the heat transfer coefficients, respectively, decreased and increased with vapor quality and mass velocity. Deng et al. [5] performed a comparison between the conventional and the structured (micro cone pin fin) microchannels. Two working fluids, namely, deionized water and ethanol were used in the experiments. Micro pin fin microchannel showed significant enhancement in flow boiling performance (water tests: from 10 to 105%, and ethanol tests: from 90 to 175%). Micro-pin-fin microchannels generated a large number of nucleation sites meaning higher bubble density. In addition, this structure boosted the fluid wetting phenomenon by creating a wicking effect, and thus prevented the local dry out on the heat transfer surface. Wan et al. [6] carried out flow boiling experiments for

four different shifted-inline micro-pin-fin heat sinks as square, circle, diamond and streamline. The photographs of the relevant heat sinks taken via scanning electron microscope are presented in Fig. 1a-d. In the experiment, deionized water was used as the refrigerant. It was concluded that the micro pin fin geometry did not have a clear influence on the onset of nucleate boiling. The square micro pin fins prevented the development of long vapor bubbles and contributed much more to the rewetting process of the channels, and thus provided better heat transfer coefficients than the other fin types. In terms of thermal success, the diamond micro pin fins with sharp corners were the worst. For all fin types, increasing heat load adversely affected the pressure drop. The diamond micro pin fin offered the lowest pressure loss. The heat sinks including square and circle micro-fins were more successful in reducing the two phase boiling flow instabilities.

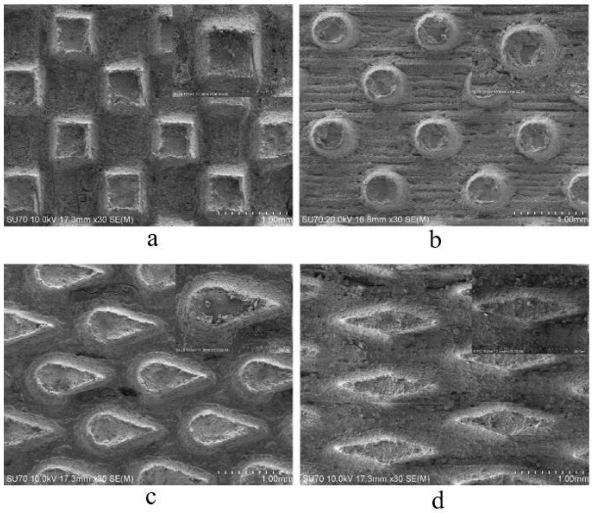

Figure 1. Four different micro pin fins: square (a), circle (b), streamline (c), diamond (d) [6]

Chien et al. [7] presented the results of an experimental study (for the refrigerant of FC-72). They used nucleated and classical type micro pin-fin microchannels, both consisting of 613 micro pin fins. Nucleated type pin fins were structured by 60 μm pore and 45 μm opening. In low and high heat fluxes, the wall superheat linearly increased with an increment in the heat flux. On the other hand, in single-phase flow, the pin fins reduced the heat transfer coefficient; while, after boiling started, they played a key role in the increase of the heat transfer coefficient. In the single-phase case with weak heat flux, the pressure drop was very low or almost constant. Once the nucleate boiling started, there was a significant increase in pressure drop, and with the increase of heat flux, the pressure drop in the micro-cavities gradually increased. Ma et al. [8] conducted experimental attempts by using HFE 7100 in the heat sinks (micro pin fin and conventional types). Contrary to the conventional type, the micro pin-fin microchannel heat sink clearly boosted the heat transfer coefficient and the critical heat flux without any significant an increment in the two-phase pressure drop. Zong et al. [9] experimentally performed a study for flow boiling instabilities. They designed a porous microchannel heat sink. The porous wall was divided into three regions: (1) dense (2) intermediate dense (3) sparsely pin fin regions (the fin gaps are 5μm, 7.5 μm, 10 μm, respectively). Due to the interconnection influence of the porous wall, early bubble nucleation occurred, and the boiling instabilities could be suppressed.

b) Oblique fins

The oblique fins are the fin types in which micro fins are cut by a certain angle. The relevant articles are summarized below.

Law et al. [10] carried out an experimental study with the working fluid of FC 72. The heat sink contained 780 oblique fins with an oblique angle of 30°. They researched the heat transfer and pressure loss during flow boiling. In low heat fluxes, the dominant heat transfer mechanism was addressed with nucleate boiling, while in the medium to high ones, thin film evaporation showed dominant character. The mass flux had no influence on the inlet pressure instability due to the nature of the inclined fin microchannels. Law and Lee [11] conducted an

experimental study including conventional and inclined fin microchannels. A dielectric fluid of FC-72 was preferred as the fluid. Better thermal performance was observed in the structured heat sink compared to the conventional one. In the cases including the nucleate boiling as the dominant mechanism, the main factor behind the enhancement was increasing bubble density; while, in the convective boiling zone, heat transfer was enhanced mainly due to the continuous development of the thin liquid film. As a measure, the heat transfer coefficients increased from 1.2 to 6.2 times compared to the conventional one. Oblique fins provided a more stable boiling process, and thus, critical heat flux increased up to 2.8 times. However, it should be noted that the sudden change of the flow direction due to the oblique geometries caused an increment in pressure drop. Law and Lee [12] conducted an experimental study (FC-72 working fluid) for flow boiling behavior in oblique fin microchannels with three secondary channel widths. Secondary channel widths of oblique fin microchannels were 0.15 mm, 0.30 mm and 0.45 mm, respectively. Larger secondary channel widths lead to a decrement in thermal performance due to the lack of suppression of flow boiling instabilities. In larger cases, much more fluid shifted its direction, and thus, two phase pressure drop also increased in addition to the deterioration in the heat transfer. Prajapati et al. [13] experimentally focused on the transient thermal behavior of inclined finned microchannels for both the single phase and flow boiling cases. Also, a comparison was conducted depending on the classical channel type. In Figs. 2a and b, the photographs of the conventional (uniform or parallel) and oblique fin microchannels are presented. The coolant was deionized water. For a wide range of heat flux, the structured heat sink maintained a stable manner compared to the conventional one. In the transition regime, the heat transfer coefficients of the oblique fin microchannel were smaller than the ones of the conventional microchannels; however, towards the steady-state, the exact opposite result was obtained. The advantage provided by the oblique fin microchannels was the unrestricted bubble growth behavior.

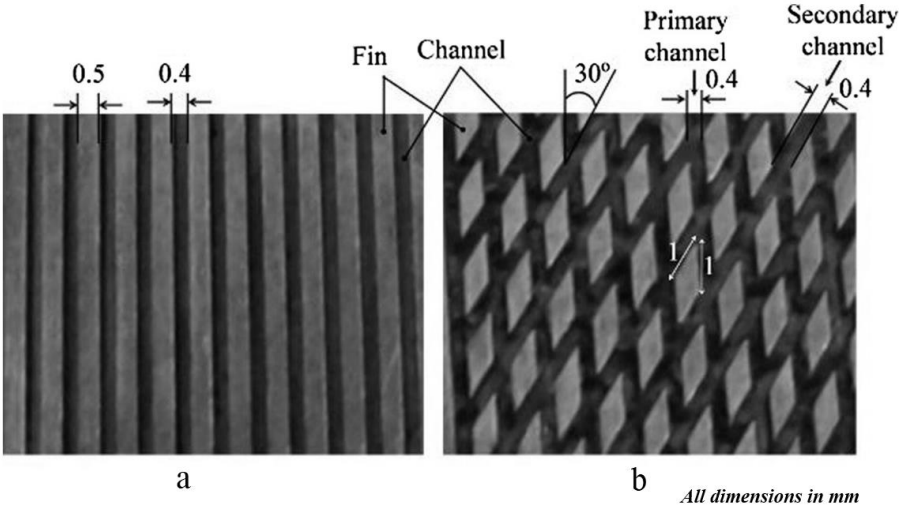

Figure 2 : Conventional (uniform) (a) and oblique (b) fin microchannels [13]

c) Reentrant geometry

In the flow boiling studies, bubble dynamic has the key importance, and thus, any modification related to bubble nucleation or movement directly influences the heat transfer and pressure drop characteristics. In some studies, researchers focused on bubble nucleation, and they carried out this aim by providing reentrant cavities on the fins, bottom walls, side walls or inlets of the channels. In this section, the relevant studies are summarized.

Kuo and Peles [14] compared the reentrant microchannels and the conventional ones depending on the flow morphology, boiling startup behavior, heat transfer coefficients and critical heat fluxes (for flow boiling). The recessed microchannels enhanced the bubble activity compared to the classical heat sink. Similar flow patterns were observed in both channels. In the structured one, lower wall superheat was obtained; the flow oscillations were suppressed, and the critical heat flux was postponed up to higher values. An experimental study was performed by Deng et al. [15] to determine the flow boiling performance of the omega shaped (Ω) reentrant

microchannel heat sinks. Deionized water was the coolant. Porous microchannels with reentrant cavities triggered the startup of boiling earlier than the conventional one. It also reduced the heat flux needed for the inception of nucleate boiling and provided an improvement in two-phase heat transfer from 2 to 5 folds. In low heat fluxes, the dominance of the nucleate boiling was shown, and the flow patterns were in the format of bubbly and slug type. On the other hand, in higher heat fluxes, churn and annular flow patterns characterizing the convective boiling were dominant. Two-phase flow instabilities were reduced due to the reentrant geometry. In their experimental study, Deng et al. [16] used three Ω-shaped reentrant microchannel heat sinks with various hydraulic diameters of 590, 781 and 858 μm. It was concluded that increasing channel cross section reduced the two phase pressure drop. However, in terms of instability suppression, the most superior one is the microchannel with the hydraulic diameter of 781 μm. In a further study, Deng et al. [17] combined the features of the pin fins and reentrant geometry with deionized water and ethanol. The relevant geometry is demonstrated in Fig. 3. The pin fin reentrant structure supported and eased the nucleation, separation and movement of the bubbles, and also, it decreased the negative effect of the bubble confinement. Therefore, in the two phase heat transfer, compared to the conventional one, a significant enhancement was observed (up to 284% for water tests and 220% for ethanol tests). In terms of working fluids, water showed better performance than ethanol as higher heat transfer, lower pressure drop and more stable boiling behavior.

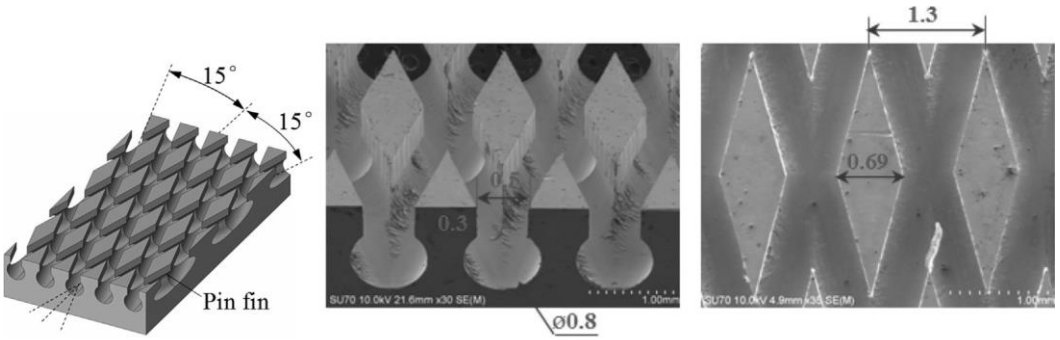

Figure 3: Pin fin interconnected reenrant microchannels [17]

Jia et al. [18] presented an experimental study regarding with flow boiling characteristics of microchannel heat sink with porous walls. The working fluid was acetone. Compared to the smooth parallel microchannel, the wall superheat for the inception of the nucleate boiling was lower and the critical heat flux was higher in the case modified channel. Also, lower pressure drop and boiling instabilities were achieved. Porous walls provided a wicking effect (related to the wetting phenomenon) and large amount of nucleation sites, which were the physical reasons for the enhancement. Li et al. [19] carried out flow boiling experiments with HFE 7100 (fluid) in micro-nozzle and reentrant silicon microchannels. The micro nozzles and reentrant structures supported bubbly flow and enhanced the mixing phenomenon; and thus, the thermal performance was improved. Compared to the conventional type heat sink, critical heat flux was raised up to 70%, and a decrement up to 82% was achieved in terms of pressure drop.

2.2 Fin alignment

The importance of the artificial nucleation cavities and the geometrical shapes of the micro pins are underlined in the previous paragraphs. Not only their shape is important, but also, their spatial arrangements are important. In this section, the relevant attempts are presented.

Qu and Siu-Ho [20] experimentally investigated the behavior of flow boiling heat transfer in a staggered square micro pin fin heat sink. The coolant was deionized water. The two phase forced convection related with the annular flow pattern was stated as the dominant mechanism for heat transfer. They underlined the importance of the interruptive features of the fin arrangement. Vapor flow including liquid droplets due to the entrainment played a key role in thermal characteristics. Also, increasing inlet subcooling improved the heat transfer in low quality region. Kosar et al. [21] focused on pressure drop behavior during unstable cases in the boiling process for three different heat sinks with the working fluids of water and R-123. Two of the heat sinks included circular

micro pin with different distance, while the remained one contains hydrofoil type pin. It should be noted that all the pins in every heat sink were arranged in staggered order. In each heat sink, once the boiling started, flow instabilities took place and a rise in the surface temperature occurred. In water tests, the magnitudes of the pressure fluctuations were insignificant before and after the unstable boiling. While a significant increase in the fluctuations was observed after initiation of instabilities in the case of R-123. Prajapati et al. [22] conducted a comparative analysis to investigate flow boiling behavior in three different channel configurations, namely, uniform cross section, segmented finned type and diverging cross section. The best performance was obtained via segmented one for both the single and two phase flow conditions. The major physical advantages provided by segmented finned channels were defined as: (1) prevention both of the bubble confinement and the reversal flow; (2) disruption of thermal boundary layer and (3) production of more bubbles. On the other hand, an increment of the total pressure drop was the penalty of segmented geometry. In their further study, Prajapati et al. [23] focused on flow boiling characteristics and bubble behavior again in the same test sections (fluid was Deionized water). Briefly, the results supported their previous study of [22] were obtained.

The useful information belongs to the studies reviewed in the present paper is briefly summarized in Table 1.

Table 1. The useful information belongs to the studies reviewed in the present paper

Study	**Remarks for fins**	**Working fluid**	**Mass flux (kg / m^{2}s)**	**Heat flux (W / cm^2) (Upper Limit)**
Lie et al. [2]	Material: Silicon Rectangular micro pin fins with 100 μm and 200 μm widths and 70 μm height	FC-72	287−431	10
Ma et al. [3]	Material: Silicon Rectangular micro pin fins with 60 μm and 120 μm different fin heights Fin thickness of 30 μm for both	FC-72	---	150
Zhuan et al. [4]	Material: Polyether Ether Ketone (PEEK) (1.5 mm x 0.15 mm x 3.5 mm) (width × depth × length) dimensional cuboid fins	R-134a	10−35	2.5
Deng et al. [5]	Material: Copper Structured micro cone pin fins with tiny cavities	Deionized water, Ethanol	200−300	106.7
Wan et al. [6]	Material: Copper Micro pin fins with various cross sections: square, circular, diamond and streamline.	Deionized water	500	59.3
Chien et al. [7]	Material: Tantalum Mikrogap pin fins with a 60 μm pore and opening of 45μm	FC-72	94−275	6

Table 1. (Continued)

Study	Remark for fins	Working fluid	Mass flux (kg / m^{2}s)	Heat flux (W / cm^2) (Upper Limit)
Ma et al. [8]	Material: Silicon Interconnected microchannels by micro slots	HFE-7100	462−1617	145 (nearly)
Zong et al. [9]	Material: Silicon Porous wall with the micro pin fins	Acetone	250−510	72
Law et al. [10]	Material: Copper Oblique-finned with 30° oblique angle	FC-72	175−350	120
Law and Lee [11]	Material: Copper Oblique-finned with 27° oblique angle	FC-72	175−350	120
Law and Lee [12]	Material: Copper Oblique-finned with 0.15, 0.30, 0.45mm secondary channel widths	FC-72	197−394	70
Prajapati et al. [13]	Material: Copper Oblique-finned with 30° oblique angle / Channel width of 400 µm and depth of 750 µm	Deionized water	100−350	30
Kuo and Peles [14]	Material: Silicon Structured reentrant cavities microchannel	Deionized water	83−303	643
Deng et al. [15]	Material: Copper Ω-shaped reentrant porous microchannels	Deionized water	125−300	52 (nearly)
Deng et al. [16]	Material: Copper Ω-shaped reentrant microchannels with a radius of reentrant cavities of 300µm, 400µm, 450µm	Deionized water	125−300	51 (nearly)
Deng et al. [17]	Material: Copper Diamond pin fins interconnected reentrant microchannels	Deionized water, ethanol	125−300	105 (nearly)
Jia et al. [18]	Material: Silicon Micro pin fin arrays with porous	Acetone	225−843	110
Li et al. [19]	Material: Silicon Micro nozzles and reentry micro-cavities	HFE-7100	231−1155	175 (nearly)
Qu and Ho [20]	Material: Copper Staggered square micro pin fins with a height of 670µm	Deionized water	183−420	248.5
Kosar et al. [21]	Material: Silicon Different circulars and hydrofoil shaped staggered micro pin fins	Deionized water, R-123	351−1351	278
Prapajati et al. [22, 23]	Material: Copper Segmented type finned	Deionized water	100−350	35

3. CONCLUSIONS

The present paper summarized the literature focusing on flow boiling characteristics in heat sinks with different geometric configurations and alignments. The effect of geometry on heat and fluid flow behavior is presented, and the underlying physical mechanisms are emphasized. The information gathered in the present paper will guide future studies. Significant results are briefly given below:

- Generally, micro pin fins and/or oblique fins improve the thermal performance compared to the conventional parallel microchannel heat sinks. However, the sudden change of the flow direction, especially for staggered designs, leads to relatively higher pressure drop.
- The existence of the secondary channels plays a key role in preventing negative effects of bubble confinement due to the providing escape ways for growing bubbles. This phenomenon leads to a decrement in flow boiling instabilities and enhances thermal characteristics. However, in oblique fins, larger secondary channel widths lead to a decrement in heat transfer performance due to increasing flow boiling instabilities. In larger cases, much more fluid shifts its direction, and thus, two phase pressure drop also increases.
- The main advantage provided by the oblique fin microchannels is the unrestricted bubble growth behavior.
- The pin fin reentrant structure supports and eases the nucleation, separation and movement of the bubbles; and also prevents or reduces the bubble confinement phenomenon.
- Porous walls and/or special pin types (such as cone type) on the bottom or side walls provide a wicking effect (related to the wetting phenomenon) and a large amount of nucleation sites. These physical facts induce the prevention of early dry-out and enhancement of nucleate boiling, which improve the thermal performance.
- Especially, reentrant walls play a key role in the bubble dynamic (bubble nucleation and leaving from the surface).
- Increasing fin height increases the heat transfer and delays the critical heat flux.

The subject of flow boiling in micro structure has a complex and difficult nature. General outputs of the available literature are summarized above. However, it should be noted that there are contradictory results in the literature. Therefore, this subject attracts the attention of the researchers.

REFERENCES

[1] Kandlikar, S. G., & Grande, W. J., Evolution of microchannel flow passages-thermohydraulic performance and fabrication technology, *Heat Transfer Engineering*, **24**(1), 3–17, 2003.

[2] Lie, Y. M., Ke, J. H., Chang, W. R., Cheng, T. C., & Lin, T. F., Saturated flow boiling heat transfer and associated bubble characteristics of FC-72 on a heated micro-pin-finned silicon chip, *International Journal of Heat and Mass Transfer*, **50**(19–20), 3862–3876, 2007.

[3] Ma, A., Wei, J., Yuan, M., & Fang, J., Enhanced flow boiling heat transfer of FC-72 on micro-pin-finned surfaces, *International Journal of Heat and Mass Transfer*, **52**(13–14), 2925–2931, 2009.

[4] Zhuan, R., & Wang, W., Boiling heat transfer characteristics in a microchannel array heat sink with low mass flow rate, *Applied Thermal Engineering*, **51**(1–2), 65–74, 2013.

[5] Deng, D., Wan, W., Qin, Y., Zhang, J., & Chu, X., Flow boiling enhancement of structured microchannels with micro pin fins, *International Journal of Heat and Mass Transfer*, **105**, 338–34, 2017.

[6] Wan, W., Deng, D., Huang, Q., Zeng, T., & Huang, Y., Experimental study and optimization of pin fin shapes in flow boiling of micro pin fin heat sinks, *Applied Thermal Engineering*, **114**, 436–449, 2017.

[7] Chien, L. H., Liao, W. R., Ghalambaz, M., & Yan, W. M., Experimental study on convective boiling flow and heat transfer in a microgap enhanced with a staggered arrangement of nucleated micro-pin-fins, *International Journal of Heat and Mass Transfer*, **144**, 118653, 2019.

[8] Ma, J., Li, W., Ren, C., Khan, J. A., & Li, C., Realizing highly coordinated, rapid and sustainable nucleate boiling in microchannels on HFE-7100, *International Journal of Heat and Mass Transfer*, **133**, 1219–1229, 2019.

[9] Zong, L. X., Xia, G. D., Jia, Y. T., Liu, L., Ma, D. D., & Wang, J., Flow boiling instability characteristics in microchannels with porous-wall, *International Journal of Heat and Mass Transfer*, **146**, 1–19, 2020.

[10] Law, M., Lee, P. S., & Balasubramanian, K., Experimental investigation of flow boiling heat transfer in novel oblique-finned microchannels, *International Journal of Heat and Mass Transfer*, **76**, 419–431, 2014.

[11] Law, M., & Lee, P. S., A comparative study of experimental flow boiling heat transfer and pressure characteristics in straight- and oblique-finned microchannels, *International Journal of Heat and Mass Transfer*, **85**, 797–810, 2015.

[12] Law, M., & Lee, P. S., Effects of varying secondary channel widths on flow boiling heat transfer and pressure characteristics in oblique-finned microchannels, *International Journal of Heat and Mass Transfer*, **101**, 313–326, 2016.

[13] Prajapati, Y. K., Pathak, M., & Khan, M. K., Transient heat transfer characteristics of segmented finned microchannels, *Experimental Thermal and Fluid Science*, **79**, 134–142, 2016.

[14] Kuo, C. J., & Peles, Y., Local measurement of flow boiling in structured surface microchannels, *International Journal of Heat and Mass Transfer*, **50**(23–24), 4513–4526, 2007.

[15] Deng, D., Tang, Y., Liang, D., He, H., & Yang, S., Flow boiling characteristics in porous heat sink with reentrant microchannels, *International Journal of Heat and Mass Transfer*, **70**, 463–477, 2014.

[16] Deng, D., Xie, Y., Huang, Q., Tang, Y., Huang, L., & Huang, X., Flow boiling performance of Ω-shaped reentrant copper microchannels with different channel sizes, *Experimental Thermal and Fluid Science*, **69**, 8–18, 2015.

[17] Deng, D., Chen, L., Wan, W., Fu, T., & Huang, X., Flow boiling performance in pin fin- interconnected reentrant microchannels heat sink in different operational conditions, *Applied Thermal Engineering*, **150**(December 2018), 1260–1272, 2019.

[18] Jia, Y. T., Xia, G. D., Zong, L. X., Ma, D. D., & Tang, Y. X., A comparative study of experimental flow boiling heat transfer and pressure drop characteristics in porous-wall microchannel heat sink, *International Journal of Heat and Mass Transfer*, **127**, 818–833, 2018.

[19] Li, W., Ma, J., Alam, T., Yang, F., Khan, J., & Li, C., Flow boiling of HFE-7100 in silicon microchannels integrated with multiple micro-nozzles and reentry micro-cavities, *International Journal of Heat and Mass Transfer*, **123**, 354–366, 2018.

[20] Qu, W., & Siu-Ho, A., Experimental study of saturated flow boiling heat transfer in an array of staggered micro-pin-fins, *International Journal of Heat and Mass Transfer*, **52**(7–8), 1853–1863, 2009.

[21] Koşar, A., Rafet Özdemir, M., & Keskinoz, M., Pressure drop across micro-pin heat sinks under unstable boiling conditions, *International Journal of Thermal Sciences*, **49**(7), 1253–1263, 2010.

[22] Prajapati, Y. K., Pathak, M., & Kaleem Khan, M., A comparative study of flow boiling heat transfer in three different configurations of microchannels, *International Journal of Heat and Mass Transfer*, **85**, 711–722, 2015.

[23] Prajapati, Y. K., Pathak, M., & Khan, M. K., Bubble dynamics and flow boiling characteristics in three different microchannel configurations, *International Journal of Thermal Sciences,* **112**, 371–382, 2017.

FLUID MECHANICS

NUMERICAL AND EXPERIMENTAL INVESTIGATION OF AIR INJECTION PROCESS WITH VENTURI PIPE PART

Ömer F. CAN[*], Tamer BAGATUR[**], Nevin ÇELİK[***]
*Dicle University, Department of Mechanical Engineering, Diyarbakir/Turkey
Email: faruk.can@dicle.edu.tr
[**]Dicle University, Department of Civil Engineering, Diyarbakir/Turkey
Email: tbagatur@dicle.edu.tr
[***]Fırat University, Department of Mechanical Engineering, Elazığ/Turkey
Email: nevincelik@firat.edu.tr

ABSTRACT

Air injector processes with venturi pipe part (VPP), simple in design and easy to operate, have been used in a wide variety of industrial, agricultural and water/waste water treatment applications in environmental engineering. The air injector process occurs when a minimal amount of differential pressure exists between the inlet and outlet regions of a venturi device. This paper introduces a numerical and experimental study of air injector process within a venturi device and its relationship with the Reynolds number for minimal flow conditions. An investigation of the air-water injector has been carried out to study the influence of operating conditions on the hydrodynamics and mass transfer characteristics of the injector by using two-fluid computational multiphase fluid dynamics (CMFD) modeling. The numerical work was performed by means of the program ANSYS CFX 11.0 software. The CMFD results are validated with experimental data. Flow field analysis and prediction of injector performance are also conducted.

Keywords: Air injection, Computational Fluid Dynamics, Venturi pipe part.

1. INTRODUCTION

In reality, the venturi is a device which has been used over many years for measuring the discharge along a water pipe in water engineering. Two-phase injectors/ejectors have recently been designed in which gas and liquid are premixed before injection into the bulk liquid, for example, the venturi in Fig. 1. Fig. 2 shows schematic diagram of air injection process with venturi pipe part.

Air injector processes with venturi, which are simple in design and easy to operate, have been used in a wide variety of industrial and water purification processes (for example, ozone and chlorine injecting/contacting for drinking water, chemical injection such as liquid fertilizers in sprinkler and drip irrigation systems and aeration/dissolved oxygen transfer in drinking and waste water treatment). The fluid flowing in the pipe is fed through a contraction section to a throat, which has a smaller cross-sectional area than the pipe, so that the velocity of the fluid through the throat is higher than that in the pipe. This increase of velocity is accompanied by a fall in pressure. Beyond the throat the fluid is decelerated in a pipe of slowly diverging section, the pressure increasing as the velocity falls. In the inlet of the venturi device, water flow has pressure energy. This pressure energy is converted to velocity in the converging cone. Water flow changes into a high-velocity jet stream. The increase in velocity through the venturi converging cone, caused by the differential pressure, results in a decrease in pressure. Thus, a vacuum is created at the suction port. Water mixes with air. Two-phase flow (bubbly flow or air–water mixture) occurs. In bubble flow the absorbed gas phase (air) flows as discrete bubbles in liquid (water). This occurs when a minimal amount of differential pressure exists between the inlet and outlet regions of the venturi device. In the outlet of the venturi device, pressure energy is regained for mass transfer of air. This device may therefore be a viable, economic alternative for gas–liquid transfer. This type of aeration equipment is useful and can be competitive with other conventional aeration equipment. In mixing, no mechanical agitation is usually employed and the pump is the only component to generate vigorous fluid motion (water and air, which

are two phase). This device also has lower energy requirements, installation, operating and maintenance costs in tanks, ponds or lagoons.

Figure 1. Air-water injection process with venturi pipe part

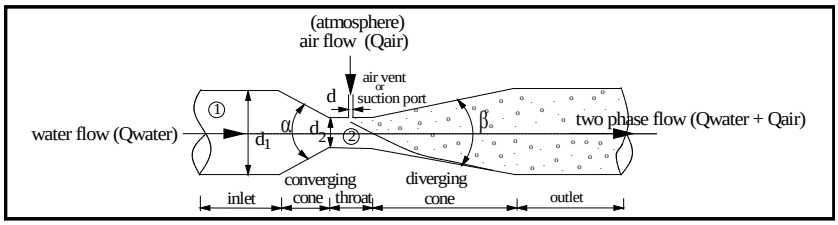

Figure 2. Schematic diagram of air injection process with venturi pipe part

Bagatur [1], summarized application fields of venturi pipe part. Venturi pipe part (VPP) can be used to solve the following problems for water treatment and irrigation:

- ✓ Excessive biochemical oxygen demand (BOD) problem in waste water treatment
- ✓ Excessive chemical oxygen demand (COD) problem
- ✓ Lack of dissolved oxygen problem
- ✓ Noise problem for packaged waste water treatment plant
- ✓ Odor problem in waste water evaporation
- ✓ Sour drinking water problem due to containing hydrogen sulfide (H_2S)
- ✓ Excessive organic matter, nutrient, and nitrogen problem
- ✓ Select of efficient aeration system problem
- ✓ Disinfection problem in drinking water treatment
- ✓ Flotation process in waste water treatment
- ✓ Improve soil aeration by entraining air (in the form of micro-bubbles) into irrigation water delivered through sub-surface drip irrigation. The added air improves growing conditions by increasing root

respiration and microbial activity. These improved soil conditions have shown significant increase in yields.

Baylar and Emiroglu [2], investigated air entrainment and oxygen transfer efficiency for a venturi in plunging jet system. Emiroglu and Baylar [3], studied the influence of air holes on venturi for aeration performance. Bagatur [1] determined minimal conditions for venturi aeration of water flows. Baylar et. al. [4], investigated influence of venturi cone angles on jet aeration. Ozkan et. al. [5], carried out experimental investigations of air and liquid injection by venturi tubes. Baylar and Ozkan [6], and Baylar et. al. [7], summarized applications of venturi principle to water aeration systems. Baylar et al. [8], determined the optimal location of the air hole in venturi aerators. Baylar et al. [9], investigated effect of air inlet hole diameter of venturi tube on air injection rate. Recently, Bagatur [10], has evaluated plant growth with aerated irrigation water using venturi pipe part.

Computational fluid dynamic (CFD) method is widely used in research due to an extensive range of features in different fields of science and engineering to improve and analyze the performance of system or design. ANSYS CFX is one of the foremost tools of CFD, which uses the finite volume technique to study the complex phenomenon such as multiphase flow, chemical reactions, turbulence and heat and mass transfer in system and design. Utomo et al. [11], investigated hydrodynamics and mass transfer characteristics of a gas-liquid ejector using three-dimensional CFD modeling. Baylar et. al. [12], studied numerical modeling of venturi flows for determining air injection rates using FLUENT CFD program. Majid et al. [13], studied CFD simulation of dust particle removal efficiency of a venturi scrubber in CFX.

This paper introduces a numerical and experimental study of air injector process within a venturi device and its relationship with the Reynolds number. An investigation of the air-water injector is carried out to study the influence of minimal operating conditions such as flow velocity on the hydrodynamics and mass transfer characteristics of the injector by using two-fluid computational multiphase fluid dynamics (CMFD) modeling. The numerical work is performed by means of the ANSYS CFX 11.0 (Academic Teaching Introductory version) computer program [14]. The CMFD results are validated with experimental data. Flow field analysis and prediction of injector performance are also conducted.

2. EXPERIMENTAL DESCRIPTION

Figure 3 shows the experimental apparatus and details of the system. The experimental apparatus consists of a recirculation pump and a water tank. A water rotameter was used to measure water discharge recirculated by the water pump. An inlet valve was settled to adjust water discharge. An air rotameter was installed on the suction port of the venturi device to measure the values of volumetric air flowrate resulting from vacuum process (injected air). Dimensional values of the venturi, which has standard dimensional values [15, 16], (ISO 5167; ASME 1995), are summarized in Table 1. The pressure difference from which the velocity of flow can be determined is measured between the inlet section 1 and the throat section 2, often by means of a U-tube manometer (as shown in Fig. 3). A U-tube manometer was used to determine the flow velocities (V_1 and V_2) at the upstream section 1 and the throat section 2. Also, the value of differential pressure difference (h) in manometer is derived from the U-tube gauge reading. The details of experimental data are given by Bagatur [1]. Table 2 shows water discharge (Q_W), injected air flowrate (Q_A), flow velocities (V_1 and V_2) and differential pressure difference (h).

Table 1. Dimensional Values of Venturı Pipe Part

Inlet diameter d_1 (10^{-3} m)	**Throat diameter d_2** (10^{-3} m)	**Hole or air vent diameter d_h** (10^{-3} m)	**Area of pipe A_1** (10^{-4} m^2)	**Area of throat A_2** (10^{-5} m^2)	**Area of hole A_h** (10^{-6} m^2)
21	10	1.5	3.46	7.85	1.66

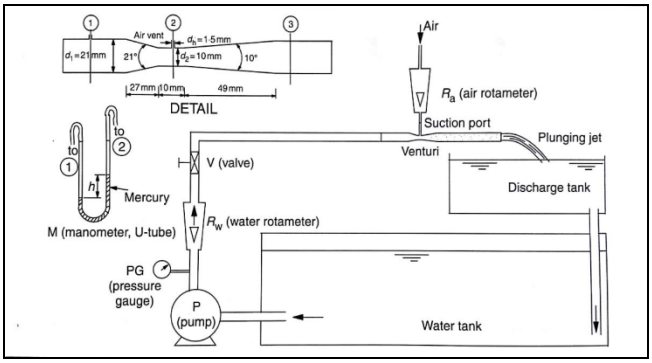

Figure 3. Experimental apparatus and its details

Table 2. Summarized Experimental Data

Water discharge Q_W (10^{-4} m^3/s)	**Volumetric air flowrate Q_A** (10^{-5} m^3/s)	**Flow velocity (section 1) V_1** (m/s)	**Flow velocity (section 2) V_2** (m/s)	**h** (cm)
3.67	2.63	0.89	3.92	4.8
4.00	2.70	0.95	4.19	5.5
4.34	2.94	1.12	4.93	7.6
4.67	3.12	1.19	5.27	8.7
5.00	3.33	1.26	5.57	9.7
5.34	3.45	1.35	5.96	11.1
5.67	3.70	1.40	6.17	11.9
6.00	3.84	1.48	6.52	13.3

3. APPLICATION OF CMFD MODELING TO VENTURI PIPE PART

CMFD (computational multiphase fluid dynamics) is a technique for solving the equations that govern fluid flow on computers. This technique has become so important that it now occupies the attention of perhaps a third of all researchers in fluid mechanics and the proportion is still increasing. One of the reasons for its popularity is that it can be used to solve real world problems. Solving the equations for fluid flow exactly is almost always impossible, except in some special cases Ferziger and Peric [17].

In CMFD, the equations of fluid flow have to be discretized, which means that the domain of interest has to be subdivided into small elements (together they are called the grid or the mesh). This also means that the solution (the velocity, pressure, etc.) is not available in the entire flow domain but only at each element. It is important to understand that a CMFD solution to a particular problem in volves approximations at several levels. The equations being solved are a model of reality, not reality itself. Secondly, when the equations are discretized, approximations are introduced. If it was possible to use an infinite number of elements it would be possible to get very close to the exact solution. But since computers are not infinite fast with infinite memory, there is a limit on the number of elements that can be used. Therefore, we cannot resolve everything inside the flowing fluid. The actual CMFD solving process is often done in steps (iterations) towards the exact solution. This process has to be stopped at some level which means that the exact solution to the discretized equations is never reached [12].

In this study, using CMFD modeling, the air injection rates of venturi pipe part are analyzed. These analyses are carried out by means of the ANSYS CFX 11.0 computer program. the ANSYS CFX is a computational fluid dynamics software package to simulate fluid flow problems. It uses the finite-volume method to solve the governing equations for a fluid. It provides the capability to use different physical models such as incompressible or compressible, inviscid or viscous, laminar or turbulent, etc.

3.1. Solution Strategies

Shear stress transport (SST) turbulence model can be used in the simulations. The SST model combines the advantages of the k–ε and k-ω models, with a blending function that activates the k-ε model in the core region of the flow, and shifts to the k–ω model for the near-wall region treatment. SST model is accurate for water flows with substantial zones of free shear/separation and it combines merits of k-ω and k-ε formulations for flows that are mixed bounded and external [14].

Shear stress transport (SST) turbulence model developed by Menter has been used for numeric simulations [18]. This model consists of three sets of coupled equations (Menter [18],; Can et al. [19]). The first set includes Reynolds-averaged Navier–Stokes equations (RANS) equations and the equation of continuity the second, which provides the turbulent viscosity μ_t needed as input to the RANS equations, is the Shear Stress Transport turbulence model. These two sets, when solved synchronous, are able to model any flow regime and to provide a smooth and automatic transformation between the flow regimes. The final equation is energy conservation. The practice of energy conservation in transition regimes is particularly challenging because a means of transforming values of μ_t to κ_t is needed. The neglect value of 0.9 was used for Pr_t.

Mass conservation is:

$$\frac{\partial u_i}{\partial x_i} = 0 \tag{1}$$

Also, Reynolds-averaged Navier–Stokes equation (RANS) is:

$$\rho\left(u_i \frac{\partial u_j}{\partial x_i}\right) = -\frac{\partial p}{\partial x_i} + \frac{\partial}{\partial x_i}\left((\mu + \mu_t)\frac{\partial u_j}{\partial x_i}\right) \quad j = 1,2,3 \tag{2}$$

Shear Stress Transport turbulence model (SST) is given as following expressions:

$$\frac{\partial(\rho u_i \kappa)}{\partial x_i} = \gamma P_\kappa - \beta_1 \rho \kappa \omega + \frac{\partial}{\partial x_i}\left[\left(\mu + \frac{\mu_t}{\sigma_\kappa}\right)\frac{\partial \kappa}{\partial x_i}\right] \tag{3}$$

$$\frac{\partial(\rho u_i \omega)}{\partial x_i} = A\rho\rho^2 - \beta_2 \rho \omega^2 + \frac{\partial}{\partial x_i}\left[\left(\mu + \frac{\mu_t}{\sigma_{\omega_1}}\right)\frac{\partial \omega}{\partial x_i}\right] + 2(1 - F_1)\rho \frac{1}{\sigma_{\omega 2}\omega}\frac{\partial \kappa}{\partial x_i}\frac{\partial \omega}{\partial x_i} \tag{4}$$

The solution of Eq. (3) and (4) yields the values of κ and ω, which are then used to evaluate the turbulent viscosity μ_t from:

$$\mu_t = \frac{a\rho\kappa}{\max(a\omega, SF_2)} \tag{5}$$

Energy conservation is:

$$\rho c_p \left(u_i \frac{\partial T}{\partial x_i} \right) = \frac{\partial}{\partial x_i} \left((k + k_t) \frac{\partial T}{\partial x_i} \right) \tag{6}$$

Turbulent Prandtl number is:

$$Pr_t = \frac{c_p \mu_t}{k_t} \tag{7}$$

Here, u term is average fluid velocity, F_1 and F_2 terms are blending functions in SST model, P is rate of production of the turbulent kinetic energy, p is pressure, α, β_1 and β_2 are SST model constants, S is absolute value of the shear strain rate, ω is specific rate of turbulence destruction, μ is dynamic viscosity, σ is Prandtl-number-like diffusivities, κ is turbulence kinetic energy, ρ is density, $_{i,j}$ are tensor notation subscripts, t is turbulent subscripts.

3.2. Boundary Conditions

The boundary conditions in the numerical model are defined as velocity inlet (water inlet), pressure inlet (air inlet with atmospheric pressure), walls (solid surfaces), and outlet (water and air outlet). The velocity inlet boundary condition is applied to determine the water flow rate at the entry of venturi pipe part. The water velocities of the boundary are changed from 0.89 m/s to 1.48 m/s, so the water discharges, Q_w, are taken into account as the range from 3.67×10^{-4} m^3/s to 6.00×10^{-4} m^3/s. The pressure inlet and the outflow are applied to the boundary of air vent (hole) and the boundary of exit of venturi, respectively (Fig.4). The pressure values in the boundary of pressure inlet and outflow are chosen as zero Pascal.

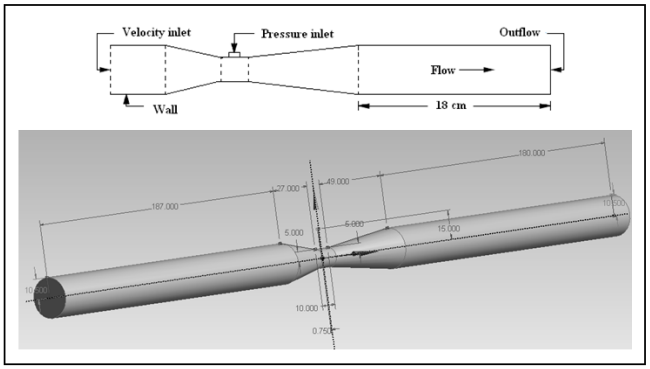

Figure 4. Boundary conditions and dimensions of the numerical model

To obtain the required flow field, solutions have been obtained by solving the basic governing equations (continuity and momentum) with inlet velocity normal to main inlet and side inlet as boundary conditions or input parameters. Further, no slip condition was imposed at the walls. The characteristics of flowing fluid was considered to rep-resent water by imposing a density and viscosity value of 997.0 kg/m^3 and 0.001 Pa s. All the simulations have been carried out assuming steady state conditions for velocities varying from 1 to 1.5 m/s. With the above velocities, Reynolds number (Re) was found to vary from 20000 to 45000 indicating turbulent flow. Hence, all the simulations have been carried using SST model. The solutions have been obtained imposing coupled solver approach using advection scheme with high resolution and a convergence limit of 1×10^{-6}.

3.3. Grid and Iterative Convergences

Geometry and grid generation is done using ANSYS workbench which is the preprocessor bundled with ANSYS CFX. In this study, the numerical model geometries are prepared with ANSYS workbench program and are divided into 45772 node numbers and 228541 element numbers (Fig. 5). The fine and coarse grids are applied in the flow domain and the convergence and stability of the solution are found to be insensitive to the grid size in the main body of the flow.

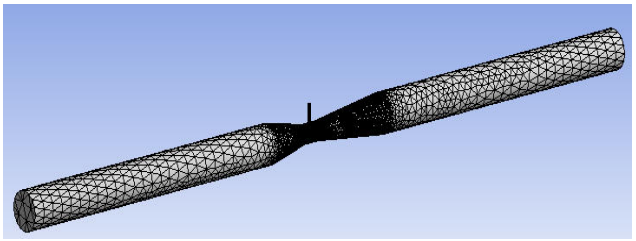

Figure 5. Meshed view of computational domain of venturi pipe part

In the iterative solutions, it must be ensured that iterative convergence is achieved with at least three orders of magnitude decrease in the normalized residuals for each equation solved. Convergence values were taken as $1x10^{-6}$. Iteration number was taken as 1000. However, values were converged to the value $1x10^{-6}$ approximately at 250-300 iterations.

4. RESULTS AND DISCUSSIONS

Using computational multiphase fluid dynamics modeling, the air injection rates of the venturi pipe part are analyzed. These analyses are performed by means of the program ANSYS CFX that uses finite volumes theory. Fig. 6 presents the air vacuum (or aeration) mechanism of the venturi pipe part for flow magnitude of air-water mixture. Also, fig.7 shows variation of air entrainment process from atmosphere with different water discharges.

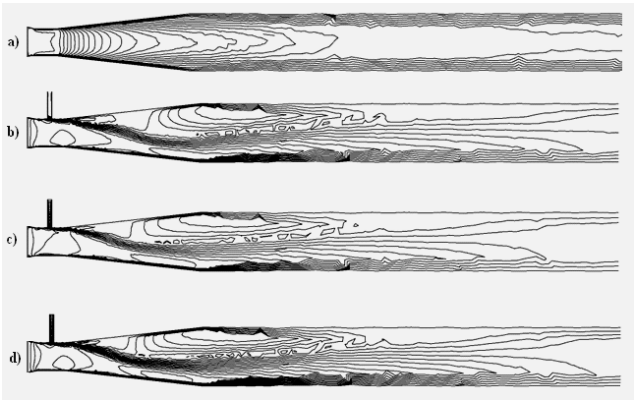

Figure 6. Contours of flow magnitude of air-water mixture: a) air vent of venturi: closed, $Q_A = 0$ (10^{-5} m^3/s); b) $Q_A = 2.63$ (10^{-5} m^3/s); c) $Q_A = 3.12$ (10^{-5} m^3/s); d) $Q_A = 3.70$ (10^{-5} m^3/s)

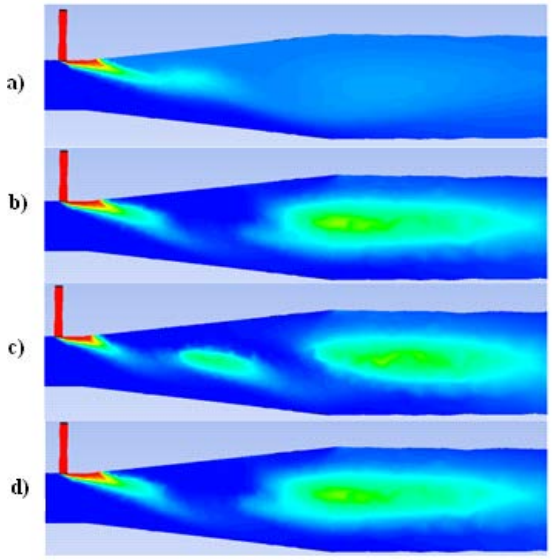

Figure 7. Variation of air entrainment process for different water discharges at steady state flow a) Q_W = 3.67 (10^{-4} m^3/s); b) Q_W = 4.67 (10^{-4} m^3/s); c) Q_W = 5.67 (10^{-4} m^3/s); d) Q_W = 6.00 (10^{-4} m^3/s)

Fig. 8 shows the air vacuum process of the venturi pipe part for flow magnitude of air-water mixture according to transient flow conditions (time, t=0-1 s). Also, Fig.9 presents velocity of entrained air from venturi vent (or hole) for transient flow conditions.

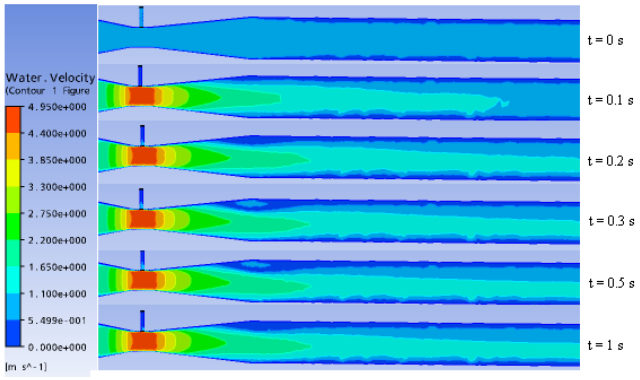

Figure 8. Air vacuum process in venturi for transient flow at Q_W = 3.67 (10^{-4} m^3/s)

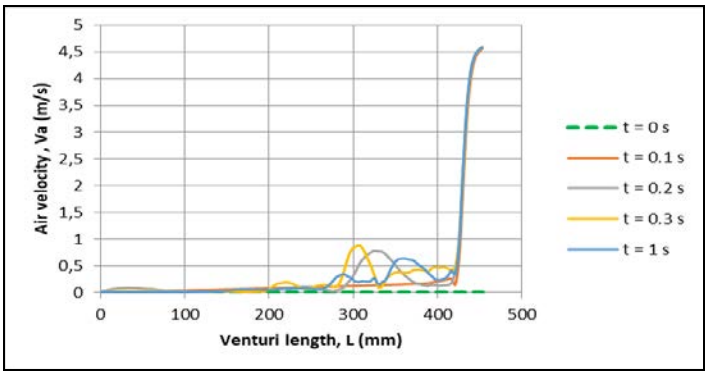

Figure 9. Variation of velocity of air from air vent for transient flow at Q_W = 3.67 (10^{-4} m^3/s)

Fig. 10 shows variation of water pressure for flow magnitude of air-water mixture according to transient flow conditions (time, t = 0-1 s). Also, fig.11 presents variation of water velocity in venturi for transient flow conditions.

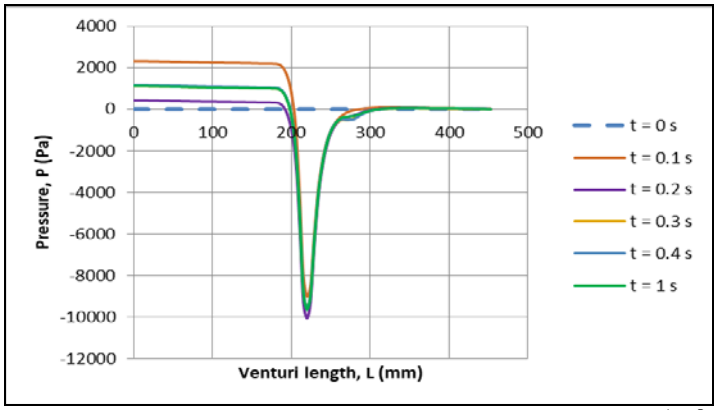

Figure 10. Variation of water pressure for transient flow at Q_W =3.67 (10^{-4} m^3/s)

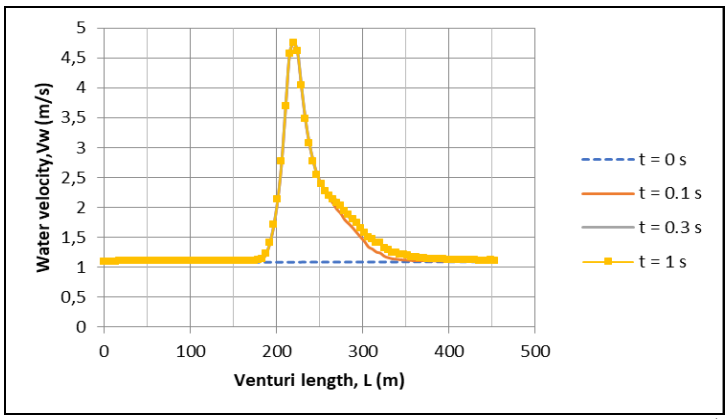

Figure 11. Variation of flow velocity in venturi for transient flow at Q_W =3.67 (10^{-4} m^3/s)

Fig. 12 presents flow velocity predictions for computational model at the middle water discharge (Q_W =4.67 (10^{-4} m^3/s) as an illustrative example. Also, fig. 12 shows the static pressure distribution on the sections. In fig. 10, as expected, the increasing of flow velocity at the throat portion accompanied by reduction in the pressure can be seen clearly. Furthermore, it is seen in Fig.13 that the static pressure before the converging cone decreases with increasing of the diameters of venturi and throat, while the negative pressure in the throat do not change too much with increasing diameter. In Fig. 13, the static pressure distribution on the sections is observed that static pressure decreases at the throat portion. According to fig. 13, it is seen that the pressure at the air suction hole decreases extremely.

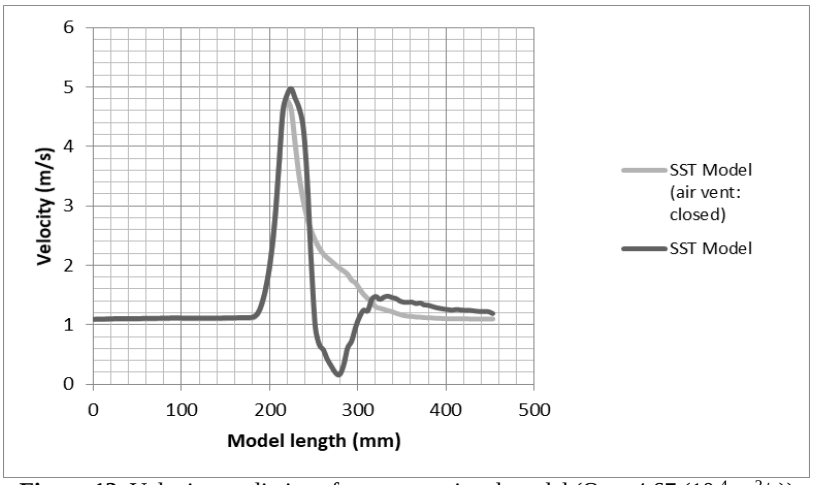

Figure 12. Velocity predictions for computational model (Q_W =4.67 (10^{-4} m^3/s))

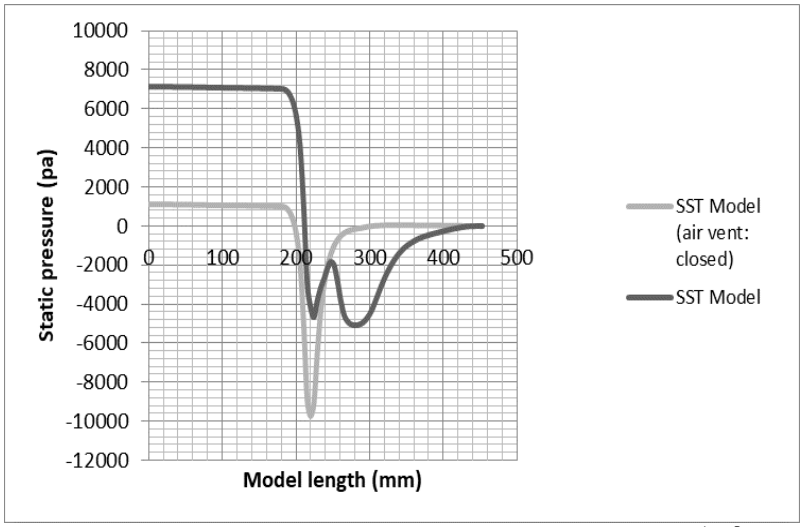

Figure 13. Pressure predictions for computational model (Q_W =4.67 (10^{-4} m^3/s)

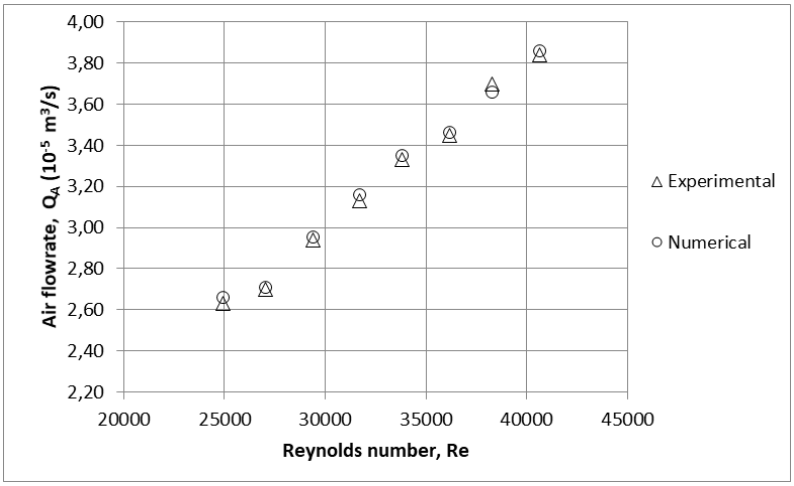

Figure 14. Plot of air flowrate (Q_A) versus Reynolds Number (Re) for experimental and numerical (CMFD model) results

The values computed from ANSYS CFX program are compared with experimental laboratory results, as shown in Fig. 14. The experimental results and those obtained with CMFD model have good agreement with each other. The mean rate of error between the experimental and numerical results is 2-3%. Thus, these errors can result from such things as selected turbulence and mathematical model for multi phase (air-water), disregarding environment conditions, grid size in numerical models and measurement faults in the experimental tests.

4. CONCLUSIONS

The computational multiphase fluid dynamics (CMFD) technique has low cost, and its computation period is shorter than experimental period, so the system parameters can be computed as much as possible. At the same time, the numerical simulation involves the concept of field, which is different from the rough mode of traditional design. It can not only reflect the practical flow characteristics inside the venturi pipe part but also obtain the relation between the self-sucking flowrate and structural parameters and therefore provide reference for the parameters design. In addition, because of the complex flow and structure inside the venturi pipe part, it is difficult to measure the flow parameters in the field. However, numerical simulation can predict the distribution of the pressure and velocity comparatively precisely, and help to further improve air entrainment (aeration) performance of the venturi pipe part. As the water passes through a restriction in a pipe, it forms a vacuum at the end of the restriction. A hole bored into the pipe at a point where this vacuum occurs will cause air to be drawn into the main flow. One example of this mechanism can be seen in the venturi pipe part with aeration process. Venturi aeration is a method of aeration that has become popular in recent years. In present paper, air injection rates of venturi pipe part were analyzed using CMFD modeling. These analyses were carried out by means of the ANSYS CFX program. Thus, this study presents air vacuum model that quantitatively predicts the rate of air entrainment and subsequent disperse bubbly flow for venturi pipe part. This model was validated against experimental data based on minimal flow velocities (from around 1 to 1.5 m/s) for air entrainment. There is a good agreement between the measured air injection rates and the computed values from ANSYS CFX depending on Reynolds Number.

REFERENCES

[1] Bagatur, T., Technical note: minimal conditions for venturi aeration of water flows. Proc. Inst. Civ. Eng. Water Manag., **158**(WM3),127–130, 2005.

[2] Baylar, A., Emiroglu, M.E. Air entrainment and oxygen transfer in a venturi., Proc. Inst. Civ. Eng.Water Marit. Energy, **156**(WM3),249–255, 2003.

[3] Emiroglu, M.E.; Baylar, A., Study of the influence of air holes along length of convergent–divergent passage of a venturi device on aeration., J. Hydraul. Res., **41**(5), 513–520, 2003.

[4] Baylar, A.; Ozkan, F.; Ozturk, M., Influence of venturi cone angles on jet aeration systems., Proc. Inst. Civ. Eng. Water Manag., **158**(WM1), 9–16, 2005.

[5] Ozkan, F., Ozturk, M., Baylar, A., Experimental investigations of air and liquid injection by venturi tubes., Water Environ. J., **20**(3), 114–122, 2006.

[6] Baylar, A., Ozkan, F., Applications of venturi principle to water aeration systems., Environ. Fluid Mech., **6**(4), 341–357, 2006.

[7] Baylar, A., Ozkan, F., Unsal, M., On the use of venturi tubes in aeration., CLEAN Soil Air Water, **35**(2), 183–185, 2007a.

[8] Baylar, A., Unsal, M., Ozkan, F., Determination of the optimal location of the air hole in venturi aerators., Clean Soil AirWater, **35**(3), 246–249, 2007b.

[9] Baylar,A., Ozkan, F., Unsal,M., Effect of air inlet hole diameter of venturi tube on air injection rate., KSCE J. Civ. Eng., **14**(4), 489–492, 2010.

[10] Bagatur, T., Evaluation of plant growth with aerated irrigation water using venturi pipe part., Arab. J. Sci. Eng., **39** (4), 2525-2533, 2014.

[11] Utomo,T., Jin, Z., Rahman, M., Jeong, H., Chung, H., Investigation on hydrodynamics and mass transfer characteristics of a gas-liquid ejector using three-dimensional CFD modeling., J. Mech. Sci. and Techn., **22**, 1821–1829, 2008.

[12] Baylar, A., Aydın, M.C., Unsal, M.,Ozkan, F., Numerical modeling of venturi flows
for determining air injection rates using FLUENT V6.2., Math. and Comp. Applica., **14** (2), 97-108, 2009.

[13] Majid, A., Changqi,Y., Zhongning, S., Jianjun,W., Haifeng, G. (2013) CFD simulation of dust particle removal efficiency of a venturi scrubber in CFX. Nuclear Eng. and Design 256, 169– 177

[14] ANSYS CFX Solver Theory Guide, 2011.

[15] ISO 5167, International organization for standardization measurement of fluid flow by means of orifice plates, nozzles, and venturi tubes inserted in circular cross-section conduits running full., ISO, Geneva, Switzerland, 1980.

[16] ASME Standard MFC-3M-1989, Reaffirmed (1995), Measurement of fluid flow in pipes using orifice, nozzle and venturi., ASME.

[17] Ferziger, J. H., Peric, M., Computational methods for fluid dynamics, Springer-Verlag, Berlin, Heidelberg, 1996.

[18] Menter, F., Two-equation eddy-viscosity turbulence models for engineering applications, AIAA Journal, **32**, 1598-1605., 1994.

[19] Can, O. F., Celik, N. , Dagtekin, I., Numerical analysis of external flow heat transfer around slightly-curved surfaces , Arab J Sci Eng, **39**, 1219–1230, 2014.

INVESTIGATION OF FLOW FIELD CHARACTERISTICS OF SYNTHETIC JET DRIVEN BY HALF SINUSOIDAL SIGNAL

Mehmet Yusuf BAYAT[*], Mustafa SARIOĞLU[*], Yahya Erkan AKANSU[**]
[*]Karadeniz Technical University, Department of Mechanical Engineering, Trabzon/Turkey
Email: sarioglu@ktu.edu.tr; bayatmehmetyusuf@gmail.com
[**]Niğde Ömer Halisdemir University, Department of Mechanical Engineering, Niğde/Turkey
Email: akansu@ohu.edu.tr

ABSTRACT

In this study, the flow field characteristics of a synthetic jet driven by a half sinusoidal signal wave were carried out experimentally and compared to a sinusoidal signal. Besides, the synthetic jet driven by the half sinusoidal signal was studied with different amplitudes and duty cycles. To elucidate the effectiveness of the actuator, the half sinusoidal signal wave was arranged with different offsets. Synthetic jet driving frequency and voltage were defined as f=4 Hz and E=5 V_{pp} respectively. To form a synthetic jet, also known as zero net mass flux jet, a woofer type loudspeaker actuator and a cylindrical nozzle having D=34 mm outlet diameter were used. Instantaneous and time-averaged jet velocities were acquired by using a hot-wire anemometer. Synthetic jet velocity flow fields were measured in the different dimensionless axial distances (H/D). The increasing amplitude of half sinusoidal signals generates tandem jets with different velocities where a jet with higher velocity can reach the preceding jet. By measuring the instantaneous velocity time history along the jet axial centerline, it was investigated whether the movements of the tandem jet would form a combined single jet structure.

Keywords: Synthetic jet, Tandem jets, Signal modulation,

1. INTRODUCTION

Synthetic jet, known as zero net mass flux (ZNMF), has recently been the focus of attention by researchers because the synthetic jet does not need to add any external mass flux. In literature, synthetic jets have been studied comprehensively by researchers from active flow control to impinging jet heat transfer, [1-10]. Active flow control is carried out using energy, and there are three types of the actuator to form the synthetic jet. The first type of actuator is piston-cylinder which can produce a high mass flow rate but has a low frequency [1], the second one is a piezoelectric actuator which has a high frequency but can produce a low mass flow rate [2] and the third one is a loudspeaker which can produce more high mass flow rate than piezoelectric actuator and has a higher frequency than piston-cylinder actuator [3]. Active flow control on bluff and streamlined bodies was investigated using a synthetic jet by many researchers [4-8]. Amitay et al. investigated using a piezoelectric actuator over a 2-D cylindrical model to reveal the effect of an increase on the lift coefficient and a decrease on the drag coefficient, respectively [4]. A delaying separation point over a spherical body can be observed using the synthetic jet [5]. Other experimental studies used synthetic jet behind models for aerodynamic drag reduction of Ahmed model and bullet [6,7]. Synthetic jets can also be used on an airfoil surface [8].

Out of the flow control, synthetic jets are also used to increase heat transfer [9-11]. It was found that the heat transfer coefficient was 11 times higher than that of natural convection obtained using an impinging synthetic jet [9]. Synthetic jets have been observed that to be three times more effective than that continuous jets having the same Reynolds number, in cooling [10].

The purpose of this study is to investigate the flow characteristics of synthetic jets. Synthetic jets were driven by different signal waves; continuous sinusoidal signal, a continuous half positive sinusoidal signal, a half

sinusoidal signal which has a 50% duty-cycle, a half sinusoidal signal which has different amplitudes, and half sinusoidal signal which has an incremental amplitude.

2. EXPERIMENTAL SETUP

The experiments were conducted using woofer type Jameson brand JW-36 model 1000 W loudspeaker. The volume of the actuator was obtained from the 10mm thickness of a Plexiglas plate and screwed on the loudspeaker. A 34 mm diameter nozzle-shaped hole was drilled in the center of the Plexiglas cover. AA Tech brand AWG-1010 model signal generator was used to drive the actuator. 2-channel Tektronix brand TDS2012 model digital oscilloscope was used to observe the produced signal. The 5-volt sinusoidal signal produced by the signal generator is amplified through the Boss brand CX750 model amplifier, and the actuator is operated.

Figure 1 shows the view of the experimental setup. The hot-wire anemometer is placed over the loudspeaker for mean and rms velocity measurements, and the probe is moved by the 2D traverse mechanism. Initially, the probe was placed in the center of the nozzle, and velocities were measured by positioning at different dimensionless axial distances (H/D=1, 2, 3, 4, 5, 6, 7, 8, 9, and 10).

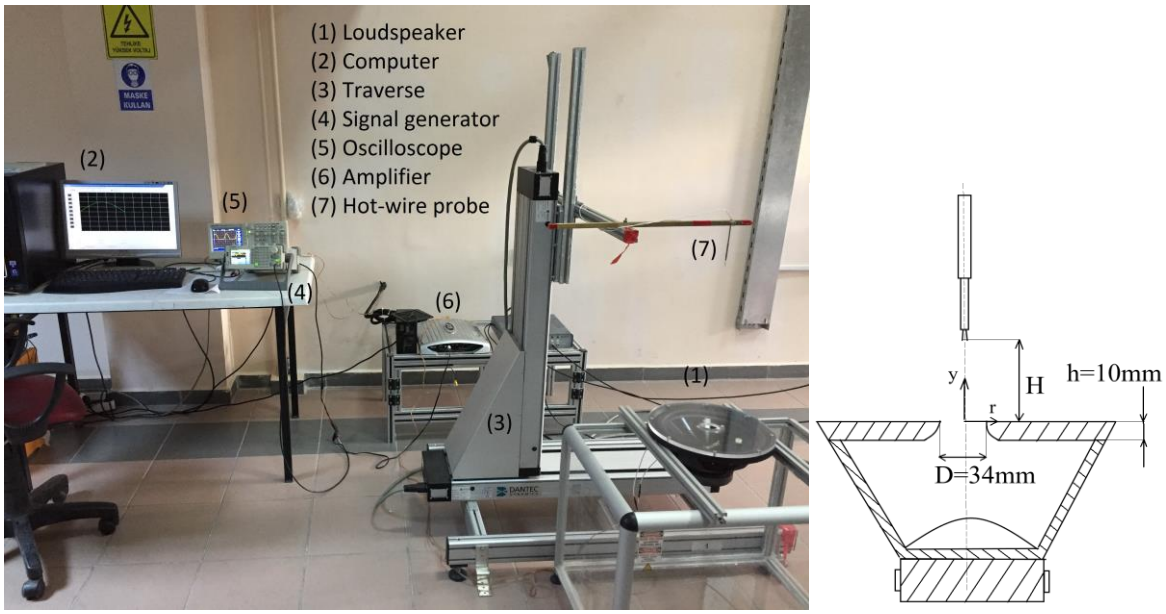

(a) **(b)**

Figure 1. a) View of the experimental setup b) schematic drawing of loudspeaker and hot-wire probe

In this study, eight different signal structures used to drive the loudspeaker are listed in table 1. To compare the amplitude effect, the Halfsin-3 is set to 2,5 V_{pp} and the Halfsin-4 set to 7,5 V_{pp}, and the remaining signal structures are set to 5 V_{pp}. Besides, Halfsin-1 was set at 100% and Halfsin-2 at 50% duty cycle to determine the effect of the duty cycle. On the other hand, experiments were carried out by adjusting the Halfsin-2, which have the same amplitude and duty cycle, but +2,5 and -2,5 V_{pp} offsets, respectively, and all other signal structures were examined at 0 V_{pp} offset. Halfsin-5, Halfsin-6, and Halfsin-7, which have a tandem signal (the first signal has a 2.5V_{pp} and the second signal has a 7.5V_{pp}), were investigated to obtain the effect of the conjoint single jet structure. These signals were set to 2Hz, and the other signals were driven at 4Hz.

Table 1. Parameters of driven signal structures

Parameters of Signal	Complete sin	Halfsin-1	Halfsin-2	Halfsin-3	Halfsin-4	Halfsin-5	Halfsin-6	Halfsin-7
Amplitude (V_{pp})	5	5	5	2,5	7,5	2.5, 7.5	2.5, 7.5	2.5, 7.5
Frequency (Hz)	4	4	4	4	4	2	2	2
Time for a half Sin signal (s)	0.125	0.125 0.125	0.125 0.125	0.125 0.125	0.125 0.125	0.125 0.125	0.125 0.125	0.125 0.125
Time gaps between two half signal (s)	0	0	0.125	0.125	0.125	0 0.250	0.0625 0.1875	0.125 0.125
Duty Cycle (%)	100	100	50	50	50	50	50	50
Shape of signals								

3. RESULTS

Figure 2 shows the instantaneous velocity time history of complete sinus and Halfsin-2. Halfsin-2 which has a 50% duty cycle and 5 V_{pp} amplitude and complete sinus which has a 5 V_{pp} amplitude instantaneous velocities of signal structures were compared. Both signal structures show similar velocity distribution time history in the same dimensionless axial distances. With increasing axial distance (H/D), the synthetic jet velocity profile expands in the radial direction and its maximum velocity decreases.

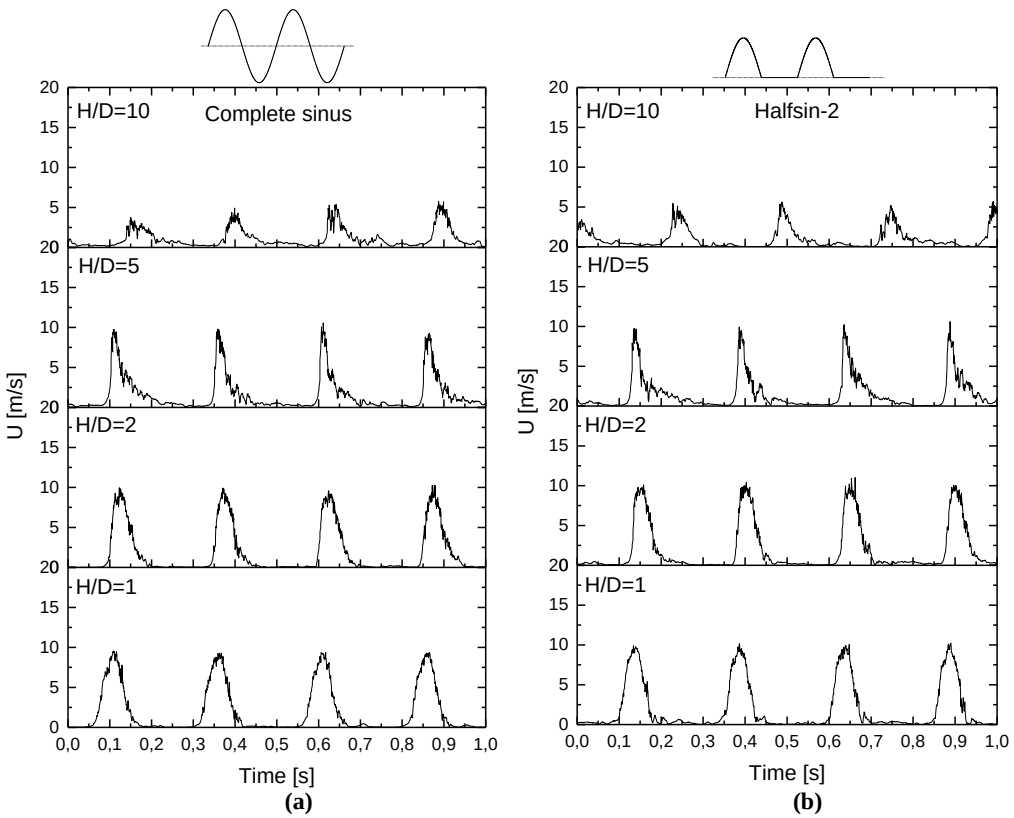

Figure 2. Instantaneous velocity time history for a) complete sinusoidal wave and b) Halfsin-2 signal.

Figure 3 shows instantaneous velocity time history to compare the Halfsin-1 and Halfsin-2 at the same axial distance H/D=2. Both signals have approximately the same maximum velocities. While Halfsin-2 has four peak

velocities, Halfsin-1 has eight peak velocities. The graph shows that Halfsin-1 has more turbulence than Halfsin-2.

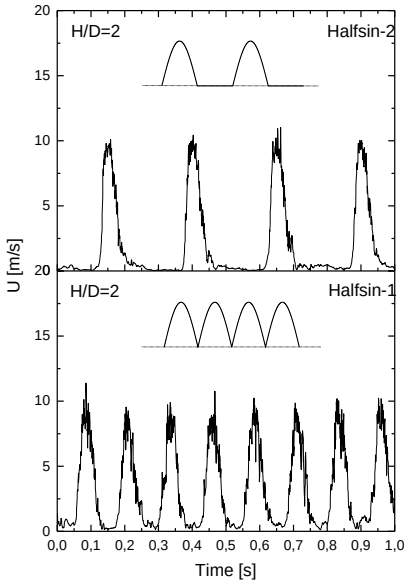

Figure 3. Instantaneous velocity time history for Halfsin-1 and Halfsin-2 at H/D=2

The signal structures which have a 50% duty cycle adjusted to different offsets are compared with the instant velocity graphs shown in figure 4. As shown in the graphics, the offset setting being +2.5, 0, or -2.5 V does not change the effectiveness of the actuator. Figure 5 reveals the change in the flow structure of the amplitude ($2.5V_{pp}$, $5V_{pp}$, and $7.5V_{pp}$). As seen in the graphs, maximum velocity values increase linearly with increasing amplitude.

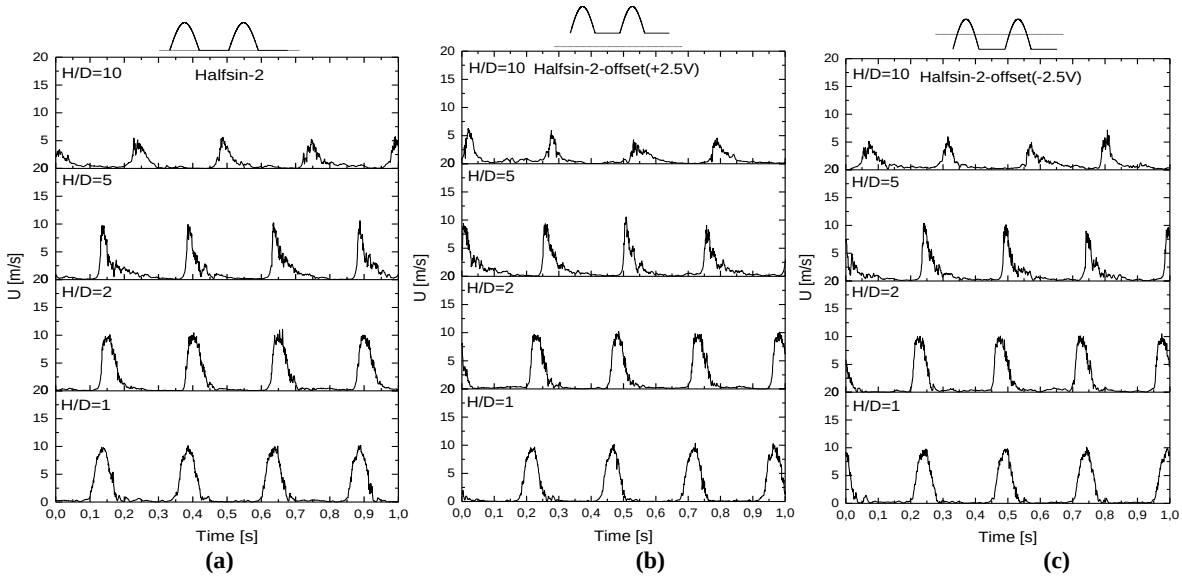

Figure 4. Instantaneous velocities of Halfsin-2 signal set to a) 0V offset, b) +2.5V offset and c) -2.5V offset

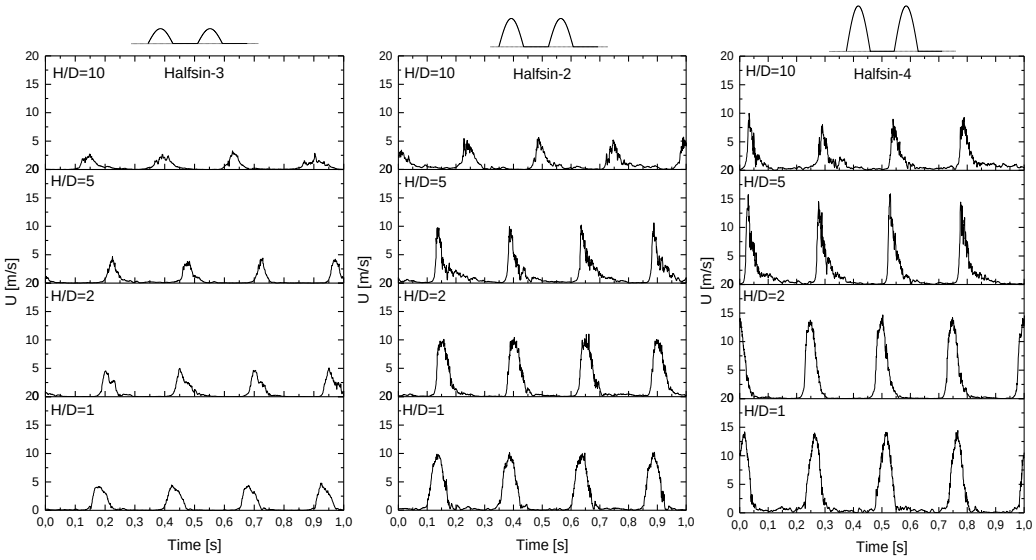

Figure 5. Instantaneous velocities of signals set to a) 2.5V_{pp} (Halfsin-3), b) 5V_{pp} (Halfsin-2) and c) 7.5V_{pp} (Halfsin-4)

In Figure 6, instantaneous velocities of the tandem two jets with different amplitudes of 2.5Vpp and 7.5Vpp and different time gaps of 0, 0.0625 and 0.125s are given. These signals cause to two jets having low and high-velocity values. The-high value jet gets close to the lower one starting previously during goes on the jet axis. In the case of the Halfsin-5 which has no time gap between the two half signals, the tandem jets occur successively, and they conjoined at H/D=8. For the Halfsin-6 signal, the fast jet could reach to slow one with a small delay at H/D=10. The effect of the time gap between the half signals of Halfsin-7, the slower primary jet loses its existence by further distance before conjoint with the fast one.

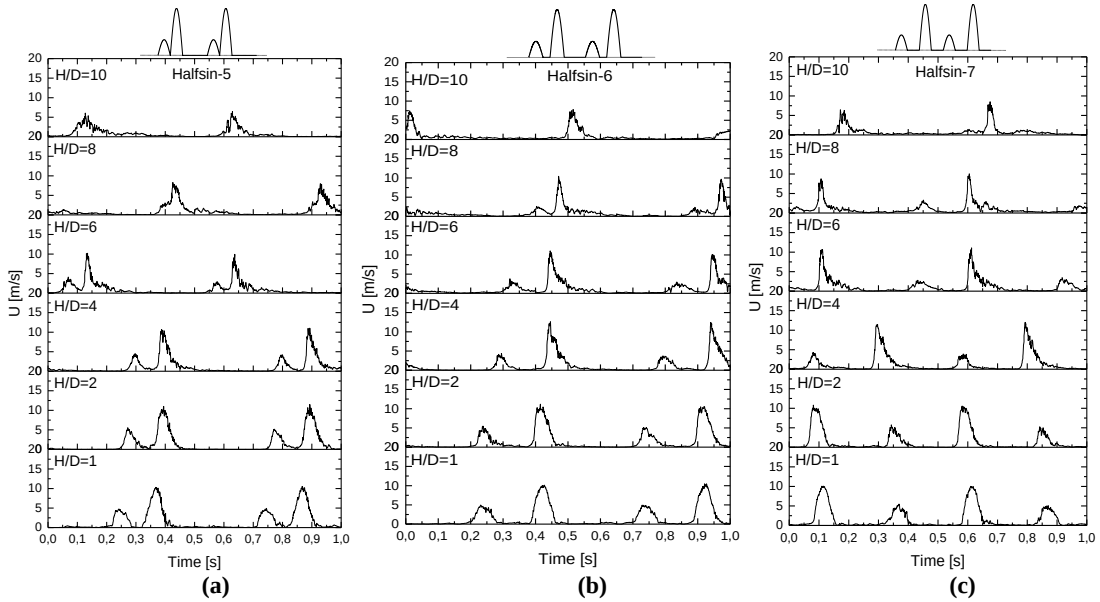

Figure 6. Instantaneous velocities of the tandem jets with increasing amplitude (2.5V_{PP} and 7.5V_{PP}) a) Halfsin-5, b) Halfsin-6, and c) Halfsin-7

In figure 7, mean velocities of all signal structures versus increasing axial distance are given. In all signal structures, it is seen that there is a rapid decrease in average velocities up to about H/D=1, whereas when H/D>1,

average velocities decrease slowly. The highest and the smallest mean velocity values were obtained in Halfsin-1 and Halfsin-3, respectively. On the other hand, the complete sinus, Halfsin-2, Halfsin-2 with +2.5V offset, and Halfsin-2 with -2.5V offset appear to have the same mean velocity values.

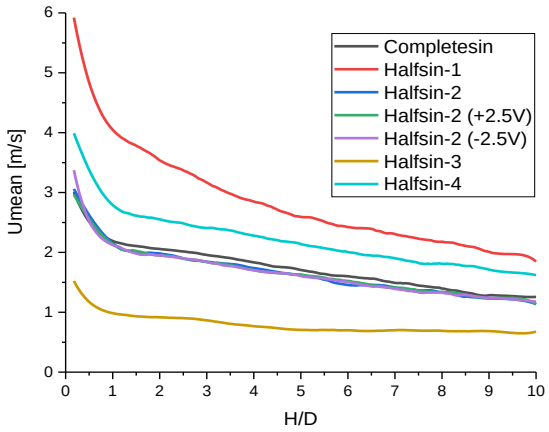

Figure 7. The variation of the mean velocities with H/D

4. CONCLUSION

The flow field characteristics of a synthetic jet driven by a half sinusoidal signal wave were investigated experimentally. The synthetic jet driven by the half sinusoidal signal was studied with different amplitudes and duty cycles. To determine the effectiveness of the actuator, the same signal structures in different offsets were examined, and changing the offset did not change the operating efficiency of the actuator. Besides, three different amplitude signals are sent to examine the effectiveness of the membrane of the actuator, and it seems that there is a consistency in membrane motion with increasing amplitude. The conjoining effect of the jets with increasing amplitude was examined sequentially. The Halfsin-5 was observed to conjoint at H/D=8 and when the time gap between the two signals increases, the effect of conjoint was observed to be delayed.

REFERENCES

[1] Gilarranz, J. L., Traub, L. W. & Rediniotis, O. K., A New Class of Synthetic Jet Actuators – Part I: Design, Fabrication and Bench Top Characterization, *Journal of Fluids Engineering*, 127, 367-376, 2005.

[2] Tan, X. M. & Zhang, J. Z., Flow and heat transfer characteristics under synthetic jets impingement driven by piezoelectric actuator, *Experimental Thermal and Fluid Science*, 48, 134-146, 2013.

[3] Kordik, J. & Travnicek, Z., Non-harmonic excitation of synthetic jet actuators based on electrodynamic transducers, *International Journal of Heat and Fluid Flow*, 73, 154-162, 2018.

[4] Amitay, M., Smith, B. L. & Glezer, A., Aerodynamic Flow Control Using Synthetic Jet Technology, *American Institude of Aeronautics and Astronautics*, 98-0208, 1997.

[5] Findanis, N. & Ahmed, N. A., The interaction of an asymmetrical localised synthetic jet on a side-supported sphere, *Journal of Fluids and Structures*, 24, 1006-1020, 2008.

[6] Park, H., Cho, J., Lee, J. Lee, D. & Kim, K., Aerodynamic Drag Reduction of Ahmed Model Using Synthetic Jet Array, *SAE Int. J. Passeng. Cars – Mech. Syst.*, 6, 01-0095, 2013.

[7] Gil, P., Bluff Body Drag Control using Synthetic Jet, *Journal of Applied Fluid Mechanics*, 12, 193-302, 2019.

[8] Amitay, M., Smith, D. R., Kibens, V., Parekh, D. E. & Glezer A., Aerodynamic Flow Control over an Unconventional Airfoil Using Synthetic Jet Actuators, *American Institude of Aeronautics and Astronautics,* 39, 3, 2001.

[9] Chaudhari, M., Puranik, B. & Agrawal A., Heat transfer characteristics of synthetic jet impingement cooling, *International Journal of Heat and Mass Transfer*, 53, 1057-1068, 2010.

[10] Pavlova A. & Amitay M., Electronic Cooling Using Synthetic Jet Impingement, *Journal of Heat Transfer*, 128, 897-907, 2006.

ANALYSIS AND DESIGN OF AN AIR TO AIR HEAT EXCHANGER USED IN ENERGY RECOVERY SYSTEMS

Helin Ülgen ELMACIOĞLU*, İrem ÖZSEVGİN, Cennet KOCABIYIK, Nezir Yağız ÇAM, Levent BİLİR
*****Yaşar University, Department of Energy Systems Engineering, İzmir/Turkey
Email: helinulgen@gmail.com

ABSTRACT

With the continuous worldwide energy use increase, energy efficiency is gaining high importance. Consequently, many methods have been investigated for potential energy savings. One of these methods is the use of heat recovery systems. These systems basically re-use waste heat and reduce energy consumption. Also, they are increasingly used to reduce the heating and cooling demands of buildings. Their main feature is to provide fresh air to the place which is heated by the exhaust air with the help of a heat exchanger working between two different temperature sources. Various heat exchangers can be used for different engineering applications with many different sizes, weights, shapes, and flow patterns. The most commonly used types of heat exchangers in ventilation systems are cross-flow heat exchangers. They have a thermal efficiency in the range of 50-75%. Many studies have been carried out to increase the efficiency of this type of heat exchanger which are preferred because of their small structure and low cost. In this study, cross-flow flat plate and dimpled plate heat exchangers were compared using Engineering Equation Solver (EES) program and ANSYS Fluent software to determine how the surface geometry affects heat transfer. Different dimple geometries were analyzed by using ANSYS Fluent software to find f friction factor and Colburn j factor in laminar and turbulent flows to develop an optimum design. As a result of the simulations, the optimum geometry required to increase efficiency was determined.
Keywords: Heat recovery, cross-flow heat exchanger, dimpled plate, heat transfer, efficiency.

Symbol List

A_s	The specific area of the heat transfer surface $[m^2]$
C	Heat capacity rate [W/K]
C_C	Heat capacity rate for cold air [W/K]
C_H	Heat capacity rate for hot air [W/K]
C_R	Heat capacity rate ratio of C_C and C_H [W/K]
C_{min}	Minimum heat capacity rate [W/K]
C_P	Specific heat at constant pressure [J/kg.K]
D_h	Hydraulic diameter [m]
NTU	Number of transfer unit [-]
Nu	Nusselt number [-]
Re	Reynolds number
Rt	net cash inflow-outflows during a single period
$T_{exhaust,inlet}$	Temperature of exhaust air inlet [℃]
$T_{supply,inlet}$	Temperature of supply air inlet [℃]
T_{in}	Inlet temperature [℃]
T_{out}	Outlet temperature [℃]
Pr	Prandtl number [-]
$\dot{Q}$	Heat transfer rate [kW]
U	Heat transfer coefficient [W/(m^2K)]
V	Velocity [m/s]
f	Friction factor [-]

h	Convective heat transfer coefficient [W/(m^2K)]
i	Discount rate or return that could be earned in alternative investments
k	Thermal conductivity [W/ (m.K)]
q	Heat flux [W]
t	Number of time period
Δt	Temperature difference [℃]
ε	Effectiveness [-]
λ	Thermal conductivity [W/ (m.K)]
ρ	Density [kg/m^3]
μ	Dynamic viscosity [kg.m/s]

1. INTRODUCTION

A significant part of the total energy used by a country is used in buildings in the residential and commercial sectors. In the project design and development process of the building, it is necessary to adopt environmentally friendly applications and solutions that lead to a reduction of energy consumption for heating, cooling, and ventilation. Since an important part of the total energy consumption is generated by air handling units, an efficient and energy-saving system is needed to minimize energy consumption in buildings. As a result of certain studies, heat recovery systems have started to be used to reduce energy consumption while increasing energy efficiency [1].

Heat recovery systems are energy recovery ventilation systems that provide fresh air that improves the indoor environment while recovering the normally wasted heat. Heat Exchanger is the main device used in the recovery of wasted heat and may have certain applications in space heating, air conditioning, and waste heat recovery. Heat exchangers are designed to efficiently transfer or "exchange" heat from one substance to another.
There are various heat exchangers tailored to different engineering applications with many different sizes, weights, shapes, and flow patterns [2]. The most used types of heat exchangers in ventilation systems are cross-flow and cross-counter-flow heat exchangers. A normal cross-flow heat exchanger has a thermal efficiency of 50-75%. If more thermal efficiency is required cross-counter-flow heat exchanger can be used, which has efficiency typically up to 75-85% [3].

The cross-flow heat exchanger has a design in which two air streams will enter the heat exchanger perpendicular to each other. A cross-flow heat exchanger is made of thin metal panels, normally aluminum. This type of airflow regulation increases efficiency but does not increase above 75% [4]. However, the cross-flow heat exchanger is a commonly used heat exchanger with a relatively small and inexpensive production unit that has sufficient efficiency. The cross-flow heat exchanger provides the compact design of the heat exchanger and does not take up much space, so it is generally preferred when space is limited.

The efficiency of heat transfer overall depends on the heat transfer area. Having different flow arrangements can increase efficiency but that does not mean that the only way to improve heat transfer is to change the flow type. A lot of research has been done on the development of heat transfer enhancement devices for internal passages. Additional design features are used for this purpose, such as rib turbulators, pins arrays, and more recently transition surfaces including dimples. This is because improvements in magnification levels are useful in a variety of practical applications such as macro and microscale heat exchangers, electronic cooling [5]. By making certain geometrical shapes on the plates such as dimples and protrusions, the heat transfer area can be increased, but at the same time, the pressure drop must be considered.

A very important parameter for the performance of a plate heat exchanger is the spacing between the plates. A narrow channel leads to high-pressure drop but also high efficiency. If a lower pressure drop is required, it is better to use a higher channel spacing. The trade-off is lower efficiency. Our goal in performing these analyzes is to understand the fluid flow and heat transfer behavior of heat transfer surfaces, to apply analytical correlations to these surfaces, and to facilitate the further enhancement of heat transfer for better heat exchanger performance.

2. METHOD

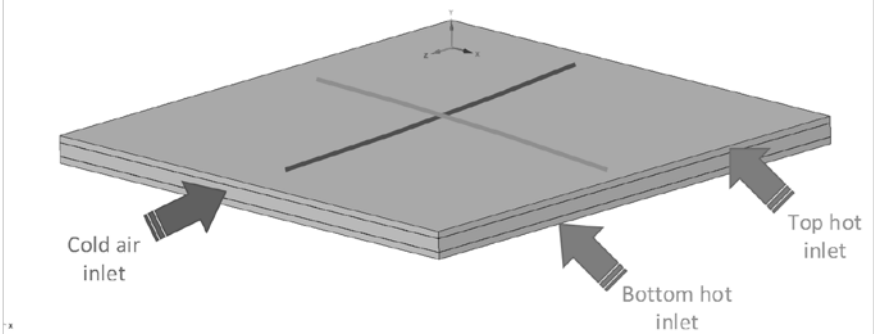

Figure 2. 1 System Schematic

In this project, three different analyzes were made on heat exchangers. The first analysis was done on the flat plate using the EES program. Later, to verify the results, ANSYS fluent program was used to determine both the solution method and the results. The second analysis was performed on a dimple plate using ANSYS fluent. Afterward, the heat transfer and pressure drop were observed by changing the dimple diameters. Finally, an economic analysis was made on the most efficient diameter dimple plate. Certain fixed parameters were used for correct interpretation in EES and ANSYS fluent comparisons (Table 2.1).

Table 2.1 System Parameter

Distance Between plate	13 mm
Thickness of plate	0.165 mm
Plate size	500mm x 500 mm
Temperature hot inlet	22°C
Temperature cold inlet	0°C
Hot and cold Inlet velocity	5 m/s
Plate material	Aluminum
Number of plates	90

2.1. Engineering Equation Solver

The main reason for doing the EES analysis is to compare the results with the ones obtained from ANSYS-Fluent simulations and ensure the correctness of ANSYS Fluent analysis. To observe the heat transfer, firstly the heat transfer coefficient for hot and cold flows was found by using the Nusselt correlations appropriate to the flow regime. Firstly, to find the Nusselt number, the flow regime must be known. [6]

The Reynolds Number was calculated to look at the flow regime (Eq.1).

$$Re = \frac{\rho \cdot v \cdot D_h}{\mu} \tag{1}$$

As the Reynolds number is higher than the given number range, it is concluded that the flow regime is turbulent. In the calculation of the Nusselt number in turbulent flows, Prandtl and friction factor parameters are required. Prandtl number is taken from thermodynamic tables in the EES database, according to the conditions given and friction factor is calculated for turbulent fully developed flow. And Nusselt number calculated by using equation (2).

$$Nu_{H,C} = \frac{\left(\frac{f}{8}\right)\cdot(Re_{H,C}-1000)\cdot Pr}{1+12.7\cdot\left(\frac{f}{8}\right)^{\frac{1}{2}}\cdot(Pr^{\frac{2}{3}}-1)} \quad (2)$$

After finding the Nusselt numbers for both air streams, an overall heat transfer coefficient is needed to find the heat transfer for the whole system. The overall heat transfer coefficient was found by using equation (3).

$$U = \frac{1}{\frac{1}{\alpha_H}+\frac{L}{k_{solid}}+\frac{1}{\alpha_C}} \quad (3)$$

The NTU method was used to find out the efficiency of the heat exchanger. The NTU number was calculated using equation (4). Finally, equation (5) was used to determine the percentage of effectiveness of the heat exchanger depending on the flow type.

$$NTU = \frac{U\cdot A_S}{C_{min}} \quad (4)$$

$$\varepsilon_{cross} = 1 - \exp\left(\frac{1}{C_r}\right)\cdot(NTU)^{0,22}\cdot\{exp[-C_r\cdot(NTU)^{0,78}]-1\} \quad (5)$$

2.2. CFD

The movement of the liquid in the physical domain depends on various properties. Speed, pressure, temperature, density, and viscosity are the main features that should be considered simultaneously when performing a fluid flow study. Thermo-fluidic events governed by equations are based on conservation laws. Navier-Stokes equations are widely applied mathematical models to examine changes in these properties during dynamic and/or thermal interactions. The equations can be adjusted according to the content of the problem and expressed on the principles of mass, momentum, and energy conservation [7]. The Navier-Stokes equations consist of time-dependent continuity equations (6,7,8,9 and10) for the conservation of mass, the conservation of the triple momentum equations, and the conservation of the energy equation over time. Equations are a combined set of differential equations and can be solved in theory for a given flow problem using methods derived from mathematics. In practice, however, it is very difficult to solve these equations analytically. Recently, high-speed computers have been used to solve approaches to equations using various techniques such as finite differences, finite volume, finite elements, and spectral methods. This field of study is called Computational Fluid Dynamics (CFD) [8].

$Continuity$:

$$\frac{\partial\rho}{\partial t}+\frac{\partial(\rho u)}{\partial x}+\frac{\partial(\rho v)}{\partial y}+\frac{\partial(\rho w)}{\partial z}=0 \quad (6)$$

$X-Momentum$:

$$\frac{\partial(\rho u)}{\partial t}+\frac{\partial(\rho u^2)}{\partial x}+\frac{\partial(\rho uv)}{\partial y}+\frac{\partial(\rho uw)}{\partial z}=-\frac{\partial\rho}{\partial x}+\frac{1}{Re_r}\left[\frac{\partial\tau_{xx}}{\partial x}+\frac{\partial\tau_{xy}}{\partial y}+\frac{\partial\tau_{xz}}{\partial z}\right] \quad (7)$$

$Y-Momentum$:

$$\frac{\partial(\rho v)}{\partial t}+\frac{\partial(\rho uv)}{\partial x}+\frac{\partial(\rho v^2)}{\partial y}+\frac{\partial(\rho vw)}{\partial z}=-\frac{\partial\rho}{\partial y}+\frac{1}{Re_r}\left[\frac{\partial\tau_{xy}}{\partial x}+\frac{\partial\tau_{yy}}{\partial y}+\frac{\partial\tau_{yz}}{\partial z}\right] \quad (8)$$

$Z-Momentum$:

$$\frac{\partial(\rho w)}{\partial t}+\frac{\partial(\rho uw)}{\partial x}+\frac{\partial(\rho vw)}{\partial y}+\frac{\partial(\rho w^2)}{\partial z}=-\frac{\partial\rho}{\partial z}+\frac{1}{Re_r}\left[\frac{\partial\tau_{xz}}{\partial x}+\frac{\partial\tau_{yz}}{\partial y}+\frac{\partial\tau_{zz}}{\partial z}\right] \quad (9)$$

$Energy$:

$$\frac{\partial(E_T)}{\partial t}+\frac{\partial(uE_T)}{\partial x}+\frac{\partial(vE_T)}{\partial y}+\frac{\partial(wE_T)}{\partial z}=-\frac{\partial(up)}{\partial x}-\frac{\partial(vp)}{\partial y}-\frac{\partial(wp)}{\partial z}-\frac{1}{Re_TPr_T}\left[\frac{\partial q_x}{\partial x}+\frac{\partial q_y}{\partial y}+\frac{\partial q_z}{\partial z}\right]+\frac{1}{Re_T}\left[\frac{\partial}{\partial x}\left(u\tau_{xx}+v\tau_{xy}+w\tau_{xz}\right)+\frac{\partial}{\partial y}\left(u\tau_{xy}+v\tau_{yy}+w\tau_{yz}\right)+\frac{\partial}{\partial z}\left(u\tau_{xz}+v\tau_{yz}+w\tau_{zz}\right)\right] \quad (10)$$

In CFD analysis, ANSYS fluent software was preferred to understand the basic theory, and calculation methods of models for heat transfer applications. This software enables monitoring of heat transfer, temperature and speed values in a modeled 3D system. Partial differential equations governing fluid flow and heat transfer are generally not suitable for analytical solutions, except in very simple cases. Therefore, to analyze fluid flows, flow fields are divided into smaller subfields. Management equations are then parsed and solved in each of these subfields. Subfields are often called elements or cells, and the summation of all elements or cells is called a mesh or grid. To understand the accuracy of the flow solution, the values obtained from the flow analysis of the flat plate were compared with the values obtained with the EES code generated by the manual calculation algorithm. The method, in which the values are close, was applied in the same way in the dimple plate analysis.

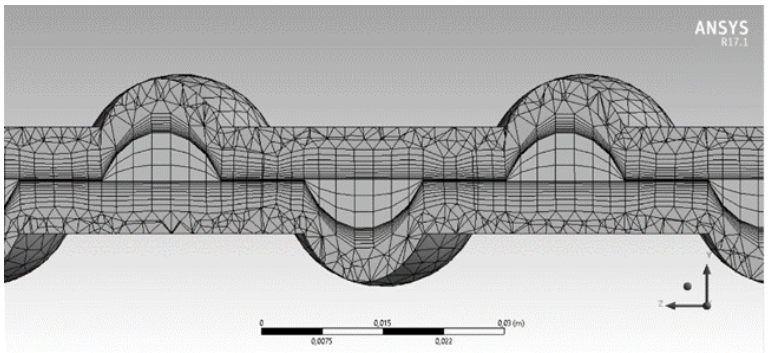

Figure 2.2 Meshed Dimpled Plate

2.3. Economics

Since dimple plate is generally used in real systems, economic analysis of the values resulting from dimple analyzes was performed. Economic analyzes were evaluated considering the gain of the heat recovery system. Heat transfer net gain in the heating period was calculated by converting it to natural gas. Then, the return time was calculated using the Discounted Payback Period method equation (11) with the investment made in the system and also Net present value was calculated using the equation (12). In economic cases, since the lifetime of the heat exchanger in ventilation systems is 10 years, the analyzes were based on this period [9].

$$Net\ Present\ Value = \sum_{t=0}^{n} \frac{R_t}{(1+i)^t} \tag{11}$$

$$Discounted\ Payback\ Period\ = A + \frac{B}{C} \tag{12}$$

A = Last period with a negative discounted cumulative cash flow;
B = Absolute value of discounted cumulative cash flow at the end of the period A; and
C = Discounted cash flow during the period after A.

3. RESULTS

Three analyzes were performed: flat plate EES, flat plate fluent and dimpled plate fluent. The results of the analyzes are presented in the section below. The results focused on heat transfer, pressure drop, fan power and thermal efficiency.

3.1. Flat Plate EES and ANSYS Fluent Results

EES program was used for the first analysis. As a result of this analysis, the following values were found.

Table 3.1 Flat Plate Results

	EES		**Fluent**	
	Hot Air	**Cold Air**	**Hot Air**	**Cold Air**
Outlet Temperature (°C)	18.22	3.5	17.8	4.02
Heat Transfer through plate (W)	73.8	73.8	80.61	80.62

As given in Table 3.1, 22°C for hot (inside) air and 0°C for cold (outside) air were taken for the winter conditions. In EES analyzes, it was observed that the hot air entering with 22°C decreased to 18.22°C degrees and the cold air entering 0°C degrees increased to 3.5°C due to the heat transfer in the heat exchanger. The heat transfer was found to be 147.6 W. However, this heat transfer value is the total value of the two streams. Therefore, the heat transfer from the single-stream through the plate can be determined as 73.8. The reason for determining the heat transfer value just for one airflow is to facilitate comparison between ANSYS fluent results because the values are flowing specifical in the software. In the ANSYS Fluent analyzes, the most appropriate geometry has been drawn to obtain correct results and different mesh methods have been tried and found to be the most suitable. In the analysis, it was observed that the hot air entering with 22°C decreased to 17.8°C degrees and the cold air entering 0°C degrees increased to 4.02°C due to the heat transfer in the heat exchanger. The heat transfer was found to be 147.6 W. This analysis was compared with EES results. Although there is not a big difference between the values, it has been observed that heat transfer value and temperature changes increase. The difference between the two analyzes may be because ANSYS fluent software performs a more detailed analysis and uses different correlations. However, despite the small differences, the values are close to each other, which means that the ANSYS fluent solution is correct and can be used in other analyzes.

3.2. Dimpled Plate ANSYS Fluent Results

As can be seen from the Table, the heat transfer of the dimpled-plate shows an increase of 156% compared to the flat-plate. With the increase of heat transfer, there was a 31.34% higher temperature increase than the flat plate in cold weather. With the increase in heat transfer and cold air temperature, the pressure drop approximately tripled.

Table 3.2 Flat-Plate Dimpled-Plate Comparison

	Flat-Plate	Dimpled-Plate
Element Size	540000	1487240
Cold Outlet Temperature (°C)	4.02	5.2
Hot Outlet Temperature (°C)	17.97	16.8
Heat Transfer (W)	80.62	207
Pressure Drop (P_{inlet}-P_{outlet}) (P)	13.88	28.78

As a result of these analyses, heat transfer was increased with the addition of dimples to the plate surface, both increasing the heat transfer area and causing more turbulence in the flow. However, the addition of dimples has also caused the pressure drop to increase. Although pressure drop is not one of the most important parameters for heat exchangers, it has an important place in heat recovery ventilation systems. The reason for this is that the fan needs more power in systems that increase the heat transfer and the pressure drop is high. More fan power is required to draw air due to pressure drop. As a result of this, certain decreases occur in energy recovery while providing heat recovery. Therefore, ideal heat recovery ventilation systems both improve heat transfer and reduce pressure drop to a minimum.

3.3. Different Dimpled Plate Analysis Results

This analysis was performed with the dimpled plate for crossflow. For this purpose, firstly, it was decided that it would be more appropriate to use one half cold air stream and one-half hot air stream geometry. To use the CFD-based symmetry feature, it was decided to design a half cold flow and one-half hot flow separated by a plate. The

reason for not taking two half hot flows is that the dimple inserts increase the heat transfer area and therefore the number of elements increases too much when meshed. Since personal computers cannot handle such a heavier process, a smaller geometry has been designed to achieve accurate analysis. 9 analyzes were made by changing the speeds in different dimple diameters. Dimpled plates were designed with 22, 26, and 30 mm diameter. Each of these designs was analyzed at 3, 5, and 8 m/s speeds. The values obtained from these analyzes and system values for 90 plates are shown in the Table.

Table 3.3 Different Dimpled-Plate ANSYS fluent Results

30 mm Dimple	**Outlet Temperatures**		**Fan power**		**Total**		**Net Gain (kW)**	**Thermal Efficiency**
Velocity (m/s)	**Cold Outlet (℃)**	**Hot Outlet (℃)**	**Cold Side (W)**	**Hot Side (W)**	**Fan Power (W)**	**Heat Transfer (W)**		
3	6.6	15.65	24.41	26.99	51.41	14222	14.17	30.00
5	5.6	16.39	96.72	106.82	203.55	19266.91	19.06	25.45
8	4.9	17.1	381.68	402	783.74	28215.88	27.43	22.27
26 mm Dimple	**Outlet Temperatures**		**Fan Power**		**Total**		**Net Gain (kW)**	**Thermal Efficiency**
Velocity (m/s)	**Cold Outlet (℃)**	**Hot Outlet (℃)**	**Cold Side (W)**	**Hot Side (W)**	**Fan Power (W)**	**Heat Transfer (W)**		
3	6.214	15.788	23.26	23.26	46.53	13390.25	13.34	28.25
5	5.257	16.442	92.38	102.17	194.56	18943.55	18.74	23.90
8	4.595	17.4	335.98	377.48	713.46	25793.94	25.08	20.89
22 mm Dimple	**Outlet Temperatures**		**Fan Power**		**Total**		**Net Gain (kW)**	**Thermal Efficiency**
Velocity (m/s)	**Cold Outlet (℃)**	**Hot Outlet (℃)**	**Cold Side (W)**	**Hot Side (W)**	**Fan Power (W)**	**Heat Transfer (W)**		
3	6.05	15.95	20.73	22.89	43.63	13036.85	12.99	27.50
5	5.19	16.8	42.07	47.23	89.31	18702.12	18.61	23.59
8	4.5	17.49	310.35	351.54	661.90	25912.54	25.25	20.45

As velocities in the same dimple's diameter were increased, an increase in heat transfer was observed. In other words, heat transfer is directly proportional to the increase in velocity in the same diameter which happens because the increase in velocity causes turbulence that improves heat transfer. According to the table, the best heat transfer is about 28.21 kW. It can be said that the cold air outlet temperature is 4.9°C and the hot air outlet temperature is 17.01°C. Total fan power was calculated by cold side fan power and hot side fan power. Total fan power increased as velocity increased in the same dimple diameter. The design with the highest total fan power and heat transfer is observed when the dimple diameter is 15mm and the velocity is 8m/s. In addition, when the diameter increased at the same velocity in the designs, an increase in net gains was observed. The design with the highest dimple diameter and the lowest velocity has the highest thermal efficiency. So, like the dimple diameter increases, thermal efficiency increases, but as velocity increases, thermal efficiency decreases. The design with the highest thermal efficiency is the design with a dimple diameter of 30 mm and a velocity of 3 m/s.

3.4. Economic Analysis

In order to make an economic analysis, firstly, the effect of the heat transfer gain of the system on heating was found. For this, based on natural gas heating needs, annual heat recovery was calculated. These values were then used in the following economic analysis methods.

Table 3.4 Yearly Saving Results

Model	Velocity (m/s)	Net Gain (kW)	Net Gain (kWh)	Natural Gas (m^3)	Cost per m^3	Yearly Saving
22 mm Dimple	5	18.61	17,865.6	1,658.44	₺ 1.86	₺3,084.70
26 mm Dimple	5	18.74	17,990.4	1,675.22		₺3,115.92
30 mm Dimple	5	19.06	18,294.6	1,703.57		₺3,168.64

An organization must make many decisions regarding the expansion of business and investments in the projects. In such cases, usually the NPV method is used to make a decision. Net present value is used in Capital budgeting to analyze the profitability of a project or investment. It is calculated by using the difference between the present value of cash inflows and the present value of cash outflows in a given period.

Table 3.5 Economic Analyzes Results

	Model	Simple Payback Period (years)	Discounted Payback Period (years)	Net Present Value
HEX	**22 mm Dimple**	0.575	0.632	₺17,181.44
	26 mm Dimple	0.569	0.626	₺17,373.45
	30 mm Dimple	0.559	0.615	₺17,697.21
AHU	**22 mm Dimple**	1.379	1.271	₺14,699.64
	26 mm Dimple	1.365	1.263	₺14,891.66
	30 mm Dimple	1.343	1.363	₺15,215.42

Since the cost of dimple pressing in different diameters did not differ, initial prices were taken the same. The average cost for 90 plates purchased from the companies is for HEX and for AHU. To find an average profit, the analysis results at 5 m/s velocities were taken as the basis. As it can be seen from Table 3.3, the 30 mm dimple model is the design with the highest heat transfer and its annual gain is higher than the others. Therefore, both the discounted payback time is less than the others and the net present value gave better results. Considering that there is no difference between the model costs, the 15 mm Dimple heat exchanger is the most profitable option when choosing.

4. CONCLUSION

We investigated the effect of cross-flow heat exchangers on the heat transfer of the shapes on the surface of the plate and changes in velocity. By comparing the values found with each other, the accuracy of the solution method and values are ensured. As a result of the analysis, was observed that;

a. The flat plate heat exchanger can heat cold air at 4 degrees
b. Dimpled plate enhances heat transfer
c. As dimple diameter increases, heat transfer, total fan power, net gain and thermal efficiency increase.
d. In the same dimple diameter designs, as speed increases, heat transfer, fan power and net gain increase, but thermal efficiency decreases.
e. With a dimpled plate, the cold air outlet temperature increases 31% more than the flat plate and the heat transfer increases 156%.

REFERENCES

[1] Fouiha, Y.E., Stabat, P., Rivière, P., Hoanga, P. & Archambault, V. 2012." Adequacy of air-to-air heat recovery ventilation system applied in low energy buildings" Energy and Building, 54, 29-39.

[2] Kotcioglu, I., Caliskan, S.& Zırzakıran, M. (2009) "Heat Transfer in A Cross-Flow Heat Recovery Ventilator with Fin." Erciyes Üniv. Fen Bilimleri Enstitüsü Dergisi 25 (1-2) 272 – 286

[3] Grundfos, 2019, Pump Encyclopedia. accessed at; https://tr.grundfos.com/ as of December 2019

[4] ASHRAE. 2004. Heating, Ventilating and Air-Conditioning Systems and Equipment

[5] Teke, I., Agra, O., Atayılmaz, S.O., Demir, H. 2010." Determining the best type of heat exchangers for heat recovery", Applied Thermal Engineering, 30, 577-583.

[6] Incropera, F. P., Dewitt, D. P., Bergman, T.L., Lavine, A.S., 2007. "Fundamentals of Heat and Mass Transfer". John Wiley & Sons, Danvers, Massachusetts

[7] White, F. M. (1991). "Viscous Fluid Flow". 3rd Edition. McGraw-Hill Mechanical Engineering. New York, NY

[8] NASA, 2015. "Navier-Stokes Equations." Glenn Research Center 2015. Accessed at https://www.grc.nasa.gov/ as of December 2019

[9] Corporate Finance Institute, 2019. "Net Present Value." Accessed at https://corporatefinanceinstitute.com/ as of February 2020

AN ENERGY-EFFICIENT MIXED FLOW SUBMERSIBLE PUMP DESIGN AND COMPUTATIONAL FLUID DYNAMICS PROCESSES IN A CASE STUDY: 7" 110 m^3/h

Manolya AKDEMİR*, M. Cevdet ÇAKMUR
*ÜSTÜNEL Pompa ve Makine A.Ş., Research and Development Center, İzmir / Turkey
Email: m.akdemir@ustunel.com.tr

ABSTRACT

With the increasing consumption of water, the usage of groundwater is gaining importance all around the world. According to some research, 96.5 % of all water is included by ocean and part of it is contained as freshwater. The freshwater value of around 68.6 % is found in glaciers; the remaining part is found as groundwater. The groundwater supply process is only possible via submersible pump systems. The energy efficiency value is determined in EU 547/2012 "Eco-design Requirements for Water Pumps" with a common criterion "Minimum Efficiency Index". This value can be calculated with an equation system, including motor rotation speed, head, and flow rate. When the efficiency values calculated for the partial load (75 %), full load and overload (110 %) value of the volumetric flow rate should be calculated depending on the MEI, and hydraulic test values are equal to or greater than the MEI values, the product can be designed according to the regulation. The study focuses on product design in accordance with the EU 547/2012 coded "Eco-design Requirements for Water Pumps". In the scope of the study, rotors and stator designs and Computational Fluid Dynamics analyses were run. First of all, the designs of the rotor were made via CFturbo® with the specifications determined when evaluated according to the customer needs and pump characteristics. After designing the final rotor design, the stator design process was started with CFX® analysis in parallel to define the stage performance criteria; head (mCW), power (kW) and efficiency (%).

After conducting the single-stage Computational Fluid Dynamics (CFD) studies of the final design, the three-stage analyses were run and the specifications of the second stage; efficiency value of 86.33%, head 11.52 mCW and 3.98 kW per stage were found.

Keywords: Mixed – Flow Pump, Pump Design, Computational Fluid Dynamics, Finite Elements Methods, Verification, Energy Efficiency, Minimum Efficiency Index, Eco-design.

NOMENCLATURE

b_2 : Outlet width (mm)
b_{in} : Stator inlet width (mm)
c_m : Absolute meridional velocity (m/s)
c_r : Absolute velocity component on r-axis (m/s)
c_z : Absolute velocity component on z-axis (m/s)
d_2 : Impeller diameter (mm)
d_H : Hub diameter (mm)
d_S : Suction diameter (mm)
Q : Flow rate (m^3/h)
H : Head (mWC)
η_c : Clearance efficiency
η_h : Hydraulic efficiency
η_v : Volumetric efficiency
n : Rotational speed (rpm)

Y : Specific work (kW)
n_q : Specific speed
δ_r : Swirl number
δ : Diameter coefficient
Ψ : Stream function
τ_1 : Blade blockage at inlet
τ_2 : Blade blockage at outlet
PL : Partial load
OL : Overload
BEP : Best Efficiency Point
MEI : Minimum Efficiency Index
ESP : Electrical Submersible Pump

1. INTRODUCTION

One of the most vital and critical resources of human beings to obtain a sustainable environment is water. Although three-quarters of the earth 's surface is covered water, the amount of fresh water suitable for human use is quite limited. As the population has increased with agricultural irrigation, building usage, drink water and other usages, the water requirement has increased. The total amount of water consumed in the last twenty years has increased by forty per cent in Turkey, which determined by the Ministry of Agriculture and Forestry [1]. With high population growth rate, industry, agriculture, energy demand and also water demand project to reach three times the last century's consumption. Significantly, the water demand leads to groundwater has become more important not only in Turkey but also all around the world and also the energy efficiency of the pump systems.

To extract clean water from reserves to ground level, a well and corresponding pump, which defines the design criteria as the capacity and the maximum diameter of the pump. In this study, a pump that fits in 8 inches borehole and has a 110 m^3/h volumetric flow rate and 10 meters of the head for a stage. As mentioned in "Ecodesign Requirements for Water Pumps", a commission regulation published on 25 June 2012, the energy consumption of water pumps was 109 TWh in 2005, and it has predicted as it will be 136 TWh in 2020. With the considerations above, the hydraulic efficiency of the pump is another design criterion.

The electrical submersible pump can classified with its impeller type and according to the requirements of the head, it can be multi-stage. Each stage of ESP consists of two main parts as a rotating set of impellers and a stationary diffuser (stator). Fluid enters the impeller eye axially with relatively low velocity and leaves the impeller with a higher velocity value due to the centrifugal forces. The stator designed with the corresponding impeller, and the kinetic energy of the fluid is converted to an increase of fluid pressure and volumetric flow rate.

Korkmaz et al. [2] studied the impacts of trailing beta progression, the number of blades and impeller discharge diameter and splitter blade lengths on energy consumption experimentally. They examined six impellers with the number of blades 5, 6, 7 and blade trailing edge angles 25°, 35° and found the highest efficiency as 0,45 for the trailing edge angle 25° at impellers with seven blades without splitters. Ling et al. [3] examined the effects of impeller width with a deep-well centrifugal pump. Two stages of the impeller with four width values and the same blade geometry is simulated with commercial CFD software. Then, two of them manufactured as prototypes to test predicted results from numerical solutions. They observed an increment of the outlet width leads to an increment in the flow area and the decline of the performance as the impeller is diffusion type. Teodor M. [4] developed a procedure for generating the inter-blade channel as radial and axial components. The domain for hydrodynamic field discretized to solve partial differential equations of the stream and flow, so that determination of the velocities and pressure fields in the solution domain is made possible. Kim et al. [5] evaluated the hydraulic efficiency in terms of geometric variables for a mixed flow pump and examined the impact of two variables related to the area of the discharge and straight length of the vane in the diffuser on the efficiency of a mixed-flow pump. The optimum results found as 0.35 and 1.55, 2.05 which is the values of

diffusion area ratio and straight vane ratios respectively. Boncinelli et al. [6] studied a bowl-type diffuser for a low specific speed and parametrized an existing geometry to reduce the radial size of the pump, and improve hydrodynamic efficiency. Ruled surface diffuser blade geometry kept unchanged; however blade turning angle distribution and the meridional channel shape is modified in order to reduce the nominal diameter of the pump and multistage configurable design. In another study, Goto et al. [7] redesigned a bowl diffuser for a low-speed pump via an program of a 3-D inverse design method. After developing a preliminary design, the meridional section of the stator structure was modified to reduce losses which were classified into five as an impeller, inter-row, guide, mixing and swirl mixing loss and results are examined by means of flow separations, pressure recovery, overall efficiency and uniformity of exit flow. The final design of the diffuser was tested for the validation of the numerical studies. Perez et al. [8] used a commercial CFD code for analyzing the internal flow of the first stage of a two-stage centrifugal pump with different interface types under transient conditions. k-epsilon model for turbulent flow is used; however a comparison between numerical simulation and experimental data shows that under-prediction of pressure values since the selected turbulent model is not suitable for flow conditions on curved faces. Hlbočan [9] compared the numerical results of k-epsilon and the shear stress transport models with experimental data of single-stage mixed flow pump and showed that the shear stress transport model is more suitable for calculating pump performance characteristics as flow rate, specific energy, and efficiency. Miner [10] analyzed the first stage of a two-stage mixed flow pump with Flotran® solver. The numerical results were compared with measured data. It showed that the most significant differences occur between measured and calculated static pressure and tangential velocity distributions induced by pre-swirl at impeller leading edge. Zhou et al. [11] studied about effects of diffuser vane numbers on efficiency. Three different diffusers were designed for the same impeller, and then numerical simulations performed for these designs. The final design which has seven vanes was manufactured as a prototype for performance tests and the results showed a wide high-efficiency range with nearly-same results of the numerical study. Stel et al. [12] simulated a multi-stage electric submersible pump and investigated flow patterns for the first, second and third stages under part and over-load conditions. It is stated that the three-stage model complies with experimental data better when compared to the five-stage model and less time-consuming.

2. METHODOLOGY

2.1. The Design Process

The hydraulic part design process is obtained via the CFturbo®, a Turbomachinery Design Program developed by the CFturbo® GmbH. In general, an impeller can be as the radial, axial or mixed flow, which can be determined with flow rate, head and revolution speed as known as specific speed, and it is defined by Equation 1.

$$n_q = n\frac{\sqrt{Q}}{H^{3/4}} \tag{1}$$

The main dimensions of a designed impeller can be specified as suction and impeller diameter, hub and shroud meridional length and outlet width. These parameters can be calculated with intake number, specific diameter and outlet width ratio as determined with equations 2:4, respectively.

$$d_S = \sqrt{d_H^2 + \frac{4Q}{\pi\eta_v\sqrt{\varepsilon^2 2Y - (1-\delta_r)^2\pi^2 d_S^2 n^2}}} \tag{2}$$

$$d_2 = \frac{\delta}{1.05(Y/Q^2)^{1/4}} \tag{3}$$

$$b_2 = (b_2/d_2)d_2 \tag{4}$$

The Cordier Diagram (Figure 1) demonstrates the approximate efficiency evaluation based on the specific speed and diameter on the rotor basis, and it defines the specific diameter of the rotor.

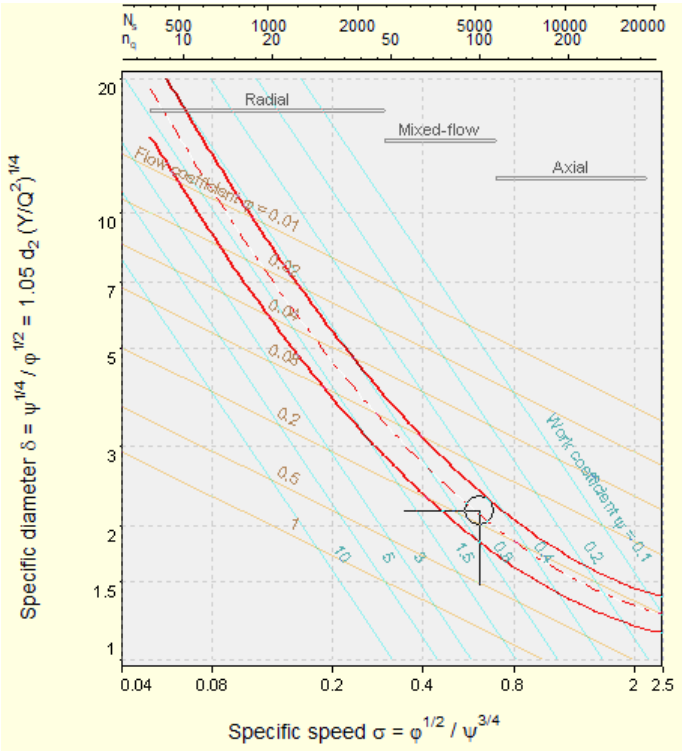

Figure 1. Cordier Diagram

The velocity distribution between the hub and shroud can be determined on a discretized area, which is meridional contour. For an incompressible fluid, stream function within the meridian structure can be expressed as follows in cylindrical coordinates as Equation 5, and the meridional velocity component can be calculated by axial and radial velocity components in Equations 6-8.

$$\frac{\partial^2\Psi}{\partial z^2}+\frac{\partial^2\Psi}{\partial r^2}-\frac{1}{r}\frac{\partial\Psi}{\partial r}=0 \tag{5}$$

$$c_z=\frac{r_r}{r}\frac{\partial\Psi}{\partial r} \tag{6}$$

$$c_r=-\frac{r_r}{r}\frac{\partial\Psi}{\partial z} \tag{7}$$

$$c_m=\sqrt{c_r^2+c_z^2} \tag{8}$$

The meridional contour design is followed by determining blade properties as thickness, blade angles, number of blades and spans. The blade angle calculations based upon shockless inflow at the leading edge and the Euler equation for the trailing edge.

$$\beta_1=\arctan\left(\frac{Q_{eff}/(\pi d_1 b_1)\tau_1}{\pi d_1 n-u_S(1-\delta_r)r_S/r_1}\right) \tag{9}$$

$$\beta_2 = \arctan\left(\frac{Q_{eff}/(\pi d_2 b_2)\,\tau_2}{\pi d_2 n - \left(Y/(\eta_h \eta_T \eta_C) - u_1^2(1-\delta_r)\right)/(\pi d_2 n)}\right) \tag{10}$$

The progression of blade angles along the mean-lines can be determined under geometric boundary conditions such as blade angles at leading and trailing edge, meridional contour and wrap angle. Blade length should be checked in order to limit the blade load.

Specific recommendations for the main dimensions of the bowl-diffuser are given by Gulich [13] as Equations 11:13, which define inlet diameter, inlet width and axial extension of the diffuser, relatively.

$$\frac{d_{in}}{d_2} = 1.04 + 0.001 \cdot (n_q - 40) \tag{11}$$

$$\frac{b_{in}}{b_2} = 1.02 \ldots 1.05 \tag{12}$$

$$\frac{\Delta z}{d_2} = 0.72 \left(\frac{n_q}{200}\right)^{0.19} \tag{13}$$

The number of stator blades is another issue to be decided to minimize pressure pulsation and mechanical loads on the blades. The pressure fields generated by the relative motion between impeller and stator blades with periodicity, however, the interference of both pressure fields cannot be calculated exactly. As a design recommendation, a difference of both periodicities is taken into consideration. The meridional contour of a designed stage is given in Figure 2.

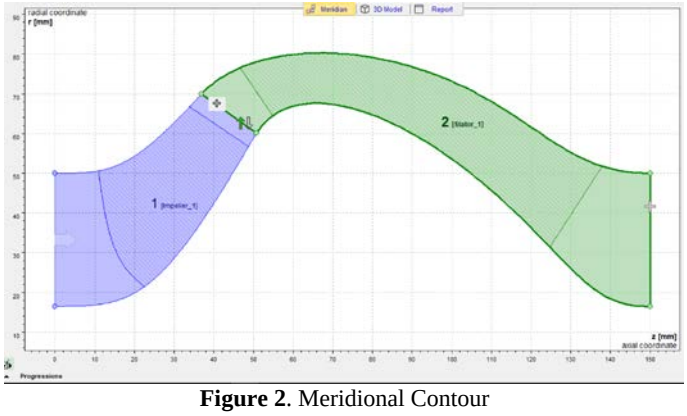

Figure 2. Meridional Contour

2.2. The Validation Process

The process followed to simulate the flow in the rotor and stator channel can expressed as follows: the volume occupied by the fluid exported from CFturbo® as a single rotor and stator and discrete to generate a mesh structure via ANSYS® meshing. First of all, to find the most optimum mesh structure and number for the segment geometry, the mesh independence studies have made. Then, boundary conditions are defined and steady-state simulations run. The mesh structure determined with advanced size function is used to generate fine mesh for designed geometry. However, it is expected that the key parameters as pressure or velocity will have higher gradients at near-wall regions such as areas close to the hub, shroud, and blades. Figure 3 shows the mesh structure of the V3 design, but the mesh structure and values are the same in all designs, approximately.

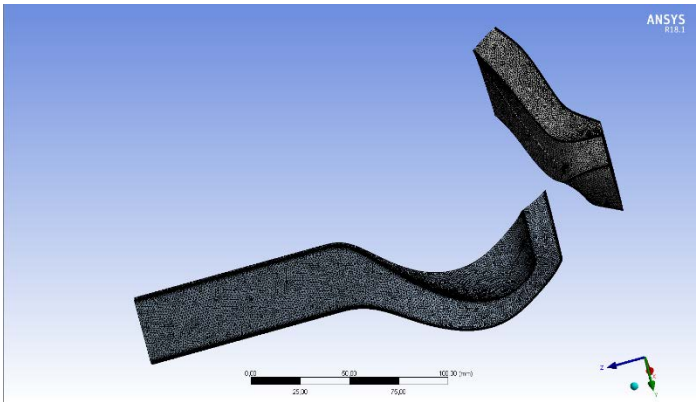

Figure 3. Mesh Structure of a Designed ESP

The solution of a single-stage analysis consists of the rotor and stator segments which are modelled as rotating and stationary domains, respectively. The blade, hub and shroud walls are specified as the smooth wall for all domains, besides sidewalls of both domains are modeled as rotational periodic around the rotation axis. Interface between rotor and stator domains specified as a stage also. Boundary conditions are determined with total pressure at the rotor inlet and mass flow rate at the outlet of the stator domain. After the final design was decided, the most efficient working range analyses started. All simulations are run with convergence criteria as residual target 10-6, and results of parameters for designed pumps as hydraulic efficiency, hydraulic power, mechanical power, pressure.

3. RESULTS

In order to obtain the multi-stage ESP, the rotor should be designed with a defined head, flow rate, and rotational speed. However, after determining a design point and corresponding rotor and stator pair, it is possible to change or modify the parameters of the components. In the first design (V0) discussed, the rotor has a different wrap angle while the V1 and V2 designs have the same, and this affects the characteristics of not the only rotor but also the rotor-stator pair. The effect of wrap angle on rotor characteristics is examined with 12 rotors that have the same properties. On the other hand, V3 has the same characteristic parameters but a completely different design. The characteristic output parameters of ESP at BEP are given in Table 1. To compare the designs, besides the hydraulic efficiency (%), head (mCW) and shaft power (kW), the production feasibility of it is taken into consideration. The final design is chosen as V3, and the HAD analyzes carried out at the best operating range values.

Table 1. Results of the Optimum Designs CFD Analysis at BEP

	Unit	V0	V1	V2	V3
Efficiency	%	86.4294	85.9997	84.5105	88.0124
Hydraulic Power	Watt	663.9820	650.5430	621.9220	610.5572
Head	mCW	13.0800	12.7800	14.1300	14.3455

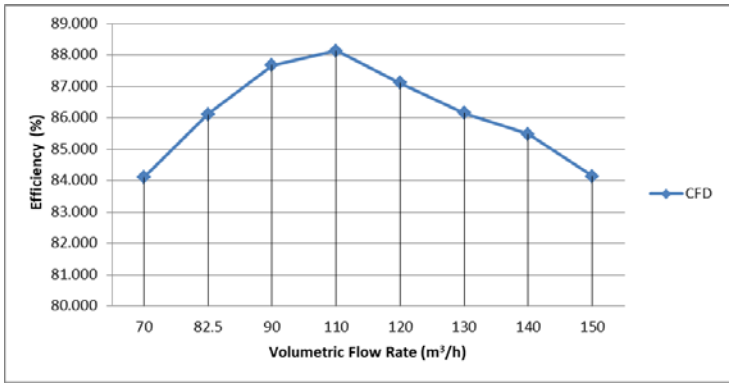

Figure 4. The CFD Results at the BER of the V3 Design

Three stages analyses of the V3 design were conducted via CFX®. According to the analyses, the most efficient operating range was revealed as Figure 5, in the BEP point, it can be seen that hydraulic efficiency, head, and shaft power were found as 86.33%, 11.52 mCW and 3.98 kW per stage, respectively. Figure 5 demonstrates the V3 design CFD results at the range above. These values were obtained in terms of the second stage to comply with real hydraulic test results, which is defined via the literature survey.

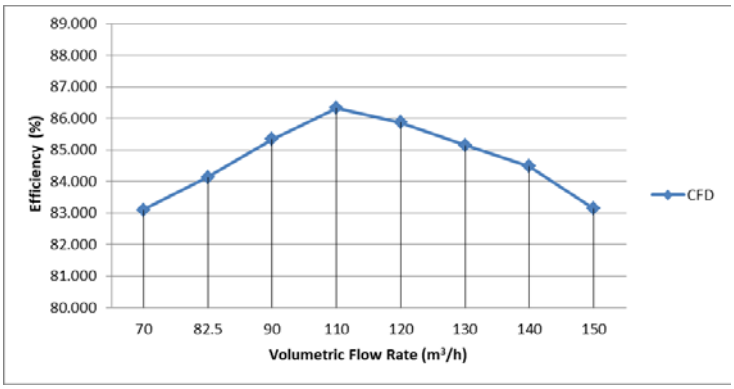

Figure 5. The Three-Stage CFD Results at the Most Efficient Operating Range of the V3 Design

4. CONCLUSION

In this study, a single - stage of a multi-stage electric submersible pump designed for corresponding design point defined with head, flow rate, and revolution speed and different design options compared with each other in terms of their efficiency, head, and hydraulic power. CFturbo® used as a design tool for components, rotor, and stator. CFD results of the designed rotor and stator components obtained from CFX® compared with each other in terms of their efficiency, head and hydraulic power. The V3 design is selected as single - stage of the multi-stage electric submersible pump, as it has the highest efficiency at the design point and analysis repeated under the same boundary conditions for three-stage one, to find the optimum design in reality. The V3 design is chosen as a prototype and further studies will be held.

REFERENCES

[1] Ulusal Su Planı 2019-2023, T.C. Tarım Orman Bakanlığı.

[2] Korkmaz E., Gölcü M., Kurbanoğlu C., Effects of Blade Discharge Angle, Blade Number, and Splitter Blade Length on Deep Well Pump Performance, Journal of Applied Fluid Mechanics, **10**(2), pp. 529-540, 2017

[3] Weidong S, Ling Z., Weigang L., Bing P., Lang T., Numerical Prediction and Performance Experiment in a Deep-well Centrifugal Pump with Different Impeller Outlet Width, Chınese Journal Of Mechanıcal Engıneerıng, **26**, 2013

[4] Milos Teodor. Impeller Design Using CAD Techniques and Conformal Mapping Method, Centrifugal Pumps, Dr. Dimitris Papantonis (Ed.), IntechOpen, 2012

[5] Kim J H, Ahn H J, Kim K Y. High-efficiency design of a mixed-flow pump. Sci China Tech Sci, **53**(1), pp.24-27, 2010

[6] Boninelli P., Biagi R., Focacci A., Corradini U., Arnone A., Bernacca M., Borghetti M., Bowl Type Diffusers for Low Specific-Speed Pumps: An Industrial Application, Journal of Turbomachinery, **130**,2008

[7] Goto A., Zangeneh M., Hydrodynamic Design of PumpDiffuser Using Inverse DesignMethod and CFD, Journal of Fluids Engineering, **124**(2), pp 319-328, 2002

[8] Perez J., Chiva S., Segala W., Morales R., Negrao C., Julia E., Hernandez L., Performance Analysıs Of Flow In A Impeller-DıffuserCentrıfugal Pumps Usıng Cfd :Sımulatıon AndExperımental Data Comparısons, V European Conference on Computational Fluid Dynamics, 2010

[9] Peter Hlbočan, Comparıson Of k-epsilon And SST Turbulence Models In CFD Sımulatıon Of The Flow In A Mıxed-Flow Pump, International Doctoral Seminar, 2011

[10] Steven M. Miner, CFD Analysis of the First-Stage Rotor and Stator in a Two-Stage Mixed Flow Pump, International Journal of Rotating Machinery, **1**, pp 23-29, 2005

[11] Zhou L, Bai L, Shi W, Li W, Wang C., Ye D., Numerical Analysis and Performance Experiment of Electric Submersible Pump with Different Diffuser Vanes Number, Journal of the Brazilian Society of Mechanical Sciences and Engineering, **40**(2), pp 40-89, 2018

[12] Stel H., Sirino T., Ponce F.J., Chiva S., Numerical Investigation Of The Flow In A Multistage Electric Submersible Pump, Journal of Petroleum Science and Engineering, Journal of Petroleum Science and Engineering, **136,** 2015

[13] Johann Freidrich Gülich, Centrifugal Pumps Second Edition, Springer, 2010

BUBBLE PUMP DESIGN AND PERFORMANCE ANALYSIS

Ahmed DALLOUL*, Mustafa ÖZBEY**
*Ondokuz Mayis University, Postgraduate Education Institute, Samsun/Turkey
Email: adalloul12@gmail.com
**Ondokuz Mayis University, Department of Mechanical Engineering, Samsun/Turkey
Email: mozbey@omu.edu.tr

ABSTRACT

Designing any refrigeration system is a critical aspect because it has to be efficient and energy saving more than the previous similar designs. In this article, an integrated cooling system in terms of lifting tube distribution, water reservoir, temperature sensors, controllers, water level sensor locations, and automatic control systems have been designed. The design conditions were assumed that a hot surface released different amounts of heat 550W, and 1500W is to be cooled and maintain the temperature under the desirable limit; the experiments have been conducted under the atmospheric pressure used many configurations such as a different number of 8mm diameter lifting tubes from 1 to 4 tubes, and different submergence ratios 0.3, 0.4, and 0.5. The design process of this system consists of a literature review of all available systems and the required components for this system. The selecting criteria were based on efficiency, costing, and energy consumption. Then the sizing has been made to find the quantity and capacity of each component. After that, an optimal arrangement of parts and components was designed, and an automatic control system has been developed to control the electrical equipment. Then the data have been recorded and tabulated, the efficiency has been calculated, the theoretical model based on the fundamentals of fluid mechanics has been compared with the experimental data, and at the last step, the conclusion has been extracted, through that, the slug flow pattern could be noticed in the experiments as the desired flow type where the heating power is 1500W. Furthermore, by comparing the results of experiments with the theoretical model, it was apparent that the performance was directly proportional to the submergence ratio and lifting tubes.

Keywords: Bubble pump, Lifting tubes, Submergence ratio, Input heating power.

1. INTRODUCTION

Heat removal in daily life plays a significant role in the industry and the electronic devices which people use, such as computers and servers. This importance stems from its impact on production levels, product quality and the efficiency of these devices work. Rapid cooling is required in many daily uses, correspondingly, cooling systems such as bubble pumps are required to provide this instant cooling effectively.

In this article, a bubble pump cooling system is designed for typical local conditions to provide cooling for electrical appliances during operation, such as servers and electrical transformers. Assuming the X device, it should dissipate at least 550W of power through the cooling system using water flow. The system relies on the bubble pump's concept, which is a rarely used device for cooling.

Bubble pumps generally consist of a single vertical lifting tube heated at the bottom with any heat source. Continuous heating produces vapour slugs that carry the liquid slugs of the mixture to a higher level (Figure 3). the advantage of the bubble pump that there are no mechanical moving parts such as pumps. When the bottom of the bubble pump is exposed to heat, it converts the liquid into vapour due to evaporation. When the vapour bubbles go up, they carry some liquid with them. According to previous studies about the subjects, there are four common flow types in the lifting tubes, which are bubbly, slug, churn, and annular. Furthermore, while rising the heat, the flow types evolve from bubbly to annular [1].

The experimental results were compared with the analytical models of bubble pump; the study aimed to find out the differences in the amount of mass flow rate resulting from the change of some variables such as the submergence ratio, the number of lifting tubes, and the amount of the heating power input to the generator in the bubble pump that uses the saturated water as the working fluid and working under the atmospheric pressure.

To reach the slug flow type, the consistency of the bubbles slug depends mainly on the input heat power in the experiment (the amount of heat dissipated by the pump) and the refrigerant boiling point, for the present work, it was nearly 99ºC for water, ammonia or R134a could be used. However, the experiment was not focused on the type of the refrigerant but the submergence ratio and the multi lifting tubes.

According to many previous works, the slug flow is the most efficient flow pattern in the airlift pump, as well as in the bubble pump as they share the basic work principle to lift liquid via bubbles without mechanical parts [2]; however the flow through the lifting tubes of the bubble pump is much complicated to analysis in compare with airlift pump because of the condensation of the steam bubble inside the lifting tubes away from the bottom due to heat loss in some cases of poor insulation of the lifting tubes, so it is vital for each bubble pump to has its pumping cycle [3], which is the time that required for the pump to form a bubble that has enough buoyancy force to lift the liquid slugs. When condensation inside the lifting tubs happens, the bubble pulls down the water slugs to the bottom of the tubes, and that affects the flow from reaching the steady-state flow.

The main types of bubble pumps: (1) Diffusion Absorption Refrigeration (DAR) Systems which consists of a vertical lifting tube filled with liquid coolant into a defined height according to the required submergence ratio, and the heat input through the bottom of the tubes works as a generator to push the liquid slugs via the generated vapour bubbles. By cutting out unnecessary electricity, this absorption technology is so important without the need for mechanical moving parts to lead the flow, provides simple mechanical design, without noise, low cost and long-time of working without maintenance. Bubble pump, widely used in percolator coffee machines, is proposed to drive domestic solar water heating systems [1]. This type of refrigeration cycles works at a single pressure level along the whole cycle, but of course, there will be some minor variations in the pressure due to friction and gravity, but they have small effects on the overall performance.

This single pressure absorption cooling system work with more than two fluids as an ammonia-water-hydrogen cycle, known as the diffusion absorption refrigeration (DAR) cycle, shown in Figure 1, patented by Swedish engineers Platen and Munter in1920 [4]. This cycle uses three working fluids to get both a low evaporation temperature and a high condensation temperature at the same pressure level. The inert fluid (hydrogen) is to maintain pressure equalization in the cooling cycle.

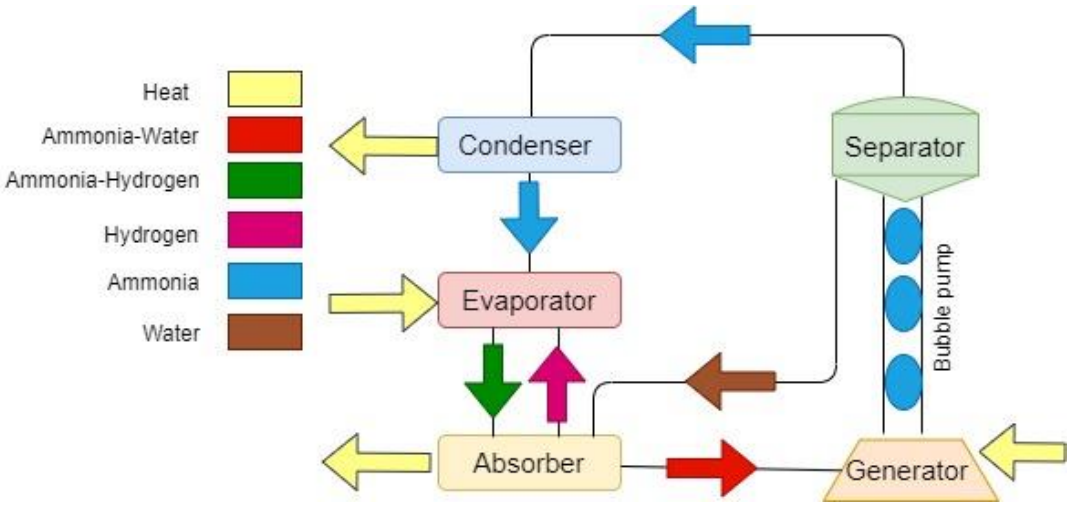

Figure 1. Schematic of diffusion absorption cooling (DAR) system

(2) Bubble-Pump-Driven Vapour Absorption Refrigeration Systems (VARS): In this system, waste heated hot water comes from manufactures, or solar energy can be used as a heat source to drive the cycle, for this system, the most common pairs work as a refrigerant are LiBr-H_2O and NH_3-H_2O, the first pair has the higher efficiency, but it is not preferable because of corrosion problems accompanying it, so the second pair are familiar in use for relatively small applications [5].

In this system, the fluid mixture is heated in the generator by the waste heat (hot water) or solar energy (by solar panels). The high-pressure coolant vapour from the generator is condensed, then it goes through the throttle valve to become at low pressure, then the fluid enters the evaporator (for example, a refrigerator). The refrigerant, after that, goes to the generator throw a pump; when the refrigerant evaporates in the generator, the remaining liquid mixture goes back through another throttle valve and flows back to the absorber; see Figure 2.

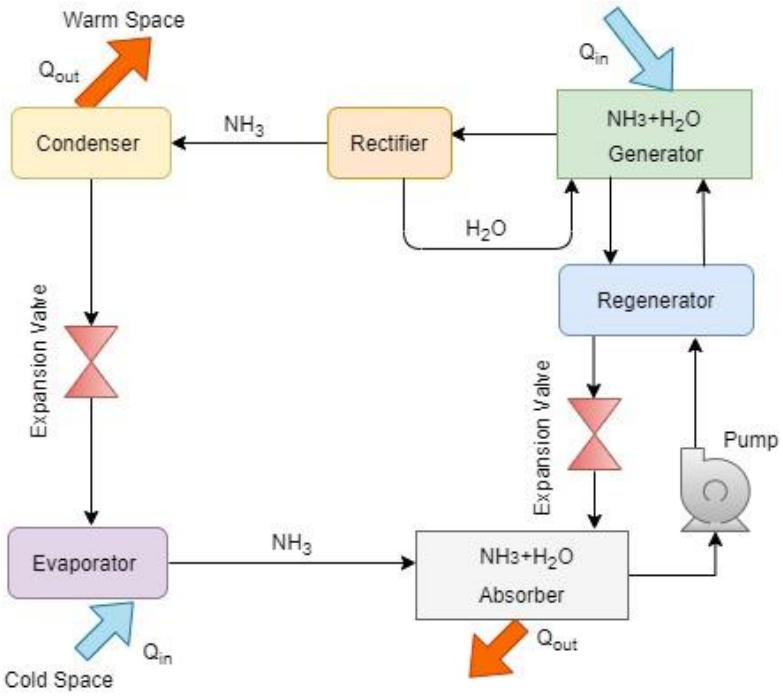

Figure 2. Bubble pump steam absorption cooling systems (VARS) schematic

2. DESIGN LAYOUT

After reviewing the previous literature and made the proper selections of the parts, and sizing the cycle, the last stage was to draw a control map to optimize the cooling system to run very efficiently with the least amount of electricity possible.

The cooling load can be defined as the amount of heat energy that has to be removed from a given space. In the case of this system, the cooling load is the heat to be removed from the hot surface by conduction, and it was chosen to be 550W and 1500W, respectively. Assumptions have been made in order to facilitate calculations:

- Assume that flow in the lift tubes is one-dimensional, adiabatic, and stable.
- Assume that the friction in the lift tubes is ignored.
- Assume that the flow head is equal to the total pressure drop of the entire cycle.
- Assume that the heat loss along the cycle is ignored.
- Assume that the refrigerant is saturated water.
- Assume that the changes in kinetic and potential energies are ignored.
- Assume that the cycle is working under atmospheric pressure.

- Assume that the electric heater under the generator is a simulator to the hot surface to be cooled.

As the water enters the cooling cycle from the water supply network to the water reservoir at an ambient temperature of nearly 23°C and then have to be heated to the saturated temperature at nearly 99°C, with the lowest cost and highest efficiency through designing an integrated cooling system in terms of bubble pump configurations, the number of the working lift tubes from 1 to 4, using the most reliable material and using an automatic control system to ensure that the device is working smoothly and to minimize human mistakes, see Figures 3 & 4.

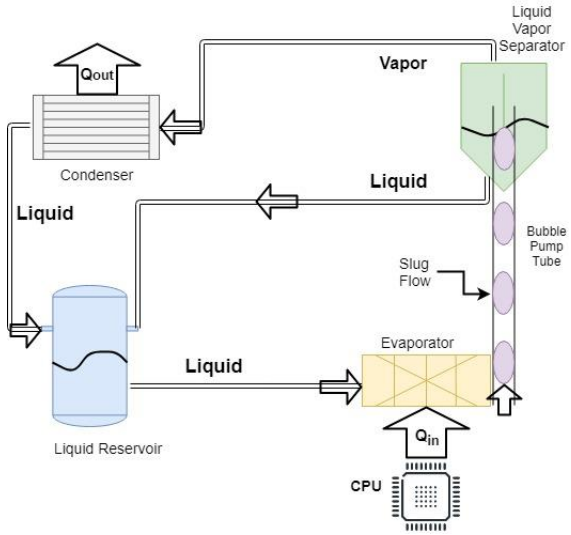

Figure 3. Working principle of bubble pump to cool up the hot surfaces

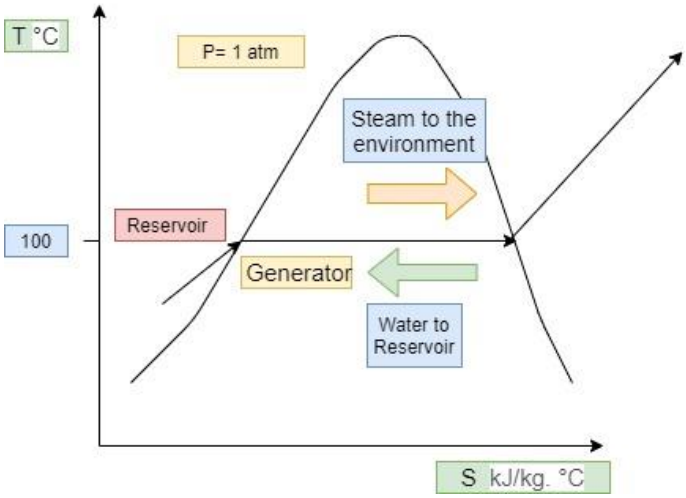

Figure 4. T-s diagram for bubble pump working environment

The main aim of this project was to design a cooling system that is an energy saver and more efficient than exists designs by considering several factors such as:

- The bubble pump system can work using different lift tube diameters, and the number of existed lift tubes can be controlled by using 1,2, 3 or 4 lift tubes according to the experiment.
- The separator is designed to return liquid hot water to the water reservoir and to release the steam into the environment if the condenser did not exist.
- The control map is designed to ensure work self-explanatory and control the solenoid valve based on the reading of temperature and liquid level sensors.

- An electric heater is to be used inside the water reservoir to maintain the refrigerant at the saturated state and control this process by the temperature sensors inside the reservoir.

3. CONTROL MAP LAYOUT

The layout controls the water circulation cycle within the bubble pump's configuration, and the water supply network and the locations of the water level sensor are to determine the submergence ratio. It is possible to make several designs for the same project with the same capacity, but the cost of any project depends on the design of the parts in the water-cooling system, so in this design, many terms were considered:

- The design's cost is confirmed to be as low as possible, whether it is the investigation cost or operating costs, and to be sure that they can work for a long time without the need for maintenance.
- In the design's layout, it was taking into account that the bubble pump parts are next to each other to reduced development costs, simplified connections to the overall system and centralized access for operations at maintenance.

3.1. The Analysis of The Control Map

Figure 5 illustrates the design of the bubble pump refrigeration cycle, including its main components, such as four lifting tubes, the generator, the separator, the condenser, the electric heaters, water tank, water reservoir, and their accessories connection like tubes and valves. However, in order to make the design less expensive and more straightforward, the condenser and water tank were abandoned. The Figure illustrates the flow of water in the cycle, which is changing its state according to heat gain due to the electric heaters, the heat rejection to the environment and heat losses.

Control system, see Figure 6, which controls the one-way solenoid valve and the constant powered electric heater by the reading of the temperature sensor inside the water reservoir. The water supply network feeds water continuously as the refrigerant to the water reservoir to compensate for the evaporation due to leakage of steam into the environment. The water level floating sensor valve type controls the water level. To maintain a constant submergence ratio.

The separation of the steam and the hot water is done by the separator, the separated steam flies to the environment, and the hot water returns to the water reservoir directly through a tube. The electric heater below the generator works as a simulator to the hot surface, should have a variable power capacity to be appropriate with all loads. The most important parts of the cooling cycle are the lifting tubes (bubble pumps); in the experiment, many working conditions have been tested to use 1, 2, 3, or 4 bubble pumps to deliver the water-steam mixture from the evaporator (generator) to the separator. Furthermore, to illustrate the flow type inside the pumps, transparent glass has been used.

The constant powered electric heater is located inside the water reservoir to deliver saturated water as the refrigerant fluid; it is connected to the control system through a temperature sensor to automatically stops when reaching the required temperature. The generator is made of steel to work as the evaporator, and the bottom works as the contact surface with the device to be cooled. The condenser is the central part of any refrigeration cycle. To bring back the vapour into the liquid refrigerant, it was not used in the experiment to minimize costs, although instead of it, water from the supply network has been used to compensate for the flying steam.

The water reservoir is an essential part of the cycle, to provide saturated water to the generator via a tube at the bottom, it was made of steel, and through it, the submergence ratio can be determined by a control system connected to the water level sensor. The purposes of the control system are to check the cycle temperatures, the water flow rates in and out, and the rate of the heat rejection from the device to be cooled, represented by the hot surface (the electric heater's power). That can be by using temperature and liquid level sensors distributed along with the bubble pump cooling device. The existing control system is on/off for both the heater inside the water reservoir and the solenoid valve. In this design, there are two control systems:

- The control system to determine the water level in the water reservoir.
- The control system to determine the temperature of the water.

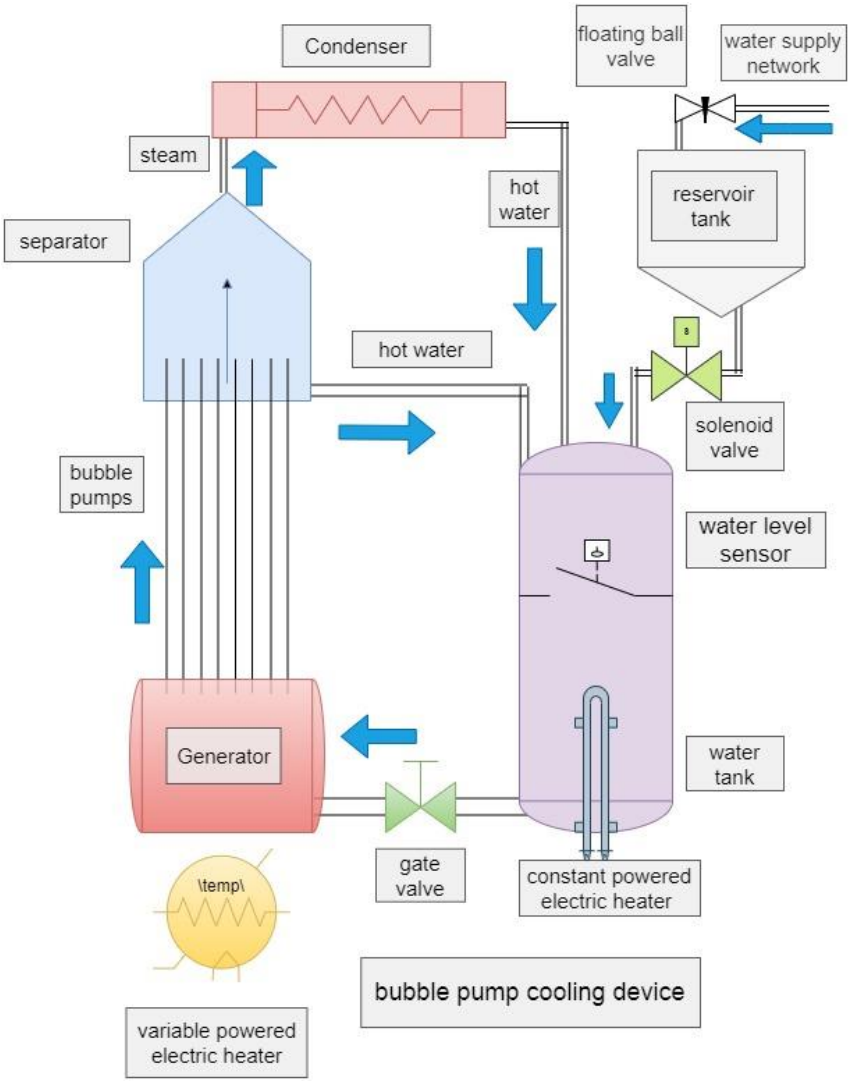

Figure 5. Closed-loop design for bubble pump schematic

Both control systems were working integrally to make an optimum operation of the system. The number of working lifting tubes can be manually controlled, by removing them or closed the inlets and outlets of the tubes via stopper rubbers. The controller type which has been used in the cooling cycle is the Aurdino UNO chip; the control system then has been simulated at program named fritzing, which is a program for simulating and drawing electrical circuits, the overall control system, including the main parts, has been drawn in Figure 6.

3.2 The Bubble Pump Performance

The protocol of the process was by using the 550W electric heater as a simulator of the hot surface to be cooled, by using firstly the total number of the lifting tubes firstly and taking the readings of the mass flow rate by utilizing a stopwatch along with measuring the weight of the hot water returning from the separator to the water reservoir by taking samples with a small bottle and by measuring the weight in gram via an electronic balance, and to obtain a more precise reading the process has been repeated five times and then the average number has been taken as the required data. Furthermore, by repeating that by resetting the water level sensor location to obtain different submergence ratios for comparing the result by using 0.3, 0.4, and 0.5 submergence ratios. To measure the device's performance with less than four lifting tubes, the previous process has been repeated three times after removing

one of the lifting tubes each time. To compare the results of the low energy hot surface with higher energy, the 550W electric heater has been replaced with a 1500W electric heater, and the whole process had been repeated.

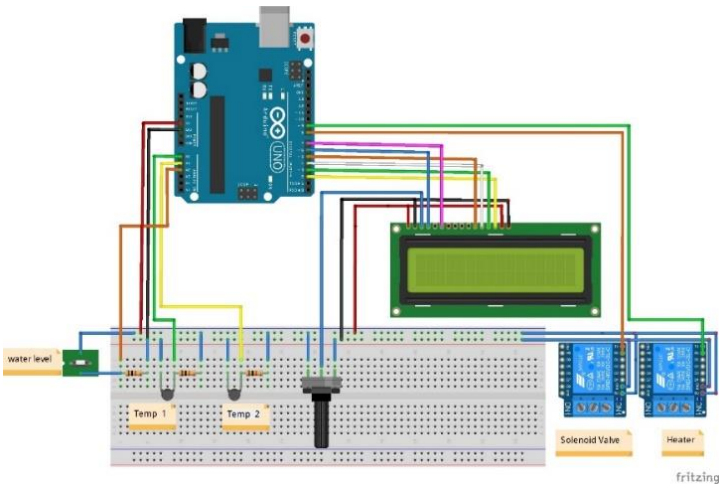

Figure 6. Control system simulated scheme in Fritzing

4. EXPERIMENTAL RESULTS

The effect of the submergence ratio and the number of lifting tubes: The liquid mass flow rate as hot water returning from the separator to the water reservoir is determined by the submergence ratio, which is defined as the ratio of the height of the liquid inside the lifting tube (H) to the whole length of the lifting tube (L), the experiments were to use different submergence ratios from 0.3 to 0.5. see Figure 7; it shows liquid mass flow rate as a function submergence ratio in a different number of lifting tubes (N=1, 2, 3, and 4) with a diameter of 8mm for two different heating power inputs 550W and 1500W.

According to the experiments, the bubble pump curves move upward when the submergence ratios increase. At the same input heating power, the mass flow rates directly proportional to the submergence ratio, because the higher the submergence ratio, the higher (H), which means that the liquid is travelling less distance to the separator. Besides, to achieve the same liquid mass flow rate value at high heating power, the submergence ratio and the number of lifting tubes at low input heating power must be increased. For example, the heating power required for liquid mass flow rates of about 18 g/s at a submergence ratio of 0.5 is about 1500W with N=1 and 550W with N=4, see Figure 7.

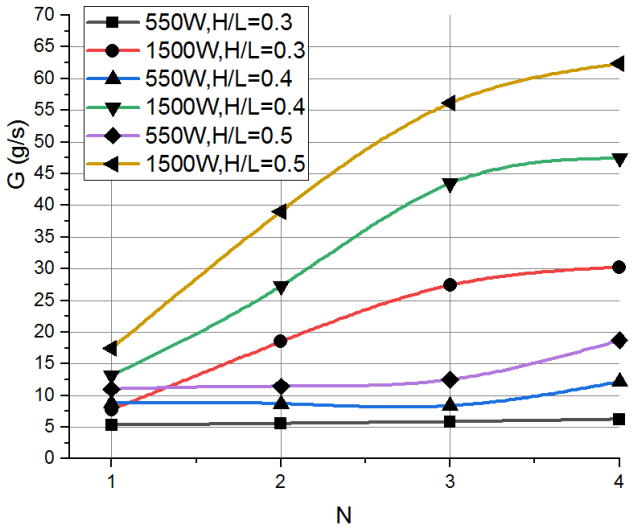

Figure 7. The effect of submergence ratio, input heating power and number of lifting tubes on the mass flow rate

In order to examine the effect of the number of lifting tubes, experiments were carried out with lifting tube numbers, N= 1, 2, 3 and 4, see Figure 7; all the performance curves have a similar trend. With the increase in the number of lifting tubes, the peak liquid mass flow rate occurs when the lifting tube number is N=4, because there is a regular heat dissipation under the generator. Nevertheless, according to the results, for the input heating power of 550W at a submergence ratio of 0.4, when N=2, it can be noticed that the mass flow rate is slightly more than the mass flow rate of the same submergence ratio when N = 3, for the same heating power, the highest performance value for N=4 is 18.7 g/s. See Figure 7, is not only related to the increase in the number of lifting tubes, but also to the higher rate of submergence ratio, which means that a different number of lifting tubes have a different effect on performance. In the 550W input heating power, the number of lifting tubes does not affect the pump's capacity. That means that the heating power assigned to each lifting tube is reduced by adding more lifting tubes and then increase the time for each tube to reach the slug flow pattern; with the increase of heating power, the liquid mass flow rate increases with the increase in the number of lifting tubes. That means that increasing the heating power of each tube allows the tube flow pattern to approach the slug flow and then improve the lifting capacity; in Figure 7, 1500W shows that at a higher heating power input, the number of lifting tubes (N) affects the overall performance of the bubble pump by comparing it with the peak mass flow rate of 62.3 g/s at a submergence ratio of 0.5 and when N=4, and the minimum mass flow rate of 7.8 g/s at N=1 and the submergence ratio of 0.3.

4.1 The Bubble Pump's Efficiency

Let the efficiency of the pump to be η. As in previous literature, it is defined as follows: the mass flow rate of the liquid refrigerant pumped per unit of input heating power to the bubble pump or can be defined as the ratio of the power output to the input heating power:

$$\eta = \frac{G\mathrm{g}(L-H)}{P_{in}} \tag{1}$$

G is the liquid mass flow rate, $(L-H)$ is the net lifting height, P_{in} is the input heating power under the generator. In Figure 8, the experimental results show the efficiency of the bubble pump of a submergence ratio of 0.5 of the 8 mm diameter lifting tubes (N) for both 550W and 1500W input heating power, regardless of the submergence ratio. The trends of the efficiency curves are consistent, and the pumping efficiency increases when the heating power increases, and the same when the number of lifting tubes increase [6].

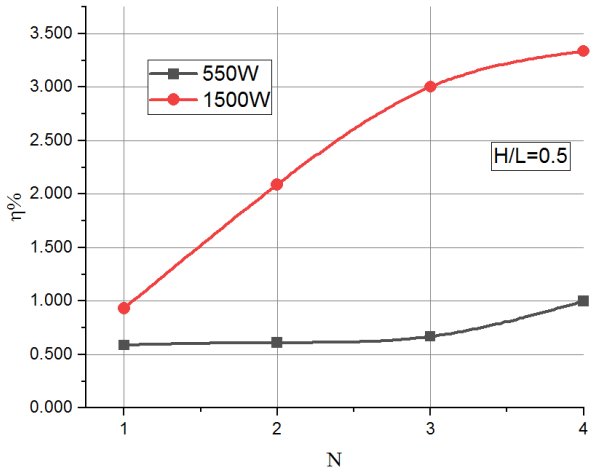

Figure 8. The effect of input heating power and the number of lifting tubes on efficiency (submergence ratio = 0.5)

In general, the higher heating efficiency was with, the more significant power input. However, for some few cases, cooling can be done using a lower heating power input and gives the same amount of efficiency for a higher input power heating, related with the higher number lifting tube, for example, the efficiency when N=4 with the input heating power 550W, is greater than the efficiency of 1500W and N=1.see Figure 8.

In the experiment, see Figure 8, when the number of the lifting tubes is 1, 2, or 3 and at low input heating power 550W, the liquid mass flow rate and the efficiency remain almost constant without a significant increase. For the higher heating power input 1500W, the increase in the number of the lifting tubes at the same submergence ratio enhanced the efficiency; also, the mass flow rate of the fluid increases with the increase of the submergence ratio. For the multi lifting tubes bubble pump to achieve more mass flow rate, low efficiency is required. Furthermore, less heating power is demanded to achieve higher efficiency. Therefore, how to choose between the liquid mass flow rate and the efficiency of the pump should be chosen according to the specific requirements of the pump system [7].

Figure 9. Bubble pump cooling device used in experiments

4.2 The Flow Patterns in The Bubble Pump

The flow in the lifting tube of a bubble pump is a complex two-phase rather than a single-phase flow, which is a direct use; the flow is upstream flow in vertical tubes. Standard vertical upstream models vary with the gas mass flow rate corresponding to the power input [8]. In previous studies [9-10], flow patterns were analyzed and categorized into four main classes of bubbly, slug, churn and annular flows.

The significant flow pattern in the vertical lifting tubes of the bubble pump is slug flow. In this experiment, gas-liquid two-phase flow is observed in four lifting tubes with a diameter of 8 mm for a tube length of 600 mm and a submergence ratio of 0.5, Flow types for 550 W and 1500W heating power shown in Figure 10 and Figure 11, respectively, were photographed. Each Figure has four photos, from (a) to (C) for 550W and (e) to (H) for 1500W heating power input, respectively, in the order of ascending lifting tubes.

For large distorted bubbles with interaction, combination, unique shapes, and system behaviours, churn flow is not enough; the number of bubbles that is interacting with each other is also not enough. This flow regime is created when there is a large gas fraction in a system with high gas and low liquid velocity. These churn bubbles occur with a relatively low heating power of 550W, see Figure 10.

In the slug flow, the bubbles are gathered together and grouped up into a stream. In Figure 11, bullet-shaped slug bubbles are shown to act as pistons that drive liquid to the top of the lifting tubes. These slug bubbles are relatively stable in high heating power (1500W), however, after increasing the heating power from 550W to 1500W, the inner volume covers more gas, and longer slug bubbles are formed. When discomfort and fracture begin to be detected in slug bubbles, which can be avoided by shake the lifting tubes gently. Lifting tubes have uneven gas distribution from bottom to top, which leads to a different flow pattern for each lifting tube.
When the heating power was 550W, in Figure 10, churn flow occurs, in Figure 10(a), when N=1, the bubbles occurred, and the steam was fast and big, in Figure 10(b), when N=2, the heat generator at the bottom of the distribution was not equal, therefore, the removal was faster in the lifting tube closest to the water reservoir, and giant bubbles did not occur, in Figure 10(c), when N=3, the steam has become slower than before, and at the same time the bubbles were giant, in Figure 10(d), when N=4, it has been noticed that the steam bubbles are larger at the bottom of the lifting tubes and become smaller and faster at the top of the lifting tubes.

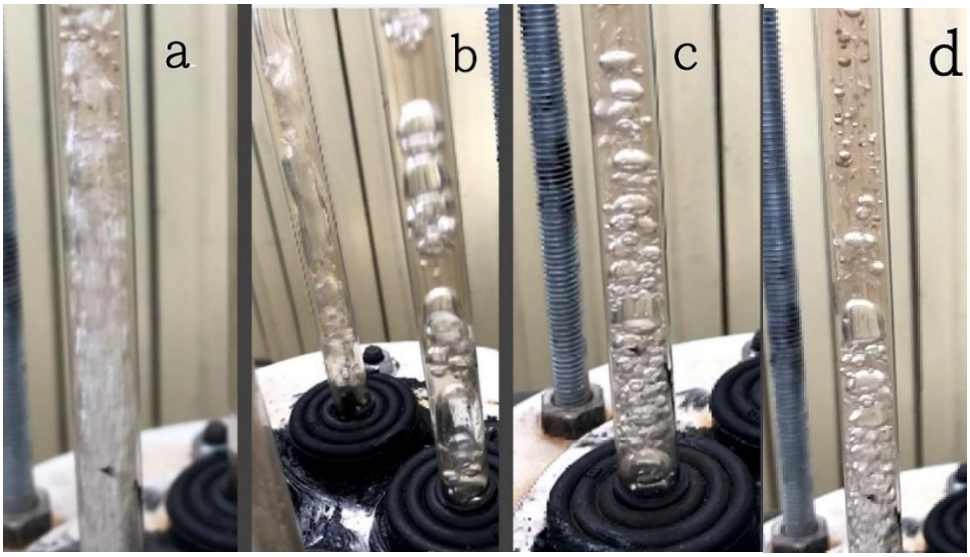

Figure 10. The flow pattern inside the lifting tubes (heating power 550W) (a) N = 1, (b) N=2, (c) N = 3, (d) N=4

At the heating power of 1500W, slug flow occurs in Figure 11; in Figure 11(e), when N=1, slug bubbles were short and fast, in Figure 11(f), when N = 2, there were differences in slug bubbles length and the flow rate of liquid

water were smaller and faster at the nearest lifting tube to the water reservoir, in Figure 11(g), when N = 3, slug bubbles were somewhat similar in terms of length and flow rate, in Figure 11(h)also, when N = 4, the slug is slower and longer than other configurations of bubbles. According to experiments, a multi-tube bubble pump can lead to the problem of uneven gas distribution.

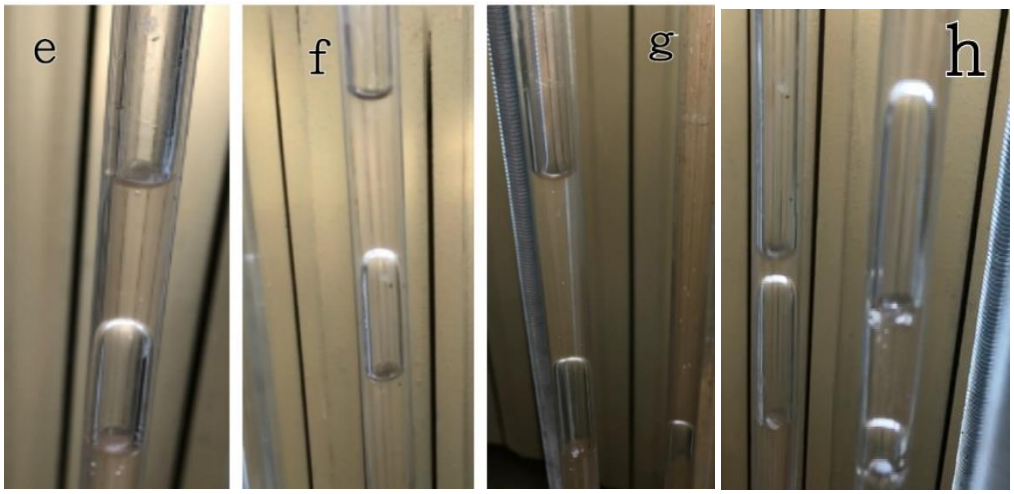

Figure 11. The flow pattern inside the lifting tubes (heating power 1500W) (e) N = 1, (f) N=2, (g) N=3, (h) N=4

5. CONCLUSION

In this article, a prototype of the open-guided Multi-Lifting tube pump system was designed and tested as the saturated water was the working fluid under the atmospheric pressure. The proposed model provides a good deal with experimental results, where the regime is slug flow and N=4 in the linear range. Besides, as the input heating power increases beyond linear, the liquid mass flow rate becomes insensitive to heating power. This model is only suitable in the slug flow zone, so it should be improved. For liquid lifting capacity, a higher submergence ratio is good. As this ratio increases, less energy will be used to remove heat from the water. However, if the submergence ratio continuously increases to unity, the importance of the bubble pump will be lost. When the liquid mass flow rate increases with higher heating power, the pumping efficiency, defined as the output power ratio to input power, has the same dependence on heating power. Despite the pumping capacity or efficiency, a first-class heating power range should be selected to displace the liquid for all conditions. Maximum pumping efficiency occurs with the maximum mass flow rate of the fluid. For a multi-lifting tubes bubble pump, it is necessary to achieve more liquid mass flow rate and less heating power to achieve higher efficiency.

Therefore, how to choose between the liquid mass flow rate and the efficiency of the pump should depend on the specific requirements of the pump's system. Multi-lifting tubes bubble pump's performance increases when the submergence ratio or the number of lifting tubes increase, also the pumping efficiency can be up to 4%. Increasing the number of lifting tubes does not cause the lifting capacity and efficiency to be directly proportional. The highest performance value for lifting tubes when N=1, 2, 3 and 4 is 17.4 g/s, 39.06 G/s, 56.12 G/s and 62.34 G/s, respectively, at a 0.5 submergence ratio of 1500W input heating power. The flow charts are observed in a different number of lifting tubes and different input heating power. The slug flow pattern is visible in the area where heating power is 1500W; therefore, the flow regime is mainly slug flow within high input heating power under experimental conditions, and for 550W input heating power, churn flow was open with the experiment. At the same time, a multi-lifting tubes bubble pump can solve the problem of uneven gas distribution. Ammonia or other common refrigerants such as R134a with the presence of the condenser can be replaced with closed-cycle cooling bubble pump runs for a commercial basis and would work well under pressure higher than atmospheric pressure, to use it to dissipate the heat emitting from large electrical transformers and many electrical devices such as central computers to save on costs resulting from the cooling of traditionally. While initial costs are not high, efficiency will be better in the long run by providing an endless cooling system without using electricity.

REFERENCES

[1] Chan, K.W. and M. McCulloch, Analysis and modelling of water-based bubble pump at atmospheric pressure. International Journal of Refrigeration, 2013. 36(5): p. 1521-1528.

[2] White, S. J. (2001). Bubble pump design and performance (Doctoral dissertation, School of Mechanical Engineering, Georgia Institute of Technology).

[3] Benhmidene, A., Chaouachi, B., Gabsi, S., & Bourouis, M. (2015). Modelling of boiling two-phase flow in the bubble pump of diffusion-absorption refrigeration cycles. Chemical engineering communications, 202(1), 15-24.

[4] Aman, J., Henshaw, P., & Ting, D. S. (2018). Bubble-pump-driven LiBr-H2O and LiCl-H2O absorption air-conditioning systems. Thermal Science and Engineering Progress, 6, 316-322.

[5] Totla, N. B., Arote, S. S., Gaikwad, S. V., Jodh, S. P., & Kattimani, S. K. (2016). Comparison of the performances of NH 3-H 2 0 and LiBr-H 2 O vapour absorption refrigeration cycles. Int J Eng Res Appl, 6, 08-13.

[6] Lin, F., Liu, D., Jiang, D., Yang, L., & Zhao, R. (2016). An experimental study on the performance of the guided bubble pump with multiple tubes. Applied Thermal Engineering, 106, 1052-1061.

[7] Shelton, S., Delano, A., & Schaefer, L. A. (1999). Second law study of the Einstein refrigeration cycle. Proceedings of the Renewable and Advanced Energy Systems for the 21st Century, 1-9.

[8] Taitel, Y., Bornea, D., & Dukler, A. E. (1980). Modelling flow pattern transitions for steady upward gas-liquid flow in vertical tubes. AIChE Journal, 26(3), 345-354.

[9] Furukawa, T., & Fukano, T. (2001). Effects of liquid viscosity on flow patterns in vertical upward gas-liquid two-phase flow. *International journal of multiphase flow*, *27*(6), 1109-1126.

[10] Mishima, K., & Hibiki, T. (1996). Some characteristics of air-water two-phase flow in small diameter vertical tubes. *International journal of multiphase flow*, *22*(4), 703-712.

THERMODYNAMICS

PERFORMANCE PREDICTION OF A TWO-BED ADSORPTION CHILLER CONSIDERING THE IMPACT OF HOT AND COOLING WATER TEMPERATURES AND HOT WATER MASS FLOW RATE

Ahmed Mohammed Shakır SHAKIR*, Türkan Üçok ERKEK, Mustafa Wahby Kanbar JABER***, Ali GÜNGÖR****
*Ege University, Institute for Natural Sciences, Izmir/Turkey
Email: ahmed_m.shaker@yahoo.com
******Ege University, Department of Mechanical Engineering, Izmir/Turkey
Email: turkan.ucok.erkek@ege.edu.tr; ali.gungor@ege.edu.tr
***Kirkuk University, Department of Mechanical Engineering, Kirkuk/Iraq
Email: musta_72@yahoo.com

ABSTRACT

Adsorption technology used in adsorption chillers is a new and environmentally benign technology. Adsorption chillers use low-quality waste heat and renewable energy resources. Silica gel–water working pair is the most frequently used adsorbent/adsorbate pair in bedded adsorption chillers. This work evaluates the impact of hot and cooling water temperature on the performance of a two-bed adsorption chiller, which uses the silica gel-water adsorbent/adsorbate pair. A mathematical model was previously developed for the theoretical analysis of adsorption chillers has adapted to this current system. Simulation work was carried out to determine the impact of hot and cold water temperatures on the COP and cooling capacity. A parametrical analysis has done to interpret the results.

Keywords: Solar energy, Adsorption cooling system, Water; Silica gel, Performance analysis

1. INTRODUCTION

Today, one of the requirements in cooling applications is to minimize the use of electrical energy, and the other one is to eliminate the harmful effects of refrigerants used in cooling systems. Likewise, a silica gel-water adsorption cooling system that can be operated by low-grade waste heat or solar energy such as a flat plate solar collector at the temperature of 55–85˚C, dependent on the industry. Two-bed adsorption cooling system developed to profit from low-temperature waste heat. Also, much accomplishment has been obtained. Zhu et al. [1] built and tested the solar dual-bed adsorption cooling system in Guangzhou. The outcome of the solar adsorption cooling system on cooling performance experimentally investigated. In the given; study, silica gel-water was used as adsorbent-adsorbate pair. The cooling capacity of 52.2 W / kg and a performance coefficient of 0.20 were obtained in 2 hours. As a result, the maximum cooling capacity and performance coefficient of the adsorption cooling system under different conditions are 180.4 W / kg and 0.29, respectively. Thakare and Deshmukh [2] examined the performance of a solar adsorption water cooling system experimentally using composite adsorbent, 25% activated carbon and 75 % silica gel. The solar performance coefficient for the 10-liter cooling water load was 0.088, and the efficiency coefficient was 0.83. It has been reported that the cooling efficiency coefficient of the system is generally dependent on the solar radiation intensity. Besides, it concluded that the cooling efficiency coefficient depends on the bed temperature. Rezk et al. [3] proposed to improve the performance of solar-powered adsorption desalination cooling (SADC) system using silica gel as an adsorbent, by optimizing the working conditions employing a new optimization algorithm. The system design shows a 70 % increase in cooling capacity by using the optimum working conditions with no change in the adsorption cooling system design or the used materials. Sayfikar and Behbahani [4] presented a transient simulation of a two-bed adsorption cooling system in Ahwaz, southern Iran. Silica gel water pair used as an adsorbent-adsorbate pair. The initial collecting area and storage tank volume used in the solar system were 55 m2 and 2750 liters. The

efficiency coefficient and cooling capacity of the modeled refrigerant were calculated as 0.575 and 8.84 kW, respectively. Alsaman et al. [5] proposed a solar adsorption desalination-cooling (ADC) system designed, built, and tested under Egypt's climate conditions. 13.5 kg silica gel, which is commercially available, is used as the adsorbent. The adsorbate used is water vapor. The results showed that the average cooling capacity was 112 W / kg, and the average specific daily water production was 4 m3/ ton of silica gel. The cooling efficiency coefficient was obtained as 0.45. Reda et al. [6], carried an experimental study on the performance of a small-sized residential solar-powered adsorption (silica gel-water) cooling system. The efficiency of the solar collector during the operation of the system varied between 50 % and 78 %. Adsorption refrigerant performance, chilled and cooling water temperatures were approximately 31 °C and 19 °C, respectively, while the average cooling capacity and daily cooling efficiency coefficient were 4.4 kW to 0.41, respectively. The results showed a 40 % increase in the cooling efficiency coefficient and a 17 % increase in cooling capacity, while city water was 27.7 °C. Raj et al. [7] studied the operation and performance parameters of the adsorption desalination system. RD-type silica gel was used as an adsorbent in the study. Dubinin Astakhov model was used to define the adsorption properties of silica gel-water adsorbent-adsorbate pair. Equations related to the mathematical model of the adsorption desalination cycle are solved using MATLAB 2017. It has been reported that better performance can be obtained from the system for low cooling water temperature, low condensation temperature, and high hot water inlet temperature. In this work, a parametric performance prediction of a two-bed adsorption chiller has made employing a numerical model. A silica gel–water adsorption chiller evaluated. As a result of the current analysis, the influence of hot and cooling water temperatures and hot water mass flow rates on the refrigeration capacity and COP is determined.

2. SYSTEM DESCRIPTION

The adsorption chiller used in this work consists of two adsorbent beds, an evaporator, a condenser, a cooler, and a heater. The illustration of the two-bed adsorption chiller is given in Figure 1. Silica gel-water is the adsorbent-adsorbate pair for the analysis in this model. Fin and tube heat exchangers, in general, are used as adsorbent beds that embed with the adsorbent material at the fin gaps. Valves that are joining each other are applied to couple the adsorbent beds with the condenser and the evaporator. The adsorption operation is a heat-releasing process in which the adsorbent bed needs to be cooled during the adsorption to remove the adsorption heat. Furthermore, the desorption process occurs as the adsorbent bed is supplied with heat. Thus the refrigerant desorbed from the adsorbent [8].

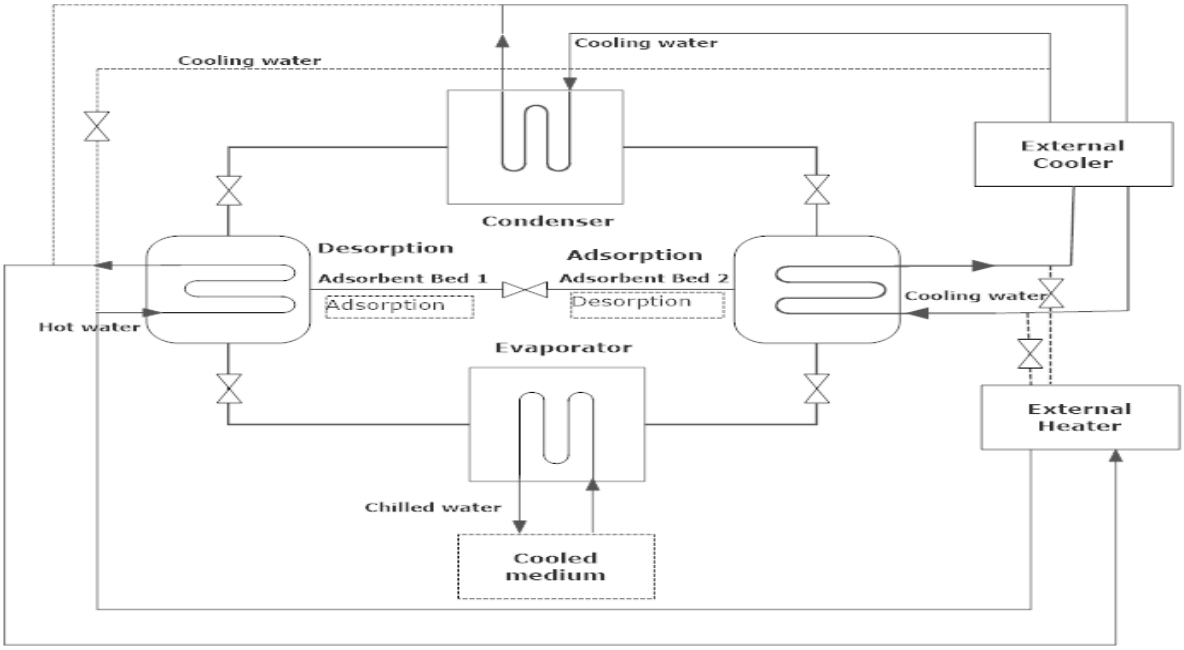

Figure 1. Illustration of the two-bed adsorption chiller**.**

3. MATHEMATICAL MODEL

The mathematical model of the two-bed adsorption chiller is built on the following assumptions [9].
The condenser's cooling capacity is infinite.
The heat loss to the environment is neglected.
In the adsorber, there is a uniform distribution of temperature and pressure.
The adsorption and desorption processes realize simultaneously without loss of switching time.
The adsorption equilibrium in this study uses the Freundlich equation. This equation supposes isobaric adsorption-desorption and an equilibrium process with no hysteresis advised by many researchers.

$$q = q_{\infty}\left(\frac{P}{P_{sat}}\right)^{1/n} \tag{1}$$

In equation (1), q designates the adsorbed amount of water vapor, q_{∞} is the adsorbed amount limit, P_{sat} symbolizes the saturation vapor pressure at the refrigerant's temperature, P is the vapor pressure inside the adsorber, and k is a constant. The refrigerant's vapor phase temperature is described by the evaporator temperature (at the adsorption phase) or condenser temperature (at the desorption phase).
The quantity of desorbed adsorbate throughout the phase of regeneration is calculated by the equation below:

$$q = q_{\infty}\left(\frac{P_{sat}(T_c)}{P_{sat}(T_{ads})}\right)^{1/n} \tag{2}$$

In equation (2), Tads represent the inner temperature of the adsorber, and Tc is the temperature of the condenser.
The quantity of water vapor adsorbed within the adsorption period is calculated by the equation below:

$$q = q_{\infty}\left(\frac{P_{sat}(T_e)}{P_{sat}(T_{ads})}\right)^{1/n} \tag{3}$$

In equation (3), Te shows the temperature of the evaporator.
The saturation pressure of the water vapor can be expressed by the equation (4) [10]:

$$P_{sat} = 0.001 \exp\left(a_s + \frac{b_s}{T}\right) \tag{4}$$

P_{sat} is in mbar, as and bs for water are 20.586 and -5098.6 respectively.
The heat is transferred to the adsorber by the heat transfer fluid at a rate of which can be stated by the equation (5):

$$\dot{Q} = \dot{m}_w C_{p,w} \varepsilon (T_w - T_{ads}) \tag{5}$$

In equation (5), $\dot{m}_w$ indicates the mass flow rate of water, $C_{p,w}$ symbolizes the specific heat of water, and Tw shows the temperature of the hot or chilled water. ε represents the effectiveness of the adsorber.
The effectiveness of the adsorber can be described by this formula below:

$$\varepsilon = 1 - \exp\left[-\frac{U A_{ads}}{\dot{m}_w C_{p,w}}\right] \tag{6}$$

In this equation, U represents the overall heat transfer coefficient and A_{ads} symbolizes the adsorber's surface area.
Energy balance in desorption is formed by the relation below:

$$\left[M_{am}C_{p,am} + M_s(C_{p,ad} + q\, C_{p,w})\right]\frac{\partial T_{ads}}{\partial t} + M_{ad}H_{ads}\frac{\partial q}{\partial t} = \dot{Q} \tag{7}$$

In equation (7) M_{am} and C_{am} indicate the mass and the specific heat of the metallic adsorber respectively, whereas M_{ad} and C_{ad} indicate the mass and the specific heat of the adsorbent.
The adsorption energy balance is written by the relation below:

$$\left[M_{am}C_{p,am} + M_s(C_{p,ad} + qC_{p,w}\right]\frac{\partial T_{ads}}{\partial t} + M_{ad}(H_{ads} + C_{p,v}(T_e - T_{ads})\frac{\partial q}{\partial t} = \dot{Q} \quad (8)$$

In equation (8), C_{pv} represents saturated water vapor's specific heat at the temperature of the evaporator.
Refrigerant's mass flow rate in the cycle is defined with the equation (9):

$$\dot{m}_{ref} = \frac{M_s\,(q_{conc} - q_{dil})}{t_{cycle}} \quad (9)$$

In equation (9), the adsorbed amount of water vapor at the end of the adsorption phase is designated with q_{conc}, the desorbed amount of water at the end of the desorption phase is q_{dil}, and the cycle time is shown by t_{cycle}. Since there are two adsorbers in the system, the equation is multiplied by 2.
In this system, the refrigeration capacity per cycle is described by equation (10). In equation (10), $h_{v(P_e)}$ symbolizes enthalpy of vapor refrigerant at the evaporator pressure and $h_{f_{(P_c)}}$ is the enthalpy of the liquid refrigerant at the condenser pressure.

$$\dot{Q}_{ref} = \dot{m}_{ref}\left(h_v(P_e) - h_f(P_c)\right) \quad (10)$$

The heat input rate for a cycle can be estimated by the equation (11):

$$\dot{Q}_{in} = (\dot{m}_{ref}H_{ads}) + \frac{\left[M_{am}C_{p,am} + M_s(C_{p,ad} + qC_{p,w}\right]}{\frac{t_{cycle}}{2}}\left(T_{g1} - T_{a1}\right) \quad (11)$$

In equation (11) the first expression has resulted from the adsorption heat, and the second expression is due to the sensible heat necessary to heat the material of the adsorber, adsorbent, and the adsorbate (water) from the temperature at the end of the adsorption phase, T_a, to the temperature at the end of the desorption phase, T_d.
The Coefficient of Performance (COP) can be obtained from the equation (12) below:

$$COP = \frac{\dot{Q}_{ref}}{\dot{Q}_{in}} \quad (12)$$

The set of parameters employed in this adsorption chiller cycle simulation are given in Table 1. Each time a single parameter is altered to analyze its influence on the refrigeration capacity and COP while the remaining parameters stay unchanged at the standard operating conditions.
The values of operating conditions employed in the simulation are demonstrated in Table 2.
The system of differential equations (1) – (12) was solved concurrently by numerical integration using Python with the functions for ODE integration.

Table 1. Specifications used in the simulation [9]

Parameters	Unit	Value
Specific heat of adsorber material, c_{am}	J / (kg. k)	448
Specific heat of adsorbent c_{ad} , (silica gel)	J / (kg. k)	920
Specific heat of water vapor, c_{pv}	J / (kg. k)	1866

Specific heat of water, c_{pw}	J / (kg. k)	4180
Heat of adsorption, H_{ad}	kJ/ kg	2800
Constant, k	-	0.799
Mass of adsorber material, M_{am}	kg	20
Mass of adsorbent, M_{ad}	kg	20
Surface area of adsorber, A_{ads}	m^2	3
Maximum adsorption	-	0.355
Overall heat transfer coefficient, adsorber, U, W /($m^2 \cdot k$)		300

Table 2. Operating conditions employed in the simulation.

Parameters Unit	Impact of hot water temperature	Impact of hot water mass flow rate	Impact of cooling water temperature
Mass flow rate of cooling/heating water kg/s	0.2	0.1/0.2/0.3/0.4/0.5	0.2
Temperature of cooling water ˚C	25	25	18/20/22/24/26/28/30/32
Temperature of heating water ˚C	40-120 ºC	90	90
Temperature of the condenser ˚C	25	25	25
Temperature of the evaporator ˚C	16	16	16
Cycle Time, t_{cycle} s	300	300	300

4. RESULTS

4.1 Impact of Hot Water Temperature on Refrigeration Capacity and COP

The impact of hot water temperature on adsorption chiller's refrigeration capacity was studied in this work. Hot water temperature ranging from 40-120℃ used in the simulation. Cycle time is arranged as 300 s and fixed along all simulations performed. Cooling water, condenser, and evaporator temperatures are kept constant. The results gained are demonstrated in Fig. 2 and 3.

As can be deduced from Figure 2, refrigeration capacity increases rapidly with the increasingly hot water temperature at temperatures between 40-70℃. The rise of the refrigeration capacity slows down Along with the temperatures between 70-100℃. Right after 100℃ temperatures, there is no increase in the refrigeration capacity. This result is the consequence of the desorption capacity of the material itself. When the desorption temperature is exceeded, there is no positive effect on desorption and shows the same effect on the refrigeration capacity.

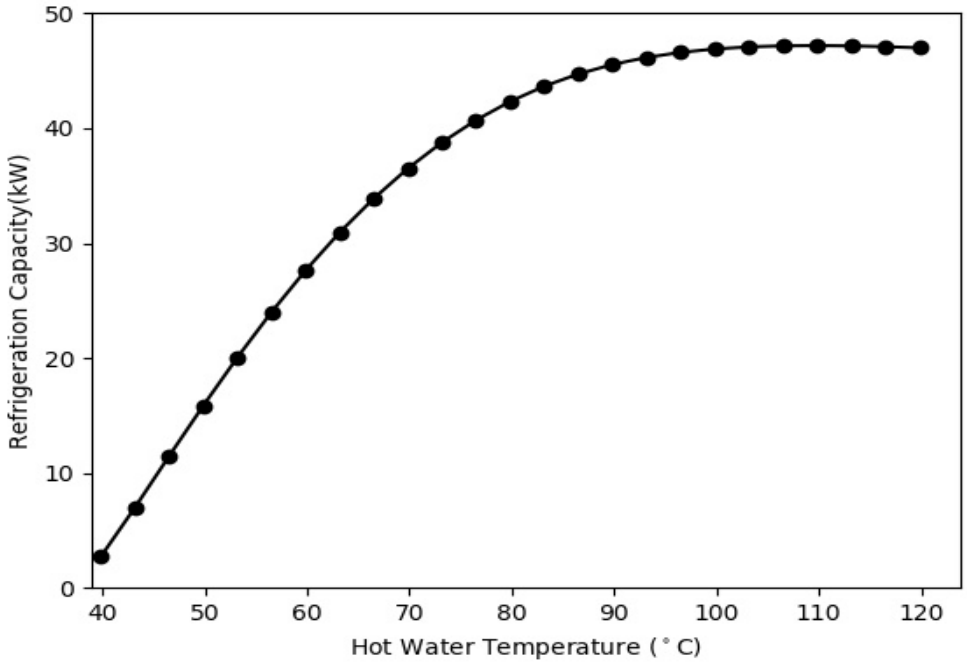

Figure 2. Impact of varying temperature of hot water on refrigeration capacity.

Figure 3 shows the impact of hot water temperature on the performance coefficient of the adsorption chiller. COP increases with increasing hot water values up to 62 °C, and after that decreases when the temperature starts to rise to 120 °C. The maximum COP obtained is roughly 0.6 at a hot water temperature of 62.4 °C.

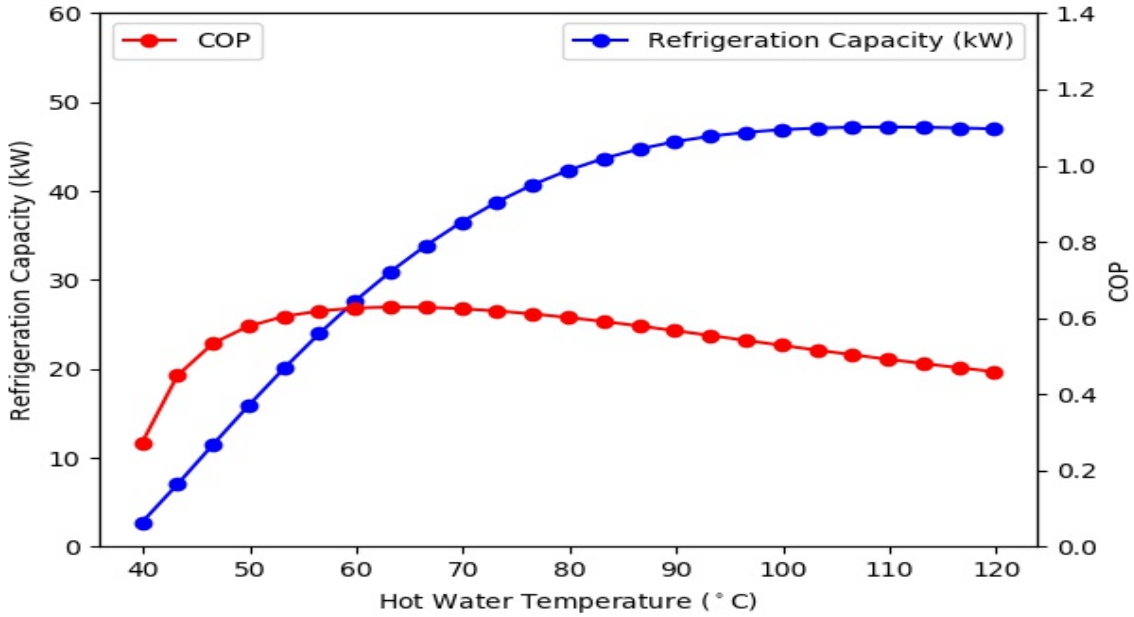

Figure 3. Impact of varying temperature of hot water on refrigeration capacity and COP.

4.2 Impact of The Variation in Hot Water Mass Flow Rate on Refrigeration Capacity and COP

The same phenomenon is observed on the impact of hot water mass flow rate on refrigeration capacity and COP, as shown in Figures 4 and 5. When the mass flow rate is ranging from 0-0.2 kg/s, there is an obvious change in refrigeration capacity and COP. If this value is exceeded, there is no change in both refrigeration capacity and COP. It is a result of more heat being supplied to the adsorber while the hot water's mass flow rate increases.

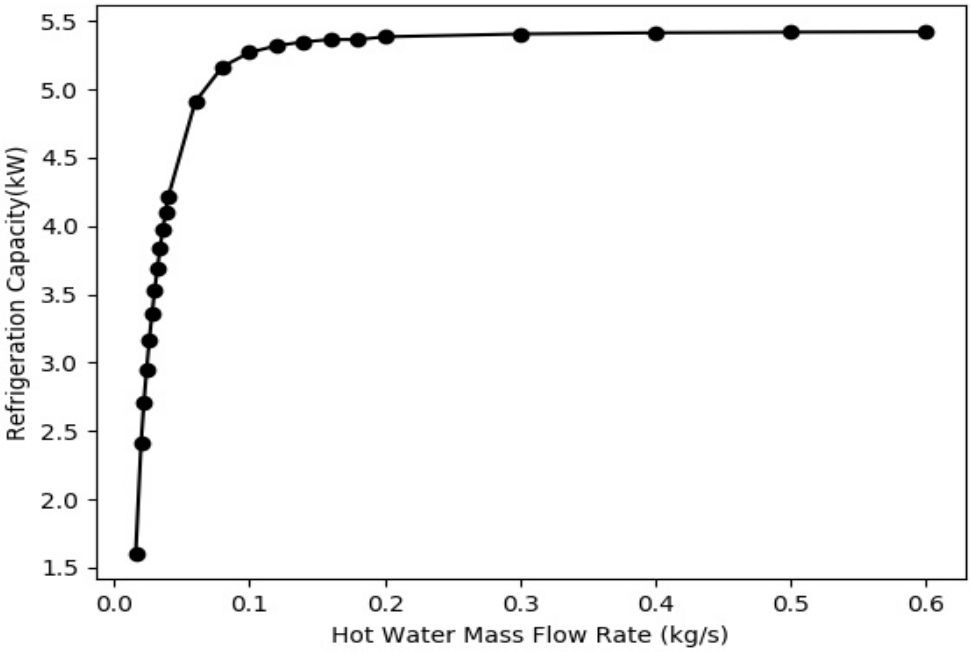

Figure 4. Impact of varying mass flow rate of hot water on refrigeration capacity.

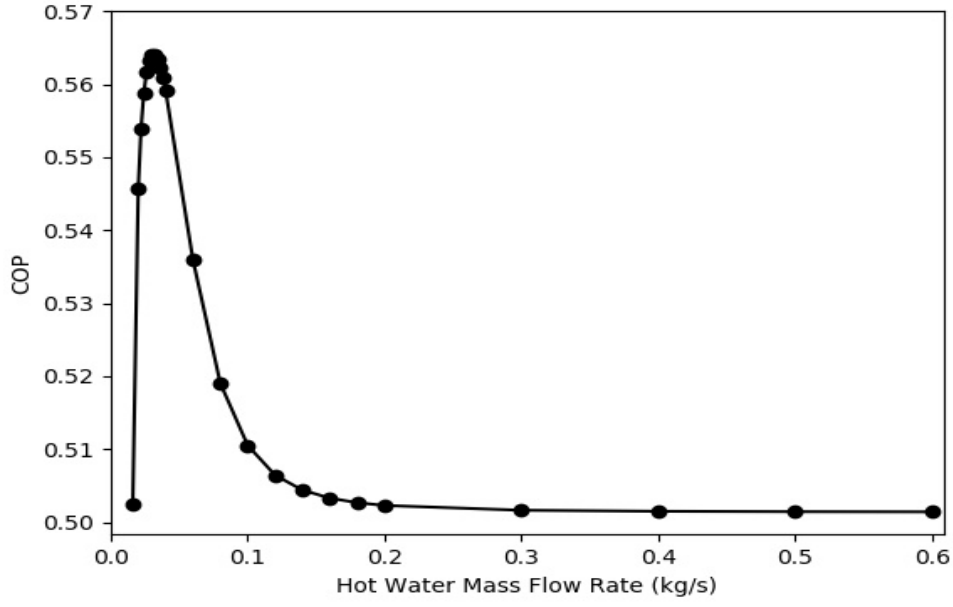

Figure 5. Impact of varying mass flow rate of hot water on COP.

4.3 Impact of The Temperature Of Cooling Water on COP and Refrigeration Capacity

Figure 6 shows the impact of cooling water temperature on the refrigeration capacity of the adsorption chiller. The refrigeration capacity decreases with increasing cooling water temperature. If the cooling water temperature increases from 18 to 32 °C, the refrigeration capacity decreases from 8 kW to 4 kW. The results show in Table 3 that the refrigeration capacity is very susceptible to any change in the cooling water temperature.

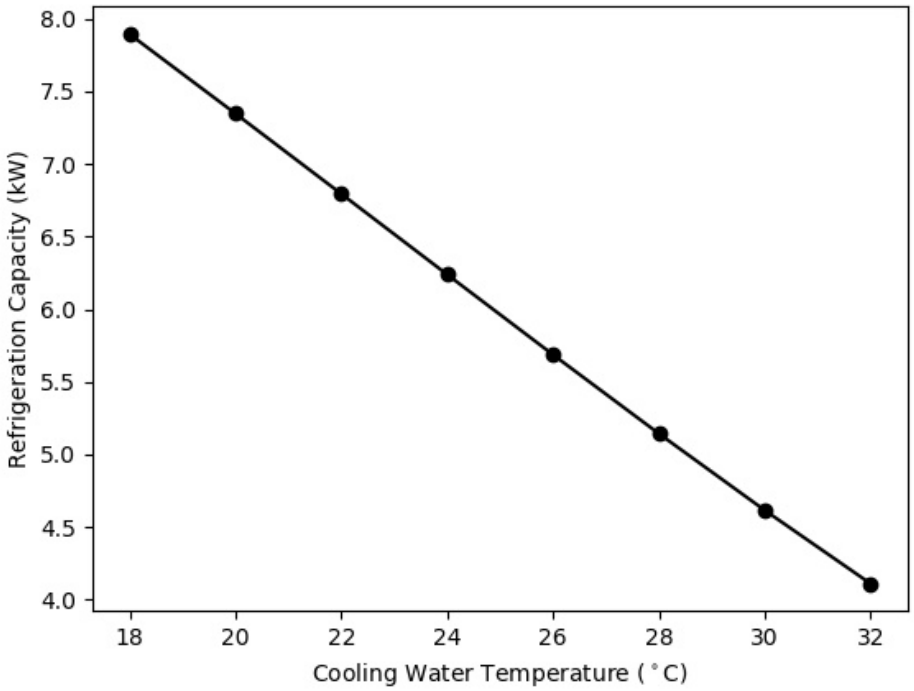

Figure 6. Impact of the varying temperature of cooling water on refrigeration capacity.

Figure 7 shows the impact of cooling water temperature on the performance coefficient of the adsorption chiller. The performance coefficient decreases with the increasing temperature of the cooling water. When the temperature of the cooling water increases, the performance coefficient value is influenced by the two factors. The first factor the refrigeration capacity decreases with increasing cooling water temperature. The second factor is the sensible heating of the adsorption. The desorption temperature reduces in the adsorption system. The decrease in performance coefficient indicates that the first factor is more effective than the second factor.

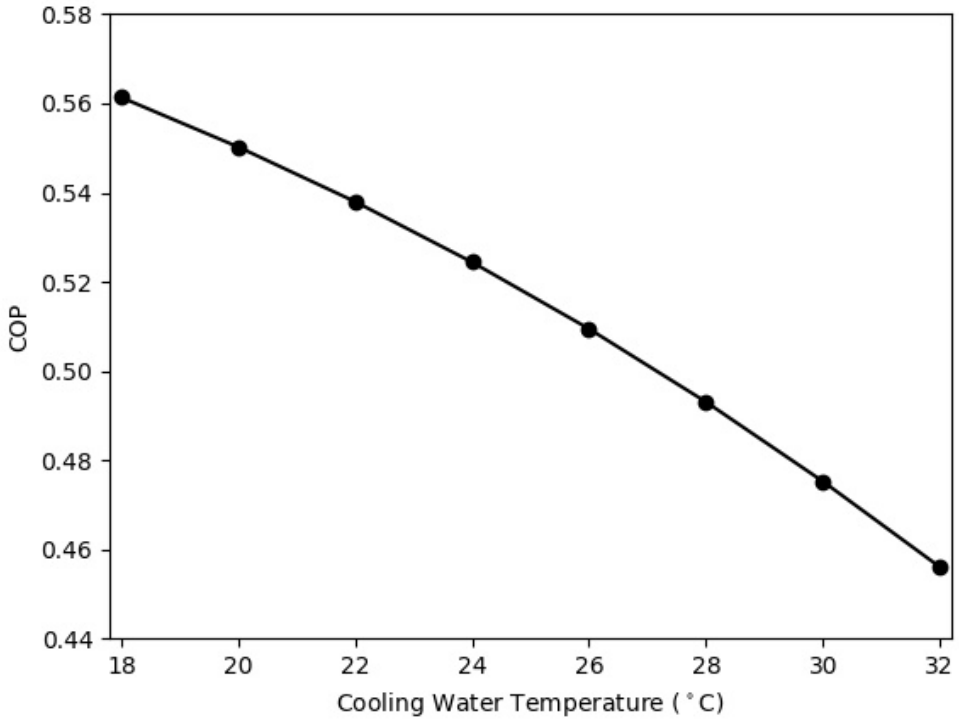

Figure 7. Impact of varying temperature of cooling water on COP.

Table 3. Impact of cooling water temperature on refrigeration capacity and COP.

Cooling water temperature (°C)	Refrigeration Capacity (kW)	COP
18	7.9	0.56
20	7.3	0.55
22	6.8	0.54
24	6.2	0.52
26	5.7	0.51
28	5.1	0.49
30	4.6	0.48
32	4.1	0.46

5. CONCLUSION

The performance of a two-bed adsorption chiller is examined under target operating conditions. The two-bed adsorption chiller uses silica gel-water as adsorbent-adsorbate working pair. The amount of silica gel used is 20 kg.

The following conclusions can be drawn from the above work:

· The impact of increasing hot water temperature on the refrigeration capacity is significant in temperatures between 40-70°C.
· There is an optimum hot water mass flow rate for the maximum attainable COP.
· When the desorption heat need is exceeded, there is any positive effect on desorption, and the same applies to the refrigeration capacity and COP.
· The performance coefficient decreases with the increasing temperature of the cooling water.
· The refrigeration capacity is very susceptible to any change in the cooling water temperature.

REFERENCES

[1] Zhu, L.Q., Tso, C .Y., , He W., Wu, C.L, Chao C.Y.H., 2017, A field investigation of a solar-powered adsorption cooling system under Guangzhou's climate with various numbers of heat exchangers in the adsorbers, *Science and Technology for the Built Environment*, 0, 1–11.

[2] Thakare A.M., Deshmukh S.J., 2018, Performance Analysis of Solar Powered Adsorption Cooling System, ICUE 2018 on *Green Energy for Sustainable Development Thavorn Palm Beach Resort Karon*, Phuket, Thailand.

[3] Rezk, H., Alsaman, A.S., Al-Dhaifallah, M., Askalany, A.A., Abdelkareem, M.A., Nassefa, A.M., 2019, Identifying optimal operating conditions of solar-driven silicagel based adsorption desalination cooling system via modern optimization, *Solar Energy*, 181, 475-489.

[4] Sayfikar M., Behbahani A., 2013, Study of the performance of a solar adsorption cooling system Energy Equipment and Systems, l1, 75-90.

[5] Alsaman A.S., Askalany A.A., Harby K., Ahmed M.S, Performance evaluation of a solar-driven adsorption desalination-cooling system, Energy, 128, 196-207.

[6] Reda A.M., Ali A.H.H., Taha İ.S., Morsy M.G., 2017, Performance of a small-scale solar-powered adsorption cooling system, *Internatıonal Journal Of Green Energy*, 14: 1, 75–85.

[7] Raj R., Baiju V., Thermodynamic Analysis of a Solar Powered Adsorption Cooling and Desalination System, Energy Procedia, 158, 885-891.

[8] Papoutsis E. G.; Koronaki I. P.; Papaefthimiou V.D., Parametric Study of a Single-Stage Two-Bed Adsorption Chiller, J. *Energy Eng.*, 04016068.

[9] Gupta, Y., 2011, Research and Development of a Small-Scale Adsorption Cooling System. *Arizona State University*.

[10] Zhang, L.Z., A three-dimensional non-equilibrium model for an intermittent adsorption cooling system, *Solar Energy* ,69 (1) (2000) 27-35.

THE PERFORMING OF THERMODYNAMIC ANALYSIS OF R134A REFRIGERANT AND ALTERNATIVE REFRIGERANTS ON THEIR APPLICATION AREAS

Ömer Faruk SEL*, Oktay HACIHAFIZOĞLU, Ünsal AYBEK***, Ahmet CİHAN******
* Trakya University, Department of Motor Vehicles and Transportation Technologies, Edirne/Turkey
Email: omerfaruksel@trakya.edu.tr
**Trakya University, Department of Mechanical Engineering, Edirne/Turkey
Email: oktayh@trakya.edu.tr
*** Tokat Gazi Osmanpaşa University, Department of Electric And Energy, Tokat/Turkey
Email: unsal.aybek@gop.edu.tr
**** Beykent University, Department of Mechanical and Architecture Engineering, İstanbul/Turkey
Email: ahmetcihan@beykent.edu.tr

ABSTRACT

Fluorocarbon and chlorofluorocarbon refrigerants are widely used in vapor-compression refrigeration systems. Due to the high ozone depletion potential (ODP) and global warming potential (GWP) of these refrigerants which are used, alternative fluid exploration studies are ongoing. In this study, alternative refrigerants for R134a refrigerant which are especially and commonly used in vehicle and household refrigerants which have zero ozone depletion potential but high global warming potential were investigated. R32, R152a and R1234yf coolants which has lower Global warming potential as alternative were used. A detailed energy and exergy analysis of these refrigerants is presented according to the theoretical vapor compression refrigeration cycle. Besides, the Performance Coefficients (COP) of the cooling cycle were theoretically compared. In addition to these, the behavior of these alternatives in different application fields and in different cooling conditions in the literature was examined.

Keywords: Energy, Exergy, RT134a-R32-R152a-R1234yf

Symbols

COP	Coefficient of Performance
ODP	Ozone Depletion Potential
GWP	Global Warming Potential
E_d	Exergy Destruction [kW]
$E_{d,cond}$	Exergy Destruction in the Condenser [kW]
$E_{d,comp}$	Exergy Destruction in the Compressor [kW]
$E_{d,ev}$	Exergy Destruction in the Evaparator [kW]
$E_{d,throttle}$	Exergy Destruction in the Expansion Valve [kW]
E_x	Exergy of Refrigerant [kW]
h	Enthalpy [kJ/kg]
$\dot{m}$	Mass Flow of Refrigerant [kg/h]
η_{exergy}	Exergy Efficiency
s	Entropy [kJ/kgK]
P	Pressure Ratio
T	Temperature [K,ºC]
T_c	Condensing Temperature [K,ºC]
T_e	Evaporation Temperature [K,ºC]
T_0	Dead-State Temperature [K,ºC]
T_r	Cooling Room Temperature [K,ºC]
W_c	Compressor Work [kW]

1. INTRODUCTION

The fact that energy generation sources are limited and energy generation costs are high has brought with it the necessity to use the available energy effectively and efficiently. With the decrease of energy sources day by day, as a result of the increase in energy consumption, the use of heat recovery systems and heat pumps have increased. Effective use of energy is also a necessity in the heating and cooling systems we need in every area of our daily life. Refrigerants are used as a transfer medium in cooling systems to transfer heat from one medium to another [1].

Considering the required features in cooling systems, many researches have been conducted on the development of refrigerants that do not damage the ozone layer and do not have a negative impact on global warming instead of the refrigerants that are prohibited or restricted to use. Effective use of energy is the basis of these studies. There is no single and perfect refrigerant in nature. Some may be suitable for high temperature applications, while others are suitable for low temperature applications. Toxicity, flammability, density, viscosity, availability and most importantly environmental effects of the refrigerant to be selected for a particular application should be taken into consideration, not only the heat-conveyance capacity. Therefore, alternative gases have been developed in place of gases that harm nature [2].

The existing refrigerant used in the automobile air conditioning systems is the R134a refrigerant, which is from the hydrofluorocarbon (HFC) refrigerant group. R134a refrigerant has a GWP value of 1430 [3].
In studies, it was determined that R152a refrigerant is a refrigerant with very good heat-conveyance and thermodynamic properties due to its high latent heat capacity and low kinematic viscosity and that R1234yf refrigerant is an environmentally friendly refrigerant due to the short term atmospheric lifetime. [4,5]. It was concluded that the R1234yf refrigerant is a long term usable fluid with acceptable performance levels [6].

In this study, R32, R152a and R1234yf refrigerants with lower global warming potential, which are alternative to R134a refrigerant, were used. A detailed energy and exergy analysis of these refrigerants was presented according to the theoretical vapor compression refrigeration cycle. In addition, the efficiency coefficients of the refrigeration cycle were theoretically compared and in addition, the behaviors of these alternatives in different application areas and different refrigeration conditions in the literature were examined.

2. CHARACTERISTICS OF REFRIGERANTS

2.1. Classes, Similarities and Application Areas of Refrigerants

Table 1. Types and chemical formulas of refrigerants [7].

Refrigerants	Type	IUPAC Chemical Name	Molecular Formula
R134a	HFC	1,1,1,2-Tetrafluoroethane	CH_2FCF_3
R32	HFC	Difluoromethane	CH_2F_2
R152a	HFC	1,1-Difluoroethane	$C_2H_4F_2$
R1234yf	HFO	2,3,3,3-Tetrafluoropropene	$C_3H_2F_4$

Similarity to R134a and Application Areas: It is the refrigerant with the most similar properties to R12 in terms of its physical and thermodynamic properties. It is the most suitable refrigerant in terms of having the ozone depletion coefficient of 0 and other features. It is the most suitable alternative for car coolers and air coolers. It is also available commercially [8].

Similarity to R152a and Application Areas: R152a, which has a better COP value than R12 and R134a, is also compatible with mineral oils. R152a , which is flammable and odorless, does not show toxic properties. Its

thermodynamic and physical properties are very close to ones of R12 and R134a. It is considered an alternative for R12 and R500 in heat pumps [8].

Similarity to R32 and Application Areas: It is a refrigerant used instead of R22. It is used in commercial coolers and industrial cooling systems. Ozone depletion potential is low [8].

Similarities to R1234yf and Application Areas: In accordance with the F-Gas regulation of the European Union, R1234yf with similar thermodynamic properties is planned to be used instead of R134A gas, which contributes to global warming. The performance ratings of the new gas, mostly used by car manufacturers and services, is very similar to the ones of R134a gas it replaces.

2.2 Environmental Properties

Ozone depletion potential, global warming potential and atmospheric lifetime are important factors that show the environmental impact of the refrigerant when released to the environment. Table 2 shows the environmental properties of the refrigerants used.

Table 2. Environmental Properties of Refrigerants [13,14].

Refrigerants	Atmospheric Lifetime	GWP	ODP
R134a	14 years	1430	0
R32	4,9 years	675	0
R152a	1,4 years	126	0
R1234yf	12 days	4	0

2.3 Physical Properties of Refrigerants

Table 3 shows the physical properties of the refrigerant. Physical properties determine the energy performance of the cooling system. High latent heat of evaporation indicates lower refrigerant mass requirement.

Table 3. Physical Properties of Refrigerants [9,10,11].

Refrigerants	Normal Boiling Point (ºC)	Critical Tempeture (ºC)	Critical Pressure (kPa)	Latent Heat (kJ/KG)
R134a	-26,09	101	4059	198,72
R32	-51,75	78,1	5780	381,86
R152a	-24	113	4516	279,36
R1234yf	-29,52	94,7	3381	172,37

3. INTRODUCTION OF THE SYSTEM

The vapor compression refrigeration cycle is the most common type of cycle used in refrigeration machines, air conditioning systems and heat pumps [12]. In this study, single-stage vapor compression refrigeration cycle was examined and its theoretical analysis was conducted.

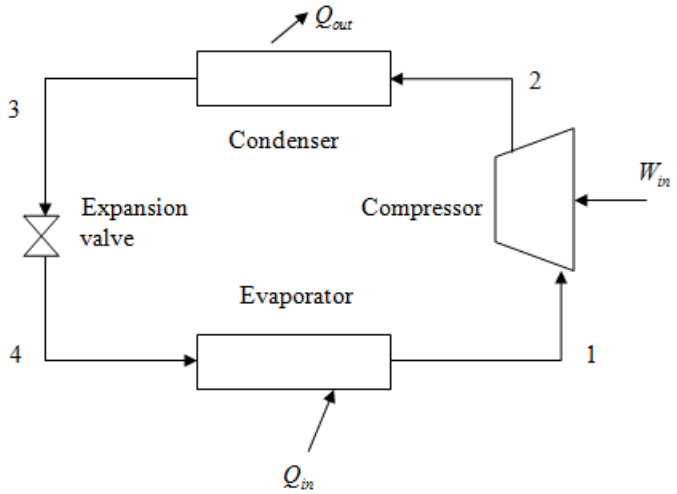

Figure 1. Schematic diagram of the single-stage vapor compression refrigeration cycle.

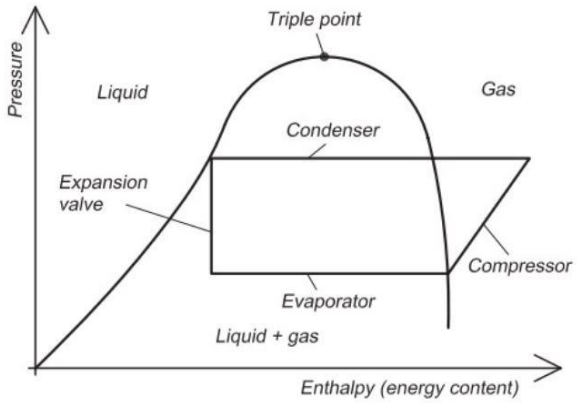

Figure 2. Single-stage vapor compression refrigeration cycle on a P-h diagram.

In the ideal vapor compression refrigerant cycle, the refrigerant enters the compressor in the saturated vapor phase and heat is released into the environment until it becomes saturated liquid in the condenser. Then, the refrigerant is throttled to the evaporator pressure in the throttle valve and the evaporator absorbs heat from the cooled medium and evaporates the refrigerant [13].

4. PERFORMANCE ANALYSIS OF THE SYSTEM

Analysis of system performance has been made according to the following assumptions:

.

- Evaporator temperature T_{evap}: Changes from –10 ºC to +15 ºC
- Condensing temperature T_{cond} = 45 ºC.
- Ambient temperature T_0 = 25 ºC. In some analyzes changes of T_0=15 ºC - 35 ºC was examined.
- There is no compression loss in the pipelines
- The compressor is isentropic.

Performance parameters were determined by using thermodynamic properties and related equations in each case. A modern approach based on the second law of thermodynamics, namely exergy analysis, can be used to measure the performance of the vapor compression refrigeration system. This analysis invents the concept of exergy, which is always destroyed due to thermodynamic irreversibilities. Exergy is formally defined as the

maximum amount of useful work that can be obtained for the system under a specific condition. The exergy balance for a control volume undergoing dead state process is expressed as follows [14,15]:

$$E_d = \sum(me_x)_{in} - \sum(me_x)_{out} + [\sum(Q(1-T_0/T_r)_{in}) - \sum(Q(1-T_0/T_r)_{out})] \pm W \quad (1)$$

Exergy Destruction in System Components (E_d):

$$E_{d,ev} = E_{x4} + Q_L(1-T_0/T_r) - E_{x1} \quad (2)$$

$$E_{d,ev} = m_r(h_4 - T_0 s_4) + Q_L(1-T_0/T_r) - m_r(h_1 - T_0 s_1)$$

$$E_{d,comp} = E_{x1} + W - E_{x2}$$

$$E_{d,comp} = m_r(T_0(s_2 - s_1)) \quad (3)$$

$$E_{d,cond} = E_{x2} - E_{x3} \quad (4)$$

$$E_{d,cond} = m_r(h_2 - T_0 s_2) - m_r(h_3 - T_0 s_3) - m_r(1-T_0/T_c)$$

$$E_{d,throttle} = E_{x3} - E_{x4} \quad (5)$$

$$E_{d,throttle} = m_r(h_3 - T_0 s_3) - m_r(h_4 - T_0 s_4)$$

$$\sum E_d = E_{d,ev} + E_{d,comp} + E_{d,cond} + E_{d,throttle} \quad (6)$$

$$\eta_{exergy} = Q_L/W_C(1-T_0/T_r) \quad (7)$$

5. RESULTS AND DISCUSSION

The compression ratio, compressor discharge temperature, exergy destruction and cooling efficiency values of the refrigerants were drawn according to the change of evaporation temperatures at constant condensation temperatures under the cooling conditions determined for the refrigeration cycle. In addition, cooling efficiency and exergy efficiencies were reexamined according to unsteady overcooling and ambient temperature conditions.

Low compression ratio in the system is desirable as volumetric and isentropic efficiencies, mass flow rate of coolant and COP of the system are expected to increase inversely to the drop in compression ratio. Figure 3 shows that the compression ratio decreases with the increase in evaporation temperature for constant condensation temperature. In all conditions, it was observed that the lowest compression rate occurs in R32 refrigerants and the highest compression rate occurs in R152 refrigerants.

With evaporation temperature increase of 25 ºC, compression ratios decreased by 58.31% in R134a, 54.49% in R32, 58.62% in R152a and 56.47% in R1234yf, respectively. Changes in compression, ratios depending on the evaporation temperature are given in Figure 3.

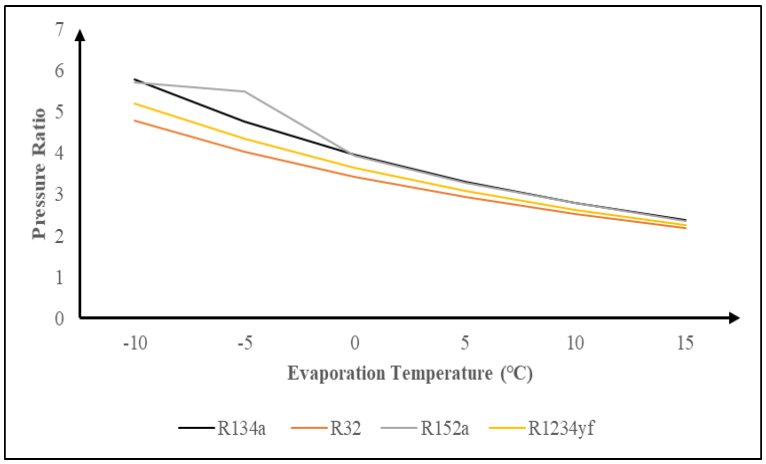

Figure 3. Change of Compression Ratios Depending on Evaporation Temperature.

Compressor discharge temperature (discharge temperature) is an important feature of an alternative refrigerant selection. Compressor discharge temperature increases the balance of the coolant and lubricant, extending the life of the compressor. It was observed that the lowest discharge temperature is in R1234yf refrigerant and the highest discharge temperature is in R32 refrigerant. The changes of discharge temperature depending on the evaporation temperature are given in Figure 4.

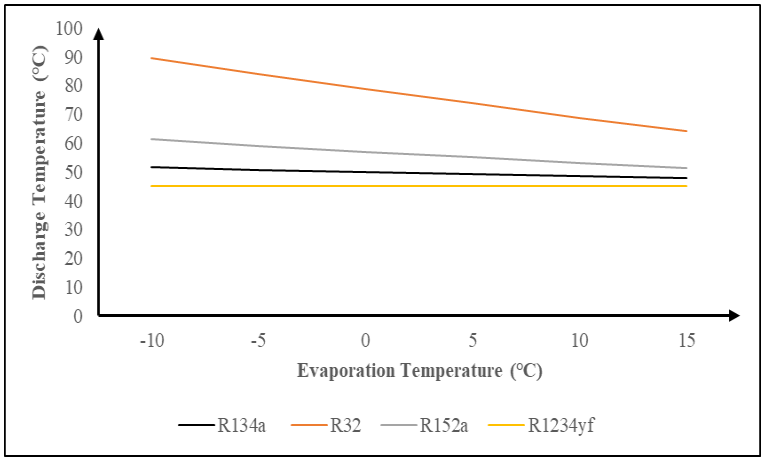

Figure 4. Change of Compressor Discharge Temperature Depending on Evaporation Temperature.

With the increase in evaporation temperature, the compression ratio decreases throughout the compressor, so the work done by the compressor decreases and the cooling capacity increases due to the increase in cooling effect. Therefore, the combined effect of these two factors increases the COP value of the vapor compression refrigeration system. Cooling efficiency was observed as large to small R152a, R134a, R32 and R1234yf, respectively. With the increase of 25 ºC of evaporation temperature, COP values increased by 124.8% in R134a, 125.5% in R32, 134.2% in R152a, and 128.8% in R1234yf respectively.

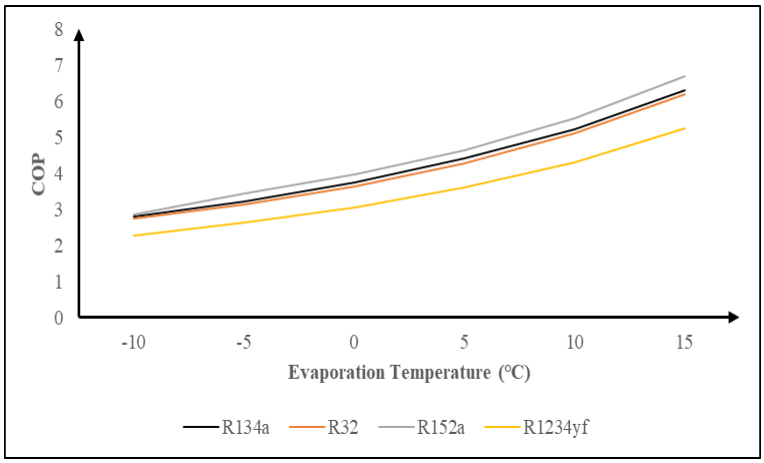

Figure 5. Change of Cooling Efficiency Depending on Evaporation Temperature.

Figure 6 and Figure 7 show the effect of evaporation temperatures on exergy destruction and exergy efficiency, respectively. Since the compressor is considered as isentropic in the system, exergy destruction in the compressor was not calculated. With the increase in the evaporation temperature, total exergy destruction was reduced. The lowest exergy destruction occurred in R134a refrigerant. But the increase of Q_L/W_C rate and decrease of T_0/T_r rate lowered exergy efficiency. R152a has the highest exergy efficiency in operating ranges. Then comes R134a, R32 and R1234yf respectively.

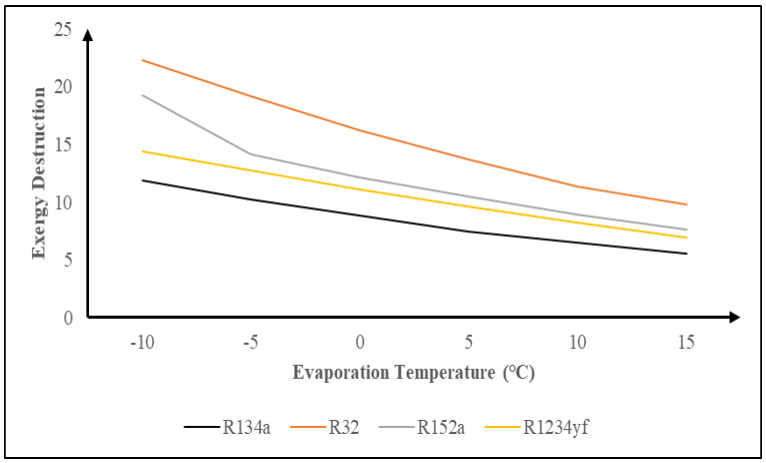

Figure 6. Change of Exergy Destruction Based on Evaporation Temperature.

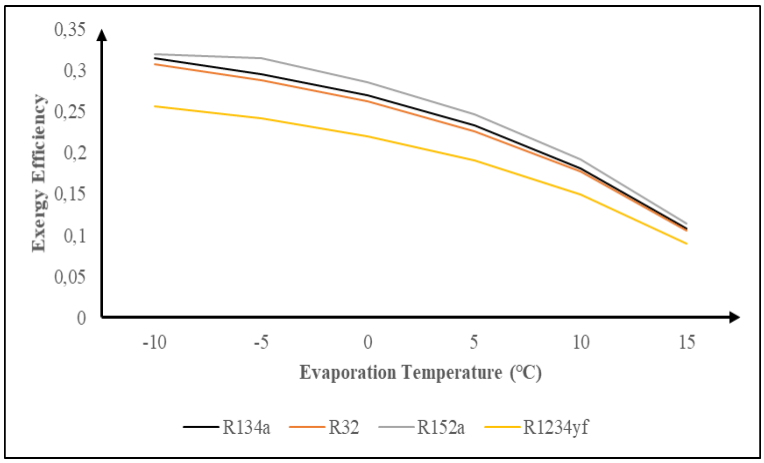

Figure 7. Change of Exergy Efficiency Depending on Evaporation Temperature.

Figure 8 shows the change of COP by overcooling the refrigerant at the condenser outlet. The increase in the degree of overcooling increased the cooling capacity and an increase in COP was observed, since there was no change in compressor operation. With the increase of 10 ºC of overcooling, cooling efficiency increased by approximately 10%.

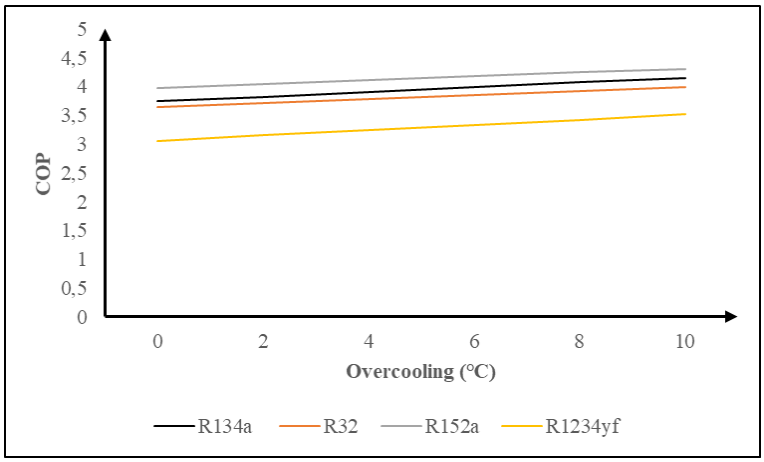

Figure 8. Replacement of COP with Overcooling.

Figure 9 and Figure 10 show the effect of overcooling on exergy destruction and exergy efficiency. Condenser exergy destruction increased due to overcooling. Despite the drop in the evaporator and throttle valve, total exergy destruction increased. It was observed that the lowest exergy destruction was in R134a while it was the highest in R32 refrigerant. With overcooling, entropy decrease at both the condenser outlet and the expansion valve outlet increased exergy efficiency. In general, we can say that overcooling has a positive effect on cooling efficiency and exergetic efficiency. For 45 ºC condensing temperature, 10 ºC overcooling increased refrigerant exergy yields by about 10% to 13%.

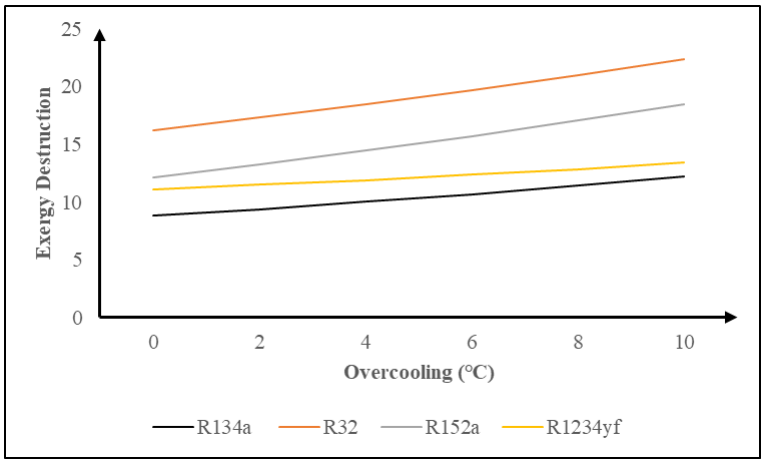

Figure 9. Change of Exergy Destruction by Overcooling.

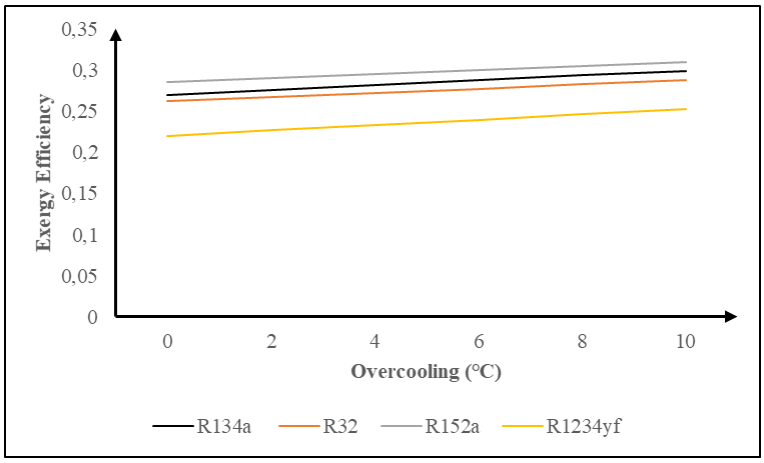

Figure 10. Change of Exergy Efficiency with Overcooling.

Figure 11 and Figure 12 show exergy destruction and exergy efficiency changes according to ambient temperature. It is a thermodynamic reality that entropy changes increase in exergy destruction as it increases at high temperature differences. It is clear that for the fact the ambient temperature and the condensing temperature are close to each other, it will increase the exergy efficiency. The lowest exergy destruction occurred in R134a refrigerant, the highest exergy efficiency occured in R152a refrigerant. The increase of 20 ºC in ambient temperature resulted in an increase of approximately 200% to 250% exergy efficiency.

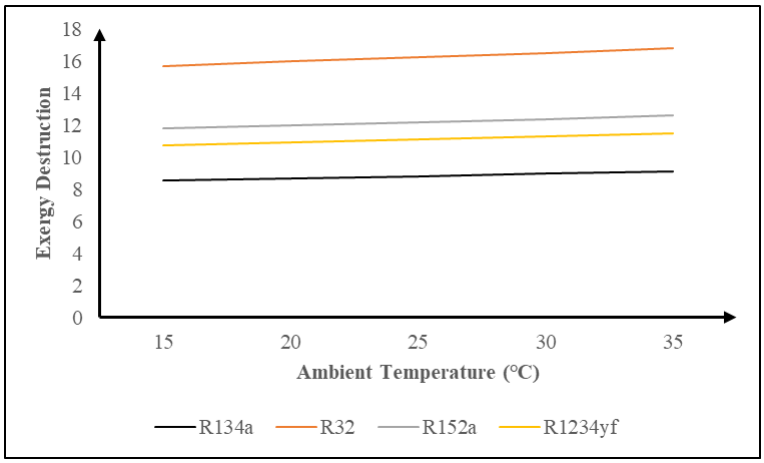

Figure 11. Change of Exergy Destruction with Ambient Temperature.

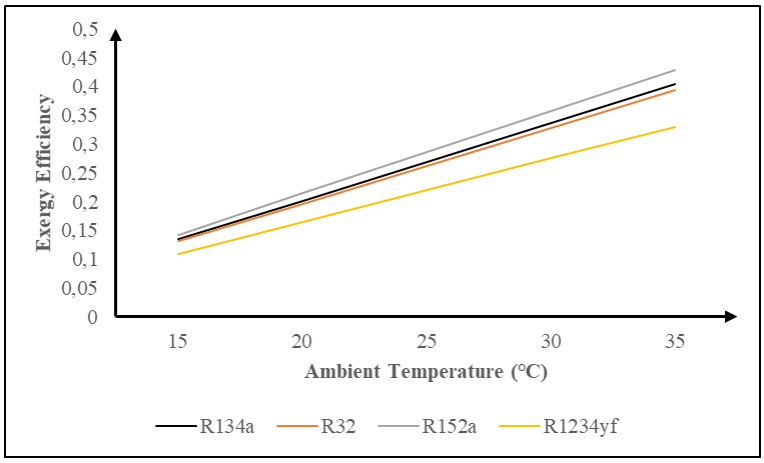

Figure 12. Change of Exergy Efficiency with Ambient Temperature.

5. CONCLUSIONS AND RECOMMENDATIONS

In this study, comparative performance analyzes of R32, R152a and R1234yf with R134a in an ideal vapor compression refrigeration cycle were performed for different evaporation temperatures at constant condensing temperature. with regard to low compression ratio, it has been observed that the best alternative is R32 refrigerant.

It has been observed that R1234yf has low compressor discharge temperature, which is an important factor that increases compressor life. In this respect, we can say that this refrigerant has superior properties in terms of being an alternative to R134a. However, the discharge temperatures of other alternatives are higher than R134a.

The cooling efficiency was observed at the highest level for R152a and it was followed by R134a, R32 and R1234yf, respectively. In terms of COP, the best alternatives to R134a are R152a and R32. In terms of exergy efficiency, R152a is superior to other alternative refrigerants. This indicates that other alternative refrigerants should be developed in terms of efficiency of both the first and second laws of thermodynamics Indeed, together with improvements on ODP and GWP effects, a reduction in energy efficiency is undesirable.

It was observed that the exergy efficiency of the refrigerants increased as the degree of overcooling increased. A similar effect is expected in the case of overheating that can be applied at the evaporator outlet. Exergy efficiency increased especially with the condensing temperature close to the ambient temperature. Since the condensing temperatures are adjusted according to the seasonal conditions at the highest temperature in order not

to interfere with cooling, exergy destruction will occur much above ideal conditions due to working conditions in cold weather conditions.

REFERENCES

[1] Özkol, N., "Applied Cooling Technique", *Chamber of Mechanical Engineers*, P. B.: MMO/2007/115/7, Ankara, 21-28, 55-72, 107-153, 2007.

[2]Gürler, S., "Exergy Analysis of Household Refrigerators Using Refrigerants R134 and R600a", *Master Thesis, Ege University Graduate School of Natural and Applied Science*, 2006.

[3]Shank, RK., "Automotive air conditioning systems historical developments the state of technology and future trends", *Heat Transfer Engineering*, 30(9):720–735, 2009.

[4] Honghyun, C., Hoseong, L., Chasik, P., "Performance characteristics of an automobile air conditioning system with internal heat exchanger using refrigerant R1234yf", *Applied Thermal Engineering*, 61(2):563–569, 2013.

[5]Navarro-Esbrí, J., "Mendoza-Miranda, J.M., Mota-Babiloni, A., Barragán-Cervera A., & Belman-FLores, J.M., "Experimental analysis of R1234yf as a drop-in replacement for R134a in a vapour compression system", *International Journal of Refrigeration*, 36:860–880, 2012.

[6]Cho, H., Lee, H. & Park, C., "Performance Characteristics of an Automobile Air Conditioning System with Internal Heat Exchanger Using Refrigerant R1234yf", *Applied Thermal Engineering*, 61:561–569, 2013.

[7]Koyun T., Koyun A. & Acar M., "Refrigerant Fluids Used in Cooling Systems and Their Effects on Ozone Layer", *Plumbing Engineering Journal N.* 88, pp. 46-53, 2005.

[8]Atalay H., "Modelling of Refrigerants Thermodynamic and Thermophysical Properties", *Master Thesis, Ege University Graduate School of Natural and Applied Science*, 2011.

[9] Yılmaz F. Tosun C., "Thermodynamic Analysis of Low Global Warming Potential hfo-1234ze with Fluid", *Erciyes University Journal of the Institute of Science and Technology*, 30(5):308-313 ISSN 1012-2354, 2014.

[10] Direk M., Yüksel F., "Effect of Environment and Flow Conditions on System Performance", *Erzincan University Journal of the Institute of Science and Technology*, 12(1), 106-115 2019, 12(1), 106-115 ISSN: 1307-9085, e-ISSN: 2149-4584, 2018.

[11] Selbaş R., YILMAZ F., "Thermodynamic Analysis of R410a and R32 Refrigerants in Vaporcompression Refrigeration Cycle", *SDU International Technologic Science*, Vol. 5, No 2, pp. 50-60, 2014.

[12] Akbulut U., Kıncay O., "Energy and Exergy Analysis in Vapor Compression Refrigeration Cycles", *Plumbing Engineering Journal*, N:94, pp. 24-32, 2006.

[13]Çengel Y. A., Boles M. A., "Thermodynamics: With an Engineering Approach", Translation Editor: Ali Pınarbaşı, İzmir, 2008.

[14] Choudhari C. S., Sapali S. N., "Performance Investigation of Natural Refrigerant R290 as a Substitute to R22 in Refrigeration Systems", *International Conference on Recent Advancement in Air Conditioning and Refrigeration*, India, 346-352, 2016.

[15] Khan N., Khan M., Ashar M., & Khan A. Z., "Energy and Exergy Analysis of Vapour Compression Refrigeration System with R12, R22, R134a", *Certified* Journal, ISSN 2250-2459, ISO 9001:2008 Volume 5, Issue 3, 210-216, 2015.

DEVELOPMENT AND THERMODYNAMIC ANALYSIS OF A HYBRID EVAPORATIVE EVAPORATOR AIR COOLING SYSTEM

Fırat ÖZDEMİR*, Ali GÜNGÖR**
*Ege University, Department of Mechanical Engineering, İzmir/Turkey
Email:firatozdemir2009@hotmail.com
** Ege University, Department of Mechanical Engineering, İzmir/Turkey
Email: ali.gungor@ege.edu.tr

ABSTRACT

In this study, performance analysis of a hybrid cooling system, which was developed by integration of an evaporative cooler and a cooling machine's evaporator, is conducted. A performance increase on a cooling machine is aimed at evaporative cooler integration. Researchers are conducted on different scenarios to indicate the highest increase of performance.

The evaporative cooler, cooling machine evaporator, and the fan, which are the primary units of the hybrid cooling system, are integrated due to six different scenarios and tested and analyzed for three different air velocities.

The variation of cooling capacity, temperature drop, energy consumption, etc., are studied for each system component and the whole system in each scenario, and these variances are linked with system performance.

Keywords: Evaporative cooling, cooling machines, air conditioning systems, humidification, evaporation

1. INTRODUCTION

Air Conditioning can be explained as a term, by adjusting spesific properties of a particular ambient air such as; humidity, temperature, and clearance to bring the environment to ideal conditions. Nowadays, air conditioning processes that are divided into branches such as heating, cooling, and ventilation, etc., are used not only to make living spaces comfortable but also to improve the quality of life indirectly. Cold storage depots that created for products in food, medicine, and medical fields without spoiling, greenhouses that allow agricultural products to be grown in different regions, cooling units that enable data centers to operate efficently in the IT field, etc., can be reproduced.

Energy spent on air conditioning has a large share in total energy consumption. Especially in the mid-generation climates, including our country, the energy spent for cooling in the summer period constitutes more than 50% of total energy consumption[1]. Evaporative cooling systems are air-conditioning devices with roots in ancient history, but are now prominent due to the many advantages they offer. These systems are efficient devices that can reach high cooling capacities with low energy consumptions. However, it is unlikely to be used in humid climates due to its nature.

This study, it is aimed to develop an energy-efficient cooling device by integrating an evaporative cooler into a cooling machine cooling coil. Combining evaporative coolers with various systems offers essential benefits in terms of providing comfort conditions. In the study, the changes in the ordering of the system components and the effects of air velocity were investigated. It has been found that the use of hybrid evaporative coolers offers significant advantages compared to conventional coolers.

2. EVAPORATIVE COOLING

The evaporative cooling process is an air conditioning process that is performed by making use of the mechanism of water to evaporate and form a cooling effect. As it is known, evaporation is an endothermic process that takes heat from the environment. During the evaporative cooling process, a certain amount of water evaporated into cooling air, and the required evaporation heat is drawn from this cooling air. This process operates based on the adiabatic evaporation. In this process, while the sensible heat is drawn from the air, the latent heat load, that is, the evaporative cooling, is the process of converting the sensible heat of the air into latent heat and proceeds along the constant enthalpy line in the psychrometric diagram. In the evaporative cooling process, the air to be cooled may only be cooled down to the wet-bulb temperature, of the inlet air. At this temperature evaporation stops because of the humidity saturation. During this process, the evaporated water vapor mixes with the cooled air, so it is released into the air as latent heat [2-4].

Since air humidification is performed in evaporative cooling, inlet airs temperature and humidity are essential parameters that directly affects the system efficiency. In hot and dry climates, because the air contains very little moisture, the evaporation amount and the evaporative cooling efficiency increases. This situation is also emphasized that moist climates decrease the efficiency of the process.

Evaporative cooling systems are applicationbased diverse systems. Basically there are three main application;
- Direct evaporative cooling (DEC)
- Indirect evaporative cooling (IEC)
- Cascade systems

However, there are also some more applications that can be divided into several subtitles.

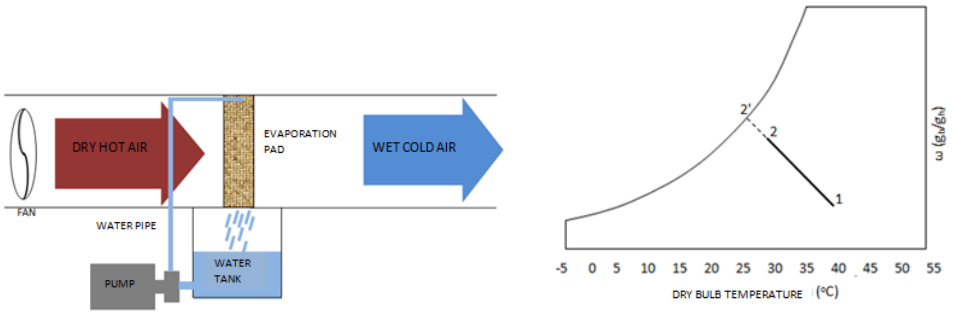

Figure 2.1 (a) Schematic and (b) Psychrometric display of a fan-pad direct evaporative cooler

.

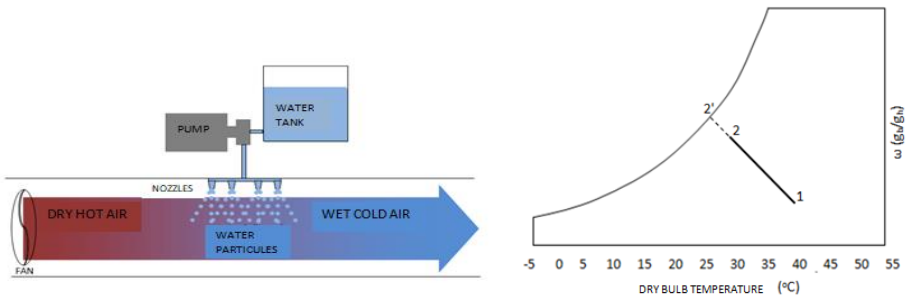

Figure 2.2 (a) Schematic and (b) Psychrometric display of a water spray direct evaporative cooler.

.

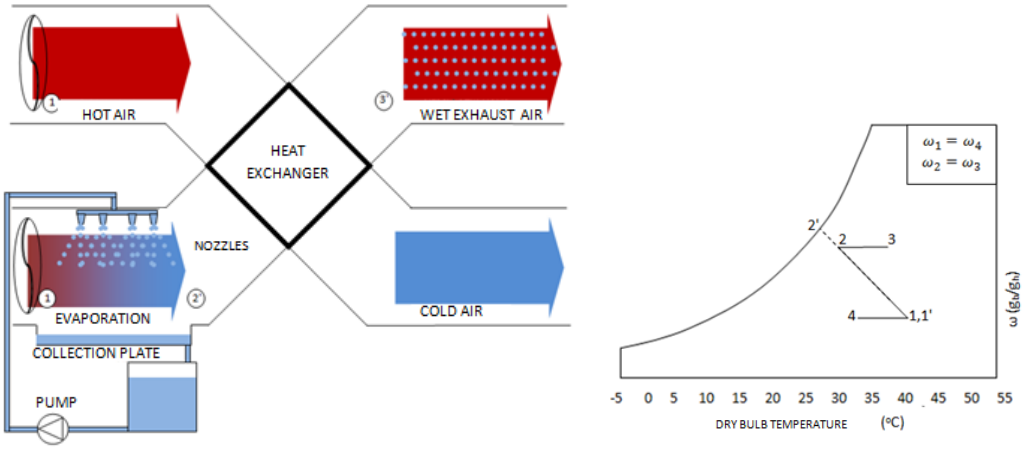

Figure 2.3 (a) Schematic and (b) Psychrometric display of an indirect evaporative cooler.

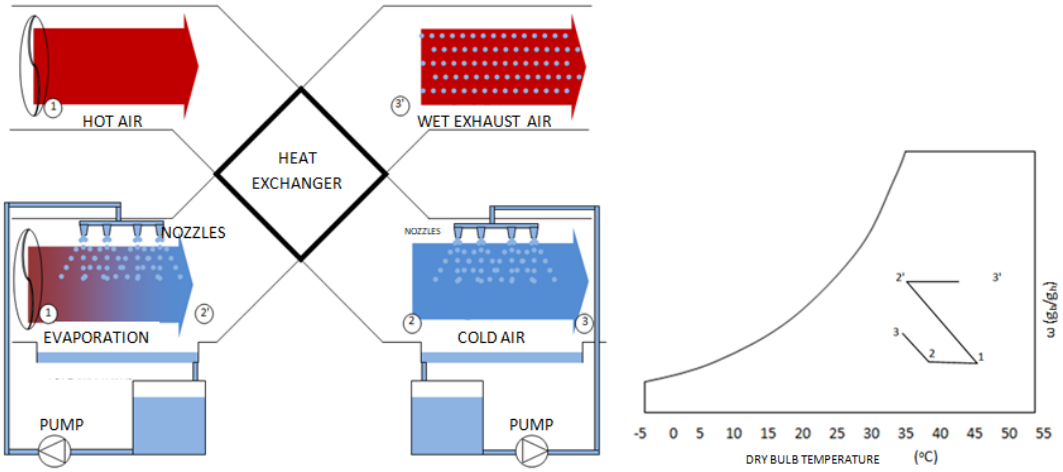

Figure 2.4. (a) Schematic and (b) Psychrometric display of a direct-indirect hybrid evaporative cooler

3. COOLING MACHINES

One of the common problems encountered in air-conditioning applications is the discharge of thermal energy drawn from a low-temperature sink to a high-temperature source. When heat transfer occurs under natural conditions, heat flows from a high-temperature source to a low-temperature sink. However, when it is necessary to condition an environment at a lower temperature than the ambient environment, for example, in the summer term, it is necessary to discharge heat from the environment to be conditioned[5].

Cooling machines are impressive devices that have can offer efficient solutions in reducing primary energy consumption while performing the heat transfer processes. Cooling machines, which are widely used in industrial and domestic applications, are systems that can be used in applications such as air conditioning and cold water production and efficiency-increasing applications like heat recovery. Basically, a simple cooling machine has four main components as;
-Compressor
-Condenser
-Expansion valve
-Evaporator.
However, there are some more complex modified systems to be able to offer more efficiency or satisfying different environmental conditions [6].

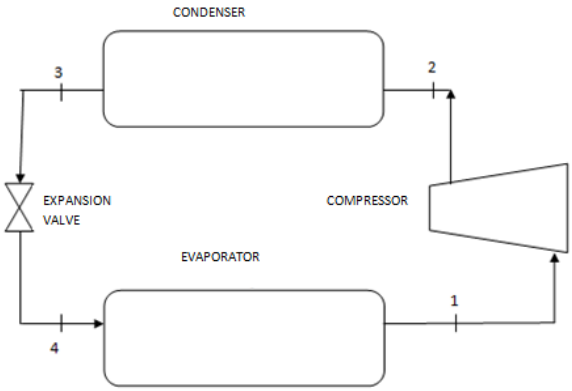

Figure 2.5 Schematic display of a basic cooling machine [7].

Schematic representation of the basic cooling machine is given in figure 2.5. The condenser and evaporator used in these systems are heat exchangers that provide heat transfer between the refrigerant used in the closed-loop and the heat sources. During the cycle, the refrigerant compressed in the compressor and converted to superheated steam, is sent to the condenser, where it draws heat from the fluid until it becomes saturated liquid. After the condenser section, the fluid entering the expansion valve to expand and cool down. Then, the fluid sent to the evaporator and draws heat from the heat source, and reaches the saturated vapor phase and it is sent back to the compressor for the second cycle. This processes (a) *T*-*s*, (b) *P*-h diagrams, shown in Figure 2.6.

.

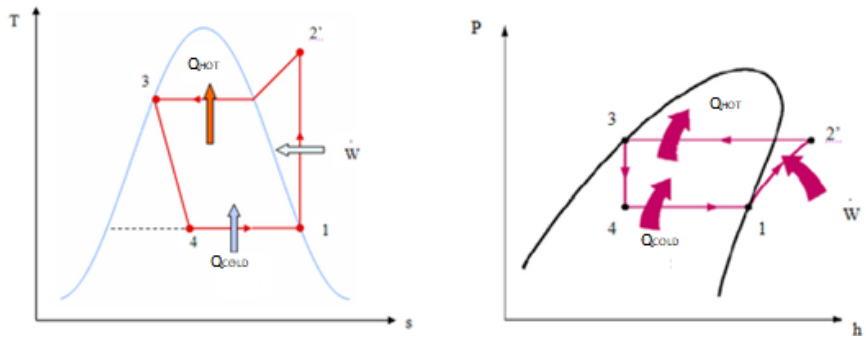

Figure 2.6 (a) T-s, (b) P-h diagrams of the cooling process which generated in a basic cooling machine [7].

In this study, an evaporative cooler pad is integrated into the evaporator of a cooling machine, operating with R-22 refrigerant. It is aimed to increase the cooling machine performance. Thermodynamic analyzes were carried out based on the experimental studies on the systems which are developed for this purpose.

4. MATERIALS AND METHODS

In the review of articles carried out, it was seen that satisfactory results were obtained from hybrid systems created with evaporative coolers. Heidarinejad et al. [8], in their study, the hot fresh air is drawn from the external environment enters the evaporative cooler after pre-cooling in the cooling coil. When the study results are examined, the average temperature drops during the 8-hour working period were recorded as 13.5ºC in total, 8ºC for the cooling coil, and 5.5ºC for the evaporative cooler. Cui et al. [9], in their research, they developed an integrated an indirect evaporative-vapor compression cooling system in order to benefit from the advantages of evaporative cooling. The cooling air is cooled in indirect cooler and vapor compression system, respectively. A numerical analysis of the system developed in the study was carried out. In line with the data obtained from the numerical analysis results, it was recorded that significant efficiency increases were realized with indirect evaporative pre-cooling in the vapor compression system. Tashtoush et al. [10] developed an open-absorption

cooling system that works by feeding on low energy sources such as waste heat and designed an integrated cooling system by coupling with an evaporative cooler. In line with the obtained results, it has been demonstrated that system performance has increased by 20% with using a combined evaporative cooling system. Camargo et al. [11], in their study, carried out a thermo-economic analysis of an evaporative cooling integrated with the absorption dehumidification system. According to results of the analyzes, it was recorded that the lowest operating costs were captured at the 71.1 ºC reactivation temperature. Sawant et al. [12] aimed to reduce the condenser pressure by pre-cooling the air entering the condenser unit of a window-type air conditioner with the evaporative cooling method improving the system COP. As a result of the experiments carried out, it was noted that the best COP value could reach 4.25.

In this study, experimental studies have been carried out using an integrated a fan-pad type evaporative cooler with an evaporator of a cooling machine. The developed system consists of three main components, one axial fan, one evaporative cooling unit, and one cooling machine.

In the evaporative cooling system designed, and manufactured, Celdek 50-90 type cellulosic evaporation pad with 340mm width, 400mm height and 100mm thickness was placed in the cassette slot in the channel. To wetting the evaporation pad, a circulation pump and the piping system placed in the water tank placed at the bottom of the evaporation pad. The water inlet into the water tank of the evaporative cooler is controlled by a solenoid valve and a float in the tank. The control mechanism of the system was maniplulated to drain the water in the tank when the system closed to avoid the grown of harmful organisms that may occur in stagnant water.

A frequency-controlled axial fan common in commercial applications, was used to ensure the flow of cooling air in the system. In the control mechanism, fan speed control is provided with a scale in the range of 1100 available. The cooling machine used in the system consists of an evaporator, a compressor, a condenser, an expansion valve, and a fan integrated on the condenser. The evaporatır of the cooling machine, where R-22 is used as the working fluid, consists of a copper tube-fin heat exchanger. In the developed system, fan, evaporative cooling unit, and cooling machine evaporator are connected with sheet metal ducts with 340×240mm cross-section and reductions.
In the study, the performance changes that occurred by replacing the system components on the developed system were investigated. In the system, six different setups have been designed with different combinations of an evaporative cooler, fan and cooling coil and experiments have been carried out in three different fan speeds, at the levels of 1, 50, and 100 on the scale ranging from 1 to 100..

Experimental setups created for each designed setup are named as System.1, System.2, System.3, System,4, System.5, and System.6.

Experimental studies were carried out at Ege University Faculty of Engineerin Mechanical Engineering Department Thermodynamics Laboratory, the tests were carried out under ASHRAE[14] Standards, in which the testing conditions of the evaporative cooling systems were described in details. The energy analyzes of the system were carried out by using the measurements that obtained from the tests have done.

In the analyzes, the evaporation efficiency of the evaporative cooling system is calculated by the process shown in equation 1. Here, system performance is defined as the ratio of the sensible cooling load provided by the system to the maximum cooling load that can be achieved.

$$\varepsilon = \frac{T_{i,DB} - T_{o,DB}}{T_{i,DB} - T_{i,WB}} \quad (1)$$

Here; ε: Evaporative cooler performance, $T_{i,DB}$: Inlet air dry-bulb temperature, $T_{i,DB}$:Inlet air wet-bulb temperature, $T_{o,DB}$: Outlet air dry bulb temperatures in Celcius.

In the analysis of the systems introduced, operations were carried out by using energy balance relations. Firstly, efficiency definitions were made, and then analyzes were carried out.

System efficiency COP (efficiency coefficient) is defined as the ratio of the cooling load obtained from the system to the power consumption.

$$COP_{System} = \frac{Systems\ Cooling\ Capacity}{Systems\ Power\ Consumption} \quad (2)$$

Here; Systems Cooling Capacity :The cooling load provided to the entire hybrid system, Systems Power Consumption The sum of cooling machine, fan and pumps energy consumptin.

In the analyzes made on the cooling machine, the efficiency was also defined over COP

$$COP_{CM} = \frac{Cooling\ Machines\ Cooling\ Capacity}{Cooling\ Machines\ Power\ Consumption} \quad (3)$$

The power consumption of each system was measured and recorded with panel type energy analyzer. Here energy and mass equations are used in the calculation of the cooling load obtained from the system.

In line with the data obtained from the system, first mass flow rates were calculated according to equation 2.

$$\dot{m} = \frac{V \times A}{\upsilon} \quad (4)$$

Here; $\dot{m}$: mass flow rate of air (kg/s), V: air velocity (m/s) A: cross-sectional area of the duct (m^2) υ: specific volume of the dry air (m^3/kg).

The specific volume values for each system were read from the psychrometric diagram, taking into account the air temperatures detected at the speed measurement points.

Mass balance of dry air:

$$\dot{m}_{a1} = \dot{m}_{a2} \quad (5)$$

energy balance:

$$\dot{m}_{a1} h_1 = \dot{m}_{a2} h_2 + \dot{Q}_s \quad (6)$$

Cooling capacity

$$\dot{Q}_s = \dot{m}_{a1}(h_1 - h_2) \quad (7)$$

Here, $\dot{m}_{a1}$: inlet air mass flow rate, $\dot{m}_{a2}$: outlet air mass flow rate h_1: inlet air enthalpy, h_2: outlet air enthalpy, $\dot{Q}_s$: The cooling capacity of the system.

The enthalpy values of the air were read from the psychrometric diagram, taking into account the temperature values measured at the inlet and outlet of each component of the system.

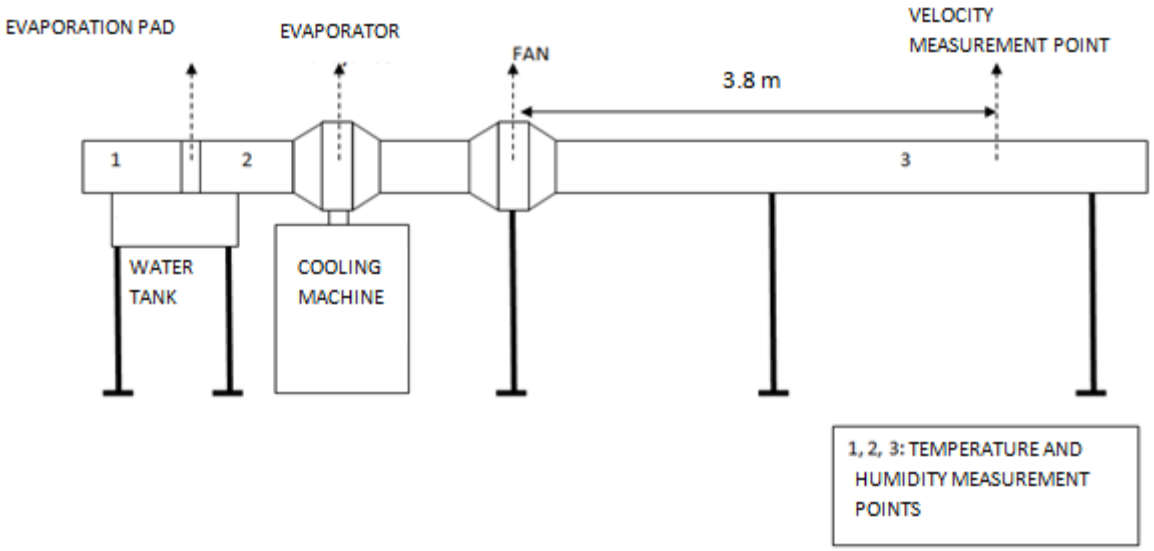

Figure 3.1 Schematic presentation of the experimental setup.

5. COMPARATIVE EVALUATIONS

In this section, changing performance, power consumption, etc., of the system created according to the constructions against the different airspeed values were examined. In Figure 4.1, changing COP values against different air velocities are given for each system and the single cooling machine.

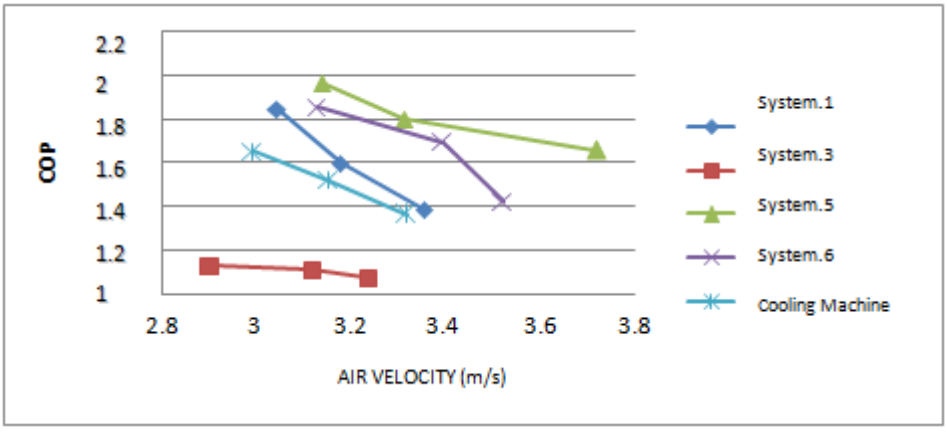

Figure 4.1 Changing COP values versus air velocity.

As can be seen in Figure 4.1, the results obtained from the tests performed on System.1, System.5, and System.6 offer higher COP values compared to the lean use of cooling machine. In system 3., it is observed that the performance has decreased significantly. Also, it is observed that the system COP decreases with increasing air velocity for the whole system.

Evaporative cooler performance was examined for each system developed in the experiments conducted. At the same time, it is known that the main factors determining the performance of evaporative coolers are inlet conditions. Performance changes against to the different air velocities are also observed. In Figure 4.2, the evaporative cooler performance for each system is examined in comparison with the lean tests of the evaporative cooling system.

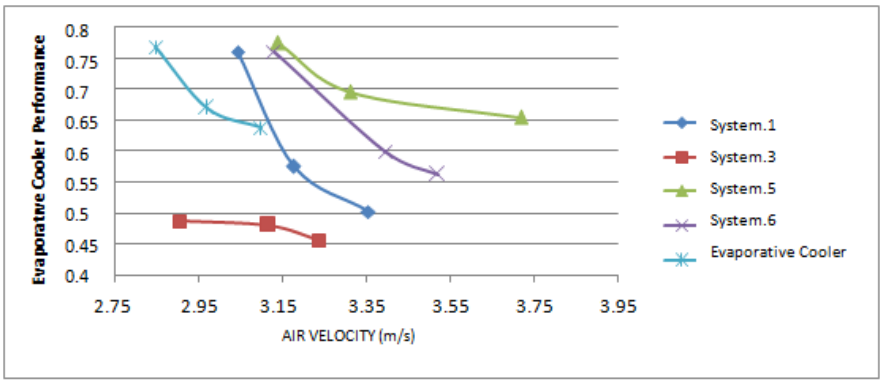

Figure 4.2 Changing evaporative cooler performance versus the air velocity.

As shown in Figure 4.2, the systems except for System.3 operate at the almost the same performance. In evaporative cooler unit, the system performance decreases with the increasing air velocity like integrated system
.

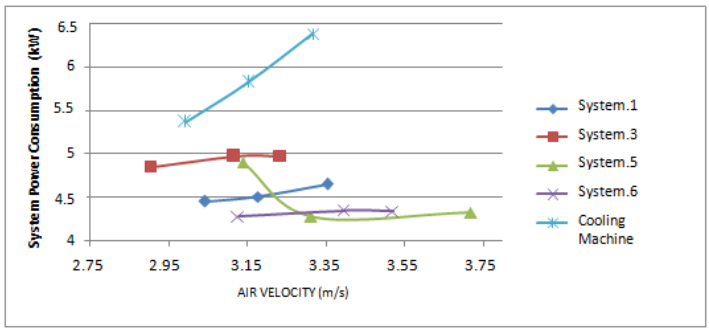

Figure 4.3 System power consumption values versus the changing air velocity.

In Figure 4.3, the changes in the total power consumption of each system against the air velocities are given. The primary variable in the effect of air velocity on system power consumption is the increasing fan power requirement to increase the air velocity. The graphics show that the cooling machine achieves the highest power consumption in lean use. The power consumption change graph for System.5 shows a decreasing curve, unlike the others.

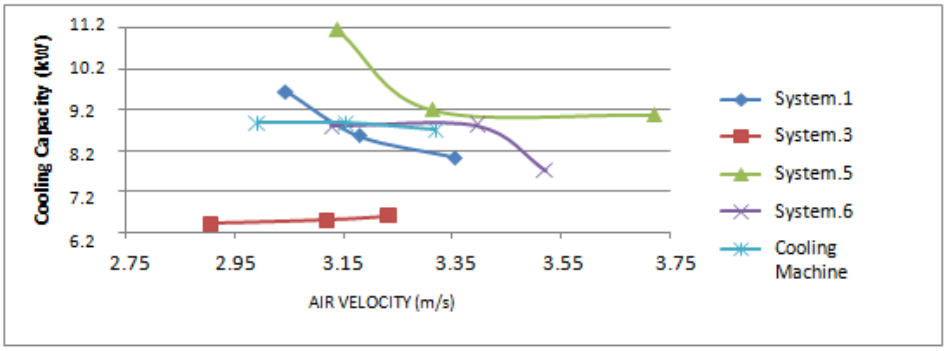

Figure 4.4 Changing cooling capacities versus the air velocity.

The changes in the cooling load values obtained from the tets from each system and the cooling machine are shown in Figure 4.4. Considering that the power consumption values of the designed systems cooling loads show

close results and it seen that the cooling load obtained from the system is one of the most crucial parameters to determine the system performance.

Table 4.1 Comparing the output air values obtained at different airflow rates for each system with the comfort conditions.

	Mass Flow Rate (kg/s)	Temperature (ºC)	Relative Humidity (%)
Comfort Standards Conditions	-	25	50
SYSTEM.1	0.51	8.3	89
	0.53	10.3	87
	0.56	10.73	89
SYSTEM.3	0.47	14.88	80
	0.51	15.88	82
	0.52	16.01	84
SYSTEM.5	0.52	10.01	85
	0.54	13.45	91
	0.61	15.38	82
SYSTEM.6	0.51	12.35	89
	0.54	14.81	84
	0.56	15.41	77

6. CONCLUSION

Compared to the results of the cooling machine, the results obtained from System.1, whiche was created as the fan-evaporation pad-cooling coil arrangement, the system COP increased by 1.6% to 11.48%. Based on the results obtained from the experimental studies, it is seen that the best performance increase is obtained for the lowest fan velocity for this system.

In the direction of the results obtained from System.3, which was constructed as cooling coil-fan-evaporation pad array, the system performance was observed to be adversely affected when the evaporation pad came after the cooling coil. The best results in three setups in which evaporation pad came after the cooling coil were obtained from the experiments on System.3. In the experiments on System.2 and System.4, where cooling coil-evaporation pad-fan and fan-cooling coil-evaporation pad sequences were applied, respectively, it was observed that no evaporation occurred on the pad. The reason for this situation is that the evaporation water temperature supplied to the pad is higher than the air temperature of the evaporation pad inlet. By reducing the temperature of the evaporation water, the system performance may be increased, and evaporation formation on the pad may be provided. However, it is anticipated that the efficiency values in applications in which the pad is placed after the coil will not be reached at the level of systems in which evaporative cooling is used as the pre-cooling system.

The results obtained from the cooling system named as System.5, and constructed as the evaporation pad-cooling coil-fan array, reveal that the highest performance increases on the integrated system are achieved with this system. It was observed that while the fan power values of this system created high power consumption values with increasing fan speed, the power consumption of the cooling machine unit decreases. It has been observed that the system COP has increased by up to 21% due to this situation.

When all systems are examined, it is seen that the relative humidity values of the cooling air are too high when compared to the comfort conditions. However, if these systems are used to cool the high volume areas, it is foreseen that the air in the space will remain in comfort conditions in terms of humidity, considering that it will form a gas mixture with the existing dry air in the environment.

As a result;

- It is observed that the coolers created by combining the evaporative cooling systems with traditional systems have obtained impressive data that offer significant performance increases.

-It has been determined that the system's efficiency has increased significantly by using the evaporative cooler as the pre-cooling unit in the integrated systems.

-In all arrays where evaporative coolers are placed after the cooling coil, these applications are not recommended because system performance is affected negatively.

-In the majority of the tested systems it was observed that the performance of the system decreased with the increase of air velocity, and it was predicted that this situation was caused by the decrease in the heat transfer process and evaporation rate at higher air velocities.

-Considering the extra cooling load provided by evaporative coolers with their low operating costs, it is seen these systems are used in their simplicity according to the climatic conditions or in the form of integration with other systems.

REFERENCES

[1]İleri, A.M.Ü., Türkiye Şehirleri için Tipik İklim Verileri, TESKON, 1998, İzmir.

[2] Cüce, P.M. and Riffat S., 2015, A State of The Art Review of Evaporative Cooling SystemsforBuilding Applications, Renewable and sustainable energy reviews, 54:1240-1249.

[3] İdiz, A., Koçak, Y.C., Özdemir, F., Akdemir, Ö., Güngör, A., İklimlendirme Sistemlerinde Evaporatif Soğutma Uygulamaları, TESKON 2017 , İzmir

[4] Genceli, O. F., Buharlaşmalı Serinletme Özellikleri ve Uygulamaları, TESKON, 1993.

[5] Büyüktür, A. R.,1985, Termodinamik Cilt 2, Uludağ üniversitesi basımevi, 445s

[6] Arpagaus, C.,Bless, F.,Schiffmann, J. andBertsch, S.S., 2016, Multi-temperature heat pumps: A literature review, International journalof refrigeration, 69: 437-465

[7] Çengel, Y., A., Boles, A., M., Thermodynamics An Engineering Approach, İzmir Güven Kitabevi, ISBN: 978-975-6240-26-7

[8] Heidarinejad, G.,Farahani, M.F. andDelfani, S., 2010, Investigation of a hybrid system of noctural radiative cooling and direct evaporative cooling, Building and environment, 45: 1521-1528

[9] Cui, X.,Chua, K.J. andYang, W.M., 2014, Use of indirectevaporative cooling as pre- cooling unit in humidtropicalclimate: an energysavingtechnique, Energyprocedia, 61:176-179

[10] Tashtoush, B, Tahat, M., Al-Hayajneh, A., Mazur, V.A. andProbert, D., 2001, Thermodynamic behaviour of an air-conditionin gsystem employing combined evaporative-water and air coolers, Applied energy, 70:305-319

[11] Camargo, J. R., Ebinuma, C. D. and Silviera, J. L., 2003, Thermoeconomic analysis of an evaporative desiccant air conditioning system, Applied thermal engineering, 23:1537-1549

[12] Sawant, A.P.,Agrawal, N. andNanda, P., 2012 performance assessment of an evaporative cooling-assisted window air conditioner, 7: 128-136(pp)

[13] ASHRAE Standard 55

PERFORMANCE ANALYSIS OF SOLAR AND GEOTHERMAL ENERGY POWERED KALINA CYCLE

Merve SENTURK ACAR*, Oguz ARSLAN
Mechanical Engineering Dept., Engineering Faculty, Bilecik Seyh Edebali University, Bilecik, Turkey
* Email: merve.senturkacar@bilecik.edu.tr
Email: oguz.arslan@bilecik.edu.tr

ABSTRACT

In this study, solar energy and geothermal energy powered Kalina cycle (SGEP-KC) was investigated according to the thermodynamic and economic analysis. The heat obtained from the parabolic solar collector integrated geothermal energy powered Kalina cycle with thermal energy storage. The geothermal energy used in Kalina cycle is a primary energy source. The energy efficiency, exergy efficiency and Net Present Values (NPV) of Kalina cycles were investigated according to solar radiation, geothermal fluid return temperature, turbine inlet pressure and condenser pressure. Solar radiation values of Kutahya Province were used in thermodynamic and economic analysis. As a result, the most effective geothermal fluid return temperature, turbine inlet pressure and condenser pressure values were respectively determined as 353.15 K, 3808 kPa and 700 kPa for all global solar radiation values according to the thermodynamic analysis. The energy efficiency and exergy efficiency values for the specified operating parameters were respectively calculated as 14.2453 % and 47.2261 % for the highest radiation value of 6.48 kWh/m^2· day. The most effective geothermal fluid return temperature, turbine inlet pressure and condenser pressure values were respectively determined as 373.15 K, 4308 kPa and 700 kPa for all global solar radiation values according to the economic analysis. The NPV values of these system configurations were determined as 23.6584 Million US$ and 101.7955 Million US$ for the highest monthly solar radiation value and the lowest monthly solar radiation value of 1.51 kWh/m^2 day, respectively. The system was found to be worth investment as a result of thermodynamic and economic analysis.

Keywords: Kalina Cycle, Energy, Exergy, Geothermal Energy, Net Present Value

1. INTRODUCTION

The use of renewable energy sources has gained importance due to the increase in energy needs parallel to the increasing world population and the environmental effects of fossil sources. For this reason, the use of low enthalpy geothermal energy resources and low temperature solar energy in power plant has been the subject of many studies in recent years.

In literature, the power plants cycle types were analyzed according to the energy and exergy analysis [1,2]. There are some investigations about system parameters and working fluids [3,4]. Moreover, there are studies about solar and geothermal integrated power plants [5,6]. Hong et. al. [7] investigated energy efficiency of Kalina Cycle powered with solar energy at a medium temperature according to the aperture area of the collector with a variation of direct radiation. They stated that solar energy energy efficiency reaches 4-20% with direct normal radiation at the limit of 100-1000 W / m^2, and the energy efficiency of annual solar power generation is about 14%. Mehrpooya and Mousavi [8] investigated the exergy destruction cost rates of the system components by conducting advanced exergy analysis for the solar-powered Kalina Cycle. As a result of advanced exergy analysis, they determined that the highest exergy destruction cost rate and exergoeconomic factors were 1.3 $/h and 85.88% for absorber and turbine, respectively. Zare and Moalemian [9] concluded that the exergy efficiency of the Kalina Cycle with the parabolic solar collector reached 14% according to the thermodynamic and economic analysis. Also, they stated that increasing the number of series-connected collectors for decreasing the electricity unit price is more effective than increasing the number of parallel-connected collectors.

In this study, annual Net Present Value (NPV), energy and exergy efficiencies of the solar and geothermal energy powered Kalina Cycle (SGEP-KC) was examined through the thermodynamic and economic analysis. The SGEP-KC was designed by taking into consideration the characteristics of Simav geothermal field and global radiation values of Simav. The solar radiation values of each month were used in the analysis and designs as a variable.

2. DESIGN OF SOLAR AND GEOTHERMAL ENERGY INTEGRATED ORGANIC RANKINE CYCLE

Diagram of SGEP-KC was given in Fig. 1. As seen in Fig. 1, the solar energy is integrated to the power cycle with the thermal energy storage tank. Thermal energy storage tank has been used to utilize solar energy equally all day. Therminol and salt were used as working fluid in the parabolic collector and TES, respectively. The heat of geothermal energy is transferred to the working fluid with the heat exchanger (H.E. 1). The heated working fluid enters to the heat exchanger (H.E. 2) and takes the heat of salt. Then, the working fluid enters to the separator and separates two flows. The vapor phase stream enters to the turbine and expanded. The properties of the system units and system parameters were given in Table 1. and Table 2.

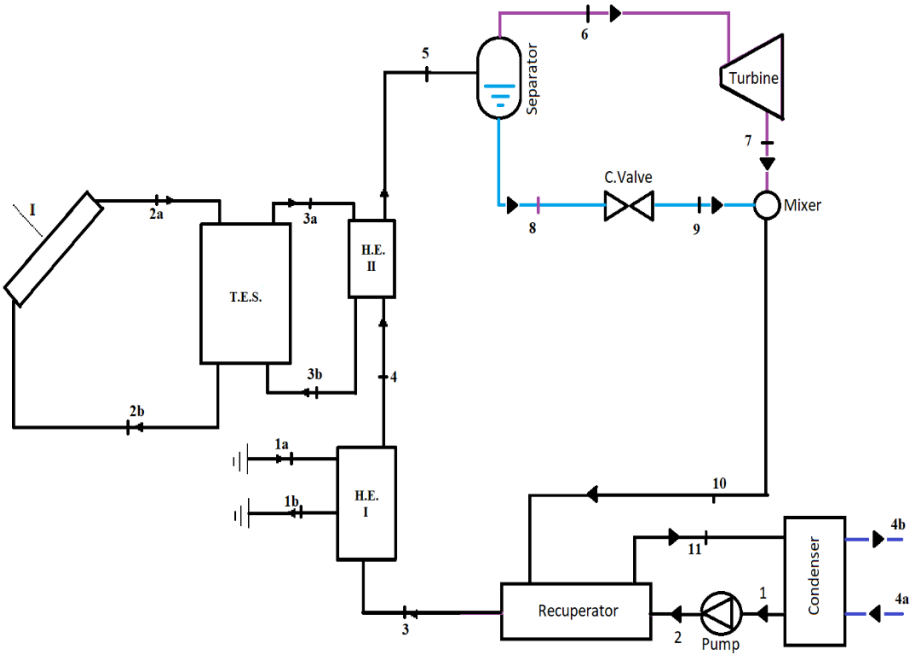

Figure 1. The flow diagram of the solar and geothermal powered KC.

Table 1. Properties of system units.

η_{TES}	Heat transfer efficiency from collectors to the thermal energy storage unit	0.98
η_T	Isentropic efficiency of turbine	0.85
η_{Coll}	Collector efficiency	0.85
η_G	Efficiency of generator	0.99
η_P	Isentropic efficiency of pump	0.90
η_{HE}	Efficiency of heat exchanger	0.98

Table 2. System parameters.

T_{1a} (K)	406,65
P_{1a} (kPa)	300
T_{1b} (K)	373,15-363,15-353,15
T_4 (K)	398,15
P_4 (kPa)	5808-5308-4808-4308-3808
T_5 (K)	401,15
P_7 (kPa)	1100-1000-900-800-700
T_{2a} (K)	593,15
T_{2b} (K)	568,15
T_{3a} (K)	588,15
T_{3b} (K)	543,15
T_{4a} (K)	288,15
T_{4b} (K)	298,15

The welding properties in Simav geothermal field were used in system design. The geothermal fluid is supplied from 9 wells. The temperature of the geothermal fluid is 406.65 K and its mass flow rate is 462 kg/s [10]. Parabolic solar collector was used in the system design and depending on the location of the geothermal source, monthly radiation values of the Simav region were taken into consideration in the analysis. Monthly global radiation values and solar time used in system designs are given in Table 3.

Table 3. Monthly global radiation values [11].

Month	**Global Radiation (kW h m^{-2}day^{-1})**	**Solar time (h)**
January	1.77	3.71
February	2.36	4.78
March	3.75	5.5
April	4.93	6.65
May	6.08	8.91
June	6.48	10.29
July	6.38	10.77
August	5.72	10.09
September	4.69	8.9
October	3.28	6.26
November	2.04	4.75
December	1.51	3.51

In the system's design, it was planned to take into account three different radiation values as a minimum, maximum and average, and the radiation values for 12 months were used in the analysis while evaluating the annual operation of the system. It is assumed that the system operates 645 h in February and 705h in other months.

3. ENERGY AND EXERGY ANALYSIS

Some assumptions such as kinetic and potential energy effects are negligible and the reference state is 25ºC and 101.325 kPa in the thermodynamic analysis. The governing energy equations of the geothermal and solar energy integrated ORC were obtained as follows.

The rate of useful heat gained for the collector can be calculated as follows [12].

$$\dot{Q}_{Coll} = I \cdot A_{coll} \cdot \eta_{Coll} \quad (1)$$

The rate of heat transfer input from the sun;

$$\dot{Q}_s = \frac{\dot{Q}_{Coll}}{\eta_{Coll}} \quad (2)$$

Mass of the heat transfer fluid calculated as;

$$\dot{m}_{terminol} = \frac{\dot{Q}_{Coll}}{(T_{2a} - T_{2b}) \cdot c_{p,terminol}} \quad (3)$$

The power output of the turbine can be calculated as;

$$\dot{W}_T = \dot{m}_{mix} \cdot (h_6 - h_7) \quad (4)$$

The electrical power output of the generator can be calculated as;

$$\dot{W}_G = \eta_G \cdot \dot{W}_T \quad (5)$$

The power consumption occurring in the pump can be calculated as;

$$\dot{W}_P = \dot{m}_{mix} \cdot (h_2 - h_1) \quad (6)$$

The energy balance of the geothermal heat exchanger;

$$\dot{Q}_{gf} = \dot{m}_{gf} \cdot (h_{1b} - h_{1a}) \cdot \eta_{HE} = \dot{m}_{mix} \cdot (h_4 - h_3) \quad (7)$$

The energy balance of the salt heat exchanger;

$$\dot{m}_{salt} \cdot (h_{3a} - h_{3b}) \cdot \eta_{HE} = \dot{m}_{mix} \cdot (h_5 - h_4) \quad (8)$$

The net power output of the system;

$$\dot{W}_{net} = \dot{W}_G - \dot{W}_P \quad (9)$$

The energy efficiency of the system calculated as;

$$\eta = \frac{\dot{W}_{net}}{\dot{Q}_s + \dot{Q}_{gf}} \quad (10)$$

The exergy balance equation for steady systems is given by the following equation:

$$\dot{E}_{X_{heat}} - \dot{E}_{X_{work}} + \dot{E}_{X_{m,i}} - \dot{E}_{X_{m,o}} = \dot{E}_{X_{dest}} \quad (11)$$

Here the exergy terms occurred by heat, work, solar radiation exergy and mass flow are given as following [12]:

$$\dot{E}_{X_{heat}} = \sum \left(1 - \frac{T_0}{T_k}\right) \cdot \dot{Q}_k \quad (12)$$

$$\dot{E}_{X_{work}} = \dot{W} \quad (13)$$

$$\dot{E}x_s = A_{Coll} \cdot I \cdot (1 + (1/3) \cdot (T_0/T_{sun})^4 - (4/3) \cdot (T_0/T_{sun})) \quad (14)$$

$$\dot{E}_{X_{m,i}} = \sum \dot{m}_i \cdot \psi_i \quad (15)$$

$$\dot{E}_{X_{m,o}} = \sum \dot{m}_o \cdot \psi_o \quad (16)$$

where ψ indicates the physical exergy term and given as:

$$\psi = (h - h_0) - T_0 \cdot (s - s_0) \tag{17}$$

where h is enthalpy, s is entropy, and the subscript zero indicates properties of fluids at the dead state. The exergetic efficiency of system is then calculated by the following equation.

$$\varepsilon = 1 - \frac{\dot{E}x_{m,total}}{\dot{E}x_{m,i}} \tag{18}$$

The reference state is 101.325kPa and 293.15K. Exergy efficiency of the system;

$$\varepsilon = \frac{\dot{W}_{net}}{(A_{Coll} \cdot I \cdot \psi_s) + (\dot{m}_{gf} \cdot (\psi_{1a} - \psi_{1b}))} \tag{19}$$

4. ECONOMIC ANALYSIS

The life cycle cost (LCC) of SGEP-KC occurs by the investment costs (C_{ic}), salvage cost (C_{sc}), operating and maintenance costs (C_{moc}) and benefit (C_b).

$$LCC_{SGEP-KC} = C_b - (C_{ic} + C_{sc} + C_{moc} + C_{OC}) \tag{20}$$

The salvage cost of the hybrid system was taken as 10% of the investment cost [10].

$$C_{sc} = C_{ic} \cdot 0.10 \tag{21}$$

The maintenance cost of the hybrid system was taken as 6% of the investment cost of the SGKC [13].

$$C_{moc} = C_{ic} \cdot 0.06 \tag{22}$$

The benefit of SGEP-KC includes electricity earning.

$$C_b = \dot{W}_{net} \cdot C_{elec} \cdot t_o \tag{23}$$

where C_{elec}; the unit price of electricity is 0.06 ($/kWh) and t_o; operating time of plant is 8400 h per annum [10]. The net cash flow;

$$C_{ncf} = (C_b - C_{moc}) \cdot (1 + i)^{t-1} \tag{24}$$

here, *i*; the interest rate and *t*; the related year time of cash flow. The Net Present Value (*NPV*) of SGEP-KC;

$$NPV = (C_{sc} - C_{ic}) + \sum_{t=0}^{ol} \frac{C_{ncf}}{(1+j)^t} \tag{25}$$

where *ol*; operating life of the hybrid system, *j*; the discount rate.

In this study, the operating life of the hybrid system has been added to calculations as 20 years. The discount and interest rates were taken as 18.5 % and 19.5%, respectively [14].

5. RESULTS AND DISCUSSION

The global radiation values (I_g) and properties of geothermal fluid were taken into account in the design of the SGEP-KC system. Handling the operating parameters as P_6 = 4308 kPa and I_g=1.51 kWh/m^{2}day the change of the NPV with different geothermal fluid outlet temperatures was obtained as shown in Figure 2.

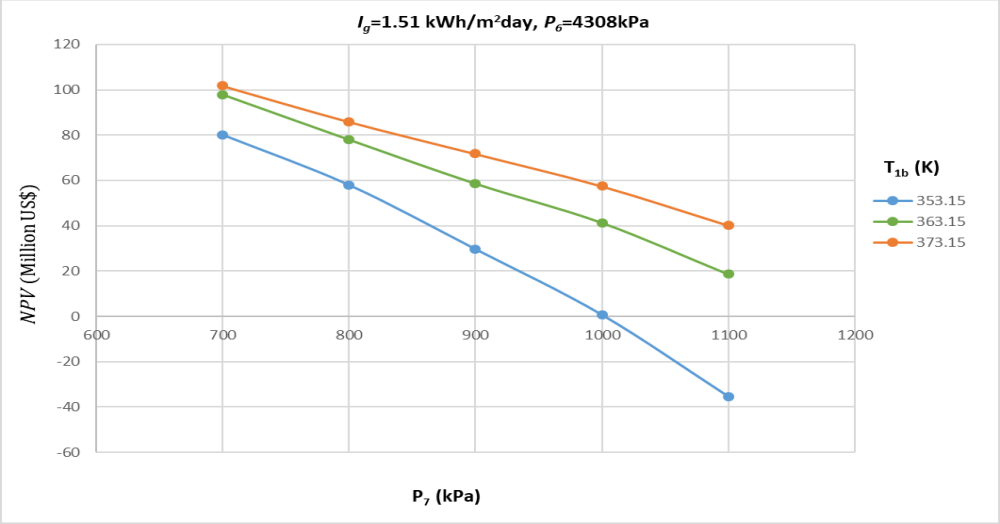

Figure 2. The variation of NPV versus T_{1b}.

Figure 2 shows that the NPV values of the SGEP-KC increase by the increase of the T_{1b} and the decrease of the turbine outlet pressure (P_7). The NPV of the proposed system ranges between -35.3727 Million US$ and 101.7955 Million US$. Taking P_6 = 4308 kPa and I_g=1.51 kWh/m^{2}day, the change of ε with different T_{1b} was obtained as shown in Figure 3.

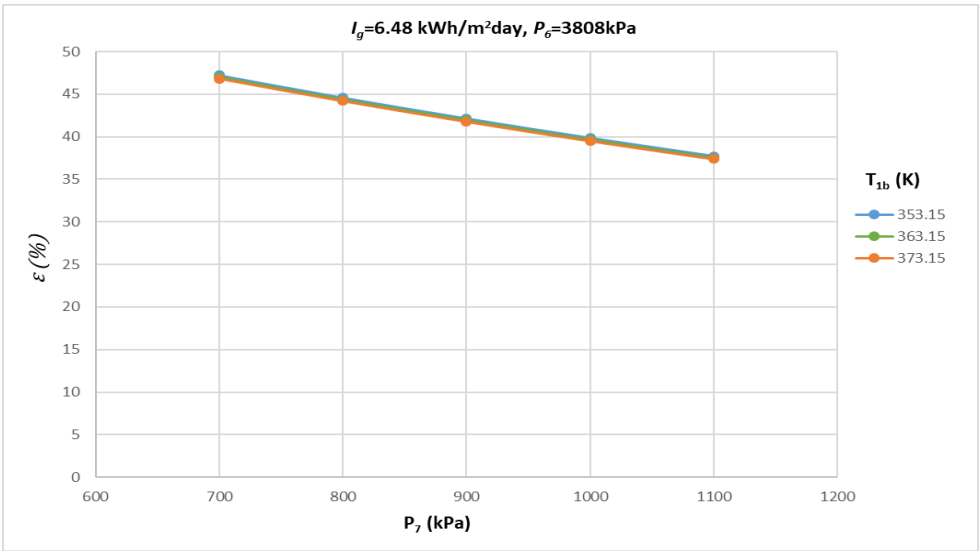

Figure 3. The variation of ε versus T_{1b}.

Figure 3 shows that the ε values of the SGEP-KC increase by the decrease of the T_{1b} and the decrease of the turbine outlet pressure (P_7). The ε of the proposed system ranges between 37.3859% and 47.2261%. Taking T_{1b} = 353.15 K and I_g=1.51 kWh/m^{2}day, the change of η with different P_6 was obtained as shown in Figure 4.

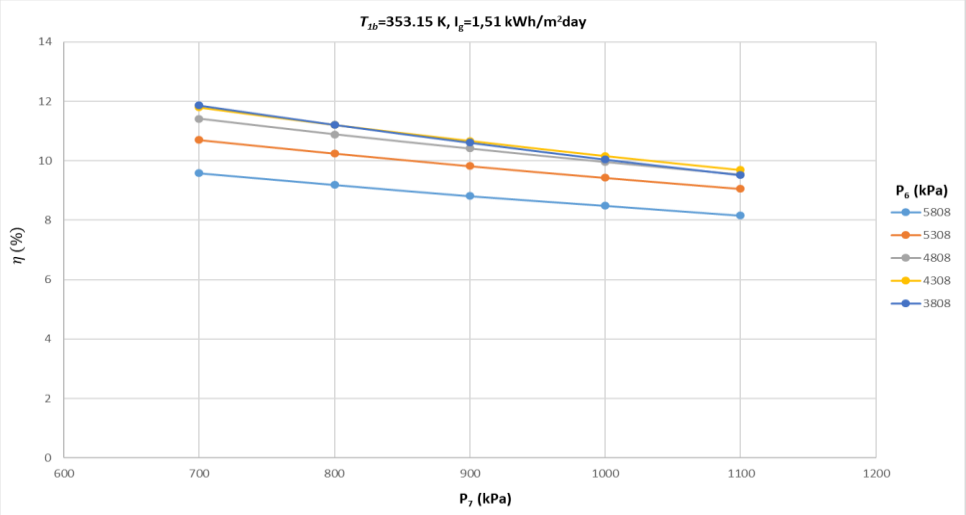

Figure 4. The variation of η versus P_6.

Figure 4 shows that the η values of the SGEP-KC increase with the decrease of the P_6 up to 4808 kPa for turbine outlet pressures higher than 900 kPa. The maximum η values of the SGEP-KC were determined for 3808 kPa turbine inlet pressure. Taking T_{1b} = 353.15 K and I_g=1.51 kWh/m^{2}day, the change of ε with different P_6 was obtained as shown in Figure 5.

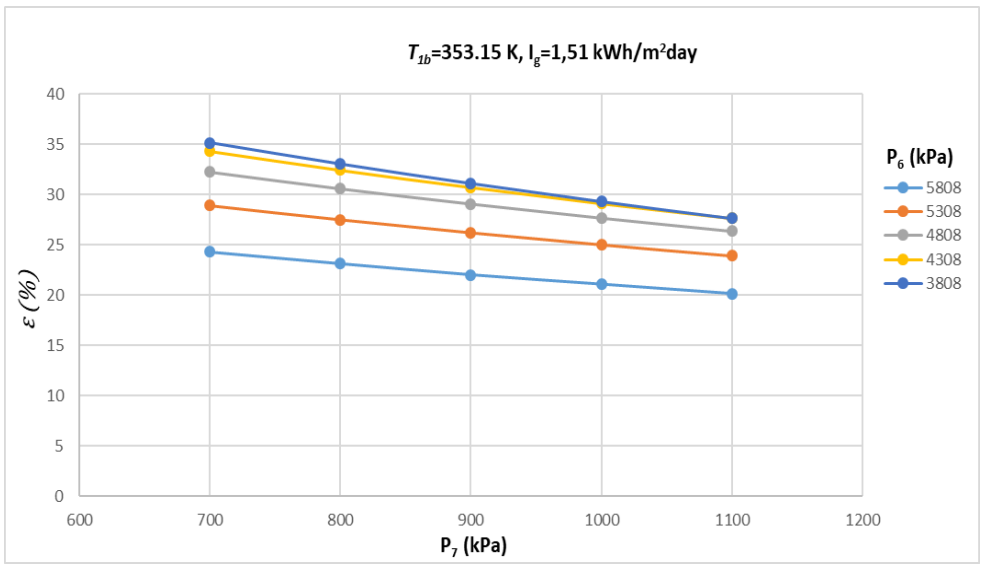

Figure 5. The variation of ε versus P_6.

Figure 5 shows that the ε values of the SGEP-KC increase with the decrease of the P_6. The ε of the proposed system ranges between 20.1444% and 35.1657%. The η of the proposed system ranges between 11.8663% and 8.1623%. Taking T_{1b} = 373.15 K and I_g=1.51 kWh/m^{2}day, the change of *NPV* with different P_6 was obtained as shown in Figure 6.

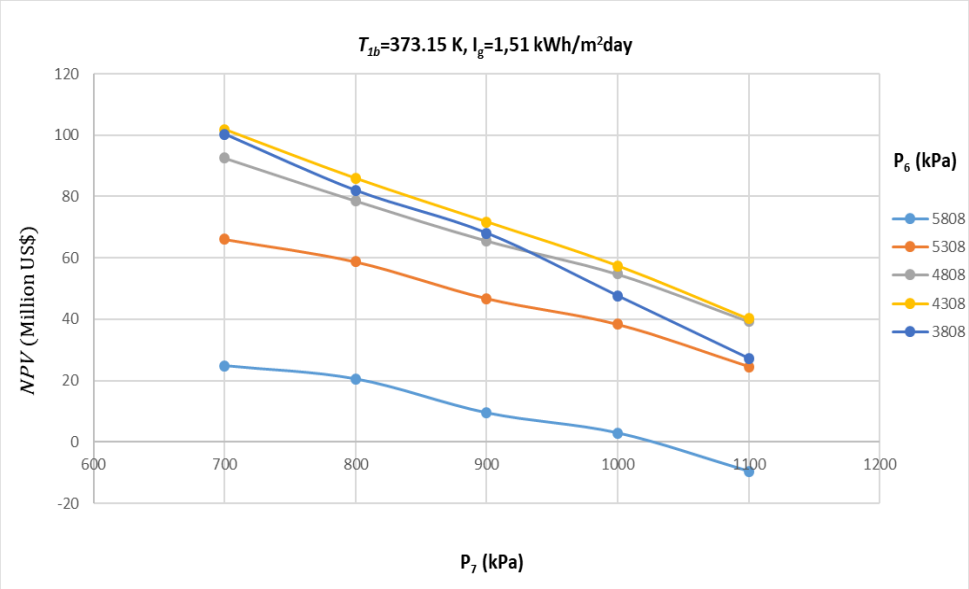

Figure 6. The variation of *NPV* versus P_6.

Figure 6 shows that the *NPV* values of the SGEP-KC increase with the decrease of the P_6 up to 4808 kPa for turbine outlet pressures lower than 900 kPa. The *NPV* of the proposed system ranges between -9.5356 Million US$ and 101.7955 Million US$. Taking T_{1b} = 373.15 K and P_6 =4308 kPa, the change of η with different I_g was obtained as shown in Figure 7.

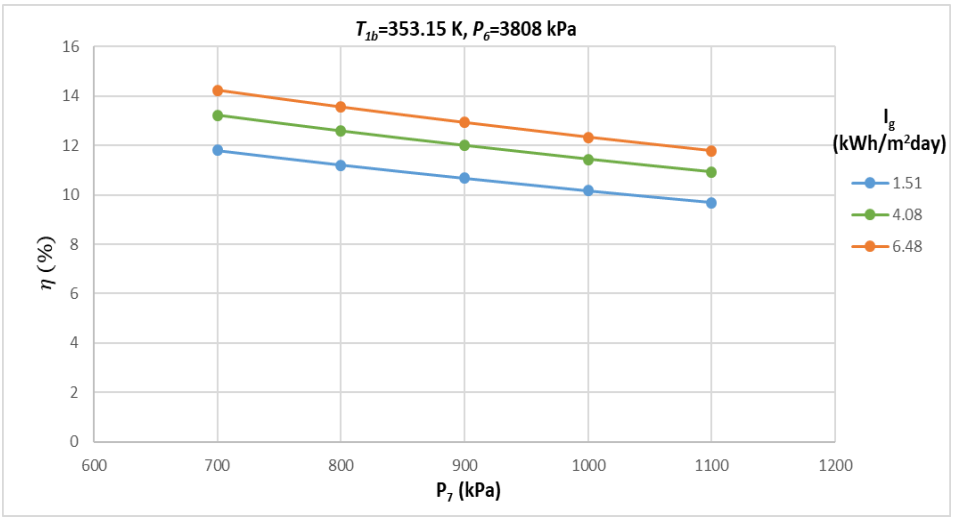

Figure 7. The variation of η versus I_g.

Figure 7 shows that the η values of the SGEP-KC increase with the increase of I_g. The η of the proposed system ranges between 9.6915% and 14.2433%. Taking T_{1b} = 353.15 K and P_6 =3808 kPa, the change of ε with different I_g was obtained as shown in Figure 8.

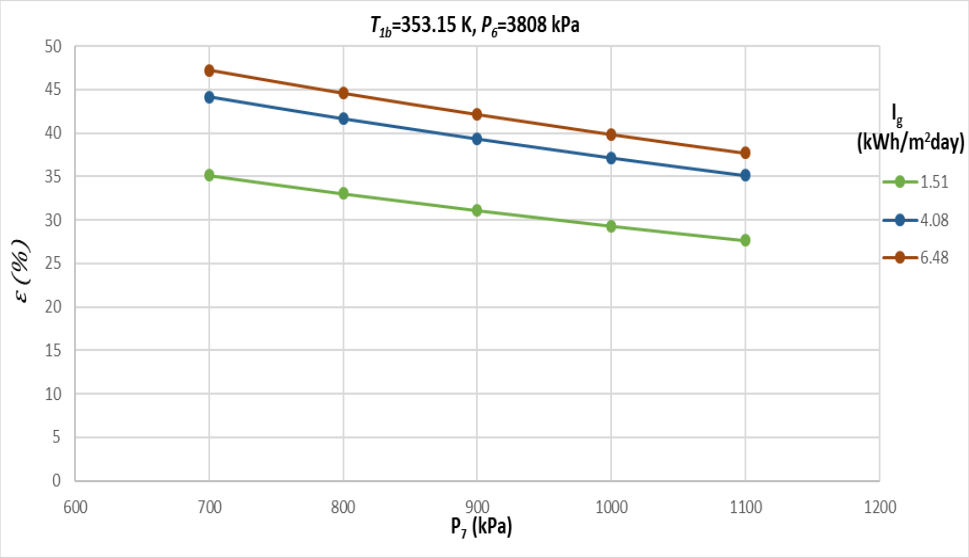

Figure 8. The variation of ε versus I_g.

Figure 8 shows that the ε values of the SGEP-KC increase with the increase of I_g. The ε of the proposed system ranges between 27.6602% and 47.2261%. Taking T_{1b} = 373.15 K and P_6 =4308 kPa, the change of *NPV* with different I_g was obtained as shown in Figure 9.

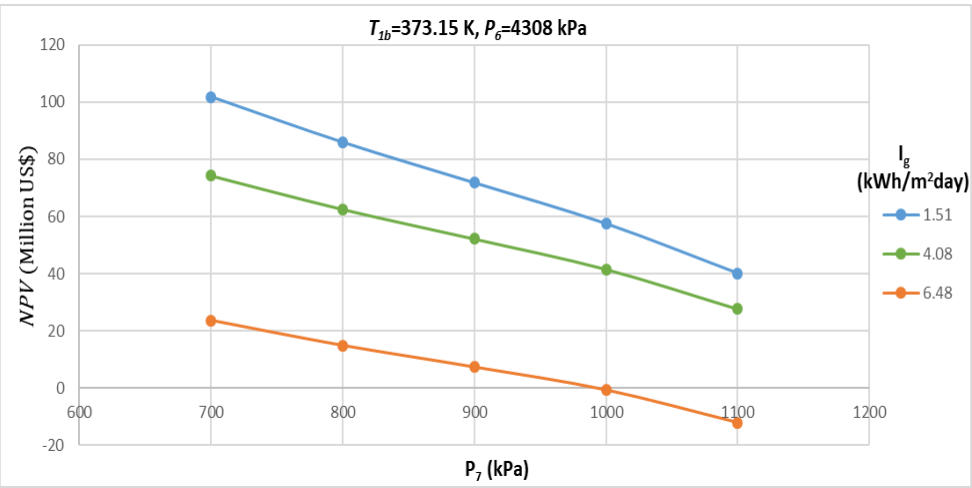

Figure 9. The variation of *NPV* versus I_g.

Figure 9 shows that the *NPV* values of the SGEP-KC increase with the decrease of the I_g. The *NPV* values of the proposed system ranges between -9.6356 Million US$ and 101.7955 Million US$.

6. CONCLUSION

In this study, the solar energy and geothermal energy powered Kalina cycle (SGEP-KC) was investigated analytically for various solar radiation, geothermal fluid return temperature, turbine inlet pressure and condenser pressure values.

As a result, the most effective geothermal fluid return temperature, turbine inlet pressure and condenser pressure values were determined respectively as 353.15 K, 3808 kPa and 700 kPa for all global solar radiation values according the thermodynamic analysis. The energy efficiency and exergy efficiency values for the specified operating parameters were respectively calculated as 14.2453 % and 47.2261 % for the highest radiation value of 6.48 kWh/m^2· day. The most effective geothermal fluid return temperature, turbine inlet pressure and condenser pressure values were determined as 373.15 K, 4308 kPa and 700 kPa for all global solar radiation values according the economic analysis. The NPV values of these system configuration were determined as 23.6584 Million US$ and 101.7955 Million US$ for the highest monthly solar radiation value of 6.48 kWh/m^2· day and the lowest monthly solar radiation value of 1.51 kWh/m^2· day, respectively. As a result, the system was found to be worth investment for lowest global solar radiation value as a result of thermodynamic and economic analysis.

REFERENCES

[1] Luo, C., Huang, L., Gong, Y., Ma, W., Thermodynamic Comparison of Different Types of Geothermal Power Plant Systems and Case Studies in China, *Renewable Energy*, 48, 155-160, 2012.

[2] Yari, M., Exergetic Analysis of Various Types of Geothermal Power Plants, *Renewable Energy*, 35, 112-121, 2010.

[3] Basaran, A., Ozgener, L., Investigation of The Effect of Different Refrigerants on Performances of Binary Geothermal Power Plants, *Energy Conversion and Management*, 76, 483-498, 2013.

[4] Heberle, F., Brüggemann, D., Exergy Based Fluid Selection for a Geothermal Organic Rankine Cycle for Combined Heat and Power Generation, *Applied Thermal Engineering*, 30, 1326-1332, 2010.

[5] Zhou, C., An In-Depth Assessment of Hybrid Solar–Geothermal Power Generation, *Energy Conversion and Management*, 74, 88-101, 2013.

[6] Ghasemi, H., Sheu, E., Tizzanini, A., Paci, M., Mitsos, A. Hybrid solar–geothermal power generation: optimal retrofitting, *Applied Energy*, 131, 158-170, 2014.

[7] Hong, H., Gao, J., Qu, W., Sun, J., Kang, Q., Li, Q. Thermodynamic Analyses of The Solar-Driven Kalina Cycle Having a Variable Concentration Ratio, *Applied Thermal Engineering*, 126, 997–1005, 2017.

[8] Mehrpooya, M., Mousavi, S.A., Advanced Exergoeconomic Assessment of a Solar-Driven Kalina Cycle, *Energy Conversion and Management*, 151, 681-692, 2017.

[9] Zare, V., Moalemian, A., Parabolic Trough Solar Collectors Integrated with a Kalina Cycle for High Temperature Applications: Energy, Exergy and Economic Analyses, *Energy Conversion and Management*, 151, 681-692, 2017.

[10] Arslan, O., Exergoeconomic Evaluation of Electricity Generation by The Medium Temperature Geothermal Resources, Using a Kalina Cycle: Simav Case Study, *International Journal of Thermal Sciences*, 49, 1866-1873, 2010.

[11] Potential atlas of solar energy, Republic of Turkey Ministry of Energy and Natural Resources, http://www.yegm.gov.tr/MyCalculator; 2020 [Accessed Feb 2020].

[12] Aydin, D., Utlu, Z., Kıncay, O., Thermal Performance Analysis of a Solar Energy Sourced Latent Heat Storage, Renewable and Sustainable Energy Reviews, 50, 1213–25, 2015.

[13] Ashouri, M., Vandani, A.M.K., Mehrpooya, M., Ahmadi, M.H., Abdollahpour, A., Techno-Economic Assessment of Kalina Cycle Driven by a Parabolic Trough Solar Collector, *Energy Conversion and Management*, 105, 1328-1339, 2015.

[14] CBRT (Central Bank of Republic of Turkish), Discount rate and interest rate of Turkey, https://www.tcmb.gov.tr/wps/wcm/connect/TR/TCMB+TR/Main+Menu/Temel+Faaliyetler/Para+Politikasi/Reeskont+ve+Avans+Faiz+Oranlari; 2019 [accessed 10 July 2019].

COMPARATIVE TECHNO-ECONOMIC-ENVIRONMENTAL ASSESSMENT OF BIOMASS FUELLED INTEGRATED ENERGY SYSTEMS

Parisa Heidarnejad*, Hadi Genceli, Zehra Yumurtaci*****
*Yildiz Technical University, Faculty of Mechanical Engineering, Istanbul/Turkey
Email: p.heidarnejad@gmail.com
** Yildiz Technical University, Faculty of Mechanical Engineering, Istanbul/Turkey
Email: hadi.Genceli@gmail.com
***Yildiz Technical University, Faculty of Mechanical Engineering, Istanbul/Turkey
Email: zyumur@ytu.edu.tr

ABSTRACT

In this research, a CHP (Combined Heating and Power) system providing electricity and heating power is proposed and investigated. With the purpose of leading designers and engineers in choosing the biomass technology type for utilizing in integrated energy systems, the considered configuration has been technically, economically, and environmentally analyzed, and their performances have been compared to each other. The CHP system is studied in two modes: 1. Heat of solid waste combustion as an input 2. Heat of biogas combustion as an input. Considering the heat values of solid waste and biogas and with purpose of providing the same amounts of products, results have been obtained. It is seen that, the thermodynamic performance of the system with biogas combustion is better than another one, while the system with solid waste combustion has better performance from thermo-economic viewpoint. Finally, the environmental assessment of the system showed that, the system with biogas combustion is more environment-friendly.

Keywords: Biogas, Environmental assessment, Solid waste, Thermodynamic analysis.

Symbols

biog	biogas
c	Cost per exergy unit ($/kW)
$\dot{C}$	Cost rate ($/s)
ex	Specific exergy (kJ/kg)
$\dot{E}x$	Exergy (kW)
F	Fuel
h	Specific enthalpy (kJ/kg)
H	Enthalpy (kJ)
i	Interest rate
η	Energy efficiency (%)
CRF	Capital Recovery Factor
PEC	Purchase Equipment Cost
$\dot{m}$	Mass flow rate (kg/s)
n	Lifetime of the system
P	Product
R	Universal gas constant
s	Specific entropy (kJ/kg.K)
T	Temperature (°C)
V	Velocity (m/s)

$\dot{W}$	Power (kW)
$\dot{Z}$	Investment cost rate ($/s)
ε	Exergy efficiency (%)
EES	Engineering Equation Solver
SW	Solid Waste

1. INTRODUCTION

With increasing of population growth (especially in developing countries), access to energy resources becomes essential. This population growth has been resulted in rising of energy demand. In this situation, combustion of fossil fuels will be responsible for the major share of the greenhouse gas emissions. In the other hand, fossil fuel resources are depleted, which has led to the energy crisis. With development of renewable energy sources such as biomass, solar, wind, geothermal and etc. as alternatives of fossil fuels, concerns have diminished somewhat. Meanwhile, the biomass is considered as a fuel with high availability which can be utilized directly or converted to other fuels. Some studies have been carried out in the field of biomass-driven CHP systems. Ghasemi et al. [1] suggested the energy of biomass combustion as a backup heat source for an integrated energy system. The technical and economic feasibilities of the system were evaluated through thermodynamic and thermo-economic analyses. Zhu et al. [2] suggested a biomass fired CHP system including ORC (Organic Rankine Cycle). Thermodynamic and economic assessments of the studied system were conducted and eleven working fluids were considered in order to investigate the system performance. In another research, Al Asfar et al. [3] studied the performance of a biomass fired power plant experimentally. They also modeled the plant thermodynamically, economically, and environmentally and validated the results with experiments. They also showed that, environmental effect of biomass combustion is disregarded due to insignificant contents of sulfur and nitrogen oxides pollutants.

Moreover, limited studies have been dealt with biogas fired CHP systems. For example, flue gases from combustion of biogas is considered as heat source for an ORC by Mudasar et al. [4], in which the results demonstrate that biogas-fired ORC systems present an efficient alternative for power generation plants in rural areas. Zhang et al. [5] examined a biogas CHP system for a rural area of China. The utilized biogas was derived from the anaerobic digestion of cow manure which yields the primary energy saving for the CHP system for most of the year.

In this research, two CHP systems are proposed with equal amounts of products. One system consumes the energy of solid waste combustion as an input, while the other system uses the energy of biogas combustion which is yielded as the anaerobic digestion of biomass. Both systems are investigated thermodynamically, economically and environmentally and are compared to each other. Finally, appropriate system is suggested according to the design objectives.

2. MATERIALS AND METHODS

2.1. System Description

The typical configuration for the CHP system is depicted in Figure 1. This system is considered with two different energy inputs separately. The one with solid waste combustion and utilizing the exhaust gasses of the combustion chamber, the other with biogas combustion and utilizing the exhaust gasses of the combustion chamber in which biogas has been collected as the production of digestion of agricultural and animal wastes.

In the proposed CHP system, the electric power and heating are achieved through a Rankine cycle. The heat transfer between exhaust gasses and steam as the working fluid is performed through a HRSG (Heat Recovery Steam Generator). The superheated steam enters the turbine and heater in order to supply electric power and heating respectively and finally is pumped into the HRSG to complete the cycle. In the CHP with solid waste combustion, the solid wastes are separated and prepared before entering the combustion chamber. On the other

hand, the CHP with biogas mainly includes reactors, mixers, feeders, gas pipes and gasholders as well as biogas fired combustion chamber.

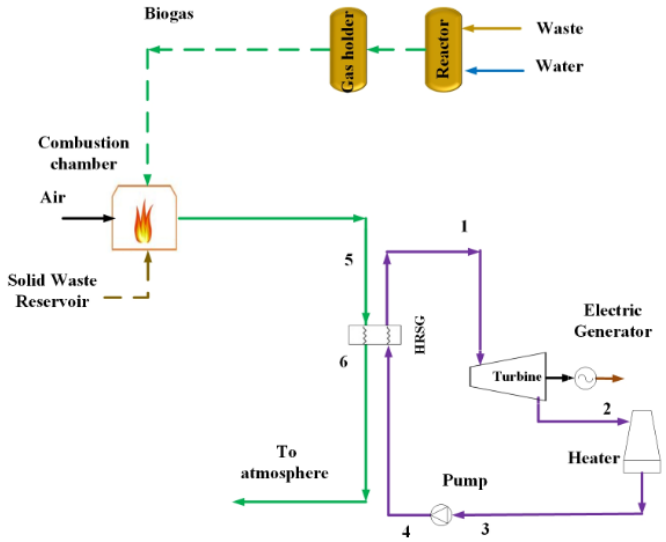

Figure 1. The layout of proposed CHP system

2.2. Thermodynamic and Thermo-economic Modeling

In this study, thermodynamic modeling is carried out based on applying energy and exergy balances on each component of the CHP system as below [6, 7]:

$$\dot{Q}+\sum \dot{m}_{in}\left(h_{in}+\frac{1}{2}V_{in}^{2}+gz_{in}\right)=\sum \dot{m}_{out}\left(h_{out}+\frac{1}{2}V_{out}^{2}+gz_{out}\right)+\dot{W} \tag{1}$$

$$\left(1-\frac{T_0}{T_i}\right)\dot{Q}_i+\sum \dot{m}_{in}ex_{in}=\sum \dot{m}_{out}ex_{out}+\dot{W}+\dot{E}x_D \tag{2}$$

$$ex=ex^{ph}+ex^{ch} \tag{3}$$

$$ex^{ph}=(h-h_0)-T_0(s-s_0) \tag{4}$$

$$ex^{ch}=\left[\sum_{i=1}^{n}x_i ex_i^{ch}+RT_0\sum_{i=1}^{n}x_i \ln x_i\right] \tag{5}$$

Also thermo-economic modeling as combined tool of exergy and economic methods is performed as the below formulation [6]:

$$\sum_k\left(c_{out}\dot{E}x_{out}\right)_k+c_{w,k}\dot{W}_k=c_{q,k}\dot{E}x_{q,k}+\sum_k\left(c_{in}\dot{E}x_{in}\right)_k+\dot{Z}_k \tag{6}$$

$$\dot{C}_i=c_i\dot{E}x_i \tag{7}$$

$$\dot{Z}_k = \dot{Z}_k^{CI} + \dot{Z}_k^{OM} = \frac{CRF \times \delta \times PEC_k}{N \times 3600} \tag{8}$$

$$CRF = \frac{i(1+i)^n}{(1+i)^n - 1} \tag{9}$$

2.3. Environmental Assessment

The amount of GHGs (Greenhouse gas) emissions and pollutions emitted by the CHP system is calculated through the obtained solid waste and biogas required for each system. Then the emission factors provided by EPA (Environmnetal protection Agency) [8] for solid waste combustion and by Benato et al. [9] for biogas combustion. These factors are used to achieve the amount of GHGs and pollutions emitted by each system.

3. RESULTS AND DISCUSSION

In this section, results of energy, exergy and thermo-economic modeling as well as environmental assessment of the CHP system with solid waste combustion and biogas combustion separately are presented and discussed. The mathematical model developed for this system is solved through Engineering Equation Solver (EES) [10] software. The outputs of the modeling are listed in Table 1 and Table 2.

Table 1. State properties of the CHP system with solid waste combustion

State	Mass flow rate (kg/s)	Temperature (°C)	Pressure (kPa)	Specific enthalpy (kJ/kg)	Specific entropy (kJ/kg.K)	Specific exergy (kJ/kg)	Cost per unit of exergy ($/GJ)	Cost rate ($/h)
1	10	450	15000	3157	6.141	1331	0.070	3.38
2	10	198.3	1500	2725	6.303	851.3	0.070	2.16
3	10	198.3	1500	844.9	2.315	159.5	0.070	0.40
4	10	201.1	15000	863.2	2.321	176.1	0.098	0.62
5	87.58	460	100	-3544	8.141	204.6	0.014	0.95
6	87.58	250	100	-3806	7.721	67.94	0.014	0.31

Table 2. State properties of the CHP system with biogas combustion

State	Mass flow rate (kg/s)	Temperature (°C)	Pressure (kPa)	Specific enthalpy (kJ/kg)	Specific entropy (kJ/kg.K)	Specific exergy (kJ/kg)	Cost per unit of exergy ($/GJ)	Cost rate ($/h)
1	10	450	15000	3157	6.141	1331	0.068	3.29
2	10	198.3	1500	2725	6.303	851.3	0.068	2.10
3	10	198.3	1500	844.9	2.315	159.5	0.068	0.39
4	10	201.1	15000	863.2	2.321	176.1	0.096	0.61
5	107.9	460	100	425.5	7.283	165.9	0.013	0.83
6	107.9	250	100	213	6.942	55.06	0.013	0.27

Based on the state properties of the system, thermodynamic, thermo-economic and environmental performances of the CHP system with solid waste combustion and biogas combustion separately are listed in Table 3.

Table 3. Thermodynamic and thermoeconomic performances of the CHP system

	$\dot{W}_{turb}$ (kW)	$\dot{Q}_{heating}$ (kW)	$\dot{m}_{SW}$ (kg/s)	$\dot{m}_{Biog}$ (kg/s)	$\dot{E}_D$ (kW)	η $(\%)$	ε $(\%)$	$\dot{C}_P$ $(\$/h)$
CHP system with solid waste combustion	4317	18801	2.05	-	40641	39.7	18.97	362.9
CHP system with biogas combustion	4317	18801	-	1.79	11779	39.7	37.99	871

The environmental assessment is performed based on the calculation of GHGs and pollutants from the CHP system with solid waste combustion and biogas combustion separately. This calculation is conducted based on the factors for solid waste combustion and biogas combustion and the results are shown in Table 4.

Table 4. GHGs and pollutants from the CHP system

CHP system with solid waste combustion			
NOx (t/y)	CO2 (t/y)	CO (t/y)	
11,822	63,633	14.99	
CHP system with solid waste combustion and biogas combustion			
NOx (t/y)	SO2 (t/y)	CO (t/y)	VOC (t/y)
366.1	45.31	561.8	18.12

4. CONCLUSION

In this research, a CHP system in two modes: 1. Heat of solid combustion as the input 2. Heat of solid combustion as the input, is proposed to provide the power and heat of a rural area. For evaluation of the feasibility of the proposed system, it is modeled from the thermodynamic and thermo-economic points of view and the environmental effects are assessed. Considering the heat values of solid waste and biogas and with purpose of providing the same amounts of products, results are obtained. It is seen that, the thermodynamic performance of the system with biogas combustion is better than another one, while the system with solid waste combustion has better performance from thermo-economic viewpoint. Finally, the environmental assessment of the system showed that, the system with biogas combustion is more environment-friendly.

REFERENCES

[1] Ghasemi A, Heidarnejad P, Noorpoor A, A novel solar-biomass based multi-generation energy system including water desalination and liquefaction of natural gas system: Thermodynamic and thermoeconomic optimization, *Journal of Cleaner Production*, **196**, 424-37, 2018.

[2] Zhu Y, et al., Thermodynamic analysis and economic assessment of biomass-fired organic Rankine cycle combined heat and power system integrated with CO2 capture, *Energy Conversion and Management*, **204**, 112310, 2020.

[3] Al Asfar J, et al., Thermodynamic analysis of a biomass-fired lab-scale power plant, *Energy*, **194**, 116843, 2020.

[4] Mudasar R, Aziz F, Kim M-H, Thermodynamic analysis of organic Rankine cycle used for flue gases from biogas combustion, *Energy Conversion and Management*, **153**, 627-40, 2017.

[5] Zhang D, Zheng Y, Wu J, Li B, Li J, Annual energy characteristics and thermodynamic evaluation of combined heating, power and biogas system in cold rural area of Northwest China, *Energy*, **192**, 116522, 2020.

[6] Bejan A, Tsatsaronis G, Moran M. Thermal design and optimization. Canada: John Wiley & Sons Inc.; 1996.

[7] Cengel AY, Boles MA. Thermodynamics: An engineering approach. New York: McGraw Hill; 2008.

[8] AP-42, Compilation of air pollutant emission factors, Volume 1: Stationary Point and Area Sources Chapter 2: Solid Waste Disposal. New York: EPA;1979. from https://www.epa.gov/air-emissions-factors-and-quantification/ap-42-compilation-air-emissions-factors.

[9] Benato A, Macor A, Rossetti A, Biogas Engine Emissions: Standards and On-Site Measurements, *Energy Procedia*, **126**, 398-405, 2017.

[10] Engineering Equation Solver (EES), 2013. Klein SA. from https://fchart.com/ees/.

THERMODYNAMIC INVESTIGATION OF FLAT PLATE COLLECTOR

Abide Banu GÜNDÜZ ALTIOKKA *, Ahmet MAVİ **, Oğuz ARSLAN***
*Bilecik Şeyh Edebali, Vocational School, Bilecik/Turkey
Email: banu.gunduz@bilecik.edu.tr
**Bilecik Şeyh Edebali, Vocational School, Bilecik/Turkey
Email: ahmet.mavi@bilecik.edu.tr
***Bilecik Şeyh Edebali, Department of Mechanical Engineering, Bilecik/Turkey
Email: oguz.arslan@bilecik.edu.tr

ABSTRACT

A flat plate collector is a heat exchanger that converts solar energy into heat energy. The solar collector transmits a part of the incoming solar radiation to the fluid. Collector efficiency is the ratio of the heat obtained from the fluid to the radiation coming on to the collector. In this study, flat plate collector modeling is done and the parameters affecting the efficiency are investigated. Thermodynamic analysis of the flat plate collector was made by taking into consideration the parameters of fluid flow, solar radiation intensity, absorber plate thickness and glazing cover.

Keywords: Flat plate collector, Collector Efficiency, Energy

1. INTRODUCTION

The flat plate collector is widely used to make solar energy useful. The reason why it is widely used is the simple design of the collector, its operation at medium and low temperatures, and its very few mechanical parts. The radiation reaching the flat plate collectors is transferred to the working fluid by conduction and convection. Collector efficiency is the ratio of heat obtained from the fluid to the radiation coming into the collector. In order to increase the collector efficiency, parameters such as glass cover number, working fluid, absorber surface material, fluid temperature, pipe diameters, pipe number were studied.

Akhtar and Mullick (2012) developed a mathematical model for calculating the inner and outer surface temperatures of the glass cover of single and double glazed flat plate collectors[1]. Föste et al. (2014) investigated the performance of glassless, single-glass and double-glass flat plate collectors. In their work, they coated glass with two different transparent conductive oxides. They observed that the coating did not cause any change in the performance of the single-glass collector, and that the thermal efficiency of the double-glass collector increased [2]. Vetrivel and Mathiazhagan (2017) examined the efficiency of collectors using single and double glass in their experimental study. Collectors of the same size are placed at an angle of 12o. As a result of the experiments, they found the collector efficiency 55% for the system using double glass and 12% for the single glass system. They measured that the outlet temperature of the fluid in the double-glass system was 10 ° C -15 ° C higher than the single-glass system [3]. Debnath et al. (2018) studied experimentally and theoretically in single and double glazed air collectors. They used flat and grooved absorber plates in the collectors. The double-glazed collector performed better due to the reduction of radiation and heat loss from the collector to the environment. They calculated that the corrugated absorber plate collector had 14% higher thermal efficiency due to the suitable turbulence effect and increased heat transfer area [4]. Sundar et al. (2018) experimentally investigated a flat plate collector with copper tubes and copper absorber plates. In the collector, 1 mm thick and 9 mm wide aluminum strips of 15, 10, 5 twists were used. Al2O3 nanofluid, which has 0.1% and 0.3% concentration as the working fluid, was used in the system with different flow rates. The thermal efficiency of the collector increased with the increase of mass flow rate and nanofluid concentration[5]. Khalil et al. (2018) conducted an exergy analysis using different absorber plates in air flat plate collectors in their experimental study. They used four types of absorber plates, namely flat plate, in-line

turbulators, staggered turbulators and inclined staggered turbulators. Simultaneous measurements were made in collectors with aluminum absorber plate and single glass cover, placed at an angle of 45 ° in the same dimensions. The least exergy loss was in the inclined staggered turbulators due to the high turbulence that occurred. Exergy analysis of the system was carried out at flow rates between 0.0125 kg / s and 0.073 kg / s. They observed that exergy loss decreased with increasing flow rate[6]. Abuska et al. (2017) conducted an experiment to investigate the energy, exergy, economical and environmental performance of a V-grooved flat plate collector at different air mass flow rates. They calculated that V-groove collectors have 6% higher heat transfer coefficient than flat plate collectors. They found that the average exergy efficiency of aluminum and copper plate collectors was between 0.06 and 0.12 and the average energy efficiency was between 0.43 and 0.60. It has been observed that the aluminum V plate collector is more efficient than the aluminum flat plate collector in terms of both energy and exergy[7]. Güven et al. (2018) modeled with the Fluent program to examine the effects of the diameters of the pipes carrying the fluid and the distance between the pipes on the efficiency in flat plate collectors. They calculated that as the distance between the pipes decreased, the efficiency increased[8]. Ehrman and Reineke-Koch (2012) coated the glass with low iron content in three layers with transparent conductive oxides by sputtering method to increase the efficiency of flat plate collectors at temperatures above 100 ° C or in low sunlight[9]. Dagdougui et al. (2011) investigated the effect of the number of transparent covers and types of transparent covers on upper heat loss and thermal performance in a flat plate collector. They used plastic, glass and combined plastic-glass as the transparent cover to calculate the upper heat losses. They calculated that when two covers are used in flat plate collectors, the upper heat loss decreases. They determined that combined plastic-glass lids are the most appropriate in terms of reducing the upper heat loss coefficient [10]. They used plastic, glass and combined plastic-glass as the transparent cover to calculate the upper heat losses. They calculated that when two covers are used in planar collectors, the upper heat loss decreases. They found that combined plastic-glass lids were the most appropriate in terms of reducing the upper heat loss coefficient [10].

In this study, a collector with glass cover and absorber flat plate whose general structure is shown in Figure 1 was modeled. The absorber plate material of the collector was chosen as aluminum and copper. In this study, solar radiation intensity, flow rate and absorber plate thickness are investigated as variable parameters.

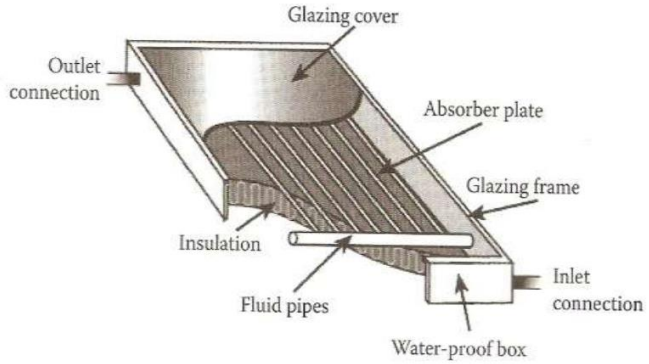

Figure 1. Flat plate collector [12]

2. MATERIAL AND METHOD

2.1 Flat plate collector

In this study, the effect of direction and slope parameters for the water fluid solar collector is not taken into account. A study was carried out for the collector facing south and placed at a fixed angle of 45° to the horizontal. The collector examined two different situations as single and double glass. The liquid flow entering the collector is 0.02, 0.04 and 0.06 kg/s; Solar radiation intensity on the collector has been taken as 400, 500, 600, 700, 800, 900 and 1000W/m^2. The ambient temperature is 293 K and the fluid inlet temperature to the collector is 295 K. Absorber plate materials are taken from copper and aluminum and thickness is 0.5 mm and 1 mm. The properties of the studied planar collector are given in table 1.

Table 1. Characteristic of the flat plate collector

Parameter	
Collector length (m)	2
Collector width (m)	1
Collector height (m)	0.15
Glass thickness (mm)	4
Emissivity of the glass	0.88
Emissivity of the plate	0.94
Pipe diameter (mm)	12
Numbers of fluid pipes	10
Distance between fluid pipes (mm)	80
Collector tilt angle (o)	45
İnsulation material	Foam
Bottom insulation material thickness (mm)	100
Bottom insulation material thickness (mm)	25

2.2 Mathematical Modeling

The sum of the solar radiation coming on the flat plate collector surface has given in equation 1.

$$I(\tau\alpha) = Q_f + Q_k + Q_d \tag{1}$$

Where, I(τα) total solar radiation, Q_f radiation passing into the carrier liquid, Q_k radiation radiating to the environment, Q_d is the radiation stored on the surface. Heat loss to the environment in the collector; have been of the collector's top, bottom and side surfaces.

$$U_T = U_{top} + U_{bottom} + U_{side} \tag{2}$$

$$U_t = \left[\frac{N}{\frac{C}{T_{y,ave}}\left[\frac{T_{y,ort}-T_a}{N+f}\right]^e} + \frac{1}{h_w}\right] + \frac{\sigma\varepsilon_c(T_{y,ave}+T_a)(T_{y,ave}{}^2+T_a{}^2)}{(\varepsilon_p+0.0059Nh_w)^{-1}+\frac{2N+f-1+0.133\varepsilon_p}{\varepsilon_g}-N} \tag{3}$$

Where N is number of glass cover, β collector tilt angle, ε_g is emissivity of the glass, ε_p is emissivity of the plate, $T_{y,ave}$ is average absorber temperature (K), T_a is ambient temperature(K), σ is Stefan Boltzman constant (5,67x10^{-8}), V_w is a wind speed (m/s). Unknown values given by equation 4,5,6 and 7 have calculated by the equations given below.

$$h_{wind}=5{,}7+3{,}8V_w \tag{4}$$

$$f = \left(1 + 0.089h_w - 0.1166h_w\varepsilon_p\right)(1 + 0.07866N) \tag{5}$$

$$e = 0.43\left(1 - \frac{100}{T_{y,ave}}\right) \tag{6}$$

$$C = 520(1 - 0.000051\beta^2) \tag{7}$$

Heat loss from the part of bottom and side of the collector is given in equation 8 and 9.

$$U_{bottom} = \frac{k}{L_{bottom}} \tag{8}$$

$$U_{side} = \frac{k\ p\ L_{side}}{L_{iso,side}}\left(\frac{1}{A_{kol}}\right) \quad (9)$$

Where is k heat transmission coefficient of the insulating material (W / mK), L_{bottom} is the thickness of the bottom insulation material (m), p is perimeter of the collector (m), L_{side} is side edge height of collector (m), A_c is a collector area (m^2), $L_{iso,side}$ is a side isolation thickness (m). Fin efficiency depends on the heat transfer coefficient of the absorbent plate, the thickness of the absorbent plate and the distance between the pipes. Fin efficiency is given equation 10.

$$F = \frac{tanh\left[m\left(\frac{W-D}{2}\right)\right]}{\left[m\left(\frac{W-D}{2}\right)\right]} \quad (10)$$

$$m = \sqrt{\left(\frac{U_T}{k_y \delta_y}\right)} \quad (11)$$

Where k_y is a thermal conductivity coefficient of absorber plate (W/mK), δ_y is absorber plate thickness (m), W is a distance between fluid pipe centers (m), D is a pipe outside diameter (m).

When the pipes are under the absorber plate, the collector efficiency factor is given in equation 12.

$$F' = \frac{\frac{1}{U_T}}{(D+W)\left(\frac{1/U_T}{D+WF}+\frac{1}{\pi D_i h_f}\right)} \quad (12)$$

Here, h_f is the heat transfer coefficient between the fluid and the tube wall (W/m^2K), D_i is inside diameter of the fluid pipe(m). Collector heat gain factor is given equation 13.

$$F_R = \frac{\dot{m}C_p}{A_c U_T}\left[1 - exp\left(-\frac{A_c U_T F'}{\dot{m}C_p}\right)\right] \quad (13)$$

Where $\dot{m}$ is the mass flow rate of the fluid inside the collector pipes (kg/s), C_p is specific heat capacity of water (J/kgK). Useful energy taken from this collector is given in equation 12.

$$Q_y = A_c F_R\left[I(\tau\alpha) - U_T\left(T_g - T_a\right)\right] \quad (14)$$

Where I is total irradiation reaching the surface of the collector (W/m^2), T_g is the inlet fluid temperature (K), $T_ç$ is the ambient temperature (K). The instantaneous efficiency of a flat plate solar collector beneficial heat obtained from working fluid it is calculated depending on the solar radiation coming on the collector [12].

$$\eta = \frac{Q_y}{A_c I} = \frac{\left[F_R A_c\left(S - U_T(T_g - T_a)\right)\right]}{A_c I} \quad (15)$$

3. RESULTS AND DISCUSSION

In this study; for aluminum and copper flat plate collectors, the variation of efficiency was investigated depending on the number of covers, the absorption plate thickness, fluid flow and solar radiation intensity. Efficiency change of copper absorbent plate collector with 0.2 kg/h flow and 0.5 mm thickness according to the number of covers is given in figure 2.

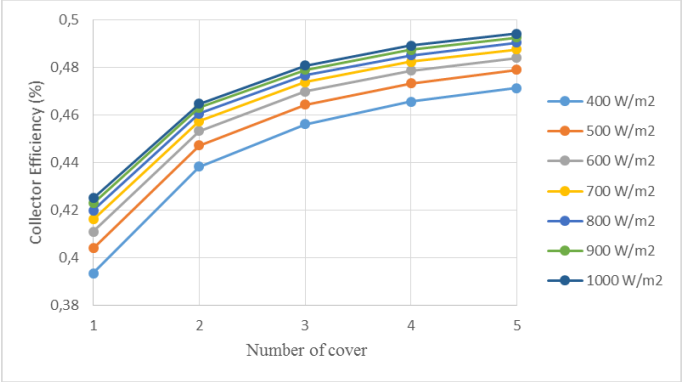

Figure 2. Change of thermal efficiency depending on the solar radiation violence according to number of glass cover in the copper flat plate collector (m=0.02 kg/s, δ_y= 0.5 mm)

When Figure 2 is examined, the efficiency value are increased when the number of glass covers is increased. However, the increase in this efficiency value due to the increase in the of covers number is in a decreasing trend. The rate of increase depending on the number of covers for 400 W / m^2 solar radiation violence varies between 0.76% and 6.48%. The number of covers over two does not provide a significant increase in efficiency. For this reason, the number of covers of the collector was taken as two.

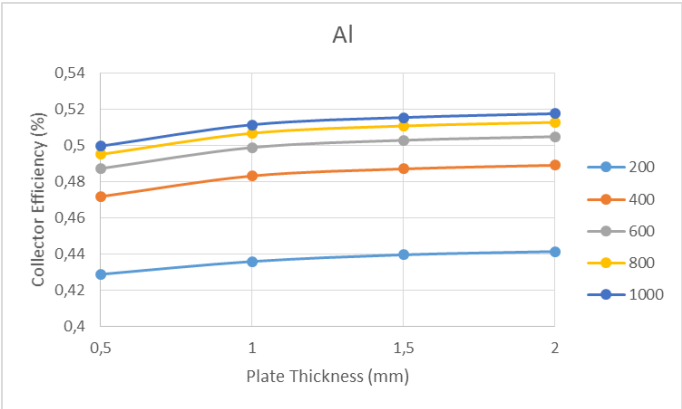

Figure 3. Efficiency change of the 2 glass cover- aluminum plate collector according to the absorbent plate thickness (0.04 kg/h).

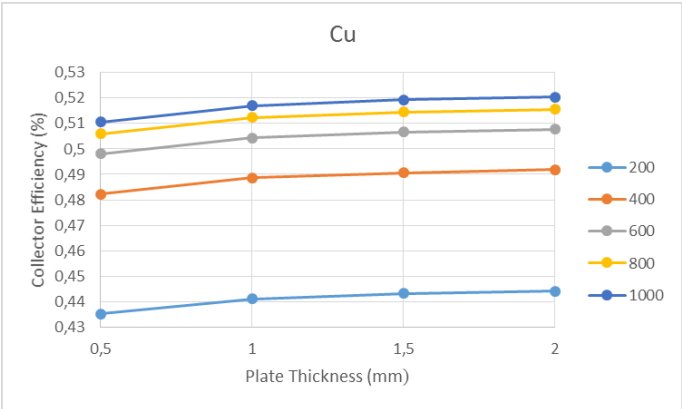

Figure 4. Efficiency change of the 2 glass cover- copper plate collector according to the absorbent plate thickness (0.04 kg/h).

In figures 3 and 4, the efficiency change is given that according to the absorber plate thickness. Efficiency value increases with increasing plate thickness. The increase in efficiency value for the aluminum plate collector between 0.25% and 1.48%, and between. 0.15% and 0.81% was calculated for the copper absorber surface. When the absorber surface thickness exceeds 1.5 mm, the amount of increase have been decreased significantly. Therefore, the plate thickness was taken as 1.5 mm.

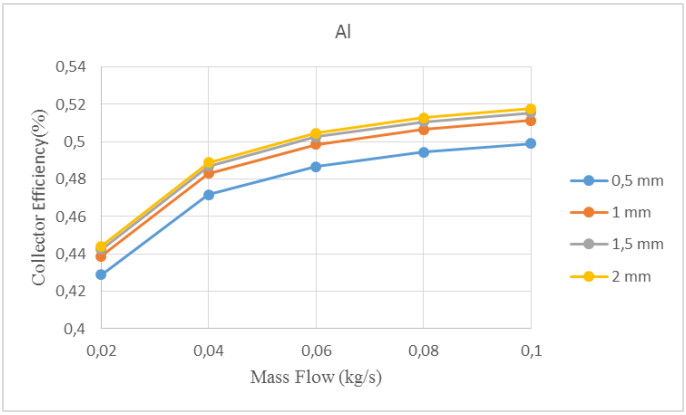

Figure 5. Efficiency change of the 2 glass cover- copper flat plate collector according to the mass flow.

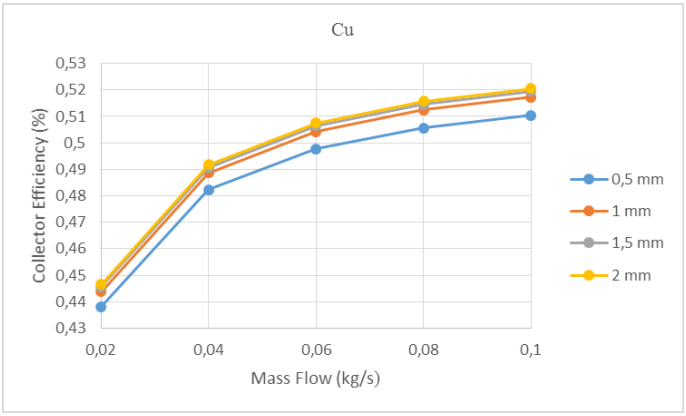

Figure 6. Efficiency change of the 2 glass cover- copper flat plate collector according to the mass flow.

In Figures 5 and 6, the mass flow change and thermal efficiency change are given. Flat plate collector thermal efficiency increased in parallel with the increase in radiation and mass flow.

4. RESULTS

With the analysis made, the yield variation for aluminum and copper plate collectors was investigated depending on the number of covers, absorber plate thickness and fluid mass.

When comparing planar collectors with different features, the efficiency will be higher as the number of glass increases, due to upper heat loss decreases. It was observed that the increase in efficiency quite decreased when the number of covers exceeded two. Therefore; ideal cover number can be determined as 2 considering the collector efficiency.

As the absorber plate thickness increases, the efficiency increases, and the ideal thickness for the examined aluminum and copper absorber surfaces can be considered 1.5 mm. For the absorbent surfaces of the same

thickness, plates with high heat transmission coefficient have higher efficiency. For this reason, they can be preferred by considering cost factors in designs.

REFERENCES

[1]Akhtar, N., & Mullick, S. C. (2012). Effect of absorption of solar radiation in glass-cover (s) on heat transfer coefficients in upward heat flow in single and double glazed flat-plate collectors. *International Journal of Heat and Mass Transfer*, 55(1-3), 125-132.

[2]Giovannetti, F., Föste, S., Ehrmann, N., & Rockendorf, G. (2014). High transmittance, low emissivity glass covers for flat plate collectors: applications and performance. *Solar Energy*, 104, 52-59.

[3]Vettrivel, H., & Mathiazhagan, P. (2017). Comparison study of solar flat plate collector with single and double glazing systems. *International Journal of Renewable Energy Research* (IJRER), 7(1), 266-274.

[4]Debnath, S., Das, B., Randive, P. R., & Pandey, K. M. (2018). Performance analysis of solar air collector in the climatic condition of North Eastern India. *Energy*, 165, 281-298.

[5]Sundar, L. S., Singh, M. K., Punnaiah, V., & Sousa, A. C. (2018). Experimental investigation of Al2O3/water nanofluids on the effectiveness of solar flat-plate collectors with and without twisted tape inserts. *Renewable energy*, 119, 820-833.

[6]Khalil, W. H., Obaid, Z. A. H., & Dawood, H. K. (2019). Exergy analysis of single-flow solar air collectors with different configurations of absorber plates. *Heat Transfer*—Asian Research.

[7] Abuşka, M., & Şevik, S. (2017). Energy, exergy, economic and environmental (4E) analyses of flat-plate and V-groove solar air collectors based on aluminium and copper. *Solar Energy*, 158, 259-277.

[8]Güven, C , Kırar, E , Işıker, Y , Aktacir, M . (2018). Düzlemsel Tip Güneş Kollektörlerde Verim Artırıcı Uygulamalar, *Harran Üniversitesi Mühendislik Dergisi*, 3 (3), 38-42 .

[9] Ehrmann, N., & Reineke-Koch, R. (2012). Selectively coated high efficiency glazing for solar-thermal flat-plate collectors. *Thin solid films*, 520(12), 4214-4218.

[10]Dagdougui, H., Ouammi, A., Robba, M., & Sacile, R. (2011). Thermal analysis and performance optimization of a solar water heater flat plate collector: Application to Tétouan (Morocco*). Renewable and Sustainable Energy Reviews*, 15(1), 630-638.

[11] Do Ango, A. M., Medale, M., & Abid, C. (2013). Optimization of the design of a polymer flat plate solar collector. *Solar Energy*, 87, 64-75.

[12] Duffie, J. A., & Beckman, W. A. (2013). Solar engineering of thermal processes. John Wiley & Sons

THERMODYNAMIC ANALYSIS OF AUTOMOBILE BRAKE SYSTEM

Ahmet MAVİ [*], Abide Banu GÜNDÜZ ALTIOKKA[*], Oğuz ARSLAN[**]
[*]Bilecik Şeyh Edebali, Vocational School, Bilecik/Turkey
Email: ahmet.mavi@bilecik.edu.tr
Email: banu.gunduz@bilecik.edu.tr
[**]Bilecik Şeyh Edebali, Department of Mechanical Engineering, Bilecik/Turkey
Email: oguz.arslan@bilecik.edu.tr

ABSTRACT

In this study, the air-ducted disc brake system of an automobile was experimentally simulated. The experiment system consisted of the brake disc, caliper, pads, the electric motor used to drive the brake disc, and a hydraulic pump to provide the oil pressure required to activate the brake unit. Rotating the brake disk at a constant speed in order to simulate the braking process, the force applied to the disk for different brake pressures and the temperature change on the disk as a result of the braking process were measured. The braking system was evaluated thermodynamically by using the measurement results obtained.

Keywords: Breaking system, Energy, Exergy

Nomenclature

Q	Heat (J)
$\dot{Q}$	Heat power (W)
P	Pressure (Pa)
W	Work (W)
$W_{Pressure}$	Brake force applied to stop the disc
W_{Turn}	Work of turning
c_p	Specific heat (J/kgK)
T	Temperature (K)
T_o	Environmenral temperature(K)
A	Disc areas (m^2).
V	Vehicle speed (km/h)
E_{in}	Input energy
E_{Out}	Output energy
Ex_{in}	Input exergy
Ex_{out}	Output exergy
Ex_d	Exergy destruction

1. INTRODUCTION

One of the most important active safety systems in cars is the brake system. Continuous improvement studies are carried out on brake systems to ensure safe and secure driving. As a result of the warming caused by friction in the brake system, changes occur in the braking force. The changes in the frictional properties of the discs, lining, etc. parts in the brake system and the loss of the properties of the parts in the brake system also affect the brake performance negatively.

Bayrakçeken and Düzgün (2005) stated in their study that the braking performance is one of the most important factors affecting vehicle safety in order to stop the vehicle safely and that the high-temperature and stopping

distance in the brakes are one of the most important indicators of braking performance [1]. The temperatures that occur in the brakes also differ according to the disc and lining materials used.

Çavdar et al. (2008) said that high temperatures generated during braking cause a decrease in brake force, brake weakening, premature wear, evaporation of brake fluid, bearing failures, and many undesirable conditions on the vehicle such as thermal cracks. Undesirable situations negatively affect the brake performance [2].

Brake systems operating with the friction principle transform the kinetic energy of the vehicle into thermal energy (heat) through friction. High temperatures adversely affect the disc and pad material properties and cause the surfaces to glaze. As a result, as the friction force between the disc and the pad decreases, various malfunctions occur in the brake system. Accordingly, the friction coefficient between the disc and the brake pad decreases. The decrease in the friction coefficient eventually causes the braking force to be negatively affected.

Düzgün ve Yıldız (2009) observed in their experimental study that the heat generated in the brake system changed in proportion to the mass and speed of the vehicle and that if the amount of heat generated by friction during braking reached high values, it created glare, glass formation, or thermal cracks on the disc surfaces over time. They also stated that the wear on the disc and lining surface increased, and the amount of wear also changed according to the lining and brake disc material used [3].

Rudolf (1995) stated in his experimental study that the performance loss (fading) due to warming can change the brake force during braking. He stated that one of the biggest problems in the vehicle brake system was that when the temperature of the linings rose above certain values (temperatures from 250°C to 315°C and above) due to friction, the linings started to slide without holding [4].

Fading is the loss of brake performance due to the heat effect. The biggest problem in the brake system of the automobile is that the brakes start to slide without holding due to excessive heat when the brakes become hot as a result of continuous use and exceed certain temperature values.

In this study, the heat energy value resulting from the high temperatures that occur in the brake systems was calculated and examined in terms of thermodynamics.

2. MATERIAL AND METHOD

2.1 Experimental System

An experimental setup was produced in order to perform the tests in accordance with the conditions specified in TS 555 and TS 9076. The friction coefficient and the brake force of the linings can be examined under the influence of factors such as different speeds, temperature, pressure. With the brake force tester, it is possible to create the friction coefficient-temperature, brake force-temperature, friction coefficient-time, temperature-time graphs.

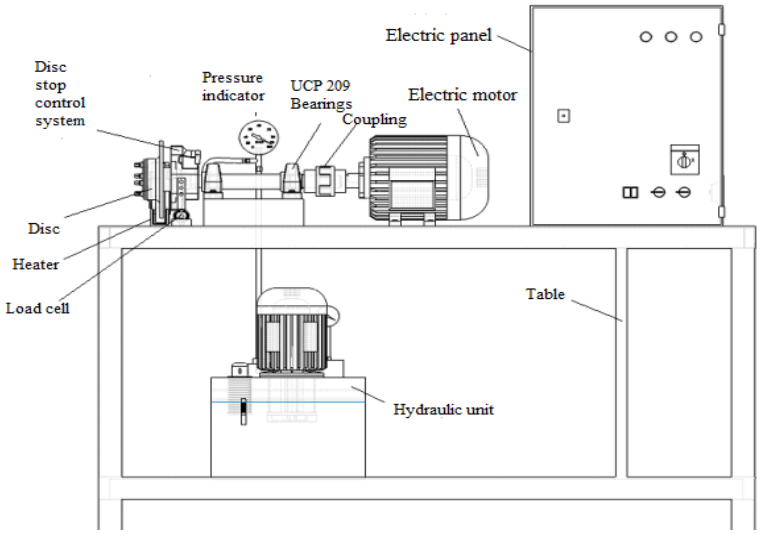

Figure 1. Schematic view of the brake force measurement test device [5].

In the friction coefficient tester shown in Figure 1, a three-phase electric motor with a power of 5.5 kW and 1400 rpm was used to rotate the disc. A transmission shaft of Ø 30 mm was used to transmit the motion obtained from the electric motor. It was aimed to prevent the shaft from swinging by placing two UCP 209 bearings on this shaft. The circular motion from the electric motor was transferred to the disc through the shaft at the desired revolutions by means of the inverter. The speeds were between 0 and 1400 rpm. The speed of the electric motor can be controlled by the computer program.

By means of the hydraulic unit in the system, desired pressure can be applied to the brake disc. During the experiments, a pressure control valve was placed between the piston and the hydraulic motor to prevent pressure irregularities and to keep the pressure constant at the desired value.

In this study, an air channel disc was used. The surfaces of the brake disc used were readied for testing by turning. The pads suitable for the caliper piston in the brake tester were made ready by performing grinding and cutting operations.

The brake disc used in the experiment and the specially prepared brake pads are shown in Figure 2.

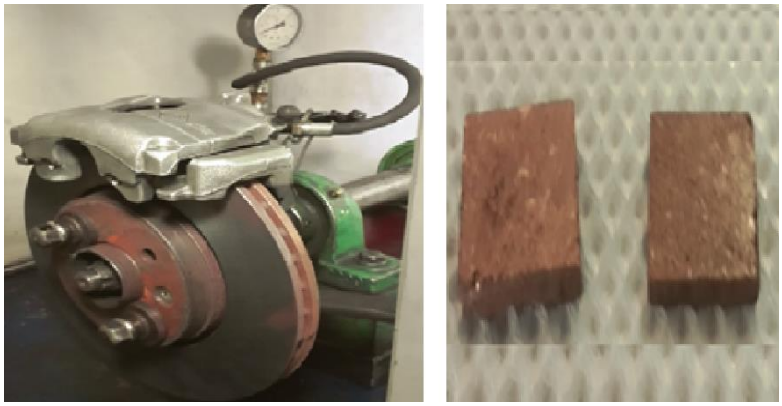

Figure 2. Brake disc and Brake lining views

The air-cooled brake disc was used in the Brake Force measuring device. Experiments were carried out at different brake pressures for vehicle speeds of 60, 80, 100 km/h. Experiments were conducted by continuously increasing

the temperature values for different brake pressures at each disc speed. Brake force values were measured for each temperature varying according to time. Temperature limit values were increased from 50°C to 400°C, and the brake force values were noted at 50°C intervals.

Elements in the brake system are shown in Figure 3a. The motion coming from the motor rotates the disk continuously. The disc is forced to stop by means of the hydraulic unit. In Figure 3b, the parameters affecting the control mass are addressed.

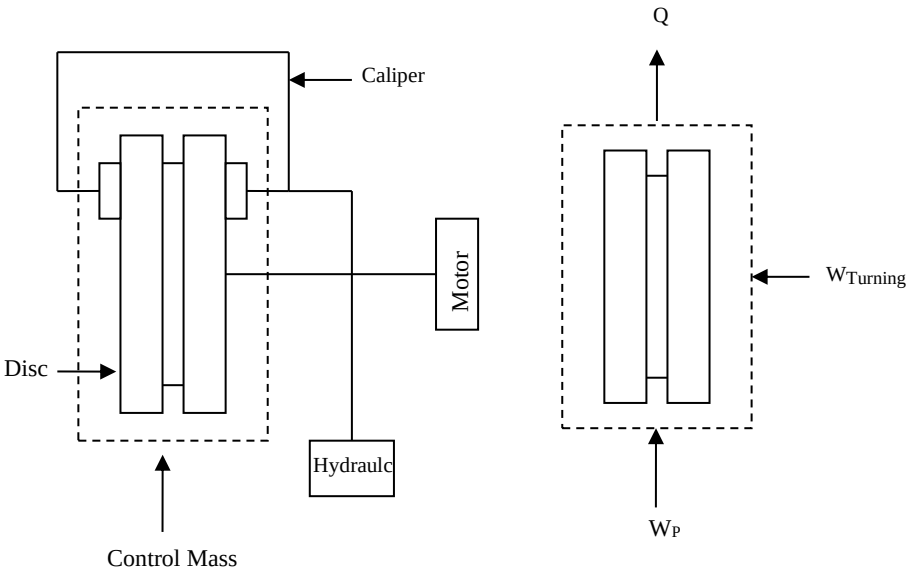

a) Elements in the brake system b) Control mass

Figure 3. Brake system schematic (a) and flow diagram (b).

2.2 Energy and Exergy Analysis

2.2.1 Energy Analysis

The first law of thermodynamics deals with the conservation of energy. It states that the net change in the total energy of a closed system during a change of state is equal to the difference between the total energy entering the system and the total energy leaving the system. General Energy Equation is given in Equation 1.

$$\dot{E}_{in} - \dot{E}_{out} = \frac{dE_{sis}}{dt} \tag{1}$$

$$\dot{Q}_{net} - \dot{W}_{net} = \frac{mc_p dT}{dt} \tag{2}$$

$$\dot{Q}_{net} - (\dot{W}_P + \dot{W}_T) = \frac{mcdT}{dt} \tag{3}$$

The pressure force applied by the brake on the system and the work obtained from the electric motor rotating the disk is shown in Equations 4 and 5.

$$\dot{W}_P = \int P d\forall = P \int d\forall = P\forall \tag{4}$$

$$\dot{W}_T = F.V \tag{5}$$

2.2.2 Exergy Analysis

Exergy is the maximum work that a system in a particular condition can do. The general exergy balance is given in Equation 6.

$$\sum \dot{E}x_{in} - \sum \dot{E}x_{Out} - \sum \dot{E}\,x_d = \sum \dot{E}x_{system} \tag{6}$$

$$(\dot{W}_P + \dot{W}_T)\text{-}\left(\left(1 - \frac{T_0}{T}\right).\dot{Q}\right) - \dot{E}x_d = \dot{E}x_2 - \dot{E}x_1 \tag{7}$$

$$\dot{E}x_d = \left(\left(1 - \frac{T_0}{T}\right).\dot{Q}\right) - (\dot{W}_P - \dot{W}_T) \tag{8}$$

3. FINDINGS AND DISCUSSION

3.1 Experimental Findings

Measurements were made for the experimental system seen in Figure 1 and the brake force values according to different vehicle speeds along with the different braking pressures depending on the temperature effect in certain time periods were measured. Measurements were taken at vehicle speeds of 60, 80, 100 km/h and in the different brake pressures of 2, 4, 6, 8, 10 bar. Subsequently, the change graph of the brake force over time was obtained. The findings of the experimental results are as given in Figure 4.

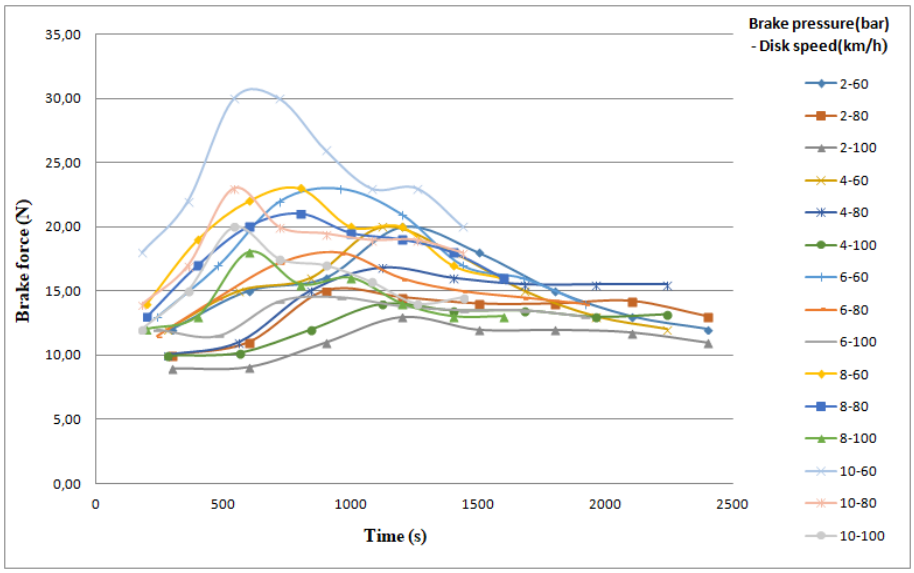

Figure 4. Brake force change [7].

When Figure 4 is examined, it is seen that the Braking Force value reached maximum levels in approximately 9 minutes for 10 bar brake pressure and 60 km/h vehicle speed and after this point, it showed a decreasing trend. There is a similar trend for other measurement parameters. The reason for this decrease is the temperature increase caused by the friction between the disc and brake lining. As a result of the increase in temperature, slipping occurs between the disc and the brake lining due to the glassy surface formation, and for this reason, the friction coefficient decreases. In addition, when we examine the brake force values obtained at different speeds, it is observed that there were more fluctuations in the brake force graphs obtained at high speeds. The reason for this can be stated as the constant change of temperature as a result of the formation of more air circulation in the experimental environment with the increase of speed [7]. The measurement values that give the temperature change of the disc are given in Figure 5.

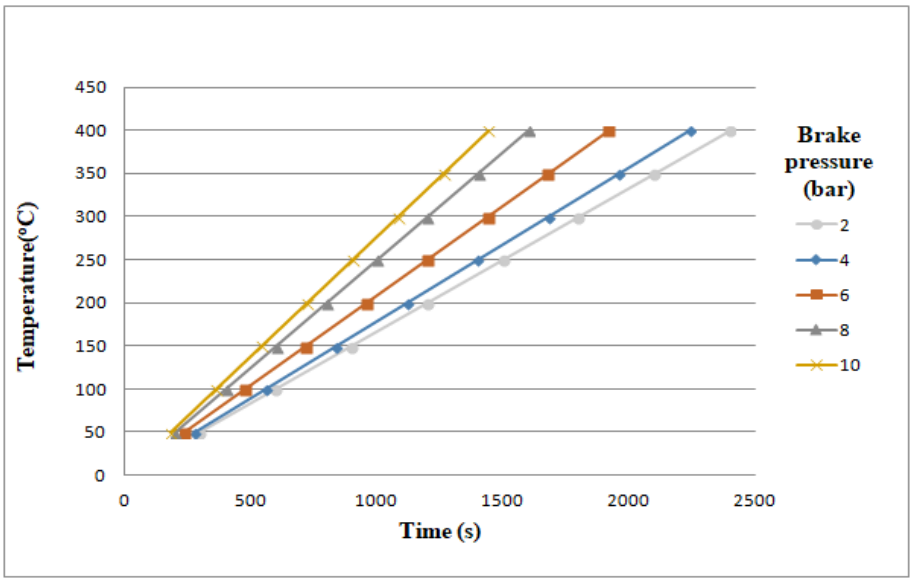

Figure 5. Disc temperature change depending on brake pressure.

As seen in Figure 5, the time to reach the maximum temperature at 10 bar brake pressure was approximately 22 minutes. It was observed that as the brake pressure increased, the duration to reach the maximum temperature decreased. Due to the reduction of brake pressures applied to the brake disc, it was noticed that the durations to reach the maximum temperature level were prolonged.

3.2 Findings of Energy Analysis

Energy analyzes were calculated according to the control mass examined (Figure 3b) and heat losses during the operation were calculated. The results of the calculations are given in Figure 6.

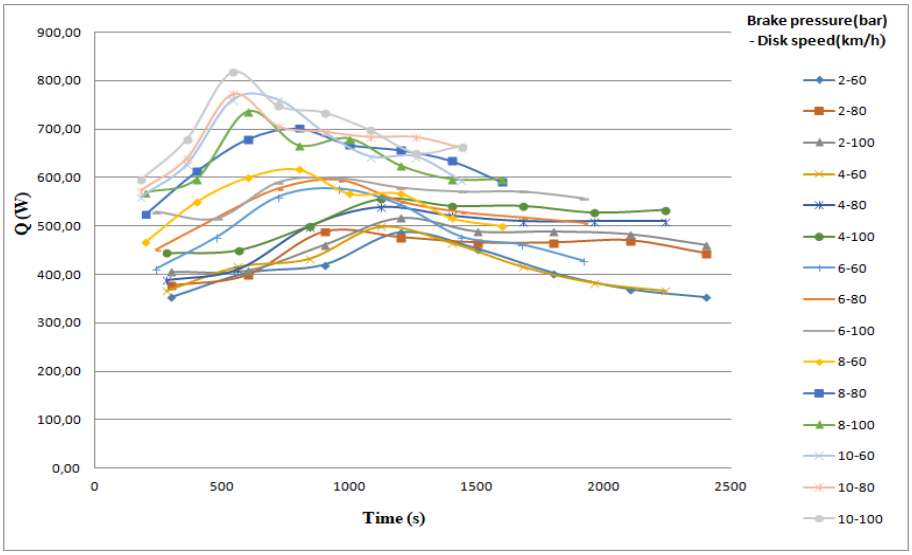

Figure 6. Heat loss values

As seen in Figure 6, heat losses increased parallel to the temperature increasing up to 200-250°C. After certain temperature values, heat losses decreased due to the slippage between the disc and the vehicle lining.

3.3 Findings of Exergy Analysis

Exergy analyzes were made according to the control mass examined (Figure 3b) and the exergy destructions occurred during the study were calculated. The results of the calculations are given in Figure 7. Exergy destructions were calculated according to these analyzes. Accordingly, the exergy destruction values appeared to be higher at high disk speeds. The reason for this change can be that the temperature values reached maximum levels in a shorter time due to the friction speed between the disc and the lining at high speeds, and the temperature values increased in a longer time at low speeds. The biggest factor in exergy destruction is the exergy component due to heat losses depending on the temperature increase. The reason why exergy destruction increased up to a certain value and then decreased was also the result of the decrease in heat losses occurring due to the decrease in the friction coefficient as a result of the slip between disc and lining.

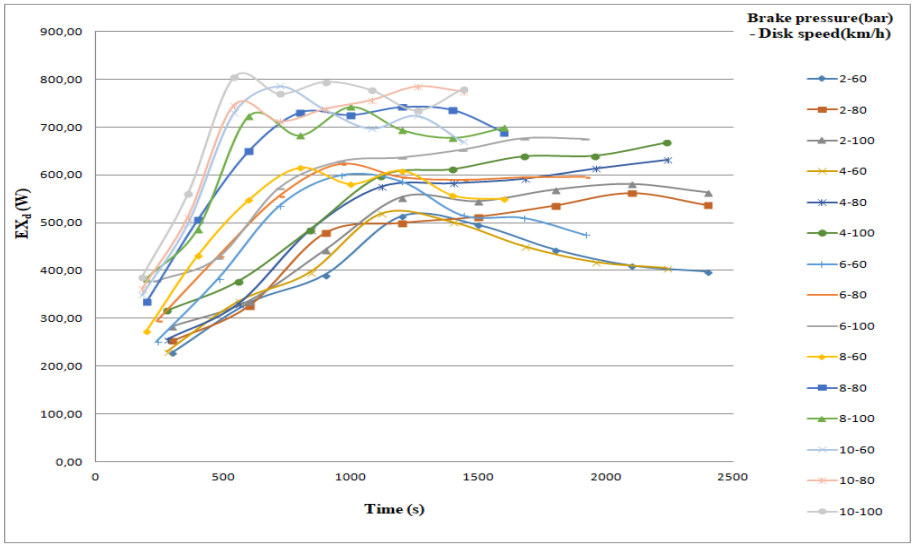

Figure 7. Exergy destruction values.

4. RESULT

In this research, we examined the effects of brake force change depending on time by evaluating the brake system energetically and exergitically. In real cases, braking times occur in short intervals and maximum braking force values are at the temperature values of 200-250ºC. When the lining or disc temperature reaches 315°C or higher, we see that slipping begins on the disc system. [4]

In this study, we determined that the most ideal brake force values were around 200ºC when we applied continuous braking in the brake test. The brake force decreased, and the braking process weakened in the temperature values of 250ºC and above. Again, due to high temperatures, heat losses and the exergy destructions caused by this also increased. Therefore, for an effective braking system temperature is one of the most important parameters to be controlled. We suggest cooling the brake discs as it is the most effective solution for reducing these losses at the maximum possible operating temperatures. Related applications are currently available, usually on air-cooled brake discs. For this purpose, constrictive applications such as holes, fins, ducts, hole-duct combination, and discs with four cooling surfaces are applied to the discs.

REFERENCES

[1] Bayrakçeken, H., Düzgün, M. (2005). Vehicles brake efficiency and braking distance analysis. Gazi University *Journal of Polytechnic* Vol: 8, No:2 pp.153-160.

[2] Çavdar, A., Demir, A. & Kılıçaslan. (2008). İ. Frenlemede zayıflama sınırının tespiti ve iyileştirme çalışmaları. OTEKON08-4. *Otomotiv Teknolojileri kongresi,* Bursa- Turkey.

[3] Düzgün, M., Yıldız, Y. (2009). Soğutma kanallı fren disklerinin frenleme kuvvetlerine ve ısı değişimine etkileri, *5. Uluslararası İleri Teknolojiler Sempozyumu* (IATS'09). Karabük, Türkiye

[4] Rudolf L. (1995). Brake Design and Safety, SAE, 51-70, 228-23.

[5] Timur M. (2007). Otomotivde kullanılan sürtünme malzemelerinin sürtünme katsayısını tespit eden test cihazı tasarımı ve imalatı. Y. Lisans Tezi, Afyon Kocatepe Üniversitesi Fen Bilimleri Enstitüsü, Afyonkarahisar.

[6] Mavi A. (2014). Taşıt frenlerinde sıcaklık etkisine bağlı olarak fren kuvveti değişiminindeneysel olarak incelenmesi. Y. Lisans Tezi, Afyon Kocatepe Üniversitesi Fen Bilimleri Enstitüsü, Afyonkarahisar.

[7] Anderson, A.E. (1992). Friction and wear of automotive brakes. *Materials Park*, OH: ASM Handbook, vol.18.

ORC SİSTEMLERİNDE KULLANILAN N-PENTANE AKIŞKANININ POMPADA SIKIŞTIRMA ORANININ GÜÇ ÜRETİMİNE VE EKSERJİ YIKIMINA ETKİSİ

Mehmet ALTINKAYNAK
Isparta Uygulamalı Bilimler Üniversitesi, Makina Mühendisliği Bölümü, Isparta/Türkiye
Email: mehmetaltinkaynak@isparta.edu.tr

ÖZET

Günümüzde atık ısıdan enerji üretimine yönelik sistem tasarımları hızla geliştirilmektedir. Burada hedeflenen amaç, tasarlanan sistemlerde düşük ısı kaynaklarında da güç üretimini sağlamaktır. Düşük sıcaklık değerleri için güç üretiminde yaygın olarak Organik Rankin Çevrimleri (ORC) kullanılmaktadır. Bu çevrimlerde yaygın olarak kullanılan akışkan n-Pentane akışkanıdır. ORC ile güç üretim sistemlerinde çevrimde kullanılan akışkanın pompada sıkıştırması güç üretimi için istenen bir durumdur. Ancak pompada akışkanı sıkıştırma, pompanın çekeceği gücü artıracaktır. Bu sıkıştırma işinden kaynaklanan entropi artışı sebebiyle, hem pompa da hem de türbinde ekserji yıkımının artmasına sebeb olacaktır. Sıkıştırma oranı 10 olarak seçildiğinde pompanın çektiği güç 14,1 kW olurken, türbinde üretilen iş 716 kW olmaktadır. Bu sıkıştırma oranına bağlı olarak enerji ve ekserji verimleri sırasıyla % 12.58 % 30,3 olarak hesaplanmıştır. Sıkıştırma oranının arttırılması sonucunda, türbine giren akışkanın basıncıda arttırılacak ve dolayısıyla güç üretimin de 660 kW'dan 812 kW'a yani % 23' lük artış meydana gelmektedir. Türbindeki ekserji yıkımı da 189 kW'dan 233 kW'a kadar çıkmaktadır. Sıkıştırma oranının güç üretiminde ve ekserji yıkımında büyük rol oynamasından dolayı optimum bir sıkıştırma aralığına bağlı sistem dizaynı yapılması, sistemin daha verimli çalışmasına ve türbinin termodinamik performansına katkı sağlayacaktır.

Keywords: n-Pentane, ORC, Sıkıştırma Oranı, Enerji, Ekserji.

1. GİRİŞ

Günümüzde dünya birçok sürdürülebilirlik sorunuyla yüzleşmektedir. Enerji, modern insan yaşamının devamı için hayati bir bileşendir ve herhangi bir ülke için sürdürülebilir kalkınmaya ulaşmak için gerekli temellerden biridir. İnsanların gelişen yaşam standartları, teknolojik ilerlemenin yanı sıra, dünyanın enerji kaynakları azalmasına rağmen enerji kullanım seviyesi artmaktadır. Yenilenebilir enerji kaynaklarının [1] geliştirilmesi ve kullanılması ve mevcut enerji kaynaklarının [2] en iyi şekilde kullanımı bu konunun ele alınmasında etkili olmuştur. İçten Yanmalı Motorlar [ICE], elektrik üretimi için geniş kapsamda kullanılmaktadır. Bu motorlar fosil yakıtların yaklaşık%60-70'ini tüketir [3]. ICE'lerin verimliliği, küçük ve büyük dizel motorlar için sırasıyla%30'dan%48'e yükselir. Araştırmalar, dizel motorların gaz türbinlerinden daha verimli olduğunu göstermektedir [4]. Fosil yakıtların yükselen fiyatları ve çevresel etkileri, araştırmacıların ICE'lerde yakıt tüketimini azaltmak için büyük çaba sarf etmeye yönelmiştir. Bu araştırmalar, motor performansını artırabilen HCCI [5], DI [6-7], yüksek basınçlı yakıt enjeksiyonu ve gelişmiş enjeksiyon süresi kontrolü [8] içerir. Ayrıca, matematiksel simülasyona dayalı sayısal yöntemler, bu motorların simülasyonu ve analizi için yaygın olarak kullanılmaktadır. Ampirik araştırma doğru olsa da, çok fazla zaman ve para gerektirir. Ancak sayısal simülasyonlar bir şekilde güvenilirdir ve gereken süreyi ve maliyeti azaltır [9].

Mevcut tüm teknolojiler arasında, Organik Rankine çevrimi (ORC), yüksek verimlilik, basit yapısı ve güvenilirliği nedeniyle orta ve düşük sıcaklıklı ısı kaynaklarının kullanımı için umut verici bir enerji dönüştürme teknolojisi olduğunu kanıtlamıştır [10]. Geleneksel buhar Rankine döngüsünden türetilen ORC çevrimi artık teknik olarak uygun kabul edilmektedir. ORC, motor atık ısı geri kazanımına ek olarak güneş, jeotermal ve biyokütle sistemlerinde yaygın olarak uygulanmaktadır.

ORC çevrimi ile egzoz atık ısı kazanımı üzerine araştırmalar yapılmıştır. Yu ve ark. dizel motordan önerdikleri atık ısı geri kazanımı için kademeli buhar / organik rankine döngüsü (RC / ORC) sisteminin üzerinde çalışmışlardır. Çalışmaları sonucunda geliştirdikleri RC / ORC sisteminin net gücünü 12,7 kW olduğunu bulmuşlardır. Sistemde kullanılan dizel motorla karşılaştırıldığında, kademeli RC / ORC sistemini entegre ederek güç artışını%5,6'ya kadar artığını hesaplamışlardır [11]. Mohammed ve ark çalışmalarında süperkritik ORC çevrimi ile dizel motorun atık ısı kazanımını araştırmışlardır. Sonuçlarında entegre edilmemiş sistemin termal verimliliği %43, R134a ve R245fa kullanıldığında sırasıyla termal verimlilikleri %59,4, %60,3 olarak bulmuşlardır. Ayrıca motordan çevreye salınan gaz emisyonunu %18 oranında azaltmışlardır [12]. Song ve ark çalışmalarında denizcilikte kullanılan ORC entegreli dizel motorun termodinamiksel performansını incelemişlerdir. Çalışma sıvısı olarak R245fa ve benzen içeren iki ayrı ORC sisteminde, toplam net güç çıkışının 101,1 kW'a deniz dizel motoru için %10,2' lik bir verimlilik artışı olduğunu bulmuşlardır. Çalışmalarında ayrıca çalışma sıvısı olarak sikloheksan (cyclohexane) kullanıldığında, optimize edilmiş sistemin maksimum net güç çıkışı, iki ayrılmış sistemden sadece % 1,4 daha düşük olarak 99,7 kW'a olduğunu hesaplamışlardır [13]. Larsen ve arkadaşları deniz motoru ısı geri kazanımı için optimum çalışma sıvısını, kazan basıncını ve Rankine döngüsü süreci düzenini belirlemek için uygulanabilir bir system olarak önermişlerdir [14]. Regner motor egzoz gazı, şarj havası soğutucusu ve EGR soğutucusundan ısıyı geri kazanmak için bir ORC-WHR sistemi geliştirmişlerdir. Analizleri sonucunda motor güç çıkışında %20'ye varan bir artış olduğunu bulmuşlardır. [15-16]. Bombarda ve arkadaşları dizel motorların atık ısı geri kazanımı için ORC ve Kalina çevriminin, termal performanslarını karşılaştırmışlardır. Elde edilen faydalı güç kapasiteleri eşit olmasına rağmen, basit tesis yapısı nedeniyle ORC daha uygun olduğunu göstermişlerdir [17].

Bu çalışmada, dizel bir motorun yüksüz durumundaki çalışma şartı için eksoz gazından ORC ile güç üretimi hedeflenmiştir. Uygulanacak güç üretim sisteminde ORC akışkanı n-Pentane seçilmiştir. Bu akışkan için pompada sıkıştırma oranının enerji ve ekserji verimine etkisi ile ekserji yıkımlarına etkisi incelenecektir.

2. SİSTEM TANITIMI VE TERMODİNAMİK ANALİZ

Dizel bir jenaratörün atık ısısından ORC ile güç üretimini gösteren sistemin şekli Şekil 1'de verilmiştir. Dizel jenaratörlerin tam yükte çalıştırılması durumunda yüksek yakıt girdisine bağlı yüksek ekszo gazı sıcakları oluşmaktadır. Ancak araştırılan bu sistemde minumum yükte çalışan bir dizel motorun eksoz gazı sıcaklığı 204 C kabul edilerek, n-Pentane akışkanın türbin girişinde 170 C'ya çıkarılması hedeflenmiştir. Böylece türbinden güç üretimi sağlanmış ve termodinamik analizi yapılmıştır.

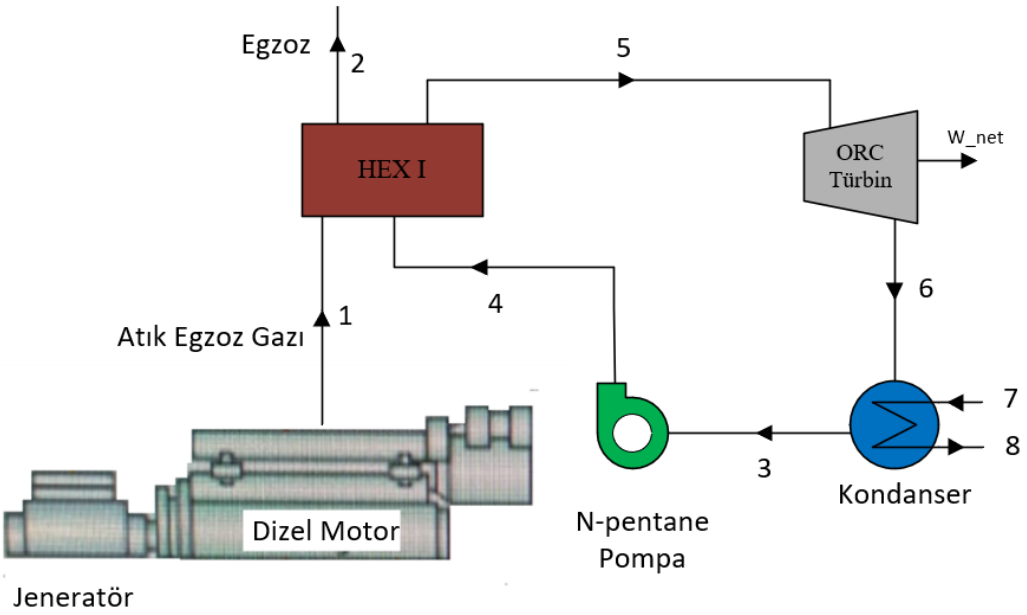

Şekil 1. Dizel Jenaratör Eksoz Gazından Güç Üretim Sistemi

Dizel jeneratör eksoz gazından güç üretimi elde etmek için kullanılan n-Pentane akışkanın fiziksel özellikleri Tablo 1.' de verilmiştir.

Tablo 1. Physical properties of n-Pentane[18]

Properties	Unit	Value
Mol Ağırlığı	g/mol	72,149
Kritik sıcaklığı	°C	196,7
Kritik basıncı	bar	33,6
Yoğunluğu	Kg/m^3	620,9
Kaynama Sıcaklığı	°C	36,06
Isı Kapasitesi (Gaz fazında)	kJ/kgK	1,66
Isı iletim katsayısı	W/m°C	0,111
Ozon Delme Potansiyeli (ODP)	0	
Küresel Isınma Potansiyeli (GWP)	20	

Organik rankine çevriminde kullanılan, dizel jenaratör eksoz gazından güç üretimi sistem elemanlarının termodinamik özellikleri Tablo 2' de verilmiştir.

Tablo 2. Sistem ekipmanlarının termodinamik özellikleri

	$\dot{m}$ (kg/s)	P (kPa)	T (°C)	s (kJ/kgK)	h (kJ/kg)
1	166,4	600	204	6,823	479,5
2	166,4	600	170	6,748	444,7
3	9,22	71,51	26	0,001741	0,2103
4	9,22	1001	26,52	0,003408	2,209
5	9,22	1001	170	1,661	631,7
6	9,22	71,51	119,7	1,738	543,6
7	78	200	22	0,3249	92,47
8	78	200	37,37	0,537	156,7

Sistemde kullanılan ekipmanların kütle, enerji, entropi ve ekserji dengeleri aşağıda verilmiştir.

HEX I ;

$\dot{m}_1 + \dot{m}_4 = \dot{m}_2 + \dot{m}_5$
$\dot{m}_1 h_1 + \dot{m}_4 h_4 = \dot{m}_2 h_2 + \dot{m}_5 h_5$
$\dot{m}_1 s_1 + \dot{m}_4 s_4 + S_{\text{üretim\_Hex-I}} = \dot{m}_2 s_2 + \dot{m}_5 s_5$
$\dot{m}_1 ex_1 + \dot{m}_4 ex_4 = \dot{m}_2 ex_2 + \dot{m}_5 ex_5 + Ex_{\text{yıkımı\_HEX-I}}$

n-Pentane Pompası ;

$\dot{m}_3 = \dot{m}_4$
$\dot{m}_3 h_3 + \dot{W}_{n-Pentane-pompa} = \dot{m}_4 h_4$
$\dot{m}_3 s_3 + \dot{S}_{\text{üretim},n-Pentane-pompa} = \dot{m}_4 s_4$
$\dot{m}_3 ex_3 + \dot{W}_{n-Pentane-pompa} = \dot{m}_4 ex_4 + \dot{E}x_{yıkım,n-Pentane\ pompa}$

ORC Türbin ;

$m_5 = m_6$

$\dot{m}_5 h_5 = \dot{m}_6 h_6 + W_{Türbin}$
$\dot{m}_5 s_5 + \dot{S}_{üretim,Türbin} = \dot{m}_6 s_6$
$\dot{m}_5 ex_5 = \dot{m}_6 ex_6 + W_{Türbin} + I_{Türbin}$

Kondanser ;

$\dot{m}_3 = \dot{m}_6 \; ; \dot{m}_7 = \dot{m}_8$
$\dot{m}_3 h_3 + \dot{m}_6 h_6 = \dot{m}_7 h_7 + \dot{m}_8 h_8$
$\dot{m}_3 s_3 + \dot{m}_6 s_6 + \dot{S}_{g,Kon} = \dot{m}_7 s_7 + \dot{m}_8 s_8$
$\dot{m}_3 ex_3 + \dot{m}_6 ex_6 = \dot{m}_7 ex_7 + \dot{m}_8 ex_8 + \dot{E}x^D_{Kon}$

3. ARAŞTIRMA VE BULGULAR

ORC ile güç üretim sistemlerinde çevrimde kullanlan akışkanın pompada sıkıştırma oranı çok önem taşımaktadır. Akışkanının pompada sıkıştırma oranı arttıkça türbin giriş basıncı artacaktır. Bu durumda pomapanın çektiği güç artacak ve sıkıştırma sonuncunda entropi artışı olacağından n-Pentane pompasının ekserji yıkımıda artacaktır. Pompanın sıkıştırma oranına bağlı güç tüketimi ve ekserji yıkımı Şekil 2'de verilmiştir. Şekilde görüldüğü gibi, sıkıştırma oranın 12 olduğu durum için; n-Pentane pompasının çektiği güç 17,8 kW olmaktadır. Sıkıştırma oranının 8'den 14'e yükseltilmesi, pompanın ekserji yıkmını 2,85 kW'tan 5,11 kW'a çıkartmıştır.

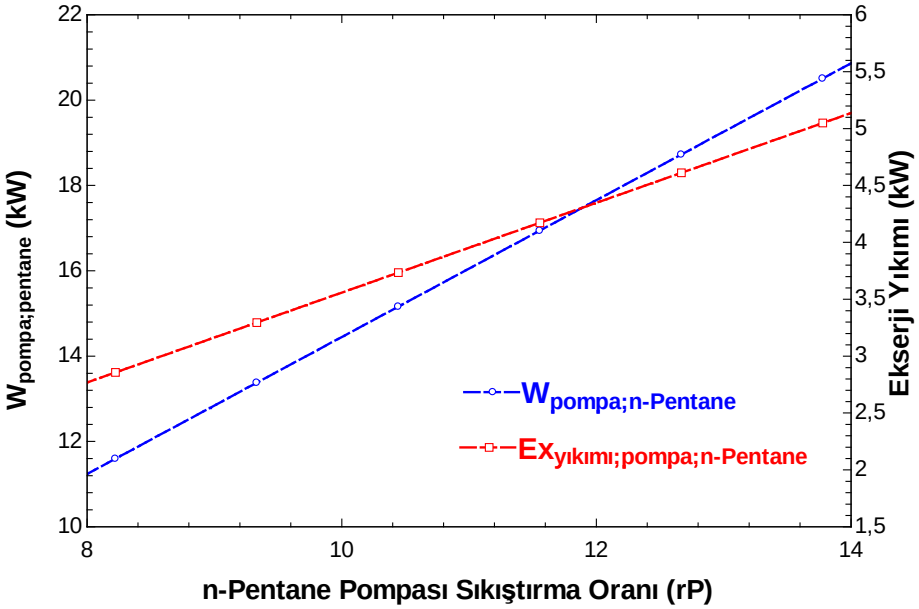

Şekil 2. Pompadaki Sıkıştırma Oranının Güç Tüketimine ve Ekserji Yıkımına Etkisi

Sıkıştırma oranının 8'den 14'e yükseltilmesi durumunda türbinde üretlen güç miktarı 660 kW'dan 812 kW'a kadar çıkmaktadır. Ancak, türbindeki entropi artışına bağlı olarak ekserji yıkımıda artmaktadır. Sıkıştırma oranının 8'den 14'e çıkarılması türbindeki ekserji yıkımınıda 189 kW'dan 233 kW'a kadar yükselmesine sebep olduğu şekil 3'te görülmüştür.

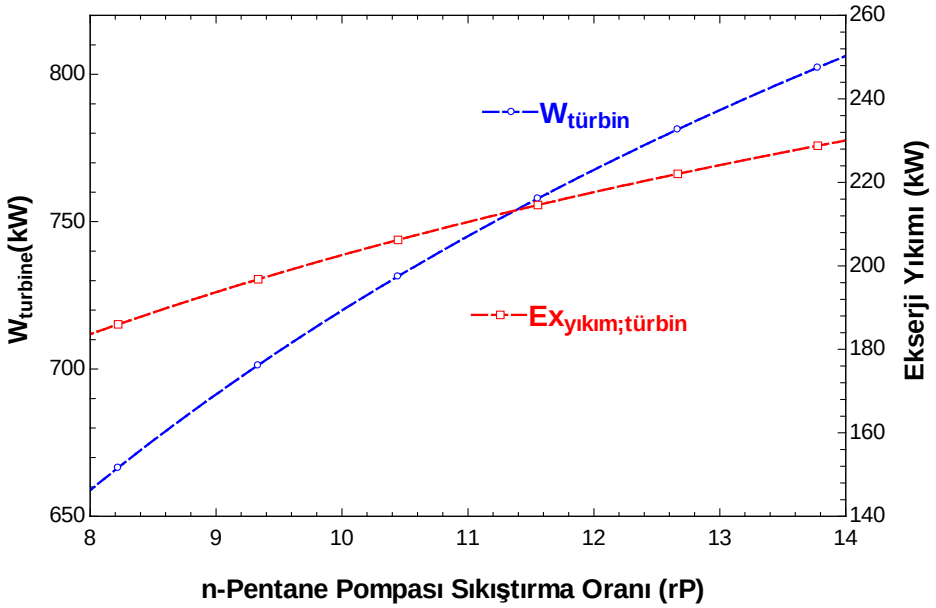

Şekil 3. Pompadaki Sıkıştırma Oranının Türbindeki Güç Üretimine ve Türbinin Ekserji Yıkımına Etkisi

4.SONUÇLAR

ORC ile güç üretim sistemlerinde çevrimde kullanlan akışkanın pompada sıkıştırması güç üretimi için istenen bir durumdur. Ancak pompada akışkanı sıkıştırma, pompanın çekeceği gücü artıracaktır. Bu sıkıştırma işinden kaynaklanan entropi artışı sebebiyle, hem pompada hem de türbinde ekserji yıkımının artmasına sebeb olacaktır. Sıkıştırma oranı 10 olarak seçildiğinde pompanın çektiği güç 14,1 kW olurken, türbinde üretilen iş 716 kW olmaktadır. Bu sıkıştırma oranına bağlı olarak enerji ve ekserji verimleri sırasıyla % 12.58 % 30,3 olarak hesaplanmıştır. Sıkıştırma oranın artırılması sonucunda, türbine giren akışkanın basıncıda arttılacak ve dolayısıyla güç üretimin de 660 kW'dan 812 kW'a yani % 23' lük artış meydana gelmektedir. Türbindeki ekserji yıkımı da 189 kW'dan 233 kW'a kadar çıkmaktadır.

Sıkıştırma oranın güç üretiminde ve ekserji yıkımında büyük rol oynamasından dolayı optimum bir sıkıştırma aralığına bağlı sistem dizaynı yapılması sistemin daha verimli çalışmasına ve türbinin termodinamik performansına katkı sağlayacaktır.

KAYNAKLAR

[1] Najafi, B., Akbarian, E., Lashkarpour, SM., Aghbashlo, M., Ghaziaskar, HS., Tabatabaei, M., Modeling of a dual-fueled diesel engine operated by a novel fuel containing glycerol triacetate additive and biodiesel using artificial neural network tuned by genetic algorithm to reduce engine emissions. Energy 168, 1128–1137 2019.

[2] Shokati, N., Mohammadkhani, F., Yari, M., Mahmoudi, SMS., Rosen, MA., A comparative exergoeconomic analysis of waste heat recovery from a gas turbine-modular helium reactor via organic Rankine cycles. Sustainability 6, 2474–2489, 2014.

[3] Shu, G., Liu, L., Tian, H., Wei, H., Yu, G., Parametric and working fluid analysis of a dual-loop organic Rankine cycle (DORC) used in engine waste heat recovery. Applied Energy, 113, 1188–1198, 2014.

[4] Renedo, CJ., Ortiz, A., Mañana, M., Silio, D., Perez, S., Study of different cogeneration alternatives for a Spanish hospital center. Energy Build, 38, 484–490, 2006.

[5] Sudheesh, K., Mallikarjuna, JM., Diethyl ether as an ignition improver for biogas homogeneous charge compression ignition (HCCI) operation-an experimental investigation. Energy, 35, 3614–3622, 2010.

[6] Poran, A., Thawko, A., Eyal, A., Tartakovsky, L., Direct injection internal combustion engine with high-pressure thermochemical recuperation–experimental study of the prototype. International Journal Hydrogen Energy, 43:11969–11980, 2018.

[7] Moon, S., Potential of direct-injection for the improvement of homogeneous-charge combustion in spark-ignition natural gas engines. Applied Thermal Engineering, 136 41–48, 2018,

[8] Hountalas, DT., Mavropoulos, GC., Zannis, TC., Schwarz, V., Possibilities to achieve future emission limits for HD DI diesel engines using internal measures. SAE Trans, 114(3) 567–583, 2005.

[9] Gogoi, TK., Baruah, DC., A cycle simulation model for predicting the performance of a diesel engine fuelled by diesel and biodiesel blends. Energy, 35,1317–1323, 2010.

[10] Lian H, Li Y, Shu G, Gu C. An overview of domestic technologies for waste heat utilization. Energy Conservation Technology, 2,123-133, 2011.

[11] Yu, G., Shu, G., Tian, H., Huo, Z., Zhu, W., Experimental investigations on a cascaded steam-/organic-Rankine cycle (RC/ORC) system for waste heat recovery (WHR) from diesel engine Energy Conversion and Management 129, 43-51, 2016.
[12] Mohammed, GA., Mosleh, M., El-Maghlany, WM., Ammar, RN., Performance analysis of supercritical ORC utilizing marine diesel engine waste heat recovery Alexandria Engineering Journal 59(2), 893-904, 2020

[13] J., Song, Y., Gu, Chun-Wei., Thermodynamic analysis and performance optimization of an Organic Rankine Cycle (ORC) waste heat recovery system for marine diesel engines, Energy, 82, 976-985, 2015
[14] Larsen, U., Pierobon, L., Haglind, F., Gabrielii, C., Design and optimization of organic Rankine cycles for waste heat recovery in marine applications using the principles of natural selection. Energy, 55, 803-812 2013.

[15] Teng, H., Regner, G., Cowland, C., Waste heat recovery of heavy-duty diesel engines by organic Rankine cycle part I: hybrid energy system of diesel and Rankine engines. SAE Technical Paper 2007.

[16] Teng, H., Regner G. Improving fuel economy for HD diesel engines with WHR Rankine cycle driven by EGR cooler heat rejection. SAE Technical Paper 2009.

[17] Bombarda, P., Invernizzi, CM., Pietra, C., Heat recovery from diesel engines: a thermodynamic comparison between Kalina and ORC cycles. Applied Thermal Engineering, 30, 212-219, 2010.

[18] Pikra, G. & Rohmah, N. Working Fluid Selection for Electricity Production Using Organic Rankine Cycle with Heat Source Temperature of 100°C, *2018 International Conference on Sustainable Energy Engineering and Application (ICSEEA)*, Tangerang, Indonesia, 2018.

COMPUTATIONAL HEAT TRANSFER AND FLUID DYNAMICS

INVESTIGATION OF AIR FLOW INSIDE AN AIRPLANE PASSENGER CABIN

Levent BİLİR*, Hasan ÇELİK, Barış ÖZERDEM*****
*Yaşar University, Department of Energy Systems Engineering, İzmir/Turkey
Email: levent.bilir@yasar.edu.tr
**İzmir University of Economics, Department of Mechanical Engineering, İzmir/Turkey
Email: hasan.celik@izmirekonomi.edu.tr
** İzmir University of Economics, Department of Aerospace Engineering, İzmir/Turkey
Email: baris.ozerdem@izmirekonomi.edu.tr

ABSTRACT

Airplane use are increasing worldwide and airplanes are the only means for long distance travels. However, the passenger cabins of airplanes could contain contaminants due to passengers and the carbon dioxide level should be controlled during the travel. In the present study, a part of the passenger cabin of a commercial airplane was modelled considering symmetrical conditions and the air flow inside the cabin was analysed numerically using Ansys-Fluent software for ceiling supply bottom return mixing ventilation. As a conclusion the streamlines of air released from air ducts was obtained and the flow path of air inside the passenger cabin was determined. The flow path of air also gives information about the contaminant spread inside the cabin.The results revealed that for the investigated air ventilation system there is no significant air mixing for different seat rows. However, the air recirculation on the seats at the same row can cause a problem and should be solved by considering a different air ventilation system.

Keywords: Airplane cabin, air flow path, ANSYS-Fluent analysis, numerical analysis, contaminant spread.

Symbol List

Re	Reynolds number
t	time [s]
u	velocity in x direction [m s^{-1}]
v	velocity in y direction [m s^{-1}]
w	velocity in z direction [m s^{-1}]

Greek Letters

ρ	Density [kg m^{-3}]
τ	Shear stress [N m^{-2}]

1. INTRODUCTION

Air travel is getting more and more inevitable due to long distances and time limitation. Hence, the passenger number using airplanes is increasing day by day. The cabin of an airplane is supplied with air by air distribution system. However, as the cabin of airplanes are confined places, the air supplied by the air distribution system can reach some remote places inside the cabin. This is important if the air contain contaminant, for ex: a virus or a germ due to some passengers. If the contaminant reaches other seats, this can cause a health issue. Mazumdar and Chen [1] considered a seat row inside an airplane cabin and established a one-dimensional analytical model for longitudinal transport of a contaminant. Fiser and Jicha [2] took a small airplane into account and modeled its passenger cabin using a computational fluid dynamics (CFD) program. They considered three different air distribution systems and investigated these systems under cold, mild and hot ambient conditions. They determined which system provides the most stable air distribution and the best quality of the cabin ventilation.

Cao et al. [3] took 2-dimensional PIV measurement of air distribution inside an airplane cabin. They presented the air velocity distribution and turbulence intensity contours using the measured data. Wang et al. [4] evaluated the performance of air distribution systems in high speed train cabins in China They modeled the cabin of three different train cabins using a CFD software. They investigated air velocity distribution inside the cabins and cough droplets removal capability in three train cabins. Yang et al. [5] investigated numerically smoke spread inside the cabin of an airplane. They determined the smoke distribution and velocity vectors at different cross sections. They also presented carbon dioxide concentrations at various cross sections inside the cabin. Maier et al. [6] evaluated thermal comfort inside the airplane cabin for different ventilation systems. They compared mixing ventilation system with displacement system and hybrid (50:50) mixing and displacement system. Zhang et al. [7] also compared different ventilation systems experimentally. They revealed advantages and disadvantages of the considered systems. Kotb and Khalil [8] evaluated the spread of a cough droplet from a moving passenger inside an aircraft cabin. They investigated the path of the cough droplet from the passenger moving with different velocities.

In the present study, a section of a commercial airplane cabin, consisting of three seat rows, was modeled using Ansys-Fluent CFD software. The ceiling supply bottom return mixing ventilation (CMV) system is chosen for air distribution. The air stream graphs were presented to illustrate how the air moves inside the cabin. The presented graphs also give information about the contaminant move inside the cabin.

2. METHOD

Ansys-Fluent program was use in order to obtain a numerical solution for the air distribution inside the evaluated cabin. Navier-Stokes equations presented in Equations (1-4) were solved with turbulence equations in order to get the flow field.

$Continuity$:

$$\frac{\partial \rho}{\partial t} + \frac{\partial\, \rho u}{\partial x} + \frac{\partial\, \rho v}{\partial y} + \frac{\partial\, \rho w}{\partial z} = 0 \tag{1}$$

$X - Momentum$:

$$\frac{\partial\, \rho u}{\partial t} + \frac{\partial\, \rho u^2}{\partial x} + \frac{\partial\, \rho uv}{\partial y} + \frac{\partial\, \rho uw}{\partial z} = -\frac{\partial \rho}{\partial x} + \frac{1}{Re_r}\frac{\partial \tau_{xx}}{\partial x} + \frac{\partial \tau_{xy}}{\partial y} + \frac{\partial \tau_{xz}}{\partial z} \tag{2}$$

$Y - Momentum$:

$$\frac{\partial\, \rho v}{\partial t} + \frac{\partial\, \rho uv}{\partial x} + \frac{\partial\, \rho v^2}{\partial y} + \frac{\partial\, \rho vw}{\partial z} = -\frac{\partial \rho}{\partial y} + \frac{1}{Re_r}\frac{\partial \tau_{xy}}{\partial x} + \frac{\partial \tau_{yy}}{\partial y} + \frac{\partial \tau_{yz}}{\partial z} \tag{3}$$

$Z - Momentum$:

$$\frac{\partial\, \rho w}{\partial t} + \frac{\partial\, \rho uw}{\partial x} + \frac{\partial\, \rho vw}{\partial y} + \frac{\partial\, \rho w^2}{\partial z} = -\frac{\partial \rho}{\partial z} + \frac{1}{Re_r}\frac{\partial \tau_{xz}}{\partial x} + \frac{\partial \tau_{yz}}{\partial y} + \frac{\partial \tau_{zz}}{\partial z} \tag{4}$$

2.1 Considered Airplane Cabin Model

The section including three seat rows of a commercial airplane cabin is taken into consideration due to symmetrical conditions. In order to obtain a numerical solution, the area of interest is divided into 8,199,032 polyhedral meshes. The view of the generated meshes is given in Figure 1.

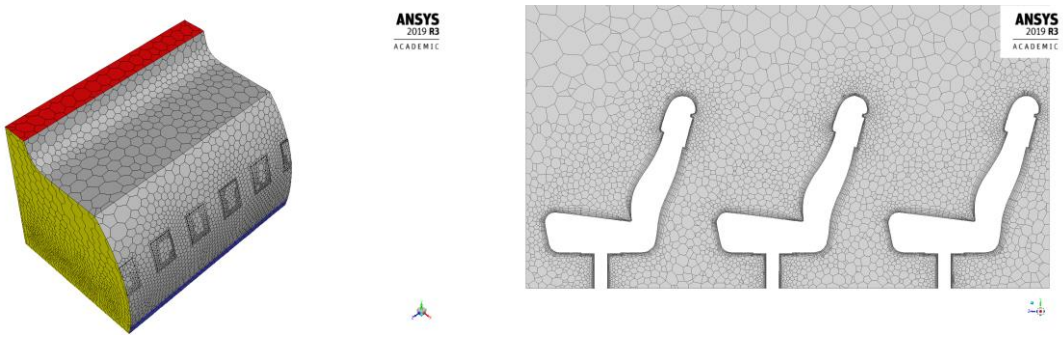

Figure 1. Polyhedral meshes generated for the model of passenger cabin.

The needed supply airflow is taken as 9.4 L/s per person [7]. As there are nine passengers in the selected cabin section the airflow is determined as 84.6 L/s and the corresponding mass flow rate is calculated as 0.11 kg/s. The air is supplied from the top side section of the cabin (blue section) and it is exhausted form the bottom side section (red section) of the model. The front, back and side (yellow section) surfaces of the cabin are defined as symmetry. Bottom surface and the outer side (gray sections) surfaces of the cabin are taken as wall.

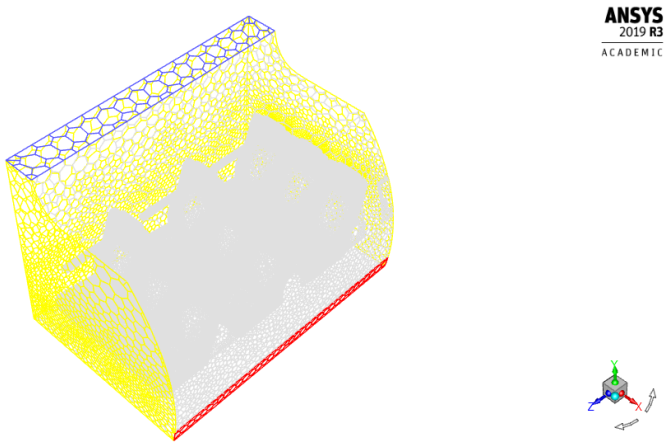

Figure 2. Boundary condition used for the numerical solution.

The realizable k-ε turbulence model with enhanced wall treatment was used as the turbulence model for the numerical solution. This turbulence model was chosen due to its accuracy and easy convergence.

3. RESULTS AND DISCUSSION

The created model is transferred to Fluent solver and iterations for numerical solution are continued until all residual values become lower than 10^{-3} (for continuity) and 10^{-6} (for all others). As a result, the streamlines for different cross sections inside the airplane cabin are presented in Figure 3.

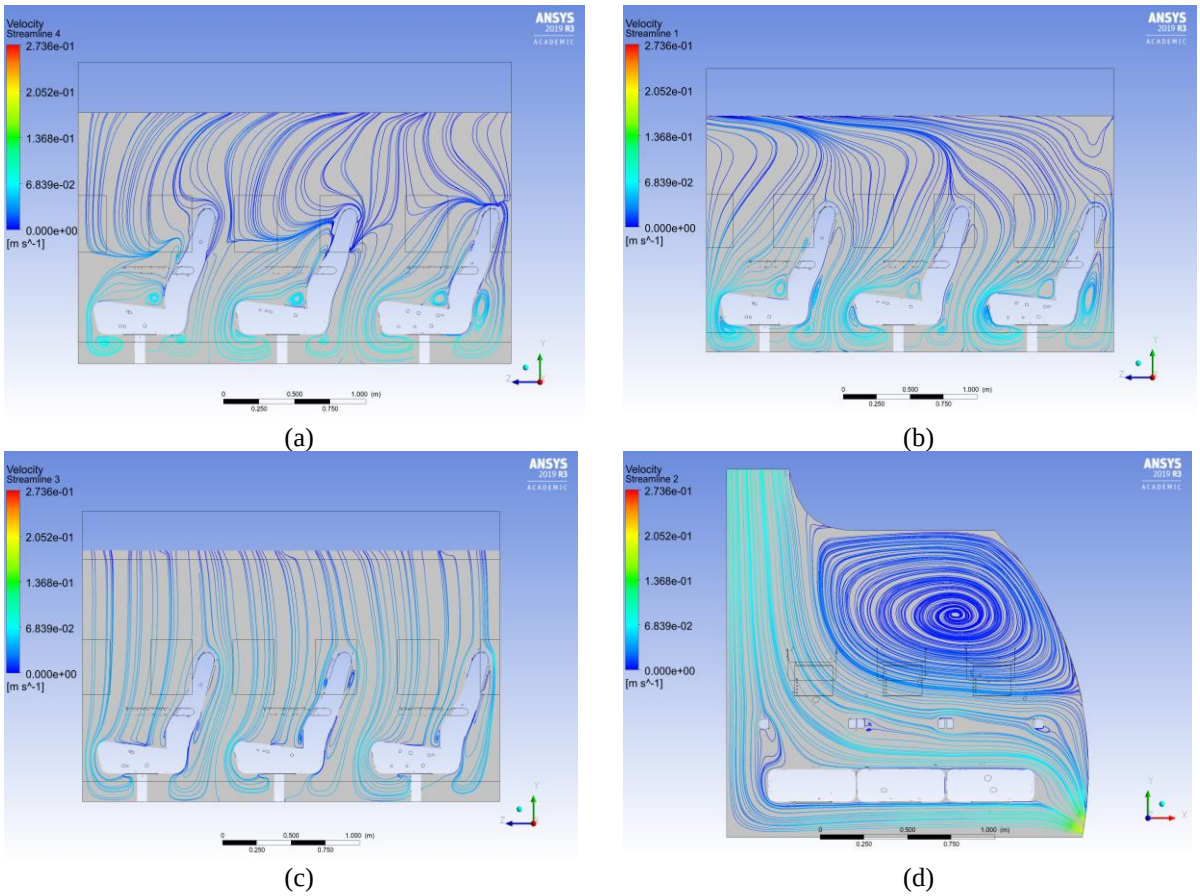

Figure 3. Streamline views at different cross sections.

The streamlines in Figure 3(a) are on the cross section which passes through the middle of the window side seats, while the streamlines in Figure 3(b) are on the cross section which passes through the middle of the middle seats. In figure 3(c), the streamlines on the cross section which passes through the middle of the aisle side seats. Lastly, the streamlines on the vertical cross section which passes through three seats on the middle row.

According to the numerical results for the air distribution inside the passenger cabin, it can be seen that the air between the seat rows is not mixed considerably for the evaluated air ventilation system. However, there is an air recirculation for the air on the same row, seen in Figure 3 (d). This recirculation can cause a health problem. In order to overcome this problem some air can also be send into the passenger cabin over the top of the window side seat or another air distribution strategy should be developed.

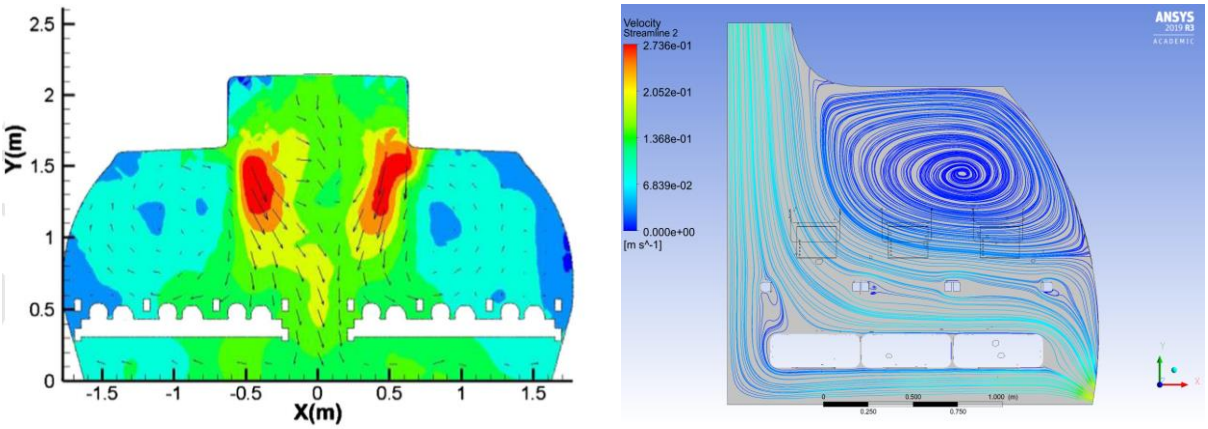

(a) (b)

Figure 4. Comparison of the streamline with the experimental findings of [7].

When the velocity distribution taken from the experimental study performed by Zhang et al. [7] (Figure 4a) is compared with the streamlines found in Figure 3 (d) (Figure 4b), it can be said that there is a very good agreement with the present study and the experimental outcome of [7]. The result shows that the numerical findings of the present study are reliable.

4. CONCLUSIONS

As the passenger number using airlines is increasing with a high trend, the air quality inside the passenger cabins is getting more important. Moreover, the danger of contaminant spread inside the cabin can cause a serious health problem. In the present study, the air distribution inside a commercial airplane cabin is investigated numerically for ceiling supply bottom return mixing ventilation system. A section of the cabin was modeled using a CFD program Ansys-Fluent and meshed with polyhedral volume elements. A total of approximately 8.2 million volume elements were generated and the numerical solution is obtained by defining appropriate boundary conditions. The results found are compared with the experimental findings of another study and it is seen that there is a good agreement between two studies. According to the air streamlines, it is found that air mixing between the rows of the seats is not significant. However, it is observed that the air recirculation is encountered for the same row seats. This problem can be solved by applying another air ventilation strategy, which is the subject of a further study.

REFERENCES

[1] Mazumdar, S., Chen, Q. A One-Dimensional Analytical Model for Airborne Contaminant Transport in Airliner Cabins, *Indoor Air*, **19**, 3-13, 2009.

[2] Fiser, J., Jicha, M. Impact of Air Distribution System on Quality of Ventilation in Small Aircraft Cabin , *Building and Environment*, **69**, 171-182, 2013.

[3] Cao, X., Liu, J., Pei, J., Zhang, Y., Li, J., Zhu, X. 2D-PIV Measurement of Aircraft Cabin Air Distribution with a High Spatial Resolution, *Building and Environment*, **82**, 9-19, 2014.

[4] Wang, H., Lin, M., Chen, Y. Performance Evaluation of Air Distribution Systems in Three Different China Railway High-Speed Train Cabins Using Numerical Simulaton, *Building Simulation*, **7**, 629-638, 2014.

[5] Yang, S., Sun, X., Yu, T, Chen, X. Research on the Numerical Simulation of Aircraft Cabin Smoke, *Procedia Engineering*,, **121**, 357-364, 2015.

[6] Maier, J., Marggraf-Micheel, C., Dehne, T, Bosbach, J. Thermal Comfort of Different Displacement Ventilation Systems in an Aircraft Passenger Cabin, *Building and Environment*, **111**, 256-264, 2017.

[7] Zhang, Y., Liu, J., Pei, J., Li, J., Wang, C. Performance evaluation of different air distribution systems in an aircraft cabin mockup, *Aerospace Science and Technology* **70**, 359-366, 2017.

[8] Kotb, H., Khalil, E.E. Numerical Simulation of Airflow and Airborne Pathogen Transport in Aircraft Cabins: Dynamic Mesh Analyses, *AIAA SCientific Forum*, Orlando, FL, 6-10 January 2020.

A NEW VORTEX PREVENTING ELEMENT DESIGN FOR FRANCIS TURBINES AND COMPARISON OF DIFFERENT GEOMETRIC SHAPES

Deniz Sarper SEMERCİ*, Tahir YAVUZ**
*Başkent University, Department of Mechanical Engineering, Ankara/Turkey
Email: dssemerci@baskent.edu.tr
** Başkent University, Department of Mechanical Engineering, Ankara/Turkey
Email: tyavuz@baskent.edu.tr

ABSTRACT

In recent years, countries have turned to renewable energy resources since fossil with limiting resources have negative effects to the environment. Hydraulic energy is one of the most effective renewable energy resources as it has high potential and ease on convertibility. Francis turbines convert potential and kinetic energy of water into mechanical energy and they have high efficiencies reaching about almost 90%. Yet, with some modifications these efficiencies could still be increased. Vortex flow in the draft tube is not only effects the performance of the turbine, but it is also has negative effects on turbine components. In this study, a new element named Vortex Preventing Element (VPE) is designed to prevent vortex flow in the draft tube. The VPE is located between the runner and draft tube. The principle of this element is to resist the outgoing flow from runner by spiral forms and regulate the flow before to draft tube. The VPE with one spiral form is analyzed with CFD in ANSYS CFX and it is seen that flow is more stabilized with respect to the case of Francis Turbine without VPE. Then, the number of spiral form is thought to be effective on preventing vortex flow so that these two case are investigated. As a result, it is seen that VPE is regulating the complex outgoing flow from runner. it is also seen that the new element increases the turbine efficiency about 2-3%.

Keywords: Francis Turbine, Vortex Structures, Efficiency, Computational Fluid Dynamics.

1. INTRODUCTION

In recent years, the increase of energy demands led countries to seek new energy resources. Renewable energy resources play an important role on supplying energy demands. There are several types of renewable energy resources such as solar energy, wind energy, wave energy, hydraulic energy, etc. Hydraulic energy is one of the most important resources because it is easily converted to the electric energy and hydraulic potential is very high almost all around the world. In hydro-electrical power plants, potential energy of water is first transformed into kinetic energy by releasing it from a determined height which is called turbine head. Then, kinetic energy of water is transformed into mechanical energy by using a hydraulic machine which is called hydraulic turbine. There are several types of hydraulic turbine types such as Kaplan, Francis, etc. But the most common one in use is Francis turbine as ıt is applicable in wide range of head and discharge.

In a Francis turbine, water enters spiral case firstly. Since it has a decreasing cross-sectional area; spiral case decreases the pressure of water and let it flow through the stay and guide vanes. These two blade profiled structures regulate the flow and increase the velocity of water and then send it to the turbine runner. The flow through the turbine runner creates torque and starts both the runner and the shaft to rotate. Then the water used in turbine is discharged from system by draft tube. As the effect of the runner water has swirling flow in the druft tube. Since the velocity of water is high and flow exits the runner in a position of swirling, there would be some stagnant regions at the entrance of draft tube. That means that some low pressure regions are generated by swirling flow. This structure is called as vortex rope. Since there is no regular pressure distribution at the entrance of draft tube, there would be some secondary flows that could decrease the performance of the suction side of turbine runner blades decreasing turbine efficiency. Besides, vortex rope may end the cavitation which is not a desired situation. So it is thought to be as if the vortex rope is eliminated or diminished at the entrance of

draft tube that would cause to increase the turbine efficiency and consequently the operation and use of turbine will be more healthful.

There are some works in literature about this topic. The runner outflow has a swirling component at the middle section of turbine runner, when Francis turbines operate at partial loads or over loads. This swirling flow causes to pressure pulsations and flow irregularities which lead to pressure fluctuations in draft tube. In partial loads, these pressure fluctuations generate a vortex rope at inlet section of draft tube and this vortex structure causes disorders on torque, axial force and radial force. Also, this structure leads vibration, noise and wear on auxiliary equipment. The reasons of vortex formation are decreasing flow velocity at the draft tube inlet section and swirling component. The swirling component rotates the low-velocity flow and that causes the vortex formation to occur. Anup et al [1] investigated the vortex structure at the inlet section of the draft tube by using different turbulence modelling. Choi, Kurokawa and Imamura [2] studied vortex structures in draft tube and they tried to prevent these structures by using J-grooves and inducer together. They obtained that the J-grooves and inducer provides runner blades' suction side to perform better at partial loads. As a consequence, they show that the hollows named J-grooves controlled the angular momentum of the flow and eliminated the swirling components. Wei, Choi and Zu [3] also and Chen and Choi [4] also investigated the effects of J-grooves on vortex structures. They showed that the quantity of vortex structures would be decreased by using J-grooves. The jet effect of these hollows decreases circumferential velocity component and eliminates a fair amount of vortex structure at partial loads. Chen and Choi studied both numerical and experimental o J-grooves' effects on vortex formation. They determined four different points on draft tube wall and measured pressure pulsations. By using Root Mean Square method, they examined magnitude of pressure fluctuations. They pointed out that these hollow structures partially prevent the vortex rope generation but they wouldn't affect turbine performance. Prof. Nishi [5] and his group determined pressure fluctuations have two parts: synchronous and asynchronous fluctuations. They carried out experimental studies and as a consequence, they obtained there is no synchronous pressure fluctuations in a straight draft tube so the elbow causes to synchronous fluctuations in a draft tube. But Stuparu and Susan-Resiga [6] claimed that pressure pulsations would always generate a vortex rope and they carried out numerical studies. Their numerical studies show that pressure fluctuations are not related with the interaction between vortex rope and draft tube elbow. Muntean et al. [7], investigated pressure pulsations caused by swirling flow in a straight draft tube. Pressure sensors are located in several points on draft tube and Fourier spectrum of measurements is determined. They also carried out numerical simulations in different turbulence models. It's seen that RNG k-ε and SAS k-ω models are better turbulence models to reveal vortex formation at the draft tube inlet. But these two models are insufficient compared to RSM to model vortex development at the onward sections of draft tube. Susan-Resiga [8] and Zhang [9] revealed the important topics on the vortex control technique. According to them, the control technique must show the reason of vortex formation, the vortex rope should be controlled at the inlet section of draft tube, the technique should aim the stagnant area located at the middle of draft tube and control technique must not decrease the turbine efficiency. Foroutan and Yavuzkurt [10] used k- ε turbulence model to simulate the vortex rope under the effect of a water jet. They determined that unsteady RANS models are not appropriate to modelling vortex rope properties. Thus, they used Detached Eddy Simulation. As a consequence, they obtain that the water jet partially controlled the pressure pulsations in draft tube. Dias and Riethmuller [11] injected air bubbles into the stagnant flow located in the inlet section of draft tube. They used Particle Image Velocimetry (PIV) to observe vortex formation. Iliescu, Ciocan and Avellan [12] showed that runner blades with constant slope angle cause cavitation phenomena. They investigated the cavitation vortex rope formation by using PIV.

In this study, a new element named Vortex Preventing Element (VPE) is designed to prevent vortex flow in the druft tube. The VPE is located between the runner and draft tube. The principle of this element is to resist the outgoing flow from runner by spiral forms and regulate the flow before to draft tube. The VPE with one spiral form is analyzed with CFD in ANSYS CFX and it is seen that flow is more stabilized with respect to the case of Francis Turbine without VPE. Then, the number of spiral form is thought to be effective on preventing vortex flow so that these two case are investigated.

2. DESIGN METHODOLOGY

Designing a Francis turbine is a complex process due to several components and complex geometries of these components. Thus, a design methodology is generated and Francis turbine is designed based on these steps in Figure 1.

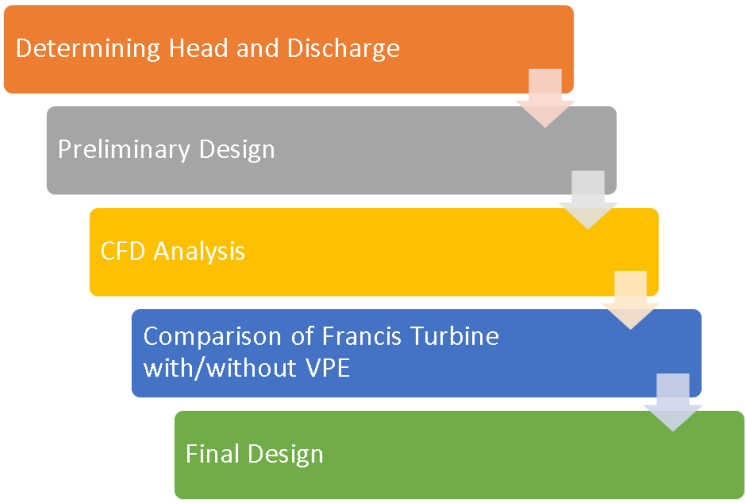

Figure 1. Design Methodology

Since the other steps depend on head and discharge values, determining head and discharge values are the first step. Then, preliminary design is made based on empirical and theoretical data from literature. After preliminary design is done, computational domains are generated in Solidworks v.18 and ANSYS v.18 BladeGEN and Design Modeler. After computational domains are created, mesh structure is generated in ANSYS Mesher. Then CFD analyses are done by ANSYS CFX for the cases that Francis turbine with/without VPE. And then the final design is determined based on efficiency values.

2.1 Vortex Preventing Element

A new design is made to prevent the possible vortex structure to occur at the entrance of draft tube. Since the water exits runner in a constant direction of rotation, a spiral structure which is located as the opposite direction of flow is considered. A resistant structure will force water to regulate its direction and it will decrease its velocity. That means low pressure region will be diminished theoretically. In Figure 2, a view of the designed VPE is given.

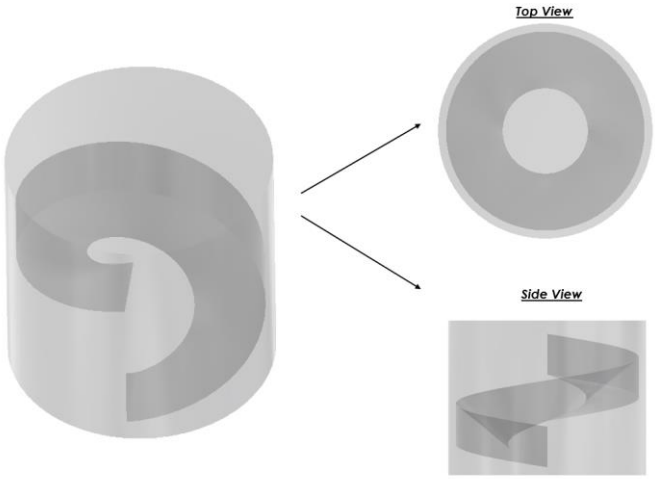

Figure 2. Vortex Preventing Element

This new component is located between the exit of runner and the entrance of draft tube. Thus, the flow with high velocity face a resistance and is forced to be slow down. The spiral shape is considered as a flow path to regulate the flow through the draft tube. The details of location are shown in Figure 3.

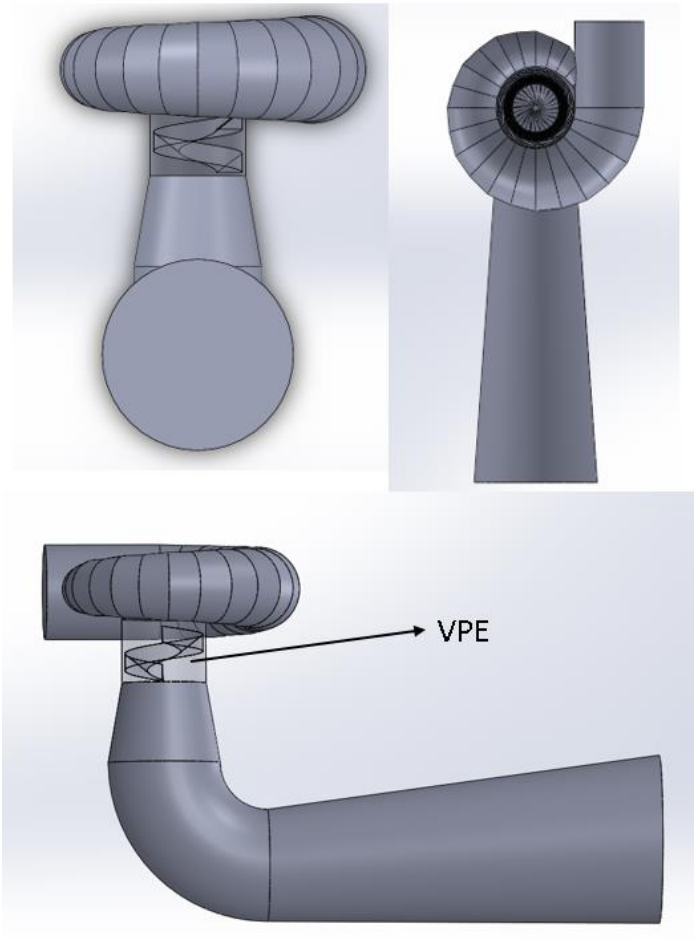

Figure 3. Francis turbine with the VPE, front, top and side views .

2.2 Geometric Differences of Two Designs

In this study, the spiral number is considered to be effective on turbine efficiency because of its location. The VPE with one spiral has less height compared to the VPE with two spirals. Since the water exits runner blades axially, there will be no tangential velocity. But with this design, the flow will be forced to rotate in the opposite direction so it is thought that there would be tangential velocity to occur. That would possibly effect runner blades badly. So, this parameter is thought to be effective on runner blades performance since there would be a resistant force and this will force water to return turbine blades suction side. Thus, two different designs based on spiral numbers are considered as shown in Figure 4.

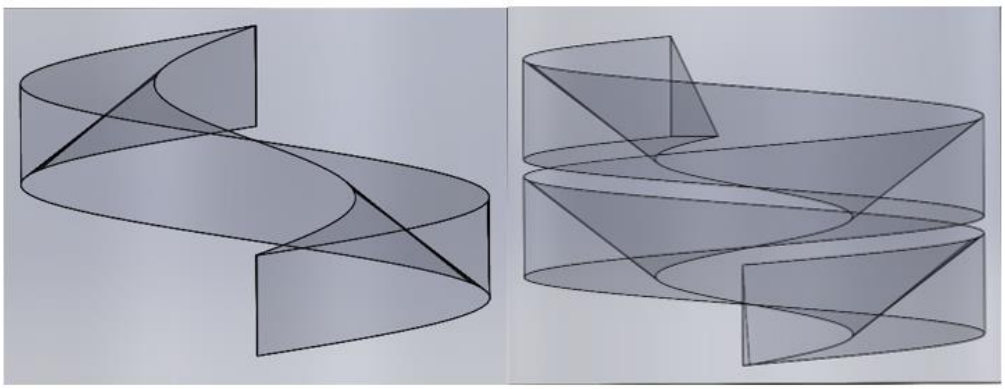

Figure 4. VPE with one spiral and two spirals

3. COMPUTATIONAL FLUID DYNAMICS

ANSYS Mesher is used for generating mesh structures of Francis turbine's components. All components are meshed separately and then combined in ANSYS CFX by using some approaches. In Figure 5, some components' mesh structures are given.

ANSYS CFX is used for generating numerical model. The turbulent flow in the Francis turbine is modelled with a Reynolds Averaged Navier-Stokes (RANS) model, RNG k-ε, because of its reliability. The equations are given as,

$$\rho\left(\frac{\partial \bar{u}}{\partial t}+u\frac{\partial \bar{u}}{\partial x}+v\frac{\partial \bar{u}}{\partial y}+w\frac{\partial \bar{u}}{\partial z}\right)=F_x-\frac{\partial \bar{p}}{\partial x}+\mu\Delta \bar{u}-\rho\left(\frac{\partial \overline{u'u'}}{\partial x}+\frac{\partial \overline{u'v'}}{\partial y}+\frac{\partial \overline{u'w'}}{\partial z}\right) \quad (1)$$

$$\rho\left(\frac{\partial \bar{v}}{\partial t}+u\frac{\partial \bar{v}}{\partial x}+v\frac{\partial \bar{v}}{\partial y}+w\frac{\partial \bar{v}}{\partial z}\right)=F_y-\frac{\partial \bar{p}}{\partial y}+\mu\Delta \bar{v}-\rho\left(\frac{\partial \overline{u'v'}}{\partial x}+\frac{\partial \overline{v'v'}}{\partial y}+\frac{\partial \overline{v'w'}}{\partial z}\right) \quad (2)$$

$$\rho\left(\frac{\partial \bar{w}}{\partial t}+u\frac{\partial \bar{w}}{\partial x}+v\frac{\partial \bar{w}}{\partial y}+w\frac{\partial \bar{w}}{\partial z}\right)=F_z-\frac{\partial \bar{p}}{\partial z}+\mu\Delta \bar{w}-\rho\left(\frac{\partial \overline{u'w'}}{\partial x}+\frac{\partial \overline{v'w'}}{\partial y}+\frac{\partial \overline{w'w'}}{\partial z}\right) \quad (3)$$

Since there are rotating and stationary parts of Francis turbine, some approaches should be applied between mesh interfaces. By using Multiple Reference Frame approach, mesh interfaces are settled. General Grid Interface is used for stationary interfaces. Frozen rotor is used for runner-draft tube and runner-guide vanes interfaces. With this method, runner is specified as rotating but its interfaces between stationary parts such as guide vanes and draft tube remain stationary.

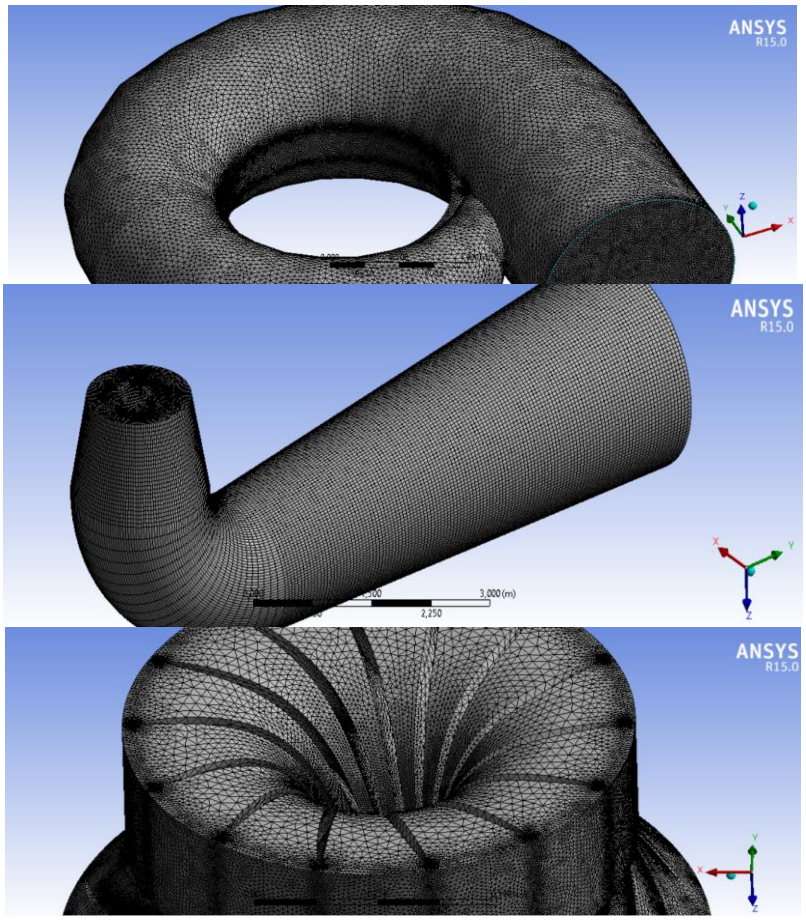

Figure 5. Mesh structures of Francis turbine's components

A discharge value is obtained for model Francis turbine. This value is specified as inlet boundary condition for spiral case inlet section. Since the water flows from draft tube to water channel, the pressure is assumed to be equal the atmospheric pressure as 1 atm. Thus, pressure outlet is defined as outlet boundary condition at draft tube outlet section.

Two different CFD analyses are carried out for Francis turbine designs with one spiraled VPE and two spiraled VPE. There are no differences between these two model and the spiral number.

4. RESULTS AND DISCUSSIONS

Results are investigated in two topics.

4.1 The VPE with one spiral

Vortex Preventing Element is designed and mounted between runner and draft tube. A CFD analysis is carried out and it is compared with standard Francis turbine. It is seen that there are some pressure fluctuations in the entrance sections. There is symmetric high pressure regions on the sharp edges located at the entrance sections. It is seen that pressure fluctuations still exist until water passes from the draft tube elbow. Then it flows uniformly.

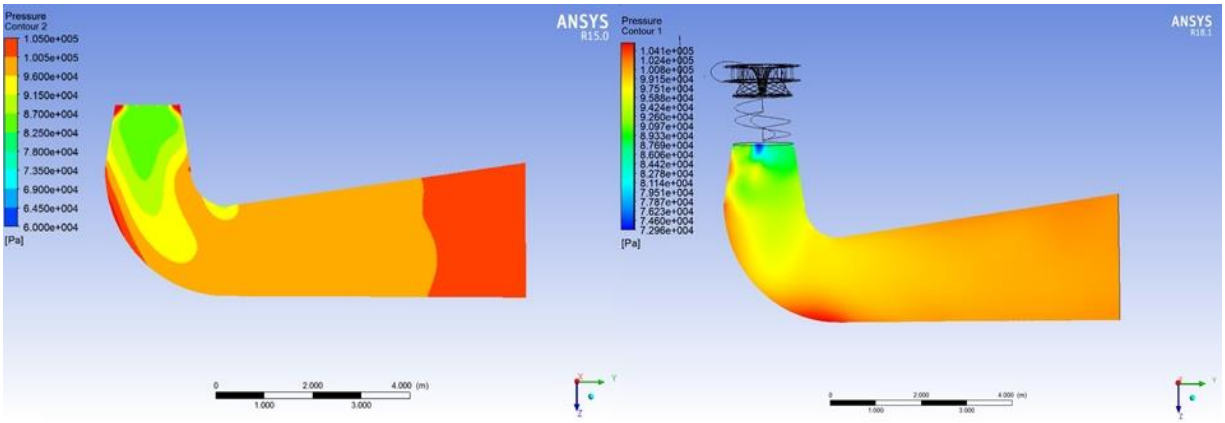

Figure 6. Pressure distributions of the draft tube of Francis Turbine with and without the VPE.

On the other hand, the right hand-side of the Figure 6 shows pressure distribution of Francis turbine draft tube with Vortex Preventing Element. It is seen that pressure fluctuations are partially diminished. The uniform flow begins earlier than the other case. Also, the symmetric high pressure regions located at entrance of draft tube do no longer exist. Pressure transitions are smoother than first case as it can be understood from contours.

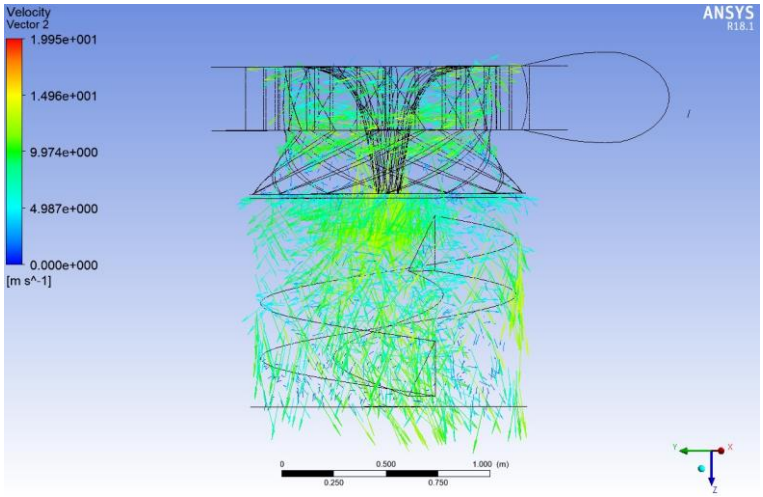

Figure 7. Velocity distribution and vectors of Francis turbine with VPE.

Figure 7 represents the velocity vectors of turbine runner and Vortex Preventing Element (VPE). Water enters radially to the runner and leaves axially. As it is seen, the outflow has swirling component and makes flow to rotate around its axis. When Vortex Preventing Element is used, it is seen that, the rotating flow turned into axial flow and the swirling component is eliminated at the outlet of component. The spiral form of VPE leads water to turn opposite direction of swirling component of velocity and makes a resistance against flow. This motion causes water to flow with minimum swirling velocity component at the outlet of VPE. The efficiencies with and without the VPE are obtained to be 92.8 % and 89 % respectively. Thus, the efficiency of turbine is increased about 4 percent by using the VPE. This is the effect of the VPE having only one spiral.

It is seen that New Vortex Preventing Element provides more uniform flow and higher efficiency at the first glance. The optimization on the number of spirals leading maximum efficiency and uniform flow in the draft tube is needed.

4.2 The VPE with two spirals

Another CFD analysis is carried out for VPE with two spirals. The same solution model is used for this case. The only difference is spiral number of vortex preventing element. In figure 8, it is seen that the velocity vectors are more regular than the case with one spiral.

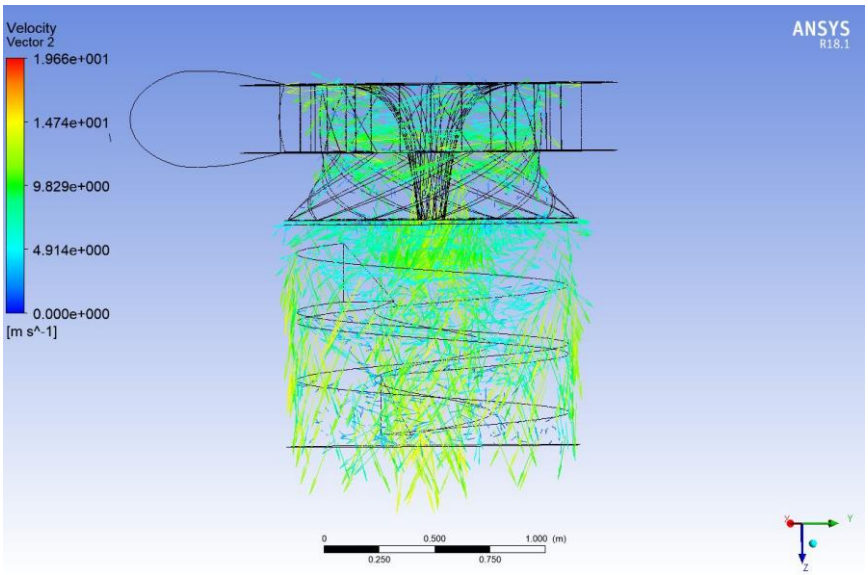

Figure 8. Velocity distribution and vectors of Francis turbine with VPE (2 spirals).

In figure 9, the pressure distribution of draft tube of the Francis turbine with VPE with two spirals is given. It is seen that the low pressure region is diminished in comparison of the designs VPE with one spiral and without VPE.

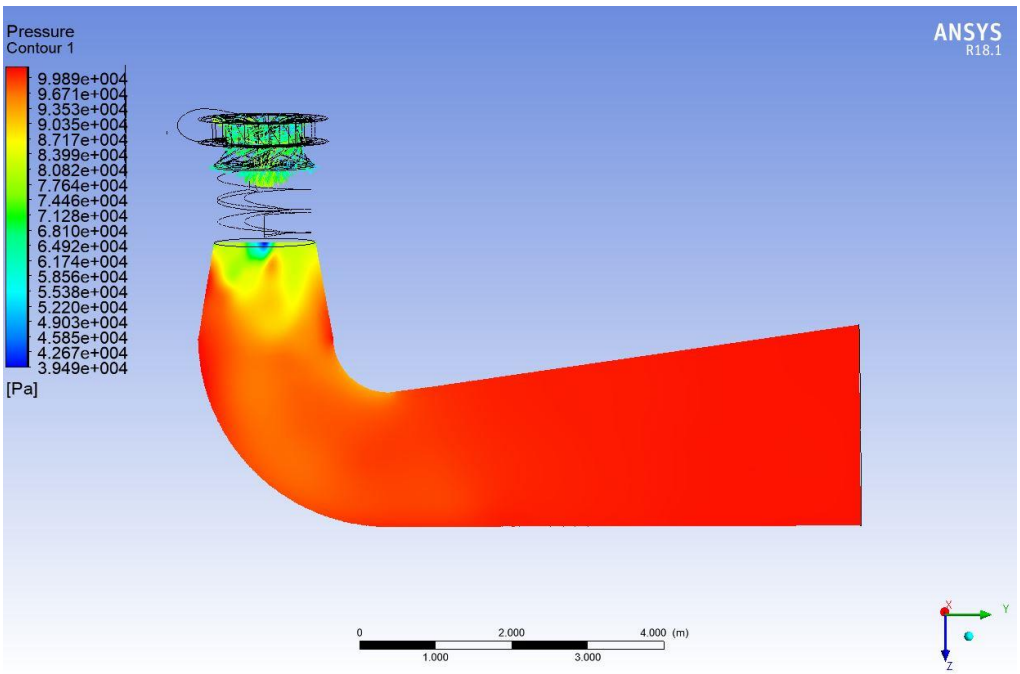

Figure 9. Pressure distribution of draft tube of the design with 2 spirals

In contrast to previous case, the pressure distribution can be evaluated as more uniform. The low pressure regions are located in a very small area at the entrance of draft tube. Also, the flow gains its pressure back faster than the other case.

But there is an undesired condition in this case. The atmospheric pressure is not re-gained at the outlet of draft tube. That may cause turbine efficiency to decrease which is not appropriate for the aim of the study.

5. CONCLUSION

In this study, a new element named Vortex Preventing Element (VPE) is designed to prevent vortex flow in the draft tube. The VPE is located between the runner and draft tube. The principle of this element is to resist the outgoing flow from runner by spiral forms and regulate the flow before to draft tube. The VPE with one spiral form is analyzed with CFD in ANSYS CFX

Conclusions drawn from the study are;

- Vortex preventing element between runner of the turbine and draft tube regulate vortex flow in the draft tube,
- The VPE with one spiral structure increase the efficiency of the turbine about 2-3 percent,
- The VPE with two spirals has more regulated effects on the vortex flow in the draft tube. But the pressure at the draft tube outlet is not equal to the atmospheric pressure. It is thought that this may cause undesirable efficiency decreases in this component. Also, since the flow is faster than the standard Francis turbine without the VPE, there may be some discharge problems in real applications.
- The numbers of the spiral in the VPE have important effect on regulating the vortex flow characteristics in the draft tube and on the efficiency of the turbine,
- More studies are needed to get optimum design of the VPE leading the maximum efficiency and more regulated flow in the draft tube.

REFERENCES

[1] Anup K.C., Young Hoo, L., Bhola, T., "CFD study on prediction of vortex shedding in draft tube of Francis turbine and vortex control technique", Renewable Energy, 86, 2016, 1406-1421.

[2] Choi Y.D., Kurokawa J., Imamura H., "Suppression of Cavitation in Inducers by J-Grooves", Journal of Fluids Engineering, 129, 2007, 15-22.

[3] Wei Q.S., Choi Y.D., Zhu B.S., "Application of J-Groove to the suppression of swirl flow in the draft tube of a Francis hydro turbine", 26th IAHR Symposium on Hydraulic Machinery and Systems, 2012.

[4] Chen Z., Choi Y.D., "Suppression of cavitation in the draft tube of Francis turbine model by J-Groove", Journal of Mechanical Engineering Science, 2018,1-11.

[5] Nishi M., Matsunaga S., Okamoto M., Uno M. and Nishitani K., "Measurement of three dimensional periodic flow on a conical draft tube at surging condition", (eds.) Flows in Non-Rotating Turbomachinery Components FED,1988, 69, 81-88.

[6] Stuparu A. and Susan-Resiga R., "The origin of the plunging pressure fluctuations for a swirling flow with precessing vortex rope in a straight diffuser", in Proc. of the 6th IAHR Int. Meeting of the Workgroup on Cavitation and Dynamic Problems in Hydraulic Machinery and Systems (Ljubljana, Slovenia) 1-8.

[7] Muntean S., Tanasa C., Bosioc A.I., Moş D.C., "Investigation of the Plunging Pressure Pulsation in a Swirling Flow with Precessing Vortex Rope in a Straight Diffuser", 28th IAHR Symposium on Hydraulic Machinery and Systems, 49,2016,1-10.

[8] Susan-Resiga, R., Vu, T. C., Muntean, S., Ciocan, G. D., and Nennemann, B., "Jet Control of the Draft Tube Vortex Rope in Francis Turbines at Partial Discharge," 23rd IAHR Symposium on Hydraulic Machinery and Systems, Yokohama, Japan,2006, October 17–21.

[9] Zhang, R. K., Mao, F., Wu, J. Z., Chen, S. Y., Wu, Y. L., and Liu, S. H., "Characteristics and Control of the Draft-Tube Flow in Part-Load Francis Turbine," ASME J. Fluids Eng., 131(2), p. 021101.

[10] Foroutan H., Yavuzkurt S., "Flow in the Simplified Draft Tube of a Francis Turbine Operating at Partial Load – Part II: Control of the Vortex Rope", Journal of Applied Mechanics, 81,061011-1.

[11] Dias, I., and Riethmuller, M. L., "Visualisation of the Forming Bubble and PIV Measurement of Surrounding Liquid Using Fluorescent Particles," Proceedings of Eigth International Symposium of Flow Visualisation, Sorrento, Italy,1998.

[12] Iliescu, M.S., Ciocan G.D., Avellan F., "Analysis of the Cavitating Draft Tube Vortex in a Francis Turbine Using Particle Image Velocimetry Measurements in Two-Phase Flow", Journal of Fluids Engineering, 130,021102-1.

[13] Siervo, J., Leva, F., "Modern trends in selecting and designing francis turbines", Water Power and Dam cont., Aug., 1976, 28-35.

[14] Akin, H., Çelebioğlu, K., Aradağ S., A CFD-Based Design Metodology For Hydraulic Turbines Applied to A Case Study in Turkey, 10th International Conference on Heat Transfer, Fluid Mechanics and Thermodynamics, Orlando-Floriad-USA, July 2014.

[15] Semerci, D.S., Yavuz, T., "Increasing Efficiency of an Exising Francis Turbine by Rehabilitation Process", The 5th IEEE International Conference on Renewable Energy Research and Applications, Birmingham/UK, 2016.

[16] Semerci, D.S., Yavuz, T., "Optimization of a Model Francis Turbine Paramaters for the Most Efficient Case", International Conference on Clean Energy, Famagurta/Cyprus, 2018.

VALIDATION STUDY OF A NATURALLY VENTILATED SOLAR FACADE

Bugra SARPER*, Soner BIRINCI, Mehmet SAGLAM**, Orhan AYDIN****
*Department of Mechanical Engineering, Tarsus University, Tarsus, 33400 Mersin, Turkey
Email: bugrasarper@tarsus.edu.tr
**Department of Mechanical Engineering, Karadeniz Technical University, 61080 Trabzon, Turkey
Email: sonerbirinci@ktu.edu.tr, mehmetsaglam@ktu.edu.tr, oaydin@ktu.edu.tr

ABSTRACT

In this study, preliminary numerical simulations of a solar facade are carried out. Two-dimensional validation studies are performed, and various turbulence models are used to predict temperature and velocity distribution initially. Then, three-dimensional numerical analysis for the building integrated solar facade, which is designed as a prototype for Tarsus in the Mediterranean region, is conducted for varying inlet-outlet positions and widths in order to increase cooling performance. Simulations are performed with ANSYS Fluent software, and surface temperatures of the absorber, local Nusselt number variation, temperature and velocity variations and streamlines within the facade are analyzed. As a result of the study, it is disclosed that the positions and widths of the openings have significant effects on temperature and velocity distribution within the facade.

Keywords: Natural convection, Solar radiation, Solar facade, Double skin facade.

1. INTRODUCTION

Rapid depletion of fossil resources and increase in environmental pollution brought the trend towards renewable energy sources, and studies for development of new and efficient technologies in this field have accelerated. According to the International Energy Agency's report [1], the buildings and construction sector are accounted for 36 % of the total energy consumption and 39 % of the CO_2 emissions related to energy and process in 2018. The European Commission [2] states that the energy consumption of buildings in Europe is about 40% of the total energy consumption, and 36% of the CO_2 emissions in Europe is caused by the buildings. In addition, 75% of the building stock in Europe consists of energy inefficient buildings. Therefore, when designing new buildings, priority should be given to the use of renewable energy sources and smart systems.

Solar energy is used extensively in solar power plants, passive heating systems, heating and cooling of buildings, water heating systems, greenhouse heating and drying of agricultural products and timber. In addition, the sun is used for natural ventilation of buildings and for reducing energy losses and energy storage applications. For this purpose, solar facades, also called double skin facade, ventilated facade, solar wall etc., are preferred on envelope of the buildings. Solar facades have benefits such as insulation, noise reduction, aesthetic appearance, natural ventilation, electricity production and reduction of carbon footprint.

Turkey, which has more potential to benefit from solar energy than most European countries, has a solar energy potential of 1400-1800 kWh/m^2-year (See Fig 1). As it is seen in Fig. 1, annular solar radiation in the Mediterranean region is higher than in other regions. The annual solar radiation potential of Tarsus is in the range of 1550-1650 kWh/m^2-year. Thus, Tarsus seems quite convenient for solar energy production and the use of solar facades and solar chimneys in buildings.

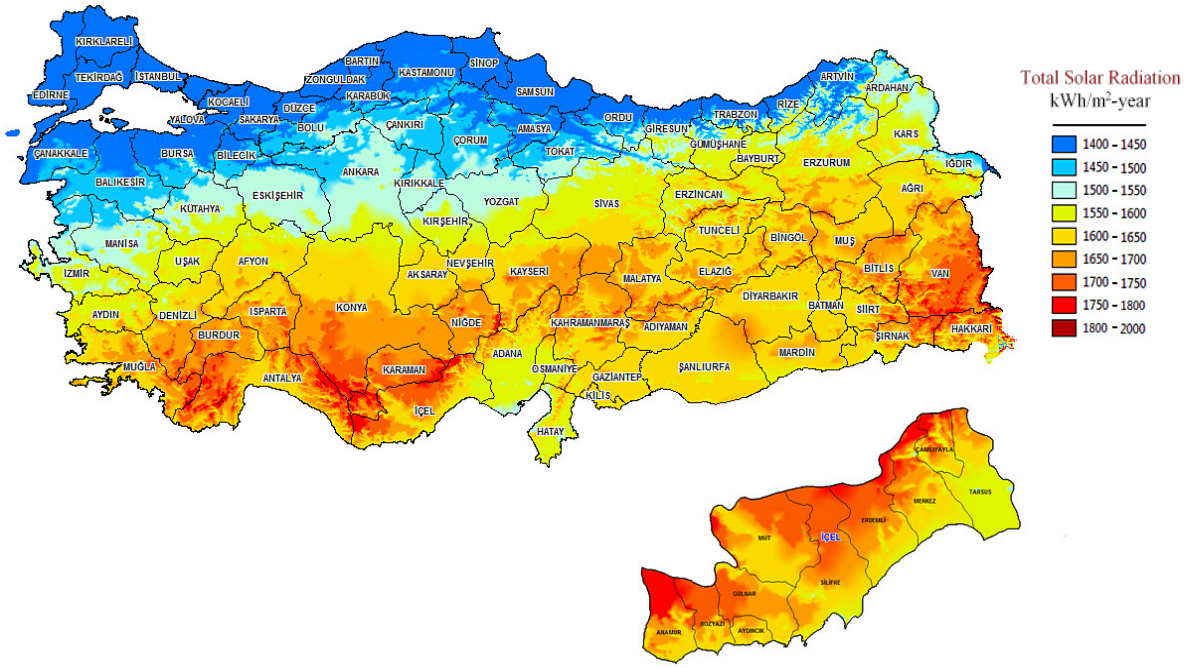

Figure 1. Annual solar radiation of Turkey [3].

The mechanisms acting on flow and heat transfer within solar facades, solar chimneys and double skin facades are addressed in the literature. Ben Yedder et al. [4] analyzed natural convection in Trombe wall systems numerically. Jubran et al. [5] investigated flow and heat transfer characteristics in a Trombe wall for varying inclination angles of the glass wall. Holmes [6] performed an optimization study for mechanically or naturally ventilated glazed facades. Mootz and Bezian [7] investigated an energy saving facade numerically for non-residential buildings. Gan [8] conducted a numerical study for passive cooling of buildings with Trombe walls. Sandberg and Moshfegh [9] performed an analytical study on natural convection in PV facades. Zalewski et al. [10] performed a validation study of solar walls. Ciampi et al. [11] investigated ventilated facades to reduce cooling loads in summer. Faggembauu et al. [12,13] investigated thermal behavior of glazed facades in Mediterranean climates. Manz et al. [14] investigated flow and thermal characteristics of a mechanically ventilated facades. Ding et al. [15] performed a numerical and experimental study on ventilation performance of a scaled multistory building with a solar chimney. Perez-Grande et al. [16] investigated glass properties on the performance of double-glazed facades. Fossa et al. [17] investigated natural convection for building integrated photovoltaic (BIPV) applications experimentally. Wong et al. [18] performed a CFD analysis for multistory double skin facade for the hot and humid climate. Baldinelli [19] investigated effects of the movable shading system in a double skin facade in warm climates. Patania [20] examined thermo-fluid dynamics of a ventilated facade. Sanjuan et al. [21] compared energy performance of an open joint ventilated facade against a conventional facade. Pasut and De Carli [22] performed CFD simulations for a naturally ventilated double skin facade. Iyi et al. [23] investigated effects of the venetian blinds within a double skin facade. Buonomo et al. [24] investigated heat transfer in a building integrated solar chimney. Manca et al. [25] investigated flow and heat transfer in building integrated solar chimneys for different inclination angles of the glass wall. Larsen et al. [26] performed thermal measurements in an office building in sunny Mediterranean climates. Nasrollahi and Salehi [27] evaluated performance of double skin facades using wind parameters in hot and dry climates. Dama et al. [28] performed a case study for a naturally ventilated double skin facade. Kim et al. [29] investigated effects of interior and exterior slat blinds on energy performance of a double skin facade. Shahrestani et al. [30] evaluated the energy performance of naturally ventilated PV facade systems. Souza et al. [31] investigated the efficiency of a naturally ventilated double skin facade. Buonomo et al. [32] performed a numerical study to investigate latent heat thermal energy storage in a building integrated solar chimney.

This study aims to carry out preliminary validation studies for a solar facade in the Mediterranean region. Initially, effects of different turbulence models on temperature and velocity fields within a solar facade are investigated. The results obtained are compared with those in the literature, and the final simulations are carried out by determining the appropriate turbulence model. After validation studies, effects of different inlet and outlet parameters on thermo-fluid dynamics of air within the solar facade are evaluated comparatively.

2. PROBLEM DESCRIPTION AND NUMERICAL MODEL

In this paper, numerical simulations of a building integrated solar facade located in Tarsus (at 36.92°N/34.89°E), are performed via ANSYS Fluent software for different positions of the openings. As described in Fig. 2, simulations are performed for four different configurations. In the first case, the openings are perpendicular to the vertical walls (absorber, glass and sidewalls), while the openings are on the unheated glass surface in other three cases. In the last three cases, positions and sum of the widths of the openings are held constant (0.4 m), while inlet and outlet widths are changed (See Fig 2). In all configurations, the height of the facade is 8 m, and its depth and width are 4 m and 0.2 m, respectively.

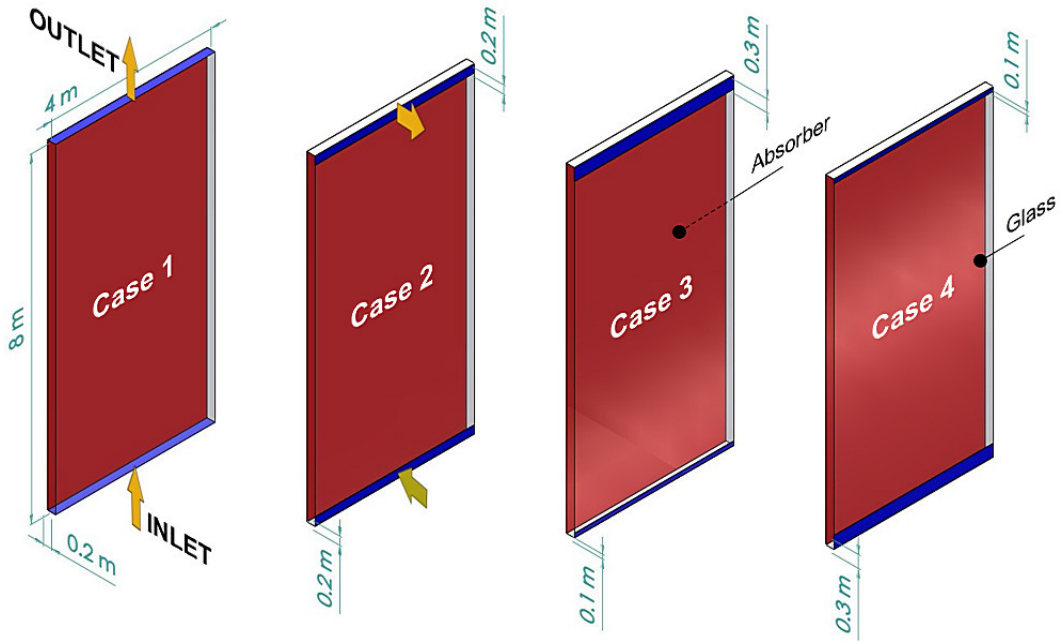

Figure 2. The studied geometry according to different cases.

Simulations are carried out by using the climatic features and solar irradiation characteristics of Tarsus. Solar irradiation is calculated using solar load model in ANSYS Fluent for the same coordinates. The studies are conducted in steady state regime. Buoyancy induced flow and heat transfer are analyzed using the data at 13 noon on June 21, 2019.

Table 1. Inlet and outlet widths of different configurations

Solar Radiation in Tarsus (36.92°N/34.89°E) at 13 noon	**Heat Flux [W/m^2]**
Direct Solar Irradiation	881.746
Diffuse Solar Irradiation Vertical Surface	78.195
Diffuse Solar Irradiation-Horizontal Surface	118.154
Ground Reflected Solar Irradıaton-Vertical Surface	97.812

Constant surface heat flux boundary condition is used on the absorber surface. The transmittence coefficient of glass opposite the absorber is taken as 0.68 as stated in [32]. The direct solar irradiation value calculated by the program is multiplied by transmittence coefficient of the glass wall, and the heat flux on the absorber is calculated as 599.587 W/m^2. Radiation heat transfer between the facade surfaces is modeled using surface to surface (S2S) radiation model [33], and surface emissivity of the absorber is 0.95 while surface emissivities of the glass wall and sidewalls are taken as 0.89 [32]. In addition, convection boundary condition is employed at the glass wall, and sidewalls are considered as adiabatic. While pressure inlet and pressure outlet boundary conditions are used at the inlet and outlet of the facade, temperature values are as the same as ambient temperature (300 K) [36].

The SIMPLE algorithm is chosen for coupling of pressure and velocity. For discretizing momentum, energy and turbulence model equations, the second order upwind scheme is used. Pressure interpolation is provided with PRESTO scheme. In the validation part, standart k-ϵ, k-ϵ RNG, k-ϵ realizable, standart k-ω, and k-ω SST models are tested, and the results of two-dimensional solutions are compared with Refs. [34,35]. As it is seen from Fig. 3, the temperature profiles obtained for each turbulence model are compatible with the literature and exhibit the same trend. However, there are differences in velocity values especially in the regions close to the walls. All the turbulence models overestimate velocity in the regions near the left wall, while underestimate velocity near the right. Especially, the difference between the results obtained with k-ω SST model and the literature is quite high. Other turbulence models give almost close results, and results of standart k-ϵ model are satisfying . Thus, the results obtained with standart k-ϵ turbulence model is used in the solutions.

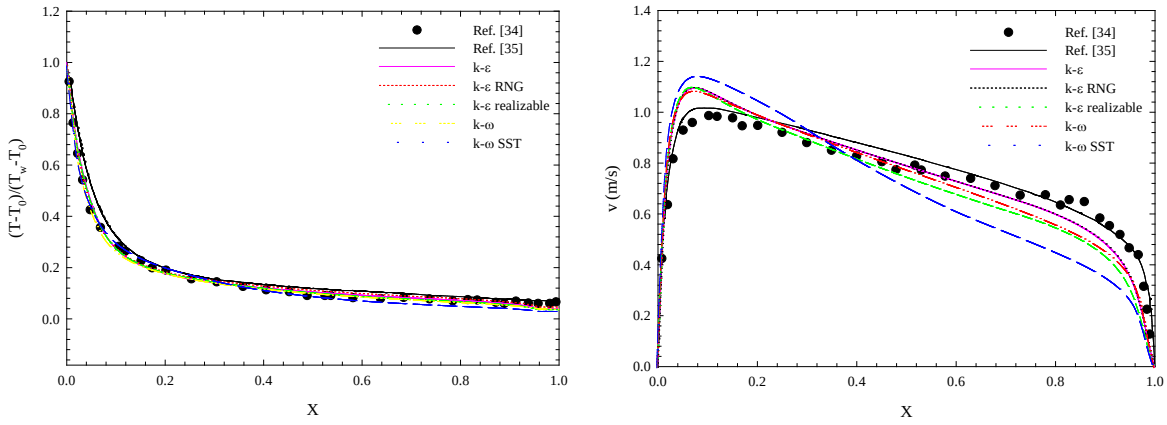

(a) (b)

Figure 3. Validation of the present study against literature: (a) Temperature profile at Y=1.0, (b) Velocity profile at Y=0.9.

2.1 Grid Structure

The grid is created using ICEM CFD. In sections close to the walls where the gradients are high, grid frequency is kept high too. The grid structure expands towards the center of the channel. Four grid sizes are tested in this study, and the results are presented in Table 2 and Fig. 4. The differences of average temperatures of the absorber and glass wall, and mass flow rate between the subsequent grid sizes are determined by calculating percentage error. When Table 2 is examined, it is seen that the solution is not affected much by grid sizes. The values obtained with 1737489 cells and 2975574 cells are found to be very close. Also, turbulent kinetic energy and velocity profiles along the X-axis at Y=0.9 (close to the outlet) are obtained in different cell numbers. As it is seen in Fig. 4, 374319 cells are not sufficient for solutions but there is no significant change in results in higher cell numbers. Consequently, when Table 2 and Fig. 4 are evaluated together, it is appropriate to use 1737489 cells.

Table 2. Grid independence study

ϕ, [K] and [kg/s]	374319 Cells	R%	895404 Cells	R%	1737489 Cells	R%	2975574 Cells
$(T-T_0)_{absorber}$	54.228	0.026	54.269	0.256	54.508	0.094	54.559
$(T-T_0)_{glass}$	10.153	0.039	10.157	0.345	10.192	0.117	10.204
$\dot{m}$	1.06135	2.519	1.08809	0.112	1.08687	0.019	1.08666

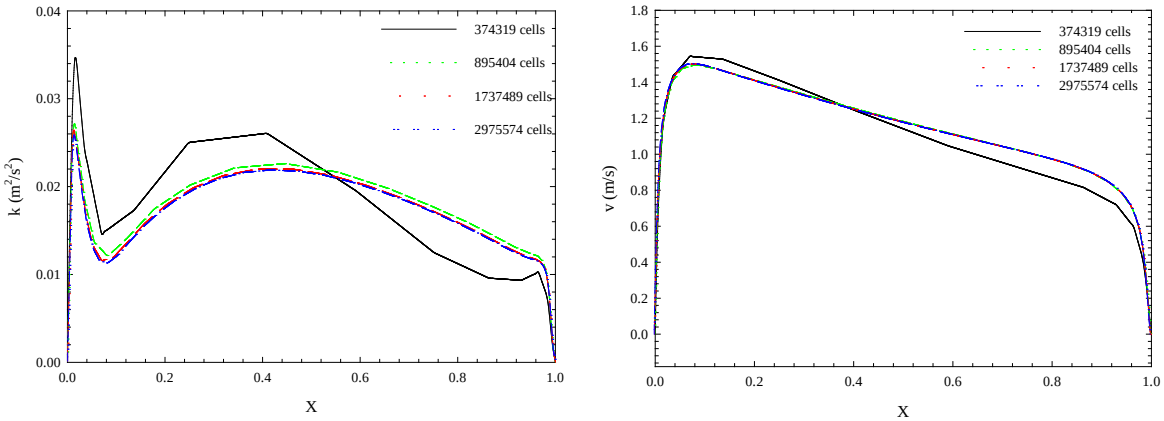

(a) (b)

Figure 4. Effects of grid size on turbulence kinetic energy (k) and velocity at Y=0.9.

3. RESULTS AND DISCUSSION

In this study, numerical analysis of a building integrated solar facade in Tarsus in the Mediterranean region is carried out. The study focuses on effects of locations and widths of the openings on heat transfer from the absorber, and velocity and temperature fields within the facade. Steady state simulations are realized for preliminary prototyping studies using Tarsus' climate features.

Figure 5 shows the variation of temperature and vertical velocity component in the X-axis at different points within the facade. Since wind speed is not taken into consideration, buoyancy induced flow occurs within the facade. Therefore, air, whose temperature increases due to the convective heat transfer, rises along the facade. The thermal boundary layer thickness increases with increasing Y distance, and air temperature increases in the sections close to the glass wall as a result of radiation heat transfer. When effect of heat transfer to the flow region is examined, it is seen that the velocity is higher in the sections close to the absorber, and velocity decreases as the X distance increases. The velocity profile is almost uniform at the facade inlet, and effect of temperature on velocity becomes evident towards the outlet (Case 1). When effects of positions and widths of the openings are examined, it is clear to see that velocity is significantly higher at Y=0.1 in the second and third cases. In the fourth case, the wider inlet cross section affects the buoyancy induced flow negatively.

Figure 6 shows the surface streamlines and velocity vectors at the mid-plane (at Z=0.5) of the facade. In the cases shown in Fig. 6, the openings are at the glass wall. As stated earlier, the openings are equal to each other (0.2 m) in the second case. In the third case, the width of the inlet is halved, while it is three times that of the third in the fourth case. In all cases except the first case, a recirculation zone occurs just above the inlet. While intensity and length of recirculation becomes evident with the reduction of the entrance width, the velocity increase in the part close to the absorber. In addition, the eye of the recirculation cell is located higher with growth of the inlet width.

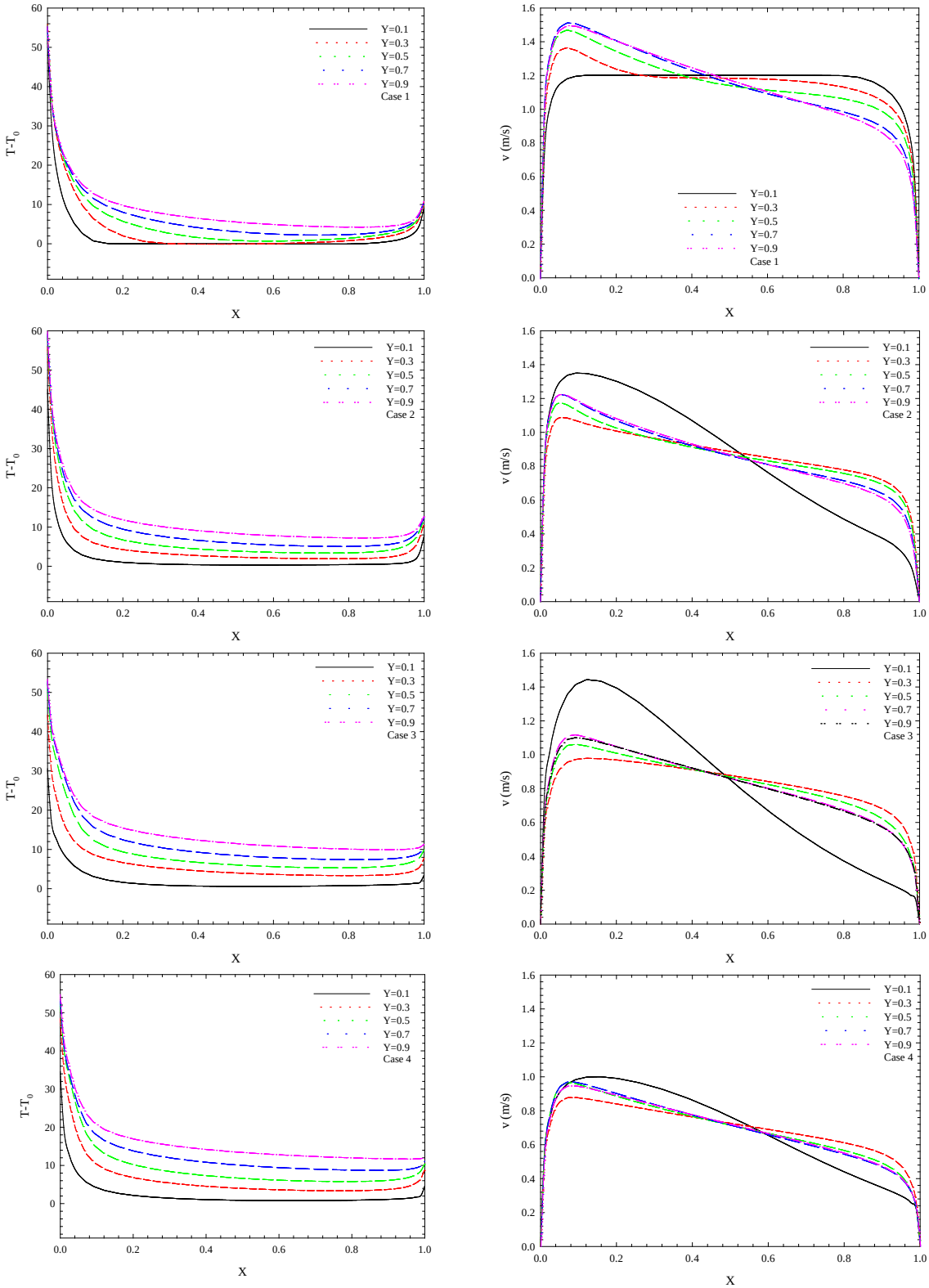

Figure 5. Temperature and velocity profiles at different coordinates.

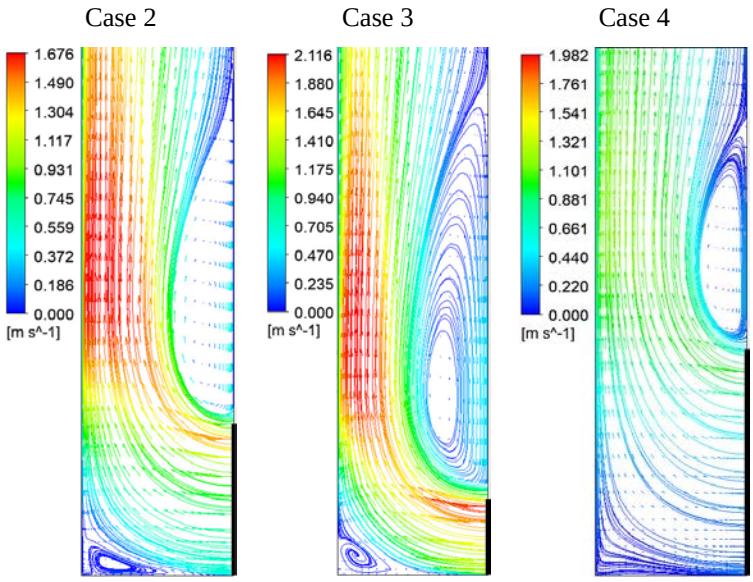

Figure 6. Surface streamlines and velocity vectors at the facade inlet at Z=0.5.

Figure 7 shows the variation of temperature and local Nusselt number at the mid-line (at Z=0.5) of the absorber. Effect of the velocity field on convective heat transfer is clearly seen when the changes in temperature and local Nusselt number along the wall are examined. In the first case, as the air warms up and rises inside the facade, convective heat transfer decreases towards the outlet. In the second case, while the local temperature at the inlet section is lower compared to the first case, there is a significant increase in local temperature towards the outlet. As mentioned above, the reduction of the inlet cross section leads to high velocities near the absorber, which increases the convective heat transfer. However, effect of the convection at the inlet section is weaker at the fourth case than that at the third. In addition, since the main flow is directed towards the outlet, the flow near the absorber side weakens and the heat transfer reduces.

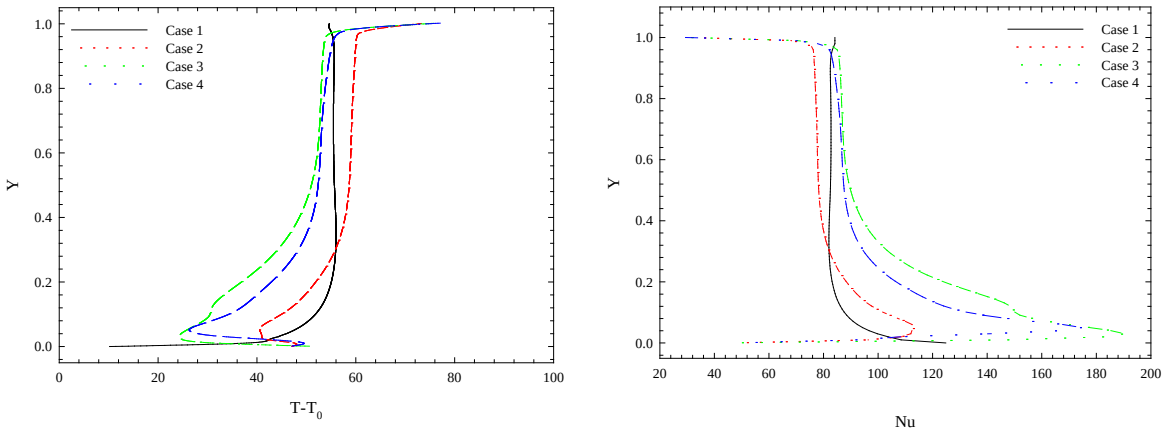

Figure 7. Temperature and local Nusselt number variation on the absorber at Z=0.5.

Figure 8 shows the average temperatures and average Nusselt numbers obtained on the absorber surface for different working conditions. As it is seen, the worst operating condition is the second case. In this case, since the average Nusselt number is minimum, the average surface temperature is maximum. In the first case, when the openings are perpendicular to the facade surfaces, cooling performance is better than in the second case. The best cooling performance is achieved in the third case. In this case, the average surface temperature is minimum depending on the convection. It is determined that equal inlet-outlet widths are not optimum in terms of cooling

performance and reducing the cross section of the inlet on the right wall maximizes cooling performance. Thus, overheating in the absorber is prevented.

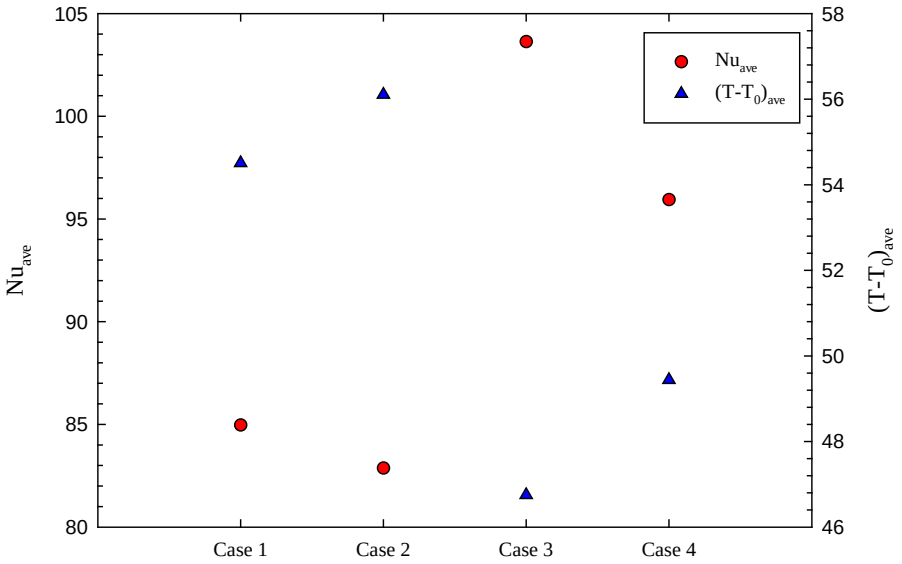

Figure 8. Average surface temperature and average Nusselt number on the absorber surface.

4. CONCLUSIONS

A numerical study has been carried out to analyze the thermal performance of a solar facade and to prevent overheating. Primarily, effects of different turbulence models have been discussed, and then parametric analysis have been performed for different working conditions. The important findings obtained in the study are as follows:

- Widths and positions of openings have significant influences on velocity profiles within the facade.
- Placing the inlet on the glass wall causes recirculation at the entrance region.
- Overheating can be prevented by changing the inlet-outlet parameters.
- The third case prevents overheating as it causes high velocities at the entrance region.

REFERENCES

[1] International Energy Agency, Global Status Report for Buildings and Construction, 2019.

[2] European Commission, Energy Performance of Buildings Directive, 2018.

[3] http://www.yegm.gov.tr/anasayfa.aspx. 22nd February 2020.

[4] Ben Yedder, R., Du, Z. G. & Bilgen, E. Numerical Study of Laminar Natural Convection in Composite Trombe Wall Systems, Solar & Wind Technology, **7**(6), 675-683, 1990.

[5] Jubran, B. A., Hamdan, M. A. & Manfalouti, W. Modelling Free Convection in a Trombe Wall, Renewable Energy, **1**(3/4), 351-361, 1991.

[6] Holmes, M. J. Optimisation of the Thermal Performance of Mechanically and Naturally Ventilated Glazed Facades, Renewable Energy, **5**(2), 1091-1098, 1994.

[7] Mootz, F. & Bezian J. J. Numerical Study of a Ventilated Facade Panel, Solar Energy, **57**(1), 29-36, 1996.

[8] Gan, G. A Parametric Study of Trombe Walls for Passive Cooling of Buildings, Energy and Buildings, **27**, 37-43, 1998.

[9] Sandberg, M., Moshfegh, B. Buoyancy-Induced Air Flow in Photovoltaic Facades Effect of Geometry of the Air Gap and Location of Solar Cell Modules, Building and Environment, **37**, 211-218, 2002.

[10] Zalewski, L., Lassue, S., Duthoit, B. & Butez, M. Study of Solar Walls-Validating a Simulation Model, Building and Environment, **37**, 109-121, 2002.

[11] Ciampi, M., Leccese, F. & Tuoni, G. Ventilated Facades Energy Performance in Summer Cooling of Buildings, **75**, 491-502, 2003.

[12] Faggembauu, D., Costa, M., Soria, M. & Oliva, A. Numerical Analysis of the Thermal Behaviour of Ventilated Glazed Facades in Mediterranean Climates. Part 1: Development and Validation of a Numerical Model, Solar Energy, **75**, 217-228, 2003.

[13] Faggembauu, D., Costa, M., Soria, M. & Oliva, A. Numerical Analysis of the Thermal Behaviour of Ventilated Glazed Facades in Mediterranean Climates. Part II: Applications and Analysis of Results, Solar Energy, **75**, 229-239, 2003.

[14] Manz, H., Schaelin, A. & Simmler, H. Airflow Patterns and Thermal Behaviour of Mechanically Ventilated Glass Double Facades, Building and Environment, **39**, 1023-1033, 2004.

[15] Ding, W., Hasemi, Y. & Yamada, T. Natural Ventilation Performance of a Double-Skin Facade with a Solar Chimney, Energy and Buildings, **37**, 411-418, 2005.

[16] Perez-Grande, I., Meseguer, J. & Alonso, G. Influence of Glass Properties on the Performance of Double-Glazed Facades, Applied Thermal Engineering, **25**, 3163-3175.

[17] Fossa, M., Menezo, C. & Leonardi, E. Experimental Natural Convection on Vertical Surfaces for Building Integrated Photovoltaic (BIPV) Applications, Experimental Thermal and Fluid Science, **32**, 980-990, 2008.

[18] Wong, P. C., Prasad, D. & Behnia, M. A New Type of Double-Skin Facade Configuration for the Hot and Humid Climate, Energy and Buildings, **40**, 1941-1945, 2008.

[19] Baldinelli, G. Double Skin Facades for Warm Climate Regions: Analysis of a Solution with an Integrated Movable Shading System, Building and Environment, **44**, 1107-1118, 2009.

[20] Patania F., Gagliano, A., Nocera, F., Ferlito, A. & Galesi, A. Thermofluid-Dynamic Analysis of Ventilated Facades, Energy and Buildings, **42**, 1148-1155, 2010.

[21] Sanjuan, C., Suarez, M. J., Gonzales, M., Pistono, J. & Blanco, E. Energy Performance of an Open-Joint Ventilated Facade Compared with a Conventional Sealed Cavity Facade, Solar Energy, **85**, 1851-1863.

[22] Pasut, W. & De Carli, M. Evaluation of Various CFD Modelling Strategies in Predicting Airflow and Temperature in a Naturally Ventilated Double Skin Facade, Applied Thermal Engineering, **37**, 267-274, 2012.

[23] Iyi, D., Hasan, R., Penlington, R. & Underwood, C. Double Skin Facade: Modelling Technique and Influence of Venetian Blinds on the Airflow and Heat Transfer, Applied Thermal Engineering, **71**, 219-239, 2014.

[24] Buonomo, B., Manca, O., Montaniero, C. & Nardini, S. Numerical Investigation of Convective-Radiative Heat Transfer in a Building-Integrated Solar Chimney, Advances in Building Energy Research, **9**(2), 253-266, 2015.

[25] Manca, O., Nardini, S., Romano, P. & Mihailov, E. Numerical Investigation of Thermal and Fluid Dynamic Behavior of Solar Chimney Building Systems, Journal of Chemical Technology and Metallurgy, **49**(1), 106-116, 2014.

[26] Larsen, S. F., Rengifo, L. & Filippin, C. Double Skin Glazed Facades in Sunny Mediterranean Climates, Energy and Buildings, **102**, 18-31, 2015.

[27] Nasrollahi, N. & Salehi, M. Performance Enhancement of Double Skin facades in Hot and Dry Climates Using Wind Parameters, Renewable Energy, **83**, 1-12, 2015.

[28] Dama, A., Angelli, D. & Larsen, O. K. Naturally Ventilated Double-Skin Facade in Modelling and Experiments, Energy and Buildings, **144**, 17-29, 2017.

[29] Kim, G. H., Kwon, H. M. & Yang, J. H. Ventilation Rate and Thermal Environment Properties of Double Skin Facade Considering Wind Profile and Direction, Journal of Asian Architecture and Building Engineering, **16**(3), 675-682, 2017.

[30] Shahrestani, M., Yao, R., Essah, E., Shao, L., Oliviera, A. C., Hepbasli, A., Biyik, E., Del Cano, T., Rico, E. & Lechon, J. L. Experimental and Numerical Studies to Asses the Energy Performance of Naturally Ventilated PV Facade Systems, Solar Energy, **147**, 37-51.

[31] Souza, L. C. O., Souza, H. A. & Rodrigues, E. F. Experimental and Numerical Analysis of a Naturally Ventilated Double-Skin Facade, Energy and Buildings, **165**, 328-339, 2018.

[32] Buonomo, B., Capasso, L., Diana, A., Manca, O. & Nardini, S. A Numerical Analysis on a Solar Chimney with an Integrated Latent Heat Thermal Energy Storage, *Proc. of the 74th ATI National Congress*, Modena-Italy, 2019.

[33] ANSYS Inc., ANSYS Fluent Theory Guide Release 15, 2013.

[34] Yilmaz, T. & Fraser, S. M. Turbulent Natural Convection in a Vertical Parallel-Plate Channel with Asymmetric Heating, International Journal of Heat and Mass Transfer, **50**, 2612-2623, 2007

[35] Zhang, T. & Yang, H. Flow and Heat Transfer Characteristics of Natural Convection in Vertical Air Channels of Double-Skin Solar Facades, Applied Energy, **242**, 107-120, 2019.

[36] www.meteoblue.com.tr/hava/historyclimate/weatherarchive/tarsus

EFFECT OF MAGNETIC FIELD ON FLOW AND HEAT TRANSFER IN HYDRODYNAMICALLY AND THERMALLY DEVELOPING COUETTE-POISEUILLE FLOW BETWEEN PARALLEL PLATES

Esra YAĞCI*, Orhan AYDIN, Tülin BALİ*****
Karadeniz Technical University, Department of Mechanical Engineering, Trabzon/Turkey
Email: esrayagci@ktu.edu.tr, oaydin@ktu.edu.tr, bali@ktu.edu.tr

ABSTRACT

In this study, a 2D numerical analysis is conducted in to investigate hydrodynamically and thermally developing flow of an electrically conducting, viscous, incompressible, and Newtonian fluid between the parallel plates a under uniform magnetic field. The problem geometry consists of two electrically insulated parallel plates of which one is stationary, and the other one is moved at a constant velocity. The fluid is heated by applied constant heat flux at the walls, and an external uniform magnetic field is applied perpendicular to the flow. Two different cases have been investigated under thermal boundary conditions: uniform heat flux at the moving wall and an adiabatic stationary wall (*Case A*) and uniform heat flux at the stationary wall and adiabatic moved wall (*Case B*). Heat generation from viscous dissipation and Joule heating are also included in the analysis Computations are performed via ANSYS 16.0. In the flow region, magnetohydrodynamic (MHD) fluid flow and heat transfer, caused by the interaction of fluid movement and electromagnetic field, are examined. For different wall velocities and heating conditions, the influence of Brinkman and Hartmann numbers on the velocity and temperature profiles and Nusselt numbers are presented.

Keywords: MHD, parallel plates, Couette, Poiseuille flow, viscous dissipation, Joule heating

Nomenclature

Br	Brinkman number
B_o	magnetic field intensity (Tesla)
c_p	specific heat at constant pressure (kJ/kg K)
h	heat transfer coefficient (W m^{-2} K^{-1})
H	channel width (m)
Ha	Hartmann Number
k	thermal conductivity (W/m K)
Nu	Nusselt number
P	pressure (Pa)
q''	constant heat flux (W/m^2)
T	temperature (K)
u	axial velocity (m/s)
v	vertical velocity (m/s)
u^*	dimensionless velocity
U^*	dimensionless velocity
x	axial coordinate (m)
X	dimensionless axial coordinate
y	vertical coordinate (m)
Y	dimensionless vertical coordinate

Greek symbols

σ	electrical conductivity (1 / Ω m)
θ	dimensionless temperature

μ dynamic viscosity (Pa s)
ρ density (kg/m^3)
υ kinematic viscosity (m^2/s)
Φ magnetic field direction

Subscripts
b bulk
m mean
x local
w wall
e entrance

1. INTRODUCTION

Magnetohydrodynamics (MHD) flows, whose fluid is electrically conductive in the presence of an external magnetic field, has an abundant number of applications such as geothermal reservoirs, petroleum reservoirs, MHD generators, accelerators, blood flow measurements, fluid journal bearings, propulsion and flight control for rocket and hypersonic aerodynamic vehicles, electromagnetic flow meters allowing to measure flow rates in a non-intrusive way, breeding blankets for fusion reactors, cooling of nuclear reactors, high-temperature plasmas, and MHD motor. The fluid motion and electromagnetic field interact with each other and depend on each other in the flow region, a complex process to analyze (complex coupling). The motion of MHD fluid interacts with an external magnetic field and generates Lorentz force, which affects the fluid motion in reverse. Consequently, different characteristics appear also to the traditional flow. Due to such a wide range of applications, electrically conductive fluid flow and heat transfer phenomena under the influence of magnetic fields have attracted the attention of many researchers.

Attia et al. [1] numerically studied the flow and heat transfer of an electrically conductive, viscous, incompressible fluid under a perpendicularly applied magnetic field between the two horizontal parallel plates where the bottom plate is held stationary, and the top plate moves at a constant speed. Attia and Sayed-Ahmed [2] conducted a numerical analysis of the heat transfer in the flow of non-Newtonian fluid between a porous parallel plate under a uniform magnetic field, including the viscous dissipation and Joule heating effect into the energy equation. In another study of Attia [3], he analyzed the non-steady Couette-Poiseuille flow of an electrically conductive, incompressible, non-Newtonian viscoelastic fluid between two porous parallel plates, taking into account the Hall Effect on the heat transfer. Suziki and Nishio [4] conducted a similar study for a non-Newtonian fluid. Beg et al. [5] included the effects of viscous dissipation and Joule heating and the Hall current and ion-slip flow into the lateral mass flow in both plates. Another study, by Ramesh [6], presented Couette, Poiseuille and generalized Couette flows of an incompressible magnetohydrodynamic Jeffrey fluid between parallel plates through homogeneous porous media. Hayat et al. [7] theoretically examined Couette flow under a uniform magnetic field applied vertically to the flow field of an electrically conductive fluid, taking into account the effect of the material constants and the applied magnetic field. Aydin and Avci [8] examined a Couette-Poiseuille flow of a Newtonian fluid between two plane-parallel plates by including the viscous dissipation effect. A similar analytical study was performed by Shigechi et al. [9]. Mokarizadeh et al. [10] examined Couette-Poiseuille of a viscoelastic fluid by including the viscous dissipation effect. In the presence of a magnetic field perpendicular to the flow field, Makinde and Onyejekwe [11] numerically studied the permanent Couette-Poiseuille flow and heat transfer electrically conductive fluid with variable viscosity and electrical conductivity between the two parallel plates. Mosayebidorcheh et al. [12] examined incompressible viscous dusty fluid, which is activated with a constant pressure gradient, in an incompressible viscous dusty fluid held under a uniform magnetic field, with a thermal temperature conductivity and viscosity depending on the temperature.

This study aims to investigate the laminar Couette-Poiseuille flow and heat transfer characteristics of an electrically conductive Newtonian fluid in the presence of a uniform magnetic field applied perpendicular to the flow by taking viscous dissipation and Joule heating effects into account. The effects of Brinkman and Hartmann

numbers on the velocity and temperature profiles, and the development of Nusselt numbers, are presented and discussed.

2. NUMERICAL STUDY

2.1 Physical Geometry of the Problem

The numerical study considers a laminar flow between two plates where one of the plates moved at constant velocity while the other kept stationary. A uniform magnetic field is applied perpendicularly through the channel. The width of the channel is chosen as 10 mm, and the length of the plates is chosen long enough to ensure that the flow reaches to fully developed state. The channel walls are maintained at uniform heat flux conditions and assumed to be electrically insulated. The geometrical characteristics of the channel are given in Fig 1.

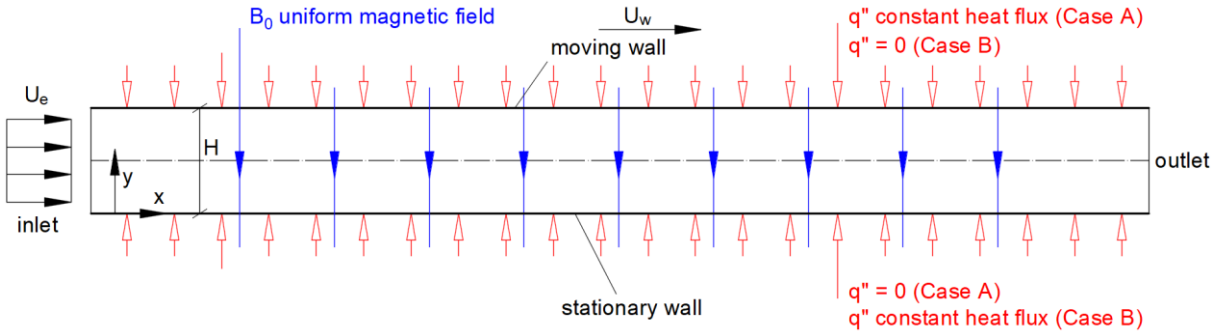

Figure 1. Physical and geometrical characteristics of the problem

2D MHD flow and heat transfer are solved numerically via ANSYS 16.0. The software requires dimensional values to solve conservation equations. Therefore, dimensional analysis is conducted. Then, all results are non-dimensionalized by using dimensionless parameters presented in the paper. Since it is aimed to present all results non-dimensional, an imaginary conducting fluid with arbitrary thermo-physical properties is used in the study. Using imaginary and varying values for working fluid gives the ability to adjusts the dimensionless numbers (*Br* and *Ha*) to a desired value easily. Thermo-physical properties of the working fluid considered in the study are given in Table 1.

Table 1. Thermo-physical properties of working fluid

Density (kg/m^3)	1.225
Dynamic viscosity (kg/ms)	1.7894x10-5
Electrical conductivity (1 / Ω m)	106
Thermal conductivity (W/m K)	0.0242
Magnetic permeability (N A−2)	1.257x10-6

2.2 Governing Equations and Boundary Conditions

Numerical simulation is conducted under the following assumptions:

- The flow regime is laminar.
- The thermo-physical properties of working fluid are constant.
- The flow is steady
- The channel walls are electrically insulated.
- Magnetic field intensity is unchanged inside the channel.

Under the above assumptions, the momentum and energy equations can be written as:

$$u\frac{\partial u}{\partial x}+v\frac{\partial u}{\partial y}=-\frac{1}{\rho}\frac{\partial p}{\partial x}+\nu\left(\frac{\partial^2 u}{\partial x^2}+\frac{\partial^2 u}{\partial y^2}\right)+\frac{\sigma {B_0}^2}{\rho}(v\sin\phi\cos\phi-u\sin^2\phi) \tag{1}$$

$$u\frac{\partial T}{\partial x}+v\frac{\partial T}{\partial y}=\frac{k}{\rho C_p}\left(\frac{\partial^2 T}{\partial x^2}+\frac{\partial^2 T}{\partial y^2}\right)+\frac{\mu}{\rho C_p}\left(\frac{\partial u}{\partial y}\right)^2+\frac{\sigma {B_0}^2}{\rho C_p}(u\sin\phi-v\cos\phi)^2 \tag{2}$$

Where σ is the electrical conductivity of fluid and B_o is the magnetic field intensity. The second and third terms on the right side of the equation in the energy equation refer to viscous dissipation and Joule heating

Hydrodynamic boundary conditions:

$$u = 0 \qquad \text{at } y = 0; \tag{3a}$$

$$u = U_w \text{ (taken as 0.1 m/s)} \qquad \text{at } y = H; \tag{3b}$$

$$u = U_e \text{ (taken as 0.1 m/s)} \qquad \text{at } x = 0; \tag{3c}$$

Introducing the following dimensionless parameters

$$u^* = \frac{u}{u_m},\ U^* = \frac{U_w}{u_m},\quad Y = \frac{y}{H},\ X = \frac{x}{H} \tag{4}$$

the boundary conditions in dimensionless form can be written as

$$u^* = 0 \qquad \text{at } Y = 0 \tag{5a}$$

$$u^* = U^* \qquad \text{at } Y = 1 \tag{5b}$$

***Case* A: The constant heat-flux at the upper plate with an adiabatic lower plate**

The thermal boundary conditions for this case can be written as:

$$\frac{dT}{dy} = 0 \qquad \text{at } y = 0 \tag{6a}$$

$$T = T_w \qquad \text{at } y = H \tag{6b}$$

$$q'' = k\frac{dT}{dy}\bigg|_{y=H} \qquad \text{at } y = H \tag{6c}$$

Introduction of the following non-dimensional temperature:

$$\theta = \frac{T - T_w}{\frac{q'' H}{k}} \tag{7}$$

Thermal boundary conditions in dimensionless form can be stated as

$$\frac{d\theta}{dY} = 0 \qquad \text{at} \quad Y = 0 \tag{8a}$$

$$\frac{d\theta}{dY} = 1, \quad \theta = 0 \qquad \text{at} \quad Y = 1 \tag{8b}$$

The bulk fluid temperature is

$$T_b = \frac{{}_A\int \rho\, u\, T\, dA}{{}_A\int \rho\, u\, dA} \tag{9}$$

In terms of dimensionless quantities, the bulk fluid temperature, θ_b can be written as

$$\theta_b = \frac{T_b - T_w}{\frac{q'' H}{k}} \tag{10}$$

The forced convective heat transfer coefficient and Nusselt number are given as follows:

$$h = \frac{k \left.\frac{dT}{dy}\right|_{y=H}}{(T_w - T_b)}, \qquad Nu = \frac{h H}{k} = -\frac{2}{\theta_b} \tag{11}$$

The Brinkman and Hartman numbers are defined as:

$$Br = \frac{u_m{}^2 \mu}{H\, q''}, \qquad Ha = \sqrt{\frac{\sigma B_0{}^2 H^2}{\mu}} \tag{12}$$

***Case* B: The constant heat flux at the lower plate with an adiabatic upper plate**

Dimensional thermal boundary conditions for *Case B* are

$$\frac{d\theta}{dY} = -1 \quad \text{and} \quad \theta = 0 \qquad \text{at} \quad Y = 0 \tag{13a}$$

$$\frac{d\theta}{dY} = 0 \qquad \text{at} \quad Y = 1 \tag{13b}$$

The continuity, momentum, and energy equations are solved with the inclusion of the MHD model of the ANYSY 16 software. The SIMPLE scheme is used for pressure-velocity coupling, and the Second-Order Upwind scheme is used for pressure, momentum, and energy equations.

3. RESULTS AND DISCUSSION

In this study, the Couette-Poiseuille flow of an electrically conducting fluid with simultaneous pressure gradient and axial movement of an upper plate under an applied uniform magnetic is numerically analyzed. The upper plate with two different axial movement conditions (U^*= 0 and 1) are studied. The influence of magnetic field with Joule heating and viscous dissipation on the flow and heat transfer characteristics of a hydrodynamically

and thermally developing MHD flow is investigated under two different values of *Ha* (0, 5), and *Br* (0, 0.01 and 0.1).

Figure 2 shows the comparison of the fully developed dimensionless velocity profiles at different wall velocities for two different Ha numbers. The movement of conductive fluid through the magnetic field generated a reverse force against the flow (Lorentz force) and changed its parabolic shape. In Figure 2 (a), where both the plates are kept stationary (*U*=0*), lower velocities are observed in the mid-region, and higher velocities are observed at the near-wall region of the channel. In Fig 2(b), where the upper plate moved at constant velocity (*U*=1*), retarding effect of the Lorentz force is found to be in a broader area in the channel. Higher velocities are seen near the lower wall region, and lower velocities are seen at the mid and upper wall region of the channel in the presence of the magnetic field.

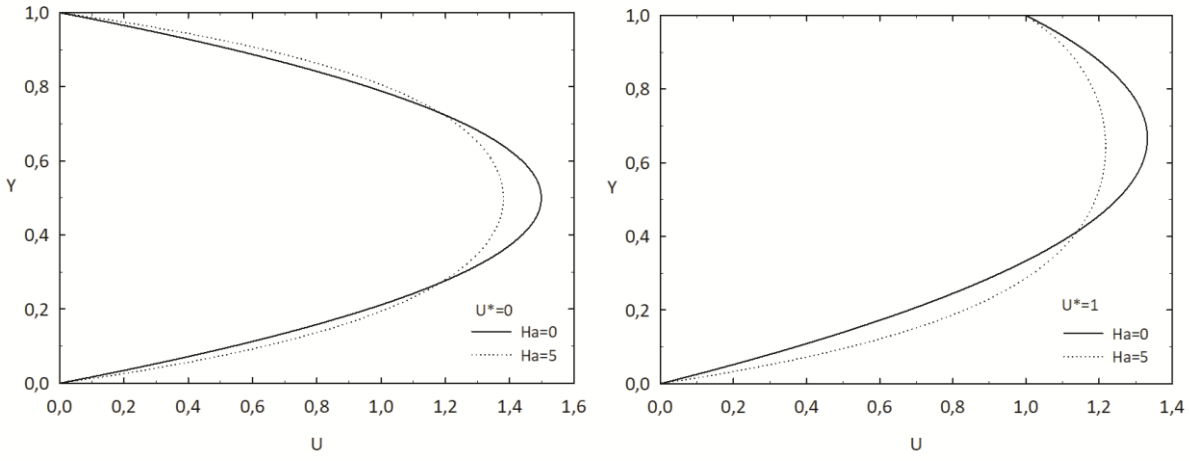

(a) (b)

Figure 2. Impact of magnetic field on dimensionless velocity profile for different movements of the upper plate

For all the cases considered, viscous dissipation and Joule heating act like a heat source. The viscous dissipation term is used to express the heat generated by shear, while the Joule heating term is used for the heat generated by electrical current flow inside the fluid (resistive heating) in the presence of the magnetic field.

Dimensionless temperature distributions and Nusselt numbers (*Nu*) of fully developed flow for upper heating condition (*Case A*) are given in Fig. 3 and Table 2, respectively. In the absence of a magnetic field (*Ha*=0), it can be shown that the fully developed Nusselt number, including the viscous dissipation effect, is precisely the same as that reported by Aydin and Avci [8], which shows the validity of the numerical procedure applied in the study. As seen from Fig 3, applying a magnetic field (*Ha=5*) increased the temperature gradient at the wall and, therefore, higher *Nu* is obtained. The difference in the temperature profiles due to the magnetic field can be attributed the change in velocity profile (Fig 2). With the inclusion of viscous dissipation and Joule heating (*Br*=0.01 and 0.1), lower *Nu* is obtained.

For the condition of moving upper plate (*U*=1*), the presence of magnetic field decreased the temperature gradient at the wall and decreased *Nu* (see Fig 3b and Table 2) for *Case A*. This decrease in *Nu* can be attributed to the reduced velocity gradient at the moving wall (Fig 2b) in the presence of the magnetic field.

Dimensionless temperature distributions and Nusselt numbers (*Nu*) of fully developed flow for upper heating condition (*Case B*) are given in Fig. 4 and Table 2, respectively. As *Case A* and *Case B* is the axial symmetry of each other for *U**=0, the temperature profile also shows the axial symmetry between *Case A* and *Case B*, and the same *Nu* numbers are obtained for fully developed flow. However for the *Case B* with moving upper plate (*U**=1), an opposite change is observed (reduced velocity gradient near in the wall region, Fig. 2b) temperature gradient and *Nu*, which can be explained by the change in velocity gradient in the presence of the magnetic field, too.

Table 2. Fully developed Nusselt numbers for different values of *Br*, *Ha*, and *U** for *Case A* and *Case B*

		Case A		*Case B*	
*U**	*Br*	*Nu, Ha=0*	*Nu, Ha=5*	*Nu, Ha=0*	*Nu, Ha=5*
0	0	5.3963	5.4766	5.3963	5.4766
	0.01	5.2879	5.4088	5.2878	5.4088
	0.1	4.4767	4.8766	4.4767	4.8766
1	0	7.2401	6.8630	4.5271	4.8304
	0.01	7.3414	6.8898	4.4321	4.7946
	0.1	8.3968	7.1435	3.7274	4.5000

An interesting situation occurs in the case of *U*=1* and *Br* > 0. For the moving upper plate, the inclusion of heat generation, increased the temperature gradient and *Nu* number at the wall. This increase can be explained by energy balance. Supplied heat flux at the wall and generated heat by viscous dissipation and Joule heating together determines the direction of the heat flow. A similar observation is done by [8] for a larger *Br* scale. In their analytical study, they found singular points in the variation of *Nu* values. They stated that in these singular points, supplied heat at the wall and generated heat is balanced, and beyond this point, the direction of heat flow is changed.

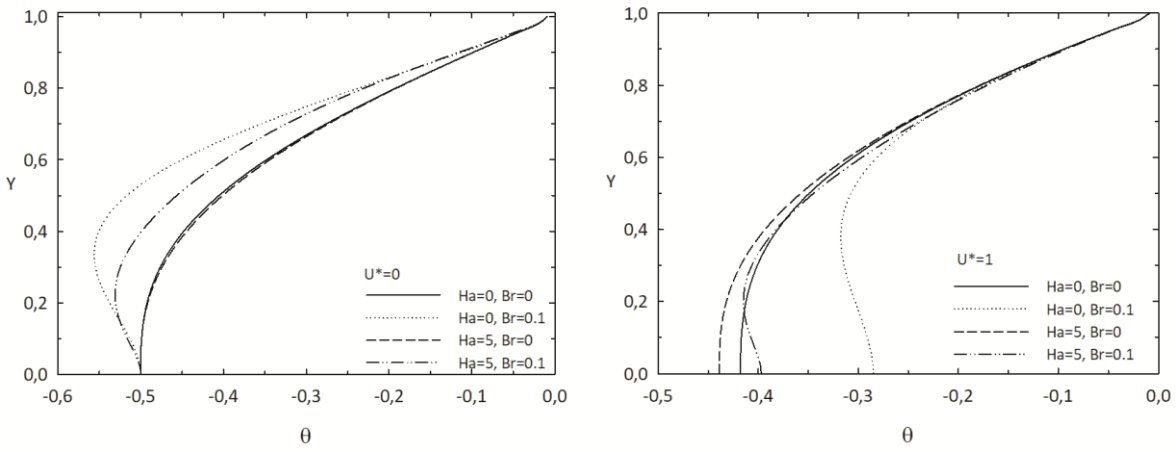

(a) (b)

Figure 3. Dimensionless temperature profiles for *Case A*

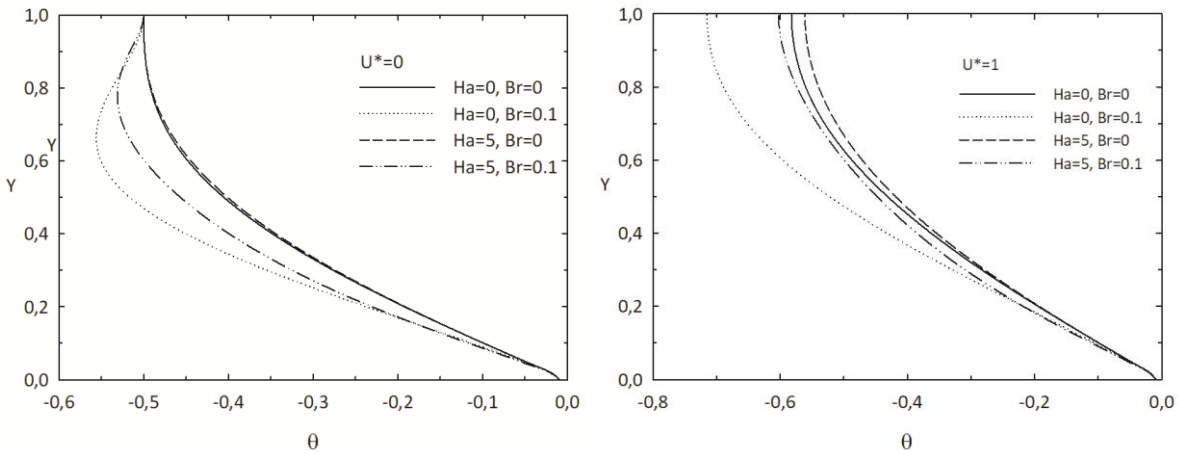

(a) (b)

Figure 4. Dimensionless temperature profiles for *Case B*

Variation of *Nu* for simultaneously developing flow is also investigated in this study. Figures 5 and 6 shows the development of *Nu* through the channel for *Case A and B*, respectively.

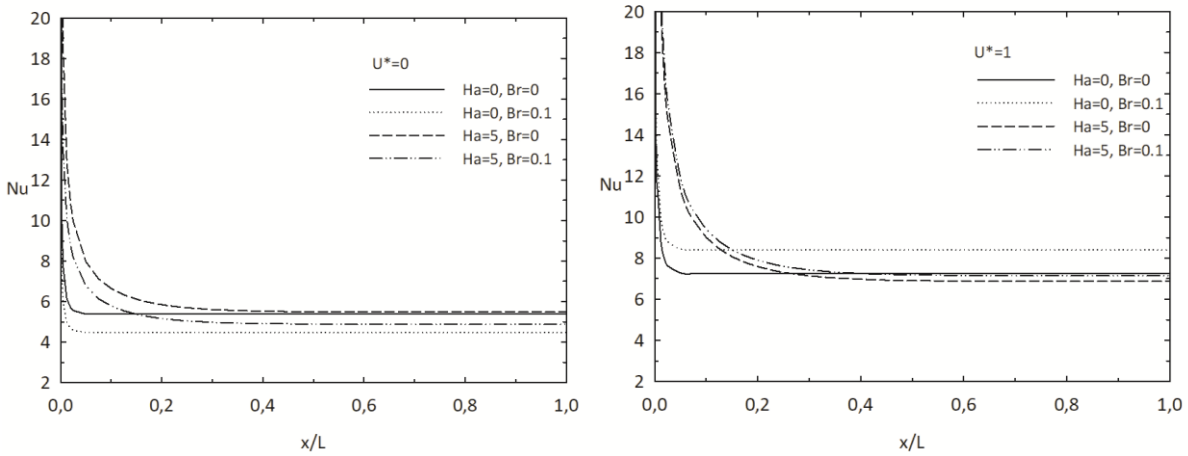

(a) (b)

Figure 5. Variation of *Nu* with respect to dimensionless axial distance for *Case A*

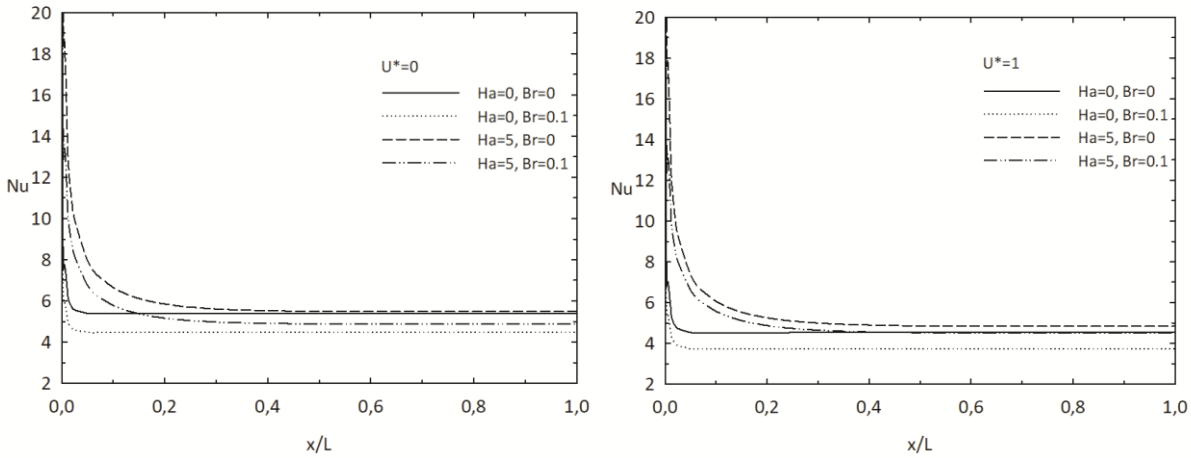

(a) (b)

Figure 6. Variation of *Nu* with respect to dimensionless axial distance for *Case B*

4. CONCLUSIONS

In this study, a 2D numerical analysis was conducted to investigate the hydrodynamically and thermally developing flow and heat transfer problem of conductive, viscous, incompressible, and Newtonian fluid between parallel plates under a uniform magnetic field. Heat generation due to viscous dissipation and Joule heating are included in the analysis. Two different cases have been investigated under thermal boundary conditions: uniform heat flux at the moving wall and the adiabatic stationary wall (*Case A*), and uniform heat flux at the stationary wall and adiabatic moved wall (*Case B*). The continuity, momentum, and energy equations are solved numerically via ANSYS 16.0. In the flow region, magnetohydrodynamic (MHD) fluid flow and heat transfer, caused by the interaction of fluid movement and electromagnetic field, are examined. For different wall velocities and heating conditions, the effects of Brinkman and Hartmann numbers on the velocity and temperature profiles and Nusselt numbers are presented and discussed. From the presented results, these conclusions can be made;

- Retarding effect of Lorentz Force acting on the electrically conductive fluid in the presence of magnetic field alters the shape of the fully developed velocity profile.

- In the presence of magnetic field, lower velocities are observed in the mid-region of the channel, and higher velocities are observed near wall regions for *U*=0* (stationary walls), which results in an increased temperature gradient in near-wall regions and enhances the heat transfer rate (for both *Case A and B*).

- For *U*=1* (moving upper wall), the presence of a magnetic field reduced the velocity gradient at the moving wall and increased the velocity gradient at the lower stationary wall. This change in the velocity profile resulted in decreased temperature gradient (reduced heat transfer rate) at the moving wall (*Case A*) while it is observed to be opposite in the lower wall (*Case B*).

- Generated heat due to viscous dissipation and Joule heating decreases the temperature gradient at stationary walls (*U*=0 Case A* and *B*, *U*=1 Case B*). An interesting case occurs where the heat is supplied from the moving wall (*U*=1 Case A*), where the inclusion of heat generation terms resulted in increased temperature gradient at the moving wall. This increase is attributed to the energy balance between generated heat near the moving wall region and supplied heat at the moving wall.

REFERENCES

[1] Attia H. A. and Kotb N. A., MHD flow between two parallel plates with heat transfer, *ActaMechanica*,117, 215-220 (1996).

[2] Attia H. A. and Sayed-Ahmed M. E. Hall effect on unsteady MHD Couette Flow and Heat Transfer of a Bingham Fluid with Suction and İnjection, *Applied Mathematical Modelling,* 28, 1027–1045, 2004.

[3] Attia H. A., Effect of Hall Current on Transient Hydromagnetic Couette–Poiseuille Flow of a Viscoelastic Fluid with Heat Transfer, *Applied Mathematical Modelling,* 32, 375–388, 2008.

[4] Suzuki K. and Nishio S., Effect of Viscous Dissipation on Fully Developed Heat Transfer of Non-Newtonian Fluids in Plane Laminar Poiseuille - Couette Flow, *Int. Comm. Heat Mass Transfer,* 663-672, 2004.

[5] Bég O. A., Zueco J., Takhar H.S., Unsteady magnetohydrodynamic Hartmann– Couette Flow and Heat Transfer in a Darcian Channel with Hall Current, İonslip, Viscous, and Joule Heating Effects: Network Numerical Solutions, *Commun Nonlinear SciNumerSimulat*, 14, 1082–1097, 2009.

[6] Ramesh K., Effects of Viscous Dissipation and Joule Heating on the Couette and Poiseuille Flows of a Jeffrey Fluid with Slip Boundary Conditions, *Propulsion and Power Research,* 7(4) 329–341, 2018.

[7] Hayat T., Khan M., Ayub M., Couette and Poiseuille Flows of an Oldroyd 6-Constant Fluid with Magnetic Field, *J. Math. Anal. Appl.*, 298, 225–244, 2004.

[8] Aydin O., Avci M., Laminar Forced Convection with Viscous Dissipationin a Couette–PoiseuilleFlow Between Parallel Plates, *Applied Energy*, 83, 856–867, 2006.

[9] Shigechi T., Momoki S., Ganbat D., Effect of Viscous Dissipation on Fully Developed Heat Transfer of Plane Couette-Poiseuille Laminar Flow, 153-156, 1999.

[10] Mokarizadeh H., Asgharian M., Raisi A., Heat Transfer in Couette-Poiseuille Flow Between Parallel Plates of the GiesekusViscoelastic Fluid, *Journal of Non-Newtonian Fluid Mechanics,* 196, 95– 101, 2013.

[11] Makinde O.D., Onyejekwe O.O., A Numerical Study of MHD Generalized Couette Flow and Heat Transfer with Variable Viscosity and Electrical Conductivity, *Journal of Magnetism and Magnetic Materials*, 323, 2757–2763, 2011.

[12] Mosayebidorcheh S., Makinde O. D., Ganji D. D., Chermahini M. A., DTM-FDM Hybrid Approach to Unsteady MHD CouetteFlow and Heat Transfer of Dusty Fluid with Variable Properties, *Thermal Science and Engineering Progress*, 2, 57–63, 2017.

NUMERICAL INVESTIGATION OF NATURALLY VENTILATED FACADE WITH PCM LOCATED IN MEDITERRANEAN REGION

Soner BIRINCI*, Mehmet SAGLAM*, Bugra SARPER, M. Yusuf YAZICI***, Mete AVCI****, Orhan AYDIN***
*Department of Mechanical Engineering, Karadeniz Technical University, 61080 Trabzon, Turkey
Email: sonerbirinci@ktu.edu.tr, mehmetsaglam@ktu.edu.tr, oaydin@ktu.edu.tr
**Department of Mechanical Engineering, Tarsus University, Tarsus, 33400 Mersin, Turkey
Email: bugrasarper@tarsus.edu.tr
*** Department of Mechanical Engineering, Samsun University
Email: myusuf.yazici@samsun.edu.tr
**** Department of Mechanical Engineering, Recep Tayyip Erdogan University, , 53100 Rize/Turkey
Email: mete.avci@erdogan.edu.tr

ABSTRACT

In recent years, with the rapid depletion of natural resources and the increasing population, there has been a need to minimize the energy consumption of buildings for ventilation and air conditioning. For this reason, solar facades have been widely used in recent years, and the use of phase change materials in building facades has become one of the main R&D studies. This paper presents a two-dimensional numerical investigation of a naturally ventilated solar facade with PCM in the Mediterranean climate. The ventilated facade consists of two regions: (i) the air duct between the outer shell and the absorber, (ii) the absorber containing PCM. The scope of this work is to emphasize effects of thickness of the PCM layer on absorber temperature, velocity and temperature of air inside the channel, phase change characteristics and latent heat storage.

Keywords: Solar facade, Double skin facade, Thermal energy storage, Natural ventilation

1. INTRODUCTION

Energy production and consumption have become highly essential all over the world. A significant part of energy production is used for the heating, cooling and ventilation of buildings, and this rate is 36% according to the International Energy Agency's report [1]. Increasing energy demand requires minimizing energy consumption of buildings. For this reason, solar facades have been widely used as one of the most efficient processes. Solar facades allow natural ventilation using passive solar energy. In addition to the conventional solar facades, the use of phase change materials (PCM) in building facades has become one of the main R&D studies for reducing energy consumption in buildings. One of the most used thermal storage methods is the latent heat storage (LHS), and the stored heat is provided with phase transition. The PCMs are employed to store energy as latent heat. Phase change materials are advantageous compared to the conventional heat storage materials. One of the most exclusive features is the high heat storage capacity, resulting in reduction of the thermal storage unit size. [2]. One of the other major advantage of PCM is isothermal phase change characteristic. This means that the heat is charged and discharged at almost constant temperature (phase-change temperature) during phase transition. This prevents temperature fluctuations and makes them ideal for providing thermal comfort [3]. A solar facade integrated with PCM can store excessive solar energy to use even at night or on a cloudy day. High thermal energy storage capacity helps to minimize the energy consumption of buildings. [4].

There are numerous studies related to solar facades with PCM in the existing literature. Ong and Chow [5] analyzed effects of the air gap and solar radiation intensity on the performance of solar chimneys. Yılmaz and Fraser [6] examined turbulent natural convection in a vertical parallel plate channel with a heated wall and an opposing glass wall experimentally and numerically. Buonomo et al. [7] carried out a numerical study to

investigate the effect of the solar chimney's height and spacing. Diarce et al. [8] investigated a new type of ventilated active facade with PCM, and they tested different radiation and turbulence models. Buonomo et al. [9] carried out a numerical study to investigate effects of the glass wall inclination. Duan et al. [10] performed a theoretical study to analyze influence of the solar radiation intensity and the height of the solar chimney on natural and mechanical ventilation rates. Lei et al. [11] conducted a numerical analysis to investigate effects of the different gap widths and inclination angles on heat transfer and fluid flow in the roof solar chimney. Sudparest et al. [12] performed a numerical study to investigate effect of the moist air on the performance of a vertical solar chimney. Li et al. [4] investigated effects of various parameters of a PCM such as melting/freezing time, and air flow rate and air temperature difference between inlet and outlet on thermal performance of a solar chimney. They stated that the phase change temperature of PCM greatly affects the thermal performance of the solar chimney. Al-Kayiem et al. [13] conducted a numerical and experimental study to analyze the influence of inlet configuration on the performance of a roof top solar chimney. Buonomo et al. [14] carried out a two-dimensional numerical study on a solar chimney with PCM. Zhang and Yang [15] investigated flow and heat transfer processes in vertical air channels of double-skin solar facades numerically.

In this paper, a two-dimensional numerical investigation of a prototypal solar facade system with PCM is presented. The PCM is located behind the absorber. Effects of thickness of the PCM layer on temperature and air velocity profiles inside the channel, phase change characteristics and latent heat storage are investigated for four cases. Simulations are carried out via a commercial computational fluid dynamic software ANSYS Fluent [16], and analyses are made on June 21 from 9 a.m. to 3 p.m. in Tarsus.

2. NUMERICAL STUDY

2.1 Geometry

The schematic view of the problem is shown in Fig. 1. The solar facade system consists of two parts: (i) the air duct between the glass and the absorber, (ii) the absorber containing PCM. Volumetric heat generation is applied within absorber of height, L_{tot}. The PCM is contained behind the absorber in a rectangular cavity of thickness, s_t. Height and width of the solar facade system are 8 m and 0.2 m, respectively. The ambient temperature is taken as T_0 = 300 K. While the flow within the channel is turbulent, it is considered as laminar within the PCM. In the study, simulations are realised for four different thicknesses of the absorber containing PCM (See Table 1).

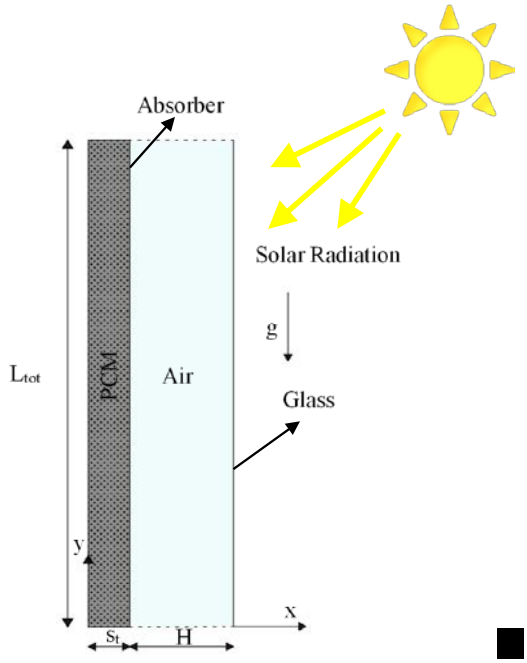

Figure 1. The schematic view of the solar facades system.

Table 1. Thickness of the PCM layer (s_t)

Case	s_t [m]
Case 1	0.1
Case 2	0.075
Case 3	0.05
Case 4	0.025

2.2 Numerical Model

In the numerical part of the study, ANSYS Fluent software [16] is used to solve governing equations. Flow is two-dimensional, unsteady, incompressible and turbulent in air region, while it is laminar in PCM region. SIMPLE algorithm is used for the pressure-velocity coupling. Momentum and energy equations are discretized by second order upwind scheme, and pressure interpolation is provided by PRESTO scheme. Turbulent flow conditions and radiative heat transfer are modeled using standard k-ϵ turbulence model and surface-to-surface (S2S) radiation model, respectively [16]. The emissivity values of the absorber and glass are considered as 0.95 and 0.89, respectively. Coupled boundary condition is used on the absorber surface and convection boundary condition is employed on the glass. Pressure inlet and pressure outlet boundary conditions are considered for inlet and outlet of the channel, respectively. The volumetric heat generation that is applied within the absorber is equal to τE. τ is the transmittance of the glass and its value is equal to 0.68 [14]. E is the solar irradiation value on June 21, and it is calculated by the solar calculator of ANSYS Fluent from 9 a.m. to 3 p.m. for Tarsus [16] (See Fig. 2).

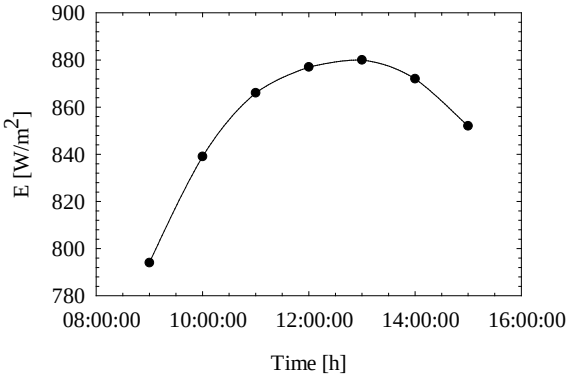

Figure 2. Solar irradiation on June 21.

The two-dimensional transient energy equation based on enthalpy-porosity technique models solidification/melting process of the PCM [18]. In this technique, liquid fraction, β which is based on an enthalpy balance is computed at each iteration. Mushy zone is defined as the region where the liquid fraction is between 0 and 1 and modeled as pseudo porous medium. As the PCM solidifies, porosity decreases from 1 to 0, and when PCM fully solidifies, the porosity gets 0 (velocity decreases to zero).

$$\begin{aligned} \beta &= 0 \quad \text{for } T < T_{solidus} \\ \beta &= 1 \quad \text{for } T > T_{liquidus} \\ \beta &= \frac{(T - T_{solidus})}{(T_{liquidus} - T_{solidus})} \quad \text{for } T_{solidus} < T < T_{liquidus} \end{aligned} \tag{1}$$

For the organic PCM material, the paraffin wax R56-58 is used, and the thermal properties of PCM are given in Table 2 [19].

Table 2. Thermal properties of paraffin wax R56-58.

Property	Value
Specific heat, *Cp* [J/kgK]	2100
Density, ρ [kg/m^3]	840
Thermal conductivity, *k* [W/mK]	0.2
Viscosity, μ [kg/ms]	0.003
Thermal expansion coefficient, γ [1/K]	0.0004
Latent heat, H_L [kJ/kg]	120.7
Solidus temperature, $T_{solidus}$ [K]	323.75
Liquidus temperature, $T_{liquidus}$ [K]	339.65

The non-uniform mesh structure is generated in this study. Grid independence studies are performed in four different cell numbers (300x20, 200x30, 300x30 and 200x40) for case 1. When the results are examined, it is found that the 200x30 cells is enough for the final computations because difference between average temperature of the absorber and mass flow rate are quite low for subsequent cell numbers. The results of the grid independence study are given in Table 3.

Table 3. Grid independence study

	300x20 Cells	Relative Error %	200x30 Cells	Relative Error %	300x30 Cells	Relative Error %	200x40 Cells
Average temperature of absorber [K]	337.9	0.23	337.1	0.089	337.07	0.1	336.7
Mass flow rate [kg/s]	0.222	1.3	0.225	0.4	0.226	0.4	0.227

The study is validated against the results of Buonomo et al. [14]. When Fig. 3 is examined, it is seen that the temperature profiles are close to each other, especially in the air region. However, the harmony in temperature profiles is not seen in velocity profiles.

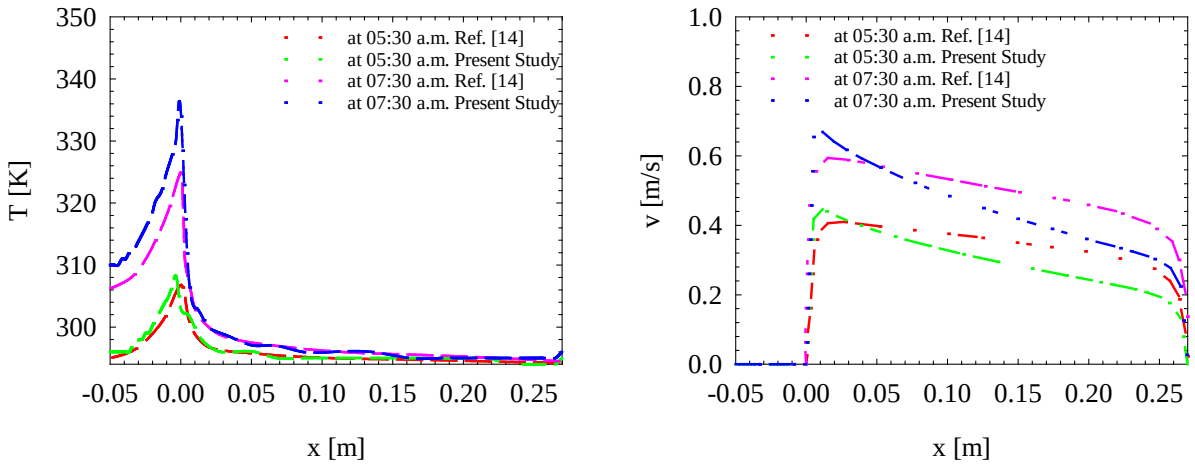

Figure 3. Comparison of temperature and velocity profiles.

3. RESULTS AND DISCUSSION

In this study, a two-dimensional numerical investigation of a prototypal solar facade system is presented. The scope of this work is to emphasize effects of thickness of the PCM layer on temperature and velocity profiles,

phase change characteristics and latent heat storage. Unsteady simulations are carried out via a commercial computational fluid dynamic software ANSYS Fluent [16]. The analyses are carried out on June 21 from 9 a.m. to 3 p.m. in Tarsus.

Figure 4 shows temperature and velocity profiles at inlet, mid-height and outlet sections at 3 p.m. for different PCM thicknesses. As it can be seen from the velocity profiles at different cases, the velocity profile within the facade is not affected by the PCM thickness. The velocity profiles are almost uniform at the inlet, and the effect of buoyancy on flow becomes clearer as the height increases. At the inlet region, temperature profile in the PCM is almost uniform in the first case. In all cases, temperatures decrease towards the inner wall with increasing PCM thickness. This indicates that the PCM layer behaves like an insulation material in the hot summer.

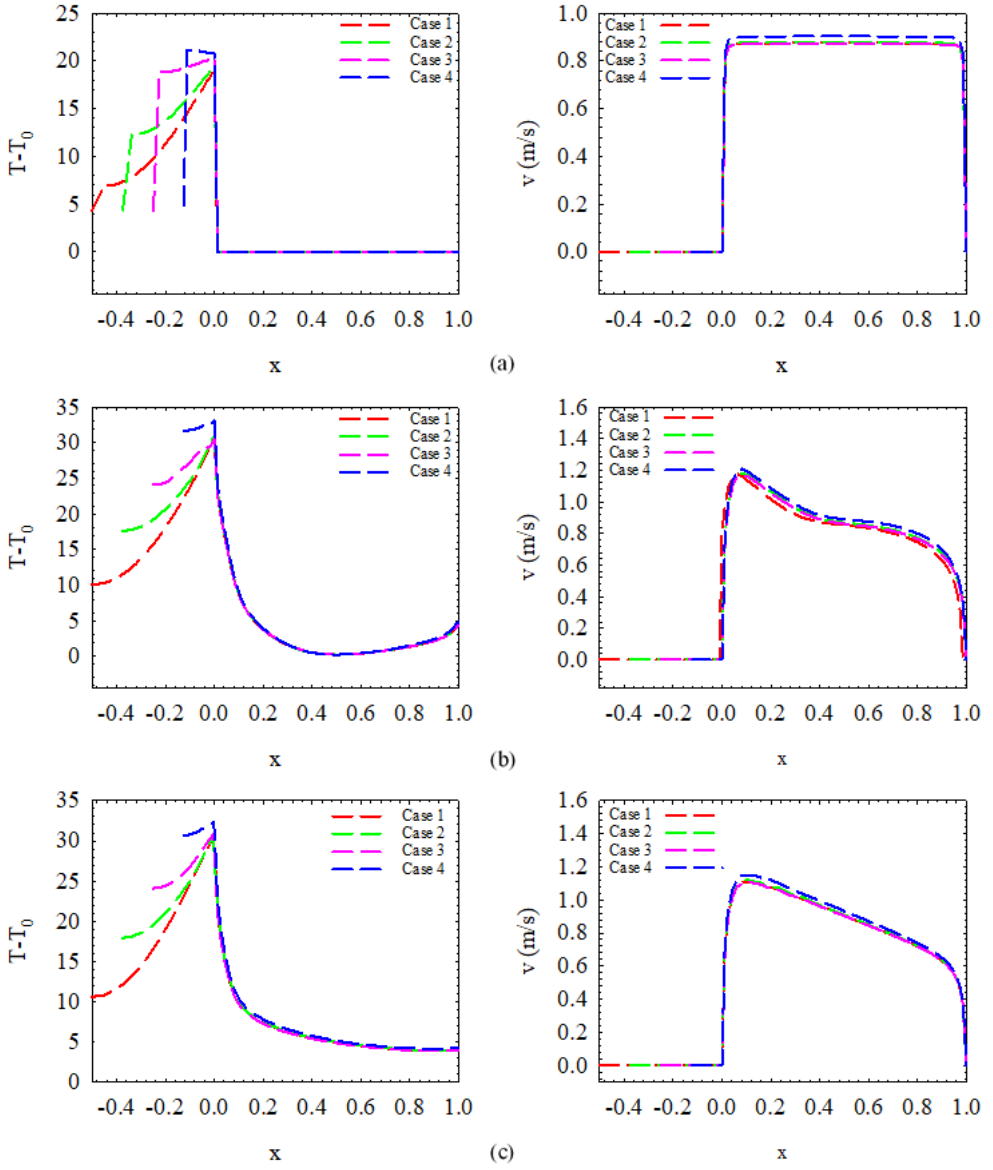

Figure 4. Temperature and velocity profiles in different positions, (a) y = 0 m, (b) y = 4 m and (c) y = 8 m at 3 p.m.

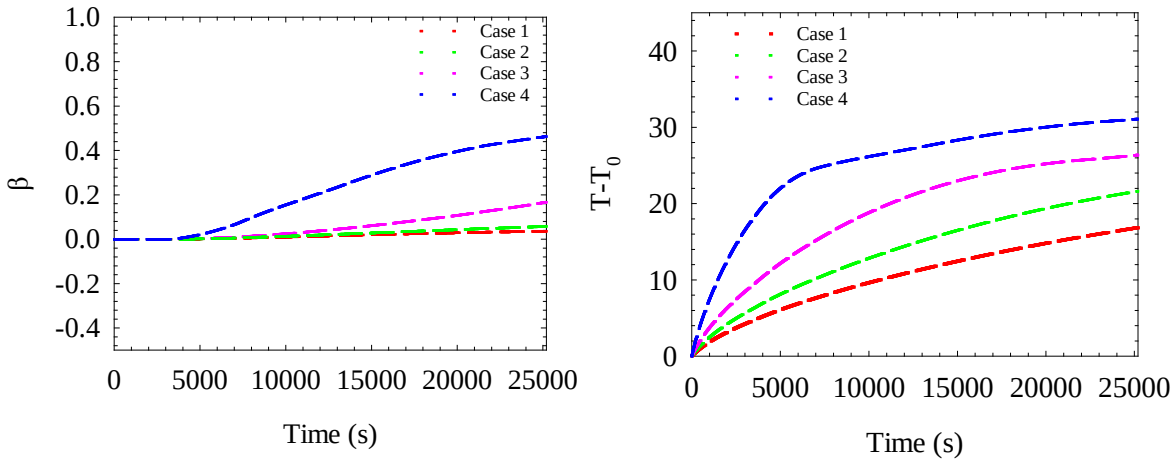

Figure 5. Variations of the liquid fraction and temperature of the PCM during simulations.

Figure 5 shows liquid fraction and temperature of the PCM at different cases. In this figure, effects of PCM on melting behavior can be seen obviously. In the first (s_t = 0.1 m) and second (s_t = 0.075 m) cases, the sensible heat is stored because the PCM does not melt enough. In the third case (s_t = 0.05 m), although PCM starts to melt, melting is not sufficient for storing latent heat. In the fourth case, melting is more pronounced, and it is four times that in the third case. However, the melting rate is still not very high, and it is not sufficient for latent heat storage. It is also seen that the melting starts at approximately 5000 seconds and continues until the end of the simulations. The results obtained in the melting graphs are also supported by temperature graphs.

4. CONCLUSION

A two-dimensional numerical study has been carried out to analyze effects of thickness of the PCM layer. Some of the important findings obtained in the study can be presented as follows:

- The velocity and temperature profiles in air duct are not affected by the PCM thickness.
- As the thickness of the PCM increases, temperature of the inner surface decreases. This indicates that the PCM can be used as an insulation material in hot summer days.
- The melting process is highly affected from the PCM thickness.
- Reducing PCM thickness makes the increase in PCM temperature evident. This accelerates melting and more latent heat is stored.

REFERENCES

[1] International Energy Agency, Global Status Report for Buildings and Construction, 2019.

[2] Ghoneim, A.A., Klein, S.A. & Duffie, J.A., Analysis of Collector Storage Building Walls Using Phase Change Materials, *Solar Energy*, **47**(3), 237 – 242, 1991.

[3] Pasupathy, A., Athanasius, L., Velraj, R. & Seeniraj, R.V., Experimental Investigation and Numerical Simulation Analysis on the Thermal Performance of a Building Roof Incorporating Phase Change Material (PCM) for Thermal Management, *Applied Thermal Engineering*, **28**, 556 – 565, 2008.

[4] Li, Y., Liu, S., & Lu, J., Effects of Various Parameters of a PCM On Thermal Performance of a Solar Chimney, *Applied Thermal Engineering*, **127**, 1119-1131, 2017.

[5] Ong, K.S., & Chow, C.C., Performance of a Solar Chimney, *Solar Energy*, **74**, 1-17, 2003.

[6] Yilmaz, T. & Fraser, S.M., Turbulent Natural Convection in a Vertical Parallel-Plate Channel with Asymmetric Heating, *International Journal of Heat and Mass Transfer*, **50**, 2612–2623, 2007.

[7] Buonomo, B., Manca, O., Nardini, S. & Tartaglione, G., Numerical Simulation of Convective-Radiative Heat Transfer in A Solar chimney, *12th Biennial Conference on Engineering Systems Design and Analysis*, Copenhagen- Denmark, 2014.

[8] Diarce, G., Campos-Celador, A., Martin, K., Urresti, A., Garcia-Romero, A. & Sala, J.M., A Comparative Study of The CFD Modeling of a Ventilated Active Façade Including Phase Change Materials, *Applied Energy*, **126**, 307-317, 2014.

[9] Buonomo, B., Manca, O., Montanioro, C. & Nardini, S., Numerical Investigation of Convective–Radiative Heat Transfer in a Building-Integrated Solar Chimney, *Advances in Building Energy Research*, **9**(2), 253-266, 2015.

[10] Duan, S., Jing, C. & Long, E., Transient Flows in Displacement Ventilation Enhanced by Solar Chimney and Fan, *Energy and Buildings*, **103**, 124-130, 2015.

[11] Lei, Y., Zhang, Y., Wang, F. & Wang, X., Enhancement of Natural Ventilation of a Novel Roof Solar Chimney with Perforated Absorber Plate for Building Energy Conservation, *Applied Thermal Engineering*, **107**, 653-661, 2016.

[12] Sudprasert, S., Chinsorranant, C. & Rattanadecho, P., Numerical Study of Vertical Solar Chimneys with Moist Air in a Hot and Humid Climate, *International Journal of Heat and Mass Transfer*, **102**, 645-656, 2016.

[13] Al-Kayiem, H.H., Sreejaye, K.V. & Chikere, A., Experimental and Numerical Analysis of The Influence of Inlet Configuration on The Performance of a Roof Top Solar Chimney, *Energy and Buildings*, **159**, 89-98, 2018.

[14] Buonomo, B., Capasso, L., Diana, A., Manca, O. & Nardini, S., A Numerical Analysis on a Solar Chimney with an Integrated Latent Heat Thermal Energy Storage, *74th ATI National Congress*, Modena-Italy, 2019.

[15] Zhang, T. & Yang, H., Flow and Heat Transfer Characteristics of Natural Convection in Vertical Air Channels of Double-Skin Solar Façades, *Applied Energy*, **242**, 107-120, 2019.

[16] ANSYS Fluent 15.0 User's Guide, Ansys Inc., 2015.

[17] Yang J., Yang L., Xu C. & Du, X., Numerical Analysis on Thermal Behavior of Solid-Liquid Phase Change Within Copper Foam with Varying Porosity, *International Journal of Heat and Mass Transfer*, **84**, 1008–1018, 2015.

[18] Voller, V.R. & Prakash, C., A Fixed-Grid Numerical Modeling Methodology for Convection-Diffusion Mushy Region Phase-Change Problems, *International Journal of Heat and Mass Transfer*, **30**, 1709–1720, 1987.

[19] Hu, X. & Gong, X., Pore-Scale Numerical Simulation of The Thermal Performance for Phase Change Material Embedded in Metal Foam with Cubic Periodic Cell Structure, *Applied Thermal Engineering*, **151**, 231 – 239, 2019.

NUMERICAL INVESTIGATION OF THE EFFECT OF AIR VELOCITY ON HEAT TRANSFER TO HEAT SINK IN THERMOELECTRIC MODULES

Seyda ÖZBEKTAŞ*, Bahattin TOPALOĞLU, Bilal SUNGUR*****
*Ondokuz Mayıs University, Faculty of Engineering, Department of Mechanical Engineering Samsun/Turkey
Email: seyda.ozbektas@omu.edu.tr
**Ondokuz Mayıs University, Faculty of Engineering, Department of Mechanical Engineering Samsun/Turkey
Email: btopal@omu.edu.tr
***Samsun University, Faculty of Engineering, Department of Mechanical Engineering
Samsun, Turkey
Email: bilal.sungur@samsun.edu.tr

ABSTRACT

Today, the demand for energy increases day by day. Energy costs also increase rapidly. There are many incentives around the world to diversify production in the field of energy. In this context, the thermoelectric module is an important source in the conversion of heat to electrical energy. The amount of electricity generation from heat depends on the temperature difference of the thermoelectric module. It can be said that more electricity is obtained with more temperature differences. This study aims to analyze the performance of a thermoelectric module with heat sink having cylindrical pin fins by using Ansys Fluent program. In this context, the effect of air velocity on heat transfer of heat sink and the thermoelectric module was investigated. Calculations were performed in three-dimensional conditions. As a result, temperature and stream function contours, temperature differences in the thermoelectric module, total thermal resistance, Nusselt numbers in relation to Reynolds numbers were evaluated and discussed. The results showed that as the Reynolds number increased, the temperature difference, Nusselt number, and heat ratio increased while the total thermal resistance decreased. Besides, the lowest and the highest temperature difference between hot and cold surfaces of the thermoelectric module were found 61.31 Kelvin at Reynolds 5000 and 71.83 Kelvin at Reynolds 15000, respectively.

Keywords: Thermoelectric Module, Heat Sink, Numerical Modelling

1. INTRODUCTION

Today, the need for energy increases with the increasing population and developing technology. To prevent such disadvantages, the trend towards renewable energy sources has accelerated all over the world. Although thermoelectric modules have not yet very efficient in producing electricity from heat, they are expected to become important in future energy technology. The thermoelectric module generates direct current electrical energy at the ends of the module when a temperature difference occurs between its surfaces. Thermo elements consisted of N and P-type semiconductor pairs are placed between ceramic plates in electrically series and thermally parallel. The thermoelectric module works according to the Seebeck effect in electricity production. In the Seebeck effect, a potential difference occurs between the circuit ends by applying different temperatures at the junction points of the materials A and B, which consist of different substances. The schematic diagram of the thermoelectric module and the Seebeck effect are shown in Figure 1 and Figure 2, respectively. Heat Sinks are cooling units that are used to lower the temperature of electronic devices, mostly by reducing the heat of the device with the help of a fan, preventing the device from overheating or burning. To increase the efficiency of the thermoelectric generators, heat sinks are often used.

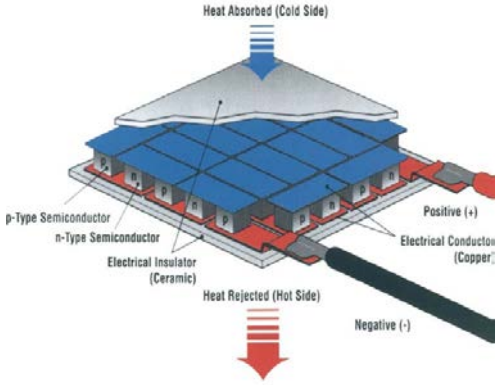

Figure 1. The schematic diagram of the thermoelectric module [17]

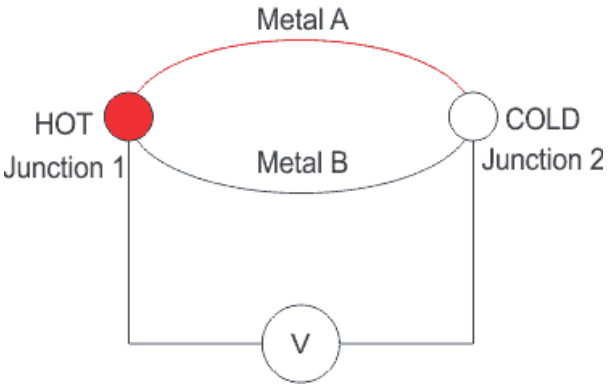

Figure 2. Seebeck effect [18]

The literature review conducted within the scope of the study has been carried out on heat sinks required for cooling the thermoelectric modules. Some of these studies are shown below. Gururatana [1] studied electronic cooling methods. He concluded that the heat transfer rate could increase with the cooling techniques widely used but with increasing heat transfer rate, the pressure drop could highly rise too, so the optimization method is required to obtain optimum cost and cooling rate. Kumar and Bartaria [2] investigated the effects of the configurations of the pin fin design. They concluded elliptical pin fin heat sink has better performance than the plate fin heat sink. Bettahar and Saidia [3] investigated the thermal and hydraulic performances of a heat sink with impinging airflow by way of numerical simulation by using C++ code personal developed in order to provide improvements on the performance of heat sink. Their results showed that as impinging Reynolds number increase, the heat transferred by the heat sink increases, and the performance of the proposed model is better than the literature results. Kumar [4] carried out a thermal analysis on the heat sink with cylindrical pin fins, which have different fin base to tip diameter ratio subjected to two turbulent impinging jets which have different velocity ratio by using Ansys Icepak. They observed that as velocity ratio increases, heat transfer coefficient and thermal resistance increase and pressure drop decreases through fins. Mohammed and Razuqi [5] aimed to predict the effectiveness of two types of closely spaced fins which are parallel cylindrical fin array and hollow parallel cylindrical fin array. In addition, there were two different locations in their study in term of the fan position. As a result of their work, they found out that the heat sink with a cooling fan fixed in the enclosure cutout template has more effect and cylindrical fins perform better in heat transfer than the hollow fins. Mendonca and Yalamarty [6] analyzed numerically heat sinks consisting of different fin geometry for led modules to compare thermal performance and airflow. They concluded that the airfoil fins with reverse orientation provide the minimum thermal resistance compared to others. Dhole et al. [7] investigated how the change in perforation geometry and the number of perforations in the heat sink with cylindrical pin fin affects heat transfer rate and pressure drop. As a result, it was found that as the number of perforations increases, Nusselt number increases and pressure drop reduces. Besides, the angle of conical perforation has an important role in generating turbulence. Lin et al. [8] investigated numerically and experimentally the heat transfer phenomena of the plate fin heat sinks under impinging jet cooling and compared the numerical and experimental results with each other. They concluded that heat removal increases obviously with the increase of Reynolds numbers, and the arrangement of the fin changes the temperature profile on the fin surface. Deshmukh and Warkhedkar [9] investigated experimentally the effects of design parameters of the heat sink with elliptical pin fins and aimed to obtain optimum design parameters. As a result, they found the effect of parameters as void fraction, the fin spacing, the fin bundle void fraction on the thermal performance of heat sink with elliptical pin fins. Junaidi et al. [10] carried out CFD modeling and simulation of heat sinks with three different designs, which are standard pin fins, splayed pin fins, and hybrid pin fins, in order to determine optimal heat sink design. Consequently, they found that splayed and hybrid heat sinks offer optimum cooling performance so that these heat sinks have better cooling performance than standard pin fin by 20% to 40%. Belarbi et al. [11] carried out an experimental analysis of a rectangular mini-channel heat sink subjected to an impinging air jet in order to improve the cooling performance of CPUs in personal computers. They concluded that the ratio of jet height/jet diameter=0.606 and longitudinal displacement of CPU 10 mm from the center offer better cooling performance.

Mamun [12] aimed to find heat transfer, optimum dimensions, temperature distributions, the fin efficiency and fin effectiveness of the cylindrical fin, which has a constant base temperature for optimum effectiveness and efficiency by using Fortran code. He found that the optimum dimension for the conditions assumed is a fin having 0.02m of length and 0.001m of the radius. This fin gives the maximum effectiveness and efficiency for the assumed condition. Yang et al. [13] analyzed experimentally pin fin heat sinks consisting of three different cross-sections and investigated the effect of fin density on heat transfer performance. They found out that fin density has an important effect in circular pin fin heat sink for an inline arrangement. In addition, for all configurations, they concluded that as fin density increases, heat transfer coefficient increases, and elliptic pin fin has the lowest pressure drops. Kim et al. [14] compared experimentally plate fin and pin fin heat sinks with impinging airflow. At the end of their study, they concluded that the pin fin heat sink has better cooling performance than the plate fin heat sink. Şara [15] investigated the heat transfer and friction characteristics of the heat sink with square cross-section pin fins, which was located staggered way. He inferred from his study that lower Reynolds number, clearance ratio, and inter-fin distance ratio provide better cooling performance.

Studies in the literature generally focused on the cooling performance of heat sinks with the flat pins for CPUs and electronic devices. In this study, the heat transfer performance of a heat sink having cylindrical pin fins on a thermoelectric module was investigated numerically. Calculations were made in three-dimensional conditions. To model the turbulent flow, the standard k-Ɛ model was used. Under these conditions, calculations have been made for different Reynolds numbers. Results have been evaluated as temperature and stream function contours, temperature differences in the thermoelectric module, total thermal resistance, and Nusselt numbers in relation to Reynolds numbers.

2. MATERIALS AND METHODS

With the developments in the field of Computational Fluid Dynamics (CFD) in recent years, it has been possible to model turbulent flows with CFD programs based on the finite volume method. In the calculation of flow problems, mass, momentum, and species conservation equations need to be solved. These differential equations are solved using boundary conditions suitable for problems. The general conservation equation is expressed in its most general form as follows:

$$\frac{\partial}{\partial t}(\rho\,\Phi) + div(\rho \upsilon\,\Phi - \Gamma_{\Phi} grad\,\Phi) = S_{\Phi} \tag{1}$$

In this equation, ρ is the density, υ is the velocity, Φ is the dependent variable, Γ_{Φ} is the transport coefficient of Φ, and S_{Φ} is the source term of the transport equation. The meanings of Φ, $\Gamma_{\Phi,}$ and S_{Φ} are provided in Table 1 for cartesian coordinates [16].

Table 1. Equations for cartesian coordinates

Equations	**Φ**	**Γ_{Φ}**	**S_{Φ}**
Continuity	1	0	0
Momentum	υ	μ_e	$-\frac{\partial p}{\partial x_i} + \frac{\partial}{\partial x_j}\left(\mu_e \frac{\partial v_j}{\partial x_i}\right) + \frac{\partial p}{\partial x_j}\left(\mu_e \frac{\partial v_i}{\partial x_j}\right) + \rho g_i$
Enthalpy	h	$\frac{\mu_e}{\sigma_h}$	S_{rad}
Turbulence Kinetic Energy	k	$\frac{\mu_e}{\sigma_k}$	$G_k - \rho_\varepsilon$
Dissipation of Turbulence Kinetic Energy	ε	$\frac{\mu_e}{\sigma_\varepsilon}$	$\frac{\varepsilon}{k}(C_1 G_k - C_2 \rho_\varepsilon)$

2.1. Boundary Conditions and Solver

The air enters through a circular cross-section of 38 mm diameter and 3 mm above the cylindrical pin fins. Velocity inlet boundary condition is used at the entrance of the air domain. Velocity inlets are specified as normal to the boundary. Reynolds numbers are specified as 5000, 7500, 10000, 15000 at the entrance of the air domain, respectively. Reynolds numbers are arranged according to the velocity of air entering through a 38 mm circular cross-section. Four sides of the air domain are set as outlet. At the outlets, the pressure outlet boundary condition is specified as atmospheric pressure. The no-slip condition has been defined at the walls in the test assembly. The temperature at the entrance of the air domain is 22℃. The hot side of the thermoelectric module is adopted at a constant temperature of 120 C. Thermoelectric module components' walls, and heat sink base walls are determined as adiabatic so that there is no heat transfer on these surfaces. Ansys Fluent package is used as CFD program. Steady-state and pressure-based solver has been employed for numerical solution. As the turbulence model, the standard k-Ɛ model was used. Spatial discretization for momentum, turbulent kinetic energy, turbulent dissipation is selected first-order upwind, and it is selected second order for pressure. SIMPLE (Semi-Implicit Method for Pressure Linked Equations) algorithm is used for pressure velocity coupling. Convergence criteria for all the equations set to 10^{-5} except energy equation which is set to 10^{-6}. The list of solid and fluid material properties used in the calculations is shown in Table 2 and Table 3, respectively.

Table 2. List of properties of solid materials used in the analysis

Materials	$\rho(kg/m^3)$	$c_p(J/kgK)$	k(W/m.K)
Ceramic	3890	880	35.4
Copper	8978	381	387.6
Aluminum	2719	871	202.4
Bismuth Telluride	7700	544	2.6

Table 3. List of properties of fluid materials used in the analysis

Materials	$\rho(kg/m^3)$	$c_p(J/kgK)$	k(W/m.K)	$\mu(kg/m.s)$
Air	1.225	1006.43	0.0242	0.00001789

2.2. Setup

The thermoelectric module with heat sink used in the analysis is designed as shown in Figure 3. This design consists of 2 ceramic plates, 256 copper plates, 128 pairs of P and N semiconductor legs, heat sink, and air domain. In this problem, the cold side of the thermoelectric module is cooled by air, and the cooling amount is increased with the cylindrical pin fin heat sink, which is made of aluminum. The ceramic plates are 40 x 40 mm in length and 0.8 mm in thickness. The copper plates are 1.4 x 3.8 mm in length and 0.5 mm in thickness, the P and N semiconductor legs are 1.4 x 1.4 mm in length and 2 mm in height. Besides, the heat sink is sized 40 mm x 40 mm in length, and 50 mm in height. The base thickness of the heat sink is 10 mm. The pin fins have a diameter of 3 mm and a height of 40 mm. The air domain is 40 x 40 mm in length and 43 mm in height, and air is blown from a circular cross-section of 38 mm in diameter at a distance of 3 mm to the pin fins.

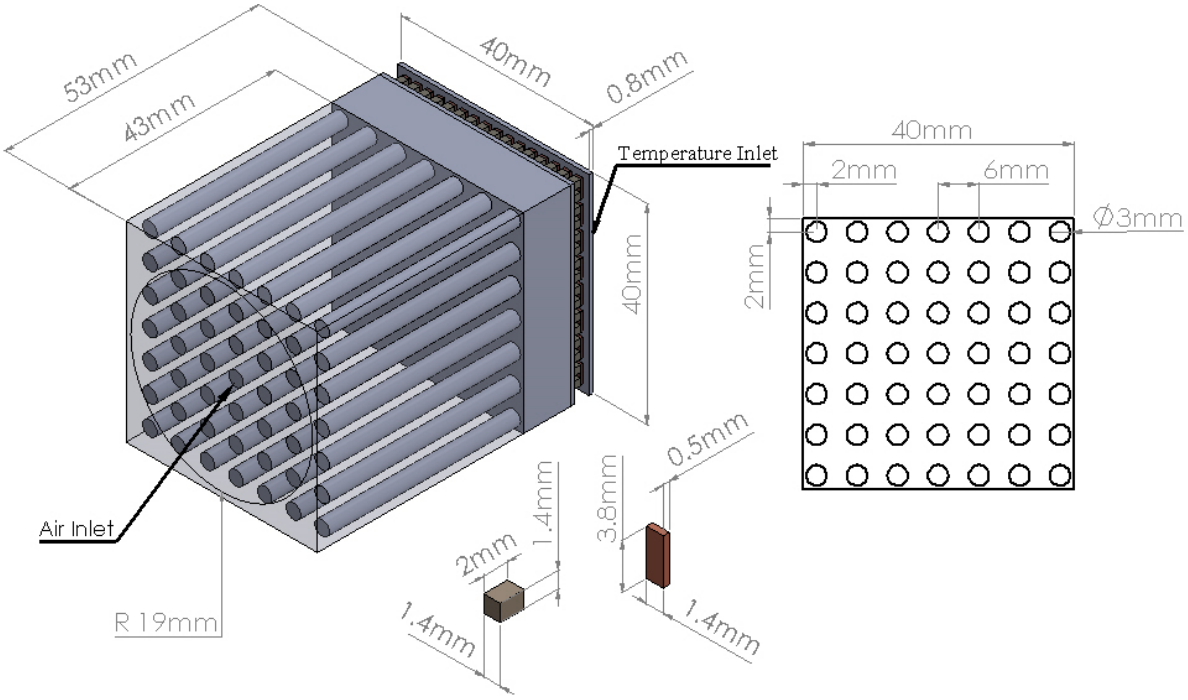

Figure 3. The dimensions and boundary conditions of thermoelectric module

The geometry must be meshed before making a solution. The average skewness value between 0 and 0.25 and average orthogonal quality between 0.75 and 1 are acceptable mesh parameters. These values are provided in this analysis, and mixed elements have been employed in the meshing process that has the number of elements 2930006 and nodes 949477. In addition, mesh size is also important. Reducing the mesh size generally has a positive effect on the quality of the mesh structure, but increases the number of nodes and elements in the mesh structure, which means more time in solutions. Therefore, an optimal mesh size must be found. In this study, three different meshing structures as coarse, medium, and fine, were compared with each other. As a result, similar results were obtained in all three meshing structures. A medium meshing structure was selected to save solution time. The medium meshing structure of the geometry is shown in Figure 4.

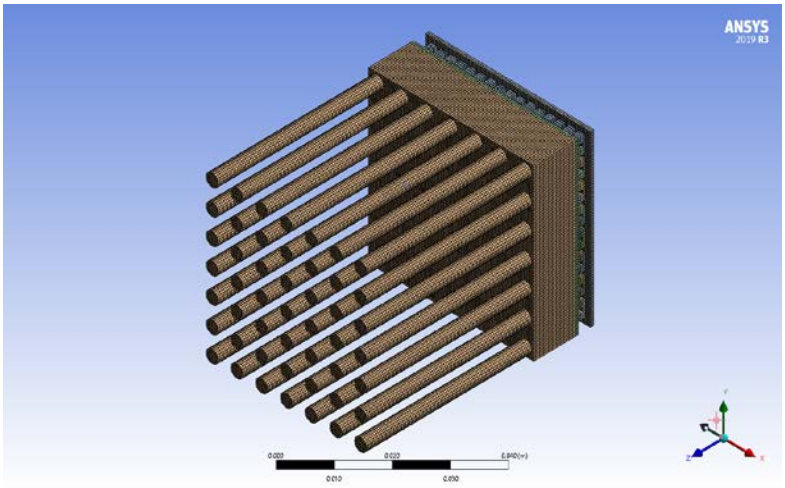

Figure 4. Meshing structure

3. RESULTS AND DISCUSSIONS

In this chapter, velocity streamlines and temperature contours of the air domain are shown in three different cross-sections. These cross-sections are placed at a distance of 16 mm to the air inlet, at the base of the heat sink, and between these two planes.

The temperature contours for four different Reynolds numbers are shown in Figure 5. According to these results, it is seen that the heat transfer from the heat sink to air increases with increasing Reynolds number. In addition, the temperature gradients on the cylindrical pin fins grow in the direction of cooling with increasing Reynolds number.

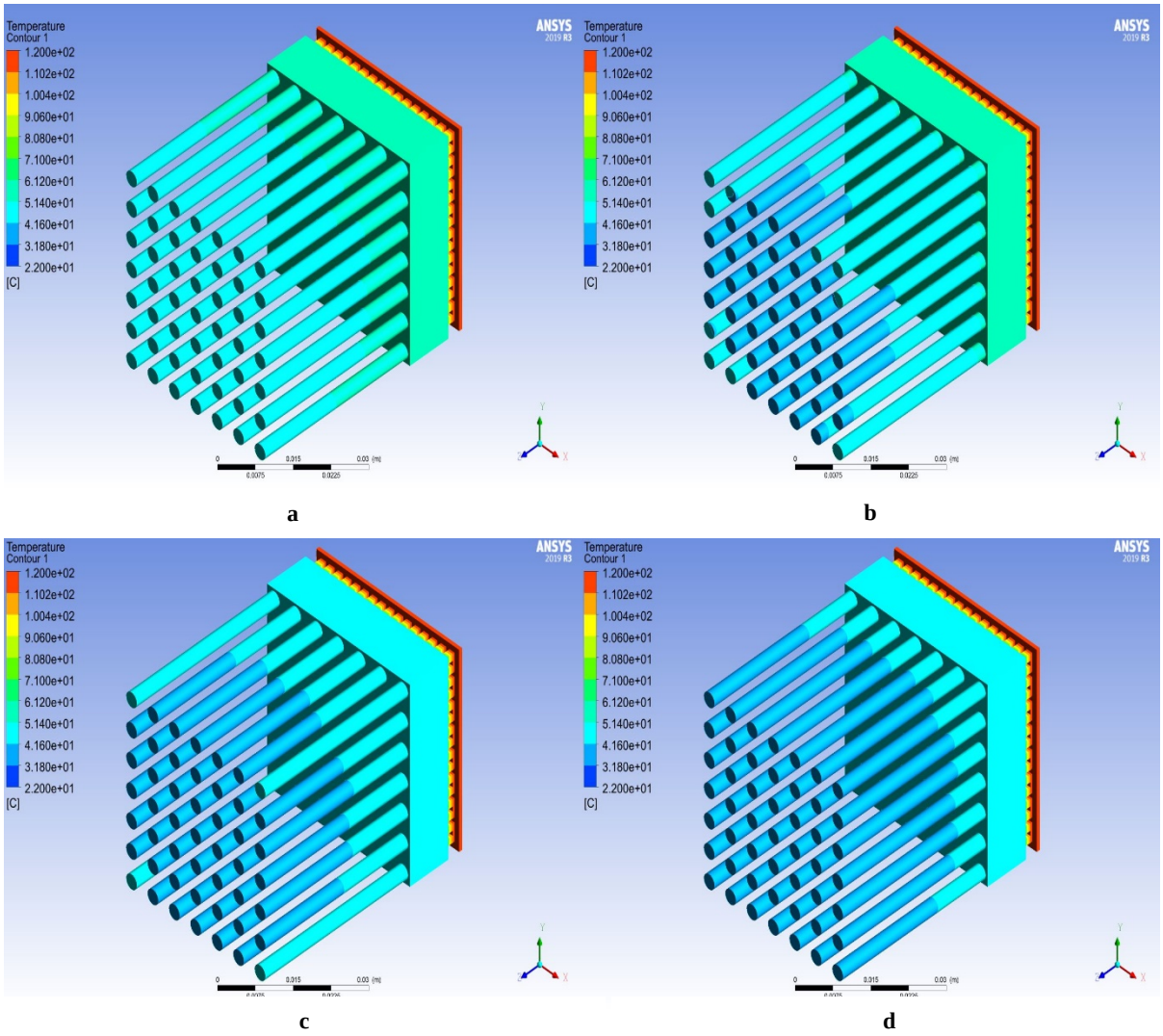

Figure 5. Temperature contours of thermoelectric module with heat sink at Reynolds **a)** 5000, **b)** 7500, **c)** 10000, **d)** 15000

The top view of the velocity streamlines in three different cross-sections at Reynolds 15000 is shown in Figure 6. The reason why showing only one Reynolds value is that there are no significant changes in the streamlines. The

figure shows that the air distributes smoothly between the cylindrical pin fins. Besides, it is observed that the air velocity increases between the cylindrical pin fins and decreases towards the outlets and the base of the heat sink.

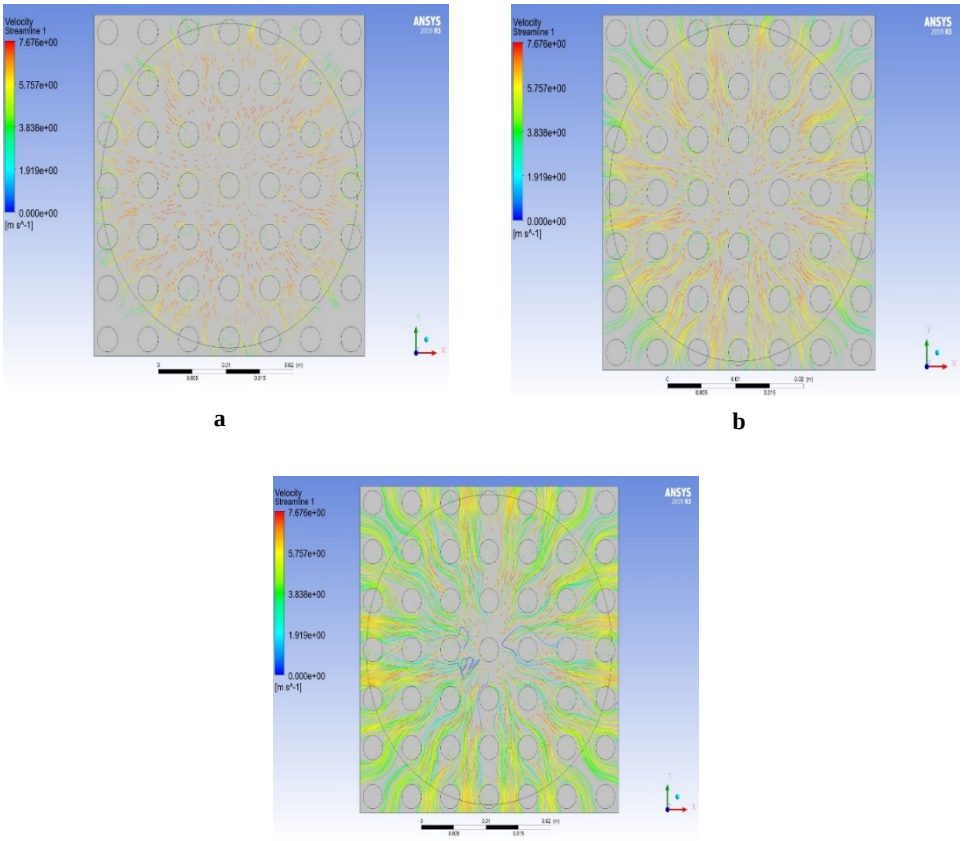

a **b**

c

Figure 6. Top view of velocity streamlines **a)** at a distance of 16 mm to the air inlet, **b)** between a and c , **c)** on the base of the heat sink at Reynolds 15000

The pressure contour at Reynolds 15000 is shown in Figure 7. The reason why showing only one Reynolds value is that there are no significant changes in the Pressure contours. The pressure contour of the air domain is shown on surfaces where the air contact with the heat sink. Being low in pressure drops is a condition wanted for good heat transfer to the air. The figure shows that there are low-pressure drops on the airside.

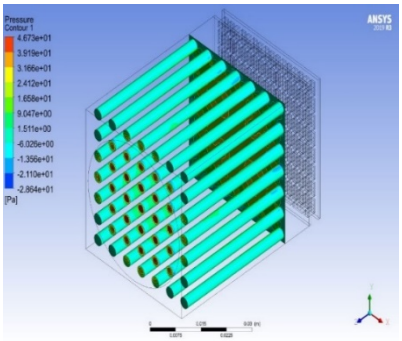

Figure 7. Pressure contour at Reynolds 15000

Temperature contours of cross-sections of the air domain for four different Reynolds numbers are shown in figure 8. The figure shows that the air temperature increases towards the base of heat sink under the effect of cylindrical pin fins, but as the Reynolds number increases, the temperature value of air decreases due to evacuation of air from the outlets rapidly. As a result, the quick evacuation of air provides better cooling.

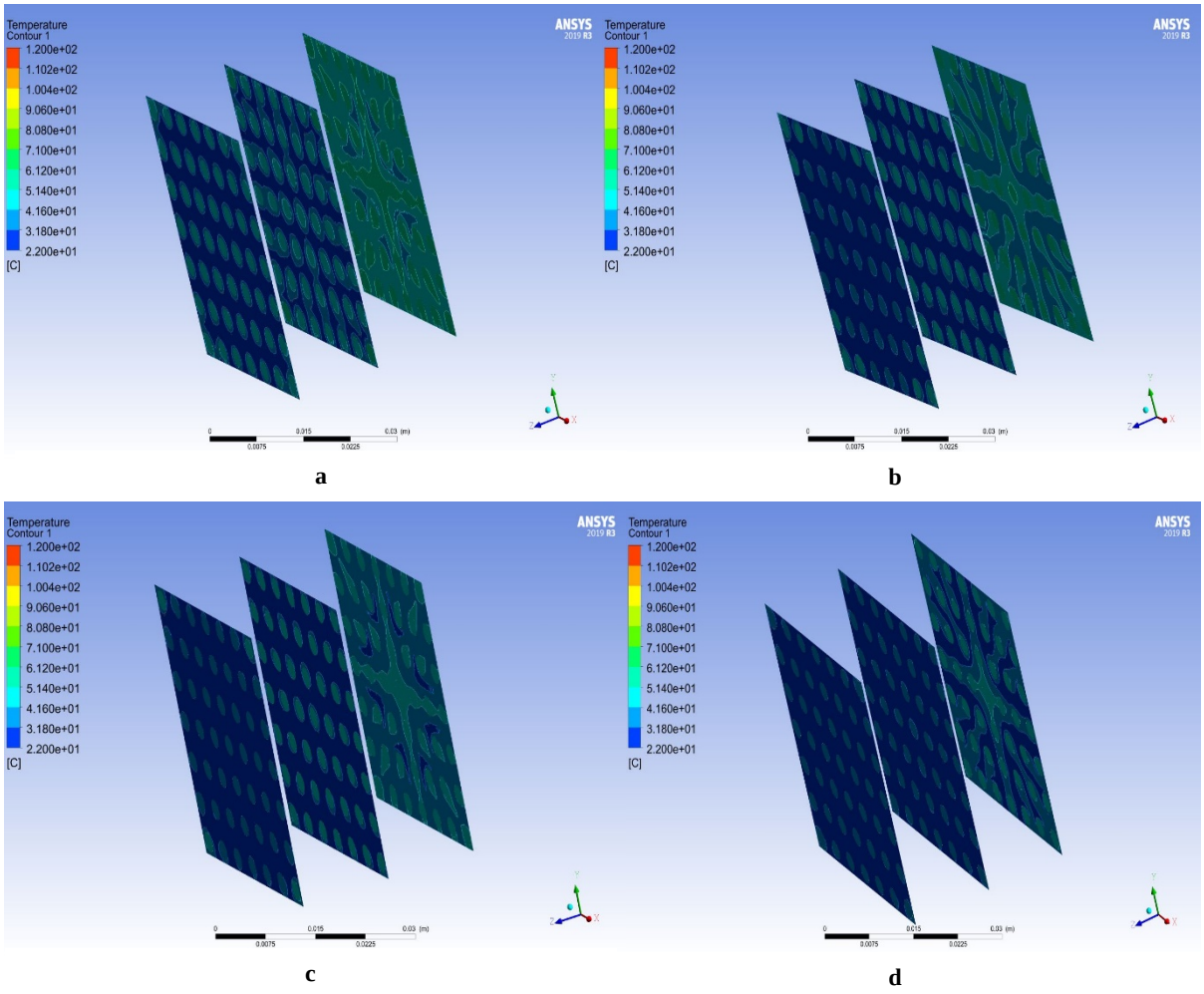

Figure 8. Temperature contours of cross-sections of air domain at Reynolds **a)** 5000, **b)** 7500, **c)** 10000, **d)** 15000

The temperature difference is the difference between the hot and cold sides of the thermoelectric module. Thermal resistance is defined as the ratio of the temperature difference between the two faces of a material to the rate of heat flow per unit area. Heat ratio is the amount of power required to keep the base of the thermoelectric module at a constant temperature of 120 degrees. The graphs of Nusselt number, temperature difference, total thermal resistance, heat ratio based on Reynolds number are shown in Figure 9. The graphs show that heat ratio, Nusselt number, and temperature difference increase with Reynolds number while total thermal resistance decreases with Reynolds number.

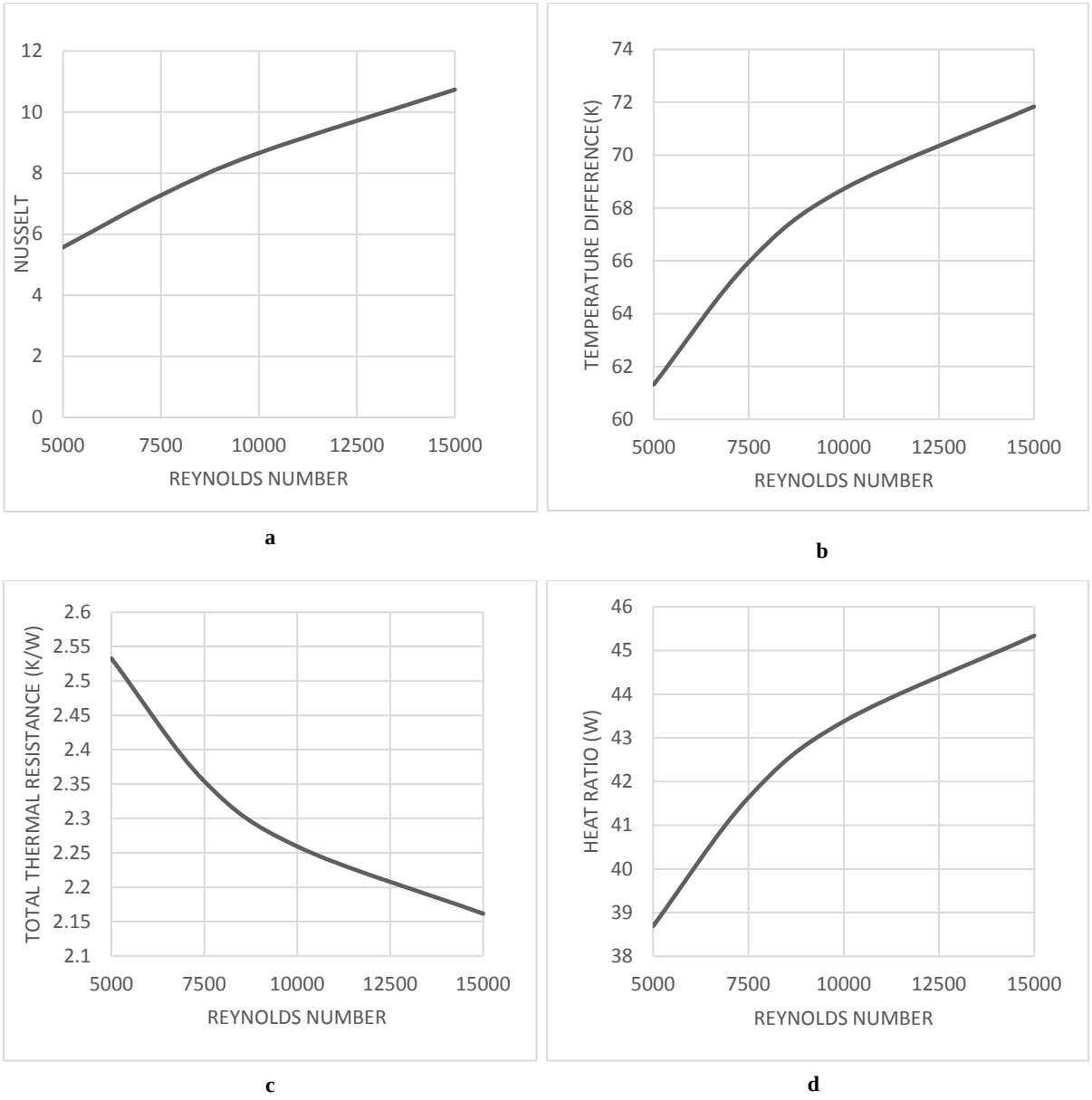

a **b** **c** **d**

Figure 9. a) Nusselt number, **b)** Temperature difference **c)** Total thermal resistance **d)** Heat ratio in relation to Reynolds Number

4. CONCLUSIONS

In this study, the performance of a thermoelectric module with heat sink having the cylindrical pin fins at different air velocities was investigated numerically. Calculations were made in three-dimensional conditions. To model the turbulent flow, the standard k-Ɛ model was used. Under these conditions, calculations have been made for different Reynolds numbers. Results have been evaluated as temperature and stream function contours, temperature differences in the thermoelectric module, total thermal resistance, and Nusselt numbers. The effect of increasing air velocity on the temperature difference in the thermoelectric generator and the air velocity needed to obtain more electricity were determined. According to the results, the lowest temperature difference is 61.31

Kelvin at Reynolds 5000, and the highest temperature difference is 71.83 Kelvin at Reynolds 15000. As can be seen from the results, as the Reynolds number increases, the heat transfer to the air increases too, and as a result, the temperature difference between the cold and hot surfaces of termoelectric module increases. In future studies, analysis of the thermoelectric module with different design heat sink can be made, and the results can be compared to this study to find which one performs better. In addition, the effect of the pin fins number on the heat sink performance can be investigated.

REFERENCES

[1] S. Gururatana, “Heat Transfer Augmentation for Electronic Cooling,” Am. J. Appl. Sci., vol. 9, no. 3, pp. 436–439, 2012.

[2] V. Kumar and D. V. N. Bartaria, “CFD Analysis of an Elliptical Pin Fin Heat Sink Using Ansys Fluent v12.1,” Int. J. Mod. Eng. Res., vol. 3, no. 2, pp. 1115–1122, 2013.

[3] M. Beriache et al., “Computation of Thermal and Hydraulic Performances of Minichannel Heat Sink with an Impinging Air Jet for Computer Cooling,” Acta Polytechnica Hungarica, vol. 9, 139-153, 2012.

[4] D. V. Kumar, “Effect Of Velocity Ratio Of Impinging Turbulent Jets On Heat Transfer Characterstics Of Heat Sink,” vol. 9, no. 8, pp. 1093–1101, 2018.

[5] A. A. Mohammed and S. A. Razuqi, “Forced Convection Heat Transfer Of Axial Air Flow With Heat sink On Uniform Heat Flux,” Heat Eng. Sustain. Dev., vol. 22, no. 2, pp. 10–21, 2018.

[6] R. Mendonca, S. Yalamarty, and C. Kini, "Numerical Analysis of Heat Sinks for Led Lighting Modules," International Journal of Research in Engineering and Technology, vol. 4, 2015.

[7] V. V Dhole, V. S. Shinde, and S. S. Kore, “Thermal and hydraulic performance analysis of cylindrical pin fin heat sink with conical perforations,” vol. 5, no. 5, pp. 436–440, 2016.

[8] D. T. W. Lin, H.-Y. Li, and Y.-C. Hu, “Study on the heat transfer of the plate-fin heat sink under impinging jet cooling,” Prog. Comput. Fluid Dyn., vol. 11, no. Nos. 3/4, pp. 237–245, 2011.

[9] P. A. Deshmukh and R. M. Warkhedkar, “Thermal performance of elliptical pin fin heat sink under combined natural and forced convection,” Exp. Therm. Fluid Sci., vol. 50, pp. 61–68, 2013.

[10] R. R. Md. Abdul Raheem Junaidi, S. I. Sadaq, and M. M. Ansari, “Thermal Analysis of Splayed Pin Fin Heat Sink,” Int. J. Mod. Commun. Technol. Res., vol. 2, no. April 2014, pp. 48–53, 2014.

[11] A. A. Belarbi, M. Beriache, and A. Bettahar, “Experimental study of aero-thermal heat sink performances subjected to impinging air flow,” Int. J. Heat Technol., vol. Vol. 36, N, no. December, pp. 1310–1317, 2018.

[12] A. Al Mamun, “Optimization of Effectiveness for a Cylindrical,” Glob. J. Res. Eng., vol. 16, no. 3, 2016.

[13] K. S. Yang, W.-H. Chu, I. Chen, and C.-C. Wang, "A comparative study of the airside performance of heat sinks having pin fin configurations," International Journal of Heat and Mass Transfer, vol. 50, pp. 4661-4667, 2007.

[14] D.-K. Kim, S. J. Kim, and J.-K. Bae, "Comparison of thermal performances of plate-fin and pin-fin heat sinks subject to an impinging flow," International Journal of Heat and Mass Transfer, vol. 52, no. 15, pp. 3510-3517, 2009.

[15] O. N. Şara, "Performance analysis of rectangular ducts with staggered square pin fins," Energy Conversion and Management, vol. 44, no. 11, pp. 1787-1803, 2003.

[16] Fluent 6.3 version. Fluent User's Guide. Fluent Incorporated. 2006.

[17] N. Totala et al., "Study and Fabrication of Thermoelectric Air Cooling and Heating System," vol. 4, pp. 2278-7461, 2014.

[18] "Electrical for us", access: 15 January 2020, http://www.sanjaysah.com.np/2016/11/seebeck-effect-and-seebeck-coefficient.html

NUMERICAL ANALYSIS OF AERODYNAMIC AND AEROACOUSTICS CHARACTERISTICS OF SUBSONIC RECTANGULAR CAVITY WITH DIFFERENT ASPECT RATIOS

Eyup Kocak, Ece Ayli, Hasmet Türkoglu*
*Cankaya University, Department of Mechanical Engineering, Ankara/Turkey
Email: eyupkocak@cankaya.edu.tr,eayli@cankaya.edu.tr, hasmet@cankaya.edu.tr

ABSTRACT

In the aerospace industry, interior storage carriages that carry items such as weapons and bombs form cavities. When the free stream flow reaches the cavity leading edge, a shear layer forms above the cavity zone. This shear layer formation changes the mean surface pressure distribution and induces pressure fluctuations in the cavity zone. Self-sustained pressure oscillations cause unsteady and complex flow fields inside the cavity. The aerodynamic noise and flow field together in cavities lead to self-sustaining oscillations. This complex flow field which comprises pressure oscillations can damage the structure of air vehicles and causes high sound pressure levels (SPL). Based on the dynamic loads and SPL levels, structural fatigue of the cavity and its characteristics can be observed. Adverse and steep pressure gradients, which prevent the safe release of stores. In this study, the flow topology of the subsonic cavity is investigated numerically. A verification study is performed comparing the numerical results obtained with experimental results from the literature. After reaching satisfactory results, the flow fields and aeroacoustics characteristics of the cavity are investigated for Mach number 0.19 and Reynolds number 1.2×10^6. The cavity aspect ratio (L/D) is varied between 2 and 10. The shear layer formation, Rossiter modes, acoustic modes, and SPL levels are obtained and compared for different L/D ratios. Obtained results show that in the closed cavities, a separation point occurs at the leading edge of the cavity, impingement point, and second separation point are at the bottom of the cavity with a stagnation point at the trailing edge of the cavity. In the open cavities, the shear layer separates at the leading edge and reattaches at the trailing edge without breaking up in the cavity.

Keywords: Cavity, Subsonic Flow, Acoustic Level, Rossiter mode, SPL

1. INTRODUCTION

Cavity flow is studied according to its numerous applications in store carriage and release. Over cavities, complex flowfields form. These complex unsteady flowfields include both the small-scale pressure fluctuations typical of turbulent shear flows and a significant resonance. The frequency and amplitude of these fluctuations depend on the cavity geometry and external flow conditions. The intense pressure fluctuations and resonant acoustic modes that are generated by the flow past an open cavity can damage the structure of the aircraft and stores and impede successful store release. Internal carriage of stores, which can be modeled by using a cavity configuration, is used for supersonic aircraft in order to reduce radar cross-section, aerodynamic drag, and aerodynamic heating. Storing weapons in internal bays of fighter aircraft offers many more benefits, including an expanded flight envelope, greater maneuverability, and higher penetration speed resulting in less time over target, which increases the survivability of the aircraft. Therefore, cavities that have complex flowfields have an indispensable application area in aerospace. In the literature, there are several studies that investigate the flow field in the cavity.

Shieh and Morris [1] numerically analyzed the two-dimensional and three-dimensional cavity flows by using the Spalart-Allmaras (S-A) model with the Unsteady Reynolds average Navier-Stokes (URANS) method. In the study, the cavity length to depth ratio is 4.4, and the width to depth ratio is 1. Mach number is 0.6 and the Reynolds number is 200.000; all parameters were kept the same with the experimental study conducted by Plentovich [2] in order to verify their numerical results. The vorticity contours were drawn for one period of

time, and it was observed that there is a vortex formation below the shear layer. Vortex gets larger through the cavity length and in the middle of the cavity, the magnitude of the vortex gets larger than the cavity length. When the vortex hits the trailing edge wall, the incoming flow pushes the vortex structure, and it is ejaculated from the cavity.

Shih et al. [3] used the k-ε turbulence model to analyze an open cavity flow for L/D=5.07 with 1.5 Mach number. They verify their numerical results with the experimental study of Kaufman et al.[4]. The flow on a two-dimensional flat plate was numerically resolved and used as an inlet boundary condition of, cavity. According to the results of the study, the flow becomes complex because of the shear layer. Mass entrance and exit occur due to the shear layer formation. Mass entrance causes pressure fluctuations inside the cavity zone, which causes aeroacoustics and aerodynamic problems.

Ashcroft and Zhang [5] modeled the subsonic cavity flow by using the k-ω turbulence model to solve compressible Navier-Stokes equations. Ashcraft and Zhang compared their numerical studies to the experimental work of Ahuja and Mendoza [6]. In the study, the L/D ratio is varied between 1.5 and 3.75. Mach number varies from 0.26 to 0.53. Rossiter modes have been in agreement with experimental values. SPL values were calculated as 5 dB more when it is compared with the experimental study. The average pressure coefficient graph was plotted depending on the location and a pressure drop has occurred in the cavity inlet and a significant increase was observed in the cavity outlet.

Peng [7] compared RANS and DES models for cavity flow at 0.85 Mach number. In the study, the L / D ratio is 5. To obtain steady-state results and minimize the numerical error analysis are performed for a 3000-time step. After reaching to steady-state operating condition for RANS method 2300 and for DES method 2800 more time step is used. According to the results of the analysis, the first mode could not be captured with either method, and the second and third modes were approximately the same in both methods. The fourth mode is better predicted with DES. With both methods, SPL values were almost 5 dB higher than experimental SPL values. A higher mean pressure coefficient was calculated with the DES method. According to the results of the study, DES gives better results in better mesh structures.

Basu et al. [8] used the DES and RANS methods to analyze the three-dimensional subsonic cavity problem. In both methods, the k-ε turbulence model is used. The Mach number is 0.128. According to the results compared with the experimental study of Driver et al. [9], the flow topology is obtained similarly to both methods. Bres and Colonius [10] used the DNS method to analyze a three-dimensional open cavity flow to investigate the mechanism that triggered cavity oscillations. The obtained results are coherent with the Rossiter mechanism.

Unalmis et al. [11] measured the oscillating pressure values for the cavity flow with Mach number =5 and L / D ratios varying from 3 to 7. According to the experimental results, the magnitude of the cavity front wall oscillations is smaller than the back wall. As the acoustic waves that travel between the back wall and the front wall are compatible with the pressure oscillation period, the oscillations are periodic in each wall.

Williams et al. [12,13] studied flow physics in the supersonic wind tunnel and also mechanisms to control cavity acoustics. They observed that the sound pressure level values changed depending on the wind tunnel pressure values. In addition, it was argued that flow characteristics change depending on the Mach number.

Chung [14] and Heller et al. [15] argued that pressure fluctuations reach to its maximum value in the trailing wall, the interaction between the shear layer and the aft wall is the major reason for the acoustic flow field.

Faure et al. [16] conducted experimental studies for different L / D ratios and Reynolds numbers. In their study, they have shown the dynamics of cavity flow. In the cavity region, there are 3 vortex formations whose sizes vary depending on the geometric properties. These structures are the main vortex, the corner vortex and the secondary vortex which is formed near the front wall.

In this study, the nature of the cavity flow is investigated with numerical methods. Numerical results are verified with the experimental study from the literature [17]. Ansys Fluent [18] software is used to calculate the compressible Navier-Stokes equations for two-dimensional and turbulent flows. The effects of cavity

geometrical parameters on the aerodynamic and aeroacoustics fields are investigated. SPL distribution, pressure fluctuations, velocity, pressure and energy contours are obtained and these outputs are analyzed in order to understand the physics of the flow.

2. METHODOLOGY

Sound is formed according to the pressure fluctuation and the sound sources are generated by motion, either by the free fluid motion or by a solidbody–fluid interaction. According to study carried out by Cosgun [21], aeroacoustics problems are divided into two parts: Fluid flow and acoustic problems. In the literature, there are several different noise prediction approaches are found as given in Fig. 1. Firstly, the time-dependent behavior of the pressure signals for the selected monitoring points is computed and secondly, using the selected aeroacoustics approach, sound pressure levels are obtained, which is a function of pressure. In 1952, Lighthill introduce the acoustic analogy for the jet noise problem. Then, Curle, Powell and Ffowcs Williams extended Lighthill's ideas and included the solid boundaries effects on the aeroacoustics regime.

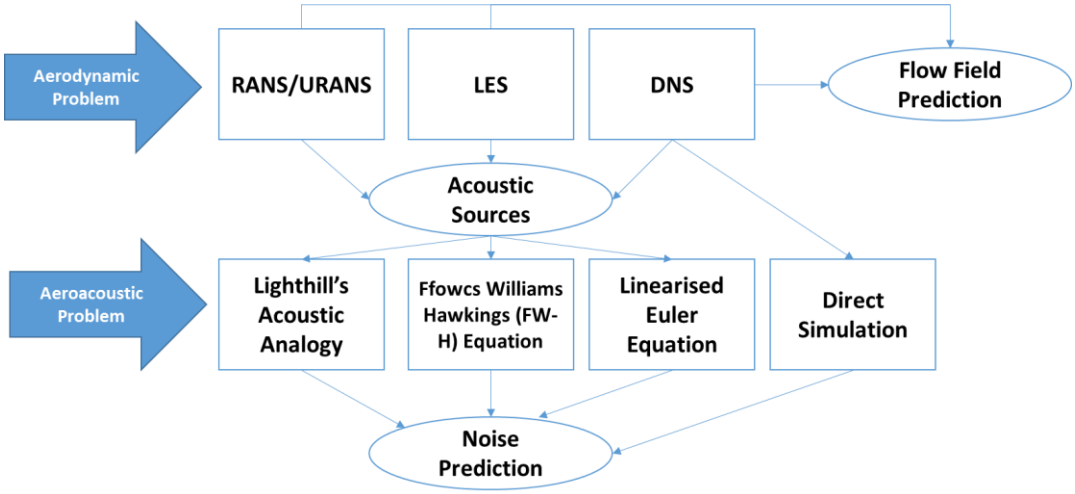

Figure 1. Aerodynamic & Aeroacoustics behavior prediction approaches [adopted from 22]

2.1. Aerodynamic Methodology

Although the cavity geometry seems to be fairly simple, the cavity flow is a highly chaotic flow with vortex formations, unstable shear layer movements and flow interactions and is a good example of turbulent flow. To solve the two-dimensional, compressible and turbulent cavity flow ANSYS Fluent software is used. To solve the compressible flow field; the conservation of mass, momentum, and energy equations given in equations (1)-(3) are solved.

$$\frac{\partial \rho}{\partial t} + \frac{\partial}{\partial x_i}(\rho u_i) = 0 \tag{1}$$

$$\frac{\partial}{\partial t}(\rho u_i) + \frac{\partial}{\partial x_j}(\rho u_i u_j) = -\frac{\partial p}{\partial x_i} + \frac{\partial t_{ji}}{\partial x_j} \tag{2}$$

$$\frac{\partial}{\partial t}\left[\rho(e + \frac{1}{2}u_i u_i)\right] + \frac{\partial}{\partial x_j}\left[\rho u_j (h + \frac{1}{2}u_i u_i)\right] = -\frac{\partial}{\partial x_i}(u_i t_{ij}) + \frac{\partial q_j}{\partial x_j} \tag{3}$$

In these equations, e is internal energy, h = e + p / ρ is the specific enthalpy value. For compressible flows t_{ij} is the stress tensor that comprises the secondary vortices term,ζ, and molecular viscosity,υ. This term is defined as follows:

$$t_{ij} = 2\mu s_{ij} + \zeta \frac{\partial u_k}{\partial x_k} \delta_{ij} \tag{4}$$

LES equations are derived from the Navier-Stokes equations given in equation (1)-(3) by a filtering procedure. In the filtering process, the small scale structures with high frequency are filtered out while large-scale motions are modeled. The flow variables are decomposed into a resolved (filtered) and unresolved (subgrid-scale or fluctuating) part as,

$$\theta_i = \overline{\theta}_i + \theta_i' \tag{5}$$

In equation (5), θ is any flow property like pressure, density, velocity, $\overline{\theta}_i$ is the filtered velocity, θ_i' is the subscale part. Consequently, by applying this filtering procedure to the Navier-Stokes equations, the LES equations can be written as [20]:

$$\frac{\partial \bar{u}_i}{\partial x_i} = 0 \tag{6}$$

$$\frac{\partial \bar{u}_i}{\partial t} + \frac{\partial}{\partial x_j}(\bar{u}_i \bar{u}_j) = -\frac{1}{\rho}\frac{\partial \bar{p}}{\partial x_j} + \frac{\partial}{\partial x_j}\left(\frac{\mu}{\rho}\sigma_{ij}\right) - \frac{\partial \tau_{ij}}{\partial x_j} \tag{7}$$

In Eq (8), τ_{ij} denotes the subgrid-scale stress and is defined by Eq. (8).

$$\tau_{ij} = \overline{\rho u_i u_j} - \bar{\rho}\bar{u}_i\bar{u}_j \tag{8}$$

This term comprises the effect of small-scale fluctuations with higher frequency values on the large-scale motions and it is modeled in order to close LES equations [20]. As an eddy viscosity model Smagorinsky model is used, which relates the filter size and resolves strain rate. The second-order implicit time-dependent solution is performed using least-square cell-based gradient evaluation.

2.2. Aeroacoustics Methodology

In this study, Ffowcs-William Hawkings Analogy is used as a noise prediction method. Curle [22] developed this analogy by taking into account the effect of immobile solid objects in the flow field and expanded the Lighthill equation. Ffowcs William–Hawkings equations are given as follow:

$$\left(\frac{\partial^2}{\partial t^2} - c_0^2 \frac{\partial^2}{\partial x_i \partial x_i}\right)\left(H(f)\rho'\right) = \frac{\partial^2}{\partial x_i \partial x_i}\left(T_{ij}H(f)\right) - \frac{\partial}{\partial x_i}\left(F_i\delta(f)\right) + \frac{\partial}{\partial t}\left(Q\delta(f)\right) \tag{9}$$

Where t, T_{ij}, Q and f represents time, Lighthill's stress tensor, and source terms, respectively. Function F denotes the domain outside the source surface. To reduce the sound, the source efficiency of the noise, the kinetic energy that is converted to the noise should be minimized and active sound waves with out-of-phase waves should be eliminated.

2.2. Computational Domain

In this study, three-dimensional cavity flow in low-speed is analyzed using numerical methods to investigate the aeroacoustics behavior of the flow. For this purpose, Navier-Stokes equations are discretized using the finite volume approach.

To solve the flow field and the sound pressure level, ANSYS FLUENT software is utilized. To model the turbulence, LES approach is utilized. Before the validation study, the mesh independency test is performed. To validate the numerical results, experimental results of study by Megennathans' [17] are used. Computational domain and boundary conditions are shown in Figure 2(a). The domain has meshed with the ANSYS Meshing software using quadrilateral elements. As an inlet boundary condition, velocity inlet is used. Mach number is set to 0.4. Pressure outlet is used as an outlet condition while all other boundaries are considered as the wall.

Boundaries are placed far enough from the cavity to avoid reflection. The cavity is placed 11 inches aft of the leading edge of the flat plate. The cavity length to depth ratio is varied between 4.5<L/D<18. For the verification study, the cavity length and depth are taken as 11 inches long and 1 inch deep. The tests are conducted for 214 ft/sec which corresponds to Reynolds number of 1200000. All of the parameters were kept the same with the experiment in the verification case.

3. RESULTS AND DISCUSSION

3.1. Verification Study

First, a mesh independency study is performed for the base case which is the same as the experimental case [17]. For this purpose, 5 different meshes are prepared. The regions that are near the leading edge, trailing edge and shear layer zone are highly clustered in order to resolve all the flow phenomena in the critical regions. The wall y+ value is less than 3.5 which is sufficient for the wall function to resolve the viscous sub-layer. The computational grid is shown in Figure 2(b).

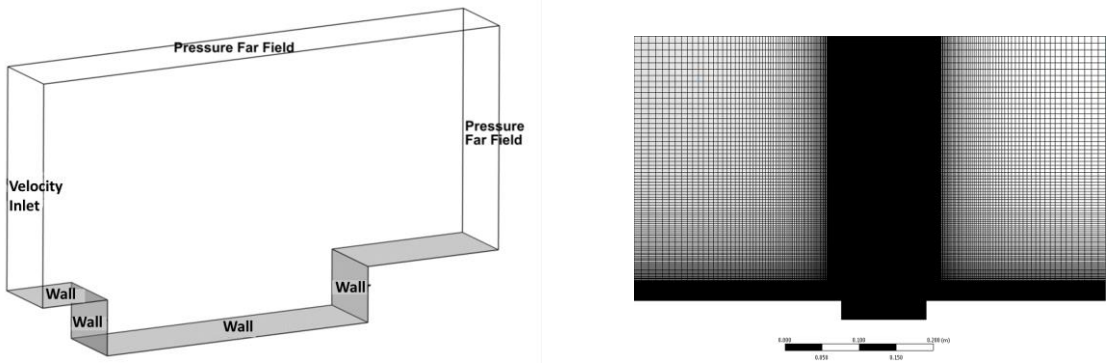

Figure 2. (a) Boundary conditions and computational domain (b) Grid domain

In Figure 3, for the first mode, sound pressure levels (SPL) obtained with different meshes are given. As seen in this figure, the results do not change after one million elements. The relative error is 0.02%. Therefore in order to reduce the computational cost and time, the mesh system with two million elements is used. For other cavity geometries, the mesh structure is conserved, and the number of mesh elements is proportionally increased.

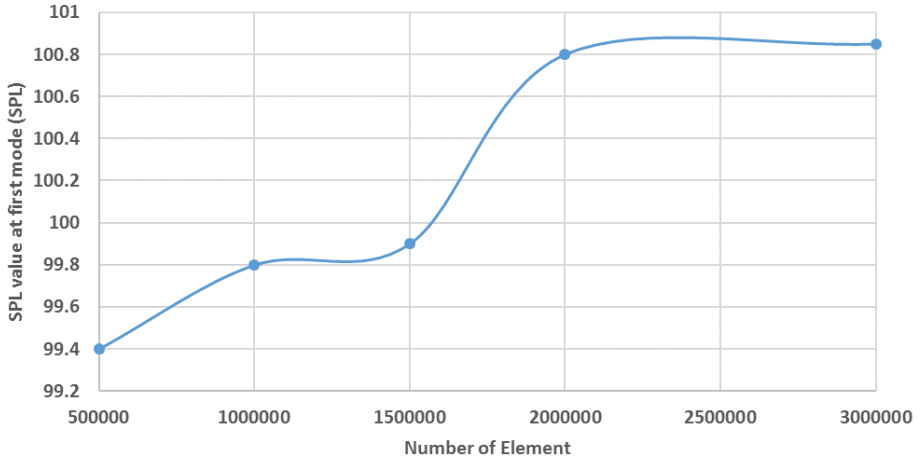

Figure 3. Mesh Independency test

In Figure 4, predicted SPL values with LES are compared with the experimental data obtained published by Meganathan [17]. According to the comparison, it is clear that SPL is sufficiently predicted and the resonance frequencies are results from the computed spectrum. The frequency of the first mode is at a higher value than the experimental one.

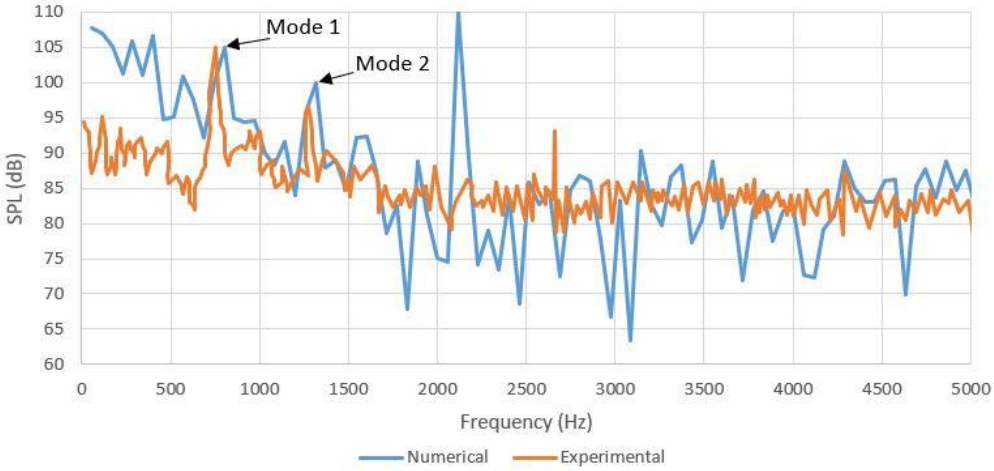

Figure 4. Numerical and experimental SPL distributions for L/D=4.5

3.2. Aerodynamic Results

Figure 5, illustrates the periodic behavior of the flow inside the cavity zone. According to the results, maximum pressure amplitude is observed in the trailing edge, while the minimum is attained in the bottom wall. The possible reason for the maximum amplitude that is seen in the trailing edge is the interaction of the shear layer and the trailing edge wall. The periodic oscillation is identified for all of the walls.

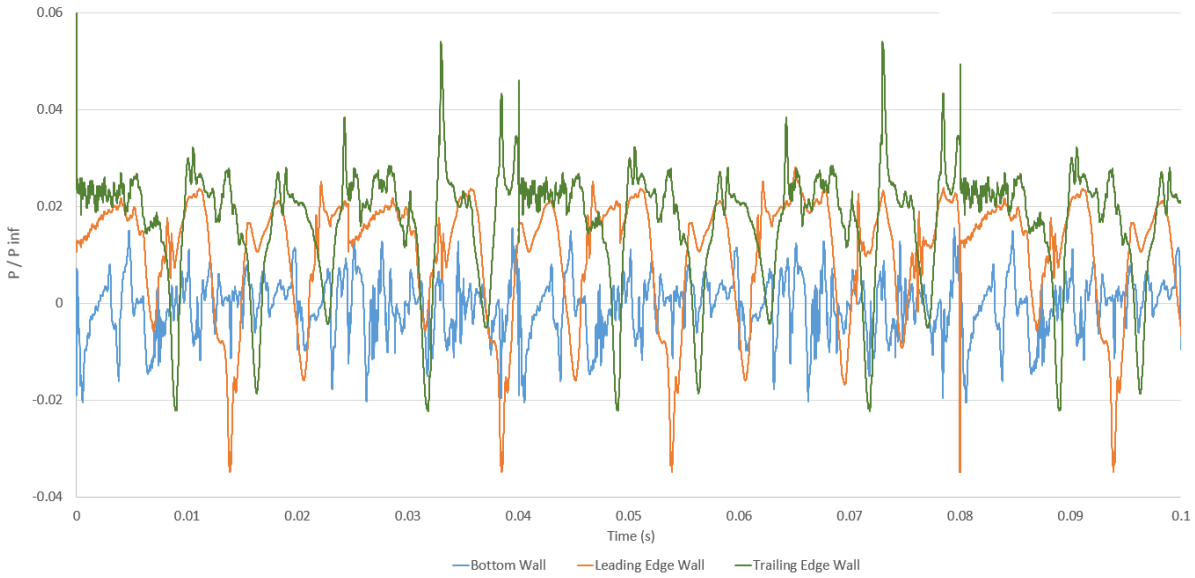

Figure 5. Pressure fluctuations for different cavity walls (L/D=4.5)

In Figure 6, for the cavity with aspect ratio, L/D=6 streamlines are shown for different instants. As it is seen in the figure, transient characteristics of the flow change with time. The shear layer is formed in the leading edge of the cavity and interacts with the trailing edge of the cavity. Due to the shear layer coupling with the pressure field in the cavity, fluid-resonant type flow is occurred. At t=0.0169 sec, the flow topology is very similar to the one that is observed at t=0.0119 s, which is also proof of the periodic flow behavior. The self-sustaining flow structure occurs in the cavity because of the shedding of the vortices inside the cavity zone.

At time t=0.0119 s, at the leading edge of the cavity, a vortex structure is formed. This vortex structure grows up through the cavity length. When it hits to the trailing edge, the upcoming vortex forces it to ejaculate. In this way, flow ejection is formed close to the downstream corner. This mass ejection begins in the last phase of the cycle (t=0.0159 s). Also, the new vortex formation starts simultaneously. So, there is a periodic flow in the cavity zone which causes instabilities in the shear layer, and multiple modes in the flow.

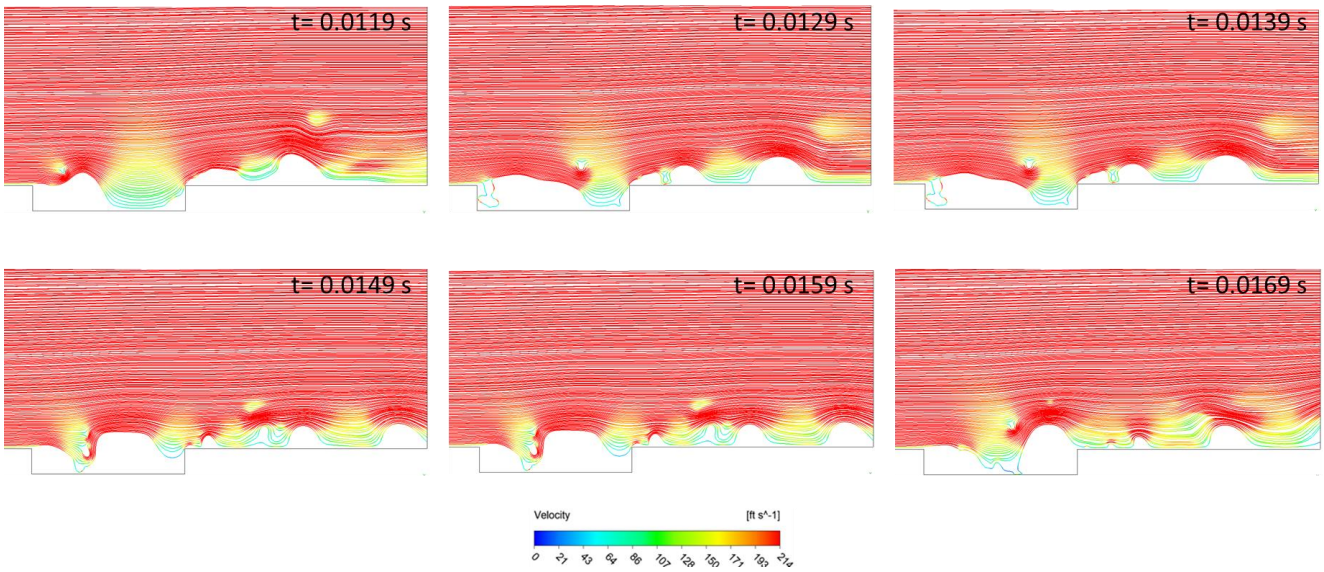

Figure 6. Unsteady flow fields at different times (L/D=4.5)

In the subsonic flow regime, when L/D<10 which is known as a closed cavity, the shear layer is formed at the leading edge of the cavity and reattach at the trailing edge. Two vertical structures are identified in the shear layer. During one period, the first vortex is just shed to the leading edge, travels through the downstream, grows with convection, and impinges to the trailing edge. The second, up-coming structure forces the first structure to ejection. This is the main mechanism in the closed cavity, as is seen in Figure 6. Also, in Figure 7, the structures that are formed in the cavity region are shown for L/D=4.5 configuration.

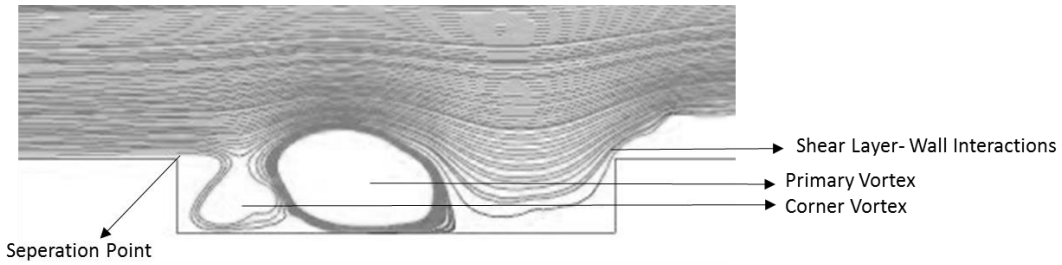

Figure 7. Flow characteristics for open cavity flow (L/D=4.5)

In Figure 8, the unsteady flow field for the open cavity is shown. According to the results, one dominant vortex structure controls the flow, which is very large compared to the corner vortex. The shear layer behavior changes with varying the cavity aspect ratio. In the closed cavity configurations, the shear layer separates at the leading edge corner, impinges to the bottom wall, and reattaches at the aft wall. On the other hand, in the open cavity shear layer does not hit the bottom wall and hits the trailing wall without any separation, which makes flow less complex when it is compared with the closed cavity flow. Shear layer instabilities decrease, and vortex mobilizations were not observed.

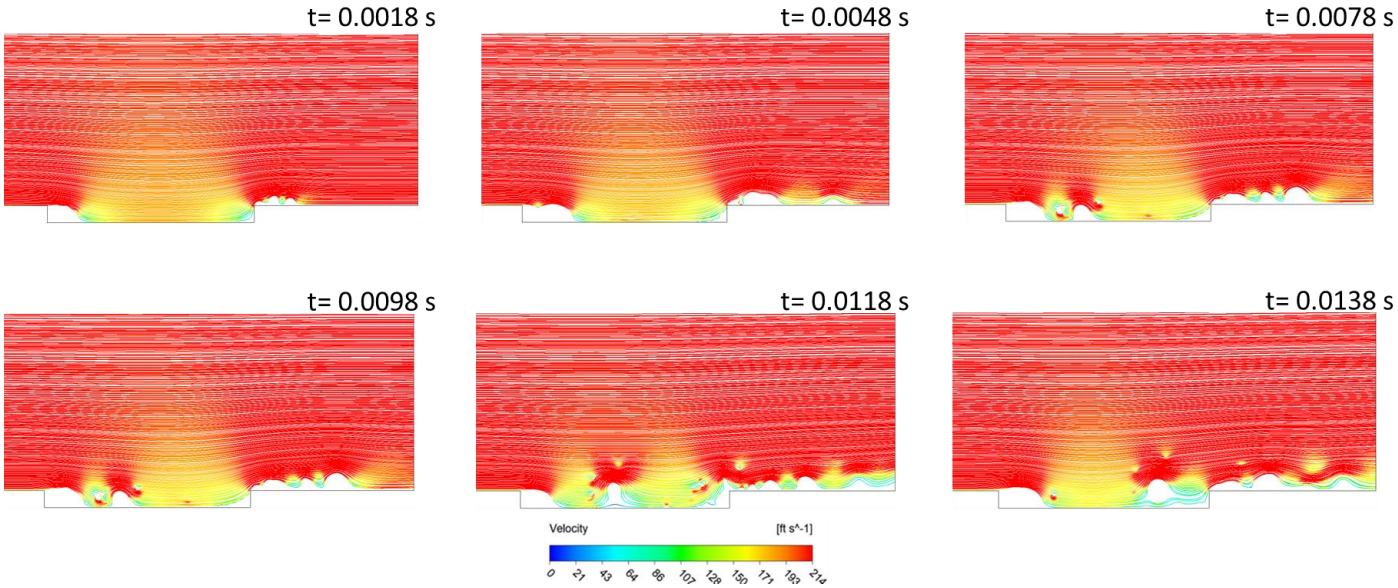

Figure 8. Unsteady flow fields at different times (L/D=12)

3.2. Aeroacoustics Results

In Figures 9 and 10, SPL distributions are presented which are obtained from the cavity rear wall. For each configuration, various modes are obtained. According to the obtained SPL distributions, energy content and spectral peak values are changing with the change of the aspect ratio. In the closed cavity configurations, the most energetic peak, which is the first peak, is obtained at lower frequency values with decreasing the L/D ratio.

Also, SPL value increases with the rising L/D ratio. As L/D increased, the mean re-circulation zone was stronger and was located at the rear of the cavity, and this is the main reason for the SPL rise. In the open cavity configurations, although the sound pressure level and frequency values change, the trend of the behavior is almost the same.

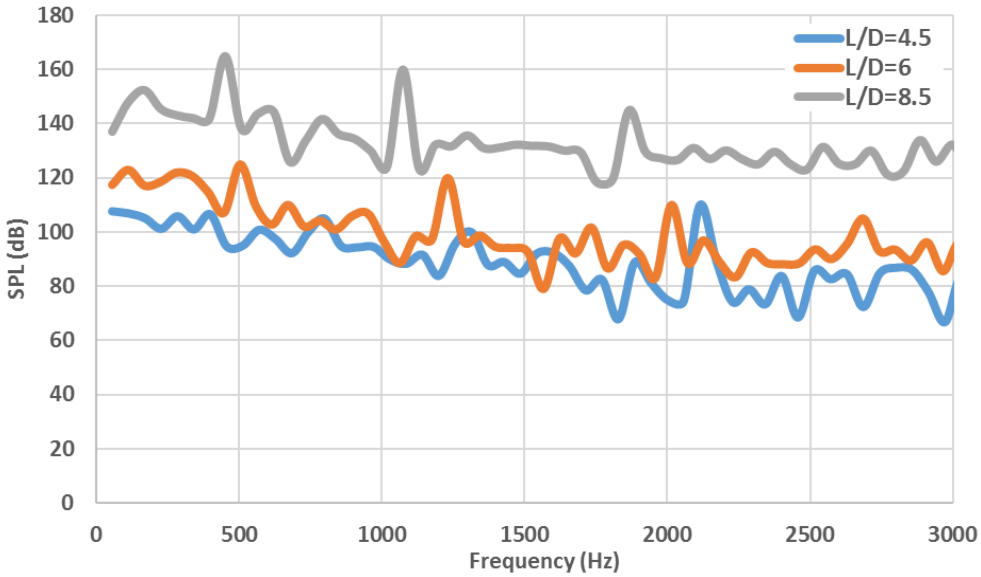

Figure 9. SPL spectra for open cavity configurations for different aspect ratios.

For the closed cavity configurations (L/D=12, 18) SPL distribution is shown in Figure 10. It is clear that the intensity of the low frequency becomes stronger while the dominant frequency value gets weaker. The lower amplitude of the dominant frequency demonstrates that the interactions in the cavity region are weaker, and the flow is less complex when it is compared with the open cavity flow phenomena.

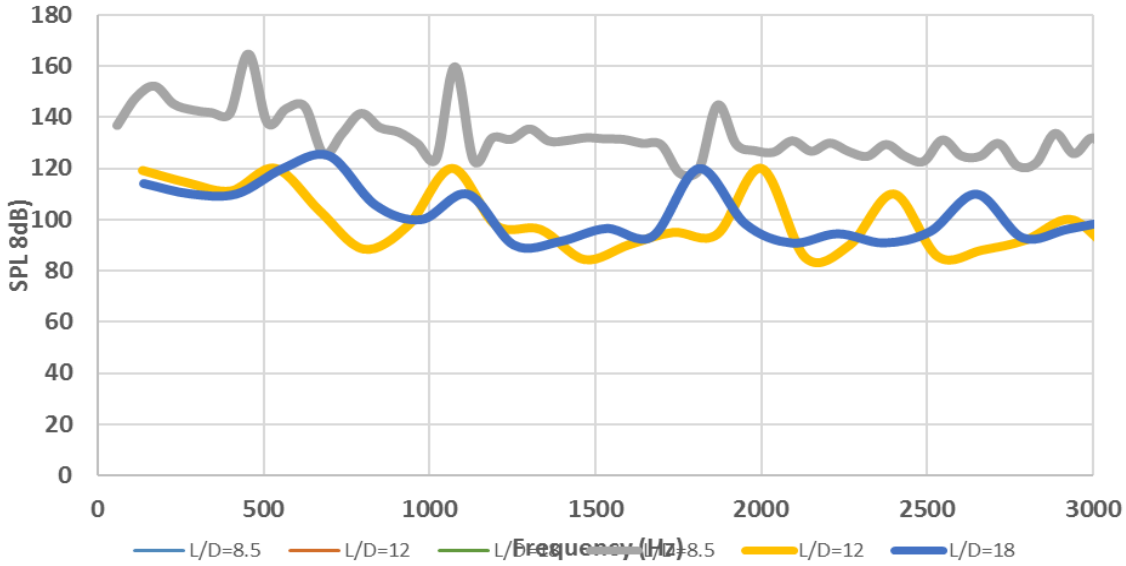

Figure 10. SPL spectra for closed cavity configurations

4. CONCLUSIONS

In this study, a numerical analysis is performed for the open and closed cavity flows with different aspect ratios solving the unsteady compressible RANS equations and Computational Aeroacoustics Equations (CAA). According to the results, cavity flow comprises (i) vortex generations in the cavity region (ii) instability of shear layer (iii) fluid-acoustic resonance. The results show that, for all of the aspect ratios, maximum pressure values are obtained in the trailing edge. The possible reason for this situation is thought of as mass ejection. In the open cavity configurations, periodic flow behavior is observed in the flow field, which comprises two vortex structures. In the closed cavities, a separation point occurs at the leading edge of the cavity, impingement point and second separation point are at the bottom of the cavity with a stagnation point at the trailing edge of the cavity. In the open cavities, the shear layer separates at the leading edge and reattaches at the trailing edge without breaking up in the cavity.

With increasing the L/D ratio, the dominant frequency value decreases in the open cavity flows. On the other hand, for closed cavity configurations, only one vortex structure is observed in the flow field, which causes a reduction in the dominant frequency value. Sound pressure levels indicate that the energy within the cavity is larger in the closed cavities when it is compared with the open cavities.

REFERENCES

[1] Shieh, M.C., Morris, P., Comparison of Two and Three Dimensional Turbulent Cavity Flows, *39th AIAA Aerospace Sciences Meeting and Exhibit*,0511, Reno,NV, Haziran 2001.

[2] Plentovich, E.B., Three Dimensional Cavity Flow Fields at Subsonic and Transonic Speeds, *NASA Technical Memorandum* 4209, Hampton, USA, 1990.

[3] Shih, S.H., Hamed, A., Yeuan, J.J., Unsteady Supersonic Cavity Flow Simulations Using Coupled k-epsilon and Navier-Stokes Equations, *AIAA Journal*, 1994, **32**(10), 2015-2021, 1994.

[4] Kaufman, L.G., Maciulaitis A., Clark, R.L., Mach 0.6 To 3.0 Flows Over Rectangular Cavities, *Air Force Wright Aeronautical Labs.*, AFWAL-TR-82-3112, New York, U.S.A., Kasım 1993.

[5] Ashcroft, G. and Zhang, X., A Computational Investigation of the Noise Radiated by Flow Induced Cavity Oscillations, *39th AIAA Aerospace Sciences Meeting and Exhibit*,0511, Reno,NV, Haziran 2001.

[6] Ahuja, K.K., Mendoza, J., Effects of Cavity Dimensions, Boundary Layer and Temperature on Cavity Noise with Emphasis on Benchmark Data to Validate Computational Aero acoustics Codes, *NASA Contractor Rep*. 4653, U.S.A., 1995.

[7] Peng S.H., Simulation of Turbulent Flow Past a Rectangular Open Cavity Using DES and Unsteady RANS, *AIAA*, 2827, 2006.

[8] Basu D., Hamed, A., Das, K., DES, Hybrid RANS/LES and PANS Models For Unsteady Separated Turbulent Flow Simulations, *Proceedings of FEDSM*, ASME, U.S.A., Haziran 2005.

[9] Driver, D.M., Seegmiller, H.M., Features of a Reattaching Turbulent Shear Layer in Divergent Channel Flow, *AIAA Journal*, **23**(2), 163-171, 1985.

[10] Bres, G.A., Colonius, T., Direct Numerical Simulations of Three Dimensional Cavity Flows, *Journal of Fluid Mechanics*: **599**, 309-339, Cambridge, UK, Mart 2008.

[11] Unalmis, O.H., Clemens, N.T., Dolling, D.S., "Experimental Study of Shear Layer/ Acoustics Coupling in Mach 5 Cavity Flow," *AIAA Journal*, **30**(2), 242-251, 2001.

[12] Williams, D.R., Cornelius, D., Rowley C.W., Closed-Loop Control of Linear Supersonic Cavity Tones, 37th *AIAA Fluid Dynamics Conference and Exhibit*, Miami, U.S.A.,2007.

[13] Williams, D.R., Cornelius, D., Rowley C.W., Supersonic Cavity Response to Open Loop Forcing, *Proceedings of the First Berlin Conference on Active Flow Control* ,Eylül 2006.

[14] Chung, K.M., Characteristics of Compressible Rectangular Cavity Flows, *Journal of Aircraft*, **37**(3), 463-468, 2000.

[15] Heller, H., Holmes, H., Covert, E.E., Flow Induced Pressure Oscillations in Shallow Cavities, *Journal of Sound and Vibration*, **18**(4), 545-545.1970.

[16] Faure, T.M., Adrianos, P., Lusseyran, F., Pastur, L., Visualizations of the Flow Inside an Open Cavity at Medium Range Reynolds Number, *Experiments in Fluids*, **42**:169-184, 2007.

[17] Meganathan, A.J., An Experimental Study of Low Speed Open Cavity Flows, *MSc Thesis*, Unıversity of Tennessee, Knoxville, 2000.

[18]Ansys 19 Manual

[19] Apaçoglu, B.,2010, Silindir Üzerindeki Laminer Ve Türbülansli Akişin Kontrolsüz Ve Kontrollü Had Analizleri, *Yüksek Lisans Tezi,* TOBB ETÜ,Fen Bilimleri Enstitüsü, Ankara, Türkiye.

[20] Cosgun, F., Düşük Mach Sayısında Kavite İçi Akışın Aeroakustik İncelenmesi, İstanbul teknik Üniversitesi, *Yüksek Lisans Tezi,* İstanbul, Türkiye, 2018.

[21] Coskun, S., Turbulent Flow and Acoustic Predictions Over Open Cavity Configurations Aa Transonic Speeds, *Yüksek Lisans Tezi*, Odtu, Ankara, Türkiye, 2019

[22] Mihaescu, M. ˇ Computational Aeroacoustics Based on Large Eddy Simulation and Acoustic Analogies. *PhD thesis*, Lund Institute of Technology, Sweden, April 2005.

A NUMERICAL STUDY ON PHASE CHANGE MATERIAL INTEGRATED BOREHOLE HEAT EXCHANGER

Nezir Yağız ÇAM*, Mehmet Akif EZAN, Levent BİLİR*****
*Dokuz Eylul University, Department of Mechanical Engineering, Izmir/Turkey
Email: neziryagiz.cam@ogr.deu.edu.tr
**Dokuz Eylul University, Department of Mechanical Engineering, Izmir/Turkey
Email: mehmet.ezan@deu.edu.tr
***Yasar University, Department of Energy Systems Engineering, Izmir/Turkey
Email: levent.bilir@yasar.edu.tr

ABSTRACT

Borehole heat exchangers are commonly used as ground source heat exchangers in ground source heat pump (GSHP) applications. Designing borehole heat exchangers is essential for GSHPs as the thermal performance of borehole heat exchangers affects the COP of GSHP systems. In this study, the thermal performance of a phase change material (PCM) integrated borehole heat exchanger was modeled under transient working conditions with a numerical code that is developed in MATLAB. The borehole exchanger is combined with a flat plate solar collector to examine the effects of real weather conditions on the heat transfer characteristics of the storage unit. A simplified lumped thermal resistance model was used for modeling the solar collector. The numerical model of PCM integrated borehole, on the other hand, was developed using the finite volume method (FVM) to discretize the governing equation. The strongly implicit solver (SIS) was used to solve the coefficient matrix. The lumped model for the flat plate collector and numerical models of the borehole and the PCM annulus were validated with available numerical and experimental studies from the literature. Short-term heat storage performance of the borehole heat exchanger with different backfill materials, i.e., PCM or soil, was investigated for selected days of each season of the year.

Keywords: Borehole, thermal energy storage, solar energy, numerical heat transfer.

List of Symbols

A	area (m^2)
C	specific heat (J/kg K)
D	diameter (m)
$\dot{E}$	rate of energy (W)
FR	collector heat removal factor (–)
F'	collector efficiency factor (–)
H	height (m)
h	convective heat transfer coefficient (W/m^2K)
I_{solar}	incident solar radiation (W/m^2)
k	thermal conductivity (W/mK)
$\dot{m}$	mass flow rate of the HTF (kg/s)
N	number (–)
Nu	Nusselt number (–)
$\dot{Q}_u$	useful heat (W)
Ra_L	Rayleigh number (–)
$R_{tot,t}$	thermal resistance of the collector (m^2K/W)
r	radial coordinate (m)
T	temperature (°C or K)
t	time (s)
U	overall heat transfer coefficient of the tank (W/m^2K)
u	velocity (m/s)

W width (m)
x cartesian coordinate (m)

Greek letters
α absorptivity of glass (–)
δ thickness (m)
η energy efficiency (–)
ρ density (kg/m^3)
σ Stefan-Boltzmann constant (W/m^2 K^4)
τ transmissivity of glass (–)
β collector tilt angle (°)

Subscripts
a air gap
amb ambient
b bottom
c glass cover
col collector
conv convective
in inlet
ins insulation
out outlet
plate absorber plate
rad radiation
t top
tube collector tube
w wind

Superscripts
BHE borehole heat exchanger
SHBHE shallow horizontal borehole heat exchanger

1.INTRODUCTION

Borehole heat exchangers (BHE) are commonly used with ground source heat pumps to transfer heat from the ground to the refrigerant. BHE consists of pipe, backfill material, and soil around the borehole. In recent years, BHE is also used as a thermal energy storage system due to the temperature distribution of the ground. Soil temperature becomes constant beyond a certain depth. However, experimental investigations are not easy for deep vertical BHEs because of their capital cost. Researchers mostly develop mathematical models to analyze the thermal performance of BHEs. One of the most comprehensive studies for BHE simulations was conducted with thermal resistance modeling by Eskilson [1]. In Eskilson's work, the thermal resistances among the components in BHE are defined as a delta circuit, and this model has provided an important opportunity to simulate BHE. Bauer et al. [2] examined the thermal performance of a BHE is using soil as a filling material in case of the heat transfer fluid has a constant inlet temperature. They concluded that the diameter of the thermal influence decreases as the depth increase. Rees and He [3] developed a numerical model with ANSYS software for the vertical borehole heat exchanger and validated the model experimentally. They varied the velocity of heat transfer fluid to investigate its influence on the thermal performance of the heat exchanger. Cui et al. [4] developed a model to simulate BHE under short-term working conditions by using the finite element method for a vertical-type heat exchanger. They validated the model against the results of Eskilson's model. In the literature, besides mathematical models related to BHE, some studies have been made for different purposes of BHE usage.

The BHE has become an essential part of underground thermal energy storage systems as well as being used as a component that provides heat exchange between the heat source and refrigerant in heat pump systems. Li et al. [5] investigated the effects of the filling material radius and also the filling material. They compared the thermal

effect radius of the concrete, and the usage of the shape stabilized PCM and the organic PCM. They concluded that the thermal energy is stored around the pipe wall when organic PCM was used as a backfill material. Bottarelli et al. [6] modeled a shallow horizontal type borehole heat exchanger. They made a comparison between other backfilling materials in a shallow horizontal borehole heat exchanger. As a result of the study, when the phase change material is integrated, the thermal energy influence radius is considerably reduced, which means that thermal energy is stored around the pipe wall of shallow horizontal BHE.

In this study, a numerical model was developed to analyze the shallow horizontal borehole heat exchanger (SHBHE). Also, a lumped model was developed to obtain the thermal behavior of the SHBHE with different backfill materials under variable weather conditions.

2.METHOD

2.1 Model Description

In this study, a numerical model is developed in MATLAB software to understand the thermal behavior of a PCM integrated with the SHBHE. A lumped flat-plate solar collector model is developed and integrated into the primary model to consider the variable weather conditions. The HTF temperature increases within the pipes of the flat plate solar collector, and then the HTF heats the backfill material while flows through the SHBHE unit. The schematic of the SHBHE unit is shown in Figure 1. The thermophysical properties of the working fluid and backfill materials, i.e., soil and PCM, are given in Table 1.

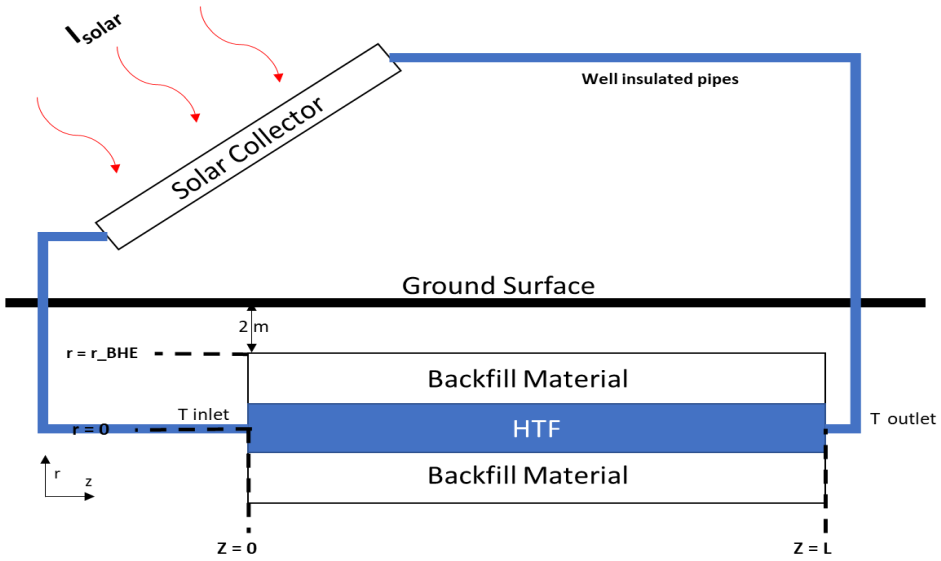

Figure 1. Schematic of SHBHE Unit

Table 1. The thermophysical properties of the HTF and backfill materials

		Density (kg/m^3)	Specific Heat (J/kg K)	Thermal Conductivity (W/m K)	Source
HTF	Liquid	1000	4180	0.58	[7]
Soil	Dry,Solid	2050	1840	0.52	[7]
PCM	Liquid	750	2400	0.19	[8]
	Solid	789	1800	0.18	

Soil as a backfill material is assumed to be dry, and the thermophysical properties of soil are taken from Incropera et al. [7]. The melting temperature of the PCM is selected as $T_m = 20℃$. The design parameters of the SHBHE and flat plate solar collector are given in Table 2. D_{pipe} denotes the diameter of the pipe within SHBHE. D_{pcm} is the diameter of the PCM layer, and D_{BHE} designate the diameter of the SHBHE.

Table 2. Design parameters of SHBHE and the flat plate solar collector [9]

Parameter	Value	Units	Parameter	Value	Units
D_{pipe}	0.0250	m	ε_{plate}	0.98	-
D_{pcm}	0.0500	m	ε_{cover}	0.88	-
D_{BHE}	0.1000	m	α	0.97	-
τ	0.90	-	β	30.30	º
W_{col}	1.0000	m	k_{plate}	0.03	W/mK
H_{col}	2.5000	m	$D_{pipe,col}$	0.02	m
$w_{s,col}$	0.1150	m	U_{inlet}	0.01	m/s

2.2 Numerical Model for SHBHE

Governing equations of the BHE are reduced by considering the following simplifications

- The fluid flow within the circular pipe is fully developed and laminar.
- The pipeline between the solar collector and the SHBHE is perfectly insulated.
- Frontal and rear surfaces of the SHBHE at $z = 0$ and $z = L$ are taken as adiabatic.
- The radiation effects are neglected.
- The thermal properties of backfill material and working fluid are constant.

The energy equation for the backfill material and fluid domains can be reduced as follows

For backfill domain:

$$\rho c \frac{\partial T}{\partial t} = \frac{\partial}{\partial z}\left(k \frac{\partial T}{\partial z}\right) + \frac{1}{r}\frac{\partial}{\partial r}\left(kr \frac{\partial T}{\partial r}\right) \tag{1}$$

For the HTF domain:

$$\rho c \frac{\partial T}{\partial t} + \rho c u \frac{\partial T}{\partial z} = \frac{\partial}{\partial z}\left(k \frac{\partial T}{\partial z}\right) + \frac{1}{r}\frac{\partial}{\partial r}\left(kr \frac{\partial T}{\partial r}\right) \tag{2}$$

As the flow is assumed laminar and fully developed within the tube, the convective heat transfer coefficient, h, between backfill material and working fluid can be calculated from the following well-known Nusselt equation, i.e., Nu = 3.66. The conduction heat transfer in phase change material is modeled by using the fixed grid numerical model of Cao and Faghri [10].

2.3 Flat plate solar collector model

The flat plate solar collector model is developed based on the procedure represented by Duffie and Beckman [9]. Radiative and convective losses from the lateral surfaces of the solar collector are neglected. The energy equation for flat plate solar collector is then written as follows:

$$\frac{d}{dt}(mcT)_{HTF} = \dot{Q_u} + \left[\dot{m}c\left(T_{col,in} - T_{col,out}\right)\right]_{HTF} \quad (3)$$

where $\dot{Q_u}$ represents the useful heat transferred to heat transfer fluid. The useful heat can be determined as

$$\dot{Q_u} = A_{col}\, F_R \left[(I_{solar}\tau\alpha) - U_L\left(T_{col,in} - T_{amb}\right)\right] \quad (4)$$

where U_L and F_R are the overall heat loss coefficient of the solar collector and the solar collector heat removal factor, respectively. Overall heat loss coefficient of the solar collector (U_L) includes the top and bottom components as followings

$$U_L = U_t + U_b \quad (5)$$

where U_t and U_b represent the heat loss coefficients of the solar collector from the top and bottom surfaces, respectively. U_t and U_b can be calculated by the thermal resistance network method. The thermal resistance network includes simply the radiative and convective heat losses from the absorber plate and the cover glass. A detailed explanation of the thermal resistance network could be found elsewhere [11]. The heat loss coefficient at the top surface of the solar collector U_t can be calculated as

$$U_t = \frac{1}{R_{tot,t}} \quad (6)$$

The radiative heat transfer coefficient between the absorber plate and glass cover is evaluated by using the Nusselt correlation that is proposed by Hollands et al. [11]. The solar collector tilt angle is defined by referring to the work of Ülgen [13], in which the optimum solar collector tilt angle of Izmir City is defined as 30.3°. The heat loss coefficient from the bottom surface can be defined as

$$U_b = \frac{1}{R_{tot,b}} = k_{ins,col}/L_{ins,col} \quad (7)$$

where $k_{ins,col}$, and $L_{ins,col}$represent the thermal conductivity of the insulation material and its thickness, respectively. The collector heat removal factor, F_R, on the other hand, is defined as

$$F_R = \frac{\dot{m}c}{A_{col}U_L}\left[1 - \exp\left(\frac{A_{col}U_L F'}{\dot{m}c}\right)\right] \quad (8)$$

where F' is the solar collector efficiency factor and could be evaluated by following the procedure described by Duffie and Beckman. [9]. To check the validity of the flat plate solar collector model, the top loss coefficient, i.e., U_t, is compared with the ones that are provided in Duffie and Beckman [9]. Comparative results show that the mean deviation between the current findings and the results given in the reference work is less than 1%.

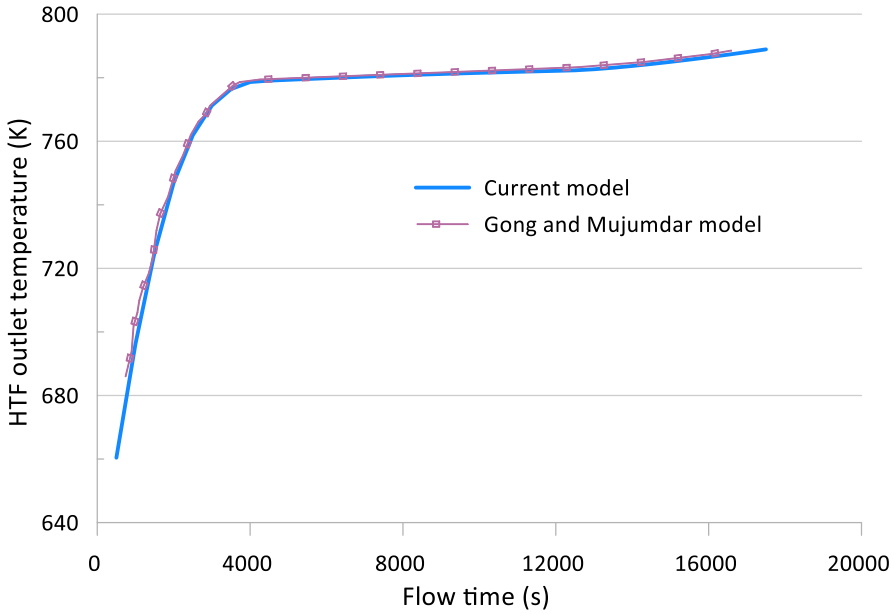

Figure 2: Model validation

In the numerical method, variable weather data of Izmir City is imported into the code, and the flat plate solar collector sub-function solves the related equations, i.e., Eqs. 3 to 8, to compute the outlet temperature of the HTF from the flat plate solar collector. The outlet temperature of the solar collector is then defined as the inlet temperature of the SHBHE unit. The control volume approach is implemented for the HTF and the backfill domains to transform the governing equations for each domain, i.e., Eqs. 1 and 2, into algebraic form. The final set of algebraic equations is then iteratively solved with SIS (Strongly Implicit Solver) algorithm [14]. The iterative solver for the integrated system, which involves the flat plate collector and the SHBHE, is codded in MATLAB software. The numerical model with PCM as a backfill material is validated with Gong & Mujumdar's [15] results with a 0.1 K difference.

3.RESULTS

In this study, the effects of *(i)* the length of the shallow horizontal borehole heat exchanger, and *(ii)* the type of the backfill material on the thermal performance of the SHBHE unit under variable weather conditions are investigated to understand the dynamic thermal performance of SHBHE unit in January. The time-wise variations of flat plate solar collector efficiency, inlet and outlet temperature of SHBHE unit, and thermal influence radius are examined. Analyses are conducted for two different pipe lengths of L = 1 m and L = 2 m with defining soil and PCM as backfill material.

In Figure 2, the HTF inlet and outlet temperature variations of SHBHE are given for two different configurations in which soil (Fig. 2a) and PCM (Fig. 2b) are implemented as backfill material. It can be observed that by increasing the length of the SHBHE unit, the inlet and outlet temperatures reduce. However, one can notice that the temperature difference between the inlet and outlet temperatures of the SHBHE increases with the length of the increasing pipe length. The SHBHE unit stores more energy due to the increased backfill material volume. Inlet and outlet temperature of the HTF reach the peak values at around t = 7 h for L = 1 m. At this instant, inlet and outlet temperatures of the HTF are obtained as 41.39°C and 40.74°C, respectively. Besides, for L = 2 m, the HTF inlet and outlet temperature reach the peak value at t = 7 h, with inlet and outlet temperatures of 35.78°C, and 34.73°C, respectively. Temperature differences between the inlet and outlet sections of the SHBHE are 0.65°C for 1 m of pipe length and 1.05°C for 2 m of pipe length. In Figure 2(b), the inlet and outlet temperatures of HTF are shown for the PCM backfilled SHBHE unit with two different pipe lengths. HTF inlet temperature for 1 m pipe length is 30.53 ℃, and the outlet temperature of HTF is 29.51 ℃ at peak. The inlet temperature of HTF for 2 m pipe length is 23.77 ℃, and the HTF outlet temperature is 22.42 ℃ at peak.

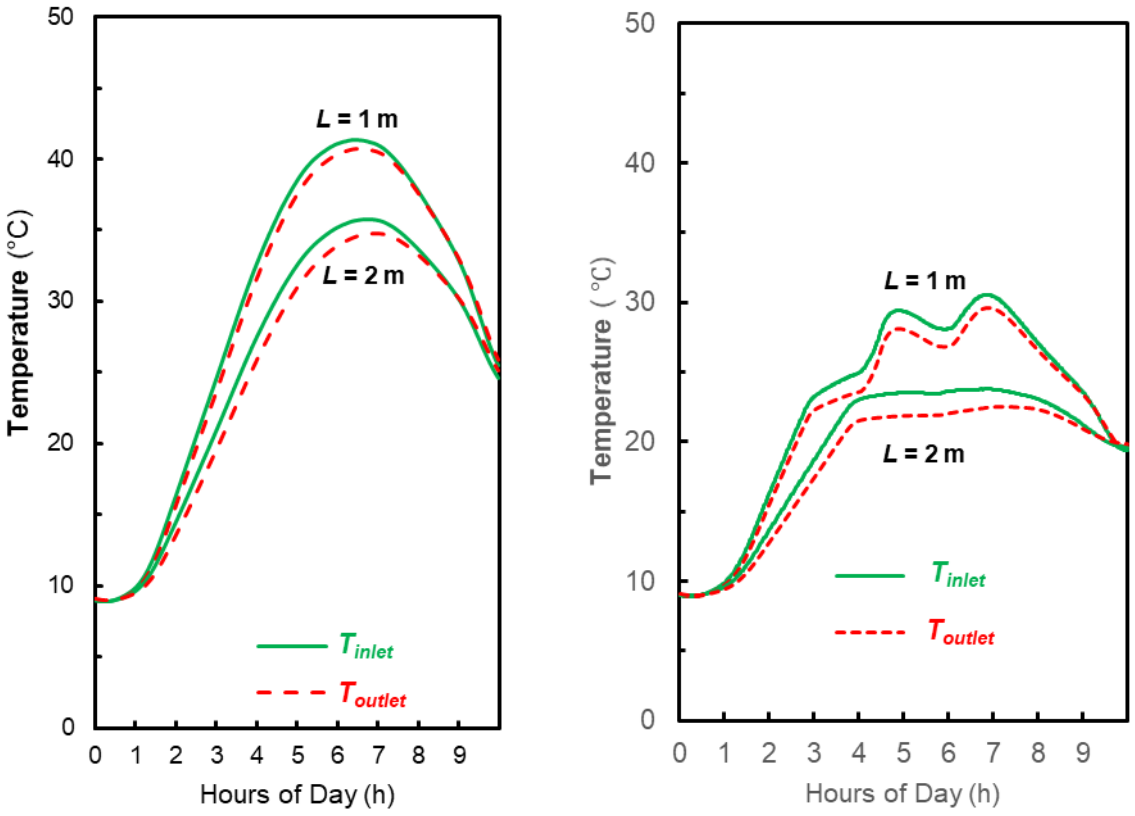

Figure 3. Inlet and Outlet Temperatures (a) soil (b) PCM as a backfill material

The HTF transfers heat with convection to backfill material, and conduction heat transfer occurs within backfill material. The temperature distribution concerning radius is computed with the MATLAB code. The temperature is calculated for 2.5 h time interval, at the same depth of $z = 0.995\ m$. Temperature distribution based on the radius within backfill material is shown in Figure 3a. Fig. 3a shows the temperature distribution based on the radius for soil backfilled SHBHE. The temperature distribution for PCM-filled SHBHE based on the radius can be observed from Fig. 3b. The thermal influence radius increases with time.

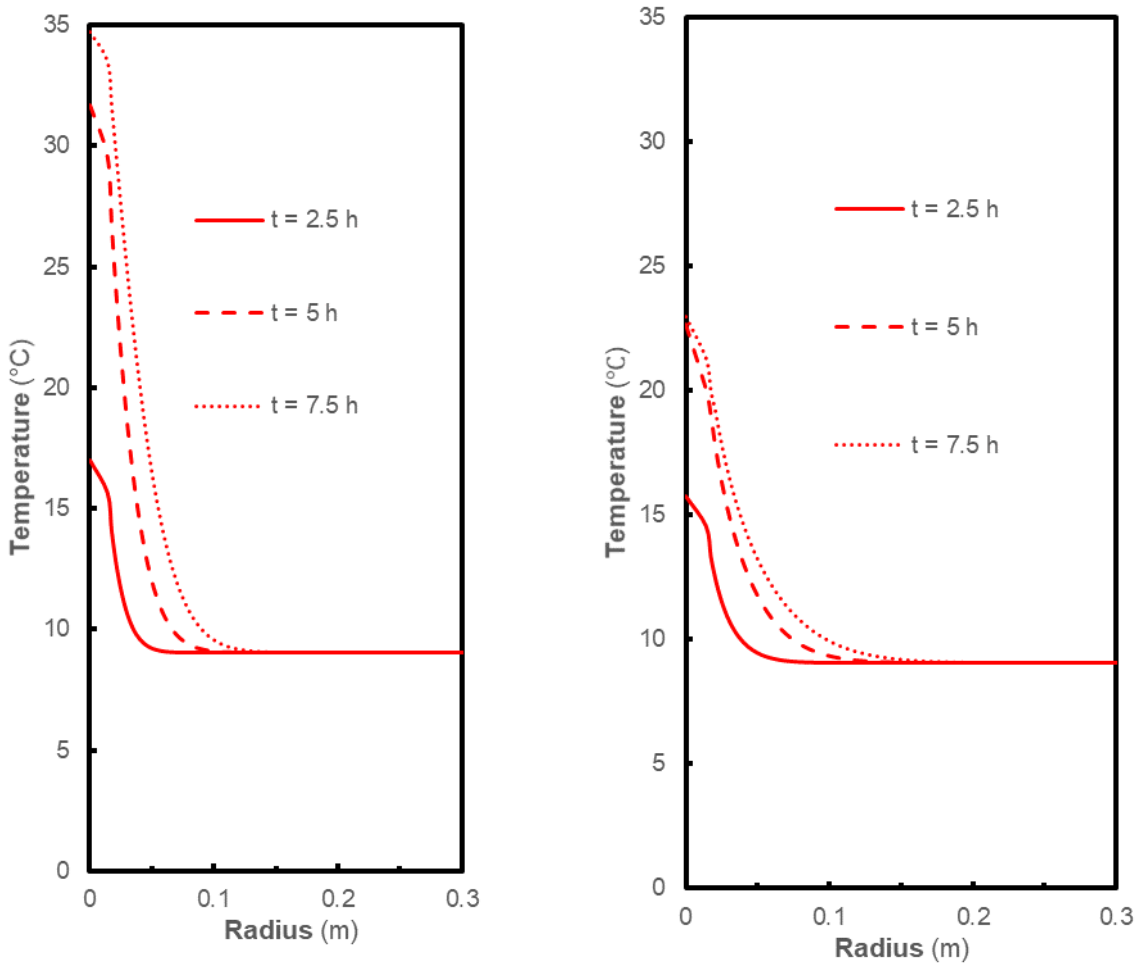

(a)Soil (b)PCM

Figure 4: Temperature distribution along with the radial direction (a) for soil and (b) PCM as a backfill material

Figure 4 represents the temperature distribution based on the radius for soil and PCM as a backfill material at t = 5 h for L = 1 m (Fig. 4a.) and L = 2 m (Fig.4b.). Temperature decreases along the radial direction. Soil as a backfill material reaches the constant temperature earlier than PCM. In Fig. 4a, temperature distribution based on the radius for L = 2 m is given. In Fig. 4b., the temperature is stabilized at r = 0.025 m because PCM volume reaches the melting temperature, and the phase change process starts.

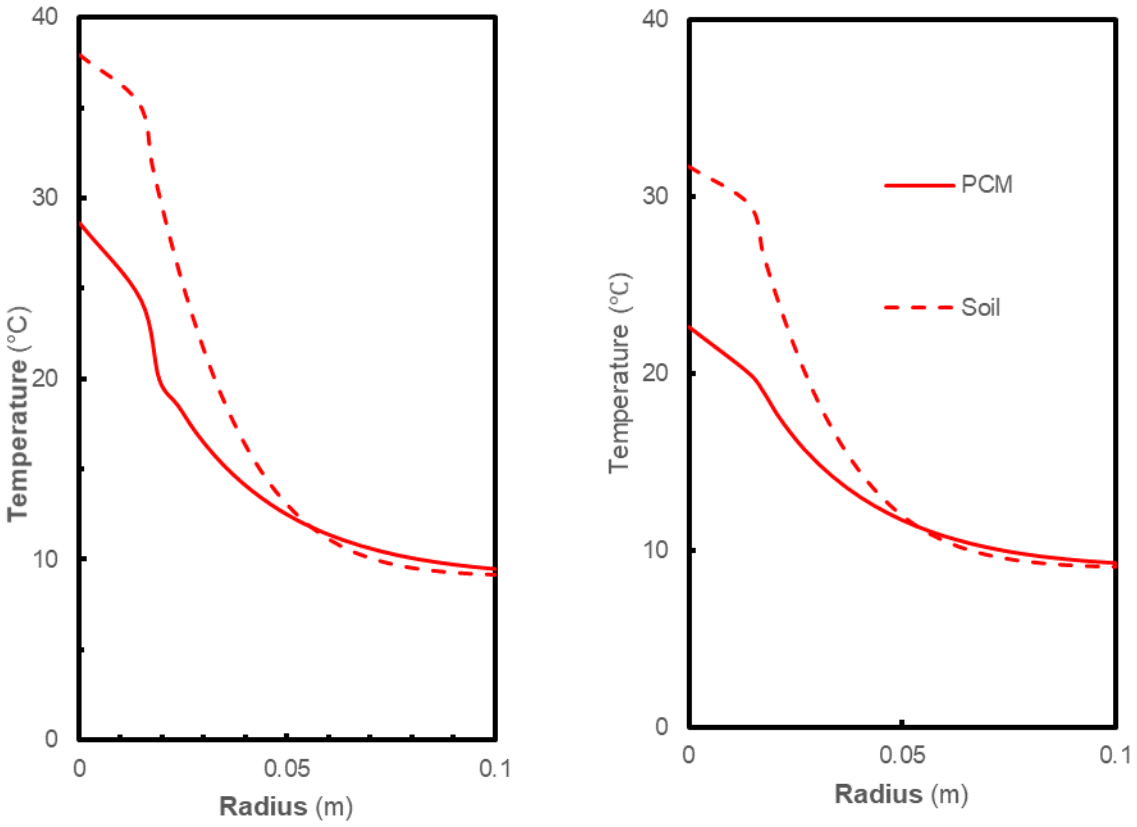

(a) L = 1 m (b) L = 2 m

Figure 5: Temperature distribution for soil and PCM as a backfill material

4.CONCLUSION

In this study, the effects of backfill materials on the thermal performance of the SHBHE unit are numerically modeled under variable weather conditions. There are several studies about BHE modeling; however, these studies investigate the thermal performance of BHE under constant inlet temperature conditions. Unlike these studies, real weather conditions implemented the mathematical model to simulate the solar energy integrated SHBHE unit. The concluding remarks are as follows

- Increasing the pipe length of the SHBHE unit decreases HTF outlet temperature; however, the temperature difference between the inlet and outlet temperature of HTF increases.
- Thermal influence radius increases with increasing time,
- When PCM is used as a backfill material, the thermal energy is stored nearby the pipe, and discharging the stored energy is easier.

In conclusion, the SHBHE unit can be used as a small-scale energy unit with different backfill materials. However, PCMs have a lower thermal conductivity, PCM as a backfill material stores energy nearby the pipe of the SHBHE due to latent heat. Since soil as a backfill material distributes the heat, it can be difficult to discharge the energy stored in the SHBHE unit. Besides, different PCM layer thicknesses in the SHBHE unit should be investigated, and cyclic performance simulations can be done for soil and PCM as backfill material in the future.

REFERENCES

[1] Eskilson, P, Claesson J., Sımulatıon Model For Thermally Interactıng Heat Extractıon Boreholes, *Numerical Heat Transfer*, 13:2, 149-165, 1988

[2] Bauer, D., Heidemann, W., & Diersch, H. J.. Transient 3D analysis of borehole heat exchanger modeling. Geothermics, 40(4), 250-260., 2011

[3] Rees, S. J., & He, M. A three-dimensional numerical model of borehole heat exchanger heat transfer and fluid flow. Geothermics, 46, 1-13. (2013).

[4] Cui, P., Yang, H., & Fang, Z. Numerical analysis and experimental validation of heat transfer in ground heat exchangers in alternative operation modes. Energy and Buildings, 40(6), 1060-1066., 2008

[5] Li, X., Tong, C., Duanmu, L., & Liu, L. Research on U-tube heat exchanger with shape-stabilized phase change backfill material. Procedia Eng, 146, 640-647., 2016

[6] Bottarelli, M., Bortoloni, M., Su, Y., Yousif, C., Aydın, A. A., & Georgiev, A.. Numerical analysis of a novel ground heat exchanger coupled with phase change materials. Applied Thermal Engineering, 88, 369-375., 2015

[7] Incropera, F. P., Lavine, A. S., Bergman, T. L., & DeWitt, D. P.. Fundamentals of heat and mass transfer. Wiley., 2007

[8] Rubitherm, R.T., Technical Data Sheet for RT 20, Rubitherm Technologies (2018)

[9] Duffie, J. A., & Beckman, W. A.. Solar energy thermal processes, John Wiley & Sons, 2013

[10] Cao, Y., & Faghri, A., Performance characteristics of a thermal energy storage module: a transient PCM/forced convection conjugate analysis. International Journal of Heat and Mass Transfer, 34(1), 93-101., 1991.

[11] Fuentes, Martin K. A simplified thermal model for flat-plate photovoltaic arrays. No. SAND-85-0330. Sandia National Labs., Albuquerque, NM (USA), 1987.

[12] Hollands, K. G. T., Unny, T. E., Raithby, G. D., & Konicek, L. Free convective heat transfer across inclined air layers.,1976

[13] Ulgen, K. Optimum tilt angle for solar collectors. Energy Sources, Part A: Recovery, Utilization, and Environmental Effects, 28(13), 1171-1180. 2006

[14] Lee, S. L. A strongly implicit solver for two-dimensional elliptic differential equations. Numerical Heat Transfer, Part B Fundamentals, 16(2), 161-178.. 1990

[15] Gong, Z. X., & Mujumdar, A. S. (1997). Finite-element analysis of cyclic heat transfer in a shell-and-tube latent heat energy storage exchanger. Applied thermal engineering, 17(6), 583-591.

EFFECTS OF INJECTION AND SUCTION THROUGH A PERFORATED CIRCULAR CYLINDER ON SOME THERMO-FLUID PARAMETERS

Mir Elyad VAKHSHOURI*, Burhan ÇUHADAROĞLU**
*Karadeniz Technical University, Department of Mechanical Engineering, Trabzon/Turkey
Email: elyadv@ktu.edu.tr
**Karadeniz Technical University, Department of Mechanical Engineering, Trabzon/Turkey
Email: burhan@ktu.edu.tr

ABSTRACT

The effects of uniform injection and suction through the surface of a perforated circular cylinder on the vortex shedding, heat transfer, and some aerodynamic parameters investigated numerically. The finite-volume method has been used for solving the ensemble-averaged Navier-Stokes equations for incompressible, turbulent near-wake flow with the *RANS* turbulence model equations. The effects of injection and suction through the surface of the cylinder with various injection/suction coefficient Γ are studied to find the optimum conditions. The results show that parameters such as drag coefficient and Nusselt number influenced drastically in some cases like flow field parameters.

Keywords: Injection and suction, Perforated circular cylinder, Heat transfer, Turbulent flow.

1. INTRODUCTION

Investigation of vortex shedding and wake region behind bluff bodies play an essential role in industrial and engineering applications such as vibration control, dynamic install, lift and drag control, reducing acoustic phenomena, thermal protection of high-speed systems, heat transfer enhancement in heat exchangers. Despite its apparent simplicity, in the case of flow past a circular cylinder, most of the phenomena found in bluff bodies' wakes, including vortex shedding, boundary layer separation, and recirculating flows, can happen. Passive and active flow control techniques are used to control flow-induced vibrations and fluctuating forces by decreasing these forces and mitigating vortex shedding. Active methods like injection and suction through a surface, electromagnetic forces, rotationally oscillating body, bleeding through a surface, using streamwise oscillating foil, exerting an external magnetic field [1–7], works with energy input. Generating secondary flow like blowing and suction through perforated surfaces of a bluff body in cross-flow can control the characteristics of boundary layers; thickening of the boundary layer, decreasing surface skin friction, decreasing drag, avoiding the boundary layer separation, and hence preventing the transition to turbulence.

Numerous papers published analyzing the effects of injection through a perforated surface to the main flow. However, limited numbers of literature studied the effects of injection/suction through a bluff body on the aerodynamic parameters and heat transfer characteristics. Schumm et al. [8] experimentally studied the Kármán-vortex shedding in the wake of different two-dimensional bluff bodies and investigated different control measures, such as wake heating, transverse body oscillations, and base bleed. Mathelin et al. [9] reveal that the dynamic and thermal boundary layers around a circular cylinder are affected strongly by blowing with the experimentally investigated study. Ling and Fang [10] numerically investigated the effects of surface suction or blowing's position and strength on the vortex structures of the circular cylinder wake, as on the drag and lift forces at $Re = 100$. The results of the study show that the suction on the shoulder of the cylinder or the blowing on the rear of the cylinder can efficiently suppress the vortex wake and significantly reduce the lift force; the suction on the shoulder of the cylinder properly chosen strength can also reduce the drag force significantly. Çuhadaroğlu and Turan [11] numerically studied the turbulent flow around a square cylinder with uniform injection or suction through various

surfaces. They resulted that the parameters such as drag coefficient, vortex shedding, and Nusselt number have been influenced by the uniform injection and suction through certain surfaces of the square cylinder. An experimental study on the effects of uniform injection through one perforated surface of a square cylinder on the pressure distribution and drag coefficient in a two-dimensional turbulent flow was presented by Çuhadaroğlu et al. [12]. The results reveal that the pressure coefficient around the square cylinder and also the drag coefficient was influenced by the position of the perforated surface and injection rate. A useful technique presented by Dong et al. [13] for suppressing the vortex-induced vibrations of bluff bodies by eliminating the von Kármán street formed in their wake. They find that small amounts of combined windward suction and leeward blowing around the body modify the wake instability and suppress the fluctuating lift force. Turhal and Çuhadaroğlu [14] experimentally investigated the impacts of the surface injection through various perforated surfaces of the horizontal and diagonal square cylinders on the drag coefficient and the Strouhal number for $Re = 10000$, 16000, and 24000. They revealed that surface injection through the top-rear, rear, and all surfaces of a diagonal square cylinder reduces the drag coefficient while the injection through all surfaces only reduces the drag of a horizontal square cylinder. Çuhadaroğlu and Turan [15] analyzed the effects of injection/suction on heat transfer via wall functions of the velocity and temperature sub layers at $Re = 21400$. The results show that suction enhances the heat transfer, while injection through the rear surface provides some thermal protection.

This review shows that the effects of the surface injection/suction through the perforated surface of the circular cylinders with different injection/suction rates on the aerodynamic parameters and heat transfer characteristics in cross-flow have not been widely investigated, especially at high Reynolds numbers and limited papers are available in the literature. Therefore, the objective of this work is to investigate that how suction and injection affect the drag coefficient and the Nusselt number in various cases.

2. GOVERNING EQUATIONS

Time-averaged Navier–Stokes and energy equations are:

$$\frac{\partial(u_j)}{\partial x_j} = 0 \tag{1}$$

$$\frac{\partial(u_i)}{\partial t} + (u_j)\frac{\partial(u_i)}{\partial x_j} = -\frac{1}{\rho}\frac{\partial(p)}{\partial x_i} + \frac{\partial}{\partial x_j}\left[\nu\left(\frac{\partial(u_i)}{\partial x_j} + \frac{\partial(u_j)}{\partial x_i}\right) - \left(u'_i u'_j\right)\right] \tag{2}$$

$$\frac{\partial(T)}{\partial t} + (u_j)\frac{\partial(T)}{\partial x_j} = \frac{\partial}{\partial x_j}\left[\frac{\nu}{Pr}\frac{\partial(T)}{\partial x_j} - \left(u'_j T'\right)\right] \tag{3}$$

By using the Boussinesq eddy viscosity hypothesis, the Reynolds stress and heat fluxes are approximated as:

$$\left(u'_i u'_j\right) = (\nu_t)\left(\frac{\partial(u_i)}{\partial x_j} + \frac{\partial(u_j)}{\partial x_i}\right) - \frac{2}{3}\delta_{ij}(k) \tag{4}$$

$$-\left(u'_j T'\right) = \frac{\nu_t}{Pr_t}\frac{\partial(T)}{\partial x_j} \tag{5}$$

The standard *k-ε* model of Reynolds-averaged Navier-Stokes (RANS) is used in a two-dimensional (2D) high Reynolds number flow. Overproduction of turbulent energy in stagnation regions and in the small regions with high deceleration and acceleration around the cylinder, which affect the vortex-shedding, is a disadvantage of standard two-equation turbulence models. A modification introduced by Kato and Launder [16] has been used to produce better results. Based on the Kato-Launder modification, the production of turbulent kinetic energy is expressed in terms of the vorticity and the strain rate. The model equations are:

$$\frac{\partial(k)}{\partial t} + (u_j)\frac{\partial(k)}{\partial x_j} = \frac{\partial}{\partial x_j}\left[\left(\nu + \frac{(\nu_t)}{\sigma_k}\right)\frac{\partial(k)}{\partial x_j}\right] + P_k - (\varepsilon) \tag{6}$$

$$\frac{\partial(\varepsilon)}{\partial t} + (u_j)\frac{\partial(\varepsilon)}{\partial x_j} = \frac{\partial}{\partial x_j}\left[\left(\nu + \frac{(\nu_t)}{\sigma_\varepsilon}\right)\frac{\partial(\varepsilon)}{\partial x_j}\right] + C_1 P_k \frac{(\varepsilon)}{(k)} - C_2 \frac{(\varepsilon)^2}{(k)} \tag{7}$$

$$(\nu_t) = \frac{C_\mu (k)^2}{(\varepsilon)} \tag{8}$$

$$P_k = C_\mu(\varepsilon) S\Omega$$

$$S = \frac{(k)}{(\varepsilon)}\sqrt{\frac{1}{2}\left[\frac{\partial(u_i)}{\partial x_j} + \frac{\partial(u_j)}{\partial x_i}\right]^2}$$

$$\Omega = \frac{(k)}{(\varepsilon)}\sqrt{\frac{1}{2}\left[\frac{\partial(u_i)}{\partial x_j} - \frac{\partial(u_j)}{\partial x_i}\right]^2}$$

In the equations above, S is the symmetric deformation tensor of the fluid, while Ω is the vorticity vector. The values of the *k*-ε model constants are σ_k=1, σ_ε=1.3, C_1=1.44, $C_2 = 1.92$, and $C_\mu = 0.09$.

The schematic of the computational domain is illustrated in Figure 1. As seen, a perforated two-dimensional circular cylinder is located at $x = 0$ (Origin of the coordinate system is in the center of the front surface of the cylinder). To reduce the effects of outer boundaries, the lengths of the upstream and downstream distance and also the width of the computational domain are chosen as 4.5H, 25.5H, and 15H, respectively.

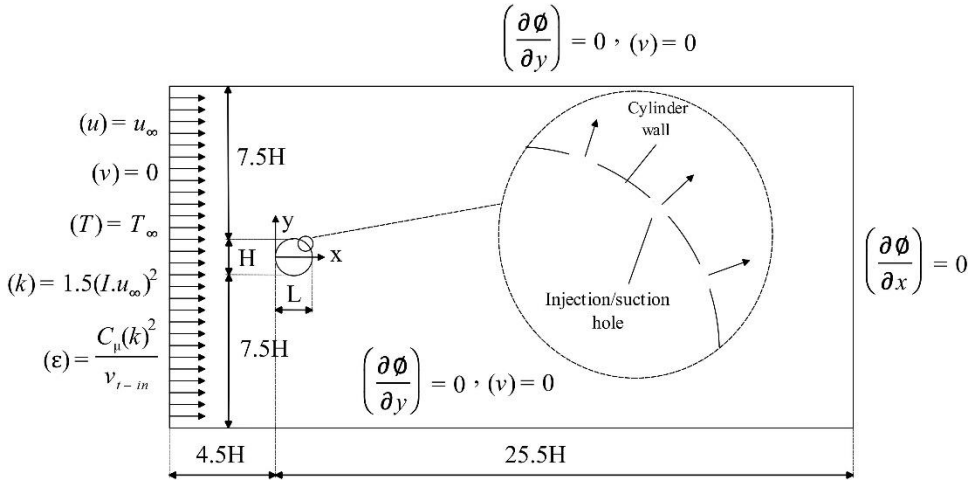

Figure. 1 Computational domain and boundary conditions.

The boundary conditions of the computational domain are as follows:

(1) At the inlet: $(u = u_\infty)$, $(k) = 1.5(I.u_\infty)^2$, $(\varepsilon) = \frac{C_\mu (k)^2}{\nu_{t-in}}$, $(T) = T_\infty$. Where The turbulence intensity (I) is 5%. The viscosity is given by Sutherland's law with three coefficients $\mu = \mu_0 \left(\frac{T}{T_0}\right)^{3/2} \frac{T_0+S}{T+S}$ with $T_0 = 273.11$ K, S = 110.56 K, the inlet viscosity $\mu = 1.7894 \times 10^{-5}$ kg/(ms), the reference viscosity $\mu_0 = 1.716 \times 10^{-5}5$ kg/(ms) and the inlet temperature $T_\infty = 373$ K. $Re = 21400$, $\rho = 1$ kg/m3, and $u_\infty = 0.38$ m/s.

(2) At the top and bottom boundaries: $\left(\frac{\partial \phi}{\partial y}\right) = 0, (v = 0)$.

(3) At the outlet: $\left(\frac{\partial \phi}{\partial x}\right) = 0$.

(4) At the cylinder boundaries: $(v = v_w)$, $\Gamma = \left(\frac{v_w}{u_\infty}\right)$, $(k) = 1.5(I.v_w)^2$, $(\varepsilon) = \frac{C_\mu (k)^2}{\nu_{t-in}}$, $(T) = T_w$ where v_w is the injection or suction velocity normal to the boundary and the temperature of the cylinder wall $T_w = 273$ K where Γ is the normalized injection or suction coefficient.

The finite volume method is used for all simulations based on an incompressible SIMPLE algorithm. The least-squares nod-based method is selected to discretize the gradient. Pressure, momentum, and energy components are discretized with the second-order method, while the first-order-upwind scheme is used to discretize other variables such as turbulent kinetic energy and dissipation rate. The second-order implicit scheme is used in transient formulation with a fixed time step method. To determine variables such as velocity and pressure fields, temperature, turbulence, etc. the hybrid interpolation method is used with the convergence criteria of 10^{-6} in all calculations.

Increasing the perforation rate of the cylinder faces provides more suction and blowing and hence increases the number of nodes on the body surface. Thus high-resolution non-uniform grid is made in the computational domain (Figure 2).

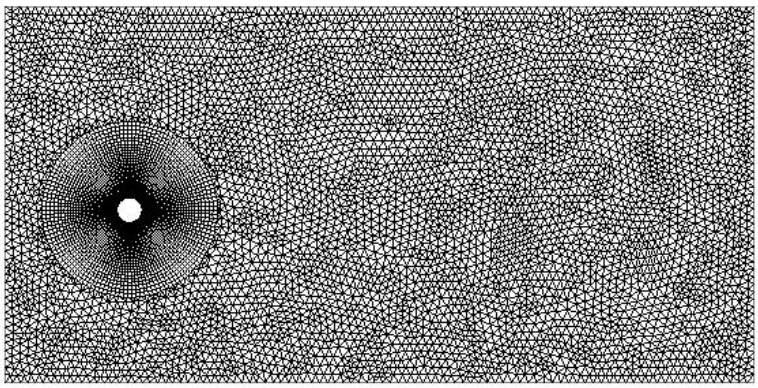

(a)

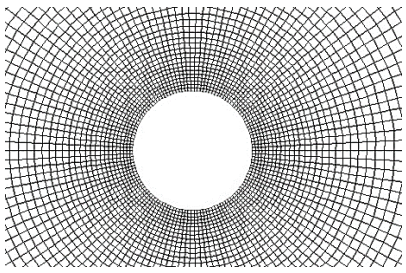

(b)

Figure. 2 Non-uniform computational grid (14666 cells, minimum grid face area (m^2) of 2.478×10^{-2} and maximum grid face area (m^2) of 4.958×10^{-1}): (a) whole domain and (b) enlarged view of the grid near the cylinder.

3. RESULTS AND DISCUSSION

Experimental and numerical achievements of the flow over non-perforated circular cylinders have been considered as reference data to investigate the influence of injection and suction through the perforated circular cylinders to validate the results of this study.

The variation of the drag coefficient with Γ for the injection/suction cases from the surface of the perforated circular cylinder is demonstrated in figure 3. It is observed that the value of the drag coefficient for the no-injection case of the present study has a good match compared to the previous results achieved by Wieselsberger [17], Cheng [18], and Achenbach [19]. It is also seen that for all values of $-0.6 < \Gamma < 0.4$, the drag coefficient decreases while for $0.4 < \Gamma < 0.6$ increases slightly compared to the no-injection case. Furthermore, the maximum increase and reduction of the drag coefficient occur at $\Gamma = 0.6$ and $\Gamma = -0.6$, about 11% and 79%.

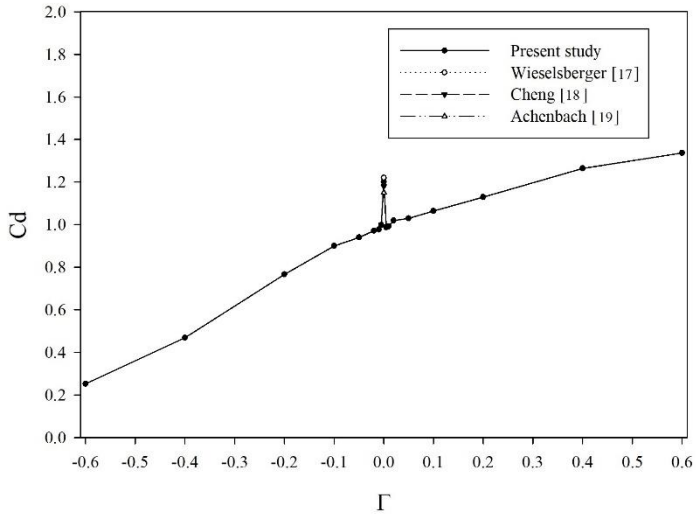

Figure. 3. Variation of drag coefficient with Γ for various injection/suction cases through the surface of a circular cylinder.

Figure 4 shows the time-averaged *Nu* number variation with all injection and suction values for flow around a circular cylinder. The results of the no-injection case obtained a good match to experimental studies by Žukauskas [20] and Kondjoyan and Daudin [21]. As seen, by increasing the suction parameter ($|\Gamma|$) in all cases, the time-averaged *Nu* number increases while on the other hand, opposite behavior occur for all injection cases. By comparing the *Nu* number of the no-injection case with all other cases, it is observed that the maximum increase and reduction of *Nu* number occur at ($|\Gamma|$) $= 0.6$, which are about 50% and 92%, respectively.

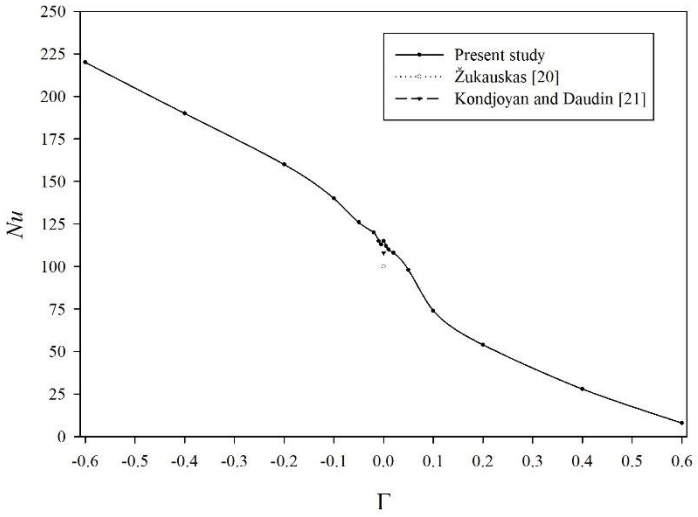

Figure. 4. Variation of time-averaged *Nu* number with Γ for various injection/suction cases.

The circumferential distribution of the mean pressure coefficient (*Cp*) is demonstrated in Figure 5. As seen, the results of the no-injection cases are almost the same compared to experimental studies by Yokuda and Ramaprian [22] and Norberg [23]. The variation of *Cp* with Γ depicted in figure 6. It is observed that the *Cp* curves have almost the same trend except for $\Gamma = -0.6$, which takes the lowest value at $\varphi = 80^{\circ}$.

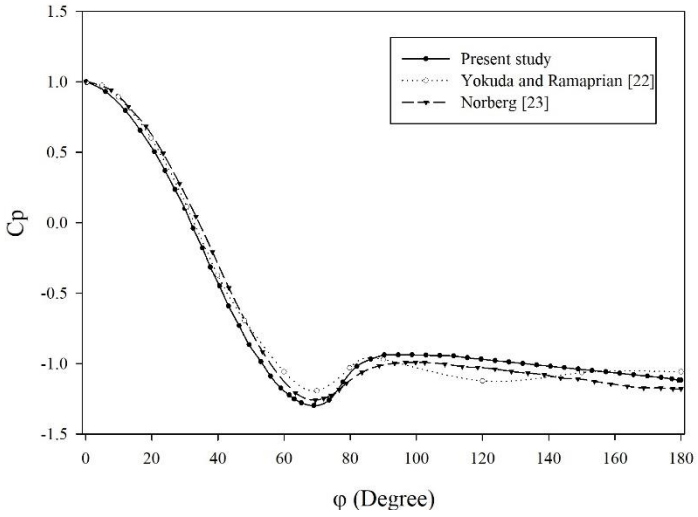

Figure. 5. Mean pressure coefficient distribution on the cylinder surfaces.

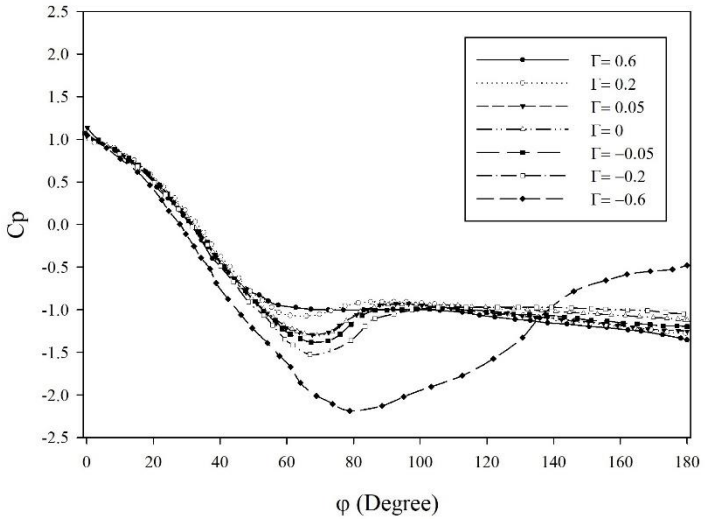

Figure. 6. Mean pressure coefficient distribution on the cylinder surfaces with various injection/suction cases.

4. CONCLUSIONS

The flow around the perforated circular and elliptical cylinders with injection or suction through various surfaces has been studied numerically by the code of ANSYS-Fluent. The effects of injection or suction coefficient on the drag coefficient and surface pressure distribution, and also heat transfer have been analyzed. The results show that although the magnitude of injection or suction is relatively lower than that of the main flow, it significantly influences drag and surface pressure as well as heat transfer depending on the injection/suction rates. It is also concluded that applying suction through the surface of a circular cylinder may also be regarded as a heat transfer enhancement application.

REFERENCES

[1] Chen, Z. & Aubry, N. Active Control of Cylinder Wake, *Communications in Nonlinear Science and Numerical Simulation*, **10(2)**, 210-216, 2005.

[2] Fujisawa, N., Asano, Y., Arakawa, C. & Hashimoto, T. Computational and Experimental Study on Flow Around a Rotationally Oscillating Circular Cylinder in a Uniform Flow, *Journal of Wind Engineering and Industrial Aerodynamics*, **93**(2), 137-153, 2005.

[3] Fransson, J.H.M., Konieczny, P. & Alfredsson, P.H. Flow around a Porous Cylinder Subject to Continuous Suction or Blowing, *Journal of Fluids and Structures*, **19**(8), 1031-1048, 2004.

[4] Sevilla, A. & Martínez-Bazán, C. Vortex Shedding in High Reynolds Number Axisymmetric Bluff-Body Wakes: Local Linear Instability and Global Bleed Control, *Physics of Fluids*, **16**, 3460, 2004.

[5] Bao, Y. & Tao, J. Active Control of a Cylinder Wake Flow by Using a Streamwise Oscillating Foil, *Physics of Fluids*, **25**, 053601, 2013.

[6] Bovand, M., Rashidi, S., Dehghan, M., Esfahani, J.A. & Valipour, M.S. Control of Wake and Vortex Shedding behind a Porous Circular Obstacle by Exerting an External Magnetic Field, *Journal of Magnetism and Magnetic Materials*, **385,** 198-206, 2015.

[7] Huang, Y., Zhou, B. & Tang, Z. Instability of Cylinder Wake under Open-Loop Active Control, *Applied Mathematics and Mechanics*, **38,** 439-52, 2017.

[8] Schumm, M., Berger, E. & Monkewitz, P.A. Self-Excited Oscillations in the Wake of Two-Dimensional Bluff Bodies and Their Control, *Journal of Fluid Mechanics*, **271,** 17-53, 1994.

[9] Mathelin, L., Bataille, F. & Lallemand, A. Flow around a Circular Cylinder with Non-Isothermal Blowing, *Experimental Thermal and Fluid Science*, **26**(2-4), 173-179, 2002.

[10] Ling, G.P. & Fang, J.W. Numerical Study on the Flow around a Circular Cylinder with Surface Suction or Blowing Using Vorticity-Velocity Method, *Applied Mathematics and Mechanics*, **23**, 1089-1096, 2002.

[11] Çuhadaroğlu, B. & Turan, O. Numerical Simulation of Turbulent Flow around a Square Cylinder with Uniform Injection or Suction and Heat Transfer, *Numerical Heat Transfer, Part A: Applications*, **55**(2), 163-184, 2009.

[12] Çuhadaroğlu, B., Akansu, Y.E. & Turhal, A.O. An Experimental Study on the Effects of Uniform Injection through One Perforated Surface of a Square Cylinder on Some Aerodynamic Parameters, *Experimental Thermal and Fluid Science*, **31**(8), 909-915, 2007.

[13] Dong, S., Triantafyllou, G.S. & Karniadakis, G.E. Elimination of Vortex Streets in Bluff-Body Flows, *Physical Review Letters*, **100**, 204501, 2008.
[14] Turhal, A.O. & Çuhadaroğlu, B. The Effects of Surface Injection through a Perforated Square Cylinder on Some Aerodynamic Parameters. *Experimental Thermal and Fluid Science*, 34(6), 725-735, 2010.

[15] Çuhadarolu, B. & Turan, O. Numerical Study on Heat Transfer between Turbulent Flow and Porous Rectangular Cylinders with Uniform Injection or Suction, *Heat Transfer Engineering*, **33**(15), 1232-1245, 2012.

[16] Kato, M. & Launder, B.E. The Modeling of Turbulent Flow around Stationary and Vibrating Square Cylinders, *Proc. 9th Symposium on Turbulent Shear Flows*, Kyoto-Japan, 10.4.1-10.4.6, 1993.

[17] Wieselsberger, C., Neuere Feststellungen über die Gesetze des Flüssigkeits- und Luftwiderstands, Physikalische Zeitschrift, **22**, 321-328, 1921.

[18] Cheng, N.S., Calculation of Drag Coefficient for Arrays of Emergent Circular Cylinders with Pseudofluid Model, *Journal of Hydraulic Engineering*, **139**(6), 602-611, 2013.

[19] Achenbach, E., Distribution of Local Pressure and Skin Friction around a Circular Cylinder in Cross-Flow up to $Re = 5 \times 10^6$, *Journal of Fluid Mechanics*, **34**(4), 625-639, 1968.

[20] Žukauskas, A., Advances in Heat Transfer, *Academic Press*, New York, 93-160, 1972.

[21] Kondjoyan, A. & Daudin, J. D. Effects of Free Stream Turbulence Intensity on Heat and Mass Transfers at the Surface of a Circular Cylinder and an Elliptical Cylinder, Axis Ratio 4, *International Journal of Heat and Mass Transfer*, **38**(10), 1735-1749 1995.

[22] Yokuda, S. & Ramaprian, B.R. The Dynamics of Flow around a Cylinder at Subcritical Reynolds Number, *Physics of Fluids, A: Fluid dynamics*, **2**(5), 10.1063/1.857732, 1990.

[23] Norberg, C., Fluctuating Lift on a Circular Cylinder: Review and New Measurements, *Journal of Fluids and Structures*, **17**, 57-96, 2003.

NUMERICAL INVESTIGATION OF THE EFFECT OF OBSTACLES CONFIGURATION IN THE FLOW CHANNEL ON HEAT TRANSFER

İrfan KURTBAS*, Mehmet SENER, Selçuk KIZILCAOĞLU*, Hüseyin DURAN***
*Hitit University, Department of Mechanical Engineering, Çorum/Turkey
Email: ikurtbas@gmail.com, selcukkizilcaoglu@gmail.com, duranhsyn@yahoo.com.tr
**Hitit University, Scientific Technical Application and Research Centre, Çorum/Turkey
Email: mehmetsener45@gmail.com
*Corresponding Author: İrfan KURTBAS

ABSTRACT

In this study, the effects of rectangular obstacles placed in a square section channel on heat transfer and pressure drop are numerically investigated. The length of the channel is determined as 200 mm. The rectangular obstacles are arranged as concave, triangular, and flat side profiles when viewed from the side surface of the channel. Each obstacle has 3, 6, and 9 rows, and the maximum heights of the obstacles are determined to be 20, 40, and 60 mm. The obstacles are selected 3 mm thickness. Flow is considered in a hydrodynamically fully developed and thermally developing region. For the boundary conditions, constant heat flux was applied to the lower surface of the test section, and other surfaces were considered adiabatic. Air (Pr=0.7) was used as a working fluid. In the turbulent flow regime, analyzes were performed for the Reynolds numbers range of 10000-30000. For numerical analyses, the k-ω SST turbulence model was used in Ansys-Fluent 14.5 commercial program. In the arrangement of the obstacles, it was seen that the type of the flat obstacles provides maximum heat transfer. However, maximum pressure loss was also obtained in the same obstacle type.

Keywords: Numerical analysis, turbulent flow, concave resistance.

NOMENCLATURE

D_h	Hydraulic diameter [m]
k	Number of obstacles
L	Length of the test section
h*	Height of obstacles
Pr	Prandtl number
Re_D	Reynolds number
n	Type of fin
Nu	Nusselt number
Nu_m	Average Nusselt number
Nu_x	Local Nusselt number
$\dot{q}$	Heat generation
q''	Heat flux [W/m^2]
U	Velocity [m/s]
f	Darcy friction coefficient
c_p	Specific heat [J/kgK]
k	Turbulent kinetic energy
W	Wide of channel
α	Thermal diffusion coefficient
ε	Dispersion rate
ω	Specific diffusion rate
ρ	Density [kg/m^3]
ϕ	Viskos dissipation

1. INTRODUCTION

The effectiveness of convective heat transfer largely depends on the geometric structure of the heat exchanger. While changing the geometric structures, high heat transfer rates are provided, the need for more pump power arises as the resulting fluid circulation increases the pressure loss. Many studies on channel flow and control, which is one of the most common problems of engineering applications, have been practiced and presented to the literature. These problems have been studied experimentally and, or numerically. When the literature is examined, it is seen that a wide range of studies has been carried out.

Friction losses and heat transfer characteristics have been investigated experimentally by Akram and Dutta [1] in the rectangular duct with inclined and perforated blades. The results indicated that the direction, distance, and geometry of the fins placed on the upper surface of the channel affect the friction losses. Promvonge et al. [2] numerical calculations were carried out by placing obstacles that cut the flow direction at different angles into the square section channel. Air was used as a fluid. The Nusselt number and friction coefficient increased with increasing resistance height. Durmaz [3], studied the effect of an offset-strip fin on heat transfer and pressure loss was investigated experimentally and numerically. Experiments were carried out under laminar flow, constant heat flux, and constant temperature boundary conditions, and solutions were repeated using different fluids to examine the effect of Pr number. The heat transfer coefficient in the channel increased with the Reynolds number. High-pressure drop occurred.

On the other hand, Promvonge and Kwankaomeng [4] carried out experimental studies in a rectangular channel with V-shaped barriers placed at different heights, distances, and angles. It has been observed that the fins increase the Nusselt number and the amount of heat transfer decreases with the increase in the distance between the fins. Uslu [5] applied a constant heat flux boundary condition in a channel with an equilateral triangular cross-section under hydrodynamically fully developed, thermally developing flow conditions, and the effects of resistances with different elevation values placed in the test section of the channel on pressure loss and Nusselt number were examined. It was determined that with the increase of Reynolds number, Nusselt number and pressure loss increased. Experimental studies have been carried out by Promvonge [6] in a rectangular channel with a V-shaped obstacle placed in different heights, distances, and angles, in the range of 5000-25000 Reynolds numbers. It was observed that the amount of heat transfer decreased. The effect of concave and convex resistors placed in a rectangular channel by Karakaş [7] on heat transfer, pressure loss, and exergy loss in the system was investigated experimentally. In the experiments, it was found that the most critical parameter on heat transfer and pressure loss is Reynolds number. However, the number of resistances, resistance height, resistance diameter, and angle of resistance, and heat transfer is directly proportional. The literature was carried out by using fixed or movable obstacles in different angles, arrays, and geometries. Also, different shapes of channels such as square, rectangular, and triangle were used in applications. In the studies, applications were made by changing the fins' distance, the fin height, and the channel section rates.

In this study, the effect of placing rectangular obstacles in a square section channel on heat transfer was investigated numerically. Flow channel length was determined as 200 mm. The rectangular obstacles are arranged as shapes of triangular, concave, and flat concerning the channel side surface. The obstacles were placed on the heating surface 3, 6, and 9 rows, and analyzed for the maximum high values of the resistors 20, 40 and 60 mm. The obstacles are selected as 3 mm thickness. In the turbulent flow regime, analyzes were performed for the Reynolds number range of 10000-30000. By considering these parameters, the experiments to be carried out using the Desing-Expert program have been determined. The k-ω SST turbulence model was used in Ansys-Fluent 14.5 commercial program for numerical analyses.

2. MATHEMATICAL FORMULATION AND NUMERICAL MODEL

2.1 Physical Model

A square channel was considered as the flow channel (Figure 1). The flow channel consists of 3 main sections: inlet section, test section, and an outlet section.

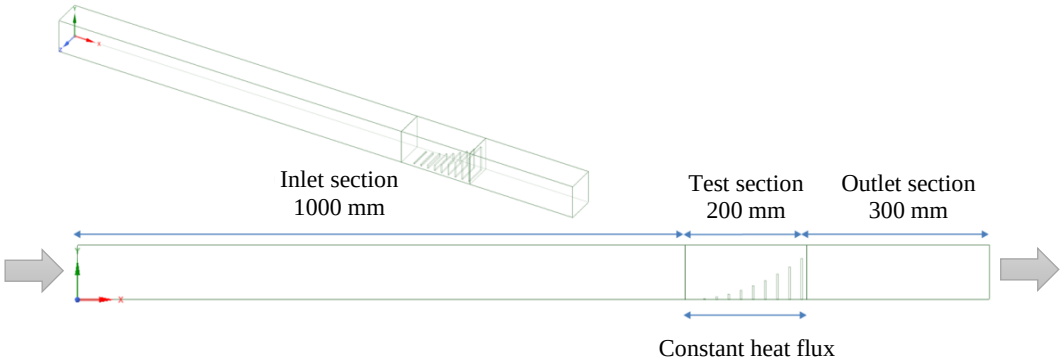

Figure 1. The view of the flow channel

The channel width and height are 80 mm. To ensure fully developed flow in the test section from hydrodynamically, the channel inlet length was determined at the inlet of the test section to be greater than ten times the channel hydraulic diameter. The channel inlet length is 1000 mm. The test section length is 200 mm, and the outlet section is 300 mm. Constant heat flux is applied to the base surface of the test section. Obstacles are placed as triangles, concave and flat shapes relative to the side surface of the test section.

In the test section, obstacles are placed in different values of the distance between the fins, and the obstacles height: triangle, concave, and flat profile. The representation of the obstacle's dimensions and the positioning of the resistance in the test section are shown in Figure 2.

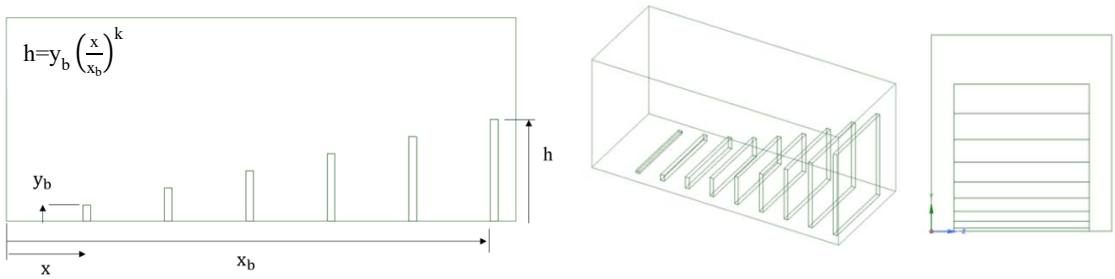

Figure 2. The view of the obstacle's position

The height of each fin is determined by using the Gardner function (Eq. 2.1). In the channel, for the k value in equation 2.1, n=1 (triangle), n=2 (concave) and n=0 (flat). Each fin in resistances is increasing to different maximum height values (y=20, y=40, y=60 mm), and there are different fin numbers (k=3, k=6, k=9). Totally 27 different models were obtained by placing resistances. The full view of the obstacle's position in the flow channel is given in Figure 2. In the test section, obstacles were placed so that the height of the resistance is triangular, concave and flat profile, and at different values of the distance between the fins. The values of geometric parameters are given in Table 1.

$$h=y_b\left(\frac{x}{x_b}\right)^k \tag{2.1}$$

The equation 2.2 has been given by Yüncü and Kakaç [8] to form a fully developed velocity profile in terms of hydrodynamics in turbulent flow conditions.

$$10\leq\frac{x_{fDh}}{D_h}\leq 60 \tag{2.2}$$

Table 1. Calculation of fin lengths for y=40 mm triangular resistance profile with six fins

S/N	x_b	y_b	x	x/x_b	y
1	190	40	30	0.157	6.32
2	190	40	62	0.326	13.05
3	190	40	94	0.494	19.79
4	190	40	126	0.663	26.53
5	190	40	158	0.831	33.26
6	190	40	190	1	40

2.2. Governing Equations

If there is motion in a material environment, the motion must behave according to the basic principles of mechanics and thermodynamics. The continuity, Reynolds averaged momentum, and time-averaged energy equations governing 3-D steady can be written in the cartesian coordinate system as follows:

Continuity;

$$\frac{\partial u}{\partial x}+\frac{\partial v}{\partial y}+\frac{\partial w}{\partial z}=0 \tag{2.3}$$

Momentum;

$$\frac{DV}{Dt}=\frac{\partial \rho}{\partial t}+\nabla.(\rho V)=0 \tag{2.4}$$

$$i\frac{\partial}{\partial x}+j\frac{\partial}{\partial y}+k\frac{\partial}{\partial z}=\nabla \tag{2.5}$$

Energy;

$$u\frac{\partial T}{\partial x}+v\frac{\partial T}{\partial x}+w\frac{\partial T}{\partial x}=\alpha\left(\frac{\partial^2 T}{\partial x^2}+\frac{\partial^2 T}{\partial y^2}+\frac{\partial^2 T}{\partial z^2}\right)+\frac{U}{c_p}\phi_u+\frac{\dot{q}}{\rho c_p} \tag{2.6}$$

2.3. Boundary Conditions

The fluid in the control volume was examined in 3-D. It is a Newtonian incompressible fluid. Its physical properties are fixed. Air is used as fluid (Pr=0.7). The fluid inlet temperature is 298 K, and inlet/outlet pressure is atmospheric pressure. Worked in the range of 10000≤Re≤30000. Radiative heat transfer and gravity effects are ignored. The air was used as a fluid at T_i=298 K temperature and inlet the channel at uniform velocity. U_i velocity for three different Reynolds numbers are defined at 1.9, 3.9, and 5.84 m/s.

$$\text{For } x=0, \qquad u=U_i \quad v=0 \quad w=0 \quad T=T_i \quad P=P_i \tag{2.7}$$

$$I= 0.16(Re_{Dh}) - \frac{1}{8} = 0.046 < \%5 \tag{2.8}$$

Turbulence intensity (I) is determined as %5 using equation 2.8. The insulated boundary condition is applied for the unheated surfaces of the channel.

$$\text{For } y=H, \qquad \frac{\partial T}{\partial y} = 0 \tag{2.9}$$

$$\text{For } z=\frac{W}{2}, \qquad \frac{\partial T}{\partial z} = 0 \tag{2.10}$$

A constant heat flux boundary condition is applied from the lower surface of the fin section of the channel (q"=2000 W/m^2).

$$\text{For y=0,} \qquad -k\left(\frac{\partial T}{\partial y}\right)=q'' \tag{2.11}$$

There is no slippage in the channel walls;

$$\text{For y=0 and y=H,} \quad u=v=w=0 \text{ and for } z=\frac{W}{2},\ u=v=w=0 \tag{2.12}$$

To shorten the solution of the problem, the symmetry boundary condition was applied to our model with a symmetrical shape at z=40 mm.

$$\text{z=40 mm,} \qquad \frac{\partial u}{\partial z}=0,\ \frac{\partial v}{\partial z}=0,\ \frac{\partial w}{\partial z}=0,\ \frac{\partial T}{\partial z}=0 \tag{2.14}$$

The fluid comes out to the environment after it leaves the channel. In Fluent, this situation was chosen a "pressure-outlet". Outdoor temperature was chosen as 298 K.

$$x=1500 \text{ mm} \qquad u=Uo,\ T=To,\ P=Po \tag{2.15}$$

$$Re=\frac{\rho u D_h}{\mu} \tag{2.16}$$

2.4. Mesh Optimization

Calibration experiments carried out in the empty channel were carried out at the highest speed value of 30000 Reynolds. As shown in Figure 3, the number of cells is changed between approximately 500000 and 3000000, and a different number of analyzes were made. Figure 3 shows that the numbers of cells of Nu and surface friction coefficients does not change much after 1000000. Therefore, it is observed that the increase in the number of mesh did not affect the solution. For this reason, the number of mesh is approximately 1000000 selected.

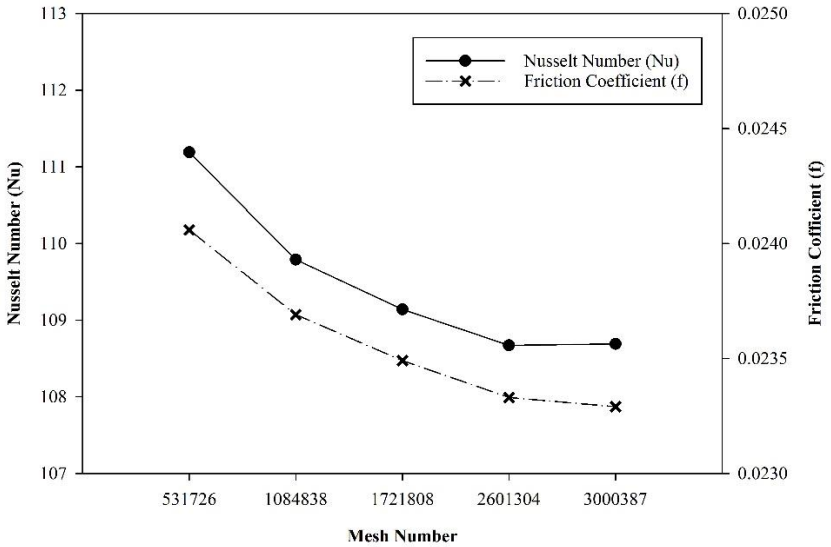

Figure 3. Grid sensitivity check of the computational results of Nusselt number and friction coefficient

The solutions were calculated up to 10^{-8} residue value as seen in Table 2. After 10^{-4}, Nusselt and the surface friction coefficient values were chosen as the residue value since it appears to have remained unchanged. Solutions were repeated several times in different cell numbers. During these solutions, iterations were stopped at certain intervals, and the difference between the results was examined. As a result of this examination

observed that Nu and f values did not change after 1000 iterations, so that the results obtained were independent of the number of iterations.

Table 2. Change of Nu and f numbers according to residual values for Re_D=30000 in an empty channel

Nusselt Number (Nu)	Friction Coefficient (f)	Nu %	f %	Residue values
110.34	0.03197	–1.495	–27.119	10^{-3}
108.69	0.023305	0	–0.024	10^{-4}
108.69	0.023299	0	–0.010	10^{-8}
108.69	0.023297			10^{-8}

3. RESULTS

In Figure 4, the effect of obstacles number (k), obstacles type (n), and Reynolds number (Re_D) on average Nusselt number (Nu_m) for the values of obstacles heights (h*=0.25 and h*=0.75) are given. For h*=0.25, the Nusselt number value varies around 50 in Reynolds number's value of 10000.

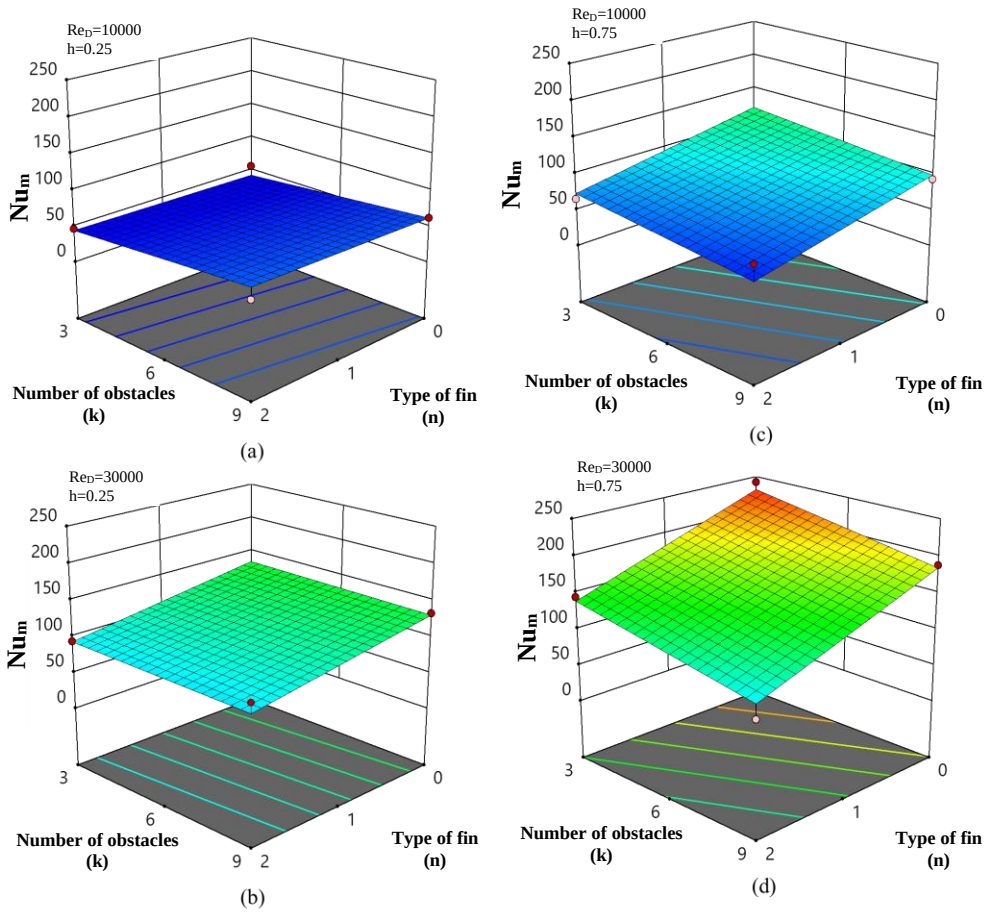

Figure 4. Variation of avarange Nusselt (Nu_m) number for the resistance height (h*=0.25 h*=0.75) with Re_D=10000-30000

At the low values of h* and Re_D, the effect of the number of resistors on Nu_m is relatively low, and as the number of obstacles increases from 3 to 9, the increase on Nu_m is about 10%. However, the effect of the type of the obstacle is negligible (Figure 4 (a)). At the high value of Re_D, the effect of the number of fins on Nu_m is almost negligible, while the number of obstacles increases linearly when it passes from concave (n=2) to level (n=0); this increase is around 55% (Figure 4 (b)).

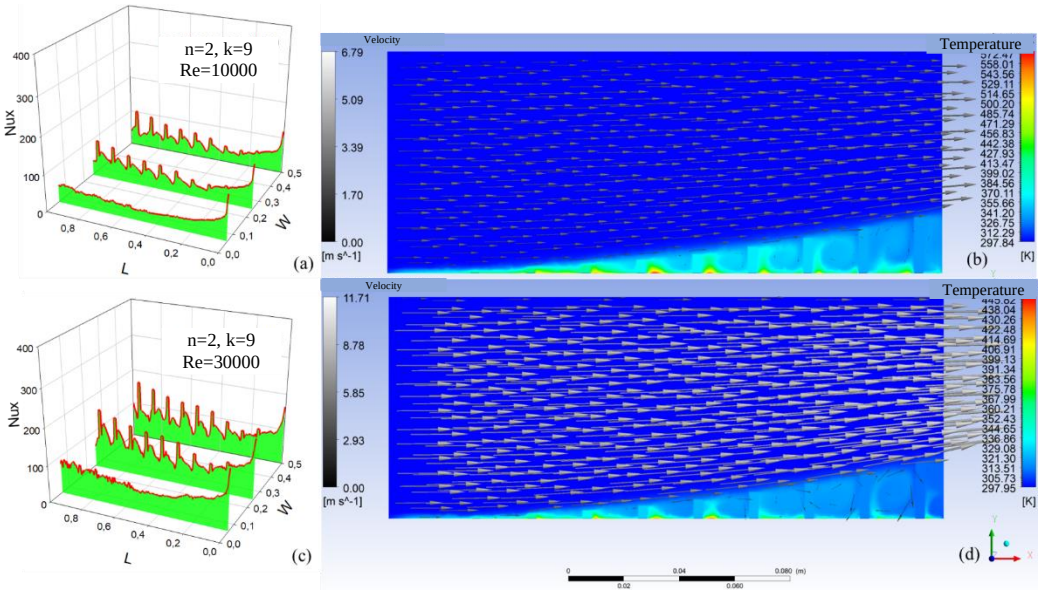

Figure 5. Velocity and temperature contours and local Nu number values for Re=10000-30000

The results have shown that in Figure 5, variation of local Nusselt number (Nu_x), velocity and temperatures distributions in the concave (n=2) type of fin with a 20 mm obstacle height (h*=0.25) and nine obstacles numbers (k) according to the Re_D numbers. As the test section approaches the symmetry surface, it is seen that the number of local Nusselt (Nu_x) increases, and as it moves away from the surface, the number of Nu_x decreases depending on the length of the channel (L). In Figure 5 (a), see that the obstacles used in the test section of the channel are both expanded and cause periodic rupture of the boundary layer.

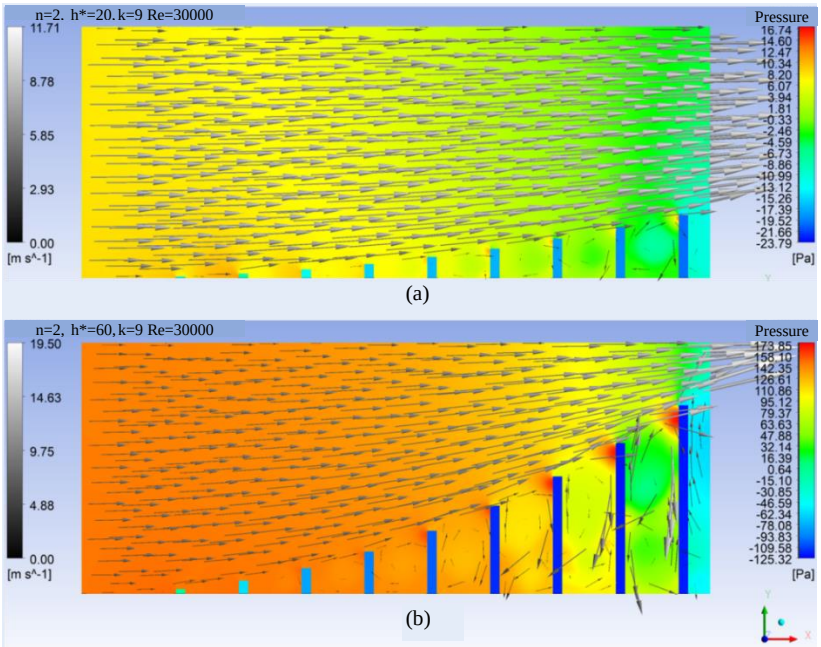

Figure 6. Velocity and pressure contours for Re=30000

In Figure 5 (b), it is seen that the velocity vectors do not make a high value difference in the entrance and exit of the test section. Accordingly, as the resistance height (h*) decreases in the concave (n=2) type of resistance, it is seen that the resistance of the fins decreases, the working fluids break off the surface, and accordingly, the heat absorption decreases. Increased obstacles height (h*) throughout the test section; increases the fin effect of the resistors, however, the results in the increases of the vortex area formed on the heating surface. The fin effect of the resistors up to a certain value of the resistance height (h*) is almost low. As Re_D=30000, the symmetry surface of the Nu_x test section rises to about 170. Similarly, in the concave (n=2) resistance configuration, it is seen that the amount of in regions with low resistance height (h*) is less. However, as the resistance height increases, the amount of heat absorption is higher (Figure 5 (c), (d)). The working fluid and surface temperature difference is higher at the entrance of the test section and this, difference decreases throughout the test section. This situation results in higher Nu_x at the inlet of the test section. In the concave (n=2) resistance geometry, the change in velocity-pressure distributions for Re_D=30000 in the resistance height values of 20 mm (h*=0.25) and 60 mm (h*=0.75) is shown in Figure 6. For the obstacle height h*=0.25, the maximum pressure occurs on the first resistance surface, and when h*=0.75, the pressure value at the same point is higher (Figure 6 (a), (b)). Increasing the obstacle height starting from the channel inlet increased the velocity of the working fluid in the test section. Figure 6 (b) shows that the working fluid velocity of the test channel is reached maximum values.

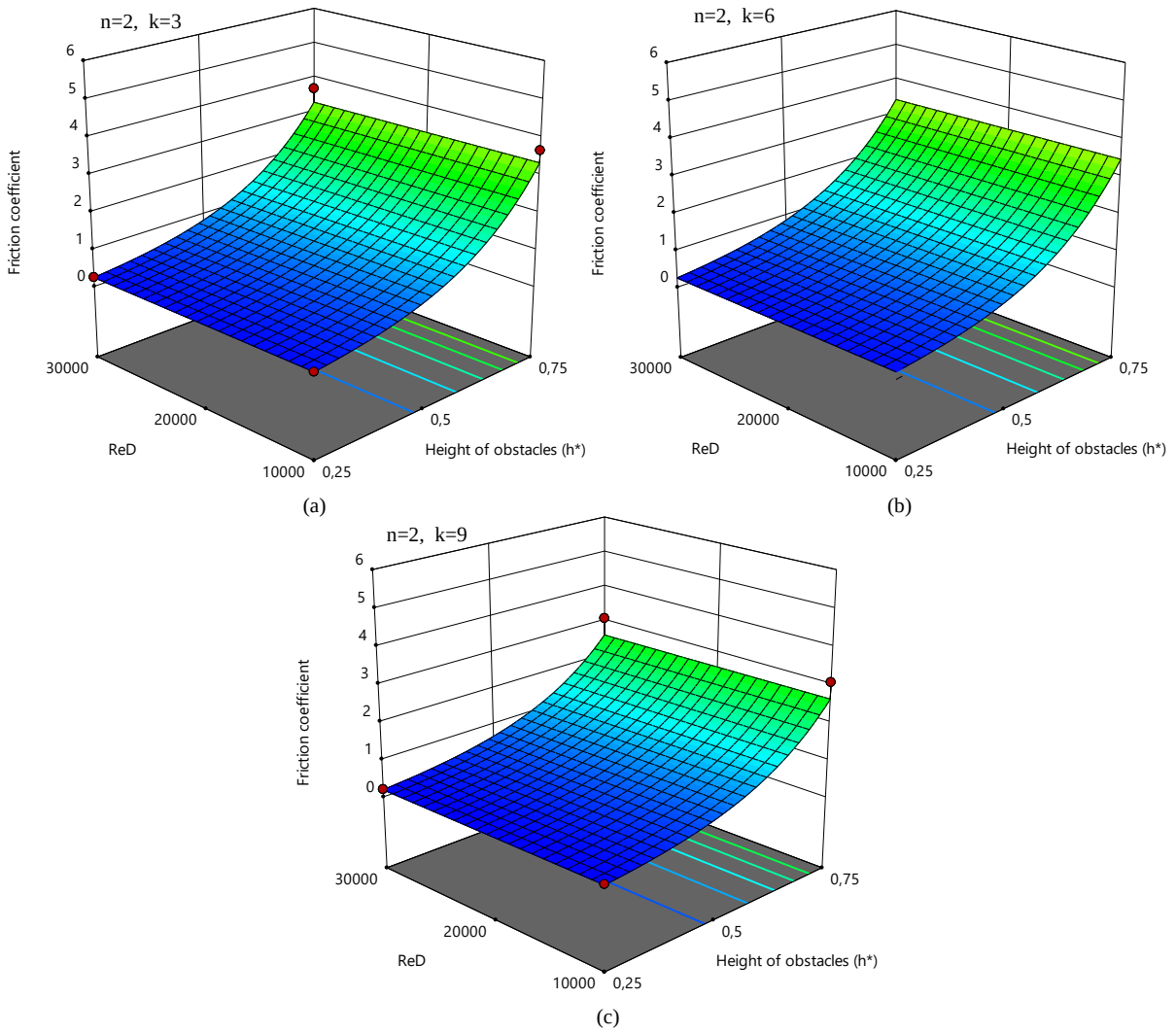

Figure 7. Effect of number of obstacles (k) on friction coefficient (f) in convex obstacle type

As seen in Figure 7 (a), (b), and (c), the effect of the inertia forces and the Reynolds number (Re_D) showing the effect of the viscous forces on the friction force (f) are lower, while the resistance height (h*) has a more significant effect. As a possible cause of this situation, obstacles placed in the test section and changes in height changes throughout the test section can be shown.

4. CONCLUSION

In this study, the effect of obstacles configurations arranged at different heights throughout the test section as flat (n=0), triangle (n=1), and concave (n=2) was investigated. Analyzes were made by changing the obstacles numbers (k) between 3 and 9, resistance height (h*) by 20-60 mm, Reynolds number (Re_D) between 10000 and 30000, and study results were obtained numerically. The findings are listed below.

- Heat transfer increased with the increase in the number of Re_D, and with this, pressure losses also increased.
- As the distance between the resistances decreases, that is, the number of resistances (k) increases, free zones are formed between the obstacles. In this case, although the fin effect increased, the amount of heat drawn from the heating surface decreased.
- As the resistance height (h*) increases, the fin behavior of the obstacles increases, and accordingly, the heat transfer increases.

ACKNOWLEDGMENT

The authors would like to thank to the Hitit University Scientific Research Project Department for the grant with the Project numbers MUH19004.13.004.

REFERENCES

[1] Akram, H., Dutta, P. 2004. Internal Cooling Augmentation In Rectangular Channel Using Two Inclined Baffles, *International Journal of Heat and Fluid Flow*. **26** (2005) 223–232.

[2] Promvonge, P., Sripattanapipat, S., Tamna, S., Kwankaomeng, S. 2009. Numerical investigation of laminar heat transfer in a square channel with 45° inclined baffles, *International Communications in Heat and Mass Transfer*. **37** (2010) 170–177.

[3] Durmaz, G. 2009. Experimental and Numerical Analysis Of Heat Transfer Performance Of Off–Set Strip Fins, Yüksek Lisans Tezi, İzmir Yüksek Teknoloji Enstitüsü, İzmir.

[4] Promvonge, P., Kwankaomeng, S. 2010. Periodic laminar flow and heat transfer in a channel with 45° staggered V–baffles, *International Communications in Heat and Mass Transfer*. **37** (2010) 841–849.

[5] Uslu, R. 2010. Üçgen Kesitli Kanallarda Zorlanmış Akış İle Isı Transferinin Sayısal Olarak İncelenmesi. Yüksek Lisans Tezi, Gazi Üniversitesi Fen Bilimleri Enstitüsü, Ankara.

[6] Promvonge, P. , 2010. Heat transfer and pressure drop in a channel with multiple 60° V–baffles, *International Communications in Heat and Mass Transfer.* **37** (2010) 835–840.

[7] Karakaş, A. 2012. Konveks ve Konkav Dirençlerin Isı Transferine Etkisinin Zorlanmış Konveksiyon Şartlarında İncelenmesi. Yüksek Lisans Tezi, Hitit Üniversitesi Fen Bilimleri Enstitüsü, Çorum.

[8] Yüncü, H., Kakaç, S. 1999. Temel Isı Transferi. Ankara: Bilim Yayıncılık

[9] Ansys, 2014, Ansys® Academic Research, Release 14.5, Ansys Fluent User's Guide, Ansys, Inc.

MODELING AND PERFORMANCE OF A THERMOELECTRIC REFRIGERATOR

Haydar KEPEKCI*, Ergin KOSA, Cuneyt EZGI*****
*Mechanical Engineering Department, Beykent University, Istanbul, Turkey.
E-mail: haydarkepekci@beykent.edu.tr
**Mechanical Engineering Department, Beykent University, Istanbul, Turkey.
E-mail: erginkosa@beykent.edu.tr
***Marine Engineering Department, Piri Reis University, Istanbul, Turkey.
E-mail: cezgi@pirireis.edu.tr

ABSTRACT

Thermoelectric refrigerators are widely used in electronics, medical, and food industry application areas. A refrigeration effect can also be achieved without using any moving parts by merely passing a small current through a closed circuit made up of two dissimilar materials. This effect is called the Peltier effect, and a refrigerator that works on this principle is called a thermoelectric refrigerator. They consist of several thermoelectric legs sandwiched between two thermally conductive plates, one cold and one hot. Thermoelectric refrigerators presently cannot compete with the vapor-compression refrigeration system because of their low-performance coefficient (COP). However, some applications have been preferred because of their small size, simplicity, quietness, and reliability. In this study, a thermoelectric cooler having a maximum cooling power of 50 W, having a dimension of 40mmx40mmx3.6 mm, is modeled in multi-physics software. Also, the performance of a thermoelectric refrigerator is investigated. It is computed the temperature difference between ceramics plates versus electric current and COP for a temperature difference between ceramics plates. The simulation results are compared with experimental values.

Keywords*:* Thermoelectric, COP, refrigerator, CFD, modeling

1. INTRODUCTION

Thermoelectric systems were initially examined about 70 years ago, and the use of these devices for air-conditioning and cooling implementations were evaluated shortly later [1]. For years, thermoelectric trading modules have been present, and their price has reduced in the time. With researchers' work, thermoelectric devices convert heat energy into electrical energy in the form of a temperature gradient or convert electrical power into a temperature gradient [2]. The thermoelectric modulus technic is the best economic remedy for causes. The thermoelectric modules are usual off-the-shelf parts, the relevance of their running voltages to series-parallel electrical circuitry, simple montage, and small size [3]. A thermoelectric cooler is a little heat pump that has the benefit that there are no moving components.
Thermoelectric modules are mini, lightweight, and can provide cooling below atmospheric temperature. Thermoelectric systems are environmentally friendly as they do not use any refrigerant during operation [4]. The positive aspects of these devices are; reliability, quiet operation, and compactness. As a result, it has attracted many researchers' attention in terms of developing and expanding thermoelectric systems. Furthermore, various reports have demonstrated the feasibility of using thermoelectric modules as a promising alternative for conventional air cooling and heating systems [5]. One reason why thermoelectric cooling systems can be widely used in electronic devices is; temperature control capacity is to provide an efficient heat transfer. It also offers advantages such as high reliability and fast thermal response [6].

The thermoelectric modulus supplies heat transfer through alteration in the energy level of the electrons. The current low energy level P-type semiconductors and high energy level N-type semiconductors transport the heat energy from the cold surface to the hot surface [7]. Another name for thermoelectric refrigerants is Peltier. The

Peltier module is created by the serial link of P-type and N-type elements. The Peltier impact happens with the direct current by the Peltier components. In this process, one surface of the thermoelectric modulus cools while the other surface heats [8]. The Peltier module is shown in Fig. 1.

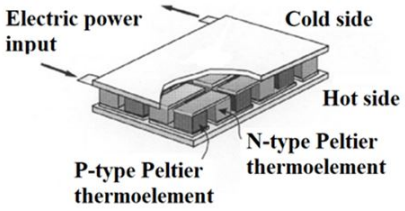

Figure 1. Thermoelectric cooler

In the system shown in Fig. 1, heat is absorbed from the refrigerated space and rejected to the warmer environment. The difference between these two quantities is the net electrical work that needs to be supplied. For the Peltier cooling systems to work correctly, the module's hot side needs to be cooled. Therefore, when designing thermoelectric cooling systems, a cooling component such as a fan should be added. Thermoelectric refrigeration based on the Peltier impact has significant benefits check against traditional vapor technology, although its COP is not as high a vapor-compression technology. Today, thermoelectric cooling's practice fields contain thermoelectric refrigeration, automobile cooling, thermoelectric air-conditioning, photovoltaic-thermoelectric hybrid system, and freshwater production [9].

Tan et al. studied a thermoelectric system for air conditioning with the combination of a phase transition matter as an option to the refrigerant. The addition of phase changer matter led to a 56% increase in thermoelectric module performance [10]. Dessel and Messac experimentally analyzed the thermoelectric performance as an air conditioning system with the combination of the PV system for the procurement of electricity with different electrical connections, input current, and other voltage values. Experimental results demonstrated that the input current alteration does not influence the temperature of the cold surface, but rather the temperature of the hot surface is much influenced. They decided that the cold side's temperature achieves steady-state and stability circumstances faster than the hot surface [11].

Chinguwa et al. designed an environmentally friendly in-car cooler. They used a thermoelectric cooler in the portable design of 20 liters. As a result of their work, they have significantly reduced exhaust gas to the environment [12]. Tan and Demirel conducted an experimental study using three different cooling systems to examine the temperature and performance of the CPU and the motherboard. The systems used are; heat sink, water cooling system, and thermoelectric cooler. Their results found that the thermoelectric cooling system had better cooling performance than the other two systems under continuous operating conditions [13]. Huang et al. devised a new style procedure for thermoelectric cooler systems in that an experimentally created performance curve of the thermoelectric module was done for design computation. Furthermore, the automated testing furnishing was devised and made to take the test. Considering the performance test outcomes, an empiric correlation was obtained for Peltier module performance, and the sequel was used in the system research of a thermoelectric cooler [14].

Karimi et al. analyzed a pyramid-type multi-stage cooling focusing on the significance of the highest achievable target heat flux and performance coefficient. As a result of the study carried out as numerical simulation, the hot side heat sink's thermal resistance, a multi-stage thermoelectric cooler, has a crucial role in determining all performance [15]. Riffat et al. developed a computer model to measure the performance of a thermoelectric heat pump system. They compared the numerical results with experimental data. They analyzed the reasons for the differences and optimized the computer model. Their work was the basis for analyzing and designing the thermoelectric heat pump system [16]. Gökçek and Sahin performed an experimental performance analysis of a mini channel water-cooled thermoelectric refrigerator. The cooling system of the fridge used in the experiment; consists of the mini-channel heat sink on the hot side and two thermoelectric modules integrated with heat distributors on the cold side. As a result, they concluded that the mini-channel heat sink's performance was as good as other liquid-cooled systems [17].

Nagy and Buist analyzed a thermoelectric cooler's performance and indicated a critical performance decrease due to the thermal resistance of heat sinks. They concluded that the thermal resistance of the heat sinks and the thermal interfaces among the modulus and the heat sinks should be reduced to reach the best feasible refrigerating performance [18].

The primary purpose of the thermoelectric refrigerator research was to investigate the cooling performance. The coefficient of performance (COP) for the refrigerator is accepted as the performance criterion. This value is the ratio between the cooling load and electrical power consumption. Refrigerators' performance is expressed in terms of the COP as ratio work input of the cooling effect.

In this paper, a thermoelectric cooler having a maximum refrigerating power of 50 W, having a dimension of 40mmx40mmx3.6mm, is modeled in computational fluid dynamics software. A prototype cooler with the same characteristics has been designed, and experimental work has been done. The data obtained from the numerical analysis and the data obtained from the experiments have been compared.

2. EXPERIMENTAL METHOD

Figure. 2. Prototype thermoelectric cooler system

As shown in Fig. 2, the experimental equipment is installed in a controlled volume. For the Peltier cooler to work well, one above the thermoelectric cooler module and the other above the closed box, two cooling fans' control volume, two cooling fans, and two heat sinks are used. The thermoelectric cooler's underside is designed as a cold area in the prototype system, and appropriate insulation is made. The dimensions of the rectangular covering are selected as 500 mm x 500 mm x 250 mm. Insulation has been provided by using approximately 50 mm thickness Styrofoam on the cooling side. The size of the cooling side is 215mm x 175mm x 130mm.

The installation also contains the electronic components necessary for the operation of the system. The model of the thermoelectric cooler used has been chosen as TEC1-12706. The dimensions of the thermoelectric cooler module used in the system shown in Fig. 3 are 40x40x3.6 mm. The specification of the TEC1-12706 conditions is provided in Table 1.

Figure. 3. Thermoelectric cooler module

Table 1. Performance specifications of TEC1-12706

Hot Side Temperature [ºC]	25 [ºC]	50 [ºC]
Q_{max} [W]	50	57
Delta T_{max} [ºC]	66	75
I_{max} [A]	6.4	6.4
V_{max} [V]	14.4	16.4
Module Resistance [Ω]	1.98	2.30

All temperatures have been measured using thermocouples with a sensitivity of ± 1 C. In this system, the ammeter has used for current measurement; the voltmeter has used for voltage measurement; the ohmmeter has used for resistance measurement. The operating range and sensitivity of the measuring devices used are given in Table 2.

Table 2. Physical properties of the devices used

Device Type	**Range**	**Sensitivity**
Thermometer	-50 [ºC] – 300 [ºC]	1 [ºC]
Voltmeter	0.1 [mV] – 600 [V]	%0.5 + 3
Ohmmeter	0.1 [Ω] – 40 [MΩ]	%0.5 + 2
Ammeter	0.1 [A] – 400 [A]	%1.5 + 3

Cooling fins (heat sink) are fabricated of aluminum and attached to the thermoelectric refrigerator's surfaces to reduce their operating temperatures. Small fans are used to induce forced convection over the fins.

3. SIMULATION METHOD

A simulation methodology has been examined on a thermoelectric cooler with the parameters used in the experimental study. After the computations are completed, the results are compared with data from the experimental.
The 3D mesh domain image of the thermoelectric cooler analyzed is, as shown in Fig. 4. This mesh has contained about 170,000 cells.

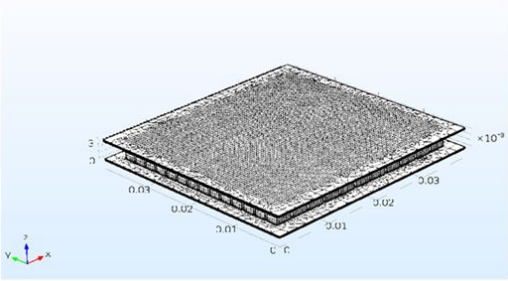

Figure 4. General view of mesh case

The mesh file's size parameters have been selected as follows; the maximum element size is $2x10^{-4}$, minimum element size is $2x10^{-6}$, the maximum element growth rate is 1.3, curvature factor is 0.2, resolution of narrow regions is 1. The geometry and their mesh have been created using computational fluid dynamics software.

The material of the P-Type and N-Type semiconductor elements of the thermoelectric cooler is selected as Bismuth Tin, the conductor's material is copper, and the ceramic material is Tungsten.

Table 3. Properties of Bismuth Tin

Property	**Expression**
Heat capacity at constant pressure (c_p)	171.6588 [J/(kg.K)]
Density (ρ)	8340 [kg/m^3]
Seebeck coefficient (α)	-55x10^{-6} [V/K]
Electrical conductivity (σ)	6.0976x10^4 [S/m]
Thermal conductivity (k)	24.5 [W/(m.K)]
Relative permittivity (ξ)	1

The meshes are structured inside of the geometry. The purpose of the analysis is to measure the coefficient of performance values at different currents. As current values, 1.5 A, 3 A, 4.5 A, and 6 A have been selected. Analyzes have been performed for both 25 ºC and 50 ºC.
SNOPT has been chosen as the solver method. SNOPT is a specific application, which is making use of a semidefinite quadratic programming solver. It is based on a finite-memory quasi-Newton approach to the Hessian of the Lagrangian and uses a Reduced-Hessian algorithm (SQOPT) for resolving the quadratic programming subproblems. It is designed for many thousands of limitations and factors but an average number of degrees of freedom [19]. In the analysis, a PC with "Intel (R) Core (TM) i7-4710HQ CPU@2.50GHz, four cores" has been used. This computational time was approximately 20 minutes.

4. RESULTS

As a result of the analysis for the surface temperature of 25 ºC, the maximum temperature difference has been calculated to be 21.150 K. The current required to obtain this value is 6 A. The required voltage is 0.44423 V. The overall electrical resistance is 0.074038 Ω. The maximum heat dissipation is 12.285 W; the maximum coefficient of performance is 1.091.

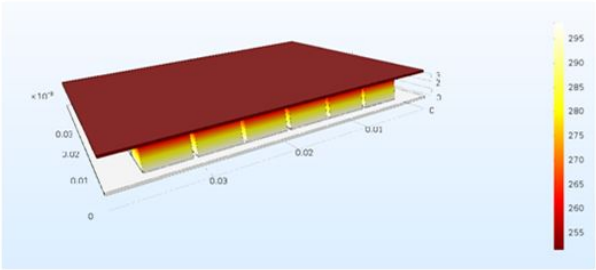

Figure 5. Surface Temperature for T_h= 25 ºC

The figure for merit is 0.0023945 1/K. As can be seen from Fig. 5, the surface temperature of the hot side goes up to 255 K, and at combining points, the temperature can be up to 295 K.

The temperature difference of the thermoelectric cooler has increased as the current has increased. The change of I (A) versus ΔT (K) for T_h= 25 ºC is illustrated in Fig. 6.

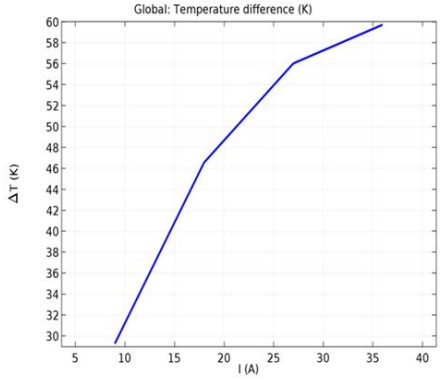

Figure 6. The change of I (A) versus ΔT (K) for T_h= 25 ºC

The temperature difference of the thermoelectric cooler has reduced as the cooling load has increased. The change of cooling load versus ΔT (K) for T_h= 25 ºC is illustrated in Fig. 7.

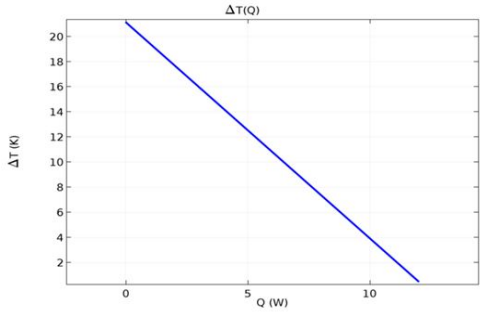

Figure 7. The change of Q (W) versus ΔT (K) for T_h = 25 ºC

For temperature differences between ceramics plates of 20 K, 40 K, and 60 K, the change of COP versus the relative applied current I/Imax, from 0.1 to 0.9, is depicted in Fig. 8.

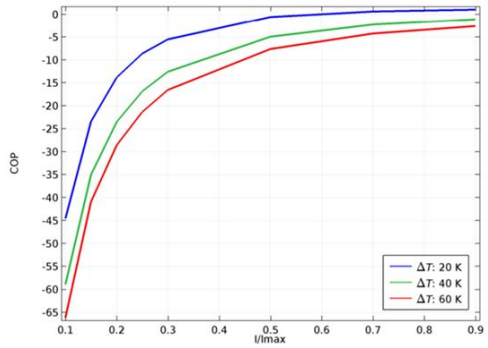

Figure 8. The change of IImax versus COP for T_h =25 ºC

In Fig. 9, Fig. 10, Fig. 11, and Fig. 12; T_h= 25 ºC; COP coefficients at different current for each ΔT value are given both experimentally and numerically. As the current has increased, the COP of the thermoelectric cooler has reduced. As indicated in the graphs, it can be said that experimental and numerical results confirm each other.

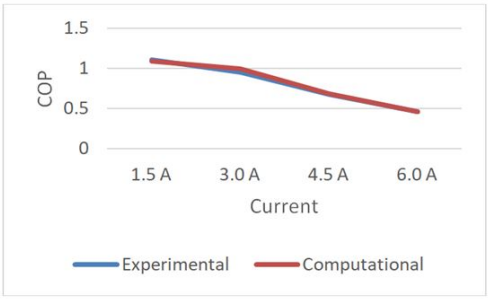

Figure 9. Current-dependent COP for T_h = 25 ºC and ΔT=20 K

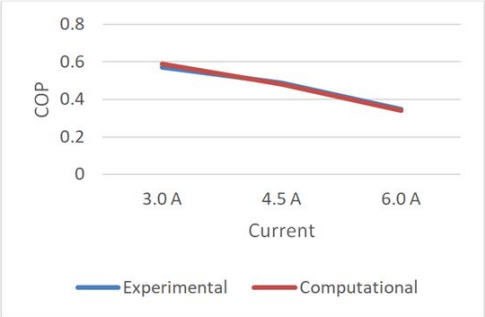

Figure 10. Current-dependent COP for T_h = 25 ºC and ΔT=30 K

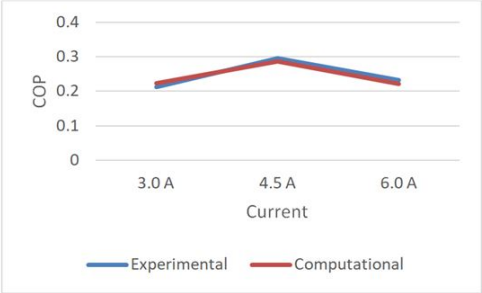

Figure 11. Current-dependent COP for T_h = 25 ºC and ΔT=40 K

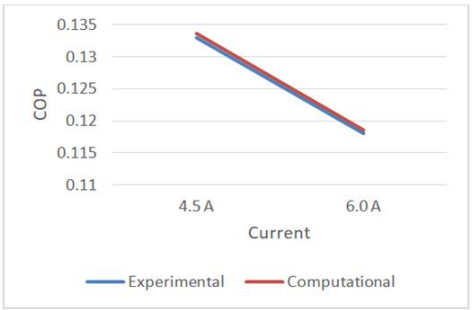

Figure 12. Current-dependent COP for T_h = 25 ºC and ΔT=50 K

Since the thermoelectric cooler's cooling load is zero at 3 A in T_h = 25 ºC and ΔT=50 K, it is not considered in Fig. 12.

As a result of the analysis for the surface temperature of 50 ºC, the maximum temperature difference has been calculated to be 24.496 K. The current required to obtain this value is 6 A. The required voltage is 0.50462 V. The overall electrical resistance is 0.084103 Ω. The maximum heat dissipation is 13.844 W; the maximum coefficient of performance is 1.445. The figure for merit is 0.0023767 1/K. The hot side's surface temperature goes up to 265 K. Surface Temperature for T_h= 50 ºC is shown as Fig. 13.

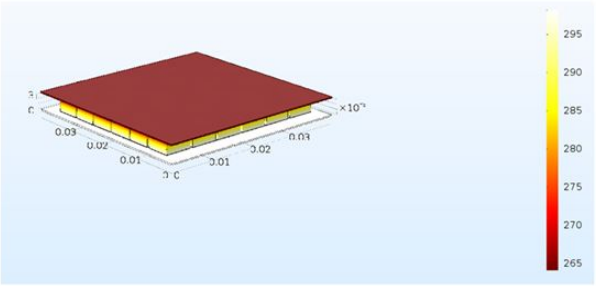

Figure 13. Surface Temperature for T_h = 50 ºC

The change of I (A) according to ΔT (K) for T_h= 50 ºC is shown in Fig. 14. The change of Q (W) according to ΔT (K) for T_h= 50 ºC is demonstrated in Fig. 15. The change of I/I_{max} according to COP for T_h= 50 ºC has been shown in Fig. 16.

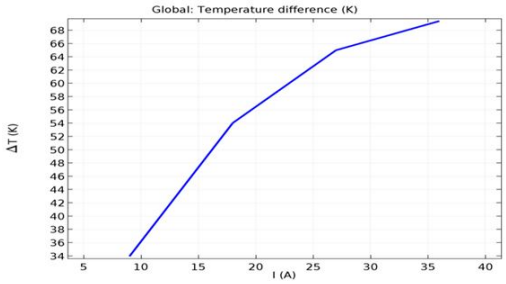

Figure 14. The change of I(A) versus ΔT(K) for T_h = 50 ºC

The temperature difference of the thermoelectric cooler has increased as the current has increased. The change of I (A) versus ΔT (K) for T_h= 50 ºC is illustrated in Fig. 14.

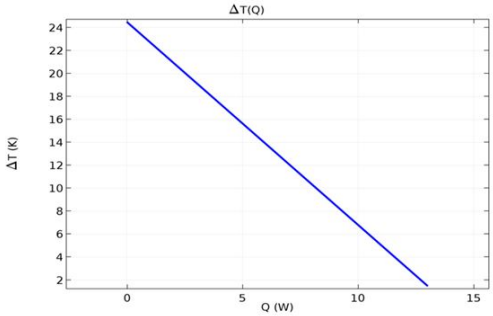

Figure 15. The change of Q(W) versus ΔT(K) for T_h =50 ºC

The temperature difference of the thermoelectric cooler has reduced as the cooling load has increased. The change of cooling load versus ΔT (K) for T_h= 50 ºC is illustrated in Fig. 15.

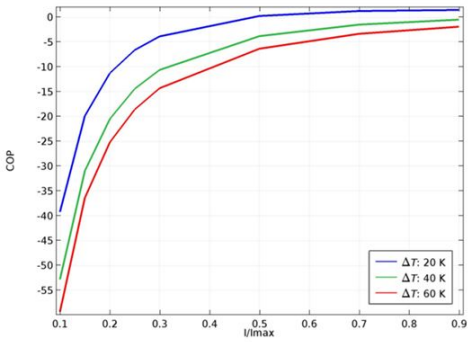

Figure 16. The change of IImax versus COP for T_h = 50 ^{O}C

For temperature differences between ceramics plates of 20 K, 40 K, and 60 K, the change of COP versus the relative applied current I/Imax, from 0.1 to 0.9, is depicted in Fig. 16.

In Fig. 17, Fig. 18, Fig. 19. 20; T_h= 50 ºC; COP coefficients at different current for each ΔT value are given both experimentally and numerically.

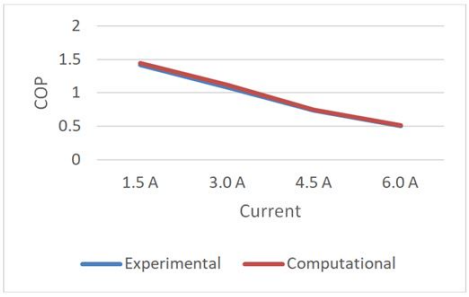

Figure 17. Current-dependent COP for T_h = 50 ºC and ΔT=20 K

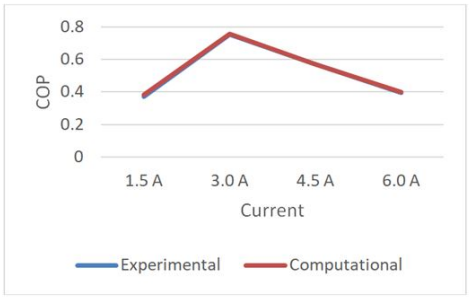

Figure 18. Current-dependent COP for T_h = 50 ºC and ΔT=30 K

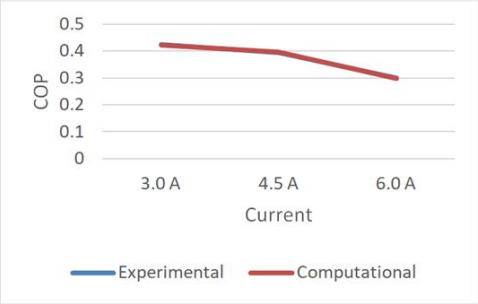

Figure 19. Current-dependent COP for T_h = 50 ºC and ΔT=40 K

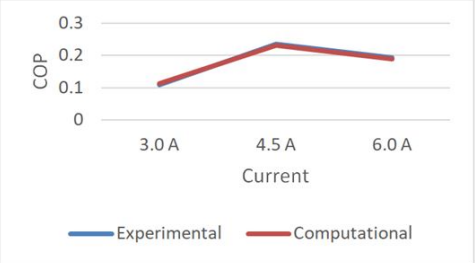

Figure 20. Current-dependent COP for T_h = 50 ºC and ΔT=50 K

Looking at the graphs obtained, it can be said that experimental and numerical results confirm each other.

5. CONCLUSION

In this study, thermoelectric refrigerators used in different sectors have been studied. The thermoelectric cooling module with 40 mm x 40 mm x 3.6 mm dimensions is used, which works with the Peltier effect principle; a prototype cooling system is designed. This design has been put into production to perform experimental studies and modeling for numerical analysis. The data obtained from the analyses have been compared with the experimental results and found to agree with each other. For the surface temperatures of 25 ºC and 50 ºC, the maximum coefficients of performance have been computed to be 1.091 and 1.445, respectively.
In general, as the temperature of hot surfaces has increased for the same temperature differences, the COP of the thermoelectric cooler has increased.

Although the coefficients of thermoelectric coolers' performance are low, due to their quiet operation, simple installation, and reliability, they are widely used in low current areas. In future studies, it will be investigated how to improve the COP of thermoelectric coolers.

REFERENCES

[1] Riffat S.B., Ma X., Wilson R. Performance simulation and experimental testing of a novel thermoelectric heat pump system, *Applied Thermal Engineering*, vol:26, 494-501, 2006.

[2] Riffat S.B., Ma X. Thermoelectrics: a review of present and potential applications, Applied *Thermal Engineering*, vol:23, 913–935, 2003.

[3] Rowe D.M. Application of thermoelectric cooling, *CRC handbook of thermoelectrics*, 617–683, 1995.

[4] Riffat S.B., Ma X. Thermoelectrics: a review of present and potential applications, *Applied Thermal Engineering*, vol:23, 913–935, 2003.

[5] Nassar M., Hegazi A. Mousa M. Combined effect of pulsating flow and magnetic field on thermoelectric cooler performance, *Case Studies in Thermal Engineering*, vol:13, 100403, 2019.

[6] Lin Z., Hongbo T., Jianlin Y. Analysis of optimal heat exchanger size of a thermoelectric cooler for electronic cooling applications, *Energy Conversion and Management*, vol:76, 685–690, 2013.

[7] Tan S.O., Demirel H. Performance and cooling efficiency of thermoelectric modules on server central processing unit and Northbridge, *Computers and Electrical Engineering*, vol:46, 46-55, 2015.

[8] Gao M., Rowe D. Cooling performance of the integrated thermoelectric micro cooler, *Solid-State Electronics*, vol:43, 923–929, 1999.

[9] Gökçek M., Sahin F. Experimental performance investigation of mini channel water cooled-thermoelectric refrigerator, *Case Studies in Thermal Engineering*, vol:10, 54-62, 2017.

[10] Tan G., Zhao D. Study of a thermoelectric space cooling system integrated with phase change material, *Applied Thermal Engineering*, vol:86, 187-198, 2015.

[11] Xu X., Dessel S.V., Messac A. (2007) Study of the performance of thermoelectric modules for use in active building envelopes, *Building and Environment Journal*, vol:3, 1489–1502, 2007.

[12] Chinguwa S., Musora C., Mushiri T. (2018) The design of portable automobile refrigerator powered by exhaust heat using thermoelectric, 15th Global Conference on Sustainable Manufacturing, *Procedia Manufacturing*, vol:21, 741-748, 2018.

[13] Tan S.O., Demirel H. Performance and cooling efficiency of thermoelectric modules on server central processing unit and Northbridge, *Computers and Electrical Engineering*, vol: 46, 46–55, 2015.

[14] Huang B.J., Chin C.J., Duang C.L. A design method of a thermoelectric cooler, *International Journal of Refrigeration*, vol:23, 208-218, 2000.

[15] Karimi G., Culham J.R., Kazerouni V. Performance analysis of multi-stage thermoelectric coolers, *International Journal of Refrigeration*, vol:34, 2129-2135, 2011.

[16] Riffat S.B., Ma X., Wilson R. Performance simulation and experimental testing of a novel thermoelectric heat pump system, *Applied Thermal Engineering*, vol:26, 494-501, 2006.

[17] Gökçek M., Sahin F. Experimental performance investigation of mini channel water cooled-thermoelectric refrigerator, *Case Studies in Thermal Engineering*, vol:10, 54-62, 2017.

[18] Nagy M.J., Buist R.J. Effect of heat sink design on thermoelectric cooling performance, *AIP Conference Proceedings*, 147-149, 1994.

[19] Gill P., Murray W., Saunders M. SNOPT: An SQP Algorithm for large-scale constrained optimization, SIAM Review, vol:12(4), 979-1006, 2002.

CFD ANALYSIS OF FLUID PASSING THROUGH VENTURIMETER

Filiz ÖZGEN*, Celal KISTAK**
*Fırat University, Department of Mechanical Engineering, Faculty of Technology, Elazığ/Turkey
Email: filizozgen@gmail.com
**Fırat University, Department of Mechanical Engineering, Faculty of Engineering, Elazığ/Turkey
Email: ckistak@firat.edu.tr

ABSTRACT

Flow analysis is an essential topic for many industrial applications. Computational Fluid Dynamics (CFD) is a branch of fluid mechanics in which the problems in which fluid behaviour is effective are solved by numerical methods and algorithms. In this study, computational fluid dynamics analysis of the fluid passing through the venturimeter performed. The venturimeter is a very suitable pipe for narrowing and re-expanding the cross-sectional pipe area to observe pressure and velocity changes. In the study, water and air used as fluids passing through the venturimeter. ANSYS-CFX program was used for analyzing the velocity and pressure changes of these fluids in different turbulence models. The parameters used in the numerical analysis are the same as those in the laboratory environment. Venturi tube dimensions are entered the same as the venturi tube dimensions used in the experiment. SST, k-Epsilon and k-Omega turbulence models were used for different fluid types. Experimental results were observed in the laboratory and numerical results were obtained with the help of these results. Velocity and flow graphs of air ,and water in different situations presented.

Keywords: Venturimeter, turbulence models, SST, k- Epsilon, k- Omega, velocity.

1. INTRODUCTION

Venturimeter is a device for measuring the flow of fluid flowing through the pipe in closed systems. The working principle based on Bernoulli and the Continuity equation. The Venturimeter test provides a practical understanding of static pressure, dynamic pressure, total pressure, energy conversion and energy losses. In this study, the venturimeter test aims to determine the volumetric flow rate of the fluid flowing at different flow rates in the pipe by applying Bernoulli and Continuity equations in the laboratory medium. When the flow in a pipe examined, it is seen that the fluid movement is uniform at low velocity, but when the velocity increase above a certain value, it becomes turbulent. The movement of high viscosity fluids at low velocities is usually laminar. The movement of low viscosity fluids such as air at high velocities is generally turbulent flow.

Fluid mechanics, which is of great importance in many engineering branches, deals with the movements of fluids and the physical effects such as velocity, acceleration, pressure, a force that cause or result from these movements. Numerous studies have been done in the literature on computational fluid dynamics analysis of the fluid passing through the venturimeter [1-3]. Bashir et al. [4] , presented CFD-based optimisation of critical geometric parameters of a cavitated venturi. It has been found that the ratio of the venturi circumference to the cross-sectional area of the narrowing determines the possible location at the beginning of the cavity. Huang et al. [5] , developed a new flow rate measurement method for gas-oil two-phase flow using electrical capacitance tomography technique and Venturimeter. Jana et al. [6] , reported the effect of the venturimeter on the liquid-liquid phase distribution during flow through a vertical pipe. Meng et al. [7] , have developed a method for an air-water two-phase flow measurement using a Venturimeter combined with an Electrical Resistive Tomography (ERT) sensor. Experimental results show that the proposed method is useful for measuring the mass flow rate of air-water flow. Sun [8] , studied the effects of a homogenous gas-liquid bubble flow on the mass flow rate using a venturi tube and a vortex flowmeter together.

In this study, the flow of air and water fluid with different turbulence models through venturimeter will be examined , and laboratory experiments will be performed numerically with the ANSYS-CFX program. The effect of fluid type will examine numerically by using air and water passing through the well-known venturimeter , which is widely used in flow experiments. Velocity and flow graphs of air and water in different situations are presented.

2. MATERIAL AND METHOD

In this study, while modelling the numerical study in the ANSYS program, water and air were taken as flow and analysis was made for each fluid. ANSYS program was used to analyze the effect of the fluid type, the effect of the turbulence models on the results and the determination of which turbulence model was closest to the actual values. In this study, the equations governing flow and heat transfer solved in three dimensions by using numerical analysis methods.

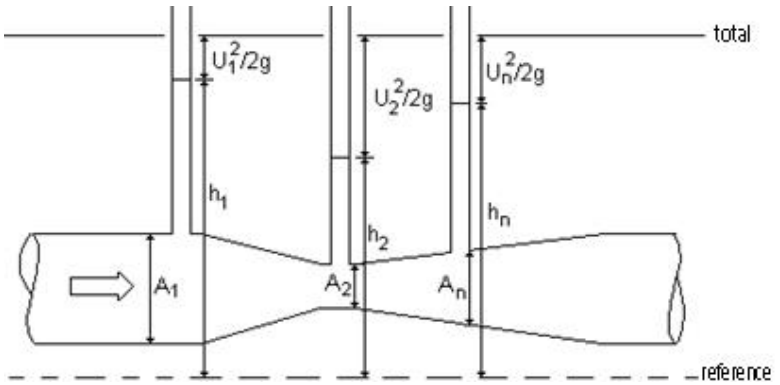

Figure 1. Ideal conditions in a venturimeter

Suppose an incompressible fluid flows from a constricted expanding venturi tube in Figure 1. Let the upper flow cross-sectional area A_1, throat cross-section A_2 and the area A_n in an arbitrary cross-section. Let the liquid heights in the piezometer tubes be h_1, h_2 and h_n , respectively from the reference level. Bernoulli equation with the assumption that velocity and piezometric considerations are constant in each of these sections and one-dimensional flow acceptance,

$$\frac{U_1^2}{2g} + h_1 = \frac{U_2^2}{2g} + h_2 = \frac{U_n^2}{2g} + h_n \tag{2.1}$$

writable. Where U_1, U_2 and U_n are the flow rates in sections 1, 2 and n. The continuity equation in these sections is given below,

$$U_1 A_1 = U_2 A_2 = U_n A_n = Q \tag{2.2}$$

U_2 velocity is calculated as follows.

$$U_2 = \sqrt{\frac{2g(h_1 - h_2)}{1-(\frac{A_2}{A_1})}} \tag{2.3}$$

In laboratory tests, results were obtained for sixteen different flow values. In this study, a comparison was made in 4 different sections for one flow result. The results obtained for the flow rate of 17 L/min are given in Figure 2.

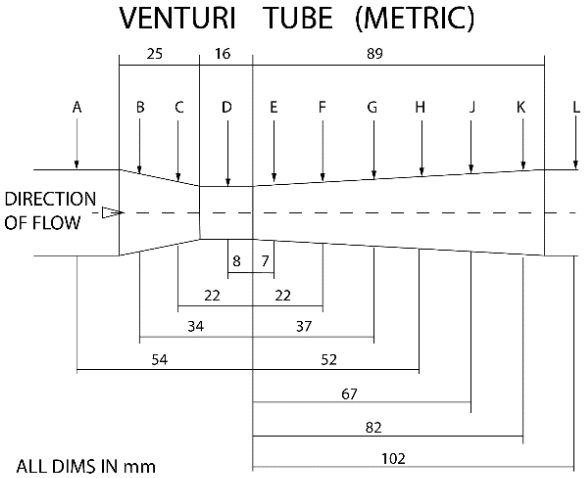

REF.	A	B	C	D	E	F	G	H	J	K	L
DIA.	26	23.2	18.4	16	16.8	18.47	20.16	21.84	23.53	25.24	26
AREA	530.9	422.7	265.9	201.1	221.7	268.0	318.8	375.0	435.0	500.8	530.9

Figure 2. Technical drawing dimensions of the venturimeter test apparatus used in the experiment

Table 1 shows the thermo-physical properties used in the ANSYS-CFX program for water and air at 19°C.

Tabel 1. Thermo-Physical Properties of Water and Air

Fluid	***T(°C)***	**ρ (kg.m^{-3})**	**μ (kg/m.s)**	**C_p (J. kg^{-1}.K^{-1})**	**k (W. m^{-1}.K^{-1})**
Water	19	998	1000	4070	0.603
Air	19	1.209	0.000018	1006	0.0255

3. RESULTS AND DISCUSSIONS

The data obtained by using the equations given in this study are indicated. These data were entered in the ANSYS-CFX program under the material properties section , and the properties of the fluids were determined. In accordance with the geometric values given in Figure 2. geometry is drawn in the ANSYS program and a mesh process is performed. The value of a single mesh length is 0.0001. As a result of the meshing process, the venturi pipe is divided into 340429 part and 169394 nodes. SST turbulence model, k-Epsilon model and k-Omega turbulence model were used to solve for water and air. The dimensions of the venturimeter tube are detailed in Figure 2. Velocity analysis was performed for three different sections on the venturimeter tube. In the ANSYS-CFX program, 1000 iterations were performed for the solution. By using turbulence flow conditions, each problem solved under different turbulence models , and different fluid values, and the resulting figures shown below.

3.1 Velocity Vectors Along Venturi

Velocity vectors along venturi shown in Figure 3 and Figure 4 for water and air. Effect of SST turbulence model, k-Epsilon model and k-Omega turbulence model investigated.

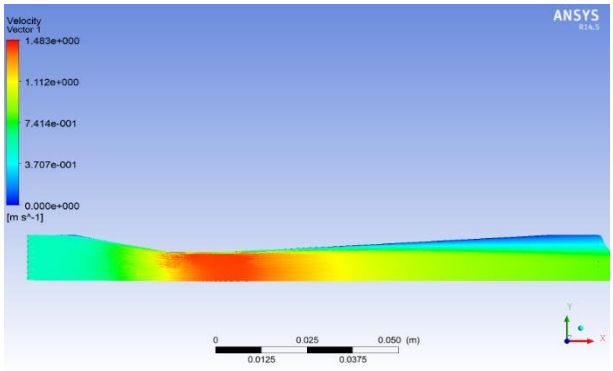

(a)

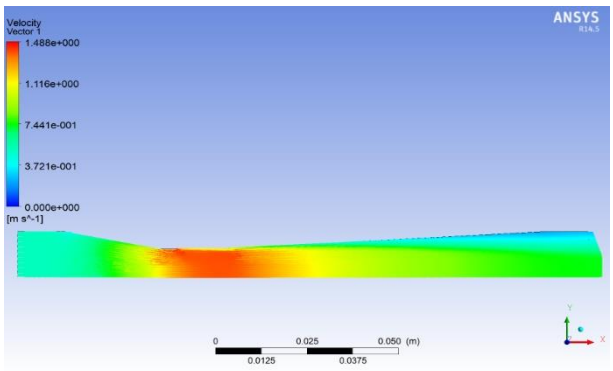

(b)

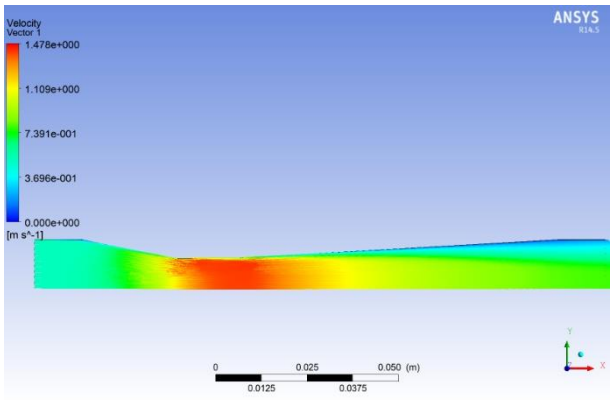

(c)

Figure 3. Velocity vectors along the venturi pipe of water: (a) SST turbulence model, (b) k-Epsilon turbulence model, (c) k-Omega turbulence model

The thermophysical properties of the water at 19°C in Table 1 defined to the fluid , and velocity vectors are generated in turbulent flow SST model, k-Epsilon model and k-Omega models. The highest velocity value was observed in the k-Epsilon turbulence model for water.

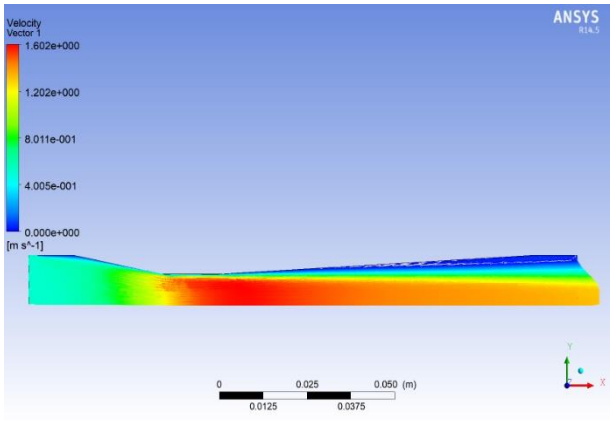

(a)

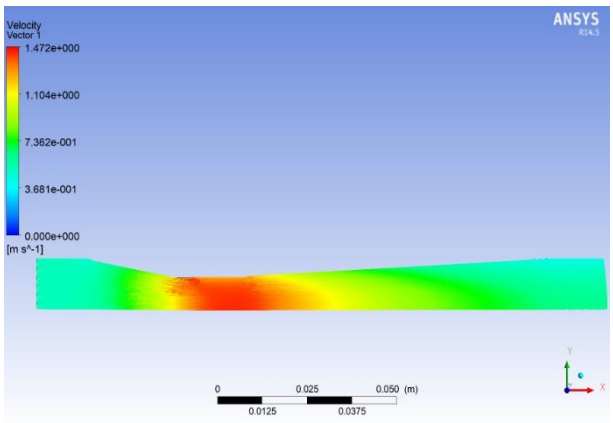

(b)

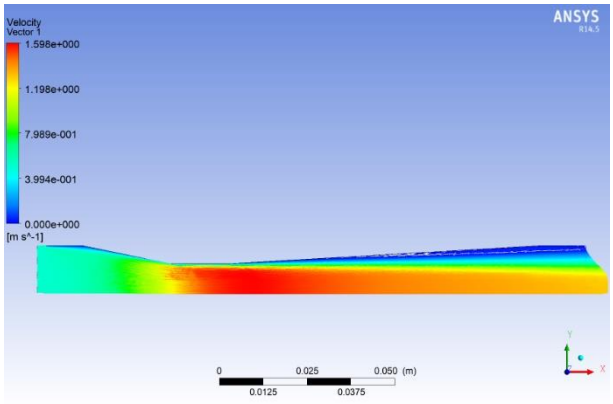

(c)

Figure 4. Velocity vectors along the venturi pipe of the air: (a) SST turbulence model, (b) k-Epsilon turbulence model, (c) k-Omega turbulence model

The thermophysical properties of the air at 19°C in Table 1 defined to the fluid , and velocity vectors were generated in the turbulent flow SST model, k-Epsilon model and k-Omega models in Figure 4. The highest velocity observed in the SST turbulence model for air.

3.2 Streamlines Along Venturi

Streamlines along venturi shown in Figure 5 and Figure 6 for water and air.

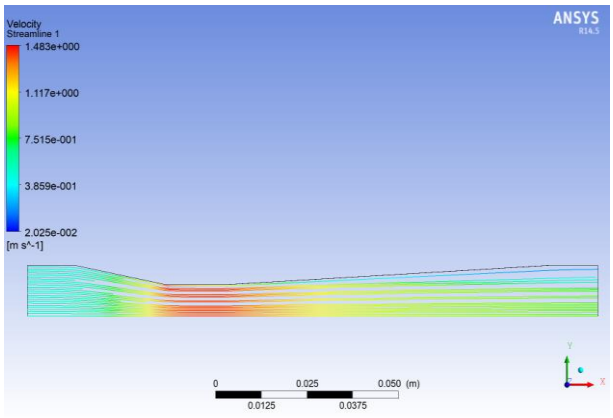

(a)

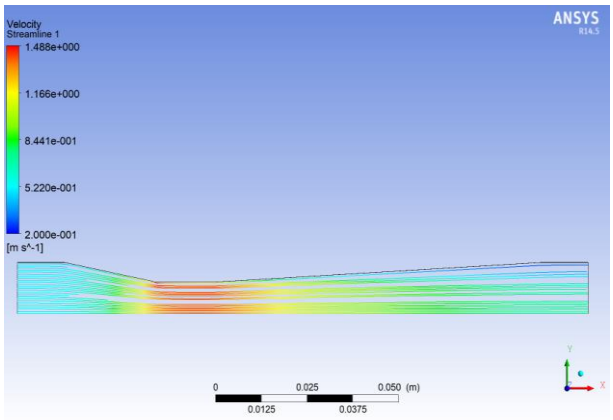

(b)

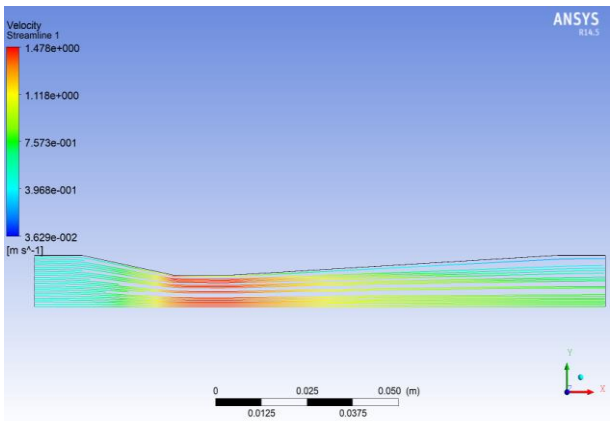

(c)

Figure 5. Streamlines along the venturi pipe for water: (a) SST turbulence model, (b) k-Epsilon turbulence model, (c) k-Omega turbulence model

The thermophysical properties of the water at 19°C in Table 1 defined to the fluid.The streamline is generated in the turbulent flow SST model, k-Epsilon model and k-Omega turbulence models in Figure 5. The highest velocity value was observed in the k-Epsilon turbulence model for water.

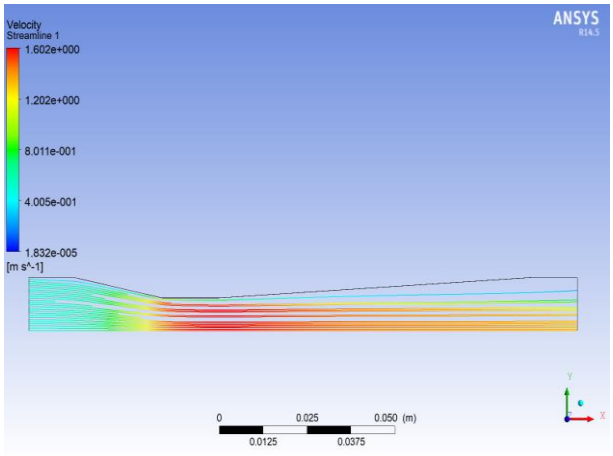

(a)

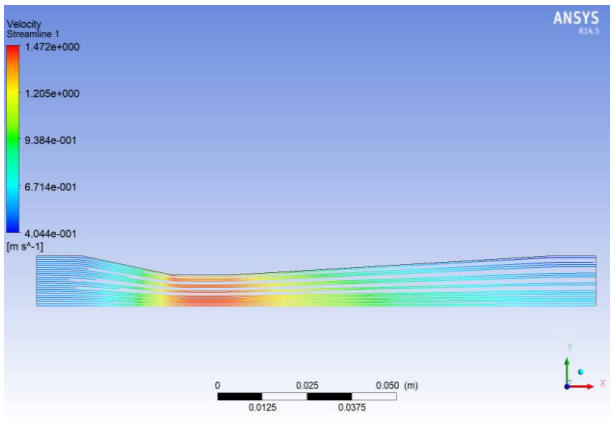

(b)

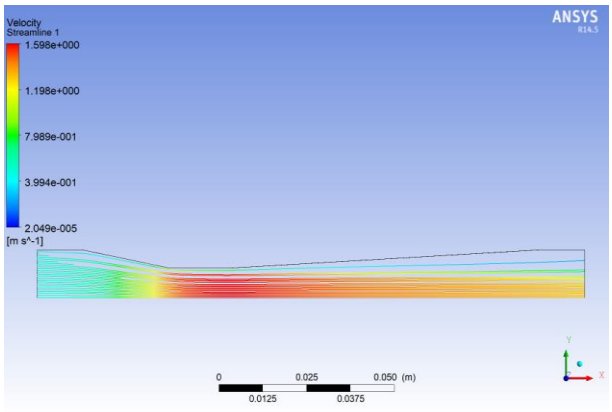

(c)

Figure 6. Streamlines along the venturi pipe for air: (a) SST turbulence model, (b) k-Epsilon turbulence model, (c) k-Omega turbulence model

The thermo-physical properties of the air at 19°C in Table 1 are defined to the fluid and in Figure 6, the turbulent flow SST model, the k-Epsilon model and the k-Omega turbulence models are generated by the streamline. The highest velocity observed in the SST turbulence model for air.

4. CONCLUSION

The thermophysical properties of water at 19°C were defined to the fluid , and the effect of different turbulence models on velocity and pressure in three different sections and the effect of fluid type on the results were examined and the following results were obtained:

- The turbulence model, which obtained the best result according to velocity data in the A-D section, was the SST turbulence model. After the SST model, the k-Epsilon and k-Omega turbulence models have almost the same values.
- According to the velocity data in the D-H section, the turbulence model , which obtained the best result was the SST turbulence model. The best result after the SST model was the k-Omega model close to this value.
- The turbulence model, which obtained the best result according to the velocity data in the H-L section was the k-Epsilon turbulence model.
- The passage of water and air separately at the same temperature value in the venturimeter of the same measured values was examined. In the A-D section, the air velocity was higher in all three turbulence models compared to water.
- According to the results of Contour values, the highest velocity value was observed in the k-Epsilon turbulence model for water and the highest velocity value was observed in the SST turbulence model for air. According to the results of contour values, the highest pressure value was observed in the SST turbulence model for water and air.

REFERENCES

[1] Hasan, A. H., and Lucas, G. P., Experimental and theoretical study of the gas-water two phase flow through a conductance multiphase Venturi meter in vertical annular (wet gas) flow. *Nuclear Engineering and Design*, 241(6), 1998-2005, 2011.

[2] Gupta, B., Nayak, A. K., Kandar, T. K., and Nair, S., Investigation of air–water two phase flow throug a venturi. *Experimental Thermal and Fluid Science*, *70*, 148-154, 2016.

[3] He, D., and Bai, B., Numerical investigation of wet gas flow in Venturi meter. *Flow Measurement and Instrumentation*, *28*, 1-6, 2012.

[4] Bashir, T. A., Soni, A. G., Mahulkar, A. V., and Pandit, A. B., The CFD driven optimisation of a modified venturi for cavitational activity. *The Canadian Journal of Chemical Engineering*, *89*(6), 1366-1375, 2011.

[5] Huang, Z., Xie, D., Zhang, H., and Li, H., Gas–oil two-phase flow measurement using an electrical capacitance tomography system and a Venturi meter. *Flow measurement and Instrumentation*, *16*(2-3), 177-182, 2005.

[6] Jana, A. K., Das, G., and Das, P. K., The hydrodynamics of liquid–liquid upflow through a venturimeter. *International Journal of Multiphase Flow*, *34*(12), 1119-1129, 2008.

[7] Meng, Z., Huang, Z., Wang, B., Ji, H., Li, H., and Yan, Y., Air–water two-phase flow measurement using a Venturi meter and an electrical resistance tomography sensor. *Flow Measurement and Instrumentation*, *21*(3), 268-276, 2010.

[8] Sun, Z., Mass flow measurement of gas–liquid bubble flow with the combined use of a Venturi tube and a vortex flowmeter. *Measurement Science and Technology*, *21*(5), 055403, 2010.

DESIGN AND PROTOTYPING OF AIR-TO-GROUND SMART FIRE EXTINGUISHER AMMUNITION

Murat TOPTAŞ*, Mehmet YILMAZ**
*İnönü University, Department of Mechanical Engineering, Malatya/Turkey
Email: inonumakine@gmail.com
**İnönü University, Department of Mechanical Engineering, Malatya/Turkey
Email: m.yilmaz@inonu.edu.tr

ABSTRACT

Fires are disasters caused by various reasons and have severe consequences, including loss of life and property. Fires especially threaten forests, strategic areas such as chemical production and storage facilities, oil and natural gas pipelines, ammunition storage areas. Firefighting organizations around the world try to combat fires effectively by using land-based and aerial firefighting methods. This study aims to design and prototype smart fire extinguishing ammunition, which is a product that can be used in aerial firefighting methods to fires and is much more effective than the existing tools. The ammunition is thrown from the aircraft to the location of the fire and cuts the contact of the flames with air and forces the fire to extinguish. The ammunition contains a powder-extinguishing agent, the primary substance of which is boron. The extinguishing ammunition is designed based on the dimensions of general-purpose ammunition from air-to-ground used by many NATO countries today. Thus, this extinguishing ammunition can quickly load onto the aircraft without any modification on it. This feature will facilitate the export of the product to all countries that use NATO standards in aircraft. A software was developed to enable the fire extinguishing ammunition to function autonomously. A prototype of fire extinguishing ammunition was produced. We predict that smart fire extinguishing ammunition will bring a new product that has never been done before to the fire extinguishing industry, which has a size of 90 billion dollars worldwide. As a result, this situation will provide a significant amount of foreign currency inflow to our country.

Keywords: Fire extinguisher ammunition, Smart ammunition, Aerial firefighting.

1. INTRODUCTION

The uncontrolled burning of solid, liquid and, or gaseous substances is called a fire. Fires cause economic severe losses and sometimes cause casualties. Fires not only threaten forests. Many points such as petrochemical plants, oil and gas transmission lines, ammunition depots, factories, and residential areas are risky places where fires are more likely to occur. According to a report in the European Forest Fire Information System (EFFIS) (EC PESETA II Project Report), in forest fires that occurred in Europe between 2000-2017, 8.5 million hectares of forests have been destroyed (480000 ha/year), 611 firefighters and civilians lost their lives (34 people/year), economic losses of up to 54 billion EUR (3 billion EUR/year) [1]. In Turkey, having a coastal to the Mediterranean, forest fire losses, which occurred between the same dates, show similarities with the European statistics.

Three elements are needed to start and continue a fire. These are flammable substances, oxidizing agents, and heat. The fire can be stopped by removing any of these three components from the environment or stopping the reaction [2].

Today, land and aerial firefighting methods are used to combat fires. These two methods are not alternative method to each other, but each of them is the fighting methods that increase other's effectiveness and emerged in time for the fire to be extinguished in time. In land fighting methods, the power of motor vehicles such as trucks, pickups, fire trucks, and construction machines are often used [3]. However, since this method of intervention is

highly dependent on geographical conditions, it is insufficient in areas that are difficult to reach where the fire occurred.

The aerial fighting method is another method that uses aircraft and helicopters to combat fires and helps with land fighting. The advantages of this method can be briefly summarized as the speed advantage of aircraft, independence from terrain conditions, and the ability to observe the entire fire area from above [4].

The method of aerial fighting takes two forms. The first method is air support activities, where fire extinguishing activities are monitored and coordination is achieved. The second method is the method of direct fighting. Here, firefighters are transported with air vehicles or fires bombarded with fire extinguishing agents. In the bombardment, water, foam, gel, or some fire retardant substances are thrown over the fire [5]. These substances are generally left on the fire about 60m higher than the tree peak in forest fires [6]. Above 60 meters, due to air resistance and weather currents which occurs on fire, very few extinguishing agents reach their destination. On lower flights, aircraft are affected by rising flames. Also, some fatal accidents have been reported by firefighting organizations of some countries that use aerial firefighting method, due to the impact force of the extinguishing agents released from the aircraft during low flights.

Briefly, aerial firefighting is a critical method that supports fighting from the land in extinguishing fires. However, leaving the extinguishing elements at a sufficient amount, at an accurate position and from a safe distance is a crucial problem waiting to be solved. Several studies have been carried out in different countries to solve this problem. One of them is the product named ASP-500, which was developed in Russia in 2004. This product is based on the extinguishing of a quenching agent on fire in a barrel-like cylindrical structure made of polyethylene [7]. The dispersing mechanism which is inside the structure provides the extinguishing material to scatter around when product hits the ground in the fire zone. However, the product has many disadvantages. The most striking one is the necessity of hitting the ground in order for the system to work. Hitting the tree-like obstacles in a fire area, the fire extinguisher materials cannot reach enough distance and loses their effect. Also, especially in forest fires, some flames jump from one tree to another at the top of the trees. This and the like design deficiencies have transformed the product into simple fire extinguisher packages left on the fire. Another product developed for the solution to this problem emerged in 2017 in China. It is a multi-barrel rocket launcher mounted on a pedestal. Rockets contain 3.6 kg of extinguishing agents to extinguish fires that occur in closed volumes of 60 m^3 at 300 m away [8]. This product uses a ground-to-ground propelling rocket with a solid-fuel rocket engine. Once fired, solid-fuel rocket engines continue to burn until all the fuel they contain is exhausted. Firing a burning rocket into the fire zone can result in disaster. Also, fuel is used up to 10 times the weight of the extinguishing agent to deliver a 3.6 kg extinguishing agent to its destination. Many laser sensors are used for targeting the rocket, and when all equipment is calculated, this product offers a very costly solution for extinguishing a fire that occurs in a volume of 60 m^3. It is also complicated to calculate the security risks of firing such rockets in confined spaces.

The aim of this study is to design and prototyping smart fire extinguisher ammunition (SFEA), which will be an effective product that has not been designed before and can be used in aerial firefighting methods. To make it practical and inexpensive, the ammunition was designed with concerning to the dimensions of the MK-84, which is a type of air-to-ground general-purpose NATO ammunition. In this way, extinguishing ammunition can be loaded without any changes on aircraft. The target of the product is open field fires such as petrochemical plants, oil, and gas transmission lines and ammunition depots outside the residential areas. The purpose of SFEA-84 is to ensure that the extinguishing agent it contains is delivered to the fire point with minimum deviation, without being affected by the weather conditions. Thanks to the sensors and software it has, the product determines the most appropriate point it will perform its duty after being thrown from the aircraft.

2. MATERIALS AND METHODS

2.1. Design of Fire Extinguisher Ammunition

Firefighting ammunition aimed to be practical, inexpensive, and effective. To ensure practical and inexpensive use, the ammunition was created with regarding to the dimensions of the general purpose ammunition type MK-

84, which is a NATO ammunition (84 code comes from here), (Fig. 1). In this way, the extinguishing ammunition would be loaded without any modification on the aircraft. This means that no extra infrastructure investment costs will arise for the countries that will purchase the extinguishing system.

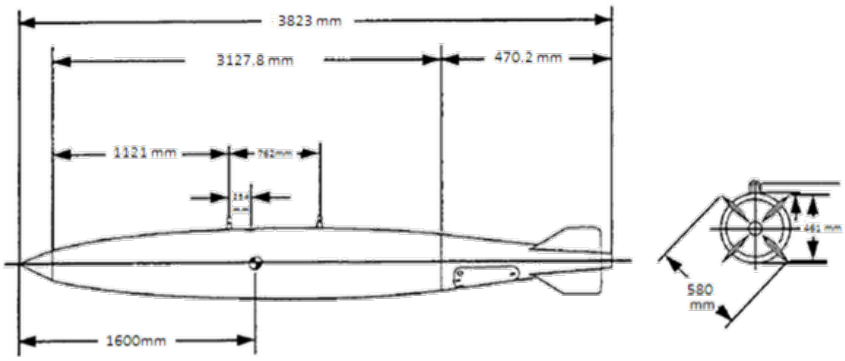

Figure1. Dimensions of MK-84 ammunition.

Fire extinguishing ammunition performs its duty at the most appropriate point and is based on the scattering of the extinguishing agent in a particular pattern and sweeping the fire zone. As a result of analyzes conducted in order to obtain a material scattering for this purpose, it was decided that the ammunition body should have a sliced structure, not a single piece, as in normal warfare ammunition. For this reason, the ammunition body designed as a six-piece structure. When these six pieces come together, they form a 32 mm diameter cylindrical space that allows the explosive to be placed in the center. Five of the slices that make up the ammunition body are empty. These cavities are designed for the extinguishing agents to fill. The sixth slice is designed as a volume to contain suspension hangers that will load the ammunition into the aircraft, and electronic sockets such as a communication socket and flight computer which enable the ammunition to be programmed by the pilot before the launch (Fig. 2). The nose part also designed in accordance with the dimensions of the MK-84 type ammunition. Slots, where some sensors belonging to the ammunition will be placed, were added in the nose cone (Fig. 3). Wings of extinguishing ammunition also designed by adhering to the MK-84 type ammunition (Fig. 4).

Catia V5.R27, a computer-aided design software, was used in prototype design and manufacturing. Also, Excel spreadsheets were used in calculations.

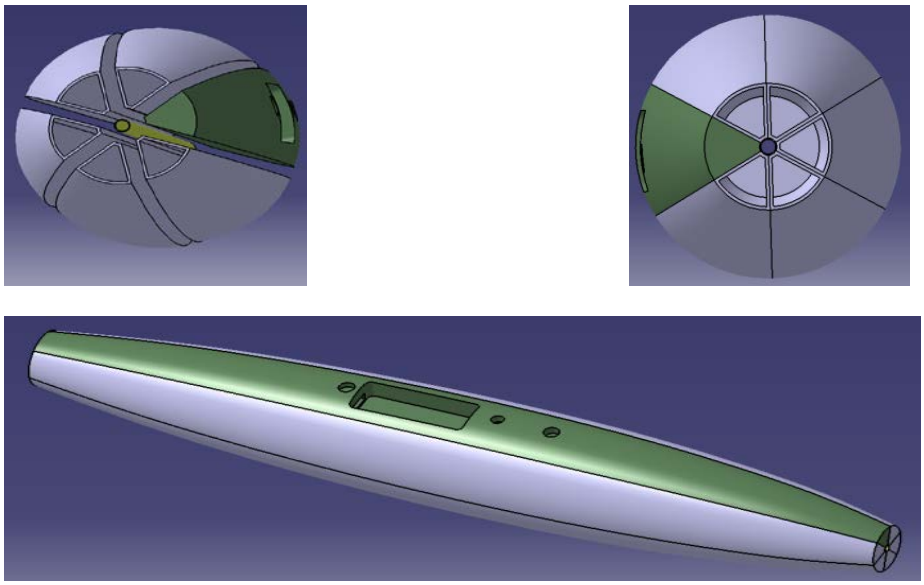

Figure 2. SFEA-84 body design.

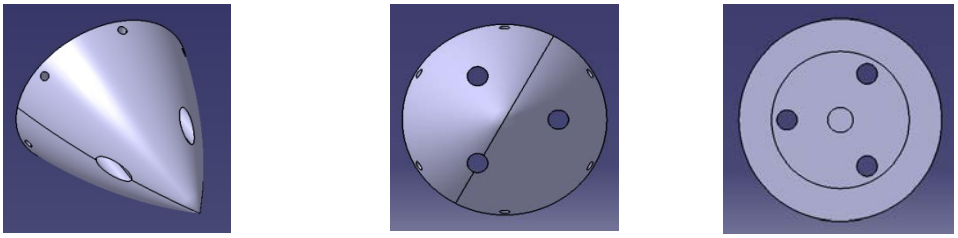

Figure3. SFEA-84 nosecone design.

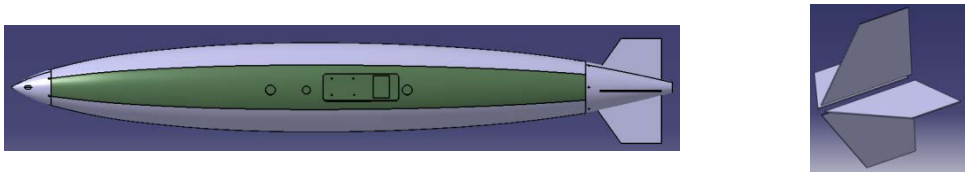

Figure4. SFEA-84 wing design.

2.2. Manufacture of Fire Extinguisher Ammunition

2.2.1. Manufacture of Ammunition Body

To create a shrapnel effect, body of the MK-84 warfare ammunition is manufactured from a single piece of brittle iron. In SFEA-84, acrylic material was used in the ammunition body. Acrylic material is a type of plastic that can be molded easily and disintegrates by showing a brittle feature when exposed to sudden impact. By using this feature of acrylic, it is aimed that the extinguishing material can easily get out during the explosion.

SFEA-84 body slices were produced by using the vacuum forming method. Slice mold was made of wood using CNC milling. A sufficient number of holes with a diameter of 5mm drilled on the mold. These holes are for the discharge of air during vacuum and to take the shape of the mold by approaching the mold surface of the plate. On the mold placed on the vacuum table, a 6 x 1000 x 4000 mm sized acrylic plate was placed in the oven at 200ºC. Then, a plate was inserted in to mold and a vacuum pump was operated. As a result, the acrylic sheet adhered to the mold and took the shape of the mold. The burrs formed in the environment were cleaned, and a slice of SFEA-84 body was obtained. The vacuum forming process was repeated six times and the production of 6 parts that make up the ammunition body was finished. The manufactured parts were joined using an adhesive with tensile strength of 0.5 N/mm^2. While choosing adhesive material, the temperature differences, possible atmospheric events, and vibrations that SFEA-84 will be exposed while carrying by air vehicles are considered.

2.2.2. Manufacture of Ammunition Wings

The wings of the ammunition were cut from a 6mm thick ST-37 steel sheet by a metal plasma cutter. After the necessary roundings of the sharp corners the wing surfaces were painted against corrosion.

2.2.3. Manufacture of Ammunition's Nose Cone

The designed nose cone part was machined on a CNC lathe using 6061 aluminum rod material. Necessary slots and holes for the placement of sensors and mounting screws were drilled using a drill and milling cutter.

2.3. Extinguishing Agent

A boron-based extinguishing material in powder form was used in the SFEA-84 extinguishing chamber. This domestically produced product does not have any carcinogenic and toxic properties due to its mineral structure. Many fire extinguishers force the fire to extinguish, preventing the flames from coming into contact with air. This situation is called drowning the fire. However, the most fires, which cannot be cooled after the drowning,

are reignited by the entry of oxygen into the environment. The powdered extinguishing material used in SFEA-84 also provides rapid cooling after the drowning. This material reduces the temperature reaching 450 ºC in fires to 24 ºC within 10 s, and is quite useful in forest fires.

Another type of material in powder form is a boron-based substance effective in metal fires. Although this substance has all the features of the first substance, it is very effective in fires of 1500 ºC and above. It was observed that 1500 ºC temperature decreased to room temperatures in a short time of 10 seconds. It can be used safely in a fire extinguisher in this domestically produced product. In summary, SEFA-84 can be used in any type of fire by replacing only the extinguishing agent that is filled.

2.4. Explosive Material

SFEA-84 contains an explosive substance that enables the extinguishing agent to explode in the fire area or above the flames and spread to a specific area. Dynamite, which can be detonated with the help of an electric detonator, was chosen as the explosive substance. In making this choice, dynamite being a civilian explosive type, relatively more straightforward and cheaper to supply than military explosives, was effective.

2.5. Electronic Equipments

There are several sensors (flame, temperature, altitude, speed, acceleration, pressure, impact) on the SFEA-84 that enable the ammunition to perform its task with high precision. Those measuring flame, temperature, distance, and impact from these sensors are located in the ammunition's nose. Other sensors are located in the chamber formed in the transport zone. Sensors are connected to an electronic card. There is a software on the card which gets and calculates the data from the sensors. All equipment is operated with a power supply (a 12V battery) and a power card binary contained in the ammunition. Figure 5 shows the electronic components of SFEA-84. Apart from these, smart fire extinguishing ammunition also has an electrical detonator which enables the activation of explosive material.

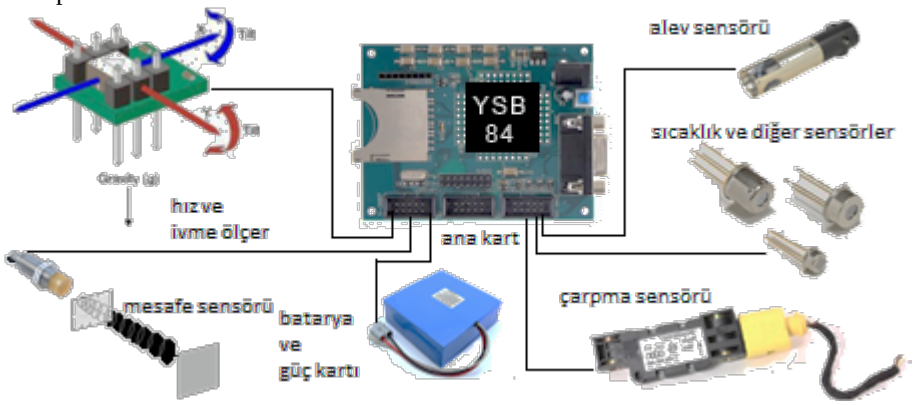

Figure 5. Electronic components of FSEA-84.

2.6. Blasting Mechanism

The explosive substance in the ammunition center activates with the help of an electric detonator. After detecting the appropriate burst point, a signal is sent from the microprocessor to the detonation board. With the signal sent, the blasting relay transfers the load it draws on the capacitor to which it is connected to the explosive, and the explosion occurs.

2.7. Software

SFEA-84 has an 84 MHz motherboard with a 32Bit microprocessor (ARM Cortex-M3). All input sensors and output relay boards are connected to this motherboard. The software is written in C programming language, and the algorithm generally works as follows (Fig. 6):

a) Detection of the fire is performed from the aircraft.

b) The pilot marks the ammunition loaded on the aircraft from the screen (HMI) of the vehicle as "top" or "bottom" ammunition.
c) Ammunitions marked as "top ammunition" explode on the flames and provide the most effective way to spread the extinguishing material over the entire area.
d) The extinguishing agent, which descends on the flames with gravity, chokes and cools the fire.
e) Ammunitions marked as "bottom" ammunition is for fires that continue on the ground (dry grass, bushes, oil pipelines, etc.). The ammunitions made with this marking fulfill their duty only when they hit the ground.

Besides, there is an audit set up in the program algorithm to prevent the ammunition from damaging the aircraft and personnel with an untimely explosion. Accordingly, it is continuously monitored (at 0.01s intervals) by sensors that the ammunition leaves the aircraft, gains a certain speed and angle meets flame and temperature.

2.8. Methods

2.8.1. Ammunition Trajectory and Angle of Impact Calculations

If the trajectory that the extinguishing ammunition will follow under the influence of the drag force after it is released from the aircraft is expressed by force equations (the direction of the ammunition is taken as "+ x", the direction of the fall (gravity direction) is taken as "–y"):

$$F_x = ma_x = -m\left(\frac{V_x}{V}\right)bV^2 \quad (1)$$

$$F_y = ma_y = -mg + m\left(\frac{V_y}{V}\right)bV^2 \quad (2)$$

$$b = C_d \rho_a A/m \quad (3)$$

b : air resistance (m^{-1})
m : mass of ammunition
ρ_{air} : density of air (kg/m^3)
A : cross-sectional area of ammunition (m^2)
C_d : drag coefficient

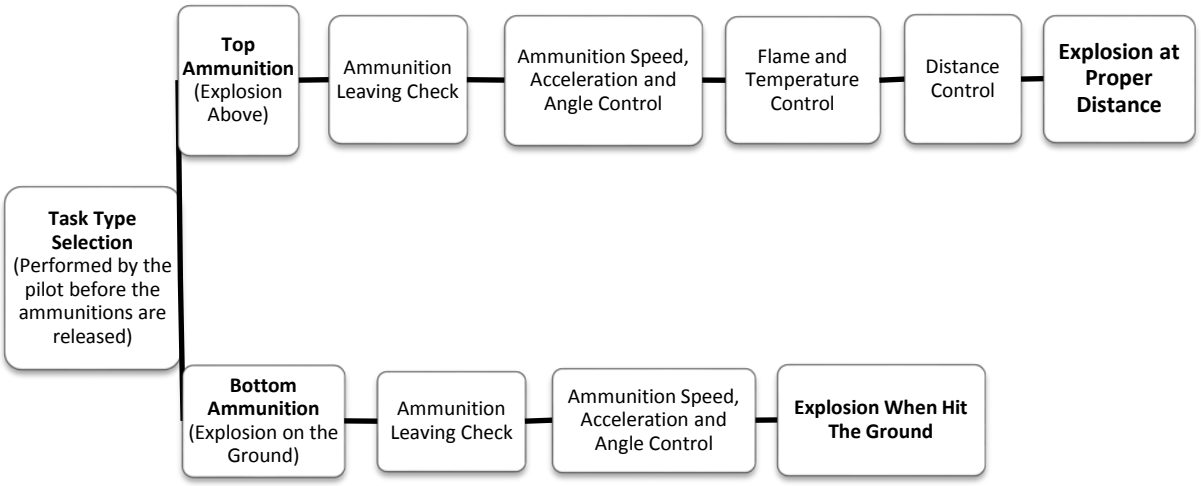

Figure 6. Scheme of work for FSEA-84 software.

Equations (1) and (2)can be simplified by dividing by the mass, and substituting: $a_x = dV_x/dt$, and $a_y = dVy/dt$, and estimating dt = Δt to obtain:

$$V_x(t+\Delta t) = V_x(t) - bV_xV\Delta t \tag{4}$$

$$V_y(t+\Delta t) = V_y(t) - g\Delta t - bV_yV\Delta t \tag{5}$$

Using these equations, a spreadsheet was set up which computed V_x,V_y, X, Y, for different drag coefficients (C_d) and heights (h). Using the found Vx and Vy speeds, the impact angle "θ" was calculated with the following equation:

$$\theta = tan^{-1}(V_y/V_x) \tag{6}$$

2.8.2. Extinguishing Agent Release Rate Calculation

In order to determine the distribution of the extinguishing agent with the explosion of the ammunition, the velocity vector in the third axis also needs to be known. For this purpose, the Gurney equation was used, which gives the shrapnel speed resulting from the explosion of cylindrical shaped ammunition. The Gurney equation for a cylindrical ammunition [9]:

$$V\sqrt{2E} = \left[(M/C_{exp}) + 1/2\right]^{-0.5} \tag{7}$$

V:Initialfragmentvelocity(m/s)
$\sqrt{2E}$: Gurney constant for a given explosive
M:Mass of fragment (kg)
C_{exp} : Explosive charge mass(kg)

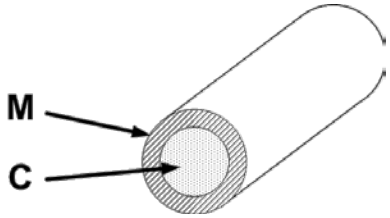

√2E value is generally very close to 1/3 of the detonation speed of explosives. However, it is necessary to look at the relative effect factor (R.E.) of the explosive for the exact value. The relative effect factor is the ratio of the energy value of the same amount of explosives to the energy value of the TNT. Dynamite was used as an explosive in SFEA-84. According to this:

$$R.E. = \frac{E_{dynamite}}{E_{TNT}} \tag{8}$$

Table 1. Gurney constants of some explosives [10].

Explosive [20]	**Density (kg/m^3)**	**Detonation Velocity [21] (m/s)**	**Gurney Constant $\sqrt{2E}$ (m/s)**
Octol 75/25	1.81	8.640	2896
PETN	1.78	8.260	2926
RDX	1.81	8.700	2926
RDX/TNT 60/40 (Cyclotol)	1.68	7.800	2402
Tetryl	1.71	7.570	2499
TNT	1.61	6.900	2438
Tritonal	1.70	5.480	2316

3. RESULTS AND DISCUSSION

3.1. Ammunition Trajectory and Impact Angle

As a result of the ammunition trajectory and impact angle calculations, the trajectories to be followed by the fire extinguishing ammunition for different altitudes and jettison speeds were determined. These trajectories were drawn for different resistance coefficient values. 300 m and 500 m in height, 50 m/s, 83.3 m/s, and 100 m/s were used as the jettison speed.
The ammunition trajectory for 500 m height and 50 m/s horizontal jettison speed is shown in Figure 7. The following conclusions can be drawn from the figure:

a) Ammunition falls horizontally 480-505 m.
b) As the resistance coefficient increases, the path taken by the ammunition decreases.
c) From the figure, it is possible to calculate the impact angles for the bottom and top bursts of the ammunition.

Figure 8. It gives the ammunition trajectory for 300 m height and the horizontal rate 83.3m/s. In this case, the ammunition falls horizontally 630-650 m. It was found that as the resistance coefficient increases, the path taken by the ammunition decreases. Figure 9 shows the ammunition trajectory obtained when the ammunition is dropped from 500 m for the same horizontal throw rate. In this case, the ammunition falls horizontally 790-840 m. This result shows that the same way the ammunition travels horizontally increases when the pulse height increases for the same pulse rates.

The ammunition trajectory for 500 m height and 100 m/s horizontal throw speed is shown in Figure 10. The figure shows that the ammunition fell 940-1010 m horizontally

Comparing of the paths taken by the ammunition horizontally for the jettison speeds and heights examined is given in Table 2. As stated in the paragraphs above, Vxo, the jettison rate, and the Cd resistance coefficient significantly affect the way the ammunition takes horizontally. Of these parameters, it was determined that the parameter that affected the path of the ammunition horizontally least was the Cd resistance coefficient, and the parameter that affected the most was Vxo velocity.

Table 2. The path taken by the ammunition horizontally for various jettison speeds and heights.

Jettison Speed and Height	**The Path of the Ammunition Horizontally**
Jettison Speed V_{xo}=50 m/s height=500 m	480-505 m
Jettison SpeedV_{xo}=83.3 m/s height h=300 m	630-650 m
Jettison Speed V_{xo}=83.3 m/s height h=500 m	790-840 m
Jettison Speed V_{xo}=100 m/s height h=500 m	940-1010 m

3.2. Release Rate of Extinguishing Agent

In SFEA-84, with a total length of 3000 mm, a diameter of 26 mm, and a reaction energy value of 4.696 MJ/kg dynamite was used in SFEA-84. When the energy value of TNT was replaced by the equation numbered (8) 4.184 MJ/kg ;

$$R.E. = \frac{4.696\ MJ/kg}{4.184\ MJ/kg} = 1.122$$

obtained. Accordingly, the relative impact factor of the explosive used in SFEA-84 is 1.122. The TNT equivalent of the explosive weight can calculate from here:

$$m_{eqv\ of\ TNT} = (R.E.)(m_{dynamite}) \tag{9}$$
$$m_{eqv\ of\ TNT} = (1.122)(1.815\ kg) = 2.036\ kg\ of\ TNT$$

From Table 1, where Gurney constants were given for explosives, by reading 2438 m/s value for TNT, the release rate of the extinguishing agent was obtained during the explosion when it is placed in the equation (7) for 572 kg ammunition weight and 2.036 kg explosive weight:

$$(V)(2438\ m/s) = [(572\ kg/2.036\ kg) + 1/2]^{-0.5}$$
$$V = 145\ \ m/s$$

was calculated. This value is the rate at which the extinguishing agent moves away in the z-direction. Sufficient information about the scattering direction and intensity of the extinguishing agent is collected when collected in vector with velocity components in the x and y directions found earlier.

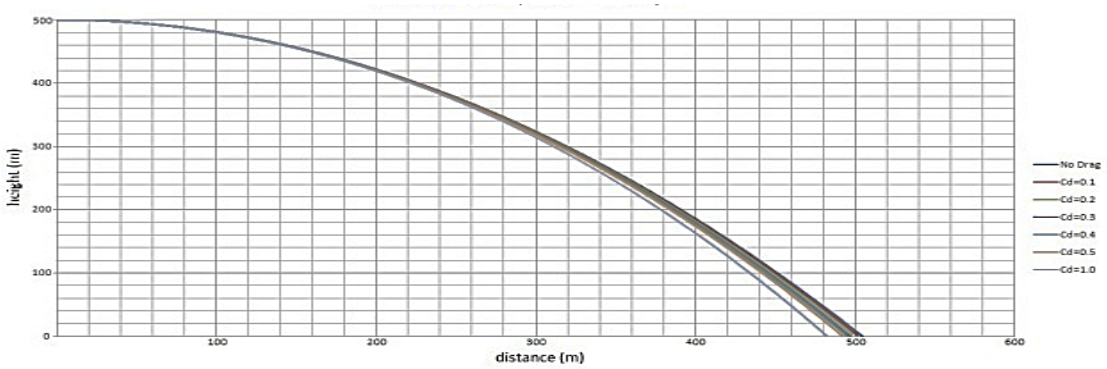

Figure 7. The trajectory followed by SFEA-84 at different altitude and jettison speeds (Vxo = 50 m / s, height = 500 m).

Figure 8. The trajectory followed by SFEA-84 at different altitude and jettison speeds (V_{xo}=83.3 m/s, height=300 m).

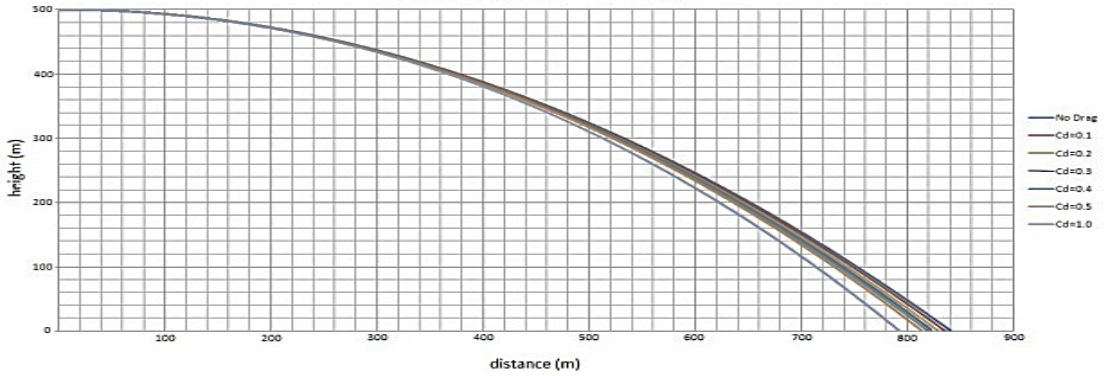

Figure 9. The trajectory followed by SFEA-84 at different altitude and jettison speeds (Vxo=83.3 m/s, height=500 m).

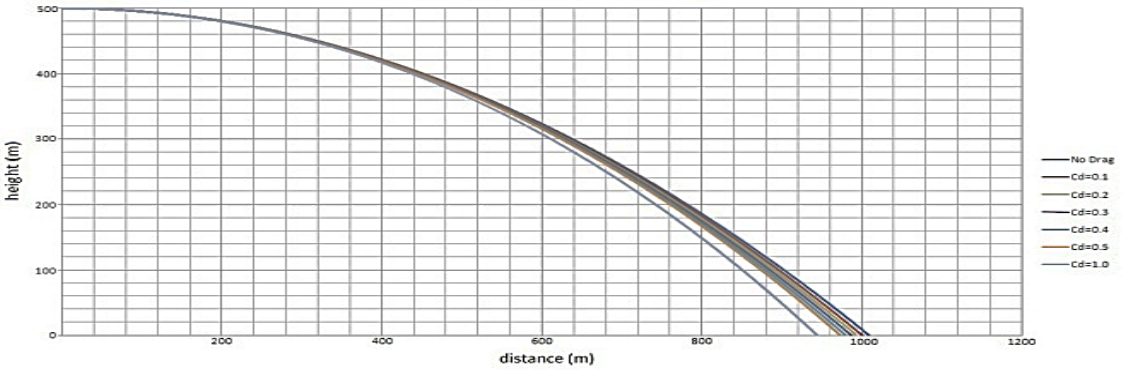

Figure 10. The trajectory followed by SFEA-84 at different altitude and jettison speeds (Vxo=100 m/s, height=500 m).

4. CONCLUSION

In this study, smart fire extinguisher ammunition (SFEA), an effective product that could not be used before and used in aerial firefighting methods, was designed and prototyped. To ensure its practicality and inexpensive use, the ammunition was created concerning to the dimensions of the MK-84 type, general air-to-ground purpose NATO ammunition. Ammunition trajectory and impact angle calculations made, and the release speed of extinguishing material calculated. The trajectories to be followed by the ammunition were visualized for different resistance coefficients. The following findings were obtained in the study:

a) As the Cd resistance coefficient increased, the path is taken by the ammunition also decreased.
b) When the jettison height of the ammunition increased, the way the ammunition travels horizontally increased.
c) The path taken by the ammunition horizontally was heavily influenced by the rate of jettison.
d) It was determined that the parameter that affects the path of the ammunition horizontally was the Cd resistance coefficient, and the parameter that affects the most was the Vxo jettison rate.
e) Depending on the Vxo jettison rate, h jettison height, and the Cd resistance coefficient, the ammunition felt horizontally 480-1010 m. further.
f) The slope of the ammunition at each point of the trajectory was determined for the bottom and top bursts.
g) For 1.815 kg of dynamite explosive used in ammunition, the extinguishing material release rate was calculated as 145 m/s.

There is no useful tool for fighting against open area fires occurring in areas such as forests, petrochemical plants, oil-gas transmission lines, and ammunition depots located outside the residential areas. The SFEA-84 smart fire fighting ammunition developed within the scope of this study is thought to close this gap and bring a new product to the civil defense or aviation field. A patent application filed for this product in 2019. In this

study, the design and manufacture of fire extinguishing ammunition made. Ammunition trajectory, impact angle and extinguishing material release rate calculated. We continue our work on the extinguishing material scatter distribution, the human-machine interface software to be used by the pilot, the determination of the explosion point, the sensors to be used, and the software that provides their coordination.

REFERENCES

[1] European Commission, Directorate-General for Research and Innovation. (2018). "*Forest Fires- Sparking fire smart policies in the EU"*. Luxembourg: Publications Office of the European Union.

[2] Hall, R. (1998). "*Essentials of Fire Fighting"*. Fourth Edition. Stillwater, OK: Fire Protection Publications

[3] Küçükosmanoğlu, A. (1993). "*Türkiye Orman Yangınlarına Ait Bazı Verilerin Değerlendirilmesi".* İstanbul Üniversitesi Orman Fakültesi Dergisi, 43, 94.

[4] Pulicinski, M.,Gould, J. (2007). "TheEffectivenessandEfficiency of AerialFirefighting in Australia (Technical Report Number A0701). Melbourne, Australia: University of Melbourne, Department of Environment andConservation.

[5] Alder, R. (1990). "Fighting Bush fires from the air. Paper presented at the Conference of the Institute of Fire Engineers, Adelaide, December 1990.

[6] Dowling, S. (2015, August 21). "The jaw-dropping missions of fire-fighting pilots." BBC Future. Retrived from https://www.bbc.com/future/article/20150821-the-jaw-dropping-missions-of-fire-fighting-pilots.

[7] Korenkov, Vladimir K. (2004). "ASP-500 Fire-extinguishing Air System" [Electronic version].
Revue Militaire Suisse, 149, 32.

[8] Lei, Z. (2017, February 2). "Chinese rockets aimed at high-rise fires". China Daily. Retrived from https://www.chinadaily.com.cn/china/2017-02/14/content_28190425.htm.

[9] Gurney, R. W. The Initial Velocities of Fragments from Bombs, Shells and Grenades, BRL-405. Ballistic Research Laboratory, Aberdeen, Maryland. USA. 1943.

[10] United Nations Office for Disarmament Affairs. (2015). "International Ammunition Technical Guideline (2nd ed.). New York, NY: United Nations Headquarters.

HVAC SYSTEMS

EFFECT OF VERTICAL SKIRT ON AIRFLOW AND PARTICLE DISTRIBUTIONS IN AN OPERATING ROOM: A NUMERICAL STUDY

Aleyna Agirman KALÇA*, Yunus Emre ÇETİN, Mete AVCI***, Orhan AYDIN***
*Karadeniz Technical University, Department of Mechanical Engineering, 61080 Trabzon/Turkey
aleynaagirman@ktu.edu.tr, oaydin@ktu.edu.tr
** Karadeniz Technical University, Arsin Vocational School, 61910 Trabzon/Turkey
yecetin@ktu.edu.tr
***Recep Tayyip Erdogan University, Department of Mechanical Engineering, 53100 Rize/Turkey
mete.avci@erdogan.edu.tr

ABSTRACT

Bacteria-carrying particles (BCPs) released from surgical staff are the main factor causing surgical site infection (SSI). Operating room (OR) ventilation plays an important role in reducing the risks of such infections. The aim of this study is to investigate the effect of the vertical skirt on airflow and particle distribution in an OR with a laminar ventilation system (LAF) via computational fluid dynamics (CFD). Two different ventilation strategies are comparatively examined: (i) with skirt, (ii) without skirt. Two different particle diameters (10 and 20μm) are considered for a constant value of the air change rate (30 ACH). The simulation results show that the vertical skirt contributes to the enhancement of the unidirectional airflow provided by LAF. It is also found out that an OR with a skirt has a great potential to reduce particle deposition in the surgical site.

Keywords: Operating room, Surgical site infection, Ventilation, Vertical skirt

Nomenclature

Latin letters

F_D	Inverse of relaxation time (s^{-1})
F_a	Additional force terms per unit particle mass ($m\ s^{-2}$)
g	Gravitational acceleration ($m\ s^{-2}$)
S_φ	Source term
t	Time (s)
u	Fluid velocity ($m\ s^{-1}$)
u_p	Particle velocity ($m\ s^{-1}$)
$\vec{V}$	Air velocity vector ($m\ s^{-1}$)

Greek letters

ρ	Fluid density ($kg\ m^{-3}$)
ρ_p	Particle density ($kg\ m^{-3}$)
Γ_φ	Diffusion coefficient ($m^2\ s^{-1}$)
φ	Velocity components (u, v, w) and mean temperature (T)

1. INTRODUCTION

During surgery, bacterial contamination of the wound is a significant risk factor in developing surgical site infection (SSI). SSIs are defined as an infection that occurs at or near the surgical incision within 30 or 90 days and are the most common nosocomial infections that originate from surgery. These infections are associated with substantial morbidity and mortality, prolong the recovery of a patient, and increase healthcare costs [1]. Leblebicioglu et al. [2] reported that SSIs occur in 4.5 % of 22 types of surgical procedures conducted at 20 hospitals in 16 cities of Turkey. It is well known that the surgical staff are the primary origin of airborne particles in an operating room (OR). The mean value of bacteria-carrying particles (BCPs) emitted from a surgical staff is considered as 100 BCP/min. This rate is based on the estimation of 1000 particles/min released per surgical staff with 10% of these BCPs [3]. The rate of deposition of an airborne particle is significantly correlated with its size. Particles can either remain suspended in the OR air (<5 µm), deposit on surfaces (between 5 and 100 µm), or settle rapidly (>100 µm) [4]. It has been reported that particles ranging from 2.5 µm to 20 µm can be considered as pathogenic particles in OR [5].

The particles, which are released by breathing or settled on sterile instruments, can contaminate the wound area. This contamination is usually reduced by using an appropriate ventilation system to maintain a low level of airborne contamination in the surgical site. Traditionally, two main types of the ventilation systems are preferred in the ORs: turbulent mixing ventilation (TMV) and laminar airflow (LAF) ventilation. TMV uses a concept of highly mixed airflow patterns in the whole OR to remove airborne bacteria. On the other hand, the LAF system is the most common ventilation system used in modern OR designs. Clean air is supplied from diffusers installed on the ceiling. This system creates a unidirectional flow field over the surgical zone. Many studies have shown that LAF ventilation is superior to TMV ventilation in terms of airborne bacteria reduction in the surgical site [6-8].

Although vertical LAF creates a sterile zone under the diffuser, it can easily be disrupted. Obstacles inside the sterile zone, such as the surgical staff and medical lamp, are considered as the main factors influencing the unidirectional airflow of a vertical LAF system [9]. In this case, BCP concentration in the wound zone may increase [10]. However, the unidirectional flow pattern can be sustained by simple modifications in the ventilation system. In this regard, the use of vertical skirts around the airflow diffuser is considered as an option in order to preserve the sweeping effect of the LAF unit [11]. Also, these skirts can avoid the short-circuiting of ceiling-supplied air [12]. Few studies have investigated the influence of vertical skirts on contaminant concentration in the surgical site. Zhai and Preechawuttidet [13] and Chow and Yang [14] indicated that the use of a vertical skirt can help to maintain unidirectional airflow over the surgical site. On the other hand, Al-Waked [15] reported that the presence of the skirt resulted in a higher particle concentration in the surgical site. Due to the contradictory findings in the literature, it is aimed to find out the effect of the vertical skirt on both airflow and BCP distribution via computational fluid dynamics (CFD) in this study.

2. NUMERICAL SIMULATION

2.1. Geometry and Layout

The considered model geometry is based on an operating room located in Karadeniz Technical University Hospital (Trabzon, Turkey). The overall dimensions of the model OR is L 6.5 m x W 9.43 m x H 2.43 m, with the physical configuration shown in Figure 1a. The OR contains a surgical table, a medical lamp (with a thermal load of 215 W/m^2), two instrument tables, medical equipment (with a thermal load of 170 W/m^2), and four surgical staff (with a thermal load of 65 W/m^2). The air is supplied to the OR by a LAF diffuser (L 1.8 m x W 2.4 m) positioned on the ceiling. Exhaust air is evacuated through four air – exhaust outlets (L 0.24 m x H 0.39 m)located close to the floor level at each corner. In addition to the original case seen in Fig 1a, a vertical skirt modification with a length of 0.6 m is added to the LAF diffuser, as shown in Fig 1b. Air is introduced to the OR with an air velocity of 0.29 m/s, giving an air exchange rate of 30 h^{-1}.

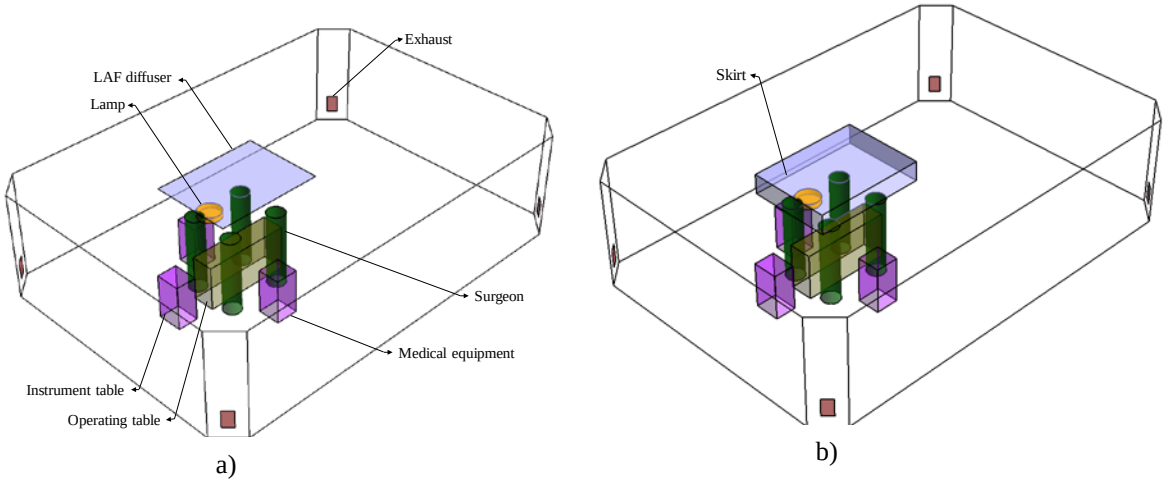

Figure 1. Geometric configuration of the operating room simulated; (a) without skirt, (b) with skirt

2.2. Numerical Model

2.2.1. Airflow Simulation Model

In the numerical analysis, the Reynolds - averaged Navier Stokes equations are employed to calculate the airflow field in the OR. The selection of a suitable turbulence model has vital importance for resolving the turbulent structure of the flow. The $k-\varepsilon$ turbulence models have been widely applied in indoor air simulations [16]. Among these models, The Realizable $k-\varepsilon$ model which is, relatively recent development of $k-\varepsilon$ models [17], is used in this simulation. The governing equations for continuity, momentum, and energy may be expressed in the general form as follows:

$$\frac{\partial(\rho\varphi)}{\partial t}+\nabla\left(\rho\varphi\vec{V}\right)=\nabla\left(\Gamma_{\varphi}\nabla\varphi\right)+S_{\varphi} \tag{1}$$

where $\vec{V}$ is the air velocity vector, ρ is the air density, φ is the transported quantity, Γ_{φ} is the diffusion coefficient of φ and S_{φ} is the source term.

The aforementioned conservation equations are discretized into algebraic equations by the finite volume method and solved by using the double–precision solver of ANSYS Fluent 16.0. Momentum and energy equations are discretized by second order upwind scheme, and pressure interpolation is provided by the PRESTO scheme. The SIMPLE algorithm is used to couple velocity and pressure. The buoyancy force is considered with the Boussinesq approximation. Velocity inlet and outflow boundary conditions are used for air inlet and exhaust outlets, respectively. The air temperature is defined as 20 ºC, and turbulence intensity is set as 10%. Convergence criteria for all the equations are set to be 1 x 10^{-5}. The surfaces of the surgical staff and medical equipment, bottom surface of the medical lamp, and the top surface of the surgical table are defined as constant heat flux boundary conditions. Also, the adiabatic boundary condition and the no-slip velocity are applied for all the solid wall boundaries. Enhanced wall treatment is employed to treat the turbulent flow properties close to wall regions. A grid independence study is performed using three different grid sizes, resulting in about 4 million, 6.5 million and 9 million cells. As results of acceptable agreements on air velocity and particle concentration distributions of 6.5 and 9 million cells, 6.5 million cells are chosen to perform the simulation.

2.2.2. Numerical model of particle motion

The Eulerian and the Lagrangian methods are used to predict particle concentration distribution for indoor environments. In this study, the Lagrangian method is applied to calculate the trajectory of each particle by integrating the force balance equation. This force balance includes particle inertia balanced by the forces acting on the particle, and can be written as follows:

$$\frac{du_p}{dt} = F_D(u - u_p) + \frac{g(\rho_p - \rho)}{\rho_p} + F_a \tag{2}$$

where ρ_p and ρ are particle and air density, u and u_p are the velocity vector of the air and particle, and g is the gravitational acceleration. The term F_D is the inverse of the relaxation time, and F_a stands for the additional forces (Saffman's lift force, Thermophoretic force or Brownian force) [18].

Particle dispersion due to turbulence is calculated using the discrete random walk (DRW) model. Due to the high computational demand, particles are injected into the OR after the turbulent airflow area is analyzed. In the current study, airborne particles with an aerodynamic diameter of 10 µm and 20 µm are released from the mouth of surgical staff to the OR air. Particles are considered to have left the OR when they arrived at the outlets (i.e., escape boundary condition). Also, particles are assumed to be 'trapped' after they hit a solid surface. This boundary condition implies that the particles that will come into contact with the surfaces will not resuspended by air.

2.2.3. Validation of the mathematical model

The experimental results of Chen et al. [19] are employed to validate the numerical approach. The room dimensions of the validated study are L x W x H = 0.8 m x 0.4 m x 0.4 m. The inlet and outlet vents are symmetrical in relation to the center plane, and the dimensions are 0.04 m x 0.04 m. Inlet velocity is 0.225 m/s. The particle size released into the chamber is 10 µm, and the material density is 1400 kg/m^3.

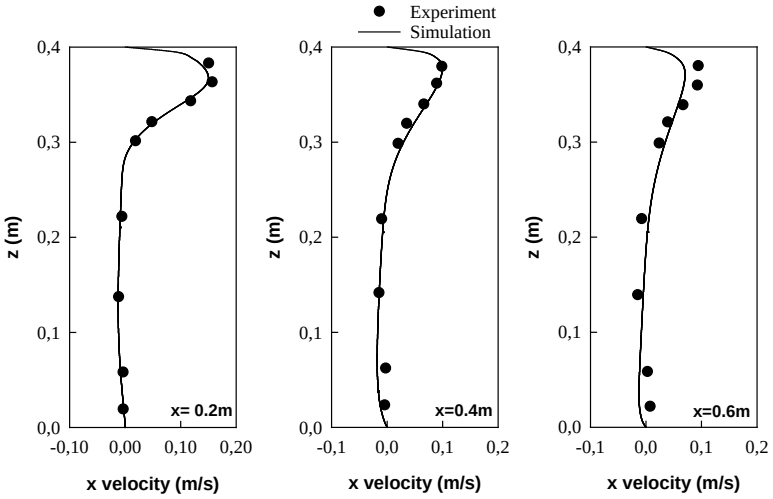

Figure 2. Comparison of measured [19] and predicted velocity at three different locations

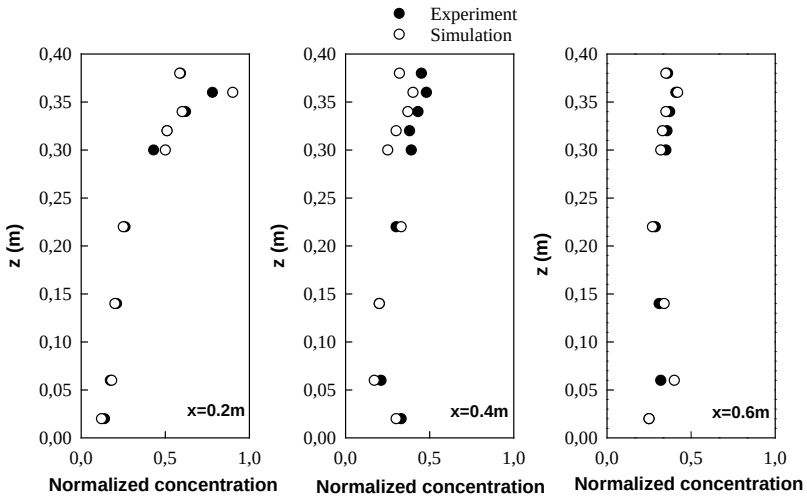

Figure 3. Comparison of measured [19] and predicted particle concentrations at three different locations

Figures 2 and 3 show a comparison of predicted x-velocity and particle concentration to experimental data [19]. Both velocity profile and Lagrangian DRW simulations are found to be compatible with measurements. Therefore, the numerical method is considered successful.

3. RESULTS AND DISCUSSION

Figure 4 shows the velocity contours and streamlines in the center plane of the operating room for two different ventilation strategies; that is, (a)without and (b)with a skirt. In the first case in which a skirt is not employed, supplied air shows a slight lateral deflection just after the LAF diffuser, although a general downflow is developed. In the other case seen in Fig.4b, there is no alteration observed in the direction of the supplied air just after the LAF face. In this particular case, the unidirectional form of the flow is preserved partially due to the skirt. As a result, the progress of the high velocity supplied air is reached nearly to the floor. It is also noticed that the medical lamp installed above the operating area disrupts the unidirectional airflow and a stagnant zone is formed in both cases. Even though this passive zone is smaller with the skirt modification, as shown in Fig. 4b, this kind of area is considered as risky since they are not taking advantage of the washing effect supplied by the LAF diffuser. Apart from the projection of the LAF diffuser, there are recirculation regions driven by very low air velocity magnitudes that exist on the upper corners of the OR and both sides of the operating table.

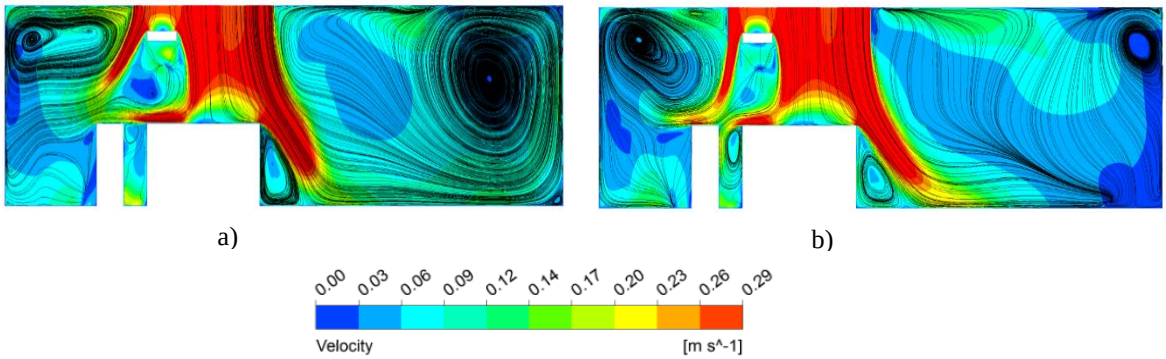

Figure 4. Velocity-contours and streamlines at the center-plane of the operating room;
(a) without skirt, (b) with skirt

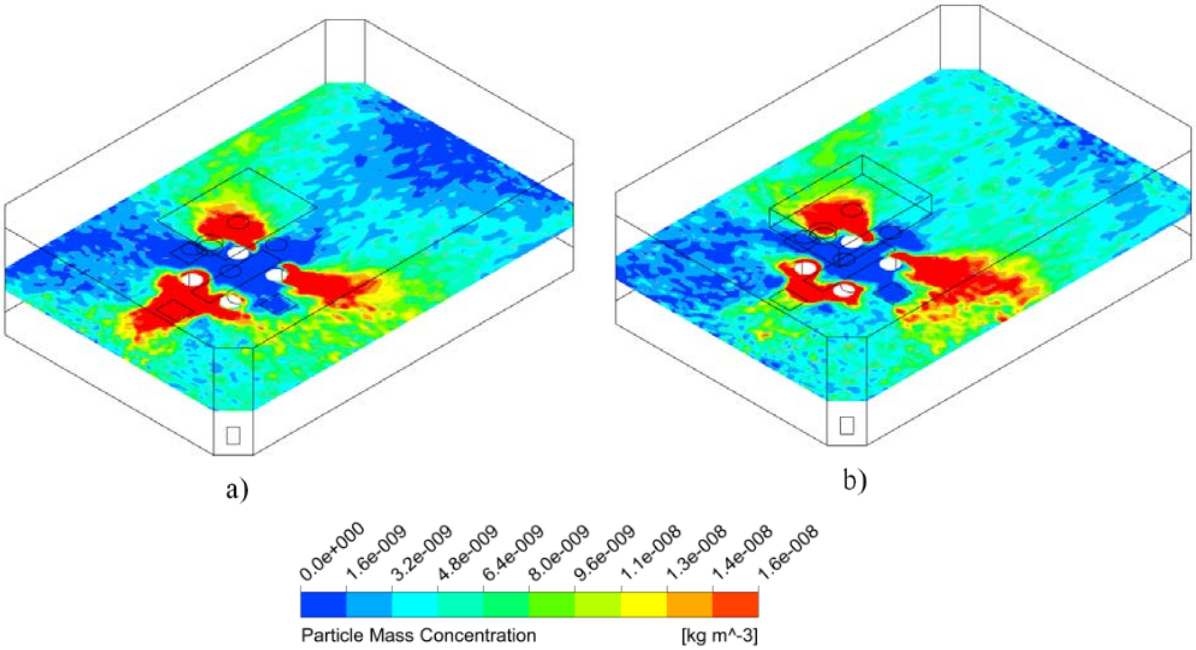

Figure 5. Particle concentration on the height of the surgical table (y=1 m) for 20µm; (a) without skirt, (b) with skirt

Figure 5 shows the concentration contours of 20 µm particles on the height of the surgical table (y=1 m) for both cases. As seen from the figure, the lowest concentration values are generally obtained on the operating table due to the effective washing effect provided by the LAF unit in both cases. In addition to this, it is seen in Fig. 5b that the skirt modification mitigates the concentration on the left side of the operating table compared to the original case depicted in Fig. 5a. The highest concentration values are reached around each of the surgical team as expected. It is also seen in both configurations that the particles released by the personnel on the right side of the operating table are swept towards out of the surgical area efficiently. A similar character is not obtained for the particles emitted by the two surgical personnel on the left side of the table. In this specific region, high particle concentration levels are obtained in the periphery of the personnel and partly on the operating table. The reason for this inadequate removal is the operating lamp that blocks the unidirectional airflow. For a more detailed analysis, the number of particles deposited on the operating table can be evaluated.

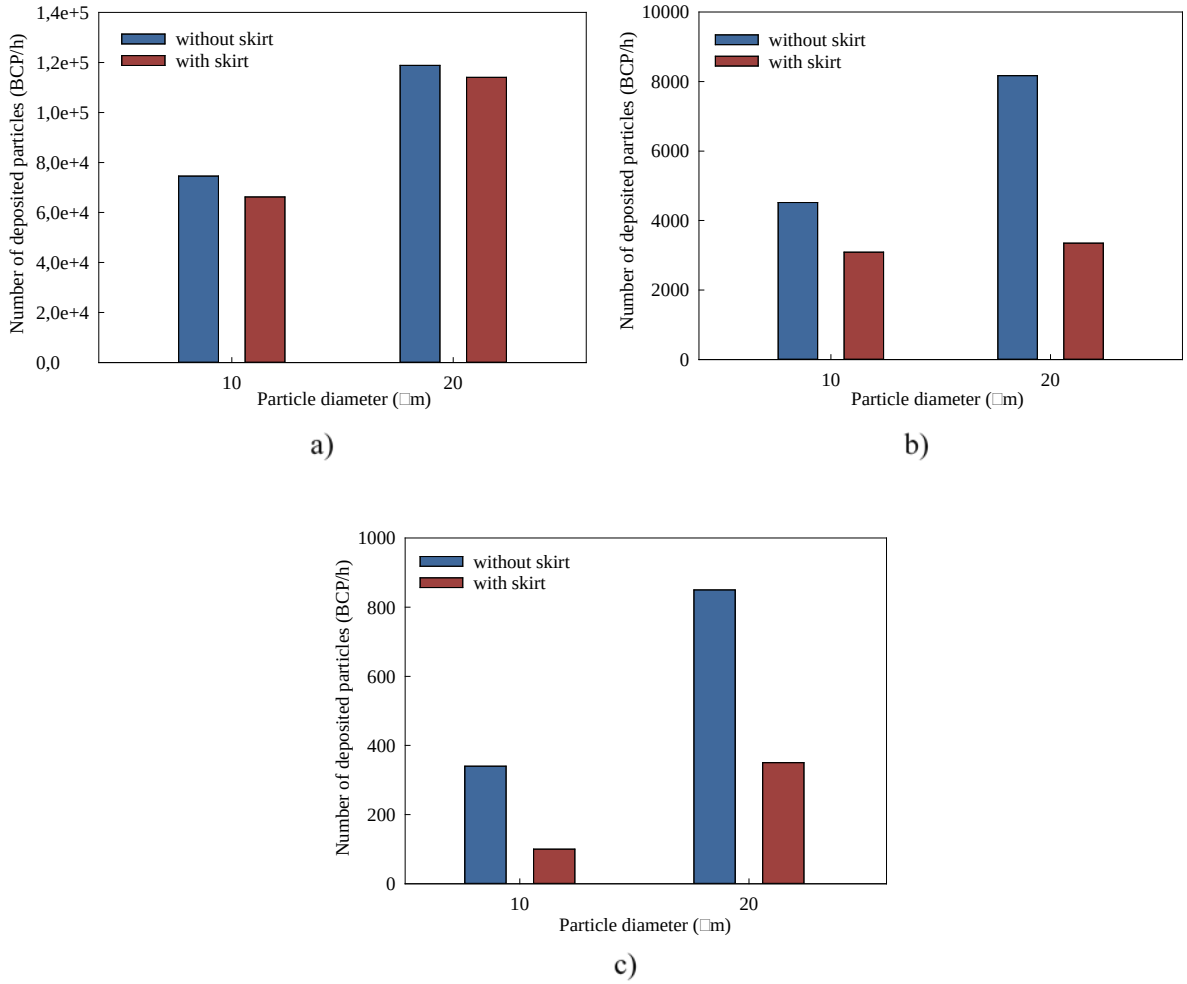

Figure 6. Comparison of the deposited particle numbers for different particle diameters and ventilation strategies: (a) whole OR, (b) equipment tables, (c) operating table

Figure 6 shows the deposited particle numbers to the whole OR surfaces (Fig.6a), the equipment tables (Fig.6b), and the operating table (Fig.6c), respectively. As a result of increasing gravitational forces deposition rates are increased with increasing particle diameters. In all cases, it is seen that the skirt modification reduces the deposited particle number and hence, it can be stated that a cleaner OR environment is sustained with the skirt configuration. Results reveal that the amount of particles deposited on the operating table in the skirt configuration decreases by 70.5% for 10 μm particle diameter and 58.8% for 20 μm particles compared to the original LAF diffuser without the skirt.

4. CONCLUSION

This study is performed to investigate the effect of the LAF diffuser with the vertical skirt on airflow and particle distribution in an operating room. The Realizable $k-\varepsilon$ turbulence model and the Lagrangian DRW model are used to simulate airflow field and particle transport, respectively. The important findings of the study are summarized as follows:

- The presence of the skirt has a significant effect on the airflow pattern, which determines the particle distribution.
- The skirt provides a stronger unidirectional downflow on the surgical site compared to the without skirt case.
- Skirt modification lowers the deposited particle numbers in the OR environment.
- Compared to the original LAF case, the amount of the particles deposited on the operating table in the skirt configuration decreased about 58.8% to 70.5%, depending on the particle diameter considered.

REFERENCES

[1] Allegranzi, B., Nejad, S.B., Combescure, C., Graafmans, W., Attar, H., Donaldson, L. & Pittet, D., Burden of Endemic Health-Care-Associated Infection in Developing Countries: Systematic Review and Meta-Analysis, *The Lancet*, **377**,228–241, 2011.

[2] Leblebicioglu, H., Nurettin, E., Victor, D.R. & Alper, S. et al., Surgical Site Infection Rates in 16 Cities in Turkey: Findings of the International Nosocomial Infection Control Consortium (INICC), *American Journal of Infection Control*, **43**, 48-52, 2015.

[3] Zamuner, N., Operating Room Environment with Turbulent Airflow, *In: ASHRAE Transactions*, 1986.

[4] Chauveaux, D., Preventing Surgical-Site Infections: Measures Other Than Antibiotics, *Orthopaedics & Traumatology: Surgery & Research*, **101**, S77–S83, 2015.

[5] Noble, W.C., Dispersal of Bacteria from Human Skin, *Proceedings of the International Symposium on Contamination Control*, 16–24, 1976.

[6] Whyte, W., Hodgson, R. & Tinkler, J., The Importance of Airborne Bacterial Contamination of Wounds, *Journal of Hospital Infection*, **3**, 123–135, 1982.

[7] Andersson, A.E., Petzold, M., Bergh, I., Karlsson, J., Eriksson, B.I. & Nilsson, K., Comparison Between Mixed and Laminar Airflow Systems in Operating Rooms and the Influence of Human Factors: Experiences from a Swedish Orthopedic Center, *American Journal of Infection Control*, **42,** 665–669, 2014.

[8] Hirsch, T., Hubert, H., Fischer, S., Lahmer, A., Lehnhardt, M., Steinau, H.U., Steinstraesser, L. & Seipp, H.M., Bacterial Burden in the Operating Room: Impact of Airflow Systems, *American Journal of Infection Control*, **40**(7): e228–e232, 2012.

[9] Chow, T. T., Lin, Z. & Bai, W., The Integrated Effect of Medical Lamp Position and Diffuser Discharge Velocity on Ultra-clean Ventilation Performance in an Operating Theatre, *Indoor and Built Environment*, **15**(4):315–331, 2006.

[10] Chow, T.T. & Wang, J., Dynamic Simulation on Impact of Surgeon Bending Movement on Bacteria-Carrying Particles Distribution in Operating Theatre, *Building and Environment*, **57**, 68–80, 2012.

[11] Whyte, W., Shaw, B.H. & Freeman, M.A.R., An Evaluation of a Partial-Walled Laminar-Flow Operating Room, *Journal of Hygiene*, **73**, 61–74, 1974.

[12] Lin, T., Zargar, O.A., Lin, K., Juina, O., Sabusap, D.L., Hu, S. & Leggett, G., An Experimental Study of the Flow Characteristics and Velocity Fields in an Operating Room with Laminar Airflow Ventilation, *Journal of Building Engineering*, **29**, 101184, 2020.

[13] Zhai, Z. & Preechawuttidet, P., Simulation and Analysis of Standard and Advanced Ventilation Systems in Hospital Operating Rooms, *IAQVEC 2016, 9th International Conference on Indoor Air Quality Ventilation & Energy Conservation in Buildings*, 2016.

[14] Chow T.T. & Yang X.Y., Ventilation Performance in the Operating Theatre Against Airborne Infection: Numerical Study on an Ultra-Clean System, *Journal of Hospital Infection*, **59**, 138–147,2005.

[15] Al-Waked, R., Effect of Ventilation Strategies on Infection Control Inside Operating Theatres, *Engineering Applications of Computational Fluid Mechanics*, **4** (1), 1-16,2010.

[16] Chen, Q., Comparison of Different $k-\varepsilon$ Models for Indoor Airflow Computations, *Journal Numerical Heat Transfer, Part B: Fundamentals*, **28**, 353-369, 1995.

[17] Srebric, J., Vukovic, V., He, G. & Yang, X., CFD Boundary Conditions for Contaminant Dispersion, Heat Transfer and Airflow Simulations around Human Occupants in Indoor Environments, *Building and Environment*, **43**, 294–303, 2008.

[18] ANSYS Fluent 15.0 User's Guide, Ansys Inc., 2013.

[19] Chen, F., Yu, S.C.M. & Lai, A.C.K., Modeling Particle Distribution and Deposition in Indoor Environments with a New Drift–Flux Model, *Atmospheric Environment*, **40**(2), 357–367, 2006.

ON THE USE OF NATURAL VENTILATION SYSTEM FOR SUCTION OF INHALED GASES IN PRODUCTION LINES FOR IMPROVED INDOOR AIR QUALITY

Onur KAYAPINAR*, Oğuz ARSLAN **
*Bilecik Şeyh Edebali University, Department of Mechanical Engineering, Bilecik/Turkey
Email: onurkayapinar1989@gmail.com
**Bilecik Şeyh Edebali University, Department of Mechanical Engineering, Bilecik/Turkey
Email: oguz.arslan@bilecik.edu.tr

ABSTRACT

The use of ventilation systems from our homes to industrial areas is increasing day by day with the growth of the population and industry. Ventilation systems used to meet the need for ventilation create energy consumption. In order to reduce energy consumption and to be able to ventilate more environmentally, natural ventilation systems are used in industrial areas. Ventilation systems that provide ventilation using pressure and temperature difference and do not have any energy consuming components are called natural ventilation. In this study, a natural ventilation system is discussed and the results are examined.

Keywords: Natural Ventilation System, Production Line, Air Quality

Nomenclature

A	Air entrance (m^2)
$C_{p,r}$	Wind pressure coefficent in wind direction
$C_{p,t}$	Wind pressure coefficent in opposite wind direction
C_d	Discharge coefficent
g	Acceleration of gravity (m/s^{-2})
Δh	Vertical distance between air inlet and outlet (m)
ΔP	Indoor and outdoor pressure difference (Pa)
P_0	Static pressure at reference altitude (Pa)
P_w	Wind pressure (Pa)
P_i	Static pressure in surface (Pa)
T_i	Indoor temperature (^0C)
T_0	Dış ortam sıcaklığı (^0C)
v	Wind velocity (m/s)
Q_T	Evacuated air with ΔT
Q_r	Evacuated air with ΔP
Q_{TH}	Total evacuated air
ρ	Air density (kg/m^3)
θ	Effectiveness of clerance

1. INTRODUCTION

The acquisition of energy, increasing costs and the use of fossil fuels are not acceptable for today's conditions. Environmental damage increases day by day. If the amount of energy used for production is not taken into account, the amount of energy consumed for ventilation and heating is serious. For these reasons, considering natural ventilation, it comes to the forefront to reduce energy consumption and reduce global damage to the environment. The use of natural ventilation in buildings enables energy-efficient environment creation by saving energy compared to mechanical systems.

In today's conditions, it is possible to see the use of natural ventilation systems individually or industrially. Natural ventilation systems have been started to be used in buildings and industrial areas against rising energy costs. Our country has examples in glass and ceramic industry. In classical Turkish and Asian architecture, there are designs that provide natural ventilation even in historical buildings from the past and there are many research subjects.Figure 1. Shows a NVS in today's modern glass manufacturing plant in top of factory roof. Natural ventilation systems used in today's conditions provide ventilation under natural conditions without any energy consumption by replacing low-quality breathing air in industrial work areas with fresh air.The important point here is that these systems renew low-quality air by allowing the external ambient air to enter the internal control volume. They are simple and primitive compared to professional systems.The quality of the ambient air and the efficiency of the system design determine the maximum benefit of the ventilation system.

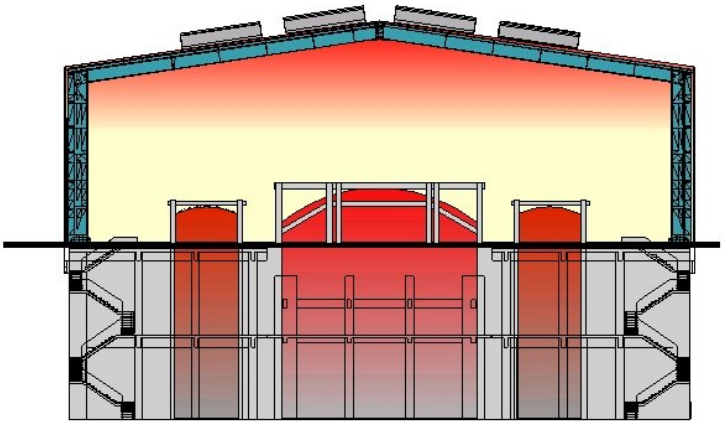

Figure 1. Natural ventilation system is in a today's glass manufacturing plant top of factory roof.

Until today, the development of natural ventilation is based on experience. Natural ventilation is nothing new, it has been around for hundreds of years. However, with the discovery of energy driven systems in the 19th century, it has remained in the secondary plan. Wind supported natural ventilation systems can be a good alternative for today's buildings. For the modern NVS named Bactolite can be given as an example [1].

The hierarchical classification of ventilation systems can be defined as shown below [2]. It is possible to see hybrid or supported natural ventilation systems among the ventilation systems. Figure.2 shows the hierarchical order of the use of today's ventilation technology. As can be seen in Figure 2, the most common systems are mixed types and the least preferred systems are natural ventilation systems.

Figure 2. The hierarchical classification of the use of today's ventilation technology.

It is difficult to reach a definitive conclusion when we compare natural ventilation according to mechanical and air conditioning systems. Considering the advantage of natural ventilation systems, the most prominent feature is that electricity consumption or the type of energy obtained from any fossil propensity is not used compared to electrically driven systems. Another advantage is that it provides sustainable benefits because it does not depend on energy.

The disadvantage of natural ventilation systems is due to climate and physical conditions. The benefits provided in some physical and climatic conditions may be limited. Especially to increase the amount of ventilation, it may be necessary to be supported with mechanical systems under such conditions. When considering natural ventilation systems in commercially, they create lower costs compared to mechanical systems in terms of application costs and operating costs. Considering volumetrically, natural ventilation systems require more space than mechanical systems.

The design of an NVS is shaped depending on the ambient conditions at which it will be applied. However, there is uncertainty in determining important variable parameters. For example, variable wind loads, internal temperature differences ,and unwanted air leaks in the applied building. Design for an NVS is divided into 5 main topics, these are respectively, applicability, selection of ventilation method, application of ventilation method, determination of internal air movements and commissioning.

Before applying the ventilation system, the degree of applicability should be determined by considering the environmental conditions and cost. Many variables such as climate conditions, physical condition of the building in need of ventilation, desired ventilation amount, adaptation to the architectural structure should be considered. Implementation of a suitable model by determining the factors that will reduce the efficiency of the ventilation system An investment made regardless of yield will have heavy costs.

The selection of the ventilation method specifies the flow model for the application of natural ventilation. The design of the NVS, which may conform to the architectural structure taken, should be shaped with the flow model. The ventilation method should be compatible with the physical model. and the outside temperature difference, the wind speed, cause inward-to-out traction. This ventilation method is suitable for study type of physical model.

After determining the natural ventilation method, it is necessary to relate the method and the optimum benefit. For example, it is necessary to know and relate the air inlet openings and the flow rates in the air outlet of the ventilation system. The air inlet openings and the location of the natural ventilation are one of the main parameters affecting the design.

It is very difficult to calculate the internal air movements in the use of natural ventilation systems. In the use of natural ventilation, the internal air movement is more sensitive to the effects. While the desired climatic conditions can be achieved in any position within the building in mechanical ventilation systems, it is necessary to consider the building applied for NVS completely. In natural ventilation systems. Controlling indoor air movement and comfort conditions can be realized by controlling the flow rates in the air inlet and outlet openings.

2.METHOD

The flow rate in the physical model to describe the flow in natural ventilation systems is defined as the envelope flow rate. Variable envelope flow rates in natural ventilation systems and air flow direction changes constitute the main differences between mechanical systems and natural ventilation. For an example , the envelope flows are shown in figure 3. Here q indicates the flow rate per unit time and the value of q depends on the value of U, ϕ w, indoor and outdoor temperature difference and A span area. The source of the flows is the momentum and buoyant force. The momentum and buoyancy vary with parameters U, ϕ, ΔT etc. In mechanical systems, the flow rate q is constant, but the change in momentum and buoyant force in natural ventilation systems For example, heating or cooling of the objects. Changing the ΔT value between indoor and outdoor affects the flow rate.

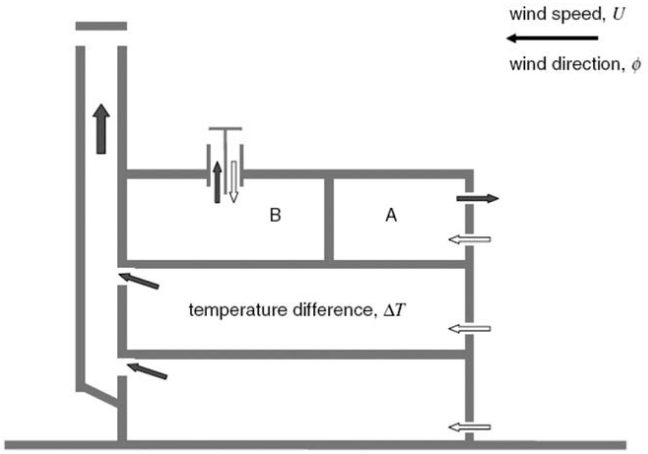

Figure 3. Multicell natural ventilation model envelope openings.

According to forced ventilation model in natural ventilation systems, any drive fan etc are not in NVS. Natural ventilation is the movement of air due to the differences in internal and external pressure from certain openings that are intentionally opened on the physical model. In this study, an industrial NVS is considered as a physical model. Figure.4 shows the general physical model of industrial NVS sectional view of this study [2]

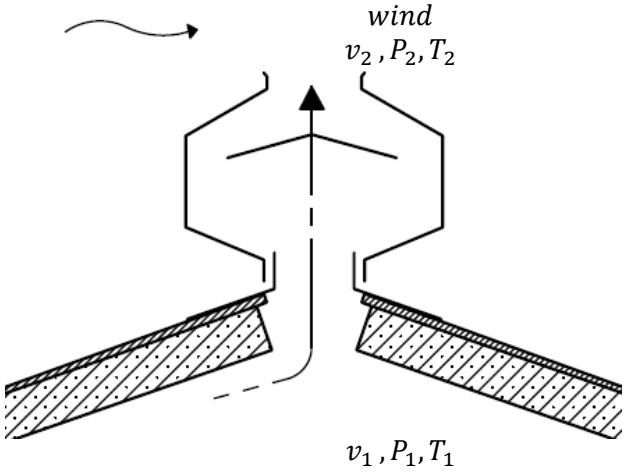

Figure 4. Shows the general physical model of industrial NVS sectional view.

The mass flow of the air flow entering into the physical model must be equal to the mass flow of the air leaving. Static pressure is formed on the surface as a result of the impact of the wind, which is one of the main causes of natural ventilation, the temperature difference is the main reason for the air movement between the difference between ΔT and ΔP. The pressure difference between indoor and outdoor is as given in equation (1). The following equation (2) is obtained to calculate the ventilation flow by using the pressure difference created by the wind.

$$\Delta P = \rho . \frac{V^2}{2} . (C_{p.r} - C_{p,t}) \quad (1)$$

In equation (1) $C_{p,r}$ and $C_{p,t}$ are the wind pressure coefficients on the wind direction and the surface opposite to the wind.

$$Q_r = C_d . A \sqrt{\frac{2\Delta P}{\rho}} \quad (2)$$

In equation (2) C_d is the discharge coefficient. The discharge coefficient is a function dependent on the dimensions of the ventilation opening and the Reynolds number.

Figure.5 shows the variation of the C_d number according to the reynolds number and pressure difference for the air vents[3]. Figure.6 indicates this change for large type openings[3]

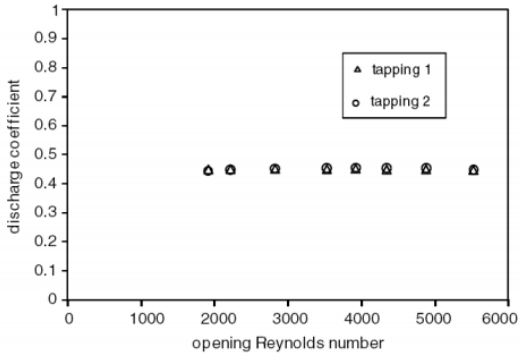

Figure 5. Variation of the C_d number according to the reynolds number and pressure difference for the air vents

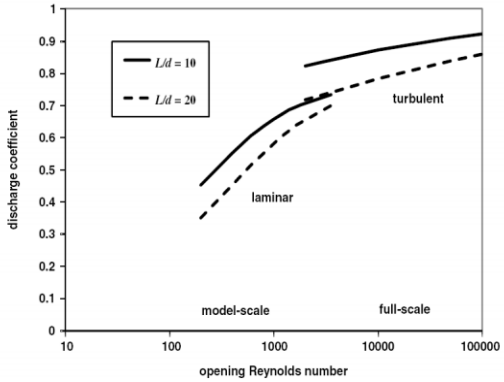

Figure 6. The change of C_d for large openings.

The ventilation flow is caused by the temperature difference is determined by the equation (3). Actual total flow of air movement is caused by temperature difference and wind speeds is reached by equation (4).

$$Q_T = C_d . A . \phi . \sqrt{2g . \Delta h . \frac{T_i - T_0}{T_i}} \tag{3}$$

$$Q_{TH} = \sqrt{{Q_r}^2 + {Q_T}^2} \tag{4}$$

3. RESULTS

In this study, NVS, which is produced by a local company, is discussed and no measurement is made on the physical model. In the building where the ventilation is applied, internal and external conditions are given by Table 1.Figure 7 .shows side view of NVS and Figure 8. shows bottom view of NVS model of local company in this study .

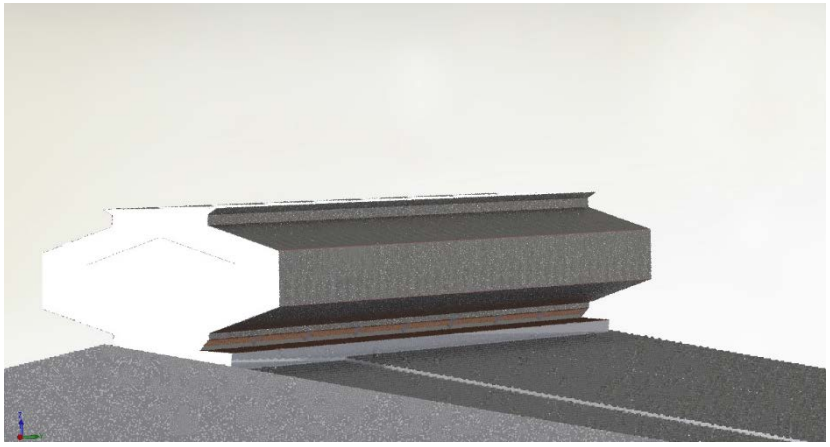

Figure 7. Side view of NVS model in a local company

Figure 8. Bottom view of NVS model in a local company

The pressure difference between ΔP indoor and outdoor environment is reached by using Equation (1). The ΔP value obtained from Equation (1) is used by Equation (2) to reach Q_r value. Equation (3) examines the different states of the ΔT value. The air reference temperature is accepted as 10,20, 30, 40, 50, 60^0 C. The total ventilation flow is achieved by using the data obtained with the equation (2) and the equation (3) in equation (4). Table.1 shows the change of Q_{TH} discharged air value depending on the model width depend on conditions.

Figure 8. According to the model width 0.5 m , ΔT indicates the relationship between temperature difference and Q_{TH} discharged air flow.Width of model is named base clearence which is size of width oof pysical model . Figure 9. According to the model width 1 m , ΔT indicates the relationship between temperature difference and Q_{TH} discharged air flow. Figure 10. According to the model width 1.5 m , ΔT indicates the relationship between temperature difference and Q_{TH} discharged air flow.

Table 1. Q_{TH} discharged air value depending on the model width.

Base clearance (m)	A ($m^{2)}$	C_d -	Φ -	h (m)	ΔT (C^0)	ρ (kg/m^3)	$C_{p,r}$ -	$C_{p,t}$ -	v (m/s)	ΔP (Pa)	Q_T (m^3/s)	Qr (m^3/s)	Q_{TH} (m^3/s)
0.5	0.5	0.2	0.6	7	0	1.164	0.65	-0.65	3.5	9268	0.994	0.399	1.071
	0.5	0.2	0.6	7	5	1.247	0.65	-0.65	3.5	9929	0.497	0.399	0.637
	0.5	0.2	0.6	7	10	1.293	0.65	-0.65	3.5	10295	0	0.399	0.399
	0.5	0.2	0.6	7	15	1.342	0.65	-0.65	3.5	10685	-0.351	0.399	0.531
	0.5	0.2	0.6	7	20	1.395	0.65	-0.65	3.5	11107	-0.444	0.399	0.597
	0.5	0.2	0.6	7	25	1.453	0.65	-0.65	3.5	11569	-0.497	0.399	0.637
1	1	0.2	0.6	7	-20	1.164	0.65	-0.65	3.5	9268	1.988	0.798	2.142
	1	0.2	0.6	7	-10	1.247	0.65	-0.65	3.5	9929	0.944	0.798	1.275
	1	0.2	0.6	7	0	1.293	0.65	-0.65	3.5	10295	0	0.798	0.798
	1	0.2	0.6	7	10	1.342	0.65	-0.65	3.5	10685	-0.703	0.798	1.063
	1	0.2	0.6	7	20	1.395	0.65	-0.65	3.5	11107	-0.889	0.798	1.195
	1	0.2	0.6	7	30	1.453	0.65	-0.65	3.5	11569	-0.994	0.798	1.275
1.5	1.5	0.2	0.6	7	-20	1.164	0.65	-0.65	3.5	9268	2.983	1.197	3.214
	1.5	0.2	0.6	7	-10	1.247	0.65	-0.65	3.5	9929	1.491	1.197	1.912
	1.5	0.2	0.6	7	0	1.293	0.65	-0.65	3.5	10295	0	1.197	1.197
	1.5	0.2	0.6	7	10	1.342	0.65	-0.65	3.5	10685	-1.054	1.197	1.595
	1.5	0.2	0.6	7	20	1.395	0.65	-0.65	3.5	11107	-1.334	1.197	1.792
	1.5	0.2	0.6	7	30	1.453	0.65	-0.65	3.5	11569	-1.491	1.197	1.912

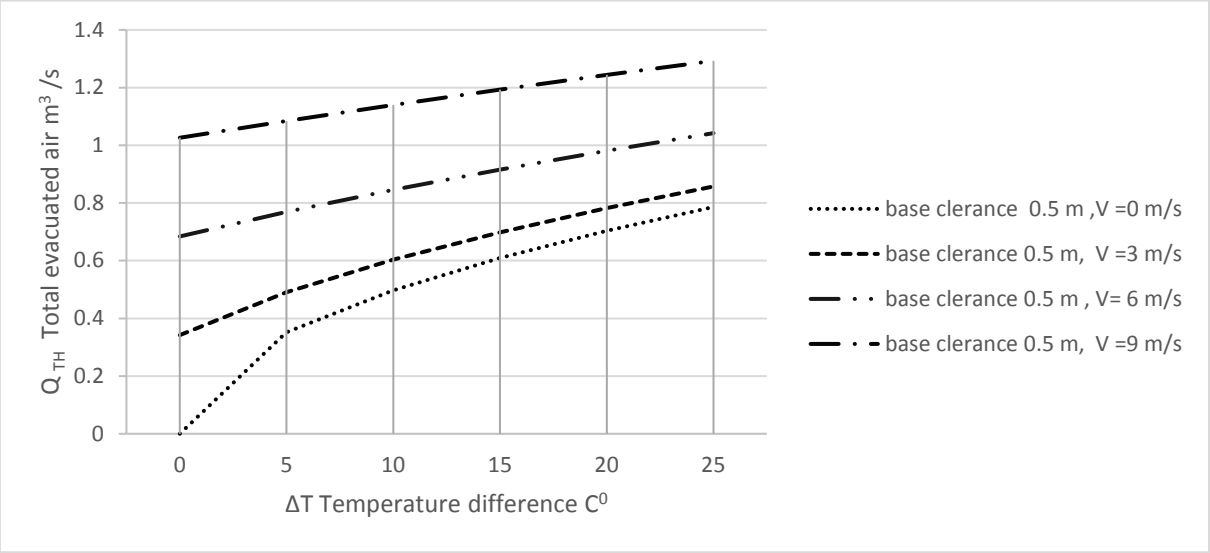

Figure 8. shows the change in the evacuated air according to base clearance 0.5 m ,wind speed and temperature

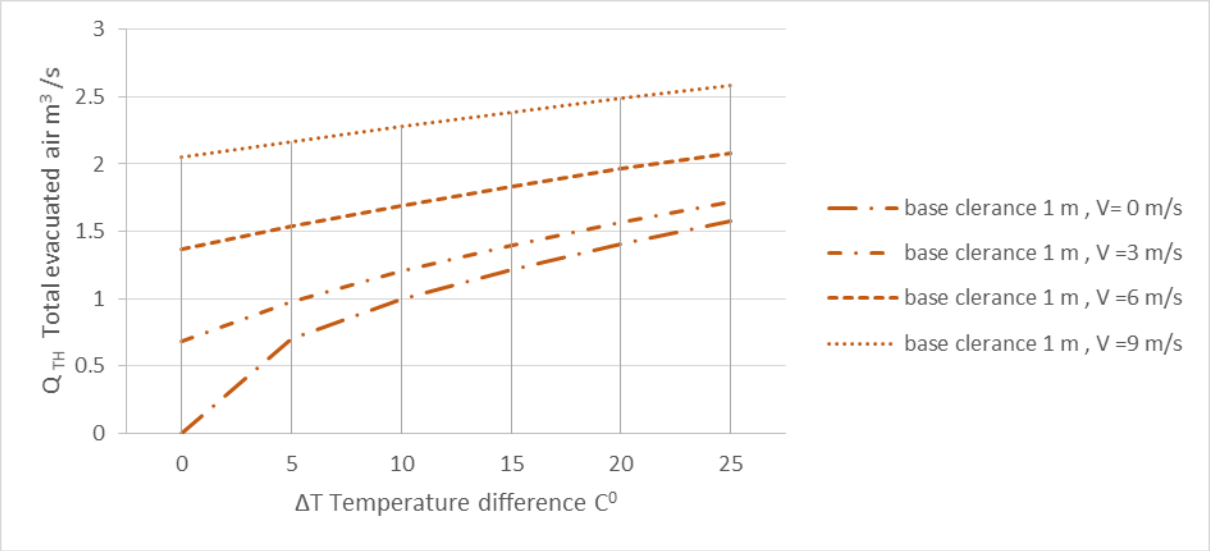

Figure 9. shows the change in the evacuated air according to base clearance 1 m ,wind speed and temperature

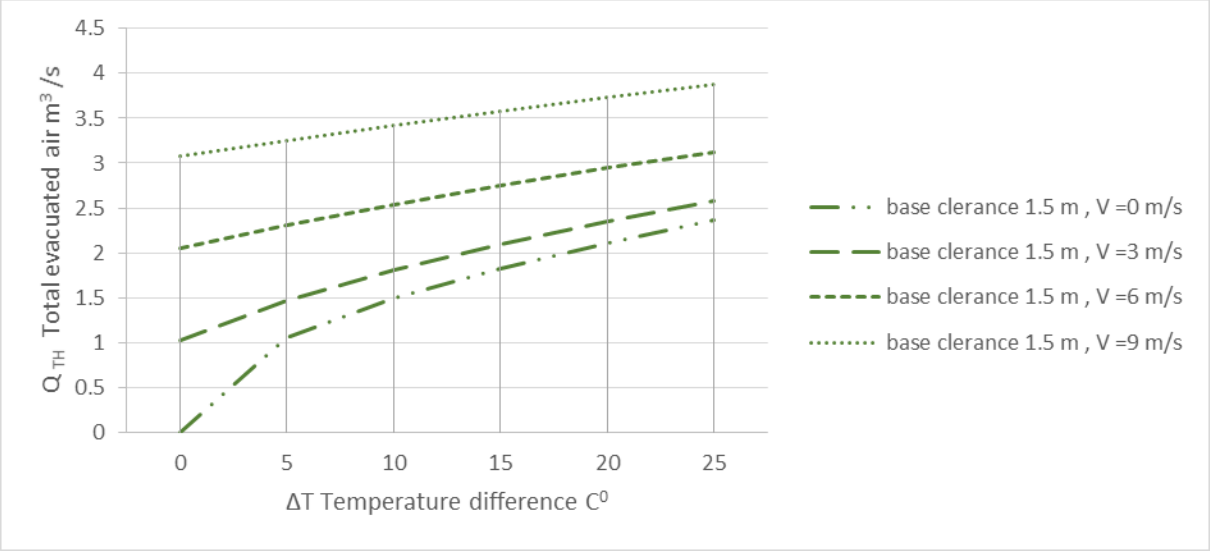

Figure 10. shows the change in the evacuated air according to base clearance 1.5 m ,wind speed and temperature.

As can be seen from the Figures, as the temperature difference and wind speed increase, the amount of discharged air flow increases for the physical model with a length of 1 m, according to the width of the base. At the point where ΔT is 0^{0} C, only the discharge air flow due to the ΔP pressure difference created by the wind appears. In this study, the amount of ventilation where ΔT is only positive is examined.

In this study, cost analysis and economic analysis were not performed, study tried to reach the functionality of the physical model in numerically and based on basic NVS principles. Calculated values of study may differ under real-life conditions, the main reason for this being that the annual average of the wind speed and temperature conditions are not being measured respectively, the flow rate is not measured on the physical model under real conditions. However, it is possible to say that the use of NVS system is innovative and noteworthy. In the face of increasing energy consumption in the industry and increasing global warming danger, NVS systems developed in the future will be a good solution for the ventilation industry.

REFERENCES

[1] Demir, H., Doğal Havalandırma Yöntemlerinin Sayısal Modellenmesi, Yüksek Lisans Tezi, *İ.T.Ü.Fen Bilimleri Enstitüsü,* 2013.

[2] Etheridge, D.. Natural Ventilation of Building: Theory, Measurement and Design. *Department of Architecture and Built Environment, University of Nottingham, UK.* 2012

[3] Küskü, B.. Eğimli Çatılarda Havalandırma, *Yüksek Lisans Tezi, Y.T.Ü.Fen Bilimleri Enstitüsü,* 2005

[4] Nikas, N., Nikolopoulos, N., Nikolopoulos A. Numerical study of a naturally cross-ventilated building, *Energy and Buildings* :Volume **42**, Issue 4, April 2010, Pages 422-434

[5] Öztürk, H., Natural and Forced Ventilation Systems in Buldings, Tesisat mühendisliği dergisi, **89**(1), 21-26, 2005.

[6] Yaşa, E.,Avlulu Binalarda Doğal Havalandırma ve Soğutma Açısından Rüzgar Etkisi ile Oluşacak Hava Akımlarına Yüzey Açıklıklarının Etkisinin Deneysel İncelenmesi, Yüksek Lisans Tezi, İ.T.Ü.Fen Bilimleri Enstitüsü, 2005.

[7] Zhai, Z., Mankibi, M., Zoubir A., Review of Natural Ventilation Models.IBPC 2015: *6th International Building Physics Conference,* Vaulx France, 2015.

INVESTIGATION OF BIM (BUILDING INFORMATION MODELING) SYSTEM IN TERMS OF PRESSURE ENERGY LOSSES IN VENTILATION SYSTEMS

Faruk DEMİRTAŞ*, Cevdet DEMİRTAŞ **
*Trabzon Provincial Health Directorate, Trabzon/Turkey
Email: fdemirtas198213@gmail.com
**Karadeniz Technical University, Department of Mechanical Engineering, Trabzon/Turkey
Email: demirtas@ktu.edu.tr

ABSTRACT

The building mechanical installation design process generally based on drawing independent projects for each installation. This method is not sufficient in terms of how the installation systems which are similar in terms of the space they occupy, should be positioned relative to each other and other engineering branches. Thus, there are many clashes in the conventional construction method. Therefore, high energy consumption occurs for the installations due to pressure loss.

Pressure loss should reduce to minimize energy costs in HVAC systems. In order to calculate pressure loss correctly, it is necessary to know exactly the types and numbers of fittings of the ventilation system. In the conventional method, the pressure loss of ventilation ducts calculate by neglecting fittings in the 3rd dimension. However, during the installation phase, fittings of the 3rd dimension are also added to the project's fittings. This causes the ventilation system to have a greater pressure loss than the values calculated in the project and create more energy-consuming systems. A ventilation system model created with BIM (Building Information Modeling) more clearly expresses the type and number of all parts of this system. With the 3D models created with BIM, you can see how to assemble before the construction phase. Thus, the dimensions of the cavity required to create a ventilation system design that would result in less pressure loss can be more clearly defined.

Keywords: Mechanical installations, Ventilation, BIM.

Symbol List

A	Major axis of the flat oval duct (m)
a	Minor axis of the flat oval duct (m)
A_c	Actual cross-sectional area of the duct (m^2)
A_e	Hypothetical area based on equivalent circular duct (m^2)
c	Loss coefficient
D	Inside diameter (m)
D_e	Equivalent diameter (m)
D_h	Hydraulic diameter (m)
ε	Absolute roughness (mm)
f	Friction factor
g_c	Gravitational constant ($kg.m/N.s^2$)
H	Height (m)
L	Length (m)
p_v	Velocity pressure (Pa)
ΔP	Pressure drop (Pa)
ΔP_f	Friction (N)
P	Perimeter of the duct (m)
q	Flow (m^3/s)
μ	Air viscosity (dynamic) (Pa.s)

ρ	Air density (kg/m^3)
Re_e	Reynolds number based on the equivalent
v	Kinematic viscosity (m^2/s)
V_c	Velocity (m/s)
V_e	Hypothetical velocity based on equivalent circular duct (m/s)
W	Width (m)

1. INTRODUCTION

Prompt response and troubleshooting HVAC-related buildings' problems are vital to providing a comfortable indoor environment for building residents. Two significant challenges in the current implementation lead to a quick troubleshooting process and resource waste: these two significant challenges; the lack of timely access to essential plant and system information and the large search space of the possible causes of a particular HVAC related problem [1]. The data obtained in BIM also save time with faster and shortened recurrence time for HVAC system calculations. There are advantages of more consistent data for pressure losses in the ducts, facilitating problems in operating the HVAC system, and reusability of stored data in BIM content [2]. Increasing the comfort conditions in the buildings also increased the energy need. The energy used in Europe buildings is around 40% of the total energy [3].

Before any building built, the area that the building will cover does not consume energy. However, while the building built, it is necessary to provide an indoor environment different from the surrounding environment [4]. Pressure loss have an essential place in HVAC systems that meet this need. Thus, almost every building creates an energy use burden to meet the requirements for HVAC systems. BIM (Building Information Modeling) technology is increasingly being used in the architecture, engineering, and construction industries [3]. When the studies reviewed, you can see that the importance of BIM technologies is increasing day by day. The use of BIM technologies in the project design phases can reduce the problems that can encounter throughout the buildings' lifetimes with the measures to be taken. Therefore, it is inevitable that such software will become more widespread in the future [3]. It is known that the traditional method is not take into account in Building energy performance (BEP) calculations due to difficulties in determining pressure losses in HVAC systems. Preparing building energy performance models involves repetitive manual operations that often lead to data losses and errors. These processes can be very different from time-consuming, accurate results, non-standard and subjective processes. For BEP models, the HVAC parameter should also be used [5]. Building Information Modeling (BIM) can help sustainability as the digitalization of product and process information provides a unique opportunity to optimize energy-efficiency-related decisions across the entire lifecycle and supply chain. BIM is considered to have several features that provide energy efficiency and potential growth in the green building marketplace. These features are; multidisciplinary integrative capacity of BIM, informed sustainability design, BIM use for monitoring building performance, educational support, and communication tools [6].

From the comparison between baseline simulation and BIM-based simulation results, it was found that the properties of the HVAC system played an important role in accurate simulation results. Therefore, more comprehensive information about the HVAC system should be provided [7].

2. TRADITIONAL METHOD AND BUILDING INFORMATION MODELING FOR HVAC SYSTEM IN BUILDINGS

HVAC are active systems that meet heating/cooling and ventilation needs within the Mechanical, Electrical, and Plumbing (MEP), also known as construction services in the industry [8]. HVAC systems design in a building according to the demands and required standards. HVAC systems play a significant role for a building in having various standards on issues, such as environmental factors, comfort conditions, and human health. The design of the HVAC system in a building is based on the principle of transporting the air required for the spaces in the building through the ducts and transporting the air from the space.

Some problems arise mechanical installation projects prepared during the design phase when apply in the field during the construction phase. The main ones are:

- Creating mechanical installation projects independently of each other causes non-coordination.
- It is not noticed whether the spaces are sufficient for mechanical installation systems in architectural and structural projects.
- Since mechanical installation projects are drawn in 2D, the elevations of the ducts, pipes, equipment, and devices of the systems are not clear, and the installations passing through the same locations clash.
- The decrease in the number of alternative solution methods in revised (application) projects.

For the solution of such problems, it is required a method by which architects and engineers who prepare building projects can create their projects with a collaborative approach. Thus, possible problems will arise during the construction phase can solve during the design phase [9]. The HVAC system design in BIM designed as an alternative to traditional design in the construction industry. Design alternatives can create with various analyzes that enable the designed structure to evaluate in energy efficiency.

In summary, traditional building design consists of these stages: A preliminary architectural project created to meet the demands and needs of the owner or the specific physical standards. After the preliminary architectural project is approved by the owner, a detailed architectural project created. The detailed architectural project transfer to the related engineering branch for the creation of the structure project. At this stage, there is coordination between architect and engineer. Copies of the created architectural project transfer to the relevant engineering branches to create MEP projects. Most of the time, engineering disciplines don't include in the project until this stage. Each engineering branch draws its own projects using architectural projects transferred to them. At this stage, projects are created independently of each other. After all the projects create, the construction phase start. Due to the lack of coordination between the projects which created at this stage, many conflicts occur during construction on site. These conflicts cause loss of time and money, as well as not being able to meet the required standards and not satisfying the owners' demands.

Building design with BIM consists of these stages: BIM brings together the people involved in the design, construction, and operation of the building, which it calls a participant, at the design phase of the building. The participants bring together to ensure that a virtual model of the building create by being aware of all processes from the design stage to demolition stage of the building. By combining architectural, structure, and MEP models of the building, clashes that may occur during the construction phase identify at the design phase, and necessary measures take, and necessary arrangements make. Clash detection software is used at this stage. With the project created by combining all models of the building, the construction phase start. The project, which was created by reducing the number of clashes greatly, causes a more efficient construction process than the traditional project. BIM brings together all participants involved in building construction. Thus, possible conflicts during the building construction phase prevent. In addition, time and money losses prevent. With this method, the standards required for the building meet more appropriately and the demands of the employers fulfill more efficiently.

3. HVAC DESIGN METHOD AND STAGES IN BIM

HVAC mainly based on the principle of thermodynamics, heat and mass transfer, and fluid dynamics. The primary purpose of HVAC is to create a comfortable thermal environment for the building and to provide the required amount of indoor air quality for the building [10]. The fact that four disciplines consisting of architects, civil, mechanical, and electrical engineering, which have been brought to the agenda with BIM technology in recent years, are aware of each other in the projects, brought up programs that will work on this platform. The most well-known of these programs in our country is Revit. Revit is a program that can make both 3D drawings and calculations that all four disciplines can use [3]. Models created with Revit, a parametric object-based program, are created with object families. You can create these object families or make changes to existing object families [10]. REVIT 2019 software is an HVAC design software used for BIM.

3.1 Architectural Model

When designing HVAC systems for a building, things to consider are building size, location, and intended use. All this information helps the mechanical engineer determine which type of HVAC system will be most suitable [11]. There are structural elements in the architectural model that can affect the ventilation design. These are elements, such as floors, walls, windows, doors, beams, and columns [12]. These structural elements whose thermal properties determined in the architectural model, contain some parameters required for HVAC design [12]. Thus, in the BIM method, it can be said that the HVAC design started with an architectural model.

3.2 Creating an HVAC Model

When a new mechanical project starts in Revit, the available mechanical template file is selected and creates a blank MEP template model set to metric units by default [11]. An HVAC model in Revit includes spaces, air terminals (vents and anemostats, etc.), ducts, mechanical equipment (AHU-Air Handling Unit-, etc.) and duct systems [12].

3.3 Linking Architectural and Structural Models

It is considered good practice to create separate models for the architectural and HVAC model and to link the architectural model to the HVAC model as a Linked Revit model. The linked architectural model mainly serves as a substrate for the HVAC model, which can be updated if necessary [12].

3.4 Coordinating and Matching Discipline Levels

When multiple disciplines work on a coordinated BIM model, it is advantageous to continually monitor the number and location of all levels in the model. Revit can do this automatically by linking levels in the MEP model to levels in the architectural model [11].

3.5 Placing Spaces

For Revit to perform HVAC load calculations, the locations must be located and defined in the mechanical model. For define these spaces, the "Room Bounding" option should mark as the Type Property of the linked model [11].

3.6 Defining Zones

Zones will be used in load calculations to determine the heating, cooling, and airflow requirements for all spaces in each zone so that HVAC equipment can be sized and selected appropriately. Here, Heating and Cooling Information (setpoints and supply air temperatures) can be entered and specified for each zone [11].

3.7 Revit Space Types

Built-in space type parameters are listed by space types set by ASHRAE standards. Revit calculates the ventilation air flows per zone. Here, it uses only the 'Outside Air Per Person', 'Outside Space Per Air' and 'Per Hour Air Changes' methods to calculate the required ventilation airflow [12].

3.8 Calculation of Loads

Heating and cooling loads can calculate by selecting the Heating and Cooling Loads option on the Analysis tab in Revit. In this dialog, there is a Parameter named Report Type; Here, the engineer can choose Simple, Standard, or Detailed load report. When the calculations complete, a load report will be displayed. Loads calculated using Revit loading software are the basis for the sizing of mechanical systems and equipment part of the HVAC model [11].

3.9 Define Project Settings

Before working on the mechanical model, some settings such as Project Information, Parameters and Units should be defined [11]. Mechanical Settings, including Duct Settings, are essential at the beginning of the HVAC system design [12].

3.10 Creating and Using the Common Object Library (COL)

The Revit Common Object Library (COL) is a collection of Revit families. This collection is included in each project model and can save in a separate folder [11].

3.11 Duct System Classifications and Duct System Types

Duct Systems are used to group different ducts, duct equipment, and mechanical equipment. In addition to the physical connection between these elements, duct systems provide a higher level of connection between these elements, allowing engineering data to flow between these elements. The Revit Duct System Category has three internal Duct System Classifications: Supply Air, Exhaust Air, and Return Air [12].

3.12 Duct Types, Flexible Duct Types, and Duct Insulation

Duct Types contain information about duct material and priority duct inserts to be used when modeling ducts. All Duct Types have a "Roughness" of 0.09 mm, a typical value for galvanized steel spiral ducts. In addition to the Duct Attachments stored in the "Routing Preferences", the user can also load other Duct Attachments from the Revit library if necessary. Revit also has a Flex Duct Category for flexible ducts. Flex Duct also has a 'Roughness' parameter, and some preferred Duct Fittings can be selected. Revit also has Duct Insulation and Duct Lining System Families [12].

3.13 Placing HVAC Equipment and Distribution Elements

When the required object families load on the mechanical model, the placement of mechanical equipment, systems, and accessories can begin [11]. The first HVAC elements to be placed on the model are supply and extract Air Terminals. At a later stage, after the AHUs and Ducts install, the exhaust and outside Air Terminals are modeled. Each of these supply and extract Air Terminals will bring air to or take air from the space where it is placed in [12].

3.14 Air Terminals, Spaces, and Airflows

The required heating and cooling loads, airflow information for all spaces and zones in the model should transfer to equipment serving these spaces, and zones. For airflow requirements, all of these begin at the air terminals in each space [11]. Each air terminal must be in the correct Revit space for workflow. If an air terminal is in the space, Revit dynamically controls it. It then reads the internal 'Flow' parameter of the air terminal and adds this value to 'Real Supply Airflow', 'Real Exhaust Airflow' or 'Real Return Airflow' [12].

3.15 Airflow in Air Handling Units

Airflow data bring to the AHU through the connected supply and extract ducts. AHU supply and extract connectors read these values and write them to the corresponding parameters of AHU [12].

3.16 AHU Settings

It is possible to add extra information to the AHU, such as fan types, calculated fan power, filter types, heat recovery efficiency, heating, and/or cooling coil types and power, if available [12].

3.17 Duct Routing

After the placement of the Air Terminals and the AHU's, the connection between these elements must make by using ducts. Revit ductwork can be modeled manually or semi-automatically using the Generate Layout and Routing Solutions tools [12].

3.18 Duct Sizing

In Revit, it is possible to use different sizing methods such as Equal Friction, Static Regain, Friction, and Velocity [12].

3.19 Duct Accessory

When the location of all Air Terminals, AHUs, and Ducts is known, it is possible to add Duct Accessory Families representing silencers, control valves, fire dampers, heating, and/or cooling coils, sensors, duct fans, cleaning covers, etc. Duct Accessory elements can be placed directly on an existing duct without having to connect them manually. The size of these elements automatically adapts to the size of the duct [12].

3.20 Duct Pressure Loss Report

Revit has a built-in tool to calculate the pressure losses of all sections of a Duct System. The tool creates a Duct Pressure Loss Report in ".html" format for each selected Duct System. In addition to the critical path, it also summarizes which calculation values use during the process. With this information, an engineer can select a suitable fan unit [12].

3.21 Local Pressure Loss

Duct Accessory and Duct Fittings Families from the Revit library typically have Instance parameters to control the pressure loss calculation. It is possible to enter a fixed value for the total local pressure loss over the element, but it is also possible to allow Revit to do to calculate of the local pressure loss based on the coefficients of ASHRAE tables, the airflow, and the duct size [12].

3.22 Linear Pressure Loss

There are three equations in Revit used to calculate linear friction losses in the ducts. These equations are the Altshul-Tsal Equation (Equation 1), Colebrook Equation (Equation 2), and Haaland Equation (Equation 3). The calculated pressure drop depends on airflow, duct size, air density, air viscosity, and duct material roughness [12].

3.22.1 Altshul-Tsal Equation

$$\text{For turbulent flow: } f^{\iota} = 0.11\left(\frac{\varepsilon}{D_h} + \frac{68}{Re_h}\right)^{0.25} \tag{1}$$

İf $(f^{\iota} \geq 0.018)$; $f = f^{\iota}$
İf $(f^{\iota} < 0{,}018)$; $f = 0.85 * f^{\iota} + 0.0028$
For laminar flow: $f = 64/Re_h$
For transitional flow: $f = 0$
$\Delta P = f\left(\frac{L}{D_h}\right)\rho\left(\frac{V_c^2}{2}\right)$

Table 1. Duct Types

Round	$A_c = \pi D^2 / 4$ $D_e = D_h = D$
Rectangular	$A_c = W * H$ $P = 2 * (W + H)$ $D_e = \frac{1.30 (A_c)^{0.625}}{(P/2)^{0.250}}$ $D_h = 4A_c/P$
Oval	$A_c = (\pi a^2/4) + a(A - a)$ $P = \pi a + 2(A - a)$ $D_e = \frac{1.55 A_c^{0.625}}{p^{0.250}}$ $D_h = 4A_c/P$

$V_c = q/A_c$
$Re_h = \frac{D_h V_c}{v}$
$v = \mu/\rho$
Flow state
Laminar: $Re_h < 2000$
Transitional: $2000 \leq Re_h < 4000$
Turbulent: $Re_h \geq 4000$
$p_v = \rho\left(\frac{V_c^2}{2}\right)$
$\Delta P_f = \Delta P/L$
$c = \Delta P/p_v$

3.22.2 Colebrook Equation

For transitional and turbulent flow: $\frac{1}{\sqrt{f}} = -2\log_{10}\left(\frac{\varepsilon}{3.7D_h} + \frac{2.51}{Re_h\sqrt{f}}\right)$ (2)

For laminar flow: $f = 64/Re_h$
$\Delta P = f\left(\frac{L}{D_h}\right)\rho\left(\frac{V_c^2}{2}\right)$

Table 2. Duct Types

Round	$A_c = \pi D^2 / 4$ $D_e = D_h = D$
Rectangular	$A_c = W * H$ $P = 2 * (W + H)$ $D_e = \frac{1.30 (A_c)^{0.625}}{(P/2)^{0.250}}$ $D_h = 4A_c/P$
Oval	$A_c = (\pi a^2/4) + a(A - a)$ $P = \pi a + 2(A - a)$ $D_e = \frac{1.55 A_c^{0.625}}{p^{0.250}}$ $D_h = 4A_c/P$

$V_c = q/A_c$
$v = \mu/\rho$
$Re_h = \frac{D_h V_c}{v}$
Flow state
Laminar: $Re_h < 2000$
Transitional: $2000 \leq Re_h < 4000$
Turbulent: $Re_h \geq 4000$
$p_v = \rho\left(\frac{V_c^2}{2}\right)$
$\Delta P_f = \Delta P/L$
$c = \Delta P/p_v$

3.22.3 Haaland Equation

$$\text{For transitional and turbulent flow: } \frac{1}{\sqrt{f}} = -1.8\log_{10}\left[\left(\frac{\varepsilon}{3.71D_e}\right)^{1.11} + \frac{6.9}{Re_e}\right] \quad (3)$$

For laminar flow: $f = 64/Re_e$
$\Delta P = f\left(\frac{L}{D_e}\right)\rho\left(\frac{V_e^2}{2}\right)$

Table 3. Duct Types

Round	$A_c = \pi D^2 / 4$ $D_e = D_h = D$
Rectangular	$A_c = W * H$ $P = 2 * (W + H)$ $D_e = \frac{1.453\ {A_c}^{0.6}}{P^{0.2}}$ $D_h = 4A_c/P$
Oval	$A_c = (\pi a^2/4) + a(A - a)$ $P = \pi a + 2(A - a)$ $D_e = \frac{1.453\ {A_c}^{0.6}}{p^{0.2}}$ $D_h = 4A_c/P$

$A_e = \frac{\pi D_e^2}{4}$
$V_c = q/A_c$
$V_e = q/A_e$
$v = \mu/\rho$
$Re_e = \frac{D_e V_e}{v}$
Flow state
Laminar: $Re_e < 2000$
Transitional: $2000 \leq Re_e < 4000$
Turbulent: $Re_e \geq 4000$
$p_v = \rho\left(\frac{V_c^2}{2}\right)$
$\Delta P_f = \Delta P/L$
$c = \Delta P/p_v$

4. DETERMINING AND COMPARING THE PRESSURE LOSSES OF THE HVAC SYSTEM IN BIM

Changes in the functions of different areas during the building construction can have a significant impact on MEP installations. To meet these changes, MEP designers tend to consider a 20-25% design safety factor in HVAC system design. However, in cases where the original design remains unchanged, the HVAC system is oversized and leads to low energy efficiency [8]. Since the design changes will decrease with the model created in BIM, the capacity values of the mechanical devices selected at the design phase can be determined more accurately [9].

In the HVAC system design, many elevation changes occur due to clashes with beams during the installation of the air ducts on the building. Due to these transitions, several fittings add to each air duct passing under the beams. In this way, many extra fittings cause increased pressure losses. As seen in Figure 1, extra fittings add to the air duct.

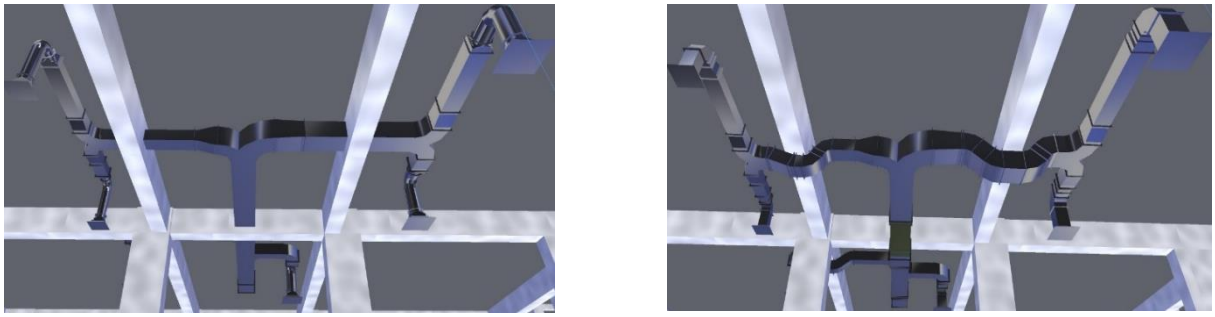

(a) Current model (b) Adjusted model

Figure 1. Clashes between beams and air ducts

While the total pressure loss of the current model calculated with Revit was 64.2 Pa, the total pressure loss of the adjusted model calculated as 66.4 Pa. This means if enough space is not creating for HVAC systems, duct crossings will consume more energy due to more pressure loss in field installations.

5. CONCLUSION

- Unlike the traditional method, it can be determined whether the space reserved for the installations is sufficient with the BIM method.

- In 2D projects, fittings formed only in 2 dimensions are included in the calculations, while in 3D projects, fittings formed in the third dimension are added to the calculations. Thus, applicable projects can create by making more accurate choices.

- The progress of the installations by changing too many levels due to clashes is a factor that will create high energy consumption due to pressure loss.

- To make HVAC systems more efficient by reducing pressure losses, the space provided for installations should be regulated.

In future studies, new objects and models for HVAC systems in complex geometry structures will develop. For this, new interfaces that will enable the HVAC model in energy simulation will use. As a study for this; An example of a set of parameters in the ModelicaBIM Class package and a set of modeling rules in the ModelicaBIM Building Sample package, an interface that automatically translates from BIM to BEM [13].

REFERENCES

[1] Yang, X., Leveraging BIM to Provide Automated Support for Efficient Troubleshooting of HVAC-Related Problems, Journal of Computing in Civil Engineering, 30(2), 1-13, 2016.

[2] Groeneveld, J., Building performance simulation from a BIM, Master Thesis, Eindhoven University of Technology, Eindhoven, 2015.

[3] Kürekci, N.A., Kaplan, S., Isıtma-Soğutma Yüklerinin HAP ve Revit Programlarıyla Hesaplanması, Tesisat Mühendisliği, 141, 5-15, 2014.

[4] Stanford, H.W. and Spach, A.F., Analysis and Design of Heating, Ventilating, and Air-Conditioning Systems. 2nd edn. CRC Press Taylor & Francis Group, 2019.

[5] Pinheiro, S., Wimmer, R., O'Donnell, J., Muhic, S., Bazjanac, V., Maile, T., Frisch, J., Treeck, C., MVD based information exchange between BIM and building energy performance simulation, Automation in Construction, 90, 91-103, 2018.

[6] Petri, I., Kubicki, S., Rezgui, Y., Guerriero, A., Li, H., Optimizing Energy Efficiency in Operating Built Environment Assets through Building Information Modeling: A Case Study, Energies, 10, 2017.

[7] Kim, S., Woo, J., Analysis Of The Differences In Energy Simulatıon Results Between Building Information Modeling (BIM)-Based Simulation Method and The Detailed Simulation Method, Winter Simulation Conference, USA, 2011.

[8] Samarasinghe, T., Mendis, P., Aye, L., Gunawardena, T., Fernando, S. ve Karunaratne, R., BIM and Modular MEP Systems For Super-Tall and Mega-Tall Buildings, 8th International Conference on Structural Engineering and Construction Management, 2017, ICSECM2017-465, 19-27.

[9] Demirtaş, F., BIM (Yapı Bilgi Modelleme) Sisteminin Bir Hastane Binası Tesisatında Kullanımı, Master Thesis, K.T.U., The Graduate School of Natural and Applied Sciences, Trabzon, 2019.

[10] Ganesh, M., Kumar, T.S., Duct Design and 3D Modeling of HVAC System for "Royal Oman Police" Building using Revit MEP, International Journal of Research in Engineering, Science and Management, V-1, Issue-5, 24-27, 2018.

[11] East, E.W., Ontology for Life-Cycle Modeling of Heating, Ventilating, and Air Conditioning (HVAC) Systems, US Army Corps of Engineers, 12-4, 2012.

[12] Bonduel, M., BIM Workflow For Mechanical Ventilation Design, Master Thesis, Tampere University of Applied Sciences, 2016.

[13] Kim, J.B., Jeong, W., Clayton, M.J., Haberl, J.S., Yan, W., Developing a physical BIMlibrary for building thermal energy simulation, Automation in Construction, 50, 16-28, 2015.

SOLAR ENERGY

FOLLOWING THE BALLOON TEMPERATURE OF A SOLAR WATER HEATER INSTALLED IN ORAN, ALGERIA

Touhami BAKI*, Mohamed TEBBAL*, Hanane BERREBAH*
*USTO-MB, Faculté de Mécanique, Laboratoire de Carburants Gazeux et Environnement, Oran, Algérie.
Email: touhami.baki@univ-usto.dz

ABSTRACT

The energy consumed for domestic hot water needs is continually increasing. The use of solar energy can contribute to a share in the energy mix. The study concerns the installation of an individual solar water heater with forced circulation for the needs of an average family installed in the climate of Oran. The energy approach compares the balance sheet of inputs and outputs and the accumulation inside the balloon. The temperature inside the balloon has been followed, indicating that it can reach peaks of more than 50 °C; performance results show that solar coverage can drop from 18% in January to 66% in July.

Keywords: Flat panel, Balloon, Temperature, Hot water, Solar energy.

Symbols:

a	Coefficient
Ap	Panel Surface (m^2)
cp	Massic heat ($J\ kg^{-1}\ K^{-1}$)
G	Solar irradiation ($W\ m^{-2}$)
$\dot{m}$	Mass flow ($kg\ s^{-1}$)
M	Ballon mass (kg)
P	Power (W)
S	External surface of the balloon (m^2)
t	Time (s)
T	Temperature (K)
U	Overall exchange coefficient ($W\ m^{-2}\ K^{-1}$)
η	Yield

1. INTRODUCTION

The increase in Algeria of the demand for energy for domestic needs follows an ascending curve, added to this a population in clear progression; a significant part of natural gas is consumed by households in cooking and heating equipment. Domestic hot water occupies a relatively high share in this consumption. The use of solar energy in the preparation of domestic hot water can provide part of this energy, knowing that Algeria has a large solar deposit and a very long period of sunshine. Solar water heaters are a solution because of their technical feasibility at a low temperature and their economic feasibility at low cost.

Yettou, F. *et al.* [01] experimented with a test bench for a solar water heater in Batna in Algeria; they designed an electronic card and developed software to manage data set, experimental results are discussed. Sahnoune, F. *et al.* [02] made a comparative study of the thermal performances of solar water heaters between two Algerian sites, namely Algiers and Adrar; results are presented in the form of tables and graphs. Hakem, S. A. *et al.* [03] studied the dimensioning of individual solar water heaters by a computer program based on a database of sensors and modeling of solar lighting in Algeria; the results are compared with data from two sites in Algeria. Burch, J. *et al.* [04] diagnosed the gain of a solar water heater based on the energy balance of the tank and deduced the time derivative of the average temperature, and the analyzes are integrated into a tool and validated by experimental

measurements from the work of other authors. Mohammed, M. N. *et al.* [05] simulated a solar water heater installation for 25 people using a forced circulation solar loop with a ten m² panel and a 600-liter storage tank; the performance of this equipment are tested with TRNSYS, the system analysis shows a maximum auxiliary energy requirement in January and February of around 1000 MJ / month.

Baki, T. *et al.* [06] simulated with the TRNSYS calculation code an individual solar water heater installed in Oran and followed the performance of the installation, which is composed of a two m² flat collector and a 300-liter tank, hot water consumption is estimated at 240 liters per day, additional electrical energy is added for the months when there is insufficient radiation, the simulation showed that during the hot months, substantial energy is saved and electrical energy is at its lowest. Lazreg, M. *et al.* [07] studied the effects of parameters on the temperature stratification of a solar water heater balloon, Baki, T. *et al.* [08] studied the performance of a solar water heater Individual with forced circulation for the needs of domestic hot water for an average family in Algeria, the results show that solar coverage can go from 7% in winter to 57% in summer.

In this article we study the evolution of the temperature inside the balloon. Based on the energy balance of the inputs and outputs and the accumulation inside the balloon. The performances are calculated by comparing the energy intake of the sun versus auxiliary energy.

2 DESCRIPTION OF THE MODEL STUDIED

The study concerns an individual solar water heater for the consumption of an average Algerian family made up of six people, a couple, and four children and living in the coastal climate of Oran.

2.1 Solar loop

The individual solar water heater is for forced circulation; it is composed of a flat solar panel and a storage tank, the two elements are connected by a set of pipes, and a circulation pump in a closed-loop, the supply of water to the city is done by the lower part and the recovery of hot water for sanitary needs by from the upper side, which is injected into the housing network, see Figure 1.
The flat solar panel captures the solar radiation and heats the liquid in circulation; the solar loop ensures the heating of the water inside the tank thanks to a heat exchanger, an auxiliary hydraulic or electric energy is integrated to fill the deficit and provide heating at the threshold of 60 ° C; a control system ensures that the pump is turned on when the panel outlet temperature is higher than the temperature at the bottom of the tank, the tank is fully insulated to minimize losses. The solar panel has a surface of 2 m² and is inclined at 45 ° to the horizontal and oriented to the south. The tank has a storage capacity of 300 liters.

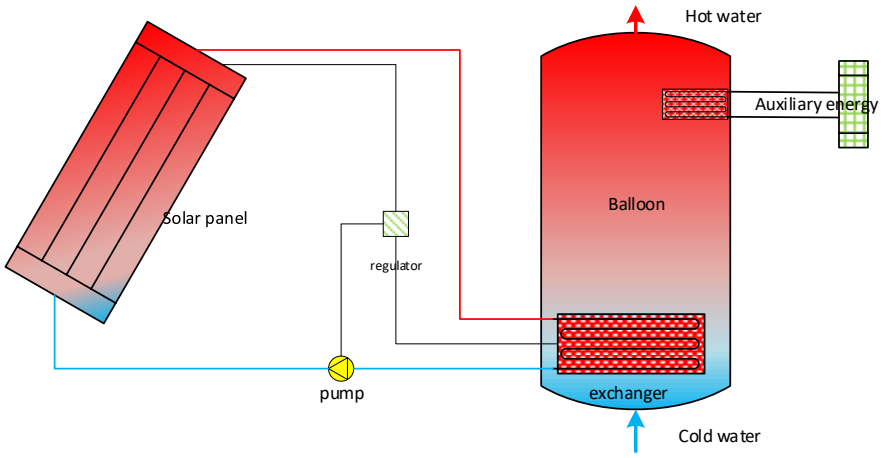

Figure 1. Installation diagram

2.2 Consumption profile

The hot water needs are 240 liters per day for an average family of 6 people, the temperature of the hot water leaving the tank is 60 ° C, the fraction of the hourly consumption of hot water follows the profile shown in Figure 2; This profile shows variability of the drawing, the consumption is zero between 2 AM and 5 AM, and it is maximum around 8 PM and 10 PM.

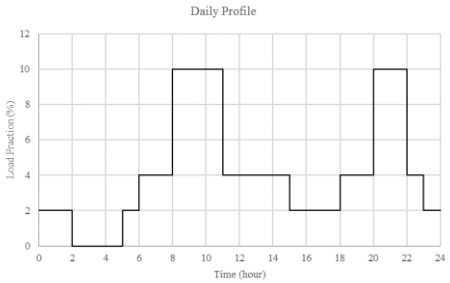

Figure 2. Domestic hot water consumption profile

2.3 Weather data

The city of Oran is a coastal city in the south of the Mediterranean Sea; it is located in the northwest of Algeria, its climate is of the warm temperate type; the average annual temperature is 18.3 ° C, it can reach the limits of 2 ° C in January and 37 ° C in July. Figure 3a shows the variation of the monthly average temperature in January, April, July, and October. The curves have the same sinusoidal shape but offset between them, the temperature peaks are reach at around 4 PM, and the minimums before sunrise around 7 a.m.; Figure 4b shows the average monthly irradiation for the months January, April, July, and October; the curve is of the parabolic type, the irradiation increases, goes through a peak and then decreases; during hot months the duration of sunshine is longer, and the maximum value is more important than winter, going from a value of 500 to almost 1000W / m² from January to July, the weather data are processed from Meteonorm file of the city of Oran.

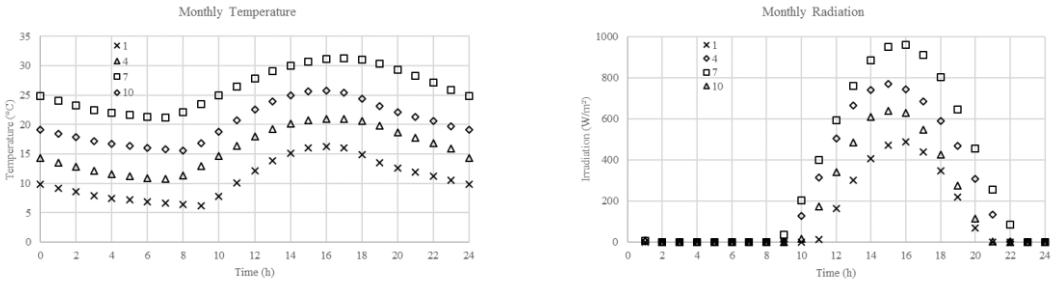

a) Ambient temperature b) Solar radiation

Figure 3. Monthly average of parameters

3. Mathematical Formulation

The energy balance of the tank highlights all the data of the installation. The tank absorbs the amount of heat coming from the solar panel, which via an exchanger will heat the water accumulated in the tank, the water cold enters below, and hot water exits from the high side for domestic consumption, the tank is wrapped in an insulating jacket to minimize losses; the injeced auxiliary power heats the water in case of conditions unfavorable weather conditions, Figure 5 shows the energy approach to the balance of system inputs and outputs.

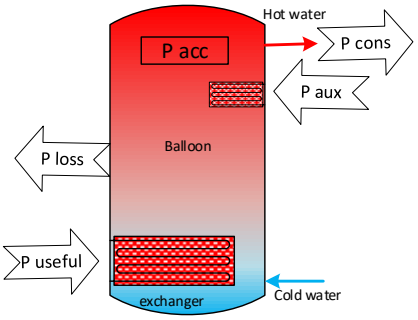

Figure 4. Energy balance of the storage balloon

The energy balance at the level of the balloon gives :

$$P_{useful} - P_{loss} - P_{cons} = P_{acc} \quad (1)$$

P_{useful} is the useful power of the solar panel; it is determined from the characteristics of the collector and is worth:

$$P_{useful} = \eta . G . A_p \quad (2)$$

The yield is calculated by:

$$\eta = \eta_0 - a_0 \frac{T_{mean} - T_{ambient}}{G} - a_1 \frac{(T_{mean} - T_{ambient})^2}{G} \quad (3)$$

P_{loss} represents the losses through the walls of the tank; this value is determined by:

$$P_{loss} = U . S . (T_{in} - T_{out}) \quad (4)$$

The consumption of the hot water drawing is:

$$P_{cons} = \dot{m} cp (T_{in} - T_{water}) \quad (5)$$

And the accumulation at the level of the balloon:

$$P_{acc} = Mcp \frac{(T_{in+1} - T_{in})}{\Delta t} \quad (6)$$

The resolution of these equations will allow the determination of the average temperature inside the balloon T_{in+1} at time $t + 1h$, knowing all the parameters at time t; the calculation makes over a 24-hour day period with a time step of 1 hour, and repeats for January, April, July, and October.

4. RESULTS AND DISCUSSIONS

4.1 The yield of the solar panel and the useful power

The yield of the solar panel calculates with the formulation (3) by introducing the parameters of the collector recovered from the study by Gherib, L. [09], namely the optical efficiency is 0.7, the coefficient $a_0 = 4.13 \mathrm{W/m^2}.\mathrm{K}$, and the second coefficient $a_1 = 0$. The average temperature of the panel is given by Kefti, O. *et al.* [10] and is valid for the summer season for July at 70 ° C, we subtract 10 ° C for each season, and we determine the average temperatures of the selected months, in October it is 60, April 50 and January 40 ° C.

Figure 6 shows the hourly yield during the solar irradiation of the day in January, April, July, and October. The yield varies from 0.2 to less than 0.5 in January, and it is around 0.5 or higher for the other months; the operating time of the panel increases depending on the season.

Figure 7 shows the power supplied by the panel in January, April, July, and October. The maximum power recovered during July when it reaches a peak of 1000W for a significant period, the powers in April and October are similar, and that of January is weak.

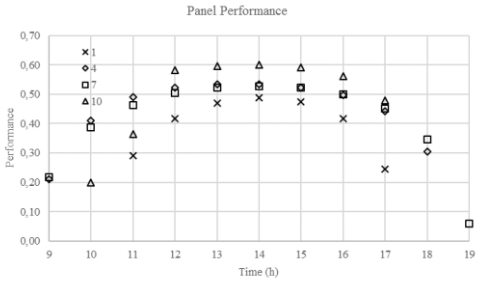

Figure 6. Hourly yield of the panel

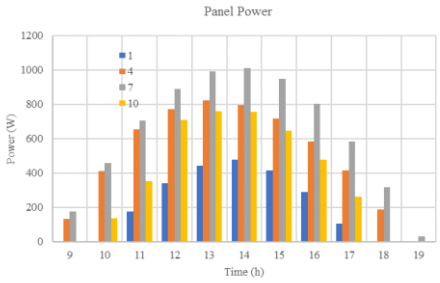

Figure 7. Useful power supplied by the panel

4.2 Balloon temperature

The determination of losses makes by assuming that the balloon is an assembly of a cylindrical part and two spherical caps, a thickness of 100 mm of glass wool covers the balloon. The internal and external exchange coefficients calculated by assuming inside the balloon an internal flow in forced convection and natural convection outside. The overall exchange coefficient by the surface has been determined and is $U.S = 1.059W/K$. The internal temperature of the tank is calculated by the formula (6), and by making the balance of entries and exits, the update is made every hour.

Figure 8 shows the evolution of the average temperature of the water in the balloon for a day in January, April, July, and October. The temperature decreases from 0 to 10 hours because of the losses and the drawing, then it increases since the solar contribution becomes more and more important, at sunset the temperature drops; the curve of January remains weak compared to the others, that of April and October are similar, and that of July is the most important, the temperature exceeds 50 °C from 16 to 20 hours.

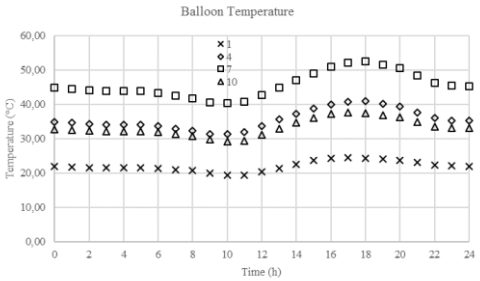

Figure 8. Internal temperature of the balloon

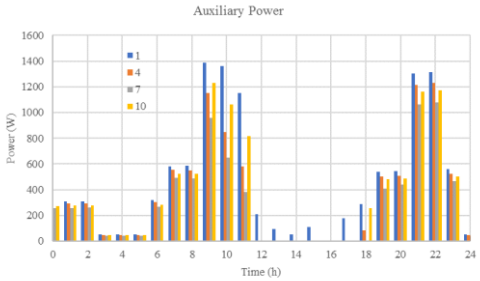

Figure 9. Auxiliary power

4.3 Auxiliary power

Figure 9 shows the auxiliary power required to supply water at 60 °C, in January, April, July, and October. This power follows the shape of the consumption profile but in the interval between 12 PM and 4 PM, heating is provided by the energy supply from the solar panel and the auxiliary power is minimal, in July we have the same trend, but the solar energy supply is more important, and the auxiliary energy is zero in the interval from 12 AM to 6 PM; between 2 AM and 6 AM consumption is zero, the auxiliary power compensates the losses.

4.4 Solar energy coverage rate

Analysis of the monthly data grouped in Table 1 shows that the solar energy coverage goes from 18% in January to 66% in July. The months of April and October covers less than half of the needs, ie, 46 and 36%.

Table 1. Monthly comparison of energy intake

Month	P Wh useful	P Wh loss	P cons Wh	P aux Wh	Coverage %
1	2247,81	1238,27	12709,60	11706,05	18
4	5492,94	1136,48	11913,58	9119,49	46
7	6915,74	999,63	10471,48	7633,44	66
10	4102,80	1077,36	11327,54	9518,51	36

5.CONCLUSION

The temperature of the cylinder of a solar water heater has been followed, indicating that it can reach the desired values. By adding auxiliary energy, we can meet the needs of the domestic hot water consumption of an average family with substantial savings.

The study of energy consumption performance has been made and has shown that solar energy coverage can reach 66% with a minimum of 18% in January for a single panel. The efficiency of such installation is proven.

REFERENCES

[1] Yettou, F., Gama, A., Hamouda, C., & Malek, A. Etude et réalisation d'un banc d'essai pour un chauffe-eau solaire à circulation forcée dans la région des Hauts Plateaux. *Revue des Energies Renouvelables*, 11(1), 119-128, 2008.

[2] Sahnoune, F., Belhamel, M., & Zelmat, M. Etude comparative des performances thermiques d'un prototype de chauffe-eau solaire pour deux sites algériens. *Revue des énergies renouvelables*, 14(3), 481-486, 2011.

[3] Hakem, S. A., Kasbadji–Merzouk, N., & Merzouk, M. Performances journalières d'un chauffe-eau solaire. *Revue des Energies Renouvelables CICME*, 8, 153-162, 2008.

[4] Burch, J., Magnuson, L., Barker, G., & Bullwinkel, M. Diagnosis of Solar Water Heaters Using Solar Storage Tank Surface Temperature Data (No. NREL/CP-550-45465). *National Renewable Energy Lab. (NREL),* Golden, CO - United States, 2009.

[5] Mohammed, M. N., Alghoul, M. A., Abulqasem, K., Mustafa, A., Glaisa, K., Ooshaksaraei, P., ... & Sopian, K. TRNSYS simulation of solar water heating system in Iraq. *Recent Researches in Geography, Geology, Energy, Environment and Biomedicine,* 153-156, 2011.

[6] T. Baki, D. Nehari, A. Remlaoui, A. Elmerieh, M. Madani, Simulation avec TRNSYS d'un chauffe-eau solaire individuel sous un climat typique d'Oran, *International Conference on Renewable Energy and Energy Conversion, ICREEC'2019,* USTO-MB Oran, 11 - 13 November 2019.

[7] Mohamed LAZREG, T. Baki, D. Nehari, Effet des paramètres sur la stratification d'un ballon de chauffe-eau solaire, *International Conference on Renewable Energy and Energy Conversion, ICREEC'2019,* USTO-MB Oran, 11 - 13 November 2019.

[8] Touhami BAKI, Mohamed TEBBAL, Hanane BERREBAH, Fatima BOUGARA, *Etude des performances d'un chauffe-eau solaire individuel installé à Oran, 1 ère Conférences Sur Les Energies Renouvelables & Les Matériaux Avancés ERMA'19* – Relizane, Algérie le 16 et 17 Décembre 2019.

[9] Lazhar Gherib, Etude et calcul des capteurs solaires plans "Application au chauffe-eau", *Option « ENERGIES RENOUVLABLES », L'université KASDI MERBAH* –OUARGLA, 2015.

[10] Ketfi, O., Merzouk, M., Merzouk, N. K., Elmetenani, S., & Lafri, D., Etude expérimentale d'un capteur solaire plan muni d'un collecteur sous forme de serpentin. *Revue des Energies Renouvelables*, 17(4), 623-630, 2014.

EXPERIMENTAL INVESTIGATION OF THERMAL GAIN IN PV PANELS

Hakan DUMRUL*, Sezayi YILMAZ*
*Karabük University, Department of Energy Systems Engineering, Karabük/Turkey
Email: hakandumrul@karabuk.edu.tr, syilmaz@karabuk.edu.tr

ABSTRACT

Photovoltaic (PV) technology, which can convert solar radiation into electric energy by the photovoltaic effect, is widely regarded as the most popular one among solar harvest. While it absorbs the sunlight across the photovoltaic panels tiny proportion is converted into electrical energy however, a large amount of this energy is turned into heat energy. Consequently, this gives rise to a significant temperature increase across the PV panels. This temperature increase causes panels' electrical efficiency to decrease, which corresponds to 1-2 % at temperatures over 30 ˚C. An easily applicable Photovoltaic thermal (PV/T) panels are developed to increase the efficiency and thermal energy gain across the PV panels, which is still under investigation.
A thermal gain application designed as a serpentine type was applied to a 20 W polycrystalline PV panel to obtain a PV-T type panel. PV/T panel's temperature and electrical efficiency were compared to a PV panel possessing the same features located at Karabuk city and this comparing carried out under Karabuk city climatic conditions on different days during September. According to the experimental results, the highest panel surface temperature was obtained with radiation value of 789 W/m^2; whose surface temperature was measured to be 59,93 ˚C, electrical power was 11,8 W, electrical efficiency was 13%, this parameters for PV/T are found to be 43,90 ˚C, 14,44 W, 16%, respectively. Thermal power and thermal efficiency obtained from PV-T panel at the same irradiance value was found to be 29.34 W, 32.60%.

Keywords: Photovoltaic/Thermal, Solar Energy, Energy Analysis.

List of symbols

A_m	Area of PV module (m^2)
I_m	Current at maximum power point (A)
T_c	Cell temperature (K)
P	Electrical power of PV module (W)
m	Fluid mass flow rate (kg/s)
C_p	Fluid-specific heat (kJ/kg K)
$I_{(t)}$	Incident total radiation (W/m^2)
Q_u	Rate of useful energy transfer (W)
T_{in}	The fluid inlet temperature (K)
T_{out}	The fluid outlet temperature (K)
V_m	Voltage at maximum power point (V)

Greek letter

η_c	Cell efficiency
η_0	Efficiency under standard test conditions
η_T	Overall efficiency
δ_c	Packing factor
η_m, η_e	PV module electrical efficiency
η_{th}	Thermal efficiency
α_c	The absorptivity of the solar cell
τ_c	Transparency for PV module glass

Abbreviations

a-Si	Amorphous silicon
CdTe	Cadmium telluride
CIS	Copper indium selenium
PV	Photovoltaic
PV/T	Photovoltaic/thermal

1. INTRODUCTION

Solar energy is considered one of the leading energy sources of the future because of its positive effects on the environment and its contribution to many technological applications. Since being environmentally friendly, it can be used in many applications. Photovoltaic (PV) continues to make human life comfortable utilizing this clean energy source. PV systems absorb 50 percent of solar radiation as thermal energy and convert 15 percent of it into electrical energy; this thermal energy causes the efficiency to decrease by disrupting the module structure. The increase in the temperature leads to decrease electrical efficiency panels. For this reason, many studies are conducted to increase the PV performance. A PV/T panel increases the usage area of solar energy, providing both electricity and heat energy. The fundamental method in the studies in PV/T technology is the cooling of PV surfaces. Different cooling techniques are used in these studies, such as thermoelectric devices, heat pipes, heat exchangers through which different fluids are passed, are tested on the back surface of the PV panel. The heat removed via this way can be used for heating applications using different systems in industrial and residential areas. PV/T is considered the best systematic method to enhance the efficiency of the photovoltaic panel. PV/T systems can generate heat and electricity simultaneously for many purposes; their efficiency is higher than the individual efficiency of PV systems and solar collectors. The installation areas of the PV/T panels cover less space than two independent systems, minimize the thermal degradation of PV panels, and extend the life span of PV panels.

There are many PV/T systems according to the type of cooling, and the most common one is water-cooled PV/T. When comparing between air- and water-cooled PV/Ts, it is stated in the literature that water-cooled PV/Ts better performs. Water or different fluid-cooled PV/T system is created by attaching a thermal collector that acts as an absorbent layer to the rear surface of the PV panel. The thermal collector can be of different types, serpentine, parallel, etc. [1-6]. Such a system is shown in figure 1.

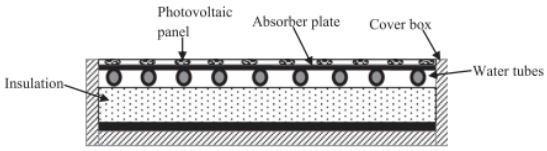

Figure 1. The basic structure of the water-cooled photovoltaic/thermal panel [5].

Different types of PV/T panels are studied by many researchers in climatic conditions in different regions of the world [6]. The studies involving these systems are reviewed below. Castanheira et al. (2018) have investigated cooling applications in the solar energy plants. They reported that used the water-cooling method in PV systems is an effective method to decrease the thermal effects. Besides, they have been recorded that water cooling systems increase energy production by about 12 percent [7]. Pang et al. (2019) also experimentally studied a water-cooled PV/T module that they had created by connecting copper-aluminum thermal collectors to the back of the monocrystalline PV panel, and they studied energy and exergy analysis. In this study, different mass flow rates and installation angles influencing the performance of the PV/T systems were investigated. In the experiment, they stated that different mass flow rates and installation angles rarely impacted the electrical efficiency of the PV/T system, but they were highly influential on its thermal efficiency. It was also found that the PV/T system has the highest performance at the mass flow rate of 0.15 kg/s of coolant, and the angle of installation is 25° [8]. Peng et al. (2017) studied the effects of PV surface temperature on outlet performance. As a result of the experimental study, It was concluded that the reimbursement period could be decreased to nearly 12 years from 15 years, and the PV efficiency could be increased by about 47 percent with cooled water [9]. Changes in the panel's efficiency when both surfaces of the PV panel were cooled using the water spraying technique while the solar radiation was

at the peak recorded by Nižetić et al. (2016). They found that under the peak solar radiation the electrical power of the PV panel was 16.3%, the electrical efficiency was 14.1%. Besides, the panel temperature has been indicated to decrease from 54 ˚C to 24 ˚C. They emphasized that this system is an effective method by explaining a 5.9% improvement in electrical efficiency and the average panel temperature is reduced by 24 degrees [10]. Ceylan et al. (2014) examined effective cooling in a PV/T system experimentally. In this study, the spiral-type heat exchanger is mounted behind the PV panel. The calculated module efficiency was about 13 percent when cooling was achieved by passing water through the spiral heat exchanger. In the non-cooling situation, it was determined as 10 percent. According to this situation, when the solar radiation increases, module temperature was found to decrease in the experimental setup. [11]. Chow et al. (2007) conducted an experimental study by combining the PV panel and the water heater collector system for use in water preheating. They manufactured PV/T wall bonded to the back surface of the PV panel consisting of six thermal collectors with 1.5 m x 1.1 m. The experiments were carried out at a constant mass flow rate of 0.011 kg/s. The thermal efficiency obtained from the experiments was recorded as 38.9%, and the average electrical efficiency was 8.56% [12].

Studies in the literature provide very serious and important data regarding the potential and performance of PV/T panels. By making comparisons between traditional PVs and PV/Ts, the theoretical principle was confirmed and explained. In this study, an efficient PV/T system was designed and experimentally analyzed. Thermal gain application designed as a serpentine type was also applied to a 20 W polycrystalline PV panel to attain a PV/T type panel. PV/T panel's temperature, electrical efficiency, and thermal efficiency were investigated compared to a PV panel of the same features at Karabuk city climatic conditions on different days in September.

2. SYSTEM DESIGN AND EXPERIMENTAL METHOD

The experimental system was designed and manufactured, as seen in Figures 2 and 3. Panels' angles were adjusted by being calculated according to the solar angles of September of Karabuk city (Turkey, 32:37 Lat., 41:12 Long.).

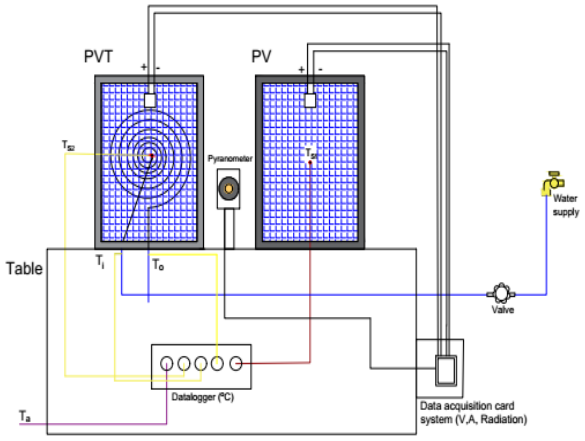

Figure 2. Designed system and measurement points.

Figure 3. Photograph of the experimental setup.

The purpose of the application was to investigate the behaviors of panels in terms of comparing their thermal and electrical efficiencies. For this purpose, the first one of two panels with the same properties was kept usually. The thermal collector designed as serpentine type is placed on the back surface of the PV panel using thermal paste. To obtain a serpentine-type of thermal collector, a 2.5 m long copper pipe with an outer diameter of 6.35 mm, and an inner diameter of 4.826 mm, and a wall thickness of 0.76 mm was intertwined spirally. Thermocouples are placed in the middle of both panels for the measurement of the back surface temperatures and at the water inlet and outlet of the PV/T panel. The manufacturing stages of the PV/T system are as in Figure 4.

Figure 4. Manufacture of PV/T system for experiments.

The time of starting the experiments was at 11:00 due to the building's shading where the panels were located, and it ended at 17:00. In the experimental setup, the ambient temperature, the backside temperature of the panels, solar radiation, and current and voltage values produced by PV panels were measured. After the experimental setup was installed, these two panels were tested under the same conditions. The experiments were carried out throughout four different days in September. During the experiment, city grid water was used as the cooling fluid in the PV/T collector, and the flow rate of the water was adjusted to 100 ml/min (0.001666 kg/s) by a valve. Considering that there might be an increase in the flow of city water, the flow rate of the fluid was manually controlled every hour using a graduated cylinder. Data acquisition card system was designed and manufactured in energy labs at Karabuk University. The data acquisition card system was used to measure the current, voltage and total radiation generated by PV, PV/T panel, and it were used to measure the total radiation on the panels. The properties of the panels are given in Table 1. The measurement points of the system are shown in Figure 2. Also, the properties of measurement devices are given in Table 2.

Table 1. Specifications of solar panels used in the experiments.

Description	Properties
Rated Maximum Power (Pmax)	20 Wp
Power Tolerance Range	+5%
Open Circuit Voltage (Voc) (Typical value)	22.10V
Max. Power Voltage (Vmp) (Typical value)	18.00V
Short Circuit Current (Isc) (Typical value)	1.35A
Max. Power Current (Imp) (Typical value)	1.11A
Max. System Voltage	1000V
Max. Series Fuse Rating	10.0A
Panel Type	Polycrystal
Number of Panel Cells	36 (4x9)
Dimensions	430x360x25 mm
All data at standard test condition: Am = 1.5 E = 1000 W/m² Tc = 25 ˚C	

Table 2. Measurement devices and properties.

Measured value	Name of the device	Device properties
Solar radiation	Pyranometer (EKO Instruments, Model: MS-602)	Irradiance range 0 - 2000 W/m²; Sensitivity, Approx. 7 µV/W/m²; Non-linearity at 1000W/m², ±1.5 %.
Temperature	Pico USB TC-08 data logger	Temperature accuracy, Sum of ±0.2% of reading and ±0.5 ˚C.
	K-type thermocouples; Ordel OM03 type	Measuring range: -40 +1200 ˚C, accuracy: ± 1 ˚C
Data acquisition card system		Accuracy, Voltage ± 0.06 V, Current ± 0.02 A

3. THERMODYNAMIC ANALYSIS OF THE SYSTEM

3.1 Energy Analysis

The energy analysis is based on the first law of thermodynamics. The electrical efficiency of PV modules can be classified into two groups as cell efficiency and module efficiency. Cell efficiency can be calculated by using the equation below:

$$\eta_c = \eta_0[1 - \beta(T_c - 25)] \quad (1)$$

The above equation, η_0 is the efficiency under standard test conditions, I(t) = 1000 W/m^2, T_c = 25, AM = 1.5 T_c is the cell temperature, and β is the thermal coefficient of electrical efficiency. β value changes depending on the material from which solar cells are produced. For crystal silicon, approximately 0.0045/K is taken, whereas 0.0035/K for CIS, 0.0025/K for CdTe, and 0.002/K for a-Si [13,14].
Module efficiency can be calculated by the equation below:

$$\eta_m = \eta_c \,.\, \alpha_c \,.\, \tau_c \,.\, \delta_c \quad (2)$$

where τ_c is the transparency for the PV module glass, α_c is the absorptivity of the solar cell and δ_c is the packing factor; the values for those are taken as 0.90, 0.95 and 0.90, respectively [15,16].
Another expression of the module electrical efficiency can be written as follows:

$$\eta_m = \frac{P}{A_m \,.\, I_{(t)}} \quad (3)$$

where P = V x I is the power delivered by the PV module. A_m is the module surface area and $I_{(t)}$ is the total radiation across the panel surface.
The overall efficiency (η_T) of the PV/T panel is the sum of its thermal and electrical efficiencies:

$$\eta_T = \eta_{th} + \eta_e \quad (4)$$

The thermal efficiency (η_{th}) of PV/T panel is calculated as:

$$\eta_{th} = \frac{Q_u}{A_m \,.\, I_{(t)}} \quad (5)$$

where Q_u is the usable heat collected, which is further calculated as:

$$Q_u = m \,.\, C_p \,.\, (T_{out} - T_{in}). \quad (6)$$

Where m is the mass flow rate of water in kg/s, C_p is the specific heat of water (4,186 kj/kgK), T_{in} is fluid inlet temperature (K) and T_{out} is fluid outlet temperature (K). The electrical efficiency (η_e) of the PV/T panel can be calculated from equation 3 [17-19].

4. RESULTS AND DISCUSSION

In this study, The PV and PV/T panel were tested between 11:00-17:00 hours on four different days during September 2019. When the measured solar radiation value falls below 300 W/m², the data were received are not reliable. For this reason, measurements were conducted at radiation values above 300 W/m². Per the measurement results, analyses were performed depending on energy law, and the results of the analyses were investigated for each different day. Figure 1 shows the panel backside temperatures, measured depending on the radiation values taken over four different days and times. Besides, the efficiency values obtained using equations 1-6 can be seen in these figures.

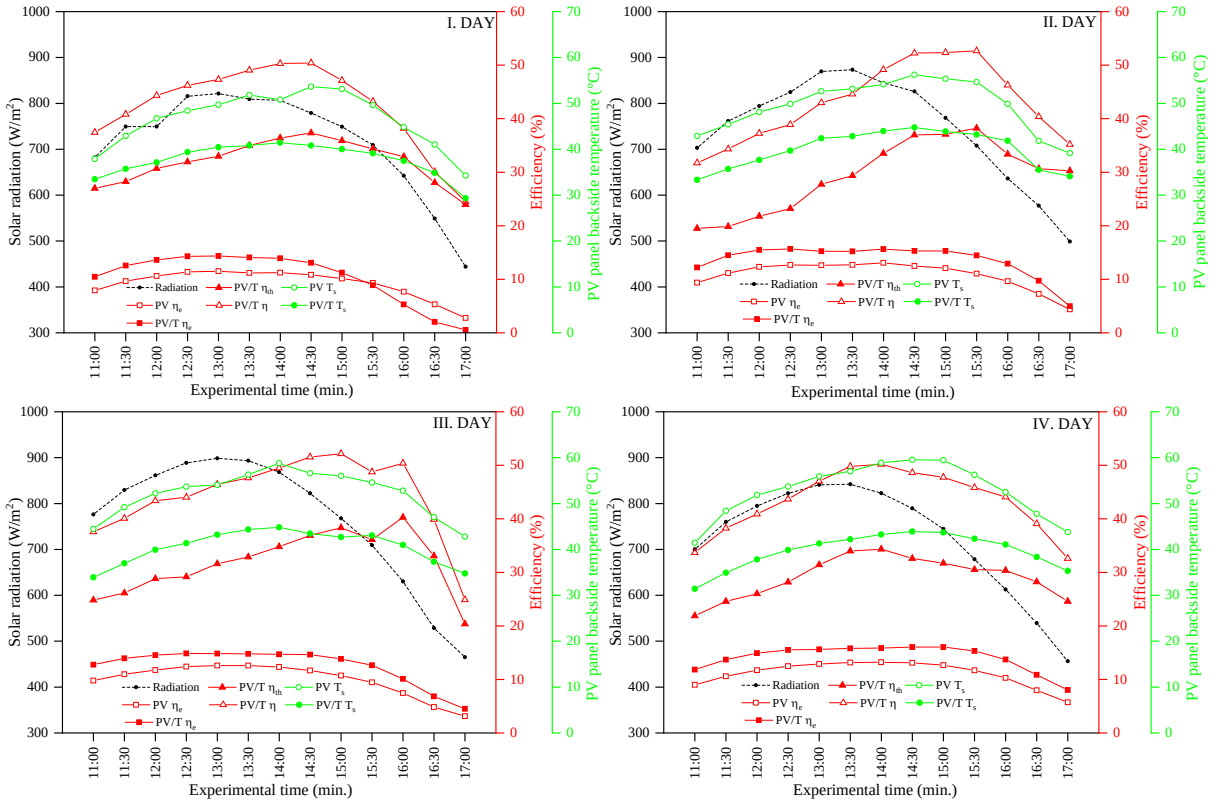

Figure 5. Variations of temperatures measured at the backside of PV panels with solar radiation for different test days and efficiency.

When the four-day test results were examined, the highest radiation values ($I_{(t)}$) were measured as 800-900 W/m² at the highest noon (13:00-13:30) hours. Theoretically, when the radiation values are highest (13: 00-13: 30), the panels are considered to have the highest values at the backside temperatures. While PV backside temperature rises to 59.5 ˚C maximum in these periods, the PV/T temperature does not exceed beyond 45 ˚C. There is a difference of about 14-15 ˚C between the PV and the backside temperature of the PV/T. When the panel efficiencies are compared, in general, it is seen that the PV/T panel is more efficient than the PV panel. The reason for this is the temperature increment in PV panel.

When the electrical, thermal, and total efficiency values of the first day depending on time and radiation are examined; at the highest radiation value (821 W/m²) at 13:00 at noon, the electrical efficiency of PV was 11.52%, the electrical efficiency of PV/T was 14.35%, the thermal efficiency was 32.97%, the total efficiency was 47.33%. The electrical efficiency values in both panels occur at noon with the highest radiation. The electrical efficiency value of PV/T is lower than PV between 16:00 and 17:00. The reason for this; It can be explained by the shadow falling on the PV/T during these periods when the radiation values begin to decrease. It can be seen that this only happens in the first day experiments and returns to normal for other days. When the data of other days are inspected; It is seen that the highest electrical efficiency values for both panels (PV, PV/T) are recorded at noon when the radiation is highest. In the case of thermal and overall efficiency, there was a decrease in the radiation values for the PV/T panel, while thermal efficiency was observed to shift towards afternoon hours due to the fact that heated panels by inertia bring about heat transfer to cooling fluid. When the effect of the temperature of the back surface of the panel on the efficiency values is examined. The most important parameter can be evaluated as an improvement in electrical efficiency. Also, the thermal gain could be achieved increases the total efficiency of the PV systems. When the experiment data are evaluated in this respect; On the fourth day, at the highest radiation value (789 W/m^2), the highest electrical efficiency values obtained from the panels were 13% for PV and 16% for PV/T. In PV/T systems, cooling processes with thermal collectors positively affect the efficiency of PV panels.

5. CONCLUSION

This experimental study expresses the comparison between a typical polycrystal silicon panel and a PV/T panel with serpentine-type copper collector attached behind a polycrystal silicon panel. Compared panels were performed at Karabuk city climate conditions and in September. Experiments were conducted during the month of September and the cloudiness factor in this month is high for the city of Karabuk. It is thought that the experimental setup in this study can give more efficient results in places with lower cloudiness factor. In the study, the fluid flow rate was kept constant. This study might be repeated for different flow rates, and the optimum flow rate could be calculated by comparing the results obtained with each other. In this study, water was used as the coolant; using different fluids can give more effective results. In terms of efficiency, especially considering Karabuk city climate conditions, experiments could also be done on monocrystal panels, and it is considered that monocrystal panels will be more appropriate for this city. As a result, we can increase the electrical efficiency by lowering the back surface temperatures of photovoltaic panels. Besides, it was seen that thermal gain could be obtained through cooling operation as well. In experiments, the thermal gain values may be very high in terms of thermal efficiency; however, they are not exergic. Different experimental studies can be done to determine the optimum parameters of the experimental system, and thus more efficient thermal gains in terms of exergy can be obtained. Thermal energy obtained from PV/T application can be used in very different applications in domestic and industrial areas.

REFERENCES

[1] Preet, S., Water and phase change material based photovoltaic thermal management systems: a review, Renewable and Sustainable Energy Reviews, 82, 791-807, 2018.

[2] Kazem, A.H., Evaluation and analysis of water-based photovoltaic/thermal (PV/T) system, Case Studies in Thermal Engineering, 13, 100401, 2019.

[3] Hasanuzzaman, M., Malek, A.B.M.A., Islam, M.M., Pandey, A.K. and Rahim, N.A., Global advancement of cooling technologies for PV systems: a review, Solar Energy, 137, 25-45, 2016.

[4] Hui, L., Tin-Tai, Chow., Jie, J., Building-integrated heat pipe photovoltaic/thermal system for use in Hong Kong, Solar Energy, 155, 1084–1091, 2017.

[5] Chow, TT., A review of photovoltaic/thermal hybrid solar technology., Applied Energy, 87, 365–379, 2010.

[6] Ergün, A., Eyinç, H., Performance assessment of novel photovoltaic thermal system using nanoparticle in phase change material, International Journal of Numerical Methods for Heat & Fluid Flow, 29(4), 1490-1505, 2019.

[7] Castanheira, A.F., Fernandes, J.F. & Branco, P.C., Demonstration project of a cooling system for existing PV power plants in Portugal, Applied Energy, 211, 1297-1307, 2018.

[8] Pang, W., Cui, Y., Zhang, Q., Yu, H., Zhang, L., Yan, H., Experimental effect of high mass flow rate and volume cooling on performance of a water-type PV/T collector, Solar Energy, 188, 1360–1368, 2019.

[9] Peng, Z., Herfatmanesh, M.R. & Liu, Y., Cooled solar PV panels for output energy efficiency optimisation, Energy Conversion and Management, 150, 949-955, 2017.

[10] Nizetic, S., Coko, D., Yadav, A., Grubisic-Cabo F., Water spray cooling technique applied on a photovoltaic panel: The performance response, Energy Conversion and Management, 108, 287–296, 2016.

[11] Ceylan, I., Gürel, A.E., Demircan, H. & Aksu, B., Cooling of a photovoltaic module with temperature controlled solar collector, Energy and Buildings, 72, 96-101, 2014.

[12] Chow, T.T., He, W., Ji, J., An experimental study of façade-integrated photovoltaic/ water-heating system, Applied Thermal Engineering, 27, 37–45, 2007.

[13] Mishra, R.K. & Tiwari, G.N., Energy and exergy analysis of hybrid photovoltaic thermal water collector for constant collection temperature mode, Solar Energy, 90, 58-67, 2013.

[14] Tiwari, G.N., & Dubey, S., Fundamentals of photovoltaic modules and their applications, Royal Society of Chemistry, London, UK, 2010.

[15] Dubey, S., Solanki, S.C. & Tiwari, A., Energy and exergy analysis of PV/T air collectors connected in series, Energy and Buildings, 41(8), 863-870, 2009.

[16] Ceylan, I., Gürel, A.E., Ergün, A., Tabak, A., Performance analysis of a concentrated photovoltaic and thermal system, Solar Energy, 129, 217–223, 2016.

[17] Park, S.R., Pandey, A.K., Tyagi, V.V. & Tyagi, S.K., Energy and exergy analysis of typical renewable energy systems, Renewable and Sustainable Energy Reviews, 30,105-123, 2014.

[18] Joshi, A.S., Dincer, I. & Reddy, B.V., Thermodynamic assessment of photovoltaic systems, Solar Energy, 83(8),1139-1149, 2009.

[19] Dincer, I., Colpan, O.C. & Kizilkan, O., Exergetic, Energetic and Environmental Dimensions, Elsevier, London, UK, 2017.

DESIGN AND ANALYSIS OF EVACUATED TUBE SOLAR COLLECTOR INTEGRATED SUPERCRITICAL BRAYTON CYCLE FOR LOW-TEMPERATURE APPLICATIONS

Gamze SOYTÜRK*, Serpil ÇELİK TOKER, Önder KIZILKAN
Isparta University of Applied Sciences, Department of Mechanical Engineering, Isparta/Turkey
*Email: gamzeyildirim@isparta.edu.tr

ABSTRACT

The objective of the current research is to investigate the performance of the evacuated tube solar collector-assisted sCO_2 Brayton cycle for low-temperature applications. sCO_2 Brayton cycle is powered by solar energy by means of 15 sets of collectors each having 13 evacuated tubes. The whole system is analyzed with the help of the first and second law of thermodynamics in order to determine the performance parameters such as energy and exergy efficiencies with exergy destruction rates. The analysis is made using the average solar radiation values for each months of the year. The EES program is used for the system design and performance assessment. According to the results, the energy and exergy efficiencies of the system are calculated as 16% and 73%, respectively for August. Among the system components, the highest exergy destruction rate occurs in the evacuated tube solar collector with a value of 8.70 kW.

Keywords: Energy, Exergy, CO_2, sCO_2 Brayton cycle, Evacuated tube.

1. INTRODUCTION

Recently, energy consumption is increasing dramatically, driven by population growth and the desire for higher living standards. Among energy consumption, conventional fossil fuels still dominate the energy sector [1]. However, due to the depletion of fossil fuel resources and causing many ecological problems, it has become necessary to use renewable energy sources such as solar energy for electricity generation [2]. At this point, using the thermodynamic power cycle, due to the technical, economic, and efficient performance advantages, the use of solar energy has attracted great attention and is increasing worldwide [3].

Nowadays, climate change caused by greenhouse gas emissions has become a serious problem worldwide. It has become essential to use natural working fluids to protect the ozone layer and prevent global warming. First of all, CO_2 is an inert gas, non-explosive, non-flammable, non-toxic, non-corrosive. It has abundant stock and a reasonable price. Due to zero ozone depletion potential (ODP) and a low global warming potential (GWP), natural carbon dioxide CO_2 is considered to be a promising alternative working fluid. It has also been very popular to be used in power cycles utilizing the energy from low to/medium grade heat sources due to its low critical properties (critical temperature, 31.1 ℃, critical pressure, 7.37 MPa). Between power generation cycles that use low-temperature heat sources, there has been increasing attention in transcritical CO_2 (tCO_2) Rankine cycle due to its safety and environment-friendly characteristics. Zhang et al. [4] researched the performance of the Rankine cycle powered by evacuated-tube solar collectors with CO_2 as working fluid. They have evaluated the system performance based on daily, monthly, and yearly experiment data. According to the results, they calculated the heat collection efficiency as 65.0–70.0% for the CO_2-based solar collector. Al-Zahrani and Dincer [5] examined experimentally and theoretically the solar-assisted reheating tCO_2 Rankine cycle consisting of parabolic trough collector, thermal energy storage facility, absorption cooling system. The tCO_2 Rankine cycle energy and energy efficiency were calculated as 34% and 82%. Li et al. [6] conducted thermo-economic performance and comparison of a CO_2 transcritical and an Organic Rankine Cycle (ORC) using R123, R245fa, R600a, and R601 as the working fluids with temperatures varying from 90℃ to 120℃ powered by the low-temperature geothermal source. They investigated these two cycles in terms of net power output, thermal efficiency, exergy efficiency, cost per net power output, and the ratio of the cost of the heat exchangers to the overall system cost. Many researchers have

theoretically studied basic solar-powered tCO_2 Rankine cycle based on their assumptions and mathematical models. Yamaguchi and his research group at Doshisha University in Japan built the first experimental set up solar-powered at low temperature for tCO_2 Rankine cycle in 2004. Yamaguchi et al. [7] examined energy and exergy analysis of the experimental solar-assisted Rankine cycle working with an environmentally friendly working fluid transcritical CO_2. They calculated the energy efficiency of the solar-powered system by 3.4% for the winter season and 5.78% for the summer season. They calculated the exergy efficiency as 7.63% for the winter season and 4.08% for the summer season.

The tCO_2 Rankine cycle includes a condensation process. After the steam coming out of the turbine is condensed, it is sent to the heater by the pump. The condensation problem in the condenser becomes the main factor limiting the development of the transcritical CO_2 Rankine cycle, as the critical temperature of CO_2 is very close to the ambient temperature or even lower than the ambient temperature in summer. In transcritical power cycles, a very low-temperature refrigerant is required to liquefy CO_2. In addition, the efficiency of the tCO_2 Rankine cycle is low. Supercritical CO_2 (sCO_2) Brayton cycles can be used instead of tCO_2 Rankine cycles to increase the efficiency of the tCO_2 Rankine cycle and solve the liquefaction problem of CO_2.

sCO_2 Brayton power generation technology has attracted considerable research interest in recent years owing to low compression work and compact turbomachinery as a result of the thermophysical of CO_2 [1]. Several research groups have a focus on the sCO_2 power generation cycles. Liao et al. [8] thoroughly studied the sCO_2 power cycles, including performance analysis, modeling, and analysis of the heat exchangers and turbomachines, the various applications of sCO_2 Brayton power cycle applications in the review. They discussed in comprehensive the mathematical models for every ingredient in the supercritical carbon dioxide cycle. Yu et al. [9] examined the current research on sCO_2 from five views: application, system types and design, mixtures with CO_2, system elements, and experimental. In the other review study, Ahn et al. [10] analyzed the present development process of the sCO_2 system and compared the performance of different sCO_2 schemes. Various sCO_2 Brayton cycle configurations are available in the literature such as simple recuperation cycle [11], recompression cycle [12], partial cooling cycle [13], reheating cycle [14], intercooling cycle [15], pre-compression cycle [16], split expansion cycle [17]. Yang et al. [14] analyzed the performance of solar-assisted four typical sCO_2 Brayton cycles, including simple recuperative cycle, reheating cycle, recompression cycle, and intercooling cycle, and they compared under part-load. Yang et al. [18] focused on the off-design performance of the system integrated s simple recuperative sCO_2 Brayton cycle, solar power tower, and thermal energy storage. They aimed at analyzing the system performance under more realistic conditions. Sing and Mishra [19] performed detailed energy and exergy analyses of solar parabolic trough collectors driven combined power plant. The combined power plant is consisting of sCO_2 Brayton cycle and organic Rankine cycle. Sing and Mishra [20] investigated the exergy and energy-centered parametric performance of parabolic trough collectors driven combined sCO_2 cycle/vapor absorption refrigeration system. They calculated the exergy and thermal efficiency of the sCO_2/vapor absorption refrigeration cycle as approximately 75.2% and 41.89% at 650 K maximum cycle temperature.

As seen from the literature overview given above, the studies on the sCO_2 Brayton cycle operating at low temperatures are limited. In most of the studies, the temperature of the heat source is above 300°C. In this study, performance analysis of a sCO_2 Brayton cycle operating at low temperature is conducted. The examined system consists of vacuum tube solar collectors and a Brayton cycle working with CO_2. The sCO_2 Brayton cycle has been integrated with a set of solar collectors. The analyses were carried out using the solar data from the city of Isparta, Turkey. Thermodynamic performance assessment of the integrated systems was performed using Engineering Equation Solver (EES) software. In addition, parametric analyses were also performed in order to examine the effects of system parameters on system performance.

2. SOLAR ASSISTED SCO_2 BRAYTON CYCLE

The schematic representation of the solar-driven sCO_2 Brayton cycle is shown in Figure 1. The system consists of a set of evacuated solar collectors, a compressor, a turbine, gas cooler. Referring to the Figure 1, the CO_2 is compressed by the compressor, and its pressure is increased. (1-2). Compressed CO_2 passes through the solar collectors, where it reaches a high-temperature (2-3). Then work is produced by expanding the carbon dioxide

fluid in the turbine. (3-4). Finally, carbon dioxide temperature is lowered down to the compressor inlet temperature in the gas cooler, thus completing the cycle.

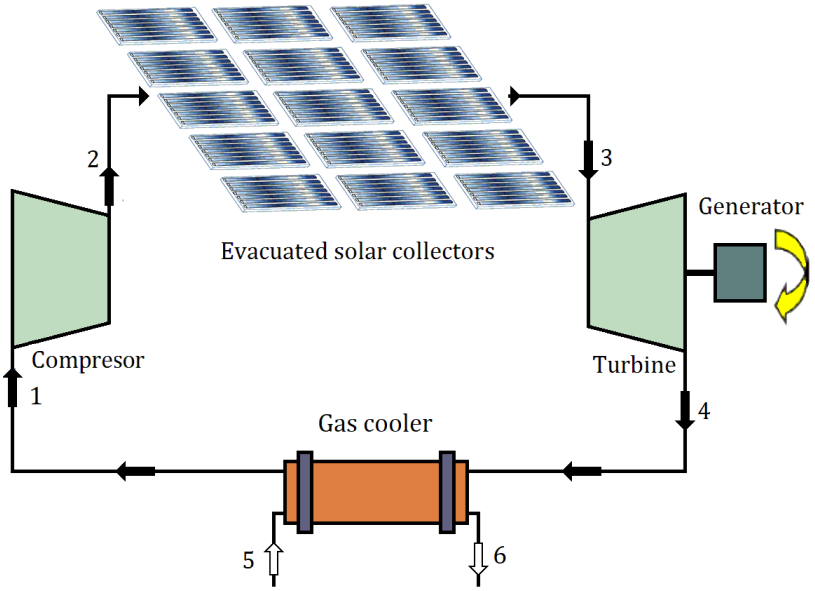

Figure 1. Solar-assisted sCO_2 Brayton cycle

3. SYSTEM MODELING

In this section, the thermal modeling of the evacuated U-tube solar collector is performed. The solar collector is heated by the solar radiation across the evacuated space, and incident solar irradiance is then absorbed by the selective coating. A large amount of absorbed solar energy is conducted aluminum fin to U-tube and then transfer to the working fluid.

The useful collected solar energy has to be determined [21].

$$\dot{Q}_u = F_R A[S - U_L(T_{in} - T_a)] \quad (1)$$

where S is the solar irradiance, F_R is the heat removal factor, U_L is the overall heat loss coefficient, A is the collector area, T_a is the temperature air, and T_{in} is the inlet CO_2 temperature. Further details associated with evacuated solar collectors can be found in Ref. [22].

For determining the CO_2 temperature at the collector exit, the useful solar energy collected by evacuated solar tubes can also be written as:

$$\dot{Q}_u = \dot{m} C_p (T_{out} - T_{in}) \quad (2)$$

The general mass balance equation for steady-state and steady-flow processes can be written as [23].

$$\sum \dot{m}_{in} = \sum \dot{m}_{out} \quad (3)$$

In the above equation, $\dot{m}$ is the mass flow rate, and the subscripts in and out stand for inlet and outlet, respectively. The energy balance equation can be written as:

$$\dot{Q} + \sum \dot{m}_{in} h_{in} = \dot{W} + \sum \dot{m}_{out} h_{out} \quad (4)$$

Here, $\dot{Q}$ is the rate of heat, $\dot{W}$ is the rate of work, and h is the specific enthalpy.

For the second law analysis of the heat generation system in steady state operation, the general exergy balance equation is given below [24].

$$\dot{E}x_Q - \dot{E}x_W = \sum \dot{m}_{out} e_{out} - \sum \dot{m}_{in} e_{in} + \dot{E}x_{dest} \quad (5)$$

Where, $\dot{E}x_Q$ and $\dot{E}x_W$ are the exergies of heat and work, respectively, e is the specific exergy and $\dot{E}x_{dest}$ is exergy destruction. In the above equation, exergies of heat and work and entropy generation rate are given below [25]:

$$\dot{E}x_{dest} = T_0 \dot{S}_{gen} \quad (6)$$

$$\dot{E}x_Q = \dot{Q}\left(\frac{T - T_0}{T}\right) \quad (7)$$

$$\dot{E}x_W = \dot{W} \quad (8)$$

The specific exergy is expressed relative to the environmental conditions as:

$$e = (h - h_0) - T_0(s - s_0) \quad (9)$$

where s is entropy and the subscript 0 indicates properties at the reference state.

The energy efficiency of the sCO_2 Brayton cycle is expressed as:

$$\eta_{en} = \frac{\dot{W}_T - \dot{W}_C}{\dot{Q}_u} \quad (10)$$

Finally, the overall exergy efficiency of the power generation system is given by:

$$\eta_{ex} = \frac{\dot{W}_T - \dot{W}_C}{\dot{E}x_{solar}} \quad (11)$$

By applying the thermodynamic equilibrium equations to each system element, the capacities and exergy destruction rate equations for each system component are given in Table 1.

Table 1. Energy capacity and exergy destruction of each system component.

	Energy capacity	**Exergy destruction**
Solar collector	$\dot{Q}_{solar} = SA$ $\dot{Q}_{coll} = \dot{m}_2 (h_3 - h_2)$	$\dot{E}x_{dest,coll} = \dot{E}x_{solar} + \dot{E}x_2 - \dot{E}x_3$
Turbine	$\dot{W}_T = \dot{m}_3(h_3 - h_4)$	$\dot{E}x_{dest,T} = \dot{E}x_3 - \dot{E}x_4 - \dot{W}_T$
Gas cooler	$\dot{Q}_{GC} = \dot{m}_4(h_4 - h_1)$	$\dot{E}x_{dest,GC} = \dot{E}x_4 + \dot{E}x_5 - \dot{E}x_1 - \dot{E}x_6$
Compressor	$\dot{W}_C = \dot{m}_1(h_2 - h_1)$	$\dot{E}x_{dest,C} = \dot{E}x_1 - \dot{E}x_2 + \dot{W}_C$

4. RESULTS

Solar assisted sCO_2 Brayton cycle was analyzed based on the energy and exergy analysis described previously. The analyses were conducted in order to determine the thermodynamic performance characteristics of the system. For the calculations, solar energy data of Isparta, Turkey, was used. The assumptions made for the calculations and operating parameters for the sCO_2 Brayton cycle analysis are given below.

- The analyses were conducted for the steady-state and steady-flow processes.
- Kinetic and potential energies can be neglected.
- Pressure losses in heat exchangers are neglected.
- Heat transfer with the ambient is negligible.
- The reference state properties are 20°C and 101.325 kPa.

The solar-assisted sCO_2 Brayton Cycle was analyzed in terms of the first and second laws of thermodynamics. The Engineering Equation Software was used for determining the thermodynamic properties of the working fluid. The analyses were made using the solar energy data of Isparta. In Figure 2, the variation of mean solar radiation for the months of the year according to the meteorological data of Isparta was given. It is clear from the figure that the mean solar radiation increases gradually from January to August and reaches a maximum value of 974 W/m^2 in August for Isparta. In addition, the lowest solar radiation rates are reported for January as 497.

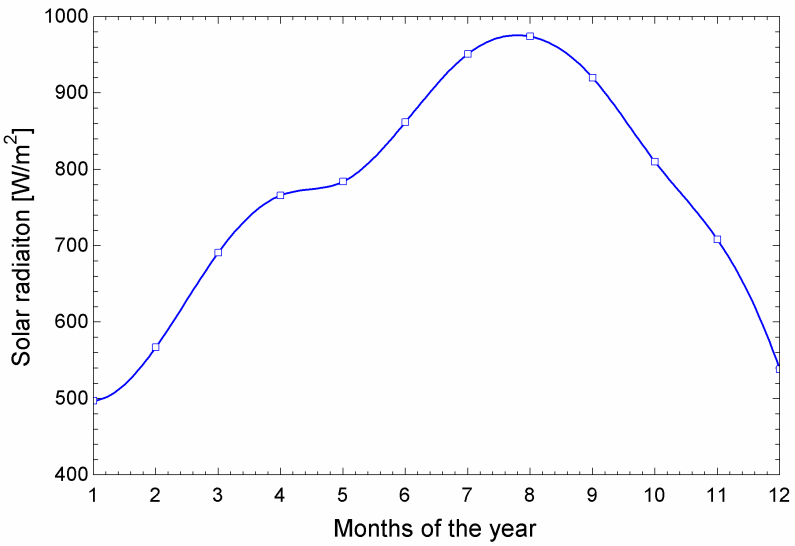

Figure 2. Monthly solar radiation data of Isparta

The CO_2 temperature at the exit of the evacuated tube solar collectors was calculated used the thermal modeling given in Ref. [22] and given in Figure 3 for the months of the year.

According to the results, calculated CO_2 temperatures at the exit of the solar collector increase from January to August and reach a maximum value of 207.2°C in August. The lowest value for the temperature was calculated for January as 110.8°C. From the simulated results, it can be understood that the exit temperature of CO_2 is sufficient enough to drive the turbine for power generation.

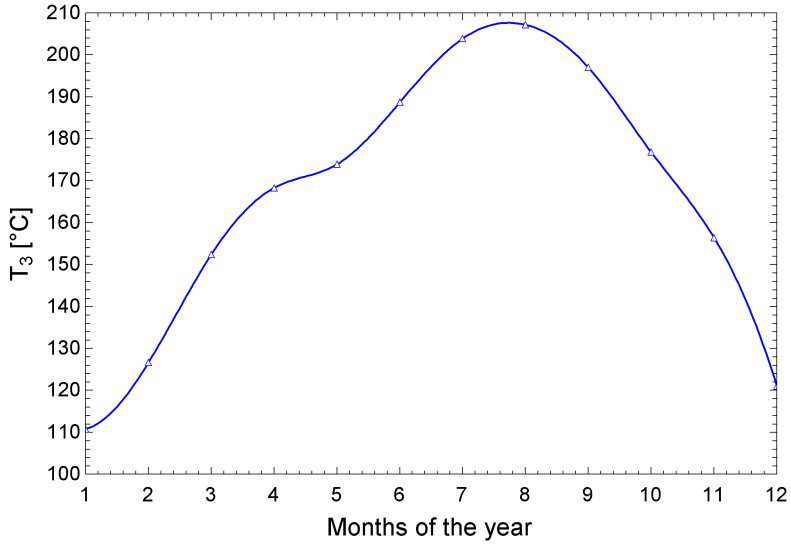

Figure 3. Variation of CO_2 temperature at the exit of solar collector

In order to determine the performance of the supercritical Brayton Cycle, the operation parameters are tabulated in Table 2. It must be noted that the compressor inlet pressure and temperature of the Brayton Cycle were taken as close to the critical properties of the CO_2 as possible for obtaining better performance.

Table 2. Initial operating parameters

Parameter	**Value**
Compressor inlet temperature	35℃
Turbine inlet temperature	207℃
Compressor inlet pressure	8000 kPa
Compressor outlet pressure	25000 kPa
Compressor isentropic efficiency	0.85
Turbine isentropic efficiency	0.94

Using the data provided in the table above, the system's performance was calculated for the whole year. According to the results, the maximum net power generation was calculated as 0.2543 kW for August. The first and second law efficiencies of the solar-powered system were calculated as 16% and 73%, respectively. According to the exergy analyses, the highest exergy efficiency for the system was calculated for the turbine with 95%. The highest exergy destruction was estimated for the solar collector as 8.7 kW. The exergy efficiency of individual system components was given in Figure 4, while the exergy destruction rates of each system element were given in Figure 5.

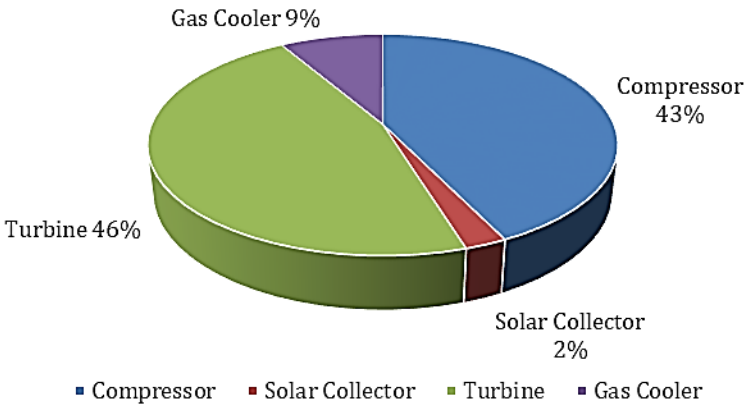

Figure 4. Exergy efficiency of individual system components

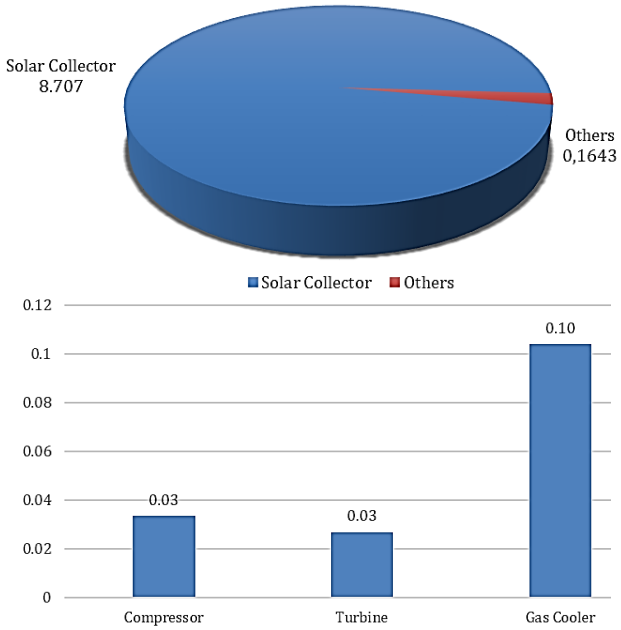

Figure 5. Exergy destruction rates of each system components (kW)

In order to examine the effects of basic parameters on the system performance, parametrical analyses were performed. In Figure 6, the effect of the turbine inlet pressure (P_T) on the net power generation was given. For the analysis, the turbine inlet pressure was varied between 20000-30000 kPa. It was determined that net power generation was increased from 248 W to 254 W from 20000 kPa to 24000 kPa. After 24000 kPa, the net power generation starts to decrease due to the increase of pressure ratio. Also, on the right-hand axes, the energy efficiency of the solar-integrated system is plotted against the high system pressure.

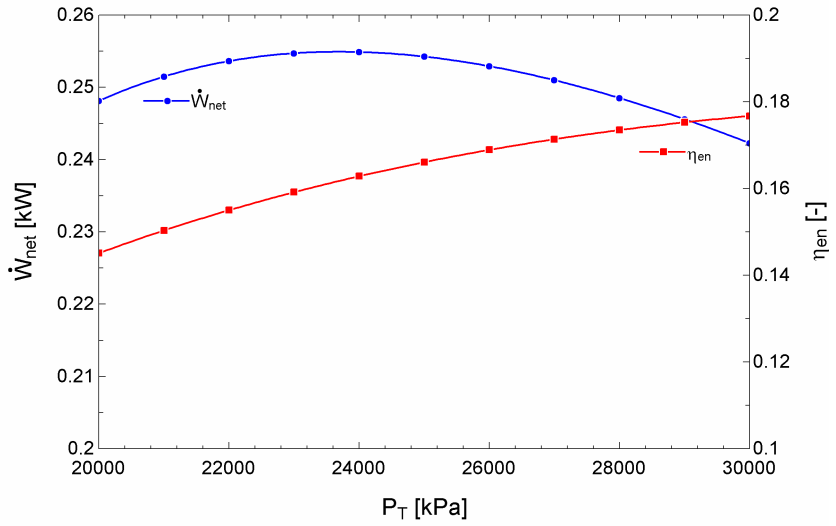

Figure 6. Variation of net power generation and energy efficiency with turbine inlet pressure

In Figure 7, the exergy destruction rate and exergy efficiency were plotted with the variation of turbine inlet pressure. On the contrary to energy analysis, the exergy destruction rate decreases a little, and after 24000 kPa, it starts to increase with the turbine inlet pressure as expected while the exergy efficiency has the same trend with the energy efficiency.

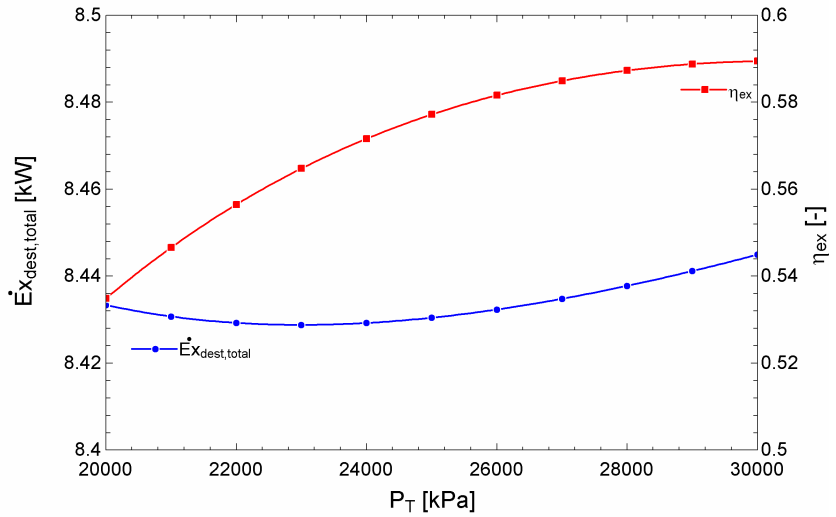

Figure 7. Variation of total exergy destruction and exergy efficiency with turbine inlet pressure

The effect of compressor pressure on the system performance was also investigated (Figures 8 and 9). In Figure 8, the variation of net power generation and energy efficiency with the compressor pressure were given. During the analyses, the compressor inlet pressure varied between 7500-10000 kPa where the lowest pressure values were taken to be close to the critical pressure of CO_2. With the increase of low-pressure values from 7500 to 8500 kPa, the net power generation increases significantly, as well as the energy efficiency. This is mainly due to the properties of the supercritical fluid CO_2. After 8500 kPa, it starts to decrease slightly.

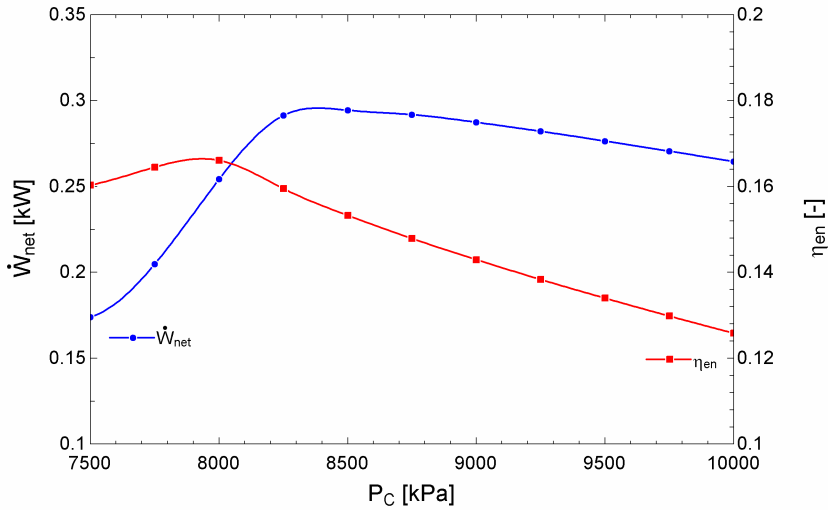

Figure 8. Variation of net power generation and energy efficiency with compressor inlet pressure

Figure 9 shows the exergy destruction and exergy efficiency variation with the compressor pressure. Conversely, the exergy destruction rate increases with the compressor pressure substantially between 7500-8500 kPa and after it starts to increases slightly with the same trend of net power generation. In addition, the exergy efficiency decreases after 8500 kPa while between 7500-8500 kPa pressure ranges, it increases. It must be noted that, during these analyses, the turbine inlet temperature and pressure were kept constant as 207°C and 25000 kPa.

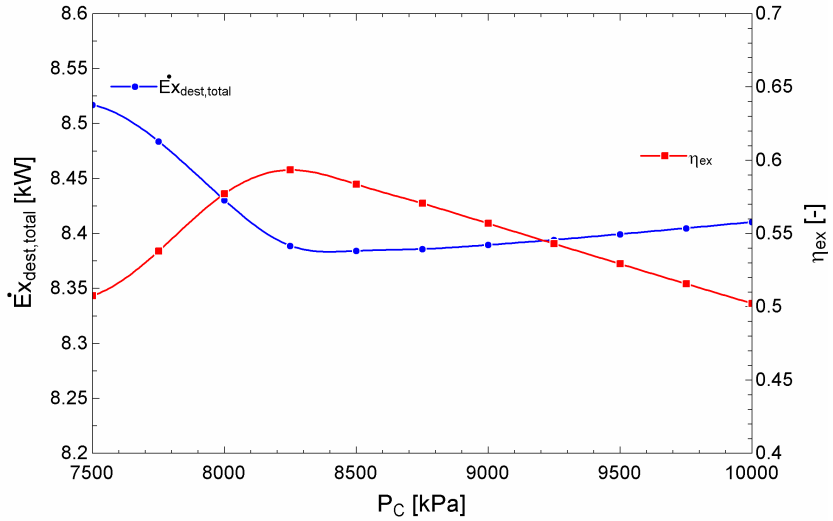

Figure 9. Variation of total exergy destruction and exergy efficiency with compressor inlet pressure

In Figure 10, net power generation and energy efficiency were given as a function of turbine inlet temperature. From the figure, it can be seen that both energy efficiency and generated electricity increase with the turbine inlet temperature. The analysis was carried out by varying the turbine inlet temperature between 150-210°C since, with the assumed parameters, the maximum turbine outlet temperature was obtained around 210°C for August. This result is harmonious with the results of the experimental study conducted by Yamaguchi and his research group [22, 26, 27]. In Figure 11, the total exergy destruction ratio and exergy efficiency were plotted against turbine inlet temperature. According to the results, with the increasing of the turbine inlet temperature, the exergy destruction

reduces from 8.58 kW to 8.42 kW. On the contrary to this, the exergy efficiency increases with the turbine inlet temperature. However, this increment is very slight around the temperature ranges of 200°C and, after this, exhibits a small decrement.

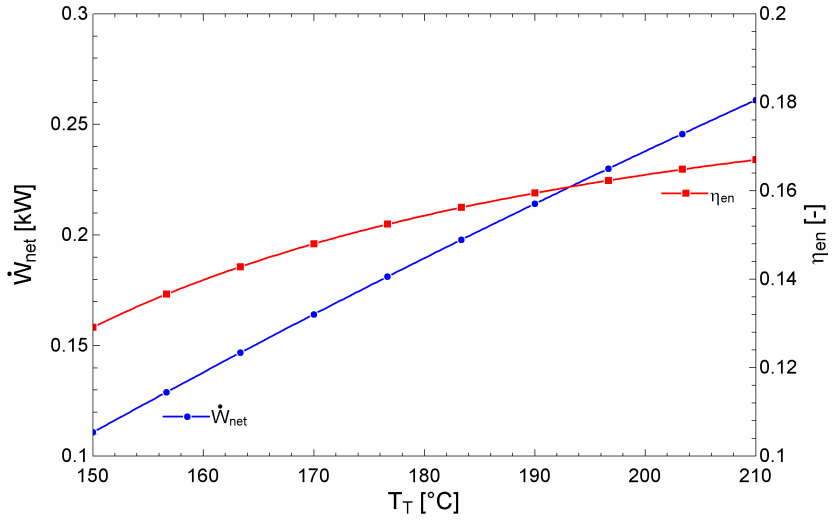

Figure 10. Variation of net power generation and energy efficiency with turbine inlet temperature

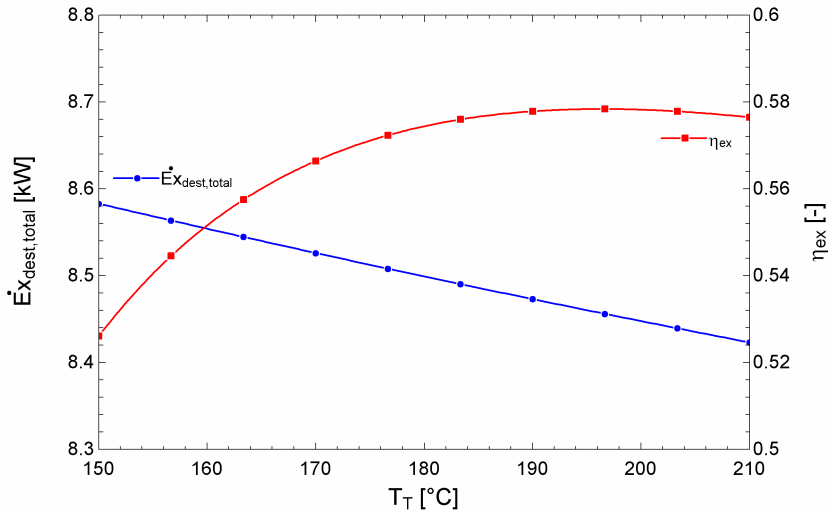

Figure 11. Variation of total exergy destruction and exergy efficiency with turbine inlet temperature

5. CONCLUSIONS

In this study, the aim was to the investigated of evacuated tube solar collector assisted sCO_2 Brayton cycle for Isparta, Turkey. Based on the investigations, the following conclusions can be drawn from the present study:

- The solar energy potential of Isparta was found to be relatively high. According to the solar data, the maximum solar radiation was 974 W/m^2 for Isparta for August.
- The results showed that CO_2 temperature at the exit of the solar collector could reach a maximum temperature of 207.2°C.
- The maximum net power generation was obtained as 0.25 kW, while the total exergy destruction was calculated to be around 8 kW.

- The energy and exergy efficiencies of the system were calculated to be 16% and 73%, respectively.
- The highest exergy efficiency within the system elements was calculated as 0.9518 for the turbine.
- Maximum exergy destruction was calculated in the solar collector as 8.7 kW.

REFERENCES

[1] Yang, Y., Huang, Y., Jiang, P. & Zhu, Y. Multi-objective Optimization of Combined Cooling, Heating and Power Systems with Supercritical CO2 Recompression Brayton Cycle, Applied Energy, 271, 115189, 2020.

[2] Kizilkan, O. & Yamaguchi, H. Feasibility Research on the Novel Experimental Solar-Assisted CO2 Based Rankine Cycle Integrated with Absorption Refrigeration, Energy Conversion and Management, 205, 112390, 2020.

[3] Meng, J., Wei, M., Song, P., Tian, R., Hao, L. & Zheng, S. Performance Evaluation of a Solar Transcritical Carbon Dioxide Rankine Cycle Integrated with Compressed Air Energy Storage, Energy Conversion and Management, 215, 112931, 2020.

[4] Zhang, X.R., Yamaguchi, H. & Uneno, D. Experimental Study on the Performance of Solar Rankine System Using Supercritical CO2, Renewable Energy, 32, 2617-2628, 2007.

[5] AlZahrani, A.A. & Dincer, I. Thermodynamic Analysis of an Integrated Transcritical Carbon Dioxide Power Cycle for Concentrated Solar Power Systems, Solar Energy, 170, 557-567, 2018.

[6] Li, M., Wang, J., Li, S., Wang, X., He, W. & Dai, Y. Thermo-economic Analysis and Comparison of a CO2 Transcritical Power Cycle and an Organic Rankine Cycle, Geothermics, 50, 101-111, 2014.

[7] Yamaguchi, H., Yamasaki, H. & Kizilkan, O. Experimental Investigation of Solar- Assisted Transcritical CO2 Rankine Cycle for Summer and Winter Conditions from Exergetic Point of View, International Journal of Energy Research, 44, 1089-1102, 2020.

[8] Liao, G., Liu, L., E, J., Zhang, F., Chen, J., Deng, Y. & Zhu, H. Effects of Technical Progress on Performance and Application of Supercritical Carbon Dioxide Power Cycle: A Review, Energy Conversion and Management, 199, 111986, 2019.

[9] Yu, A., Wen, S., Lin, X. & Zhou, N. Recent Trends of Supercritical CO2 Brayton Cycle: Bibliometric Analysis and Research Review, Nuclear Engineering and Technology, Article In Press.

[10] Ahn, Y., Bea, S.J., Kim, M., Cho, S.K., Baik, S., Lee, J.I. and Cha, J.E. N. Review of Supercritical CO2 Power Cycle Technology and Current Status of Research and Development, Nuclear Engineering and Technolog, 47, 647-661, 2015.

[11] Teng, L. & Xuan, Y. Design of a Composite Receiver for Solar-Driven Supercritical CO2 Brayton cycle, Journal of CO2 Utilization, 32, 290-298, 2019.

[12] Mohammadi, Z., Fallah, M. & Seyed Mahmoudi, S.M. Advanced Exergy Analysis of Recompression Supercritical CO2 Cycle, Energy, 178, 631-643, 2019.

[13] Milani, D., Luu, M.T., McNaugton, R. & Abbas A. A comparative Study of Solar Heliostat Assisted Supercritical CO2 Recompression Brayton Cycle: Dynamic Modeling and Control Strategies, The Journal of Supercritical Fluids, 120, 113-124, 2017.

[14] Yang, J., Yang, Z. & Duan, Y. Part-load Performance Analysis and Comparison of Supercritical CO2 Brayton Cycles, Energy Conversion and Management, 214, 112832, 2020.

[15] Padilla, R.V., Too, Y.C.S., Benito, R. & Stein, W. Exergetic Analysis of Supercritical CO2 Brayton Cycles Integrated with Solar Central Receivers, Applied Energy, 148, 348-365, 2015.

[16] Zhu, H.H., Wang, K. & He, YL Thermodynamic Analysis and Comparison for Different Direct-Heated Supercritical CO2 Brayton Cycles Integrated into a Solar Thermal Power Tower System, Energy, 140, 144-157, 2017.

[17] Kulhanek, M. & Dostal, V. Supercritical Carbon Dioxide Cycles Thermodynamic Analysis and Comparison, Supercritical CO2 Power Cycle Symp. Boulder, CO, May, 2011.

[18] Yang, J., Yang, Z. & Duan, Y. Off-design Performance of a Supercritical CO2 Brayton Cycle Integrated with a Solar Power Tower System, Energy, 201, 117676, 2020.

[19] Mishra, R.S. & Singh, H. Detailed Parametric Analysis of Solar Driven Supercritical CO2 Based Combined Cycle for Power Generation, Cooling and Heating Effect by Vapor Absorption Refrigeration as a Bottoming Cycle, Thermal Science and Engineering Progress, 8, 397-410, 2018.

[20] Singh, H. & Mishra, R.S. Performance Analysis of Solar Parabolic Trough Collectors Driven Combined Supercritical CO2 and Organic Rankine Cycle, Engineering Science and Technology, an International Journal, 21, 451-464, 2018.

[21] Kalogirou SA. Solar Energy Engineering: Processes and Systems. Academic Press: Oxford 2009.

[22] Kizilkan, O., Yamaguchi, H. A feasibility study of CO2-based solar-assisted Rankine cycle: a comparative case study for Isparta, Turkey. Greenhouse Gas Sci Technol., 10, 840–854, 2020.

[23] Cengel, Y.A. & Boles, M.A. Thermodynamics: an engineering approach. 5th ed., McGraw-Hill, New York, USA, 2006.

[24] Dincer, I., Rosen, M.A. Exergy: Energy, Environment and Sustainable Development. 1st ed., Elsevier Science; Oxford, UK, 2007.

[25] Kotas T.J. The exergy method of thermal plant analysis. Butter-Worths, London, UK, 1985.

[26] Kizilkan, O., Khanmohammadi, S., Yamaguchi, H. Two-objective optimization of a transcritical carbon dioxide based Rankine cycle integrated with evacuated tube solar collector for power and heat generation. Applied Thermal Engineering, 182, 116079, 2021.

[27] Yamaguchi, H., Yamasaki, H., Kizilkan, O. Experimental investigation of solar-assisted transcritical CO2 Rankine cycle for summer and winter conditions from exergetic point of view. International Journal of Energy Research, 44, 1089–1102, 2020.

ANALYSIS AND DESIGN OF A COOLING CHANNEL FOR A PHOTOVOLTAIC PANEL

Zeynep ÖZCAN, Miray GÜLGÜN, Ecem ŞEN, Nezir Yağız ÇAM, Levent BİLİR
Yaşar University, Department of Energy Systems Engineering, İzmir/Turkey
Email: zeynepppozcan@gmail.com

ABSTRACT

Photovoltaic panels are attracting more attention in Turkey as the solar potential is very high in many regions. It is a well-known fact that even though the electricity generation is higher when the solar radiation is high on the panel, the efficiency of the panel drops as its temperature increases. In this study, it intended to achieve a cooling effect using an air duct placed under a photovoltaic (PV) panel, thereby increasing the panel's efficiency of electricity generation. The PV selected as a Panasonic monocrystalline panel of 1.67 square meters with a capacity of 330 W. An aluminum channel placed under the panel and the cooling fluid used as air. Hourly electricity generation, PV efficiency and cell temperature values over a year calculated using measured ambient temperature, global and diffuse radiation data by using MATLAB software. Furthermore, the same calculations made using PV SOL software for the chosen PV and compared with obtained values in MATLAB. An excellent agreement accomplished between the results obtained from MATLAB program and the results provided by PV SOL software. Maximum cell temperature determined as 57.91 °C on June 21st at 13:00 as a result of hourly calculations. The incident solar radiation found as 976 W/m^2 when the panel reached maximum temperature. The PV and cooling channel modeled in ANSYS Fluent software and cooling effect investigated for different air velocities for the hour when maximum cell temperature reached. Additionally, the effects of some protrusions attached on the cooling channel on heat transfer and pressure drop also investigated.

Keywords: Photovoltaic panel, efficiency, cooling channel, ANSYS Fluent analysis.

Symbol List

A	Cross Sectional Area (m^2)
A_{PV}	PV Panel Area (m^2)
C	Specific Heat (J/kgK)
E_i	Hourly PV Electricity Generation (W)
G_{ref}	Ground Reflection
I_d	Diffuse Radiation (W/m^2)
I_G	Global Radiation (W/m^2)
I_T	Hourly Radiation Incident of the Tilted PV Panel
k	Thermal Conductivity (Wm/K)
$\dot{m}$	Mass Flow Rate (kg/s)
n	Day Number
n_{pv}	Number of PV Panel
$\dot{Q}$	Heat Transfer (kW)
R_b	Beam Radiation
T	Temperature (°C)
T_a	Ambient Temperature (°C)
T_c	Cell Temperature (°C)
T_{ref}	Reference Temperature (°C)
W	Hour Angle (°)
w_s	Sunset Hour Angle (°)

Greek Letters

β	Slope angle of PV (°)
δ	Declination Angle, Solar Radiation Coefficient (°)
η	Efficiency
$\eta_{mp,ref}$	PV Panel Efficiency(%)
μ_{mp}	Temperature Coefficient of Maximum Power Point
ρ	Density (kg/m^3)
ρ_g	Ground Reflectivity
φ	Latitude
ΔT	Temperature Difference between Outlet and Inlet (°C)

1. INTRODUCTION

In today's society, renewable energy seeking and its usage are becoming mandatory with the increase of the human population and the environmental issues. Especially society started to use a solar energy. The solar energy is essential renewable energy source that is clean, sustainable, and easy to reach, does not require complex technology, does not harm to the environment, has high power density, has lower reducing costs source of energy. Because of these factors, the solar energy usage has increased. However, the most important issue in today's world is the efficient usage of energy. Decreasing the initial costs, reducing waste usage, recovering the waste energy and the most effective and efficient usage of energy are the main research topics. Researchers often emphasize that one of the improvement studies for the PV panels is to increase the efficiency of PV cells by cooling. [1]

Mittelman et al. (2009) aimed that cooling the PV panel with radiation and free convection. Therefore, they prepared the cooling channel due to passive cooling and used air as a cooling material in their project. [2] Erkan et al. (2018) investigated the cooling of a single crystalline photovoltaic cell using the computational fluid dynamics method by taking water as a cooling material. They observed the effect of the mass flow velocity of water on cooling. [1] Bayrak et al. (2019) experimentally investigated the performance of polycrystalline 75W PV panel with a cell structure for Elazıg, Turkey climatic conditions. At the end of their project, they found that Aluminum fins placed behind the photovoltaic panels kept the PV panel temperature below the maximum allowable temperature. [3] Zou et al. (2019) focused on the passive air-cooling system for PV; they showed the effect of channel geometry on the cooling performance of the system. [4] Han et al. (2019) investigated two-dimensional numerical analysis of the fluid flow and heat transfer behaviors of the natural convection driven by the buoyancy force in the passive cooling air duct formed by the two vertical parallel walls. At the end, they showed the passive cooling air duct under the PV module is an effective way of thermal regulation of the PV module. [5]

In this study, it aimed to cool the solar panel based on the hottest value by means of heat transfer by giving air at different velocities to the flat plate and finned cooling channel located under four-layer solar panel with ANSYS Fluent software to increase panel's efficiency for electricity generation.

2. METHOD

In this study, the cooling channel that has different geometrical designs and pursue performance analysis on a PV panel made with Computational Fluid Dynamics. The PV panel selected as Panasonic N330 type. PV panel's cells are monocrystalline-silicon and have maximum 19.4 % efficiency under standard test conditions (air mass=1.5, Radiation=1000W/m², cell temperature=25°C). [6] PV panel layers are with the cooling channel; glass, airgap, PV cells, aluminum plate and cooling channel, respectively. In the PV panel, the cooling channel has been used to cool the PV cells, the air has been transmitted that used as a refrigerant to the channels with the help of a fan.

The inclined PV panel has been located in Izmir. In summer, radiation is higher than the other seasons in Izmir. Due to high radiation, cell temperature has increased rapidly. Cell temperature calculations determined with MATLAB. According to temperature rising, the PV module's efficiency is decreasing. Therefore, the PV panel must be cooled to prevent temperature rising. For this reason, the cooling channel installed under the PV panel.

A comprehensive numerical analysis of the PV panel performed using the MATLAB program to simulate time-dependent changes. In this parametric study, the effects of change of design parameter investigated using hourly diffuse, global radiation and ambient temperature data for one year. For obtaining the optimal design, a reference temperature taken as 25 degrees and a slope angle of the PV taken as 30 degrees. Moreover, it aimed to calculate the monthly electricity production of this PV panel and to compare the values obtained in the PVSOL software, and observed to the change in the cooling amount, electricity production and PV panel efficiency depending on the velocity of the air supplied to the cooling channel using ANSYS Fluent program. The hourly electricity generation steps of the PV panel are as follows; [7]

Declination Angle (δ):

$$\delta = 23.42\sin\left(360\times\frac{284+n}{365}\right) \quad (1)$$

Where n days of the year from 1 to 365.

Hour Angle (w):

$$w = (\text{Solar time}-12)\times 15° \quad (2)$$

Where solar time is hours of the day from 1 to 24.

Sunset Hour Angle (w_s):

$$w_s = \min[\arccos(-\tan\varphi\tan\delta), \arccos(-\tan(\varphi-ß)\tan\delta] \quad (3)$$

Where φ is the latitude of Izmir and ß is the slope angle of PV.

The ratio of beam radiation on the inclined surface to a horizontal surface for the collector directed south in the northern hemisphere (R_b) :

$$R_b = \frac{\cos(\varphi-ß)\cos\delta\cos w+\sin(\varphi-ß)\sin\delta}{\cos\varphi\cos\delta\cos w+\sin\varphi\sin\delta} \quad (4)$$

Hourly radiation incident of the tilted PV panel (I_T):

$$I_T = (I_G - I_d)\, R_b + I_d\left(\frac{1+\cos ß}{2}\right) + I_G\rho_g\left(\frac{1-\cos ß}{2}\right) \quad (5)$$

Where I_G is the global radiation, I_d is the diffuse radiation and ρ_g is ground reflection.

Cell temperature (T_c):

$$T_c = T_a \times k \times I_T \quad (6)$$

Where T_a is the ambient temperature for each hour and k is the thermal conductivity.

Hourly PV efficiency (η):

$$\eta = \eta_{mp,ref} \times (1 - \mu_{mp}\,(T_c - T_{ref}) + \delta.\ln\left(\frac{IT}{Gref}\right) \quad (7)$$

Where $\eta_{mp,ref}$ is PV panel efficiency , μ_{mp} is the temperature coefficient of maximum power point efficiency which is 0.00258 and T_{ref} is the reference temperature.

Hourly PV electricity generation (E_i):

$$E_i = \eta \times n_{pv} \times A_{pv} \times I_T \quad (8)$$

Where n_{pv} is number of PV and A_{pv} is PV area.

Some amount of solar radiation has been absorbed by glass and PV cells. Therefore, net heat flux(W/m^2) is:

$$\text{Heat flux } (W/m^2) \times \text{Glass transmissivity} \times \text{PV transmissivity} \quad (9)$$

Heat transfer provided with the air transmitted through the channel with the help of the fan, so PV panel's cooling performed. With using ANSYS Fluent software, modeling performed according to specific temperature and cooling channels with different air velocities and different geometrical shapes.

In ANSYS Fluent, The Navier-Stokes equations used. These equations can be derived from the basic conservation and continuity equations applied to properties of fluids. In order to derive the equations of fluid motion, we must first derive the continuity equation, apply the equation to conservation of mass and momentum, and finally combine the conservation equations with a physical understanding of what a fluid is. [8]

The models of the cooling channels were rectangular. For CFD analysis of the PV module, cooling channels located. First the cooling channel had 71 rectangular fins. Fins dimensions were: 5 mm width, 8 mm height and the air distance between 2 fins was 10 mm. In the second model, cooling channel had 82 rectangular fins. Fins dimensions were: 3mm width, 8mm height and the air distance between two fins was 10 mm. In the third model, air distance between 2 curved fins was 30 mm. The cooling refrigerant selected air and same in every simulation. Air's temperature that was coming to the cooling channels and ambient temperature selected 25°C. Constant heat flux was giving to the system and it was equal to 597 W/m^2. Simulations performed for both cooling channel with 3m/s and 5m/s.

3.VALIDATION

Baloch et al. (2015) analyzed a convergent water channel cooling which aimed to obtain low and uniform temperature on the PV panel surface. They made evaluations for an uncooled PV system and a converged channel-cooled PV system due to the climate of Saudi Arabia during June and December. Before cooling the PV string, the maximum temperature recorded as 71.2°C and 48.2°C in June and December, respectively. The mesh methods applied in this study similarly applied to the study of the Baloch et al. (2015).

Table 1. Comparison of water outlet temperatures and cell temperatures between the applied mesh methods into Baloch et al. (2015)

Water velocity (m/s)	Water outlet temperature (°C)	Cell temperature (°C)
0.012	30.5	45.1
0.012	29.77	42.79

As it is seen in the Table 1., when water with a temperature of 27°C given to the cooling channel at a velocity of 0.012 m/s, the outlet temperature was 29.77°C, while the temperature of the cell before cooling was 71.2°C, this value dropped to 42.79°C aftercooling in the applied mesh methods into Baloch et al. (2015).

In Baloch et al (2015), the temperature of the water entering the cooling channel at a velocity of 0.012 m/s increased from 27°C to 30.5. The cell temperature decreased from 71.2 °C to 45.1°C. According to the modeling, in both studies, it observed that the cooling amount varied according to applied mesh methods. Furthermore, when looking at the results obtained, it was seen that while the cell temperature and water outlet temperature values are near in both studies.

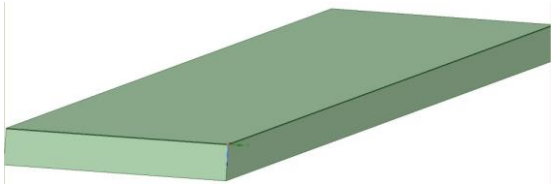

Figure 1. Geometry Design of PV Panel with the cooling channel in ANSYS Fluent Panel based on the system investigated in Baloch et al. (2015)

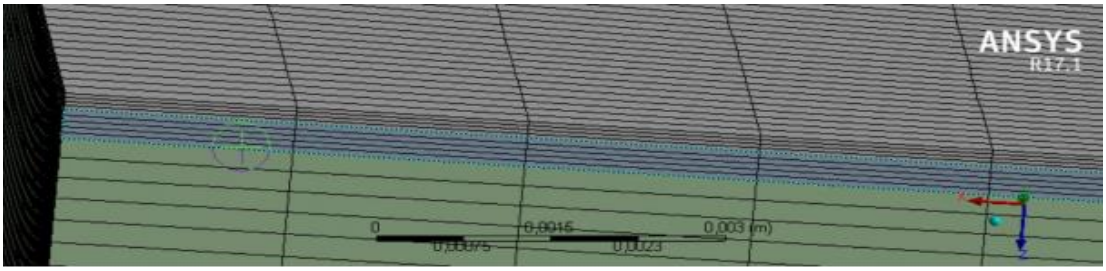

Figure 2. Mesh view of PV Panel from right side based on the system investigated in Baloch et al. (2015)

4. RESULTS AND DISCUSSION

In this section firstly, monthly electricity generation of the PV has been presented. Secondly, comparison of electricity generation data between MATLAB and PVSOL has been made. Next, heat transfer characteristic and temperature differences occurred during heat transfer between PV and channel have been examined due to calculated data from ANSYS Fluent programme. Finally, all results and graphs from Fluent software have been discussed.

Yearly and monthly electricity generation values calculated by MATLAB software. These calculations made according to 2018 yearly solar data. Monthly electricity generation values that calculated by MATLAB are almost as same as values that founded by PVSOL. The results are presented in Figure 3. The most electricity generation obtained in and the annual electricity generation founded as 561 kWh in MATLAB.

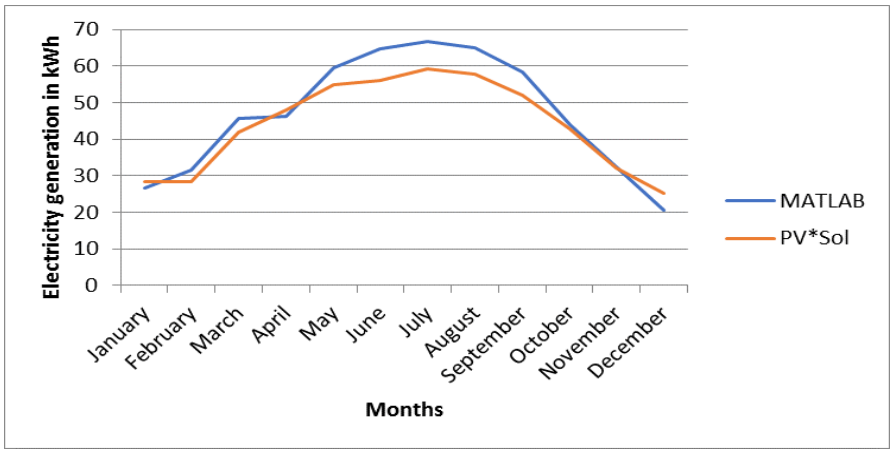

Figure 3. Graph of Monthly Electricity Generation in MATLAB and PVSOL software.

According to the results that calculated with MATLAB, the highest cell temperature value has been determined as 21st of July at 13.00. Moreover at that day cell temperature founded as 57.91°C and PV efficiency founded as 18%. In addition hourly solar irradiance determined as 975.97 W/m^2 and 293 W electricity generated by PV. Therefore, ANSYS Fluent programme analyzes have been made by basing on 57.91°C cell temperature because

as it mentioned in earlier the main aim of this study have been provided cooling due to the temperature rising. Likewise in the following path ANSYS Fluent analyzes for flat plate have been made according to different air velocities which were 5,7,10 m/s respectively. Cooling has been provided to cell temperature with channel during heat transfer. The model created for the simulations for the PV with flat plate channel is illustrated in Figure 4.

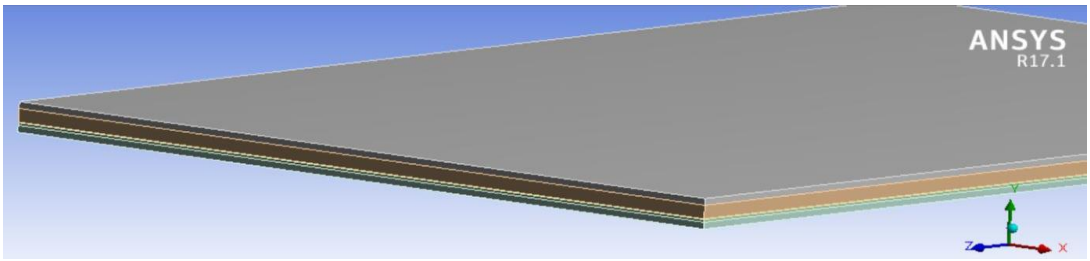

Figure 4. The PV panel's geometry for flat plate design in ANSYS Fluent software.

Table 2. Comparison of the results due to 5 m/s, 7 m/s and 10 m/s for flat plate.

Inlet Velocity(m/s)	Cell Temperature(°C)	Temperature Difference (°C)	Electricity Generation(W)	PV Efficiency(%)
5	46.4	11.51	302.95	18.59
7	41.49	16.42	307.01	18.84
10	37.4	20.51	310.4	19.04

After completing flat plate analysis, different geometrical shapes for cooling channel designed.

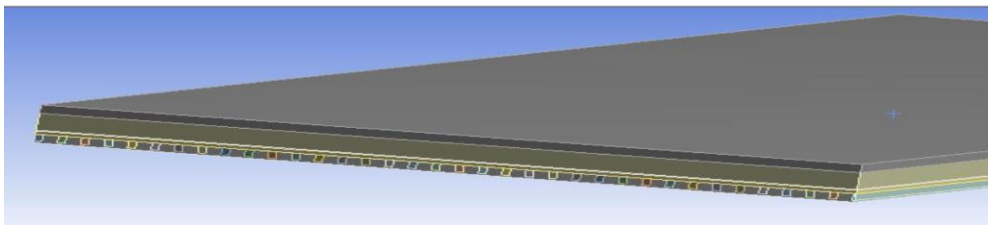

Figure 5. The front view of the PV's geometrical symmetry of the rectangular cooling channel with 71 fins in ANSYS Fluent software.

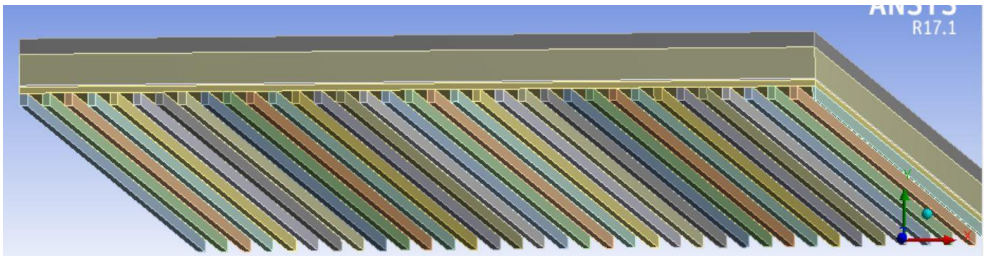

Figure 6. The bottom view of the PV's geometrical symmetry of the rectangular cooling channel with 71 fins in ANSYS Fluent software.

Table 3. Comparison of the results due to 3 m/s and 5 m/s for th rectangular cooling channel.

	Inlet Velocity(m/s)	Cell Temperature(°C)	Temperature Difference (°C)	Electricity Generation(W)	PV Efficiency(%)
71 Fins	3	49.74	8.17	300.18	18.42
	5	41.36	16.55	307.12	18.84
82 Fins	3	47.48	10.43	302.05	18.53
	5	39.82	18.02	308.40	18.92

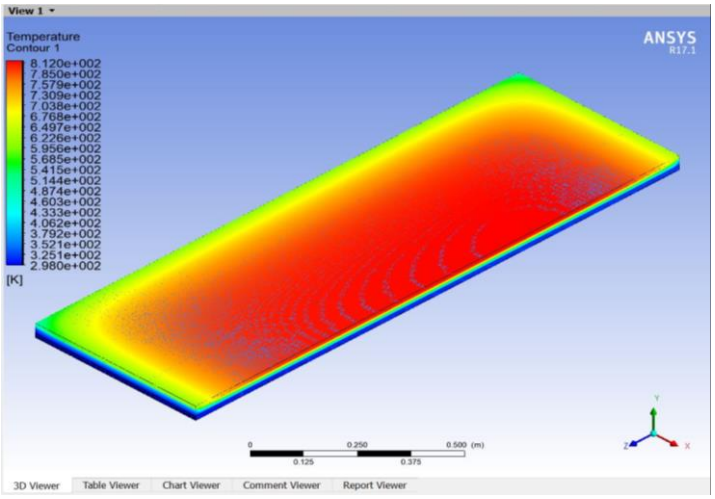

Figure 7. Temperature Contour of the PV module with 71 fins for 5 m/s in ANSYS Fluent.

In table 3, it shown that the channel with fins provided much more cooling than the channel with flat plate.

Without fins in 3m/s velocity, the cooling could not be observed but with fins even in 3m/s the cooling process observed.

As it seen in table 3, with 82 fins and 3m/s the cooling obtained close to the without fins and 5m/s value. In addition, with 71 fins and 5m/s same value observed with in 7m/s without fins and 82 fins with 5m/s almost reached the cooling value that observed in without fins and 10m/s.

After every step of analysis, the pressure drop values recorded.

Table 4. Pressure drops according to the channel geometry.

Channel geometry	Pressure Drop
Without fins (5m/s)	56.83 Pa
With 71 fins (5m/s)	126.41 Pa
With 71 fins (3m/s)	58.49 Pa
With 82 fins (5m/s)	121.25 Pa
With 82 fins (3m/s)	56.15 Pa

Pressure drop values increased with velocity rising on the other hand when pressure drops are compared in same velocity value it is seen that in the Table 4., when the fin numbers rose pressure drop values decreased.

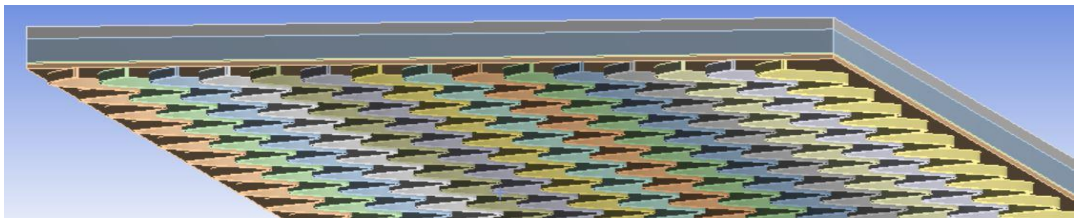

Figure 8. The bottom view of PV's geometrical symmetry for curved cooling channel with 30 mm fin distance in ANSYS.

Table 5. The results due to 3 and 5 m/s for the curved fins cooling channel

Fin Distance	Inlet Velocity(m/s)	Cell Temperature(°C)	Temperature Difference (°C)	Electricity Generation(W)	PV Efficiency(%)
30 mm	3	42.61	15.3	306.09	18.78
	5	36.66	21.25	311.01	19.08

5. CONCLUSION

As a result, the monthly electricity production, panel efficiency, solar radiation and cell temperatures found by using the hourly data of 2018 in MATLAB programme. The cooling channel designed by adhering to the highest cell temperature and observed how much electricity production and panel efficiency could increase depending on the drop in cell temperature by sending air at different velocities to this channel by using ANSYS Fluent programme. Cooling process provided to PV cells with different geometrical cooling channels during heat transfer. Different geometrical shapes of the cooling channel designed with fins and cooling processes provided to PV cells with these channels. At the end rising in cooling observed in PV with these new channels. Pressure drop values discussed.

It is observed that with the curved fin cooling channel it is possible to cool PV temperature more than with the flat cooling channel and finned cooling channel. It is also observed that cooling the PV from its maximum cell temperature which recorded as 57.91 °C to low temperature that recorded as 36.66 °C with the curved fin cooling channel and 5 m/s. In addition, electricity production and efficiency of PV scaled up when the flat, finned (82fins) and curved fin cooling channel compared in the same velocities and it is recorded as from 302.95 to 308.40W, 311.01 and from 18.59% to 18.92% and 19.08% respectively. It understood that increasing the contact area, increase the heat transfer and thus the efficiency increases.

REFERENCES

[1] Erkan, O., Özkan M., Arslan, O. 2018. "Mini-Channel Cooling of a Photovoltaic CellMini-Channel Cooling of a Photovoltaic Cell".

[2] Mittelman, G., Alshare, A., Davidson, J.H. 2009. "A model and heat transfer correlation for rooftop integrated photovoltaics with a passive air-cooling channel".

[3] Bayrak,F., Oztop H. F., Selimefendigil, F.2019. "Effects of different fin parameters on temperature and efficiency for cooling of photovoltaic panels under natural convection".

[4] Zheng, Z., Yan, W., Gong, H., Wang, Y., Shao, J.2019. "Quantifying the performance advantage of the novel passive air cooling system for PV array and system structure optimization".

[5] Han, J., Lu, L., Yang, H., Cheng, Y.2019. "Thermal regulation of PV façade integrated with thin-film solar cells through a naturally ventilated open air channel".

[6] Panasonic N330 Catalogue. :: Retrieved from https://lstr.panasonic.com/panel/upload/N330_325_en.pdf

[7] Duffie, J. A., & Beckman, W. A. (2013). *Solar engineering of thermal processes* (4th ed.). Hoboken, N.J.: John Wiley & Sons.

[8] Gibiansky, A. (n.d.). Andrew Gibiansky :: Math → [Code]. Retrieved from http://andrew.gibiansky.com/blog/physics/fluid-dynamics-the-navier-stokes-equations/

[9] Baloch, A. A. B., Bahaidarah, H. M. S., Gandhidasan, P. 2015a. "An Experimental Study of the Effect of Converging Channel Heat Exchanger on PV System".

A MACHINE LEARNING APPROACH FOR SOLAR POWER PLANT ELECTRICAL POWER ESTIMATION

Tayfun UYANIK[1a], Onur YILMAZ[2a], Yasin ARSLANOĞLU[3a]
[a]İstanbul Technical University, Maritime Faculty, 34940, Tuzla, İstanbul, Turkey
Email: uyanikt@itu.edu.tr[1], yilmazon@itu.edu.tr[2],arslanoglu@itu.edu.tr[3]

ABSTRACT

Environmental pollution is caused by fossil fuels, so the importance and use of renewable sources of energy have grown in recent years. Instead of fossil fuels, harvesting energy from renewable sources such as wind, solar, and water will minimize emissions accumulated in the atmosphere and thereby provide a sustainable environment.

In this study, electrical power obtained from a solar power plant in İkitelli, Istanbul, was estimated by machine learning methods. Multiple Linear Regression algorithm delivered more accurate findings than Random Forest and Support Vector Regression approaches as a result of the calculations. The simulation results showed that the electrical power generated by the solar power plant can be successfully estimated from the real data set. With the widespread use of data collection systems, it has been determined that methods such as machine learning and deep learning can be functional in predicting electrical power by using actual data instead of different solar energy simulation programs.

Keywords: Machine Learning, Electrical power, solar energy, Solar power.

1. INTRODUCTION

The increasing effects of global warming and climate change in recent years significantly affect the living standards of humanity. Fossil fuels stand out as one of the most important causes of global warming and climate change. It is known that the destruction of the environment by human beings has caused global warming of approximately 1° C in recent years. If the increase continues in this way, it is foreseen to reach a figure of 1.5° C after 2030 [1]. In order to reduce global warming and climate change, the demand for alternative energy sources instead of fossil fuels is increasing day by day. Especially photovoltaic energy is one of the well-known and cleanest energy generation methods of alternative energy sources. In addition, the relatively low maintenance costs of solar power plants and decreasing PV panel costs increase the use of solar energy.

Turkey is an energy importer due to the scarcity of fossil energy resources and aims to reduce this import with the help of alternative energy resources. In recent years the country has been increasing investment in this area. A large number of solar power plants are established to make more use of this energy source. When considering the potential of solar energy, Turkey can be regarded as lucky than most countries thanks to its geographical location. According to GEPA data, there are 2737 hours of Turkey's annual solar radiation and 1527 kWh/m^2 solar energy has the potential in a year [2]. Due to these advantages, it is inevitable for the country to work to increase production in this field. The development of solar power plants in Turkey in recent years is given in Figure 1. When the figure is examined, especially in the last few years, solar power plants and the amount of power obtained from these plants have increased significantly.

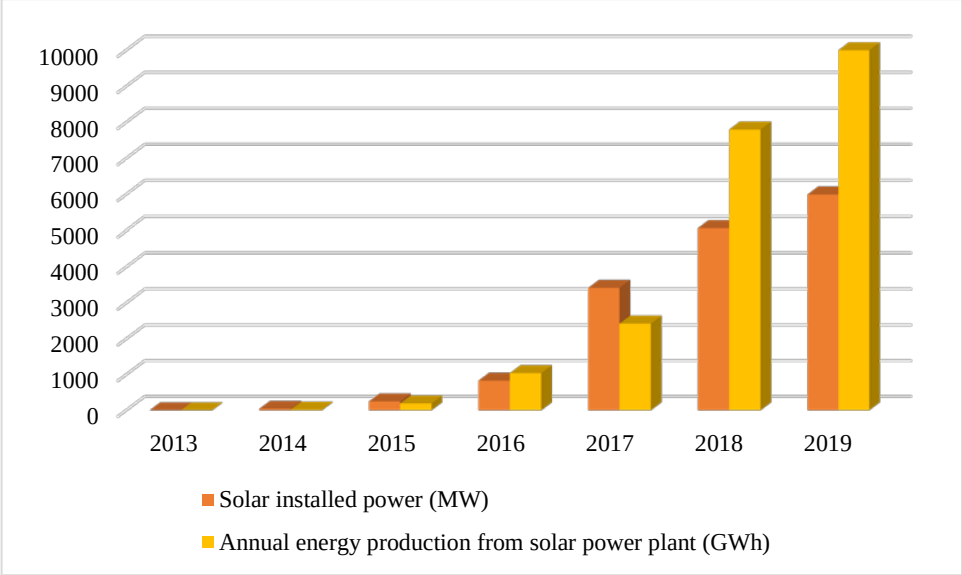

Figure 1. The development of solar power plants over the years in Turkey [3]

Organizations use SPPs for generating electrical energy, reduce energy costs and increase energy efficiency. A large number of SPPs have been established in Istanbul for this purpose. The GES examined in this study is located in İkitelli Water Treatment Plant and has a size of 1200 kWp [4].

The issue of estimating electrical power in solar becomes increasingly important. The power generation process needs to be accurately estimated to return the investment. Various simulation programs are used to estimate the electrical power in solar power plants. These programs give realistic results up to a certain stage. However, due to the climate change experienced in recent years, inconsistencies in power estimation have started to emerge.

In recent years, machine learning algorithms are increasingly used in solving various problems [5-7]. In this study, the electrical power generation estimation of the solar power plant was made with the help of the 2099 sample data set for June 2018. MAE (Mean Absolute Error) error metric was used to compare the algorithms [8]. As a result of the case study, it was determined that the Multiple-Linear Regression method made more successful predictions than Random Forest and the SVM algorithms with a MAE score of 1.3242. Also, considering these successful results, it has been revealed that machine learning algorithms can be functional in estimating the electrical power generated in solar power plants.

The following parts of the study are as follows, in the second part, the material and method are explained, in the third part a case study is made and simulation results are shown, and in the fourth section, the results of the study are examined.

2. MATERIAL AND METHODS

2.1 Machine Learning Algorithms

Multiple-Linear Regression

It is an algorithm that uses independent variables to predict the value of the dependent variable. The equation used by the algorithm for predictions is given below [5]. In this equation, a: dependent variable, b_i: independent variable, x_i: coefficient.

$$a = b_0 + b_1 x_1 + b_2 x_2 + \cdots + b_n x_n \quad (1)$$

Random Forest Regression

The random forest algorithm is a method formed by coming together of many decision trees. The random forest method is explained as follows [5].

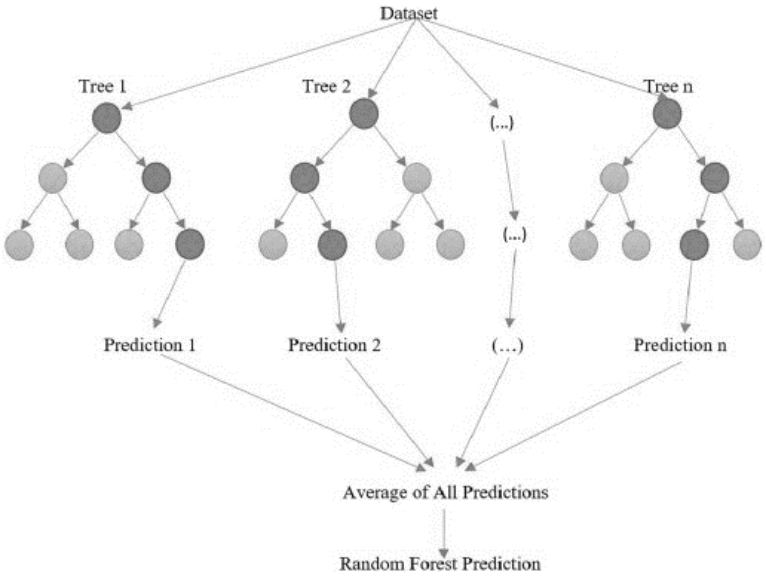

Figure 3. Random forest regression algorithm [5]

Support Vector Regression

Support vector machine (SVM) algorithm is a frequently used machine learning algorithm. The purpose of the algorithm is to make predictions in the margin allowed by two support vectors [5]. The algorithm is explained in the figure below.

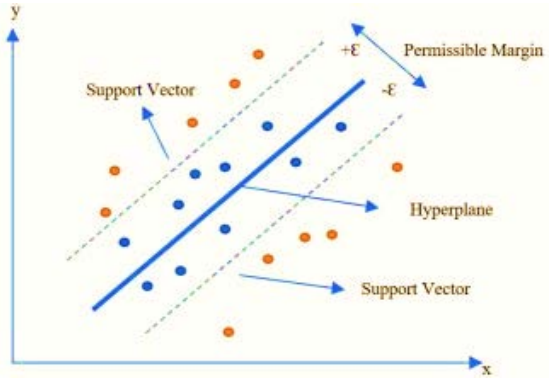

Figure 4. Support vector machine [5,9]

2.2 Mean Absolute Error

In statistical methods, it is an expression of the length between predictions and actual values in absolute value. Calculation of Mean Absolute Error is shown in the following equation [10].

$$MAE = \frac{1}{n}\sum_{i=1}^{n}|a_i - p_i| \quad (2)$$

In this equation, a_i : actual values, p_i : predicted values.

3. CASE STUDY & SIMULATION RESULTS

In this study, the electrical power generation in the solar power plant located in the İkitelli region of Istanbul is estimated. 2099 sample data set was used in the simulations. The data set consists of electrical power generation, hour, minute, day and other meteorological variables. The randomly selected 2/3 of the data set was taught to the algorithms as training data. The remainder was saved as test data and, algorithms made the test data prediction process. Mean Absolute Error is used as an error metric to evaluate the prediction results and to select the most successful algorithm for this problem. The processes of estimating electrical power generation in the solar power plant using machine learning algorithms are explained in the following figure.

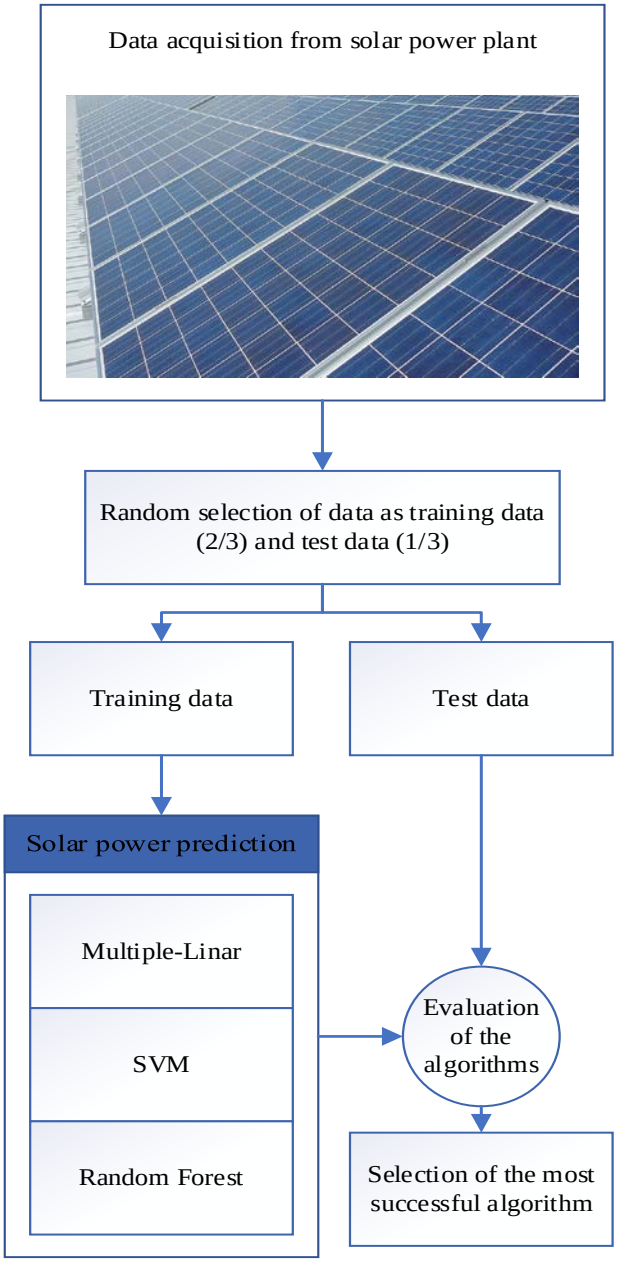

Figure 5. Electrical power prediction with machine learning algorithms in solar power plant

Spyder 4.1 interface of Python 3.0 programming language was used in simulations. The electrical power estimation results are given in the table below.

Table 1. Mean Absolute Error values

Multiple-Linear	Random Forest	SVM
1,3242	3,746	3,522

In order to better examine the predictions made by the algorithms, 50 randomly selected test data and the predictions are shown in the figure below.

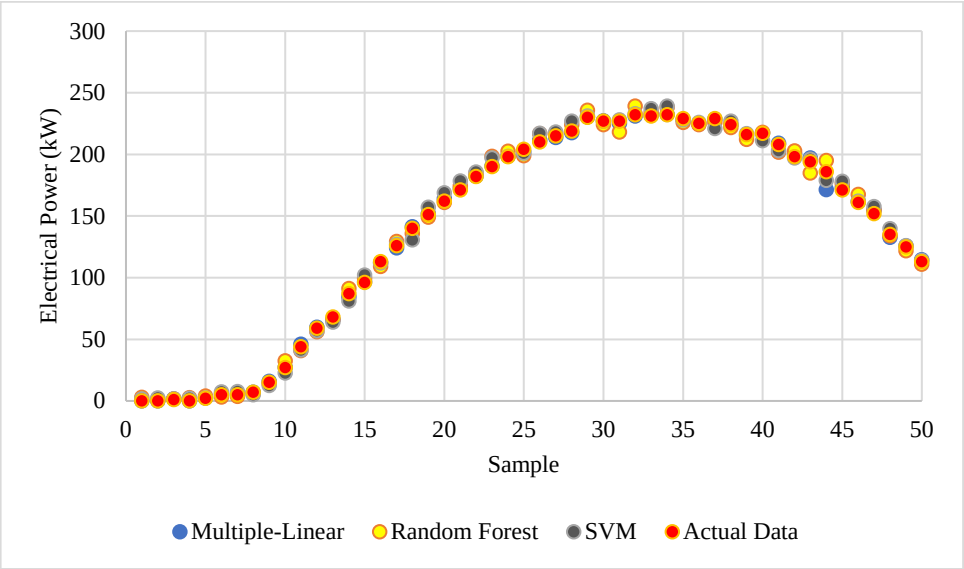

Figure 6. Comparison of predicted values and actual values in a random day

4. CONCLUSION

In this study, the electrical power generation of a solar power plant in Istanbul-İkitelli is estimated with the help of machine learning algorithms. As a result of the estimation process, it was determined that the Multiple-Linear Regression method made more successful predictions than Random Forest and SVM algorithms with Mean Absolute Error score of 1.3242. When the SVM and Random Forest algorithms are compared, it can be said that the SVM algorithm is slightly more successful than the Random Forest algorithm. As can be seen from the simulation results, the electrical power generation of solar power plants can be successfully predicted with machine learning algorithms. This study has shown that erroneous situations that occur in the predictions made by solar energy simulation programs due to global climate change can be eliminated with the help of machine learning algorithms.

REFERENCES

[1] M. James C. Crabbe, Climate change, global warming and coral reefs: Modelling the effects of temperature, Computational Biology and Chemistry, Volume 32, Issue 5, 2008, Pages 311-314, ISSN 1476-9271, https://doi.org/10.1016/j.compbiolchem.2008.04.001.

[2] Emre Tercan, Abdurrahman Eymen, Tuğrul Urfalı, Burak Omer Saracoglu, A sustainable framework for spatial planning of photovoltaic solar farms using GIS and multi-criteria assessment approach in Central Anatolia, Turkey, Land Use Policy, Volume 102, 2021, 105272, ISSN 0264-8377, https://doi.org/10.1016/j.landusepol.2020.105272.

[3] H. Ebru Colak, Tugba Memisoglu, Yasin Gercek, Optimal site selection for solar photovoltaic (PV) power plants using GIS and AHP: A case study of Malatya Province, Turkey, Renewable Energy, Volume 149, 2020, Pages 565-576, ISSN 0960-1481, https://doi.org/10.1016/j.renene.2019.12.078.

[4] Istanbul Metropolitan Municipality İkitelli solar power plant production amounts: data.ibb.gov.tr/dataset/ikitelli-gunes-enerjisi-santrali-elektrik-uretim-miktarlari, Accessed 11th Feb 2021.

[5] Tayfun Uyanık, Çağlar Karatuğ, Yasin Arslanoğlu, Machine learning approach to ship fuel consumption: A case of container vessel, Transportation Research Part D: Transport and Environment, Volume 84, 2020, 102389, ISSN 1361-9209, https://doi.org/10.1016/j.trd.2020.102389.

[6] Gizem Elidolu, Tayfun Uyanık , Pınar Karabıyık, Yasin Arslanoğlu, Hull cleaning effects on CO_2 emissions: estimation with machine learning methods. 5th International Mediterranean Science and Engineering Congress (IMSEC 2020) Alanya Lonicera Resort & Spa Hotel, October 21-23, 2020 – Alanya, Antalya / TÜRKİYE Pages: 203-208, Paper ID:127

[7] Atak Ü., Kaya T., Arslanoğlu Y. (2021) Container Terminal Workload Modeling Using Machine Learning Techniques. In: Kahraman C., Cevik Onar S., Oztaysi B., Sari I., Cebi S., Tolga A. (eds) Intelligent and Fuzzy Techniques: Smart and Innovative Solutions. INFUS 2020. Advances in Intelligent Systems and Computing, vol 1197. Springer, Cham. https://doi.org/10.1007/978-3-030-51156-2_134

[8] Xin (Shane) Wang, Jun Hyun (Joseph) Ryoo, Neil Bendle, Praveen K. Kopalle, The role of machine learning analytics and metrics in retailing research, Journal of Retailing, 2020, ISSN 0022-4359, https://doi.org/10.1016/j.jretai.2020.12.001.

[9] Mostafa Jalal, Poura Arabali, Zachary Grasley, Jeffrey W. Bullard, Hamid Jalal, Behavior assessment, regression analysis and support vector machine (SVM) modeling of waste tire rubberized concrete, Journal of Cleaner Production, Volume 273, 2020, 122960, ISSN 0959-6526, https://doi.org/10.1016/j.jclepro.2020.122960.

[10] Lap-Ming Wun, Wen Lea Pearn, Assessing the statistical characteristics of the mean absolute error or forecasting, International Journal of Forecasting, Volume 7, Issue 3, 1991, Pages 335-337, ISSN 0169-2070, https://doi.org/10.1016/0169-2070(91)90007-I.

NANOAKIŞKAN KULLANILAN PARABOLİK OLUK TİPİ GÜNEŞ KOLEKTÖRLÜ ORGANİK RANKİNE ÇEVRİMİNİN TEORİK MODELLENMESİ VE SİSTEM PARAMETRELERİNİN İNCELENMESİ

Erhan KIRTEPE*, Oğuz Emrah TURGUT**
*Şırnak University, Department of Mechanical Engineering, Şırnak/Turkey
Email: erhan.kirtepe@sirnak.edu.tr
** Bakırçay University, Department of Industrial Engineering, İzmir/Turkey
Email: oguzemrah.turgut@bakircay.edu.tr

ÖZET

Bu çalışmada parabolik oluk tipi güneş kolektörlü Organik Rankine Çevriminin (ORÇ) teorik modellenmesi yapılmıştır. Parabolik oluk tip güneş kolektörü için oluşturulan teorik modelin geçerliliği literatürde yapılmış olan çalışma sonuçları ile karşılaştırılarak kanıtlanmıştır. Parabolik oluk tipi güneş kolektöründe kullanılan ısı transfer akışkanına (Therminol VP-1, Syltherm 800) farklı türde ve konsantrasyon oranlarında nanopartiküller (Al_2O_3, CuO, Cu, SiO_2, TiO_2) eklemenin ve ORÇ'de farklı soğutkanların (Toluene, MDM, cyclohexane, n-pentane, n-Hexane, R11, R123, R113, R141b) kullanımının sistem verimliliğine ve performansına etkisi incelenmiştir. En yüksek sistem verimi ısı transfer akışkanı olarak Therminol VP-1, nanopartikül olarak Cu ve soğutkan olarak Toluene seçildiği durumda %17,7 olarak bulunmuştur.

Anahtar Kelimeler: Güneş enerjisi, parabolik oluk tipi güneş kolektörü, Organik Rankine Çevrimi, nanoakışkan.

THEORETICAL MODELING AND INVESTIGATION OF SYSTEM PARAMETERS OF ORGANIC RANKINE CYCLE WITH NANOFLUID USED SOLAR PARABOLIC TROUGH COLLECTOR

ABSTRACT

In this study, theoretical modeling of Organic Rankine Cycle with solar parabolic trough collector has been done. The validity of the theoretical model has been proved by comparing it with the results of the study done in the literature. The effects on system efficiency and performance of adding nanoparticles (Al_2O_3, CuO, Cu, SiO_2, TiO_2) of different types and concentrations to the working fluid (Therminol VP-1, Syltherm 800) used in solar parabolic trough collector and the use of different refrigerants (Toluene, MDM, cyclohexane, n-pentane, n-Hexane, R11, R123, R113, R141b) in Organic Rankine Cycle are examined, and optimum system parameters are determined. The highest system efficiency was found to be 17.7% when Therminol VP-1 was chosen as the heat transfer fluid, Cu as the nanoparticle, and Toluene as the refrigerant.

Keywords: Solar energy, solar parabolic trough collector, Organic Rankine Cycle, nanofluid.

1. GİRİŞ

Dünya genelinde enerjiye olan talebin artması ve fosil kökenli yakıtların çevreye verdikleri zararın yanı sıra tükenmekte olması yenilenebilir enerji kaynaklarına olan gereksinimin artmasına yol açmıştır. Yenilenebilir enerji kaynaklarından enerji üretimi için gerekli sistemlerin performanslarının geliştirilmesi bu kaynaklardan maksimum miktarda faydalanmamızı sağlayacaktır. Özellikle, yenilebilir enerji kaynaklarından biri olan güneşten enerji üretmek için kullanılan sistemlerde farklı çalışma akışkanlarına nanopartikül eklenmesinin ve bu sistemlerin başka sistemlerle beraber entegre bir şekilde kullanılmasının sistemin performans ve verimliliği üzerine etkileri ile ilgili birçok bilimsel çalışma yapılmaktadır.

Abubakr vd. (2020) [1] yapmış oldukları çalışmalarında nanoakışkan kullanılan parabolik oluk tipi güneş kolektörünün (POTGK) Multi-objective genetik algoritması (MOGA) ile enerji ve ekserji optimizasyonunu gerçekleştirmişlerdir. Çalışma kapsamında ısı transfer akışkanı olarak Therminol VP-1, Syltherm 800, ve Dowtherm Q kullanılmış ve bu akışkanlara farklı konsantrasyon oranlarında Al_2O_3, CuO, ve SiO_2 isimli nanopartiküller eklenerek performans incelemeleri yapılmıştır. Risi vd. (2013) [2] POTGK'de kullanılan ısı transfer akışkanına gaz fazında ve farklı konstantrasyon oranlarında nanopartikül (CuO ve Ni) eklenmesinin POTGK'nin termal verimine etkisini incelemişlerdir. Ayrıca POTGK'nin performansının geliştirilmesi ve optimizasyonunun yapılması için genetik algoritma optimizasyonunu (MOGA II) kullanmışlardır. Yapılan analizler sonucunda POTGK için maksimum termal verim %62,5 olarak bulunmuştur. Ehyaei vd. (2019) [3] tarafından yapılan çalışmada POTGK'nin enerji, ekserji ve ekonomik analizi gerçekleştirilmiştir. Multi-objective swarm optimizasyon (MOPSO) tekniği uygulanarak maksimum ekserji verimliliği ve minimum enerji maliyeti araştırılmıştır. Optimum sonuçlara göre ekserji verimliliği, enerji verimliliği ve ısı maliyeti sırasıyla %29,22; %35,55 ve 0,0142 $/kWh olarak bulunmuştur. Bellos ve Tzivanidis (2017) [4] ORÇ ile birlikte çalışan POTGK'nin teorik analizini gerçekleştirmişlerdir. Temel ısı transfer akışkanı olarak Syltherm 800'ü kullanmışlar ve bu akışkana farklı nanpartiküller (Al_2O_3, CuO, TiO_2, Cu) eklenmesinin ve ORÇ'de farklı soğutkanların (Toluene, MDM, cyclohexane, n-pentane) denenmesinin sistem performansına etkisini araştırmışlar, sistemim parametrik analizini ve optimizasyonunu gerçekleştirmişlerdir. Moloodpoor vd. (2019) [5] POTGK'nin bir boyutlu ısıl modelini geliştirmişler ve modelden elde ettikleri sonuçları literatürdeki mevcut deneysel sonuçlar ile karşılaştırarak modelin geçerliliğini kanıtlamışlardır. Ayrıca İPSO (integrated particle swarm optimization) tekniğini kullanarak POTGK'nin ısıl analizlerini gerçekleştirmişlerdir. Huang vd. (2016) [6] POTGK için 2 boyutlu ısıl model ve 3 boyutlu optik model geliştirmişlerdir. Geliştirilen nümerik modele göre hesaplanan teorik sonuçlar literatürde verilen deneysel çalışma sonuçları ile karşılaştırılmış ve modelin geçerliliği kanıtlanmıştır. Alirahmi vd. [7] jeotermal ve güneş enerjisini kullanarak hidrojen, tatlı su, soğutma yükü ve sıcak suyun birlikte üretildiği bir sistemin termodinamik analizini, ekonomik analizini ve çok amaçlı (multi-objective) optimizasyonunu gerçekleştirmiştir. Optimizasyon algoritması olarak NSGAII (Non-Dominated Sorted Genetic Algorithm) kullanmışlardır. Coccia vd. (2016) [8] POTGK'nin nümerik analizini gerçekleştirmişlerdir. Yaptıkları çalışmada POTGK'nin ısıl veriminin arttırılması amacıyla farklı ağırlık konsantrasyonlardaki su bazlı nanoakışkanlar denemişlerdir. İncelenen nanoakışkanlar içerisinde farklı nanopartiküller (Fe_2O_3, SiO_2, TiO_2, ZnO, Al_2O_3 ve Au) kullanmışlardır. Nümerik olarak hesaplanan sonuçların doğruluğu ısı transfer akışkanı olarak suyun kullanıldığı deneysel çalışma sonuçları ile karşılaştırılarak kanıtlanmıştır. Mwesigye vd. (2016) [9] ısı transfer akışkanı olarak Cu-Therminol VP-1 nanoakışkan kullanan yüksek konsantrasyon oranlı POTGK'nin ısıl ve termodinamik performansı üzerine nümerik bir çalışma yapmışlardır. Yapılan analizler sonucunda POTGK'nin ısıl veriminin nanoakışkan içerisinde ki nanopartikül hacim oranı ile birlikte arttığı belirlenmiştir.

Bu çalışmada da Parabolik Oluk Tipi Güneş Kolektörlü Organik Rankine Çevriminin (POTGK-ORÇ) teorik modellenmesi yapılacaktır. POTGK için oluşturulan teorik modelin doğruluğu literatürde yapılmış olan çalışma sonuçları ile karşılaştırılarak kanıtlanacaktır. POTGK'de kullanılan çalışma akışkanına (Therminol VP-1, Syltherm 800) farklı türde ve konsantrasyon oranlarında nanopartiküller (Al_2O_3, CuO, Cu, SiO_2, TiO_2) eklemenin ve ORÇ'de farklı soğutucu akışkanların (Toluene, MDM, cyclohexane, n-pentane, n-Hexane, R11, R123, R113, R141b) kullanımının sistem verimliliğine ve performansına etkileri incelenecektir.

2. MATEMATİKSEL MODEL

Bu çalışmada incelenen POTGK-ORÇ sisteminin şematik resmi Şekil 1'de görülmektedir. Bu şekilden de görüleceği üzere POTGK ile güneş enerjisinden elde edilen ısıl enerji depoya aktarılmaktadır. Depo saf Therminol VP-1 akışkanı ile doludur ve kolektörlerden gelen toplam ısıl enerji uygun bir ısı değiştirici ile depo içerisindeki akışkana transfer edilmektedir. Depo ile ORÇ arasında dolaşan ısı transfer akışkanı ile depodan alınan ısıl enerji ORÇ'nin kazanında ORÇ'de dolaşan soğutkana aktarılmaktadır. ORÇ'nin kazanında yüksek basınç ve sıcaklığa ulaşan soğutkan türbinde genişleyerek düşük basınç ve sıcaklığa inmektedir. Türbinde soğutkanın genişlemesi ile mekanik enerji elde edilmekte ve bu mekanik enerji jeneratör yardımı ile elektrik enerjisine çevrilmektedir.

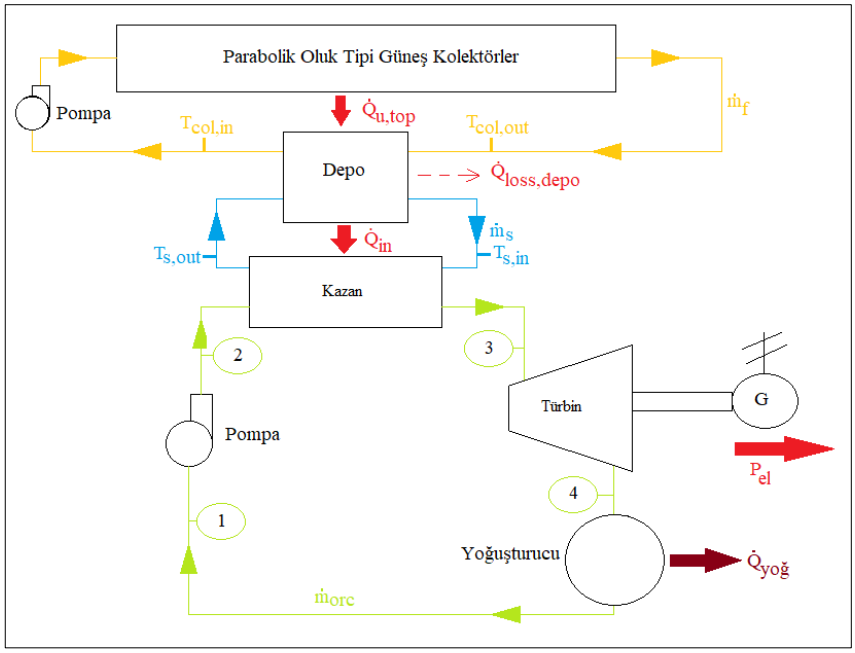

Şekil 1. POTGK-ORÇ sisteminin şematik resmi.

2.1 Parabolik oluk tipi güneş kolektörü

POTGK'de bulunan silindirik alıcı yüzey tarafından yutulan ışınım POTGK'nin optik özelliklerine bağlı olduğu kadar sistem elemanlarının kurulumundan geometrik özelliklerinden ve kullanım sonucu oluşan kirlenme gibi faktörlerin de etkisine bağlıdır. POTGK'nin ısıl performansına etki eden hatalar Tablo 1'de gösterilmiştir.

Tablo 1. POTGK'nin ısıl performansını etkileyen hatalar [10]

Optik Özellikler	**Değer**
Destek elemanlarının, uzama kompensatörünün gölge etkisi (γ1)	0,974
İzleme hatası (γ2)	0,994
Yansıtıcı yüzeyin geometrik hassasiyeti (γ3)	0,980
Yansıtıcı yüzeyin kirlenmesi (γ4)	0,995
Sistem elemanlarının kirlenmesi (γ5)	0,997
Diğer etkenler (γ6)	0,960
Yansıtıcı yüzeyin temiz koşuldaki yansıtma oranı (ρ)	0,935

Cam örtüde ve silindirik alıcı yüzeyde yutulan ışınım akısı sırasıyla Eşitlik 1 ve 2'den elde edilir.

$$S_c = I_b\ \rho\ (\prod_{i=1}^{6} \gamma_i)\ \alpha_c K \tag{1}$$

$$S_r = I_b\ \rho (\prod_{i=1}^{6} \gamma_i) \tau_c\ \alpha_r K \tag{2}$$

Cam örtü ile dış ortam arasında taşınım ve ışınım ile olan ısı geçişi Eşitlik 3'den hesaplanır.

$$Q_{c-a} = \varepsilon_c \pi D_{c,o} L \sigma \left(T_{c,o}^4 - T_{gök y}^4\right) + h \pi D_{c,o} L \left(T_{c,o} - T_a\right) \tag{3}$$

Buradaki gökyüzü sıcaklığı Eşitlik 4'te görüldüğü üzere dış ortam hava sıcaklığına bağlı olarak hesaplanır [11].

$$T_{gök y} = 0.0552 T_a^{1.5} \tag{4}$$

Cam örtü ile çevre arasında olan ısı taşınım katsayısının bulunması için McAdams (1954) tarafından önerilen bağıntı kullanılmıştır [12].

$$Nu_{air} = 0{,}40 + 0{,}54Re_{air}^{0{,}52} \qquad 0{,}1 < Re_{air} < 1000 \tag{5}$$

$$Nu_{air} = 0{,}30\, Re_{air}^{0{,}6} \qquad 1000 < Re_{air} < 50000 \tag{6}$$

$$Re_{air} = \frac{\rho_{air} V_{wind} D_{c,o}}{\mu_{air}} \tag{7}$$

Burada havanın termodinamik özelikleri (ρ_{air} ve μ_{air}) çevre hava ve cam örtü dış yüzeyinin ortalama sıcaklığından ($T_{m,air}$) hesaplanmıştır.

$$T_{m,air} = \frac{T_{c,o} + T_{air}}{2} \tag{8}$$

Cam örtüde iletim ile olan ısı geçişi Eşitlik 9 kullanılarak belirlenmiştir.

$$Q_c = \frac{2\pi k_c L(Tc,i - Tc,o)}{ln\left(\frac{D_{c,o}}{D_{c,i}}\right)} \tag{9}$$

Cam örtünün iç yüzeyi ile silindirik alıcının dış yüzeyi arasında gerçekleşen ısı geçişi Eşitlik 10 kullanılarak belirlenmiştir. Bu çalışmada cam örtünün iç yüzeyi ile silindirik alıcının dış yüzeyi arasında oluşan bölgede vakum olduğu varsayıldığından k_{eff} değeri sıfır olarak alınmıştır.

$$Q_{c,i-r,o} = \frac{\pi D_{r,o} L\, \sigma(T_{r,o}^4 - T_{c,i}^4)}{\frac{1}{\varepsilon_r} + \frac{1-\varepsilon_c}{\varepsilon_c}\left(\frac{D_{r,o}}{D_{c,i}}\right)} + \frac{2\pi k_{eff} L(T_{r,o} - T_{c,i})}{ln\frac{D_{c,i}}{D_{r,o}}} \tag{10}$$

Silindirik alıcının dış yüzeyinin sermet seçici yüzey olduğu dikkate alınmış ve bu yüzeyin yayma oranı silindirik alıcının dış yüzey sıcaklığına bağlı olarak Eşitlik 11'den bulunmuştur [10].

$$\varepsilon_r = 0{,}000327 \times T_{r,o} - 0{,}06597 \tag{11}$$

POTGK'de ısı transfer akışkanına aktarılan yararlı ısı, akışkan giriş ve çevre hava sıcaklığına bağlı olarak Eşitlik 12'den hesaplanmıştır.

$$Q_u = A_a\, F_R \left[S - \frac{A_r}{A_a} U_L\left(T_{f,i} - T_a\right)\right] \tag{12}$$

Buradaki toplayıcı ısı kazanım faktörü (F_R) aşağıdaki Eşitlik 13'den bulunabilir.

$$F_R = F'' \times F' \tag{13}$$

Eşitlik 13'de gösterilen F'' ve F' sırasıyla kolektör akış faktörü ve kolektör verim faktörü olup Eşitlik 14 ve 15'te nasıl hesaplanacağı gösterilmiştir.

$$F'' = \frac{\dot{m} c_p}{A_r U_L F'}\left(1 - exp\left(-\frac{A_r U_L F'}{\dot{m} c_p}\right)\right) \tag{14}$$

$$F' = \frac{1/U_L}{\frac{1}{U_L} + \frac{D_{r,o}}{h_{f,i} D_{r,i}} + \frac{D_{r,o}\ln\left(D_{r,o}/D_{r,i}\right)}{2k_r}} \tag{15}$$

Isı transfer akışkanının akış rejiminin laminer olması durumunda ($Re_{f,i} < 2300$), silindirik alıcının iç yüzeyi ile ısı transfer akışkanı arasındaki Nusselt sayısı 4,36 $\left(Nu_{f,i} = 4{,}36\right)$ olarak sabit alınmış, ve sürtünme faktörü Eşitlik 16 çözülerek belirlenmiştir [13].

$$f = 64/Re_{f,i} \tag{16}$$

Isı transfer akışkanının akış rejiminin türbülanslı olması durumunda ise silindirik alıcının iç yüzeyi ile ısı transfer akışkanı arasındaki Nusselt sayısının hesaplanmasında Gnielinski tarafından önerilen bağıntı kullanılmış ve Eşitlik 17 ve 18 çözülerek hesaplanmıştır. Bu bağıntı $0{,}5 \leq \mathrm{Pr} \leq 2000$ ve $3 \times 10^3 < \mathrm{Re} < 5 \times 10^6$ koşullarında geçerlidir [13].

$$Nu_{f,i} = \frac{(f/8)\,(Re_w - 1000\,)Pr_{f,i}}{1+12.7(f/8)^{0.5}\left(Pr_{f,i}^{(2/3)}-1\right)} \tag{17}$$

$$f = (1.58\,ln\,Re_w - 3.28)^{(-2)} \tag{18}$$

2.2 Nanoakışkan Özelikleri

Bu çalışmada POTGK'de Syltherm 800 ve Therminol VP-1 olarak iki temel ısı transfer akışkanı kullanılmıştır. Bu akışkanlardan ısıl verimlilik açısından uygun olanı seçilip içerisine farklı konstantrasyon oranlarında nanpartiküller eklenmiştir. Temel ısı transfer akışkanına eklenen nanopartüküllerin (Al_2O_3, CuO, TiO_2, Cu, SiO_2) özelikleri Tablo 2'de görülmektedir.

Tablo 2. Nanopartikül özelikleri [1, 4].

Nanopartükül	$\boldsymbol{\rho_{np}}$ **(kg/m^3)**	$\boldsymbol{k_{np}}$ **(W/mK)**	$\boldsymbol{c_{p,np}}$ **(J/kgK)**
Al_2O_3	3970	40	765
CuO	6320	77	532
TiO_2	4250	8.95	686
Cu	8933	401	385
SiO_2	3970	1.4	765

Nanoakışkanların ısıl özelikleri 19, 20, 21 ve 22 numaralı eşitlikler kullanılarak belirlenmiştir. Burada bf ve np alt indisleri sırasıyla kullanılan temel akışkanı ve nanopartikülü göstermektedir [4].

$$\rho_{nf} = \rho_{bf}(1 - \emptyset) + \rho_{np}\emptyset \tag{19}$$

$$c_{p,nf} = \frac{\rho_{bf}(1-\emptyset)}{\rho_{nf}} \cdot c_{p,bf} + \frac{\rho_{np}\emptyset}{\rho_{nf}} \cdot c_{p,np} \tag{20}$$

$$k_{nf} = k_{bf}\frac{k_{np}+2k_{bf}+2\left(k_{np}-k_{bf}\right)(1+\beta)^3\emptyset}{k_{np}+2k_{bf}-\left(k_{np}-k_{bf}\right)(1+\beta)^3\emptyset} \tag{21}$$

Buradaki β parametresi, nanotabaka kalınlığının orjinal partükülün yarıçapına oranıdır ve nanoakışkanlarda ısıl iletim katsayısı hesaplanırken genellikle 0,1'e eşit alınır [4].

$$\mu_{nf} = \mu_{bf}(1 + 2{,}5\emptyset + 6{,}5\emptyset^2) \tag{22}$$

2.3 Organik Rankine Çevrimi ve Deponun Matematiksel Modeli

POTGK'de güneşten elde edilen yararlı ısının, sistemin kararlı durumunda (steady-state) yapılan analizinde tümüyle depolama tankına aktarıldığı varsayılmıştır. Bu değerlendirme kararlı durumda oluşturulan model için uygundur [4]. Bu modelleme için Eşitlik 23 kullanılır.

$$Q_{u,top} = (UA)_{col-st} \cdot \frac{(T_{col,out} - T_{col,in})}{ln\left[\frac{T_{col,out} - T_{st}}{T_{col,in} - T_{st}}\right]} \tag{23}$$

Burada depo içerisinde bulunan akışkan sıcaklığının (T_{st}) uniform olduğu varsayılmış ve $(UA)_{col-st}$ değeri 12 kW/m^{2}K' e eşit alınmıştır [4]. Depo için genel enerji dengesi Eşitlik 24'te gösterilmiştir.

$$Q_{stored} = Q_{u,top} - Q_{loss,st} - \dot{m}_s c_{p,s}\left(T_{s,in} - T_{s,out}\right) \tag{24}$$

Kararlı durumda depoda depolanan enerji (Q_{stored}) sıfıra eşit olur. Depodan dış ortama olan ısı kaybı Eşitlik 25'den hesaplanmıştır.

$$Q_{loss,st} = U_{st} A_{st} (T_{st} - T_a) \tag{25}$$

Depodan dış ortama olan ışınım, taşınım ve iletimle olan ısı kaybını içeren toplam ısı kayıp katsayısı (U_{st}) 0,5 W/m^{2}K'e eşit alınmıştır [4]. Deponun yüzey alanı Eşitlik 26'dan hesaplanmıştır.

$$A_{st} = \frac{\pi D_{st}^2}{2} + \pi D_{st} L_{st} \tag{26}$$

ORÇ'nin kazanında soğutkanın buharlaşması için verilen ısı $\left(Q_{in,orc}\right)$ Eşitlik 27'den hesaplanmıştır.

$$Q_{in,orc} = \dot{m}_s c_{p,s}\left(T_{s,in} - T_{s,out}\right) = \dot{m}_{orc}(h_3 - h_2) \tag{27}$$

ORÇ'de basınç oranı (PR), yüksek basıncın (P_{max}) kullanılan soğutkanın kritik basıncına oranına basınç oranı (P_{cr}) şeklinde tanımlanır.

$$PR = \frac{P_{max}}{P_{cr}} \tag{28}$$

ORÇ'de kullanılan türbinin ve pompanın izantropik verimleri sırasıyla Eşitlik 29 ve 30 ile gösterilmektedir.

$$\eta_{turb,orc} = \frac{h_3 - h_{4g}}{h_3 - h_{4s}} \tag{29}$$

$$\eta_{pump,orc} = \frac{w_{pump,s}}{w_{pump,g}} = \frac{h_{2s} - h_1}{h_{2g} - h_1} \tag{30}$$

Pompa için izantropik ve gerçek durumda gereken enerji sırasıyla 31 ve 32 numaralı eşitlikler kullanılarak hesaplanmıştır.

$$w_{pump,s} = v_1(P_2 - P_1) \tag{31}$$

$$w_{pump,g} = \frac{w_{pump,s}}{\eta_{pump}} = \frac{v_1(P_2 - P_1)}{\eta_{pump}} \tag{32}$$

ORÇ'de türbinden elde edilen mekanik enerjinin jeneratör vasıtası ile elektrik enerjisine dönüştürülmektedir. Elde edilen elektrik gücü Eşitlik 33 kullanılarak belirlenmiştir.

$$P_{el} = \eta_{mg} \dot{m}_{orc}\left(h_3 - h_{4g}\right) \tag{33}$$

ORÇ'de elde edilen net elektrik güç üretimi ve ORÇ'nin verimi sırasıyla Eşitlik 34 ve 35 ile hesaplanmıştır.

$$P_{net,orc} = P_{el} - W_{pump,orc} \tag{34}$$

$$\eta_{orc} = \frac{\mathrm{P_{net,orc}}}{\mathrm{Q_{in,orc}}} \tag{35}$$

Güneş enerjisinden elde edilen ısıl enerjinin elektrik enerjisine dönüştüren POTGK-ORÇ'de sisteminde üretilen net elektrik gücü ve sisteminin termodinamik verimi sırasıyla Eşitlik 36 ve 37 kullanılarak bulunmuştur.

$$P_{net,sys} = P_{el} - W_{pump,orc} - W_{pump,POTGK} \tag{36}$$

$$\eta_{sys} = \frac{P_{net,sys}}{N[I_b(D_a - D_{c,o})]L} \tag{37}$$

Yapılan çalışmada kullanılan POTGK-ORÇ sisteminin sabit parametreleri Tablo 3'de görülmektedir.

Tablo 3. POTGK-ORÇ sisteminin sabit parametreleri [4, 5, 14]

Parametre	**Değer**	**Parametre**	**Değer**
Çevre hava sıcaklığı ($\boldsymbol{T_a}$)	25 ºC	Silindirik alıcının yutma oranı ($\boldsymbol{\alpha_r}$)	0,96
Güneş ışınımı ($\boldsymbol{I_b}$)	800 W/mK	Silindirik alıcının ısı iletim katsayısı ($\boldsymbol{k_r}$)	54 W/mK
Yoğuşturucu sıcaklığı ($\boldsymbol{T_{yoğ}}$)	40 ºC	Cam örtü dış çapı ($\boldsymbol{D_{c,o}}$)	0.125 m
Depo taban çapı ($\boldsymbol{D_{st}}$)	2 m	Cam örtü iç çapı ($\boldsymbol{D_{c,i}}$)	0.120 m
Depo yüksekliği($\boldsymbol{L_{st}}$)	3.2 m	Cam örtünün yayma katsayısı ($\boldsymbol{\varepsilon_c}$)	0,90
Isı değiştirici etkinliği ($\boldsymbol{UA}$)$_{\boldsymbol{col-st}}$	12 kW/m^2	Camın örtünün geçirgenliği ($\boldsymbol{\tau_c}$)	0,95
POTGK'deki ısı transfer akışkanın hacimsel debisi ($\boldsymbol{\dot{V}_f}$)	3 m^3/saat	Camın örtünün ısı iletim katsayısı ($\boldsymbol{k_c}$)	1.2
POTGK modül sayısı ($\boldsymbol{N}$)	30	POTGK açıklık alanı	5x8 m^2
POTGK modül uzunluğu ($\boldsymbol{L}$)	8 m	Rüzgar hızı (V)	1 m/s
Işınım geliş açısı düzeltme faktörü ($\boldsymbol{K}$)	1	Türbinin izantropik verimi ($\boldsymbol{\eta_{turbin}}$)	0,85
Silindirik alıcı dış çapı ($\boldsymbol{D_{r,o}}$)	0.07 m	Pompanın izantropik verimi ($\boldsymbol{\eta_{pump}}$)	0,70
Silindirik alıcı iç çapı ($\boldsymbol{D_{r,i}}$)	0.066 m	Jeneratörün elektromekanik verimi ($\boldsymbol{\eta_{jenerator}}$)	0,98

3. POTGK İÇİN OLUŞTURULAN TEORİK MODELİN GEÇERLİLİĞİ

Bu çalışmada POTGK için geliştirilen teorik modelin geçerliliği, Sandia Ulusal Laboratuvarı (Sandia National Laboratory) [14] deneysel sonuçları ile karşılaştırılarak kontrol edilmiştir. Yapılan deneysel çalışmada POTGK'de ısı transfer akışkanı olarak Syltherm 800 kullanılmış ve silindirik alıcı yüzey ile cam örtü arasındaki halkasal bölgede vakum olduğu durum incelenmiştir. Karşılaştırma sonuçları Tablo 4'de görülmektedir. Geliştirilen teorik model ile deney sonuçları arasında, akışkanın kolektörden çıkış sıcaklığına ve POTGK verimine göre oluşan maksimum belirsizlik değeri sırasıyla 1,23 ºC ve % 2,82'dir.

Tablo 4. Bu çalışmada geliştirilen teorik modelin deney sonuçları ile karşılaştırılması

Deney No	**Işınım (W/m^2)**	**Rüzgar Hızı (m/s)**	**Çevre Sıcaklığı (ºC)**	**Debi (L/d)**	**Syltherm 800 Giriş (ºC)**	**Syltherm 800 Çıkış (ºC)**		**Model Belirsizliği (ºC)**	**Isıl Verim (%)**		**Isıl Verim Belirsizliği (%)**	
						Deney	**Model**		**Deney**	**Model**	**Deney**	**Model**
1	933,7	2,6	21,2	47,7	102,2	124,0	122,95	1,05	72,51	69,91	1,95	2,60
2	968,2	3,7	22,4	47,8	151,0	173,3	172,74	0,56	70,90	70,42	1,92	0,48
3	982,3	2,5	24,3	49,1	197,5	219,5	219,04	0,46	70,17	69,85	1,81	0,32
4	909,5	3,3	26,2	54,7	250,7	269,4	268,77	0,63	70,25	68,87	1,90	1,38
5	937,9	1,0	28,8	55,5	297,8	316,9	316,08	0,82	67,98	66,37	1,86	1,61
6	880,6	2,9	27,5	55,6	299,0	317,2	316,10	1,10	68,92	66,17	2,06	2,75
7	920,9	2,6	29,5	56,8	379,5	398,0	396,77	1,23	62,34	59,52	2,41	2,82
8	903,2	4,2	31,1	56,3	355,9	374,0	373,02	0,98	63,82	61,62	2,36	2,20

4. BULGULAR

POTGK için geliştirilen teorik modelin geçerliliği literatürdeki mevcut deneysel çalışma sonuçları ile karşılaştırılarak kanıtlandıktan sonra, Tablo 3'de sabit parametreleri verilen POTGK-ORÇ sisteminin teorik olarak optimum sistem parametreleri incelenmiştir. İlk olarak POTGK'de Syltherm 800 ve Therminol VP-1 akışkanlarının kullanımının POTGK'nin ısıl performansına etkisine bakılmıştır. Şekil 2'de görüldüğü üzere ısı transfer akışkanı olarak Therminol VP-1 kullanımı ısıl performansı arttırmaktadır. Bu nedenle Therminol VP-1, çalışma kapsamında yapılan diğer analizlerde, POTGK'de kullanılan temel ısı transfer akışkanı olarak seçilmiştir.

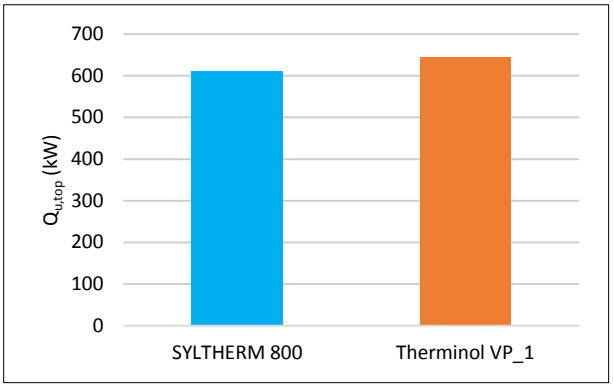

Şekil 2. POTGK'de Syltherm 800 ve Therminol VP-1 kullanımının ısıl performansa etkisi.

Temel ısı transfer akışkanın seçiminden sonra hangi nanopartikülün kullanılması gerektiği araştırılmıştır. Bunun için Şekil 3'de görüldüğü üzere farklı konstrasyon oranlarındaki beş farklı nanapartikülün (Al_2O_3, CuO, Cu, SiO_2, TiO_2) POTGK'nin ısıl verimine etkisi incelenmiştir. Burada konstarasyon oranının sıfır olması ısı transfer akışkanın saf halini göstermektedir. İncelenen nanopartiküllere bakıldığında konstrasyon oranının arttırılmasının verime etkisinin olumlu yönde olduğu ve en iyi verimin nanopartikül olarak Cu kullanılması ile elde edildiği belirlenmiştir.

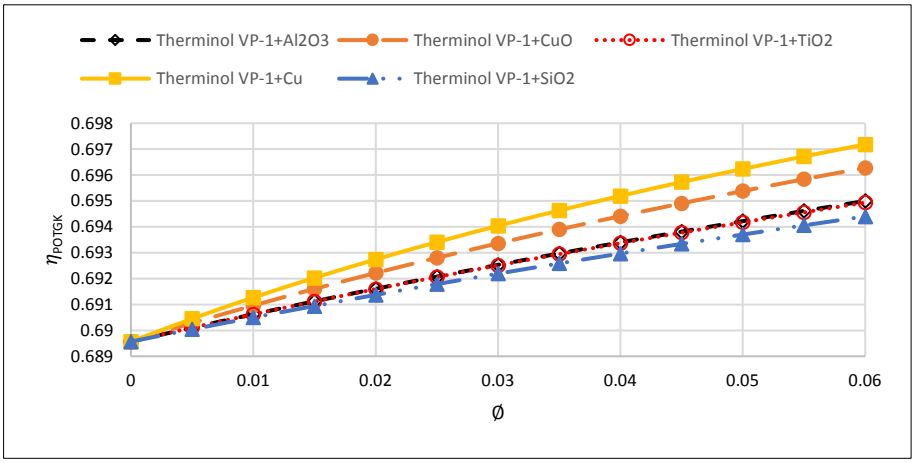

Şekil 3. Farklı nanopartiküllerin POTGK verimine etkisinin nanopartikül konsantrasyon oranı ile değişimi.

ORÇ'de farklı soğutkanlar (Toluene, MDM, cyclohexane, n-pentane, n-Hexane, R11, R123, R113, R141b) kullanılmış ve bu soğutkanların ORÇ verimine etkisi incelenmiştir. Teorik olarak yapılan analizler sonucunda ve Şekil 4'de de görüldüğü üzere en yüksek ORÇ verimi soğutkan olarak Toluene kullanıldığı durumda elde edilmiştir.

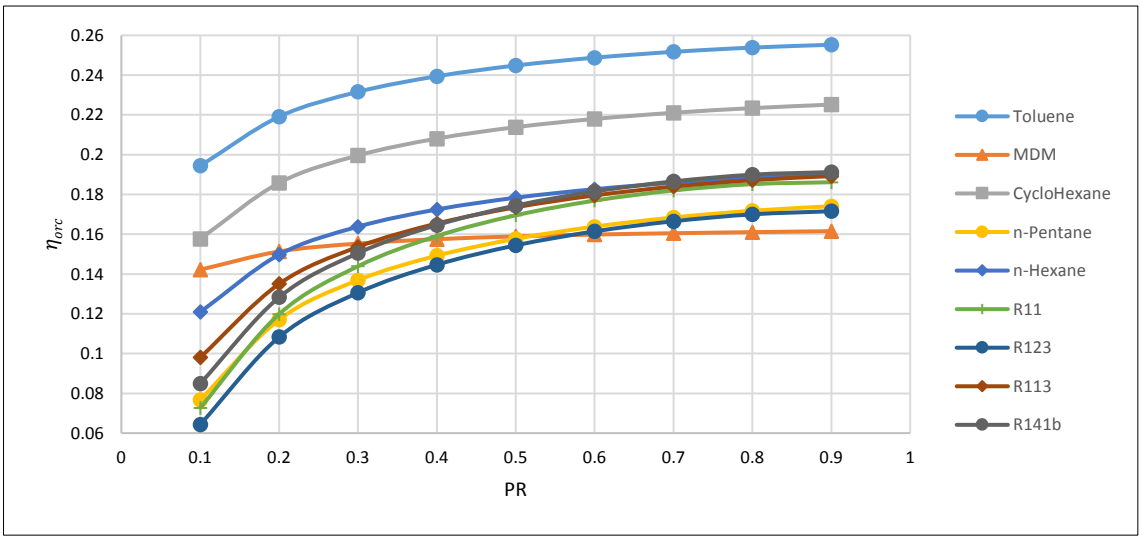

Şekil 4. Farklı soğutkanların ORÇ verimine etkisinin basıç oranı ile değişimi.

POTGK'de temel ısı transfer akışkanı olarak Therminol VP-1, nanopartikül olarak Cu ve ORÇ'de soğutkan olarak Toluene kullanıldığı durumda sistemden performansı incelenmiştir. Belirtilen koşullarda yapılan analizler sonucunda değişen nanopartikül konsantrasyon oranı ve basınç oranına bağlı olarak sistemden elde edilen net elektrik gücünün ve sistem veriminin değişimi sırası ile Şekil 5 ve 6'da görülmektedir. Belirlenen koşullarda yapılan analizler sonucunda en yüksek elektrik gücü ve sistem verimi sırasıyla 165,652 kW ve %17,7 olarak bulunmuştur.

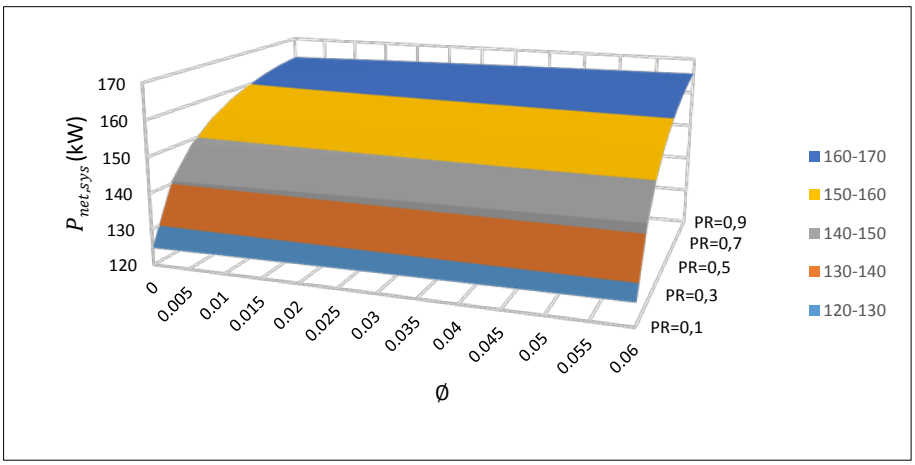

Şekil 5. Sistemden elde edilen net elektrik gücünün nanopartikül konsantrasyon ve basınç oranı ile değişimi.

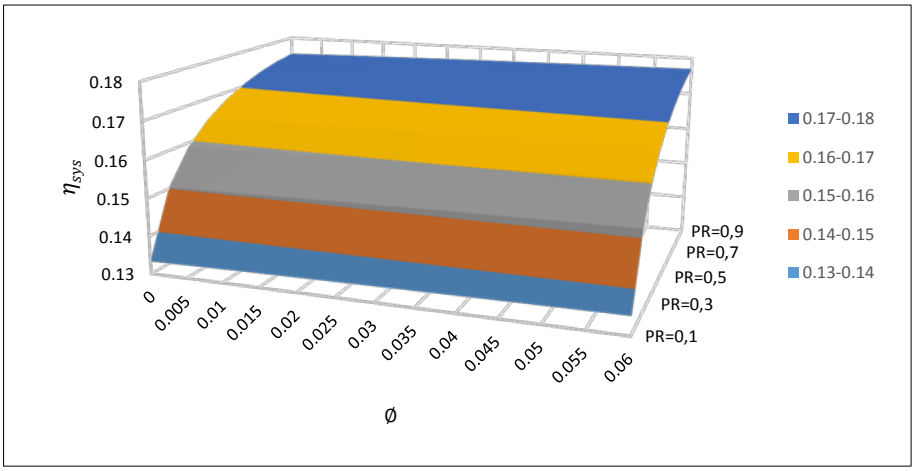

Şekil 6. Sistem veriminin nanopartikül konsantrasyon ve basınç oranı ile değişimi.

5. SONUÇ VE ÖNERİLER

Yapılan bu çalışmada POTGK'de farklı ısı transfer akışkanların (Syltherm 800, Therminol VP-1) ve farklı nanopartiküller (Al_2O_3, CuO, Cu, SiO_2, TiO_2) eklenmesinin POTGK'nin ısıl performansına etkisi araştırılmıştır. ORÇ'de farklı soğutkanların kullanımının çevrim verimine etkisi araştırılmıştır. Uygun nanoakışkan ve soğutkanın seçiminden sonra POTGK-ORÇ sistem veriminin, basınç oranı ve nanopartikül konsantrasyon oranı ile değişimi incelenmiş ve sistemin en yüksek verimi %17,7 olarak bulunmuştur. Gelecekte yapılacak çalışmalarda bu gibi bütünleşik uygulamalar denenerek sistem verimleri arttırılabilir. Ayrıca farklı nanoakışkanların ve soğutkanların incelenmesi ile sistem performansları geliştirilebilir.

KAYNAKLAR

[1] Abubakr, M., Amein, H., Akoush , B.M., El-Bakry, M.M. & Hassan, M.A., An intuitive framework for optimizing energetic and exergetic performances of parabolic trough solar collectors operating with nanofluids, *Renewable Energy*, **157,** 130-149, 2020.

[2] Risi, A., Milanese, M. & Laforgia, D., Modelling and optimization of transparent parabolic trough collector based on gas-phase nanofluids, *Renewable Energy*, **58**, 134-139, 2013.

[3] Ehyaei, M.A., Ahmadi, A., El Haj Assad, M. & Salameh, T., Optimization of parabolic through collector (PTC) with multi objective swarm optimization (MOPSO) and energy, exergy and economic analyses, *Journal of Cleaner Production*, **234**, 285-296, 2019.

[4] Bellos, E. & Tzivanidis, C., Parametric analysis and optimization of an Organic Rankine Cycle with nanofluid based solar parabolic trough collectors, *Renewable Energy*, **114**, 1376-1393, 2017.

[5] Moloodpoora, M., Mortazavib, A. & Ozbalta, N., Thermal analysis of parabolic trough collectors via a swarm intelligence optimizer, *Solar Energy*, **181**, 264-275, 2019.

[6] Huang, W., Xu, Q. & Hu, P., Coupling 2D thermal and 3D optical model for performance prediction of a parabolic trough solar collector, *Solar Energy*, **139**, 365-380, 2016.

[7] Alirahmi, S.M., Rostami, M. & Farajollahi, A.H., Multi-criteria design optimization and thermodynamic analysis of a novel multigeneration energy system for hydrogen, cooling, heating, power, and freshwater, *International journal of hydrogen energy*, **45**, 15047- 15062, 2020.

[8] Coccia, G., Nicola, G.D., Colla, L., Fedele, L. & Scattolini, M., Adoption of nanofluids in low-enthalpy parabolic trough solar collectors: Numerical simulation of the yearly yield, *Energy Conversion and Management*, **118**, 306-319, 2016.

[9] Mwesigye, A., Huan, Z. & Meyer, J.P., Thermal performance and entropy generation analysis of a high concentration ratio parabolic trough solar collector with Cu-Therminol VP-1 nanofluid, *Energy Conversion and Management*, **120**, 449-465, 2016.

[10] Forristall R., Heat Transfer Analysis and Modelling of A Parabolic Trough Solar Receiver Implemented in Engineering Equation Solver, *NREL/TP-550-34169*, 2003.

[11] Kırtepe, E., Yılmaz, R. & Özbalta, N., Parabolik Yoğunlaştiran Toplayicilarin Teorik Modellenmesi ve Farklı Sistem Parametrelerinin Verime Etkisinin İncelenmesi, *22. Ulusal Isı Bilimi ve Tekniği Kongresi*, 781-790, 11-14 Eylül, 2019.

[12] Duffie, J.A. & Beckman, W.A., Solar Engineering of Thermal Processes, 4th ed., *John Wiley and Sons*., 2013.

[13] Çengel, Y.A. & Ghajar, A.J., Isı ve Kütle Transferi, *Palme Yayıncılık*, 2015.

[14] Dudley, V.E., Kolb, G.J., Mahoney, A.R., Mancini, T.R., Matthews, C.W., Sloan M. & Kearney D., Test Results: SEGS LS-2 Solar Collector, *Report of Sandia National Laboratories (SANDIA-94-1884)*, 1994.

BIDIRECTIONAL FLYBACK BASED DIFFERENTIAL POWER PROCESSING CONVERTER FOR PHOTOVOLTAIC APPLICATIONS

Erkan KARAKAŞ*, Yusuf ÖNER*, Selami KESLER*
*Pamukkale University, Department of Electrical Electronics Engineering, Denizli/Turkey
Email: erkank@pau.edu.tr, yoner@pau.edu.tr, skesler@pau.edu.tr

ABSTRACT

Conventional photovoltaic (PV) energy conversion architectures are often forced to trade off efficiency and cost for increased power production. In many applications, cells or modules are connected in series as high voltage is required. When PV cells are connected in series, they experience internal and external mismatch that reduces output power. The differential power processing (DPP) approach overcomes this drawback by enabling each PV element to operate at its maximum power point (MPP) while only processing a small fraction of the total power produced. DPP converters are used to control PV elements, sub-panel strings, or individual PV cells. DPP converters process only the difference in power between PV elements. This paper includes a bidirectional flyback converter (BFC) based PV to Bus DPP architecture at the submodule level. When a mismatch occurs, bidirectional DPP converters can inject or subtract current to the string. If there is no mismatch between serial cells, the DPPs are shut down and process any energy. The PV to Bus architecture and voltage equalization control method has been validated by simulation results using bidirectional flyback-based DPP converters on a standard 36 cell PV module light and no mismatch conditions.

Keywords: Bidirectional flyback, Differential Power Processing, Photovoltaic, MPPT

1. INTRODUCTION

In photovoltaic (PV) energy systems, PV modules are often connected in series for increased string voltage. However, there is usually a mismatch between the I/V characteristics of the series-connected PV modules; this is typically the result of partial shading, manufacturing variability, and thermal gradients [1]. The mismatches have disproportional effects on the overall available power due to the reduction in current through the series-connected cells. Typically, bypass diodes are connected in parallel with groups (substrings) of cells to prevent cell failures due to hot spots induced by power losses on reverse-biased cells operating in breakdown [2]. However, these diodes cannot recover the power loss caused by the mismatch [3]. To overcome this severe power reduction due to series connection, the concept of individual converters was introduced, which connected each PV module to an individual converter controlling the PV module's operation. Examples of this kind of system architecture are cascaded converters, Dc optimizers, and microinverters [4]. Dc optimizers connected with a cascaded architecture to reduce mismatch by using a dedicated converter to control each module at its maximum power point. Thus, maximum power is extracted regardless of any mismatch among the substrings. The Dc optimizer has the disadvantage in that each converter process full of generated power even when there is no mismatch on the series modules. This architecture resolves mismatch, but the converter processes all the PV power with conversation losses.

Another architecture developed against incompatibility is differential power processors. These power converter systems with different types are used to balance the currents of series-connected PV modules. The power of the module, which creates a mismatch with the balancing of the serial module currents, is added to the system again. DPPs are structures that become active only in case of mismatch and provide power transfer. Therefore, they do not process power and do not cause losses when no mismatch. DPPs are processed only a part of the power generated from PV modules to balance the serial current. So, fewer energy losses occur compared to full power processors.

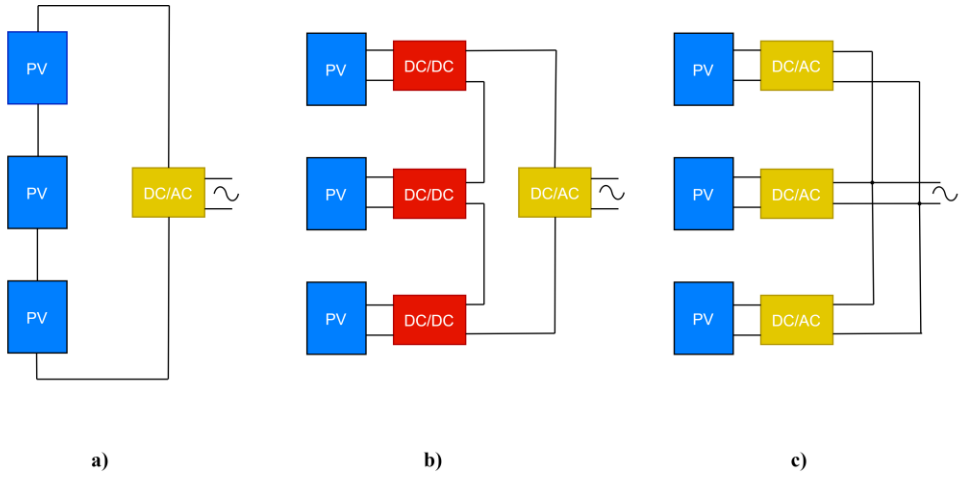

Figure 1. PV system topologies a) series string with a central inverter, b) cascaded Dc optimizer, c) microinverter

2. DIFFERENTIAL POWER PROCESSING ARCHITECTURES

In PV systems, there are three main differential power processing architectures named PV to PV, PV to Bus, and PV to Isolated Bus. Some of dc-dc converters can be applied to create differential power processors such as buck-boost, flyback, and sepic. When PV modules currents mismatch, differential power processors add or remove current to balance line current. In this way, the mismatch condition is eliminated, and almost all the powers produced from PV modules are harvested.

2.1 PV to PV

In the PV-to-PV architecture, each DPP converter is connected between two PV elements, as shown in Fig 2 (a). These converters transfer power according to the needs of the system from one PV to another. Each converter is bidirectional so, current can be added or removed to balance PV modules. For a string of *n* PV modules, there should be an *n-1* converter to control PV modules. This architecture allows two techniques for controlling the PV modules. The first method is the exact MPPT, which controls PV modules at its MPP. DPP converter tracks each PV module's current and voltage to extract maximum power from the PV module. This technique requires current and voltage sensors on the DPP converter. Another solution is voltage balancing. In this method, all the series PV modules voltages are equalized. Equal PV module voltages allow each PV to operate close to its MPP. Voltage balance requires only line current and PV module voltages. In this way, a cheaper converter solution can be realized.
For the PV to PV DPP converter topology, a bidirectional buck-boost converter is commonly used [5-6-7-8]. Alternatively, the resonant switched-capacitor converter is used which allows higher efficiency. In some cases, unidirectional converters are used to reduce magnetic components. PV to PV topologies are relatively low-cost converters due to non-isolated architecture. Most of studies focused on the voltage balance of PV elements when using the central inverter with MPPT algorithm. This technique provides that the PV element works near the MPP thanks to central MPPT. Voltage balance control in DPP converter requires less sensor and simple algorithm while exact MPPT requires more sensors and complex algorithm.

2.2 PV to Bus

PV to bus architecture, each DPP converter is connected between a PV module and the system Dc bus, as shown in Fig 2 (b). Bidirectional DPP converters can add or remove the current needed to the MPP operation of every PV module. Typically, an isolated converter topology should be chosen in PV to bus architecture due to possible short circuits with Dc bus and PV elements. This architecture allows exact MPPT and voltage equalization methods for PV elements. The critical goal is the least amount of power processing than a full power processor. This architecture has a unique minimum power point at every work condition. This is called "least power point

tracking" [8]. Also, unidirectional DPP converters have been used to simplify control and implementation in the literature [9].

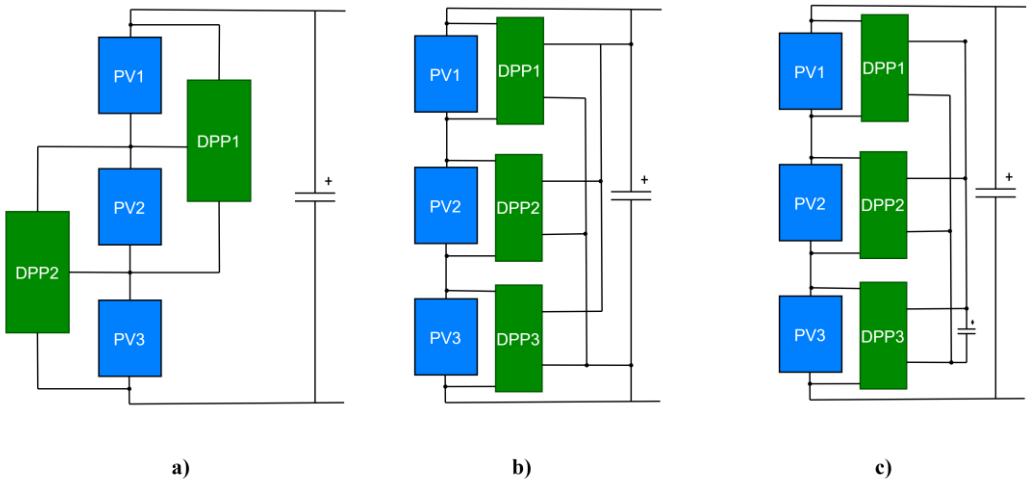

Figure 2. DPP architectures a) PV to PV, b) PV to Bus, c) PV to Isolated Bus

In this work, PV to bus architecture has been selected and simulated with a bidirectional flyback converter. The main objective of the DPPs is to balance the serial modules, which is called voltage equalization control. The goal of this control strategy is to equal all serial modules voltages.

2.3 PV to Isolated Bus

The third topology is similar from PV to Bus and is called PV to the isolated bus. The only difference from the PV to bus architecture is the secondary side of the DPP converter is connected. The second sides of DPPs are connected at an isolated point from the Dc bus. This isolated point is used for energy transfer between PV modules. DPP converters are worked in bidirectional mode and transferred energy to balance line current.

3. BIDIRECTIONAL FLYBACK CONVERTER

In this paper, bidirectional flyback topology is selected since it can achieve voltage isolation, high efficiency for a wide range, and easy control. The bidirectional flyback converter is easily made from the unidirectional by adding a switch instead of a rectifier. The energy flow of DPP can be selected to control primary and secondary switch. So, DPP can extract or add current to balance serial line current and prevent a mismatch.
There are two types of control algorithms for DPPs: exact MPPT control and voltage equalization. The exact MPPT achieves the theoretical maximum output power for each module. However, the control is relatively complex and needs extra data. Voltage equalization is not an exact MPPT but equalized voltage of each module at close to its MPP. Close-loop control is used to balance module voltages. When a mismatch occurs, the control algorithm detects module voltages difference and set DPPs energy flow direction. Each PV module voltages the equalize at a maximum of PV voltage. In Equation 1, V_{pri} and V_{sec} are primary and secondary voltages of converter. D is the duty cycle of the converter control signal.

$$V_{\text{sec}} = V_{pri} \frac{D}{1-D} \tag{1}$$

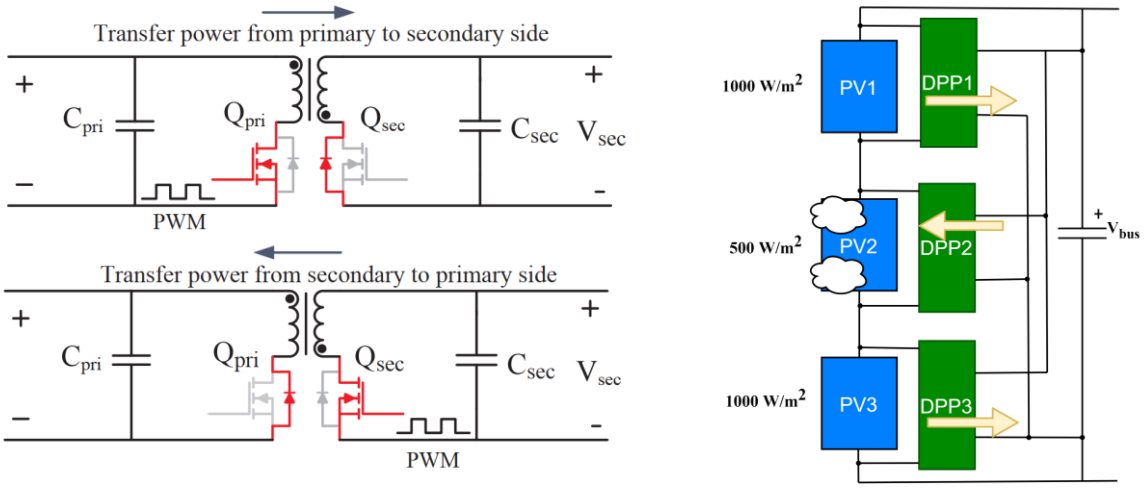

Figure 3. Bidirectional flyback converters energy flow [10] and applied DPP architecture

The mismatch scenario has been realized like in Figure 3. The solar radiation for the upper and lower PV modules is set to 1000 W / m2 and the middle module to 850 W/m^2. When running voltage balance algorithm, DPP1 and DPP3 transfer power to Dc bus to extract current from the serial line. DPP2 transfers power from the Dc bus to PV2 to balance its voltage. Bidirectional flyback converter switching frequency selected as 30 kHz. Primary and secondary inductances are equal and 10 mH.

Table 1. PV module parameters

Parameter	Value
V_{OC} (Open circuit voltage)	22.77V
V_{MPP} (Maximum power point voltage)	18.3V
I_{SC} (Short circuit current)	2.93A
I_{MPP} (Maximum power point current)	2.75A
Cells per module	36

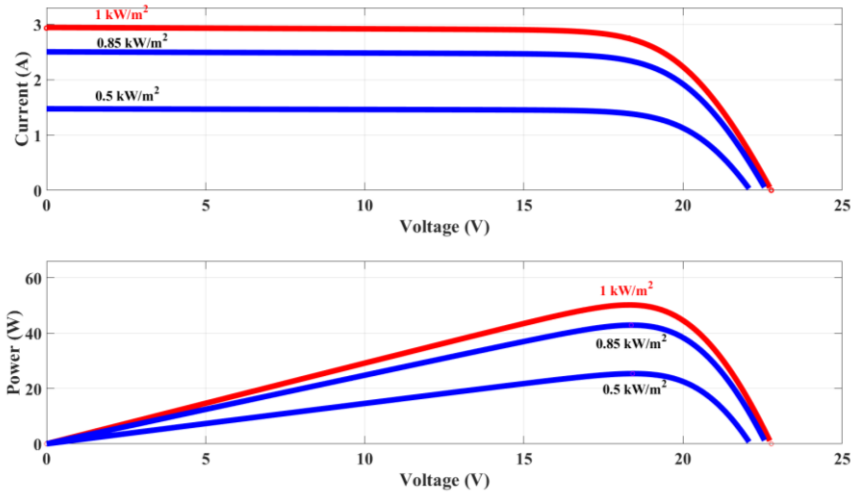

Figure 4. PV module characteristic curves

PV module characteristic and parameters are given in Table 1 and Figure 4. The proposed DPP architecture with a bidirectional converter is simulated in Simulink PC program. A mismatch condition is modeled, and DPPs performances were examined.

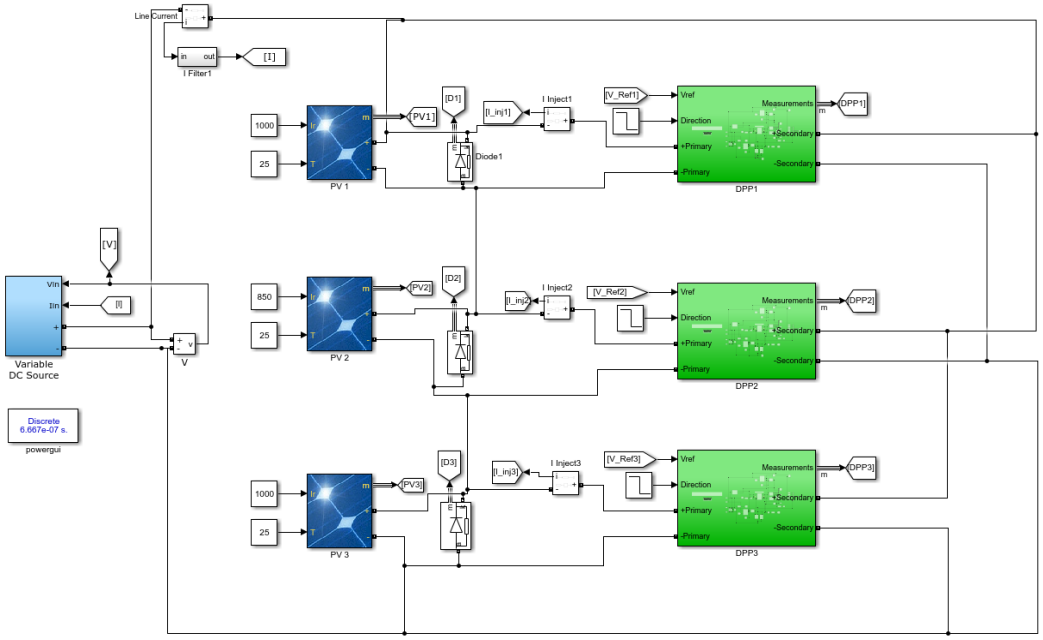

Figure 5. Bidirectional flyback converters energy flow and applied DPP architecture

4. RESULTS

Since the DPP concept for PV systems was introduced in recent years, various work has been developed and published in the literature. In this paper, the problem of module mismatch in partially shaded PV modules has been simulated using bidirectional flyback-based differential power processing for isolated PV to bus topology.

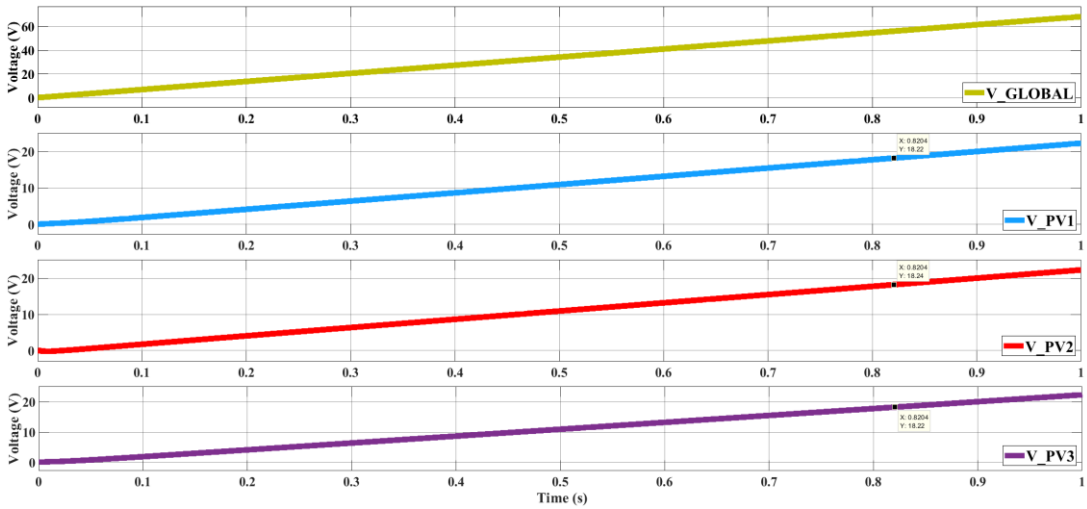

Figure 5. Voltages of modules and Dc bus

Voltage equalization was selected as the control method to apply at DPP converters cause of the simplicity and minimal measurement required. A PID block controls the PWM duty cycle on both sides of the bidirectional

converter. So, PV module voltages are regulated close to each other. The main control block detects mismatch, and set DPP converters active or inactive, bidirectional converter power flow and reference voltages.

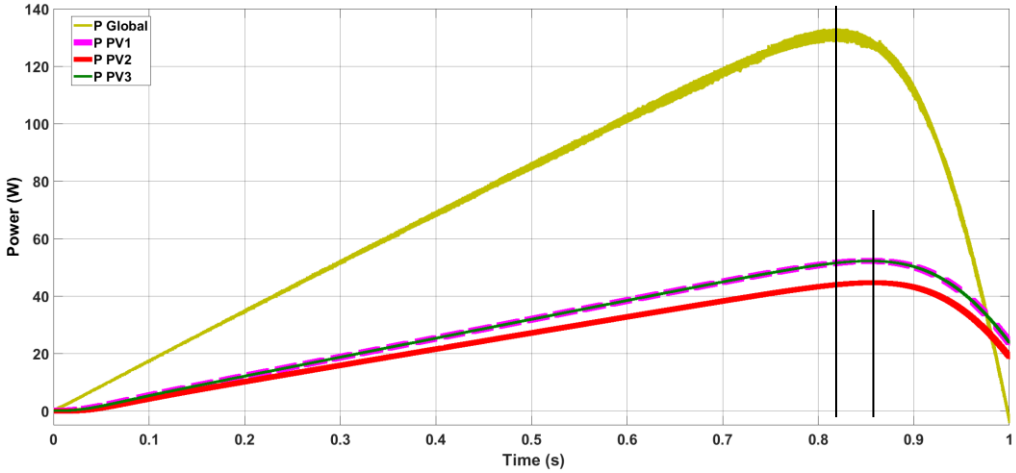

Figure 6. Power of modules and string

In this simulation work, a light mismatch condition was created as PV1 and PV3 module irradiances are %100, and the PV2 irradiance is set to %85. In mismatch condition DPP2 equalizes PV2 voltage to PV1 or PV3 voltage. DPP1 and DPP3 regulate DC bus voltage. To regulate the serial current, DPP1 and DPP3 remove current and DPP1 adds current. In Figure 5, PV voltages are shown. It is seen that the voltages are equal. Figure 6 shows global and PV modules power. A power graph was obtained by changing the array load over time.

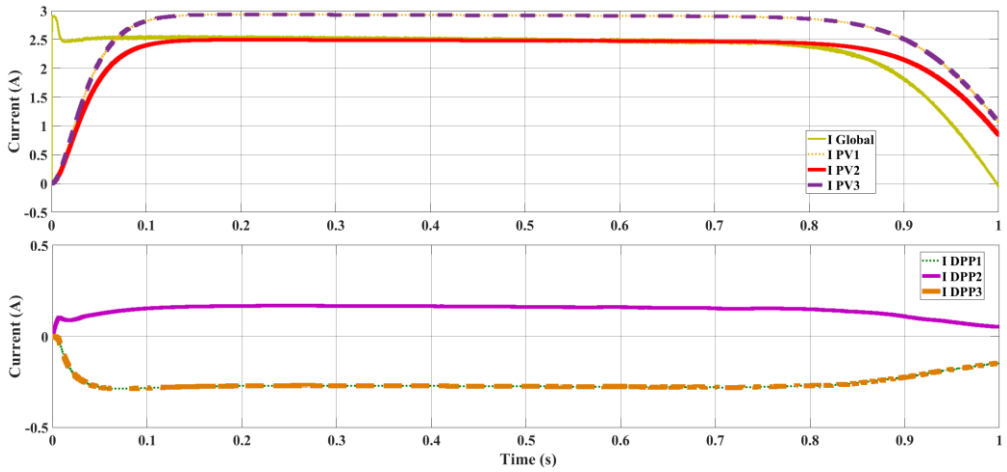

Figure 7. Currents of PV modules and DPP converters

The string power has only one peak point, as shown in Figure 6. This means a central inverter can easily track maximum power points of the string. The local maximum power points are close to the global MPP. PV modules and DPP converter currents are shown in Figure 7. DPP1 and DPP3 currents are the negative causes of remove current from the serial line. DPP2 current is positive because this converter adds current to the serial line.

Simulation results show that the DPP converter solves mismatch and equalizes PV voltages. DPP solutions improve the system efficiency and reinject unusable energy to the Dc bus. In future works, it may be planned severe mismatch conditions, exact MPPT control of per modules, and implementation of a prototype.

REFERENCES

[1] Qin, S. et al., "A distributed approach to MPPT for PV sub-module differential power processing", in *2013 IEEE Energy Conversion Congress and Exposition, ECCE 2013*, 2778–2785, 2013.

[2] Olalla, C. et al., "Architectures and control of submodule integrated dc-dc converters for photovoltaic applications", *IEEE Transactions on Power Electronics*, 2013.

[3] MacAlpine, S. M., Brandemuehl, M. J., and Erickson, R. W., "Analysis of potential for mitigation of building-integrated PV array shading losses through use of distributed power converters", in *ASME 2010 4th International Conference on Energy Sustainability, ES 2010*, 2010.

[4] Jeong, H. et al., "Review of Differential Power Processing Converter Techniques for Photovoltaic Applications", *IEEE Transactions on Energy Conversion*, 2019.

[5] Badawy, M. and Sozer, Y., "Differential power processing of photovoltaic systems for high energy capture and reduced cost", in *2017 IEEE Energy Conversion Congress and Exposition, ECCE 2017*, 475–481, 2017.

[6] Qin, S. et al., "A distributed approach to maximum power point tracking for photovoltaic submodule differential power processing", *IEEE Transactions on Power Electronics*, 2015.

[7] Wang, F. et al., "An improved submodule differential power processing-based PV system with flexible multi-MPPT control", *IEEE Journal of Emerging and Selected Topics in Power Electronics*, 2018.

[8] Jeon, Y.-T. et al., "Least Power Point Tracking Method for Photovoltaic Differential Power Processing Systems", *IEEE Transactions on Power Electronics*, 2017.

[9] Biswas, J. et al., "Design, Architecture, and Real-Time Distributed Coordination DMPPT Algorithm for PV Systems", *IEEE Journal of Emerging and Selected Topics in Power Electronics*, 2018.

[10] Chu, G. et al., "Bidirectional flyback based isolated-port submodule differential power processing optimizer for photovoltaic applications", *Solar Energy*, 158May, 929–940, 2017.

DYNAMIC SIMULATION OF A FLAT PLATE SOLAR COLLECTOR SYSTEM UNDER HOT AND HUMID CLIMATIC CONDITIONS

Hadi GENCELİ*, Akın ÖZDOĞAN, Mustafa ASKER*****
* Yildiz Technical University, Faculty of Mechanical Engineering, Istanbul/Turkey
Email: hadi.genceli@gmail.com
** ELPARTS ENTERPRISES LTD, Nicosia / North Cyprus
Email: ayumusak331@gmail.com
*** Aydın Adnan Menderes University, Department of Mechanical Engineering, Aydın/Turkey
Email: mustafa.asker@adu.edu.tr

ABSTRACT

The system's design, testing, modification and adaptation are costly and time-consuming every time. Simulation programs are often used to prevent time loss and reduce costs. A numerical investigation is applied to depict the transient performance of a flat plate solar collector (FPSC) under hot and humid climate conditions. In this regard, a real-time stand-alone FPSC system is modeled by using the TRNSYS program. This research study is addressed, taking into account the real climatic conditions of Trabzon and Izmir, the topical cities placed in Turkey. Throughout the year, the amount of energy consumed during the year is calculated. Besides, the performances of FPSC for both weather data are compared, including the temperature changes and the amount of solar energy for both weather data.

Keywords: Flat plat solar collector, Thermal performance, TRNSYS.

1. INTRODUCTION

Solar energy utilization needs further development to regulate the high demand and consumption of fossil fuels due to the ever-increasing cost and the threats they bring to the environment. The use of collectors is getting more attention from researchers, but still, their performance needs improvement. The sun is the most powerful energy generator of the solar system. Solar hot water systems collect energy from the sun in panels or tubes to produce domestic hot water used in a home or building. With over 110 days of sunshine per year in Turkey, most of Turkey's cities are good choices for the solar domestic hot water system.

The solar domestic hot water system (SDHW) consists of three components: a solar collector panel, a storage tank, and a circulation system to transfer the heat from the panel to the store. The solar collector converts sunlight to heat energy. The storage tank stores hot water when it is not in use. A pump from the circulation system controls the transfer fluid flow through the collector and storage tank [1].

A flat plate solar collector (FPSC) is the most straightforward and user-friendly means available for solar energy usage. The purpose of using an FPSC is to utilize the absorbed sun's radiation to raise the working fluid temperature to a new one which can be used for various low and medium applications. They use both diffuse and beam solar radiation and are easy to maintain (Duffie and Beckman 2013). Buchberg and Roulet (1968) developed a thermal model of a house heating system, simulated its operation with a year's hourly meteorological data, and applied a pattern search optimization procedure in finding optimum designs. Andres and Lopez [4] have modeled a thermosyphon solar water heater by using TRNSYS. Genc et al. 2018 [5] performed a transient numerical study on the thermal performance of an FPSC using Al_2O_3/water nanofluid with a volume fraction range of 1-3% for three different months in the city of Izmir, Turkey. The effect of the nanofluid thermophysical properties and at different flow regions was investigated by varying the flow rate. The results obtained showed that at 0.004kg/s and volume fraction of 3%, the outlet temperature is at its maximum increase (7.20%) in the month of July. The efficiency is also at its highest increase (83.90%) at 0.06kg/s and

volume fraction of 1%. Hawwash et al. [6] developed a model by using ANSYS software to test the performance of FPSC using double distilled water (DDW) as well as Al_2O_3 nanofluid at different volume fractions. Mahian et al. [7] conducted first and second law analysis to examine the efficiency of FPSC connect to minichannel using various nanofluids. Bellos and Tzivanidis] [8 applied multi-objective optimization for FPSC integrated with an absorption chiller driven. Koholé and Tchuen 2018 [9] presented an optimization of a FPSC for the thermosiphon water heating system by using a genetic algorithm to obtain suitable design parameters of the system. Asker and Gadanya [10] applied a numerical study in order to examine the performance of a FPSC using five different nanofluids.

2. SYSTEM DESCRIPTION

SDHW is the simplest and most direct application of solar energy (see Figure 1). It consists of two major parts: a solar collector and a storage tank, with the collector been the most important part. The collector receives the solar radiation and transforms it to heat, then transfers the heat into a working fluid, mainly water or oil. Solar water heating systems can either be active or passive. The active system requires a mechanical system (e.g. pump) to transfer the liquid to the collector, while the passive system depends on gravity and natural circulation to circulate the liquid (En 1996). A list of the collector specifications is shown in Table 1.

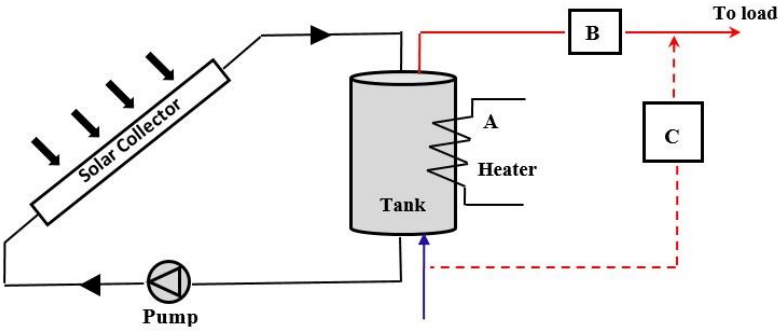

Figure 1. Schematic representation of flat plate solar collector.

Table 1. Simulation data used for Trabzon and İzmir provinces in February and July.

Parameters	TRABZON	IZMIR
Flow rate of water ($\dot{m}$)	dependent variable	dependent variable
Collector Outlet temperature (T_{out})	dependent variable	dependent variable
Collector Inlet temperature (T_{in})	dependent variable	dependent variable
Fluid specific heat (c_p)	4190 J/kg.K	4190 J/kg.K
Area of collector (A_{col})	5 m^2	5 m^2
Incident solar radiation		
February	2253 W/m^2	2200 W/m^2
July	5412 W/m^2	6300 W/m^2

3. ANALYSIS

The performance of a collector is expressed by applying an energy balance on FPSC. The useful energy output can be written as [2]

$$Q_u = F_R A_c \left\lfloor I_T (\tau\alpha) - U_L (T_i - T_{amb}) \right\rfloor \quad (1)$$

The thermal efficiency is given as follows.

$$\eta_{collector} = \dot{m} c_p \frac{T_{out} - T_{in}}{A I_T} \quad (2)$$

Where ṁ is the flow rate of water, c_p is the fluid specific heat, T_{out} is the outlet temperature of water from the collector, T_{in} is the inlet temperature of water from the collector, A is the area of collector and I_T is the incident radiation from the sun.

4. RESULTS AND DISCUSSION

The dynamic simulation of FPSC system for two different city of Tukey is carried out by using TRNSYS modeling software. Hourly water flow in solar collector for solar water heating system during the day in February and July are shown in Figure 3a and Figure 3b. The proposed time table for hourly water flow in solar collector is the same for both provinces.

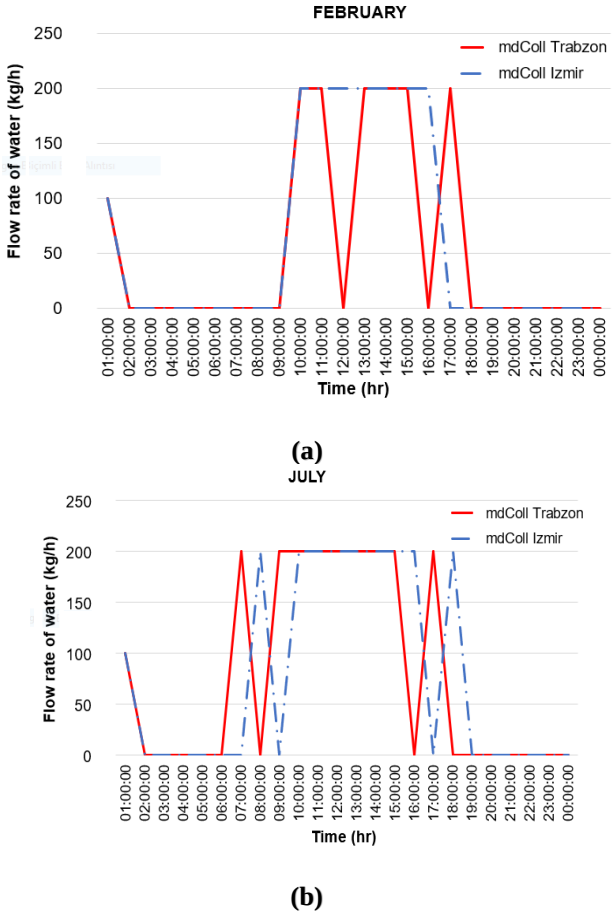

Figure 3. Time-dependent change of the collector water flow for Trabzon and Izmir provinces in (a) February and (b) July.

The outlet temperature of the collector as well as Auxiliary heater power in February and July are shown in Figure 4a and Figure 4b. In summer, solar radiation started earlier in July, so more solar energy is provided than in February. When the solar radiation reaches its minimum level, auxiliary heaters in the system are active. The maximum obtained level of solar radiation in July is higher than in February. The auxiliary heater in the tank is not used after 11:00 AM in both provinces is the maximum limit of water temperature at the top of the storage

tank is about 60 °C. In July, more efficiency than solar energy was achieved for both provinces compared to February (the average coldest month). Collector temperatures are shown in red and red dashed lines and the auxiliary heater distributions are expressed in blue and blue dashed lines.

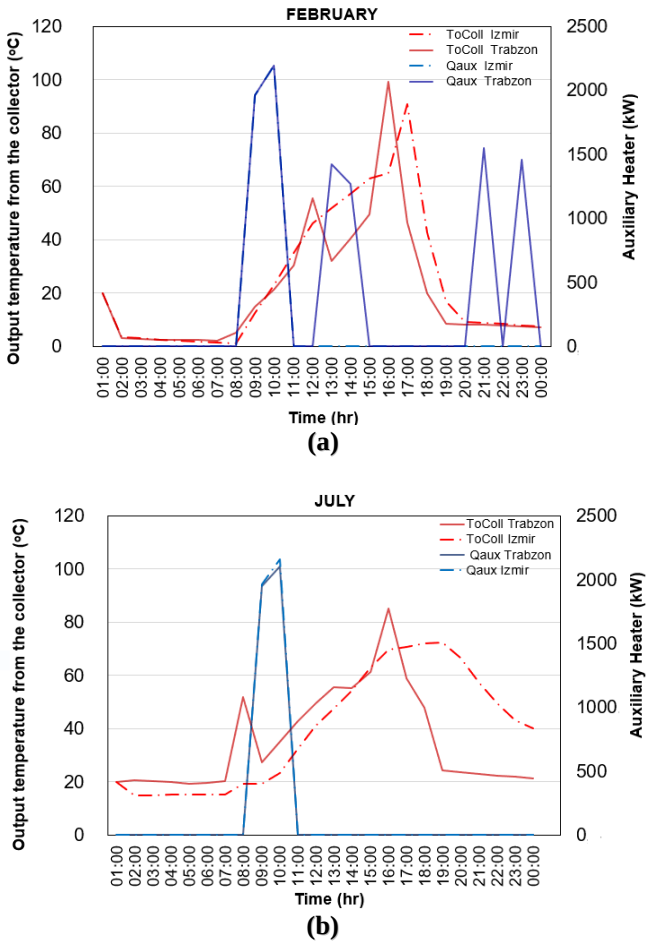

Figure 4. Comparison of water temperature from the collector and auxiliary heater in February (a) and July (b) for Trabzon and İzmir provinces.

Comparing power consumption of the auxiliary heater for Izmir and Trabzon provinces in February and July is illustrated in Figure 5a and Figure 5b. As shown in Figure 5a, the total power consumption of the auxiliary heater in Trabzon for 24 hours in February is about 9847.3 kW. However, the total power consumption of the auxiliary heater in Izmir for 24 hours in February is about 4152 kW. The results showed that the total power consumption of the auxiliary heater in Trabzon is 2.3 times higher than the power consumption in Izmir.

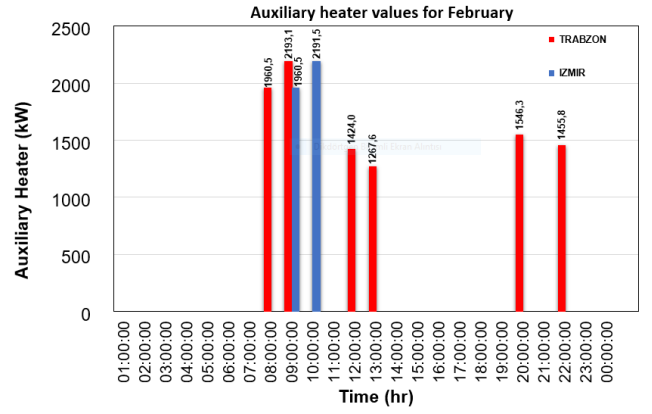

(a)

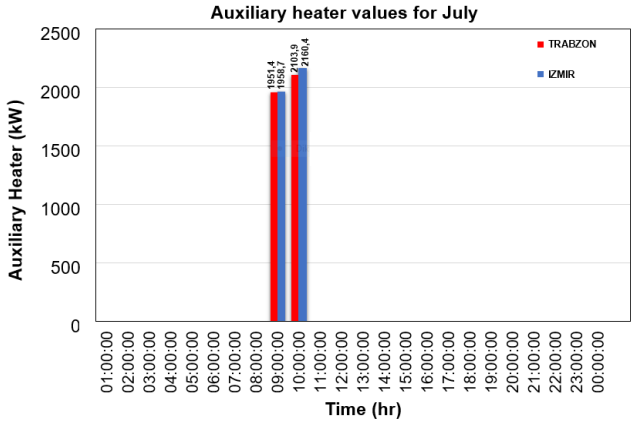

(b)

Figure 5. Auxiliary heater values for Izmir and Trabzon in February (a) and July (b)

The comparison of the efficiency of solar collector for Izmir and Trabzon provinces for February and July are depicted in Figure 6a and Figure 6b. In the cases where the solar radiation is insufficient or water demand is zero, the efficiency is also zero for the solar collector in both provinces. In addition, when the solar radiation decreases, the collector is not efficient and the required energy for heating water is provided with auxiliary heaters in the tank. The highest efficiency from the collector for both provinces is seen between 12:00 and 13:00 PM due to higher solar radiation.

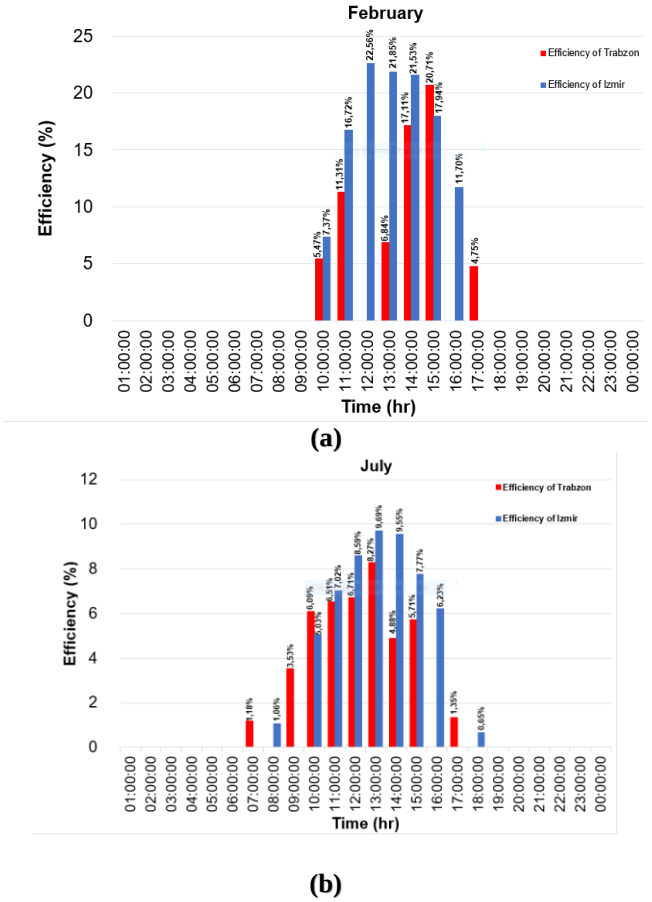

Figure 6. Comparison of collector efficiencies of Trabzon and Izmir provinces in (a) February and (b) July.

5. CONCLUSIONS

This research paper performs a flat plate solar collector for Trabzon and Izmir provinces in February and July months. In this regard, simulation programs (TRNSYS) were used to determine the efficiency of the system. The results showed that the total power consumption of the auxiliary heater in Trabzon in February is 2.3 times higher than the power consumption in Izmir to provide the same amounts of hot water.

REFERENCES

[1] Ksenya, Components of a Solar Hot Water Heating System, https://solartribune.com/solar-hot-water-parts/ Agust 8,2011.

[2] Duffie,J.A.,Beckman,W.A., Solar Engineering of Thermal Processes, *4th ed.*, New Jersey, Wiley, (2013).

[3] Buchberg, H.,. Roulet J. R., Simulation and Optimization of Solar Collection and Storage for House Heating, *Solar Energy*, 12, 31 (1968).

[4] Carrilo Andres, A., Cejudo Lopez, J.M., TRNSYS model of a thermosyphon solar water heater with a horizontal store and mantle heat exchanger, *Solar Energy*, 72, 89-98,2002.

[5] Genc A.M., Ezan M.A, Turgut A., Thermal performance of a nanofluid-based flat plate solar collector: A transient numerical study. *Applied Thermal Engineering* 130, 395–407, 2018.

[6] Hawwash A. A., Abdel Rahman A. K. and Nada S. A., Ookawara S. "Numerical Investigation and Experimental Verification of Performance Enhancement of Flat Plate Solar Collector Using Nanofluids", Applied Thermal Engineering, 130: 363-374, 2018.

[7]Mahian O., Kianifar A., Sahin A. Z. and Wongwises S., Performance analysis of a minichannel-based solar collector using different nanofluids, Energy Conversion and Management, 88, 129-138, 2014.

[8] Bellos E. and Tzivanidis C., Performance analysis and optimization of an absorption chiller driven by nano fluid based solar flat plate collector, Journal of Cleaner Production, 174: 256-272, 2018.

[9] Koholé, Y.W. & Tchuen, G., Experimental and numerical investigation of a thermosyphon solar water heater. *International Journal of Ambient Energy***,** pp.1–11,2018.

[10] Asker M., Gadanya T.S., Performance Assessment of Flat Plate Solar Collector Using Different Nanofluids, *Hittite Journal of Science and Engineering*, 6 (3) 193-200, 2019.

ARTIFICIAL NEURAL NETWORK MODELING OF PARABOLIC TROUGH TYPE SOLAR THERMAL POWER PLANT

Damla KILIC*, Oguz ARSLAN*
* Bilecik Seyh Edebali University, Mechanical Engineering Department, Bilecik/Turkey
Email: damla.kilic@bilecik.edu.tr, oguz.arslan@bilecik.edu.tr

ABSTRACT

In this study, thermo-economic analysis of the parabolic trough type solar thermal power plant was performed. The economic analysis of this system was made using the NPV method. Then, it was compared to the analysis result and NPV result obtained by the ANN. A total of 900 designs were realized according to different operating parameters determined for R-134a refrigerant. TheANN model was realized by using the MATLAB program. The back-propagation learning algorithm with three different variants, namely LevenbergeMarguardt, Pola - Ribiere Conjugate Gradient, and Scaled Conjugate Gradient were used in the network to find the best approach. The best results were obtained in the LM-10 algorithm during the training and testing steps. When the obtained results are examined, the analysis results of the most suitable system are as follows; the energy efficiency 18.4 %, exergy efficiency 23.6 % and generated power of the system 281.9 MWh. Besides, the profitability value of the system has been determined as 1.317 million US$. When the analysis results and the ANN results were compared, the error percentage was found to be 0.013 %. This value is an acceptable error rate.

Keywords: Solar Power Plant, Parabolic Trough Type Solar Collectors, Artificial Neural Network

List of Symbols

ANN = Artificial Neural Network
C = Cost ($)
CGP = Pola- Ribiere Conjugate Gradient
E = Energy (kW)
Ex = Exergy (kW)
h = Enthalpy (kj/kg)
LM = LevenbergeMarguardt
$\dot{m}$ = Mass flow (kg/s)
NPV = Net Present Value
ORC = Organic Rankine Cycle
P = Pressure (kPa)
PTTSTPP = Parabolic Trough Type Solar Thermal Power Plant
s = Entropy $(kj/kg.K)$
T = Temperature (℃)
TES = Thermal Energy Storage
$\dot{Q}$ = Heat Energy (kW)
$\dot{W}$ = Power (kW)
η = Energy efficiency (%)
ε = Exergy efficiency
ψ = Specific exergy (kj/kg)

1. INTRODUCTION

The rapidly growing population and technological developments in the world bring energy demand. Today 80% of the energy demand in the world is provided by fossil fuels. However, renewable energy sources have gained importance due to the depletion of fossil fuels and their environmental damage. Solar energy, one of the renewable energy sources, is preferred not only because it is a free and endless source but also an easily accessible source. There are two ways to generate electricity from solar energy. One of them is photovoltaic solar cells and the other is solar power plants. This study is based on solar power plants. There are many studies on these systems in the literature. Some of these studies; Ferrara et al.[1], designed a system using different working fluids (R134a, R245fa, Acetone) for a small-scale solar power plant with 20 kWe. Kumar and Kaur [2], determined the solar radiation values using the ANN model for a region in India. Arslan and Yetik [3] designed a system for the Simav region based on the $ORC - Binary$ geothermal power plant. To determine the most appropriate design, they used the ANN model, including the life cycle cost. Three different algorithms, LM, CGP and SCG, were used to find the best approach in the network. As a result of the study, the most suitable algorithm was LM-16 in the s1 type cycle and LM-14 in the s2 type cycle. Sencan et al.[4], in their study, they used ANN to determine the thermodynamic properties of Li-Br water and Li-Clewater fluid pairs in an absorption heat pump system. Sozen et al.[5] investigated solar energy potential using ANN methods for 17 different cities in Turkey. LM, CGP, and SCG learning algorithms and logistic sigmoid transfer functions were used in the network. Arslan [6] examined the electricity production in the Simav geothermal field using the Kalina Cycle. The optimization of the system was realized with the ANN model. In this study, three different types of backpropagation learning algorithms, $M\ CGP$, and SCG have been tried to find the best approach in the network. As a result, the most suitable algorithm was determined to be LM with seven neurons. Al-Sulaiman [7], has performed an exergy analysis of parabolic trough solar collectors integrated with steam and ORC cycles. Boukelia et al. [8], in their study, PTTSTPP have designed that with and without integrated the thermal energy storage system and fuel backup systems. Eight different configurations were created. The configurations are analyzed as Energy, Exergy, Economic and Environmental. Senkal [9], using the ANN method Turkey's solar radiation values have been determined by selecting 19 different regions. Boukelia et al. [10], in the study, the level of electricity cost of the power plant using parabolic trough type solar collectors was determined using the ANN model. Gunasekar et al. [11] In their work, the ANN model have used to determine the energy performance of a photovoltaic-thermal evaporator used in solar-assisted heat pumps. Kalogirou [12], using the TRNSYS program, modeled the solar energy system according to the meteorological values of Cyprus. To determine the most economical value of the solar energy system, the system has been optimized by using the ANN.

In this study, the PTTSTPP was analyzed according to the first and second laws of thermodynamics by considering different parametric values. The economic analysis of this system was made using the NPV method. Then, it was compared the analysis result and the NPV result obtained by ANN. Three different backpropagation algorithms were used to find the best approach in the network. These are Levenberge Marguardt (LM), Pola- Ribiere Conjugate Gradient (CGP), and Scaled Conjugate Gradient (SCG), respectively. The accuracy rate of ANN in applications was discussed by determining the error rate between the ANN results and analysis results.

2. MATERIAL AND METHOD

Turkey's solar radiation values are average. In this paper, Bilecik is determined as the study area. Bilecik is located between 40.1° latitude and 29.9° longitude. Figure 1 shows the average solar radiation values, monthly average temperature values and sunshine times for Bilecik.

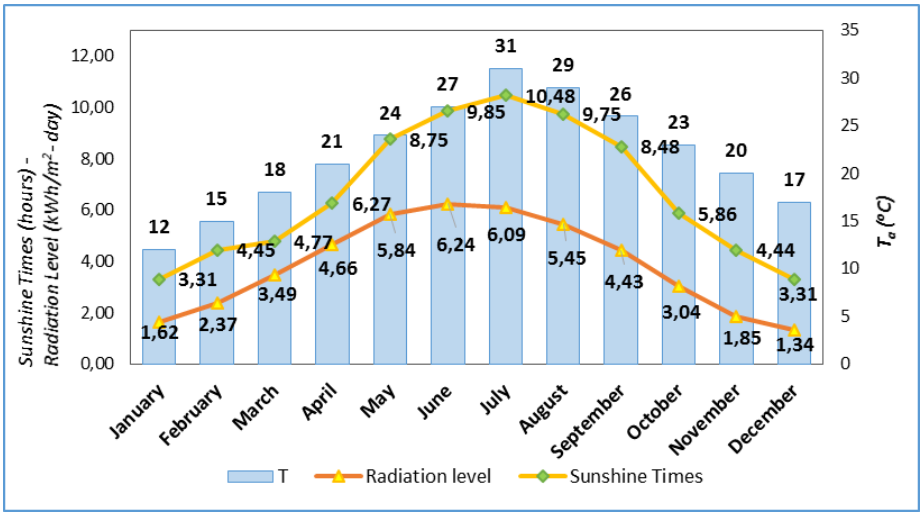

Figure 1. Monthly average values of Bilecik [13].

When Figure 1 is examined, Bilecik has a radiation range between 1.34-6.24 kWh/m^2-day. The solar radiation value is the highest in June and the lowest in December. Similarly, the lowest times were observed in January and December as 3.31 hours and the highest sunshine time was observed in July as 10.48 hours. The temperature values shown in the graph belong to 2018. These values are taken for Bilecik from Meteorology General Directorate. The highest temperature value is 31 ^{o}C in July and the lowest temperature is 17 ^{o}C in January. Considering these values, a solar power plant was designed according to Bilecik's conditions. Figure 2 shows the flow diagram of the designed solar power plant.

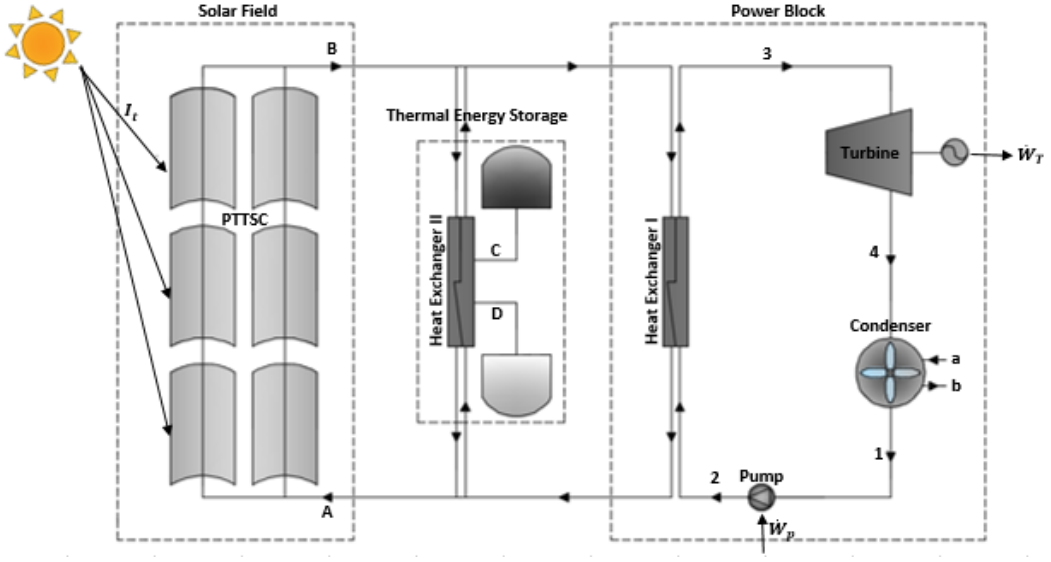

Figure 2. Flow diagram of the system.

The system consists of three main sections: Solar field, Thermal energy storage and power block. In the Solar field, the most commonly used among the condenser systems parabolic trough type solar collectors have selected. These systems in which the sun rays come to the surface of the parabolic collectors, reflect the receiving pipe in the center of the collector. In this way, the fluid in the solar field becomes the heat source. Then, this fluid is transferred to the power cycle to obtain steam. The technical details of the parabolic trough type solar collectors used in system design are given in Table 1.

Table 1. Technical Details of Parabolic Collectors [14].

Parabolic Collectors	Values
Receiver outside diameter ($D_{o,r}$)	0.07 m
Receiver inside diameter ($D_{o,i}$)	0.066 m
Heat transfer coefficient inside the receiver (h_{fi})	300 W/m^2
Thermal conductivity of the receiver (κ)	16 W/m ^{o}C
Transmissivity of the cover glazing (τ_{cover})	0.90
Effective transmissivity of PTC (τ_{PTC})	0.94
Absorptivity of the receiver (α_r)	0.87
Correction factor for diffuse radiation (γ)	0.95
Single collector width (W)	1.5
Single collector length (L)	5

The TES system is basically a storage for hot or cold fluid to be used when necessary. These systems feed the turbine during cloudy or bad weather without the sun and during the night. Thus, ensuring the operation of the power plant and preventing the decrease of efficiency. Thanks to the TES systems, it is possible to increase the uptime of solar power plants up to 24 hours. In this study, the TES system with a hot and cold storage tank is considered.

The heat obtained from the solar energy is transferred to the refrigerant fluid by the heat exchanger in the ORC. At high temperatures and pressure, the refrigerant fluid exiting the heat exchanger operates the turbine to generate electrical energy. The expanding fluid in the turbine is converted to liquid in the condenser. Then, the pressure of the fluid entering the pump increase. The fluid exiting the pump is sent to the heat exchanger and completes the cycle.

The Therminol VP-1, molten salt and R-134a have been used as a working fluid in the solar field, thermal energy storage and power block, respectively. The properties of the fluids are given in Table 2.

Table 2. The properties of the working fluids.[15,16,17]

Properties	Therminol VP-1	Molten Salt	R-134a
Boiling Point (℃)	257	-	-26.074
Freezing Point (℃)	12	221.85	-103.3
Critical Temp. (℃)	400	-	101.06
Critical Pres. (MPa)	-	-	4.059
Density (kg/m^3)	1068	1840	511.9
C_p (kj/kg.K)	1.53	1.56	1.5

While determining the system parameters, both the studies in the literature have been examined and the values suitable for the properties of the fluid have been selected. Accordingly, different parameters for collector inlet and outlet temperatures, hot and cold storage tank temperatures have been determined. For refrigerant fluids, different parametric values have been determined for the pump inlet and outlet pressures and the steam temperature suitable for operating the turbine. The main parameters of the PTTSTPP are given in Table 3.

Table 3. The main parameters of the PTTSTPP.

Parameters	Values
Number of collectors	2531
T_A (℃)	290-310
T_B (℃)	390-410
T_C (℃)	380-400
T_D (℃)	280-300
P_1 (kPa)	610-1045
P_2 (kPa)	2000-3000
T_3 (℃)	100-120
η_{th}	0.88
η_P	0.8

2.1. Energy and Exergy Analysis

The system was analyzed according to the first and second laws of thermodynamics. Thermodynamic analysis of the system was carried out for steady regime conditions and the pressure losses in the system are neglected. For a continuous flow system, the mass balance is expressed in terms of the mass flow rate entering and exiting the system [18];

$$\Sigma \dot{m}_i = \Sigma \dot{m}_o \tag{1}$$

For continuous flow systems, the conservation of energy in terms of energy entering and exiting the system;

$$\sum \dot{E}_i - \sum \dot{E}_o = 0 \tag{2}$$

In a continuous flow system, the energy conservation equation for the energy transmitted by heat, work and mass is written as follows;

$$\dot{Q} + \dot{W} = \Sigma \dot{m}_o h_o - \Sigma \dot{m}_i h_i \tag{3}$$

Thermal efficiency is as follows [18];

$$\eta = \frac{\dot{W}_{net}}{\dot{Q}_i} \tag{4}$$

General exergy balance [18];

$$\Sigma \dot{E}x_i - \Sigma \dot{E}x_o = \Sigma \dot{E}x_d \tag{5}$$

$$\dot{E}x_{heat} + \dot{E}x_{work} + \dot{E}x_{mass,i} - \dot{E}x_{mass,o} = \dot{E}x_d \tag{6}$$

The expression on the right side of equality refers to exergy destruction. The expressions on the left side of the same equation, exergy generated by the heat interaction ($\dot{E}x_{heat}$), exergy generated by the interaction of the work ($\dot{E}x_{work}$) and exergy entering ($\dot{E}x_{mass,i}$) and exiting ($\dot{E}x_{mass,o}$) the mass due to the mass flow is defined as follows [18];

$$\dot{E}x_{heat} = \Sigma \left(1 - \frac{T_0}{T}\right) \dot{Q} \tag{7}$$

$$\dot{E}x_{work} = \Sigma \dot{W} \tag{8}$$

$$\dot{E}x_{mass,i} = \Sigma \dot{m}_i \psi_i \tag{9}$$

$$\dot{E}x_{mass,o} = \Sigma \dot{m}_o \psi_o \tag{10}$$

Exergy flow is calculated as follows;

$$\psi = (h - h_0) - T(s - s_0) \tag{11}$$

where h_0 ve s_0 refer to enthalpy and entropy values of the fluid at the dead state pressure and temperature, respectively.

Exergy efficiency can be defined as follows [18];

$$\varepsilon = \frac{\dot{E}x_{\text{ç}}}{\dot{E}x_g} = 1 - \frac{\dot{E}x_d}{\dot{E}x_g} \tag{12}$$

2.2. Economic Evaluation

NPV method is used in the economic analysis of the system. In this method, the cash flows of the project to be invested are determined according to the time value of money. Investments incurred due to cash outflow are taken as negative and earnings are taken as positive and a net result is obtained. If the result is negative, the investment project cannot be done and if it is positive, the decision to make is correct. NPV method can be expressed mathematically as follows;

$$NPV = \sum_{t=0}^{n} \frac{B_t}{(1+r)^t} \tag{13}$$

where n; the useful life of the project, B_t; cash flow in t year, r; discount rate. The B_t value is calculated by the following equation;

$$B_t = -C_{mr} - C_r - C_p + C_e \tag{14}$$

Cash flow contains the cost of maintenance and repair, the cost of refrigerant, the total annual personnel expenses and the cost of electricity. Cost data for the economic model is given in Table 4.

Table 4. Cost data for the economic model [10]

Parameters	Values
Solar Field	270.00 $\$/m^2$
Thermal Energy Storage System	80.00 $\$/kWh$
Power Block	830.00 $\$/kWe$
Minimum Wage	485.46 $
Electricity Unit Cost	0.13 $\$/kWh$
Discount Rate	13%

Maintenance and repair costs are included in the calculations as 2% of the initial investment cost. Initial investment cost consists of total cost and assembly cost. The total cost consists of the solar field cost, thermal energy storage system cost and power block cost given in Table 5. The assembly cost is 10% of the total cost. Refrigerant cost constitutes 10% of the power block cost. Personnel expenses were calculated using equation (15). The labor force requirement of the power plant has been included in the calculations by considering 1 manager, 1 engineer and 9 workers to meet the system operation. The minimum wage average of 2019 is based on [19].

$$C_p = 485.46 \cdot 12 \cdot (5 \cdot 1 + 3 \cdot 1 + 1.5 \cdot 9) \tag{15}$$

While calculating the cost of electricity for the system, the unit cost of electricity was included in accounts as 0.13 $\$/kWh$ [20]. Accordingly, the cost of electricity;

$$C_e = \dot{W}_p \cdot 0.13 \cdot 24 \cdot 300 \tag{16}$$

The useful life of the PTTSTPP has been determined as 20 years and the cost of the system was investigated by the NPV method.

2.3. Artificial Neural Network Modeling

The *ANN* model, which mimics the human brain in general, is inspired by biological neurons. It has emerged as a result of artificially simulation of the work system of the human brain. Various learning algorithms are available to obtain the relationships between inputs and outputs. The most widely used algorithm is forward feed backpropagation learning algorithm, and the most common variants to be adapted for this algorithm in the field of energy systems are LM, SCG and CGP. With the feedback propagation algorithm, ANN learns by changing link weights and these changes are stored as information.[10]

The performance of PTTSTPP was calculated using four average statistical parameters: Root Mean Square Error ($RMSE$), Mean Percentage Error (MPE), Coefficient of Variation (CoV) and Absolute Change Percentage (R^2) [10].

$$RMSE = \sqrt{\frac{1}{n}\sum_{i=1}^{n}(y_{output} - y_{actual})^2} \tag{17}$$

$$MPE = \frac{1}{n}\sum_{i=1}^{n}\left(\frac{y_{output}-y_{actual}}{y_{output}}\right) \tag{18}$$

$$CoV = \frac{\sum_{i=1}^{n}(y_{output}-\bar{y}_{output})(y_{actual}-\bar{y}_{actual})}{n} \cdot 100 \tag{19}$$

$$R^2 = \left[\frac{\sum_{i=1}^{n}(y_{output}-\bar{y}_{output})(y_{actual}-\bar{y}_{actual})}{\sum_{i=1}^{n}(y_{output}-\bar{y}_{output})^2 \sum_{i=1}^{n}(y_{actual}-\bar{y}_{actual})^2}\right]^2 \tag{20}$$

LM, SCG and CGP variants of feed-forward back-propagation algorithm were applied and logarithmic sigmoid (logsig) was used;

$$f(ze) = \frac{1}{1+e^{-ze_j}} \tag{21}$$

$$ze_j = \sum_{i=1}^{n} w_{ij}y_i + b_j \tag{22}$$

Although the ideal values of statistical tests such as $RMSE, MPE$ and CoV are close to 0 or 0, the value of R^2 should be close to 1 or 1[10]. ANN model of the system design is given in figure 3.

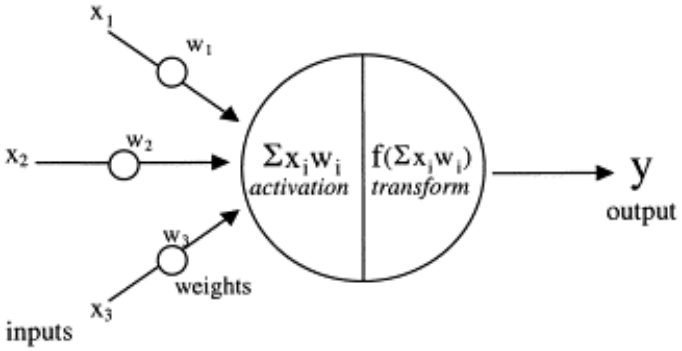

Figure 3. Model of the Artificial Neural Network neuron. [21].

3. RESULTS

The PTTSTPP system was designed by considering Bilecik's conditions. Thermodynamic analysis of this system was made according to different parametric values. In this context, the energy and exergy efficiencies of this system were calculated between 13.14-20.34 %, 16.83-23.88 %, respectively. Besides, the generated power of the system was determined to change between 78.1-281.9 MWh. The maximum generated power was observed when T_B is 390 ℃, T_A is 290 ℃, P_1 is 865 kPa, P_2 is 3 MPa and T_3 is 100 ℃. The energy and exergy efficiencies of the system in these conditions are 18.4 % and 23.6 %, respectively. The NPV values of the system, designed according to different parameters, have changed between 38 million US$ and 1.317 million US$.

In the ANN modeling of the PTTSTPP, the number of 10 inputs; solar radiations (I_t), ambient temperatures (T_0), inlet and outlet temperatures of the parabolic collector (T_A and T_B), temperatures of storage tanks (T_C and T_D), inlet and outlet pressures of the pump (P_1 and P_2), inlet temperatures of the turbine (T_3) and sunshine times (Δt) were used. NPV was obtained as the output. Using the MATLAB software, the *ANN* model was created. A total of 900 different data were used. In the training phase, 630 data were used. The remaining 270 data were reserved for testing. Increasing neuron numbers between 6 – 14 that gave the output closest to the actual value for 1000 iterations were used. The statistical results obtained are given in Table 5.

Table 5. The statistical results of the training and test data according to the NPV values.

Algorithm	Training				Test			
	R^2	*MPE*	*CoV*	*RMSE*	R^2	*MPE*	*CoV*	*RMSE*
LM-6	0.9994	0.5414	0.3874	0.0037	0.9993	0.6220	0.3231	0.0040
LM-8	0.9995	0.5911	0.3843	0.0037	0.9995	0.6313	0.3192	0.0039
LM-10	**0.9999**	**0.5100**	**0.3807**	**0.0031**	**0.9996**	**0.5602**	**0.3114**	**0.0030**
LM-12	0.9983	0.7255	0.4130	0.0053	0.9983	0.7182	0.3520	0.0052
LM-14	0.9996	0.4860	0.3975	0.0027	0.9996	0.5060	0.3322	0.0028
CGP-10	0.9985	0.7916	0.4065	0.0050	0.9981	0.8606	0.3440	0.0053
SCG-10	0.9978	0.0104	0.4053	0.0058	0.9973	0.0702	0.3435	0.0061

As shown in Table 5, obtained the statistical results are extremely satisfactory. The best results were obtained both in the training and testing stages in the LM-10 algorithm. The values of R^2, MPE, CoV and $RMSE$ were determined as 0.9999, 0.5100, 0.3807 and 0.0031, respectively for the output of NPV in training steps. These values were 0.9996, 0.5602, 0.3114 and 0.0030, respectively in the testing step. The comparison of the analysis and ANN values of the NPV is given in figure 4.

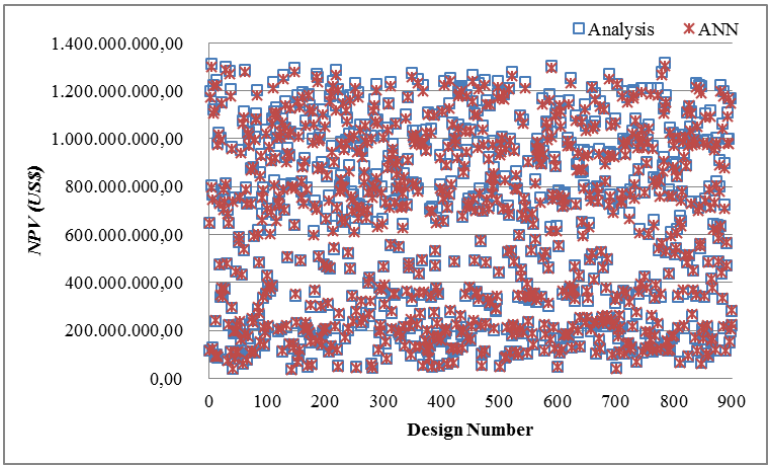

Figure 4. The comparison of the Analysis and ANN values of the NPV.

As shown in the figures, the results of the analysis and ANN values very close to each other. Similarly, excellent results were obtained even with unspecified test values. Therefore, it was concluded that these values were statistically acceptable. According to the results obtained, the error percentage of the analysis results and the ANN results were found to be 0.013%.

4. CONCLUSION

In this paper, the thermo-economic analysis of PTTSTPP was made. ANN algorithm with feed-forward back-propagation learning algorithm and LM, CGP, SCG variants were used to predict of the NPV. These algorithms were evaluated by statistical methods, such as R^2, MPE, CoV and $RMSE$. The best results were obtained in the LM-10 algorithm during the training and testing steps. As a result of the thermodynamic analysis, the energy and exergy efficiencies, that the system with maximum generated power, were determined as 18.4% and 23.6%, respectively. In addition, the profitability value of the system has been determined as 1.317 million US$. When the analysis results and ANN results were compared, the error percentage was found to be 0.013 %. This value is an acceptable error rate. As a result, ANN has given acceptable results in the solution of very complex power plants. Therefore, it can be easily used in the design and optimization of many engineering applications.

5. REFERENCES

[1] Ferrara, F., Gimelli, A., & Luongo, A. (2014). Small-scale concentrated solar power (CSP) plant: ORCs comparison for different organic fluids. *Energy Procedia*, 45(68th), 217-226.

[2] Kumar, S., & Kaur, T. (2016). Development of ANN based model for solar potential assessment using various meteorological parameters. *Energy Procedia*, *90*, 587-592.

[3] Arslan, O., & Yetik, O. (2011). ANN based optimization of supercritical ORC-Binary geothermal power plant: Simav case study. *Applied Thermal Engineering*, 31(17-18), 3922-3928.

[4] Şencan, A., Yakut, K. A., & Kalogirou, S. A. (2006). Thermodynamic analysis of absorption systems using artificial neural network. *Renewable Energy*, *31*(1), 29-43.

[5] Sozen, A., Ozalp, M., Arcaklioglu, E., & Galip Kanit, E. (2004). A study for estimating solar resources in Turkey using artificial neural networks. *Energy Sources*, *26*(14), 1369-1378.

[6] Arslan, O. (2011). Power generation from medium temperature geothermal resources: ANN-based optimization of Kalina cycle system-34. *Energy*, *36*(5), 2528-2534

[7] Al-Sulaiman, F. A. (2014). Exergy analysis of parabolic trough solar collectors integrated with combined steam and organic Rankine cycles. *Energy Conversion and Management*, *77*, 441-449.

[8] Boukelia, T. E., Mecibah, M. S., Kumar, B. N., & Reddy, K. S. (2015). Investigation of solar parabolic trough power plants with and without integrated TES (thermal energy storage) and FBS (fuel backup system) using thermic oil and solar salt. *Energy*, *88*, 292-303.

[9] Şenkal, O. (2010). Modeling of solar radiation using remote sensing and artificial neural network in Turkey. *Energy*, *35*(12), 4795-4801.

[10] Boukelia, T. E., Arslan, O., & Mecibah, M. S. (2017). Potential assessment of a parabolic trough solar thermal power plant considering hourly analysis: ANN-based approach. *Renewable Energy*, *105*, 324-333.

[11] Gunasekar, N., Mohanraj, M., & Velmurugan, V. (2015). Artificial neural network modeling of a photovoltaic-thermal evaporator of solar assisted heat pumps. *Energy*, *93*, 908-922.

[12] Kalogirou, S. A. (2004). Optimization of solar systems using artificial neural-networks and genetic algorithms. *Applied Energy*, *77*(4), 383-405.

[13] General directorate of renewable energy. www.yegm.gov.tr/MyCalculator/pages/11.aspx (date of access 10.06.2019), in Turkey

[14] Yüksel, Y. E. (2018). Thermodynamic assessment of modified Organic Rankine Cycle integrated with parabolic trough collector for hydrogen production. *International Journal of Hydrogen Energy*, 43(11), 5832-5841.

[15] THERMINOL VP1 br\376 .pdf. http://www.lubratech.com.tr. (date of access 10.09.2018) in Tukey.

[16] Sohal M.S., Ebner, M.A., Sabharwall, P., Sharpe, P. (2010). "*Engineering Database of Liquid Salt Thermophysical and Thermochemical Properties*", Idaho National Laboratory.

[17] REFPROP. (2010). Reference Fluid Thermodynamics and Transport Properties. NIST Reference Database. Version 9.0. *National Institute of Standards and Technology*, NIST, USA.

[18] Cengel, Y., & Boles, M. (1996). Thermodynamics with Engineering Approach. (Translation: T. Derbentli). Istanbul: McGraw-Hill- Literature Publishing.

[19]Ministry of Family, Labor and Social Services Turkish Republic. https://ailevecalisma.gov.tr/istatistikler/calisma-hayati-istatistikleri/asgari-ucret/asgari-ucret-2019/(date of access 2018, January).

[20] Ministry Of Energy And Natural Resources of Turkish Republic. https://www.enerji.gov.tr/tr-TR/Sayfalar/Elektrik. (date of access 2018, August).

[21] Agatonovic-Kustrin, S., & Beresford, R. (2000). Basic concepts of artificial neural network (ANN) modeling and its application in pharmaceutical research. *Journal Of Pharmaceutical And Biomedical Analysis*, 22(5), 717-727.

A STUDY OF THE EFFECT OF BAFFLES INSIDE SOLAR COLLECTOR

Burcu GÜLMEZ*, Ayşe Bilgen AKSOY**
*Manisa Celal Bayar University, Mechanical Engineering, Manisa/Turkey
Email: burcugulmez@gmail.com
** Manisa Celal Bayar University, Energy Systems Engineering, Manisa/Turkey
Email: aysebilgen.aksoy@cbu.edu.tr

ABSTRACT

Nowadays, solar collectors are used in many areas such as space heating, hot water production, drying of agricultural products. In order to improve the solar collector technology, it is essential to analyze the flat plate solar collector performance and their optimum condition. In this study, air solar collectors using air as carrier fluid are discussed. The finite element method was used to analyze the standard-sized solar air collector with baffles in the airflow path and the flat absorber plate. The effect of baffle geometries on the efficiency of the collector is discussed. 3D models of absorbent plates, glass cover, and baffles were modeled by ANSYS Workbench. It was found that the outlet temperature is lower in the case of flat plate air collectors than baffled solar air collectors. With the installation of the internal baffles, the outlet temperature of the collector has been increased, and its efficiency has been improved by approximately 5% on an hourly basis.

Keywords: Solar Collector, efficiency, ANSYS.

1. INTRODUCTION

Due to environmental issues and limited fossil fuel resources, increasing attention is being given to renewable energy sources [1]. Increasing clean and renewable energy sources, generating electricity from renewable energy, and increasing energy efficiency gain importance due to the rapid decline of fossil fuels and adverse effects on the environment. Among the different renewable energy technologies, solar energy is the best option because of its advantages, such as abundant availability, sustainability, and production on a larger scale at a relatively lower cost than other renewable energy sources [2].

The solar collectors can be classified according to the working fluid they use. The most commonly used working fluid is fluid water and air. Air solar collectors collect the sun's radiation and transfer it to the air used as a fluid. In this process, the air entering the collector absorbs heat energy as it passes through the channel between the absorbent surface and the transparent upper surface. This heat energy, which is taken into the air, is sent to the environment where the process will be carried out by being conditioned.

Operating parameters such as ambient temperature and solar radiation intensity have a significant effect on temperature rise but have little effect on collector efficiency [3]. When the literature studies are examined, increasing the collector efficiency is based on increasing the heat transfer area and reducing the heat losses. Attaching the baffles and partitions to the absorber plate is one of the effective techniques used to increase the heat transfer rate in solar air heaters as they extend the heat transfer area and create more turbulence [4]. Wei et al. [5] developed a geometric optimization method for the design of baffles and compartments to be placed in the airflow compartment. Promvonge [6] used V-shaped baffles and observed a significant increase in the Nusselt number. Daliran and Ajabshirchi [7] determined that attaching rectangular fins to the airflow path improves the performance of the solar collector. Amraoui and Aliane [8] increased the outlet air temperature using baffle structures.

In this study, air solar collectors using air as carrier fluid are discussed. The finite element method was used to analyze the standard-sized solar air collector with baffles in the airflow path and the flat absorber plate. The

effect of baffle geometries on the efficiency of the collector is discussed. ANSYS FLUENT is used to analyze and visualize the flow across the duct of a solar air heater. The 3D models of the solar air collectors involving air inlet, absorber plate, glass cover, and insulation are model by ANSYS Workbench. The numerical solution is obtained in ANSYS FLUENT, which uses a finite volume method for solving the governing continuity, momentum, energy, and k-ε model equations [9]. CFD is a numerical simulation technique that does not require prototyping, is not obstructed by measurement capabilities, and can provide highly detailed data when required. Using CFD analysis saves time as many options can be tested before production [10].

2. NUMERICAL MODEL

2.1 Geometry

In this study, two solar air collectors, with baffles and one without baffles, were examined, as shown in Figure 1. The overall dimension for the solar air collector is 1940x936x94 mm^3 with a 4 mm thick glass plate placed at the top side of the collector. Baffles size 600x77 mm with a 4 mm thickness, of rectangular shape, which placed at equal distances. Glass wool is used as insulation material. Material properties are shown in Table 1.

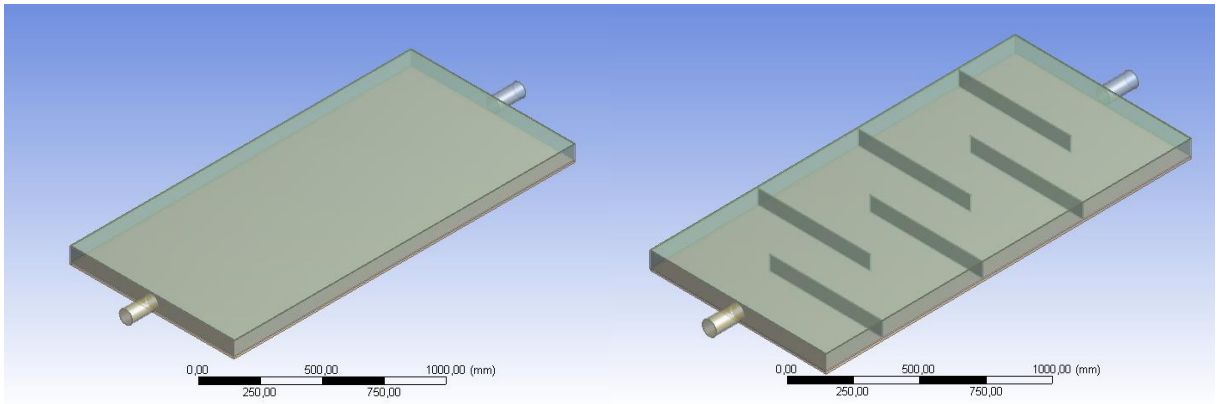

Figure 1. Solar Air Collectors

Table 1. Physical Properties of Materials [11]

Material	Density (kg/m3)	Thermal Conductivity (W/mK)	Specific Heat (J/kgK)
Aluminum	2719	202.4	871
Glass	2800	1,1	750
Glass Wool	52	0.034	657

To improve mesh quality, mesh parameters such as element quality, skewness, and orthogonal quality were considered. An average element mesh quality of 0.8 and above is considered acceptable [12]. Standard skewness and orthogonal quality mesh metrics spectrums were shown in Figure 2.

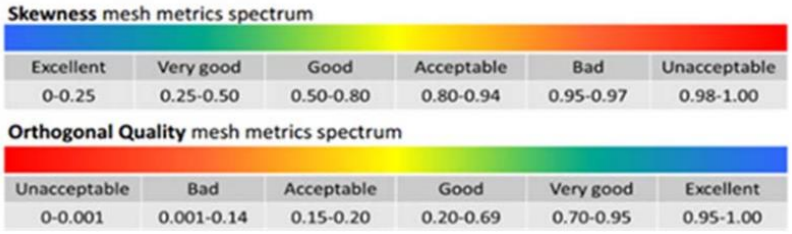

Figure 2. Skewness and orthogonal quality mesh metrics spectrums [12].

The mesh selection was made by running the same simulation with different dimensions and comparing the results' accuracy. In this study, the range of maximum skewness varies between 0.82 – 0.89.

2.2 Numerical Setup

Numerical simulations were carried out with transient state and pressure-based solver. For turbulence modeling, realizable k-ε model with standard wall functions has been used. Heating of surfaces due to radiation can be achieved in CFD model using Discrete Transfer Radiation Model, or P-1 Radiation Model, or Rosseland Radiation Model, or Surface-to-Surface (S2S) Radiation Model, or Discrete Ordinates (DO) Radiation Model [13]. In this paper, Rosseland Radiation Model is used. The solar calculator is used to track the solar irradiation for the analysis by taking 7th July as the day for the sunshine with fair weather conditions. The location has a longitude and latitude angle of 38,42373 and 27,14283. The analysis is carried out from 10 am to 3 pm of the day. Radiation and convection from the glass cover to the ambient is modeled using mixed boundary condition.

In both simulations, boundary conditions are specified as; 'Velocity Inlet' for collector inlet and 'Pressure Outlet' for collector outlet. Air at the inlet has a turbulence specification method of turbulent intensity and viscosity ratio with 5 % and %10, respectively. The glass cover surface is exposed to sunlight. No-slip condition has been used on the walls. Pressure outlet boundary condition with zero gauge pressure has been used at the outlet.

The following assumptions are made in the analysis for both simulations:

1. The system is considered in transient state conditions.
2. The ambient temperature is 300 K and considered a constant.
3. Pressure outlet boundary condition with zero gauge pressure has been used at the outlet.

2.3 Efficiency

Flow analysis can be done experimentally and theoretically. In the theoretical analysis, it is divided into two as Control volume and differential analysis. In the energy analysis of the collectors, the control volume approach is often used for theoretical analysis. The theoretical analysis of the collector with the acceptance of control volume can be done with the results of the experimental analysis using the following equations.

Usable heat transferred to the working fluid [14]:

$$Q_u = m.c_p.(T_{out} - T_{in}) \quad (1)$$

"m" in the equation refers to the mass flow of air, "C_p" refers to the specific heat value of the air at constant pressure, "T_{in}" refers to the collector inlet temperature of the air, "T_{out}" refers to the collector outlet temperature of the air.

Heat from solar energy:

$$Q_g = I.A_c \tag{2}$$

In the equation, I (W / m^2) is the radiation intensity from the sun per unit area, and A_c (m^2) is the collector area.

The collector efficiency can be found from the amount of heat passing into the fluid to the amount of heat coming from the sun [15].

$$\eta = \frac{Q}{Q_g} \tag{3}$$

3. RESULTS

Numerical analysis of two collectors was carried out using the same boundary conditions, the outlet temperatures and efficiencies were compared in the results. When the results are analyzed, natural transport has occurred due to the low flow rate, and therefore, the efficiency is low. Despite low efficiency, it was found that the outlet temperature is lower in the case for flat plate air collector than baffled solar air collector. As shown in Figure 3. and Figure 4., with the installation of the internal baffles, the output temperature of the collector has been increased, and its efficiency has been improved.

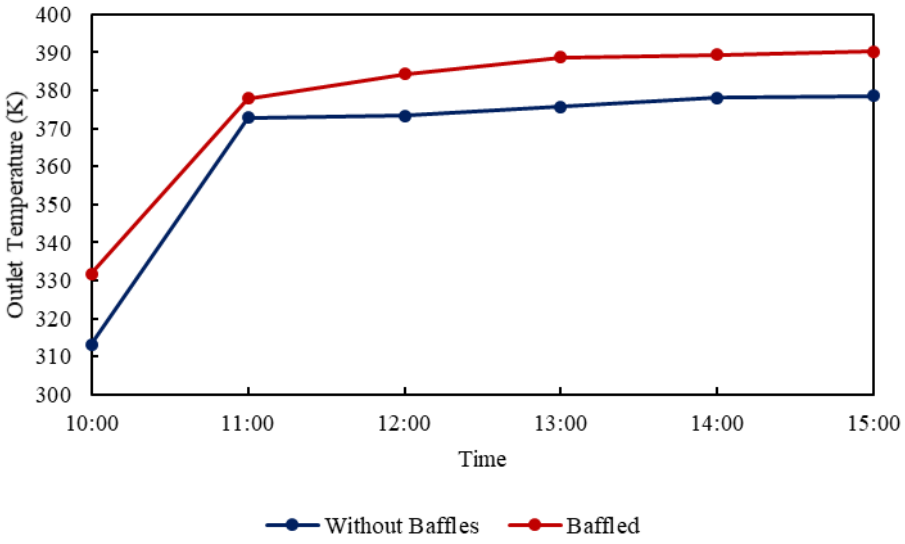

Figure 3. Comparison of Outlet Temperatures

During the day, the collector output temperature difference was calculated as maximum 18 ºC and minimum 5 ºC. While the outlet temperature in the collector reached 105 ºC, the outlet temperature in the baffled collector reached about 120 ºC. With the addition of the baffle structure to the collector, the efficiency increases of approximately 5% were achieved on an hourly basis, as shown in Figure 4.

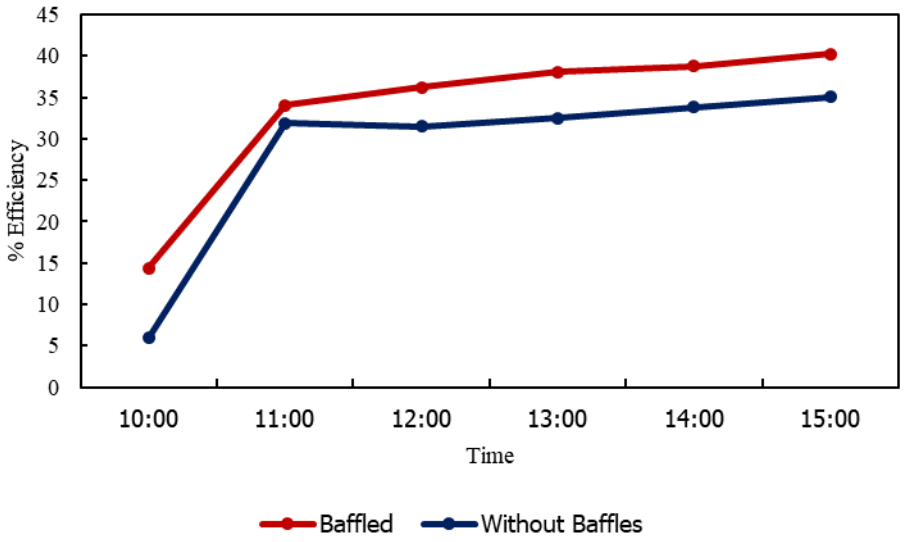

Figure 4. Comparison of Efficiency

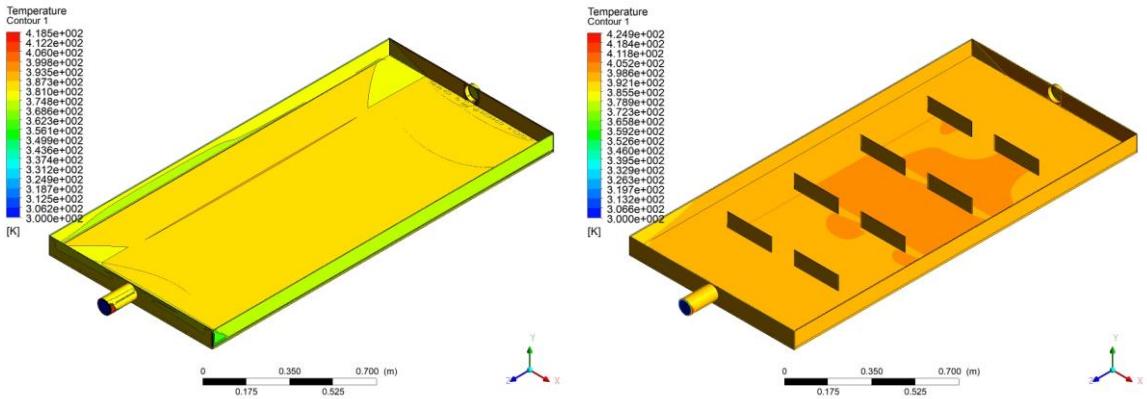

Figure 5. Temperature Contours of Collectors

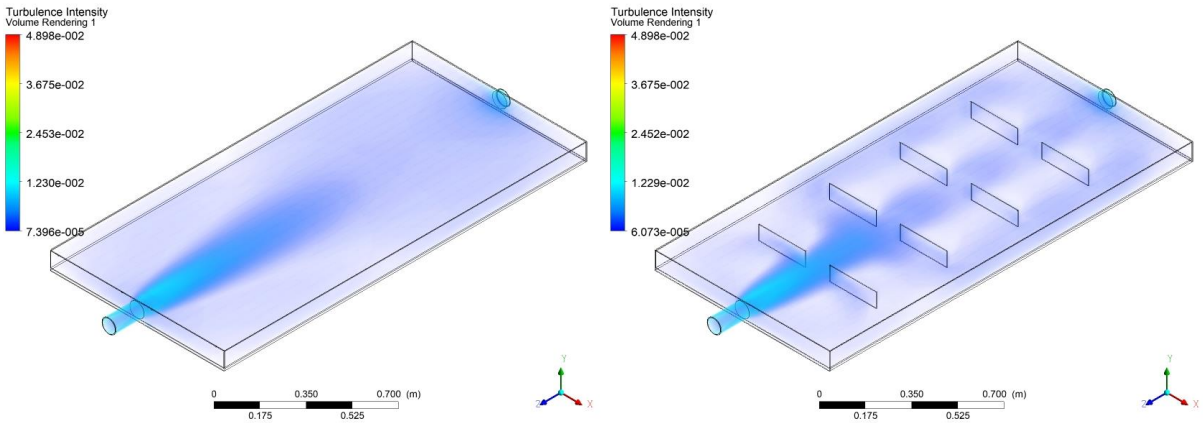

Figure 6. Turbulence Intensity of Collectors

Due to the current design, the two designs did not differ much in turbulence, as shown in Figure 6. In future studies, in order to obtain more efficient results, different baffle designs can be made by calculating the optimum baffle number. The increased temperature obtained can be integrated into many industrial systems such as space heating, food drying, and timber drying.

ACKNOWLEDGEMENTS

The experiments of this work are realized with the support of Manisa Celal Bayar University BAP project of number 2019-057.

REFERENCES

[1] Zima, W., Dziewa, P. Modelling of liquid flat-plate solar collector operation in transient states, Proceedings of the Institution of Mechanical Engineers, Part A: Journal of Power and Energy, 225, 53–62, 2011.

[2] Imtiaz Hussain, M., Ménézo, C., Kim, J. T. Advances in solar thermal harvesting technology based on surface solar absorption collectors: A review. Solar Energy Materials and Solar Cells, 187, 123–139, 2018.

[3] Hu, J., Sun, X., Xu, J., Li, Z. Numerical analysis of mechanical ventilation solar air collector with internal baffles. Energy and Buildings, 62, 230–238, 2013.

[4] Sabzpooshani, M., Mohammadi, K., Khorasanizadeh, H. Exergetic performance evaluation of a single pass baffled solar air heater. Energy, 64, 697–706, 2014.

[5] Luo, L., Wei, M., Fan, Y. Design and optimization of baffled fluid distributor for realizing target flow distribution in a tubular solar receiver. Energy, 136, 1236-134, 2018.

[6] Baissi, M. T., Brima, A., Aoues, K., Khanniche, R., Moummi, N. Thermal behavior in a solar air heater channel roughened with delta-shaped vortex generators. Applied Thermal Engineering, 165, 2019.

[7] Daliran, A., Ajabshirchi, Y. Theoretical and experimental research on effect of fins attachment on operating parameters and thermal efficiency of solar air collector. Information Processing in Agriculture, 5, 411–421, 2018.

[8] Amraoui, M. A. & Aliane, K. Three-dimensional analysis of air flow in a flat plate solar collector, Periodica Polytechnica Mechanical Engineering, 62, 126–135, 2018.

[9] Mwesigye, A., Bello-Ochende, T., Meyer, J. P. Minimum entropy generation due to heat transfer and fluid friction in a parabolic trough receiver with non-uniform heat flux at different rim angles and concentration ratios. Energy, 73, 606–617, 2014.

[10] Yadav, A. S. & Bhagoria, J. L. Modeling and simulation of turbulent flows through a solar air heater having square-sectioned transverse rib roughness on the absorber plate, The Scientific World Journal, 2013, 964–971, 2013.

[11] ASHRAE, 2017, 2017 Ashrae handbook: Fundamentals: Si edition.

[12] Fatchurrohman, N., Chia, S.T. Performance of hybrid nano-micro reinforced mg metal matrix composites brake calliper: Simulation approach, IOP Conference Series: Materials Science and Engineering , 257, 2017.

[13] Ali, B. H., Gilani, S. I., Al-Kayiem, H. H. A three dimensional performance analysis of a developed evacuated tube collector using a CFD fluent solar load model. MATEC Web of Conferences, 13, 3–7, 2014.

[14] Bellos, E., Tzivanidis, C. Investigation of a star flow insert in a parabolic trough solar collector. *Applied Energy*, **224**, 86–102, 2018.

[15] Bensaci, C., Moummi, A., Labed, A. Experimental Investigation on Heat Transfer Coefficient and Thermal Efficiency of Solar Air Heaters Having Different Baffle, *Environmentally-Benign Energy Solutions*, 309-321, 2020.

EXERGY ANALYSIS OF A SOLAR POWER PLANT AND COMPARISON OF PRODUCTION VALUES WITH SOFTWARE

Burcu GÜLMEZ*, Ramazan KÖSE, Oğuz Ozan YOLCAN*****
*Manisa Celal Bayar University, Department of Mechanical Engineering, Manisa / Turkey
Email: burcugulmez@gmail.com
**Kütahya Dumlupınar University, Department of Mechanical Engineering, Kütahya / Turkey
Email: ramazan.kose@dpu.edu.tr
***Kütahya Dumlupınar University, Department of Mechanical Engineering, Kütahya / Turkey
Email: oguzozan.yolcan@dpu.edu.tr

ABSTRACT

In this study, one-year production values of a 910 kW solar power plant in Eskişehir were compared with the simulation in computer software, and energy and exergy analyses was performed for a photovoltaic panel with 250 W power used throughout the year. The values obtained in the simulation made with the System Advisor Model software were found to be 2% different from the actual production values. Annual energy and exergy analysis were performed by using the production values and technical characteristics of the panel and meteorological data. After the energy and exergy analysis, the average annual energy efficiency was calculated as 13.5% ,and the annual average exergy efficiency was calculated as 12.6%. According to the values obtained, it was observed that energy and exergy efficiencies decreased as the ambient temperature increase.

Keywords: Solar energy, simulation, exergy analysis

1. INTRODUCTION

Due to the negativities caused by fossil fuels and their limited amounts, the demand for renewable energy sources in Turkey and in the world has been high in recent years. High investment costs and generally low efficiency of renewable energy systems make it necessary to increase the efficiency of the systems as much as possible. For this purpose, energy and exergy analyzes are applied.

There are many studies in the literature on energy and exergy analysis of photovoltaic panels. Akyüz et al. Proposed a new method to determine the maximum amount of exergy from the sun to formulate exergy efficiency when applied to a photovoltaic (PV) system. Exergy differences in productivity, which have been investigated using real experimental data obtained from the installation of a PV system in Turkey. A new computer program has been produced for data analysis in Matlab-Simulink software environment. Then, all results were compared [1]. Colombo et al. Constitute a general thermoeconomic method, taking into account the economic and environmental impacts of energy cycle integration, the impact of life cycle inefficiencies. The method here is a comparison of the productive mixture between a photovoltaic power plant (PV) and a standard commercial, non-cogenerated gas turbine plant (GT). The effects of different methods on both monetary and electricity exergy costs are evaluated. While the economic cost assessment is made with standard thermoeconomic techniques, exergy costs are evaluated using both Extended Exergy Accounting (EEA) and Thermo-Ecological Cost (TEC) methods [2]. Bayat et al. Conducted experimental work on a polycrystalline solar photovoltaic (PV) module to determine its performance characteristics through energy, exergy, and execonomic analysis. Energy and exergy analyzes were made according to the first and second laws of thermodynamics. Thus, energy and maximum electricity, power conversion and exergy efficiency are calculated as functions of environmental, operational and design parameters. Exejoeconomic analysis was found by calculating the exergy breakdown and energy loss rate of PV in order to determine the actual product cost of the system. According to the analyzes conducted in this study, power conversion efficiency varies between 9.6% and

18.3%, while maximum electrical efficiency ranges between 12.6% and 23.12% [3]. Rajoria et al. Conducted energy and exergy analysis for different configurations of the hybrid photovoltaic thermal (PVT) array. Hybrid PVT array are serial and parallel combinations of PV modules. A one-dimensional temporary model has been developed for the hybrid PVT array using basic heat transfer equations. Based on this temporary model, they proposed to choose a hybrid PVT array suitable for different climatic conditions of India [4]. Fujisawa et al. Have designed and manufactured a photovoltaic-thermal hybrid collector. The collector consists of a liquid heating flat plate solar collector with mono-Si PV cells on the aluminum absorber plate. In the study, concepts based on exergy theory were adopted. From an exergy-based annual experimental evaluation, it was concluded that the PV / T collector can produce higher output density from a unit PV module or liquid heating flat plate solar collector [5]. Bayrak et al. Conducted a comprehensive study on exergy analysis and performance evaluation of various solar energy methods. Exergy analysis is a useful analysis to evaluate and improve energy systems. The systems studied include photovoltaic (PV) and hybrid solar collectors [6].

2. MATERIAL AND METHOD

In this study, hourly data of a photovoltaic panel with a power of 250 W was obtained with the help of System Advisor Model (SAM) [7] software using the meteorological data of Eskişehir province and with the help of these data, the exergy inputs and outputs, energy and exergy efficiencies of the system were calculated. In the calculations, hourly environmental temperature, hourly wind speed and solar radiation values of Eskişehir were used on a yearly basis.

2.1. Material

As can be seen in Figure 1, the highest temperature average in Eskişehir, located in the Northern Hemisphere, is observed in July and August. The average temperature in July and August has been reported as approximately 23.5 ºC. In January, which has the lowest average temperature, the average temperature was specified as approximately 0.7 ºC. The lowest ambient temperature was stated as -11.5 ºC on January 12, the highest air temperature as 35.5 ºC on July 21. The annual average environmental temperature of Eskişehir is specified as 12 ºC. As seen in Figure 2, the highest monthly average wind speed value in Eskişehir was measured in July with a value of 3 m / s. The lowest monthly average wind speed value is observed in November with 2.1 m / s. The highest wind speed was specified on September 8 with a value of 16.7 m / s. The average annual wind speed of Eskişehir is 2.5 m / s. In Figure 3, hourly solar radiation values of Eskişehir province are shared on a yearly basis. As expected, the highest solar radiation values are seen in the summer months.

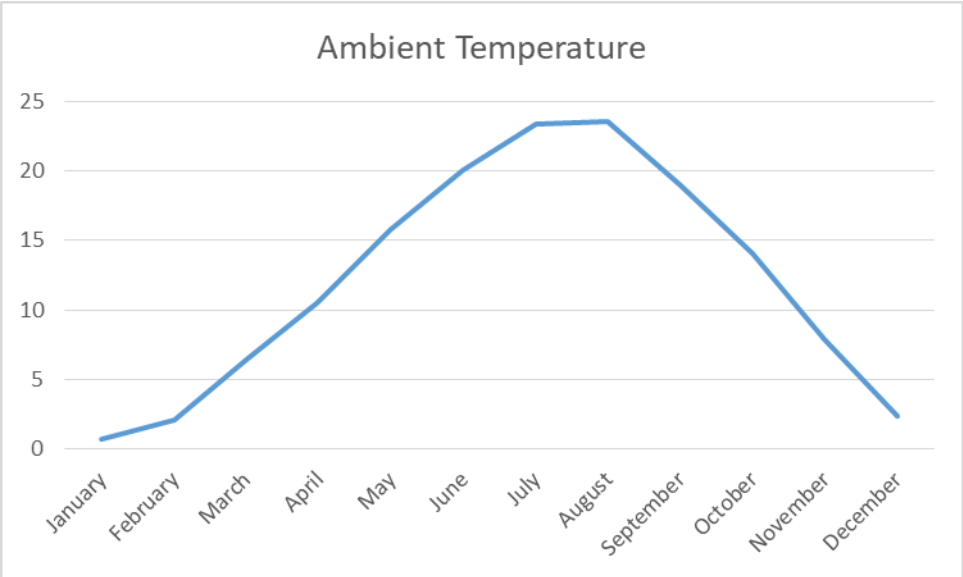

Figure 1. Ambient temperature of Eskişehir

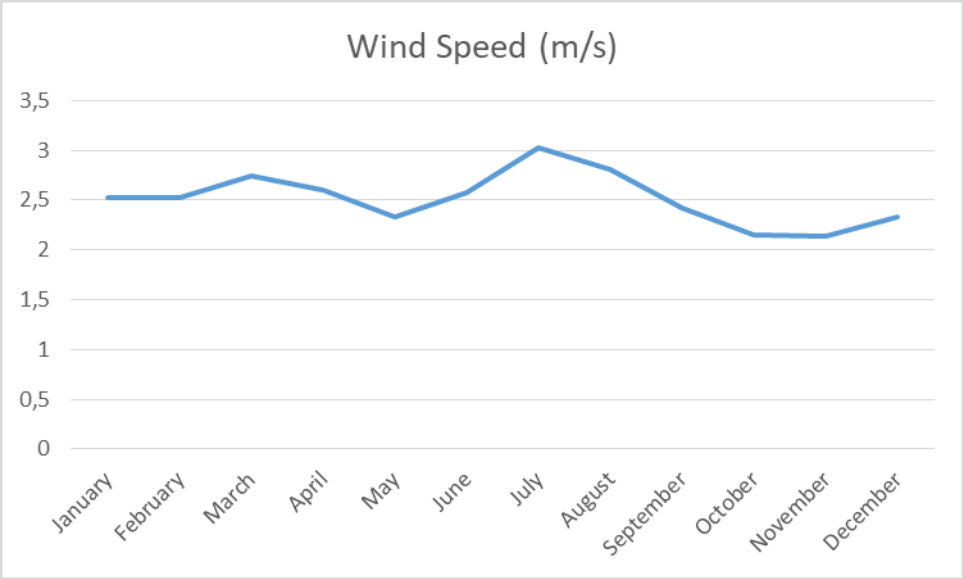

Figure 2. Average wind speed of Eskişehir

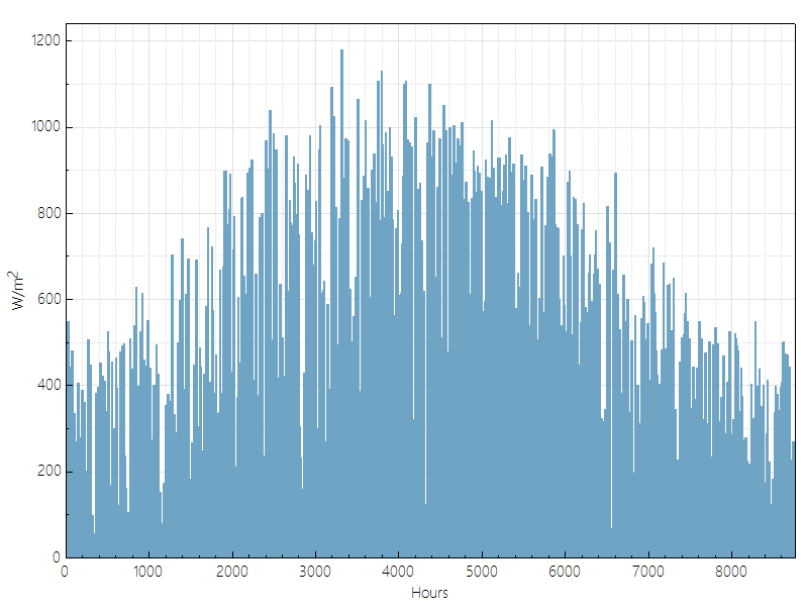

Figure 3. Radiation values of Eskişehir

2.2. Method

Various thermodynamic analysis methods were applied for the photovoltaic panel selected in the study. The efficiency of photovoltaic panels are the ratio of the product of maximum voltage (V_m) and maximum current (I_m) to the product of solar radiation (I_m) and panel area (A). Energy efficiency of photovoltaic panels can be calculated with Eq. 1;

$$\eta = \frac{V_m . I_m}{S_t . A} \quad (1)$$

Exergy transfer to the photovoltaic panel can be calculated with Equation 2 and Equation 3;

$$\sum \dot{E}x_g = \sum \dot{E}x_ç + \sum \dot{E}x_d + \sum \dot{E}x_k \tag{2}$$

$$\dot{E}x_ç = \dot{E}x_m - \sum \dot{\Gamma} - \dot{E}x_k \tag{3}$$

In these equations; $\dot{E}x_g$, the incoming exergy; $\dot{E}x_ç$, the outcoming exergy; $\dot{E}x_d$, exergy destruction; $\dot{E}x_k$, thermal exergy; $\dot{E}x_m$, the maximum exergy output; $\dot{\Gamma}$ denotes irreversibilities. The electrical exergy output of the system can be calculated by subtracting irreversibilities from the maximum exergy output (Equation 4);

$$\dot{E}x_m - \sum \dot{\Gamma} = V_{ad} I_{kd} - (V_{ad} I_{kd} - V_m I_m) = V_m I_m \tag{4}$$

In this equation, V_{ad} denotes open circuit voltage, I_{kd} short circuit current. Heat transfer from the system by convection can be calculated with Equation 5;

$$Q = h_c . A . (T_{hüc} - T_0) \tag{5}$$

In this equation, h_c is the heat transfer coefficient; $T_{hüc}$, cell temperature; T_0 expresses the ambient temperature. The heat transfer coefficient can be calculated with Equation 6;

$$h_c = 5{,}7 + 3{,}8 . V \tag{6}$$

In this equation, V represents the wind speed. Thermal exergy can be calculated with Equation 7;

$$\sum \dot{E}x_k = (1 - \frac{T_0}{T_{hüc}})[(5{,}7 + 3{,}8 . V) . A . (T_{hüc} - T_0)] \tag{7}$$

After performing the necessary actions, exergy from the system and exergy entering the system are expressed as Equation 8 and Equation 9;

$$\sum \dot{E}x_ç = V_m I_m - (1 - \frac{T_0}{T_{hüc}}) . [h_c . A . (T_{hüc} - T_0)] \tag{8}$$

$$\sum \dot{E}x_g = S_t . A . (1 - \frac{T_0}{T_G}) \tag{9}$$

In this equation, T_G represents the solar surface temperature. The exergy efficiency of the system can be calculated with Equation 10;

$$\Psi = \frac{\dot{E}x_ç}{\dot{E}x_g} = \frac{V_m I_m - (1 - \frac{T_0}{T_{hüc}}) . [h_c . A . (T_{hüc} - T_0)]}{S_t . A . (1 - \frac{T_0}{T_G})} \tag{10}$$

3. COMPARISON OF PRODUCTION VALUES

The installed photovoltaic power plant with a power of 910 kW was simulated in the System Advisor Model software. The difference of the simulation values from the actual production values was calculated as an average of 2%.

Table 1. Simulation of solar power plant

	Production 2017	Production 2018	SAM	Prod. Average	SAM Difference
January	74,580	92,670	83,700	83,625	-0,0009
February	97,710	83,970	87,699	90,840	0,034577
March	136,220	109,460	121,798	122,840	0,008483
April	157,410	178,110	141,443	167,760	0,156873
May	152,820	158,970	146,761	155,895	0,058591
June	168,110	165,090	161,756	166,600	0,029076
July	202,490	179,220	178,666	190,855	0,063865
August	182,230	181,500	175,232	181,865	0,036472
September	171,600	168,760	146,446	170,180	0,139464
October	133,920	134,310	119,182	134,115	0,111345
November	94,760	96,150.60	107,583	95,455.3	-0,12705
December	89,300	59,049.90	94,087	74,174.95	-0,26845
					2%

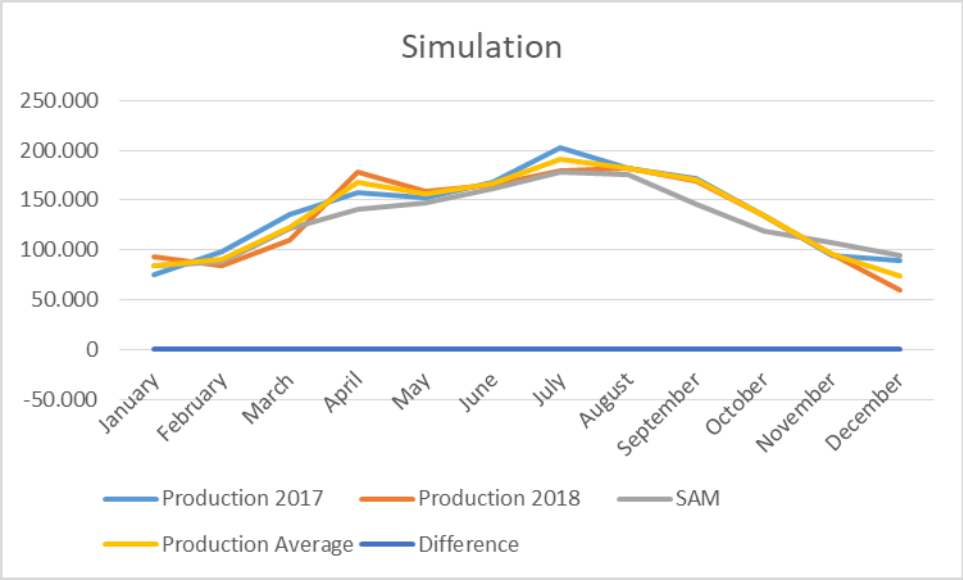

Figure 4. Simulation of solar power plant

4. RESULTS AND DISCUSSIONS

Temperature values of photovoltaic cells on an hourly basis are shown in Figure 5. Energy efficiency of the photovoltaic panel calculated as; 17.93% for January, 15.75% for February, 13.99% for March, 12.72% for

April, 11.61% for May, 10.59% for June, July 10.58% for August, 11.49% for August, 12.62% for September, 14.5% for October, 16.83% for November, 18.31% for December. Exergy efficiency of the photovoltaic panel calculated as; 17.0% for January, 14.98% for February, 13.13% for March, 11.78% for April, 10.75% for May, 9.56% for June, July % 9.48 for August, 10.35% for August, 11.48% for September, 13.52% for October, 15.64% for November, 17.39% for December.

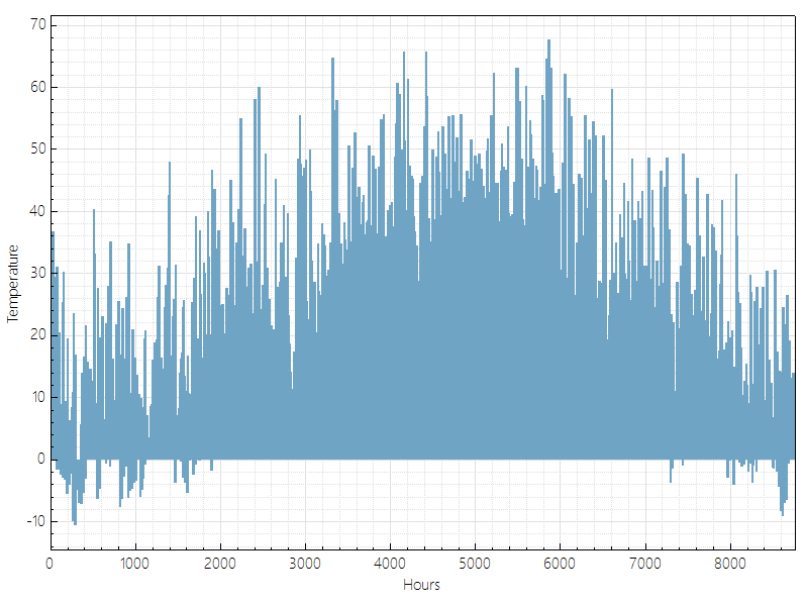

Figure 5. Hourly temperature values of solar cells

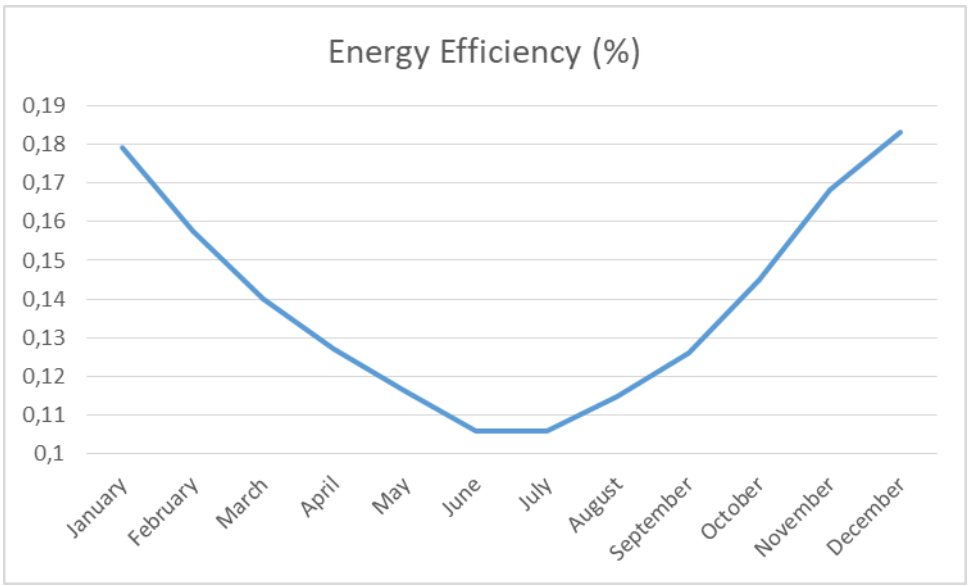

Figure 6. Energy efficiency of photovoltaic panel

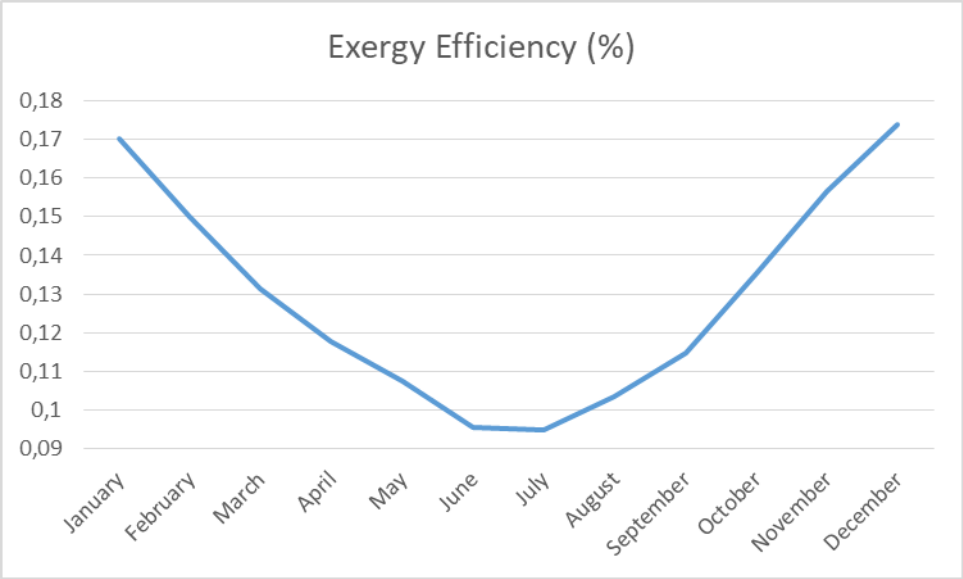

Figure 7. Exergy efficiency of photovoltaic panel

The energy efficiency, exergy efficiency and temperature relationship of the photovoltaic panel can be seen in Figure 8. As the ambient temperature rises, the energy efficiency and exergy efficiency of the photovoltaic panel decrease.

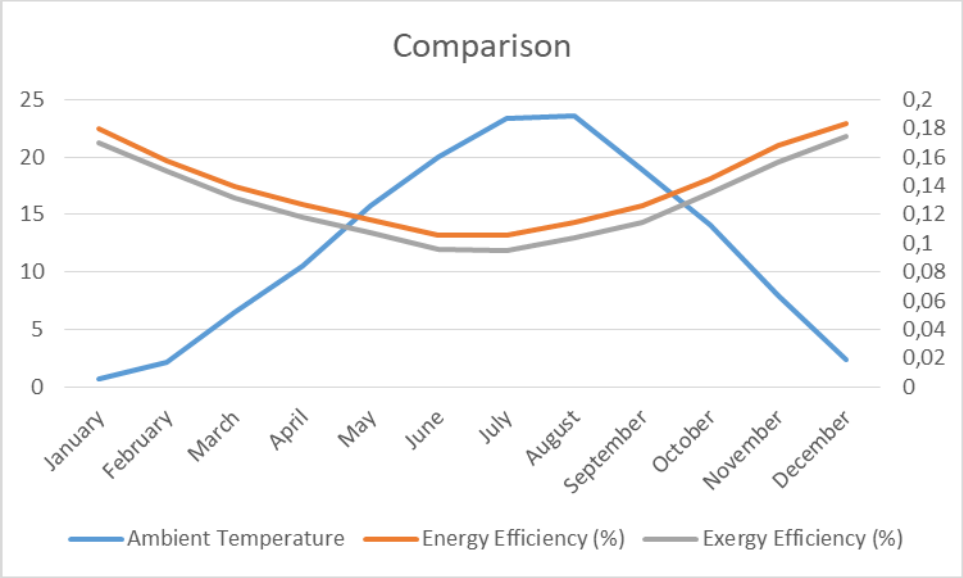

Figure 8. Energy efficiency, exergy efficiency and temperature relationship.

REFERENCES

[1] Akyuz, E., Coskun, C., Oktay, Z., & Dincer, I. (2012). A novel approach for estimation of photovoltaic exergy efficiency. Energy, 44(1), 1059–1066. doi: 10.1016/j.energy.2012.04.036

[2] Colombo, E., Rocco, M. V., Toro, C., & Sciubba, E. (2015). An exergy-based approach to the joint economic and environmental impact assessment of possible photovoltaic scenarios: A case study at a regional level in Italy. Ecological Modelling, 318, 64–74. doi: 10.1016/j.ecolmodel.2014.11.006

[3] Bayat, M., & Ozalp, M. (2018). Energy, Exergy and Exergoeconomic Analysis of a Solar Photovoltaic Module. Exergetic, Energetic and Environmental Dimensions, 383–402. doi: 10.1016/b978-0-12-813734-5.00022-6

[4] Rajoria, C., Agrawal, S., & Tiwari, G. (2012). Overall thermal energy and exergy analysis of hybrid photovoltaic thermal array. Solar Energy, 86(5), 1531–1538. doi: 10.1016/j.solener.2012.02.014

[5] Fujisawa, T., & Tani, T. (1997). Annual exergy evaluation on photovoltaic-thermal hybrid collector. Solar Energy Materials and Solar Cells, 47(1-4), 135–148. doi: 10.1016/s0927-0248(97)00034-2

[6] Bayrak, F., Abu-Hamdeh, N., Alnefaie, K. and Öztop, H. (2017). A review on exergy analysis of solar electricity production. Renewable and Sustainable Energy Reviews, 74, pp.755-770.

[7] http://sam.nrel.gov Available on: 26.08.2019

IMPORTANT PARAMETERS IN SOLAR POWER PLANT INSTALLATION AND ANALYTICAL HIERARCHY PROCESS

Burcu GÜLMEZ*, Ramazan KÖSE, Oğuz Ozan YOLCAN*****
*Manisa Celal Bayar University, Department of Mechanical Engineering, Manisa / Turkey
Email: burcugulmez@gmail.com
**Kütahya Dumlupınar University, Department of Mechanical Engineering, Kütahya / Turkey
Email: ramazan.kose@dpu.edu.tr
***Kütahya Dumlupınar University, Department of Mechanical Engineering, Kütahya / Turkey
Email: oguzozan.yolcan@dpu.edu.tr

ABSTRACT

The limited reserve problems of fossil-based fuels, their environmental impacts, and being imported fuel for our country increase the importance of renewable energy sources. Our country has an important potential in terms of solar energy. Solar power installed in our country has increased substantially in recent years and continues to increase.

In this study, Turkey's energy situation was examined and evaluated by our country's installed capacity of renewable energy sources and production values. Important criteria in determining the solar power plant site were mentioned, and information was given about the Analytical Hierarchy Process, one of the algorithms used in determining the power plant site.

Keywords: Solar energy, renewable energy, solar powerplant site selection

1. INTRODUCTION

In our world, where energy consumption is increasing day by day, the rate of benefiting from renewable energy sources is increasing rapidly due to the limited reserves of fossil fuels and the environmental damage. In Table 1, electricity energy production rates of some countries on the basis of 2016 are given [1]. As can be seen from Table 1, Canada meets most of its electricity generation from renewable energy sources. Looking at the world average, it is seen that renewable energy sources have an important rate of 22.9%. On the world average, the rate of coal is 40.6%, the rate of oil is 4.3%, the rate of natural gas is 21.6% and the rate of nuclear energy is 10.6%. China, and the USA, which are the countries with the highest electricity generation in the world, provide electricity to a large extent from fossil fuels.

Table 1. Electricity generation rates of some countries ona source basis [1]

Country	Coal (%)	Oil (%)	Natural Gas (%)	Nuclear (%)	Renewables (%)	Others (%)
France	2.1	0.3	2.3	77.6	17.5	0.2
Germany	45.4	0.9	9.9	15.5	28.0	0.3
USA	39.5	0.9	26.8	19.1	13.6	0.1
Canada	9.9	1.2	9.3	16.4	62.8	0.3
China	72.5	0.2	2.0	2.3	23.0	0.0
India	75.1	1.8	4.9	2.8	15.5	0.0
Russia	14.9	1.0	50.1	17.0	17.0	0.0
World	40.6	4.3	21.6	10.6	22.9	0.1

When the licensed electricity generation installed power of our country is examined, the total licensed electricity generation installed power was 83.2 GW in 2018 this, value increased to about 85 GW by the end of 2019 [2]. Among the renewable energy sources, the installed power of wind energy from 6.9 GW to 7.5 GW; The installed power of geothermal energy has increased from 1.3 GW to 1.5 GW, and the installed power of solar energy from 82 MW to 170 MW [2].

Table 2. Turkey' s licensed electricity generation installed capacity [2]

Resource Type	2018 (MW)	Share (%)	2019 (MW)	Share (%)	Change 2018-2019(%)
Natural gas	25,731.93	30.93	25,935.41	30.53	0.79
Hydro dam	20,534.80	24.69	20,642.51	24.3	0.52
Lignite	9,597.12	11.54	10,101.03	11.89	5.25
Import coal	8,938.85	10.75	8,966.85	10.55	0.31
Run of river	7,748.90	9.32	7,851.85	9.24	1.33
Wind	6,942.27	8.35	7,520.33	8.85	8.33
Geothermal	1,282.52	1.54	1,514.69	1.78	18.1
Hard coal	616.15	0.74	810.77	0.95	31.59
Biomass	590.92	0.71	725.92	0.85	22.85
Asphaltite coal	405	0.49	405	0.48	0
Fuel oil	709.21	0.85	305.93	0.36	-56.86
Solar	81.66	0.1	169.7	0.2	107.81
Naphta	4.74	0.01	4.74	0.01	-0.08
Lng	1.95	0	1.95	0	0
Diesel	1.04	0	1.04	0	0
Total	83,187.05	100	84,957.72	100	2.13

When the licensed electricity generation values of our country are examined, it is seen that the total generation value in 2018 was 296 billion kWh, while this value was realized as 294.2 billion kWh in 2019 [2]. Among the production values of 2018, natural gas has the highest share with a share of 30.96%, while in 2019, power plants with a dam have the highest share with a share of 30.2%. The electrical energy obtained from wind energy from 19.8 billion kWh to 21.6 billion kWh; The electrical energy obtained from geothermal energy has increased from 7.4 billion kWh to 8.9 billion kWh. The electrical energy obtained from licensed solar power plants decreased from 386 GWh to 194 GWh [2].

Table 3. Turkey' s licensed electricity generation installed power generation values [2]

Resource Type	2018 (GWh)	Share (%)	2019 (GWh)	Share (%)	Change 2018-2019(%)
Hydro dam	59,902.04	20.24	88,850.17	30.2	48.33
Import coal	62,988.54	21.28	60,381.27	20.52	-4.14
Natural gas	91,639.14	30.96	56,522.71	19.21	-38.32
Lignite	45,087.00	15.23	46,893.73	15.94	4.01
Wind	19,827.00	6.7	21,636.28	7.35	9.13
Geothermal	7,430.98	2.51	8,929.73	3.03	20.17

Biomass	3,240.96	1.09	4,266.32	1.45	31.64
Hard coal	2,844.58	0.96	3,518.87	1.2	23.7
Asphalite coal	2,328.50	0.79	2,323.95	0.79	-0.2
Fuel oil	328.89	0.11	732.92	0.25	122.84
Solar	385.86	0.13	194.37	0.07	-49.63
Diesel	0.22	0	1	0	349.3
Total	296,003.71	100	294,251.32	100	-0.59

When the unlicensed electricity generation installed capacity of our country is examined, the total unlicensed electricity generation installed power was 5.3 GW in 2018, while this value increased to 6.3 GW by the end of 2019 [2]. Solar energy has the highest share in unlicensed electricity generation installed power values. While the unlicensed solar energy installed power of our country was 5 GW in 2018, it increased by 16% in 2019 and reached 5.8 GW. Unlicensed wind power installed power, on the other hand, increased from 52 MW in 2018 to approximately 71 MW in 2019 [2].

Table 4. Unlicensed electricity generation installed capacity of Turkey [2]

Resource Type	2018		2019	
	Installed Capacity (MWe)	Share (%)	Installed Capacity (MWe)	Share (%)
Solar	5,016.99	94.47	5,825.46	92.33
Natural Gas	153.04	2.88	328.66	5.21
Biomass	79.18	1.49	75.67	1.2
Wind	51.95	0.98	70.83	1.12
Hydraulic	8.91	0.17	8.65	0.14
Total	5,310.57	100	6,309.27	100

When the unlicensed electricity generation values of our country are examined, it is seen that the total generation value in 2018 was 8.2 billion kWh, while this value was realized as 9.8 billion kWh in 2019 [2]. Generation values from unlicensed solar energy have a 96% share among all sources in 2018 and 2019. While electricity generation from unlicensed solar energy was 7.9 billion kWh in 2018, this value increased to 9.4 billion kWh in 2019. While electricity generation from unlicensed wind energy was 111.5 million kWh in 2018, it reached 113.6 million kWh in 2019 [2].

Table 5. Unlicensed electricity generation installed power generation values of our country [2]

Resource Type	2018		2019	
	The amount of energy given to the system as surplus (MWh)	Share (%)	The amount of energy given to the system as surplus (MWh)	Share (%)
Solar	7,860,576.89	95.71	9,425,965.29	95.9
Biomass	205,901.95	2.51	255,486.79	2.6
Wind	111,542.03	1.36	113,558.01	1.16
Hydraulic	34,750.58	0.42	34,437.65	0.34
Total	8,212,771.44	100	9,829,447.73	100

When the years 2016-2019 are examined, the licensed installed power of our country in 2016 was 77.6 GW, it increased by 9.5% to 85 GW in 2019; The licensed electricity generation in 2016 increased by 8% from 272.6 billion kWh to 294.3 billion kWh in 2019. In the same time period, unlicensed installed power increased by 500% from 1.05 GW in 2016 to 6.31 GW in 2019; unlicensed electricity generation increased from 1.1 billion kWh in 2016 to 9.8 billion kWh by increasing 765% [2,3].

2. SOLAR POWER PLANT SITE SELECTION

Energy resources are evaluated according to various criteria [4]. Various criteria should also be taken into account in the evaluation of solar energy and determination of the solar power plant site. Power plant site efficiency and legal regulations are some of them [5].

2.1. Land Determination

Solar energy has many uses. Electricity generation with photovoltaic panels is one of them[6].There are basic criteria such as solar potential, climate condition, land structure, land use status, network connection, distance to energy consumption regions, accessibility, water resources, geological structure, land condition and land cost in choosing suitable photovoltaic power plants These criteria and requirements can be summarized as follows [7-9];

Table 6. SPP site selection criteria and requirements [7]

Criteria	Solar Radiation	Slope	Prox. to the Res. Area	Prox. to enterprises	Prox. to the Road Network	Temperature	Land Cover
Neccessity	>1100 kWh/m^2.yr	<5^o – 15^o	>500 meters	<3500 meters	<500 meters	15 ^{o}C – 40 ^{o}C	Away from forests, settlements, agriculture areas

The intensity of solar radiation of the region, the distance of the land to the settlements and industrial areas, the condition of the land are among the parameters that affect the selection of photovoltaic power plants [7-9].

2.2. Legal Regulations

Legal regulations and implementation regulations that are made in the selection of the location of solar power plants need to be evaluated [5]. It is especially useful to examine the legal regulations regarding potential power plant areas under the authority of various institutions separately [5].

2.3. Determination of Plant Site with Algorithms

In determining solar power plant site, using the criteria specified in the previous sections, the most suitable location can be selected with the help of various algorithms. There are many studies in the literature on determining the photovoltaic solar power plant area with algorithms [10-20]. One of the algorithms frequently used in the literature is the Analytical Hierarchy Process (AHP). Analytical Hierarchy Process was developed by Thomas Saaty in 1980 [21]. In the Analytical Hierarchy Process, the determined criteria are ranked according to each other [22]. By analyzing the listed criteria according to each other, the weight ratio of the criterion is obtained. The grading criteria prepared by Saaty are given below[22].

Table 7. Analytical Hiearchy Process fundamental scale [22]

Intensity of importance	**Definition**
1	Equal importance
3	Moderate importance of one over another
5	Essential or strong importance
7	Very strong importance
9	Extreme importance
2, 4, 6, 8	Intermadiate values between the two adjacent judgements

3. RESULTS AND DISCUSSIONS

The importance of renewable energy sources in the world and Turkey and its use is increasing day by day.Given the fact that solar energy is a clean and infinite source of energy and the solar energy potential of our country is quite high and is currently dependent on energy in terms of energy, increasing investments in solar energy in our country should be strongly encouraged. In this study, the energy and solar energy situation of our country has been mentioned and the criteria that are important in the selection of the solar power plant have been evaluated under three main headings. These criteria directly affect costs during plant installation and operation. In addition, the location selection of the solar power plant was examined with the help of algorithms using various criteria, and the studies were emphasized. In addition, Analytical Hierarchy Process, which is frequently used in solar power plant site selection, was also mentioned.

REFERENCES

[1] http://www.enerji.gov.tr/tr-TR/Enerji-ve-Tabii-Kaynaklar-Gorunumleri Available on: 15.01.2020

[2] https://www.epdk.gov.tr/Detay/Icerik/3-0-24/yillik-sektor-raporu Available on: 15.08.2020

[3] https://www.epdk.gov.tr/Detay/Icerik/3-0-23/elektrikaylik-sektor-raporlar Available on: 15.08.2020

[4] Köse, R., Enerji Kaynaklarının Değerlendirilmesi, 3e Dergisi S 68-72, 1998.

[5] Şenlik, İ., Güneş Enerjisi Santrallarının Yer Seçimi, Elektrik Mühendisliği S 462 S 94-98, 2017.

[6] https://www.yenienerji.com/gunes-enerjisi-ve-kullanim-alanlari Available on: 15.01.2020

[7] Kereush, D., Perovych, I., Determining Criteria For Optimal Site Selection For Solar Power Plants, Geomatics, Landmanagement and Landscape C 4 S 39-54, 2017.

[8] Brewer, J., Ames, D.P., Solan, D., Lee, R., Carlisle, J., Using GIS analytics and social preference data to evaluate utility-scale solar power site suitability. Renewable Energy S 81 S 825-836, 2015.

[9] Charabi, Y., Gastli, A., PV site suitability analysis using GIS-based spatial fuzzy multi-criteria evaluation. Renewable Energy S 36 S 2554-2561, 2011.

[10] Dhunny, A., Doorga, J., Allam, Z., Lollchund, M., Boojhawon, R., Identification of optimal wind, solar and hybrid wind-solar farming sites using fuzzy logic modelling. Energy S 188 116056, 2019.

[11] Jung, J., Han, S., Kim, B., Digital numerical map-oriented estimation of solar energy potential for site selection of photovoltaic solar panels on national highway slopes. Applied Energy S 242 S 57–68, 2019.

[12] Palmer, D., Gottschalg, R., Betts, T., The future scope of large-scale solar in the UK: Site suitability and target analysis. Renewable Energy S 133 S 1136–1146, 2019.

[13] Doorga, J. R., Rughooputh, S. D., Boojhawon, R., Multi-criteria GIS-based modelling technique for identifying potential solar farm sites: A case study in Mauritius. Renewable Energy S 133 S 1201–1219, 2019.
[14] Ali, S., Taweekun, J., Techato, K., Waewsak, J., Gyawali, S., GIS based site suitability assessment for wind and solar farms in Songkhla, Thailand. Renewable Energy S 132 S 1360–1372, 2019.

[15] Wu, Y., Zhang, B., Wu, C., Zhang, T., Liu, F., Optimal site selection for parabolic trough concentrating solar power plant using extended PROMETHEE method: A case in China. Renewable Energy S 143 S 1910–1927, 2019.

[16] Shorabeh, S. N., Firozjaei, M. K., Nematollahi, O., Firozjaei, H. K., Jelokhani-Niaraki, M., A risk-based multi-criteria spatial decision analysis for solar power plant site selection in different climates: A case study in Iran. Renewable Energy S 143 S 958–973, 2019.

[17] Garni, H. Z. A., Awasthi, A., Solar PV power plant site selection using a GIS-AHP based approach with application in Saudi Arabia. Applied Energy S 206 S 1225–1240, 2017.

[18] Zoghi, M., Ehsani, A. H., Sadat, M., Amiri, M. J., Karimi, S., Optimization solar site selection by fuzzy logic model and weighted linear combination method in arid and semi-arid region: A case study Isfahan-IRAN. Renewable and Sustainable Energy Reviews S 68 S 986–996, 2017.

[19] Abdul-Wahab, S., Charabi, Y., Al-Mahruqi, A. M., Osman, I., Osman, S., Selection of the best solar photovoltaic (PV) for Oman. Solar Energy S 188 S 1156–1168, 2019.

[20] Cho, Y., Shaygan, A., Daim, T. U., Energy technology adoption: Case of solar photovoltaic in the Pacific Northwest USA. Sustainable Energy Technologies and Assessments S 34 S 187–199, 2019.

[21] Saaty, T.L., The Analytic Hierarchy Process, McGraw-Hill, New York, 1980.

[22] Saaty, R.W., The analytic hierarchy process—what it is and how it is used . Math Model 9:161–76, 1987

STATE OF THE ART REVIEW ON THE Cu(InGa)Se2 THIN-FILM SOLAR CELLS

Mohammad Anwar OMID* Ömer Necati CORA,**
*Karadeniz Technical University, Mechanical Engineering Department, Trabzon/Turkey
*Kabul Polytechnic University, Department of Auto-Mechanical Engineering, Kabul/Afghanistan
Email: ma.omid@kpu.edu.af
**Karadeniz Technical University, Department of Mechanical Engineering, Trabzon/Turkey
Email: oncora@ktu.edu.tr

ABSTRACT

Increasing solar cell efficiency and durability are some of the critical research issues in the field of photovoltaic (PV) technology. Thin-film PV cells can be used increasingly in many industries and applications such as wearable electronics, self-energizing systems, the roof of electric vehicles, trains, solar boats, *etc*. Various types of thin-film solar cells have been investigated, produced, and exploited around the world. There are used different types of chalcopyrite semiconductors in high-efficiency thin-film solar cells, specifically in flexible solar cells. Cu(InGa)Se2 (CIGS) solar cells are promising technology among the thin-film solar cells due to their unique features. However, there are many challenges towards the development of the photovoltaic performance of thin-films and ultra-thin-film solar cells. Thickness and surface roughness of thin-film layer which has a significant effect on the performance of cells, electron recombination, interface contact between thin-film layers, grain size, and grain boundaries, can be mentioned as existing problems. Among the proposed solutions, alkali post-deposition treatment was noted to reduce the thickness of the absorber. Reduction in the absorber thickness leads to a significant decrease in electron recombination, which improves the PV performance of CIGS solar cells. Cs post-deposition treatment (Cs-PDT) improves cell performance by creating conduction band upward, and valence band downshifts. Low thickness of absorber increases crystallinity and surface roughness of CIGS absorber. On the other hand, a high amount of Ga concentration reduces the grain size and major loss of charge carrier. In addition to the high Ga amount, Sulfurization decreases the grain size and the fill factor (FF) of the PV cell.

Keywords: Chalcopyrite semiconductors. Cu(InGa)Se2, CIGS, thin-film solar cells, flexible solar cells, alkali treatment.

ANALYSIS OF 100 KW SOLAR PHOTOVOLTAIC POWER PLANT WHICH CAN BE INSTALLED IN TRABZON

Ramazan KÖSE*, Ayşe Bilgen AKSOY, Burcu GÜLMEZ***, Oğuz Ozan YOLCAN******
*Kütahya Dumlupınar University, Department of Mechanical Engineering, Kütahya / Turkey
Email: ramazan.kose@dpu.edu.tr
**Manisa Celal Bayar University, Department of Energy Systems Engineering, Kütahya / Turkey
Email: aysebilgen.aksoy@cbu.edu.tr
***Manisa Celal Bayar University, Department of Mechanical Engineering, Kütahya / Turkey
Email: burcugulmez@gmail.com
****Kütahya Dumlupınar University, Department of Mechanical Engineering, Kütahya / Turkey
Email: oguzozan.yolcan@dpu.edu.tr

ABSTRACT

In this study, 100 kW solar photovoltaic power plant is modeled and simulated by using System Advisor Model (SAM) software using meteorological data of Trabzon province. As a result of these studies, annual electricity generation amounts, initial investment cost, net present value and repayment period of the power plant were calculated. According to the results, the annual photovoltaic solar power plant has an annual electricity production of 106,844 kWh, an initial investment cost of $ 85,700 and a payback period of 9.2 years. Monthly production values of the plant are as follows; 6,269.5 kWh for January, 7,466.9 kWh for February, 9,670.3 kWh for March, 10,242.5 kWh for April, 11,346 kWh for May, 11,642.8 kWh for May, 10,539 for July , 1 kWh, 10,626.1 kWh for August, 9,269 kWh for September, 7,979.5 kWh for October, 6,165.2 kWh for November and 5,626.4 kWh for December. The net present value of the modeled power plant is calculated as $ 25,750.

Keywords: Solar energy, photovoltaics, net present value, renewable energy

1. INTRODUCTION

Feasibility is important before establishing large capacity facilities. In this way, data such as payback period of the facility can be calculated. Photovoltaic power plants can be simulated using meteorological data, panel and inverter features and other data. There are studies related to this subject in the literature.

Colmenar-Santos et al. have developed an integrated PV plant model with HVDC (High Voltage Direct Current) or HVAC (High Voltage Alternating Current) network using power electronics PSIM software. This model was developed by functional blocks, including the photovoltaic field itself, the conversion units suitable for the integration of each network, and the type of network for production. Models enable transmission loss for any combination of three variables to which they depend; network length (km), temperature (°C) and radiation (W / m^2). The use of HVDC networks may be suitable for such power generation plants to verify the validity of the model and show the distribution advantages for HVDC-relatively low photovoltaic power plants compared to the currently used applications in HVDC networks [1]. Schumacher et al. have developed and tested an integrated

monitoring and simulation method for very precise online simulation of photovoltaic power plants. The method is based on detailed modeling of one or two diode current-voltage curves of the photovoltaic generator. The parameters are derived either from the data sheet information of the PV modules or more precisely from the measured IV curves of the modules at different irradiance levels. A simulation accuracy of 2% has been achieved. Using internet-based communication technology for data exchange, online simulation can be performed directly at the photovoltaic power plant's location or from any remote location. To demonstrate the method, online simulation of several grid connected PV generators has been carried out up to MW power range during commissioning and operation of photovoltaic plants. Powerful visualization in the same software environment includes both monitored and simulated online datasets [2]. Saint-Drenan et al. have developed an algorithm that can use historical PV power measurements to create parameters of a physical model for power generation. The approach chosen consists in evaluating the parameters of a PV model, which maximizes the likelihood that simulations match the power measurements. It is possible to interpret and control the algorithm output. The performance of the proposed approach was evaluated and analyzed using measurements from two PV plants. It has been shown that the proposed approach can identify orientation angles with an accuracy of less than 2 in optimal cases. The situations were also found with a difference between the predicted and true 5 angles, which lead to better simulation / prediction accuracy than the actual parameters, as the predicted parameters compensate for the systematic error of the selected PV model [3]. Robles-Campos et al. have created an electro-thermal modular model for a photovoltaic system of any size and includes the effects of both photovoltaic cells and bypass diodes. A detailed analysis of the proposed model was made and later verified on both PSCAD / EMTDC and Matlab – Simscape. The proposed model was then verified using actual ambient temperature, cell temperature, wind speed measurements and then performance analysis of several maximum power point monitoring algorithms [4]. Huang et al. investigated the degradation process of photovoltaic modules with simulation studies. A circuit-based model has been used to define photovoltaic properties for environmental conditions and aging factors of photovoltaic modules. Analysis of each aging factor shows that the reduction of short circuit current, which is the main cause of power loss, is mainly caused by optical distortion. The deterioration of the filling factor worsens the power output, mainly due to the deterioration of the parasite resistors. Statistical analysis of photovoltaic characteristic parameters based on multiple photovoltaic modules with the same technology shows that the deterioration process can be very complex due to the deterioration models of aging factors. Overall, power loss is increasing, and mismatch between photovoltaic modules becomes more noticeable over time [5].

2. MATERIAL

Trabzon is located in Turkey's eastern Black Sea region. Trabzon province has a Black Sea climate. Sunshine duration, less than the province in the south of Turkey. The solar energy potential of Trabzon is shown in Figure 1 [6]. As seen in the figure, the solar energy potential of Trabzon province is in the range of 1400-1600 kWh / m^2.

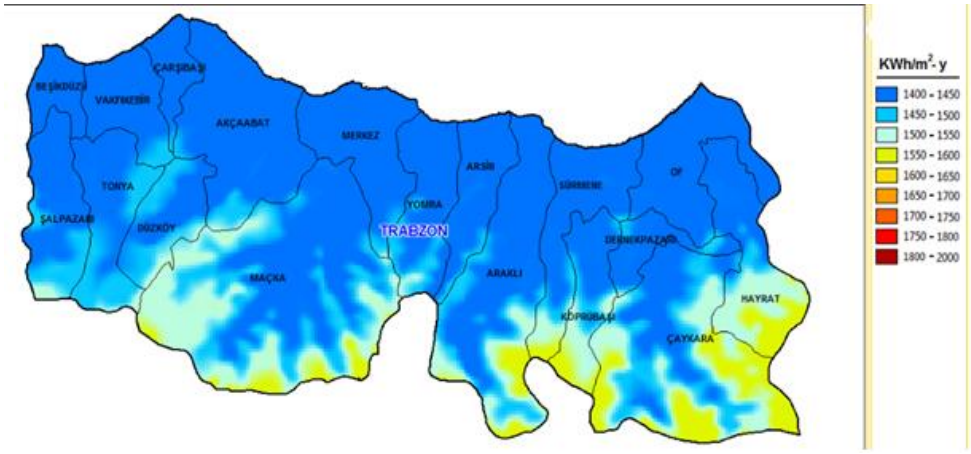

Figure 1. Solar energy potential of Trabzon

Monthly average temperature values of Trabzon province are shared in Figure 2 [7]. As seen in the figure, the approximate average temperatures of Trabzon province; 7.5 ºC for January, 7.7 ºC for February, 9.3 ºC for March, 11.2 ºC for April, 15.7 ºC for May, 20.1 ºC for June, 23.8 ºC for July, 24.7 ºC for August, 21.8 ºC for September, 18.1 ºC for October, 13.5 ºC for November and 9.2 ºC for December. Monthly average wind speed values of Trabzon province are shared in Figure 3 [7]. As seen in the figure, the approximate average wind speed values of Trabzon province; 2.92 m / s for January, 2.93 m / s for February, 3.04 m / s for March, 2.49 m / s for April, 2.24 m / s for May, 2.37 m / s for June, 2.74 m / s for July, 2.6 m / s for August, 2.87 m / s for September, 2.65 m / s for October, 2.75 m / s for November and 2.81 m / s for December. Hourly solar radiation values of Trabzon province on year basis are shown in Figure 4 [7].

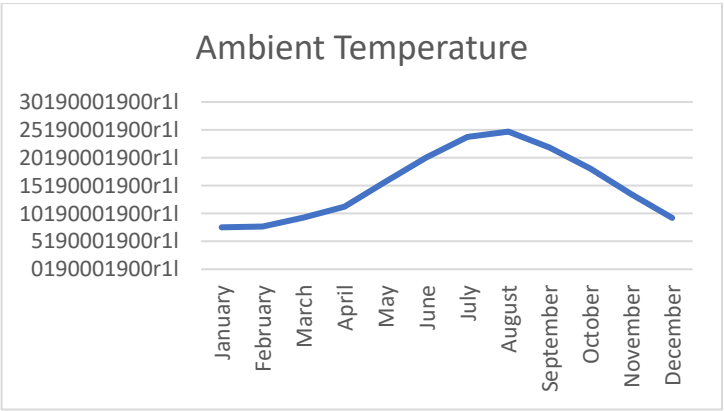

Figure 2. Monthly average temperature values of Trabzon

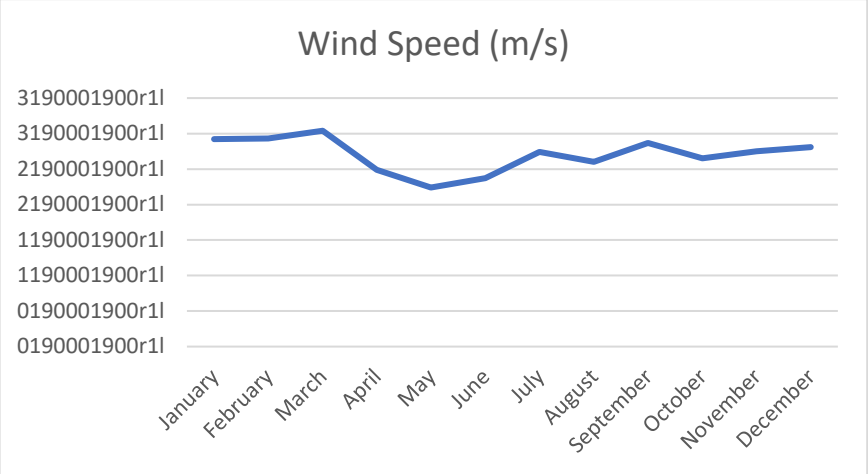

Figure 3. Monthly average wind speed values of Trabzon

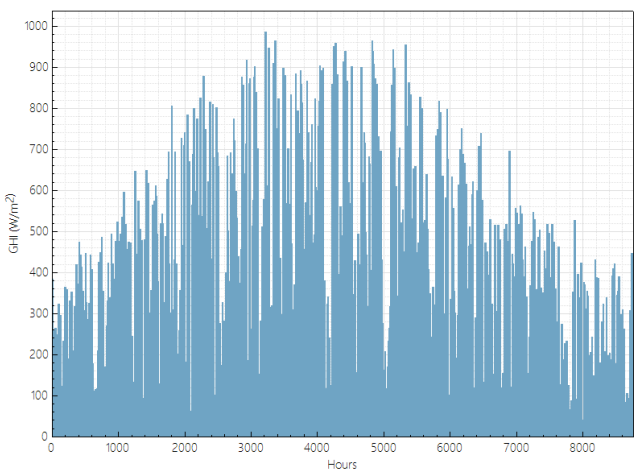

Figure 4. Hourly solar radiation values of Trabzon province on year basis

3. METHOD

Yingli Solar YL250P-29b panels and TRIO-27.6-TL-OUTD inverters were used in the simulated solar power plant. Technical characteristics of panels and inverters can be seen in Figure 5 and Figure 6 [7].

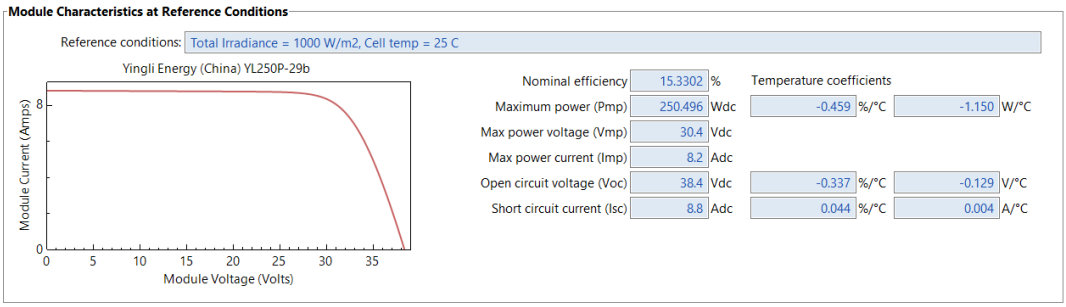

Figure 5. Technical properties of solar panels

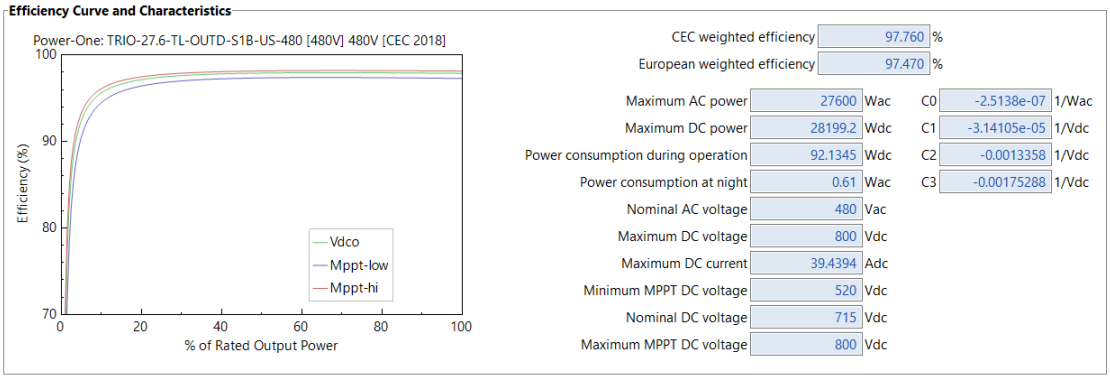

Figure 6. Technical properties of inverters

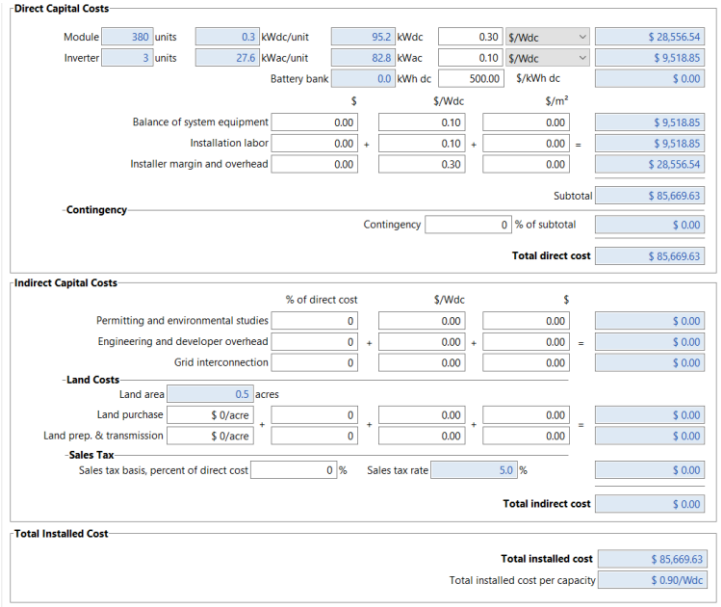

Figure 7. Installation cost of solar photovoltaic power plant

The plant cost is shown in Figure 7 as the sum of the individual costs. The cost of the simulated power plant is determined as $ 85.700 [7]. Monthly production values of the simulated power plant are shown in Figure 8. Production values of the power plant; 6,269.5 kWh in January, 7,466.9 kWh in February, 9,670.3 kWh in March, 10,242.5 kWh in April, 11,346 kWh in May, 11,642.8 kWh in June, 10,539.1 kWh in July, 10,626.1 in August kWh, 9,269 kWh in September, 7,979.5 kWh in October, 6,165.2 kWh in November and 5,626.4 kWh in December. Annual production values of the power plant for 25 years are shown in Figure 9. The power plant, which produced 106,844 kWh of electricity in the first year, produces 94,733 kWh of electricity in its 25th year.

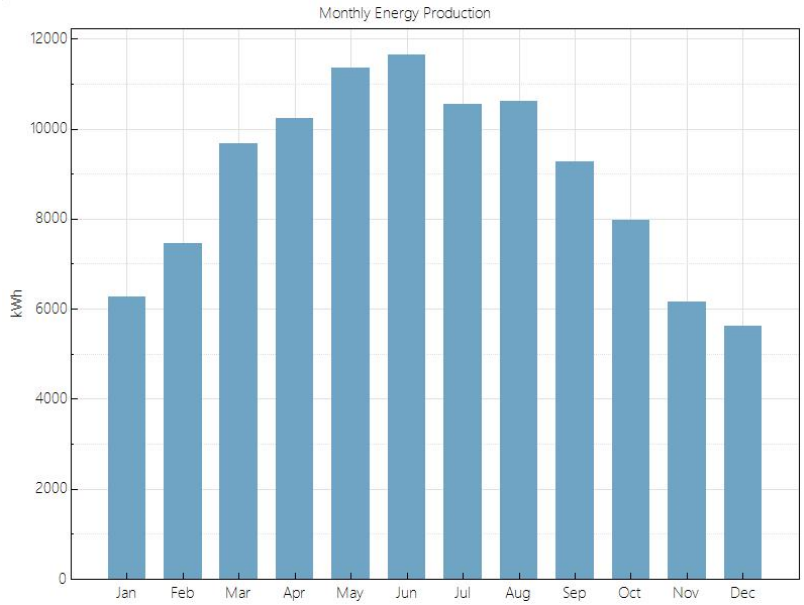

Figure 8. Monthly production values of the simulated power plant

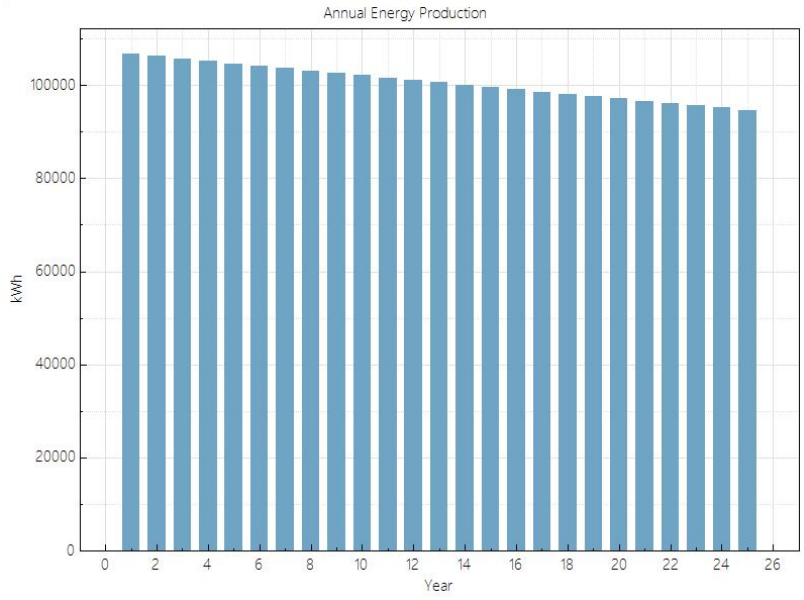

Figure 9. Annual production values of the power plant for 25 years

Various values calculated for the power plant are shown in Table 1. The LCOE (Levelized cost of energy) value of the power plant is 3.62 c / kWh, the net present value of the power plant is $ 25.747 and the payback period of the power plant is 9.2 years [7].

Table 1. Various values for power plant

Metric	Value
Annual energy (year 1)	106,844 kWh
Capacity factor (year 1)	12.8%
Energy yield (year 1)	1,122 kWh/kW
Performance ratio (year 1)	0.83
Levelized COE (nominal)	4.58 ¢/kWh
Levelized COE (real)	3.62 ¢/kWh
Electricity bill without system (year 1)	$826,030
Electricity bill with system (year 1)	$816,797
Net savings with system (year 1)	$9,233
Net present value	$25,747
Payback period	9.2 years
Discounted payback period	16.5 years
Net capital cost	$85,670

4. RESULTS

Using the meteorological data of the city of Trabzon, with the help of System Advisor Model software, a solar power plant with a power of 100 kW was simulated. The production value of the power plant in the first year has been calculated as 106,844 kWh. The plant's installation cost has been calculated as $ 85,700, its net present value is $ 25,747 and the payback period is 9.2 years.

REFERENCES

[1] Colmenar-Santos, A., Guinduláin-Argandoña, T., Rosales-Asensio, E., Molina-Ibáñez, E.-L., & Blanes-Peiró, J.-J. (2018). Simulation of modeling of multi-megawatt photovoltaic plants with high voltage direct current grid integration. *Solar Energy*, *166*, 28–41. doi: 10.1016/j.solener.2018.02.016

[2] Schumacher, J., Pietruschka, D., & Eicker, U. (2014). Commissioning and Operational Control of Photovoltaic Power Plants through Online Simulation. *Energy Procedia*, *57*, 152–160. doi: 10.1016/j.egypro.2014.10.019

[3] Saint-Drenan, Y., Bofinger, S., Fritz, R., Vogt, S., Good, G., & Dobschinski, J. (2015). An empirical approach to parameterizing photovoltaic plants for power forecasting and simulation. *Solar Energy*, *120*, 479–493. doi: 10.1016/j.solener.2015.07.024

[4] Robles–Campos, H. R., Azuaje–Berbecí, B. J., Scheller, C. J., Angulo, A., & Mancilla–David, F. (2019). Detailed modeling of large scale photovoltaic power plants under partial shading conditions. *Solar Energy*, *194*, 485–498. doi: 10.1016/j.solener.2019.10.043

[5] Huang, C., & Wang, L. (2018). Simulation study on the degradation process of photovoltaic modules. *Energy Conversion and Management*, *165*, 236–243. doi: 10.1016/j.enconman.2018.03.056

[6] http://www.yegm.gov.tr/MyCalculator/pages/61.aspx Available on: 19.10.2019

[7] http://sam.nrel.gov Available on: 10.12.2019

POTENTIAL FOR THE USE OF SOLAR ENERGY IN THE FOOD INDUSTRY

Damla BAYANA*, Filiz İÇİER**
*Ege University, Graduate School of Natural and Applied Sciences, Food Engineering Department, Bornova/Izmir/Turkey
Email: damlabayana@gmail.com
** Ege University, Faculty of Engineering, Department of Food Engineering, Bornova/Izmir,/Turkey
Email: filiz.icier@ege.edu.tr

ABSTRACT

The food industry has strategic importance for the country's economies because of the evaluation of agricultural products, supplying raw materials to industry, feeding the society, contributing to employment and foreign trade. A large amount of energy is used for the production, transport, processing and storage of food products. It is very important to discuss the sustainability of food production as food needs are expected to be double in the next 50 years. The energy used during the safe delivery of food products to end consumer is provided by fossil fuels. Nowadays, the studies on increasing the applicability of renewable energy sources in food production have increasing trend since the current consumption of the existing fossil fuel resources are impressive.

The novel methods such as solar power generation by photovoltaic and solar thermal, solar refrigeration, solar cooking, solar cooling/heating and solar drying, etc. are applicable in the food industry. The most common use of solar energy is sun drying. In the traditional drying processes carried out under natural conditions, the climatic conditions are sufficient on control of the process, the hygienic problems due to pollutions by dust, birds, insects, and living organisms, etc. could be possible, and thus the assurance of the food quality is questionable. The use of solar energy by its storage or its assistance in the form of heat energy is often preferred due to the high energy costs during the artificial drying process.

In this study, the use of solar energy, one of the primary renewable energy sources, as an alternative in the food processing applications requiring high fuel consumption is discussed. In this regard, the potential for different aims of using solar energy is examined and their applicability in food industry is discussed. This study is financially supported by projects; Ege University BAP-FDK2019-20627 and TUBİTAK 119O132.

Keywords: Drying, Energy, Food, Renewable, Solar

WIND ENERGY

INVESTIGATION OF VERTICAL AXIS WIND TURBINES AND THEIR COMPONENTS DESIGN

Ayetullah BOZTAŞ*, Oğuzhan DEMİRBAŞ*, Mustafa Ergin ŞAHİN[*]
[*]Recep Tayyip Erdoğan University, Department of Electrical and Electronic Engineering, Rize/Turkey
E-mail: mustafa.sahin@erdogan.edu.tr

ABSTRACT

Wind energy and developments of wind turbine design are getting important today all around the world. To increase the efficiency of wind turbines, the scientists have many researches. One of these topics to increase the efficiency is vertical axis wind turbines, blades, and motors design. Also, the generated energy and connection to the grid are causes some problems and have to study.

In this study, vertical axis wind turbine blades and developments to increase efficiency are investigated firstly. Design steps and magnetic equation of an axial flux, permanent magnets, coreless stator, and rotor designed for a small wind turbine application are investigated in this paper. Stator voltages depending on the magnetic flux distribution have been obtained for different operating speeds and load conditions. The stator voltages for the three-phase are rectified and connected to a buck-boost converter to regulate bus voltage. How electricity is connected to the grid or A DC bus is investigated and given a proposal with power electronic converters and simulated with MATLAB/Simulink.

Keywords: Wind turbine, Axial flux permanent magnet generator, vertical axis wind turbine, buck-boost converter, PID controller.

1. INTRODUCTION

In our world, where the need for energy is increasing, the interest in renewable energy sources is increasing day by day. Among these sources, wind energy attracts the most attention after solar energy. The turbines used to convert wind energy into electrical energy can be produced with a gear system or directly connected. These systems are need overhaul, additional costs, and generates noise even with low-speed power generation with geared wind turbines [1].

The high coercivity and low permeability properties of hard magnetic materials make it difficult to magnetize and demagnetize. These materials are referred to as permanent magnets because they are magnetized once and then retain their magnetization for a long time [2]. With the emergence of NdFeB magnets in the 1980s, permanent magnet machine technology gained high momentum. Today, permanent magnet machines are used in many fields, from electric vehicles to the space industry. One of these areas is wind energy systems. Losses are reduced by using magnets for excitation, and the efficiency of the system increases [3, 4].

Permanent magnet machines are used for all the energy conversion devices where magnet makes the magnetic excitation [5]. High-density magnetic materials are now widely used in both motor applications and generator applications. Permanent magnet machines are examined in two main sections, radial and axial, depending on the magnetic flux situation. In wind turbine applications, different versions of both structures may be used depending on the rotor position [6]. The axial flux permanent magnet (AFPM) machine, also called a disc type, is more suitable for wind turbines due to its structural feature. In wind generator applications, axial flux permanent magnet generators with corrugated cores in the stator can also be used [7]. However, in a coreless stator and surface-mounted axial flux machine, the yield and the hysteresis current losses are eliminated**.**

The generator output voltage is not stable, and the DC voltage supplies a load quickly. There are required some components to adjust the output voltage to do the desired voltage level [8]. For single-phase or three-phase generator output voltages are rectified with a full-bridge converter to DC voltage. However, this DC voltage is not stable and constant to supply the loads and batteries [9-12]. So there is a buck-boost DC to DC converter circuit to adjust the output voltage required bus voltage. If the rectifier output voltage is lower than the DC bus voltage depends on the wind speed, the converter works in a boost mode to increase the input voltage. If the rectifier output voltage is higher than the DC bus voltage depends on the high wind speeds converter work in a buck mode to decreases the input voltage. However, this converter regulates the output voltages ripples and fluctuations. This system is proposed for off-grid street lighting with battery energy storage.

This paper is aimed to production and analysis of a small power vertical axis wind turbine, which is handmade and can be a solution option in remote rural areas where electricity is not available. In the proposed system, the stator windings are fixed to each other after they are formed in desired windings and sizes and embedded in the material formed with a mixture of epoxy resin, talcum powder, and hardener. Rotor structures are also embedded in the same mixture. Thus, the magnets are protected against structural stresses and corrosion. The generated electricity from the turbine is rectified with a full bridge rectifier. A buck-boost converter is used to increase or decrease these voltages to the desired voltage levels for the batteries' charge. The simulations and design steps are given in this paper as a preliminary study. The general structure of the proposed vertical axis wind turbine and its components are given in Figure 1.

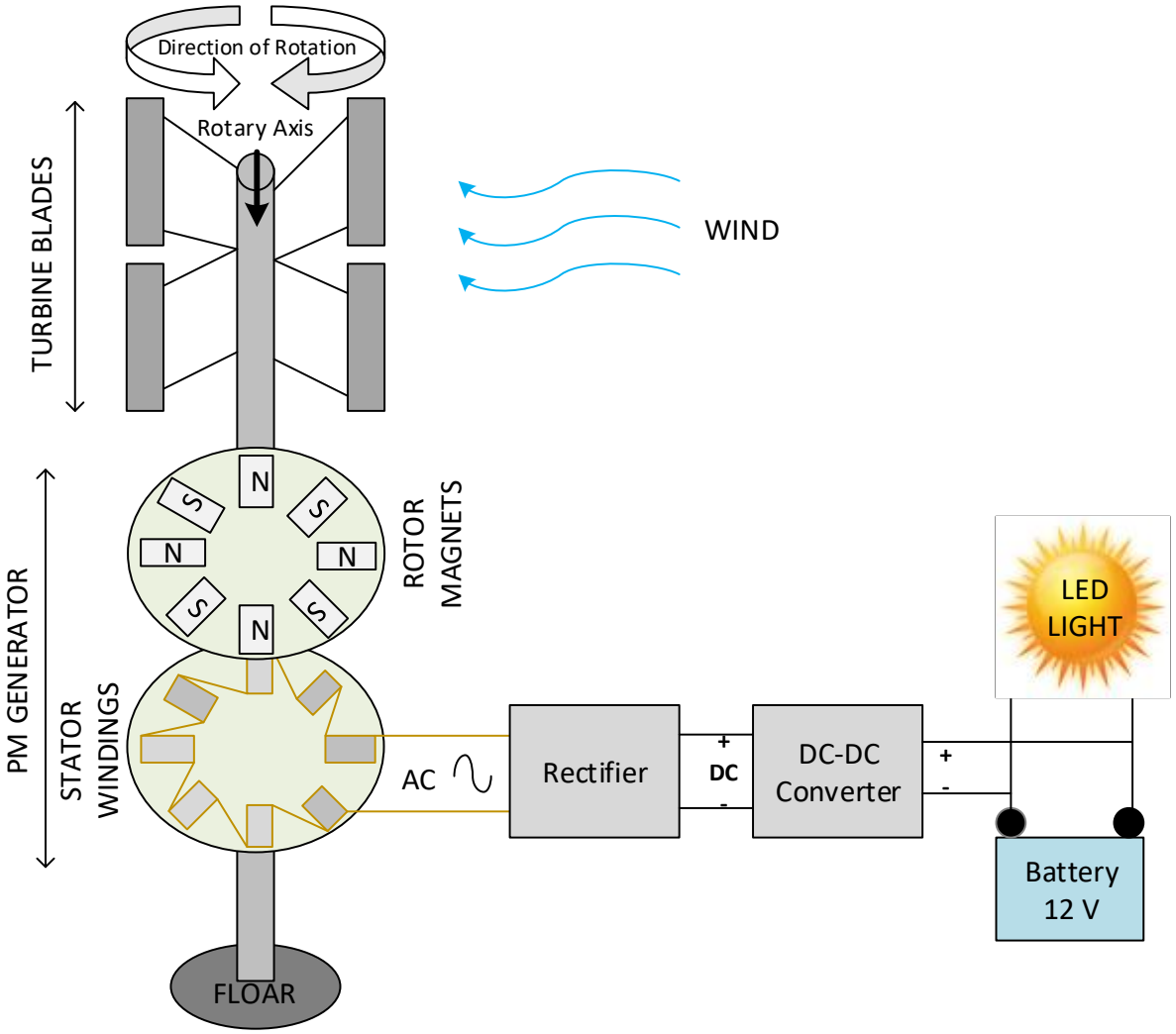

Figure 1. The general structure of the vertical axis wind turbine and its components.

3. COMPONENTS OF INSTALLED SYSTEM

In this article, the investigation of production and analysis of a handmade small power wind turbine can be a solution option in remote rural areas where electricity is not available is aimed [13]. In the installed system, the stator windings are fixed after they are formed in desired windings and sizes. Rotor structures are also embedded in the same mixture, and the magnets are protected against structural stresses and corrosion, and also attached rectifier and converter circuits for the DC bus voltage for an off-grid system. To connect the generator and on-grid system is required some complex inverter applications [14, 15]. The following section introduces the components of the system.

3.1 Blades

The rotation axis of the vertical axis wind turbine systems is perpendicular to the direction of the wind. Thus, these turbines can take the wind from all ways and generate electricity by rotating accordingly. For this reason, it has an advantage compared to horizontal axis wind turbines. It is less efficient than horizontal axis turbines in terms of efficiency, and the efficiency of these turbines, which lift the wind by dragging, is approximately 35%. These turbines can operate at low wind speeds without the need for any tower also [16].

Three basic types of vertical axis wind turbine models are given in Figure 2. The Savonius turbine creates a moment in the inner part of the cylinder with the wind effect coming in any direction while it creates a negative moment in the outer part of the cylinder, and thus it rotates [17]. Darrieur rotors are highly efficient but difficult to operate. The H rotor Darrieur model was formed by the development of the vertical axis Darrieur wind turbine and which was replaced by the curved rotor blades in the Darrieur wind turbine are the smooth aerodynamic profile and the application of pitch control to the blades [16]. Many companies apply the experiences of horizontal turbine design to vertical turbines because of the lack of design theories and design basis, and some companies design a vertical turbine based on their preference [18].

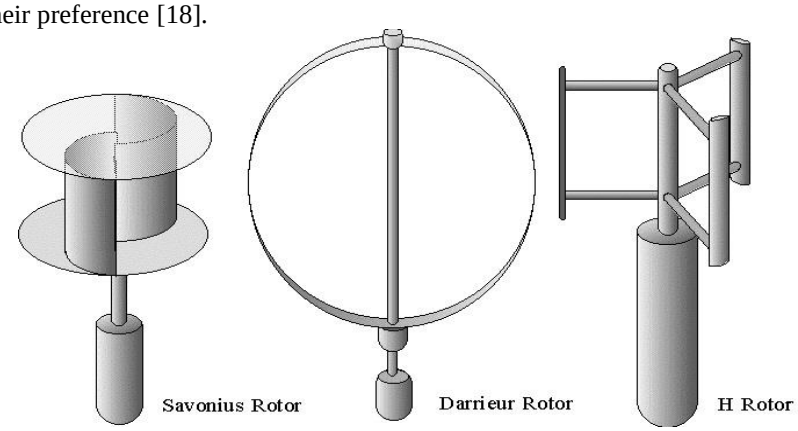

Figure 2. Three types of vertical axis wind turbine models [18].

3.2 Generator Part

The Axial Flux Permanent Magnet (AFPM) machine model is shown in Figure 3(a). Disc-type rotors in the machine consist of permanent magnets placed on steel. An equal number of permanent magnets in both rotors must have reverse polarity with the magnet placed on the opposite rotor steel in the same position and with the magnet next to it on the same steel. Thus, magnets, air gap, stator windings, and rotor as a closed magnetic circuit are obtained through the steel [12]. The distribution of magnetic fields in a coreless axial flux machine is shown in Figure 3(b). These AFPM models can be designed as a single rotor single stator, double rotor single stator (TORUS), single rotor double stator (AFIR), multirotor multi stator, and obtained various topologies [19].

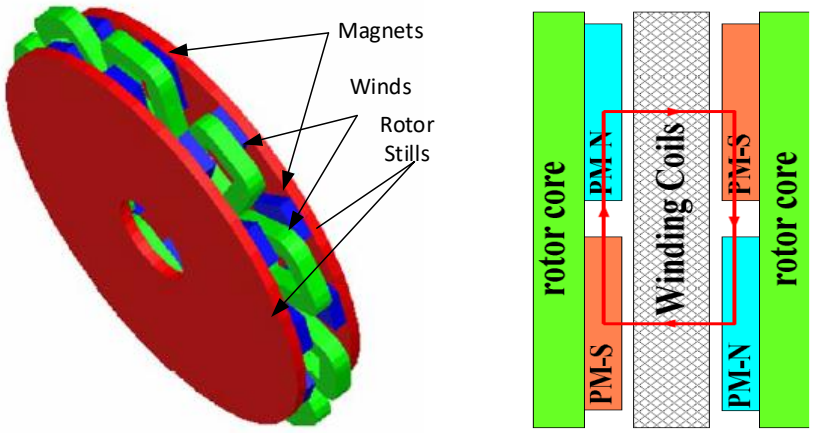

(a) (b)

Figure 3. Coreless EASM model (a), Cross section and distribution of magnetic field (b) [12, 19].

The finite element method used in magnetic field analysis utilizes Maxwell's equations as seen in Equation 1 [8]. The application of the finite element method to the design of electrical machines allows the determination of important design parameters such as; flux bond, induced voltages, core losses, winding inductances, and magnetic moment with very high accuracy [11, 12].

$$\Phi = \int_S B.dS \qquad e(t) = N.\frac{d\Phi}{dt} \qquad e(t) = N.\frac{d\Phi}{d\theta}.\frac{d\theta}{dt} \tag{1}$$

The change of the rotor position with time will give the angular velocity, and the voltage expression can be written as is seen in Equation 2. The number of windings (N), Angular velocity (*w)*, Air gap magnetic flux (Øg), Rotor angular position (θ) are the parameters in this equation.

$$e(t) = N.w.\frac{d\emptyset g}{d\theta} \tag{2}$$

2-D or 3-D analysis may be preferred when performing the analysis with the finite element method. In the 2-D analysis, it is possible to reach the approximate result in a shorter time; 2-D analysis does not process the entire radial and axial geometry and therefore cannot accurately calculate flux distributions on the structure. In the 3-D analysis, almost exactly the right result is achieved in a slightly longer time [19].

The windings must be appropriately positioned, so that the windings make the best use of the magnetic field generated by the magnets. The induced winding voltages are sinusoidal, and the phase difference between the winding voltages is the same. Figure 4 shows the windings diagram and the position of the windings.

If the magnetic property of the materials can quickly deteriorate, such materials are called soft magnetic material [3]. When performing the analysis of the BH curves steel, which is a soft magnetic material, must be specified. Today, the most widely used magnet in permanent magnet machines is the NdFeB magnet. In the axial flux machine produced, 12 magnets on rotor steel are uniformly spaced. The magnets are mounted in reverse polarity with the magnet on one side when mounting on steel [19, 20]. Figure 4 shows one of the rotor discs plotted in cad software.

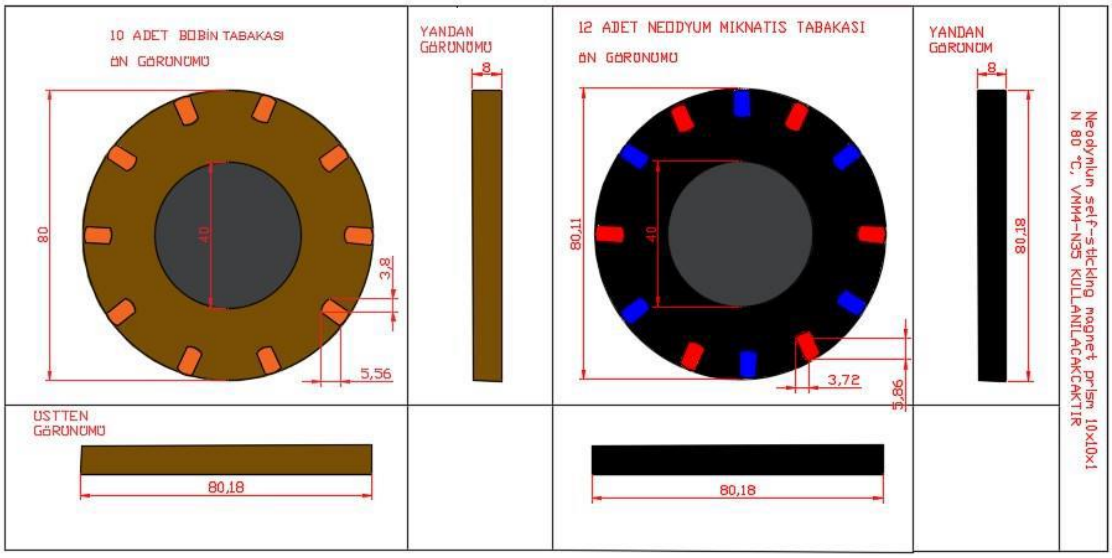

Figure 4. The winding diagram and the position of the magnets on the rotor disk.

For the blades, it utilizes a primary component of plastics or plywood. It is in connection with rods having a cover of sturdy aluminum. There are two separate steel discs with magnets on them for the alternator. On the other hand, copper wires are fixed to the main shaft around their axis. The proposed vertical axis wind turbine and the components are shown in Figure 5. This single component can generate 50 kWh of energy per month for eight battery packs by connecting the rectifier to the generator at an optimum wind speed of 10 km – 36 km/hr [20, 21, 22].

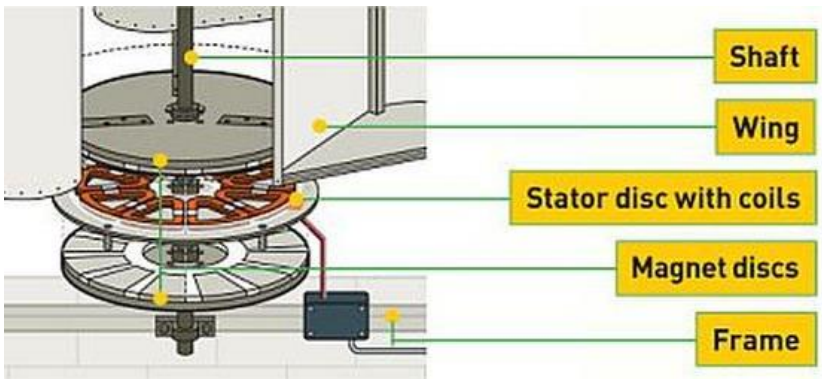

Figure 5. The constructed vertical axis wind turbine and the components [21].

3.3 Rectifier and Converter

The obtained voltages from the wind turbines are applied to a rectifier circuit to rectify the DC voltages. There is used a three-phase rectifier circuit to convert the three-phase AC voltages to DC voltages. The rectifier circuit is shown in Figure 6 (a). The rectified DC voltages are applied to a converter circuit. This converter is selected as a buck-boost converter to increase or decrease the input voltages. The DC to DC buck-boost converter circuit is given in Figure 6 (b). The converter circuit output voltage is adjusted to the desired voltage using a PID controller. This controller compared the output voltage with the desired reference voltage and obtained a PWM signal to drive the converter to be adjusted the output voltage [23].

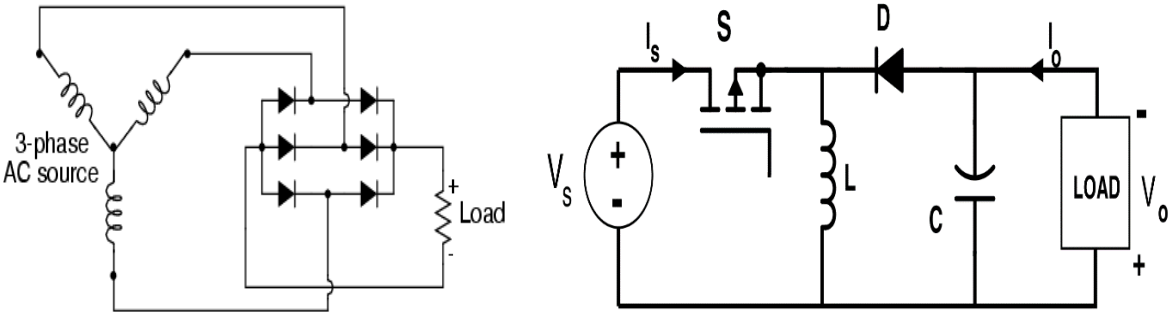

(a) (b)

Figure 6. (a) Three-phase rectifier circuit, (b) The DC-DC buck-boost converter.

4. SIMULATIONS AND RESULTS

The proposed AFPM wind system electrical part is simulated in MATLAB/Simulink and shown in Figure 7. The AFPM accepted a three-phase AC source, and the voltage is changed from 0 to 50 V. The first block in Figure 7 shows the three-phase wind turbine sources and rectifier circuit consisting of six diodes. The rectified single-phase voltage is applied to the buck-boost converter circuit. The converter output voltage is controlled by the PID controller, which compares with a reference voltage and output voltage as an error signal. This error signal is applied to the PID controller, and the obtained error amplifier signal is compared to a high frequency sawtooth to generate the PWM switching signal. The PWM signal drives the MOSFET switching component.

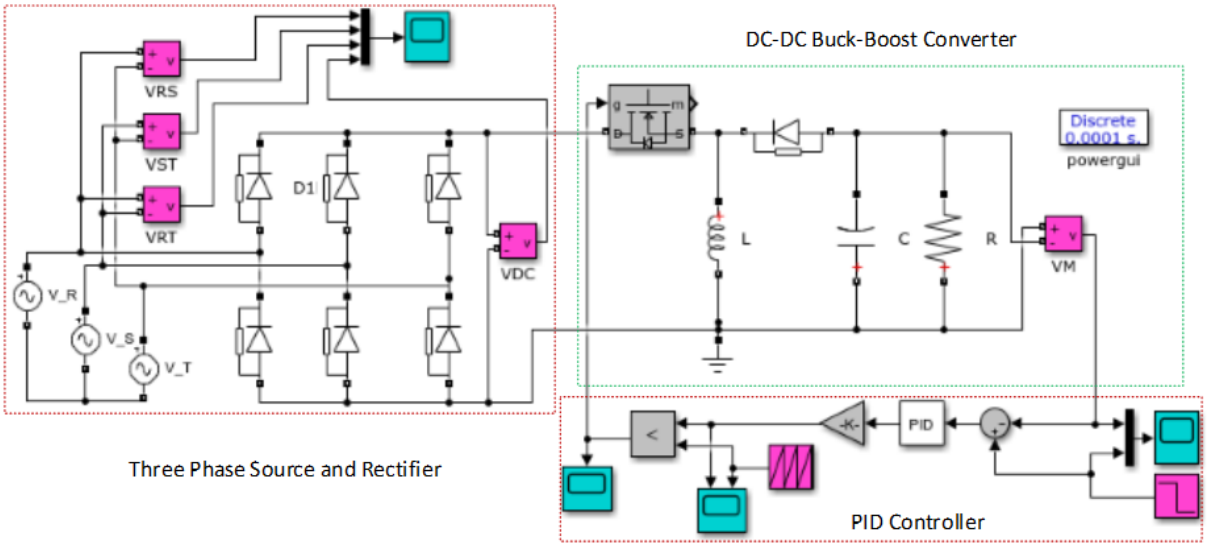

Figure 7. Simulation model of the total system.

The simulation results for three-phase to phase inputs (V_{RS}, V_{ST}, V_{RT}) and three-phase rectifier outputs (V_{DC}) are for different input voltages are shown in Figure 8. Figure 8 (a, b, c) shows the three input voltage for 5 V, 12 V, 30 V maximum phase voltage, and rectifier output voltage. The rectifier output voltages are near the phase to phase maximum voltage with small voltage drops on diodes. So the rectifier output voltages nearly 8 V, 19 V, and 50 V with small ripples.

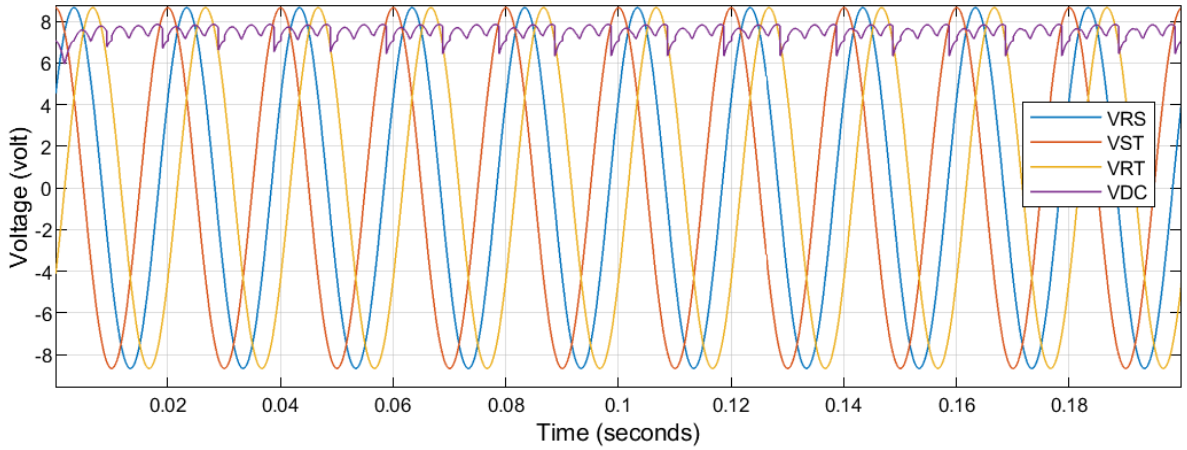

(a)

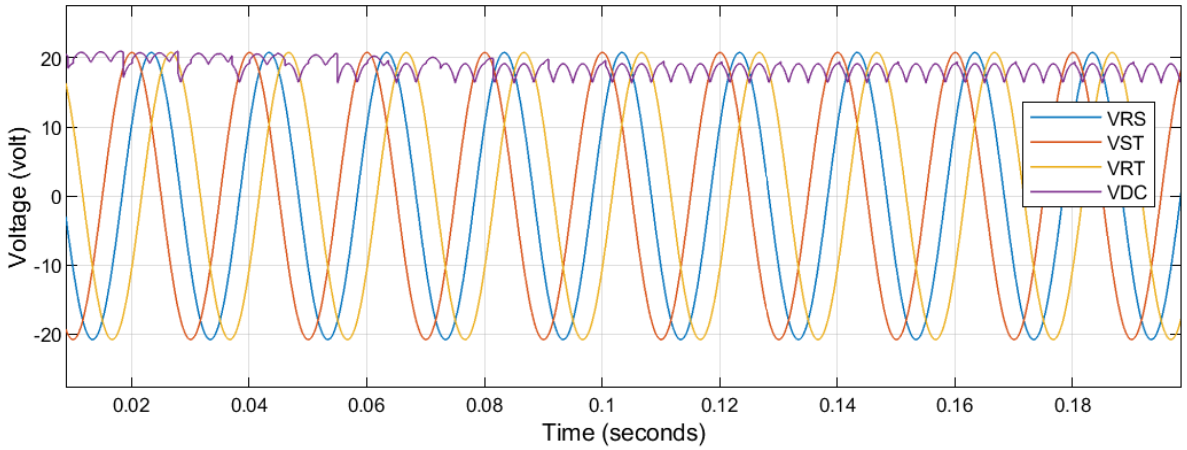

(b)

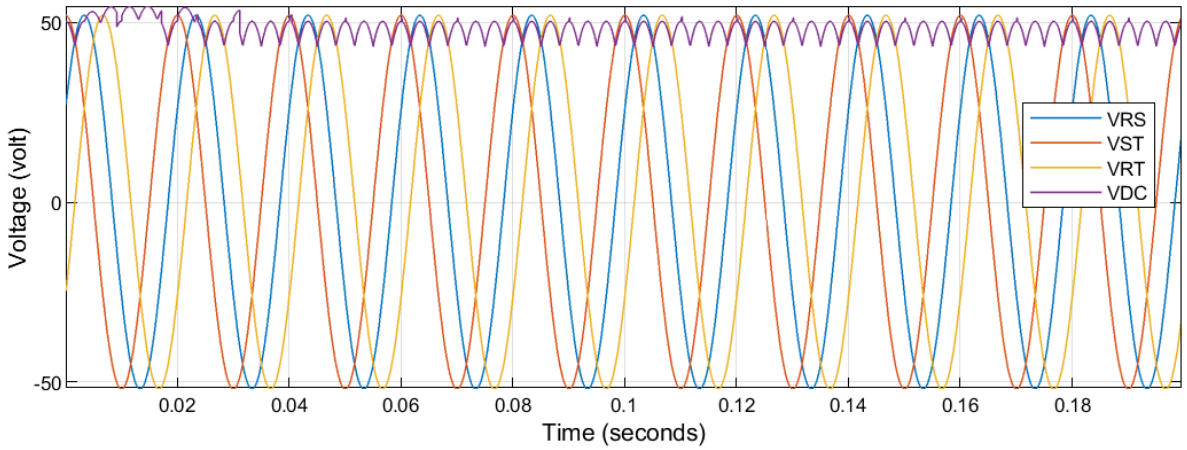

(c)

Figure 8. Three input voltage for (a) 5V, (b) 12 V, (c) 30 V maximum phase and rectifier output voltages.

The simulation results for rectified input voltages (8 V, 19 V, 50 V) are shown in Figure 9 (a, b, c). The converter output voltage variations are given for 12V and 24 V reference output voltage. For 8 V input voltage and 10 Ω load resistance, for 19 V input voltage and 6 Ω load resistance, for 50 V input voltage and 6 Ω load resistance output voltages are given in Figure 9 (a, b, c) respectively.

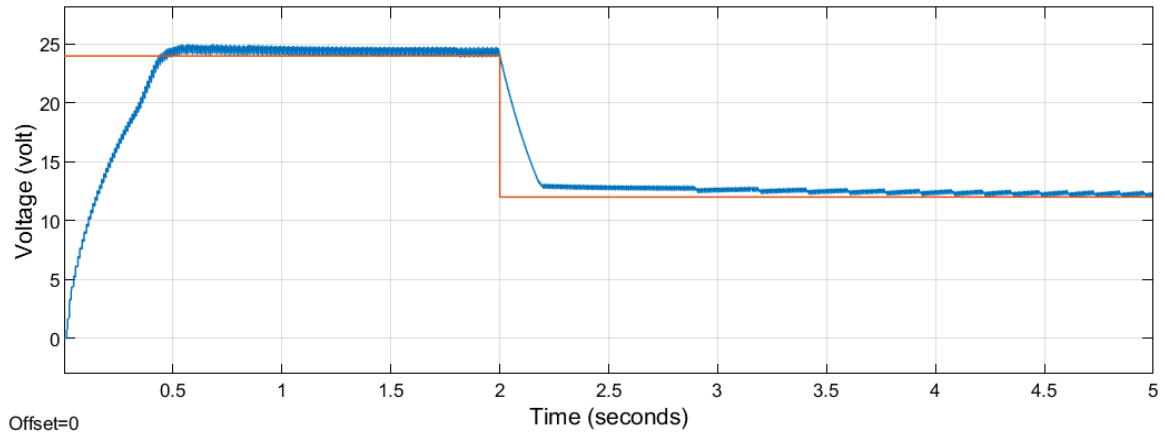

(a)

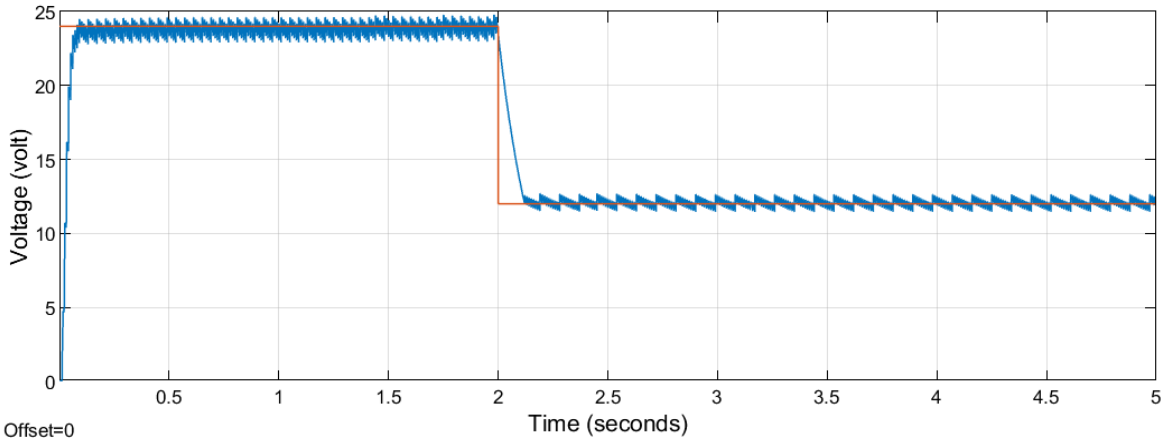

(b)

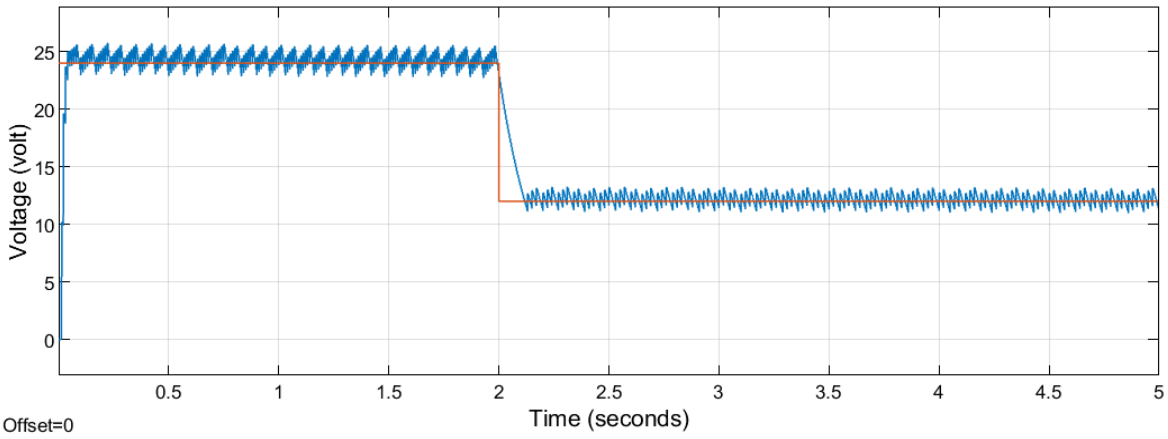

(c)

Figure 9. The simulation results for rectified input voltages (a) 8V, (b) 19V, (c) 50V and for different references (12 V, 24 V).

The simulation results show different input voltages depend on different wind speeds are rectified by the DC voltages. These DC voltages can be reduced or enlarged to the desired voltage levels by the buck-boost converter and PID controllers. The controller works as expected, and the results catch the desired reference values with small ripples. These reference values are selected 12 V and 24 V in simulations for the different bus voltages.

Table 1. All the simulation parameters of the designed system.

Parameters	Values
Phase voltages (V_R=V_S =V_T)	V_{R,S,T_max} = 5V, 12 V, 30 V
Phase to phase voltages (V_{RS}, V_{ST}, V_{RT})	V_{RS,ST,TR_max} = 8V, 19 V, 50 V
Load resistance (R)	R=6 Ω and 10 Ω
Output reference voltages (VR)	V_R=12 V, 24 V
Output power for R=6 Ω, V_R=12V and 24 V	P_{max_24}= 100 W, P_{max}_12=25 W
Inductance value (L)	1,5 mH
Capacitor value (C)	30 mF
Switching components	MOSFETs
Rectifier components	Power diodes

4. CONCLUSION

The AFPM generator and a power converter system were used to design a wind energy system in this paper. The AFPM generator specifications, design steps, and the other components were also explained in this study. The rectifier and converter parts were used to obtained DC voltage at the desired levels. Accepted to generator generates 0-30 V three-phase AC voltages the rectifier and converter parts were designed and simulated in MATLAB/Simulink. The simulation results are obtained for rectifier output and converter outputs using different input voltages and output reference voltages. The simulation results give the expected values with small ripples and response time without a high overshoot and long smoothing. These results show that the power converter and rectifier part can be used to regulate the irregular input voltages depend on the variable wind speeds. Also, the axial axis permanent magnet generator design principles are given in this paper. The authors aim to perform this proposed system experimentally to be used in lightening using power LEDs and batteries without the grid.

REFERENCES

[1] Chalmers, B.J., Wu, W., Spooner, E., An Axial Flux Permanent-Magnet Generator for a Gearless Wind Energy System, *IEEE Transaction on Energy Conversion*, **14,** 251-257, 1999.

[2] Gieras, F.J., Wang, R., Kamper M. J., Axial Flux Permanent Magnet Brushless Machine, *Kluwer Academic Publishers*, USA, 2004.

[3] Aydin, M., Huang S., Lipo T. A., Axial Flux Permanent Magnet Disc Machines: A Review, *SPEEDAM Conf.*, Capri-Italy, 61-71., May 2004.

[4] Aydin, M., Axial Flux Surface Mounted Permanent Magnet Disc Motors for Smooth Torque Traction Drive Applications, *Ph.D. Dissertation*, University of Wisconsin-Madison, 2004.

[5] Rizk, J., Nagrial, M.H., Permanent-magnet generators for wind turbines, *The Third International Power Electronics and Motion Control Conference***, 1**, 208-212, 2000.

[6] Chen, Y., Pillay, P., Khan, A., PM Wind Generator Comparison of Different Topologies, *IEEE 39th Industry Applications Conference,* **3,** 1405- 1412, 2004.

[7] Chen, Y., Pillay, P., Axial-Flux PM Wind Generator with A Soft Magnetic Composite Core, *IEEE 48th Industry Applications Conference,* **1,** 231-237, 2005.

[8] Yang, X., Gong, X. ve Qiao, W., Mechanical Sensorless Maximum Power Tracking Control for Direct- Drive PMSG Wind Turbines, *IEEE Energy Conversion Congress and Exposition*, 4091-4095, 2010.

[9] Şahin, M. E., and Okumuş, H. İ., The Design Steps of a Hybrid Energy System, *Acta Physica Polonica A* **132**, 1160-1164, 2017.

[10] Uyar, M., Gençoğlu, M. T., and Yıldırım, S., Değişken hızlı rüzgar türbinleri için generatör sistemleri, *III. Yenilenebilir Enerji Kaynakları Sempozyumu,* Mersin, Türkiye, 2005, 2-5.

[11] Vyas, R., Effect of Toothless Stator Design on the Dynamic Performance of Permanent Magnet Generators, *Ph.D. Dissertation,* Marquette University, Milwaukee, Wisconsin, 1992.

[12] Yıldırız, E., & Aydemir, M. T. Küçük Güçlü Bir Rüzgar Jeneratöründe Kullanım için Eksenel Akılı Bir Sürekli Mıknatıslı Motorun Analizi, Tasarımı ve Gerçekleştirilmesi, *Journal of the Faculty of Engineering & Architecture of Gazi University,* **24(3),** 2009.

[13] Dursun, E. ve Binark, E. K., Rüzgar Türbinlerinde Kullanılan Generatörler, *UTES*, 667-674, 2008.

[14] Hendawi, E., Khater, F. ve Shaltout, A., "Anlysis, Simulation and Implementation of Space Vector Pulse Width Modulation Inverter", *9th WSEAS International Conference*, 124-131, 2009.

[15] Pradeep, J. Devanathan, R., Comparative Analysis and Simulation of PWM and SVPWM Inverter Fed Permanent Magnet Synchronous Motor, *ICETEEEM Conference*, 299-305, India, 2012.

[16] Çetin, S. K., Genç, M. S., & Daldaban, F., Dikey Eksenli Rüzgâr Türbinleri-Küçük Ölçekli Uygulamalar, *Bilecik Şeyh Edebali Üniversitesi Fen Bilimleri Dergisi*, **6(2),** 539-551, 2019.

[17] Mojola, O. O., On the aerodynamic design of the Savonius windmill rotor, *Journal of Wind Engineering and Industrial Aerodynamics*, **21(2),** 223-231, 1985.

[18] Volker Quaschning: Regenerative Energiesysteme. (2007). Hanser Verlag, München.

[19] Mahmoudi, A., Rahim, N. A., and Hew, W. P., Axial-flux permanent-magnet machine modeling, design, simulation, and analysis, *Scientific Research and Essays*, **6(12)**, 2525-2549, 2011.

[20] Parviainen, A., Pyrhonen, J., and Kontkanen, P., Axial flux permanent magnet generator with a concentrated winding for small wind power applications, *In IEEE International Conference on Electric Machines and Drives*, 1187-1191, 2005.

[21] Diy Vertical Axis Wind Turbine Designs and Much More, https://ecofriend.com/5-diy-vertical-axis-wind-turbine-designs-generate-clean-energy.html, (Accessed 26.11.2020).

[22] A. Boztaş. O. Demirtaş, Rüzgar Enerjisinde Sürekli Mıknatıslı Jeneratör, RTE Üniveritesi Bitirme Tezi, 2020.

[23] Şahin, M. E., and Okumuş, H. İ., Comparison of different controllers and stability analysis for photovoltaic powered buck-boost DC-DC converter, E*lectric Power Components and Systems* 46(2), 149-161, 2018.

DESIGN AND AERODYNAMIC PERFORMANCE ANALYSIS OF MICRO WIND TURBINE BLADE

Kadir KAYA*, Erdem KOÇ**
*Ondokuz Mayis University, Department of Mechanical Engineering, Samsun/Turkey
Email: kadir.kaya@omu.edu.tr
** Ondokuz Mayis University, Department of Mechanical Engineering, Samsun/Turkey
Email: erdemkoc@omu.edu.tr

ABSTRACT

In the near future, due to the depleting fossil fuels and increasing energy demand, countries tend to use more renewable energy sources. Wind energy is one of the most important renewable energy sources and wind turbines are used to utilize this energy. The blade that is a part of the wind turbine, is the first ring of the energy production chain and transmits the kinetic energy taken from the air to mechanical parts as mechanical energy. Aerodynamic and mechanical parameters are taken into consideration during the design phase of the blade. The power taken from the air is directly affected by the aerodynamic design of the blade. In this study, aerodynamic design methodology of horizontal axis wind turbine blades being widely used nowadays have been considered and basic blade aerodynamic design parameters namely, power (N), tip speed ratio (λ), blade number (B), aerofoil selection, aerofoil drag coefficient (C_D), aerofoil lift coefficient (C_L), twist angle (φ), chord (c) have been evaluated. Aerodynamic design case study of 1 m micro-scale wind turbine blade has also been conducted by using the Q Blade software.

Keywords: Wind Energy, Wind Turbines, Wind Turbine Blade Design and Performance.

1. INTRODUCTION

Energy being the most essential input for all sectors, has become a vital component at homes, workplaces, education, health, transportation, industry, shortly all living spaces. Energy sources can be divided into two groups as renewable and non-renewable energy sources and countries tend to use renewable energy sources because of the harmful effects of the non-renewable energy sources.

Wind energy, one of the most important renewable energy sources, is an indirect product of solar energy. Wind power plants are used in order to utilize this source. Wind turbines are generally consist of elements such as rotor, tower, body, gearbox, low and high speed shaft, electric generator, pitch mechanism, anemometer and wind rose, hub and blades (Figure 1). The general principle of these plants energy is based on the combination of the kinetic energy, mechanical energy and electrical energy cycle. In wind turbines, the kinetic energy of the wind is captured by blades. After converting into mechanical energy, this energy is transmitted to generator by using the low speed and high speed shafts. The generator is the wind turbine component where mechanical energy is converted into electrical energy.

In wind turbines, the blade being the first ring of energy production chain of wind turbines, need to be designed by taken into consideration the aerodynamic and mechanical parameters. The aerodynamic parameters affect the amount of power can be obtained from the turbine; the mechanical parameters provide the required strength under the working conditions. Thus, the blade design can be categorised into two groups as the aerodynamic design and the mechanical design. While creating the aerodynamic form or outer geometry of the blade is generated by considering the aerodynamic design procedure (Figure 1c); the dimensions of the blade and the blade elements are determined taking into account of the mechanical design procedure (Figure 1d) [1, 2].

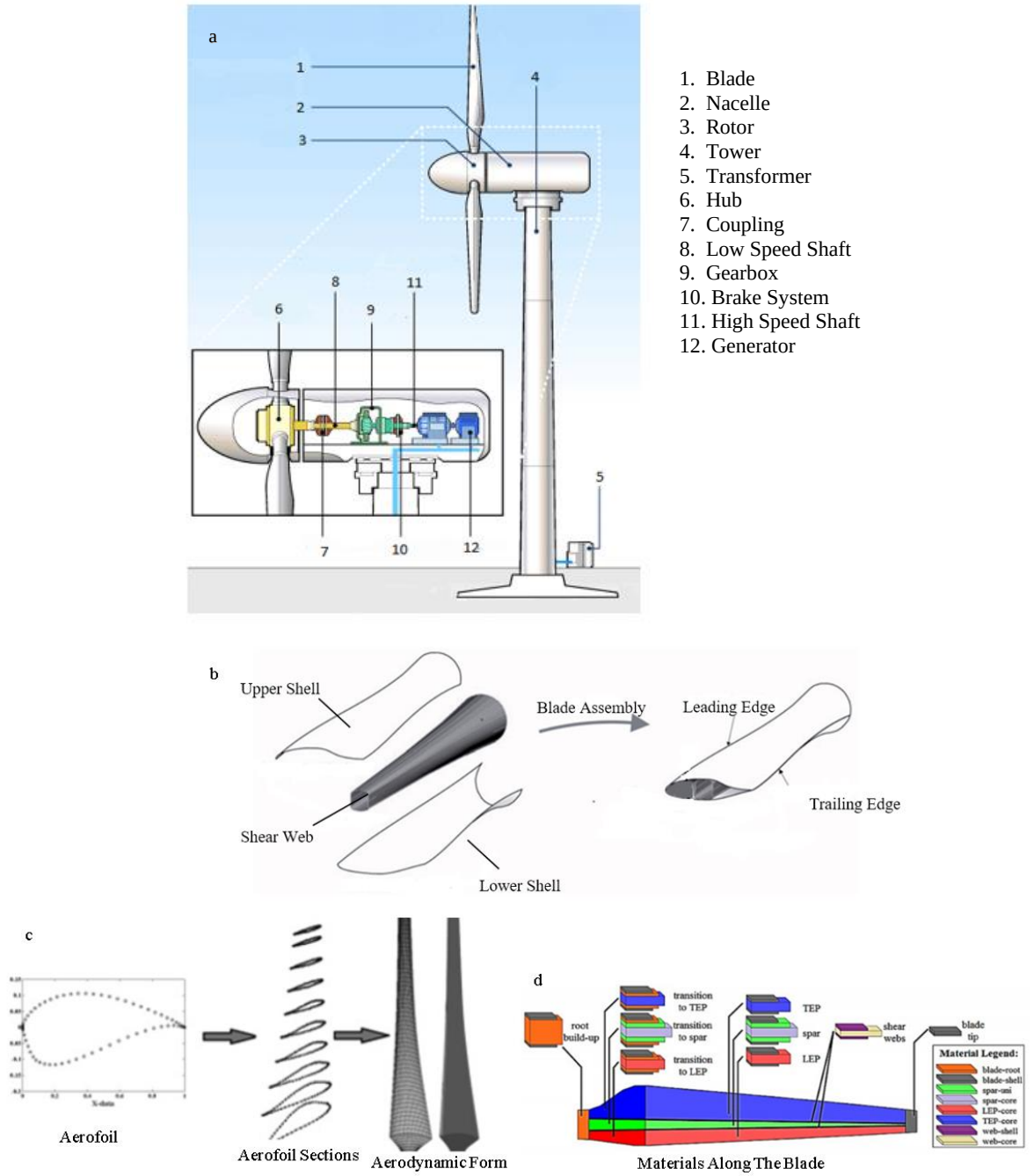

Figure 1. HWAT (a) and Blade (b) General Structure, Aerodynamic (c) and Mechanical (d) Design of the Blade [1-4]

In this study, the aerodynamic design methodology of horizontal axis wind turbine blade, being widely used today, is discussed. The aerodynamic design parameters of the 1 m long blade have been determined and the aerodynamic model of the blade has been generated. In addition, the aerodynamic performance of the blade designed has been evaluated by using the open source software namely Qblade.

2. AERODYNAMIC DESIGN AND PERFORMANCE ANALYSIS OF WIND TURBINE BLADE

The main function of wind turbines is harvesting the wind energy. This energy is directly linked to the aerodynamic design parameters and aerodynamic form of the blade. Some design parameters need to be comprehended for the aerodynamic design of the wind turbine and blade. So these parameters are summarized in this section.

2.1 Basic Aerodynamic Design Parameters

Parameters such as wind power (N), tip-speed ratio (λ) , power coefficient (C_p) and blade number (N) are known as basic aerodynamic design parameters. These parameters and definitions are given below [5-8].

Wind power (N); Wind power depending on the density of the air (ρ), the sweep area (A) of the blade and the wind speed (v) can be determined by using the equation below

$$N = \frac{1}{2}\rho A v^3 \tag{1}$$

The tip-speed ratio (λ): The tip-speed ratio being one of the important parameters for determining the aerodynamic performance is calculated by the ratio of the blade tip speed and wind speed.

$$\lambda = V_{tip}/V_{wind} = \omega x R/V_{wind} \tag{2}$$

Power Coefficient (C_p): Power Coefficient is used to determine the percentage of harvesting power to wind power and this ratio is also known as the efficiency of the turbine. It is calculated by using following equation.

$$C_p = \frac{N_R}{N_o} \tag{3}$$

Blade Number (N): One of the main parameters affecting the aerodynamic performance of wind turbines is the number of blades. In wind turbines, the number of blades and the rotational speed of the blades are inversely proportional. In wind turbines, the rotational speed of the blade decreases as the number of blades increases, therefore, as the number of blades in wind turbines increases, the tip-to-speed ratio decreases.

2.2 Aerodynamic Design Parameters of the Blade

As mentioned before, the aerodynamic design of the blade affects the amount of power can be obtained from the wind turbine. The aerodynamic form or geometry of the blade is generated by using the aerodynamic design parameters. These parameters are summarised as follows [5-8].

- The output of the wind turbine is determined by using the equation below.
- $$N = C_p \eta \frac{1}{2}\rho \pi R^2 v^3 \tag{4}$$

  Here, N Power, the power factor of the turbine, electrical and mechanical efficiency.

- The selection of the turbine tip speed ratio
  The tip speed ratio is selected between 1-3 for wind turbines produce mechanical energy; 4-12 for wind turbines generate electricity. This ratio is selected between 9-10 for two bladed wind turbines; 6-8 for three bladed turbines generate electricity.
- The selection of the blade number
  Wind turbines with 3 blades are widely used today. Although more power can obtained from the wind turbine as the number of blades increases, the optimal wind turbine is 3-bladed turbines considering the turbine cost, mechanical behavior and performance criterias of the wind turbine.
- Selection of aerofoil according to the selected tip speed ratio

In wind turbine blade, Unique aerodynamic sections namely aerofoil are used to capture the kinetic energy of the wind. These profiles ensure pressure difference between the upper and lower surfaces of the blade creating an aerodynamic lift force.

- Determination of lift (C_L) and drag (C_D) coefficients of the selected aerofoil
  C_L and C_D coefficients of aerofoils are determined by using the experimental studies at different Reynolds numbers.
- Determination of the twist angle (φ) and chord length (c) of the blade
  According to the Modified Blade Element Momentum Theory, the twist angle (φ) and chord lengths (c) of the blade sections are determined by using the following equations.

$$\varphi = \frac{2}{3}\tan^{-1}\frac{1}{\lambda_r} - \alpha_D \tag{5}$$

$$c = \frac{16\pi r}{BC_L}\left(sin\left(\frac{1}{3}\tan^{-1}\frac{1}{\lambda_r}\right)\right)^2 \tag{6}$$

The aerodynamic design parameters of the blade such as chord length (c) and twist angle (φ) are shown in Figure 2.

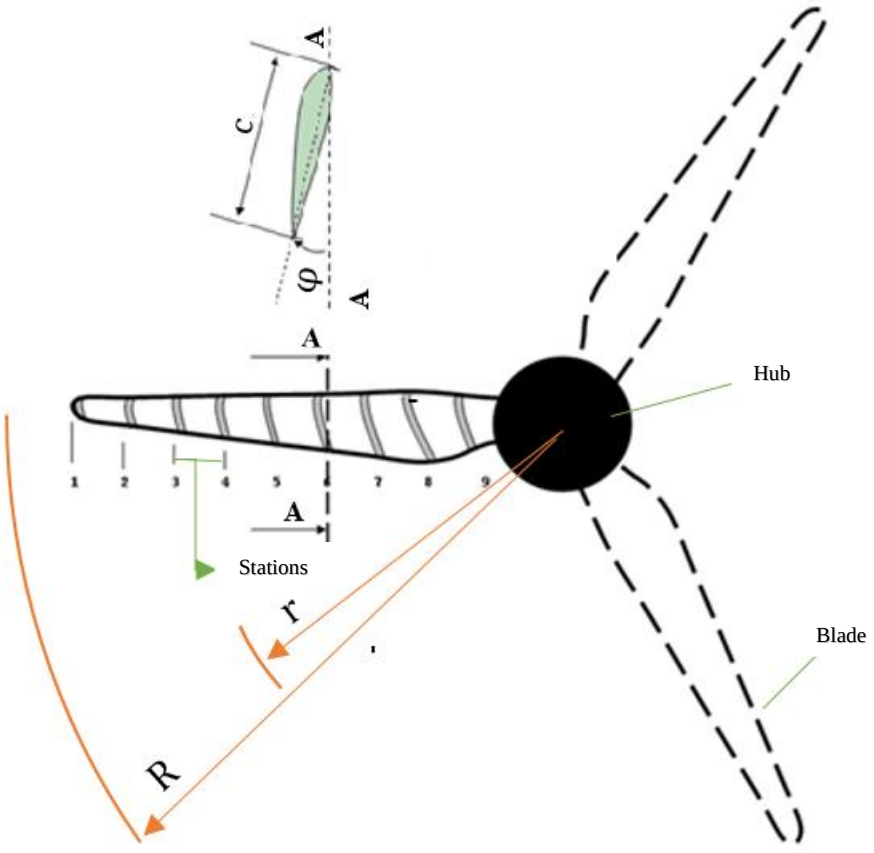

Figure 2. Aerodynamic Design Parameters of the Blade [1,2]

The aerodynamic form or geometry of the blade is generated by using the aerodynamic design parameters such as the twist angle (φ) and chord length (c) determined.

2.3 Aerodynamic Design of the Blade

The aerodynamic shape of the blade is formed by combining sections having different shape and size. The blade has three different sections from root to tip. The first cross-section is circular near the root and the second cross-section is the transition section between first circular section and last section. The last cross-section is the aerofoil section that ensures generating the aerodynamic lift force.

The aerodynamic design of the blade is the process of generating the aerodynamic form of the blade using the design parameters determined. In this study, the aerodynamic design of the 1 m blade has been done. For this purpose, the aerodynamic design parameters of the blade have been determined as aforementioned and given in Table 1. Due to the fact that S835, S834 and S833 aerofoils have been recommended to use in the blade structure of 1-3 m blade by National Renewable Energy Laboratory (NREL), the aerofoils used in this study are selected as NREL S835, S834 and S833 [9, 10]. In this study, tip-speed ratio and blade number parameters are selected as 7 and 3 respectively.

Table 1. Aerodynamic Design Parameters of Blade Designed

Stations	r/R	r	Angle of Twist (φ)	Chord (c, m)	Aerofoil Section
1	0.1	0.1	-	-	Circular
2	0.2	0.2	18.78700	0.2095230	S835
3	0.3	0.3	15.44905	0.1865170	S835/S833
4	0.4	0.4	12.11111	0.1635110	S835/S833
5	0.5	0.5	8.773164	0.1405050	S835/S833
6	0.6	0.6	5.435218	0.1174990	S835/S833
7	0.7	0.7	2.097273	0.0944930	S835/S833
8	0.75	0.75	0.42830	0.0829900	S833
9	0.8	0.8	0.25926	0.0744792	S833/S834
10	0.9	0.9	0.09022	0.0659684	S833/S834
11	0.95	0.95	-0.00570	0.0617130	S834
12	1	1	-0.00570	0.0617130	S834

The aerodynamic form of the blade have been generated by using the aerodynamic design parameters given in Table 1 and the blade geometry designed within the scope of this study.

2.4 Investigating the Aerodynamic Performance of Blade by Using the Qblade Software

Qblade is an open source software for wind turbines developed by Hermann Föttinger Institute of Berlin Technical University. This software is adequate for teaching, design and simulation capabilities for horizontal axis wind turbines (HAWT) and vertical axis wind turbines (VAWT) rotor design and shows all the fundamental relationships of design concepts and turbine performance in an easy and intuitive way [11].

In this aerodynamic model of 1 m HWAT blade have been generated (Figure 3) and aerodynamic performance of this blade have been investigated by using Qblade software.

3. AERODYNAMIC PERFORMANCE OF BLADE

In this study, Qblade software has been used for evaluation the aerodynamic performance of the blade. For this purpose, firstly aerodynamic geometry of the blade has been generated with help the Qblade software (Figure 3).

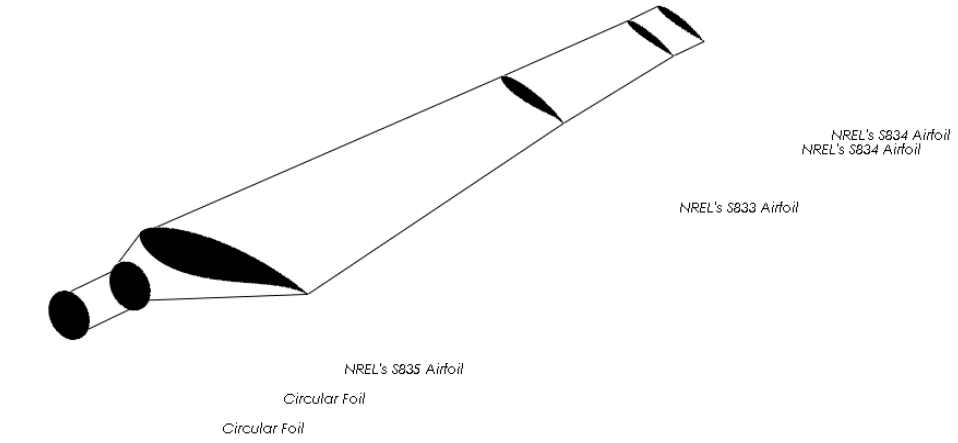

(a)

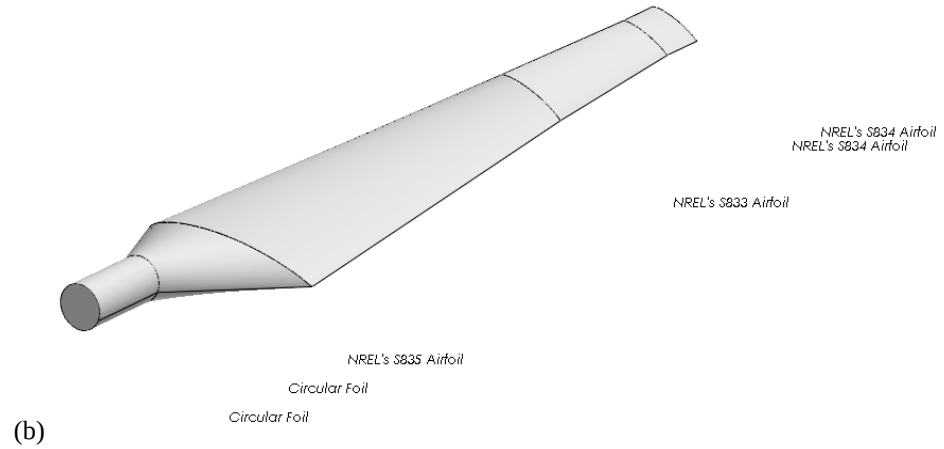

(b)

Figure 3. Aerodynamic Form of the Blade Designed

The power occours at this blade for different wind speeds has been determined by using Qblade (Figure 4). It can be seen from the figure that the pressure coefficient (C_p) takes the greatest value of 0.45 with the tip-speed ratio (λ) of the blade being equal to 6.

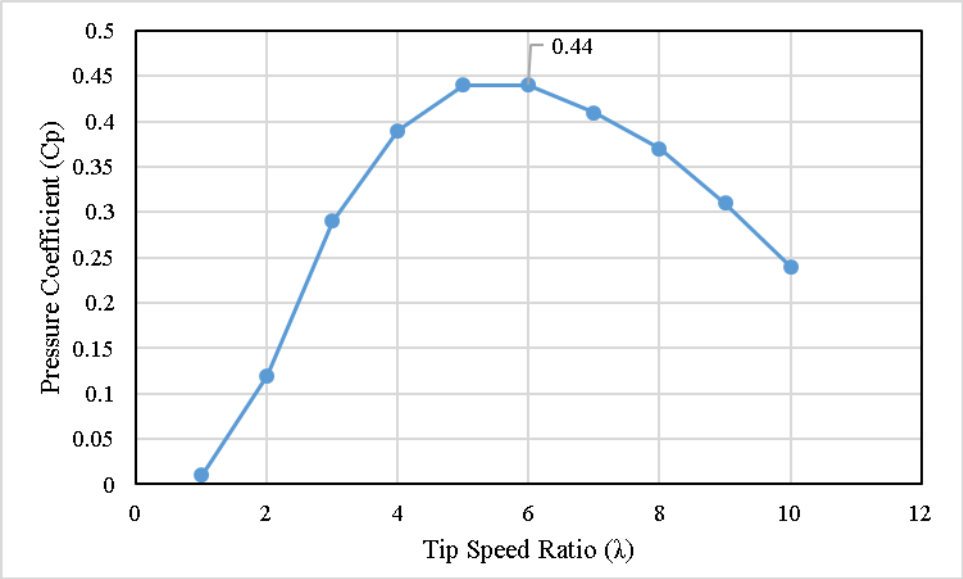

Figure 4. The Variation of the Pressure Coefficient (C_p) by Tip-Speed Ratio (λ)

The output power (N) of the blade has been determined according to wind speed of the blade (Figure 5). It can be seen from the figure that the blade starts to operate at a wind speed of 2 m/s and produces the maximum power (444.14 Watt) at wind speed of 11.5 m/s.

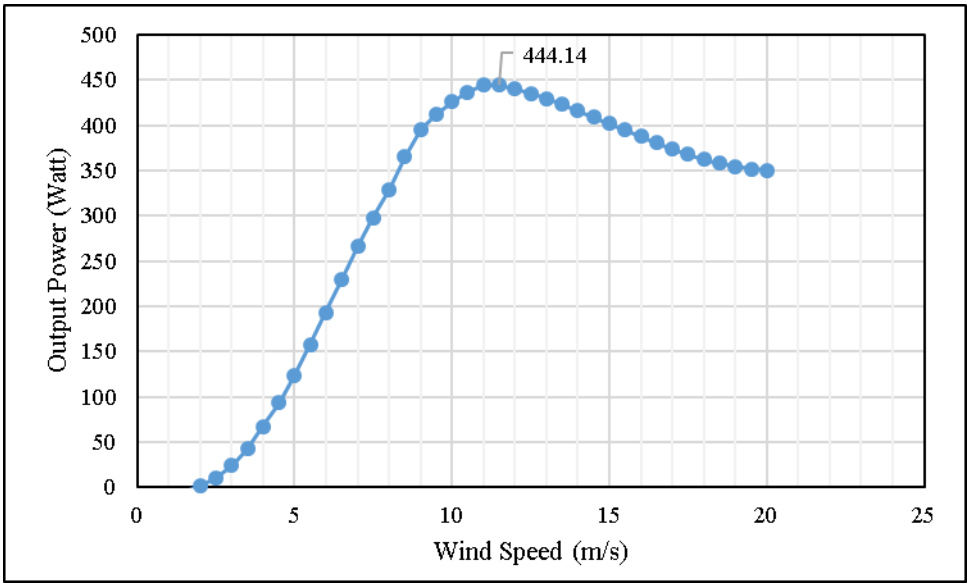

Figure 5. The Variation of Output Power with Wind Speed

4. RESULTS

In wind turbines, the blade being the first ring of energy production chain of wind turbines, need to be designed by taken into consideration the aerodynamic and mechanical parameters. The aerodynamic parameters affect the amount of power can be obtained from the turbine; the mechanical parameters provide the required strength under the working conditions. In this study, the aerodynamic design methodology of horizontal axis wind turbine blade is discussed. The aerodynamic design parameters of the blade 1 m long have been determined and the

aerodynamic performance has been evaluated by using the open source software namely Qblade. Important results obtained from this study are summarized below.

- The aerodynamic design of the blade affects the amount of power can be obtained from the wind turbine.
- Qblade is an open source software for wind turbines for teaching, design and simulation capabilities for horizontal axis wind turbines (HAWT) and vertical axis wind turbines (VAWT) rotor design and shows all the fundamental relationships of design concepts and turbine performance.
- The pressure coefficient takes the greatest value of 0.45 with the tip-speed ratio (λ) of the blade being equal to 6.
- The blade starts to operate at a wind speed of 2 m/s and produce the maximum power at wind speed of 11-11.5 m/s.
- It is suggested to perform the aerodynamic performance analysis experimentally after manufacturing the blade designed.

REFERENCES

[1] Kaya, K. Rüzgar Türbini Kanadının Mekanik Tasarım Esasları, Yüksek Lisans Tezi, Ondokuz Mayıs Üniversitesi Fen Bilimleri Enstitüsü, Samsun, s. 19, 2014.

[2] Kaya, K., Koç., E. Yatay Eksenli Rüzgâr Türbinlerinde Kanat Profil Tasarımı ve Üretim Esasları, *Mühendis ve Makina*, 56(670), 38-48, 2015.

[3] Sale, D., Aliseda, A. Structural Design of Composite Blades for Wind and Hydrokinetic Turbines, University of Washington, Northwest National Marine Renewable Energy Center, 2012.

[4] Layton J., How Wind Power Works, URL: https://science.howstuffworks.com/environmental/green-science/wind-power2.ht, Accessed Date: 15.02.2020.

[5] Hau, E. Wind Turbines Fundamentals, Technology, Application, Economics, *Springer-Verlag*, Second Edition, ISBN 10-3-540-24240-5, , Berlin, Heidelberg, Germany, 2006.

[6] Burton, T., Sharpe, D., Jenkins, N., Bossanyi, E., Wind Energy Handbook, *John Wiley&Sons Ltd*., 608, England, 2001.

[7] Schubel, P. J., Crossley, R. J., "Wind turbine blade design," *Enegies*, 5, 3245-3449, 2012.

[8] Manwell, J. F., McGowan, J. G., Rogers, A. L. Wind Turbine Explained, Theory Design And Application, *John Wiley&Sons*, ISBN 0-471-49972-2, England, 2002.

[9] Somers, D.M., The S833, S834, and S835 Airfoils Subcontract Report NREL/SR-500-36340, National Renewable Energy Laboratory (NREL), 2005, URL:
https://wind.nrel.gov/airfoils/Documents/S833,S834,S835_Design.pdf.

[10] Wind Turbine Airfoil Families, NREL, URL: https://wind.nrel.gov/airfoils/AirfoilFamilies.html, Accessed Date: 15.02.2020.

[11] Qblade Wind Turbine Design and Simulation Software, URL: http://www.q-blade.org/#welcome, Accessed Date: 15.02.2020.

DESIGN OF THE DEFORMABLE WIND TURBINE BLADE TO KEEP EFFICIENCY HIGH

Yalım GÜLTEKİN*, Emre KOÇ, Tahir YAVUZ****
*Başkent University, Anadolu OSB Vocational School Machinery Program, Ankara/Turkey
Email: ygultekin@baskent.edu.tr
**Başkent University, Department of Mechanical Engineering, Ankara/Turkey
Email: ekoc@baskent.edu.tr, tyavuz@baskent.edu.tr

ABSTRACT

Wind turbines are conventionally used for converting the wind's kinetic energy into electrical energy. In wind turbines, wind energy is converted to mechanical energy by turning the turbine blades and then to electrical energy with the help of a generator. The maximum efficiency of the horizontal axis turbine has obtained the conditions at which the maximum ratio of the lift to drag force. However, when the wind speed changes, of the design condition, efficiency decreases accordingly. This study aims by using deformable blades to keep the value of the C_l/C_d ratio at about the design condition in the range of the wind speed for a horizontal wind turbine. In the optimization, Ansys Fluent Adjoint Solver with the k-ε is used. The simulation model created is validated with data on Cornel University Confluence. Reference airfoil NACA0012 is chosen. At the design angle of attacks, $\alpha=4^o$ and $\alpha=10^o$ the value of C_l/C_d is obtained to be about 13 and 10 and kept constant in the range of wind speed between 5 m/s and 25 m/s. A deformable blade can be used to get maximum high and constant efficiency at wind speeds in wind turbine applications.

Keywords: Deformable wind turbine blades, Airfoils, k-epsilon turbulence model, C_l/C_d optimization, Ansys Fluent Adjoint Solver.

Symbols

k-ε	k-epsilon turbulence model
C_l	Lift coefficient
C_d	Drag coefficient
α	Angle of attack

1. INTRODUCTION

A wind turbine could be defined simply as a device that converts kinetic energy from the wind into electrical power. Wind turbines are manufactured in a wide range of vertical and horizontal axis types. The small type turbines are used for applications such as battery charging for auxiliary power for boats or caravans or to power traffic warning signs. Slightly larger turbines can be used for making small contributions to a domestic power supply while selling unused power back to the utility supplier via the electrical grid. Arrays of large turbines, known as wind farms, are becoming an increasingly important source of renewable energy and are used by many countries as part of a strategy to reduce their reliance on fossil fuels.

With the globalization process, the developments in science and technology, and the increase in quality of life, and population growth concordantly, the demand for energy requirement is rapidly increasing year by year in World and Turkey. According to the Strategic Plan of the Ministry of Energy between 2019-2023, the energy demand of Turkey will increase by an annual rate of 6% [1]. Energy sources meeting this demand can be divided into "conventional energy sources" and "renewable energy sources". Conventional sources are the sources that produce energy by burning carbon-based fuels, which are used in energy production until now and renewable energy sources are sources that can renew themselves in a short period. According to the 2019-2023

Strategic Plan of the T.R. Ministry of Energy and Natural Resources report; it is anticipated that the ratio of the installed power based on the domestic and renewable resources of our country's energy requirement to the total installed power will increase from 59% to 65%. This installed power increase mainly depends on the increase of renewable energy sources. Renewable energy sources in a wide range of sources can be sampled as solar, hydraulic, tidal, hydrogen, wave, and wind [2-4].

Today, depending on technological developments, the wind turbine can operate to produce electric energy in the range of the wind speed between 4 m/s and 25 m/s. Some region has not enough wind performance to generate electricity from a wind turbine. The formation of wind energy depends on local factors such as geographical formations, land-sea transitions, temperature, and pressure differences, as well as the shape of the earth, the morphological structure of the earth, and the sun. Therefore the speed of the wind, as dependent on many parameters, is not constant but changes continuously with time over a day. As wind speed changes, the energy produced by the wind turbine also changes accordingly. All wind turbines are designed at some reference parameters such as reference wind speed, operation rate, and so on. The efficiency of the wind turbine is the most important parameter on energy production from a wind turbine and their efficiency is given at these design parameters. When wind speed changes the efficiency of the wind turbine has to change. Accordingly, the energy produced from the wind turbine also has to be decreased. To get more energy from the wind turbine, the efficiency of the turbine has to be kept constant over the operation wind speed ranges. To keep the efficiency of the turbine at a high level at the wind speed, the deformable wind blade may be the solution.

There are studies in the literature on deformable blades. Li et al. [8] have conducted studies on modeling and analysis of deformable blades until today. Morgado et al. [9] studied the performance outputs of XFOIL and CFD methods on high lifting force at low Reynold numbers. The outputs of these studies showed that the X-FOIL programs with k-kl-ω and k-ε models resulted from more accurate numerical results in C_d and C_l values Wang et al. [10] provided a reduction in the dynamic stall characteristic by airfoil optimization. They created the optimum calculation method with the function adaptation method for optimization and so reducing the time spent for CFD implementation and optimizing the airfoil worked on. Wang et al. [11] worked on the backed, monitoring, and control of flexible blades with piezo composite actuators that can be replaced dynamically. As a result of this study, it has been found that the voltage applied to piezo composite actuators, which provide transitions between predetermined airfoil shapes, causes deviations in the profile along the blade and causes vibration. To be able to come through this situation, it has been suggested to use dynamic control and backfeed systems instead of static control (system control with voltage difference only). Açıkel and Genç [12] worked on laminar decomposition bubble control on the wind turbine blade suction surface with partial flexibility. In the study, it was tried to decrease the friction force with the partial elastic membrane on the suction surface in different Re numbers. It was observed that the friction force decreased significantly compared to the solid turbine blades without deformation if there is a membrane deformation at an equal frequency to the frequency of the deformation in the flow. Marinić-Kragić et al. [13] worked on the subjects of numerical analysis and shape optimization of Savonius type vertical axis wind turbines with flexible blade structure. Bilgen and Friswell [14] worked on profile design with variable hump level in solid-phase with Piezoceramic composite actuators. As a result of this study, voltages were applied on blade profiles using MFC actuators and different airfoil profiles were created. Xiaoqiang et al. [15] studied the geometric parameter method for the airfoil. In this study, shape adaptation and aerodynamic calculations were made over 8 control parameters that can be considered to be less than conventional calculation methods using the IGP method. Gonzales et al. [16] studied the control and maintenance of turbine rolling movements. As a result of this study, undesired flips were tried to be eliminated while using the maximum wind potential with pitch movement by using 4 parameters. In the suggestion part of the study, it was addressed that pitch adjustments can be made with learning algorithms. Thumthae [17] has worked on optimum blade profiles for variable-speed wind turbines in low wind speed regions. In the study, CFD and BEM-based SuWiT program was used and it was observed that the outcomes were the same. The turbine based on in the study is 300 kW and found the power coefficient as 50.5% (Betz limit is 59.63%) since it was exposed to a wind speed of 10 m/s.

The aim of the study is that, to sustain the energy production of the wind turbine at a reasonable domain. To obtain that the airfoil of the wind turbine blade changes shape to overcome the handicaps of the wind speed changes. The study is subdued into 2 parts. In the first part, the confirmation study has been achieved. Later the

airfoil is studied in one of the inefficient points at 10º and one of the most efficient angles of attack of 4º. To able to achieve this morphing airfoil ANSYS-FLUENT package program with ADJOINT SOLVER is used.

2. MATERIAL AND METHOD

The deformation of the wind turbine blade profile fundamentally begins with defining the blade profile that is used. In the study, the NACA 0012 symmetric airfoil with a small cross-section area is chosen. To increase the energy transmitted to the turbine at low wind speeds, the blade profile has been transformed into a new shape where more lifting force can be obtained. When the wind speed exceeds the safe value, the blade profile has evolved in such a way to achieve a less lifting force reducing the energy transmitted to the turbine. For the emergency state, the blade shape transferred a shape producing zero lift and stop the system.

The CFD analyses for the system care carried out by using ANSYS-FLUENT with ADJOINT SOLVER. The FLUENT code solves the RANS equations using the finite volume method. Steady-state, SIMPLE pressure-based, and Green-Gauss cell-based discretization method are chosen as a solver in the CFD analyses. Also, the second-order scheme is used for the momentum and turbulence equations discretization. The k-ε turbulence transition model has been used to solve the incompressible Navier-Stokes equations. The external rectangular flow domain is chosen. The air entrance surface of the domain is defined as "Velocity Inlet" and the air exit surface of the domain is defined as "Pressure Outlet" boundary conditions. The mesh structure is created using the Ansys Fluent Program. To get a more precise solution 72400 nodes are chosen. The mesh structure is shown in Figure 1.

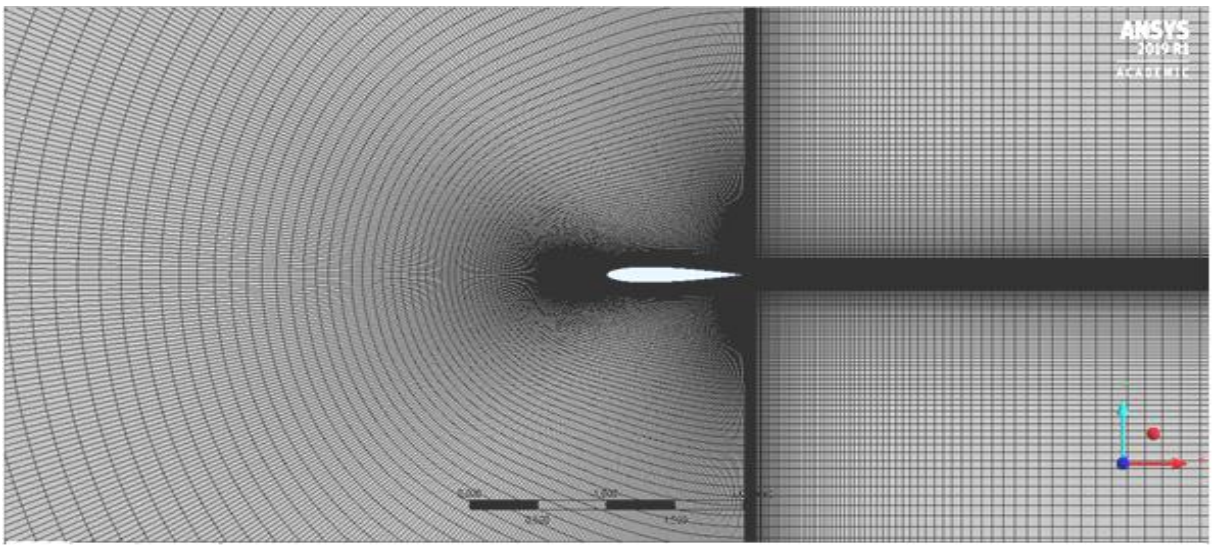

Figure 1. Mesh structure for NACA0012

In the validation of the program, the Airfoil Database Search-2015 [18] is used. In the validation study, as the NACA0012 blade gives the maximum value of C_l/C_d the angle of attack, 4º, and 1 m/s wind speed is chosen. The simulation study gives the value of C_l = 0.65785139 comparing the value of C_l = 0.6630 by Cornel University Data Base. There is about % 0.7 difference which is considered to be acceptable.

3. RESULTS AND DISCUSSIONS

The symmetric airfoil, NACA0012 is chosen as the primary airfoil. The airfoil gives the maximum value of C_l/C_d at the angle of attack 10º considering the maximum value of the C_l/C_d is about 13.2 at α=4º [18]. Static pressure distributions obtained about airfoil with changing airfoil shape are shown in Figure 2 at various wind speeds.

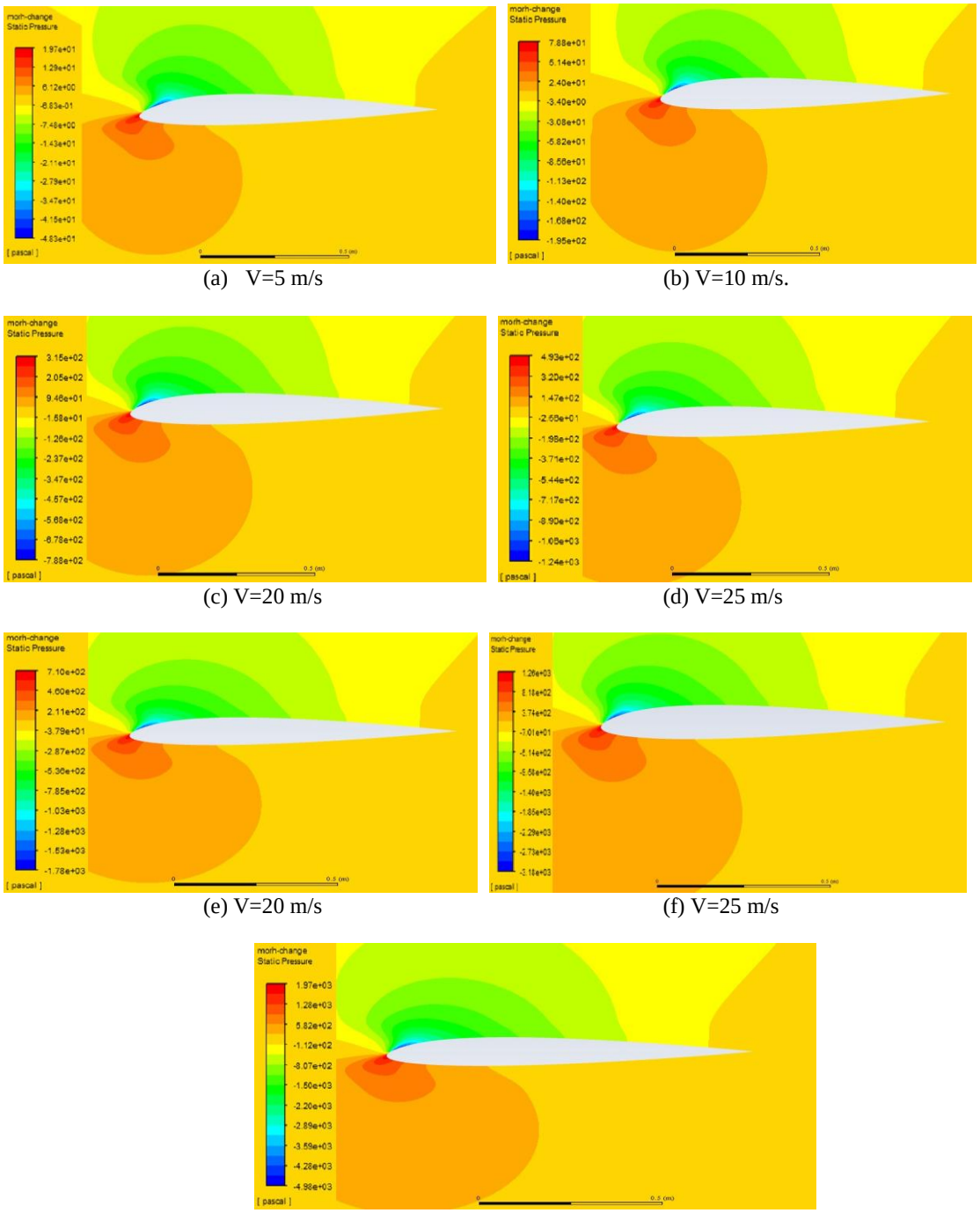

(a) V=5 m/s (b) V=10 m/s.

(c) V=20 m/s (d) V=25 m/s

(e) V=20 m/s (f) V=25 m/s

(g)V=25 m/s

Figure 2. Static pressure distriubitons for morphed airfoil at α =10^o for (a) V=5 m/s (b) V=10 m/s (c) V=20 m/s (d) V=25 m/s (e) V=30 m/s (f) V=40 m/s (g) V=50 m/s

The symmetric airfoil, NACA0012 is chosen. The airfoil gives the maximum value of C_l/C_d at the angle of attack α 10^o considering the maximum value of the C_l/C_d is about 13.2 at α=4^o.

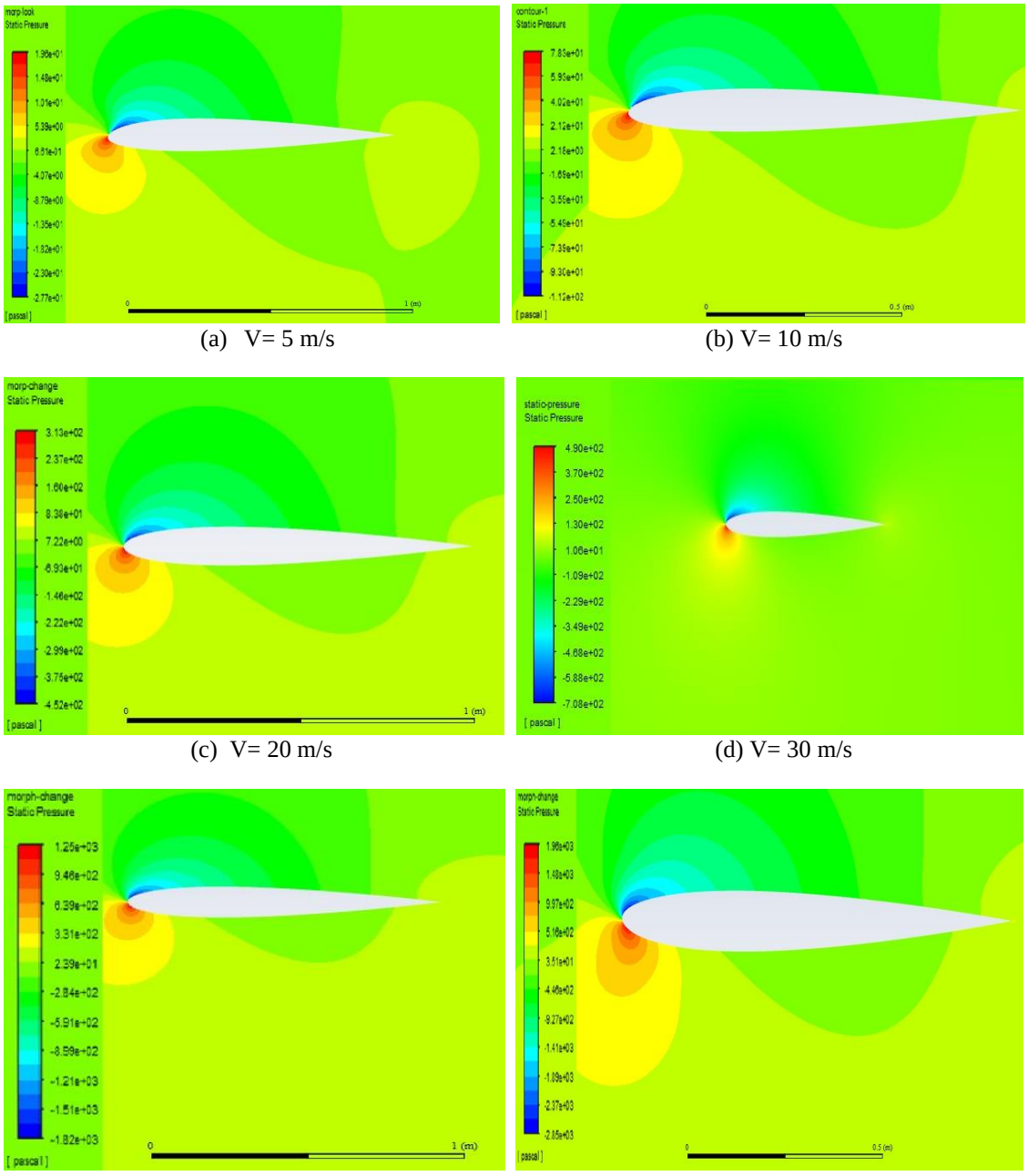

(a) V= 5 m/s (b) V= 10 m/s

(c) V= 20 m/s (d) V= 30 m/s

(e) V= 40 m/s (f) V= 50 m/s

Figure 3. Static pressure distriubitons for morphed airfoil at $\alpha = 4^o$ for (a) V=5 m/s (b) V=10 m/s (c) V=20 m/s (d) V=30 m/s (e) V=40 m/s (f) V=50 m/s

As shown in the figure the geometry of the airfoil changes at different wind speed to keep the ratio of C_l/C_d to be constant and the airfoil changes the shape to get approximately the constant value of the C_l/C_d at wind speeds. The ratio of the C_l/C_d obtained in this simulation at various wind speed is given in the Table,

Table1. Variation of the C_l/C_d at wind speed at α=10º and α= 4º

10º Angle of Attack		
Speed	**C_l/C_d**	**$\Delta C_l/C_d$**
5 m/s	9,787826	3,417799
10 m/s	10,059530	3,148991
20 m/s	10,285000	2,949397
25 m/s	10,349620	3,241208
30 m/s	10,399910	2,967532
40 m/s	10,474970	2,753032
50 m/s	10,529850	2,677229

4º Angle of Attack		
Speed	**C_l/C_d**	**$\Delta C_l/C_d$**
5 m/s	12,013490	1,212100
10 m/s	12,574420	1,075796
20 m/s	13,061780	0,115193
25 m/s	13,205625	0,000000
30 m/s	13,318910	-0,011938
40 m/s	13,490370	-0,122248
50 m/s	13,359180	-0,317247

Green values in the table indicate the increase while red values the decrease required to be made by the airfoils to keep the values of the C_l/C_d approxşimatelly constant. As shown in the table, the ratio of the C_l/C_d has kept approximately constant values at two angles of attacks as 13 at α=4º and at α=10º respectively by changing the shape of the airfoil at wind speeds.

4. CONCLUSION

The efficiency of the wind turbine is the most important parameter on energy production from wind turbines. The efficiency of wind turbines is given at the design parameters such as free wind speed, airfoil type, and revolution rate, and so on. When wind speed changes, the efficiency of wind turbines has to be changed too. To get more energy from the wind turbine, the efficiency of the turbine has to be kept constant over the operation wind various speeds. To keep the efficiency of the turbine at a high level at the wind speed, the deformable wind blade may be the solution. In the analysis, ANSYS-FLUENT package program with ADJOINT SOLVER is used.

Conclusions from the study based on the master thesis studies conducted by Gültekin under the supervision of Prof. Yavuz at Başkent University are;

-Deformable blade can be used to get maximum high and constant efficiency at wind speeds,
-At the angle of attack, 4º, the ratio of C_l/C_d = 13 is obtained in the range of the free wind speed between 5 m/s and 25 m/s
- At the angle of attack, 10º, the ratio of C_l/C_d = 10 is obtained in the range of the free wind speed between 5 m/s and 25 m/s.

The efficiency of the wind turbine should be re-calculated at each case to compare the values of the efficiencies at the wind speed. It is considered to be as remaining work.

5. REFERENCES

[1] *Strategic Plan 2015-2019 of the T.R. Ministry of Energy and Natural Resources*. Retrieved from *https://www.enerji.gov.tr/File/?path=ROOT%2f1%2fDocuments%2fStratejik%20Plan%2fETKB%202015-2019%20Stratejik%20Plani.pdf*.

[2] Koç, E. & Şenel, M. C., Dünyada ve Türkiye'de Enerji Durumu-Genel Değerlendirme, *Mühendis ve Makine Dergisi- Journal of Engineer and Machine*, **54** (639), 32-44, 2013.

[3] Yılmaz, M., Türkiye'nin Enerji Potansiyeli ve Yenilenebilir Enerji Kaynaklarının Elektrik Enerjisi Üretimi Açısından Önemi, *Ankara Üniversitesi Çevrebilimleri Dergisi- Ankara University Journal of Environmental Science,* **4** (2), 33-54, 2012.

[4] Koç, E. & Kaya, K. (2015). Enerji Kaynakları-Yenilenebilir Enerji Durumu, *Mühendis ve Makine Dergisi-Journal of Engineering and Machine*, **56** (668): 36-47, 2015.

[5] Keleş, D., Ayhan, V., Parlak, A., Cesur, İ., Boru, B. & Koç, T., Bir Rüzgar Türbini Tasarımı ve Geliştirilmesi. *Sakarya Üniversitesi Fen Bilimleri Enstitüsü Dergisi-Sakarya University Journal of Science*, **17** (2), 207-216, 2013.

[6] Şenel, K. & Koç, E., Kanat Tasarım Parametrelerinın Rüzgâr Türbini Aerodinamik Performansına Etkisi, *5. Ulusal Havacılık ve Uzay Konferansı Tam Metin Kitabı- Proc. of 5th National Aviation and Space Conference*, Kayseri-Türkiye, 2014.

[7] Elibüyük, U. & Üçgül, İ., Rüzgar Türbinleri, Çeşitleri ve Rüzgar Enerjisi Depolama Yöntemleri. *SDÜ YEKARUM e-Dergi-Süleyman Demirel University e-Journal of YEKARUM,* **2** (3),1-19, 2014.

[8] Li, D., Zhao, S., Ronch, A. D., Xiang, J., Drofelnik, J., Li, Y. & Breuker, R. D., A Review Of Modelling and Analysis of Morphing Wings, *Progress in Aerospace Sciences*,**100**, 46-62, 2018.

[9] Morgado, J., Vizinho, R., Silvestre, M. & Páscoa, J., XFOIL vs CFD Performance Predictions For High Lift Low Reynolds Number Airfoils, *Aerospace Science and Technology*, **52**, 207-214, 2016.

[10] Wang, Q. & Zhao, Q., Rotor Airfoil Profile Optimization For Alleviating Dynamic Stall Characteristics, *Aerospace Science and* Technology, **72**, 502-515, 2018.

[11] Wang, X., Zhou, W. & Wu, Z. Feedback Tracking Control For Dynamic Morphing of Piezocomposite Actuated Flexible Wings, *Journal of Sound and Vibration*, **416**, 17-28, 2018.

[12] Açıkel, H. H. & Genç, M. S. Control of Laminar Separation Bubble Over Wind Turbine Airfoil Using Partial Flexibility on Suction Surface, *Energy*,**165**(PA),176-190, 2018.

[13] Marinić-Kragıć, I., Vučina, D. & Milas, Z., Concept of Flexible Vertical-Axis Wind Turbine with Numerical Simulation and Shape Optimization, *Energy*, **167** (PA), 841-852, 2019.

[14] Bilgen, O. & Friswell, M. I., Piezoceramic Composite Actuators for A Solid-State Variable-Camber Wing, *Journal of Intelligent Material Systems and Structures*, **25** (7), 806-817, 2013.

[15] Lu, X., Huang, J., Song, L. & Li, J., An Improved Geometric Parameter Airfoil Parameterization Method, *Aerospace Science and Technology*, **78**, 241–247, 2018.

[16] González, A., Cortadi, A. J., Galar, D. & Ciani, L., Condition Monitoring of Wind Turbine Pitch Controller: A Maintenance Approach, *Measurement*, **123**,80-93, 2018.

[17] Thumthae, C., Optimum Blade Profiles for A Variable-Speed Wind Turbine in Low Wind Area, *Energy Procedia*,**75**, 651-657, 2015.

[18] Airfoil Tools, 2015. Retrieved from.http://airfoiltools.com/airfoil/details?airfoil=n0012-il.

WIND ENERGY POTENTIAL ASSESSMENT OF SUSURLUK REGION IN BALIKESİR

Abdullah DÜZCAN*, Yusuf Ali KARA**
*Bursa Technical University, Department of Mechanical Engineering, Bursa/Turkey
Email: abdullah.duzcan@btu.edu.tr
** Bursa Technical University, Department of Mechanical Engineering, Bursa/Turkey
Email: yusufali.kara@btu.edu.tr

ABSTRACT

The energy demand has been rapidly growing due to increasing industrialization and increasing population. Countries implement new policies of renewable energy resources instead of building fossil-based conventional power plants to meet this increasing demand. Among many renewable energy resources, wind energy is one of the top ones. That's why wind power plant investments are augmented in the last decade in Turkey. In this study, the wind potential of Susurluk region is investigated with the aid of Windsim, a commercial CFD software. Windsim solves the governing equations by using hourly wind speed data gathered from the Turkish Meteorological Service and the roughness of the Susurluk region. The analysis result showed that Susurluk has an enormous wind potential. Establishing a new power plant in the Susurluk region will help the environment a lot.

Keywords: Wind energy potential, Susurluk, Windsim, CFD

1. INTRODUCTION

Renewable energy power plants are built to meet the high energy demand created due to industrialization and population growth. The reason why renewable energy sources, mostly wind power plants, are chosen instead of fossil-based power plants is greenhouse gas emissions such as CO_2 and water vapor, harmful to nature.

There are a lot of wind assessment studies in the literature. Some of them considered land-based analysis, and some of them considered offshore. Aries et al. [1] studied wind assessment in Algeria. Yan et al. [2] conducted a CFD-based wind resource assessment analysis. Niyomthan et al. [3] carried out wind resource assessment analysis on the coast of Thailand, and the capacity factor for the region was 58%. Ramadan [4] researched on wind assessment in Egypt. The wind speed is 6.52 and 7.21 at the altitude of 10 meters and 25 meters, respectively. The wind power plant capacity is 200 MW. The net annual energy production is 840.62 GWh per year.

In this study, the wind potential of the Susurluk region in Balıkesir Province has been assessed. The proper locations for the wind power plant are selected.

2. MATERIAL METHOD

The wind speed and direction data supplied by the Turkish State Meteorological Service [5] at 10 meters are transferred to the hub height of the wind turbines, which is 80 meters, by a Windsim [6], a CFD-based software. That data is then combined with the elevation and roughness data derived from ASTER GDEM worldwide elevation and VCF Tree Cover worldwide data. Windsim solves RANS equations to assess the wind potential for a specified region by using all these datasets.

Figure 1 illustrates the locations of six Vestas V90 [7] commercial wind turbines shown as triangles and measurement mast of Turkish State Meteorological Service shown as a dot in Susurluk Region.

Figure 1. Layout of the wind farm, triangles (turbines), and a dot (meteorological measurement mast)

3. RESULTS AND DISCUSSION

Figure 2 indicates the Weibull distribution and wind speed frequency for 10 meters and 80 meters for Susurluk territory. The Shape and scale factors for 10 meters elevation are 1.72 and 3.41, whereas they are 1.68 and 5.8 according to the results gathered by solving RANS equations.

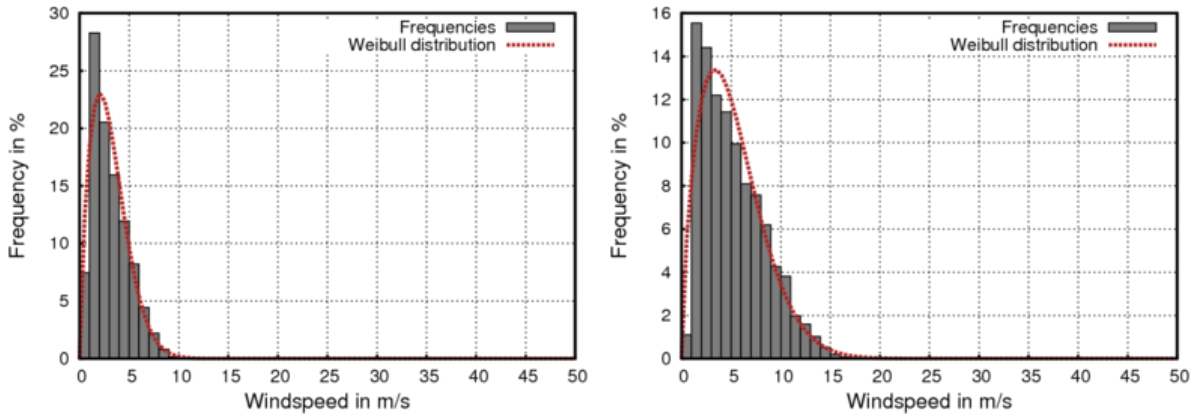

Figure 2. Weibull distribution of 10 meters and 80 meters, respectively.

Figure 3 shows the wind rose of the specified territory. According to wind rose, the turbines are located perpendicular to the direction where the wind is intense to get rid of wake losses for selected regions. Annual Energy Production (AEP) is 31.308 GWh/y. The loss of AEP due to wake loss is 0.004 GWh/y, which is very tiny compared to AEP. All six turbines work 2700 h per year approximately. The capacity factor for the region is 30.2%.

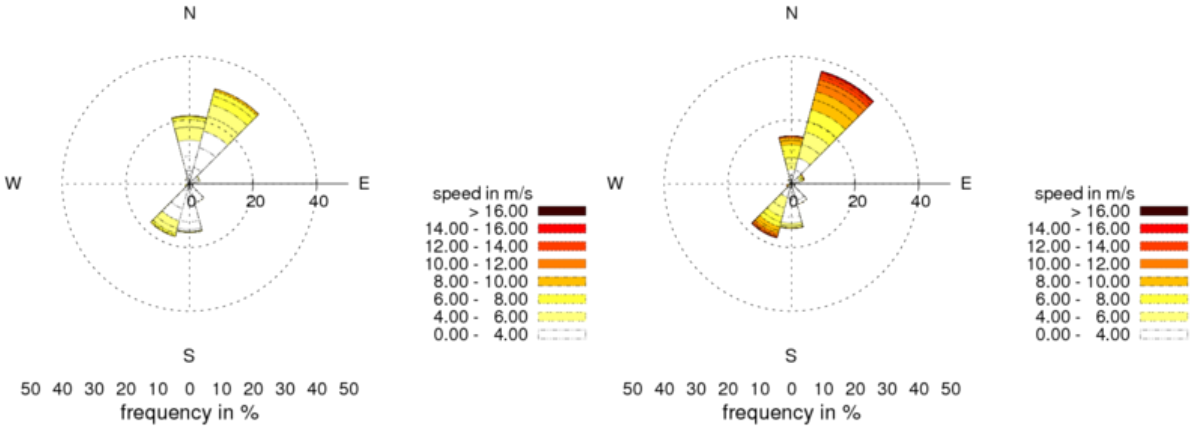

Figure 3. The wind rose at the location of the meteorological measurement station at 10 meters and 80 meters, respectively.

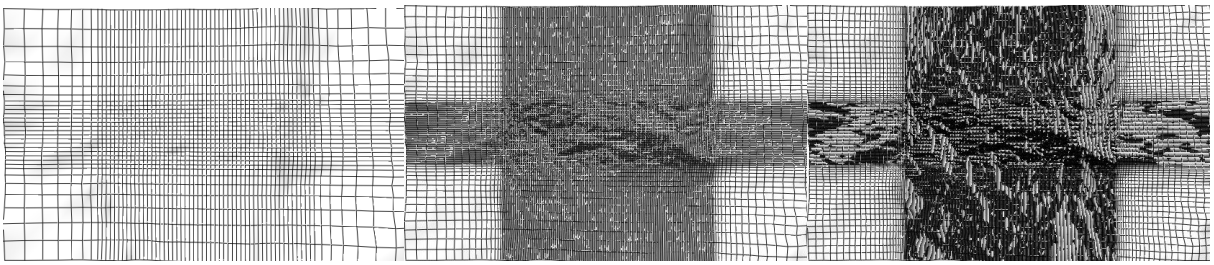

Figure 4. Horizontal grid line from coarse mesh to fine mesh.

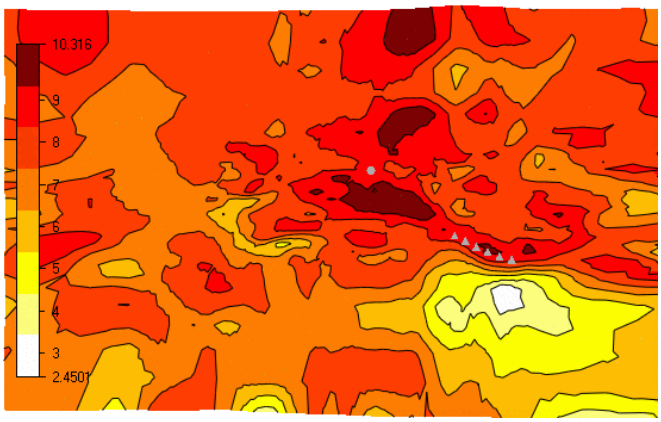

Figure 5. Average wind speed at 80 meters

4. CONCLUSION

The energy requirement has been quickly rising all over the world, especially in Turkey. To handle this increase, Turkey implements new policies to increase renewable energy investments especially wind energy.

The average wind speed is 6.1 m/s at an altitude of 80 meters. The shape and scale factors for the region at 80 meters elevation is 1.68 and 5.8, respectively. Six Vestas V90 wind turbine operates 2700 h per year roughly. Annual Energy Production (AEP) from those turbines are 31.308 GWh/y with a negligible wake loss effect.

ACKNOWLEDGMENT

The authors appreciate to Turkish State Meteorological Service for the provided meteorological data.

REFERENCES

[1] Aries, N., Boudia, S. M., & Ounis, H. (2018). Deep assessment of wind speed distribution models: A case study of four sites in Algeria. Energy Conversion and Management, 155, 78-90.

[2] Yan, B. W., & Li, Q. S. (2016). Coupled on-site measurement/CFD based approach for high-resolution wind resource assessment over complex terrains. Energy Conversion and Management, 117, 351-366.

[3] Niyomtham, L., Lertsathittanakorn, C., Waewsak, J., & Gagnon, Y. (2017). On the Wind Resource Assessment along the Western Coast of Thailand. Energy Procedia, 138, 1190-1195.

[4] Ramadan, H. S. (2017). Wind energy farm sizing and resource assessment for optimal energy yield in Sinai Peninsula, Egypt. Journal of Cleaner Production, 161, 1283-1293.

[5] Turkish State Meteorological Service, https://www.mgm.gov.tr/

[6] Windsim (2019), Wind Simulation Software, https://windsim.com

[7] Vestas (2019), https://www.vestas.com/en/products/2-mw-platform/v90-2_0_mw

THE STATE OF ENERGY IN WORLD AND TURKEY – WIND ENERGY

Kadir KAYA*, Erdem KOÇ**
*Ondokuz Mayis University, Department of Mechanical Engineering, Samsun/Turkey
Email: kadir.kaya@omu.edu.tr
** Ondokuz Mayis University, Department of Mechanical Engineering, Samsun/Turkey
Email: erdemkoc@omu.edu.tr

ABSTRACT

Nowadays, energy has become one of the vital components for the survival of humanity and countries tend to use renewable energy sources to provide their growing energy demands. Also, Countries aim to reduce the use of non-renewable energy sources that are predicted to be depleted shortly and are known for their environmental damage. The usage of wind energy, which one of the most important renewable energy sources, has increased in Turkey and the World. In this study, the general state of wind energy in Turkey has been evaluated. For this purpose, the wind energy potential and developments for Turkey were examined then, wind energy activities in Turkey from the past to the present time have been evaluated and the current status has been determined. It has been tried to shed light on the renewable energy policies of our country by evaluating the committed and planned activities with this work.

Keywords: Wind Energy, Wind Turbines, Wind Energy Policies.

1. INTRODUCTION

Energy being the most critical input for all sectors has become a vital component at homes, workplaces, transportation, industry shortly in all living spaces. Energy sources that can remain the same in a natural cycle process are known as renewable energy sources (Solar, Wind, Hydraulics, Biomass, etc.). On the other hand, energy sources that cannot renew themselves once used are known as non-renewable energy sources (Coal, Petroleum, Natural Gas etc.). Countries tend to use renewable energy sources due to the depletion of non-renewable energy resource reserves and the environmental damage of non-renewable energy sources.

Wind energy, one of the most important renewable energy sources, is an indirect product of solar energy. As a result of different sea warming, air moves from high pressure to low pressure and this movement is known as wind. The wind has kinetic energy and this energy can be used by converting it into mechanical energy or electrical energy by using Wind Plants [1].

Because of the fact that growing population, rising welfare level and technological developments, the demand for energy in Turkey is increasing as well as in the World. Thecurrent status of renewable energy sources in Turkey needs to be identified meeting the demand increasing, ensure the use of the existing non-renewable energy sources in a planned manner and benefit more from the renewable energy sources [1-4]. In this study, the current status of wind energy is one of the most important renewable energy sources in Turkey and the World has been evaluated based on the recent data and the points that could shed light on the energy policy of Turkey has tried to determine.

2. THE STATE OF WIND ENERGY IN THE WORLD

In order to evaluate the wind energy status of the countries, the wind power plant capacities of countries and forecasts about wind energy in the World in 2030 and 2050 have been investigated in this section. The countries that have high installed wind power are given in Table 1. It can be seen from the table that China is the country

making the wind energy investments most with 206804 MW onshore and 4588 MW offshore wind power plant capacity as of 2018. Turkey's 7370 MW of installed wind power plant capacity can also be monitored from the table.

Table 1. Wind Power Plant Capacities of Selected Countries [MW] [5-7]

Rank	Countries	Years					
		2006	2010	2013	2016	2017	2018
1	China	2,599	44,733	91,412	168,690	185,604 2,788*	206,804 4,588*
	Europe Union	48,122	84,278	117,384	153,730	168,715	178,826
2	USA	11,603	40,200	61,110	82,183	89,047 30*	96,635 30*
3	Germany	20,622	27,214	34,250	50,019	50,779 5,411*	53.180 6,380*
4	India	6,270	13,064	20,150	28,665	32,938	35,129
5	Spain	11,630	20,676	22,959	23,075	23,097	23,494
6	UK	1,963	5,203	10,711	14,542	12,412 6,651*	13,001 1,312*
7	France	1,589	5,660	8,243	12,065	13,757	15,307
8	Brazil	237	932	3,466	10,740	12.769	14,707
9	Canada	1,460	4,008	7,823	11,898	12,240	12.816
10	İtaly	2,123	5,797	8,558	9,257	9,506	9,958
11	Turkey	65	1,329	2,958	6,081	6,872	7,370
12	Sweeden	571	2,163	4,382	6,519	6,499	7,216
13	Poland	153	1,107	3,390	5,782	5,848	5,864
14	Portugal	1,716	3,702	4,730	5,316	5,313	5,380
15	Denmark	3,140	3,752	4,807	5,227	5,477	5.758

As of 2018, onshore (Figure 1a) and offshore (Figure 1b) wind plants installed are given in Figure 1. It can be seen from the figure that the country having highest installed onshore wind plant in the world is China (% 36) and the country having the highest installed offshore wind plant in the world is UK (% 34) as of 2018.

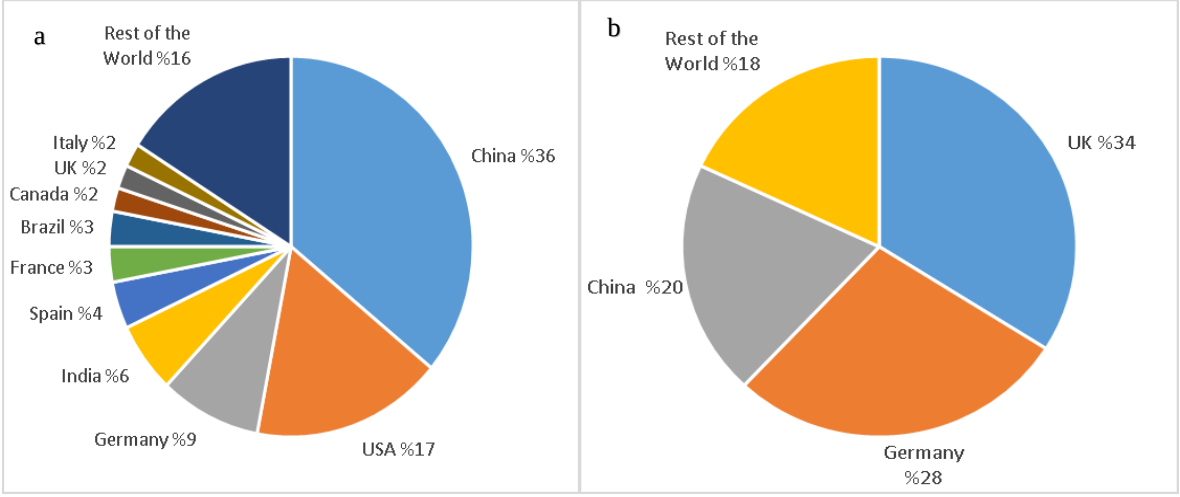

Figure 1. The Distribution of Onshore (a) Offshore (b) Wind Power Plant Capacities in The World as of 2018 [6]

The total wind power installed in the World and the distribution of this power by continents and the predictions is given in Table 2. It is seen from the table that 231 GW of the total installed power of 542 GW onshore wind power plant has been located in the Asia continent, where China is also located. In 2050, it can be seen from the table that more than half (52 %) of the 5044 GW wind power plant in the World is expected to be located in Asia.

Table 2. Current Status and Predictions of Wind Power Plant Capacities by Continent [8]

Wind Turbine	Years	North America	Latin America	Europe	The Middle East and Africa	Asia	Oceanica	Total
Onshore (GW)	2018	107	25	164	6	231	7	542
	2030	330	71	215	84	1067	19	1187
	2050	1146	182	483	525	2646	62	5044
Offshore (GW)	2018	0	0	19	-	5	0	23
	2030	23	1	78	-	126	1	228
	2050	164	5	215	-	613	3	1000

The status and future predictions of various wind energy economy parameters such as Total Installation Cost, Levelised Cost of Electricity, Average Annual Investment, Capacity Factors, Employment are given in Table 3. The total investment cost and levelised cost of electricity show the cost need be paid for the installation of a 1 kW wind energy plant and the cost for producing the 1 kWh electric energy respectively. The table also includes the annual investments of onshore and offshore wind plants in selected years and future predictions. Moreover, the table includes the capacity factor parameter that is an indicates how much wind energy can be utilized by using wind plants and information on employment in the wind energy industry.

It can be seen from the table that wind power plant installation costs and unit energy production costs are expected to decrease; average annual investment, capacity factors and employment parameters are expected to increase in the future. It can also be followed from the table that employment in the wind energy sector, being 0.75 million in 2010, is expected to increase 3.74 million and 6.06 million in 2030 and 2050 respectively.

Table 3. The status and Predictions of Various Wind Energy Economy [8]

Parameter	**Wind Turbine Type**	**2010**	**2018**	**2030**	**2050**
Total Installation Cost (USD/kW)	Onshore	1913	1497	800-1350	650-1000
	Offshore	4572	4353	1700-3200	1400-2800
Levelised Cost of Electricity (USD/kWh)	Onshore	0.08	0.06	0.03-0.05	0.02-0.03
	Offshore	0.16	0.13	0.05-0.09	0.03-0.07
Average Annual Investment (USD Billion/Year)	Onshore	57	67	146	211
	Offshore	4.2	19.4	61	100
Capacity Factors (%)	Onshore	27	34	30-55	32-58
	Offshore	38	43	36-58	43-60
Employment (Million)		0.75	1.12	3.74	6.06

3. THE STATE OF WIND ENERGY IN TURKEY

According to data from the Turkish State Meteorological Service for the wind speeds more than 6.5 m/h, the onshore wind energy potential of Turkey is 131,756.4 MW and the offshore wind energy potential of Turkey is 17393.2 MW. The average wind speed at the height of 50 m on the place where the turbine will be installed needs to be a minimum of 7 m/s in order to make an economic investment for wind power plants. Therefore, the onshore wind energy potential is 48000 MW and the offshore wind potential is 5300 MW in Turkey considering the wind speeds that is more than 7 m/h [1].

The variation of total Wind Power Plant Installed Capacity in Turkey between 2007-July 2019 are given in Figure 2. It can be seen from the figure that wind power plant capacity in Turkey is 7615 MW as of July 2019, whereas 146.3 MW in 2007.

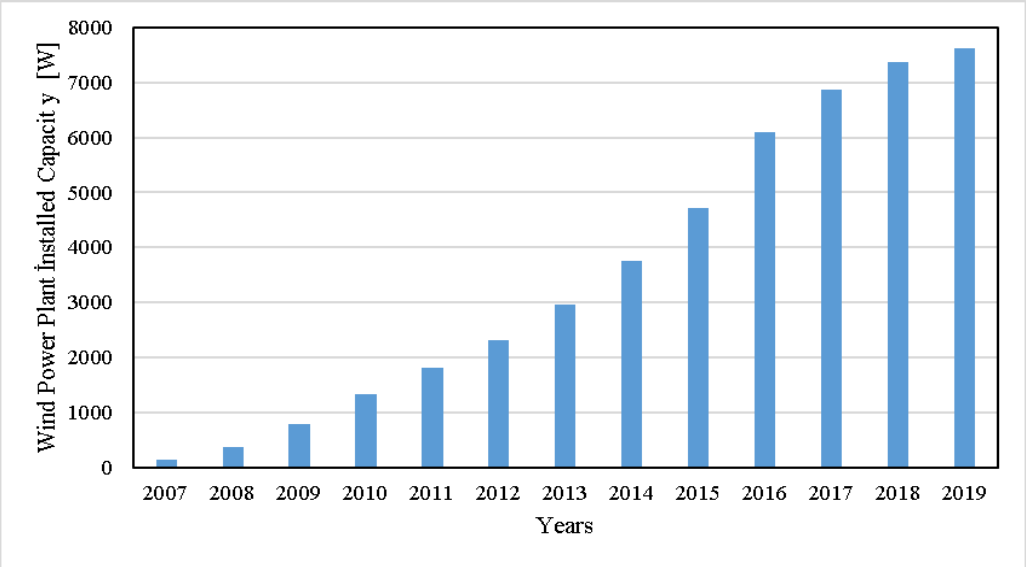

Figure 2. The variation of Windpower installed capacity in Turkey between 2007 and July 2019 [9]

The produced electricity from wind plants and the percentage of the electricity demand covered by wind energy in Turkey between 1998 and July 2019 are shown in Figure 3. It can be seen from the figure that Electric Energy Generated by Wind Plants and percentage of the electricity demand covered by wind have been increased rapidly after 2006 and become 10498 GWh and 7.4 % were as of July 2019.

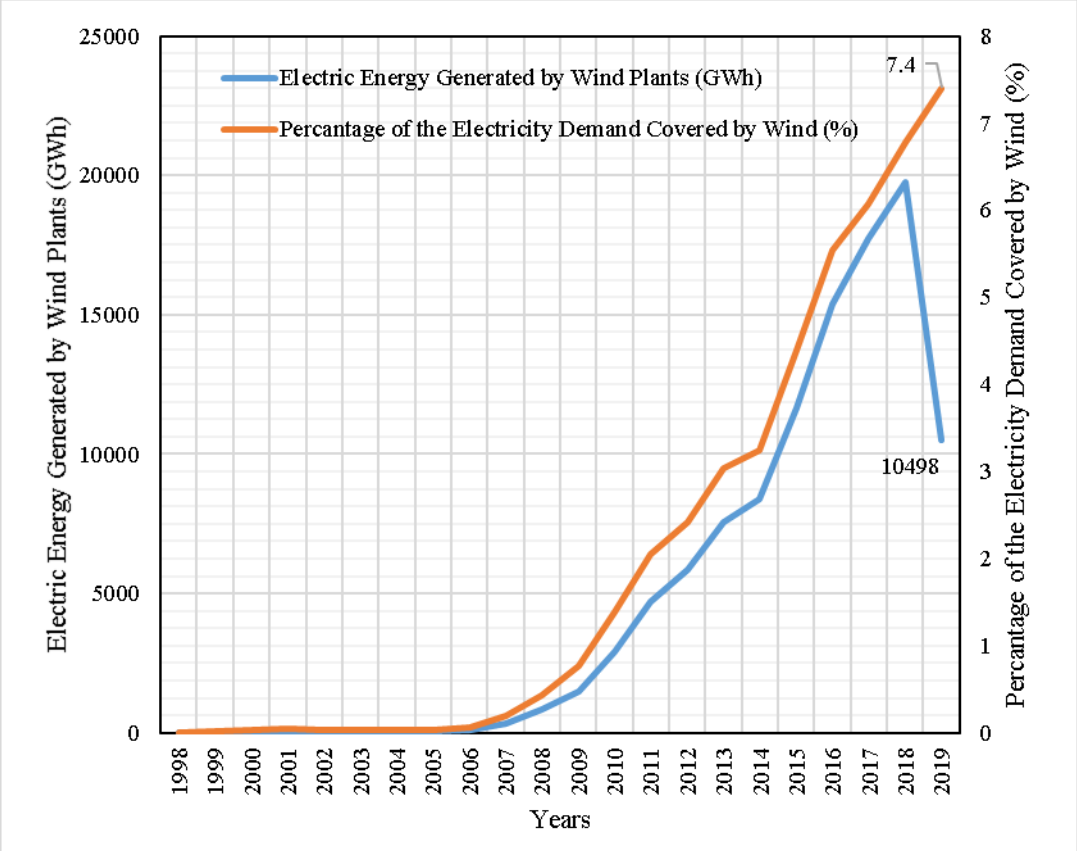

Figure 3. The Variation of Electric Energy Generated by Wind Plants and The Percentage of Electricity Demand Covered by Wind Energy in Turkey [9-12]

As of July 2019, statistical data about the wind plants in operation, wind plants under construction and wind plants pre-licensed in are given in Table 4. It is seen from the table that the city having the most wind power installed capacity in operation is İzmir. It can also be seen from the table that the wind turbines under construction and wind turbines pre-licensed in İzmir are 125.9 MW and 72.95 MW respectively. Moreover, after setting up the wind plants under construction and wind plants pre-licensed, wind power plant installed capacity in Turkey will be nearly 12,500 MW. It can be concluded from the table that Turkey will be benefited from only % 26 of its potential as thought that the onshore wind power potential in Turkey is 48,000 MW.

Table 4. The status of Wind Energy Plants in Turkey [MW] [9]

City	Installed Wind Turbine Capacity in Operation	Wind Turbine Capacity under Construction	Wind Turbines Pre-Licenced	Total
İzmir	1462.2	125.9	72.95	1661.05
Balıkesir	1135	133.8	229.6	1498.4
Çanakkale	505.6	81.2	290.55	877.35
Manisa	669.95	-	30	699.95
İstanbul	256.9	40.2	290	587.1
Sivas	155.3	-	330	485.3
Hatay	364.5	-	60	424.5
Mersin	218.7	-	154.6	373.3
Bursa	128.4	-	240.8	369.2
Kayseri	275.1	-	80	355.1
Edirne	85.6	-	254.2	339.8
Tekirdağ	155.8	18.4	160.9	335.1
Kırklareli	199.6	72	44	315.6
Afyon	268.45	-	30	298.45
Aydın	237.2	36	-	273.2
Osmaniye	265.3	-	-	265.3
Muğla	197.25	-	25.7	222.95
Konya	164.9	-	48	212.9
Yalova	86.4	-	110	196.4
Tokat	140.7	-	40	180.7
Kırşehir	168	-	-	168
Amasya	139	-	11	150
Karaman	-	-	136.2	136.2
Kahramanmaraş	86.4	-	40	126.4
Isparta	61.2	-	60	121.2
Adana	-	-	120	120
Sakarya	-	-	110	110
Antalya	-	-	101.5	101.5
Uşak	54	-	47	101
Malatya	11.7		80	91.7
Kocaeli	10.2	5	70	85.2
Ankara	-	-	80	80
Denizli	-	74.8	-	74.8
Bilecik	40	32	-	72
Gaziantep	65.55	-	-	65.55

Table 4. The status of Wind Energy Plants in Turkey [MW] (Continue**)** [9]

City	Installed Wind Turbine Capacity in Operation	Wind Turbine Capacity under Construction	Wind Turbines Pre-Licenced	Total
Çorum	-	-	65	65
Adıyaman	27.5		35	62.5
Mardin	-	-	60	60
Yozgat	-	-	52	52
Ordu	-	-	50.8	50.8
Erzincan	-	-	50.3	50.3
Ağrı	-	-	50	50
Çankırı	-	-	50	50
Erzurum	-	-	50	50
Eskişehir	-	-	50	50
Kütahya	-	-	50	50
Bingöl	-	-	49.5	49.5
Samsun	-	-	49	49
Bitlis	-	-	40	40
Elazığ	-	-	40	40
Giresun	-	-	40	40
Kilis	-	-	40	40
Sinop	-	-	40	40
Karabük	-	-	30	30
Kars	-	-	20	20
Burdur	-	-	3	3
Total	7615	619.3	4261.6	12495.9

4. RESULTS

The current status of renewable energy sources in Turkey needs to be identified for the purpose of meeting the demand increasing, ensure the use of the existing non-renewable energy sources in a planned manner and benefit more from the renewable energy sources. In this study, the current status of wind energy being one of the most important renewable energy sources in Turkey and in the world have been evaluated based on the recent data and the points that could shed light on the energy policy of Turkey has tried to determine. Important results obtained from this study are summarized as follows.

- China is the country making the wind energy investments most with 206804 MW onshore and 4588 MW offshore wind power plant capacity as of 2018.
- The country having the highest installed onshore wind plant in the World is China (36 %) and the country having the highest installed offshore wind plant in the World is UK (34 %) as of 2018.
- 231 GW of the total installed power of 542 GW onshore wind power plant has been located in Asia, where China is also located. More than half (52 %) of the 5044 GW wind power plant in the world is expected to be located in Asia In 2050.

- Power plant installation costs and unit energy production costs are expected to decrease; average annual investment, capacity factors and employment parameters are expected to increase in the future.
- Employment in wind energy sector being 0.75 million in 2010 is expected to increase 3.74 million and 6.06 million in 2030 and 2050 respectively.
- Therefore, the onshore wind energy potential is 48000 MW and the offshore wind potential is 5300 MW in Turkey considering the wind speeds being more than 7 m/h.
- Wind power plant capacity in Turkey is 7615 MW as of July 2019, whereas 146.3 MW in 2007.
- Electric Energy Generated by Wind Plants and percentage of the electricity demand covered by wind in Turkey have been increased rapidly after 2006 and become 10498 GWh and 7.4 % were as of July 2019.
- In Turkey, the city having the most wind power installed capacity in operation is İzmir
- After setting up the wind plants under construction and wind plants pre-licensed, wind power plant installed capacity in Turkey will be nearly 12,500 MW and Turkey will be benefited from only the % 26 of its potential as thought that the onshore wind power potential in Turkey is 48,000 MW.
- Turkey also has 5300 MW of offshore wind power potential so incentive activities need to be done to benefit from this potential.

REFERENCES

[1] Koç, E., Kaya, K. Enerji Kaynakları–Yenilenebilir Enerji Durumu, *Mühendis ve Makina*, 56 (668), 36-47, 2015.

[2] Kaplan, Y. A., Overview of Wind Energy in the World and Assessment of Current Wind Energy Policies in Turkey, *Renewable and Sustainable Energy Reviews*, 43, 562- 568, 2015.

[3] Camadan, E., An Assessment on the Current Status and Future of Wind Energy in Turkish Electricity Industry, *Renewable and Sustainable Energy Reviews*, 15, 4994- 5002, 2011.

[4] Dincer, F. The Analysis on Wind Energy Electricity Generation Status, Potential and Policies in the World, *Renewable and Sustainable Energy Reviews*, 15, 5135- 5142, 2011.

[5] Koca, T., Aksungur, S., Dünyada ve Türkiye'de Rüzgar Enerjisi ile Elektrik Üretim Potansiyeli, 23. Uluslararası Enerji ve Çevre Fuarı ve Konferansı (ICCI 2017), İstanbul, 2017.

[6] Global Wind Energy Report 2018, Global Wind Energy Coincil (GWEC), April 2019. URL: https://gwec.net/wp-content/uploads/2019/04/GWEC-Global-Wind-Report-2018.pdf, Accessed date: 15.02.2020.

[7] Wind Energy in Europe in 2019 – Trends and Statistics, Wind Europe, 2020, URL: https://windeurope.org/wp-content/uploads/files/about-wind/statistics/WindEurope-Annual-Statistics-2019.pdf,Accessed date: 15.02.2020.

[8] Future of Wind – Deployment, Investment, Technology, Grid Generation and Socio-Economic Aspects, International Renewable Energy Agency (IRENA), 2019.

[9] Turkish Wind Energy Statistic Report July 2019, Turkish Wind Energy Association (TWEA). URL: https://www.tureb.com.tr/files/bilgi_bankasi/turkiye_res_durumu/istatistik_raporu_temmuz_2019.pdf, Accessed date: 15.02.2020.

[10] Turkish Wind Energy Statistic Report Jan 2019, Turkish Wind Energy Association (TWEA). URL: https://www.tureb.com.tr/files/bilgi_bankasi/turkiye_res_durumu/istatistik_raporu_ocak_2019.pdf, Accessed date: 15.02.2020.

[11] Turkish Wind Energy Statistic Report July 2018, Turkish Wind Energy Association (TWEA). URL: https://www.tureb.com.tr/files/tureb_sayfa/duyurular/2018/03/turkiye_ruzgar_enerjisi_istatistik_raporu_ocak_2018.pdf, Accessed date: 15.02.2020.

[12] Statistics on Generation Electricity by Wind Energy, URL: https://www.enerjiatlasi.com/elektrik-uretimi/ruzgar, Accessed date: 15.02.2020.

FUEL CELLS

DEVELOPMENT OF A DYNAMIC SYSTEM-LEVEL THERMODYNAMIC MODEL OF SOLID OXIDE FUEL CELL (SOFC) INTEGRATED GAS TURBINE (GT) POWER PLANT

Miraç Burak KAYA *, Alper Can İNCE*, Fevzi BEDİR*, Mustafa Fazıl SERİNCAN*
*Gebze Technical University, Department of Mechanical Engineering, Kocaeli/Turkey
Email: mbkaya@gtu.edu.tr

ABSTRACT

The increasing demand to obtain green energy due to growing awareness on global warming and decreasing fossil fuel sources has made fuel cell (FC) technology more popular in the last years. Especially, solid oxide fuel cell (SOFC) is a promising technology to be used in the stationary application (e.g. combined heat and power generation, cogeneration and trigeneration) due to fact that it has higher conversion efficiency and no environmental impact compared to conventional power systems. However, high cost of SOFC materials has been considered as an important issue for the SOFC system commercialization. In addition, system integration of SOFC based on interaction between the balance of plant (BOP) components is another significant problem. Typical main components of the SOFC system are SOFC stack included internal reformer, gas turbine (GT), compressor, valves, and heat exchangers. In the present work, the transient zero-dimensional (0-D) SOFC model is developed in the MATLAB/Simulink environment. This model is then employed the dynamic thermodynamic model which includes mass and energy balances for the system components of hybrid SOFC/GT power plant. Through this model, a dynamic performance of hybrid SOFC/GT system is investigated.

Keywords: SOFC/GT Cycle, System-Level Modelling, Dynamic Model, Thermodynamic Model.

1. INTRODUCTION

The demand of conventional power sources has been decreased due to low conversion efficiency and, its usage of fossil fuel sources. Therefore, solid oxide fuel cell (SOFC) technology has become popular due to high energy conversion efficiency and low environmental impact. In addition to this, SOFC can be integrated combined heat and power systems. For example, SOFC and gas turbine (GT) hybrid system has a great potential to generate power. However, the design and real-time problems of these systems are drawbacks to hinder their commercialization. To face these problems, dynamic simulations of system-level of SOFC/GT are developed in the literature.

Zhang et al. [1] developed dynamic model of hybrid system SOFC/GT. They presented inlet and outlet temperature of SOFC, voltage output of SOFC and molar fraction of gas species at the inlet and outlet of SOFC. They found that the temperature of SOFC outlet increases while the air temperature of SOFC inlet decreases with increasing current density. Roberts and Brouwer [2] performed dynamic model of a pressurized 220 kW SOFC/GT hybrid system. Reliable experimental data were used to validate the model. Rossi et al. [3] presented a simplified dynamic approach applied to three different test-rigs. The ability of these test-rigs was revealed. The dynamic model capability of SOFC/GT system was presented by Hughes et al. [4]. In that study, 1-D transient mathematical model of SOFC stack which includes electrochemical, thermal and diffusion models is integrated into the system-level model of hybrid SOFC/GT. The polarization losses and reactant compositions were presented according to real time simulation. Another dynamic model of SOFC-based combine heat and power system was developed by Barelli et al. [5]. They first developed Aspen Plus model to understand the effect of operating conditions on the system components. Then, this model integrated into MATLAB/Simulink model to reveal dynamic behavior of the system. The delay time to reach next operating conditions was found as 220 s when the electric load is supplied from 2200 W – 3000 W. In that case, the requirement of hydrogen molar flow rate increased from 2.2×10^{-5} kmol·s^{-1} to 3.4×10^{-5} kmol·s^{-1}.

In this study, dynamic performance of system components of SOFC/GT hybrid system is investigated. For this purpose, the electrochemical and thermodynamic model for SOFC implemented internal reformer, and thermodynamic model

for system components are developed using MATLAB/Simulink software. The load electrical profile is presented. According to this profile, electrochemical performance (polarization and power) of SOFC is presented under different cell operating temperatures. The thermodynamic performance (temperature and power output) of turbine is also investigated under different electrical load.

2. System Model Description and Equations

The scheme of working principles of SOFC/GT system is shown Fig. 1. Pre-reformed fuel is send to anode side of SOFC. The pre-reformed methane is fully reformed inside the cell. The reactions of steam methane reforming, water gas shift, overall fuel cell reactions are occured inside the cell (equations (1)-(3)). Reforming reaction rates are taken into consideration in this study. The exhaust gas of SOFC is fed to gas turbine. The power is generated by the turbine. The air temperature entering heat exchanger is heated by the heat transfer of gas leaving the gas turbine. Heated air is send to compressor. Here, the air is compressed and send to cathode side of SOFC.

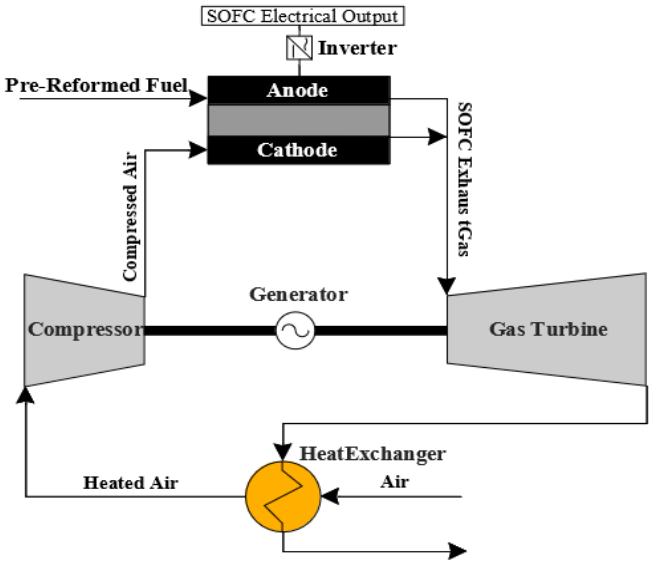

Figure 1. SOFC/ GT system schematic

$$CH_4(\dot{x}) + H_2O \leftrightarrow CO + 3H_2 \text{ (Steam Reforming Reaction)} \quad (1)$$

$$CO(\dot{y}) + H_2O \leftrightarrow CO_2 + H_2 \text{ (Water-Gas Shift Reaction)} \quad (2)$$

$$H_2(\dot{z}) + \frac{1}{2}O_2 \leftrightarrow H_2O \text{ (Chemical Reaction)} \quad (3)$$

The assumptions used in this model are given as follows:

- 0-D approach is performed.
- All external walls of all components of the SOFC are considered as adiabatic.
- The fuel fed into anode side as %30 pre-reformed.
- The pressure drop within the cell channels is neglected.
- Fuel utilization rate is constant.
- The gases behave as an ideal gas.

2.1 Electrochemical Model

Nerst potential which represents the maximum theoretical cell voltage is calculated by the following equation [6];

$$E_{nernst} = E_0 + \frac{R \cdot T}{2 \cdot F} \ln\left(\frac{P_{H_2} \cdot P_{O_2}^{0.5}}{P_{H_2O}}\right) \quad (4)$$

where E_0 is standart potential and is represented by the following empiric expression [7];

$$E_o = a + b \cdot T \quad (5)$$

Three main overpotentials, e.g. ohmic (V_{ohm}), activation for anode and cathode ($V_{act,cell}$), and concentration ($V_{con,cell}$) are considered and calculated through the equations (6)-(9).

$$E = E_{nernst} - V_{ohm} - V_{act,cell} - V_{con,cell} \quad (6)$$

Ohmic overpotential is caused by the resistance of ion and free electrons passing through the electrolyte and the open circuit respectively. V_{ohm} is calculated by using Ohm law;

$$V_{ohm} = i \cdot (R_{anode} + R_{cathode} + R_{electrolyte}) \quad (7)$$

Activation overpatential is directly related to the condition of the reaction rate. This value must be exceeded for the start of chemical reactions. In this study exchange current density (i_o) is taken constant value as $0.2\ A \cdot cm^{-2}$ from study of Badur et al. [8], as shown Table 1 with other model parameters. Activation overpotentials for anode and cathode can be calculated by the following expression [9];

$$V_{act,cell} = \frac{R \cdot T}{F} \cdot \sinh^{-1}\left(\frac{i}{2 \cdot i_0}\right) \quad (8)$$

The limited current density (i_l) is taken constant value as $0.67\ A \cdot cm^{-2}$ from study of Badur et al. [8]. Concentration overpotential can be calculated by the following expression [10].

$$V_{con,cell} = \left|\frac{R \cdot T}{2 \cdot F} \cdot \ln\left(1 - \frac{i}{i_l}\right)\right| \quad (9)$$

Table 1. Parameters of mathematical model

Parameters	Unit	Value	Ref.
Conductivity of Electrolyte (σ_e)	$\Omega^{-1} \cdot cm^{-1}$	$33.4 \cdot 10^3 e^{(10300/T}$	[9]
Conductivity of Anode (σ_a)	$\Omega^{-1} \cdot cm^{-1}$	$9.5 \cdot 10^7 e^{(-1150/T)}$	[9]
Conductivity of Cathode (σ_c)	$\Omega^{-1} \cdot cm^{-1}$	$4.2 \cdot 10^7 e^{(1200/T)}$	[9]
Electrolyte Thickness (t_e)	cm	$4 \cdot 10^{-3}$	[9]
Anode Thickness (t_a)	cm	$1 \cdot 10^{-2}$	[9]
Cathode Thickness (t_c)	cm	$2.2 \cdot 10^{-1}$	[9]
Limited Current Density (i_l)	A$\cdot cm^{-2}$	0.67	[8]
Exchange Current Density(i_o)	A$\cdot cm^{-2}$	0.2	[8]
Universal Gas Constant (R)	$J \cdot mol^{-1} \cdot K^{-1}$	8.314	
Faraday Constant (F)	A$\cdot s \cdot mol^{-1}\cdot$	96485	
Fuel Utilization Rate (U_f)	-	0.85	
Air Utilization Rate (U_a)	-	0.25	
a	V	1.272	[6]
b	V$\cdot K^{-1}$	$2.76 \cdot 10^{-4}$	[6]
A_c	m^2	0.1	

Table 2. Operating conditions for both cases.

Case	A	B
Fuel Inlet Temperature	973 K	1073 *K*
Air Inlet Temperature	873 K	873 K
Operating Pressure	1 atm	1 atm

2.2 Thermodynamic Model

2.2.1 SOFC Model

The cell cross-sectional scheme and heat transfer events in tubular SOFC are shown in Fig.2. The energy balance around the control volume enclosing the fuel cell is given (10) and (11). Here, the power output ($\dot{Q}_{elec}$) can be calculated using the Eq. (12). In addition, heat transfer rates occured inside cell due to chemical reaction $\dot{Q}_{chem}$, convection of air ($\dot{Q}_{conv,air}$) and fuel ($\dot{Q}_{conv,fuel}$), radiation ($\dot{Q}_{rad}$) and reforming ($\dot{Q}_{reform}$) are found through the Eqs. (13)-(17), respectively.

$$m_{cell} \cdot C_{p,cell} \cdot \frac{dT_{cell}}{dt} = \dot{Q}_{chem} - \dot{Q}_{elec} - \dot{Q}_{conv,fuel} - \dot{Q}_{conv,air} - \dot{Q}_{rad} - \dot{Q}_{reform} \quad (10)$$

$$m_{inj} \cdot C_{p,inj} \cdot \frac{dT_{inj}}{dt} = \dot{Q}_{rad} - \dot{Q}_{conv,inner} - \dot{Q}_{conv,outer} \quad (11)$$

$$\dot{Q}_{elec} = V_{out} \cdot I \quad (12)$$

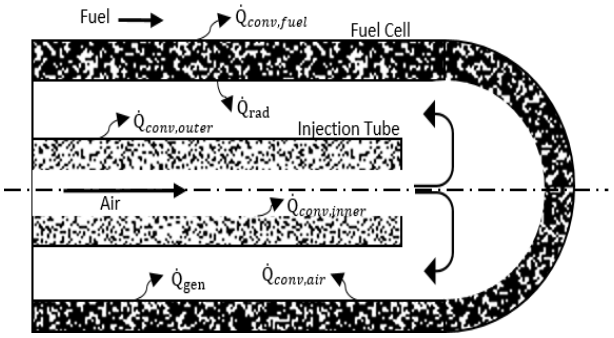

Figure 2. Operating principle of a single tubular of SOFC

$$\dot{Q}_{chem} = \frac{I}{2 \cdot F} \cdot H_{H_2} + \frac{I}{4 \cdot F} \cdot H_{O_2} + \frac{I}{2 \cdot F} \cdot H_{O_2} \quad (13)$$

$$\dot{Q}_{conv,air} = h_c \cdot A_{c,inner} \cdot (T_{cell} - T_{air}) \quad (14)$$

$$\dot{Q}_{conv,fuel} = h_a \cdot A_{c,outer} \cdot (T_{cell} - T_{fuel}) \quad (15)$$

$$\dot{Q}_{rad} = \varepsilon \cdot \sigma \cdot A_c \cdot ({T_{cell}}^4 - {T_{inj}}^4) \quad (16)$$

$$\dot{Q}_{reform} = r_{rmsr} . \Delta H \quad (17)$$

where r_{msr} is steam reforming reaction rate at the Ni-YSZ anode and ΔH is formation enthalpy. H is the molar enthaply of species. ha and hc represent the heat transfer coefficients at the air and fuel, respectively.

2.2.2 Compressor Model

It is used to compress the ambient air that is send to cathode side of SOFC. The thermodynamic model of compressor is based on the polytropic transformations. Equations used in this model are given through equations (18)-(20) [11];

$$T_o = T_i \cdot (r_c)^{\frac{(k_a-1)}{k_a \cdot \eta_c}} \tag{18}$$

$$\eta_c = \left(\frac{1-(r_c)^{\frac{(k_a-1)}{k_a}}}{1-(r_c)^{\frac{(k_a-1)}{k_a \cdot \eta_c}}} \right) \tag{19}$$

where η_c is compressor polytropic efficiency and k_a is specific heat ratio of air. Power is consumed by the compressor;

$$P_c = \eta_c \cdot \dot{m}_{air} \cdot \Delta H_{air} \tag{20}$$

2.2.3 Turbine Model

In the gas turbine cycle, the turbine is used to obtain secondary electrical power. Turbine generates power by using high pressure and temperature stream.. Model equations are given as follows;

$$T_o = T_i \cdot (1/r_e)^{\frac{(k_e-1)}{k_e \cdot \eta_t}} \tag{21}$$

$$\eta_t = \left(\frac{1-(1/r_e)^{\frac{(k_e-1)}{k_e \cdot \eta_t}}}{1-(1/r_e)^{\frac{(k_e-1)}{k_e}}} \right) \tag{22}$$

where η_t is compressor polytropic efficiency and k_e is specific heat ratio of exhaust gas. Mechanical power generated by the gas turbine can be calculated as;

$$P_t = \eta_t \cdot \dot{m}_e \cdot \Delta H_e \tag{23}$$

3. RESULTS AND DISCUSSION

In this section, the results of dynamic performance of SOFC/GT system are presented and discussed. In the Fig. 3, validation of SOFC model with Singhal experiment is shown [11]. Quite similar results with the Singhal experiment were obtained from the simulation. Accordance between simulation results which are power-current density curve and voltage- current density curve and experiment results prove quality of model data. Model error is mainly caused by difference of fuel gas composition. Electrical load for the system is given in Fig. 4a. The simulation time is determined as 1000 s. According to this figure, the current load is increased from 150 A to 250 A at the simulation time of 500 s.

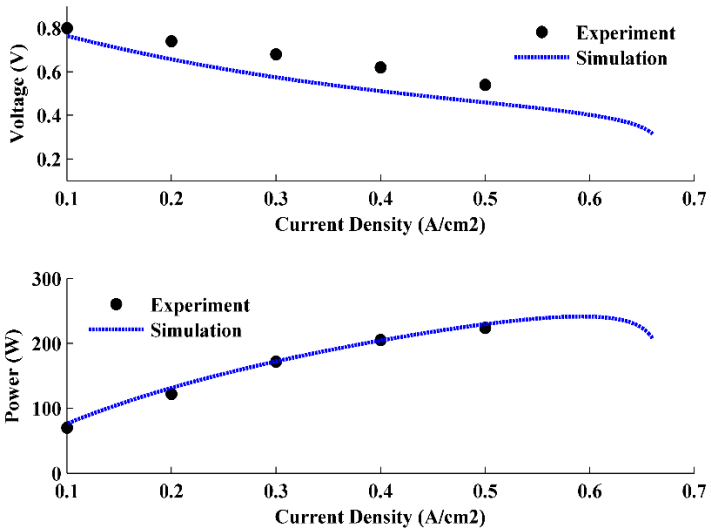

Figure 3. SOFC performance graphs- comparison of the simulation outputs with Singhal experiment [11].

The dynamic performance of polarization and power output are shown in Fig. 4b and 4c at case A and B. When the cell operating temperature decreases, the cell voltage decreases. A decrement of cell voltage is found as 0.1 V and 0.12 V at case A and B, respectively. When the cell is operated at A condition , time delay in the response of voltage is very fast to reach steady-state operational regime when the compared with the case B. These results are very compatible with the study of Yadav at al. [12].

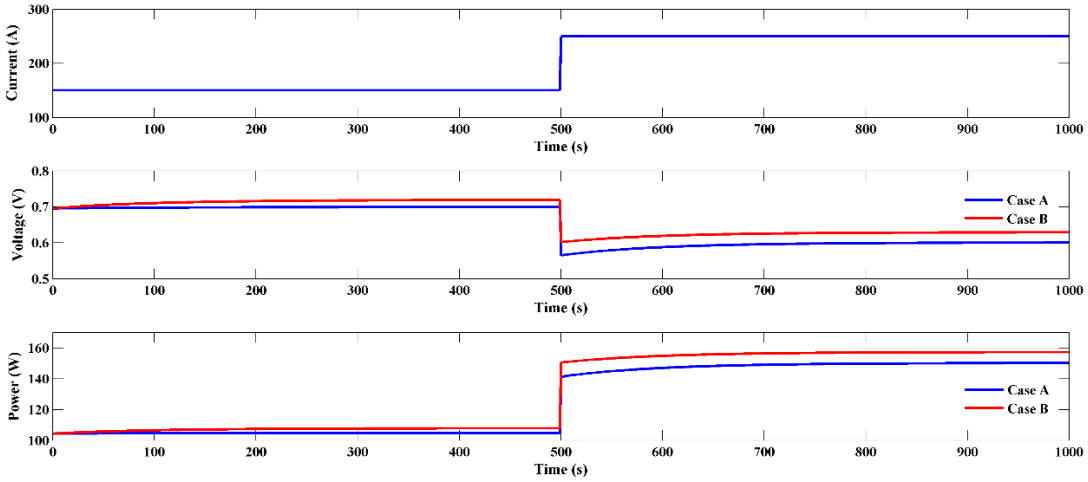

Figure 4. The dynamic performance of SOFC a) current load b) polarization and c) power output for different operating conditions at a constant fuel utilization rate

The turbine power and temperature outputs are also investigated under the change of electric load in Fig.4a and Fig.4b, respectively. When the electric load increases from 150 A to 250 A, an increment of turbine power and turbine outlet temperature are found as 70 W and 9 K, respectively. It is explained that when the current density increases, the mass flow rate of SOFC exhaust gas increases, and thus mass flow rate entering the turbine increases. In this case, an increase of mass flow rate at the turbine inlet leads to an increment power output of turbine according to equation (23). In addition, time delay response of turbine output temperature is relatively slow. For example, time delay response of turbine outlet temperature is found as 400 s to ensure steady-state operation regime.

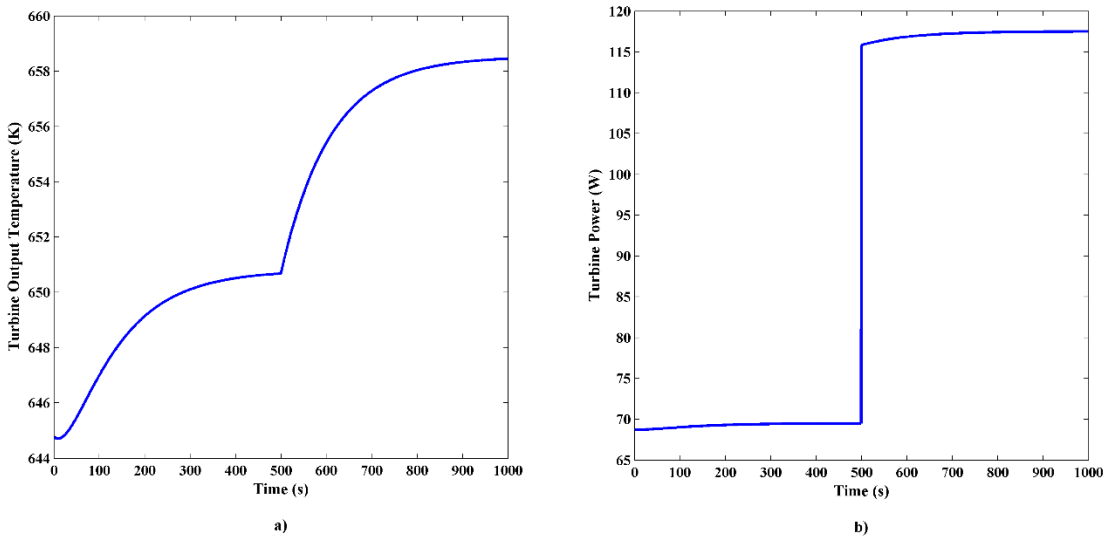

Figure 5. Turbine outputs a) temperature and b) power when the electric load is increased from 150 A to 250 A

3. CONCLUSION

In the present paper, the dynamic behavior of SOFC/GT system is investigated under different electric loads. For this purpose, the electrochemical and thermodynamic model for SOFC implemented internal reformer, and thermodynamic model for system components are developed using MATLAB/Simulink software. A higher time delay in the response of voltage output of SOFC is found at low operating cell temperature when the compared with the high operating cell temperature. Similarly, the time response of turbine outlet temperature to reach steady-state operation time of turbine is quite slow. On the other hand, the time delay in the response of turbine power output is very fast. In the future study, exergy and exergy economy model are integrated into this model to obtain thermoeconomic performance of SOFC/GT systems.

REFERENCES

[1] Zhang, X., Li, J., Li, G., & Feng, Z. Dynamic modeling of a hybrid system of the solid oxide fuel cell and recuperative gas turbine. *Journal of Power Sources*, **163**, 523-531, 2006.

[2] Roberts, R. A., & Brouwer, J. Dynamic simulation of a pressurized 220kw solid oxide fuel-cell–gas-turbine hybrid system: modeled performance compared to measured results. *Journal of Fuel Cell Science and Technology*, 18-25, 2006.

[3] Rossi, I., Traverso, A., & Tucker, D. SOFC/Gas Turbine Hybrid System: A simplified framework for dynamic simulation. *Applied energy*, **238**, 1543-1550, 2019.

[4] Hughes, D., Wepfer, W. J., Davies, K., Ford, J. C., Haynes, C., & Tucker, D. A real-time spatial SOFC model for hardware-based simulation of hybrid systems. *In ASME 2011 9th International Conference on Fuel Cell Science, Engineering and Technology collocated with ASME 2011 5th International Conference on Energy Sustainability*, 2011.

[5] Barelli, L., Bidini, G., Gallorini, F., & Ottaviano, P. A. Design optimization of a SOFC-based CHP system through dynamic analysis. *International journal of hydrogen energy*, **38**, 354-369, 2013.

[6] Gebregergis, A., Pillay, P., Bhattacharyya, D., & Rengaswemy, R. Solid oxide fuel cell modeling. *IEEE Transactions on Industrial Electronics*, **56**, 139-148, 2008.

[7] Campanari, S., & Iora, P. Definition and sensitivity analysis of a finite volume SOFC model for a tubular cell geometry. *Journal of Power Sources*, **132**, 113-126, 2004.

[8] Badur, J., Lemański, M., Kowalczyk, T., Ziółkowski, P., & Kornet, S. Zero-dimensional robust model of an SOFC with internal reforming for hybrid energy cycles. *Energy*, **158**, 128-138, 2018.

[8] Janardhanan, V. M., & Deutschmann, O. Modeling of solid-oxide fuel cells. Zeitschrift für Physikalische Chemie, 221, 443-478, 2007.

[9] Saisirirat, P. The solid oxide fuel cell (SOFC) and gas turbine (GT) hybrid system numerical model. *Energy Procedia*, **79**, 845-850, 2015.

[10] F. Incropera, "Fundamentals of Heat and Mass Transfer", 7th ed. Hoboken,NJ: *John Wiley*, 2011

[11] Singhal S.C., 2000. Advances in solid oxide fuel cell technology. Solid State Ionics, 135, 305–313. DOI: 10.1016/ S0167-2738(00)00452-5

[12] Yadav, R., & Shankar, G. Modelling and Simulation of Solid Oxide Fuel Cell. *International Conference On Computation Of Power, Energy, Information And Communication (ICCPEIC)*, 2014.

THERMAL EXPANSION, POROSITY, AND MICROHARDNESS PROPERTIES OF SOLID OXIDE FUEL CELL METALLIC INTERCONNECTS MANUFACTURED BY POWDER METALLURGY APPROACH

Alparslan TOPCU*, Ömer Faruk YALÇIN, Bülent ÖZTÜRK**, Ömer Necati CORA*****
*Adana Alparslan Türkeş Science and Technology University, Department of Mechanical Engineering, Adana/Turkey
Email: alparslan.topcu.01@gmail.com
**Karadeniz Technical University, Department of Metallurgical and Materials Engineering, Trabzon/Turkey
Email: ofrkylcn@gmail.com, bozturk@ktu.edu.tr
***Karadeniz Technical University, Department of Mechanical Engineering, Trabzon/Turkey
Email: oncora@ktu.edu.tr

ABSTRACT

This study aimed to investigate the effects of manufacturing parameters on the physical, thermal and mechanical properties of solid oxide fuel cell (SOFC) metallic interconnects through the powder metallurgy (P/M) method. To this goal, interconnect samples were manufactured through P/M methods using Nickel, stainless steel 316L, Inconel 600, SUS 445J1, 1C44Mo20, and Crofer®22 APU powders. Different manufacturing parameters were employed (compaction pressure, compaction temperature, and sintering temperature) to obtain sound samples. Porosity, microhardness, and coefficient of thermal expansion (CTE) measurements were performed. Porosities of samples were measured through optical microscope images. Image J software was used to binarize the photos taken on samples. Five different measurement points were selected on the samples' surface (randomly) in the microhardness process. Vickers microhardness values were determined by applying 50 g.f loads. CTE values of samples were measured using dilatometer equipment at 800 °C in the air atmosphere.

Results showed that the porosity and CTE values of samples decreased with the increasing compaction pressure compaction temperature, and sintering temperature while microhardness values increased. Porosity values were measured between 2-36% considering all samples depending on used powder size and manufacturing parameters. Microhardness values were in the range of 99-261 HV. The coefficient of thermal expansion values was measured between 13.4-34.6x10^{-6} K^{-1} for Nickel, stainless steel 316L, Inconel 600, SUS 445J1, and 1C44Mo20 samples while 11.4-13.1x10^{-6} K^{-1} for Crofer®22 APU sample. As an overall conclusion, it was shown that only the Crofer®22 APU powder could be used as interconnect material when manufactured by the P/M approach as its coefficient of thermal expansion is in the suggested range (9-12x10^{-6} K^{-1}) for SOFC system requirements.

Keywords: SOFC, Metallic interconnect, Powder metallurgy, CTE, Porosity, Microhardness.

1. INTRODUCTION

Solid oxide fuel cells (SOFCs) are highly efficient energy conversion devices used as a power supply or electricity generator for stationary applications [1]. The main advantages of the SOFC system are operating at high temperatures (600-1000 °C), not required an expensive catalyst layer, fuel flexibility, and appropriate for cogeneration applications [2,3]. A SOFC stack consists of membrane electrolyte assembly (MEA), sealant, and interconnect components. Today, yttria-stabilized zirconia (YSZ) based ceramic materials using as MEA, and glass-ceramic materials using as a sealant in SOFC system generally [4,5]. Interconnect is one of the critical components of SOFCs stack through which multiple cells are connected in series [6]. Moreover, interconnects provide electrical contacts between cells, distribute reactive gases on both sides of the cell (anode and cathode sides), and separate the anodes and cathodes of adjacent cells in the stack [6-8]. Interconnects are usually made from stainless steel materials due to their excellent features such as high electrically and thermally conductivity,

corrosion resistance, and high-density structure. Interconnects manufactured using casting and machining (wire erosion) operations in general [9,10]. On the other hand, they can manufacture using the powder metallurgy (P/M) method. P/M approach has some advantages on traditional manufacturing such as reduction of machining steps and scrap material, and near-net-shape production [11,12]. Production of porous Ti – 5.4% Si material by powder metallurgy method studied by Brodnikovskii et al. [13] and examined its structural and mechanical properties. Different groups carried out researches about metallic interconnect manufacturing by powder metallurgy approach [14-16]. Glatz et al. [17-19], Köck et al. [20], and Janousek et al. [21] manufactured different net-shaped interconnect materials with the P/M method. They indicated that the powder metallurgy method is more comfortable than the traditional manufacturing process, and manufactured interconnects by P/M were appropriate for interconnect application in the SOFC system.

In this study, some metallic interconnect powders used as interconnect in literature were manufactured by the P/M method and investigated whether appropriate as interconnect application for the SOFC systems. Samples were fabricated from nickel, stainless steel 316L, Inconel 600, SUS 445J1, 1C44Mo20, and Crofer®22 APU powders in different manufacturing parameters. Afterward, the effects of manufacturing parameters on CTE, porosity, and microhardness were scrutinized.

2. EXPERIMENTAL

Interconnect powders were acquired from different countries and companies. Physical specifications and chemical compositions of powders are listed in Table 1 and Table 2, respectively. Also, SEM images of powders were presented in Figure 1.

Table 1. Physical specifications of powders

Metal Powder	Particle Size Distribution (µm)	Density (g/cm^3)	Melting Temperature (°C)
Nickel	0-125	8,9	1455
Stainless Steel 316L	0-125	8,0	1400
Inconel 600	0-125	8,4	1350
SUS 445J1	0-58	7,7	1500
1C44Mo20	0-38	7,9	1490
Crofer®22 APU	0-63	7,7	1510

Table 2. Chemical compositions of powders

Element % (wt)	Ni	Fe	Cr	Mo	Mn	Si	Ti	Nb	Mn	La	Other
Nickel	99,8	-	-	-	-	-	-	-	-	-	0,2
Stainless Steel 316L	10-14	67,5	17	2,5	0-2	-	-	-	-	-	-
Inconel 600	72	6-10	14-17	-	-	-	-	-	-	-	-
SUS 445J1	0,09	Bal.	22,3	1,2	0,08	0,28	0,19	0,26	0,1	-	-
1C44Mo20	0,02	Bal.	22,1	1,0	0,31	0,04	0,02	0,73	-	0,1	-
Crofer®22 APU	0,03	Bal.	22,8	0,1	0,44	0,5	0,2	0,1	-	0,1	-

Table 3. Sample manufacturing parameters

Metal Powder	Sample Code #	Compaction Temperature (°C)	Compaction Pressure (MPa)	Sintering Temperature (°C)
Nikel	101	300	200	1200
	102	300	300	1200
	103	300	400	1200
	104	375	200	1200
	105	375	300	1200
	106	375	400	1200
	107	450	200	1200
	108	450	300	1200
	109	450	400	1200
Stainless Steel 316L	201	300	200	1200
	202	300	300	1200
	203	300	400	1200
	204	375	200	1200
	205	375	300	1200
	206	375	400	1200
	207	450	200	1200
	208	450	300	1200
	209	450	400	1200
Inconel 600	301	300	200	1200
	302	300	300	1200
	303	300	400	1200
	304	375	200	1200
	305	375	300	1200
	306	375	400	1200
	307	450	200	1200
	308	450	300	1200
	309	450	400	1200
SUS 445J1	401	300	200	900
	402	300	300	1050
	403	300	400	1200
	404	375	200	900
	405	375	300	1050
	406	375	400	1200
	407	450	200	900
	408	450	300	1050
	409	450	400	1200
1C44Mo20	501	300	200	900
	502	300	300	1050
	503	300	400	1200
	504	375	200	900
	505	375	300	1050
	506	375	400	1200
	507	450	200	900
	508	450	300	1050
	509	450	400	1200
Crofer® 22 APU	601	300	200	900
	602	300	300	1050
	603	300	400	1200

	604	375	200	900
	605	375	300	1050
	606	375	400	1200
	607	450	200	900
	608	450	300	1050
	609	450	400	1200

Powder size is significant for interconnect manufacturing by the P/M method. Because it directly affects the adhesion surfaces and porosity during pressing. The melting temperatures of the powders are one of the most critical parameters to be considered during sintering. Powders consist of iron-based materials, as seen in Table 2. At the same time, the chromium ratio is very high without 'Nickel' powder. Chromium additives increase chemical stability, oxidation resistance, and anti-corrosion levels. Sample manufacturing parameters are given in Table 3. Compaction temperature was considered as 300, 375, and 450 °C (warm pressing conditions). Compaction pressure was varied at the range of 200-400 MPa. Moreover, 900, 1050, and 1200 °C sintering temperatures were evaluated. Hydraulic press (60 tons capacity) and die set (have 30 mm^2 areas) mechanism (Figure 2) were used in sample manufacturing with the P/M approach.

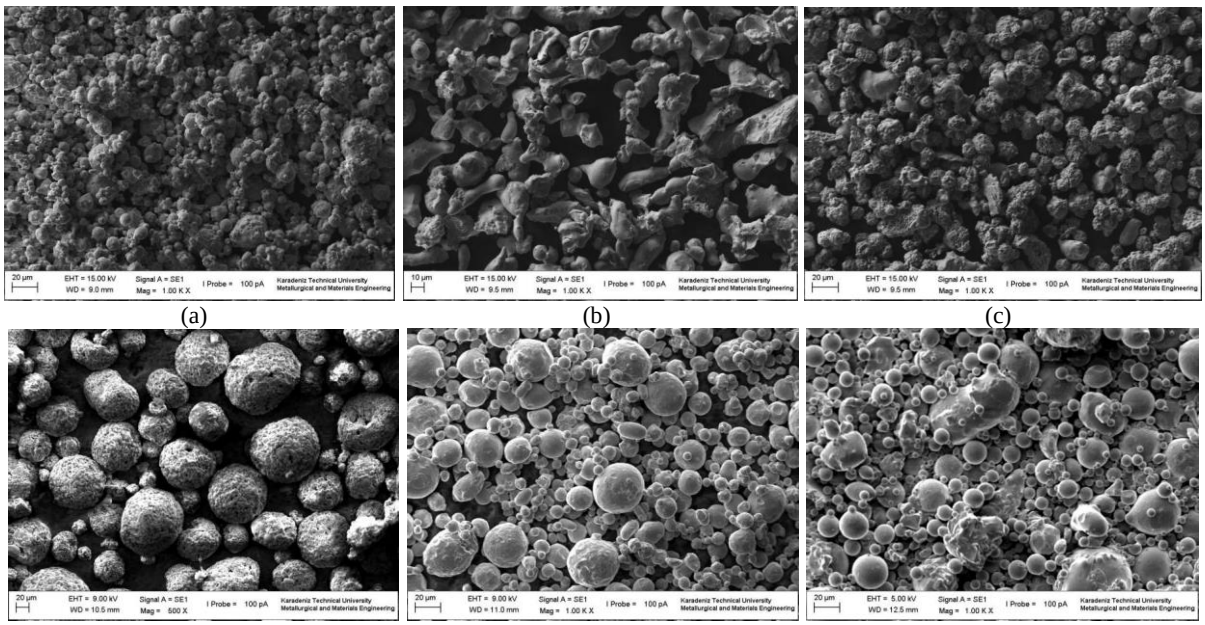

Figure 1. SEM images of powders; (a) Nickel, (b) Stainless steel 316L, (c) Inconel 600, (d) Stainless steel SUS 445J1, (e) 1C44Mo20, (f) Crofer ®22 APU

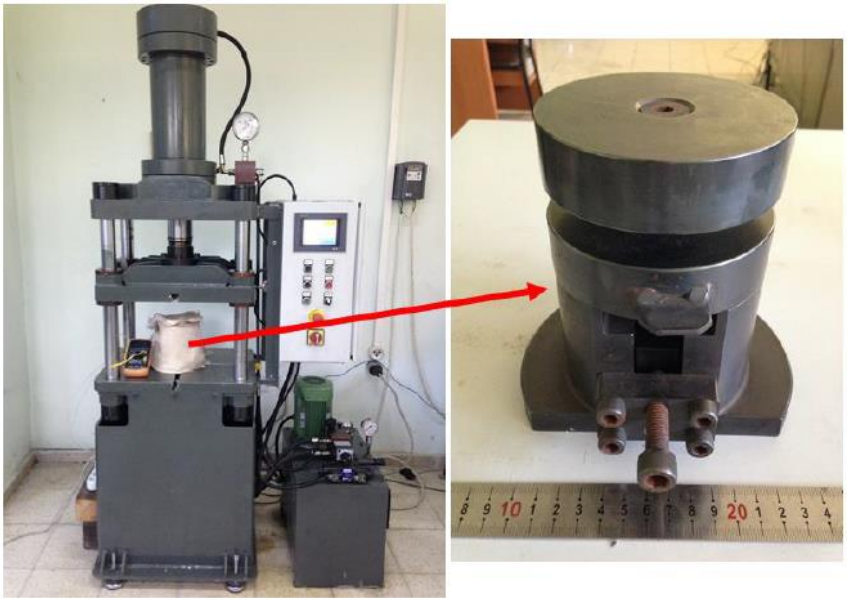

Figure 2. Used hydraulic press and die set in sample manufacturing

2.1 Porosity Measurements

Porosity values affect the coefficient of thermal expansion (CTE) directly. At the same time, interconnects should dense as possible, because reactant and oxidant gases can pass from interconnect to outside. So, firstly porosity values of powders were determined. Samples were molded using the cold molding method, and after grinding and polishing processes were carried out. Microscope images of samples were obtained, and then porosity values were determined using Image J software. Porosity measurement process steps were given in Figure 3. Firstly, the original microscope image was uploaded to the software, as seen in Figure 3 (a). This image was converted into black and white areas (binarization), as seen in Figure 3 (b). Then, black and white areas (Figure 3-c) were selected (red rectangle areas). The ratio of black and white areas on all areas was determined, and the porosity value was calculated.

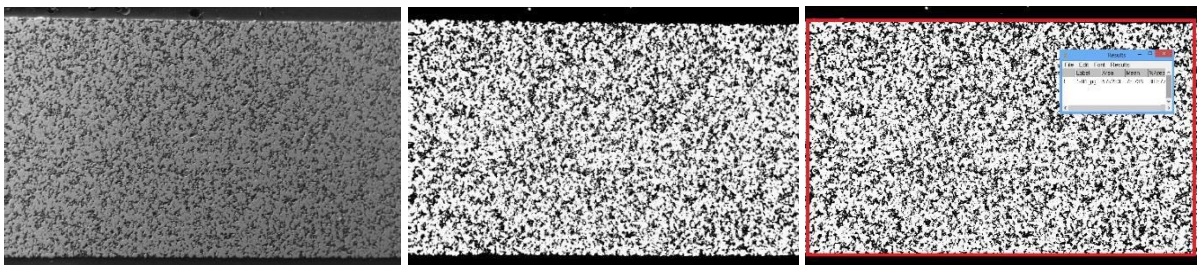

(a) (b) (c)

Figure 3. Porosity measurements using Image J software; (a) original microscope image, (b) binarization, (c) determining black and white areas

2.2 Microhardness Measurements

Interconnects should provide strengthen mechanically because they exposed mechanical loads under operating conditions. Vickers microhardness measurements were carried out using the Innova microhardness test device. 50 g.f load was applied to the samples and 10 seconds waited. Measurements were saved from five different places on a sample.

2.3 CTE Measurements

Coefficient of thermal expansion (CTE) values of SOFC system components should close and match as possible. Usually, the CTE of system components is changing between 9-12 x 10^{-6} K^{-1}. Thus, CTE values of interconnect should match with these values. Besides, differences in the CTE of components can cause thermal stresses and cracks in the system. For this purpose, samples were prepared with 20x10x3 mm^3 dimensions by the P/M method. Measurements were carried out using a dilatometer device. Samples were heated from room temperature to 800 °C, and CTE was measured at this point.

3. RESULTS AND DISCUSSION

3.1 Porosity Values

The porosity value was found for sample#101 as 7.4% and sample#109 as 3.2% for Nickel powders. Porosity values decrease with the increase of production pressure and temperature for all powders. The highest porosity value for the stainless steel 316L sample was 11% with sample#201. The lowest porosity for the same group was calculated as 5.8% with sample#209. The same trends were observed for other powder groups. The porosity values of all samples were presented in Figure 4. Crofer®22 APU powder was observed as the most porous sample, while Nickel powder has the lowest porosity value. Therefore, porosity is a natural result of the powder metallurgy approach and can control the changing of manufacturing parameters (sintering temperature, compaction pressure, and compaction temperature).

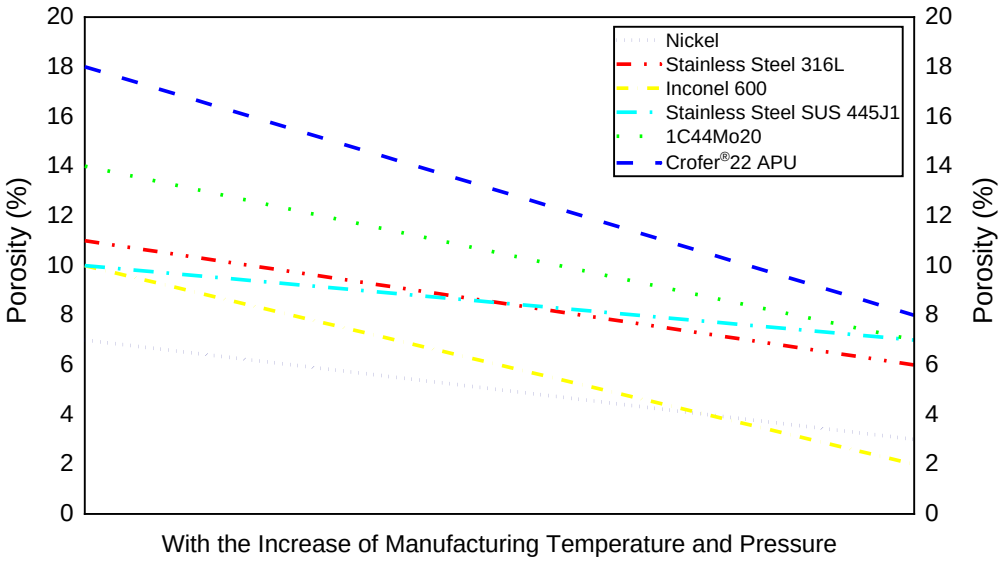

Figure 4. Porosity values changing of samples with the increase of temperature and pressure

3.2 Microhardness Values

Microhardness values of samples were presented in Table 4. Microhardness values increased with the increase of production pressure, temperature and sintering temperature.

Table 4. Microhardness values of samples

Metal Powder	Sample Code #	Compaction Temperature (°C)	Compaction Pressure (MPa)	Sintering Temperature (°C)	Microhardness ($HV_{0.05}$)
Nikel	101	300	200	1200	104.4
	102	300	300	1200	113.1
	103	300	400	1200	121.4
	104	375	200	1200	107.0
	105	375	300	1200	115.6
	106	375	400	1200	123.5
	107	450	200	1200	108.4
	108	450	300	1200	118.2
	109	450	400	1200	125.9
Stainless Steel 316L	201	300	200	1200	134.3
	202	300	300	1200	139.5
	203	300	400	1200	142.8
	204	375	200	1200	145.4
	205	375	300	1200	151.1
	206	375	400	1200	159.6
	207	450	200	1200	162.3
	208	450	300	1200	175.4
	209	450	400	1200	178.6
Inconel 600	301	300	200	1200	123.7
	302	300	300	1200	125.2
	303	300	400	1200	128.4
	304	375	200	1200	127.3
	305	375	300	1200	130.6
	306	375	400	1200	133.8
	307	450	200	1200	131.7
	308	450	300	1200	134.9
	309	450	400	1200	136.3
SUS 445J1	401	300	200	900	111.4
	402	375	200	1050	116.8
	403	450	200	1200	121.1
	404	300	300	900	126.5
	405	375	300	1050	134.9
	406	450	300	1200	144.3
	407	300	400	900	146.8
	408	375	400	1050	149.4
	409	450	400	1200	151.2
1C44Mo20	501	300	200	900	129.1
	502	375	200	1050	147.4
	503	450	200	1200	153.6
	504	300	300	900	136.3
	505	375	300	1050	167.6
	506	450	300	1200	173.8
	507	300	400	900	219.7
	508	375	400	1050	234.3
	509	450	400	1200	241.2

3.3 CTE Values

CTE values of samples were measured, and it was observed that CTE values of samples were decreased with the increase of production pressure and temperature. CTE of Nickel samples was found at the range of 22-29x10^{-6} K^{-1}. CTE of Stainless steel 316L samples was found between 24-31x10^{-6} K^{-1}. CTE values of Inconel 600 samples were determined between 18-22x10^{-6} K^{-1}. The lowest CTE value was found as 15.82x10^{-6} K^{-1} for stainless steel SUS 445J1 in sample #409. And, the lowest CTE value was found as 13.82x10^{-6} K^{-1} for 1C44Mo20 in sample #509.

CTE values of all samples were found to mismatch for the SOFC system, without Crofer®22 APU powders. 11.42-13.08x10^{-6} K^{-1} CTE values obtained for Crofer®22 APU powders. Thus, only Crofer®22 APU appropriate for interconnect application for SOFC system. Changing of CTE values of all interconnect samples with the increase of manufacturing temperature and pressure were illustrated in Figure 5.

Figure 4 and Figure 5 have comparable specifications. Crofer®22 APU sample has the highest porosity value and has the lowest CTE, at the same time. Stainless steel 316L sample is one of the most porous powders and one of the lowest CTE. The other powders are in the same tendency. In conclusion, porous samples have lower CTE while lower porous samples have higher CTE.

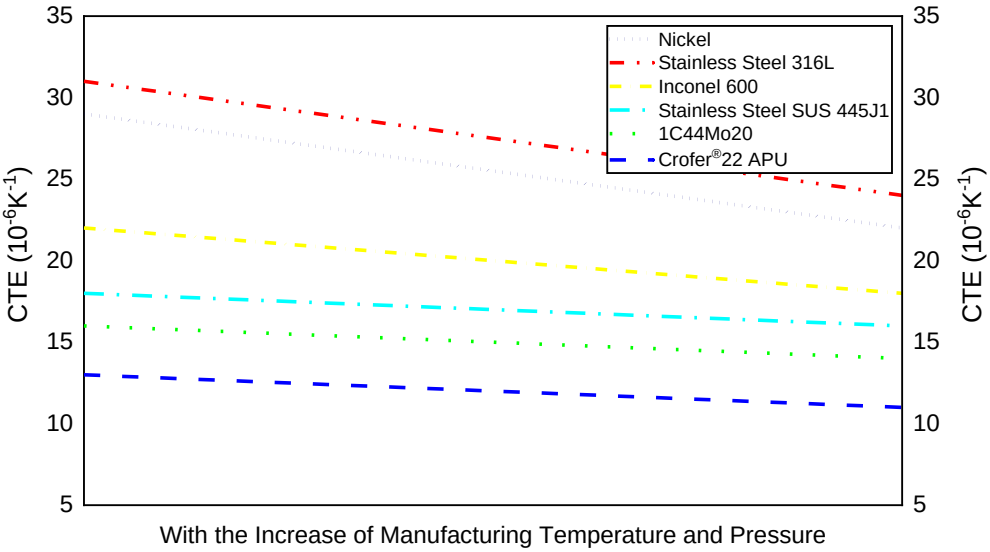

Figure 5. CTE values changing of samples with the increase of temperature and pressure

4. CONCLUSION

In this study, some metallic powders were manufactured by the P/M approach and checked appropriately for interconnect application in the SOFC system. Samples were manufactured considering different compaction pressure, compaction temperature, and sintering temperature. Effects of these production parameters on porosity, microhardness, and CTE values of powders were investigated. Results showed that the porosity and CTE values of samples decreased with the increasing compaction pressure and temperature as well as sintering temperature while microhardness values increased. All samples have sufficient strength mechanically according to microhardness test results. Besides, Crofer®22 APU powders (in the range of 11-13x10^{-6} K^{-1}) were found compatible with other components of SOFC (9-12x10^{-6} K^{-1}) in terms of CTE, and other powders (14-31x10^{-6} K^{-1}) were found mismatch. Also, there is an inverse correlation between the porosity and CTE magnitudes.

ACKNOWLEDGMENTS

This study was supported by the Scientific and Technological Research Council of Turkey (TUBITAK) through project grant #114M502.

REFERENCES

[1] Flores, J.J.A., Rodríguez, M.L.Á., Espinosa, G.A., Vera, J.V.A., Advances in the Development of Titanates for Anodes in SOFC, *International Journal of Hydrogen Energy*, **44**, 12529-12542, 2019.

[2] Yu, Z., Han, J., Cao, X., Chen, W., Zhang, B., Analysis of Total Energy System Based on Solid Oxide Fuel Cell for Combined Cooling and Power Applications, *International Journal of Hydrogen Energy*, **35**, 2703-2707, 2010.

[3] Choudhury, A., Chandra, H., Arora, A. Application of Solid Oxide Fuel Cell Technology for Power Generation - A Review, *Renewable and Sustainable Energy Reviews*, **20**, 430-442, 2013.

[4] Fergus, J., Metallic Interconnects for Solid Oxide Fuel Cells, *Material Science and Engineering A*, **397**, 271-283, 2005.

[5] Guan, W., Wang, G., Zhou, X.D., Mechanism of the Cathode Current Collector on Cell Performance in a Solid Oxide Fuel Cell Stack: Short Communication, *Journal of Power Sources*, **351**, 169-173, 2017.

[6] Swaminathan, S., Ko, Y.S., Lee, Y-S., Kim, D-I., Oxidation Behavior and Area Specific Resistance of La, Cu and B Alloyed Fe-22Cr Ferritic Steels for Solid Oxide Fuel Cell Interconnects, *Journal of Power Sources*, **369**, 13-26, 2017.

[7] Mah, J.C.W., Muchtar, A., Somalu, M.R., Ghazali, M.J., Metallic Interconnects for Solid Oxide Fuel Cell: A Review on Protective Coating and Deposition Techniques, *International Journal of Hydrogen Energy*, **42**, 9219-9229, 2017.

[8] Rubio, D., Suciu, C., Waernhus, I., Vik, A., Hoffman, A.C., Tape Casting of Lanthanum Chromite for Solid Oxide Fuel Cell Interconnects, *Journal of Materials Processing Technology*, **250**, 270-279, 2017.

[9] Tietz, F., Buchkremer, H.-P., Stöver, D., Components Manufacturing for Solid Oxide Fuel Cells, *Solid State Ionics*, **152**, 373-381, 2002.

[10] Scott, J.A., Dunand, D.C., Processing and Mechanical Properties of Porous Fe-26Cr-1Mo for Solid Oxide Fuel Cell Interconnects, *Acta Materialia*, **58**, 6125-6133, 2010.

[11] Venskutonis, A., Glatz, W., Kunschert, G., P/M Processing of ODS Cr- and FeCr-based Alloys for Solid Oxide Fuel Cell Applications, *International Symposium on SOFC IX*, **2**, 534-544, 2005.

[12] Herchen, H., Karuppaiah, C., Armstrong, T., Method of Making Fuel Cell Interconnect Using Powder Metallurgy, United States Patent App. Public, US 2013/0129557 A1, 2013.

[13] Brodnikovskii, D.N., Lugovoi, N.I., Brodnikovskii, N.P., Slyunyaev, V.N., Kuz'menko, N.N., Vasil'ev, A.D., Firstov, S.A., Powder Metallurgy Production of Ti-5.4 wt.% Si Alloy. II. Structure and Strength of the Sintered Material, *Powder Metallurgy and Metal Ceramics*, **52**, 539-544, 2014.

[14] Venskutonis, A., Brander, M., Kraussler, W., Sigl, L.S., High Volume Fabrication of Ready-to-Stack Components for Planar SOFC Concepts, *ECS Transactions*, **25(2)**, 1353-1359, 2009.

[15] Franco, T., Brandner, M., Rüttinger, M., Kunschert, G., Venskutonis, A., Sigl, L.S., Recent Development Aspects of Metal Supported Thin-Film SOFC, *ECS Transactions*, **25(2)**, 681-688, 2009.

[16] Haydn, M., Ortner, K., Franco, T., Menzler, N.H., Venskutonis, A., Sigl, L.S., Development of Metal Supported Solid Oxide Fuel Cells Based on Powder Metallurgical Manufacturing Route, *Powder Metallurgy*, **56(5)**, 382-387, 2013.

[17] Glatz, W., Batawi, E., Janousek, M., Kraussler, W., Zach, R., Zobl, G., A New Low Cost Mass Production Route for Metallic SOFC-Interconnectors, *Solid Oxide Fuel Cells VI, The Electrochemical Society Proceedings Series PV*, **99-19** (S.C.Singhal, M.Dokiya, Editors), Pennington, NJ., 1999.

[18] Glatz, W., Janousek, M., Batawi, E., Honegger, K., Cost Efficient Industrial Manufacturing Routes for Intermediate and High Temperature SOFC Interconnects, *Proceedings of 4th European SOFC Forum*, **2**, (A.J.McEvoy, Ed.), Lucerne/Switzerland, 2000.

[19] Glatz, W., Kunschert, G., Janousek, M., Powder Metallurgical Processing and Properties of High-Performance Metallic SOFC Interconnect Materials, *Proceedings of 6th European SOFC Forum*, **3**, (M. Mogensen, Ed.), Lucerne/Switzerland, 2004.

[20] Köck, W., Martinz, H.P., Greiner, H., Janousek, M., Development and Processing of Metallic Cr Based Materials for SOFC Parts, *Solid Oxide Fuel Cells IV, The Electrochemical Society* (M.Dokiya, O.Yamamoto, H.Tagawa and S.C.Singhal, Editors) *Proceedings Series PV* **95**-1, 1995.

[21] Janousek, M., Köck, W., Baumgärtner, M., Greiner, H., Development and Processing of Chromium based Alloys for Structural Parts in Solid Oxide Fuel Cells, *Solid Oxide Fuel Cells V, The Electrochemical* (U.Stimming, S.C.Singhal, H.Tagawa and W.Lehnert, Editors) *Society Proceedings Series* PV **97-18**, 1997.

HYDROGEN ENERGY

EXERGY AND THERMOECONOMIC ANALYSES OF SOLAR HYDROGEN PRODUCTION AND LIQUEFACTION PROCESS

Tansel KOYUN*, Emin Fuad KENT**
*Süleyman Demirel University, Engineering Faculty, Batı kampusu, Çünür, Isparta/Turkey
Email: tanselkoyun@sdu.edu.tr
**Istanbul Technical University, Mechanical Engineering Faculty, İnönü Cad. No:87, Gümüşsuyu, Istanbul/Turkey
Email: kente@itu.edu.tr

ABSTRACT

This study attempts to perform energy and exergy analyses of solar hydrogen production and liquefaction process. It is possible to produce hydrogen using conventional or renewable energy sources. Hydrogen produced from conventional sources (about 97% of total production), i. e., produced from steam reforming of natural gas and other fossil fuels, couses greenhouse gases and other climate-changing emissions release into the environment. On the other hand, there is no such harmfull effect on the environment for the hydrogen produced from renewable energy sources (using electrolysis), i. e., from solar energy using photovoltaics for direct conversion, from solar thermal energy, wind power, hydropower and biomass. The idea of using solar energy is to protect the environment from unwanted greenhouse gas emissions. It must be stressed that hydrogen produced from the use of renewable energy sources could only become a clean energy carrier. In the present work, solar energy is utilized to produce electricity, and this electricity is used for the PEM (Proton Exchange Membrane) water electrolysis to produce hydrogen. The exergy analyses are carried out in two stages. In the first phase, exergy analysis of the solar hydrogen production system (including electrolysis) has been performed. Then the exergy efficiencies for these processes have been determined. The liquefaction porocess is also taken into account as hydrogen is transported in liquid form. It is worth mentioning that the hydrogen liquefaction process is very energy intensive, and thus, it requires much exergies. It has a significant impact on the final exergy efficiency of all processes. In the second phase, the exergy efficiency for the liquefaction process is found. In this work, we presented the exergy efficiencies of the system before and after the liquefaction process. The exergy analysis has revealed exergy efficiencies in the solar-receiver system, organic Rankine cycle and electrolysis unit, and liquefaction process. The exergy efficiency of the system is calculated by multiplying the individual efficiencies. The exergy efficiencies of the system before and after the liquefaction process, are found to be 3.91% and 0.52%, respectively.

Keywords: Hydrogen, Exergy, Electrolysis, Solar energy, Second law efficiency, Liquefaction.

Symbols

E	Energy (kJ)
$\dot{E}_{in}$	The rate of net energy transfer in (kW)
$\dot{E}_{out}$	The rate of net energy transfer out (kW)
$\dot{Ex}$	Exergy (kW)
$\dot{Ex}_{dest}$	Exergy destroyed (kW)
$\dot{Ex}_{in}$	Exergy in (kW)
$\dot{Ex}_{out}$	Exergy out (kW)
$E_{kin,in}$	The kinetic energy in (kJ)
$E_{kin,out}$	The kinetic energy out (kJ)
$E_{pot,in}$	The potential energy in (kJ)
$E_{pot,out}$	The potential energy out (kJ)
ex	Specific exergy (kW/kg)
ex_{ch}	The chemical exergy (kW/kg)

ex_{tm}	The thermo-mechanical flow of exergy (kW/kg)
H	Enthalpy (kJ)
h	Specific enthalpy (kJ/kg)
h_{in}	Inlet enthalpy (kJ/kg)
h_{out}	Outlet enthalpy (kJ/kg)
h_0	Dead state enthalpy (kJ/kg)
m	The mass (kg)
$\dot{m}$	Mass flow rate (kg/s)
$\dot{m}_{in}$	Mass flow rate in (kg/s)
$\dot{m}_{out}$	Mass flow rate out (kg/s)
Q	Heat (kJ)
$\dot{Q}$	The rate of heat transfer (kW)
$\dot{Q}_k$	Heat transfer rate through the boundary at location k (kW)
$\dot{Q}_{net}$	Net heat transfer rate (kW)
s	Entropy (kJ/kg.K)
s_0	Dead state entropy (kJ/kg K)
T	Temperature (K)
T_0	Dead State Environment temperature (K)
T_k	The boundary temperature at location k (K)
W	Work (kJ)
$\dot{W}$	Work rate (kW)
$\dot{W}_{net}$	Net work transfer rate (kW)

1. INTRODUCTION

The decreases in fossil energy sources, such as coal, oil and, natural gas, and; the harmful gaseous emissions make renewable energy sources and carbon-free fuels (such as hydrogen) a priority. Hydrogen produced from the use of renewable energy sources could only become a clean energy carrier. Currently, the steam reforming process is the most economical way of producing hydrogen. As much as 96% of hydrogen is produced from hydrocarbon fuels [1], which neither address the dependence on finite resources nor reduce the amount of carbon from the energy structure. The renewable energy sources used are wind power, solar energy, hydroelectric power and, biomass.

[2] performed exergy analysis of renewable energy sources. [3] gave a review on exergy comparison of hydrogen production methods from renewable energy sources. [4] presented life cycle assessment of hydrogen production processes]. [5] carried out exergetic assessment of solar hydrogen production methods. In their work, various solar-based hydrogen production processes were assessed and compared in terms of exergy efficiency. [6] investigated exergy analysis and the thermodynamic performance of hydrogen production from heat and water by electrolysis. The flows of energy and exergy through the various steps comprising the entire process were considered. Energy and exergy analyses of electrolytic hydrogen production were performed by [7]. It was also noted that their work formed part of a broader program to examine, with energy and exergy analyses, several production processes and hydrogen-derived fuels. The thermodynamic performance of the steam methane reforming process for producing hydrogen from natural gas was investigated by examining the flows of energy and exergy using a computer code [8]. Analysis and assessment of advanced novel hydrogen liquefaction systems were performed in [9] and [10]. An advanced hydrogen liquefaction system with catalyst-infused heat exchangers was proposed, analysed and, assessed energetically and exergetically in [9]. A novel supercritical hydrogen liquefaction process based on helium-cooled hydrogen liquefaction cycles to produce liquid hydrogen was thermodynamically analysed and, assessed in [10]. A detailed thermodynamic analysis of a multi-generation system producing electricity, hydrogen, hot water, heating and cooling based on geothermal energy is presented in [11].

In this work, exergy analysis of solar hydrogen production and liquefaction process has been performed. Solar energy is used to produce electricity (photo-thermal or solar-thermal methods), and this electricity is used for the

PEM (Proton Exchange Membrane) water electrolysis process to produce hydrogen (and oxygen). The idea of using solar energy is to protect the environment from unwanted greenhouse gas emissions. The thermal energy from solar energy in high-temperature applications is also called concentrated solar energy. Concentrated solar energy can be utilised to produce steam in a solar concentrated parabolic trough solar collector-receiver system and then, using the steam, ammonia organic Rankine cycle (ORC) produced electricity. By using this electricity in the PEM water electrolysis process, we produce hydrogen. Figure 1shows the basic idea of the solar energy route to produce hydrogen.

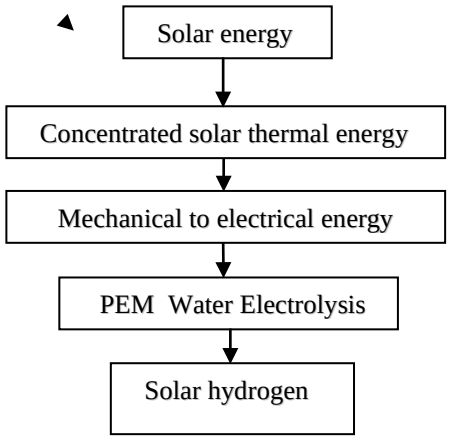

Figure 1. Solar hydrogen production.

Because hydrogen is transported in liquid form, the liquefaction process is also taken into account in this work. The hydrogen liquefaction process is very energy-intensive and, thus, it requires much exegies. It has a significant impact on the final exergy efficiency of all processes and thus hydrogen production cost.

2. SYSTEM DESCRIPTION

The schematic diagram of the solar hydrogen production and liquefaction system investigated is presented in figure 2. This figure shows all components included in the overall system and the hydrogen liquefaction process used in this application, where a closed nitrogen loop is used for additional cooling.

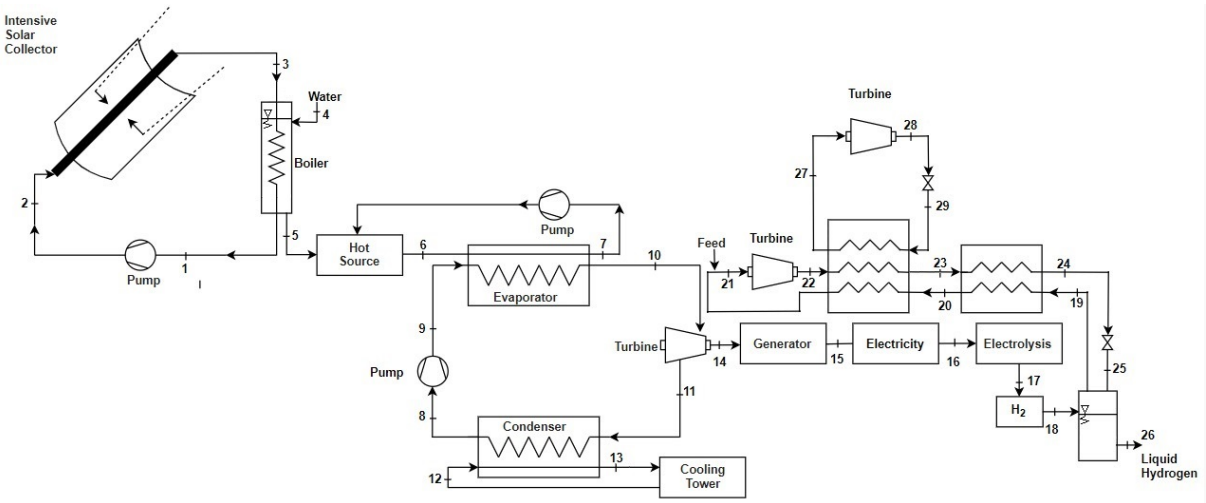

Figure 2. Schematic diagram of the solar hydrogen production and liquefaction system.

PEM (Proton Exchange Membrane) water electrolysis process is used to produce hydrogen (and oxygen). Water electrolysis technologies are classified into three categories based on the applied electrolyte: alkaline water electrolysis, proton exchange membrane (PEM) water electrolysis, and solid oxide water electrolysis [12-13]. PEM water electrolysis systems provide several advantages over the other two electrolysis technologies, such a higher hydrogen production rate, more compact design, and greater energy efficiency [14–17].

3. EXERGY ANALYSIS

The objective of exergy analysis is to determine the exergy efficiencies of the process under consideration. The hydrogen production and liquefaction system studied all assumed to operate in steady-state. For a steady-state system, the mass balance equation yields

$$\sum \dot{m}_{in} = \sum \dot{m}_{out} \tag{1}$$

where $\dot{m}$ is the mass flow rate, and the subscript *in* stands for inlet and *out* for outlet [3]. The general energy balance can be written as

$$\sum \dot{E}_{in} = \sum \dot{E}_{out} \tag{2}$$

$$\mathrm{E_{kin,in} + E_{pot,in} + eventual\ other\ forms\ of\ energy + Q + m_{in}h_{in} =}$$

$$\mathrm{= E_{kin,out} + E_{pot,out} + eventual\ other\ forms\ of\ energy + W + m_{out}h_{out}} \tag{3}$$

where $\dot{E_{in}}$ is the rate of net energy transfer in, $\dot{E_{out}}$ is the rate of net energy transfer out by heat, work and mass; $\dot{Q} = \dot{Q_{net}}$ is the rate of net heat input, $\dot{W} = \dot{W_{net}}$ is the rate of net work output, and h is the specific enthalpy.

The changes in kinetic and potential energy are negligible, equation (3) can then be written as follows:

$$\dot{Q} + \sum \dot{m}_{in} h_{in} = \dot{W} + \sum \dot{m}_{out} h_{out} \tag{4}$$

This equation expresses the total amount of energy input of the system is equal to the total amount of energy output. The energy efficiency of the system can be expressed as

$$\eta_I = \frac{\sum \dot{E}_{in}}{\sum \dot{E}_{out}} \tag{5}$$

The exergy of the system can be expressed by the following equations:

$$\sum \dot{E}x_{in} - \sum \dot{E}x_{out} = \sum \dot{E}x_{dest} \tag{6}$$

or

$$\sum((1 - \frac{T_0}{T_k})\dot{Q}_k - \dot{W}) + \sum \dot{m}\,(ex_{tm,in} + ex_{ch,in}) - \sum \dot{m}_{out}\left(ex_{tm,out} + ex_{ch,out}\right) = \sum \dot{E}\,x_{dest} \tag{7}$$

with

$$ex_{tm} = (h - h_0) - T_0(s - s_0) \tag{8}$$

where $\dot{Q}_k$ is the heat transfer rate through the boundary at temperature T_k at location k, $\dot{W}$ is the work rate, ex_{tm} is the thermo-mechanical flow of exergy, s is the specific entropy and the subscript zero indicates properties at the temperature and pressure of the environment of the system considered.

Equation (8) can be expanded to the form of equation (9)

$$ex_{tm} = (h - h_0) - (T_0 s - T_0 s_0) \quad (9)$$

The term $T_0 s - T_0 s_0$ represents the exergy that has been destroyed, and it is presented as Ex_{dest}.

It must be noted that in the present work Energy Equation Solver (EES) program [18] is used in the calculation of all fluid properties of the system.

The energy and exergy efficiency of the collector-receiver system, are found to be 35% and 28%, respectively. For the ammonia Organic Rankine Cycle, the energy and exergy efficiencies, are found to be 9% and 43%, respectively. Exergy efficiency of the electrolysis unit is 67.5%. The exergy efficiency of the liquefaction process is 13.3%. The exergy efficiency of the system is calculated by multiplying the individual efficiencies. The exergy efficiencies of the system before and after the liquefaction process, are found to be 3.91% and 0.52%, respectively.

Overall efficiency analyses for solar thermal and PV hydrogen production systems were performed in [19]. It was found that the overall energy and exergy efficiency of the solar thermal hydrogen production system ranges between 10.42 – 12.92% and 3.06 – 6.31%, respectively. It is worth noting that these efficiencies are for hydrogen production systems only. They do not take into account the hydrogen liquefaction process. Therefore, the results are in agreement with our presented corresponding results. (3.91% before liquefaction process versus 3.06 -6.31%).

In another work [20], an advanced hydrogen liquefaction system with catalyst-infused heat exchangers is proposed, analyzed and, assessed energetically and exergetically. A comprehensive thermodynamic analysis was performed using the energy and exergy efficiencies of each component and overall system. The proposed hydrogen liquefaction system was simulated in the Aspen plus and, the performance of the system was measured energy and exergy efficiencies. The resulting energy efficiency of the system was calculated to be 15.4%; and the exergy efficiency was found to be 11.58%. It must be stressed that in this aforementioned advanced hydrogen liquefaction system proposed, both energy and exergy efficiencies are much more significant than our presented results and those of the results given in [19].

Energy and exergy analyses of an integrated solar-based hydrogen production and liquefaction system were carried out in [21]. In that work, an integrated system capable of producing and liquefaction hydrogen using the solar energy source was analyzed. The integrated system studied consists of the Heliostat field system, Cu-Cl cycle, Kalina cycle, OIsobutane cycle, and Linde-Hampson cycle. The overall energy efficiency was found to be 4.1%; the overall exergy efficiency was found to be 4.9%. The effect of a rise in solar light intensity on the production and liquefaction rate was studied. The overall energy and exergy efficiencies were found to be increasing from 4.1% to 7.3% and 4.9% to 8.2%, respectively; with rising in solar light intensity. Parametric studies were carried out to see the effect of variation in solar light intensity, makeup water flow rate and ambient temperature on hydrogen production rate, hydrogen liquefaction rate, and overall energy and exergy efficiencies. The increase in the supplied rate of makeup water results in an increase in overall exergy efficiency of the integrated system from 8.2% to 9.6%.

4. TECHNO-ECONOMIC HYDROGEN PRODUCTION PATHWAYS COST ANALYSIS

4.1 Production Cost of Hydrogen

There is a specific report which summarizes work conducted under a three-year Department of Energy (DOE) funded project to Strategic Analysis, Inc. (SA) [22] to analyze multiple hydrogen production technologies and

project their corresponding levelized production cost of hydrogen. The analysis was conducted using the H2A Hydrogen Analysis Tool developed by the DOE and National Renewable Energy Laboratory (NREL). In their work, in-depth techno-economic analysis (TEA) of five different hydrogen production methods was conducted. These TEAs developed projections for capital costs, fuel/feedstock usage, energy usage, indirect capital costs, land usage, labor requirements, and, other parameters, for each hydrogen production pathway, and, use the resulting cost and, system parameters as inputs into the H2A discounted cash flow model to project the production cost of hydrogen ($/kg$H_2$).

The technologies analyzed in this report as part of the project are:

Proton Exchange Membrane technology (PEM),
High-temperature solid oxide electrolysis cell technology (SOEC),
Dark fermentation of biomass for H_2 production,
H_2 production via Monolithic Piston-Type Reactors with rapid swing reforming and regeneration reactions, and Reformer-Electrolyzer-Purifier (REP) technology developed by Fuel Cell Energy, Inc. (FCE).

Methods as mentioned above for hydrogen production are summerized in [22]. Optimization efforts specifically targeted meeting multi-year production plan goal of H_2 production costs of less than \$2/kg H_2.

Results for four of the five H_2 production system studies are presented as a levelized cost of H_2 and appear as \$/kg H_2. The hydrogen production costs for PEM water electrolysis, SOEC, REP integrated and fermentation are given as, \$5.14/kg H_2, \$4.96/kg H_2, \$2.58/kg H_2 and \$51.02/kg H_2 , respectively in this work. The range of H_2 production costs for Projected Current case studies is \$2.58 - \$51.02/kg H_2. It is worth noting that the Projected Current fermentation hydrogen cost (\$51.02/kg H_2) represents a significant outlier within the data due to its low level of commercial readiness; without this particular data point, the range of costs for hydrogen production from the Projected Current cases narrows to \$2.58 - \$5.14/kg H_2. It must be noted that the range of hydrogen production costs for Projected Future case studies is given \$3.82 - \$5.65/kg H_2 in this report.

Electricity is the main parameter driving the cost of the PEM electrolysis process. Hydrogen production cost in \$/kg H_2 for PEM water electrolysis is presented in Table 1.

The price of electricity in Turkey is about 2.45 times greater than that of the price of electricity in the USA. So, hydrogen production cost in Turkey is much more expensive than the corresponding cost in the USA. In both Forecourt and Central cases, the Projected Current stack and BOP capital costs are also high contributors to the overall cost structure.

Table 1. Hydrogen production cost in \$/kg H_2 for PEM water electrolysis.

Component	**Projected current forecourt**	**Projected future forecourt**
Stack capital cost	\$0.42	\$0.16
BOP capital cost	\$0.61	\$0.25
Indirect capital cost and Replacement	\$0.32	\$0.16
Decommission	\$0.02	\$0.01
Fixed operations and maintenance (O&M)	\$0.42	\$0.18
Average electricity price (USA)	0.0612 \$/kWh	0.0688 \$/kWh
Average electricity price (TURKEY)	0.15 \$/kWh	0.15 \$/kWh
Electricity Feedstock (USA)	\$3.34	\$3.46
Electricity Feedstock (TURKEY)	\$8.186	\$8.186
Variable O&M	\$0.01	\$0.01
Total H_2 production cost in \$/kg H_2 (USA)	\$5.14	\$4.23
Total H_2 production cost in \$/kg H_2 (TURKEY)	\$9.98	\$9.98

4.2 Liquefaction Cost of Hydrogen

It is worth mentioning that the hydrogen liquefaction process is very energy intensive, and thus, it requires much exergies. Thus, hydrogen production cost will be found much higher than the indicated values. The hydrogen liquefaction cost in Turkey will also be higher than that of in the USA. This difference is due to the higher average electrical price in Turkey.

The required theoretical minimum energy to produce liquid hydrogen, in a reversible Carnot process is 2.88 kWh/kg, assuming an inlet pressure of 20 bar. Twenty bar is the typical outlet pressure of steam methane reformers (SMR), which are primarily used to produce hydrogen for existing liquefaction plants. Today's industrial liquefiers, however, have an energy requirement in the range of 10–20 kWh/kg [23]

Once hydrogen is produced, the conventional hydrogen liquefaction process includes consecutive compression, cooling and, expansion steps. The liquefier capital cost contribution to the levelized cost of hydrogen with liquid delivery is presented [23]. The capital cost contribution of the liquefier tends to decrease as capacity increases (mainly when capacity is over 10,000 kg/day). The capital contribution is ~$1.40/kg for a liquefier with a capacity of 27,000 kg/day. Additional recurring costs (e.g., electricity) result in an overall levelized cost of ~$2.75/kg total for a 27,000 kg/day liquefier. It is important to note that there are other distribution costs associated with the terminal and tankers used to distribute liquid hydrogen to the stations. As a result, this work concludes a profited hydrogen production cost of $2.24/kg H_2. Liquefaction and terminal profited costs are $2.75/kg and $0.39/kg, respectively, for a plant-gate hydrogen cost of $5.38/kg H_2 for liquid hydrogen supply chain cost estimation for the California market. Energy costs for natural gas, electricity, and diesel were taken into account in the calculations. It is worth mentioning that in their work, delivery via liquid trucks adds $0.68/kg to the cost of hydrogen, and retail station costs add another $8.18/kg; and, thus, making a total dispensed profited cost of liquid hydrogen of $14.24/kg H_2.

An economic analysis of three hydrogen liquefaction systems with an associated cost comparison was given in [24]. The first of the considered systems was a simple conceptual system having an efficiency of 17%. The second was a two-stage compressor Claude system with a 24% efficiency, and, the third was an optimized large-scale type system whose efficiency is 31.5 %. This analysis took into account the energy cost, operation and maintenance, and fixed charges on capital investment. The analysis showed that the cost of liquefying hydrogen is lowest for an optimized large-scale type liquid hydrogen plant and is highest for a simple conceptual liquid hydrogen plant. The ideal (reversible) work is the Carnot work required to liquefy hydrogen at 20 K from gaseous hydrogen at 300 K. This is equal to 3.3 kW h/kg (2.88 kW h/kg in [23]). It is concluded that the cost of liquefaction decreases as the production rates increase and come to a value of $0.63/kg H_2 for the optimized large-scale type liquid hydrogen plant at a production rate of 30,000 kg/h when the cost of electricity is $0.04/(kW h).

Thermodynamic analysis of a new renewable energy-based hybrid system for hydrogen liquefaction is presented in [25]. In this paper, a parametric study of the triple effect absorption cooling system (TEACS) integrated with solar photo-voltaic/thermal (PV/T), geothermal, and Lindee-Hampson cycle is conducted. [26] conducted a study on the cost of hydrogen production and liquefaction ranges between 0.979 $/ kg H_2 and 2.615 $/ kg H_2 for different models studied. [27] investigated a case study concerning exergoeconomic analysis and genetic algorithm optimization of the performance of a hydrogen liquefaction cycle assisted by geothermal absorption precooling cycle. The objective was to minimize the unit cost of hydrogen liquefaction of the composed system. In that study, the actual work consumption in the hydrogen liquefaction was 10.06 kW h/kg H_2. The unit exergetic liquefaction cost of hydrogen is calculated to be 1.114 $/kg H_2 in the optimum case.
[28] presented process optimization and analysis of a novel hydrogen liquefaction. In that work, after optimization, the specific energy consumption of the system (taken as the objective function), was found to be 7.1329 kWh/ kg H_2.

From the above-mentioned considerations, the total cost of production and liquefaction of the hydrogen was about to 13.12 $/kg H_2, when the cost of electricity in Turkey was taken as 0.15 $/ kW h.

5. CONCLUSIONS

This work presents exergy analysis of solar hydrogen production and liquefaction process. The exergy efficiency of the system is calculated by multiplying the individual efficiencies. The exergy efficiencies of the system before and after the liquefaction process, are found to be 3.91% and 0.52%, respectively. These results are in agreement with the corresponding results in the literature.

Techno-economic hydrogen production pathways cost analysis reveals that total H_2 production costs in the USA and Turkey are \$5.14/ kg H_2, \$9.98/ kg H_2, respectively. This difference is due to the higher average electrical price in Turkey. The total cost of production and liquefaction of the hydrogen is about to 13.12 \$/kg H_2.

ACKNOWLEDGEMENT

The authors wish to express their sincere thanks to the anonymous referees for their valuable comments which improves the quality of this work.

REFERENCES

[1] Bennaceur K., Clark, B., Franklin, M. J., Ramakrishnan, T. S., Roulet C. & Stout, E., Hydrogen: A future energy carrier? *Oilfield Review*. 2005, 17, 30-41.

[2] Koroneos, C., Spachos, T. & Moussiopoulos, N., Exergy analysis of renewable energy sources, *Renewable Energy*, **28**, 295-310, 2003.

[3] Koroneos, C. & Rovas, D., A review on exergy comparison of hydrogen production methods from renewable energy sources, *Energy Environ. Sci.*, **5**, 6640-6651, 2012.

[4] Koroneos, C., Dompros, A., Roumbas, G. & M. Moussiopoulos, M., Life cycle assessment of hydrogen fuel production processes, *Int. J. Hydrogen Energy*, **29**, 1443-1450, 2004.

[5] Joshi, A. S., Dincer, I. & Reddy, B.V., Exergetic assessment of solar hydrogen production methods", *Int. J. Hydrogen Energy*, **35**, 4901-4908, 2010.

[6] Rosen, M. A. & Scott, D. S., Exergy analysis of hydrogen production from heat and water by electrolysis, *Int. J. Hydrogen Energy*, **17**(3), 199-204, 1992.

[7] Rosen, M. A., Energy and exergy analysis of electrolytic hydrogen production, *Int. J. Hydrogen Energy*, 2**0**(7), 547-553, 1995.

[8] Rosen, M. A., Thermodynamic investigation of hydrogen production by steam-methane reforming, *Int. J. Hydrogen Energy*, **16** (3), 207-217, 1991.

[9] Hammad, A. & Dincer, I., Analysis and assessment of an advanced hydrogen liquefaction system, *Int. J. Hydrogen Energy*, **43**, 1139-1151, 2018.

[10] Yuksel, Y. E., Ozturk, M. & Dincer, I., Analysis and assessment of a novel hydrogen liquefaction process, *Int. J. Hydrogen Energy*, **42**, 11429-11438, 2017.

[11] Yuksel, Y. E. & Ozturk, M., Thermodynamic analysis of a multi-generation energy system based geothermal energy, *Pamukkale Univ. Muh. Bilim. Derg*., **26**(1), 113-121, 2020.

[12] Buttler A., & Spliethoff, H., Current status of water electrolysis for energy storage, grid balancing and sector coupling via power-to-gas and power-to-liquids: A review. *Renewable and Sustainable Energy Reviews*. **82**, 2440-245, 2018.

[13] Maric R. & Yu H., *Nanostructures in Energy Generation, Transmission and Storage*, DOI: 10.5772/intechopen., 78339, 2018.

[14] Marshall, A., Børresen, B., Hagen, H., Tsypkin, M. & Tunold, R., Hydrogen production by advanced proton exchange membrane (PEM) water electrolyzers—Reduced energy consumption by improved electro-catalysis, *Energy*, **32**, 431-436, 2007.

[15] Millet, P., Ngameni R., Grigoriev, S. A., Mbemba, N., Brisset, F. & Ranjbari, A., PEM water electrolyzes: From electro catalysis to stack development, *Int. J. Hydrogen Energy*, **35**, 5043-5052, 2010.

[16] Millet, P., Mbemba, N., Grigoriev, S. A., Fateev, V. N., Aukauloo, A. & Etievant, C., Electrochemical performances of PEM water electrolysis cells and perspectives, , *Int. J. Hydrogen Energy*, **36**, 4134-4142, 2011.

[17] Carmo, M., Fritz, D. L., Mergel, J. & Stolten, D., A comprehensive review on PEM water electrolysis, *Int. J. Hydrogen Energy*, **38**, 4901-4934, 2013.

[18] Engineering Equation Solver, EES, F-Chart software, P. Box 444042, Madison, WI 53744, www.fchart.com

[19] Dincer, I. & Joshi, A. S., Solar based hydrogen production systems, *Springer-Verlag New York, 2013*.

[20] Hammad, A. & Dincer, I., Analysis and assessment of an advanced hydrogen liquefaction system, *Int. J. Hydrogen Energy,*, **43**, 1139-1151, 2018.

[21] Ratlamwala, T. A. H. & Dincer, I., Energy and exergy analyses of an Integrated solar based hydrogen production and liquefaction system, *Progress in exergy, energy and environment, Chapter 9, 90-110, Springer International Publishing, 2014.*

[22] James, B. D., DeSantis, D. A. & Saur, G., Hydrogen production pathways cost analysis (2013-2016), *DOE-Strategic Analysis Inc.-6231-1*, 2016.

[23] Connelly, E., Penev, M., Elgowainy, A. & Hunter, C. Current Status of Hydrogen Liquefaction Costs, *DOE Hydrogen and Fuel Cells Program Record, Record #: 19001*, 2019.

[24] Syed, M. T., Sherift, S. A., Veziroglu, T. N. & Sheffield, S. A, An economic analysis of three hydrogen liquefaction systems, *International Journal of Hydrogen Energy*, **23** (7), 565-5762, 1998.

[25] Ratlamwala, T. A. H., Dincer, I., Gadalla, M. A. & Kanoglu, M., Thermodynamic analysis of a new renewable energy based hybrid system for hydrogen liquefaction, *Int. J. Hydrogen Energy*, **37**, 18108-18117, 2012.

[26] Yılmaz, C., Kanoglu, M., Bolatturk, A. & Gadalla, M. Economics of hydrogen production and liquefaction by geothermal energy, *Int. J. Hydrogen Energy*, **37**, 2058-2069, 2012.

[27] Yilmaz, C., A case study: exergoeconomic analysis and genetic algorithm optimization of performance of a hydrogen liquefaction cycle assisted by geothermal absorption precooling cycle, *Renewable Energy*, **128**, 68-80, 2018.

[28] Yin, L. & Ju, Y., Process optimization and analysis of a novel hydrogen liquefaction, *International Journal of Refrigeration*, **110**, 219-230 2020.

HİDROJEN TEDARİK ZİNCİRİ VE TÜRKİYE ÖRNEĞİ

Ahmet ERDOĞAN*, Ebru GEÇİCİ, Mehmet Güray GÜLER *****
* Endüstri Mühendisliği Bölümü, Makine Fakültesi, Yıldız Teknik Üniversitesi, İstanbul, Türkiye
Email: a.erdogan8787@gmail.com
** Endüstri Mühendisliği Bölümü, Makine Fakültesi, Yıldız Teknik Üniversitesi, İstanbul, Türkiye
Email: egecici@yildiz.edu.tr
*** Endüstri Mühendisliği Bölümü, Makine Fakültesi, Yıldız Teknik Üniversitesi, İstanbul, Türkiye
Email: mgguler@yildiz.edu.tr

ÖZET

Petrol gibi mevcut enerji kaynakları, yakın gelecekte artan talebi karşılamak için yeterli olmayacak. Bu nedenle ülkelerin stratejik planlarının gündeminde enerji, öncelikli konulardan biri olacaktır. Ancak günümüzde hidrojen enerjisi teknolojileri aktif kullanılmadığından, altyapı yeterli değildir ve kritik altyapının tesisi dikkatli planlanmalıdır. Hidrojen enerjisinin üretimden son kullanıcılara iletilmesini sağlayan sistemlere hidrojen tedarik zinciri (HSC) denir. HSC tasarımı, tedarik zinciri yönetiminin ilk adımıdır ve amacı, üretim ve tesis türlerini ve nakliye tiplerini belirlemektir. HSC, dört önemli aşamadan oluşmaktadır: (i) birincil enerji kaynakları, (ii) üretim, (iii) depolama ve (iv) nakliye. Hidrojen enerjisi üretmek için üretim tesislerinde gerekli hammadde birincil enerji kaynaklarından karşılanırken, son kullanıcıların ve depoların talepleri üretilen enerjinin farklı taşıma modları ile aktarılmasıyla karşılanmaktadır. Yapmış olduğumuz bu çalışmada, 2021 ile 2050 yılları arasındaki dönemin taşıma sektörüne ait hidrojen talebini karşılamak amacıyla Türkiye'nin HSC'ni analiz ediyoruz. Amacımız, talebi karşılarken HSC'nin toplam maliyetini en aza indirmektir. Bu kapsamda HSC için karma tamsayılı programlama modelini çözüyoruz. Elde ettiğimiz sonuçlar önceki benzer çalışmalarla tutarlıdır. İlk dönemde yerel üretim tesislerinden gelen talebi karşılayabilme %12 iken, planlama ufku sonunda bu oranın %48'e çıktığı görülmektedir. Analiz aynı zamanda, hemen hemen tüm şebekelerin aynı anda hem hidrojen üretmeyip hem de ithal etmediğini, yani ya hidrojen ürettiklerini ya da ithal ettiklerini ortaya koyuyor. Optimal çözüme farklı uzaklıktaki çözümler karşılaştırıldığında ise kurulu tesisler açısından sadece küçük farklılıklar olduğu ortaya çıkıyor.

Anahtar Kelimeler: Hidrojen Tedarik Zinciri, Çok Dönemli Model, Karma Tamsayılı Programlama

DESIGN OF A FUTURE HYDROGEN SUPPLY CHAIN: A MULTI-PERIOD MODEL FOR TURKEY

Mehmet Güray GÜLER*, Ebru GEÇİCİ, Ahmet ERDOĞAN*****
* Department of Industrial Engineering, Faculty of Mechanical Engineering, Yıldız Technical University, Istanbul, Turkey
Email: mgguler2@gmail.com
** Department of Industrial Engineering, Faculty of Mechanical Engineering, Yıldız Technical University, Istanbul, Turkey
Email: geciciebru@gmail.com
*** Department of Industrial Engineering, Faculty of Mechanical Engineering, Yıldız Technical University, Istanbul, Turkey
Email: a.erdogan8787@gmail.com

ABSTRACT

Energy resources such as petroleum will not be sufficient in the near future to fulfill increased demand. For this reason, energy will become one of the priority issues in the strategic plan of the countries. Hydrogen is one of the most promising alternative energy sources because of its advantages. However, as the hydrogen technologies are not used actively, the required infrastructure is not enough. For this reason, it should be designed carefully. Systems that enable the transmission of hydrogen energy from production to end users are called hydrogen supply chains (HSC). Design of the HSC is the first step of supply chain management, and its aim is to define the modes of production, facility, and transportation. HSC consists of four important stages: primary energy sources, production, storage, and transportation. While the required raw material to produce hydrogen is provided from the primary energy sources, the demands of end-users and warehouses are fulfilled by transferring the produced energy with different transportation modes. In this study, the HSC of Turkey, with the aim of meeting the hydrogen demand for the transportation sector was analyzed for the period between 2021 and 2050. Our goal is to minimize the total cost of HSC while meeting demand. Thus, the mixed integer programming model was solved for HSC. Results of this study are consistent with previous similar studies. While meeting the demand from local production facilities was 12% in the first period, it is seen that this ratio increased to 48% at the end of the planning horizon. The analysis also reveals that almost all networks do not simultaneously produce and import hydrogen; that is, they either produce or import hydrogen. The results are robust as there are small differences in terms of installed facilities compared to solutions of different optimality gaps.

Keywords: Hydrogen Supply Chain, Multi-Period Model, Mixed Integer Programming

ENERGY TECHNOLOGIES

SMART THERMOS DESIGN INTEGRATED WITH THERMOELECTRIC MODULE

Erkan ÖZTÜRK*, Alpay HİNDİSTAN*, Kemal YILDIZLI*
*Ondokuz Mayıs Üniversitesi, Mühendislik Fakültesi, Makina Mühendisliği Bölümü
Email: erkan.ozturk@omu.edu.tr, alpayhindistan@gmail.com, kyildizli@omu.edu.tr

ABSTRACT

Thermoses are the devices that keep the temperature of the food and beverages inside stable for a long time. In this study, a new smart thermos design and prototype manufacturing which keeps the liquid temperature constant at desired value were realized for small cooling volume by modification and controlling a standard thermos cup. A microcontroller was adapted to the design for keeping the temperature constant for both cold and hot beverages. The smart thermos contains a thermocouple, fan, thermoelectric module, a different type of sensors / electronic components and a control unit which is coded using a microcontroller. The prototype was run actively in laboratory conditions, and temperature changes of water in the smart thermos were monitored. The proposed smart thermos can be used for daily life of people, and it can be commercialized by a compact and economical design.

Keywords: Smart, Microcontroller, Thermoelectric module, Peltier, Thermos

1. INTRODUCTION

While the removing the heat of materials in solid, liquid or gas phase is called cooling, the process of giving heat to materials is called heating. Different heating and/or cooling systems and techniques are used for cooling and heating depending on environmental conditions/working locations. A thermoelectric module (thermoelectric cooler) is a tool that is generally used for cooling recent days; however, it can be used for both cooling and heating purposes. When the thermoelectric module is powered with electricity, one of its surfaces cools down while the other surface heats up. Also, the more efficiently cooling on the high-temperature surface, the better cooling on the low-temperature surface can be achieved. The capability of using upper or lower surface of it will enable to develop new heating and/or cooling applications/systems. A thermoelectric module cooler is a tool used for two purposes. When the temperature difference is applied to both surfaces, it is possible to generate electricity from the device. Thermoelectric coolers, which we call thermoelectric module/Peltier, are used in many fields today such as medical fields, military/space research (e.g., cabin cooling for radio stations), individually in-home refrigerators, car coolers, beverage built-in coolers, portable insulin coolers etc. Thermoses facilitate our daily life, where food and drinks can be stored either hot or cold for a long time. They can maintain their temperature for a long time. However, different approaches are still required to increase the efficient storage period of thermoses. For that reason, cutting-edge thermoses integrated with thermoelectric modules may be designed, and these designs can promise to create useful products for the market. When the literature is examined, some studies are concentrated to thermoelectric modules. Although the studies related on smart thermos are at the beginning level, the exciting studies can be summarized as below.

Şimşek focused on air conditioning design with thermoelectric module for cars in his thesis. He emphasized that standard air conditioners in cars decrease cars' performance and increase fuel consumption. Thus, he revealed that the thermoelectric modules could be adapted to the air conditioning system in cars [1]. Tan emphasized that it is possible to cool the central processor unit (CPU) and the motherboard with different methods in his thesis, and he compared three different cooling methods during the CPU working at full capacity. In his study, he used a heat sink, water cooling module and thermoelectric cooler module, respectively. The author claimed that the thermoelectric cooler module cools more effectively than other methods [2]. In a different and interesting study, Taşpınar designed and manufactured an organ transporter device integrated with a thermoelectric module. After

manufacturing the device compactly, he investigated the performance analysis of it [3]. Erel et al. aimed to produce electrical energy from solar energy using a mechatronic-based parabolic reflector. They claimed that they made the thermoelectric module-based generator operational by absorbing the heat energy coming from reflected sun rays on the reflective surfaces [4]. Ahıska et al. examined the properties of the two-phase heat transfer system CPU cooler integrated with a thermoelectric module. They compared the two-phase CPU cooler integrated with the thermoelectric module to the cooler systems-based fans. As a result, they observed that the two-phase CPU cooler integrated with thermoelectric module was nine times better [5]. Hacı and his friend developed a food carrying module for industrial kitchens, which have two different compartments at different temperatures to store foods and drinks. In addition, it can provide heating and cooling skills simultaneously. While a thermoelectric module was used in the cooling compartment, a resistance was used in the heating compartment of their design. Computational Fluid Dynamics (CFD) analysis was benefited to optimize that the designed cabin was able to reach the desired temperature for the compartments of the food carrying module [6]. Vasant et al. presented a review article in which they examined recent studies to improve the performance and efficiency of thermoelectric module coolers [7]. Karls et al. modeled the change of temperature according to time and water position for a thermos filled with ice water using CFD analysis [8]. Alsaif and colleagues revealed a recent and interesting study. In their study, they designed and manufactured portable smart cup for hot and cold drinks, especially used in extreme sports. The authors claimed that they compared the temperature change in the cup with the CFD model. Their design might be familiar to ours due to use thermoelectric module and fan. However, the control and operation procedure of their designed did not described in detail [9]. Zeberjadi focused on improving a new heat sink design with new material and geometry instead of the standard copper rectangular heat sinks to improve thermoelectric module performance in the electronic cooling applications [10]. Alomair et al. designed and manufactured a low-cost air conditioner integrated with solar powered thermoelectric module for usage in tents or homes for living areas where electricity is still not available [11]. Al-Madhhachi et al. designed and produced a thermoelectric water purification system for drinking water. While water evaporation on the hot surface of the thermoelectric module was realized, water condensation was made on the cold surface of the thermoelectric module for their water purification device. In addition, they emphasized that the system worked more efficiently by consuming less energy [12]. Gao et al. stated that two-stage thermoelectric modules could achieve a greater temperature drop than single-stage thermoelectric modules when working in steady-state conditions. They fed the thermoelectric modules with current pulses and stated that more temperature drops/cooling and the hot surface reached the highest temperature faster. They emphasized that they had a long-lasting operation by feeding with current pulses, and also this method can be used in time-dependent supercooling applications in the future [13]. They produced a jacket integrated with thermoelectric modules that had temperature control skills for different climate conditions. They set up a system capable of heating and cooling, and set three different temperature limits. The jacket allowed temperature adjustment by the user, and could work according to the climatic conditions [14].

In this study, a standard thermos cup for the small cooling volume, a thermoelectric module, an aluminum heat sink and a fan were selected to design and manufacture a smart thermos that had cooling and heating talents. For the temperature control capability, the design of the system was consisting of different sensors and electronic circuit elements communicated directly with a micro control unit. Also, the smart thermos had own software and being manufactured as a prototype. The proposed design promised a potential to be used in people's daily lives. For that reason, the design criteria and needs were explained in detail in the study.

2. MATERIALS AND METHOD

The use of thermoelectric modules and thermoses together is currently researchable topic. In this framework, a new smart thermos design and prototype manufacturing were made. Then, the principles of design and operation were described in detail in this section.

The necessary tools and equipment were listed below.

- Thermos cup
- TEC-12073, Thermoelectric module
- Fan
- Microcontroller board

- LCD screen
- Potentiometer
- K-Type Thermocouple voltage converter
- Thermocouple
- 12 V Dc power supply
- Relay

The features can be requested by the users from the smart thermos are listed below. During the smart thermos prototype production, these features were paid attention as much as possible.

Necessaries and technical features:
1. Small cooling/heating volume
2. Portability
3. Economic
4. Appealing to all age groups
5. Having heating and cooling
6. It could be assembled and disassembled

Hot drinks such as tea, hot chocolate and coffee are usually served at temperatures between 71.1 ° C and 85 ° C. Liquids consumed at these temperatures can cause significant burns in mouth and throat. However, hot drinks should be served at a temperature high enough to give the consumer a satisfying taste. Recent data in the literature described the coffee drinking temperature preferred by the consumers as about 57.8 ° C for a population of 300 subjects [15]. For hot drinks, 58 °C can be preferred as the critical operating temperature for the manufactured prototype. Although there is no clear information about the preferred temperature for cold beverages in the literature, it has been assumed between 15-20 ° C via personal trials. Thus, 19 °C, at which the produced prototype worked most effectively, was chosen as the critical value for the cooling mode.

Since the thermos cup had a small volume, controlling temperature and monitoring trials could be more comfortable. For this reason, a thermos cup was chosen as control volume to be cooled and heated. In the design, a fan, an aluminum heat sink and a thermoelectric module were assembled as **Figure 1.a**. They had small sizes so that they could be easily assembled to the thermos cup. An aluminum material apparatus was designed for assembling or disassembling to the bottom of the thermos cup via threads. Disassembling allowed the thermos cup to be removed and washed easily. Glass wool was used between the inner chamber and the outer plastic layer for thermal insulation in the thermos cup. In the designed apparatus, there were gaps to let the fan blow out the air comfortably (**Figure 1.b-c**). The designed smart thermos was presented in **Figure 1**.

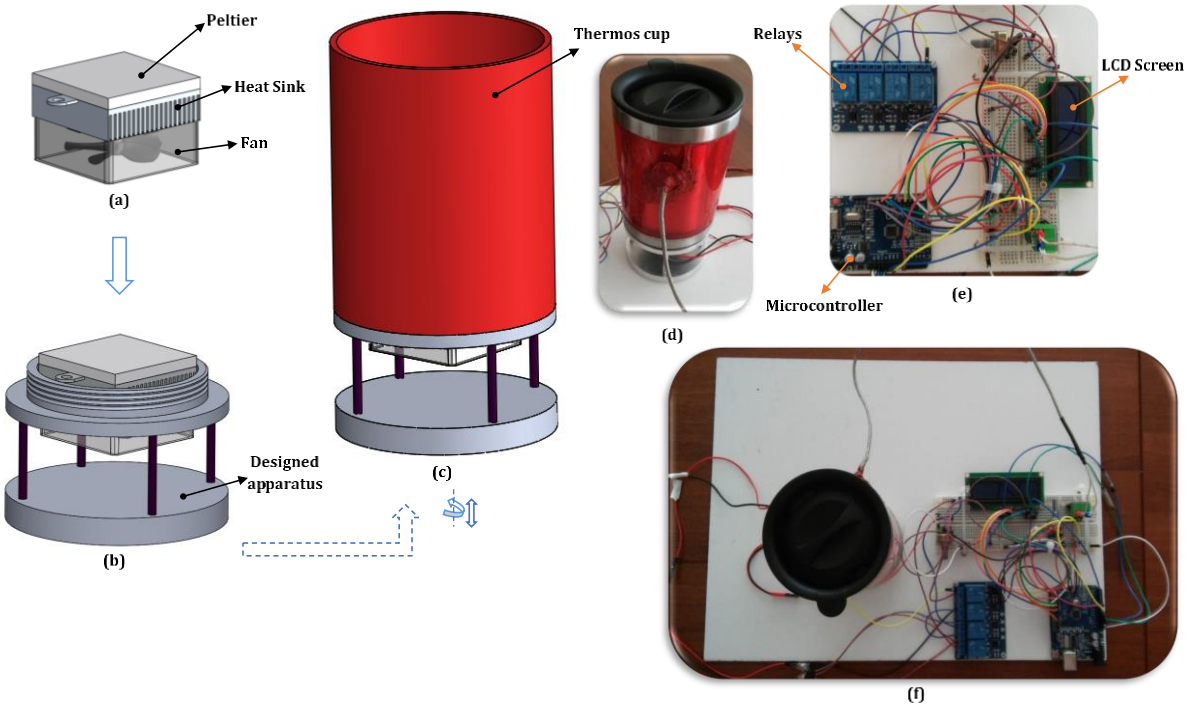

Figure 1. Designed and manufactured smart thermos

The purposes of the designed smart thermos were cooling/heating the liquid placed in the thermos and keeping the desired temperature for longer times. In this context, a system with both cooling and heating modules had been planned and installed. A schematic view of the system was shown in **Figure 2**.

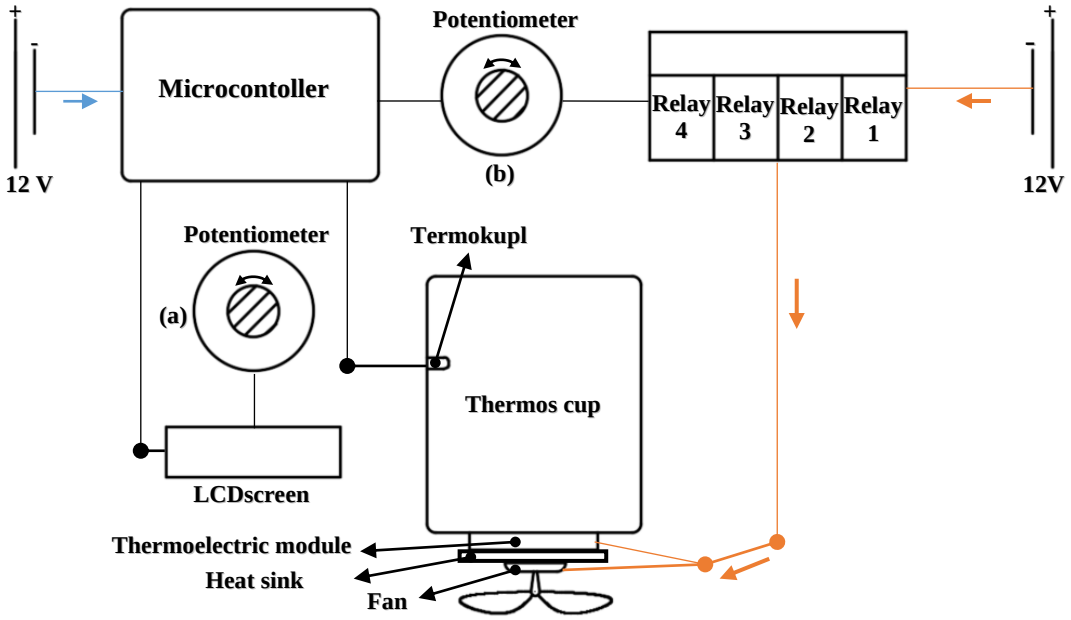

Figure 2. Schematic view of the smart thermos cup

A microcontroller was used for controlling the temperature variations in the smart thermos system. The microcontroller can communicate with potentiometer b, thermocouple, relays, LCD screen, fan and thermoelectric module in the system. The user determines the operation mode of the smart thermos with potentiometer b (Heating, cooling or standby mode). According to the input data received from the potentiometer, the microcontroller determines the operation mode, then reads temperature changes by communicating directly with thermocouple. When the boundary conditions are exceeded, the microcontroller operates the fan and thermoelectric module via controlling the relays. In addition, the microcontroller collects temperature changes as feedback at certain intervals and turns the system on or off. Thus, the temperature of the liquid in the thermos could be kept stable. The microcontroller can be supplied from the USB or 12 V power supply (**Figure 2**).

Thermoelectric module, fan and heat sink trio were used for heating or cooling the thermos chamber. The thermoelectric module is assembled with a fan and heat sink on one side to remove the generated heat on that surface. The inner volume of the cup is heated or cooled with the other surface of thermoelectric module according to the operation mode. The heating and cooling abilities of the thermoelectric module are provided by changing the direction of the electric current with the relays (**Figure 2**). This triple system was assembled in designed apparatus. Thus, they can be removed and attached to the thermos cup. The side surfaces of the apparatus were designed to be left open. In this way, airflow is provided efficiently with the help of a fan (**Figure 1.c-d**). The thermoelectric module and fan system were powered by a 12 V DC power supply.

While the operation mode of the smart thermos cup can be determined from the potentiometer b, the contrast of the LCD screen can be adjusted with the potentiometer a by users (**Figure 2**). A K-type thermocouple was connected with a thermocouple voltage converter, and this converter can be controlled by the coded microcontroller. The tip of the thermocouple was mounted in the thermos cup to measure liquid temperature as not to leak (**Figure 2 and Figure 1.b-d**). In this way, temperature measurements could be taken directly from the liquid, and the temperature change could be controlled in certain periods. These measured temperatures can be instantly displayed on the LCD screen.

In the system, relays were mounted to turn off or on the thermoelectric module-fan couple at the right moments without exceeding the critical temperatures. The all relays can be controlled by the coded microcontroller, and they can be activated or deactivated in different combinations of hot and cold modes (**Figure 2**). The operation strategy of the relays and the prevention of short circuit were explained in detail with the help of **Figure 3**.

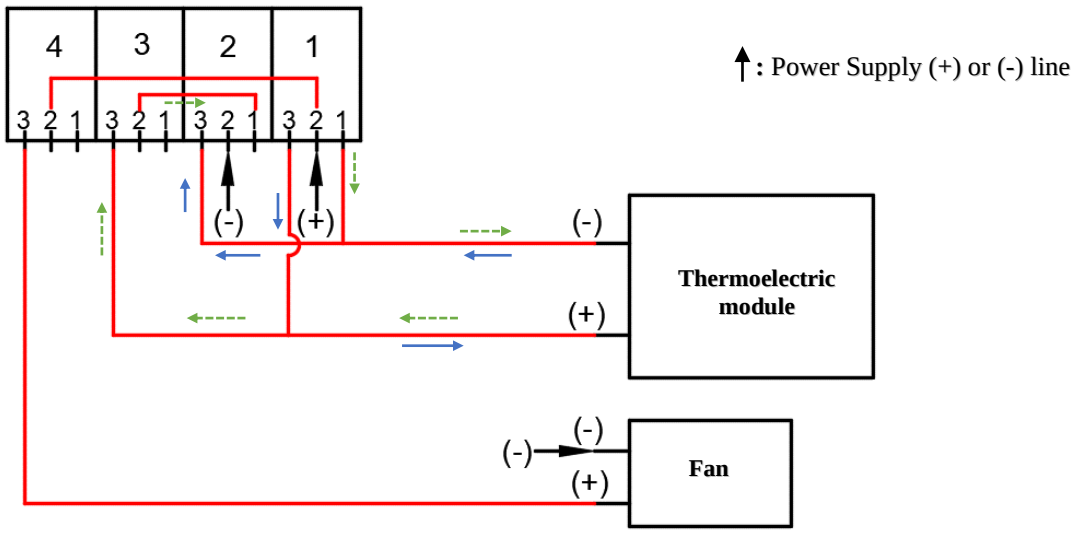

Figure 3. Relay, fan and thermoelectric module electric circuit

When each relay is activated, the lines 2 and 3 are in contact (the electric current is permittable on this line), line 1 is nonconductive. When the relays are passive position, the lines 1 and 2 are in contact and line 3 is nonconductive. The thermoelectric module and fan are controlled by the microcontroller for three basic states namely; cooling, heating and standby modes. While relays 1,2 and 4 are active except relay 3, the smart thermos is in cooling mode. The electric power line will follow the blue arrows as shown in **Figure 3** to make the thermoelectric module run. The by-pass is prevented owing to relay 3. The fan is powered by relay 4, which is directly connected to the line 2 (power supply line) of the 1st relay. While relays 3 and 4 are active in the heating mode, relays 1 and 2 are passive. In this case, the thermoelectric module is supplied by the electric current with the reverse of its' operation direction. Therefore, the thermos cup begins to heat the liquid inside. The system has the same logic for the fan as cooling mode, and by-pass is prevented similarly. In standby mode, all relays are passive. Thus, the circulation of electric current is prevented.

The coded microcontroller monitors the temperature changes in the thermos according to the mode of the user selection. Then, it collects the feedback of the temperature to ensure that the liquid inside remains at the same temperature.

3. EXPERIMENTAL PROCESS

The steps of the experiment process were briefly explained below.

- When the system is in standby mode, it is connected to the power supply. Also, this system can be power by lithium-polymer batteries.
- Water (330ml) is added to the empty thermos cup at the desired temperature.
- Potentiometer is set in the appropriate position for operating mode (hot/cold).
- When the temperature of the water reaches the critical temperature that set for the operating mode, the microcontroller controls the relays, and adjusts the operation of the fan and thermoelectric module.
- The Fan and thermoelectric module work continuously for a certain period for the selected operation mode (Hot mode 5 min-cold mode 10 min). When the working time is completed, the microcontroller measures the water temperature with the help of thermocouple, and displays it on the LCD screen.
- The time until the water temperature reaches the critical value is observed.
- When the liquid temperature reaches the critical temperature, the system becomes active again to cool or warm according to the operating mode. This process can be continued at the desired repetition.
- When the system is wanted to be closed, the system is put into standby mode by users.

4. DISCUSSION AND RESULTS

Smart thermos design and prototype production were realized and tested in working conditions. Thermos cup was chosen for the smart thermos design due to have small chamber volume and be capable of making experiments quickly. The water in the smart thermos were preserved at healthy-friendly temperatures for cold and hot drinking. The experiments were carried out with water in thermos at room temperature of 26 ºC, and the working process was monitored. The use of thermoses with the thermoelectric modules is a new subject, and a portable travel cup was designed for extreme athletes with a familiar thermoelectric module system in the current study by Alsaif et al. [9]. However, how the designed cup works and be controlled in their study has not been explained in detail. In this study, the working principle of the designed smart thermos was given in detail. This design has the potential to be easily used for thermos of different sizes.

The experiments were repeated 5 times, and the temperature change-time (ΔT-t) graphics were obtained as shown in **Figure 4-5** for cooling and heating modes. In heating mode, the thermoelectric module-fan couple operates continuously for 5 minutes when the water temperature equals the critical temperature (58 ºC). Then, the system checks the temperature of the water, and keeps the thermoelectric module and fan off until the temperature drops the critical value again. This waiting period was observed for about 2 minutes during the experiments. On the other hand, cooling mode operates with the same logic as heating mode, but the critical temperature value is considered as 19 ºC. The system runs the thermoelectric module fan couple at critical

temperature for 10 minutes without interruption. The waiting time of the cold mode was observed for approximately 2 minutes and 15 seconds. All experiments were carried out at room temperature of 26 ºC.

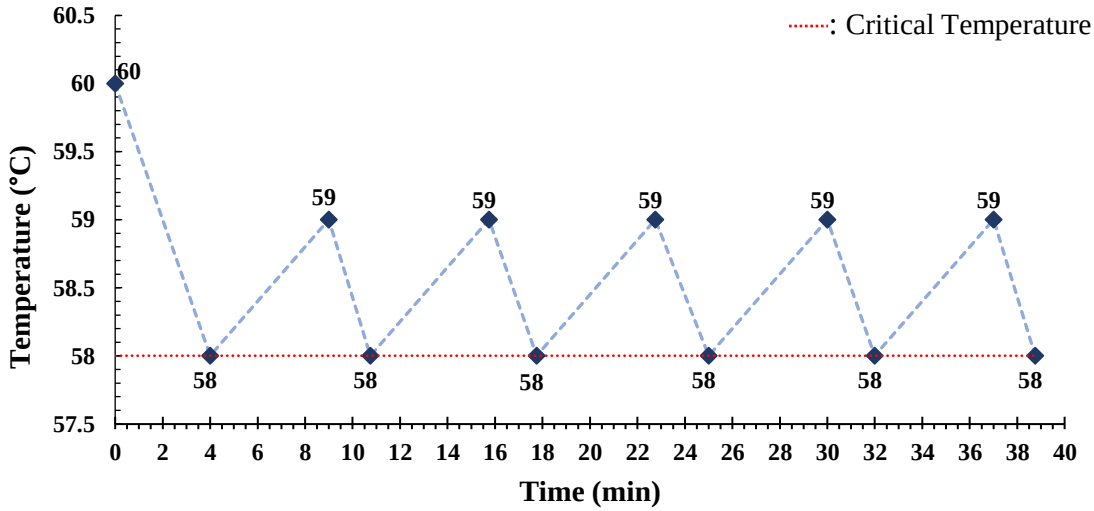

Figure 1. 5 times repetition working process for heating mode

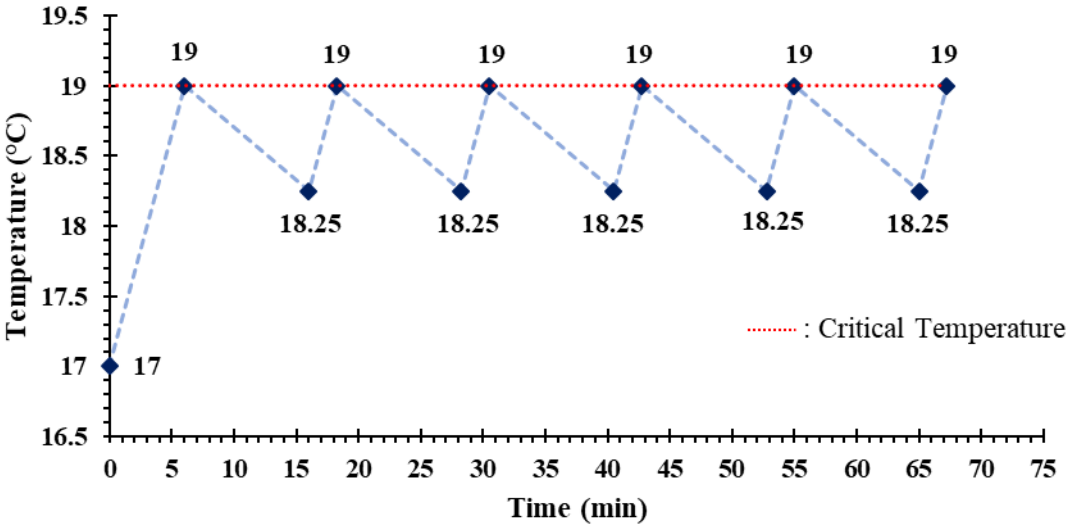

Figure 2. 5 times repetition working process for cooling mode

In the smart thermos design, a 12 V DC power supply instead of li-po battery was used to reduce the prototype cost and make experiments ease. Also, it is possible to use li-po or li-on batteries, which are trendy in this design. However, it may not be appropriate to feed this system with small batteries sold in the market. With recent battery technology (cost-effective), it can be difficult to find products that can provide long-term operation to cool/heat small-volume thermos or chambers. However, it is possible to make portable new designs. Small size 12 V accumulators can be preferred for larger size thermos designs. The products used in the smart thermos prototype are easily accessible and economical products. Despite the large size of the electronic circuit elements in the designed and produced prototype, it is possible to make these electronic elements small sizes. Thus, these electronic elements can be fit in a smaller design and optimum, compact and commercially promising thermoses can be manufactured.

Besides, this design can be researched in the field of climbing and camping equipment, in travel companies, baby bottles, auto icebox and thermoses, and also smart thermos of different sizes.

5. CONCLUSION

In this study, a smart thermos was designed and produced. The operation of the thermos was observed by experiments. Approximately 330ml of water was used in the experiments. In the heating experiment, water was kept constant in the temperature range of 58-59 ºC. Although the system could reach 60 ºC and above, exceeding 60 ºC was prevented by coding the microcontroller. It was observed that the minimum temperature value reached in cooling experiments was 18 ºC. For the effective operation of the system, the 19 ºC limit was accepted, and the water temperature was kept in the range of 18.25-19 ºC in experiments. In the design, the working volume was small for the thermoelectric module fan and heat sink. Therefore, it made difficult to cool effectively the heated surface of the thermoelectric module. Although the thermoelectric module cold surface decreased up to 5 ºC, water was not able to cool lower than 18 ºC in experiments. However, there is no problem operation logic of the designed thermos at any temperature. During the temperature measurements, the temperatures displayed by the thermos were confirmed by measuring with a digital thermometer put in the thermos. In order to improve this study, suggestions for future studies can be listed as below. If batteries of small sizes are used to provide the necessary power (li-ion, li-po batteries, etc.), the thermos can be made portable.

- Different types thermoelectric modules can be selected, and the insulation of the reservoir can be improved to be more effective.
- Cooling at lower temperatures can be possible with selecting a suitable fan that can remove heat more quickly from the heated surface of the thermoelectric module.
- This approach can be applied to larger size thermoses. Also, 12 V accumulators can be used efficiently for power supply.
- This design can be commercialized in the field of climbing and camping equipment, in travel companies, baby bottles, auto icebox and thermoses, and also smart thermos of different sizes.

REFERENCES

[1] Şimşek M., Peltier Modül ile Taşıt Klima Tasarımı, Master Thesis, Afyon Kocatepe University, Institute of Science, Afyon, 2015.

[2] Tan O.S., Sunucuların Peltier Modüller ile Soğutulması sisteminin Tasarımı ve Gerçekleştirilmesi, Master Thesis, Karabük University, Institute of Science, Karabük, 2013.

[3] Taşpınar S. Y., Organ Taşıma Amaçlı Termoelektrik Soğutma Sistem Tasarım ve Uygulaması, Master Thesis, Selçuk University, Institute of Science, Konya, 2012.

[4] Erel Ş., Akdaş M. & Tugay M., Güneş Enerjisi ile Çalışan Bir Termoelektrik Jeneratörde Sıcaklık Faktörünün Etkisi, Int.J.Eng.Research & Development, 2, (1), 7-10, 2010.

[5] Ahıska R., Ahıska K., Flexible Two Phase Thermoelectric CPU Cooler, J. Fac. Eng. Arch. Gazi Univ., 22, (2), 347-351, 2007.

[6] Hacı M., Kahraman Z., Termoelektrik Sistemli Yemek Taşıma Modülü Tasarımı ve Analizi, he International Journal of Fuels, Fire and Combustion in Engineering (FCE), 4, 2016.

[7] Vasant P., Kose U. & Watada J., Metaheuristic Techniques in Enhancing the Efficiency and Performance of Thermo-Electric Cooling Devices, Energies, 10, 1703, 2017, doi:10.3390/en10111703.

[8] Karls M. A., Scherschel J.E:, Modeling Heat Flow in a Thermos, Am. J. Phys., 71, 678, 2003.

[9] Alsaif H. F., Almaghrabi M. A., Smart Travel Mug for Hot and Cold Beverages, Proceedings of the ASME, International Mechanical Engineering Congress and Exposition IMECE2017, November 3-9, Florida, USA, 2018.

[10] Zearjadi M., Elektronic Cooling Using Thermoelectric Devices, Applied Physics Letters, 106, 2015.

[11] Alomair M., Alomair Y., Mahmud S., & Abdullah H., Theoretical and Experimental Investigations of SolarThermoelectric Air-Conditioning System for Remote Applications, Journal of Thermal Science and Engineering Applications, 7, (021013), 1-10, 2015.

[12] Al-Madhhachi H., Min G., Effective use of thermal energy at both hot and cold side of thermoelectric module for developing efficient thermoelectric water distillation system, Energy Conversion and Management, 133, 14–19, 2017.

[13] Gao Y.W., Lv H., Wang X. D., & Yan W. M., Enhanced Thermoelectric module Cooling of Two-Stage Thermoelectric Cooler via Pulse Currents, International Journal of Heat and Mass Transfer, 114, 656–663, 2017.

[14] Poikayil J.R., Francis J., & Saju D., Peltier Integrated Heating & Cooling Jacket, International Conference on Electronics, Communication and Aerospace Technology ICECA 2017, 260-263, 2017.

[15] Brown F., Diller KR., Calculating the Optimum Temperature for Serving Hot Beverages, Burns, 34, (5), 648-54, 2008.

CALIBRATION OF A LOW-COST GLOBE THERMOMETER WITH LINEAR COMPARATIVE CALIBRATION METHOD

Mehmet Furkan ÖZBEY*, Cihan TURHAN**
* Atılım University, Department of Mechanical Engineering, 06830 İncek, Gölbaşı – Ankara/Turkey
Email: ozbey.mehmetfurkan@student.atilim.edu.tr
**Atılım University, Department of Energy Systems Engineering, 06830 İncek, Gölbaşı –Ankara/Turkey
Email: cihan.turhan@atilim.edu.tr

ABSTRACT

Mean Radiant Temperature (MRT) shows direct and reflected wave radiation fluxes on a human body. On the other hand, the MRT measurement is vital to determine the thermal comfort of occupants. Traditionally, MRT can obtain by calculation or measurement methods. Calculation methods are very complex due to the nature of radiation flux components. Besides, measurement methods are not cost-effective since the methods require a high number of pricey sensors. A Globe Thermometer is one of the ways to obtain MRT. However, the calibration of these devices is significant in their accuracy. In this study, a low-cost globe thermometer is developed and calibrated with a well-known commercial globe thermometer. First, a 135 mm matt-black painted copper globe thermometer was produced to measure MRT cost-effectively. A measurement campaign was conducted in a university office located in Ankara, Turkey. These data are then compared with the data of the commercial globe thermometer. As a final step, the low-cost globe thermometer is calibrated with Linear Comparative Calibration Method (LLCM), a commonly used calibration technique. Results showed that MRT could be easily measured using a low-cost globe thermometer with low error rates and high accuracy.

Keywords: Globe Thermometer, Mean Radiant Temperature, Radiation, Calibration.

1. INTRODUCTION

The definition of thermal comfort is "the condition of mind that expresses satisfaction with the thermal environment" [1]. Thermal comfort is affected by environmental parameters such as relative humidity (RH), indoor air temperature (T_i), air velocity (v_a), and mean radiant temperature (MRT), and personal parameters, which are clothing insulation (clo) and metabolic rate (met) [1]. The most complex variable on the thermal comfort is undoubtedly the MRT, described as "the uniform temperature of an imaginary enclosure in which radiant heat transfer from the human body is equal to the of radiant heat transfer in the actual non-uniform enclosure" [2,3]. Heat gain/loss due to radiation is a crucial factor for thermal comfort, especially in indoor environments. This phenomenon might cause the occupant to feel cooler or warmer due to radiative heat transfer between the human body and surroundings such as walls, windows, ceiling, and ground [4].

Different methods are used to determine the MRT in indoor environments, including calculation, measurement, and estimation approaches [5-8]. Calculation methods include the process based on the surrounding surfaces' temperature and angle factors based on plane radiant temperature [2,9]. The main radiant flux density (S_{str}) of the human body should be first determined to use calculation methods. As a second step in the calculation, six individual measurements of the short and long-wave radiation fluxes must multiply by angular factors (F_i) between the occupant and surrounding surfaces [10].

Even though the calculation of angle factors is very complicated, it is vital for the MRT calculation methods. Besides, the position and orientation of occupants highly affect their Fi values [11]. For instance, F_i is taken as 0.06 for radiation fluxes from above and below, while 0.22 is used for radiation fluxes from the east, west, south, and north directions for standing or walking occupant. Finally, MRT is calculated with the help of Equation (1) [12];

$$MRT(°C) = \sqrt[4]{\frac{S_{str}}{\varepsilon_p \sigma}} - 273 \quad (1)$$

In Equation (1) σ is the Stefan-Boltzmann Constant (5.67 10^{-8} W/m^2K^{-4}).

The most important advantage of using calculation methods is high accuracy using angle factors of the human body. On the other hand, the complexity of the calculation of angle factors and difficulty in measuring the environment's surface temperatures can be counted as the disadvantage of the method [7,13]. For these reasons, some researchers prefer estimation methods to determine the MRT. For instance, Turhan and Akkurt [8] estimated MRT from operative temperature (OT) and T_i, while Calis et al. [14] estimated MRT using approximately the same T_i.

Another method to determine the MRT is the measurement methods. Measurement methods are commonly used approaches by the researchers to abstain the complexity of the calculation methods. ISO 7726 [3] defines three different measurement devices to obtain the MRT, namely radiometer, globe thermometer (GT), and constant-air temperature sensors. The radiometer is a device that measures net radiation transfer between the environment and surface element [3]. However, radiometers are highly expensive and require more sensors in three directions for the MRT measurement.

On the other hand, using constant-air temperature sensors in MRT measurements constitutes some uncertainties due to the different emissivity values, various diameters, and sizes of the sensors. On the other hand, GTs are introduced as a simple measurement method that includes a thermometer located in the matt black sphere center. The standard GT is a 150 mm diameter, 0.4mm thick black hollow copper sphere, and a thermometer with a positioned in the middle of the copper sphere [15]. Essentially, the first GTs are used in the 1970s to determine indoor and outdoor thermal comfort [16,17]. On the other hand, GT is started to determine MRT in the 1980s [18]. The advantages of GTs are their low cost compared to other measurement devices and their easy usages [7].

Despite the simplicity of the GTs, these devices' cost is still quite expensive in the industry. Data logger and temperature sensor in the device increase the price while providing the copper globe is very difficult. On the other hand, user interfaces are quite different to understand and vary for each GT. These limitations encourage them to develop their GT by the researchers.

However, developed GTs are only reliable when they are well-calibrated. The calibration is the process of checking the accuracy of the measurement of the devices. A simple and effective calibration method is Linear Comparative Calibration Method (LCCM) using a linear regression [19,20]. Calibration of instruments is processed by comparing their results with the calibrated ones by choosing different test temperature values specifically for temperature sensors and the GTs [21-24]. For instance, O Brien et al. [23] calibrated their devices with three different temperatures, while Hunt and Stewart [24] used nine different test temperatures to use the linear comparative calibration. Alhashimi [25] indicates that other calibration algorithms and static sensors methods are linear Gaussian models, mixture models, and Bayesian models. More information about other calibration techniques is described in [19,26-28].

The GTs are commonly used devices to determine the MRT and evaluate occupants' thermal comfort in the buildings. The high cost of the GT and the complexity of deciding MRT encouraged researchers to develop their GT. This study aims to enlighten thermal comfort researchers to develop and calibrate a self-sufficient low-cost GT capable of long-lived field deployment. Finally, it is worth saying that this work also gives an example of a simple calibration method by using LCCM for the developed sensors in the thermal comfort field.

2. METHODS

The study's methodology consists of three different sections: development of a novel globe thermometer (GT), measurement campaign, and calibration of the developed GT. Figure 1 is depicted the method of the study.

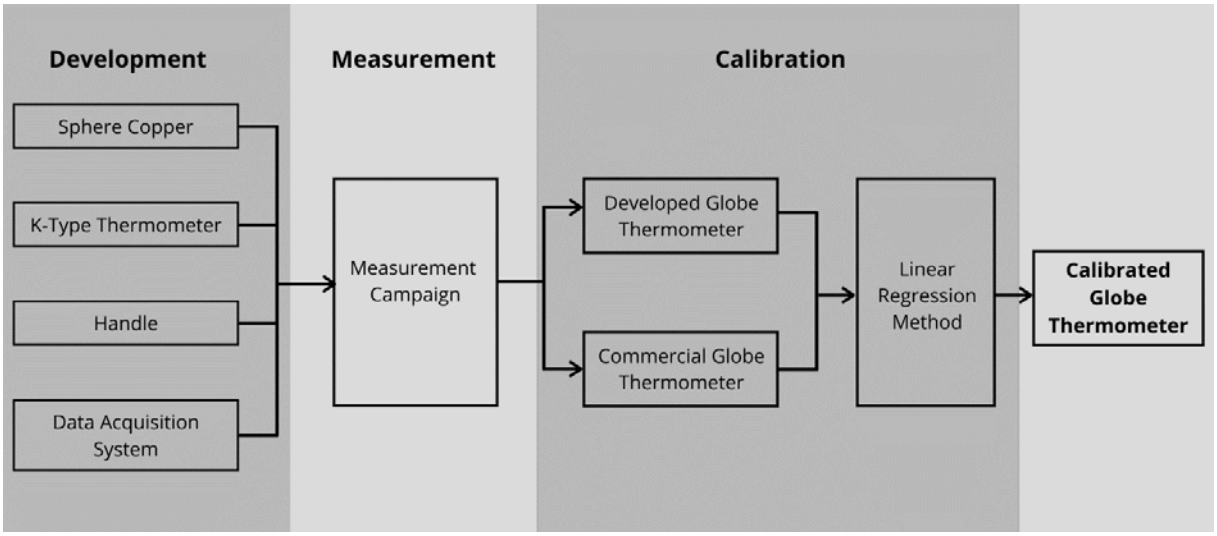

Figure 1. The methodology of the Study

2.1 Development of The Novel Globe Thermometer

The developed GT mainly includes a 135 mm diametric and 0.6 mm in thicknesses matt-black painted copper sphere, a data acquisition system, a k-type temperature sensor (DS18B20 sensor), and a non-conductive handle. The data acquisition system takes data from a k-type temperature sensor located in the copper sphere's center. It calculates MRT by combining them with indoor air temperature and air velocity data according to Equation (2) [3].

$$MRT(°C) = \left[\left(T_g + 273\right)^4 + \frac{0.25 \times 10^8}{\varepsilon_g} \times \left(\frac{|T_g - T_i|}{D} \right)^{1/4} \times \left(T_g - T_i\right) \right]^{1/4} - 273 \qquad (2)$$

In Equation (2), T_g represents the black globe temperature; T_i defines the air temperature, D is the matt-black GT's diameter, and ε_g is the matt black globe's emission coefficient, which is equal to 0.96 [3,29]. It is worth reminding that most commercial GTs use a standard 150 mm diameter copper sphere. However, the reason for using a 135 mm diameter-GT is its advantage of shorter response time. On the other hand, the developed GT uses a k-type thermometer inside the copper sphere. The minimum requirements of temperature sensors used for GTs are indicated in ISO 7243 [30]. The maximum tolerance value is specified ± 0.5 °C for the range between 20°C to 50°C and ±1°C for the range between 50°C to 120°C [30]. To this aim, DS18B20 k-type thermometer selected due to its pertinence of the range of accuracies (± 0.5 °C accuracy from -10 °C to 85°C range) [31]. Moreover, Arduino Uno [32] used as a microcontroller connected to a micro-SD card to store the MRT data. Finally, a non-conductive handle is mounted in the middle of the copper sphere to measure MRT values at 1.1 m height according to the ASHRAE 55 [1]. The technical drawing of the developed GT is given in Figure 2.

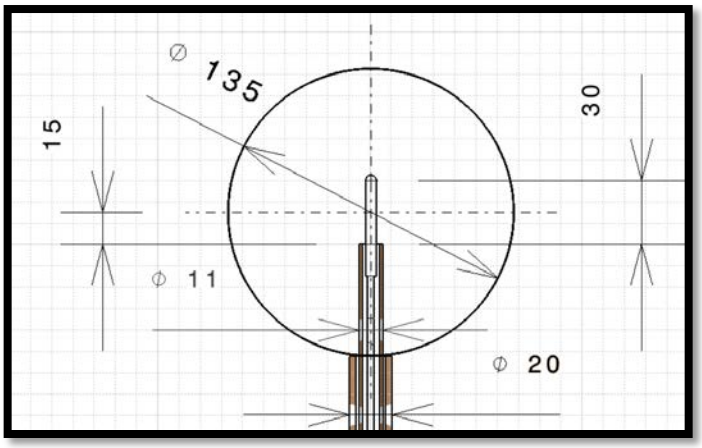

Figure 2. Technical Drawing of Inside the Matt-Blacked Copper Sphere.

The developed GT is also cost-effective compared to commercial GTs. A commercial GT cost is approximately 500 $ [33] while the developed one is 60 $.

2.2 Measurement Campaign

A measurement campaign is conducted to calibrate the developed GT in a university office in Ankara, Turkey, between the 23rd of January to 1st of February during the winter season. The university office has a total dimension of 5 m in length, 3 m in width, and 2.8 m in height. The office walls, except the south wall (it has a large window), are all internal walls. The temperature data collected by arranging set temperatures between 16 to 22 °C via mechanical ventilation. Thus, v_a is calculated as 0.1 m/s in the office [1].

Furthermore, to prevent v_a disturbances, the window and door are kept closed during the measurement. The office's window to wall ratio is 3.6, which results that MRT highly differs from T_i. The T_i was measured with a temperature sensor of DHT22 [34], which is mounted on the developed GT handle. Simultaneously, a well-known calibrated commercial GT operated to compare its data with a developed one. The MRT data collected at 5-minute intervals during office hours (8 hours per day). The office room with the positions of the novel GT and commercial GT shown in Figure 3.

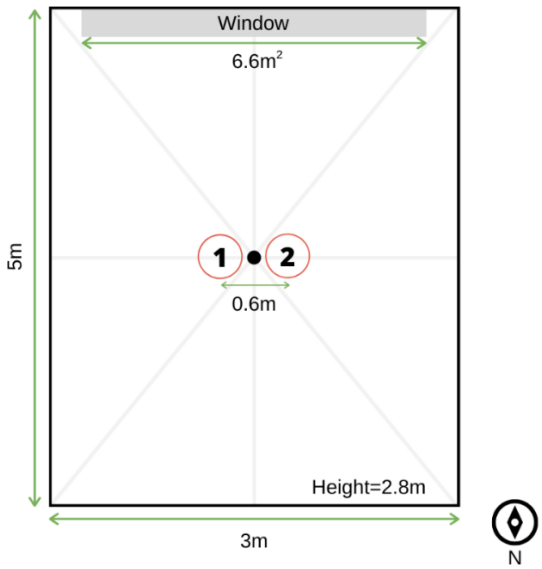

Figure 3. The positioning of the Novel GT (1) and Commercial GT (2) in the University Office

2.3 Calibration of The Novel Globe Thermometer

The developed GT was calibrated with Linear Comparative Calibration Method (LCCM). LCCM tries to predict the interaction between two different variables by transforming the measurement data into a linear equation [27]. The linear regression model represented in Equation (3);

$$y = \beta_0 + \beta_1 x + e \tag{3}$$

Equation (3) β_0 defines the intercept, β_1 delineates the slope, x enacts the independent variable, y is called the dependent variable, and e represents an error, which is the difference between the observed value of the y and the straight line ($\beta_0 + \beta_1 x$) [28].

The collected data of both developed and commercial GTs are plotted in the x-y chart of the MATLAB [35] to perform a regression analysis. Plotting data is the first step to determine the relationship between dependent and independent variables. Our dependent variable is the MRT values of the novel GT, while the independent variable is the MRT values of the commercial GT. The data are then correlated and plotted. The regression model fit line is obtained through the middle of all points in the chart by using a computer program, MATLAB [35]. Note that the more considerable error value (e) represents the line's less definite [27,28]. Besides, the commonly used statistical criteria, Mean Squared Error (MSE) and Determination of Multiple Coefficient (R^2), are used to understand the accuracy of the developed GT according to Equation (4) and (5), respectively [36].

$$MSE = \frac{1}{p}\sum \left| t_i - o_i \right|^2 \tag{4}$$

$$R^2 = 1 - \left(\frac{\sum_i \left| t_i - o_i \right|^2}{\sum_i \left(o_i \right)^2} \right) \tag{5}$$

In equations (4) and (5), t_i is the target, o_i specifies the output, and p represents the number of input-output pairs of i^{th} data. Finally, it should be noted that the copper sphere contains a particular air volume and the k-type thermometer inside, which must reach the equilibrium when the heat gain by radiation is equal to the heat loss by radiation and convection. To this aim, the calibration process started after waiting 20 minutes to reach equilibrium in both GT [15].

3. RESULTS AND DISCUSSION

For the calibration process, the developed globe thermometer (GT) was used to measure the MRT in the case office for eight days, including 872 different MRT data. The results of the novel GT were then compared with a well-known calibrated commercial GT. Figure 4 depicts the comparison of the measured MRT values for both developed and commercial GTs.

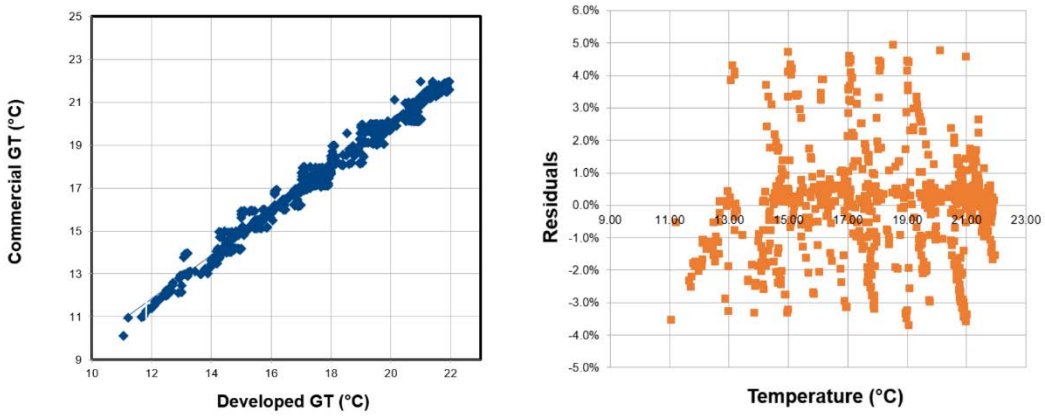

Figure 4. Comparison of Measured Data for Linear Comparative Comparison Method

The figure 4 indicates that the developed GT measured slightly higher values than commercial GT under a certain temperature of 16 °C. The reason for the difference could be the response time of the comparatively smaller diameter of the copper sphere. It is worth reminding that the commercial GTs use 150 mm diameter of the sphere; however, the novel GT has a 135 mm diameter. Small GTs reach the equilibrium rapidly due to the less air volume inside the sphere [37,38].

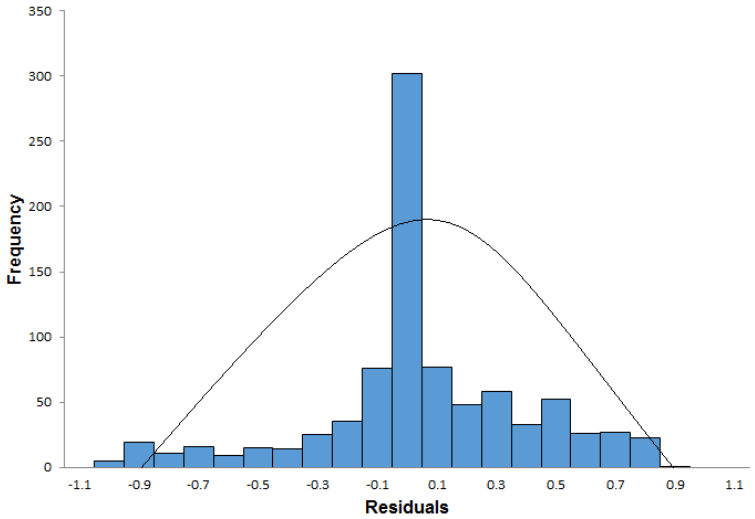

Figure 5. Distribution of the Residuals

Histogram graphs show to represent a normality distribution of the measurement data [36]. The normality assumption is correct if the values spread equally classified around zero. Figure 5 depicts the normality of the residuals for the calibration process. The residuals distributed normally, which indicates that the developed GT successfully measures MRT values. On the other hand, Table 1 gives descriptive LCCM statistics of the developed GT. The calibration results suggested that the MRT values show an excellent coherence with an R^2 of 0.98 while the MSE value is 0.12.

Table 1. Results of Regression Analysis

Variables	Values
Slope	1.0114
Intercept	-0.2925
MSE	0.1256
R^2	0.9842

This paper also considers the cost analysis of the developed GT. The developed GT was manufactured at a 60 $ price, but it is worth considering that this cost can vary depending on the model or type of sensors and materials. The prices of components can be seen in Table 2. The most expensive component is producing a hollow copper sphere. The sphere is created with the metal spinning process, which requires experts and neat work. This case increased the total price of the developed GT.

Table 2. Components Used in the Developed GT with Their Prices

Products	Price ($)
Copper Sphere	35$
Silicone (Adhesive)	3$
K-Type Thermometer	4$
Microcontroller with Connection Cables	10$
Matt-Black Color Spray	4$
Handle	4$
Total Price	**60$**

4. CONCLUSIONS

Mean Radiant Temperature (MRT) is crucial for thermal comfort, affecting radiative heat transfer between occupant and occupant's surrounding area. Globe thermometers are using to determine MRT as a measurement method. However, the high prices of these instruments encourage researchers to design and develop their GT. On the other hand, these developed GTs are only valid if they are well-calibrated. To this aim, this paper describes a simple method to calibrate a low-cost developed GT with a well-known commercial device. A total of 872 different temperature data measured with varying temperatures of the set was used to calibrate developed GT by Linear Comparative Calibration Method. The developed GT was calibrated with a high value of R^2 and normally distributed residuals. Moreover, the developed GT was constructed with considering reasonable standards for instruments while providing a significant cost-saving.

In the study, the copper sphere was constructed as a diameter of 135 mm instead of a standard 150 mm owing to the lack of a 150 mm sphere mould. More accurate results could be obtained using a traditional copper hollow sphere since the equilibrium time would be the same. Another limitation of the study was the lack of calibration experts during in-situ measurements. The operator caused temperature variations during the calibration period by opening the door to check the results. Finally, future works will compare different calibration methods mentioned in the introduction part of this paper.

REFERENCES

[1] American National Standards Institute, ASHRAE-55 STANDARD, Thermal Environmental Conditions for Human Occupancy (2004).

[2] Kántor, N., & Unger, J. (2011). The most problematic variable in the course of human-biometeorological comfort assessment — the mean radiant temperature. Open Geosciences, **3**(1). https://doi.org/10.2478/s13533-011-0010-x

[3] ISO, E. (1998). 7726. *Ergonomics of the thermal environment-Instruments for measuring physical quantities* (ISO 7726: 1998).

[4] Atmaca, I., Kaynakli, O., & Yigit, A. (2007). Effects of radiant temperature on thermal comfort. Building and Environment, **42**(9), 3210–3220. https://doi.org/10.1016/j.buildenv.2006.08.009

[5] Lindberg, F., Holmer, B., & Thorsson, S. (2008). SOLWEIG 1.0–Modelling spatial variations of 3D radiant fluxes and mean radiant temperature in complex urban settings. International journal of biometeorology, **52**(7), 697-713.

[6] Walikewitz, N., Jänicke, B., Langner, M., Meier, F., & Endlicher, W. (2015). The difference between the mean radiant temperature and the air temperature within indoor environments: A case study during summer conditions. Building and Environment, **84**, 151–161. https://doi.org/10.1016/j.buildenv.2014.11.004

[7] d'Ambrosio Alfano, F. R., Dell'Isola, M., Palella, B. I., Riccio, G., & Russi, A. (2013). On the measurement of the mean radiant temperature and its influence on the indoor thermal environment assessment. Building and Environment, **63**, 79–88. https://doi.org/10.1016/j.buildenv.2013.01.026

[8] Turhan, C., & Akkurt, G. G. (2019). The relation between thermal comfort and human-body exergy consumption in a temperate climate zone. Energy and Buildings, **205**, 109548.

[9] La Gennusa, M., Nucara, A., Rizzo, G., & Scaccianoce, G. (2005). The calculation of the mean radiant temperature of a subject exposed to the solar radiation—a generalized algorithm. *Building and Environment*, **40**(3), 367-375.

[10] Höppe P., Ein neues Verfahren zur Bestimmung der mittleren Strahlungstemperatur in Freien. [A new measurement procedure to obtain the mean radiant temperature outdoors]. Wetter und Leben, 1992, **44**, 147-151 (in German)

[11] Fanger PO. 1972. Thermal comfort. Analysis and Application in Environment Engineering. McGraw Hill: New York.

[12] Thorsson, S., Lindberg, F., Eliasson, I., & Holmer, B. (2007). Different methods for estimating the mean radiant temperature in an outdoor urban setting. International Journal of Climatology: A Journal of the Royal Meteorological Society, **27**(14), 1983-1993.

[13] Wang, Y., Meng, X., Zhang, L., Liu, Y., & Long, E. (2014). Angle factor calculation for the thermal radiation environment of the human body. In Proceedings of the 8th International Symposium on Heating, Ventilation and Air Conditioning (pp. 447-455). Springer, Berlin, Heidelberg.

[14] Calis, G., Alt, B., & Kuru, M. (2015). Thermal Comfort and Occupant Satisfaction of a Mosque in a Hot and Humid Climate. Computing in Civil Engineering 2015. Presented at the 2015 International Workshop on Computing in Civil Engineering. https://doi.org/10.1061/9780784479247.018

[15] Vernon, H. M. (1932). The measurement of radiant heat in relation to human comfort. Journal of Commercial Hygiene, **14**, 95-111.

[16] Kuehn, L. A., Stubbs, R. A., & Weaver, R. S. (1970). Theory of the globe thermometer. Journal of applied physiology, **29**(5), 750-757.

[17] Clarke, J. F., & Bach, W. (1971). Comparison of the comfort conditions in different urban and suburban microenvironments. International journal of biometeorology, **15**(1), 41-54.

[18] De Dear, R. (1987). Ping-pong globe thermometers for mean radiant temperatures. Heating and Ventilating Engineer, **60**(681), 10–12.

[19] Wimmer, G., & Witkovský, V. (2012). Two models for linear comparative calibration. International Journal of Metrology and Quality Engineering, **3**(3), 179–184. doi:10.1051/ijmqe/2012026

[20] Mulholland, M., & Hibbert, D. B. (1997). Linearity and the limitations of least squares calibration. Journal of Chromatography A, 762(1-2), 73-82

[21] J. L. Purswell, & J. D. Davis. (2008). Technical Note: Construction of a Low-Cost Black Globe Thermometer. Applied Engineering in Agriculture, **24**(3), 379–381. https://doi.org/10.13031/2013.24500

[22] Ekici, C. (2017). Calibration of Heat Stress Monitor and its Measurement Uncertainty. International Journal of Thermophysics, **38**(6). https://doi.org/10.1007/s10765-017-2224-8

[23] O'Brien C, Hoyt R, Buller M, Castellani J and Young A 1998 Telemetry pill measurement of core temperature in humans during active heating and cooling Med. Sci. Sports. Exerc. **30**, 468–72.

[24] Hunt, A. P., & Stewart, I. B. (2008). Calibration of an ingestible temperature sensor. Physiological Measurement, **29**(11), N71–N78. https://doi.org/10.1088/0967-3334/29/11/n01

[25] Alhashimi, A. (2018). Statistical Sensor Calibration Algorithms (Doctoral dissertation, Luleå University of Technology).

[26] Betta, G., & Dell'Isola, M. (1996). Optimum choice of measurement points for sensor calibration. Measurement, **17**(2), 115-125.

[27] Seber, G. A., & Lee, A. J. (2012). Linear regression analysis (Vol. 329). John Wiley & Sons.

[28] Montgomery, D. C., Peck, E. A., & Vining, G. G. (2012). Introduction to linear regression analysis (Vol. 821). John Wiley & Sons.

[29] J. Carvill, 3 - Thermodynamics and heat transfer, Editor(s): J. Carvill, Mechanical Engineer's Data Handbook, Butterworth-Heinemann, 1993, Pages 102-145, ISBN 9780080511351, https://doi.org/10.1016/B978-0-08-051135-1.50008-X.

[30] ISO7243 Ergonomics of the thermal environment — Assessment of heat stress using the WBGT (wet bulb globe temperature) index – 2017

[31] https://datasheets.maximintegrated.com/en/ds/DS18B20.pdf (Accessed on 21/01/2020)

[32] https://store.arduino.cc/usa/arduino-uno-rev3 (Accessed on 22/01/2020)

[33] https://www.testo.com/en-US/globe-probe-o-5-9/p/0602-0743 (Accessed on 22/01/2020)

[34] https://www.sparkfun.com/datasheets/Sensors/Temperature/DHT22.pdf (Accessed on 22/01/2020)

[35] MATLAB ver. R2018b

[36] Turhan, C., Kazanasmaz, T., Uygun, I. E., Ekmen, K. E., & Akkurt, G. G. (2014). Comparative study of a building energy performance software (KEP-IYTE-ESS) and ANN-based building heat load estimation. *Energy and Buildings*, ***85***, 115-125.

[37] Humphreys, M. A. (1977). The optimum diameter for a globe thermometer for use indoors. Annals of Occupational Hygiene, **20**(2), 135–140

[38] Hey, E. N. (1968). Small globe thermometers. Journal of Physics E: Scientific Instruments, **1**(9), 955.

THE THERMAL DECOMPOSITION OF THE LIQUID HOT WATER & ALKALI PRETREATED COTTON FIBER

Sevim ÖZGÜL[a], Günnur KOÇAR[b]
[a]Ege University, Solar Energy Institute, Izmir/Turkey
[b] Ege University Biomass Energy Systems and Technologies Application and Research Center, Izmir/Turkey
Email: sevimozgul88@gmail.com, gunnur.kocar@ege.edu.tr

ABSTRACT

Besides green energy production, exploiting renewable sources in materials production has recently gained interest in being eco-friendly and sustainable. Due to the abundance of agricultural wastes, easy accessibility, eco-friendly and lightweight, the interest in using agricultural wastes for the production of plant fiber has increased. Plant fibers can be used as a reinforcement material for bio-composite. Thermal degradation of the natural fibers has a high significance on the extrusion temperature of thermoplastic composites and the curing temperature of thermosets. Pretreatments of plant fiber improve the thermal degradation of fiber. These research aims are to investigate the thermal analysis of liquid hot water (LHW) and alkali pretreated cotton fibers. Experiments of liquid hot water are carried out by varying temperature (140, 160, and 180 °C), reaction time (30 and 60 min). Cotton fibers are pretreated with NaOH solution (5% in weight) for one h, two h, three h, and four h at room temperature. According to the result of thermogravimetric analysis of LHW and alkali pretreatments, alkali pretreatment (5% w/v, three h) was applied to LHW (180 °C, 60 min) pretreated fibers. The results of liquid hot water and alkali pretreatments, and co-pretreatment were compared with the thermal behavior.

Keywords: Plant fiber, Liquid Hot Water pretreatment, Alkali pretreatment, Thermogravimetric analysis.

1. INTRODUCTION

Besides green energy production, exploiting renewable sources in materials production has recently gained interest in being eco-friendly and sustainable. The interest in using agricultural wastes for production of fiber has increased due to abundance, easy accessibility, eco-friendly and lightweight of agricultural wastes. The use of lignocellulosic biomass-based materials over petro-materials has received increased attention due to growing environmental awareness, environmental sustainability concerns, increasing global waste problems, and depletion of fossil fuels [1]. The abundant availability and accessibility of plant fibers are the primary reasons for an emerging new interest in sustainable technology. Research shows that the energy used in the production of plant fibers is less than half of the energy required to produce synthetic fibers. Besides, plant fibers are non-abrasive, non-irritant, non-flammable, and non-toxic materials. They are biodegradable materials, as well [2]. Plant fibers can be used as an alternative to glass, carbon, and other human-made fibers [3,4]. Besides, it is estimated that by 2020, fibers from biomass sources will account for 28% of the support material market [5]. Manufacture of currently used materials is quite tricky regarding the consumption of energy, raw materials, and cost. The readily available renewable material resources are significant also from the point of sustainability of material resources. Plant fibers are renewable resources, so they are suitable alternative material resources for the reinforcement of composite. Therefore, using these ‘‘sustainable” natural fibers will reduce structural cost and weight, improve structural performance and increase energy efficiency [6].

Many lignocellulosic fibers, such as jute fiber, hemp fiber, sisal fiber, abaca fiber, and cotton, are used as reinforcement materials for biomaterials with their excellent mechanical properties and low specific mass. [7]. Furthermore, cotton fiber has high specific strength and modulus in lignocellulosic fiber, which is especially meaningful to enhance composites. However, cotton fiber also has disadvantages as a reinforcing material: the high moisture absorption and the low processing temperature permissible. Processing temperatures must be maintained below 200 °C to avoid the properties' deterioration due to the cotton degradation. Surface

modification is often use for decreasing moisture absorption and improving the interfacial properties in composites [8]. Pretreatment methods can improve the interfacial bonding quality between fiber and matrix. Liquid hot water (LHW) is one of the physical treatments [9]. LHW pretreatment uses hot water, which is an environmentally friendly approach due to chemical-free. Also, it has low operational costs and high potential for hemicelluloses dissolution [10]. During the treatment, water itself acts as a hydrolytic catalyst, especially at a higher temperature. The LHW pretreatment of biomass provides not only degrades most of the hemicellulose and part of the cellulose, but also eliminates the sugar, starch, and protein on the surface of plant fiber. Thus, plant fiber has lower molecule polarity and it has better interfacial compatibility with the polymer matrix. There are many types of research on lignocellulosic fibers reinforced polymer matrix composites after surface pretreatment of fibers. Results showed improved strength and a better thermal property of the composites [11, 12, 13, 14]. Alkali pretreatment or mercerization is one of the most uses chemical pretreatments for natural fibers. The necessary modification done by alkaline treatment is the disruption of hydrogen bonding in the network structure, thereby increasing surface roughness. This treatment removes a certain amount of lignin, wax, and oils, depolymerizes cellulose, and exposes the short-length crystallites [15]. It is reported that alkali treatment has two effects on the fiber: (1) it increases surface roughness resulting in better mechanical interlocking; and (2) it increases the amount of cellulose exposed on the fiber surface, thus increasing the number of possible reaction sites [16]. Several researchers employed different percentages of an alkali solution (5%, 7%, 10%, and 15% in weight) and immersion times (1, 3, and 24 h) to treated natural fibers [17-21].

Materials are subject to thermal decomposition and combustion depending on conditions exposed to fire or any other high-intensity heat source. The combustibility of a natural fiber reinforced polymer composite depends on many factors. These factors are type of raw materials (fibers, polymer, and additives), composite density, structure, thermal conductivity, and humidity [22, 23]. Several methods can help to analyze the thermal properties of a material. The mass change, thermal degradation temperature, and thermal stability of composite materials can measure by thermogravimetric analysis (TGA). In general, the thermal degradation process of natural fiber-polymer composites can be roughly divided into five parts [24-27]. The evaporation of water on the fiber surfaces starts at 100°C, thermal decomposition of hemicelluloses, celluloses, and lignin starts at 200°C, 250°C, and 280°C, respectively. Also, polymer matrix macromolecular degradation or depolymerization starts at 200°C. The thermal degradation of natural fibers has a high significance on the extrusion temperature for thermoplastic composites and the curing temperature of thermosets, as well [24]. Natural fiber polymer composites are typically manufactured below 200 °C to avoid the thermal degradation of natural fibers [28]. Hemicellulose and lignin are removed from the fibers through pretreatments. Thus, thermal decomposition of pretreated fibers is started at high temperatures. Also, untreated fibers have higher content of hemicellulose and lignin compared to pretreated fibers, and so they begin to degrade at a lower temperature.

2. EXPERIMENTAL

2.1 Material

The cotton stalk was obtained from a field in İzmir, which is in the west of Turkey. The particle size of the cotton stalk was minimized for storing at dry and room temperature by using a cutting mill. Cotton stalks were separated in 2 mm particle size by the sieve. Sieved samples were used for the liquid hot water and alkali pretreatment processes.

2.2 Method

2.2.1 Proximate analysis

Moisture content and an ash content of the cotton fibers were determined according to TS 1562 standard for each experiment. All samples were dried at 105 °C for 24 h, and then moisture content was determined by the loss of mass. For ash content, 1 g of the oven-dried sample was kept in a muffle furnace at 575 °C for three h. The ash content was determined as the residue.

2.2.2 Ultimate analysis

The ultimate analysis of the cotton fibers was carried out using a Leco TruSpec® CHN-S Analyzer in order to determine the carbon (C), hydrogen (H), nitrogen (N), and sulfur (S) contents of the samples.

2.2. Calorific value

The higher heating value (HHV) of raw cotton fiber was measured using a bomb calorimeter (Parr 6300, Parr Instrument Co., Illinois, USA) according to ASTM D 5865 [29]. For each test, a sample pellet of 1.0 g was taken into the crucible and then combusted under a pressurized oxygen atmosphere (3000 kPa). All of the samples were tested in three replicates.

2.2.1 Liquid Hot Water Pretreatment

Before treatment, untreated fibers were washed with distilled water to remove dirt. Afterward, fibers were dried in an oven at 80 °C for 48 h [30]. LHW was carried out on the dried cotton stalk in 1 dm^3 Erlenmeyer flasks (100 water and 10 g cotton stalk in each flask) at three different temperatures (140 °C, 160 °C, and 180 °C) for 30 and 60 min in an oven. After the pretreatment, the hydrolysates were collected, and the product was put on filter paper and washed with deionized water three times. Afterward, the fibers were dried at 80 °C for 12 h and stored in plastic containers until thermogravimetric analysis.

2.2.2 Alkali Pretreatment

Untreated fibers were immersed in sodium hydroxide solution (5% w/v) for one h, two h, three h and, four h at room temperature. The suspension was further filtered. The residue was washed with distilled water until the filtrate pH was 7. Afterward, the filtered fibers were dried at 80 °C for 12 h.

2.2.3 Co-Pretreatment of Liquid Hot Water and Alkali

According to the thermogravimetric analysis of LHW and alkali pretreatments, alkali pretreatment was applied to LHW pretreated fibers. LHW pretreated fibers (180 °C, 60 min) were immersed in sodium hydroxide solution (5% w/v) for three h. The suspension was further filtered. The residue was washed with distilled water until the filtrate pH was 7. Afterward, the filtered fibers were dried at 80 °C for 12 h.

2.2.3 Thermogravimetric analysis

Thermogravimetric analysis (TGA) of untreated and pretreated cotton fibers was measured using Setaram TG-DTA / DSC instrument. About 15 mg of samples were heated from 30 °C to 600 °C at a rate of 10 °C/min under argon flow.

3. RESULTS AND DISCUSSION

3.1 Properties of untreated cotton fiber

The proximate and ultimate analyses of cotton fiber samples are listed in Table 1. The moisture value of raw cotton fiber was high. The moisture content of the fibers has a critical effect on the quality of the final product. That is due to the high temperatures used during the processing, which causes water to evaporate from the composite melt. The evaporation of water leads the formation of bubbles, which increase the porosity of the composite and consequently deteriorates the properties of the composite. For this reason, before pretreatments, fibers were dried in an oven at 80 °C for 48 h to remove the moisture.

Table 1. Properties of raw cotton fiber

	% C	*% H*	*% N*	*% S*	*% Moisture*	*% Ash*	*HHV (MJ/kg)*
Cotton fiber	41,52	5,91	0,09	0,47	12,90	8,55	4043,93

3.2 Thermogravimetric analysis

TGA analysis was carried out to observe the distinct process of weight loss of fibers at different pretreatment conditions. The thermogravimetric analysis of raw cotton fiber is shown in Figure 1. Figure 1 shows three stages of the weight loss process with a long temperature range. From the curve, the first stage of weight loss, which started from 30 °C to 200 °C, is due to removing of the moisture content of the fiber. Significant degradation occurred at the second stage with the temperature range of 200–350 °C, which is related to the degradations of lignin and hemicelluloses of the fiber. The last stage of weight loss ranging from 350 °C to 500 °C, indicates the degradation of cellulosic and other non-cellulosic materials in the fiber. Also, the temperature at which the most mass loss occurs was 385,68 ° C. The thermal decomposition of untreated cotton fiber is similar to the study of Dobircau et al.[31].

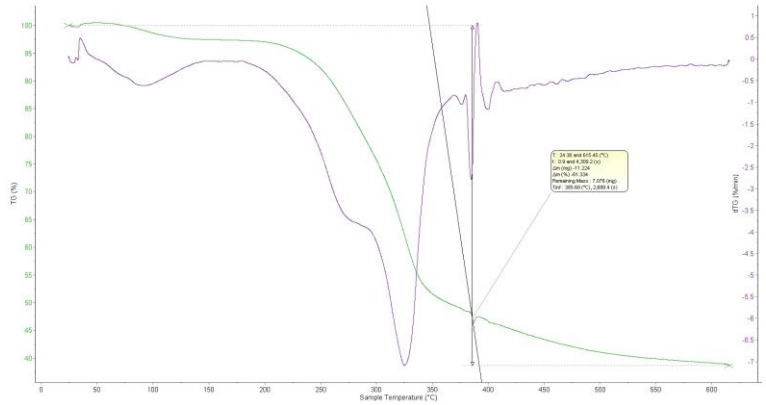

Figure 1. Thermal decomposition of untreated cotton fiber

It was examined that untreated cotton fiber started degrading at 200 °C. When TGA analysis of biomass is interpreted, in the first stage, mass loss at temperatures below 100 °C, loss of volatile substances quickly, loss of moisture in the range of 100-130 °C, loss of volatile matter at 130-250 °C. In the next stage, volatile matter, hemicellulose, cellulose, and lignin are removed due to structural deterioration in the range of 150-600 °C, and a significant mass loss occurs [32]. Hemicellulose degrades in a wide range of 160-900 °C, starting from 220-300 °C, cellulose 275-350 °C and 400 °C by weight [33, 34, 35]. However, the start temperature of degradation for the LHW pretreated fibers increased, and also, the fibers showed higher thermal stability. Thermal degradation of raw material begins at lower temperatures compared to the pretreated one. Since pretreated fibers have a lower percentage of moisture and hemicellulose, they begin to degrade at higher temperatures. The highest mass loss occurred at LHW-180 °C-60 min condition. As the temperature and residence time was increased, mass loss was increased too. The mass loss was % 61,33 for untreated cotton fiber while it was % 73,39 at LHW-180 °C-60 min. Figure 2 presents TGA analysis of the LHW treated fiber samples.

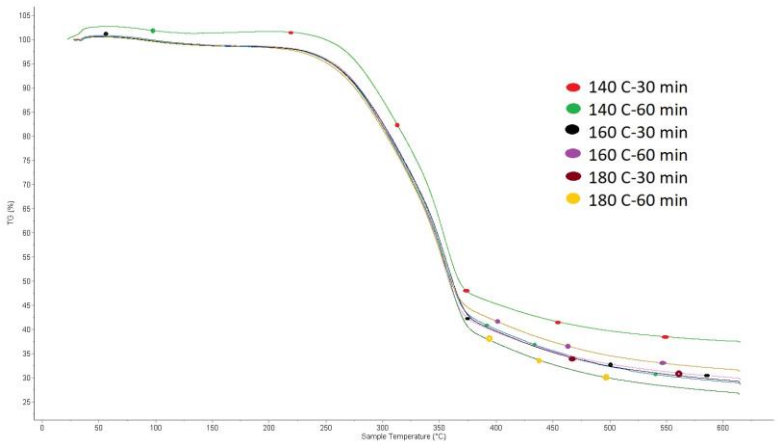

Figure 2. TGA analysis of the LHW treated fiber samples.

Similar results were observed in pretreated alkali fibers. The amount of degradation of pretreated fibers increased compared with the untreated fiber with increasing residence time. It might be cause by the alkali treatment, which reduced the hemicelluloses and lignin content of the fiber. As a result, fibers became more hydrophobic and enhanced the better possibility to adhere with the matrix. Fig. 3 presents TGA analysis of the alkali-treated fiber samples. The characteristics of thermal degradation of the treated fibers show similarity, and the best result was observed for 5%-NaOH-3h pretreated fiber sample.

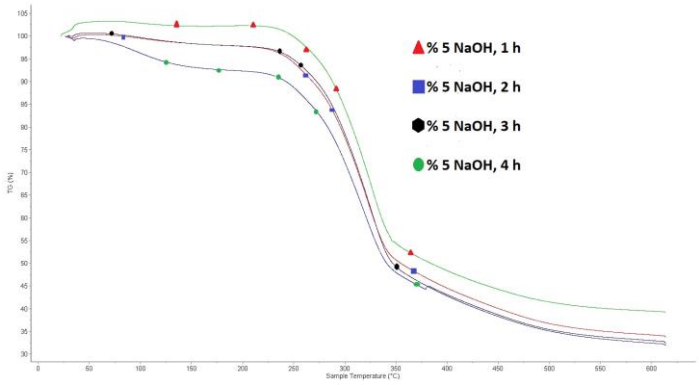

Figure 3. TGA analysis of the alkali-treated fiber samples

It was observed that the co-pretreatment of LHW and alkali causes lower mass loss than individual pretreatment. Fig. 4 presents TGA analysis of the co- pretreatment fiber.

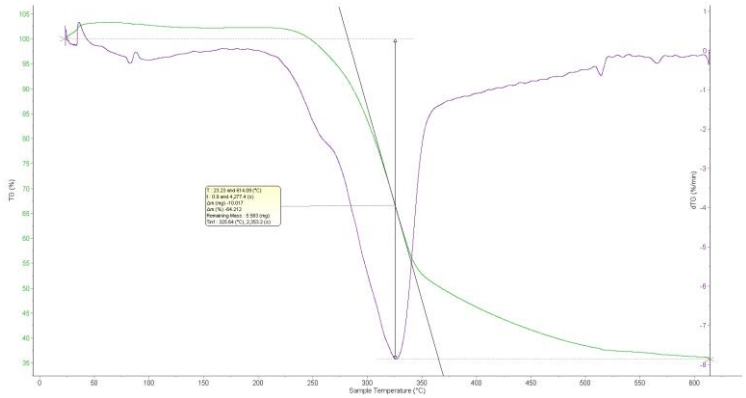

Figure 4. TGA analysis of the co- pretreatment fiber

The residual mass for all samples at 600 °C is shown in Table 2.

Table 2. Values of residual mass for samples

Type of material	***Residual mass at 600 °C (%)***
Untreated cotton fiber	38,666
LHW-140 °C-30 min	37,155
LHW-140 °C-60 min	28,544
LHW-160 °C-30 min	29,567
LHW-160 °C-60 min	31,266
LHW-180 °C-30 min	28,906
LHW-180 °C-60 min	26,602
%5 NaOH-1 h	38,655
%5 NaOH-2 h	33,649
%5 NaOH-3 h	32,015
%5 NaOH-4 h	32,443
LHW-180 °C-60 min -%5 NaOH-3 h	35,788

Based on the literature, after pretreatment of LHW and alkali, the content of hemicellulose decreases is observed. The high crystalline nature of cellulose has been reported to improve the mechanical properties of fiber-reinforced plastics. Lignins and hemicelluloses have no free hydroxyl groups to react with the PP chains, leads to lower interfacial adhesion between fibers and matrices when the contents of lignin and hemicellulose are higher. Therefore, low hemicellulose contents are desirable. It is because high contents can degrade thermal stability and increase moisture absorption. Lignin is advantageous in that it inhibits water absorption and enhances thermal stability. Lignin also increases the resistance of the biomass to chemical and biological degradation [36].

4. CONCLUSION

Recently, the increase of environmental awareness has impacted materials design and manufacturing; many products and structures made by non-renewable resources and required a substantial amount of energy for productions that would excessively generate carbon dioxide, which is put into scrutiny. The introduction of natural fibers to composites may cause environmentally beneficial consequences such as bio-degradability and natural availability. The low fire resistance of plant fibers is a significant disadvantage of these materials. The thermal degradation of the fibers begins at 200 °C approximately, and it has high significant effect on the extrusion temperature of thermoplastic composites and the curing temperature of thermosets. Pretreatments of plant fiber improve the thermal degradation of fiber; also, it increases surface roughness resulting in better

mechanical interlocking and increases the amount of cellulose exposed on the fiber surface, thus increasing the number of possible reaction sites. In this study, different pretreatments were conducted, and the thermal behaviors of pretreated fibers were observed.

REFERENCES

[1] Rinaldi, R., Jastrzebski, R., Clough, M.T., Ralph, J., Kennema, M., Bruijnincx, P.C., Weckhuysen, B.M., Paving the way for lignin valorisation: recent advances in bioengineering, biorefining and catalysis, Angewandte Chemie International Edition, **55** (29): 8164-8215, 2016.

[2] Shekar, H.S. and Ramachandra, M., Green Composites: A Review, Materials Today: Proceedings, **5**: 2518–2526, 2018.

[3] Vimal, R., Subramanian, K.H.H, Aswin, C., Logeswaran, V. and Ramesh, M., Comparisonal study of succinylation and phthalicylation of jute fibres: Study of mechanical properties of modified fibre reinforced epoxy composites, Materials Today: Proceedings, **2**:2918–27, 2015.

[4] Ramesh, M., Palanikumar, K. and Reddy, K.H., Plant fibre based bio-composites: sustainable and renewable green materials, *Renewable and Sustainable Energy Reviews*, 79: 558–584, 2017.

[5] Shah, D., Developing plant fibre composites for structural applications by optimising composite parameters: a critical review, *Journal of Materials Science*, **48**(18):6083–107, 2013.

[6] Yan, L., Chouw, N., Huang, L., Kasal, B., Effect of alkali treatment on microstructure and mechanical properties of coir fibres, coir fibre reinforced-polymer composites and reinforced-cementitious composites, *Construction and Building Materials*, **112**:168–182, 2016.

[7] Liu, L., Yu, J., Cheng, L., Yang, X., Biodegradability of poly(butylene succinate) (PBS) composite reinforced with jute fibre, *Polymer Degradation and Stability*, **94**, 90–94, 2009.

[8] Väisänen, T., Das, O., Tomppo, L., A review on new bio-based constituents for natural fiber-polymer composites, Journal of Cleaner Production, **149**, 582-596, 2017.

[9] Wang, L., Li, A., Chang, Y., Relationship between enhanced dewaterability and structural properties of hydrothermal sludge after hydrothermal treatment of excess sludge, *Water Res.*, **112**, 72-82. DOI:10.1016/i.watres.2017.01.034

[10] Wang, N., Cai, C.J., Cai, D.Q., Cheng, J.J., Li, S.L., Wu, Z.Y., Hydrothermal fabrication of hydroxyapatite on the PEG-grafted surface of wood from Chinese glossy Privet, *Appl Surf Sci*, **259**:643-649, 2012.

[11] Hamzeh, Y., Ashori, A., Marvast, E.H., Rashedi, K., Olfat, A.M., A comparative study on the effects of coriolus versicolor on properties of HDPE/wood flour/paper sludge composites, *Compos B Eng*, **43**(5):2409-14, 2012.

[12] Gregorova, A., Hrabalova, M., Kovalcik, R., Wimmer, R., Surface modification of spruce wood flour and effects on the dynamic fragility of PLA/wood composites, *Polym Eng Sci*, **51**(1):143-50, 2011.

[13] Bledzki, A. and Gassan, J., Composites reinforced with cellulose based fibres, *Prog Polym Sci*, **24**(2):221-74, 1999.

[14] Doan, T.T.L., Brodowsky, H., Mäder, E., Jute fibre/polypropylene composites II. Thermal, hydrothermal and dynamic mechanical behaviour. *Compos Sci Techno*, **67**(13):2707-14, 2007.

[15] Mohanty, A.K., Misra, M., Drzal, L.T., Compos Interfaces **8**:313, 2001.

[16] Valadez-Gonzalez, A., Cervantes-Uc, J.M., Olayo, R., Herrera-Franco, P.J., *Compos B: Eng*, **30**:309, 1999.

[17] Alawar, A., Hamed, A.M., Al-Kaabi, K., Characterization of treated date palm tree fiber as composite reinforcement, *Compos B*, **40**:601–6, 2009.

[18] Mishra, S., Mohanty, A.K., Drzal, L.T., Misra, M., Parija, S., Nayak, S.K., Studies on mechanical performance of biofibre/glass reinforced polyester hybrid composites, *Compos Sci Technol*, **63**:1377–85, 2003.

[19] Mylsamy, K., Rajendran, I., Investigation on physio-chemical and mechanical properties of raw and alkali-treated Agave Americana fibre, *J Reinf Plast Compos*, **29**:2925–35, 2010.

[20] Ramadevi, P., Sampathkumar, D., Srinivasa, C.V., Bennehalli, B., Effect of alkali on water absorption of single cellulose abaca fiber, *Bioresources*, **7**:3515–24, 2012.

[21] Edeerozey, A.M.M., Akil, H.M., Azhar, A.B., Ariffin, M.I.Z., Chemical modification of kenaf fibers, *Mater Lett* **61**:2023–5, 2007.

[22] Horrocks, A., Kandola, B., Flammability and fire resistance of composites. In: Long, A.C. (Ed.), Design and Manufacture of Textile Composites. Woodhead Publishing, Cambridge, UK, pp. 330-363, 2005.

[23] Kozłowski, R., Władyka-Przybylak, M., Flammability and fire resistance of composites reinforced by natural fibers, *Polym. Adv. Technol*, **6**, 446-453, 2008.

[24] Saheb, D.N. and Jog, J., Natural fiber polymer composites: a review. Adv. Polym. Technol. 18, 351–363, 1999.

[25] Monteiro, S.N., Calado, V., Rodriguez, R.J., Margem, F.M., Thermogravimetric stability of polymer composites reinforced with less common lignocellulosic fibers–an Overview. *J. Mater. Res. Technol.* 1, 117–126, 2012.

[26] Stokke, D.D., Wu, Q., Han, G., 2014, Introduction to Wood and Natural Fiber Composites. John Wiley & Sons, West Sussex, UK.

[27] Beyler, C.L., Hirschler, M.M., Thermal decomposition of polymers. In: DiNenno, P. (Ed.), SFPE Handbook of Fire Protection Engineering. National Fire Protection Association, Quincy, Massachusetts, US, pp. 110–131, 2001.

[28] Yao, F., Wu, Q., Lei, Y., Guo, W., Xu, Y., Thermal decomposition kinetics of natural fibers: activation energy with dynamic thermogravimetric analysis. *Polym. Degrad. Stab.* **93**, 90–98, 2008.

[29] Singh., Kaushlendra and Zondlo., John, Characterization of fuel properties for coal and torrefied biomass mixtures, *Journal of the Energy Institute*, **90**(4):505-512, 2017, https://doi.org/10.1016/j.joei.2016.05.012.

[30] Sawpan, M.A., Pickering, K.L., Fernyhough, A., Flexural properties of hemp fibre reinforced polylactide and unsaturated polyester composites, *Composites: Part A*, **43**, 519–526, 2012.

[31] Dobircau, L., Sreekumar, P.A., Saiah, R., Leblanc, N., Terrié, C., Gattin, R., Saiter, J.M., Wheat flour thermoplastic matrix reinforced by waste cotton fibre: Agro-green-composites, *Composites: Part A*, **40**, 329–334, 2009.

[32] Singh, R., Babu, J.N., Kumar, R., Srivastava, P., Singh, P., Raghubanshi, A.S., 2015. Multifaceted application of crop residue biochar as a tool for sustainable agriculture: an ecological perspective. Ecol. Eng. **77**, 324–347.

[33] Basu, P., 2018. Biomass Gasification, Pyrolysis and Torrefaction: Practical Design and Theory. Academic Press. Bridgwater A.V., 2012, Review of fast pyrolysis of biomass and product upgrading, Biomass Bioenergy, **38**:68–94.

[34] Chen, W.-H., Lu, K.-M., Tsai, C.-M., 2012, An experimental analysis on property and structure variations of agricultural wastes undergoing torrefaction. Appl. Energy **100**, 318–325.

[35] Zhao, C., Jiang, E., Chen, A., 2017. Volatile production from pyrolysis of cellulose, hemicellulose and lignin. J. Energy Inst. **90** (6), 902–913.

[36] Yiga, V.A., Pagel, S., Lubwama, M., Epple, S., Olupot, P.W., Bonten, C., Development of fiberreinforced polypropylene with NaOH pretreated rice and coffee husks as fillers: Mechanical and thermal properties, *Journal of Thermoplastic Composite Materials,* 1–23, 2019.

DEVELOPMENT OF A NOVEL TEMPERATURE AND RELATIVE HUMIDITY DATA LOGGER

Ahmet Yaser BAYHAN*, Cihan TURHAN*
*Atılım University, Department of Energy Systems Engineering, Ankara/Turkey
Email: bayhan.ahmetyaser@student.atilim.edu.tr, cihan.turhan@atilim.edu.tr

ABSTRACT

Data loggers measure indoor air parameters such as temperature and relative humidity by using several sensors in buildings. These parameters are the most important factor in calibrating energy simulation programs. However, data loggers are very expensive and require hard-to-understand hardware in order to store data. In addition, these devices use standard Lithium batteries to supply the energy of sensors, however, some of the data can be missed due to the low battery life of the data loggers. Furthermore, tracking of the measured data is very difficult since they require additional software's which are very confusing for engineers and architects.

The purpose of this study is to develop a novel low-cost data logger and record the measured data as an excel file into the microSD card. For hardware purposes; a temperature and humidity sensor, an Arduino microcontroller, a microSD card module, a solar panel and a battery unit are used while software codes are written in order to generate permanent data. The prototype of the novel low-cost temperature and relative humidity data logger is manufactured and tested in a case building at Atilim University in Ankara/Turkey. Then, the novel data logger is compared with well-known commercial data logger during four days. The results show that the cost of the data logger can be decreased by approximately 82% while the accuracy of the data is 98% and 97% for temperature and relative humidity, respectively, compared to the commercial data logger.

Keywords: Thermal comfort, data logger, renewable energy, measurement

1. INTRODUCTION

Buildings are responsible of 40% and 32% of total energy consumption in Europe and Turkey, respectively [1]. Considering developing countries, such as Turkey, have limited energy resources, decreasing energy consumption of the buildings becomes a vital issue. On the other hand, environmental impact of carbon dioxide (CO_2) emissions of the building sector is increasing in even developed countries. It is worth to note that buildings require to consume a certain amount of energy according to heating and cooling loads, zone, location and type of the building [2]. However, the building sector also represents 50% of energy saving potential in total energy consumption [3]. Here, usage of energy-efficient Heating, Ventilating and Air-Conditioning (HVAC) systems, well-insulating of building elements such as walls and windows and occupant-centric control systems are some of significant examples in order to decrease energy consumption of the building [4,5]. However, as a first step, it is necessary to determine energy consumption of the building to apply these retrofits to the building. Considering large and complex constructions, in-situ measurement of energy consumption of the buildings is very complicating since energy consumption is highly affected by multi-parameters which are inter-related [6]. In this context, dynamic building energy simulation programs (DBESP) are one of the most efficient tools to estimate the total energy consumption and, therefore, foresee early inaccuracies in the construction [7,8]. DBESPs provide simulation predictions which match closely with real energy consumption of the buildings [9]. However, the DBESP model of the building must be calibrated by using monitored data in order to get more accurate results [10]. For calibration, annual outdoor and indoor air temperature and relative humidity values of the case building are required.

In this case, data loggers are used to accurately record the temperature and humidity data of the building on an annual basis. In other words, data loggers form the accuracy of the DBESPs [11]. Here, it is worth to remind that data loggers are not only essential for these programs, but also for occupants who want to monitor the temperature

and humidity of their buildings. Data loggers use several sensors and communication systems between sensors and a main server [12]. Commercially, there exists many temperature and relative humidity data loggers in the building market, however, their prices are quite expensive. In addition, many producers prefer to use their own user-interfaces which are difficult to understand by the occupants. These limitations force many researchers in various fields to develop their own data loggers [13]. For instance, Frisby et al. [14] developed a unique temperature monitoring device to assess pig meat quality. The system consisted of two temperature probes attached to a Radio-Frequency (RF) data logging unit which transmits temperature data to the RF base station with the help of low power radio frequency communications. Similarly, Abu Bakar Sidik et al. [15] developed a novel Arduino-based data logger in order to measure temperature and humidity for meteorology and geoscience fields (Fig.1).

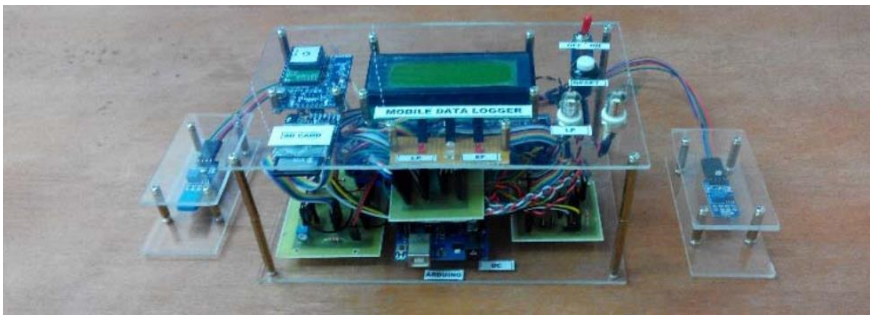

Figure 1. An example of a developed temperature and relative humidity data logger [15]

The authors used a mobile data logger which included a microcontroller, a GPS module, LEDs, an LCD module, and an SD Card module. In order to verify the operation of the temperature and humidity data logger, a test was conducted by comparing the temperature and humidity data from the prototype device with a commercial certificated device. The authors concluded that developed data logger measured temperature with an error of 3.1 ^{o}C.

On the other hand, limited studies used novel developed data loggers in the building sector. For instance, Syad Ali et al. [16], developed an inexpensive open-source platform for logging building environmental data. The novel data logger included air temperature, relative humidity, occupancy, light, and CO_2 sensors (Fig.2). An NTC thermistor and Sensirion SHT15-type digital humidity sensor were chosen for temperature and relative humidity measurements, respectively. The authors indicated that researchers could save approximately 50% of total cost by developing their own data loggers. However, there exists limited studies on development of low-cost and energy efficient data loggers in the literature.

Figure 2. A developed data logger for building environmental data monitoring [16]

To this aim, the purpose of this study is to develop a novel low-cost data logger and save the monitored data into the microSD card as an excel file. The diversity of this data logger is infinite battery life since it uses renewable energy sources to charge battery. A test office room located in Atılım University/Ankara-Turkey is selected as a case study for testing the developed data logger. A short measurement campaign of four days, during the winter season, is investigated for comparison and calibration of developed data logger on a 5-minutes interval basis.

2. METHODS

The methodology of the study lays on two main sections. The first section gives the development of a novel low-cost and energy efficient temperature and relative humidity (T&RH) data logger while the developed data logger is compared with a well-known commercial T&RH data logger in the second section.

2.1. Development of the novel data logger

The purposed data logger consists of a microcontroller, a T&RH sensor, an LCD display, a potentiometer, a micro SD card, a resistor and two solar panels. Arduino Uno, which uses Atmega 2560 base controller, is used to execute logical operations of the data logger [17]. The controller has 14 digital input / output pins (6 of them can be used as PWM outputs), 6 analog inputs, 16Mhz crystal, an USB socket, a power socket, ICSP connector and a reset button. The developed data logger distinguishes from other commercial products with its infinite battery life since the device uses renewable energy source. The data logger provides its energy from two 3.7 V Li-Ion batteries which can charge itself permanently with two 5.5 V monocrystalline solar panels. As a battery charging unit, the 2S Li-Ion Battery Charge Circuit is used to charge 2S batteries operating between 4.2V - 3.6V x 2 with the TP4056 linear charging integrated on it. The data logger measures T&RH via a DHT22-type sensor which provides a calibrated digital signal output [18, 19]. In addition, a MicroSD card is used to store measured data in an Excel file. The data logger also displays the measured T&RH values on an LCD screen which has 2x16 character dimensions. It is worth to note that a mini-rheostat is also added in order to adjust the backlight of the LCD display. The full list of components of data logger and their specifications are depicted in Table 1.

Table 1. Specifications of all components of developed data logger

Components	Pictures	Properties	Components	Pictures	Properties
Arduino Uno R3 control card		Working voltage 5 V Input Voltage 7-12V 14 Digital I / O Pin (6 PWM output) 40 mA current for I / O pins 6 Analog Inputs (A0-A6) 16 Mhz speed	RTC and SD Cart data logger shield	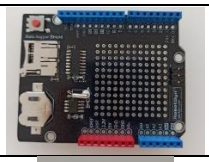	DS1307 RTC integrated CD4050 MicroSD card IC driver Automatically control 3.3V Compatible with Arduino UNO R3
2x16 LCD display		Working voltage: + 5V Working temperature: -20 - +70 Dimensions: 80x36x9.4mm	Potentiometer	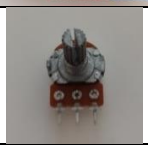	Resistance range: 0 ~ 10,000 ohm
DHT22		Resolution accuracy: 0.1 Humidity measurement range: 0-100% RH Temperature Measuring range: -40 ~ 80 ºC Humidity measurement accuracy: ± 2% RH Temperature measurement accuracy: ± 0.5 ºC	MicroSD Card		Capacity: 2 GB
5.5 V Solar panel	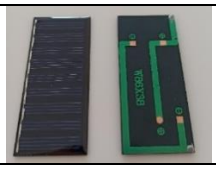	High efficiency output Excellent weak light effect Material: Monocrystalline Voltage: 5.5V Current: 100mA Powe: 0.6 Watt Size: 86 x 38 mm	Li-Ion battery		Voltage: 3.6v-4.2v Capacity: 2600mAh Nominal Voltage: 3.63V Charging Method: CC-CV Weight: 48g Size: 65mm x 18mm
Battery charging circuit			Size: 36x6x1mm Overload Voltage Range: 4.25-4.35v ± 0.05v Over-discharge Voltage Range: 2.3-3.0v ± 0.05v Working Current: 3A Instantaneous Current: 5A Static Current: <3μA Working Temperature: -40 ~ + 50 ºC Storage Temperature: -40 ~ + 80 ºC Internal Resistance: <45mΩ Short Circuit Protection: Yes		

Figure 3 depicts the circuit connection diagram of the developed data logger (right) and an exemplary screenshot of data logger programming (left). The data logger uses C-based programming language which can be easily adjusted by the user according to the desired specifications. After wiring and connections, the data logger is packed in a storage box.

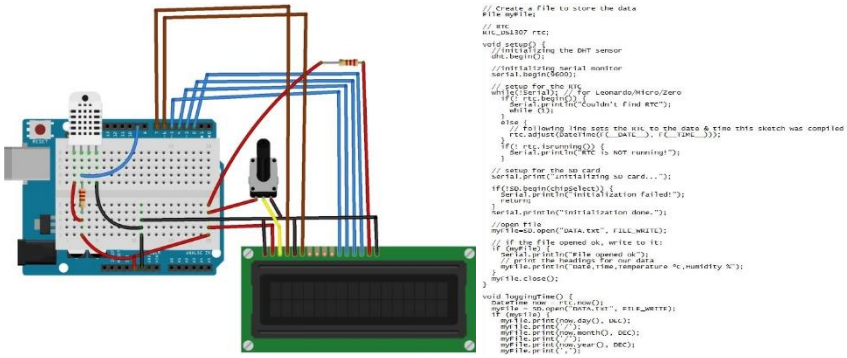

Figure 3. Circuit connection diagram (left) and screenshot of data logger programming (right)

The produced storage box is 158 gr with a total dimension of 90 x 51 x 38 mm. T&RH sensor is placed inside the box since the sensor is not affected by the sunlight while solar panels are located on the lateral surface (Fig.4-5). Finally, it is worth to note that the developed data logger can be placed on walls with the help of bracket.

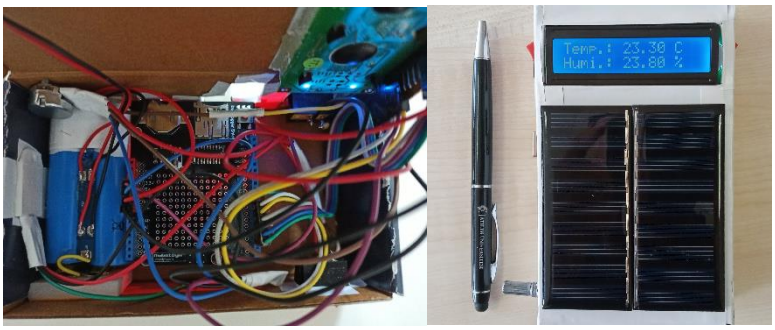

Figure 4. Inside (left) and front view of developed data logger (right)

2.2 Comparison of the data loggers

A measurement campaign is designed in order to evaluate the accuracy of the developed data logger. The measurements are taken between 28th and 31th of January in an office room which is located at Atılım University Campus, Ankara, Turkey (at 32.52ºE 39.56ºN). The dimension of the office room is 5 x 3 x 2.8 m with 3 internal and an external wall facing south direction (Fig.5). On the external wall, a 6.7 m^2 window exists while window to wall ratio of south facade is 3.6. The developed data logger is compared with a well-known calibrated T&RH data logger which is commonly used sensor in dynamic energy simulation tools. The data are taken with 5-minutes interval at the same time with commercial data logger. Then, measured data are compared with linear calibration curve and assessed with multiple correlation coefficient (R^2) which is calculated according to Eqn.1 [20].

$$R^2 = 1 - \left(\frac{\sum_i |t_i - o_i|^2}{\sum_i (o_i)^2}\right) \quad (1)$$

Here, t_i is the data of developed data logger, o_i specifies the data of commercial data logger, and p represents the number of input-output pairs of i^{th} data. Finally, the cost analysis of two data loggers are conducted.

Figure 5. Case office room used for the study

3. RESULTS AND DISCUSSIONS

A total number of 656 T&RH data were recorded between 28th of January and 31th of January, 2020 in case office room. The results of developed data logger were then compared with a well-known commercial data logger. The measurements were carried out every 5 mins during the measurement campaign. Figure 6 depicts the comparison of the measured temperature values for both developed and commercial T&RH data loggers. The figure indicates that the developed data logger measured T values with an accuracy of R^2 =98.3% compared to the commercial one.

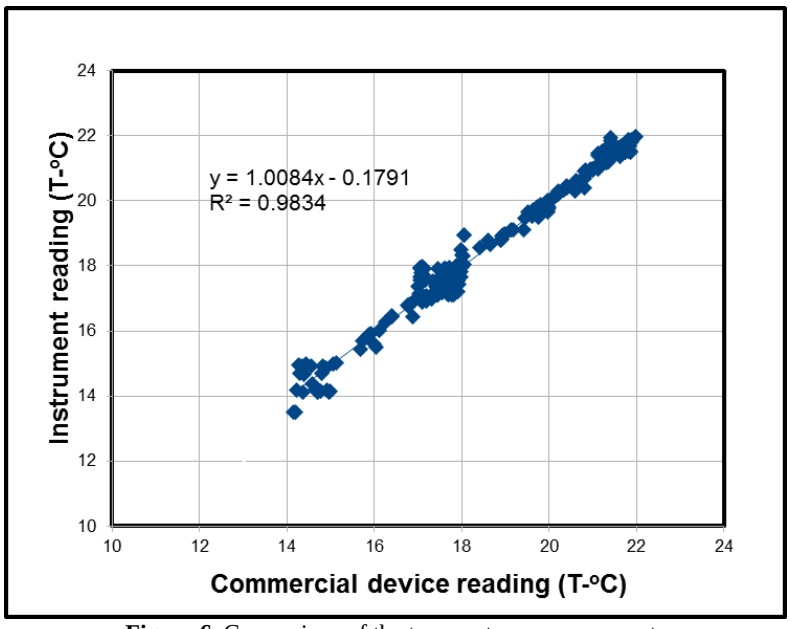

Figure 6. Comparison of the temperature measurements

Figure 7 represents the distribution of the residuals for temperature measurements. It is worth to note that the developed data logger under-measured temperature values below 18 ˚C while over-measured above 22˚C. The reason could be the design of storage box of the data logger. In commercial data loggers, the temperature sensor is located inside the box. However, in order to avoid internal heat gains coming from electronical devices such as microcontroller used in the data logger, the temperature sensor is located on the storage box. This means that developed data logger was highly affected from sudden temperature changes.

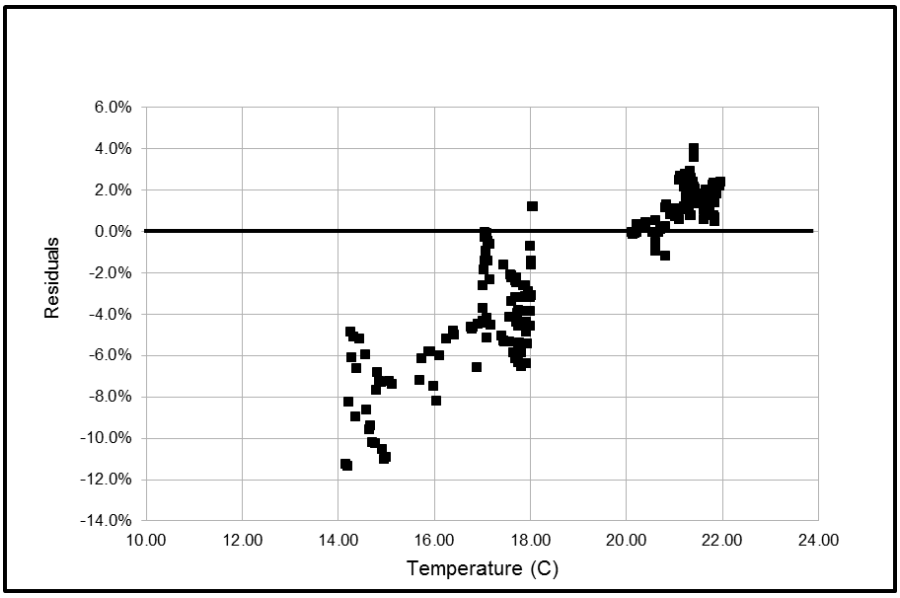

Figure 7. Residual distribution for temperature measurements

Figures 8 and 9 show the comparison of the RH measurements and the distribution of residuals, respectively. The figures clearly indicate that the developed data logger was successfully accomplished since the data fits with commercial data logger's data. This result is also supported by the fact that R^2 value was 97.5%. In addition, a strong linear trend in the Figure 9 indicated the normality of the errors. However, the same problem with temperature measurements can be drawn here again for RH measurements.

When developing of the novel data logger can be taken into account, the effect of design factors should be also considered. The commercial products combine optimum design parameters with suitable material properties. However, this case is not handy for developing a new prototype. For this reason, the accuracy and response time of the device could increase upwards after serial manufacturing.

Finally, the cost of the components of the developed data logger was shown in Table 2. The developed data logger merely costs 27.1$ while commercial data logger is 150$ [21]. In addition, an extra payment is also required for launching the device and reading data from commercial data logger which costs an additional $100 [22]. The researchers can save 82% of total price by developing their own data loggers. PV panels are the most expensive parts (cost approximately 6$) of the developed data logger. However, considering a battery life of 8 months for commercial products, they supply infinite battery life to the device.

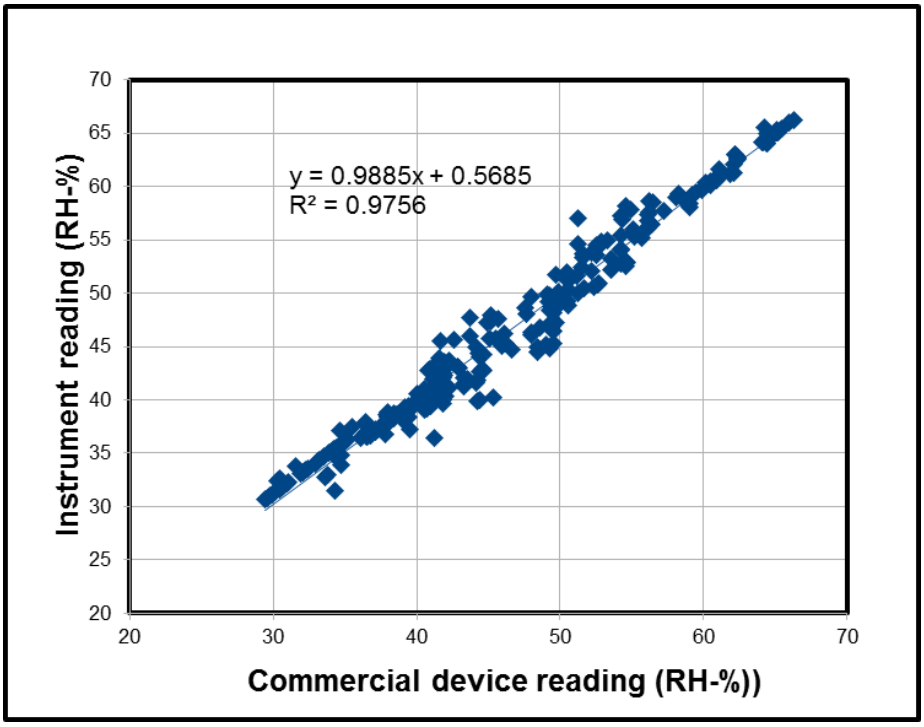

Figure 8. Comparison of the RH measurements

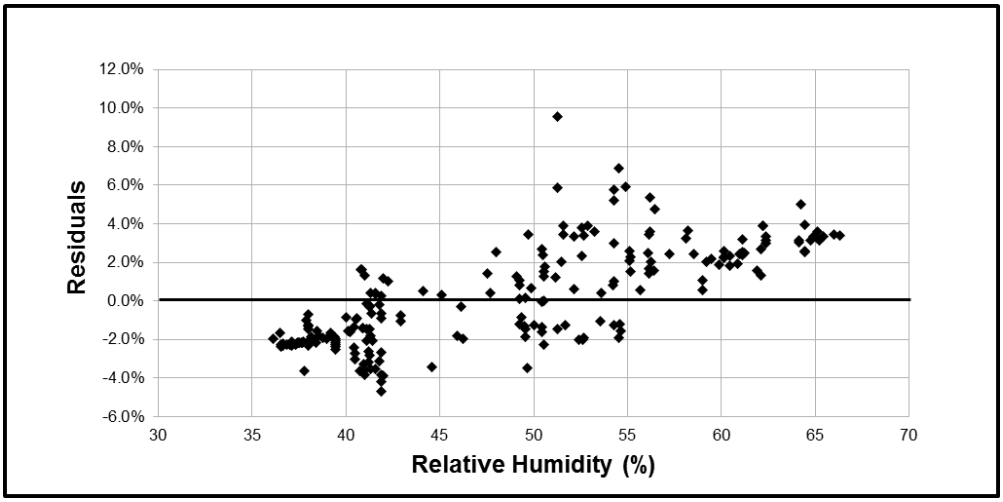

Figure 9. Residuals for RH measurements

Table 1. Cost analysis of developed data logger

Component	Piece	Unit price	Total price
Arduino Uno R3 control card	1	5.9 $	5.9 $
RTC and MicroSD Cart data logger shield	1	3.5 $	3.5 $
2x16 LCD display	1	1.6 $	1.6 $
Potentiometer	1	0.3 $	0.3 $
DHT22	1	3.8 $	3.8 $

2 Gb Micro SD Card	1	1.5 $	1.5 $
5.5 V 0.6 W solar panel	2	3.2 $	6.4 $
Rechargeable Li-Ion battery 3.7 V	2	1.5 $	3.0 $
2S Battery charging circuit	1	1.1 $	1.1 $
TOTAL PRICE			**27.1 $**

4. CONCLUSIONS

Temperature and relative humidity data loggers are now very popular in many application areas, from basic home applications to the usage in dynamic building energy simulation programs. However, these data loggers are very expensive and not user friendly due to the limitations and complexity of the user interfaces. To this aim, this study proposed to design a novel low-cost energy efficient and a reliable temperature and relative humidity data logger. The novel data logger included a microcontroller, a T&RH sensor, an LCD display, a potentiometer, a micro SD card, a resistor and two solar panels. The developed data logger then compared with a well-known commercial data logger. The results showed that researchers can save approximately 82% of total price with the accuracy of the results by R^2 of 98% and 97% for temperature and relative humidity, respectively.

This paper guides the researchers to develop their own temperature and relative humidity data loggers to avoid high costs and complexity of hardware's of commercial products. Furthermore, the accuracy of the device can serve to highlight the potential application of the control strategies to air conditioning systems. Further studies will include testing the developed data logger in larger areas with different environmental variables.

REFERENCES

[1] Nurdil Eskin, H. T, Analysis of annual heating and cooling energy requirements for office buildings in different climates in Turkey, *Energy and Buildings,* **40 (5)**, 763-773, 2008.

[2] Andrew H. & Buchanan, B. G., Energy and carbon dioxide implications of building construction, *Energy and Buildings*, **20 (3)**, 205-2017, 1994.

[3] Ignacio Zabalza Bribián, A. C., Life cycle assessment of building materials: Comparative analysis of energy and environmental impacts and evaluation of the eco-efficiency improvement potential. *Building and Environment,* **46**, 1133-1140, 2011.

[4] John E. Games, W. W, *United States Patent No. US4205381A,* 1997.

[5] Faye C. & McQuiston, J. D, Heating, *Ventilating, and Air Conditioning: Analysis and Design.* John Wiley & Sons, 2004.

[6] Bing Dong, C. S., Applying support vector machines to predict building energy consumption in tropical region, *Energy and Buildings*, **37 (5)**, 545-553, 2005.

[7] Barbason, M. & Reiter, S., Coupling building energy simulation and computational fluid dynamics: Application to a two-storey house in a temperate climate, *Building and Environment*, **75**, 30-39, 2014.

[8] Nadarajan, M. & Kirubakaran, V., SIMULATION TOOLS FOR RESIDENTIAL BUILDINGS-A REVIEW ON CONCEPTS AND TECHNOLOGIES, ARPN *Journal of Engineering and Applied Sciences*, **11 (5)**, 2098-3007, 2016.

[9] Reddy, T. A., Literature Review on Calibration of Building Energy Simulation Programs: Uses, Problems, Procedures, Uncertainty, and Tools, *ASHRAE*, **112 (1)**, 226-240, 2006.

[10] Manfren, M., Aste, N., Moshkar, R., Calibration and uncertainty analysis for computer models – A meta-model based approach for integrated building energy simulation, *Applied Energy*, 103, 627-641, 2013.

[11] Waghmare, M.B. & Chatur, D. P., Temperature and Humidity Analysis using Data Logger of Data Acquisition System, *International Journal of Emerging Technology and Advanced Engineering*, **2 (1)**, 102-106, 2012.

[12] Nhivekar, G. S. & Mudholker, R.R., DATA LOGGER AND REMOTE MONITORING SYSTEM FOR MULTIPLE PARAMETER MEASUREMENT APPLICATIONS. *e-Journal of Science & Technology*, **1**, 55-62, 2011.

[13] Haghighat, F. & de Bellis, L., Material emission rates: Literature review, and the impact of indoor air temperature and relative humidity. In *Building and Environment*, **33 (5)**, 261-277, 1998.

[14] Frisby, J., Raftery, D., Kerry, J.P., Diamond, D., Development of an autonomous, wireless pH and temperature sensing system for monitoring pig meat quality, *Meat Science* , **70 (2)**, 329-360, 2005.

[15] Sidik, M. A. B. ,Rusli, M. Q. A. , Adzis, Z. ,Buntat, Z. , Arief, Y. Z., Shahroom, H. , Nawawi, Z. , Jambak, M. I., Arduino-Uno Based Mobile Data Logger with GPS. *TELKOMNIKA*, **13 (1)**, 250-259, 2015.

[16] Syed Ali, A., Zanzinger, Z., Debose, D., Stephens, B., Open Source Building Science Sensors (OSBSS): A low-cost Arduino-based platform for long-term indoor environmental data collection, Building *and Environment*, **100,** 114-126, 2016.

[17] Shuvo, A.M., Rahman, M.D., Nahian, A.T., Himel, M.T.F., Design & Implementation of a Low Cost Data Logger for Solar Home, *International Journal of Engineering and Management Research*, **9 (1)**, 32-40, 2019.

[18] Bogdan, M., How to Use the DHT22 Sensor for Measuring Temperature and Humidity with the Arduino Board, *Acta Universitatis Cibiniensis, Technical Series*, 22-25, 2006.

[19] Wen, C.-Y., Jhu, C-Y., Wang, Y-W., Chiang, C-C., Shu, C-S., Thermal runaway features of 18650 lithium-ion batteries for LiFePO4 cathode material by DSC and VSP2, *Journal of Thermal Analysis and Calorimetry*, **109**, 1297-1302, 2012.

[20] Moosavi, S.W. & Ghassabian, S., Linearity of Calibration Curves for Analytical Methods: A Review of Criteria for Assessment of Method Reliability, *Calibration and Validation of Analytical Methods - A Sampling of Current Approaches*, 2018.

[21] Onset HOBO Temperature/Relative Humidity/2 External Channel Data Logger, https://www.onsetcomp.com/products/data-loggers/u12-013 (retrieved date: 11.01.2020).

INFLUENCES OF VANISPERSE IN NEGATIVE ACTIVE MATERIAL ON THE PERFORMANCE OF LEAD-ACID BATTERY

Yakup ŞİRİN, Yıldırım EYDEMİR, Çağatay AYHAN, Enes DEMİRYÜREK, Emre KOÇ
Abdulkadir Özcan Otomotiv Lastik Sanayi ve Ticaret Anonim Şirketi, R&D Center, Cankırı, Turkey.
Email: yakup.sirin@akoaku.com

ABSTRACT

The organic additive lignosulfonate known as a commercial name vanisperse (modified lignin derivative) has been produced for lead-acid batteries. The main advantages of this additive are enhancing some properties of lead-acid batteries, which are cycle life, cold-cranking performance, and the capacity. It also counteracts the formation and also increasing of a new non-permeable layer of big sulfate crystals on the negative active material (NAM) surface.

This study is aimed to increase the electrical performance of standard lead-acid batteries by developing chemical properties and changing chemical composition of the negative electrodes. For that purpose, different types (VN-X, VN-Y) and ratios (wt.%) of vanisperse (lignosulfonate) were used as an additive in the negative paste. This study consists of three steps. In the first step, different types of vanisperse (lignosulfonate) were characterized. In the second step, the negative active materials were prepared. In the last step, lead-acid batteries (12V 66Ah 610A EN) were produced and electrical performance tests were carried out in the laboratory.

Electrical performance tests were executed in reference to Turkish Standards Institute (TSI) 50342-1 standard. The electrical test results of the lead-acid batteries which are contained different types of vanisperse (lignosulfonate) were compared with the standard battery. As a result, the porosity of the electrode increased due to the vanisperse additive (lignosulfonate) used in the negative active material (NAM), so the electrical test results positively affected. When vanisperse X (0,3 wt.%) is added to the negative active material (NAM) recipe, capacity, cold cranking ampere, internal resistance test, charge acceptance and life-cycle performance of lead-acid battery have enhanced significantly.

Keywords: Lead-acid battery, vanisperse (lignosulfonate), negative active material (NAM).

1. INTRODUCTION

1.1. History of Lead-Acid Battery

The battery is a chemical energy storage that converts chemical energy to electrical energy. The primary task in vehicles is to run the starter that gives the engine the first movement Lead-acid batteries are used in start-stop and hybrid automotive applications to provide CO_2 savings and economic benefits to our society. Besides, in state of problems with the charger, the air conditioner, heater, radio, a headlight is needed to operate such systems [1]. The main elements of the lead-acid battery were found place approximately 100 years ago. Gaston Plante was the first to submit that a beneficial discharge current could be withdrawn from a double of lead plates (positive-negative plate) that had been submerged in sulfuric acid and subjected to a charging current [2].

Lead-acid batteries form the basis of rechargeable battery systems. Lead-acid batteries' reliability, low-cost, and life span for many years. Despite the developing technology of new battery systems, lead-acid batteries are still the most preferred battery in the world as the most widely used system. On the other hand, the using of lead-acid batteries was limited owing to the slow production process of the electrodes and their very low capacity. In the late 1870s, there was an excessive need of new technologies for lead-acid production [3].

In 1881, Camille Fauré added red lead (II) oxide (Pb_3O_4) to the battery paste, water, and sulfuric acid within the lead positive plates. The positive paste was converted to active bulk with charging to form PbO_2 and Pb. Consequently, the specific energy of the lead-acid batteries was raised [3].

The research group of Gladstone (1882) brought into the open the reactions that occurred at the two electrodes during battery performance and reported double sulfate theory [4].

In 1883, Hermann Aron explored the charge and the discharge period of lead-acid batteries, and also indicated a correlation between the discharge time and specific density of H_2SO_4 electrolyte [3].

1.2. Lead-Acid Battery Components

Lead–acid battery composed of negative/positive electrodes, separators, connections, terminals, polypropylene case, and lids and sulfuric acid solution as an electrolyte. These compound types are shown in Figure 1.
The functions of the four basic components in the lead-acid battery;

1-The active material: It is a chemical mixture that is pasting on the grid's surface and transforms the grid into a plate. Namely, the negative and positive active materials are applied to the surface of the grids to form positive and negative electrodes in the battery.

2- Negative electrode: Before charging process, the negative electrode consists of metallic lead (Pb), lead oxide (PbO), and additives (carbon black, barium sulfate, lignin derivative, etc.) in the lead-acid battery. With the charging process, the negative electrode ingredients transform to metallic lead (Pb) and lead sulfate ($PbSO_4$) in the lead-acid battery.

3- Positive electrode: Before charging process, the positive electrode includes metallic lead (Pb), lead oxide (PbO) and red lead (II) oxide (Pb_3O_4) in the lead-acid battery. After charging process, the positive electrode constituents convert into the lead dioxide (PbO_2) in the lead-acid battery.

4-The electrolyte: Distilled water and sulfuric acid solution are mixed, which occurs electrolyte in the lead-acid battery. Sulfuric acid provides ionic charge transfer between the positive and negative electrodes.

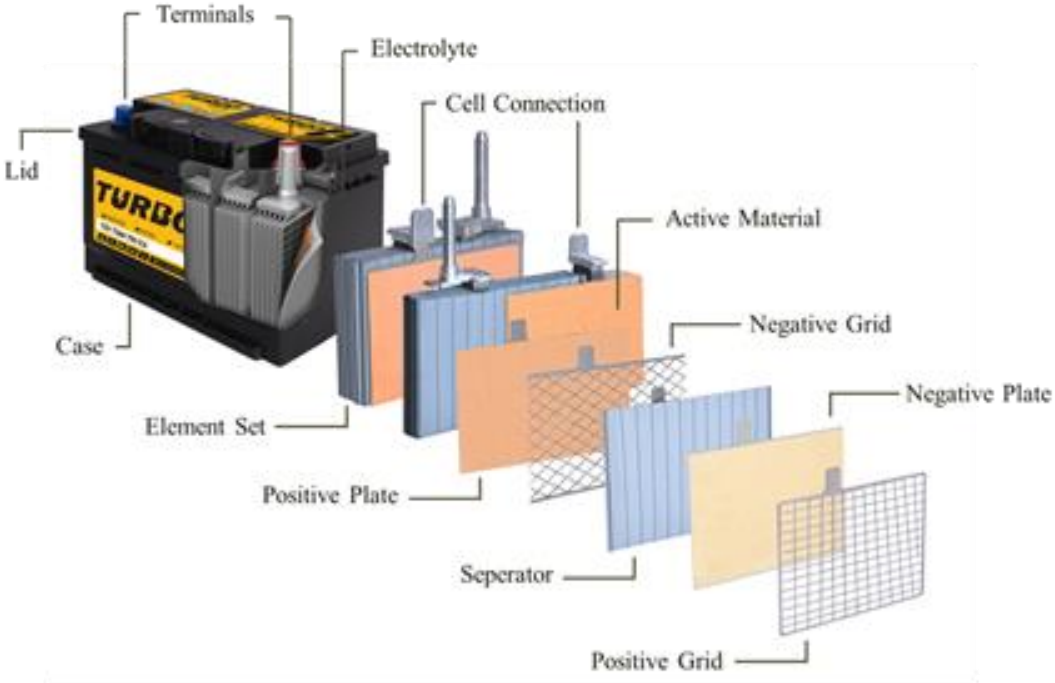

Figure 1: Standard lead-acid battery

1.3. Lead-Acid Battery Production Process

Lead-acid battery production is composed of many different processes, which are oxide manufacturing, strip/grid manufacturing, paste mixing, pasting, curing, assembly, formation, laboratory, and test processes [5].

1.4. Reaction of Lead-Acid Battery

The charge and discharge reactions of lead-acid batteries for the positive and negative electrode respectively are as follow;
E_0 is the normal electrode potential for lead acid battery electrodes while the electrode is in a normal state.

$$\text{Positive Electrode;}\quad PbO_2 + 3H^+ + HSO_4^- + 2e^- \underset{\text{charge}}{\overset{\text{discharge}}{\rightleftharpoons}} PbSO_4 + 2H_2O \quad (E^0_{(+)}=+1{,}740\ V)$$

$$\text{Negative Electrode;}\quad Pb + HSO_4^- \underset{\text{charge}}{\overset{\text{discharge}}{\rightleftharpoons}} PbSO_4 + H^+ + 2e^- \quad (E^0_{(+)}=-0{,}270\ V)$$

$$\text{Total Reaction;}\quad PbO_2 + Pb + 2H^+ + HSO_4^- \underset{\text{charge}}{\overset{\text{discharge}}{\rightleftharpoons}} 2PbSO_4 + 2H_2O \quad (E^0_{(+)}=+2{,}010\ V)$$

1.5. The Use of Vanisperse in Lead-Acid Battery

Vanisperse additive which is known as a lignosulfonate (modified lignin derivative) increases the cycle-life performance of the lead-acid batteries. It also enhances the specific surface area of the NAM (negative active material). The progressing surface exhibits a strong trend to beginning oxidative reaction using atmospheric oxygen. It also increases the cold-cranking performance of lead acid batteries. As well as all these positive results, excessive using of vanisperse can have an adverse effect on lead-acid battery performance [6].
In this study, the effects of vanisperse used in NAM (negative active material) on the battery performance were investigated. Therefore, a negative electrode with two different brands of vanisperse and a negative electrode with no vanisperse were used. Batteries (12V 66 Ah 610 CCA (EN)) were manufactured by these electrodes.

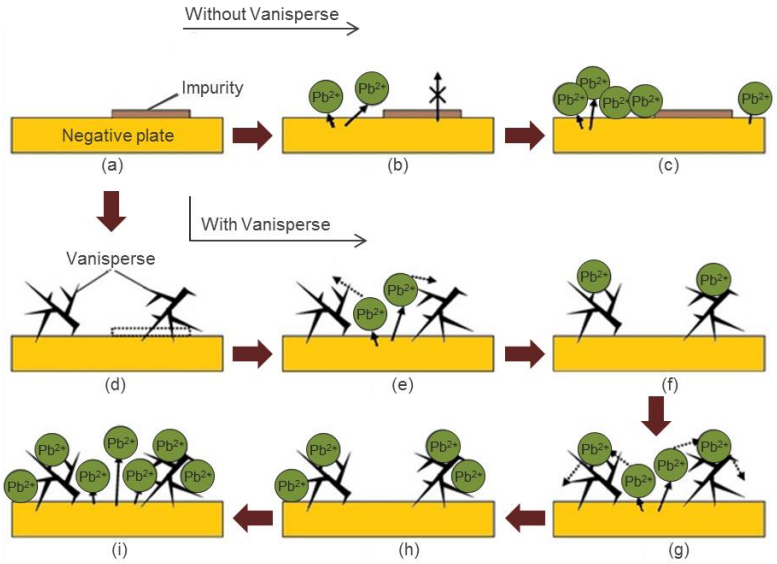

Figure 2. Model of vanisperse effect on lead acid battery during oxidation

2. MATERIALS AND METHODS

2.1. Lead-Acid Battery Negative Active Material Component

Lead (II) oxide and sulfuric acid as main components in the negative active material recipe, expanders (carbon black+lignosulfonate+barium sulfate), fiberglass as an additive were used in this study.

2.2. Plate Preparation and Battery Design (Vanisperse Materials Added to NAM)

The pre-prepared vanisperse additives have similar active surface area and different particle size range from several microns. Vanisperse-free negative active material was used for comparison.

2.3. Negative Paste Preparation and Characterization

Experimental groups of vanisperse additives added to negative pastes are shown in Table 1. Paste without vanisperse was also prepared and used for assembling reference plates. The paste was made by mixing all chemicals for all studies. All the plates were cured and dried at 55-85 ˚C for 24 h. Before formation process, the samples of NAM and HRPSoC cycling were characterized by Brunauer–Emmett–Teller (BET) Surface Analyzer.

Table 1. Experimental groups of vanisperse additives to the negative plate

Signature	Composition	Amount of NAM (wt.%)
VN-0	Non-vanisperse	-
VN-A1	VN-A1 brand vanisperse	0,1
VN-A2	VN-A2 brand vanisperse	0,2
VN-A3	VN-A3 brand vanisperse	0,3
VN-A4	VN-A4 brand vanisperse	0,4
VN-A5	VN-A5 brand vanisperse	0,5
VN-B1	VN-B1 brand vanisperse	0,1
VN-B2	VN-B2 brand vanisperse	0,2
VN-B3	VN-B3 brand vanisperse	0,3
VN-B4	VN-B4 brand vanisperse	0,4
VN-B5	VN-B5 brand vanisperse	0,5

2.4. Lead-Acid Battery Design and Production

The influence of vanisperse additives on the performance of the negative lead-acid battery plate was investigated on 12 V 66 Ah 610 CCA (EN) lead -acid batteries.

2.5. Charging of the Produced Batteries

There is no difference between the batteries except the types of the vanisperse in the paste of the negative plate. All founded differences are according to the vanisperse used in different brands.
In this study, batteries contain seven (7) positive and seven (7) negative plates in each cell. This battery has 66 (Ah) capacity and 610 (A) CCA (EN) features as standard. Batteries were charged with a constant current in the charging pools (35˚C) in the laboratory.

2.6. After Charging: Open Circuit Voltage (OCV)/ Cold-Cranking Ampere (CCA) Specification

OCV and CCA of the batteries were measured by means of the Mitronics device, which is accepted as the norm for all battery companies at the end of charging. OCV refers to the total voltage of the six cells of the battery

value that should be minimum 12,72 V at the end of two hours. CCA is known as the battery's cold-cranking ampere, which should be, after two hours, minimum 610 (A) is suitable with respect to standards. (EN: European Norm)

2.7. Capacity Test

capacity (C_n) is 20 h capacity (C20-Ah) defined for the temperature of 25°C ± 2°C. The capacity test was performed according to TS EN 50342-1.
The battery must be discharged with the in current, which is kept constant at ± 1% of the rated value, until the voltage between the terminals drops to 10,50 V ± 0,05 V. This discharge time, t (h), should be recorded. The beginning of the discharge should be within the period of 1 hour to 5 hours from the end of the charge. The nominal 20 h capacity C_n is the electric charge (in Ah) that a battery can supply with a current: $I_n = C_n /20$ h
C_e = t x I_n (Ah)

2.8. Cranking Performance Test

The cranking performance test was applied according to TS EN 50342-1. The battery temperature should be brought to -18˚C ± 1˚C. The battery must be discharged with I_{cc} current. After 10 s discharge, the voltage U_f between the terminals should be recorded and the current cut off. The Uf voltage should not be less than 7.50 V. The battery should then be discharged with a current of 0,6 I_{cc}. Discharge should be terminated when the battery voltage reaches 6V. Discharge time (t'_{6V}) up to 6V at 0,6 I_{cc} should be recorded in seconds.

2.9. Charge Acceptance Test

The battery shall be discharged at a temperature of 25 °C ± 2 °C at a current I_0 (A) for 5 h where:

$I_0 = C_e/10h$

The value C_e shall be taken as the maximum value C_e of the previous discharges. Within 10 min after the discharge, the battery shall be placed in a cooling chamber with (forced) air circulation at a temperature of 0 °C ± 1 °C until the temperature of the middle cells is 0 °C ± 1 °C. It is generally accepted that the required temperature will be achieved after a minimum period of 15 h in the cooling chamber. At this temperature, the battery should be charged at a constant voltage of 14,40 V ± 0,05 V and I_{max} = 50 A for batteries having sizes defined in EN 50342-2 and I_{max} = 100 A for batteries having sizes defined in EN 50342-4. After 10 min, the charging current ($I_{ca)}$ should be recorded. Requirements: I_{ca} should be ≥ 2 I_0

2.10. Cycle Life Test

Batteries should be placed in a water bath and stored at +40 ± ˚C ± 2˚C. The charge voltage U 15,6 V and charge rate CR of the battery to be tested will be used as 1,08. Batteries will be connected to series of cycles. Each cycle consists of the following:
-The battery will be discharged with a constant current at I = 5 I_n for 2 hours. If the voltage drops below 10,5 V, the test will be terminated.
-In the first step, the battery will be charged for a maximum of 5 hours under constant voltage and a current limitation at of I_n.
-During discharge, the above steps are implemented until the voltage is attained upper limit or until the number of 360 cycles is reached.

3. RESULTS

3.1. Vanisperse Materials Specification

The pre-prepared vanisperse additives have the similar active surface area and different particle size range from several microns. Vanisperse-free negative active material was used for comparison. The characteristics of vanisperse additives are given in below.

Table 2. Characteristics of vanisperse additives under investigation

Characteristic	Value	Vanisperse X	Vanisperse Y
BET Surface	m^2/g	0,3218	0,2987
Dry Matter	%	95,48	94,12
pH	pH	7,69	10,17
Insoluble	%	0,012	0,036
Ash	%	18,95	23,98
Iron (Fe)	ppm	9,89	47,56
Calcium (Ca)	ppm	29,4	218,69
Magnesium (Mg)	ppm	21,45	25,68

3.2. Charging Features

The current (A), voltage (V), ampere-hour (Ah), and temperature (°C) graphs of the test batteries during the charging are as follows.

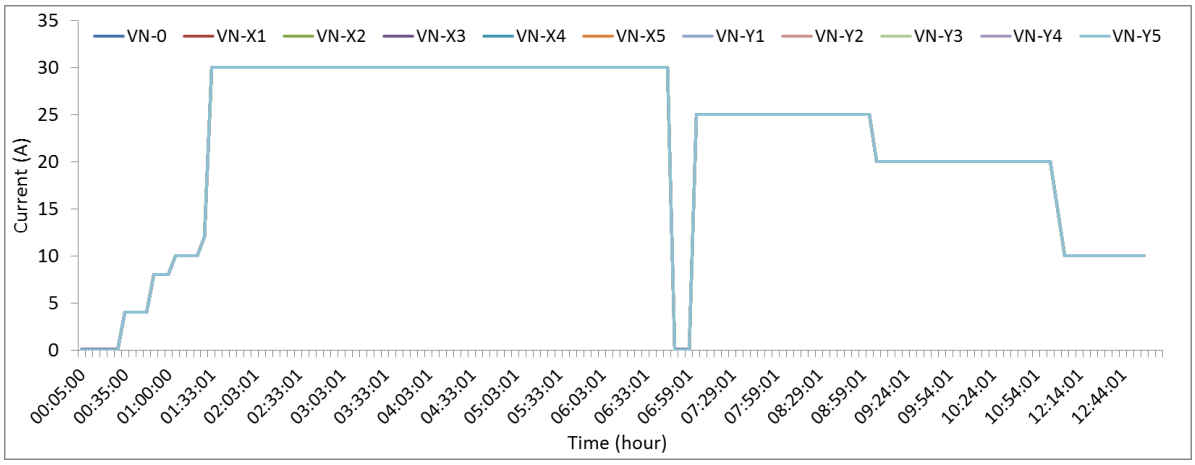

Figure 3. The graph shows the current of the batteries during charging

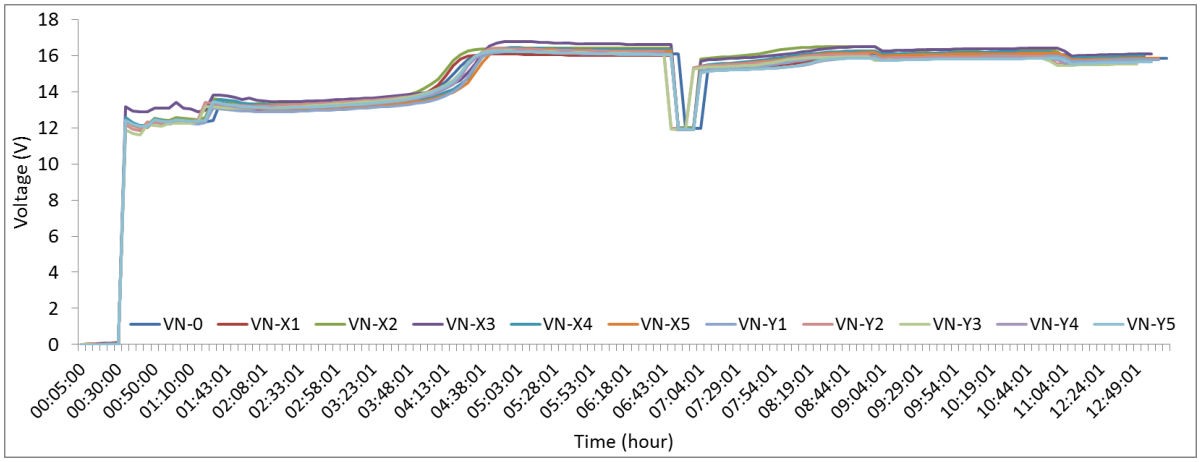

Figure 4. The graph shows the voltage change of the batteries during charging.

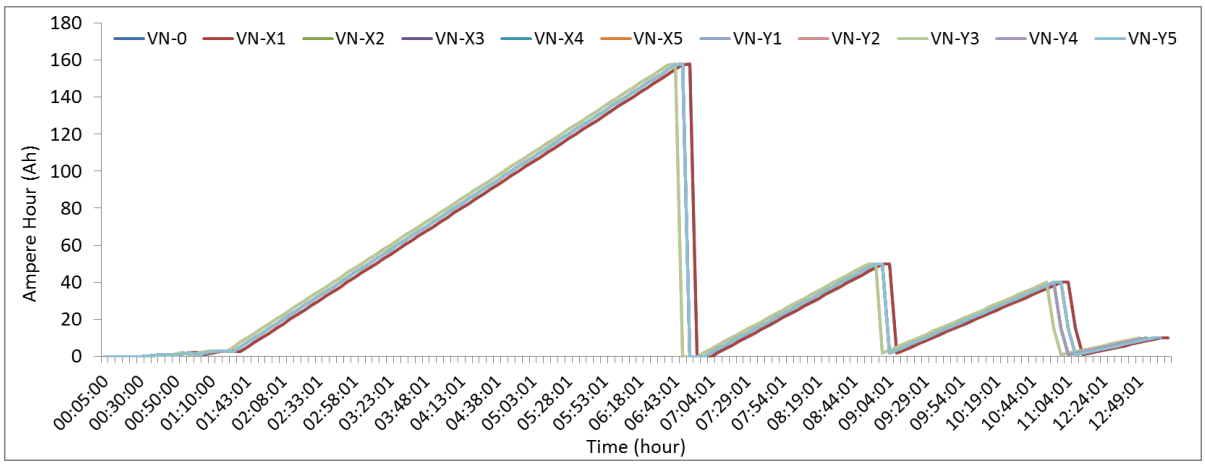

Figure 5. Total ampere-hours are given to the batteries during charging.

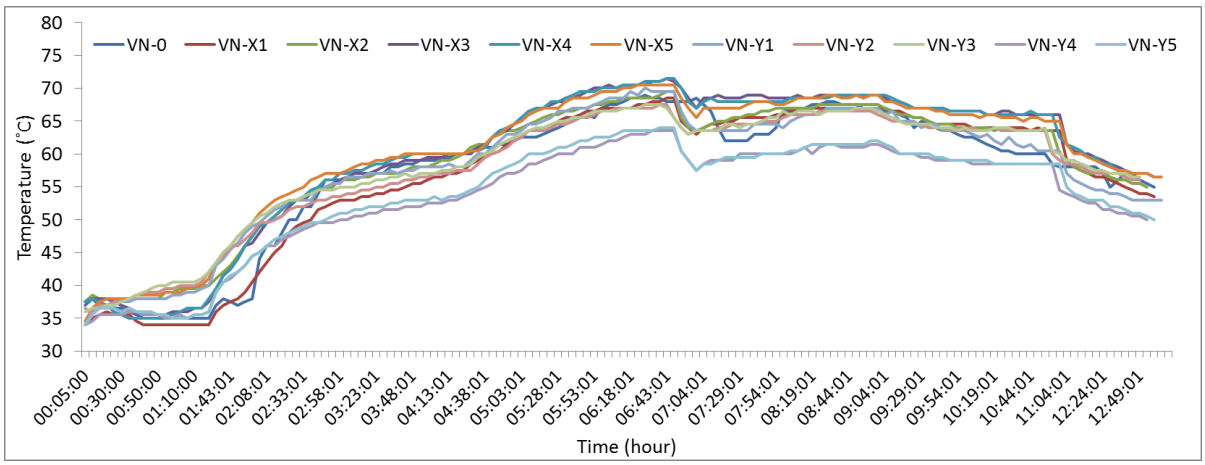

Figure 6. The graph shows the internal temperature of the batteries while charging.

3.3. After Charging OCV and CCA Results

Electrical performances results as an OCV and CCA, of the batteries are shown in Figure 7 and Figure 8, respectively.

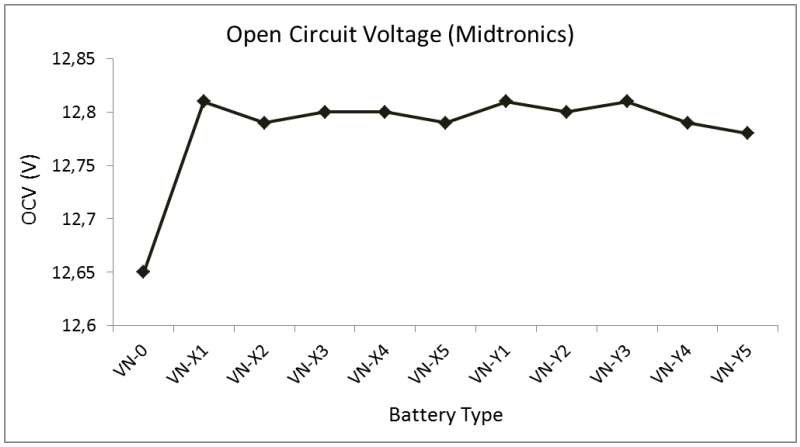

Figure 7. OCV graphic after charging.

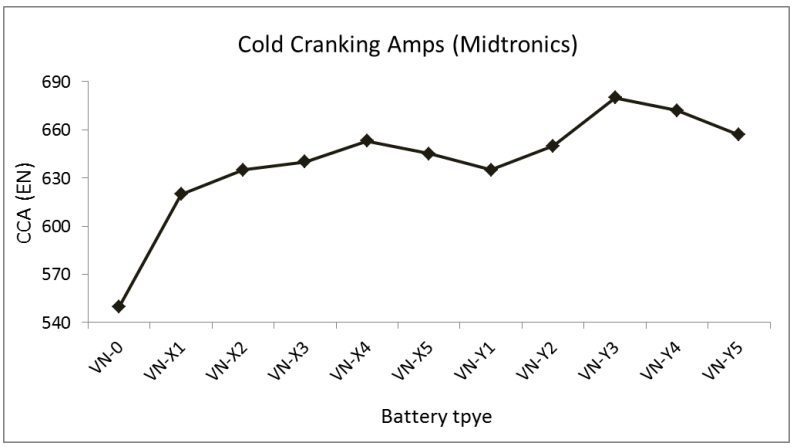

Figure 8. CCA graphic after charging.

3.4 Internal Resistance Test

Electrical performances results as an internal resistance of the battery are shown in Figure 9.

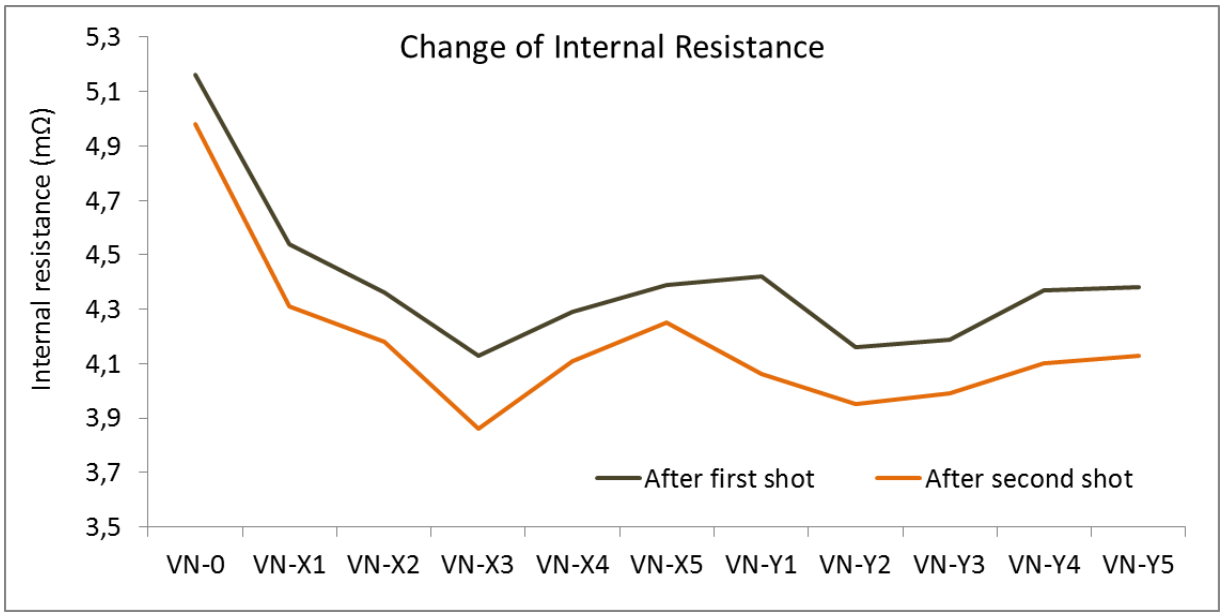

Figure 9. Internal resistance graphic after charging.

3.5. Capacity Test

Electrical performance results as a capacity are demonstrated in Figure 10.

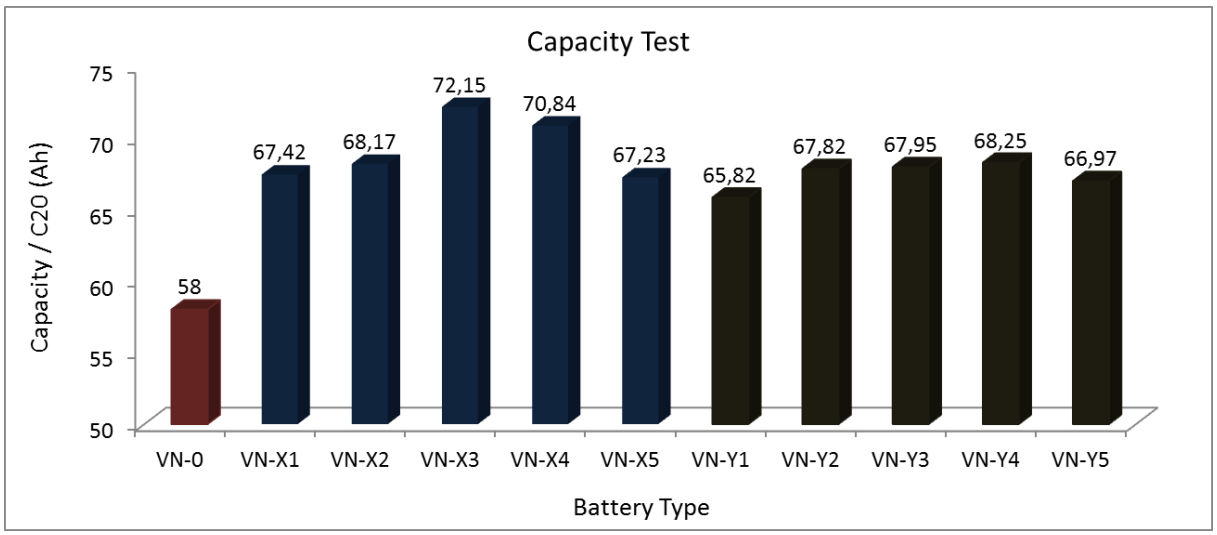

Figure 10. Capacity graph

3.6. Cranking Performance Test

Results of cold-cranking ampere (CCA) of lead-acid batteries are given in Table 3.

Table 3. Cold-cranking ampere results

Vanisperse Type	**Current draw**	**U_f**	**After U_f voltage ≥ 7,5**	**t'_{6v}≥90s**
VN-0	610	7,6	7,5	101
VN-X1	610	10,4	7,5	160
VN-X2	610	10,2	7,5	168
VN-X3	610	11,2	7,5	175
VN-X4	610	10,8	7,5	163
VN-X5	610	10,6	7,5	152
VN-Y1	610	10,1	7,5	123
VN-Y2	610	10,1	7,5	136
VN-Y3	610	10,3	7,5	143
VN-Y4	610	10,4	7,5	157
VN-Y5	610	10,2	7,5	139

3.7. Charge Acceptance Test

Charge acceptance results of lead-acid batteries vanisperse are shown in Figure 11.

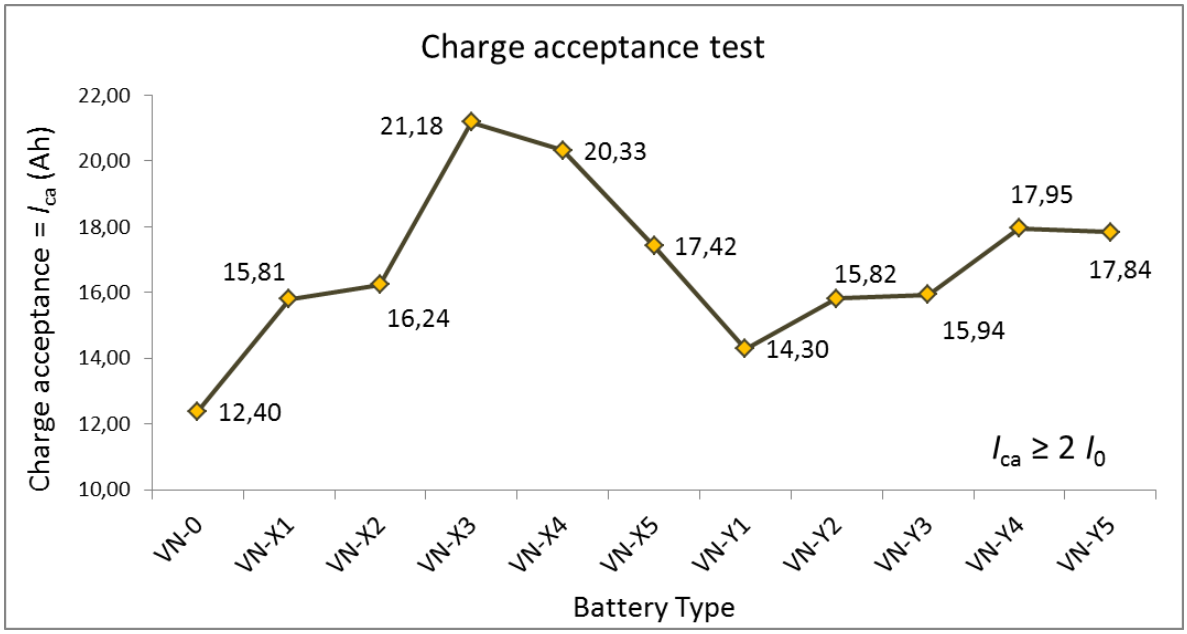

Figure 11. Charge acceptance test graph.

3.8. Cycle Life Test

Cycle-life test results of lead-acid batteries are shown in the Figure 12.

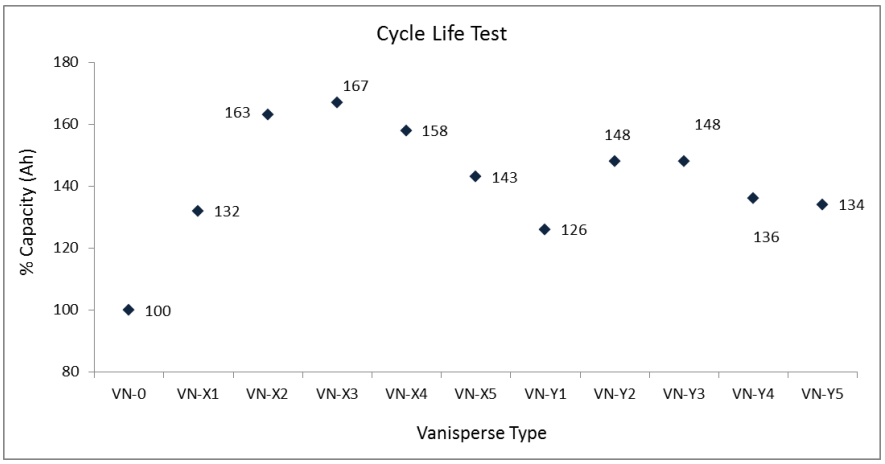

Figure 12. Cycle life test graph.

4. RESULTS

As a result of this study, 0,4% vanisperse Y battery achieved 130 units increase in CCA. Batteries containing 0,3% vanisperse X increased 24% in capacity. Besides batteries containing 0,3% vanisperse X increased 75% in the cranking performance test. Also, batteries that contain 0,3% vanisperse X increased 70% in the charge acceptance test. Finally, battery cycle life is increased by 67% with 0,3% vanisperse X additive. Future research will be conducted to improve the electrical properties of batteries by using vanisperse in more different types and ratios in weight.

ACKNOWLEDGEMENTS

We acknowledge to Abdulkadir Özcan Otomotiv A.Ş. board of directors for their financial and moral support.

REFERENCES

[1] Boden, D.P., Improved oxides for production of lead/acid battery plates, *Journal of power sources*, **73**(1), 56-59, 1998.

[2] Planté, G., Nouvelle pile secondaire d'une grande puissance, *Mallet-Bachelier*, *Comptes rendus de l'Académie des Sciences*, **50**(1), 640-642, 1860.

[3] Pavlov, D., Lead-acid batteries: science and technology, *Elsevier*, pp. 11-12, 2011.

[4] Gladstone, J. H., Tribe, A., The chemistry of the Plante and Faure accumulators, *Nature*, **25**, 221-223, 1882.

[5] Eydemir, Y., Strengthened battery design for start-stop vehicles, *Gazi University, Energy Systems Engineering, Ankara*, pp. 12-28, 2019.

[6] Zimáková, J., Fryda, D., Vaculik, S., Bača, P., & Bouška, M., Examination of impact of lignosulfonates added to the negative active mass of a lead–acid battery electrode, *Journal of Energy Storage*, **18**, 229-238, 2018.

ELECTROCHEMICAL CHARACTERIZATION OF TEMPERATURE DEPENDENCE IN LITHIUM-ION BATTERY

Ongun Bora SABAN*, Eda GÜZEL, Mustafa Fazıl SERİNCAN*, Mehmet Ali ARSLAN***
*Gebze Technical University, Department of Mechanical Engineering, Kocaeli/Turkey
Email: obsaban@gtu.edu.tr, mfserincan@gtu.edu.tr, mehmet.arslan@gtu.edu.tr
** Gebze Technical University, Department of Electronics Engineering, Kocaeli/Turkey
Email: e.guzel@gtu.edu.tr

ABSTRACT

Lithium ion batteries are the one of the most preferred energy storage devices for today's world due to their high capacity and high power density. Cylindrical ones such as 18650 commercial lithium batteries are commonly used in automotive, IT and space industry since their stability, sustainability and applicability. Thus, in order to investigate the performance of the battery and develop its technology, analyzing the electrochemical reactions occurred in the battery is crucial. Electrochemical Impedance Spectroscopy (EIS) and pulse tests are frequently used methods to understand the electrochemical performance of the batteries. The EIS measurements of fully charged battery are conducted in the frequency range of 200 kHz and 10 mHz for the deep understand of polarization processes. In this study, we interpreted the electrochemical stability of Nickel Manganese Cobalt oxide cathode and graphite anode material cylindrical SONY Murata 18650-lithium battery in different temperatures. In addition, equivalent circuit modeling of the commercial lithium battery has obtained in order to understand the physical meaning of the electrochemical kinetics.

Keywords: Energy systems, Battery, Impedance, Electrochemistry

Symbols

C	C-rate factor
T	Temperature (°C)
V	Voltage (V)
I	Ampers (A)
R	Resistance (ohm)
CPE	Constant-phase element (Farad)
α	Exponent in the equation for the CPE.

1. INTRODUCTION

Due to the promising energy rate and stability of lithium-ion batteries, automotive, defense, space industries, technology companies mostly use these electrochemical energy storage systems. [1] Hence, in order to understand the detailed performance of those devices in different working conditions performance characteristics should be analyzed. Batteries can be arranged into various classifications by considering the chemical composition, size and use cases and yet, there are two principle kinds of batteries, which are Primary batteries and Secondary batteries. [2] While primary batteries are not rechargeable, secondary batteries can switch chemical responses to electrical power many times. Also, secondary batteries can be arranged in several different types such as Nickel Cadmium (Ni-Cd), Nickel-Metal Hydride (Ni-MH), Lead Acid and Lithium-ion (Li-ion) due to their chemical decompositions.

The characteristics of widely used batteries, such as voltage values, operating temperature range, are listed in Table 1 [3]. According to the studies, it is possible to reach 300-2000 cycles depending on the chemical structure of the

battery in rechargeable Li-ion batteries. At the end of each cycle, the battery loses its initial nominal energy capacity to some degree. Temperature is one of the most significant factors that abbreviates battery life. [4] Dependence between voltage and temperature in the battery are commonly used monitoring method in order to understand the most significant variables influencing chemical responses. [5] Furthermore, electrochemical Impedance Spectroscopy (EIS), which is a frequency based method that measures the resultant voltage or current behavior of a system with the application of sinusoidal current or voltage is widely used approach to analyze the internal kinetics of this kind of energy conversion systems. EIS is a powerful method to detect the internal reaction characteristics. [6-8] One of the commonly used way to show EIS is the Nyquist plot, which is a parametric plot of the complex part of feedback and real part of transfer function. Nevertheless, frequency characteristics, reactance and resistance characteristics may be determined by using Nyquist plots of batteries.

Table 1. Properties of widely used batteries

Battery Type	Nominal Voltage (V)	Energy Density (Wh/kg)	Life Cycle	Min. Operating Temp. (°C)	Max. Operating Temp. (°C)
Lead Acid	2	35	1000	-15	50
Nickel-Cadmium	1.2	50-80	2000	-20	50
Lithium-Ion	3.6	118-250	2000	-20	60
Lithium-Ion Polymer	3.7	130-225	1200	-20	60
Lithium-Iron Phosphate	3.2	120	2000	-45	70
Lithium-Air	2.9	1300-2000	100	-10	70

2. METHODOLOGY

The experimental part of this study consists of three processes under various ambient temperatures (0 °C, 25 °C and 40 °C), measurements of discharge test, battery load test and electrochemical impedance measurements. Three identical commercial Sony US18650VTC5 Cylindrical 2.5 Ah (battery properties are shown in Table 2.) 18650 type cylindrical lithium-ion batteries are used for the experiments in order to project the temperature dependence of electrochemical characteristics. The cells were made from Lithium Nickel Manganese Cobalt Oxide (NMC) material as positive electrode, which provides high power, high energy density and high cycle life, graphite material as negative electrode and LP-30 as electrolyte. Battery tests are performed in Nüve Climatic Chambers in order to set and control the desired ambient temperature. Gamry 5000E and ARBIN BT2000 Battery Tester devices are used for measuring and monitoring the discharge tests, load tests and electrochemical impedance spectroscopy.

The charge and discharge measurements are performed constant current-constant voltage technique. Batteries are charged until 4.2 V with constant current (2.5 A) and constant voltage (4.2 V) until the current drops below 100 mA and the discharge process is performed under constant current (2.5 A) until the cut-off voltage (2.5 V) limit in desired ambient temperatures. Discharge load tests were carried out using ARBIN BT2000 Battery Tester and Nüve Climate Chamber with the desired pulse current discharge rate and in a controlled temperature environment. These tests were repeated at three different temperatures to fully charged batteries with the application of 20 pulses with 90 minutes relaxation times until the cut-off voltage limit with 2.5 A discharge current. In order to calculate the resistance and capacitance values 1 RC model developed by MatLab is used.

Electrochemical impedance measurements are performed with the frequency range between 100 kHz – 10 mHz and 5 mV/s scanning rate in different state of charges of the batteries. State of charge of the lithium ion battery isn't related with open circuit potential directly. Therefore, in order to calculate the state of charge, battery's voltage-capacity graphs are obtained from discharge tests and discharge load tests.

Table 2. Properties of SONY Murata VTC5 18650-type cylindrical lithium-ion cell.

Property	Unit	Value
Diameter	mm	18.35
Length	mm	65.2
Weight	g	44.3
Nominal Voltage	V	3.6
Charge-up Voltage	V	4.2
Discharge cut-off Voltage	V	2.5
Internal Impedance at AC-1 kHz	mΩ	13.0
Nominal Capacity (0.2 C discharge at 25 °C)	mAh	2577

3. RESULTS AND DISCUSSION

The electrochemical performance of the batteries is highly dependent to the ambient temperature. Many studies show that low diffusivity and conductivity in the electrolyte and the slow-moving charge transfer kinetics and solid-state diffusion in the anode and cathode materials occurs in low ambient temperature. Hence, at the first step of the investigation of the temperature dependence of the battery, capacity fade at various temperatures should be monitored with Voltage vs. Capacity graph while the battery is in discharging process. Figure 1 indicates that while the capacity loss occurs in low ambient thermal conditions at different discharging currents, lower discharging current also affects the capacity of the batteries positively.

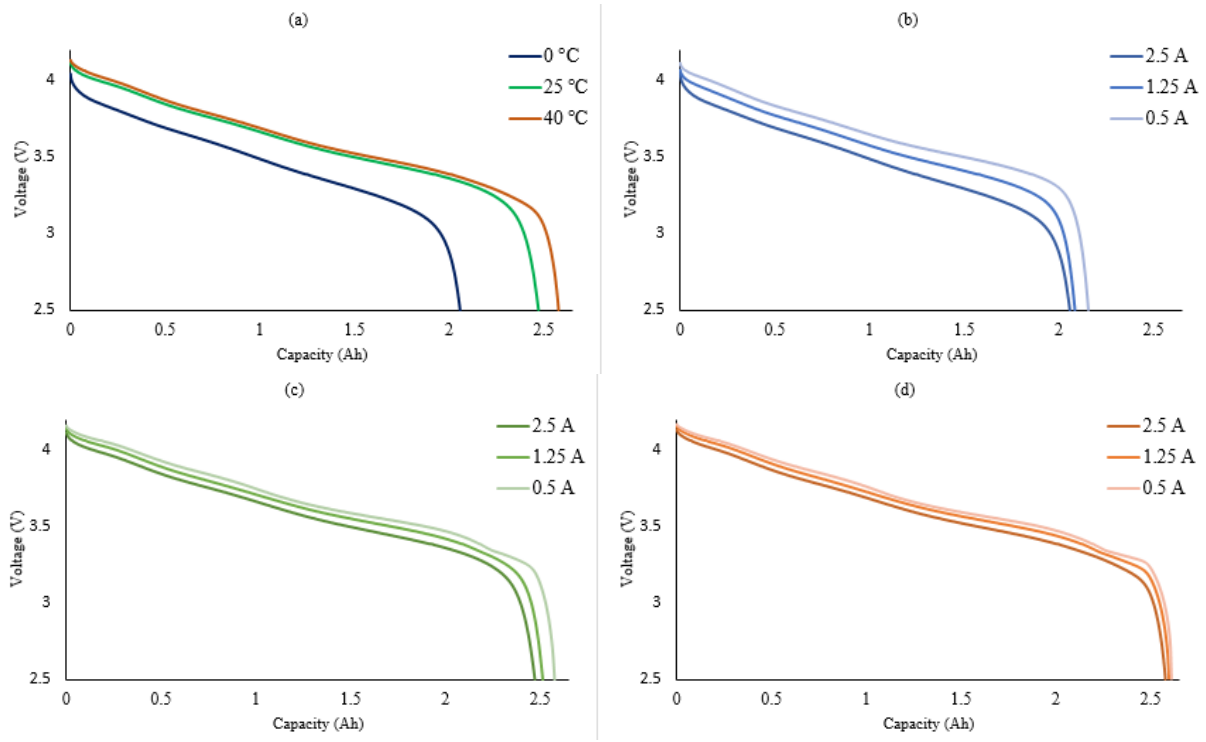

Figure 1. Temperature dependence of discharge process of the battery. (a) 2.5 A discharge current at different ambient temperatures. (b), (c) and (d) represents various discharge currents at 0 °C, 25 °C and 40 °C respectively.

Moreover, in this study, Electrochemical Impedance Spectroscopy (EIS) method, which provides highly accurate results is used to interpret the electrochemical data vs. state-of-charge (SoC) of the battery. SoC values are calculated by using Coulomb-counting method with the help of voltage vs. capacity data and SoC vs. battery's capacity values are tabulated in Table 3.

Table 3. SoC vs. Discharge capacity and Voltage values of experimental cells at different ambient temperatures.

	0 °C		25 °C		40 °C	
SoC (%)	**Discharge Capacity (mAh)**	**Voltage (V)**	**Discharge Capacity (mAh)**	**Voltage (V)**	**Discharge Capacity (mAh)**	**Voltage (V)**
100	0	4.07	0	4.14	0	4.16
80	417.21	3.81	502.90	3.89	519.45	3.90
60	834.01	3.64	1005.48	3.71	1038.69	3.71
40	1251.23	3.49	1508.99	3.55	1558.23	3.56
20	1668.07	3.35	2011.15	3.42	2077.73	3.41
0	2085.61	2.50	2514.34	2.50	2597.10	2.51

In order to analyze the performance of the battery modeling the equivalent circuits is very useful approach for energy storage systems. As shown in Figure 2, the battery used in this study modeled with two elements, which are constant-phase element (CPE) and resistance (R). Here, R_i indicates ohmic resistance and it is related with electrolyte, separator, current collector and electric conductivity, while R1 and CPE1 represent the first semi-circle as resistance of solid electrolyte interface layer and the decomposition of organic electrolyte compounds on the surface of graphite electrode, respectively. R2 and CPE2 correspond to the second semi-circle, which indicate the charge transfer impedance of NMC material, and lastly CPE3 is assigned with Li diffusion in the solid phase, which is most likely observed in low frequency range in impedance spectra.

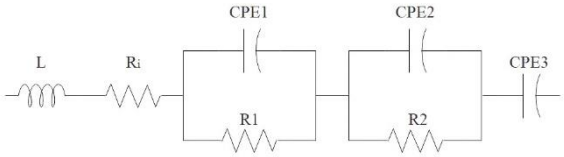

Figure 2. Equivalent circuit model for fitting the experimental impedance data of the cells.

Figure 3 shows the Nyquist plots of the impedance spectra in different SoC values at different ambient temperatures.

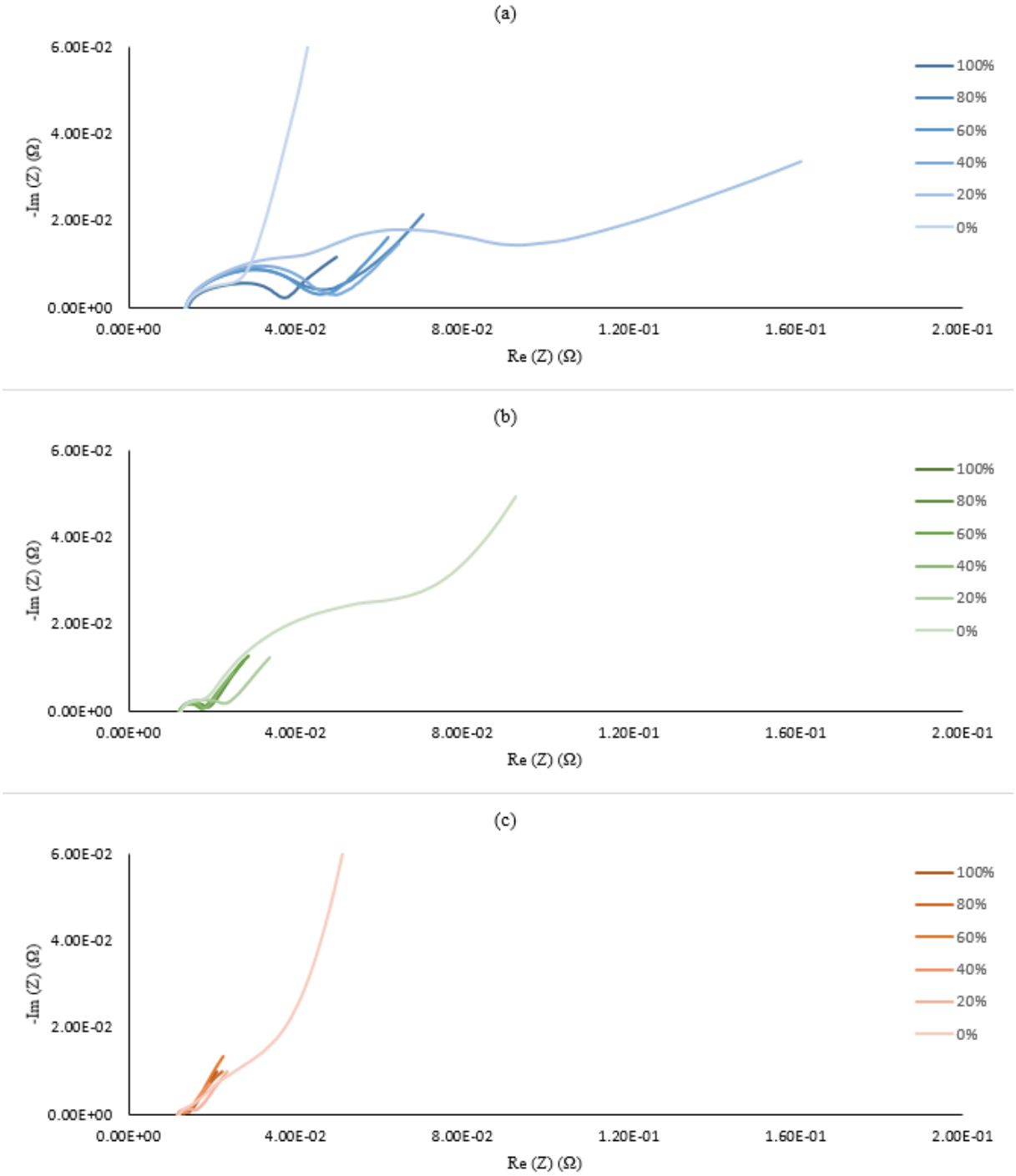

Figure 3. (a), (b) and (c) represents the EIS results of the battery at different SoC values at 0 °C, 25 °C and 40 °C respectively.

It can be seen that from Figure 4, the first semi-circle observed in the middle frequency range of the Nyquist impedance plot is growing while the ambient temperature increasing.

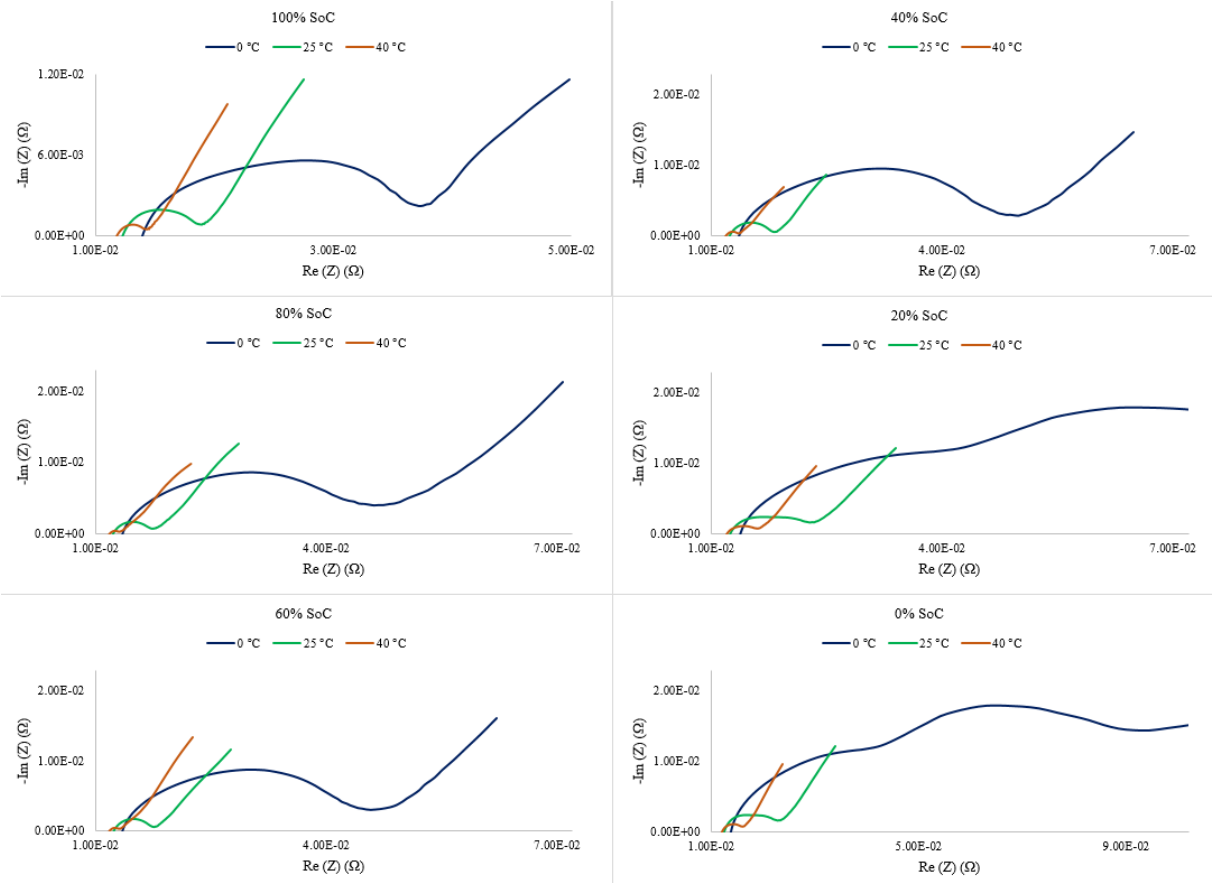

Figure 4. Temperature dependence of EIS at each SoC.

As detailed in Figure 5, in the high frequency range of the Nyquist diagram, R_i, which is the first intersection point with Re (Z) axis, is not changing within the change in SoC but increases while temperature is decreasing. Besides, the change in SoC does not affect the value of R1 element noticeably until SoC is 0%; however, CPE1 element has highest values when the SoC is 100% in different ambient temperatures during the experiment. Therefore, the solid electrolyte interface formation is most likely to be stable in different ambient temperatures, but at low temperatures, it is understandable that electrolyte channels are blocked since SEI film layer got thicker. The second semi-circle, which corresponds to R2 and CPE2 elements has observed after 20% SoC. The results show that the charge transfer impedance is increasing while the capacity of the battery is at lower states. On the other hand, the resistance of Li+ insertion into the electrode became higher in low temperatures, because of the fact that SEI film layer has thickened. CPE3, the capacitive behavior of Warburg diffusion is after 40% SoC is slightly decreasing.

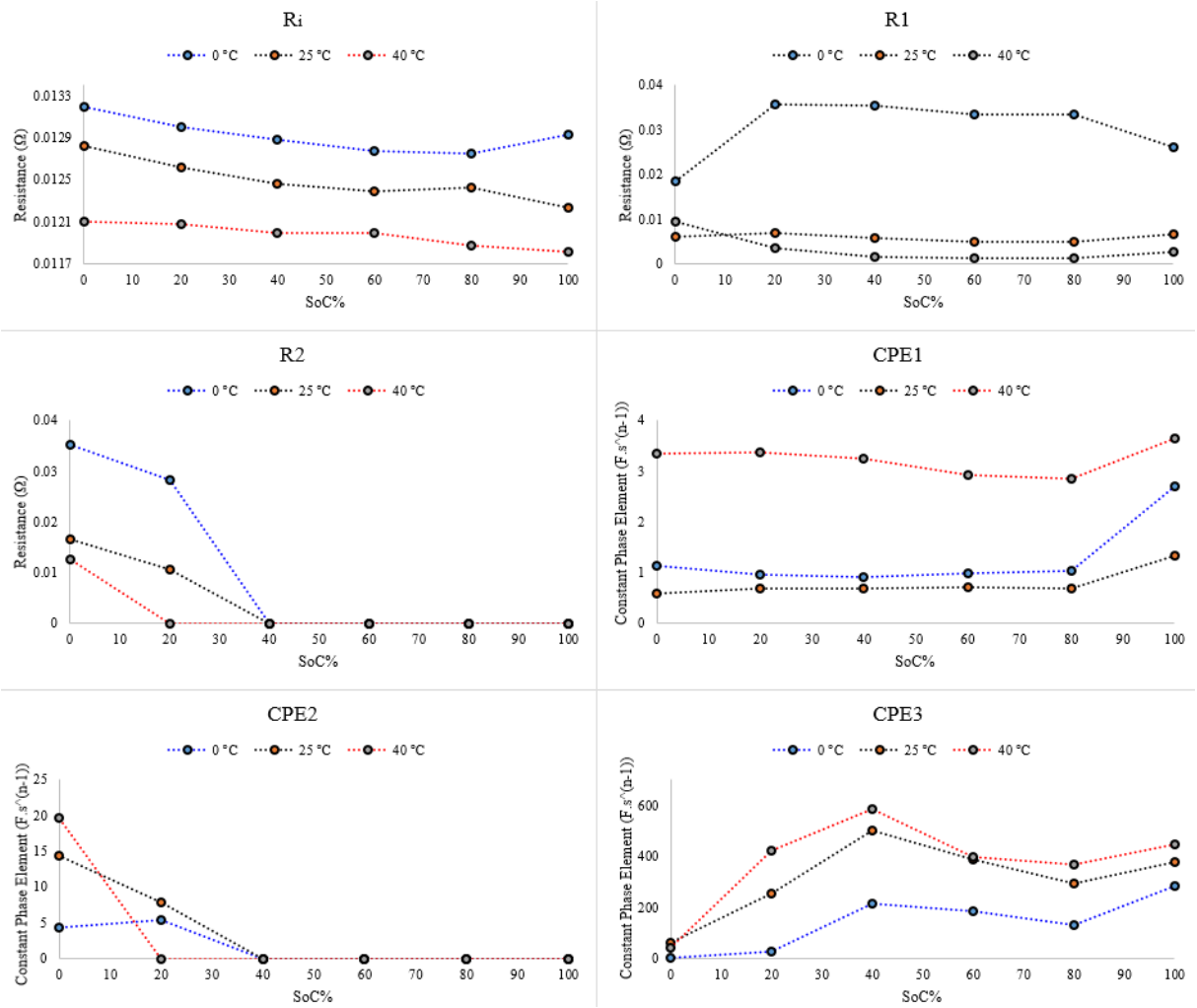

Figure 5. Temperature dependence of R and CPE elements vs. SoC.

In order to compare the R and C parameters obtained from the load tests and impedance data, Brug's (1) formula is used for the calculation of capacitance value of the constant phase element value of the first semi-circle. Table 4 shows that the resultant capacitance values of the first semi-circle.

$$C_{CPE} = \left[CPE_n . \left(\frac{1}{R_n}\right)^{\alpha-1}\right]^{\frac{1}{\alpha}} \quad (1)$$

In equation (1), C_{CPE} indicates the capacitance calculated from constant-phase element, CPE1 and R1 are the values of corresponded semi-circle (n=1 for the first semi-circle) and α (assumed α=0.48) is the exponent in the equation for the CPE.

Table 4. Capacitance values of the first semi-circle.

Ambient Temperature	**Capacitance (F)**					
40 °C	11648.8	12769.3	14947.7	14016.8	7531.4	3613.0
25 °C	672.9	200.5	210.2	186.9	166.3	129.4
0 °C	1369.3	174.1	153.2	131.4	139.2	253.4

As shown in Figure 6, discharge load tests are obtained at different ambient temperatures. Due to the low temperature behavior of electrochemical characteristics, at 0 °C, voltage gains of pulses responded higher with respect to discharge trend of the battery.

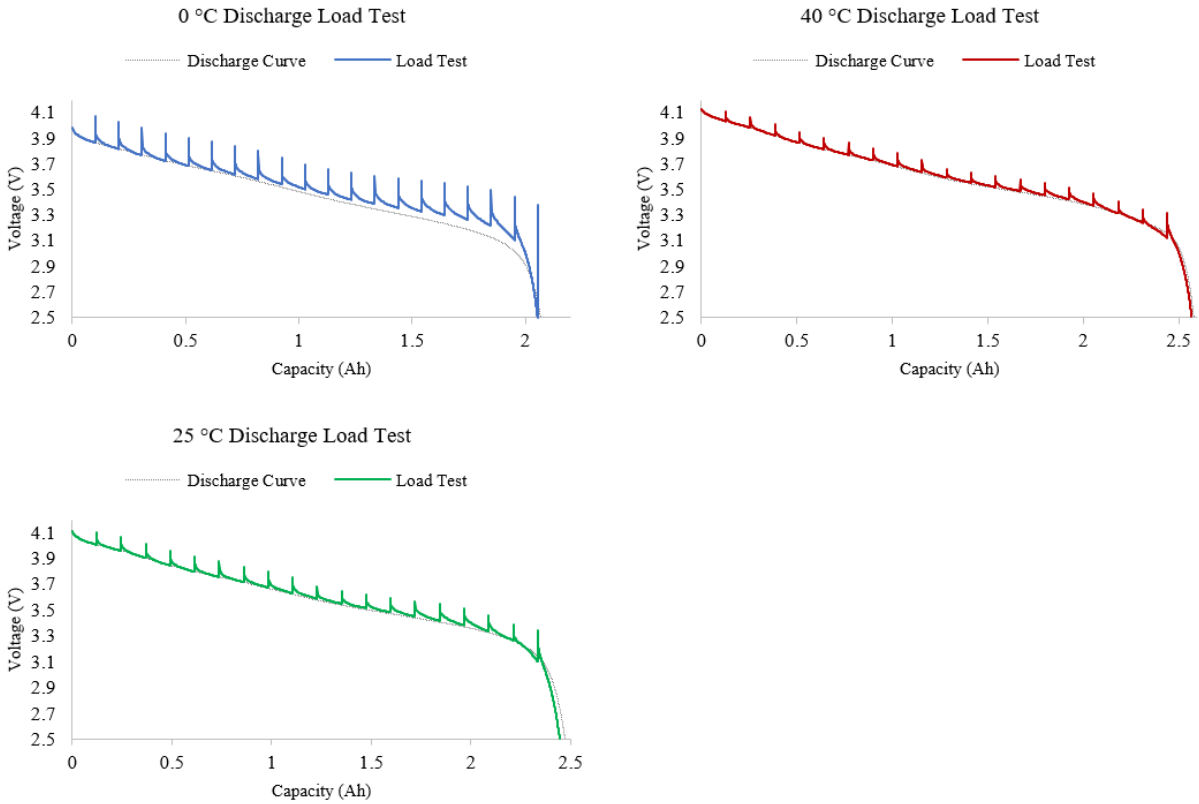

Figure 6. Discharge load characteristics of the batteries under different ambient temperatures.

Load tests are widely used method of estimation of the SoC of the batteries and their electrochemical characteristics. In this study, the resistance and capacitance values of the batteries in different temperatures modeled with 1 R-C circuit from discharge load tests as seen in the Figure 7. Hence, while R_i indicates the ohmic losses, the R1 and C1 values related with charge transfer kinetics. Figure 8 shows the results obtained from load tests. The circuit equation of the cells can be derived by using Kirchhoff law as shown in Equation (2) and (3).

$$\frac{dVc}{d(t)} = -\frac{1}{R1.C1} \times Vc(t) + \frac{1}{C1} \times i(t) \quad (2)$$

$$V(t) = Voc(t) - Vc(t) - Ri \times i(t) \quad (3)$$

In equation (2), while R1 indicates the equivalent polarization resistance and C1 indicates the equivalent polarization capacitance, i corresponds to the current applied on cell.

In equation (3), V_{oc} corresponds to open circuit potential and R_i denoted as internal resistance of the battery.

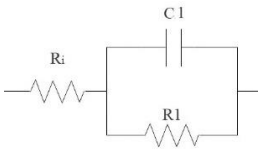

Figure 7. Equivalent circuit modeling for the calculation of the R and C parameters obtained from discharge load tests data.

R1 and C1 values can be calculated by considering the diffusion kinetics and charge transfer processes between the electrodes and electrolyte with the use of the time constant τ.

$$\tau = R1 \times C1 \tag{4}$$

$$R1 = \frac{Voc - Vt'}{I} \tag{5}$$

In equation (5), V_t' corresponds to the terminal voltage of the battery after discharging process.

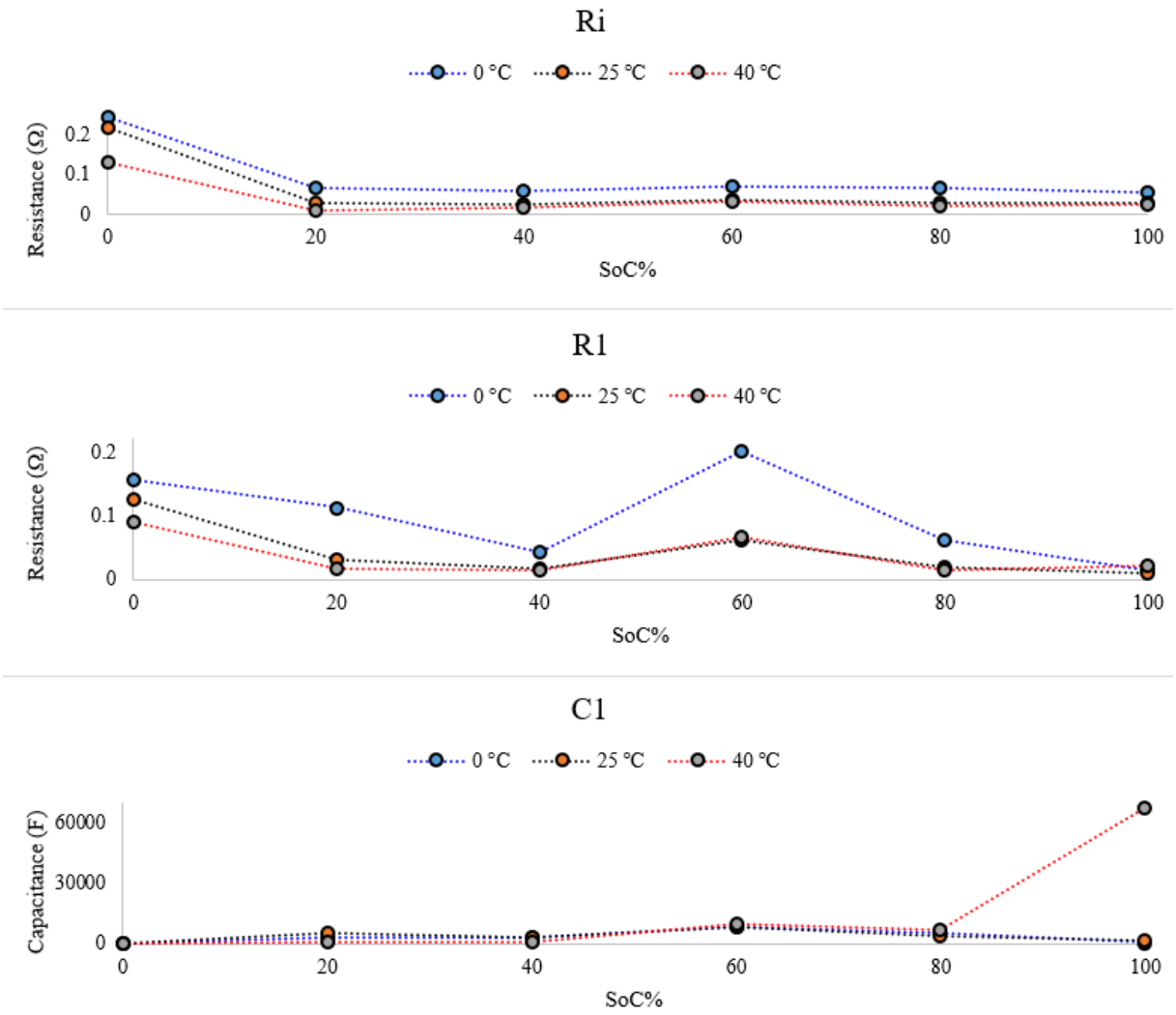

Figure 8. R and C parameters of the batteries at different ambient temperatures obtained from discharge load tests.

R_i values obtained from discharge load tests are higher than EIS results because of the fact that the different accuracies of the experimental equipment. Moreover, at 0% SoC, R_i values tend to be higher at each ambient temperature. R1 values correspond to the serial connection of charge transfer resistance and solid electrolyte interface resistance. As seen in the figure, while the resistance and capacitance values show a pick at all ambient temperatures at 60% SoC as expected, but at 40 °C, slightly high capacitive behavior seen at 100% SoC.

4. CONCLUSION

The electrochemical performance of the batteries can be investigated by using different approaches. In this study, equivalent circuit modeling is used to understand the electrochemical kinetics of 18650 cylindrical li-ion cells consisting of NMC - graphite electrodes and LP30 electrolyte at different operational temperatures. The parameters are obtained from discharge load tests and electrochemical impedance spectroscopy and the results are summarized. As we discussed above, the low temperature performance of the batteries is slightly decreased since the SEI and charge transfer resistances are increased. Furthermore, it is clearly seen that the temperature impacts on the electrochemical performance of the batteries is relatively higher than the change in SoC.

REFERENCES

[1] J. M. Tarascon, M. Armand, Issues and Challenges Facing Rechargeable Lithium Batteries, *Nature*, **414**, 359-367, 2001.

[2] https://depts.washington.edu/matseed/batteries/MSE/classification.html

[3] Yong, Jia Ying, et al. A Review On The State-Of-The-Art Technologies of Electric Vehicle, Its Impacts and Prospects, *Renewable and Sustainable Energy Reviews*, **49**, 365-385, 2015.

[4] E. Prada, D. Domenico et al. Simplified Electrochemical and Thermal Model of LiFePO4-Graphite Li-Ion Batteries for Fast Charge Applications, *Journal of Electrochemical Society*, **159(9)**, 1508-1519, 2012.

[5] T. Huria, M. Ceraolo, J. Gazzarri, R. Jackey, High Fidelity Electrical Model With Thermal Dependence For Characterization and Simulation Of High Power Lithium Battery Cells, *Electric Vehicle Conference (IEVC)*, Greenville (SC)-USA, 2012.

[6] D. Andre, M. Meiler, K. Steiner, H. Walz, T. Soczka-Guth, D.U. Sauer, Characterization of High-Power Lithium-ion Batteries By Electrochemical Impedance Spectroscopy. II: Modelling, *Journal of Power Sources*, **196**, 5349-5356, 2011.

[7] P. L. Moss, G. Au, E. J. Plichta, J. P. Zheng, An Electrical Circuit for Modeling the Dynamic Response of Li-Ion Polymer Batteries, *Journal of The Electrochemical Society*, **155**, 986-994, 2008.

[8] H. Schichlein, A.C. Muller, M. Voigts, A. Krugel, I. Tiffee, Deconvolution Of Electrochemical Impedance Spectra for the Identification Of Electrode Reaction Mechanisms In Solid Oxide Fuel Cells, *Journal of Applied Electrochemistry*, **32(8)**, 2002.

TURKEY'S PUMPED HYDRO STORAGE STATUS: CURRENT SCHEME AND POTENTIAL

Serpil ÇELİK TOKER*, Gamze SOYTÜRK, Önder KIZILKAN
*Isparta University of Applied Sciences, Department of Mechanical Engineering, Isparta/Turkey
Email: serpilcelik@isparta.edu.tr

ABSTRACT

With the rapid increase in energy demand, the search for new and clean energy sources has gained significant importance. Renewable energy resources arising from this search have become of great importance for countries by spreading rapidly worldwide. Besides, the increase in the number of renewable energy plants such as wind-solar and the high stopping costs of baseload power plants have created the need for storing electrical energy. Among the storing technologies, pumped hydro energy storage (PHES) is widely used worldwide as it is very costly to store large amounts of energy as electricity. With the growing interest in PHES around the world, global PHES capacity is projected to grow by 78 GW by 2030, significantly more than other energy storage technologies. The objective of this study is to investigate the current situation PHES potential of Turkey. For this aim, the working principle, types, and advantages of PHES are examined at first. After, the PHES utilization potential of the world is investigated, followed by the prospect of Turkey. It is estimated that the PHES systems can significantly benefit Turkey's energy reliability, continuity, and dependence on foreign energy sources.

Keywords: Pumped hydro, energy, efficiency, energy storage.

1. INTRODUCTION

Energy demand is increasing all over the world with technological developments and rapid population growth. Most of the energy needs are met from fossil fuels, which cause severe changes in our environment. Global warming, ozone depletion, and the greenhouse effect are some of the environmental threats [1]. As a result of fossil fuel energy consumption, CO_2 emissions are increasing. Atmospheric accumulation of greenhouse gases such as CO_2, NO_X causes global warming. In order to lower the limit of global warming below 2°C, greenhouse gas emissions must be at least 25% lower by 2030 than in 2018 [2]. In this respect, renewable energy sources make a vital contribution to achieving this goal. Among the clean energies, renewables play an essential role, mostly because of their local origin. Renewable energies such as solar, wind, and hydraulic are the most suitable supply options for sustainable energy generation [3]. Although it is a clean and free energy source, renewable energy sources depend heavily on weather conditions and are therefore not sustainable. In this case, the importance of storage systems has increased. By storing electrical energy when it is not needed, the stored energy can be used when wind or solar energy is not sufficient. Thus, renewable energy resources are stored and utilized continuously [4].

The energy storage system can be classified into five groups: mechanical (pumped hydro-storage, compressed air, flywheels), electric (superconductors, capacitors), thermal, electrochemical (batteries), and chemicals (fuel cells) [5]. PHES plants are one of the most extended energy storage systems at the worldwide level [6]. Pumped hydro storage dominates the total operational storage capacity with a 98% share, which corresponds to 167.8 GW [7]. Basically, a pumped hydro energy storage system utilizes the potential energy of water by pumping and discharging it between upper and lower reservoirs [8]. During periods with low power demand, these systems pump water from a lower reservoir to an upper one. In contrast, when electricity demand increases, the PHES system generates electricity just like a conventional hydroelectric power station [9]. Since it was first used in the 1890s, the use of PHES has made considerable progress. PHES surged through the 1960s, 70s, and 80s in Europe, the United States, and Japan, where the rapid growth of nuclear energy and coal-fired units continued [10]. According to International Hydropower Association (IHA) 's Hydropower Status Report 2020, PHES has a

global share of 94% in total installed energy storage capacity with 157.99 GW by the end of 2019 [11]. Countries with the highest amounts of this technology's installed power capacity are China with a total capacity of 32 GW, Japan 28 GW, European University Association (EUA) 22 GW, and Spain 8 GW [9].

Researchers have performed in-depth studies in recent years to plan various pumped hydro storage stand-alone hybrid energy systems. Kocaman and Modi proposed a programming model for sizing an integrated hybrid energy system with PHES [12]. Koko et al. introduced an optimal energy management model for a pumped hydro energy storage system to reduce the grid consumption costs and increase the energy sales revenue [13]. Lu et al. studied the prospective sites for PHES systems in South Australia [14]. Kizilkan et al. investigated the applicability of a pumped-storage hydropower system in Isparta to use energy efficiently, contribute to the energy supply-demand balance, and ensure the continuity of renewable energy sources. They thought of two scenarios for analysis. In the first scenario, the energy required for the water's pumping operation to be stored was supplied from the grid line when electricity unit prices are low. In the second scenario, the energy required for the pumping process was provided by the theoretically calculated solar power plant. In the first case, they calculated the depreciation period as 15 years, in the second case as 21.5 years. They also stated that Turkey's PHES potential is very high, and Egirdir lake and its surroundings are suitable for such power plants [15]. Barboros et al. studied the Turkish power grid, and they have analyzed the electricity market in detail to investigate the necessity of a PHES of Turkey. They chose Gökçekaya, Turkey's most prominent PHES alternative, as a model and used real-time energy ratios and production-consumption values from public and private perspectives [16]. Dursun and Alboyaci comprehensively examined the importance and necessity of wind-hydro pumped storage systems for Turkey. The contribution of wind-hydro pumped storage systems was emphasized in meeting Turkey's electric energy demand [17]. Melikoglu analyzed the global development of PHES. He investigated hydroelectric, wind, and solar energy development plans in Turkey in the next 7 years, based on the Vision 2023 energy targets. And he evaluated, from a global to local perspective, the potential role of PHES as a synergistic energy storage option for Turkey [18].

The purpose of this study is to investigate Turkey's PHES potential by examining the global PHES applications. The structure of this paper is as follows: a) definition of PHES, types, advantages, b) the importance of PHES utilization, c) investigation of world's PHES applications with samples and the current state of PHES in the world d) examining Turkish PHES potential.

2. PUMPED HYDRO ENERGY STORAGE SYSTEMS

For many years, PHES has been the most suitable and efficient way to store electricity. The illustration of a PHES system is shown in Figure 1. The main components of a typical PHES are an upper reservoir, lower reservoir, penstock, tunnels, turbine, pump, and generator (Figure 1). Like hydropower itself, PHES is a simple technology. In the conventional hydro energy power plant (HEPP), the reservoir water is stored with the help of a dam. The stored water is released to the turbine through channels to generate electricity. PHES systems pump water from the lower reservoir to higher with an additional reservoir's aid when energy demand is low. It produces energy in the same way as traditional hydroelectric power when the energy demand is high [19].

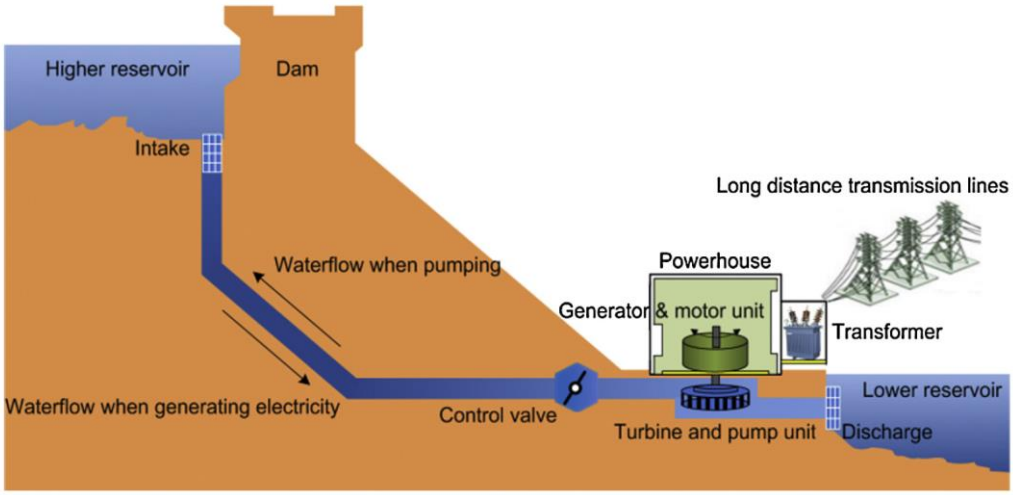

Figure 1. Schematic representation of a PHES plant [20].

In fact, during the pumping process, PHES is an energy-consuming plant, and the amount of energy consumed is more significant than that produced when it is in production mode. Nevertheless, the difference in electricity price between peak and off-peak hours makes PHES profitable. PHES is commonly used, particularly in developed countries such as China, the United States (US), Japan, Germany, and France, because of the high value of peak electricity [21]. The importance of PHES is to balance energy demand instead of generating electricity. The main advantage of PHES is to ensure the reliability of the electrical network. If the power produced is excessive, the system frequency increases. If the demand exceeds production, the frequency decreases. PHES helps keep the frequency in the grid constant with pumping or turbine operating modes [22].

To meet peak demands, each power grid must have the capacity to respond quickly. If the power plants do not generate power immediately, the system frequency falls, and therefore, a power cut may happen. In contrast to other power plants, PHES also can be started quickly, as in traditional HEPPs. The startup times of various power plants following an 8-hour shutdown are shown in Table 1 [23].

Table 1. Startup times following an 8-hour shutdown [23]

Plant Type	Startup Time
Hydroelectric Power Plant	3-5 minutes
Natural Gas Power Plant	1 hours
Oil Power Plant	3 hours
Coal Power Plant	4 hours
Nuclear Power Plant	5 days

As mentioned above, PHES has many advantages. Some of these advantages are as follows:
PHES can provide a large amount of flexible storage capacity and increase the reliability of electrical systems. PHES enables increased use of intermittent renewable resources such as wind and solar energy. PHES has the highest cycle efficiency with the range of 75-85% currently available [24]. PHES provides more output by supporting low-carbon production facilities. It also lowers emissions of greenhouse gases.

A standard PHES has two reservoirs connected with water conductors that transfer water from one to the other. Although it is a standard, there are different types of PHES applications. PHES classification is under three main groups: Pure or closed-cycle, on-stream integral or open cycle, and hybrid cycle [21]. Closed-cycle projects produce power only from water that has been previously pumped to an upper reservoir. There is no significant natural inflow of water to either reservoir [25]. The closed-cycle type is environmentally advantageous since it has no interference in the aquatic ecosystem. However, this type constitutes a challenge: Water losses due to

evaporation and leakage and finding a suitable location for constructing two reservoirs [26]. Open-cycle projects have either an upper or lower reservoir that is continuously connected to a naturally flowing water feature. Some open-cycle projects can have significant natural inflows to the upper reservoir, meaning that electricity may be generated without the requirement for pumping as in a storage hydropower facility without pumping ability [27]. An already existing dam can be converted into a PHES with additional pump-turbine equipment and a lower reservoir at the end of outflow. On-stream integral seems more convenient for a potential decrease in construction investment as the upper reservoir already exists [28]. In hybrid systems, PHES cooperates with discontinuous wind power plants and solar power plants. The primary purpose of hybrid systems is to meet the necessary pumping energy of PHES from wind and solar energy. Thus, profit increase is achieved by continuously utilizing intermittent renewable energy sources [21]. Figure 2. and Figure 3. show some examples of the closed pumped storage and the open pumped storage plants, respectively.

Figure 2. Goldisthal closed system PHES [29].

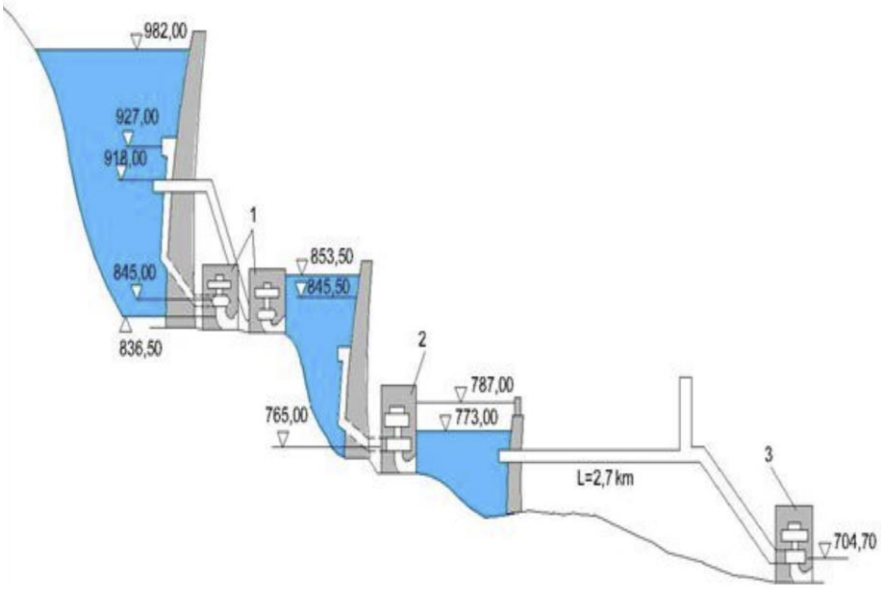

Figure 3. Azumi, Midano, and Sinrusima open system PHES located on the Azusa River [30].

3. GLOBAL PHES STATUS

The only large-scale, low-cost electricity storage solutions available today include pumped storage and traditional hydropower with reservoir storage [15]. Pumped storage represents about 2.2 % of all generation capacity in the United States, 18 % in Japan, and 19 % in Austria [31]. According to the end of 2017, the worldwide installed capacity stood at 161 GW at the IHA. With almost 15 GW of capacity added since 2010, China has contributed to much of the recent growth, driven by ambitious government goals for renewables [15].

In Europe, PHES capacity is expected to grow between 8- 11 GW by 2030, driven by the need for increased flexibility due to variable renewable energy growth. Most additions in Europe are expected in Switzerland, UK, Austria, Portugal, and France, while some prospective projects in Romania, Ireland, and Ukraine may also go ahead [25].

The majority of PHES additions outside China and Europe are projected to occur in the Asia-Pacific region, with some notable additions in the Middle East's non-traditional PHES markets. India, Indonesia, the Philippines, and Thailand are all in the pipeline for projects. The federal government in Australia has announced funding for various PHES schemes, particularly the 2 GW Snowy 2.0 project, to offset higher shares of variable renewable resources and the planned removal of existing coal generation from the baseload. Projects under construction are planned to add approximately 1 GW in Israel, Morocco, and Iran. Simultaneously, the UAE (United Arab Emirates) and Egypt have also recently announced plans to add PHES to their grids. In Figure 4. PHES power plants existing and planned around the world are shown on the map [31].

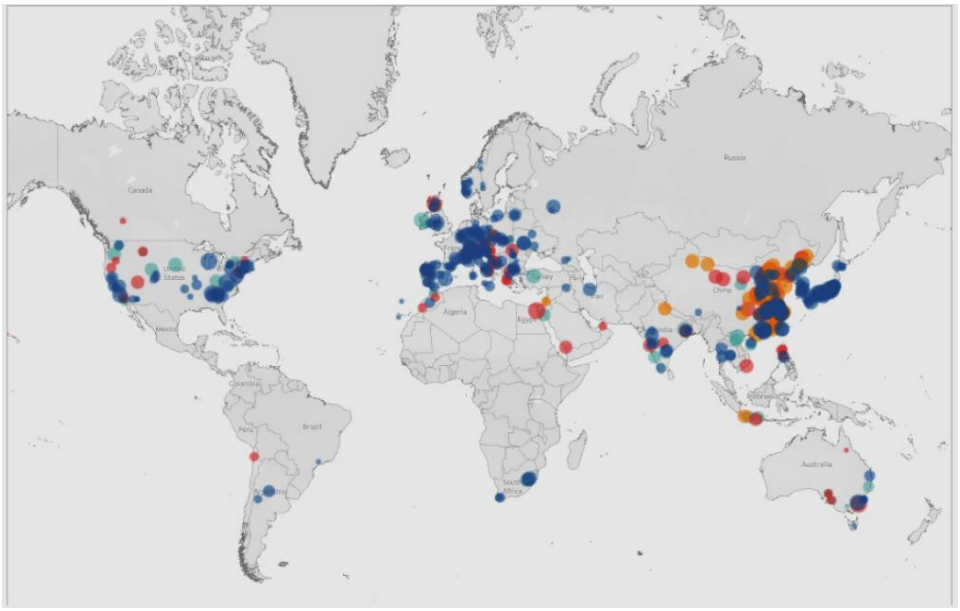

Figure 4. Existing and planned PHES projects worldwide according to IHA [31].

PHES currently accounts for over 94 % of installed global energy storage capacity and over 96 % of stored energy in grid-scale applications. During 2019, the installed capacity of pumped storage hydropower worldwide increased by 304 MW. According to IHA's Hydropower Status Report, the total installed pumped storage hydropower capacity was estimated at 158 GW in 2019. The pumped-storage hydroelectric capacity (GW) of the top 10 countries and the rest of the world in 2019 is shown in Figure 5 [11].

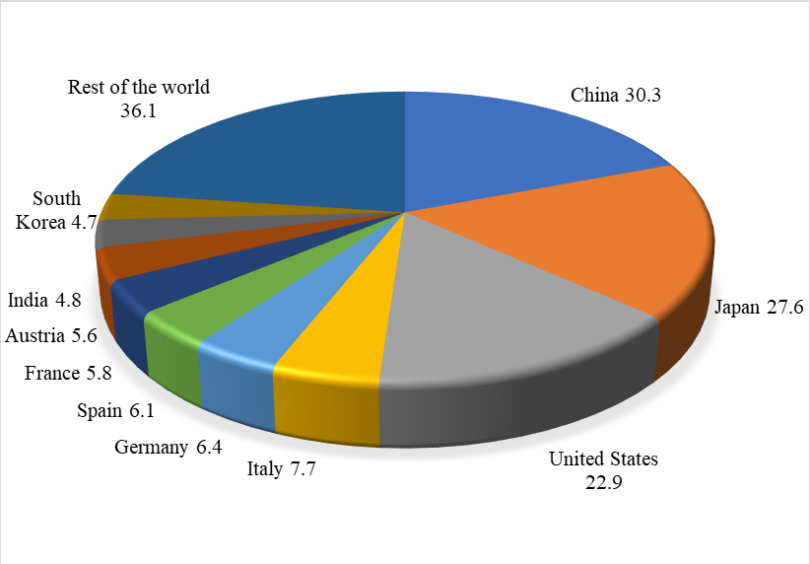

Figure 5. Pumped storage hydropower capacity (GW) of top 10 countries and rest of the world in 2019 [11].

Among the hydroelectricity producers, Japan is one of the largest electricity generators from hydropower. Hydroelectricity is Japan's primary renewable energy source, with an installed capacity of about 50 GW, and most of the Japanese hydroelectric power plants are pumped-storage plants. According to the Federation of Electric Power Companies of Japan (FEPC), nearly 93% of the principal hydroelectric power plants whose capacities are above 360 MW are pumped storage types [32]. Besides, the country is surrounded by seas, and Japan's topography is very suitable for the construction of storage facilities pumped by seawater. Okinawa is the world's first seawater pumped storage facility (Figure 6). The project is 26 m^3/s flow, height 136 m, and installed power 30 MW [33]. Because it is surrounded by sea on three sides, seawater pumped storage hydropower may be suitable also the Turkey [33].

Figure 6. Okinawa seawater PHES facility [33].

The world's largest PHES is Kanagawa in Japan, which was put into operation in 2005, shown in Figure 7. The facility has six pump-turbines, each with a power of 470 MW [34].

Figure 7. World's largest PHES facility, Kannagawa, Japan [34].

Ludington PHES was established in America between 1969 and 1973. It consists of a 34 m deep, 4 km long, and 6 km long reservoir on Lake Michigan's shores with a volume of 100 million m^3. The total installed power is 1872 MW, there are 6 reversible turbines, each with a capacity of 312 MW and 6 pipes of 340 m in length [34].

Figure 8. PHES facility in Ludington, USA [34].

4. PHES POTENTIAL IN TURKEY

Turkey has a significant hydropower capacity and potential. Increasing the security of supply, energy dependence, and reducing greenhouse gas emissions constitutes significant advantages of hydropower for the country. Moreover, Turkey is situated through a mountainous topography (average altitude = 1132 m) and owns an annual average run off the value of 186 billion m^3, favoring ideal locations for hydropower development [35]. The first nuclear power plant (NPP) of Turkey, Akkuyu NPP, is known to start generating by 2023. Although this nuclear facility is controversial in terms of environmental and economic concerns, it is essential to develop and diversify Turkey's energy resources. Due to these advantages, Turkey has a high potential for PHES applications. The variation of electrical energy generation by years is given in Figure 9 [36].

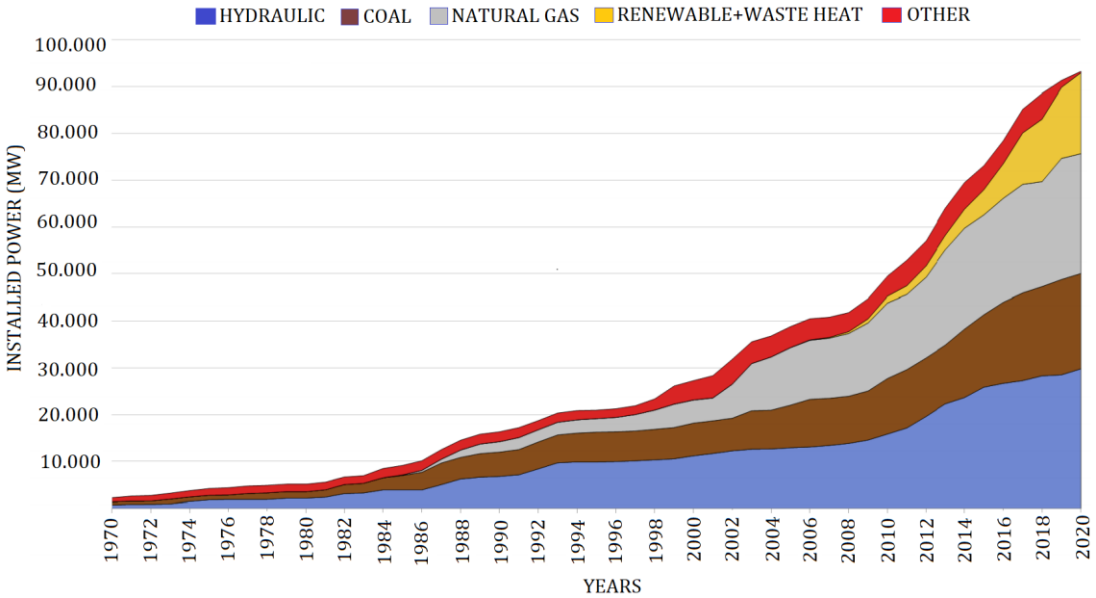

Figure 9. Electric energy production between 1970-2019 [36].

Turkey's installed capacity reached 93,207 MW by the end of 2019. Natural gas power is plants have a share of 25,634 MW, coal 11,313 MW, hydropower 29,789 MW, geothermal 1,514 MW, wind 8,077, and solar 6,361. Figure 10. Shows the distribution of resources of Turkey's installed capacity [36].

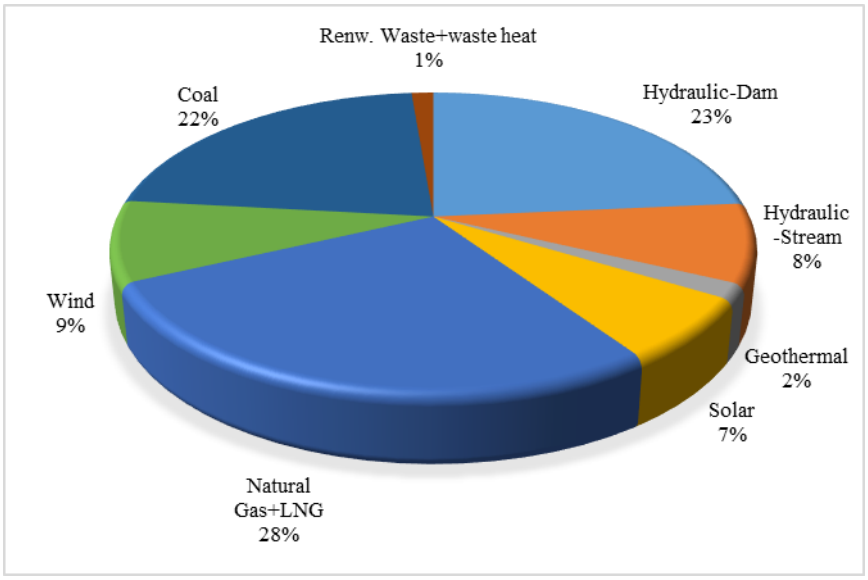

Figure 10. Distribution of installed capacity by resources in 2019 [33].

In Turkey, although PHES power plant works were started for the first time in 2005 by the Electrical Works Study Administration (EIE) General Directorate, there is no power plant established yet [37]. Many feasibility studies have been conducted in Turkey since 2005. Possible PHES projects specified in the Strategy Plan of the EIE General Directorate are shown in Table 2. below [30].

Table 2. Information on the facilities proposed by EIE [30].

Project Name	Location	Installed Capacity (MW)	Project Discharge (m^3/sec)	Gross Head (m)
Kargı PSH	Ankara	1000	238	496
Sarıyar PSH	Ankara	1000	270	434
Gökçekaya PSH	Eskişehir	1600	193	962
İznik-I PSH	Bursa	1500	687	255
İznik-I PSH	Bursa	500	221	263
Yalova PSH	Yalova	500	147	400
Demirköprü	Manisa	300	166	213
Adıgüzel	Denizli	1000	484	242
Burdur Gölü PSH	Burdur	1000	316	370
Eğirdir Gölü PSH	Isparta	1000	175	672
Karacaören-II PSH	Burdur	1000	190	615
Oymapınar PSH	Antalya	500	156	372
Aslantaş PSH	Osmaniye	500	379	154
Bayramhacılı PSH	Kayseri	1000	720	161
Yamula PSH	Kayseri	500	228	260
Hasan Uğurlu PSH	Samsun	1000	204	570

According to IHA data, it has been declared that only one PHES power plant will be established, and it is predicted to be completed in 2025. This power plant announced is the Gökçekaya PHES power plant. The power plant has a fixed speed, a lower and upper reservoir height difference of 389 m, a capacity of 1400 MW, and an energy storage capacity of 234.18 GWh [38].

According to the Anatolia agency, General Electricity Company (GE) has said that 1000 MW pumped storage hydroelectric power plant to be established in Isparta-Eğirdir lake, Turkey, is significant renewable energy conversion. The company stated that 4 special 250 MW bi-directional turbines and equipment would be used in the plant. It is expected that the construction of the power plant will begin by January 2022 [39].

Figure 11. Eğirdir Lake [40].

The researchers reported that Turkey's realizable PHES potential was estimated as 19.63 TWh, which was about 68% of total Europe potential (Figure 12). They analyzed the PHES potential according to some different

scenarios. They concluded PHES potential the countries with the largest were Turkey, Albania, Spain, Switzerland, Norway, Italy, and France [41].

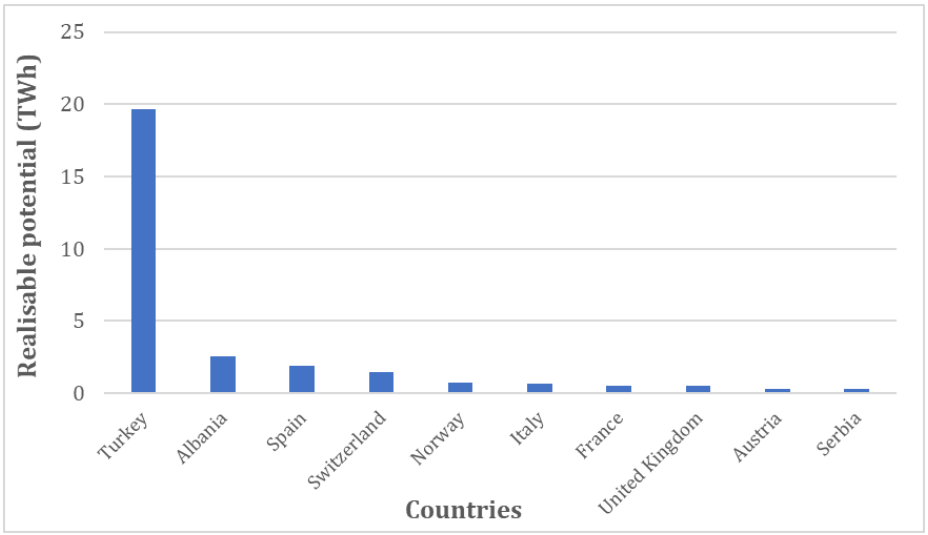

Figure 12. Estimated realizable PHES potential at 20 km distance (Reproduced from Ref. [41]).

5. CONCLUSIONS

The status of PHES in Turkey's energy policies and its standing in the existing HEPP has been examined. PHES makes the energy supply reliable by integrating with intermittent renewable energy sources and nuclear power plants; those systems respond quickly to high capacity energy storage potential and peak demand. The investment required per unit of energy in hydroelectric systems with pumped storage is high. Pumped storage systems should be made attractive with government support and new laws and incentives. Turkey has got the massive potential for PHES applications. Also, considering the installed hydropower plants, PHES systems can be a strong alternative for supporting the country's energy needs. As far as we know, it is seen that feasibility studies are carried out only for Eskişehir Gökçekaya PHES in Turkey. It is thought that taking more concrete steps in this area will be beneficial for our rapidly developing country. It must be given critical importance to PHES to achieve sustainable economic growth, energy security and reduce foreign dependency on energy. It is predicted that the PHES systems discussed in this study can significantly benefit Turkey's energy reliability and sustainability.

REFERENCES

[1] El-Emam, R., Analysis, Assessment and Optimization of Integrated Solar Energy Systems for Multigeneration, *PhD Thesis, University of Ontario Institute of Technology*, 2014.

[2] Olhoff, A., Rogelj, J., Kuramochi, T. & Höhne N. Emissions Gap Report 2019, United Nations Environment Programme, 109p, 2019.

[3] Kusakana, K., Feasibility Analysis of River Off-Grid Hydrokinetic Systems with Pumped Hydro Storage in Rural Applications, *Energy Conversion and Management*, **96**, 352–362, 2015.

[4] Karataş, M., Investigation of Pumped Hydro Stotage Application in Isparta Province, *Master Thesis, Isparta University of Applied Sciences*, 59p, 2019 (In Turkish).

[5] Baumann, M., Weil, M., Peters, J.F., Chibeles-Martins, N. & Moniz, A.B. A review of multi-criteria decision making approaches for evaluating energy storage systems for grid applications, *Renewable and Sustainable Energy Reviews*, **107**, 516-534, 2019.

[6] Rehman, S., Al-Hadhrami L.M. & Alam M.M. Pumped hydro energy storage system: A technological review, *Renewable and Sustainable Energy Reviews*, **44**, 586–598, 2015.

[7] DOE Global Energy Storage Database, 2014.

[8] Üstündağ, O,. Utilization Of Realistic Pumped Hydroelectric Storage System Model For Various Optimal Short Term Control Strategies, *Master Thesis, Middle East Technical University*, 81p, 2019.

[9] Gonzalo, E.A., Operation of Pumped Storage Hydropower Plants Through Optimization for Power Systems, *Energy*, **202**, 117797, 2020.

[10] Lu, B., Stocks, M., Blakers, A. & Anderson, K. Geographic Information System Algorithms to Locate Prospective Sites for Pumped Hydro Energy Storage, *Applied Energy*, **222**, 300–312, 2018.

[11] Hydropower IHA. Status report 2020: sector trends and insights, London, 2020.

[12] Kocaman, A.S., Modi, V., Value of Pumped Hydro Storage in a Hybrid Energy Generation and Allocation System, *Applied Energy*, **205**, 1202–1215, 2017.

[13] Koko, S.P., Kusakana, K. & Vermaak, H.J. Optimal Power Dispatch of a Grid-Interactive Micro-Hydrokinetic -Pumped Hydro Storage System, *Journal of Energy Storage*, **17**, 63–72, 2018.

[14] Lu, B., Stocks, M., Blakers A. & Anderson K. Geographic Information System Algorithms to Locate Prospective Sites for Pumped Hydro Energy Storage, *Applied Energy*, **222**, 300–312, 2018.

[15] Kizilkan, Ö., Korkmaz, E. & Karataş, M. A Feasibility Study of Pumped Hydro Storage Facility for Isparta, Turkey, *11th International Exergy, Energy, and Environment Symposium (IEEES-11)*, China, 2019.

[16] Barbaros, E., Aydın, İsmail. & Celebioğlu, Kutay. Feasibility of Pumped Storage Hydropower with Existing Pricing Policy in Turkey, *Renewable and Sustainable Energy Reviews*, **136**, 110449,2021.

[17] Dursun, Bahtiyar., Alboyaci, B., The Contribution of Wind-Hydro Pumped Storage Systems in Meeting Turkey's Electric Energy Demand, *Renewable and Sustainable Energy Reviews*, **14**, 1979-1988, 2010.

[18] Melikoglu, M., Pumped hydroelectric energy storage: Analysing global development and assessing potential applications in Turkey based on Vision 2023 hydroelectricity wind and solar energy targets, *Renewable and Sustainable Energy Reviews*, **72**, 146-153, 2017.

[19] Ghorbani, N., Makian, H. & Breyer, C. A GIS-Based Method to Identify Potential Sites for Pumped Hydro Energy Storage - Case of Iran, *Energy*, **169**, 854–867, 2019.

[20] Luo, X., Wang, J., Dooner, M. & Clarke, J. Overview of Current Development in Electrical Energy Storage Technologies and the Application Potential in Power System Operation, *Applied Energy*, **137**, 511–536, 2015.

[21] Barbaros, E., Feasibility Of Pumped-Storage Hydraulic Systems Based On Hourly Variation Of Electricity Prices, *Master Thesis, Middle East Technical University*, 130p, 2019.

[22] Nielsen, T.K, Hydropower and Pumped Storage, In The World Scientific Handbook of Energy, 275–306, 2013.

[23] Japan International Cooperation Agency (JICA), Final Report on Feasibility Study on Adjustable Speed Pumped Storage Generation Technology, Japan, 2012.

[24] Cavazzini, G., Pérez-Díaz, J.I. & Blázquez F. Pumped-Storage Hydropower Plants: The New Generation, *In World Scientific Series in Current Energy Issues*, **4,** 27–80, 2017.

[25] The world's water battery: Pumped hydropower storage and the clean energy transition, IHA working paper, 2018.

[26] US Army Corps of Engineers, Technical Analysis of Pumped Storage and Integration with Wind Power in the Pacific Northwest Final Report, Washington, 2009.

[27] The world's water battery: Pumped hydropower storage and the clean energy transition, IHA working paper, 2018.

[28] Breeze, P., Pumped Storage Hydropower, In Power System Energy Storage Technologies, *Elsevier*, 13–22, 2018.

[29] https://www.vgb.org/en/hv_11_praesentationen-dfid-39900.html (Accessible date: 31.12.2020).

[30] Sertkaya, A.A., Saraç, M. & Omar, M.A. The Importance of Pumped Storage Hydro-Electric Power Plants for Turkey, *Gazi Journal of Engineering Science*, **1/3,** 369-382, 2015 (In Turkish).

[31] https://www.hydropower.org/publications/2018-hydropowerstatus-report (Accessible date: 28.12.2020).

[32] https://www.fepc.or.jp/english/energy_electricity/location/hydroelectric/index.html (Accessible date: 31.12.2010).

[33] http://www.yegm.gov.tr/duyurular_haberler/phes_calistay.aspx. (Accessible date: 28.12.2020).

[34] Ayder, D. E., Hydroelectric Power Plants with Pumped Storage, Technical Report, 22, 2015.

[35] Kucukali S., Finding the Most Suitable Existing Hydropower Reservoirs for the Development of Pumped-Storage Schemes: An integrated approach, *Renewable and Sustainable Energy Reviews*, **37,** 502–508, 2014.

[36] https://www.emo.org.tr/genel/bizden_detay.php?kod = 88369 (Accessible date: 27.12.2020).

[37] Karaçay, P., Pumped Storage Power Plant and Its' Status in Turkey, *Master Thesis, Istanbul Technical University*, 53p, 2010 (In Turkish).

[38] https://www.hydropower.org/hydropower-pumped-storage-tool (Accessible date: 26.12.2020).

[39]https://www.aa.com.tr/tr/ekonomi/turkiyenin-enerjisine-1-5-milyar-dolarlik-yatirim/1798440 (Accessible date: 29.12.2020).

[40] Aktaş, S., Egirdir Lake Nutrition Basin and Future of the Lake, *Master Thesis, Suleyman Demirel University*, 72p, 2018 (In Turkish).

[41] Gutiérrez, M.G., Arántegui, R.L., Assessment of the European Potential for Pumped Hydropower Energy Storage Based on Two Existing Reservoirs, *Renewable Energy,* **75**, 856-868, 2015.

INDIGENOUS OIL YIELDING PLANTS AS ENERGY SOURCES IN PAKISTAN

Muhammad ZAFAR[*], Mushtaq AHMAD[*], Ömer KILIÇ[**], Shazia SULTANA[*], Javaria ZAHOOR[*], Erkan YILMAZ[**]

[*] Department of Plant Sciences, Quaid-I-Azam University, Islamabad, Pakistan
[**] Adıyaman University, Faculty of Pharmacy, Department of Basic Science of Pharmacy, Adıyaman, Turkey
*Corresponding author Email: zafar@qau.edu.pk

ABSTRACT

Pakistan is a country which lies in between tropic of Capricorn and tropic of Cancer with diverse climatic conditions. Pakistan has rich biodiversity of oil yielding plants; some cultivated by local farmers while majority are wildly distributed in various zones of Pakistan. Among these oil yielding plants there is rich diversity of biodiesel yielding wild resources e.g. pongame, castor beans, mustard etc. Current energy crises throughout the world generally and Pakistan particularly need the energy from renewable sources like biodiesel. Biodiesel is an emerging solution for the present day concerns about rising oil prices and depletion of fossil fuel resources throughout the world. In current scenario due to shortage of energy resources, biodiesel is very good option for energy security in Pakistan. There are large arable lands with good climatic conditions for large biomass production of biodiesel yielding species. In this project we have identified rich diversity of oil yielding plants with biodiesel potential are identified based on biodiversity assessment, biodiesel production through transesterfication and fuel properties comparison with ASTM standards. This study will provide pictorials of oil yielding plants, biodiesel samples, byproducts and their botanical aspects for wider interest which might be adopted by other countries to utilize these natural resources for biomass energy.

Keywords: Oil yielding plants, Pakistan, biodiesel, biomass energy.

RF SPUTTERED TIO_2 THIN FILMS WITH VARIOUS DEPOSITION CONDITIONS FOR TRIBOELECTRIC FRICTION LAYER

Gizem DURAK YÜZÜAK, Seray ÖZKAN, Ercüment YÜZÜAK
Recep Tayyip Erdoğan University, Department of Energy Systems Engineering, Rize/Turkey
Email: gizemyuzuak@erdogan.edu.tr, serayozkan79@gmail.com, ercument.yuzuak@erdogan.edu.tr

ABSTRACT

During the last decade, with the incredible presence of electronic devices in our daily lives, alternative solutions to unravel the energy requirement have begun to be assembled. Triboelectric nanogenerators (TENGs) emerge to transform energy from the existing conditions into electricity as an exceptional energy harvesting technology. TENGs maintains several advantages such as cost-smart, energy-saving, and adaptability with material choices, which originated in the coupling of working mechanisms between triboelectrification and electrostatic induction.

Instead of using unpractical polymers for long-term usage in severe conditions as a friction layer in TENGs using durable TiO_2 thin films are one of the suitable choices through semiconductor materials. With good chemical and mechanical stability, TiO_2 films are the most widely used oxide for electronic applications owing to low cost and high activity. Mainly, the low-temperature phase - anatase exhibits different surface charge density properties with varying surface modifications to affect TENGs performance.

TiO_2 films deposited on Si(100) substrate by using the RF magnetron sputtering method with various working powers and partial O_2 pressures. To manage the triboelectric performance of the TiO_2 films, structural and electrical characterizations were accomplished with X-ray diffraction, scanning electron microscopy, semi-logarithmic current-voltage, and frequency-dependent capacitance measurements. The variations in the working power and partial O_2 pressures affect the crystal and surface structure under sputtering conditions caused by development in the particle distributions. The surface charge density characteristics received by variation in the working power and partial O_2 pressures concerned from the frequency-dependent capacitance measurements. The maximum capacitance value at very low frequencies regarded as a further contribution for the triboelectric is quite close to the natural oscillation frequency due to the coupling of triboelectrification and electrostatic induction.

Keywords: Triboelectric Effect, TiO_2, Triboelectric Nanogenerator, Friction Layer

ACKNOWLEDGMENTS

This work was supported by the Scientific and Technological Research Council of Turkey (TÜBİTAK) under the grant number of 119M972.

THERMOELECTRIC THIN FILM MODULES

Seray ÖZKAN, Gizem DURAK YÜZÜAK, Ercüment YÜZÜAK
Recep Tayyip Erdoğan University, Department of Energy Systems Engineering, Rize/Turkey
Email: serayozkan79@gmail.com, gizemyuzuak@erdogan.edu.tr, ercument.yuzuak@erdogan.edu.tr

ABSTRACT

Energy is undoubtedly one of our most important needs, whose consumption is constantly increasing and will continue to increase in the future. Developing technology and increasing the number of people cause an increase in energy needs. Many methods are used to handle the energy need. One of the most important factors in handling the required energy is to provide high efficiency at a low cost. In this study, to overcome these energy problems, the development of thermoelectric thin-film modules will be studied.

The thermoelectric effect is determined by measuring the electrical properties resulting from the temperature difference between the two different types of materials. When a current is passed through a circuit composed of two different metals connected, depending on the direction of the current, heat is absorbed from one of the metals and released from another.

In engines, industrial processes, various boilers, and many other energy-consuming devices, the waste heat released into the environment can be recycled and reused as clean energy. If waste heat recovery and management are done correctly, more efficient and cheaper operation of systems in companies can be used to reduce operating costs and greenhouse gas emissions.

For this purpose, thin films were grown on glass, Kapton tape and Si (100) substrates by using two different BiSeTe / BiSbTe alloy materials which are placed in industrial Peltier as a n and p-type semiconductor. The thermal evaporation method has been used to develop thermoelectric modules nanoscale form. The thermoelectric properties of n, p, and n-p cells obtained during this study were investigated by forming certain temperature gradients on them by making serial connections. To find the temperature gradient, data, and images, a thermal camera is used.

Keywords: Termoelectric Effect, BiTe, Seebeck

COOLING TECHNOLOGIES

EXPERIMENTAL INVESTIGATION OF THE PULSATING HEAT PIPES HAVING LARGER FLOW SECTIONS IN THE EVAPORATOR REGION

Ayse CANDERE*, Burak MARKAL,Orhan AYDIN* , Mete AVCI****
*Karadeniz Technical University, Department of Mechanical Engineering, Trabzon/Turkey
Email: aysecandan@ktu.edu.tr, oydin@ktu.edu.tr
**Recep Tayyip Erdogan University, Department of Mechanical Engineering, Rize/Turkey
burak.markal@erdogan.edu.tr, mete.avci@erdogan.edu.tr

ABSTRACT

In this study, influence of the inclination angle on thermal performance and flow characteristics of a flat plate closed-loop pulsating heat pipe is investigated experimentally. The heat pipe has a novel geometry including, larger flow sections in the evaporator region (in the one branch of the relevant U-turns), which also provides a variation of the channel widths in the relevant region. Ethanol is used as the working fluid. Experiments are carried out for different inclination angles (-90°, 0°, 30°, 60° and 90°) and thermal powers (5W – 60W) at a constant filling ratio of 50%. A high-speed camera is used to obtain the images of pulsating flow in the heat pipe. At the positions including positive inclination angles (30º, 60º and 90º), it is observed that thermal resistance significantly reduces with the increasing thermal power. On the other hand, at the top heating mode (-90°) and the horizontal orientation (0°), the thermal resistance showed a horizontal trend with increasing thermal power. The relevant results are also supported by flow visualizations.

Keywords: Pulsating heat pipe, Thermal performance, Flow visualization.

1. INTRODUCTION

With the development of manufacturing technology, the size of electronic devices increasingly shrinks, which causing the release of high amounts of heat, and thus overheating problems. Therefore, the number of studies investigating alternative thermal management methods for cooling electronic devices increases. Pulsating heat pipes (PHPs) are passive cooling devices operating depending on the thermally induced oscillations. Unlike the active cooling technologies, the heat pipes do not require any mechanical device (a pump and or a fan) for operation. For this reason, pulsating heat pipes are one of the most suitable thermal control tools for cooling electronic components.

The working principle of PHP can be summarized as follows: during the operation, continuous condensation of fluid in the condenser and continuous evaporation of it in the evaporator generates a pulsating/unbalanced vapor pressure field. This situation ensures liquid and vapor motion between adjacent channels. Therefore, heat is transferred from the evaporator to the condenser section due to the oscillating motion engendered by the periodic phase variation of the fluid. Generally, PHP is created by bending a long capillary tube (in the form of multiple U loops) or the engraving meandering channels on a flat plate. Also, two different flow loop configurations have used in PHPs as closed and open ones. In some studies (e.g., Chien et al. [1]), it is explained that closed types have better heat transfer merits due to flow circulation. Also, PHP created by engraving of the surface of a flat plate is more advantageous as the sharp corners of the channels create a capillary effect [2].

It has been shown by previous researches that the flow regimes and thermal performance in PHPs are affected by various experimental parameters such as internal diameter, channel shape, filling ratio, heat input, working fluid, orientation and total number of turns. Khandekar et al. [3] studied the rectangular and circular cross-section PHPs with a hydraulic diameter of about 2 mm. The filling ratio, heat load and orientation were changed as parameters. Charoensawan et al. [4] investigated the effects of gravity, number of turns and thermophysical properties of working fluids on the thermal performance of closed type pulsating heat pipes (CLPHPs). The heat

pipes were made of copper tubes with an inner diameter of 2 mm and 1 mm. The fluids were water, ethanol and R-123. The experimental results showed that the parameters mentioned above, have quite essential effects on the performance of CLPHPs. Xu et al. [5] performed a parametrical study to see the effetcs of fluid type (HFC - 134a and butane), orientation, condenser area on the performance. They pointed that the working fluid has an aiding effect on the thermal performace. Borgmeyer and Ma [6] experimentally focused on the motion of the liquid-vapor interface under different inclination angles. They found that the amplitude of the oscillating motion increases when the position is changed from horizontal to vertical. Yang. et al. [2] examined flat plate CLPHPs with 1x1 mm^2 and 2x2 mm^2 channel cross-sectionals. They stated that the thermosiphon effect was appeared at low filling ratios (< 20%) for vertical position. On the other hand, PHPs operated in every position between 40% and 70% filling ratio, and so, the effect of gravity was relatively insignificant. Lips et al. [7] performed several experiments on two PHPs with different tube diameters, number of turns, and working fluids. It was concluded that PHP performance depended on orientation in low heat fluxes, while it was independent of orientation in high heat fluxes.

Chien et al. [1] designed a FP-CLPHP having an asymmetric channel with dimensions of 2 mm in height and 1 mm in width to create additional unbalancing capillary force, and also, compared its thermal performance against the uniform channel (2 mm x 2 mm). Experiments were conducted at different filling ratios ranging between 40-70% and at inclination angles ranging between 0−90º. They concluded that the uniform one did not operate in a horizontal position, while the non-uniform PHP worked under a sufficient filling ratio (≥ %60). The role of uniform and alternating tube diameters were experimentally studied by Tseng et al. [8] for vertical and horizontal positions. Water, methanol and HFE-7000 were selected as the working fluids. They reported that the alternating configuration had smaller thermal resistance in the horizontal position compared to the uniform one. A similar kind of study was performed by Yang et al. [9] for a PHP with alternate microchannel widths (0.5 mm and 0.3 mm) for two different working fluids as methanol and water. Kwon and Kim [10] examined the asymmetric ratio influence on the heat transport in a flat plate pulsating micro heat pipe.

As it is seen from the above paragraphs, the subject of the heat pipe is one of the most attractive research fields in recent years. In this respect, the objective of this study is to experimentally research the influence of inclination angle on thermal characteristics and flow behavior of a novel PHP having larger flow sections in the evaporator region (in the one branch of the relevant U-turns).

2. EXPERIMENTAL SETUP AND DATA REDUCTION

2.1. Experimental Setup

The schematic of the experimental setup is given in Fig. 1. It includes test section, cooling water loop for the condenser, heating section, flow visualization and data acquisition section.

The test section consists of teflon chassis (PTFE, Polytetrafluoroethylene), heat pipe, heater plate and heat sink. Teflon chassis is designed to connect the heat pipe, the heater plate and the heat sink. The FP-CLPHP is made of copper plate with a total size of 116 mm x 55.5 mm x 4mm (having 16 parallel channels or 8 turns). The schematic picture representing the channel width values of the heat pipe is given in Fig. 2. The height value of the channels is kept constant as 2 mm. The top surface of the heat pipe is covered with a glass plate (thickness of 6 mm). An o-ring is utilized in order to create a sealed volume in the heat pipe. The supporting frame made of brass is placed on the glass and attached to the heat pipe with bolts. Channels are engraved on the back surface of the heat pipe to place the thermocouples in the evaporator, adiabatic and condenser sections. The heater plate is made of copper material with dimensions of 20 mm x 40 mm x 9 mm. The evaporator section of the heat pipe is heated with two cartridge heaters put into the heater block. The electrical supply of the cartridge heaters is provided by the AC power source. The heat sink with the total size of 40 mm x 40 mm x 12 mm is made of two parts. The upper part of the heat sink is made of 2 mm-thick copper plate. The lower part of the heat sink is the 10 mm-thick polycarbonate plate (including meandering passages). The cooling water loop is associated with the heat sink. The cooling water loop comprises a micropump integrated with a digital pump driver, a temperature bath, a flow controller and a manometer. Via a micro gear pump, the cooling loop provides the circulation of the cooling water with 20ºC and 20 ml/min. The flow controller device controls the flow rate of water. The digital

manometer is placed at the outlet of the micro gear pump for the reading of system pressure in the circulation loop. The flow visualization section in the experimental setup consists of a high-speed camera and a light source. Temperature measurements in the test area are recorded via a computer and data acquisition system.

2.2. Data Reduction

Thermal resistance (R_{th}) is calculated to determine the performance of the heat pipe at different inclination angles.

$$R_{th} = \frac{T_e - T_c}{Q} \tag{1}$$

In the equation, Te and Tc are the average values for the temperature in the evaporator and condenser zones, respectively; Q, shows the mean value of the heat input applied by the power supply to the evaporator (Q_i) and the heat removed to the heat sink (Q_o).

The heat value removed by the heat sink in the condenser section is calculated as follows:

$$Q_o = \dot{m} c_p \left(T_{out} - T_{in} \right) \tag{2}$$

In the equation, T shows the temperature (the subscripts of in and out are for inlet and outlet of cooling water), C_p means the specific heat and $\dot{m}$ is used to represent the mass flow rate of the water. Also, according to the uncertainty approach (Kline and McClintock [11]), the relevant values for the thermal resistance are calculated as 4.20% − 5.81%.

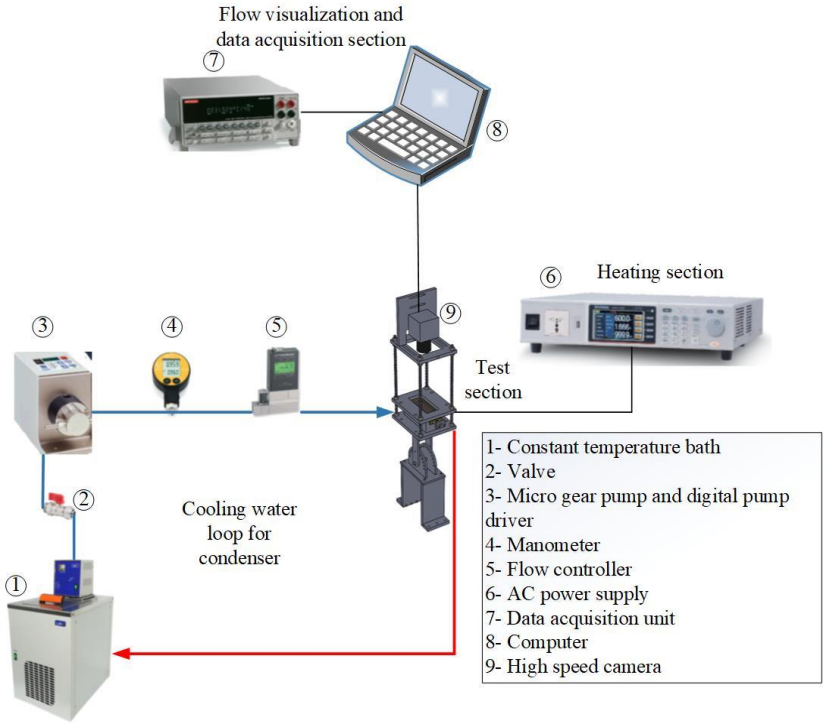

Figure 1. The schematic of the experimental setup

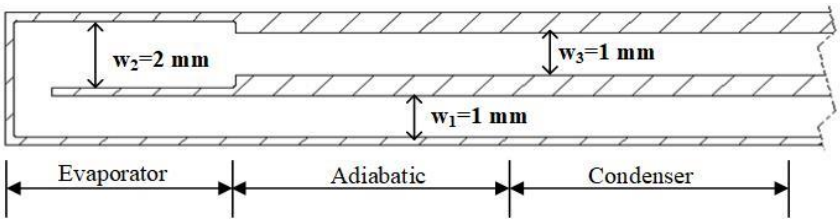

Figure 2. The schematic picture representing the channel width values of the heat pipe

4. RESULTS AND DISCUSSIONS

In this experimental study, effect of the inclination angle on thermal performance and flow characteristics of a FP-CLPHP is examined. Ethanol has been used as the working fluid and experiments have been carried out at 50% filling ratio under different heat loads (there is a temperature limitation as 110 °C for evaporator temperature).

In Fig. 3, the variation of the thermal resistance with the applied heat load is given as a function of the inclination angle. The thermal resistance is significantly reduced with the heat load for the inclination angles of 30, 60 and 90°, and, in this angle range, the thermal resistance is nearly independent from the orientation. In the relevant angle range, the reason of decreasing trend of resistance with heating power can be explained by the increase in the circulation speed and oscillation amplitudes. Also, as it can be seen from the relevant figure, in the input power range of 5−15 W, the thermal resistance is relatively higher since the oscillation motion is not yet active (the startup phenomenon of the PHP does not actualize, yet.). However, as the heating power continues to increase, oscillation amplitudes begin to increase. Also, the flow images are included in order to better understand the physical mechanism in the heat pipe. Figures 4a, b and c are given as the flow images with different input powers (20, 45 and 60 W) at the inclination of 90°. As shown in Fig. 4a, at the input power of 20 W, the flow in the heat pipe has low oscillation amplitude and frequency, in which case, most of the channels have a passive character. In the evaporator zone, the vapor plugs move towards the larger sections. In Fig. 4b, it is observed that as the input power value increases, the number of vapor plugs and velocity of the flow increase. The liquid slugs and the vapor plugs motion are actively observed in all passages. For the evaporator side, the vaporization rate is high for higher input powers (see Fig. 4c), the bubble population and the contribution of nucleate boiling increase (especially in the larger passage). The complexity of the flow field and the pumping power are increased depending on the higher heat loads.

Differently from the angles of 30, 60 and 90º, in the horizontal (0º) and top heating modes (−90º) , the trend of the thermal resistance curve has a horizontal character despite increasing heat input. This shows unsuccessful startup, or in other words, failure of the heat pipe. The relevant phenomenon is also observed during the visualization tests. Therefore, it is understood that, in the relevant conditions (for the range of the present study) gravity is an essential factor in the operation of the heat pipe.

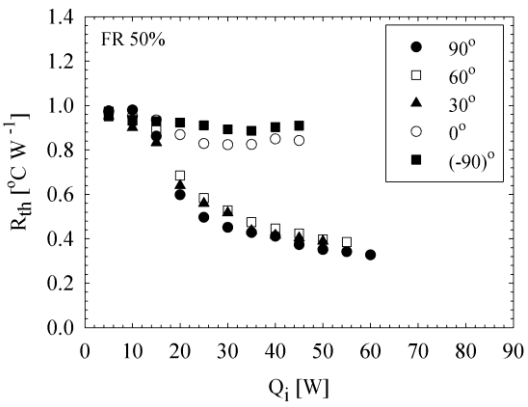

Figure 3. The variation of the thermal resistance with the heat input for different inclination angles

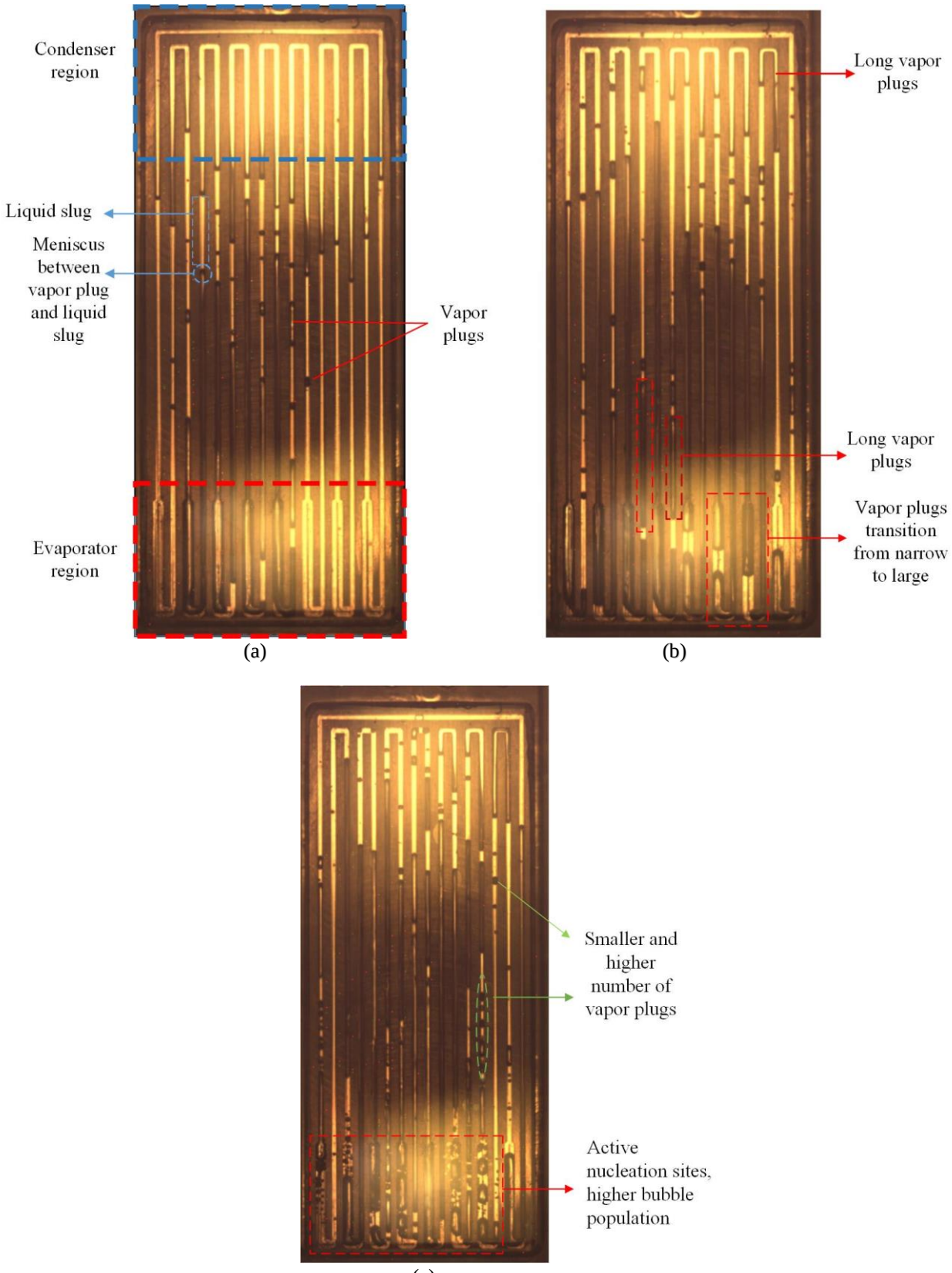

Figure 4. Photographs for PHP at the conditions: 90°, 20 W (a), 45 W (b) and 60 W (c).

5. CONCLUSIONS

In this paper, the influence of the inclination angle on the flat plate closed-loop pulsating heat pipe (FP-CLPHP) performance is presented. The FP-CLPHP is made of copper plate with 8 turns (16 parallel channels). The heat pipe is designed to be included larger flow passages in the evaporator section (in the one branch of the relevant U-turns). The following results are obtained:

- The thermal resistance is significantly reduced with the heat load for the inclination angles of 30, 60 and 90°, and in this angle range, the thermal resistance is nearly independent from the orientation.
- In the input power range of 5−15 W, the thermal resistance is relatively higher since the oscillation motion is not yet active (the startup phenomenon of the PHP does not actualize, yet.)
- Differently from the angles of 30, 60 and 90º, in the horizontal (0º) and top heating modes (−90º) , the trend of the thermal resistance curve has a horizontal character in spite of increasing heat input. This shows the failure of the heat pipe. Therefore, it is understood that, in the relevant conditions (for the range of the present study) gravity is an important factor in the operation of the heat pipe.

ACKNOWLEDGEMENT

This study is supported by The Scientific and Technological Research Council of Turkey (TUBITAK) with the project number of 217M341.

REFERENCES

[1] Chien, K., Lin, Y., Chen, Y., Yang, K. & Wang, C. A Novel Design of Pulsating Heat Pipe with Fewer Turns Applicable to All Orientations, *International Journal of Heat and Mass Transfer*, **55**, 5722–5728, 2012.

[2] Yang, H., Khandekar, S. & Groll M. Performance Characteristics of Pulsating Heat Pipes as Integral Thermal Spreaders, *International Journal of Thermal Sciences*, **48**, 815–824, 2009.

[3] Khandekar, S., Schneider, M., Schafer, P., Kulenovic, R. & Groll, M. Thermofluid Dynamics Study of Flat-Plate Closed-Loop Pulsating Heat Pipes, *Microscale Thermophysical Engineering*, **6**, 303-317, 2002.

[4] Charoensawan, P., Khandekar, S., Groll, M. & Terdtoon, P. Closed Loop Pulsating Heat Pipes Part A: Parametric Experimental Investigations, *Appl. Therm. Eng.*, **23**, 2009–2020, 2003.

[5] Xu, G., Liang, S. & Vogel, M. Thermal Characterization of Pulsating Heat Pipes, *10th Intersociety Conference on Phenomena in Electronics Systems,* 552-556, 2006.

[6] Borgmeyer, B. & Ma, H.B. Experimental Investigation of Oscillating Motions in a Flat Plate Pulsating Heat Pipe, *Journal of Thermophysics and Heat Transfer*, **21**(2), 405-409, 2007.

[7] Lips, S., Bensalem, A., Bertin, Y., Ayel, V., Romestant, C. & Bonjour, J. Experimental Evidences of Distinct Heat Transfer Regimes in Pulsating Heat Pipes, *Applied Thermal Engineering*, **30**, 900–907, 2010.

[8] Tseng, C., Yang, K., Chien, K., Jeng, M. & Wang, C. Investigation of the Performance of Pulsating Heat Pipe Subject to Uniform/Alternating Tube Diameters, *Experimental Thermal and Fluid Science*, **54,** 85–92, 2014.

[9] Yang, K., Cheng, Y., Liu, M. & Shyu, J. Micro Pulsating Heat Pipes with Alternate Microchannel Widths, *Applied Thermal Engineering***, 83**, 131-138, 2015.

[10] Kwon, G. H. & Kim, S.J. Experimental Investigation on the Thermal Performance of a Micro Pulsating Heat Pipe with a Dual-Diameter Channel, *International Journal of Heat and Mass Transfer*, **89**, 817–828, 2015.

[11] Kline, S.J. & McClintock, F.A. Describing Uncertainties in Single-Sample Experiments. *Mech. Eng*. **75**, 3–8, 1953.

HEAT TRANSFER AND THERMAL MANAGEMENT OF LITHIUM-ION BATTERY PACK SYSTEM WITH FORCED AIR CONVECTION

İsmail HOŞ*, Göker TÜRKAKAR**
*Zonguldak Bulent Ecevit University, Department of Mechanical Engineering, Zonguldak/Turkey
Email: ismaill.hoss@gmail.com
**Zonguldak Bulent Ecevit University, Department of Mechanical Engineering, Zonguldak/Turkey
Email: turkakar@beun.edu.tr

ABSTRACT

Studies on battery cooling systems gain momentum every new year owing to its limited operating temperature range. As lithium-ion batteries are one of the critical components of electric vehicles, researchers have recently focused on them. A two-dimensional analysis of a battery pack has been carried out. A hydrodynamic and thermal study has been conducted for an air-cooled 6x6 battery pack (36 batteries in total) system. The system is analyzed using the ANSYS / FLUENT software for aligned and staggered battery arrangements for steady-state conditions. The system's temperature distribution and pressure drop are scrutinized for the mean air velocities of 0.5 m/s, 0.75 m/s, and 1 m/s for the aligned order. Same analyses have been executed for the staggered order, with the help of keeping the mass flow rate constant. The battery pack is composed of Lithium-ion 26650, $LiFePO_4$ batteries. Numerical analyses are performed for the discharge conditions of the batteries. Uniform and constant heat generation are assumed for the batteries during the discharge process. Heat generation is attributed as 1.43 W and 2.75 W per battery, corresponding to 2C and 3C discharge rates, respectively. The effect of battery arrangement and the air mean velocity on the temperature distribution and the total pressure drop in the system are inspected.

Keywords: Battery Cooling, Lithium-ion battery, air forced convection, Thermal battery management

Symbols

c_p	Specific heat capacity (J $kg^{-1}K^{-1}$)
D	The diameter of battery (m)
k	Thermal conductivity (W m^{-1} K^{-1})
l_a	Distance between first battery and fluid inlet (m)
l_b	Distance between first and last battery (m)
l_c	Distance between the last battery and the fluid outlet (m)
r_{+x}	+ radius in x-direction (m)
r_{-x}	- radius in x-direction (m)
P	pressure
Pr	Prandtl number
Re	Reynold's number
S_y	Distance between two battery centers in Y direction (m)
S_x	Distance between two battery centers in X direction (m)
$T_{initial}$	Initial temperature (K)
U	Nondimensional axial velocity
v	Velocity (used in a vectorial form)
V	Inlet velocity (m s^{-1})
x	horizontal coordinate

y	vertical coordinate
ρ	Density (kg m^{-3})
μ	Dynamic viscosity (kg $m^{-1}s^{-1}$)

1. INTRODUCTION

Electric vehicles (EV's) and hybrid electric vehicles (HEV's) have gained popularity recently. Compared to the other types of batteries, lithium-ion batteries are much more preferred due to their longer cycle and efficiency [1]. However, lithium-ion batteries have some drawbacks. In literature, it is known that the best operating temperature of lithium-ion batteries is 25-40°C, and a maximum 5°C temperature difference in the battery pack is permitted [2]. Batteries generate heat while they are charged or discharged. The generated heat's not being dissipated results in heat storage inside the battery, leading to an increment in the batteries' temperature.

As the fluid temperature increases in the streamwise direction, non-uniform temperature distribution might be observed in the battery pack. This non-uniformity may result in a breakdown in the battery system. Most importantly, some studies have indicated that the batteries' performance decreases with rising temperature [3,4].

All these reasons explained above necessitates various types of cooling methods on the batteries. Many studies on the cooling of battery systems are available in the literature, such as liquid cooling, air cooling, cooling with phase change materials, and cooling with heat exchangers. Each method has its advantages disadvantages. In this study, a battery pack cooling system with forced air cooling is investigated. There are many studies and comparisons about air cooling of the battery packs in the literature [5,6,7,8]. Sabbah et al. [5] compared active (air cooling) and passive (phase change material) cooling methods. They asserted that the air cooling without high fan power makes it impossible to dissipate heat, especially under high operating or ambient temperatures. On the other hand, using the passive cooling techniques (using phase changing materials) satisfies the operating temperature requirements. For this reason, forced convection cooling for battery packs needs special attention. It is crucial to achieving a uniform temperature distribution. Therefore, pack arrangement comes into prominence. Li et al. [6] conducted experimental and numerical studies to determine the battery pack's maximum cell temperature and temperature variation. They have used the forced convection method. They indicated that the CFD model and the experimental model showed consistency. However, they stated that optimization studies in the field should continue. Besides, they pointed out that different turbulence models and many parameters should be carefully investigated. H. Park [7] used a numerical model for forced air-cooled lithium-ion batteries to be used in hybrid electric vehicles. Results indicated that the required cooling performance could be achieved using conical manifold and pressure relief ventilation. Zhang et al. [8] examined the air velocity effect on the battery pack system's temperature for different battery arrangements. Mahamud and Park [9] used reciprocating airflow to improve temperature homogeneity for a cylindrical Li-ion (LiMn204 / C) cell. They aimed to reduce the maximum battery temperature. They used a 2D computational fluid dynamics, CFD model. Also, they conducted experiments. They noted that a 3D CFD model would be much better to estimate the battery life and temperature. He et al. [10] performed experiments and numerical simulations to establish optimal cooling effectiveness regarding the maximum temperature rise, temperature non-uniformity between the cells, and reducing the parasitic power consumption. They mounted two identical fans at both ends of the setup, creating reciprocating airflow in the battery module. Their optimization strategy was based on exploiting the reciprocating cooling flows. Results revealed that a combination of hysteresis control and reciprocating cooling flow could reduce the parasitic power by 84%. The temperature uniformity is enhanced, but a slight increment is observed in the cells. Lu et al. [11] numerically analyzed the three-dimensional geometry of a staggered battery pack to investigate the effects of cooling channel size and air supply strategy on the battery pack's thermal behaviors. 18650 li-ion battery was chosen. They sought the impact of the location of the inlet and the outlet ports on the thermal performance. They concluded that the best cooling performance is obtained if the airflow inlet and outlet are positioned at the top of the battery pack. They noted that packing more cells in the flow direction works very well in terms of the battery power density and cooling requirement. Although there are many studies related to forced air battery pack cooling in the literature, just a few of them have focused on the pack's temperature non-uniformity.

In this study, the air is used as the fluid. Battery pack temperature distribution and pressure drop are examined for different volumetric flow rates. Besides, the battery arrangement effect on the maximum temperature and the temperature uniformity is studied. There are 6×6 batteries located as aligned or staggered (36 batteries in total). Pressure drop and the pumping power is among the examined parameters in the present study. Two different heat generation values are investigated. These are 1.43 W and 2.75 W corresponding to approximately 2C and 3C discharge rates of Lithium-ion 26650 $LiFePO_4$ batteries [12,13]. It should be noted that the heat generation depends on the temperature and the state of charge of the battery, but some studies employ mean heat generation value during discharge [12,13]. It is assumed that there is uniform heat generation inside the batteries.

2. PROBLEM DEFINITION AND METHOD

A transient analysis has been performed, but the simulation has been sustained until the steady-state conditions are reached. A two-dimensional model is formed. Air is used as a working fluid, and it flows in the x-direction (Fig. 1). The initial temperature of the batteries and the fluid inlet temperature are taken as the ambient temperature ($T_{initial} = 296$ K). Symmetry boundary condition was applied for the battery pack during the analysis to reduce the computational effort. Velocity inlet and pressure outlet boundary conditions are applied at the channel inlet and the outlet.

The geometry modeled is illustrated in Fig. 1 (a) and (b) is demonstrated in detail for the aligned battery arrangement and the staggered battery arrangement, respectively.

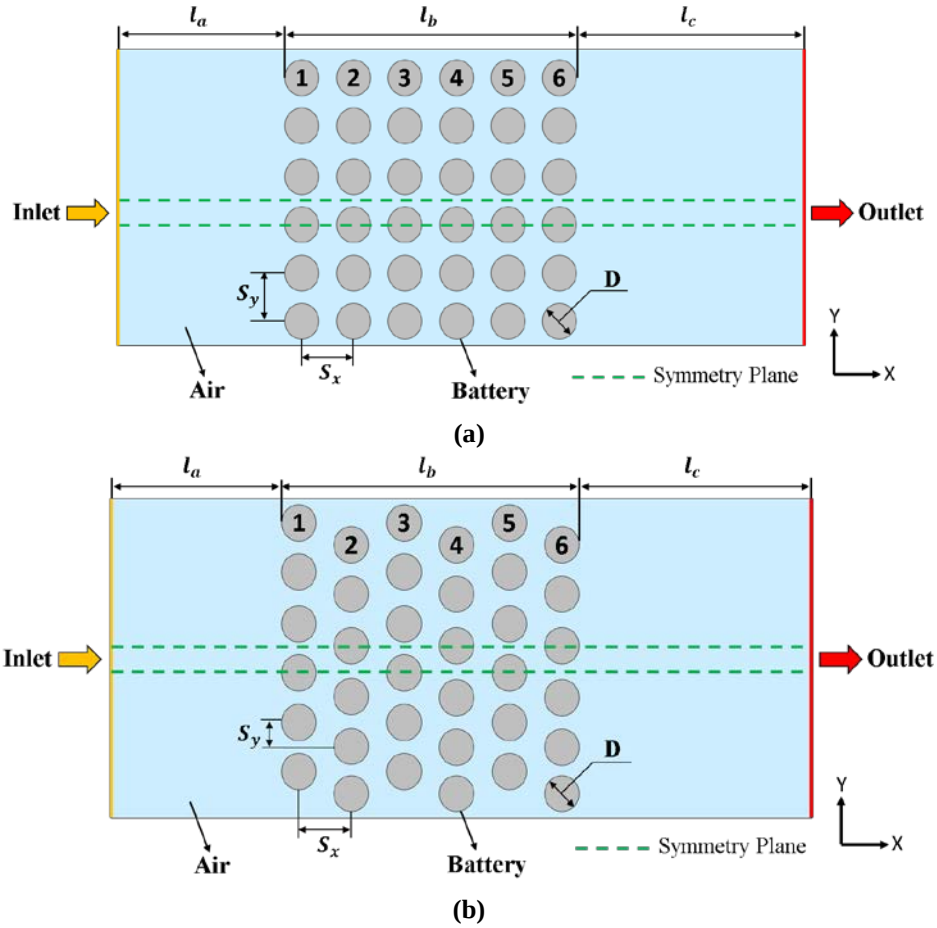

Figure 1. Modeled 2-D Geometry **(a)** Aligned arrangement **(b)** Staggered arrangement

The diameter of each battery cell is $D = 26$ mm. The distance between batteries in the x-direction is $S_x = 35.2$ mm and $S_y = 35$ mm in the y-direction for the aligned battery arrangement. For the staggered battery arrangement, $S_x = 35.2$ mm and $S_y = 17.5$ mm.

Moreover, the distance between the inlet and the first battery cell is $l_a = 137$ mm, and the distance between the outlet and the last battery cell is $l_c = 237$ mm as projected in Fig.1. The total length of 6 batteries is $l_b = 202$ mm.

The meshed model is simulated in ANSYS FLUENT R2 STUDENT. The equation of momentum and turbulent kinetic energy are discretized using the second-order upwind scheme. The Semi-Implicit Method for Pressure-Linked Equation (SIMPLE) algorithm is used for the pressure and velocity coupling. As a turbulent flow model, the k – ε turbulence model (enhanced wall improvement) [6,9] is used. The mesh quality and size are important because it significantly improves the accuracy of the results. It is important to note that the boundary layer effect over the cylinder and the separation point are considered.

The meshed geometry is given in Figure 2.

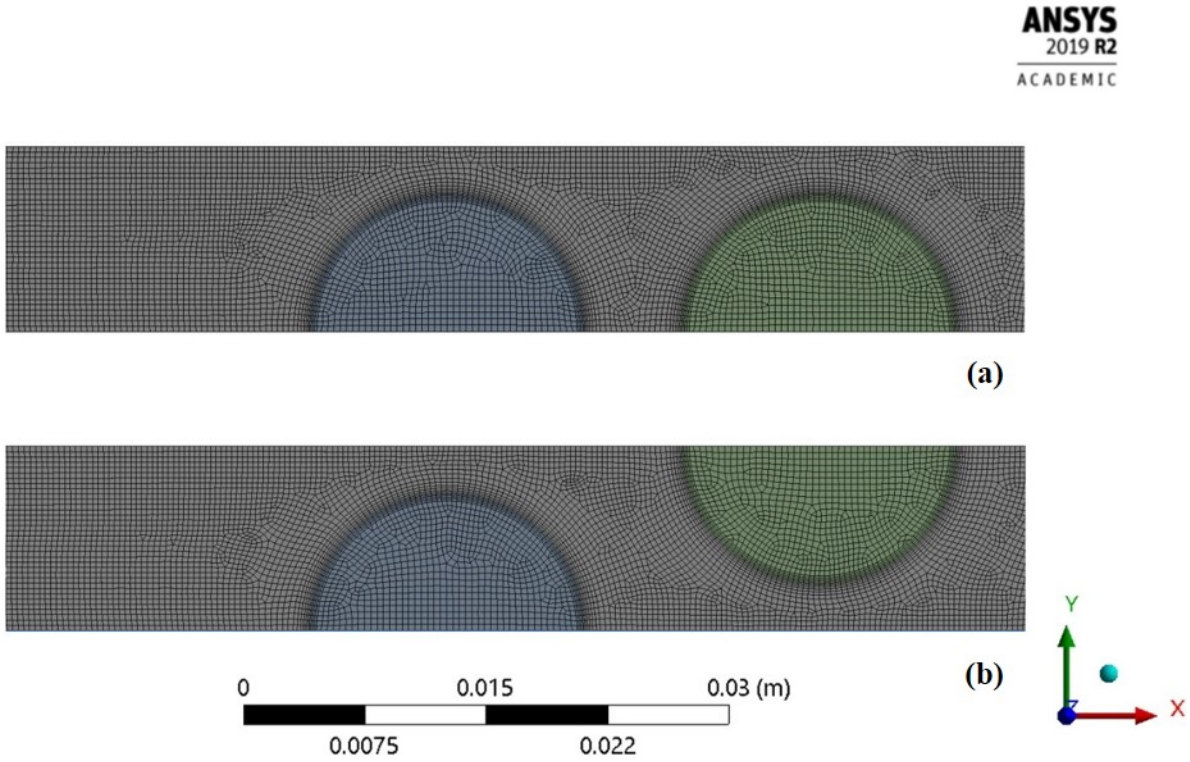

Figure 2. Mesh model of design geometry **(a)** Aligned battery arrangement **(b)** Staggered battery arrangement

Skewness, orthogonal quality, aspect ratio, and mesh element size for both modeled geometries are summarized in Table 1.

Table 1. Meshing and quality parameters

Parameters	Aligned	Staggered
Skewness	0.60	0.69
Orthogonal Quality	0.65	0.62
Aspect Ratio	3.42	3.43
Element Size	40,093	39,803

The mesh independence is an essential parameter in CFD analysis and has been verified in this analysis. If the mesh number (for the aligned arrangement in Figure 2, for 1.43 W heat generation) is increased by 60%, the system's maximum temperature changed by approximately 0.03%.

Mass, momentum, and energy equations for the two-dimensional airflow with negligible viscous dissipation and body force (in momentum eq) can be written as:

Continuity:

$$\frac{\partial \rho_a}{\partial t} + \boldsymbol{\nabla} \cdot (\rho_a \vec{v}) = 0 \tag{1}$$

Momentum:

$$\frac{\partial}{\partial t}(\rho_a \vec{v}) + \rho_a(\vec{v} \cdot \boldsymbol{\nabla})\vec{v} = -\boldsymbol{\nabla} \mathrm{P} + \mu \nabla^2 \vec{v} \tag{2}$$

Energy:

$$\frac{\partial}{\partial t}\left(\rho_a C_{p,a} T_a\right) + \rho_a C_{p,a}(\vec{v} \cdot \boldsymbol{\nabla} T_a) = \boldsymbol{\nabla} \cdot (k_a \boldsymbol{\nabla} T_a) \tag{3}$$

For the battery domain, the classical energy equation is employed with uniform and constant heat generation. In Table 2, the thermophysical properties of the fluid and the battery are summarized.

Table 2. Thermophysical properties of air (at T = 296 K) and battery

Properties	Density, kg m^{-3}	Specific Heat Capacity, J $kg^{-1}K^{-1}$	Thermal Conductivity, W m^{-1} K^{-1}	Dynamic Viscosity, kg $m^{-1}s^{-1}$
Battery, [12]	2047	1075	3.91 [14]	-
Air	1.180064	1006.92	0.02598	$1.826 \cdot 10^{-5}$

In Table 2, thermophysical properties of the battery were taken from Lazrak et al. [12]. The battery's thermal conductivity was also taken from Zhao et al. [14] as it was not provided in Lazrak et al. [12].

3. RESULTS AND DISCUSSION

This section is presented with subtitles as "Temperature Distribution" and "Pressure Drop and Cooling Index."

3.1 Temperature Distribution

The temperature values when the system reaches the steady-state regime at total (battery pack) volumetric flow rates of $6.825 \times 10^{-3}\ m^3 s^{-1}$, $10.238 \times 10^{-3}\ m^3 s^{-1}$ and $13.650 \times 10^{-3}\ m^3 s^{-1}$ for the aligned and staggered battery arrangement system are summarized in Tables 3 and 4, respectively.

Table 3. Battery temperatures at specified velocities for the aligned battery arrangement

Aligned		**Battery Temperatures, K (1.43 W)**					
Vol. Flow Rate, m^3s^{-1}	**Velocity, m s^{-1}**	**Battery-1**	**Battery-2**	**Battery-3**	**Battery-4**	**Battery-5**	**Battery-6**
6.825×10^{-3}	0.5	306.7	306.9	307.7	308.6	309.6	310.1
10.238×10^{-3}	0.75	304.6	304.8	305.2	305.8	306.5	306.7
13.650×10^{-3}	1	303.3	303.5	303.8	304.2	304.7	304.9
		Battery Temperature, K (2.75 W)					
6.825×10^{-3}	0.5	316.6	317.1	318.5	320.3	322.2	323.1
10.238×10^{-3}	0.75	312.5	312.9	313.7	314.9	316.1	316.6
13.650×10^{-3}	1	310.1	310.4	311.0	311.9	312.8	313.1

Table 4. Battery temperatures at specified velocities for the staggered battery arrangement

Staggered		**Battery Temperatures, K (1.43 W)**					
Vol. Flow Rate,m^3s^{-1}	**Velocity, m s^{-1}**	**Battery-1**	**Battery-2**	**Battery-3**	**Battery-4**	**Battery-5**	**Battery-6**
6.825×10^{-3}	0.46	306,3	305.0	306.5	307.6	308.8	309.9
10.238×10^{-3}	0.69	304.2	303.1	304.2	304.9	305.7	306.4
13.650×10^{-3}	0.92	303.1	302.1	302.9	303.4	304.0	304.6
		Battery Temperature, K (2.75 W)					
6.825×10^{-3}	0.46	315.7	313.2	316.2	318.3	320.5	322.7
10.238×10^{-3}	0.69	311.9	309.7	311.7	313.1	314.6	316.1
13.650×10^{-3}	0.92	309.6	307.7	309.2	310.2	311.3	312.5

When Tables 3 and 4 are examined, the temperature non-uniformity remained below the critical temperature value of 5°C for all cases of 1.43 W heat generation. In the case of 2.75 W heat generation, it is seen that this critical value is exceeded at the lowest flow rate value for both battery arrangements. The non-uniform temperature distribution is observed for the volumetric flow rate value of $6.825 \times 10^{-3}\ m^3s^{-1}$ in the battery pack system for both arrangements.

When the temperature distribution is examined, it is seen for both battery arrangements that more homogeneous temperature distribution is obtained for higher airflow rates.

When Tables 3 and 4 are examined, slightly better heat removal is obtained for staggered battery arrangement. The heat transfer rate is slightly higher since the turbulence effect is promoted in this battery arrangement; hence, the staggered order's battery temperature values are lower. However, when the temperature distribution is studied, a more uniform temperature distribution is obtained for the aligned battery arrangement. This can be improved by modifying the distance between them. The last battery row in the flow direction is the most critical one in terms of temperature. Hence; only 6th battery's transient analyses are provided in Fig. 3.

The time-dependent temperature change in the 6th battery for 1.43 W and 2.75 W heat generation is given for both battery arrangements in Figure 3 (a) and (b), respectively.

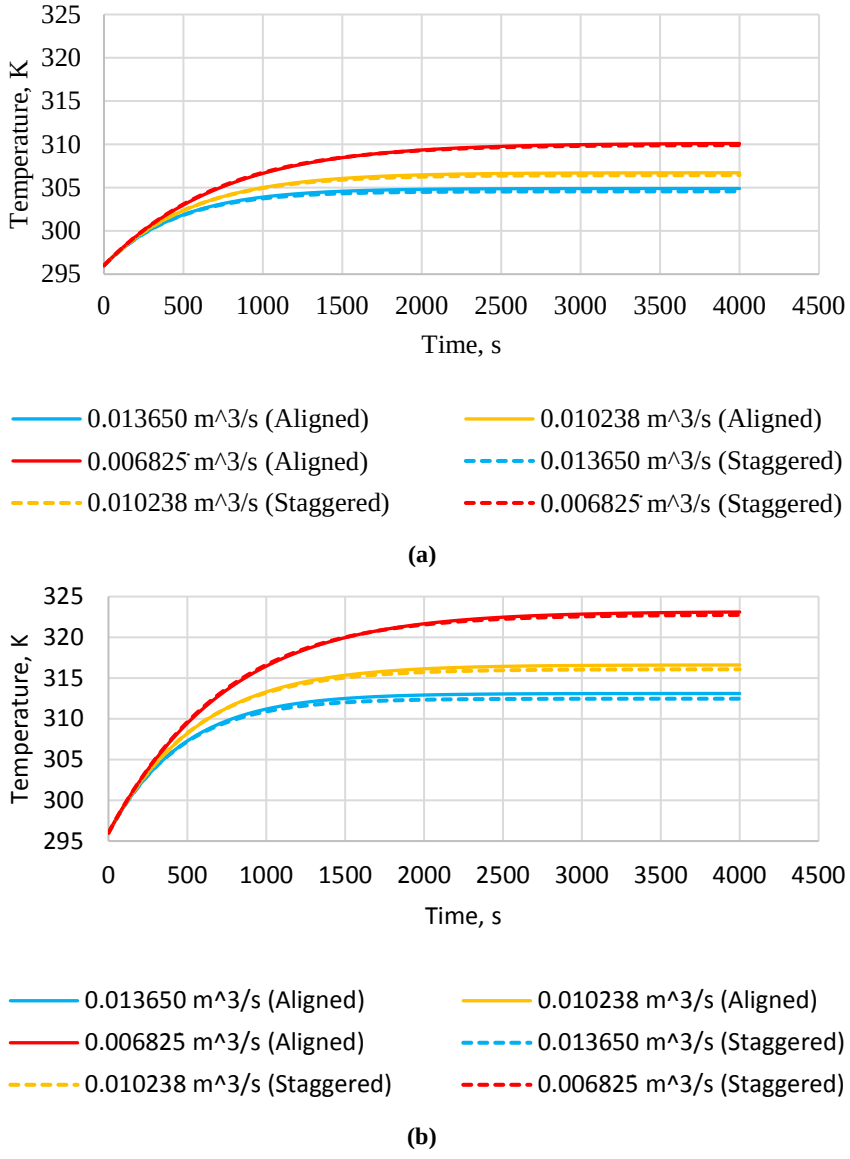

Figure 3. Time-dependent battery temperature for the 6th battery **(a)** 1.43 W heat generation **(b)** 2.75 W heat generation

The maximum allowable temperature difference between batteries also applies to the temperature non-uniformity in the battery itself. Accordingly, the temperature non-uniformity for a battery is also vital for the system. Thus, the temperature distribution inside the batteries ought to be investigated. Thanks to the lines depicted in red color in Fig 4, temperature variation inside the batteries can be observed.

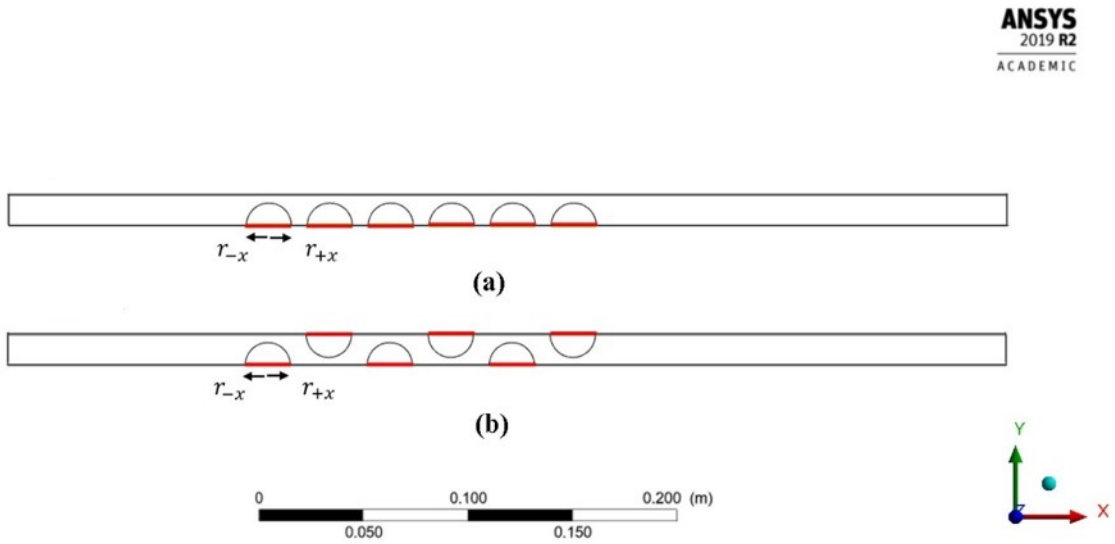

Figure 4. The lines on which the temperature variation is examined **(a)** Aligned battery arrangement **(b)** Staggered battery arrangement

The simulation has been carried out at a flow rate of $13.650 \times 10^{-3}\ m^3 s^{-1}$ and for 2.75 W heat generation. The temperature distribution inside the batteries for the steady-state regime is represented in Figure 5.

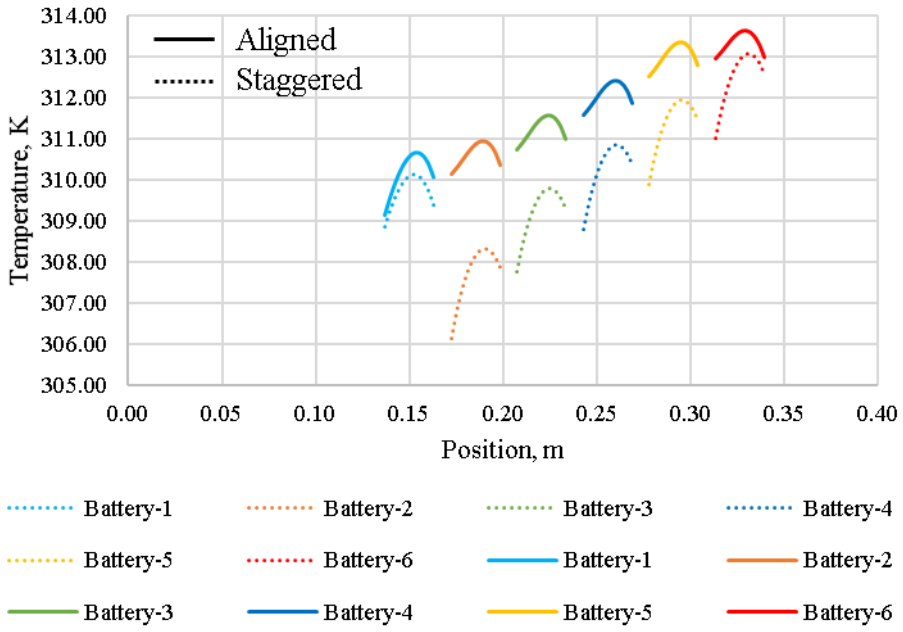

Figure 5. Temperature change along the diameter of each battery (For $\dot{\forall} = 13.650 \cdot 10^{-3}\ m^3 s^{-1}$ and 2.75 W heat generation)

As shown in Figure 5, while the temperature distribution is more uniform for aligned order, there is significant temperature variation in the batteries positioned according to staggered order. As the batteries meet the air in the upstream direction first, the temperature of that side of the batteries is lower for all cases.

Although the temperature values are quite close for staggered and aligned orders for the first battery, battery arrangement comes to the foreground after the first battery. The turbulence effect gets dominated for the staggered order after the first battery row. Consequently, if a comparison is made for the same row, the average temperature of a battery is lower for the staggered order.

3.2 Pressure Drop and Cooling Index

The pressure drop through the battery pack is crucial for the design. Besides, pressure drop and pumping power is desired to be low in these systems. A cooling index parameter is defined as the ratio of the total heat rejection to the power consumed by the fan while the steady-state condition prevails [8]. Pressure drop, pumping power, and cooling index parameters are presented for different velocities in Table 5.

Table 5. Pressure drop, fan power, and cooling index occurring in both battery arrangements

Vol. Flow Rate, m^3s^{-1}	Aligned				Staggered			
	Pressure Drop, Pa	Pumping Power, W	Cooling Index 1.43 W	Cooling Index 2.75 W	Pressure Drop, Pa	Pumping Power, W	Cooling Index 1.43 W	Cooling Index 2.75 W
$\mathbf{6.825 \times 10^{-3}}$	5.7	0.0389	1323.4	2545	7.4	0.0505	1019.4	1960.4
$\mathbf{10.238 \times 10^{-3}}$	11.5	0.1177	437.4	841.1	15.3	0.1566	328.7	632.2
$\mathbf{13.650 \times 10^{-3}}$	18.5	0.2525	203.9	392.1	24.8	0.3385	152.1	292.5

It can be concluded from Table 5 that the cooling index is better for the aligned order when compared to staggered order at the same flow rate. Nevertheless, the average temperature observed in the aligned order is higher. Lower pressure drop and pumping power are the reasons behind the aligned order's better cooling index. As long as the operating temperature is in the safe range, the aligned order battery arrangement can be preferable due to its low fan energy consumption.

4. CONCLUSION

- The temperature difference between the batteries might be kept at a minimum level at high volumetric flow rates. By doing so, the temperature difference between the batteries is ensured to be under critical levels.
- The 6th-row battery owns the highest average temperature. When compared at the same flow rates, the average temperature is lower for the staggered order.
- Much as the use of staggered order placement resulted in lower temperature values at the same battery row compared to the aligned order placement, temperature uniformity inside the batteries deteriorated.
- The cooling index is better for the aligned order than the staggered order at a constant flow rate. However, the average temperature observed in the aligned order is higher.
- So long as the operating temperature is in the safe range, aligned order battery arrangement can be preferred thanks to its low fan energy consumption.
- It is better to compromise from the cooling index and use at least a moderate flowrate ($10.238 \times 10^{-3}\ m^3\ s^{-1}$) for 2.75 heat generation case as it much safer in terms of the cell temperature.
- The maximum temperature deviation between the cells during 2.75 W heat generation is 4°C for the aligned order. On the other hand, it is 7°C for the staggered order.

REFERENCES

[1] Deng, Y., Feng, C., Jiaqiang, E., Zhu, H., Chen, J., Wen, M. & Yin, H., Effects of Different Coolants and Cooling Strategies on The Cooling Performance of The Power Lithium-Ion Battery System: A Review, *Applied Thermal Engineering*, **142**, 10-29, 2018.

[2] Pesaran, A. A., Battery Thermal Models for Hybrid Vehicle Simulations, *Journal of Power Sources*, **110(2)**, 377-382, 2002.

[3] Sato, N., Thermal Behavior Analysis of Lithium-Ion Batteries for Electric and Hybrid Vehicles, *Journal of Power Sources*, **99(1-2)**, 70-77, 2001.

[4] Ramadass, P., Haran, B., White, R. & Popov, B. N., Capacity Fade of Sony 18650 Cells Cycled at Elevated Temperatures: Part II. Capacity Fade Analysis, *Journal of Power Sources*, **112 (2)**, 614-620, 2002.

[5] Sabbah, R., Kizilel, R., Selman, J. R. & Al-Hallaj, S., Active (Air-Cooled) Vs. Passive (Phase Change Material) Thermal Management of High-Power Lithium-Ion Packs: Limitation of Temperature Rise and Uniformity of Temperature Distribution, *Journal of Power Sources*, **182**(2), 630-638, 2008.

[6] Li, X., He, F. & Ma, L., Thermal Management of Cylindrical Batteries Investigated Using Wind Tunnel Testing and Computational Fluid Dynamics Simulation, *Journal of Power Sources*, **238**, 395-402, 2013.

[7] Park, H., A Design of Air Flow Configuration for Cooling Lithium-Ion Battery in Hybrid Electric Vehicles, *Journal of Power Sources*, **239**, 30-36, 2013.

[8] Yang, N., Zhang, X., Li, G. & Hua, D., Assessment of The Forced Air-Cooling Performance for Cylindrical Lithium-Ion Battery Packs: A Comparative Analysis Between Aligned and Staggered Cell Arrangements, *Applied Thermal Engineering*, **80**, 55-65, 2015.

[9] Mahamud, R. & Park, C Reciprocating Air Flow for Li-Ion Battery Thermal Management to Improve Temperature Uniformity, *Journal of Power Sources*, **196** (13), 5685-5696, 2011.

[10] He, F., Wang, H., & Ma, L., Experimental Demonstration of Active Thermal Control of A Battery Module Consisting of Multiple Li-İon Cells, *International Journal of Heat and Mass Transfer*, **91**, 630-639, 2015.

[11] Lu, Z., Yu, X., Wei, L., Qiu, Y., Zhang, L., Meng, X., & Jin, L., Parametric Study of Forced Air-Cooling Strategy for Lithium-İon Battery Pack with Staggered Arrangement, *Applied Thermal Engineering*, **136**, 28-40, 2018.

[12] Lazrak, A., Fourmigué, J. F. & Robin, J. F., An Innovative Practical Battery Thermal Management System Based on Phase Change Materials: Numerical and Experimental Investigations, *Applied Thermal Engineering*, **128**, 20-32, 2018.

[13] Hémery, C. V., Pra, F., Robin, J. F. & Marty, P., Experimental Performances of A Battery Thermal Management System Using A Phase Change Material, *Journal of Power Sources*, **270**, 349-358, 2014.

[14] Zhao, J., Rao, Z., Huo, Y., Liu, X. & Li, Y., Thermal Management of Cylindrical Power Battery Module for Extending The Life of New Energy Electric Vehicles, *Applied Thermal Engineering*, **85**, 33-43, 2015.

MAGNETIC REFRIGERATION TECHNOLOGY AND APPLICATIONS

Arda ZAİM*, Haydar ARAS**
*Eskişehir Osmangazi University, Department of Mechanical Engineering, Eskişehir/Turkey
Email: arda.zaim@gmail.com
**Eskişehir Osmangazi University, Department of Mechanical Engineering, Eskişehir/Turkey
Email: haras@ogu.edu.tr

ABSTRACT

Up to this time, conventional vapor compression refrigeration systems have been widely used for cooling applications. Refrigerants that contain chlorofluorocarbon and hydrochlorofluorocarbon used in these systems damage the ozone layer. Vapor compression refrigeration systems have both direct and indirect effects on global warming in two ways. Leakage of refrigerant from the system components or it is being spread to the outside during service can be considered as a direct effect. The indirect effect is using a carbon-emitting power plant for the generation of electrical energy used by the refrigeration system. Besides, indirect effects are directly related to the cooling performance coefficient of the system. Nowadays, as system efficiency and environmental impacts are taken into consideration, alternative methods are being searched for refrigeration applications instead of vapor compression refrigeration systems. Researches on magnetocaloric materials and the development of magnetic refrigeration technologies provide an alternative to the conventional vapor-compression refrigeration cycle. Magnetic refrigeration is based on the principle that a ferromagnetic or paramagnetic material exhibits a magnetocaloric effect and this effect allows heat exchange from the environment using a heat transfer fluid in the heat exchanger. These systems have no negative effects on the environment in terms of global warming and the ozone layer. On the other hand, since there are no compression and throttling processes in magnetic refrigeration systems, they are theoretically more efficient than vapor compression systems. Besides, moving parts are reduced in the system, and noise generated during compressor operation is eliminated in magnetic refrigeration. In this study, magnetic refrigeration technology was compared to conventional vapor compression systems in terms of working principle, energy efficiency, cooling performance, and environmental effect. Besides, its application fields were investigated. Thermodynamic cycles that can be used in magnetic refrigeration systems were also examined.

Keywords: Energy efficiency, magnetic refrigeration, magnetocaloric effect.

AMR	Active magnetic regenerator
CFC	Chlorofluorocarbon
COP	Coefficient of performance
Gd	Gadolinium
H	Magnetic field
HCFC	Hydrochlorofluorocarbon
s	Entropy
T	Temperature (^{o}C)
T	Tesla

1. INTRODUCTION

Increasing population and developing technology require more energy, which necessitates new technological methods for energy supply and makes efficient use of energy essential. The main purpose of new methods is energy production and operation costs, environmentally friendly, sensitive to social values, and effective. The issues on the world energy agenda can be listed as follows; efficient use of energy, effective energy

management, alternative fuel options and applicability, renewable energy sources, and environmental problems caused by energy use [1,2].

Nowadays, although conventional vapor compression refrigeration technology is widely used in many places from vehicles to industrial plants, various limitations in the system result in low efficiency. Also, chlorofluorocarbon and the hydrochlorofluorocarbon-containing refrigerant used in these systems damage the ozone layer and affect global warming. Vapor compression refrigeration systems have direct and indirect effects on global warming in two ways. Leakage of the refrigerant from the system components or it is being spread to the outside during service can be considered as a direct effect. The indirect effect is the use of a carbon-emitting powerplant for the generation of electrical energy used by the cooling system compressor. The substantial disadvantage of the vapor compression refrigeration system is that it requires a compressor to compress a large amount of refrigerant vapor which requires a great deal of power to operate. Additionally, environmental factors limit the lowest temperature of the refrigeration cycle and therefore have lower COP than the Carnot cycle [3,4].

Considering the system efficiency and environmental impacts, alternative methods for refrigeration applications are being used instead of vapor compression refrigeration systems. Research on magnetocaloric materials and the development of magnetic refrigeration technologies provide an alternative to the conventional vapor compression refrigeration systems. Magnetic refrigeration is based on the principle that a ferromagnetic or paramagnetic material exhibits a magnetocaloric effect and this effect allows heat exchange from the environment using a heat transfer fluid in the heat exchanger. These systems have no adverse effects on the environment in terms of global warming and the ozone layer. On the other hand, since there are no compression and throttling processes in magnetic refrigeration systems, they are theoretically more efficient than vapor compression systems. Also, moving parts are reduced in the system, and noise generated during compressor operation is eliminated in magnetic refrigeration [5-7].

In this study, the magnetocaloric effect which is the basic principle of magnetic refrigeration technology is explained and the working principle of the magnetic refrigeration system is mentioned, magnetic refrigeration technology was compared to conventional vapor compression systems in terms of working principle, energy efficiency, cooling performance and environmental effect and its application fields were investigated.

2. PRINCIPLES OF MAGNETIC REFRIGERATION SYSTEM

The working principle of magnetic refrigerators is based on the magnetocaloric effect, perceived as an adiabatic temperature change or isothermal entropy change. The magnetocaloric effect was discovered by Emil Warburg in 1881 with its effect on iron. Debye and Giauque also independently defined the magnetocaloric effect. Besides, these scientists have guided practical use of the magnetocaloric effect, such as removal of adiabatic demagnetization and reaching lower temperatures than liquid helium, the lowest experimental temperature that can be obtained [8,9].

To define the magnetocaloric effect, thermodynamic relations are used to associate the magnetic variables with magnetization and magnetic field with entropy and temperature. All materials have magnetocaloric effects, but the intensity of this effect depends on the properties of the material. The physical origin of the magnetocaloric effect is that the applied magnetic field causes a change in the entropy of the material [10].

As shown in Figure 1, the isothermal magnetization of a paramagnet or ferromagnet is similar to the isothermal compression of a gas. The magnetic field is applied and entropy is reduced. The pressure is applied and entropy is reduced. Adiabatic demagnetization is similar to the adiabatic expansion of a gas temperature decreases when the pressure decreases in constant entropy. The total entropy remains constant when the magnetic field acting on the material is removed and the temperature decreases due to the increase in magnetic entropy [11].

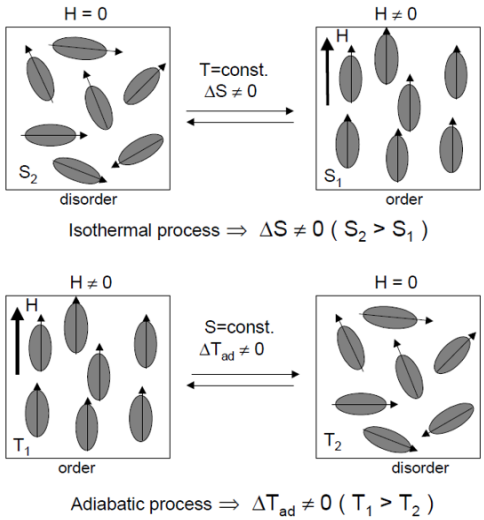

Figure 1. The isothermal process causing entropy change in magnetocaloric effect and adiabatic process with temperature change observed.

One of the most essential examples in which the magnetocaloric effect can be observed is the chemical element gadolinium and some alloys. Gadolinium and its alloys have gained an important place in magnetic cooling systems thanks to their unique magnetic properties. Furthermore, these magnetocaloric materials are the best available materials for magnetic refrigeration close to room temperature since they are subject to second-order phase transitions. Curie temperature is the critical temperature at which a ferromagnetic material loses its permanent magnetism and becomes paramagnetic. Gadolinium, a typical magnetocaloric material, can exhibit a maximum adiabatic temperature change of 2.5 ^{o}C at Curie temperature and 1 Tesla magnetic field strength. As shown in Figure 2, this value increase in proportion to the magnetic field strength [12].

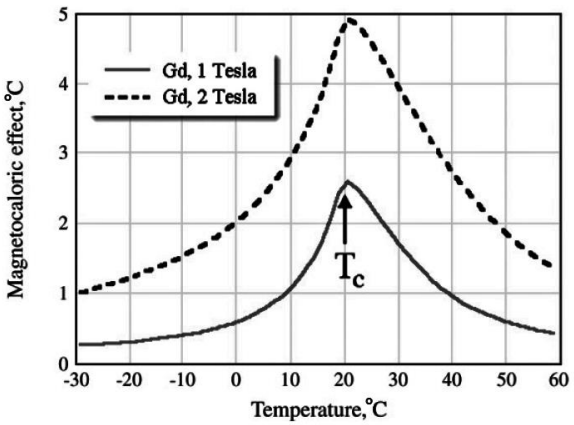

Figure 2. Gadolinium adiabatic temperature change.

In the conventional vapor compression cycle, the refrigerant fluid is compressed its temperature is increased, then the compressed gas gives heat to the environment through a condenser, the fluid decreases in temperature, the expanded gas draws heat from the environment to be cooled, and the cycle starts again.

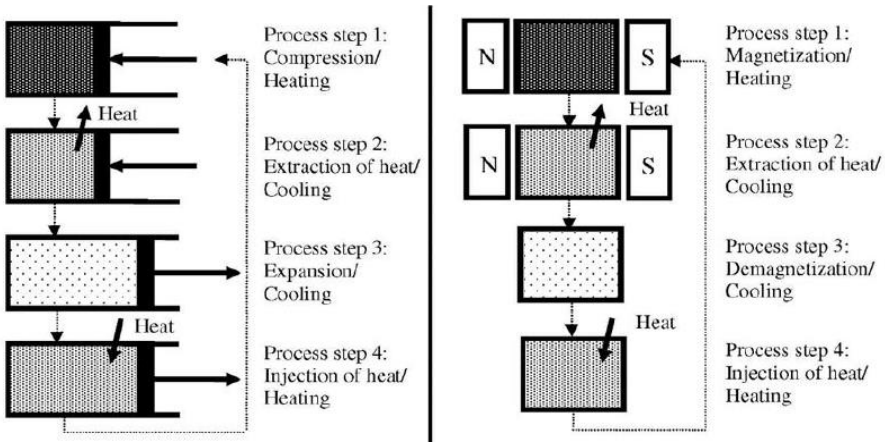

Figure 3. Similarities between the vapor compression system and the magnetic refrigeration systems.

Magnetic refrigeration is based on the principle that a ferromagnetic or paramagnetic material exhibits a magnetocaloric effect, and this effect allows heat exchange from the environment using a heat transfer fluid in the heat exchanger. In the magnetic refrigeration cycle, the heat is increased by exposing the magnetocaloric material to the magnetic field. The magnetized magnetocaloric material gives heat to the environment. The material is demagnetized, and its temperature is lowered, the fluid draws heat from the environment to be cooled, and the cycle begins again. To carry heat transfer on magnetocaloric material under the influence of the magnetic field, water, and ethyl alcohol derivative fluids are used as a refrigerant in the system. The fact that the magnetocaloric material enters and exits the magnetic field along with gradually flowing liquid flow replaces the function of the compressor in a conventional vapor cycle. Figure 3 shows the similarities between the vapor compression system and the magnetic refrigeration systems [13].

Since the 1930s, magnetic cooling has been used as a laboratory technique to reach shallow temperatures. However, working close to room temperature has recently been possible with rare earth metals and transition metal-based refrigerants and permanent high field and superconducting magnets. Although gadolinium is one of the best magnetocaloric materials available, the temperature differences that can be achieved with the magnetocaloric effect are low. For this reason, it is very complicated to describe the use of the magnetocaloric effect in many cooling applications. This technical obstacle was overcome by integrating the active magnetic regenerator into the system. Regeneration in magnetic refrigeration systems ensures that the heat discharged by the system is taken back at any step of the cycle and sent back to the system in another step in the same cycle. Thus, the capacity used for cooling the network load can be used effectively to increase the actual change of entropy and the obtained temperature difference [14].

The sample active magnetic regenerative cycle is operated as shown in Figure 4 for a steady-state condition. In the first stage (a), the initial temperature profile (dashed line) is for the zero magnetic fields. When the magnetic field is applied, each particle in the bed heats up with a magnetocaloric effect (solid line). The amount that each particle warms up is equal to the adiabatic temperature change upon magnetization at the initial temperature of the particle. This value decreases with the effect of the heat capacity of the liquid in the pores between the particles. In the next stage (b), the cold fluid flows from the cold end in the bed to the hot end. The bed is cooled by the fluid, and the fluid reaches a value close to the bed temperature at the hot end, reducing the temperature profile across the bed. Since the temperature reached by the fluid is above the ambient temperature, heat is removed from the environment with the hot end heat exchanger. Then (c) the fluid flow is stopped, and the bed is cooled by removing the magnetic field effect. The cycle continues by forcing the fluid to flow from the hot end of the bed to the cold end. The fluid is lowered below the ambient temperature to be cooled by the bed (d). The cold fluid draws heat from the medium to be cooled by the cold end heat exchanger and the cycle is completed [15,16].

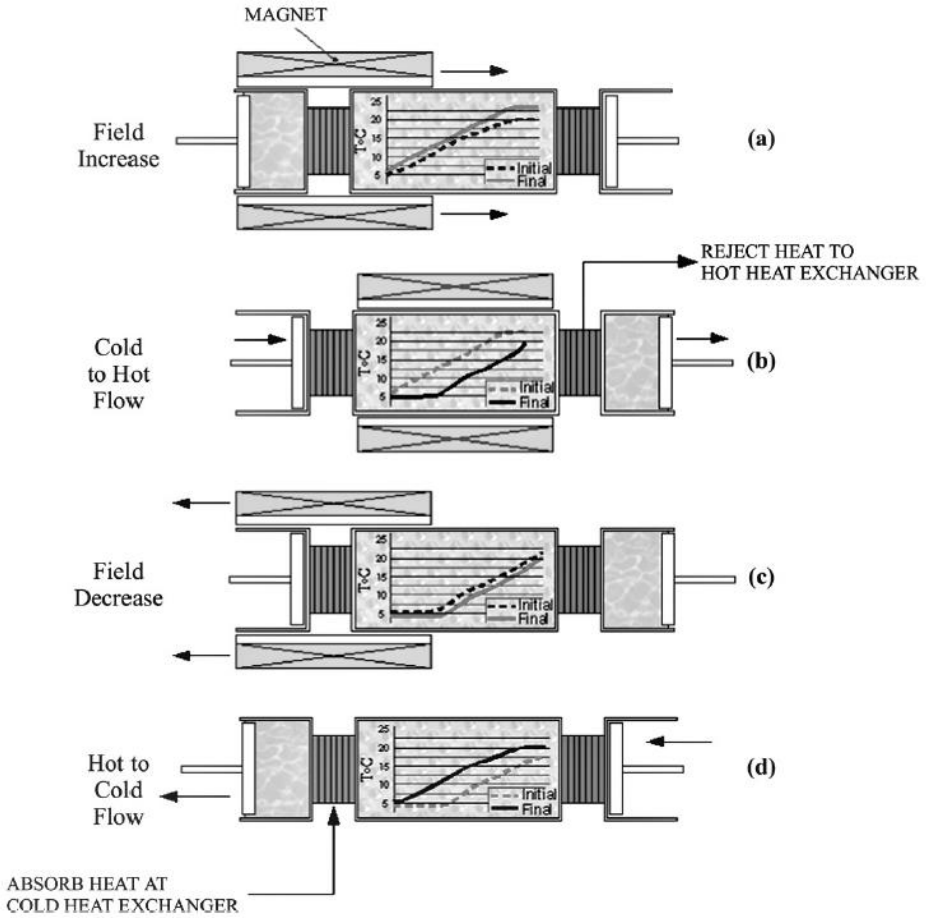

Figure 4. Active magnetic regenerator cycle.

3. THERMODYNAMICS OF MAGNETIC REFRIGERATION SYSTEMS

Carnot, Ericsson, and Brayton cycles are used for thermodynamically magnetic refrigeration systems. However, the most suitable cycles for room temperature applications are the Ericsson and Brayton cycles, where high cooling efficiency in magnetic materials can be achieved [17].

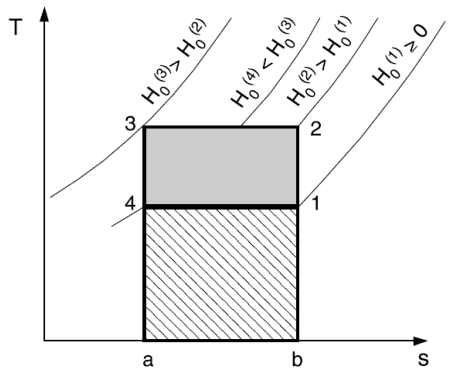

Figure 5. Carnot cycle T-s diagram for magnetic refrigeration.

As seen in Figure 5, the Carnot cycle process (1-2) is the adiabatic magnetization step. While the magnetization process (2-3) continues increasingly, it becomes isothermal magnetization. The heat generated during this process is removed from the system. The next step (3-4) is adiabatic demagnetization. The cycle is completed when the system combines with the heat source during the adiabatic demagnetization phase (4-1). It appears that the Carnot cycle can only be operated if the magnetocaloric material is moved and at least four different magnetic fields are created. In the process (1-2) the magnetic field strength should be changed quickly to prevent heat losses. For isothermal magnetization conditions to occur (2-3) magnetic field change and heat removal from the system must be simultaneous. The area between (1-2-3-4) represents the work required, and the area (1-4-a-b) is related to thermal cooling energy [18].

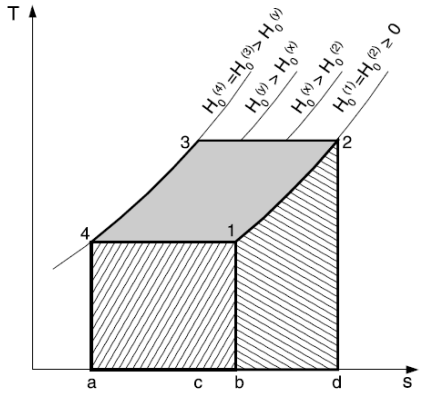

Figure 6. Ericsson cycle T-s diagram for magnetic refrigeration.

The magnetic refrigerator, where the Ericsson cycle is preferred, operates within two iso-therms and two iso-magnetic fields, as can be shown in Figure 6. This process requires heat regeneration. During the iso-magnetic field process (1-2), heat is absorbed from the opposite side (3-4) using a regenerator. For this reason, in ideal regeneration, the area (2-1-b-d), representing thermal energy absorption from the magnetocaloric material has to correspond to (3-4-a-c), representing the heat extraction of the refrigerant material. Regeneration can only be done if there is a temperature difference. The efficiency of the Ericsson cycle decreases due to the irreversible heat transfer. A simultaneous alteration of the magnetic field and heat absorption or rejection leads to the isothermal processes (2-3), and (4-1). The area (1-2-3-4) represents the work required for the Ericsson cycle and the area (1-4-a-b) is identical to the cooling energy [19].

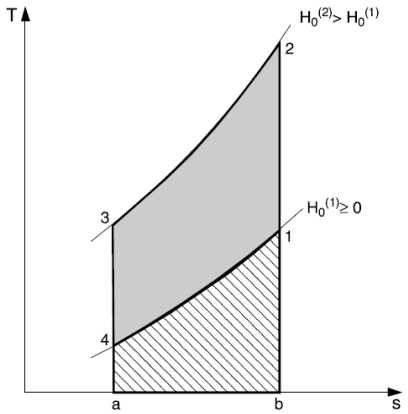

Figure 7. Brayton cycle T-s diagram for magnetic refrigeration.

Figure 7 shows the Brayton cycle, one of the most fundamental cycles of magnetic refrigeration. The magnetic refrigerator, where the Brayton cycle is preferred, operates between two iso-fields (constant magnetic fields) and

two isentropic curves (constant total specific entropy). Total entropy remains constant by processing the magnetocaloric material through the transition to a magnetic field (1-2). In this case, adiabatic magnetization increases the temperature of the magnetocaloric material. The heat of the material is rejected at this high temperature (2-3). In the adiabatic demagnetization process (3-4), the temperature of the material decreases. At the last stage (4-1), an external device is cooled by absorbing heat in the heat source [19].

4. RESULTS

Today, it is aimed to develop new technologies that use energy efficiently, are sensitive to social values, and are environmentally friendly due to the limited energy resources, increasing energy consumption and demand, and global problems such as global warming. Conventional vapor compression refrigeration systems have been widely used in many fields from industrial facilities to the automotive industry for many years. Research on magnetocaloric materials and the development of magnetic refrigeration technologies provide an alternative to the conventional vapor compression refrigeration systems.

Magnetic refrigeration is a green and environmentally friendly technology considering the desired properties on the minimum effect on global warming. Due to the unavoidable installation leaks, a certain amount of CFC or HCFC gases are mixed directly into the atmosphere every year from the vapor compression refrigeration systems. Since the refrigerants used in magnetic refrigeration are water and ethyl alcohol derivatives which are environmentally friendly liquids, they do not pose an environmental hazard in case of mixing into the atmosphere due to leaks. Magnetic refrigeration technology has the potential to reduce operating and maintenance costs compared to the conventional vapor compression method. Since there is no compressor in magnetic refrigeration systems, the moving parts are reduced and the noise generated during operation is eliminated. It can replace the conventional method by eliminating the high initial investment cost of the compressor and reducing the cost of electrical energy required to operate the system. On the other hand, since there are no compression and throttling processes, they theoretically more efficient than vapor compression refrigeration. Low refrigerant pressure increases the usability of the system in the automotive industry and local air conditioning.

REFERENCES

[1] Abdeen M.Ö., Energy, Environment and Sustainable Development, *Renewable and Sustainable Energy Reviews,* **12**(9), 2265-2300, 2008.

[2] Dresselhaues M.S., Thomas I.L., Alternative Energy Technologies, *Nature,* **414**, 332-337, 2001.

[3] Aprea C., Greco A., Maiorino A., Masselli C., Magnetic Refrigeration: An Eco-friendly Technology for the Refrigeration at Room Temperature, *Journal of Physics: Conference Series,* **655,** 012026, 2015.

[4] Wu C., Chen L., Sun F., Chen W., General Performance Characteristics of a Finite-speed Carnot Refrigerator, *Applied Thermal Engineering,* **16**(4), 299-303, 1996.

[5] Gschneidner K.A., Pecharsky V.K., Tsokol A.O., Recent Developments in Magnetocaloric Materials, *Report on Progress in Physics,* **68**(6), 2005.

[6] Brown J.S., Domanski P.A., Review of Alternative Cooling Technologies, *Applied Thermal Engineering,* **64**(1-2), 252-262, 2014.

[7] Rowe A., Tura A., Dikeos J., Chahine R., Near Room Temperature Magnetic Refrigeration, *The 1.International Green Energy Conference Proceedings,* **84,** 2005.

[8] Pecharsky V.K., Gschneidner K.A., Magnetocaloric Effect and Magnetic Refrigeration, *Journal of Magnetism and Magnetic Materials*, **200**(1-3), 44-56, 1999.

[9] Tusek J., Zupan S., Prebil I., Poredos A., Magnetic Cooling – Development of Magnetic Refrigerator, *International Journal of Mechanical Engineering*, **55(**5), 293-302, 2009.

[10] Tishin A.M., Spichkin Y.I., The Magnetocaloric Effect and its Applications, *Institute of Physics Publishing Bristol and Philadelphia*, 2003.

[11] Gomez J.R., Garcia R.F., Catoira A.D.M., Gomez M.R., Magnetocaloric Effect: A Review of the Thermodynamic Cycles in Magnetic Refrigeration, *Renewable and Sustainable Energy Reviews*, **17**, 74-82, 2013.

[12] Bahl C.R.H., Nielsen K.K., The Effect of Demagnetization on the Magnetocaloric Properties of Gadolinium, *Journal of Applied Physics*, **105**, 013916, 2009.

[13] Mezaal N.A., Osintsev K.V., Zhirgalova T.B., Review of Magnetic Refrigeration System as Alternative to Conventional Refrigeration System, *IOP Conference Series: Earth and Environmental Science*, **87**, 032024, 2017.

[14] Rowe A., Tura A., Experimental Investigation of a Three-material Layered Active Magnetic Regenerator, *International Journal of Refrigeration*, **29**(8), 1286-1293, 2006.

[15] Russek S.L., Zimm C.B., Potential for Cost-Effective Magnetocaloric Air Conditioning Systems, *International Journal of Refrigeration*, **29**, 1366-1373, 2006.

[16] Jacobs S., Auringer J., Boeder A., Chell J., Komorowski L., Leonard J., Russek S., Zimm C., The Performance of a Large-scale Rotary Magnetic Refrigerator, *International Journal of Refrigeration*, **37,** 84-91, 2014.

[17] Bouchekara H., Recherche sur les Systèmes de Réfrigération Magnétique: Modélisation Numérique, Conception et Optimisation, *Grenoble Institut National Polytechnique*, Thèse de Doctorat, 2008.

[18] Kitanovski A., Plaznik U., Tusek J., Poredos A., New Thermodynamic Cycles for Magnetic Refrigeration, *International Journal of Refrigeration*, **37**, 28-35, 2014.

[19] Kitanovski A., Egolf P., Thermodynamics of Magnetic Refrigeration, *International Journal of Refrigeration*, **29**, 3-21, 2006.

SUPERELASTIC PROPERTIES OF NI-TI FOR NEW GENERATION COOLING TECHNOLOGIES

Seray ÖZKAN, Ezgi DEMİRTAŞ, Gizem DURAK YÜZÜAK, Ercüment YÜZÜAK
Recep Tayyip Erdoğan University, Department of Energy Systems Engineering, Rize/Turkey
Email: serayozkan79@gmail.com, ezgidemirtaaas@gmail.com, gizemyuzuak@erdogan.edu.tr, ercument.yuzuak@erdogan.edu.tr

ABSTRACT

Refrigeration technologies used in modern societies are used to meet various needs from the operation of technological devices to the storage of fresh foods and ventilation systems. The working principle of today's traditional refrigeration technologies is based on traditional gas compression systems. The gases contained in the cooling technologies can cause environmentally harmful liquids and greenhouse gas production. To minimize these environmental problems, more cost-effective, environmentally friendly energy-free cooling system is being investigated as an alternative to traditional methods. Moreover, one of the main problems of conventional cooling systems is their low efficiency. Instead of these energy-intensive systems, high-efficiency alternative cooling technologies should be developed. For this purpose, solid-state cooling systems that exhibit magnetocaloric, electrocaloric and superelastic effects are being investigated extensively worldwide. The development of superelastic cooling applications is directly proportional to the development of high-performance superelastic materials. Among the properties of a good superelastic material, the mechanical strength under stress must have a high entropy change.

The best-known alloys with these properties are composed of alloys having shape memory properties. Due to the martensitic properties of these Ni-based and Cu-based alloys, major changes in structural phase transition and entropy are observed. This entropy change causes a temperature change in the material. Superelastic cooler designs can be made by using these materials in suitable mechanisms by removing this temperature change from the environment with the help of coolant.

This study covers the examination of superelastic cooling systems that promise efficient and environmentally friendly energy that will not increase carbon emissions and will not produce harmful gases and greenhouse effects. To achieve this result, NiTi alloys are produced by using arc melter method and investigate the structural properties by using the X-ray diffraction, scanning electron microscope and temperature changes in the material due to stress within the home-made mechanical measurement system.

Keywords: superelastic, NiTi, cooling technologies

ELASTOCALORIC PROPERTIES OF THE OPTIMIZED NI-TI ALLOY

Gizem Durak YÜZÜAK, Ercüment YÜZÜAK
Recep Tayyip Erdoğan University, Department of Energy Systems Engineering, Rize/Turkey
Email: gizemyuzuak@erdogan.edu.tr, ercument.yuzuak@erdogan.edu.tr

ABSTRACT

Cooling /heating technologies have great importance for sustaining and maintaining the comfort of life in modern societies, such as long-term food storage, home, and office air conditioning. The problems of global warming caused by damages to the nature of materials used in existing cooling technologies operating in the traditional vapor compression cycle increase the concerns about environmental issues in society. For this reason, worldwide vapor compression technologies are being abandoned gradually, according to developing technology. Systems based on solid state-caloric effects, which are an alternative to existing cooling technology, have been attracting attention with the studies carried out in recent years. In solid-state cooling technologies of magnetocaloric and electrocaloric requires a high driving external field to achieve very uniform thermal entropy changes. Among these, elastocaloric can be defined as different from others because having stress-induced phase transitions. This mechanical stress field can be easily produced with the current technological possibilities and the relatively cheaper than the initial investment, maintenance and repair costs.

In this study, direct temperature changes under stress based on the elastocaloric effect near room temperature of systems obtained in NiTi alloy are investigated. NiTi alloy is obtained through an arc melting furnace under vacuum with Ni and Ti elements and then heat-treated. Surface and composition measurements were performed by electron microscopy and the crystal structures were determined before, and after heat treatment by X-ray powder diffraction technique. The alloy transforms from B2 (Pm3m) ordered cubic structure to a monoclinic B19 (P2/m) martensitic phase according to the XRD results. The phase transition temperatures of the materials are measured by the temperature-dependent resistivity measurement system. A home-made system that sensed the temperature change of the material under mechanical stress fields in the vicinity of room temperature is used to examine the elastocaloric temperature change.

Keywords: Elastocaloric, Ni-Ti, Phase transition

FUELS AND COMBUSTION

ENGINE PERFORMANCE AND EXHAUST EMISSIONS OF A SPARK IGNITION ENGINE OPERATING ON 2.5 % n-BUTANOL/GASOLINE BLEND AND 2.5 % n-BUTANOL/GASOLINE BLEND WITH 9 % WATER INJECTION TO INTAKE AIR

Zehra ŞAHİN*, Orhan Nazım AKSU, Coşkun BAYRAM*****
*Karadeniz Technical University, Faculty of Engineering, Mechanical Eng. Dep.,Trabzon
Email: zsahin@ktu.edu.tr
**Karadeniz Technical University, Sürmene Abdullah Kanca High School, Trabzon
Email: onaksu@ktu.edu.tr
***Karadeniz Technical University, Of Technology Faculty, Energy Engineering Dep., Trabzon
Email: cbayram@ktu.edu.tr

ABSTRACT

The aim of the present paper was to investigate the effects of 2.5 % n-butanol/gasoline blend (nBGB2.5) and 2.5 % n-butanol/gasoline blend with 9 % water introduction to intake air (nBGB2.5-WI9) on the engine performance, total fuel cost, and exhaust emissions in an automobile spark ignition engine (SIE). nBGB2.5 contains 2.5 % n-butanol and 97.5 % gasoline in volume basis. Here, experiments for neat gasoline (NG) and 2.5 % n-butanol/gasoline blend (nBGB2.5) for five different loads have been performed at 3000 and 5000 rpms. Then, an adapted carburetor was mounted on the intake manifold on this engine, and tests for 2.5 % n-butanol/gasoline blend with 9 % water introduction to intake air (nBGB2.5-WI9) have been conducted at the same loads and engine speeds.

The test results showed that nBGB2.5 generally decreases brake specific fuel consumption (BSFC), carbon monoxide (CO), and total hydrocarbon (THC) emissions at all of the selected loads at 3000 and 5000 rpms. Nitrogen oxides (NO_x) increase at 3000 rpm, but they decrease at 5000 rpm with applying nBGB2.5. As NO_x could not reduce to the desired extent for only nBGB2.5, nBGB2.5 was applied by injecting 9 % water into the intake air (nBGB2.5-WI9). At 3000 rpm, NO_x decrease with nBGB2.5-WI9 compared to nBGB2.5. However, in both applications, NO_x emissions are higher than that of NG at 3000 rpm. At 5000 rpm, NO_x decrease with nBGB2.5-WI9 and nBGB2.5. However, decrement ratios of NO_x of nBG2.5-WI9 are higher than that of nBGB2.5. nBGB2.5-WI9 and nBGB2.5 decrease NO_x approximately 49 % and 9 %, respectively for 90 Nm load at 5000 rpm. The use of nBGB2.5-WI9 and nBGB2.5 has generally reduced CO at two engine speeds. However, the applying of nBGB2.5-WI9 has increased THC and BSFC more than the applying of nBGB2.5. Total fuel costs for nBGB2.5 and nBGB2.5-WI9 have become higher than NG.

Keywords: Spark Ignition Engine, N-butanol, Water Introduction to Intake Air

Symbols:

BSFC, b_e	Brake specific fuel consumption $[kg/kWh]$
C_1	Cost of gasoline $[\mathrm{TL}/lt]$
C_2	Cost of n-butanol $[\mathrm{TL}/lt]$
CO	Carbon monoxide (%)
LHV	Lover heating value $[kJ/kg]$
NG	Neat gasoline
nB2.5	2.5 vol. % n-butanol and 97.5 vol. % gasoline
nBGBs	n-butanol/gasoline blends
nB2.5-WI9	2.5 % n-butanol/97.5 % gasoline blend with 9 % water injection into the intake air
NO_x	Nitrogen oxides (ppm)
SIE	Spark ignition engine

THC	Total hydrocarbon (ppm)
VRs	Variation ratios (%)
α	Excess air coefficient

1. INTRODUCTION

It is known from the press and relevant literature that the use of diesel cars in the capitals of some European countries and the major metropolitan cities will be banned after 2020 due to increased environmental pollution [1]. Besides, the use of spark-ignition engines (SIEs) would become the most widespread solution for hybrid vehicles which are considered to be the solution of the near future. However, the vehicles used on highways are noted as to be the major emission contributor to the environment, which is dangerous to human health. For this reason, scientists, politicians, and automotive companies have been working intensively to reduce environmental pollution nowadays [2-4]. In this context, many different studies are carried out on the SIEs [2-4]. The use of different alternative fuels, especially alcohols [2, 5-7] and water addition [3, 4, 8-12] can be given as examples of these studies and the numbers of these studies have been increased in recent years.

As is known from the literature, studies on the use of ethanol in SIEs are very common [2, 6, 9]. However, butanol is an alternative fuel that has attracted the attention of researchers, and studies on n-butanol have been intensified in recent years. Also, water addition studies in SIE have been carried out in recent years [10-12]. It is known that nitrogen oxides can be reduced significantly with the use of water, especially in diesel engines [9, 13, 14]. Besides, the use of water is effective at sequestering knock through multiple mechanisms in SIEs [11]. The effects of different water addition to intake air on engine performance and exhaust emission have been carried out in KTU Mechanical Engineering Department [12]. The useful results have been obtained for engine performance and exhaust emissions in this experimental study. Additionally, the best water ratio has been determined as 9 %. Three different n-butanol-gasoline blends studies have also been carried out in this department, and 2.5 % n-butanol ratio has given the best results in terms of engine performance and exhaust emissions [15]. However, the desired reduction in NO_x has not been achieved for nBGB2.5. For this reason, here, an experimental study was performed to investigate 2.5 % n-butanol-gasoline blend with 9 % water addition into intake air (nBGB2.5-WI9) in the same engine.

2. EXPERIMENTAL SYSTEM AND MEASUREMENT

2.1 Experimental Setup

Experiments for neat gasoline (NG), 2.5 % n-butanol and 97.5 % gasoline blend (nBGB2.5), and 2.5 % n-butanol gasoline blend with 9 % water introduction to the intake air (nBGB2.5–WI9) were conducted in a four-cylinder, water-cooled automotive SIE. The engine's main technical specifications are given in Table 1. Also, Figure 1 shows a schematic diagram of the test system. A water brake dynamometer was used to measure the brake moment and effective power of this engine in the test system. An exhaust gas analyzer (MDS 450, AVL) was used to measure exhaust gases. The accuracies of CO_2, CO, and O_2 ratios are within ±0.3% vol, ±0.02 % vol, and ±0.02 % vol, respectively. Also, the accuracies of THC and NO_x measurements are within ±4 ppm and ±5 ppm, respectively. This exhaust gas analyzer also measures the excess air coefficient calculated from the CO_2, CO, O_2, and THC ratios.

2.2 Experimental Procedure

Here, NG and nBGB2.5 tests were conducted under five different loads of (105, 95, 85, 75, and 65) Nm at 3000 and (95, 85, 75, 65, and 55) Nm at 5000 rpms. Firstly, NG experiments were performed. Then, nBGB2.5 was carried out. For the nBGB2.5 examination, no modifications are made to this engine. In the present study, 99.9 % purity n-butanol was purchased from a commercial supplier (Sigma Aldrich firm representative of Turkey). The main properties of gasoline, n-butanol, and ethanol were presented in Table 2. After NG and nBGB2.5 tests were completed, an adapted carburetor was mounted on the intake manifold of the used engine to introduce ~9 % water into the intake air. The technical drawing of the adapted carburetor and other elements of the water

addition unit are shown in Figure 1. Here, a small water tank, a scaled-glass bulb, and a flexible pipe were used to measure the amount of the introduction water. Any other change on the experimental system and the used engine for water addition tests are not made. After these minor modifications, nBGB2.5-WI9 experiments were conducted for the above-selected loads at 3000 and 5000 rpms.

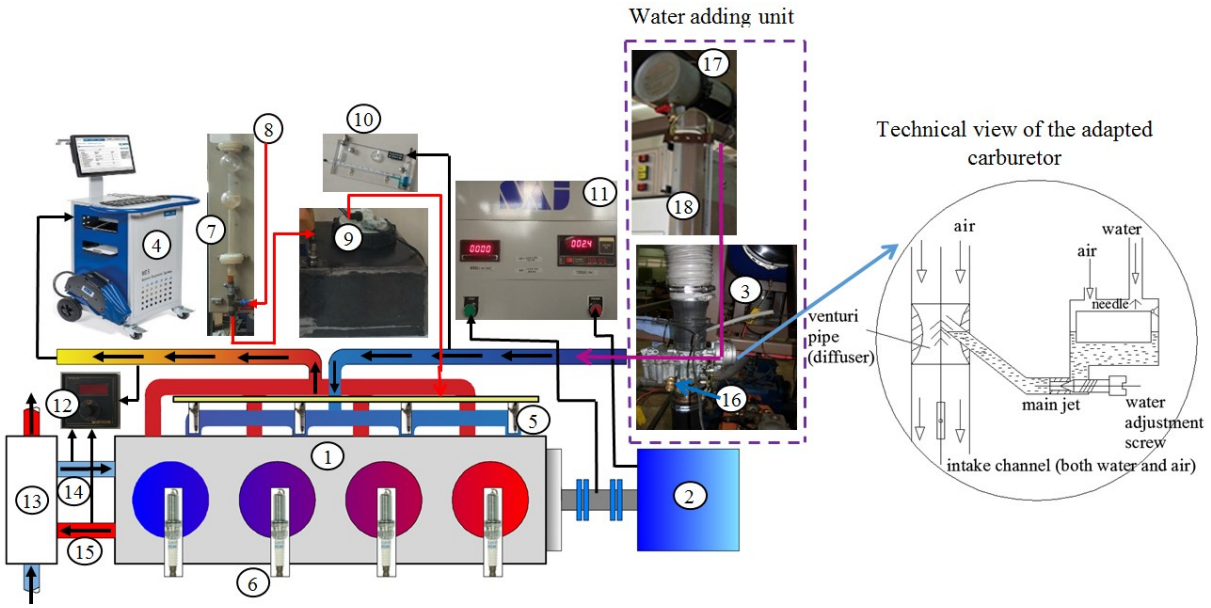

Figure 1. Experimental system. 1. Spark-ignition engine (Renault K7J700), 2. Hydraulic dynamometer, 3. Carburetor, 4. Gas analyzer (AVL, MDS 450), 5. Injector, 6. Spark plug, 7. Fuel measurement unit, 8. Fuel and control valve, 9. Fuel pump and tank, 10. Air measurement manometer, 11. Dynamometer control and instrument panel, 12. Digital temperature display (Engine coolant inlet and outlet temperatures, exhaust gases temperature, etc.), 13. Cooling unit, 14. Engine coolant inlet pipe, 15. Engine coolant outlet pipe, 16. Water adjustment screw, 17. Water tank, 18. Scaled glass bulb.

Table 1. The test engine specifications

Engine	Renault Clio
Displacement	1.4 liter
Cylinder numbers and compression ratio	4 & 9.5:1
Stroke & Bore	70 & 79.5 mm
Max output	55 kW @ 5800 rpm
Max torque	114 Nm @ 4250

2.3 Engine Performance Calculation and Properties of nBGB2.5 Determination

For NG, nBGB2.5, and nBGB2.5-WI9, engine performance parameters calculation, and the fuel properties determination are summarized as follows. The detailed information on this calculation method can be found in references [16, 17]. Using the measured data during the experiments, the engine performance characteristics have been calculated by using the following relations. In the following relations, N_e is effective power and B and b_e are total fuel consumption and brake specific fuel consumption (BSFC), respectively, and η_e is effective efficiency.

$$N_e[kW] = \frac{0.1013}{1000} \cdot \frac{T_b \cdot \omega}{P_0} \cdot \sqrt{T_0/293} \cdot X_{hum} \quad (1)$$

$$B[kg/h] = \frac{\Delta m_{nBGB}}{\Delta t} = \frac{(\Delta V_{nBGB} \cdot \rho_{nBGB}) \cdot 3600}{\Delta t \cdot 10^6} \quad (2)$$

$$b_e[kg/kWh] = \frac{B}{N_e} \quad (3)$$

$$\eta_e = \frac{3600}{LHV_{nBGB} \cdot b_e} \quad (4)$$

In Eq. (1); T_b $[Nm]$ and ω are brake torque and angular velocity, respectively. P_0 $[MPa]$ and T_0 $[K]$ are ambient air pressure and ambient air temperatures, respectively. X_{hum} is the humidity correction factor. In Eqs. (2); ΔV_{nBGB} is the volume of consumed nBGB, Δt $[s]$ is the duration of consumption of ΔV_{nBGB} volume (50 mL) of nBGB, ρ_{nBGB} is the density of nBGB, and LHV_{nBGB} is the lower heating value (LHV) of nBGB. Here, Mendeleyev formula [16, 17] has been used to calculate LHV of NG and n-butanol.

$$LHV[kJ/kg] = [33.91 \cdot c' + 125.6 \cdot h' - 10.89 \cdot (oy' - s') - 2.51 \cdot (9h' - w')] \cdot 10^3 \quad (5)$$

In Eq. (5) c', h', oy', s', and w' represent the elemental composition of the fuel and their values for gasoline and n-butanol have been given in Table 2. For nBGBs, density and LHVs have been determined by using the following relations given by Durgun [16, 17].

$$\rho_{nBGB}[kg/m^3] = \frac{x_{NG} \cdot \rho_{GN} + x_{nB} \cdot \rho_{nB}}{x_{NG} + x_{nB}} \quad (6)$$

$$LHV_{nBGB}[kJ/kg] = \frac{\sum_{i=1}^{n}(x_i \cdot \rho_i \cdot LHV_i)}{\sum_{i=1}^{n}(x_i \cdot \rho_i)} = \frac{x_G \cdot \rho_{NG} \cdot LHV_{NG} + x_{nB} \cdot \rho_{nB} \cdot LHV_{nB}}{x_{GN} \cdot \rho_{NG} + x_{nB} \cdot \rho_{nB}} \quad (7)$$

where ρ_{NG} and ρ_{nB} are the densities of gasoline and n-butanol, respectively, and x_{NG} and x_{nB} are the volumetric percentages of gasoline and n-butanol in the mixture, respectively. For the determination of the variation ratio of BSFC, the following relation has been used. The variation ratios (VRs) of the other engine characteristics and also exhaust emissions have been calculated in a similar way.

$$\frac{\Delta b_e}{b_e} \cdot 100\ [\%] = \left[\left(b_{e,nBGB} - b_{e,NG}\right)/b_{e,G}\right] \cdot 100 \quad (8)$$

where $b_{e,nBGB}$ and $b_{e,NG}$ are BSFC values for nBGB and gasoline, respectively.

2.4 Cost Analysis, Error Analysis, and Uncertainties

For cost analysis, the following formula proposed originally by Durgun [16, 17] has been used.

$$\frac{\Delta C}{C_1} \cdot 100\ [\%] = [(C_2 - C_1)/C_1] \cdot 100 = \left[\frac{x_1 + \sum_2^n x_i \cdot r_i}{x_1 + \sum_2^n x_i \cdot s_i} \cdot \left(1 + \frac{\Delta b_e}{b_e}\right) - 1\right] \cdot 100 \quad (9)$$

where

$$r_i = C_i/C_1;\ r_1 = C_1/C_1 = 1, r_2 = C_2/C_1 = 132.16/6.95 = 19.01583 \quad (9a)$$

$$s_i = \rho_i/\rho_1;\ s_1 = \rho_1/\rho_1 = 1, s_2 = \rho_2/\rho_1 = 810.6/732.9 = 1.10601 \quad (9b)$$

C_1 is the cost of gasoline, C_2 is the cost of n-butanol, and $\Delta b_e/b_e$ is the difference ratio of BSFC. ρ_1 and ρ_2 are densities of gasoline and n-butanol, respectively. Here, units of (C_1, C_2), (ρ_1, ρ_2), and b_e are $[TL/lt]$, $[kg/m^3]$

and $[kg/kWh]$ respectively. Table 2 presents the costs and other main properties of gasoline and n-butanol (and also ethanol).

Table 2. Fuel properties of gasoline, ethanol, and n-butanol [1, 5, 7]

	Gasoline	**Ethanol**	**n-Butanol**
Chemical formula	C_8H_{15}	C_2H_5OH	C_4H_9OH
Molecular mass $[kg/kmol]$	111.028	46.07	74.123
Density $[kg/m^3]$	732.9*	785	810.6*
Lower heating value $[kJ/kg]$	43238.5**	27423.24**	33630.8**
Octane number	87	86	100
Stoichiometric air-fuel ratio	14.7	8.95	11.28
Latent heat of evaporation $[kJ/kg]$	349	904	581.4
Kinematic viscosity, $[at\ 40\ ℃\ cSt]$	0.60	1.20	3.64
Composition, mass [%]	$c' = 0.873$ $h' = 0.127$	$c' = 0.521$ $h' = 0.131$ $oy' = 0.347$	$c' = 0.648$ $h' = 0.136$ $oy' = 0.216$
Cost $[TL/lt]$, July 2019, $1\$ = 5.65\ TL$***	6.95 -	50.72 (99,5 % purity)	132.16 (99,9 % purity)

*measured in laboratory, **calculated from Mendeleyev formula, *** TL: Turkish Lira

Here, from the results of applying the error analysis to the measured values [18], uncertainties for effective power and BSFC were computed and they took values at the interval of (0.365-1.486) % and (0.995-5.445) %, respectively. Thus, it can be said that these uncertainties are within acceptable limits.

3. RESULTS AND DISCUSSIONS

In this paper, influences of the nBGB2.5 and nBGB2.5-WI9 on BSFC, exhaust emissions, and total fuel cost at two engine speeds have been presented and evaluated in the following sections.

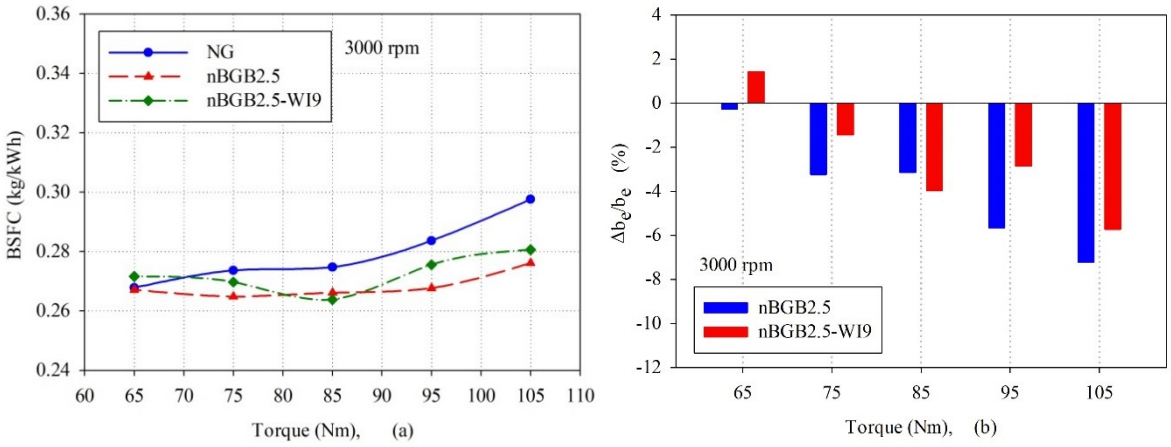

Figure 2 (a-b). Variations and VRs of BSFC with different loads at 3000 rpm, respectively.

Figures 2 (a-b) show the variations and VRs of BSFC versus different loads at 3000 rpm, respectively. It is observed that nBGB2.5 and nBGB2.5-WI9 generally decrease BSFC. But, the reduction ratios in BSFC for nBGB2.5 have become higher than that of nBGB2.5-WI9. It can be seen in Figure 2 (a-b) that the reductions in BSFC at high loads have been more effective in both applications. It is assumed that cylinder temperatures for high loads are higher than that of lower loads, which helps in the evaporation of n-butanol and mixing better

with air. The obtained maximum reduction ratios of BSFC for nBGB2.5 and nBGB2.5-WI9 are 7.23 % and 5.73 % under 105 Nm load, respectively.

The variations and VRs of BSFC versus different loads at 5000 rpm have been shown in Figures 3 (a-b), respectively. It can be observed from these figures that BSFC decreases for nBGB2.5 and nBGB2.5-WI9. However, the reductions in BSFC for nBGB2.5 have been more effective than that of nBGB2.5-WI9. The obtained maximum reduction ratios of BSFC for nBGB2.5 and nBGB2.5-WI9 are 9.95 % and 6.97 % under 55 Nm load at this engine speed.

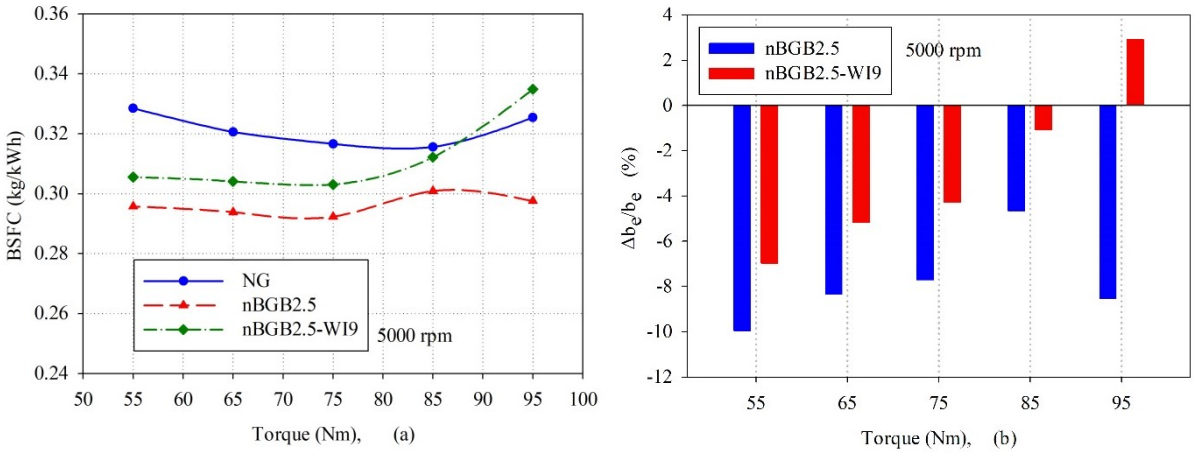

Figure 3 (a-b). Variations and VRs of BSFC with different loads at 5000 rpm, respectively.

The reasons for the reduction of BSFC when applied n-butanol-gasoline blend can be given as follows. It is known from the literature that n-butanol has more oxygen content than gasoline; this enhances combustion efficiency and also decreases BSFC. Besides, the latent heat of evaporation temperature of n-butanol is higher than gasoline. Therefore, the cylinder temperatures of the butanol-gasoline blend (nBGB2.5) may be lower, which reduces the loss of heat transfer through to cylinder wall to outside. This phenomenon helps to reduce BSFC [19]. Finally, compared to NG, laminar flame propagation speed and combustion speed of n-butanol are fast, which improves BSFC. When water is injected into intake air, the cylinder temperature values before the combustion process are through to drop further compared to n-butanol-gasoline blend and neat gasoline. Also, the vaporized water occupies some cylinder volume so that the density of the oxygen is diluted. These two factors slow down the combustion rate and lead to a longer combustion duration. Thus, BSFC increases slightly compared to nBGB2.5. However, the BSFC of nBGB2.5-WI9 is quite lower than that of NG.

Figures 4 (a-b) show the variations and VRs of CO versus different loads at 3000 rpm, respectively. It is observed that nBGB2.5 and nBGB2.5-WI9 significantly decrease CO. However, the reduction ratios in CO for nBGB2.5-WI9 have become higher than that of nBGB2.5 at this engine speed. The obtained maximum reduction ratios of CO for nBGB2.5 and nBGB2.5-WI9 are 6.82 % and 10.14 % under 85 Nm load.

Figures 5 (a-b) show the variations and VRs of CO versus different loads at 5000 rpms, respectively. It is observed that nBGB2.5 and nBGB2.5-WI9 generally decrease CO. The obtained maximum reduction ratios of CO for nBGB2.5 and nBGB2.5-WI9 are 5.12 % under 55 Nm load and 4.95 % under 75 Nm load at 5000 rpm.

The presence of n-butanol oxygen contributes to the combustion process, which can reduce CO emissions. It is also through that the use of both nBGB2.5 and nBGB2.5-WI9 may decrease cylinder temperatures during the combustion process. Thus, CO emissions formation may decrease at low temperatures [19]. Also, the extra oxygen in the n-butanol can contribute to the reduction of CO. In the case of water addition, CO could react with water vapor (H_2O) to form CO_2 and hydrogen over the temperature range of 600–2000 K, which could result in reducing of CO [9]. Similar results were found in the studies conducted in the literature [9, 20, 21].

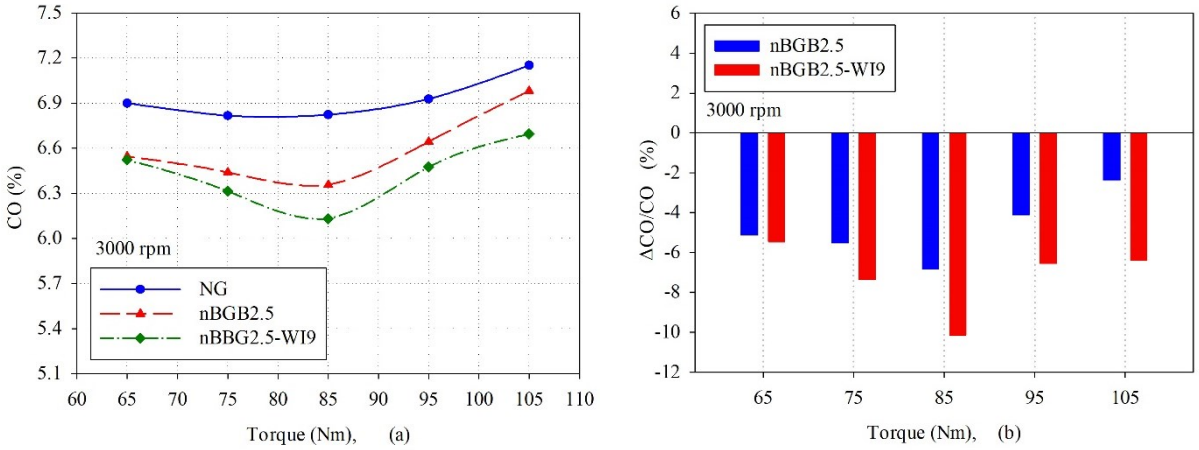

Figure 4 (a-b). Variations and VRs of CO with different loads at 5000 rpm, respectively.

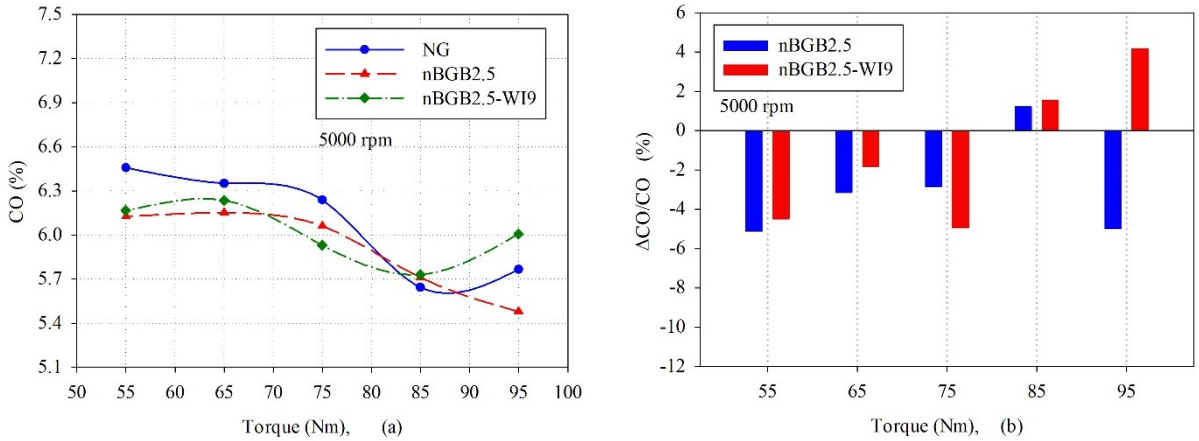

Figure 5 (a-b). Variations and VRs of CO with different loads at 5000 rpm, respectively.

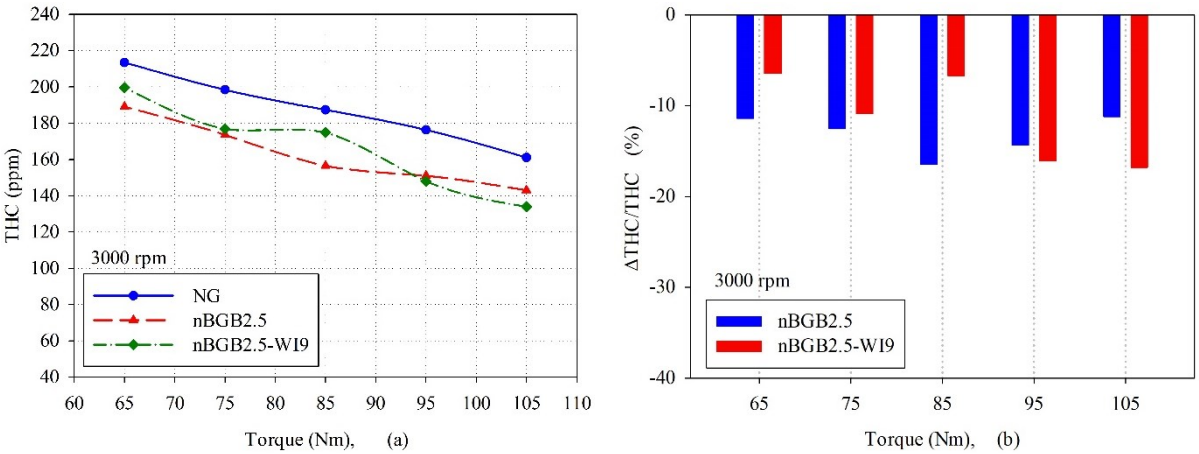

Figure 6 (a-b). Variations and VRs of THC with different loads at 3000 rpm, respectively.

Figures 6 (a-b) and Figures 7 (a-b) show the variations and VRs of THC versus different loads at 3000 and 5000 rpms respectively. It is observed that nBGB2.5 and nBGB2.5-WI9 decrease THC at 3000 and 5000 rpms. THC

formation in spark-ignition engines is mainly incomplete combustion of fuel, wall quenching effect, slit effect, wall oil film, and carbon adsorption [19]. The wall quenching effect of nBGB2.5-WI9 is more dominant than nBGB2.5 due to lower temperatures for water addition into the intake air. Therefore, THC values have been slightly higher than nBGB2.5 in the case of water addition. However, in the case of water addition, THC values are lower than NG.

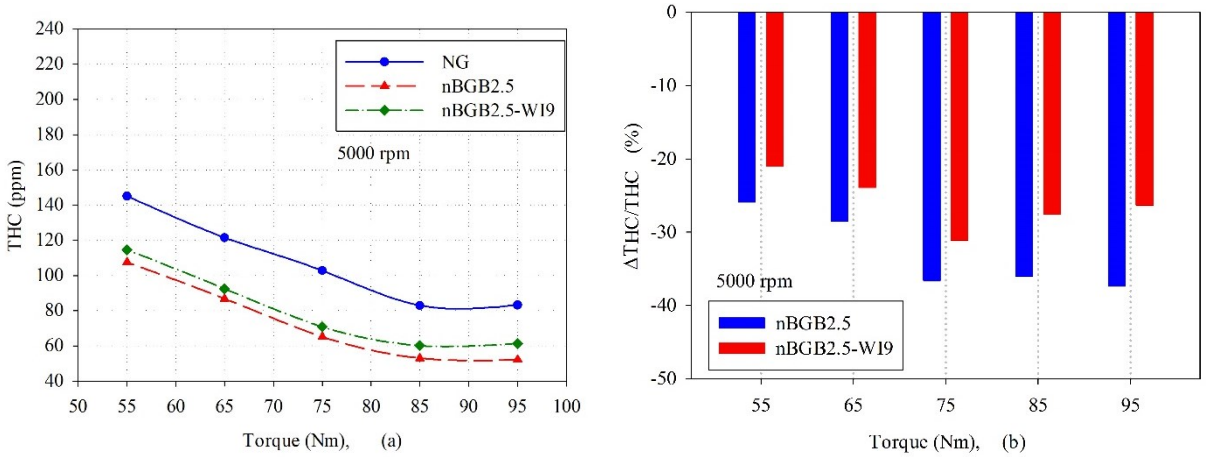

Figure 7 (a-b). Variations and VRs of THC with different loads at 5000 rpm, respectively.

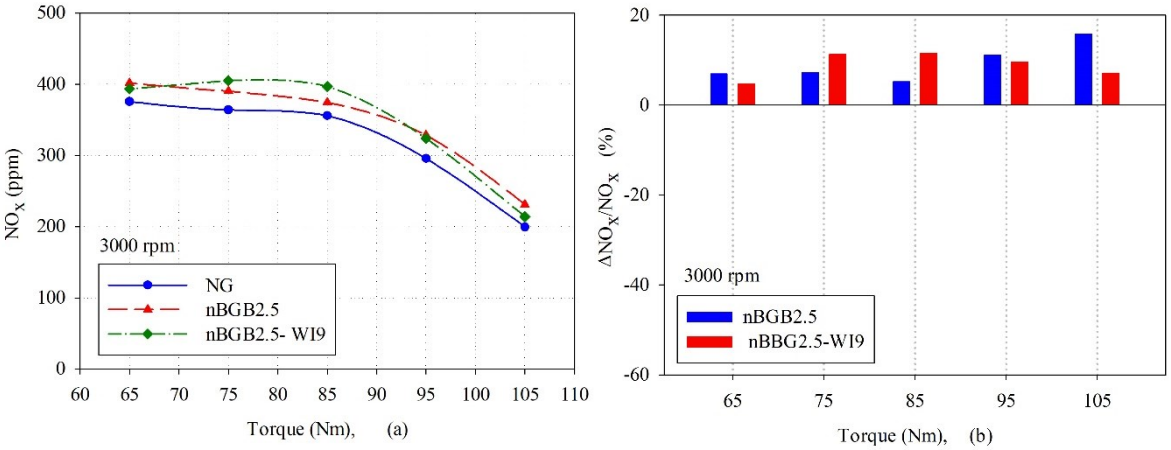

Figure 8 (a-b). Variations and VRs of NO_x with different loads at 5000 rpm, respectively.

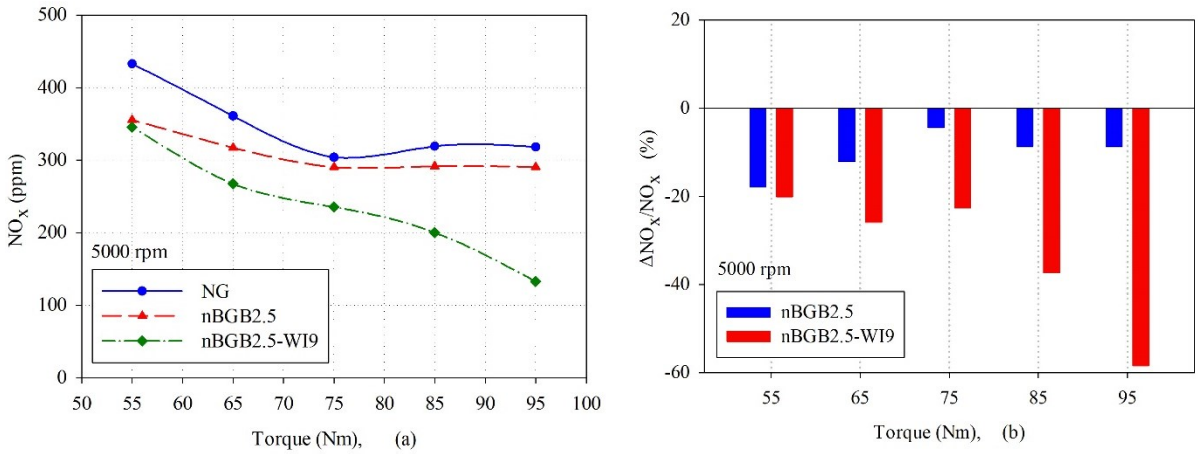

Figure 9 (a-b). Variations and VRs of NO_x with different loads at 5000 rpm, respectively.

Figures 8 (a-b) and Figures 9 (a-b) show the variations and VRs of NO_x versus different loads at 3000 and 5000 rpms respectively. Also, VRs of excess air coefficient values versus different loads at these engine speeds are presented in Figure 10 (a-b). It is observed that nBGB2.5 and nBGB2.5-WI9 increase NO_x at 3000 rpm, but they decrease NO_x at 5000 rpm. At 3000 rpm, nBGB2.5 and nBGB2.5-WI9 could not fully reflect its beneficial effect on NO_x. In some studies, in the literature, NO_x emissions were found to increase for n-butanol-gasoline blends [5, 7, 20]. NO_x emissions were found to be significantly reduced when only about 9 % water injection into the intake air was applied for this engine [12]. For example, 23%, 37%, 23%, and 13% reductions for NO_x emissions were found under (100, 90, 80, and 70) Nm load at 3000 rpm [12]. Thus, the increases in NO_x are thought to result from the addition of n-butanol to gasoline.

nBGB2.5 and nBGB2.5-WI9 significantly have reduced NO_x at 5000 rpm. The reduction rate in water addition has been more effective. It is known from the literature that the higher combustion temperature and local oxygen concentration in the peak temperature zone were favorable to NO_x emissions formation [22]. At 5000 rpm, combustion temperatures, especially the high combustion zone temperatures, are thought to decrease for nBGB2.5 and nBGB2.5-WI9. Therefore, NO_x emissions have decreased for both nBGB2.5 and nBGB2.5-WI9. Also, as can be seen in Figure 10b that excess air coefficient values slightly increase for nBGB2.5, but they decrease significantly for nBGB2.5-WI9. For this reason, the reductions in NO_x for nBGB2.5-WI9 have been more effective. The obtained maximum decrease ratios of NO_x for nBGB2.5 and nBGB2.5-WI9 are 17.86 % under 55 Nm load and 25.85 % under 65 Nm load at 5000 rpm respectively. Similar results were found in the studies conducted in the literature [9, 12, 23].

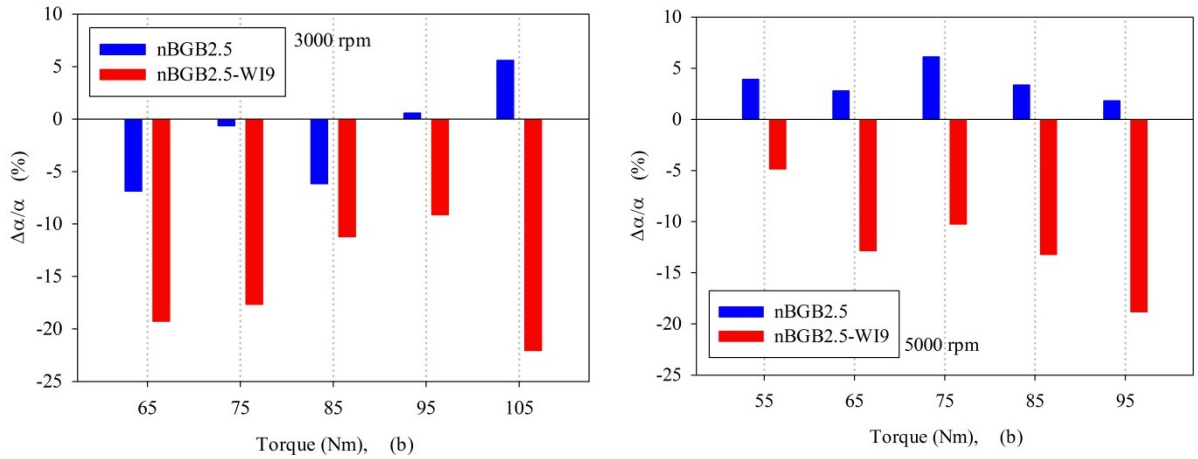

Figure 10 (a-b). VRs of excess air coefficient with different loads at 3000 and 5000 rpms, respectively.

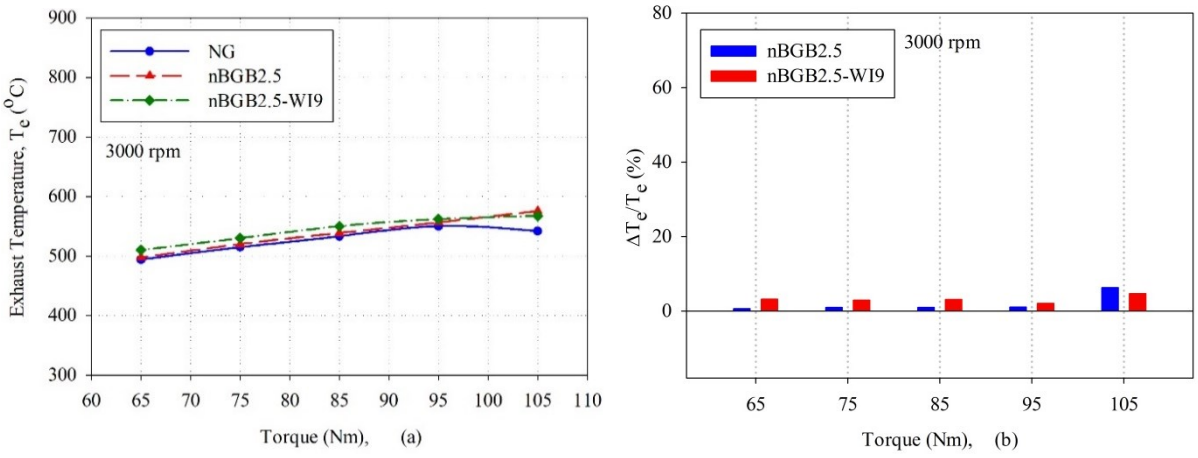

Figure 11 (a-b). Variations and VRs of T_e with different loads at 3000 rpm, respectively.

Figures 11 (a-b) and Figures 12 (a-b) show the variations and VRs of exhaust temperatures versus different loads at 3000 and 5000 rpms respectively. In both applications, the exhaust temperatures have increased at 3000 and 5000 rpms. The increase in exhaust temperature values has been lower at 3000 rpm compared to 5000 rpm. Increases in exhaust temperature values have been almost the same in cases of using both nBGB2.5 and nBGB2.5-WI9 at 3000 and 5000 rpms. In both applications, exhaust temperatures were become high, although local zone temperatures were thought to be lower in the combustion chamber.

Figures 13 (a-b) depict VRs of the total fuel cost at 3000 and 5000 rpms, respectively. It can be noticed that the total cost of fuels of nBGB2.5 and nBGB2.5-WI9 take higher values than that of NG at all of the selected test conditions. This is because the n-butanol price is nineteen times more times expensive than gasoline in Turkey.

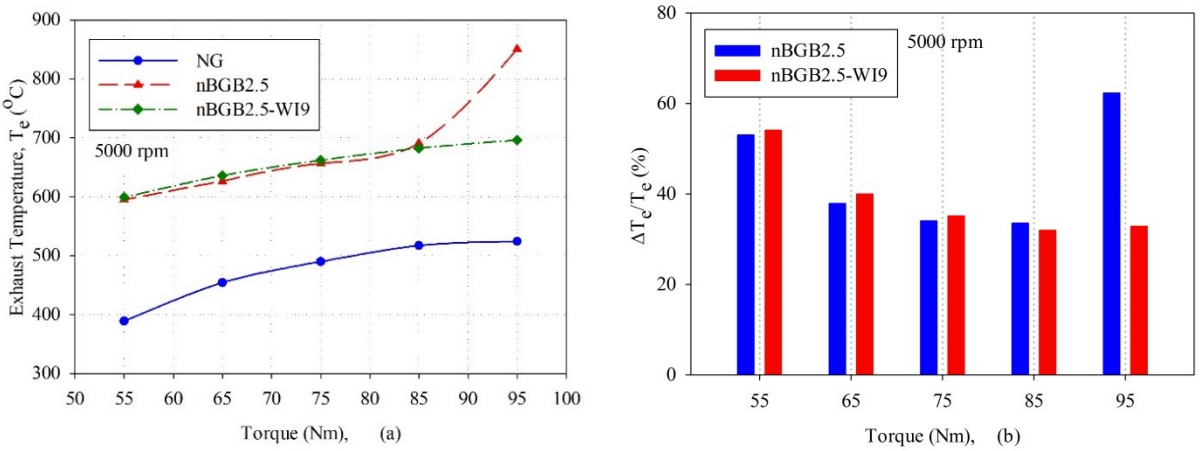

Figure 12 (a-b). Variations and VRs of T_e with different loads at 3000 rpm, respectively.

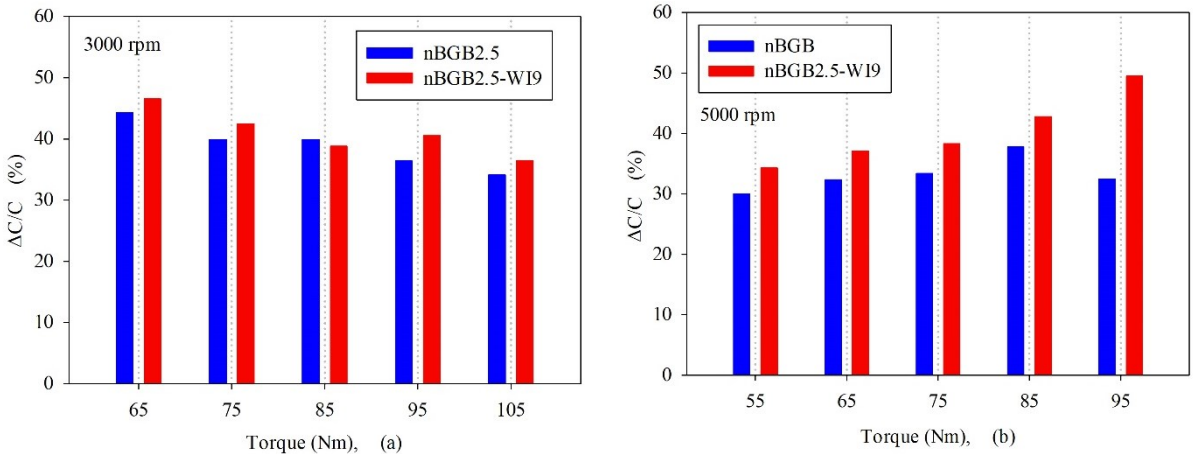

Figure 13 (a-b). VRs of cost with different loads at 3000 and 5000 rpms, respectively.

4. CONCLUSION

In this study, the effects of nBGB2.5 and nBGB2.5-WI9 on BSFC, fuel cost, and emission characteristics were investigated experimentally and compared with that of NG in an automotive SIE. Based on the experimental results the main effects of nBGB2.5 and nBGB2.5-WI9 can be summarized as follows:

1. nBGB2.5 and nBGB2.5-WI9 generally decrease BSFC at 3000 and 5000 rpms, but the reduction ratios in BSFC for nBGB2.5 have been higher than that of nBGB2.5-WI9 at two selected engine speeds. The obtained maximum reduction ratios of BSFC for nBGB2.5 and nBGB2.5-WI9 are 7.23 % and 5.73 % under 105 Nm load at 3000 rpm, 9.95 %, and 6.97 % under 55 Nm load at 5000 rpm, respectively.

2. nBGB2.5 and nBGB2.5-WI9 importantly decrease CO at 3000 rpm. However, they decrease generally decrease CO at 5000 rpm. At selected engine speeds, the reduction ratios in CO for nBGB2.5-WI9 have been higher than that of nBGB2.5. The obtained maximum reduction ratios of CO for nBGB2.5 and nBGB2.5-WI9 are 6.82 %, and 10.14 % under 85 Nm load at 3000 rpm and 5.12 % under 55 Nm load, and 4.95 % under 75 Nm load at 5000 rpm, respectively.

3. nBGB2.5 and nBGB2.5-WI9 decrease THC at 3000 and 5000 rpms. THC emissions have been slightly higher than nBGB2.5 in the case of water addition. However, in the case of water addition, THC emissions are lower than NG.

4. nBGB2.5 and nBGB2.5-WI9 increase NO_x at 3000 rpm, but they decrease NO_x at 5000 rpm. The obtained maximum decrease ratios of NO_x for nBGB2.5 and nBGB2.5-WI9 are 17.86 % under 55 Nm load and 25.85 % under 65 Nm load at 5000 rpm respectively.

5. The total cost of fuels of nBGB2.5 and nBGB2.5-WI9 take higher values than that of NG at all of the selected test conditions. This is because the n-butanol price is nineteen times more times expensive than gasoline in Turkey.

6. It is advisable to apply nBGB2.5 and nBGB2.5-WI9 to this engine. In both applications, beneficial results were obtained in terms of engine performance characteristics and exhaust emissions. nBGB2.5 results were generally better than nBGB2.5-WI9. Only reductions in NO_x emissions were more effective in the use of nBGB2.5-WI9 than that of nBGB2.5.

REFERENCES

[1] Şahin, Z., Aksu, O.N. & Durgun, O., Experimental Investigation of the Effects of n-Butanol Fumigation on Engine Performance and Exhaust Emissions in a Turbocharged DI Diesel Engine, *II. International Conference of Advanced Engineering Technologies (ICADET)*, 708-717, 2017.

[2] Awad, O. I., Mamat, R., Ibrahim, T. K., Hammid, A. T., Yusri, I. M., Hamidi, M. A., Humada A. M. & Yusop, A. F., Overview of the Oxygenated Fuels in Spark Ignition Engine: Environmental and Performance, *Renewable and Sustainable Energy Reviews*, 91, 394-408, 2018.

[3] Bozza, F., Bellis V. D. & Teodosio L., Potentials of Cooled EGR and Water Injection for Knock Resistance and Fuel Consumption Improvements of Gasoline Engines, *Applied Energy*, 169, 112–125, 2016.

[4] Nguyen, Q-A. & Wu, Y-Y., Experimental Investigations of Using Water-Gasoline Emulsions as a NOx Treatment and its Effects on Performance and Emissions of Lean-Burn Spark-Ignition Engine, *Proceedings of the International Conference on Power Engineering-09 (ICOPE-09)*, Kobe-Japan, November 2009.

[5] Wigg, B. R. A study on the emissions of butanol using a spark ignition engine and their reduction using electrostatically assisted injection, Master Thesis, University of Illinois at Urbana-Champaign, 2011.

[6] Chansauria P., Mandloi RK. Effects of ethanol blends on performance of spark ignition engine- A Review, *Materials Today: Proceedings*, 2(5): 4066–4077, 2018.

[7] Wang, Y., Yu, X., Ding, Y., Du, Y., Chen Z. & Zuo X., Experimental Comparative Study on Combustion and Particle Emission of n-Butanol and Gasoline Adopting Different Injection Approaches in a Spark Engine Equipped with Dual-Injection System, *Fuel*, 211, 837-849, 2018.

[8] Mingrui, W., Sa, N. T., Turkson, R. F., Jinping, L. & Guanlun G., Water Injection for Higher Engine Performance and Lower Emissions, *Journal of the Energy Institute*, 90(2), 285-299, 2017.

[9] Li, Y., Chen, Y., Wu, G. & Liu, J., Experimental evaluation of water-containing isopropanol-n-butanol-ethanol and gasoline blend as a fuel candidate in spark-ignition engine, *Applied Energy*, 219, 42-52, 2018.

[10] Wilson, J. P., Effects of Water Injection and Increased Compression Ratio in a Gasoline Spark Ignition Engine, Master Thesis, University of Idaho, USA, 2011.

[11] Worm, J., Naber, J., Duncan, J., Barros, S. & Atkinson, W., Water Injection as an Enabler for Increased Efficiency at High-Load in a Direct Injected, Boosted, SI Engine, *SAE International*, 10(3), 951-958, 2017, (doi:10.4271/2017-01-0663).

[12] Soysal, D., Şahin, Z. & Durgun, O., Experimental Investigation of the Effects of Water Adding to the Intake Air on the Engine Performance and Exhaust Emissions, *22nd Congress on Thermal Science and Technology*, Kocaeli-Turkey, pp.705-711, 2019.

[13] Lanzafame, R., Water Injection Effects In A Single-Cylinder CFR Engine, *SAE Technical Paper*, 1999-01-0568, 1999.

[14] Subramanian, K. A., A comparison of water–diesel emulsion and timed injection of water into the intake manifold of a diesel engine for simultaneous control of NO and smoke emissions, *Energy Conversion &Management,* 52 (2), 849-857, 2011.

[15] Şahin, Z., Aksu, O. N. & Bayram, C., Experimental Investigation of the effects of n-butanol/gasoline blends on Engine Performance and Exhaust Emissions in a Spark Ignition Engine, *International Conference on Advanced Engineering Technologies (ICADET 2019)*, Bayburt-Turkey, 2019.

[16] Durgun, O., Experimental Methods in Engines, Lecturer notes for laboratory, Karadeniz Technical University, Engineering Faculty, Mechanical Engineering Department, 1990.

[17] Durgun, O., Internal Combustion Engines, Basic Principles. TMMOB Chamber of Naval Eng., İstanbul, 2018.

[18] Holman, J. P., Experimental Methods for Engineers. McGraw Hill Press, New York, 2001.

[19] Tian, Z., Zhen, X., Wang, Y., Liu, D. & Li, X., Combustion and emission characteristics of n-butanol-gasoline blends in SI direct injection gasoline engine, *Renewable Energy*, 146, 267-279, 2020.

[20] Li, Y., Nithyanandan, K., Zhang, J., Lee, C.F. & Liao, S., Combustion and Emissions Performance of a Spark Ignition Engine Fueled with Water Containing Acetone-Butanol-Ethanol and Gasoline Blends, *SAE Technical Paper*, 2015-01-0908, 2015.

[21] Feng R., Yang J., Zhang D., Deng B., Fu J., Liu J., Liu, X., Experimental study on SI engine fuelled with butanol–gasoline blend and H_2O addition, Energy Conversion and Management, 74, 192-200, 2013.

[22] Heywood, J.B., Internal Combustion Engine Fundamental. McGraw-Hill Book Company, New York, 1988.

[23] Rohit, A., Satpathy, S., Choi, J., Hoard, J., Surnilla G. & Hakeem M., Literature Survey of Water Injection Benefits on Boosted Spark Ignited Engines, *SAE Technical Paper*, 2017-01-0658, 2017.

THEORETICAL INVESTIGATION OF ENGINE PERFORMANCE AND EXHAUST EMISSIONS IN ETHANOL-FUELED DUAL-PLUG SI ENGINE

İsmail ALTIN*, Atilla BİLGİN, İsmet SEZER*****
*Karadeniz Technical University, Department of Naval Architecture and Marine Engineering, Trabzon/Turkey
Email: isaltin@ktu.edu.tr
** Karadeniz Technical University, Department of Mechanical Engineering, Trabzon/Turkey
Email: bilgin@ktu.edu.tr
***Gümüşhane University, Department of Mechanical Engineering, Gümüşhane/Turkey
Email: isezer@gumushane.edu.tr

ABSTRACT

Most of the on-road vehicles with two and four wheels have spark ignition (SI) engines. The effect of equivalence ratio, spark timing, and spark-plug location on engine performance and exhaust emission characteristics was investigated by using theoretical model in ethanol-fueled dual-plug SI engine. Findings showed that dual-spark plug configuration (SpL@d) in SI engine is the convenient solution to continue improved engine performance and exhaust emission characteristics if there are some design constraints in contrast to the centrally located single plug (SpL@c) configuration gives the best engine performance and fuel economy.

Keywords: SI engine, Dual-plug, Ethanol, Engine performance, Exhaust emission.

Symbols

be	Brake specific fuel consumption
CA	Crank angle (°)
CO	Carbon monoxide
CO_2	Carbon dioxide
F_s	Stoichiometric fuel/air ratio (-)
h	Specific enthalpy (kJ kg^{-1})
H_u	Lower heating value (kJ kg^{-1})
k	Constant (k=2 for 4-stroke engines)
m	Mass (kg)
n	Engine speed (rpm)
NO_x	Nitrogen oxide
p	Cylinder pressure (bar)
P_0	Ambient pressure (bar)
P_e	Brake power (kW)
P_{me}	Mean effective pressure (bar)
P_{mi}	Mean indicated pressure (bar)
$P_{m,m}$	Mean pressure of mechanical losses (bar)
Q	Heat loss (J)
QD	Quasi-dimensional
rf	Flame radius (mm)
R	Ideal gas constant (J g^{-1} K^{-1})
SpL@c	Centrally-located single plug
SpL@d	Diagonally located dual-plugs
T	Temperature (K)
T	Engine torque (Nm)
T_0	Ambient temperature (K)
u	Specific internal energy (kJ kg^{-1})
V	Instantaneous cylinder volume (m^3)
V_h	Displacement volume (m^3)
W	Work (J)

x	Mass fraction burned (-)
y_{CO}	Volumetric ratio of CO in combustion products (ppm)
y_{CO2}	Volumetric ratio of CO_2 in combustion products (ppm)
y_{NO}	Volumetric ratio of NO in combustion products (ppm)
z	Cylinder number (-)
ϕ	Equivalence ratio [-]
η_e	Brake thermal efficiency (-)
η_v	Volumetric efficiency (-)
θ	Crank angle (°)
ω	Angular velocity (s^{-1})
b	Burned
i	Indicated
u	Unburned
L	Loss

1. INTRODUCTION

Numerous researchers have focused on the performance and the exhaust emission characteristics of spark ignition (SI) engines [1-3]. Operation with lower exhaust emissions in SI engines has become a critical challenge for the automotive industry [4]. Also, it was requested the improved engine performance as well. The usage of dual-plug in SI engines has the potential to achieve all expectations on performance and emissions [1]. Dual-plug configuration in SI engine ensures robust and stable combustions [6]. Alternative fuels associated with engine configuration are of great significance in SI engines [7]. Ethanol is of great importance among biofuels [5]. Ethanol (C_2H_5OH) is obtained from any fermentable material [8] and has high octane number and flame speed [7]. Also, ethanol fuel can be used as pure or mixed with gasoline in SI engines without modification [8]. The disadvantage of ethanol is a bit high production cost relative to gasoline. Engine performance characteristics in an ethanol- fueled dual-plug SI engine were experimentally investigated by Almeida [9]. It was found that there was an improvement in the performance parameters at all test conditions [9]. Nakayama et al. investigated a new engine concept (gasoline-fueled 1.3L 2-plug SI engine-L13A). This engine achieved both low fuel consumption and low emissions [10]. Wada et al. investigated fuel economy, power, and low emission technology of i-DSI 2-plug engine. They found improvement in fuel consumption and maximum engine torque-speed [11]. Nakata et al. studied effects of high RON fuels (ethanol and ethanol blends) on engine thermal efficiency in the dual-plug engine [12]. The use of ethanol obtained an improvement in the thermal efficiency of the SI engine and mitigated exhaust emissions (HC, NO_x, and CO_2) [12]. Raja et al. considered various gasoline-ethanol blends for twin spark ignition engine in the study [13]. High ethanol percentage contributed to increasing brake specific fuel consumption and volumetric efficiency while it decreased exhaust emissions [13]. Yontar numerically investigated the effects ethanol and blending fuels on engine performance characteristics in a sequential ignition dual-plug SI engine. The use of E85 fuel increased engine performance value when compared to gasoline [14].
Literature survey showed that there were various studies on the investigation of engine performance and exhaust emissions of dual-plug SI engine. However, it could not be found comprehensive study including the effect of equivalence ratio, spark timings, and spark plug locations on these characteristics.

This study aims to clarify the effect of equivalence ratio, spark timing, and spark plug location on the performance and the exhaust emissions of ethanol-fueled dual-plug SI engine.

2. THEORETICAL MODEL

A two-zone quasi-dimensional (QD) thermodynamic cycle simulation model was used to investigate the performance and exhaust emission characteristics of ethanol-fueled dual-plug SI engine. The model uses flame propagation model approach to meet quasi-dimensional concept. An infinitesimally thin spherical flame front divides the enclosed combustion chamber into two regions called burned and unburned zone. The schematic presentation of thermodynamic model is shown in Figure 1. The governing equations of the thermodynamic model are a differential form of energy conservation equation and obtained by applying an open thermodynamic

system approach to SI engine combustion chamber. Further detail of the QD thermodynamic model can be found in Ref. [8].

Table 1 contains specifications of reference engine and fuel properties. Three spark plug locations (diagonally located two (SpL@d), centrally located single (SpL@c), and side located single spark plug (SpL@s) on cylinder head), equivalence ratios (from 0.8 to 1.1 by 0.1), spark timings (from -35 CA to -20 CA by 5 CA), and nominal engine speed (5700 rpm) were considered in the simulation studies. The equation set of the QD thermodynamic model was simultaneously solved by computer code written in FORTRAN. Two validation tests were carried out: (a) comparison of performance (engine power output and engine torque) parameters at specific engine speed and using mean absolute percentage error (MAPE) [5]. Figure 2, which contains engine torque and power, shows validation of the presented theoretical model. Numerical results of the validation tests are also given in Table 2. Validation tests (Figure 2 and MAPE) show that the presented model complies with available literature.

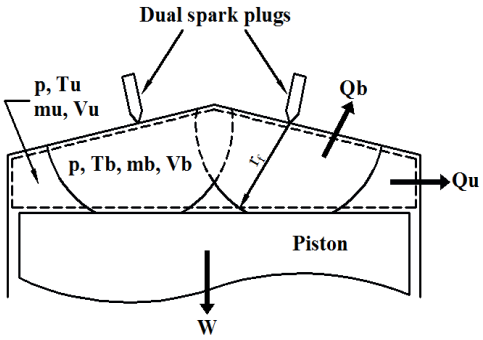

$$\dot{Q} - p\dot{V} = m\dot{u} + u\dot{m} + \dot{m}_L\, h_L/\omega \quad (1)$$

$$\dot{p} = f_1(\theta, p, T_b, T_u) \quad (2)$$

$$\dot{T}_b = f_2(\theta, p, T_b, T_u) \quad (3)$$

$$\dot{T}_u = f_3(\theta, p, T_u) \quad (4)$$

Figure 1. Schematic presentation of thermodynamic model and governing equations of the model [6].

Table 1. Engine specifications and fuel properties [5].

Bore x Stroke (mm)	73 x 80	Chemical formula	C_2H_5OH
Connecting rod length (mm)	135	Molecular weight (kg/kmol)	46.07
Compression ratio (-)	10.8:1	Stoichiometric AFR by mass (-)	8.94
Ignition system	DPSI	Lower heating value (MJ/kg)	≈27
Maximum power (kW@rpm)	63@5700	Research octane number (-)	111
Maximum torque (Nm@rpm)	119@2800	Laminar flame speed (cm/s)	≈ 39

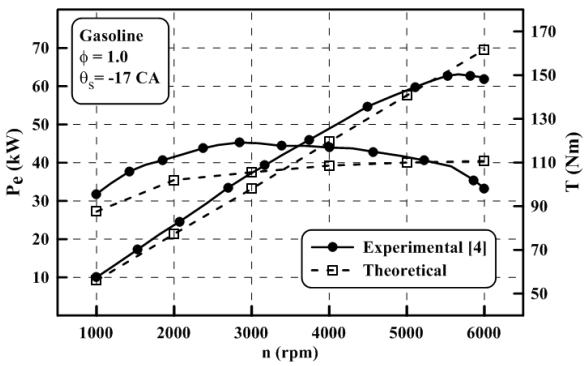

$$p_{mi} = \frac{W_i}{V_h} \quad (5)$$

$$p_{me} = p_{mi} - p_{m,m} \quad (6)$$

$$P_e = \frac{p_{me} V_h z n}{k 60} \quad (7)$$

$$\eta_e = \frac{p_{me} R T_o}{F_s \phi H_u p_o \eta_v} \quad (8)$$

$$b_e = \frac{3600}{H_u \eta_e} \quad (9)$$

Figure 2. Validation of the QD thermodynamic model (1st column) and the governing equations for the computation of engine performance characteristics (2nd column).

Table 2. Numerical results of the validation tests

Performance parameters	Test 1 (deviation from the exp. data)	Test 2 (MAPE)
Engine torque	11.3% @ 2800 rpm	7.69%
Engine power	3.84% @ 5700 rpm	8.51%

4. RESULTS AND DISCUSSION

4.1 Evaluation of performance parameters

Figure 3-(a), (b), and (c) show the effect of equivalence ratio on brake power, brake specific fuel consumption, and maximum burned gas temperature of ethanol-fueled dual-plug SI engine, respectively. The highest brake power in the simulation was obtained at SpL@c configuration, having the shortest flame travel distance throughout all equivalence ratios (Figure 3-a). The data of brake power at SpL@d case were close to SpL@c case because dual ignition accelerated the combustion process by increased flame front area. Enhanced combustion led to increasing brake power of the SI engine. Maximum brake power was obtained for the vicinity of the stoichiometric ratio (ϕ=1) in all three cases. 2.2% higher brake power at SpL@c was obtained for stoichiometric ratio in comparison with SpL@d case. Operating with a higher equivalence value (in other words, rich mixture) did not affect brake power. Brake specific fuel consumptions (bsfc) were indicated in Figure 3-b. bsfc at SpL@c case was minimum throughout all equivalence ratios. There were significant differences among brake specific fuel consumptions at lower equivalence ratios. After the stoichiometric ratio, it was determined that the equivalence ratio did not dominate at higher equivalence (more than stoichiometric) ratios. Equivalence ratio ϕ=0.9 led to minimum bsfc in the ethanol-fueled dual-plug engine. Figure 4-(a), (b), and (c) show the effect of spark timing on brake power, brake specific fuel consumption, and maximum burned gas temperature of ethanol-fueled dual-plug SI engine, respectively. Spark timing close to the top dead center resulted in higher brake power and lower brake specific fuel consumption. SpL@c case can be reported here as the best configuration, as well. Maximum burned gas temperature is another critical parameter in SI engines since the higher burned gas temperature can result in higher NO_x emissions. Maximum burned gas temperature was obtained at SpL@c and SpL@d cases, as shown in Figure 3-(c) and Figure 4-(c).

4.2 Evaluation of exhaust emissions

Figure 5 shows effects of equivalence ratio on exhaust emissions (CO_2, CO, and NO). CO_2 emission indicates combustion efficiency. A large quantity of CO_2 emission, which is a harmful combustion product, leads to global warming. Figure 5-(a) relates to CO_2 emission. The highest CO_2 emission was at a stoichiometric ratio with various spark plug configurations. Improvement in the combustion process with dual-plug can be indicated according to CO_2 emission levels in Figure 5-(a). CO emission increased as the equivalence ratio increased because of the lack of oxygen in the combustion chamber. NO emission was the highest at ϕ=0.9 (a bit lean mixture). This finding complies with the literature [15].

The effect of spark timing on exhaust emissions was presented in Figure 6. The spark timing did mostly not affect NO emission and CO_2 emission in general. CO emission decreased at advanced spark timing, i.e., -20 CA.

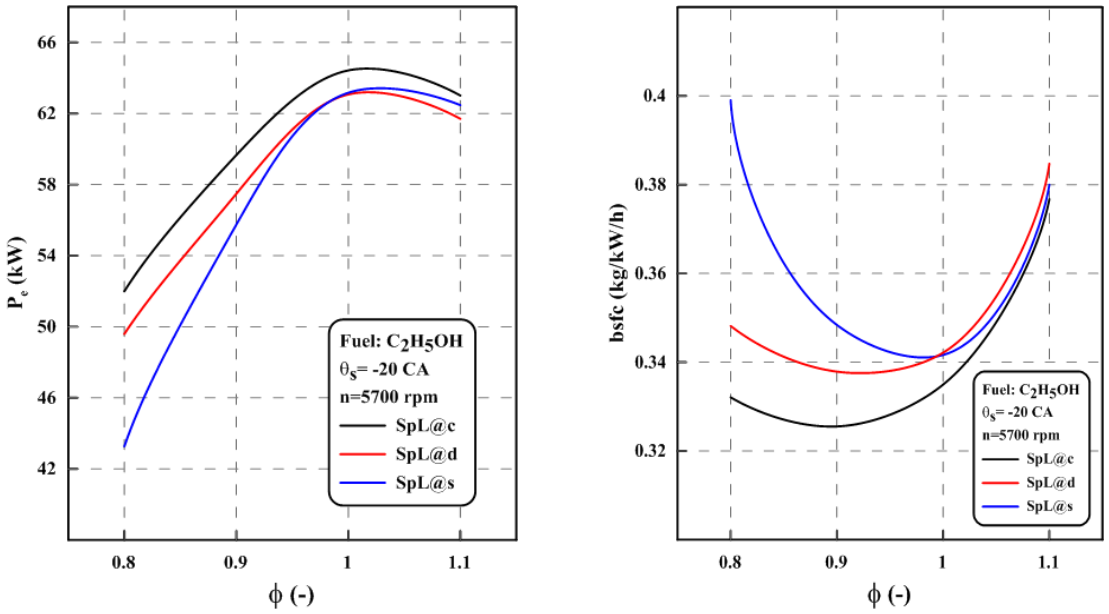

(a) (b)

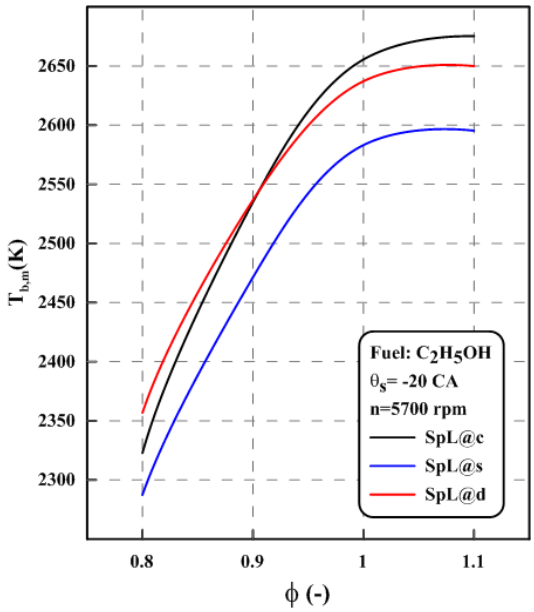

(c)

Figure 3. Effect of equivalence ratio on the performance parameters: (a) brake power, (b) brake specific fuel consumption, and (c) maximum burned gas temperature

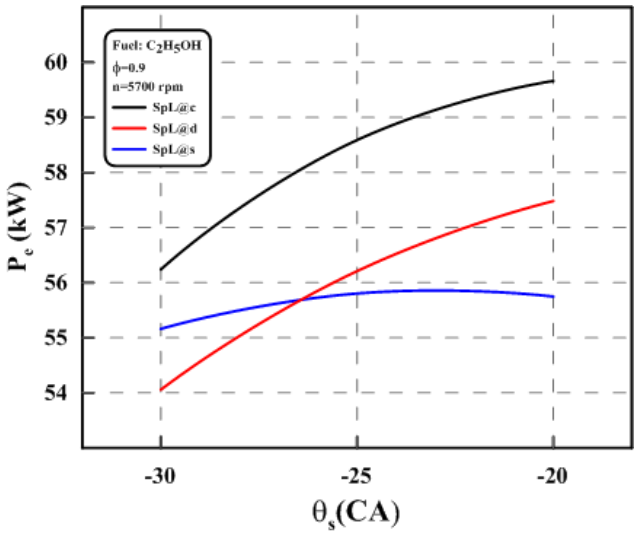

(a)

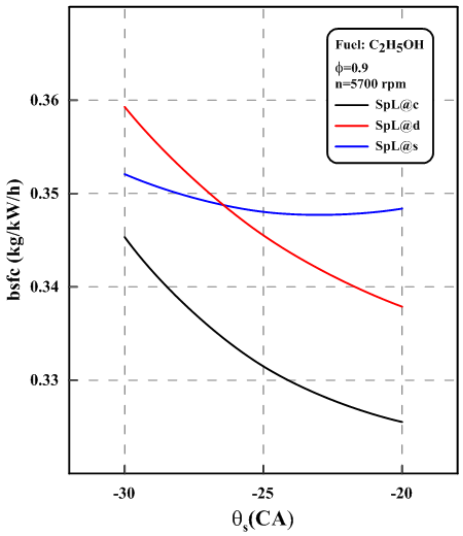

(b)

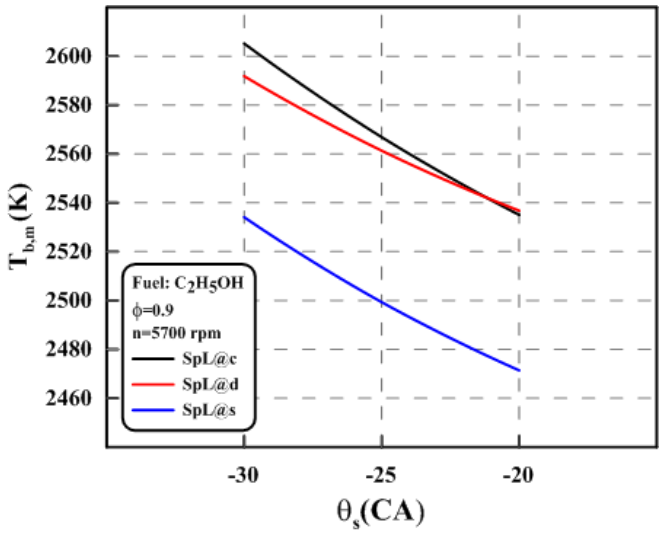

(c)

Figure 4. Effect of spark timings on the performance parameters: (a) brake power, (b) brake specific fuel consumption, and (c) maximum burned gas temperature

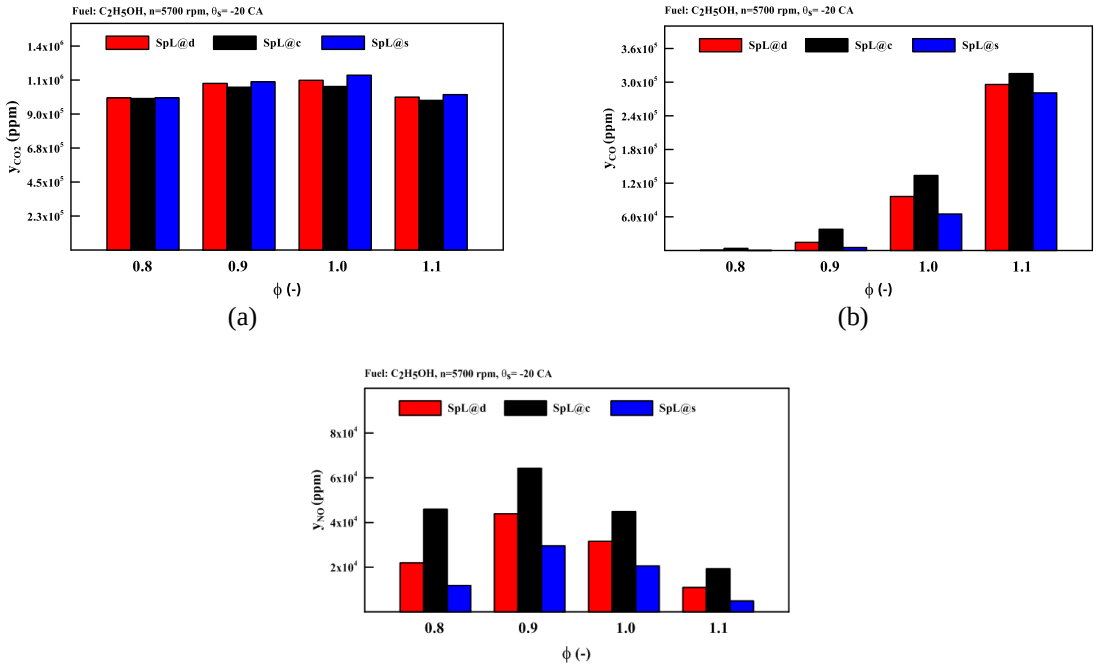

Figure 5. Effect of equivalence ratio on exhaust emissions: (a) CO_2, (b) CO, and (c) NO

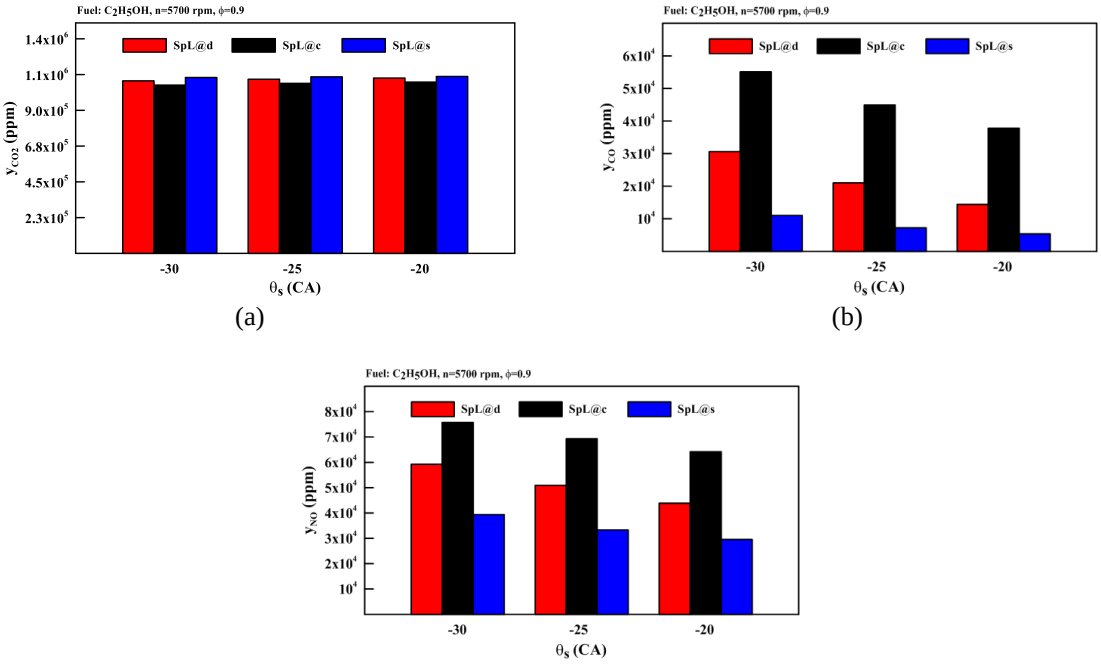

Figure 6. Effect of spark timing on exhaust emissions: (a) CO_2, (b) CO, and (c) NO

5. CONCLUSIONS

In this study, the effect of equivalence ratio, spark timing, and spark plug location on engine performance and exhaust emission characteristics was theoretically investigated in ethanol-fueled dual-plug SI engine. The findings of the present study lead to the following conclusions:

- The centrally located single plug configuration (SpL@c) gives the best engine performance and fuel economy.
- Dual-spark plug configuration (SpL@d) in an SI engine is the convenient solution to continue improved engine performance characteristics if there are some design constraints.
- Equivalence ratio ϕ=0.9 led to minimum bsfc in the ethanol-fueled dual-plug engine.
- 2.2% higher brake power at SpL@c was obtained for ϕ=1.0 in comparison with the SpL@d case.
- SpL@c case has maximum burned gas temperature.
- The highest CO_2 emissions were at stoichiometric ratio with various spark plug configurations.
- The highest NO emission was obtained at ϕ=0.9 (a bit lean mixture).
- CO emission decreased at advanced spark timing.

REFERENCES

[1] Altın, İ. & Bilgin A., A parametric study on the performance parameters of a twin-spark SI engine, *Energy Conversion and Management*, **50**(8), 1902-1907, 2009.

[2] Altin, İ., Sezer İ. & Bilgin, A., Effects of the stroke/bore ratio on the performance parameters of a dual-spark-ignition (DSI) engine. *Energy & Fuels*, **23**(4), 1825-1831, 2008.

[3] Altın, İ. & Bilgin, A., Farkli buji sayıları ve konumularına sahip buji ateşlemeli bir motorda ateşleme avansının motor performans parametreleri üzerindeki etkisi, *Gazi Üniversitesi Mühendislik Mimarlık Fakültesi Dergisi*, , **31**(2), 361-368, 2016.

[4] Migita, H., Amemiya, T., Yokoo, K. & Iizuka, Y., The new 1.3-liter 2-plug engine for the 2002 Honda Fit, *JSAE Review*, **23**(4), 507-511, 2002.

[5] Altın, İ., Bilgin, A. & Sezer, İ., Theoretical investigation on combustion characteristics of ethanol-fueled dual-plug SI engine, *Fuel*, **257**, 116068, 2019.

[6] Altın, İ. & Bilgin, A., Quasi-dimensional modeling of a fast-burn combustion dual-plug spark-ignition engine with complex combustion chamber geometries, *Applied Thermal Engineering*, **87**, 678-687,2015.

[7] Nakata, K., Utsumi, S., Ota, A., Kawatake, K., Kawai, T. & Tsunooka, T., The effect of ethanol fuel on a spark ignition engine, *SAE Technical Paper*, 1-7, 2006.

[8] Bayraktar, H., Experimental and theoretical investigation of using gasoline–ethanol blends in spark-ignition engines, *Renewable Energy*, **30**(11), 1733-1747, 2005.

[9] Almeida, A.A.,Tests on a dual ignition alcohol SI engine (in Brazilian), *MSc Thesis, Mechanical Engineering Faculty, State University of Campinas*, 2005.

[10] Nakayama, Y., Suzuki, M., Iwata, Y. & Yamano J., Development of a 1.3 lt 2-plug engine for the 2002 model fit, *Honda R&D Technical Review*, **13**, 43-52, 2001.

[11] Wada, Y., Ohtsu, K., Narita, K. & Shinohara T., Development of i-DSI 2plug engine for 2004 model year Honda LIFE, *Honda R&D Technical Review*,**16**, 93-101, 2004.

[12] Nakata, K., Uchida, D., Ota, A., Utsumi, S. & Kawatake, K., The impact of RON on SI engine thermal efficiency, *SAE Technical Paper*, 456-462, 2007.

[13] Raja, A.S., Arasu, A.V. & Sornakumar, T., Effect of gasoline-ethanol blends on performance and emission characteristics of a single cylinder air cooled motor bike SI engine, *Journal of Engineering Science and Technology*,**10**(12),1540-1552, 2015.

[14] Yontar, A.A., Numerical comparative mapping study to evaluate performance of a dual sequential spark ignition engine fuelled with Ethanol and E85, *International Journal of Automotive Engineering and Technologies*, **7**(3), 98-106, 2018.

[15] Heywood, J.B., Internal combustion engine fundamentals, New York McGraw-Hill, 1988.

SESAME HARVESTING WASTE: THERMAL CHARACTERIZATION AND CONVERSION FOR BIOFUEL AND BIOCHAR PRODUCTION

Elif GÖDEKMERDAN*, Benginur BAŞTABAK*, Günnur KOÇAR*
* Ege University, Solar Energy Institute, Biomass Energy and Technology Center, İzmir/Turkey
Email: elifgodekmerdan@gmail.com, benginurbastabak@outlook.com, gkocer@gmail.com

ABSTRACT

Plant residues and agricultural wastes are considered green energy sources since their sustainable use could substantially minimize the environmental impacts of fossil fuels. This study examines the potential use of sesame harvesting waste for biofuel production through the pyrolysis process. The impact of temperatures (from 400 to 600 °C) and residence time (15 and 30 min) were investigated for analyzing biofuel production through the slow pyrolysis of sesame harvesting waste. The physicochemical and combustion characteristics of the sesame waste biochars were investigated. In particular, the raw biomass and biochars properties were analyzed using numerous analytical techniques such as thermogravimetric analyses (TGA/DTG) and calorific value (MJ/kg) analyses. It indicates that the thermal behavior of biochars is suitable for combustion as solid fuel. The results revealed that sesame harvesting waste could be used as a good precursor for the production of high energy density biofuels. The biochar produced at low temperatures was a good solid fuel in terms of the improvement of the combustion and emission quality.

Keywords: Sesame harvesting waste, slow pyrolysis, biochar, biofuel.

1. INTRODUCTION

The accelerating population growth and rapid industrialization continuously increase the global energy demand and cause severe environmental problems [1]. Therefore, clean and renewable energy sources like biomass have drawn attention recently [2]. Agricultural waste and crop residues are considered as promising alternatives to produce clean bioenergy and ensure sustainable biofuel production without impacting food security [3]. Moreover, agricultural residue like sesame crops generates large amounts of waste with enormous energy potential in case of conversion thermochemically through pyrolysis as an organic matter source [20]. Sesame (Sesamum indicum L.) is cultivated in China, Turkey, Sudan, India, Myanmar, Lebanon, and South Asian countries [4]. In 2018, the average global sesame production was 6 million tonnes grown on an area of 11.7 million hectares, according to the Food and Agriculture Organization Statistical Database (FAOSTAT). Besides, sesame seeds are used in medicinal and herbal products because of their high oil yield, quality, and stability [5]. After the oil is extracted, the residue of sesame is used as a soil conditioner or animal feed due to its rich protein content [6]. In addition to this, the high carbon content of sesame residues can be utilized for the production of low-cost biofuels through thermochemical conversion methods such as pyrolysis and gasification [7].

Pyrolysis is a thermochemical decomposition of organic materials by heating above 300 °C under an inert atmosphere in the absence of oxygen [8]. Biochar, the solid by-product of pyrolysis, is a suitable fuel for boilers or as pre-material for activated carbon production with high fixed carbon content, enhanced grind ability, higher calorific value, and porosity. Moreover, bio-oil and syngas can be used as biofuel and biomaterial [9]. Depending upon the operating conditions, pyrolysis can be categorized as fast pyrolysis and slow pyrolysis. [10]. Fast pyrolysis produces more bio-oil and less biochar with high temperature and short residence time [11]. In slow pyrolysis, the biomass is heated with a heating rate of about 0.1 to1 °C/s for a time ranging between 5 and 30 min at the low-temperature range between 400–500 °C. The slow pyrolysis process produces more biochar and less bio-oil [12].

This paper aimed to explore the usability of sesame residue for biofuel production through slow pyrolysis and evaluate the thermal characteristic of biochars. In this study, the slow pyrolysis of sesame harvesting waste was carried out using a fixed bed reactor. Pyrolysis was conducted to determine the effects of torrefaction at different temperatures (400 °C, 500 °C, and 600 °C) and residence time (15 and 30 min) on the weight yield and high heating value of the biochars. The physicochemical properties and thermal characterization of the sesame harvesting waste and biochar were also investigated.

2. MATERIALS AND METHODS

2.1 Feedstock Material Preparation

Sesame harvesting wastes were obtained from Muğla, Turkey. The moisture content of the sesame harvesting waste was approximately 8.4 wt%. The samples were dried in an oven at 105 °C for 24 hours. The samples were grounded and sieved by using a mesh screen (2 mm sieve opening).

2.2 Pyrolysis Process

Grounded sesame harvesting wastes were collected and pyrolyzed at different temperature values (400, 500, and 600 °C) in a fixed bed horizontal tubular furnace. 100 g of sesame harvesting wastes were fed into the reactor. When the reactor reached the desired temperature with a heating rate of 10 °C min^{-1}, the sample was kept in the reactor for 15 and 30 min. The condensable fraction (bio-oil) was stored in a tubular condenser tank, and non-condensable gases have been washed and stored in a gas tank. After each experiment, biochar, syngas, and bio-oil samples were collected for further analysis.

2.3 Proximate Analysis

Proximate analysis was achieved to identify moisture, ash, volatile matter (VM), and fixed carbon (FC) contents using a thermogravimetric analyzer (PrepASH Thermogravimetric Analyser) according to the standard method ASTM D7582. For moisture content determination, the weight loss associated with moisture is obtained by heating the samples under nitrogen from room temperature to 105 °C. Fixed carbon and volatile matter of samples were determined after combusting at 950 °C in a muffle furnace for 7 min. The ash content was determined after furnacing at 600 °C with oxygen.

2.4 Ultimate Analysis

The ultimate analysis of the feedstock and torrefied samples were performed using a Leco TruSpec® CHN-S Analyzer to detect the carbon (C), hydrogen (H), and nitrogen (N) contents of the samples. Apart from this, oxygen (O) content was calculated by the difference are given in Eqs. (1) [13].

$$O(\%w/w) = 100 - Ash(\%w/w) - C(\%w/w) - H(\%w/w) - N(\%w/w) \quad (1)$$

2.5 Calorific Value

The higher heating value (HHV) of feedstock and biochars were measured using a bomb calorimeter (Parr 6300, Parr Instrument Co., Illinois, USA) according to ASTM D 5865. Briefly, 0.5 g of sample pellet was introduced into the crucible and combusted under a pressurized oxygen atmosphere (3000 kPa). The calorimeter was calibrated with benzoic acid. It should also be noted that all of the samples were tested in three replicates. The results were obtained in cal per g dry sample.

2.6 Thermogravimetric Analysis (TGA)

The thermogravimetric analyzer (Setaram-Labsys Evo-Simultaneous TGA–DSC) was used to measure the weight loss of biomass during heating. For thermogravimetric analysis, approximately 10 mg of powdered

sample was taken into the Al_2O_3 crucible and then was heated with increasing temperature from 30 °C to 1000 °C at a constant heating rate of 20 K/min under argon gas to investigate the mass loss and derivative mass loss. DTG analysis (wt. %/min) was carried out to determine the thermal degradation behavior and the reactivity of samples.

3. RESULTS AND DISCUSSION

3.1 Properties of Raw Biomass and Biochars

The proximate, ultimate, and elemental analyses of the sesame waste and biochar samples were illustrated in Table 1 and Fig. 1. As shown in Table 1, the carbon (C) and nitrogen (N) content of the biochars ranged from 52 to 41.13 % and 2.62 to 1.71%, respectively. The sesame waste biochar obtained at 400 °C contained the highest C content (52 %), whereas biochar obtained at 600 °C contained the lowest C content (41.13 %). However, it was observed that the carbon content of biochar produced at higher temperatures (> 400 ° C) was lower than that of biochar obtained at 400 °C. Besides, the high operating temperature negatively affects the carbon content of sesame waste biochar due to the high ash content of the sesame waste (9.62%) and the conversion of oil content into volatile forms at high temperatures.

Table 1. Ultimate analysis of biochars and sesame waste at different conditions

	C (%)	H (%)	N (%)	S (%)	O (%)
Sesame waste	44,52	5,76	2,13	-	37,97
400 °C/15 min	52,00	3,20	2,62	0,40	8,97
400 °C /30 min	47,05	2,74	2,08	0,32	15,41
500 °C /30 min	47,54	1,89	2,18	0,37	13,24
500 °C /45 min	45,66	1,65	1,71	0,40	13,75
600 °C /15 min	41,68	1,64	2,01	0,31	17,21
600 °C /30 min	41,13	1,38	2,06	0,40	10,58

As shown in Fig. 1, increasing the temperature from 400 °C to 600 °C causes a considerable increase in ash content due to the removal of volatiles in the biomasses and accumulation of inorganics. It can be seen from the proximate analysis results that the volatile matter of biochar obtained at lower temperatures had more volatile matter than that of the higher temperature biochar.

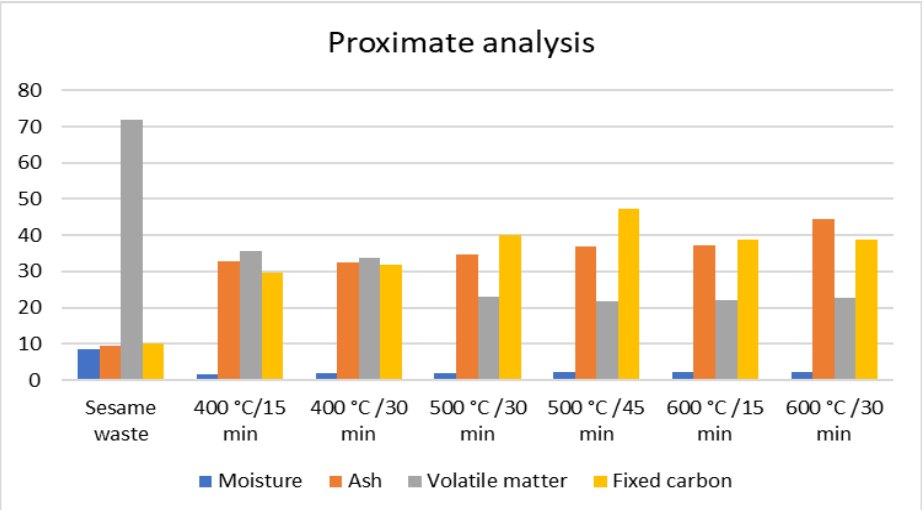

Figure 1. Proximate analysis of biochars and sesame waste at different conditions

3.2 The High Heating Value (HHV) of Biochar and Gas Products

The effects of pyrolysis temperature and residence time on the high heating value (HHV) of the gas products and biochars and the composition of syngas are shown in Table 2. The primary composition of syngas produced from the pyrolysis of sesame wastes consists of H_2, CO, CH_4, and CO_2. It was observed that the highest gas product released from the pyrolysis of sesame wastes was CO_2, followed by CH_4, H_2, and CO, respectively. It is evident in Table 2 that a higher yield of H_2 was obtained at high temperatures because of increasing the rate of decomposition of volatile matter with increasing temperature and residence time during pyrolysis of sesame wastes [14].

Table 2. The HHV of the biochar and gas products

	$HHV_{biochar}$ (MJ/kg)	**CO_2 (%)**	**CO (%)**	**CH_4 (%)**	**H_2 (%)**	**HHV_{syngas} (MJ/m^3)**
400 °C/15 min	19,63	43.70	10.22	5.64	1.25	6.550
400 °C /30 min	17,53	39.18	10.62	15.13	2.53	7.728
500 °C /30 min	16,84	32.66	12.64	26.12	12.57	13.640
500 °C /45 min	16,40	28.59	13.52	26.27	14.15	14.006
600 °C /15 min	14,63	28.76	13.68	25.75	15.95	14.020
600 °C /30 min	14,55	27.81	15.20	24.59	18.30	14.142

The high heating value (HHV) of the gas products increases with increasing temperature and residence time because the decomposition of organic matter is fast at high pyrolysis temperatures [15]. According to the results of this study, the maximum HHV of syngas was 14.142 MJ/m3 at 600 °C for 30 minutes, whereas the minimum HHV of syngas was 6.55 MJ/m3 at 400 °C for 15 minutes. The HHV of the gas products was in the range of 6.55–14.14 MJ/m3, which is higher than the average HHV of fuel gas (4–7 MJ/m3) generated by non-catalytic gasification of biomass [16]. This study showed that the sesame wastes is a suitable feedstock for clean energy production via slow pyrolysis. As depicted in Table 2, the HHV of the biochar decreased with increasing temperature and residence time since the high ash content of raw materials led to an adverse effect on HHV.

3.3 Weight Yields of Biochar, Bio-oil, and Syngas

As shown in Table 3, the yield of biochar, bio-oil, and syngas differ depending on temperature and residence time. The highest char yield was produced by sesame waste with a value of 47,3 wt.% at 400 °C for 15 minutes, and the lowest char production yield was 34,9 wt.% at 600 °C for 30 minutes. The results demonstrate that the yield decreased gradually when the reaction temperature increased from 400 °C to 600 °C. Thus the yield of biochar decreased rapidly from 47.3% to 34.9%.

The results show that the highest total syngas volume of 17,78 liter/100 g sesame waste was produced at 600 °C for 15 minutes. At the time, the production of bio-oil increased with higher reaction temperature from 14,8 wt.% to 32 wt.%. As shown in Table 3, there was a significant relationship between the yield of products and pyrolysis temperatures. The rise in bio-oil and syngas production is connected with the increasing temperature because of the increased carbon conversion rate of gases during pyrolysis [15].

Table 3. Yields of biochars, bio-oil, and syngas produced at different pyrolysis temperatures

	Biochar (g)	**Bio-oil (ml)**	**Syngas (liter/100 g)**
400 °C/15 min	47,3	14,8	10,52
400 °C /30 min	46,9	26	10,52
500 °C /30 min	38	32	15,60
500 °C /45 min	35,9	27,2	15,96
600 °C /15 min	36,2	30	17,78
600 °C /30 min	34,9	14,2	17,42

3.4 Thermogravimetric Analysis (TGA)

Table 4 depicts the results of thermogravimetric (TG) analysis in wt% and derivative thermogravimetric (DTG) analysis in wt% min^{-1} for sesame waste biochar. The weight loss during the decomposition process occurred in three major stages. The TG-DTG curves were divided into three major stages as vaporization of moisture, followed by devolatilization of hemicellulose and cellulose and lignin decomposition. All the TG curves showed a similar trend for weight loss of biochars. At around 30–150 °C, the release of moisture causes a mass loss for all the sesame biochar prepared at different temperatures. [17]. The second mass loss occurred between 150 and 600 °C due to the degradation of the hemicellulose and cellulose [19]. As shown in Table 4, a rapid weight loss through the TG curve occurred between 600 and 1000 °C because of the decomposition of the remaining lignin content.

Table 4. Degradation temperature, weight loss, and maximum degradation rate values of sesame waste in pyrolysis for biochars

	1. decomposition zone			**2. decomposition zone**			**3. decomposition zone**		
	T	$-DTG_{max}$ (%/min)	Weight loss (%)	T	$-DTG_{max}$ (%/min)	Weight loss (%)	T	$-DTG_{max}$ (%/min)	Weight loss (%)
400 °C	30-150	0.05	0.98	151-600	0.3	16.75	601-1000	0.35	16.82
500 °C	30-150	0.25	0.162	151-600	0.2	4.252	601-1000	2.45	17.657
600 °C	30-150	0.5	0.573	151-600	0.25	2.528	601-1000	2.91	18.694

Furthermore, the mass loss of sesame waste biochar prepared at 400 °C (34.51%) was highest as compared to 500 °C biochar (22.02 %) and 600 °C (21.75 %) biochar. According to the results of thermogravimetric (TG) analysis, the thermal stability of sesame waste biochar prepared at 500 °C and 600 °C was more than that of biochar at 400 °C.

4. CONCLUSION

The thermal degradation behavior and yields of pyrolysis of sesame waste had been analyzed in this study. Temperature and residence time had an exceptionally significant influence on the yield of biofuel. Although the highest char yield was obtained at 400 °C, the thermal stability of sesame waste biochar prepared at 500 °C and 600 °C was more than that of biochar at 400 °C. Therefore, the optimal pyrolysis temperature for char production was determined at 400 °C. According to the results of this study, the maximum HHV of syngas (14.142 MJ/m3) was obtained at 600 °C for 30 minutes whereas the minimum HHV of syngas (6.55 MJ/m3) was obtained at 400 °C for 15 minutes. Thus, the best suitable conditions of syngas production were at a higher temperature and residence time (600 °C for 30 minutes). This study has shown that sesame waste can be effectively used as a raw material to prepare biochar, bio-oil, and syngas. The crop residue and agricultural waste were found more suitable feedstock for biofuel production.

REFERENCES

[1] Fadhil, A.B., Evaluation of apricot (Prunus armeniaca L.) seed kernel as a potential feedstock for the production of liquid biofuels and activated carbons, Energy Conversion and Management, 133, 307-317, 2017.

[2] Ali M., Saleem M., Khan Z., Watson I.A., The use of crop residues for biofuel production, Biomass, Biopolymer-Based Materials, and Bioenergy, 369-395, 2019.

[3] Casazza A. A., Spennati E., Converti A., Busca G., Production of carbon-based biofuels by pyrolysis of exhausted Arthrospira platensis biomass after protein or lipid recovery, Fuel Processing Technology, 201, 106336, 2020.

[4] Dawodu F.A., Ayodele O.O., Bolanle-Ojo T., Biodiesel production from Sesamum indicum L. seed oil: An optimization study, Egyptian Journal of Petroleum, 23 (2), 191-199, 2014.

[5] Dossa K., Li, D., Dossa L., Wang L., Zheng X., Yu J., Wei X., Fonceka D., Diouf D., Liao B., Cisse N., Zhang X., Dynamic transcriptome landscape of sesame (Sesamum indicum L.) under progressive drought and after rewatering, Genomics Data, 11, 122-124, 2017.

[6] Mujtaba M.A., Cho H.M., Masjuki H.H., Kalam M.A., Ong H.C., Gul M., Harith M.H., Yusoff M.N.A.M., Critical review on sesame seed oil and its methyl ester on cold flow and oxidation stability, Energy Reports, 6, 40-54, 2020.

[7] Kumar P., Kumar V., Kumar S., Singh J., Kumar P., Bioethanol production from sesame (Sesamum indicum L.) plant residue by combined physical, microbial and chemical pretreatments, Bioresource Technology, 297, 122484, 2020.

[8] Guilhen S.N., Mašek O., Ortiz N., Izidoro J.C., Fungaro D.A., Pyrolytic temperature evaluation of macauba biochar for uranium adsorption from aqueous solutions, Biomass and Bioenergy, 122, 381-390, 2019.

[9] Khiari B., Ghouma I., Ferjani A.I., Azzaz A.A., Jellali S., Limousy L., Jeguirim M., Kenaf stems: Thermal characterization and conversion for biofuel and biochar production, Fuel, 262, 116654, 2020.

[10] Tripathi M., Sahu J.N., Ganesan P., Effect of process parameters on production of biochar from biomass waste through pyrolysis: A review, Renewable and Sustainable Energy Reviews, 55, 467-481, 2016.

[11] Sharifzadeh M., Sharifzadeh M., Guo M., Borhani T.N., Murthy Konda N.V.S.N., Garcia M.C., Wang L., Hallett J., Shah N., The multi-scale challenges of biomass fast pyrolysis and bio-oil upgrading: Review of the state of art and future research directions, Progress in Energy and Combustion Science, 71, 1-80, 2019.

[12] Patel S., Kundu S., Halder P., Veluswamy G., Pramanik B., Paz-Ferreiro J., Surapaneni A., Shah K., Slow pyrolysis of biosolids in a bubbling fluidized bed reactor using biochar, activated char and lime, Journal of Analytical and Applied Pyrolysis, 144, 104697, 2019.

[13] Mimmo T., Panzacchi P., Baratieri M., Davies C.A., Tonon G., Effect of pyrolysis temperature on miscanthus (Miscanthus x giganteus) biochar physical, chemical and functional properties, Biomass and Bioenergy, DOI: 10.1016/j.biombioe.2014.01.004

[14] Déparrois N., Singh P., Burra K.G., Gupta A.K., Syngas production from co-pyrolysis and co-gasification of polystyrene and paper with CO2, Applied Energy, 246, 1-10, 2019.

[15] Hong Z., Zhong F., Niu W., Zhang K., Su J., Liu J., Li L., Wu F., Effects of temperature and particle size on the compositions, energy conversions and structural characteristics of pyrolysis products from different crop residues, Energy, 190, 116413, 2020.

[16] Loy A.C.M., Yusup S., Chin B.L.F., Gan D.K.W., Shahbaz M., Acda M.N., Unrean P., Rianawati E., Comparative study of in-situ catalytic pyrolysis of rice husk for syngas production: Kinetics modelling and product gas analysis, Journal of Cleaner Production, 197, Part 1, 1231-1243, 2018.

[17] Pariyar P., Kumari K., Jain M.K., Jadhao P.S., Evaluation of change in biochar properties derived from different feedstock and pyrolysis temperature for environmental and agricultural application, Science of The Total Environment, 713, 136433, 2020.

[18] Yang X., Kang K., Qiu L., Zhao L., Sun R., Effects of carbonization conditions on the yield and fixed carbon content of biochar from pruned apple tree branches, Renewable Energy, 146, 1691-1699, 2020.

[19] Afif R.A., Anayah S.S., Pfeifer C., Batch pyrolysis of cotton stalks for evaluation of biochar energy potential, Renewable Energy, 147, Part 1, 2250-2258, 2020.

[20] Zhou J., Chen L.H., Peng L., Luo S., Zeng Q.R., Phytoremediation of heavy metals under an oil crop rotation and treatment of biochar from contaminated biomass for safe use Chemosphere, 247, 125856, 2020.

HEAT INSULATION

THERMAL COMFORT ANALYSIS OF HISTORICAL MOSQUES. CASE STUDY: THE ULU MOSQUE, MANISA, TURKEY

Yusuf DİLER*, Cihan TURHAN, Zeynep DURMUŞ ARSAN***, Gülden GÖKÇEN AKKURT******
*Izmir Institute of Technology, MSc.in Energy Engineering, Gulbahce Campus, 35430 Urla, Izmir,Turkey
Email: yusufdiler@windowslive.com
**Atılım University, Department of Energy Systems Engineering, 06830 Incek, Ankara, Turkey
Email: cihan.turhan@atilim.edu.tr
***Izmir Institute of Technology, Department of Architecture, Gulbahce Campus, 35430 Urla, Izmir, Turkey
Email: zeynepdurmus@iyte.edu.tr
****Izmir Institute of Technology, Department of Energy Systems Engineering, Gulbahce Campus, 35430 Urla, Izmir, Turkey
Email: guldengokcen@iyte.edu.tr

ABSTRACT

Mosques are sanctuary places for Muslims where they can communicate with each other and perform their religious activities. On the other hand, historical mosques contain lots of artworks that have cultural heritage values. These mosques initially do not have any Heating, Ventilating, and Air-Conditioning (HVAC) systems. For this reason, obtaining thermal comfort becomes a significant issue. In this study, a systematic approach to monitoring and evaluating the microclimate and thermal comfort of historical mosques was developed. As a case study, The Ulu Mosque, Manisa/Turkey, was monitored between 2015 and 2018, and thermal comfort evaluation of the mosque was conducted during worship periods based on the method provided by ISO 7730 Standard. A dynamic Building Energy Performance Software, Design Builder, was used to model the mosque, and the model was calibrated by using hourly indoor temperature data. The calibrated model was then used to develop retrofitting scenarios. Thirteen different scenarios were proposed to improve the thermal comfort of prayers during worship periods. The results were evaluated according to EN 16883 Standard for the conservation of cultural heritage. Electrical radiator heating with intermittent operation schedule was obtained as the best scenario to protect the cultural heritage value of the mosque, while decreasing the Predicted Percentage of Dissatisfied (PPD) from 45% to 10% in winter months. Additionally, intermittent operation saved 46.9% of energy compared to continuous operating schedule.

Keywords: Thermal comfort, Historic mosques, Retrofitting, Energy analysis

1. INTRODUCTION

The first studies on thermal comfort assumed as conducted by Socrates in the early 5th century BC, examining how a house should be built to ensure thermal comfort. On the other hand, thermal comfort was not a practical issue until the industrial revolution. A fire pit in the middle of the houses was used for heating, while hand-held fans were used for cooling. While heating technologies were improved in the 18th century, cooling technologies had to wait two centuries more [1]. At 1923, Houghton and Yaglou [2] used the "comfort zone" term for the first time and described it as "*a thermal condition in which little or no effort is required by occupants to adjust their bodies to surrounding environmental conditions.*" Following World War II, the number of studies on "thermal comfort" was increased, and many disciplines from engineering to architecture, physiology, medicine, and geography brought their findings on thermal comfort together in an interdisciplinary manner [3-4].

Thermal comfort is described as "*the condition of human's feeling express the thermal environment,*" which depends on two main parameters: personal and environmental [5]. Personal parameters depend on activity level (met) and clothing insulation (clo), while environmental parameters are mean radiant temperature (MRT), relative humidity (RH), air temperature (T_i), and air velocity (v_a). These parameters are input parameters of a

mathematical model for predicting thermal comfort and thermal dissatisfaction levels, which was presented by Fanger as Predicted Mean Vote (PMV) and Predicted Percentage of Dissatisfied (PPD), respectively [6]. The PMV is described as an index that predicts the mean value of thermal sensation votes of a large group which is calculated from heat balance equations of the body and environment, and refers to a thermal sensation scale [7]. The thermal sensation scale is based on seven ratings from -3 to +3, which describes occupants' feeling as -3 for cold, -2 for cool, -1 for slightly cool, 0 for neutral, +1 for slightly warm, +2 for warm, and +3 for hot [6]. On the other hand, PPD establishes a quantitative prediction of percentages of thermally dissatisfied people. The PPD is a function of PMV, and the indoor environment is accepted as "comfortable" if 85% of the occupants are satisfied with the environment; in other words, 15% of the people are dissatisfied [7].

In recent years, numerous reports and articles have been published on the improvement of thermal comfort in different types of buildings such as offices, public and residential buildings [8]. Although each type of buildings has its occupancy and operation schedule, the mosques are very similar to other religious buildings with a intermittent occupation, and the occupation period changes throughout the year [9]. For this reason, heating and cooling strategies must be carefully designed. Although many studies encountered thermal comfort in living and working areas, dwellings, offices, classrooms, and schools, according to the authors' knowledge, there are few studies exist on thermal comfort of historical mosques [8, 10]. To this aim, this study investigates thermal comfort of prayers on only prayer times in a historical mosque located in the temperate climate and also performs a risk assessment study which aims to preserve cultural heritage.

2. METARIALS AND METHODS

The methodology of conducting thermal comfort evaluation of a historic mosque consists of three main phases: detailed data collection, development of a dynamic building energy model, and analysis of retrofitting strategies to improve thermal comfort without deteriorating the heritage value of the building. The first phase involves long-term measurements of indoor and outdoor climatic conditions (temperature and relative humidity), collection of data on structural characteristics of the building, thermal properties of building materials, heating/cooling system, ventilation strategies, and the number of occupants and occupation time. The second phase is to model the building to reflect formal, structural, and occupancy characteristics. The model is then calibrated by hourly indoor air temperature data. The calibrated model (baseline), which meets ASHRAE 14 requirements [11], can be used to evaluate the indoor climate of the mosque, and to develop an analysis of retrofitting proposals. The third phase includes discussion and simulation of retrofitting strategies. Simulation results are compared based mainly on thermal comfort and protection of cultural heritage assets along with energy consumption data of the proposed strategies. Fig. 1 gives the flow diagram of the methodology [12].

2.1 Case Study

The Ulu Mosque Complex, which is located on the northern skirts of Spil Mountain in Manisa-Turkey, was built in 1366 [13]. The location of the Complex is given in Figure 2. The Complex consists of a mosque, a madrasah, a tomb, and a courtyard. Besides, there is a bath on the 80 m north-east side of the complex (Fig. 3). In this study, the mosque is selected as a case study for thermal comfort analysis of prayers.

2.2 Data Collection

The data collection process includes collecting existing data of mosque, and indoor and outdoor data measurement campaign. Existing data, including structural characteristics of the building, thermal properties of building materials, heating/cooling system, ventilation strategies, and the number of occupants and occupation time, were collected from architectural and restoration projects, reports, books, surveys, and personal communications with staff of the mosque. In addition, long-term measurements of indoor and outdoor climatic data (temperature and relative humidity) were conducted by mini data loggers. Five dataloggers were installed in the prayer hall, while one data logger is located outside the courtyard (Fig. 4). Temperature (T) and Relative Humidity (RH) data were recorded every 10 minutes between April 4th, 2016-March 11th, 2018.

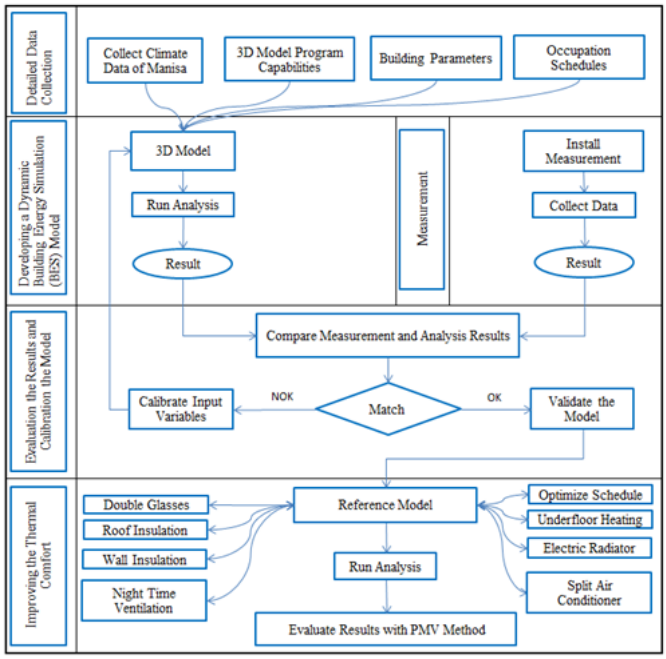

Figure 1. Flow diagram of the methodology [12].

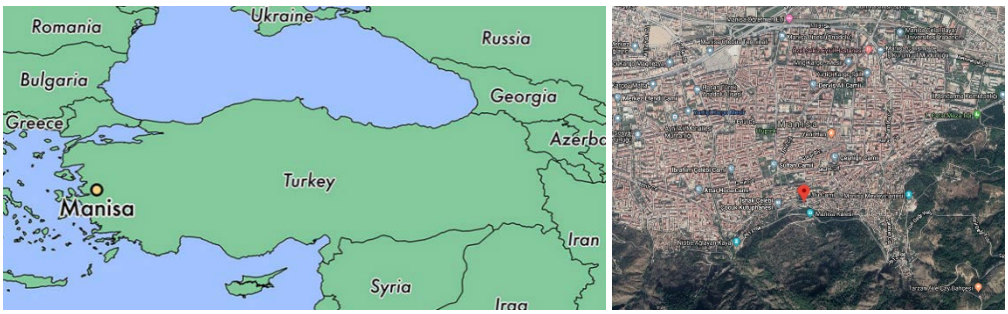

Figure 2. Location of the Ulu Mosque complex-Manisa-Turkey.

2.2 Development of a Dynamic Building Energy Simulation (BES) Model

The Ulu Mosque was modeled, and the model was calibrated to determine thermal comfort conditions at the baseline. The proposed retrofit interventions to improve thermal comfort are simulated by this calibrated model. DesignBuilder v.5.0.3.007 [14] software was chosen for BES modeling because of the integration with Energy Plus, which enables completion of the simulation within the DesignBuilder interface. In this way, results were displayed and analyzed effectively in different intervals.

2.3 Thermal Comfort Analysis

Following the calibration period, PMV and PPD values were calculated to determine the thermal comfort of the prayers according to ASHRAE Guideline 14 [11]. Indoor environment conditions were investigated to understand if the conditions meet the recommended threshold values specified in EN ISO 7730 [7].

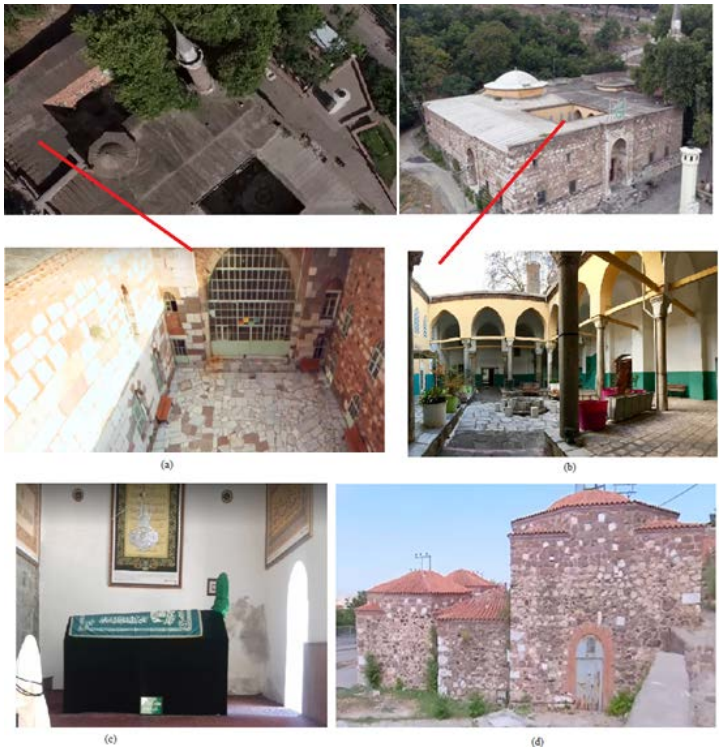

Figure 3. The Ulu Mosque Complex a) Fethiye Madrasah, b) Courtyard, c) Tomb, d) Çukur Hamam.

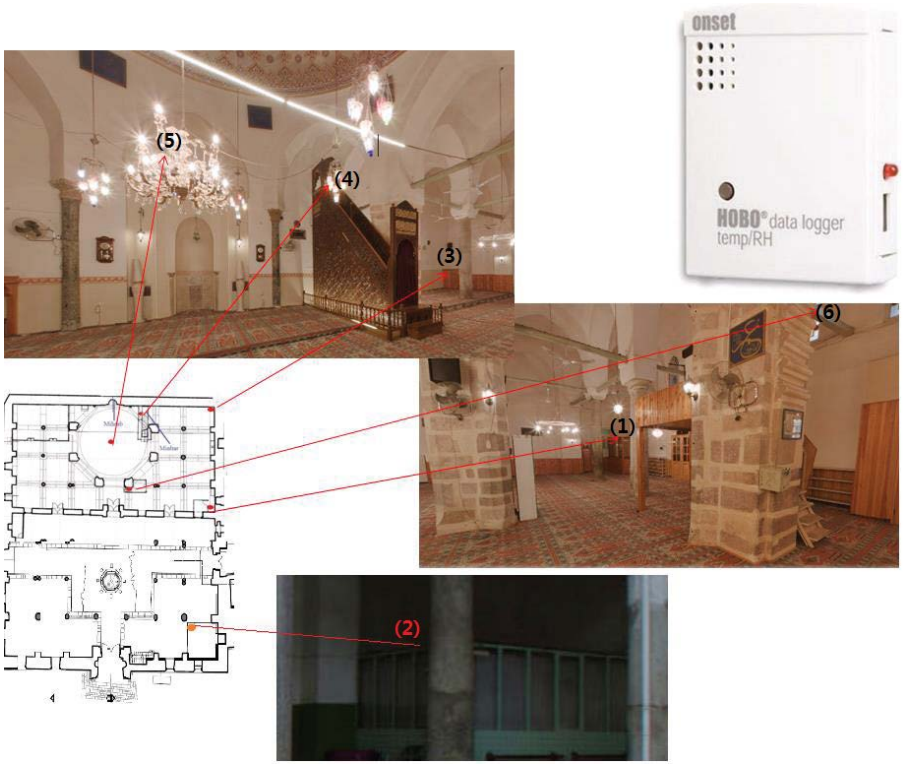

Figure 4. Location of dataloggers.

2.4 Retrofitting Strategies

The main aim of proposing retrofitting scenarios was to improve the thermal comfort of the prayers in the mosque. The developed scenarios were classified as passive and active retrofitting scenarios. The aim of passive design scenarios is to achieve thermal comfort without consuming any energy source such as electricity or natural gas [12], such as changing the windows with double glazing and low emissivity glass, night-time ventilation, roof, and wall insulation while active scenarios were implementing an underfloor heating system, electric radiator and split air-conditioning system. The active and passive scenarios were simulated using the calibrated model, then PMV and PPD values were obtained for each case.

Besides thermal comfort analysis, the effect of retrofit interventions on heritage value was also evaluated to find the most appropriate solutions for the components of building's envelope based on EN 16883 "Conservation of cultural heritage-Guidelines for improving the energy performance of historic buildings" standard [15]. The standard utilizes five-level assessment criteria as presented in Table 1. Finally, the results are compared with the baseline model based on four measures: heritage value protection, thermal comfort, energy consumption, and energy cost.

Table 1. Five-level assessment scale of EN 16883 [15].

Assessment scale				
High risk	Low risk	Neutral	Low benefit	High benefit

3. RESULTS

As a first step, the baseline model was developed in DesignBuilder v.5.0.3.007 by using input data and architectural drawings (Fig.5). It is worth noting that the mosque was modeled with surrounding buildings and trees to evaluate the shading effects. Then, the model was calibrated according to ASHRAE Guideline 14 [11]. By using the calibrated model, thermal comfort analysis and retrofitting scenarios were developed and simulated. Simulation results were evaluated based on thermal comfort, energy consumption, and risk on cultural heritage.

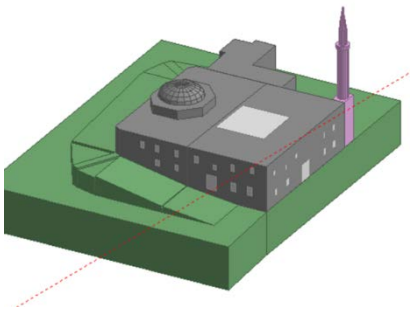

Figure 5. BES model of the Ulu Mosque.

Once the calibration was completed, the energy consumption of the mosque and thermal comfort indices of the prayers were obtained with the help of DesignBuilder software. Then, the data were separated concerning the prayer times. It is worth reminding that PMV and PPD values were taken from DesignBuilder, which was calculated according to ISO 7730 [7]. Based on the calculation of PMV values (baseline model) on prayer times, occupants of the mosque generally felt cool in winter and almost neutral in summer. In the summer season, the PMV value was found between -0.57 and 0.33 (Fig. 6).

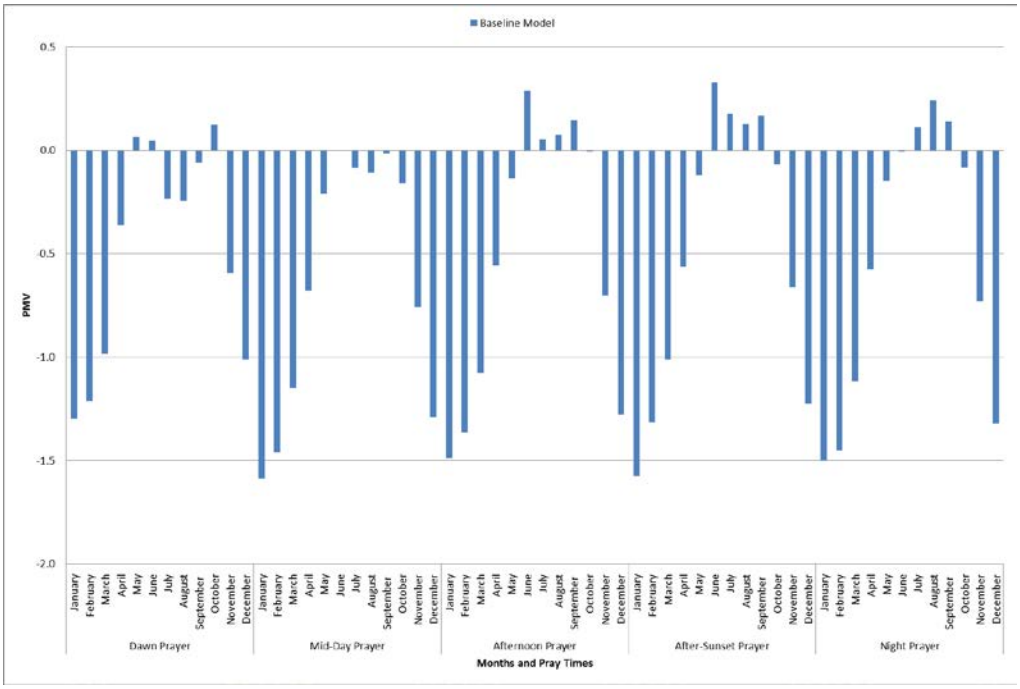

Figure 6. PMV values of prayers (baseline model).

PPD values indicated that prayers were not satisfied during the winter season. Fig.7 depicts that the dissatisfaction level reached 55.3% in January during mid-day prayer time. From December to March, the lowest PPD was obtained for dawn prayer times compared to the other prayer times in the same month since prayers preferred thick clothes. Although PPD started to decrease in March, the results were still outside the threshold limits. However, PPD values were in the acceptable range between April and October. In addition, May had the lowest PPD as 5.4% in dawn prayer times. Occupants felt comfortable between May and October since PPD was below 15% on these months.

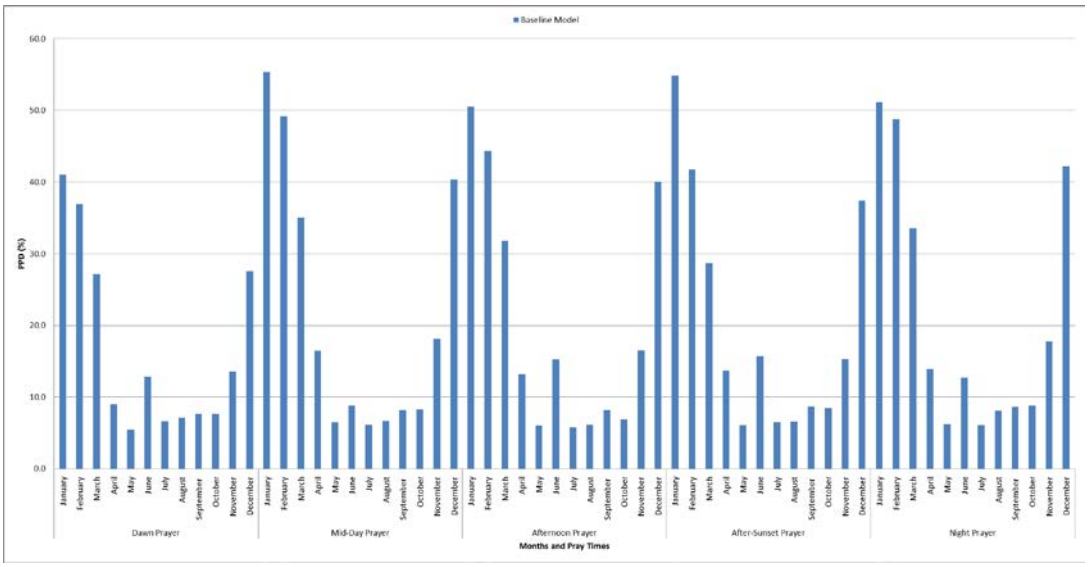

Figure 7. PPD levels of prayers (baseline model).

According to the baseline model results, prayers were not satisfied with their thermal environment in winter. Thus, various retrofitting scenarios were developed in order to increase the thermal comfort of prayers during winter.

In the study, four passive retrofitting strategies, namely, windows with double low emissivity glazing, nighttime ventilation, roof insulation, and wall insulation, were developed. All PPD levels of the strategies and baseline model are presented in Fig. 8.

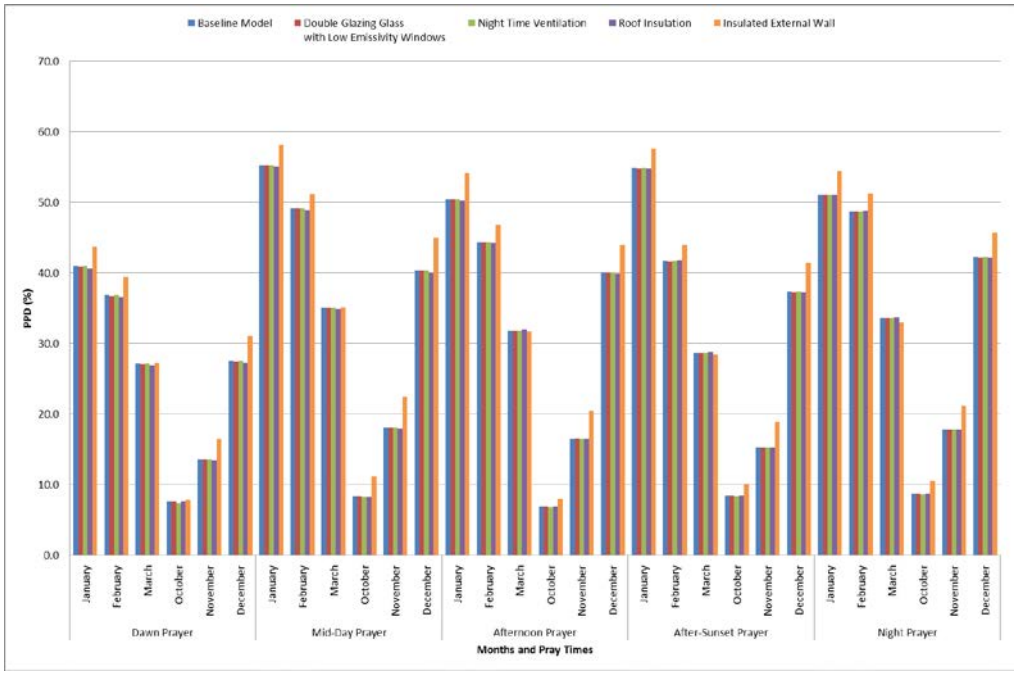

Figure 8. Comparison passive retrofitting strategies with baseline model.

Active retrofitting strategies proposed in the study were adding an underfloor heating system, electric radiator, and split type air-conditioner. Proposed systems were operated in two different schedules: intermittent and continuous (5:00-20:00) heating types. The heating season was considered as of January, February, March, April, November, and December, where the PPD level reached 50%. Set-point temperature during the heating season was fixed as 22°C. Fig.9 depicts the comparison of PPD levels for active retrofitting strategies.

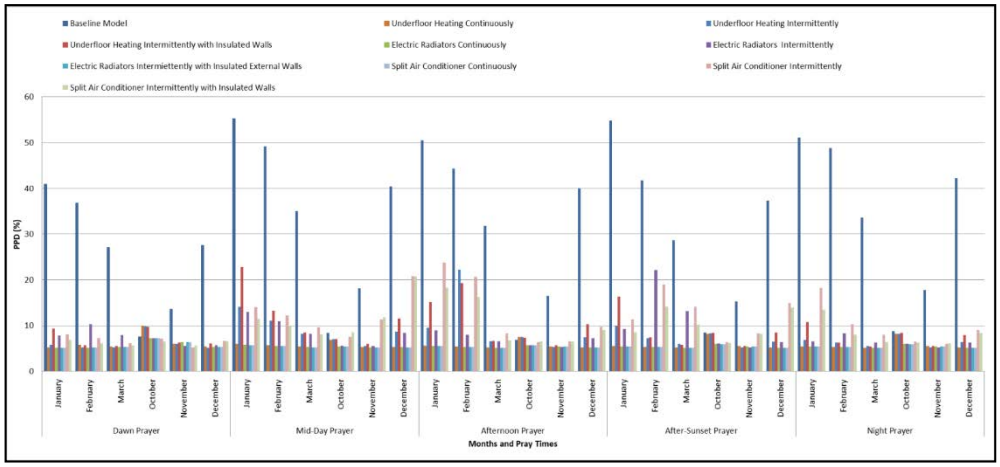

Figure 9. Comparison active retrofitting strategies with baseline model.

According to Fig.s 8 and 9, changing windows with double glazing and low emissivity glass, nighttime ventilation, and roof insulation had no effect on thermal comfort. Insulation of the walls had a negative effect on thermal comfort if there was no heating system. If a heating system was installed, insulation could cause a decrease in energy consumption while maintaining thermal comfort. Energy-saving rates for the portable electric radiator, split type air-conditioner and underfloor heating systems were 18.4%, 11.8%, and 23.2%, respectively. PPD levels of active retrofitting strategies decreased from 45% to below 15% for winter, which was considered "acceptable" by ISO 7730 [7]. Even though the PPD level of baseline model was below 15% for the autumn, active retrofitting strategies enhanced thermal comfort.

Significant reduction in annual energy consumption of the Ulu Mosque could be obtained while maintaining thermal comfort when an intermittently operated heating system was properly designed. Compared to the continuous operating schedule, intermittent operation decreases annual energy consumption by approximately 46.9% for the portable electric radiator, 56.6% for split type air-conditioner, and 26.9% for the underfloor heating system.

The effect of retrofit interventions on heritage value was also evaluated via four measures, namely, heritage value protection, thermal comfort, energy consumption, and energy cost according to EN 16883 [15], as shown in Table 2.

Table 2. Risk assessment according to EN 16883 [15].

Retrofit Impact Assessment				
Type of retrofit	Heritage value protection	Thermal comfort	Energy consumption	Energy cost
Windows with double glazing with low emissivity glass				
Night-time ventilation				
Roof insulation				
Insulated external wall				
Electric radiators continuously				
Electric radiators intermittently				
Electric radiators intermittently with insulated external walls				
Split air-conditioner continuously				
Split air-conditioner intermittently				
Split air-conditioner intermittently with insulated walls				
Underfloor heating continuously				
Underfloor heating intermittently				
Underfloor heating intermittently with insulated walls				

Thermal comfort assessment of retrofit scenarios was transferred to Table 2 based on heritage value protection measure, window change, and roof insulation were accepted as having a low effect on building envelope and cultural heritage. External wall insulation could lead to the loss of historical appearance and indicates a high risk on the heritage value and historical building character. Portable electric radiators could be placed away from sensitive surfaces or objects not to cause damage as particle deposition. Night-time ventilation has no harmful effect on cultural heritage. Even though particle deposition on surfaces may be inconspicuous with underfloor heating, the impact on the floor was considerable. Therefore, it was evaluated as risky [16].

5. CONCLUSIONS

Thermal comfort analysis was conducted during prayer times at a historical and naturally ventilated mosque, the Ulu Mosque, located in Manisa, Turkey. On-site indoor and outdoor T and RH measurements were taken for almost two years. The mosque was then modeled by DesignBuilder software, and the model was calibrated according to ASHRAE Guideline 14. Baseline model results were concentrated on prayer times only, and it showed that thermal comfort of the prayers was not satisfied at certain periods during prayer times. Therefore, retrofitting scenarios were proposed to be able to improve the thermal comfort level of the mosque. Thirteen retrofitting scenarios were simulated by the model, and results were discussed. All scenarios were evaluated according to EN 16883 to analyze the risks in terms of cultural heritage.

Retrofitting scenarios must be carefully selected not to compromise the cultural value of historical buildings. Therefore, the number of scenarios applicable to the mosque was limited. Electric radiator heating with an intermittent operating schedule was the best option to protect cultural heritage, while providing thermal comfort with lower energy consumption. In addition, thermal comfort should be evaluated in mosques that differ from other building types in terms of occupancy period during a day because of their unique function and intermittent operating schedule. Therefore, thermal comfort was analyzed five times a day with various numbers of prayers at all prayer times during the year according to the motion of the moon. Furthermore, software like DesignBuilder allows different scenarios to be used in the selection of retrofitting strategies to be applied in historical buildings. Implementation of these scenarios should be consistent with the heritage value of the building, and risk assessments should be done according to EN 16883 for a systematic approach. Lastly, owing to the fact that thermal comfort is a situation where each person reacts differently to the same environmental condition, a further thermal comfort survey should be conducted to the prayers to obtain their preferences and compare with the model.

REFERENCES

[1] Szokolay S.V. Advances in Solar Energy, Thermal Comfort and Passive Design, Advances in Solar Energy. (2nd Ed.), Springer, Boston, 257-296, 1985.

[2] Houghton, F.C. & Yaglou, C.P. Determining Lines of Equal Comfort. *Journal of the American Society of Heating and Ventilating Engineers Trans.* **29**,163-176 and 361-384, 1923.

[3] Panchyk K. Solar Interiors: Energy-Efficient Spaces Designed for Comfort, Van Nostrand Reinhold Company Inc., USA, 1984.

[4] Auliciems A. & Szokolay SV. Thermal Comfort, (2nd Ed.), PLEA, 1997.

[5] ASHRAE Standard 55, Thermal Environmental Conditions for Human Occupancy. ASHRAE Standards Committee, 2013.

[6] Fanger, P. Thermal Comfort: Analysis and applications in environmental engineering. Mc Graw-Hill, 1970.

[7] ISO 7730:2005. Ergonomics of the thermal environment. Analytical determination and interpretation of thermal comfort using calculation of the PMV and PPD indices and local thermal comfort criteria, CEN, Switzerland.

[8] Atmaca A.B. & Gedik G.Z. Evaluation of Mosques in Terms of Thermal Comfort and Energy Consumption in a Temperate-Humid Climate. *Energy & Buildings*, **195**, 195-204, 2019.

[9] Jaafar R., Khalil E. & Abou-Deif T. Numerical Investigations of Indoor Air Quality inside Al-Haram Mosque in Makkah. *Procedia Engineering*, **205**, 4179-4186, 2017.

[10] Bughrara K., Arsan Z. & Akkurt G. G. Applying Underfloor Heating System for Improvement of Thermal Comfort in Historic Mosques: The Case Study of Salepçioğlu Mosque, İzmir, Turkey. *Energy Procedia,* **133**, 290-299, 2017.

[11] ASHRAE Guideline 14: 2002. Measurement of Energy and Demand Savings. ASHRAE Standards Committee.

[12] Bughrara K. Adaptive thermal comfort analysis of historical mosque: The case study of Salepçioğlu Mosque, MSc thesis, IZTECH, İzmir, Turkey, 2016.

[13] TC Ministry of Culture and Tourism. Retrieved from http://www.manisakulturturizm.gov.tr/TR,73021/ulu-camii-ve--kulliyesi-manisa-merkez.html, (2017, June 02).

[14] DesignBuilder version 6.1.3.008, 2017.

[15] EN 16883:2017. Conservation of cultural heritage-Guidelines for improving the energy performance of historic buildings. Brussels, Belgium.

[16] EN 15759-1:2011. Conservation of cultural property-Indoor climate-Part 1: Guidelines for heating churches, chapels, and other places of worship, CEN, Switzerland.

OPTIMIZATION OF INSULATION THICKNESS FOR PIPES IN A LOW TEMPERATURE DISTRICT HEATING NETWORK

Meryem TERHAN*
*Gumushane University, Department of Mechanical Engineering, Gumushane/Turkey
Email: meryem.terhan@gumushane.edu.tr

ABSTRACT

In the study, a thermo-economic analysis has investigated using Equivalent Annual Worth (EAW) Analysis Method to determine the optimum insulation thickness of pipes such as supply and return water pipes; hot water and circulation pipes existed in a low-temperature district heating network. In the analysis, energy savings over a lifetime and payback periods of the pipe insulation material (glass wool) have calculated depending on the different nominal pipe sizes (20-150 mm). The results show that the optimum insulation thicknesses found between 30 mm and 40 mm. The investment cost of the pipe insulation material changes over the range 0.53-11.78 $/m, while total energy savings of the insulation material wave to 102.17 $/m from 19.24 $/m according to the variable pipe insulation thickness like 25-100 mm. The payback periods of the different insulation thicknesses have calculated between 0.06 and 2.53 years.

Keywords: low-temperature district heating network, pipes, optimum insulation thickness, energy savings, equivalent annual worth (EAW) analysis

Symbol List

β	Volume expansion coefficient (1/K)
C_f	Fuel cost ($/m^3)
C_{fl}	Annual fuel consumption cost occurred heat losses from pipes ($/year)
C_i	Cost of insulation material per unit volume ($/m^3)
C_{ins}	Insulation cost ($)
C_m	Maintenance and operation cost ($)
C_{tot}	Total cost ($)
d	Inflation rate (%)
D_t	Diameter of insulation pipe (m)
E_s	Energy savings ($/m)
g	Gravitational acceleration (m/s^2)
h	Heat convection coefficient (W/m^2.K)
H_u	Lower heating value of the fuel (kJ/m^3)
i	Interest rate (%)
k	Thermal conductivity coefficient (W/m.K)
L	Length (m)
N	Lifetime years
N_u	Nusselt number
Pr	Prandtl number
r_v	Ratio of resale value to the first cost
R	Thermal resistance (m^2.K/W)
Ra	Rayleigh number
Q	Heat transfer rate (kJ/s)
Q_f	Annual fuel energy consumed from the heating system (kJ/year)
t_c	Canal thickness (m)
T	Temperature (°C)
T_b	Base temperature (°C)

T_{sa}	Solar-air temperature (°C)
ύ	Volumetric flow rate (m^3/s)
V	Volume (m^3)
V_f	Annual fuel consumption of heating system (m^3/year)
V_{pl}	Annual fuel consumption occurred heat losses from pipes (m^3/year)
x_{cp}	Canal perimeter (m)
x_c	Canal deepness (m)
α	Heat diffusion coefficient (m^2/s)
η_s	Efficiency of heating system (%)
υ	Kinematic viscosity (m^2/s)

1. INTRODUCTION

Energy plays an essential role in increasing economic development and welfare level. Energy consumption has been quickly increased depending on life standard improvement, rising population, and urbanization because of migration to big cities. Besides, environmental pollution related to fossil fuels has become a severe threat to human wealth and the ecosystem. Thus, the main idea is to maximize energy savings and minimize energy consumption in the design stage of the power and heating systems with fossil fuel. The building sector is numerous remarked on energy consumption because of high heat losses. In the world, the most significant part of global energy demand consists of the building sector with a percent of 40% [1-6]. Used to cover space heating and domestic hot water needs, heat produced in a plant is transferred to the buildings in a campus or region in the district heating systems (DHS) [7]. The district heating systems are provided solutions for the increasing energy problems in high population cities such as remediation of air quality because of reducing CO_2 emissions, increasing renewable energy sources share, reducing energy export owing to control of energy demands [8]. The advantages of DHS can be sorted as high efficiency in heat generation, fuel used diversity, and low interaction on the environment [9]. The first investment cost, operation cost, and total energy cost go up depending on increasing heat loss in DHS's distribution network. Thus there is a needs decreasing of heat losses from pipes in the network. Heat loss from the network corresponds percent of 5-20% transferred energy, and this loss is higher than the other losses in the heating system. Heat losses from the network depend on many factors such as outdoor conditions, insulation of pipes, and length of distribution network [7-11].

Using suitable insulation material reduces significantly energy consumption in space heating thus decreasing fossil fuel consumption and pollution effect on the environment. Especially, district heating systems have confused and expensive pipe configurations. Un-insulation supply and return pipes of the heating system are essential sources of waste energy. Applications of insulation on pipe systems for energy savings not only decrease heat losses from the pipes but also reduce environmental pollution due to fuel savings. Thermal insulation material used is an effective method for thermal impact protection in buildings and pipes. For these reasons, the selection of suitable insulation material and determination of optimum insulation thickness is quite essential [4-12]. Using suitable insulation material is one of the effective ways for energy savings on pipe networks in the district heating system. The insulation decreases fuel consumption and undesirable carbon emissions from fossil fuel combustion in the system [3]. The insulation material thickness must determine considering the factors such as thermal conductivity and cost of insulation material, and outdoor temperature of the region. Increase the insulation thickness not only energy savings but also contributes to the decrease of environmental pollution. However, the insulation thickness supplied no heat losses is neither practical nor economical. Thus, a balance point must determine between the insulation material cost with energy savings obtained, and this point shows the optimum insulation thickness [1-13].

There are many studies related to the optimum thickness of distribution networks in the district heating system. Comakli et al. [14] investigated the energy and exergy losses of heat distribution networks consisted of 11988 m length and 65-250 mm nominal size pipes of Ataturk University. The heat loss of the district heating networks pipes found as 8.62%. As a result of the study, the insulation material thickness is the most influential factor because of decreasing heat losses from the pipes. In case the insulation thickness of 20 cm uses instead of 8 cm on the pipes, the heat losses from the pipes decreases percent by 25. Keçebaş et al. [1] calculated the optimum insulation thickness, energy savings, and payback periods of pipes used district heating network existed

Afyonkarahisar Province in Turkey for five different nominal sizes of pipes and four fuel types during ten years of economic life. In the study, an optimum model developed based on Life Cycle Cost Analysis Method. Rockwool considered insulation material, and the network consisted of network 50-200 mm nominal size pipes. According to the study results, the optimum insulation thickness, energy-saving, and payback period were shown a change respectively between 0.085-0.228 m, 10.041 $/m-175.171 $/m, and 0.442-0.808 years depending on different pipe diameters. Rosti et al. [2] proposed the determination of optimum insulation thickness by first investment cost of insulation and payback period all climatic zones in Iran. In the study, the optimization carried out by using the Life Cycle Cost Analysis method with a numeric solution. Kayfeci [3] determined energy saving significantly can be obtained by insulating pipe networks, and the incredible number of heat losses stem from the network of heat losses in the district heating system. In the study, the optimum insulation thickness, energy-saving, annual operation cost, and payback period calculated using the Life Cycle Cost Analysis method for different nominal pipe sizes, various insulation materials, and heating degree days (HDD). In the study results, the optimum insulation thickness showed a change between 0.048-0.134 m; while energy-saving and payback period were found respectively between 10.84 $/m-49.78 $/m and 0.74-1.29 years. Zhang et al. [13] calculated the optimum insulation thickness, energy-saving, and payback period of direct-buried pipes used district heating network for various pipe diameters, different soil deepness for Xion Province in China by using the Life Cycle Cost Analysis method in this study. According to the study results, the optimum insulation thickness, energy-saving, and payback period respectively changed between 0.060-0.121 m, 36.395 $/m-194.682 $/m, and 0.445-1.691 years.

In this study, optimum insulation thicknesses, energy savings, first investment costs and payback periods of the pipes in the network of a low-temperature district heating system investigated using Equivalent Annual Worth (EAW) Analysis method for natural gas. The total length of the district heating system's network is 1470 m; and supply-return pipes for space heating, hot water pipes, and circulation pipes locate in the heat canals under the soil. Optimum insulation thicknesses calculated for different nominal sizes pipes (Ø20mm-Ø150 mm) for the fourth climatic zone (the coldest zone) and glass wool.

2. METHOD

2.1 Heat losses from the pipes in the network (heat canals under the soil)

A resistance model is shown in Figure 1for calculating heat losses from the pipes in the canals under soil per unit length [14].

Insulation material resistance;

$$R_i = \frac{1}{2 \times \pi \times k_i} \times In\left(\frac{r_2}{r_1}\right) \quad (1)$$

Canal resistance;

$$r_c = \frac{x_{cp}}{2 \times \pi} \quad (2)$$

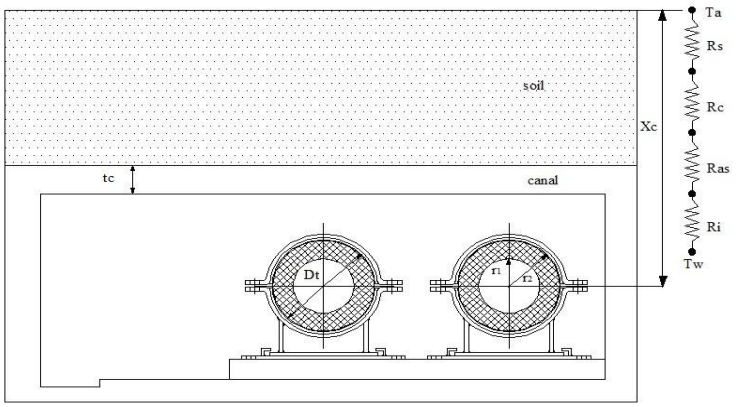

Figure 1. The sectional view of heat canal and the resistance model

$$R_c = \frac{1}{2 \times \pi \times k_c} \times In\left(\frac{r_{c+} t_c}{t_c}\right) \tag{3}$$

The convection resistance of the air in the canal;

$$R_a = \frac{1}{2 \times \pi \times h_{a\times} r_i} \tag{4}$$

The air convection coefficient can found by the following formula [14].

$$h_a = \frac{k_a}{D} \times Nu_D \tag{5}$$

The following formula can be used for calculating the local Nusselt number at constant temperature and around a cylinder.

$$Nu_D = \left[0.6 + \frac{0.387 \times Ra_D^{1/6}}{\left[\left(1 + (0.559/Pr^{9/16})\right)\right]^{8/27}}\right]^2 \tag{6}$$

$$Ra_D = \frac{g \times \beta \times (T_s - T_\infty) \times D}{\vartheta \times \alpha} \tag{7}$$

Soil resistance;

$$R_s = \frac{1}{2 \times \pi \times k_s} \times In\left[\frac{x_c}{r_c} \times \left(1 + \sqrt{1 - (D_t/x_c)^2}\right)\right] \tag{8}$$

Heat losses from the pipes in the heat canals per unit length calculate with the following formula.

$$\dot{Q_{pl}} = \left[\frac{T_w - T_a}{R_i + R_a + R_c + R_s}\right] \tag{9}$$

Annual fuel consumption corresponding heat losses from the pipes,

$$\dot{V_{pl}} = \frac{\dot{V_f} \times \dot{Q_{pl}}}{\dot{Q_f} \times \eta_s} \tag{10}$$

Annual total fuel energy consumed of the heating system,

$$\dot{Q}_f = \dot{V}_f x H_u \tag{11}$$

Annual fuel consumption cost corresponding heat losses from the pipes,

$$C_{fl} = \dot{V}_{pl} x C_f \tag{12}$$

The volume and cost of insulation material,

$$V_i = \pi \times (r_2^2 - r_1^2) \times L \tag{13}$$

$$C_{ins} = \mathrm{V}_i x C_i \tag{14}$$

Energy savings can calculate as follows:

$$\dot{Q_{es}} = \dot{Q}_{un-ins} - \dot{Q}_{ins} = \left[\left(\frac{1}{R_a + R_c + R_s}\right) - \left(\frac{1}{R_i + R_a + R_c + R_s}\right)\right] \times (T_w - T_a) \tag{15}$$

In the economic analysis, it is necessary determining some parameters such as first investment cost, lifetime period, annual maintenance and operation costs, annual savings, and interest rate. Equivalent Annual Worth analysis is used as the economic analysis method. In the annual equivalent worth analysis, the aim is to transform money into an equivalent uniform annual cost or savings [15]. Equivalent Annual Worth (EAW) and payback period calculate in the following equations. F, C, and IC in the equations show respectively income, cost, and first investment cost.

$$EAW = \left[\sum_{n=1}^{t} \frac{F_n}{(1+i)^n} - \sum_{n=1}^{t} \frac{C_n}{(1+i)^n}\right] \times \frac{(1+i)^n \times i}{(1+i)^n - 1} \tag{16}$$

$$PP = \frac{IC}{EAW} \tag{17}$$

2.2 System description

Space heating and hot water need of buildings in the 18. Regional Directorate of Highway's campus, located in Kars city of Turkey, is satisfied by 4th Generation a low-temperature heating system (LTDH). Kars is the coldest city, situated in the fourth climatic zone of Turkey. Annual fuel (natural gas) consumption of district heating system is on average 809,793.50 Nm^3. Supply and return water temperatures of the district heating networks vary between 60°C/50°C. The heat distribution network's length is 1470 m, and the diameters of the pipes in the heat canals are varied from Ø20 mm to Ø150 mm. The layout plan of the district heating network gives in Figure 2.

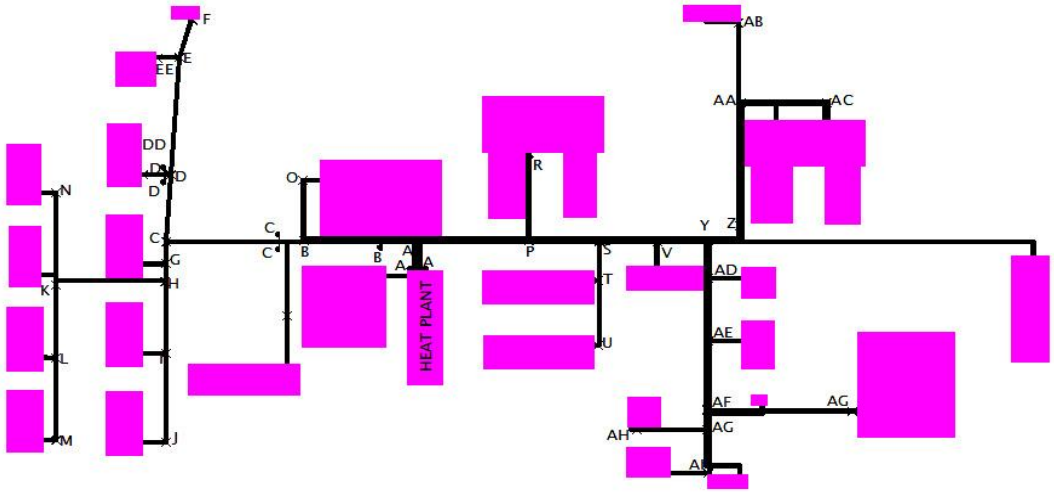

Figure 2. The layout plan of the district heating network

Equivalent Annual Worth (EAW) Analysis method is used to investigate optimum insulation thicknesses of the pipes in heat canals. For the analysis of the heating system, annual fuel consumption values were taken from the regional natural gas company. Supply and return water temperature values of the system measured by the system's thermometers.

3. RESULTS

There are different diameters of heating pipes (supply and return pipes) between Ø25-Ø150 mm, and the total length of 1760 m in the network consists of heat canals. Besides, while a total of 1500 m length of hot water pipes has existed the different diameters Ø25-Ø110 mm, there is a total of 1498 m length of the circulation pipes (Ø20-Ø76 mm). The total length of the pipes in the canals is 4758 m, and supply and return water temperatures of the network vary between 60° and 50°C. At the under soil, the deepness of the canal is an average of 1.2 m. In the system's network in four different sizes, heat canals exist, and the values of the canal resistance change to 0.4403 from 0.3763.

Table 1. Results of the resistant model

Parameter	Value
Canal material	Concrete
k_c	2.1 W/m.K
R_c	0.376-0.441 W/m^2.K
t_c	20 cm
Insulation material	Glass wool
k_i	0.035 W/m.K
R_i	2.679-5.697 W/m^2.K
Deepness of soil x_c	1.2 m
k_s	2 W/m.K
R_s	1.378-1.413 W/m.K
h_a	6.902-7.897 W/m^2.K
Ra_D	$1.25x10^6$-$7.18x10^7$
Nu_D	20.48-69.05

Supply and return heating pipes, hot water pipes, and circulation pipes in heat canals are insulated with glass wool to decrease heat losses. The thermal conductivity coefficient of insulation material has been taken as k=0.035 W/m.K, and soil resistance values have been found between 1.3781-1.4130. Parameters and values used in resistance calculations show in Table 1.

Heat loss from the pipes in the district heating network has been calculated as 46.48 kW, and 31.07 kW of this loss stems from supply and return pipes and 15.41 kW of this loss from hot water and circulation pipes. Considering all district heating system annual heat loss value and heat loss ratio from all pipes in the network has been found respectively as $14.45x10^8$ kJ and 5.44%.

To minimize this high amount of heat loss and save fuel, the pipes should investigate in terms of optimum insulation thickness. Parameters and values used in the economic analysis show in Table 2.

Table 2. Parameters used in the economic analysis

Parameter	Value
Heating degree-days (HDD)	3860°C days
Insulation material	Glass wool
k_i	0.035 W/m^2.K
Fuel	Natural gas
Price, C_f	0.3601 \$/m^3
H_u	8250 kcal/m^3
The efficiency of heating system	95%
Annual fuel consumption, V_f	809,793.50 Nm^3
The interest rate, i	15%
Inflation rate, d	13%
Lifetime, N	Ten years

Total costs, insulation costs and energy, and fuel savings have been calculated for the different pipe diameters and glass wool insulation material according to the different insulation thicknesses in the district heating networks. Change of annual fuel cost, insulation, and total costs according to the insulation thicknesses for a pipe (Ø 90 mm) shows in Figure 3. While depending on different insulation thicknesses, the insulation costs of supply and return pipes (Ø150 mm-Ø20 mm) are changed between 11.78\$/m-0.53\$/m; the insulation costs of hot water pipes (Ø110mm-Ø25 mm) and circulation pipes (Ø76 mm-Ø20 mm) are respectively between 4.94\$/m-0.29\$/m and 2.94\$/m-0.27\$/m.

Insulation thickness, where minimizes total cost, is shown the optimum insulation thickness. The optimum insulation thickness has been investigated for all pipes in the network and compared to the current insulation thickness of the pipes. Optimum and current insulation thicknesses are given for supply and return water pipes in Figure 4. Optimum insulation thicknesses change between 30-40 mm for all pipes.

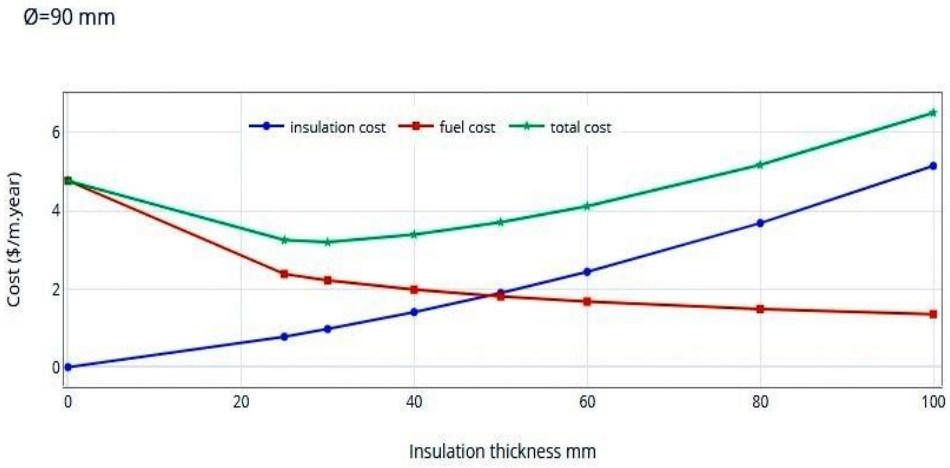

Figure 3. Change of annual costs depending on different insulation thicknesses

The heat loss from the pipes decreases together with the increasing insulation thickness, and fuel savings provides. The chancing of energy savings shows in Figure 5 depending on the increasing insulation thickness for circulation pipes with different nominal sizes. Energy savings are reached a maximum point at the insulation thickness between 25-40 mm and observed no change hardly ever at values between 50-80 mm. Though the insulation costs increase, energy savings is no change at the insulation thickness of 50 mm and over. Therefore, this value and over are not economical.

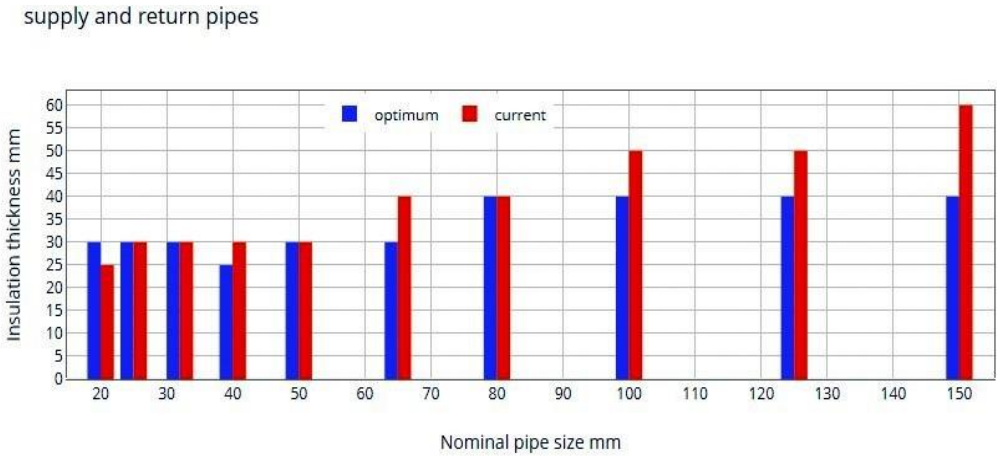

Figure 4. Current and optimum insulation thicknesses of supply and return pipes

Energy savings are respectively changed between 61.60 $/m-102.127 $/m for supply and return pipes depending on the different pipe diameters (Ø150mm-Ø20 mm) during the economic life of 10 years. While energy savings during economic life are obtained as 19.25$/m-29.07$/m for hot water pipes (Ø110mm-Ø25 mm), they are between 20.71$/m-29.91$/m for circulation pipes (Ø76 mm-Ø20 mm).

Payback periods, which to be compensated first investment cost with the energy savings provided, are calculated for various diameters of all pipes in the network. The change of payback periods by different insulation thickness for the supply and return pipes gives in Figure 6.

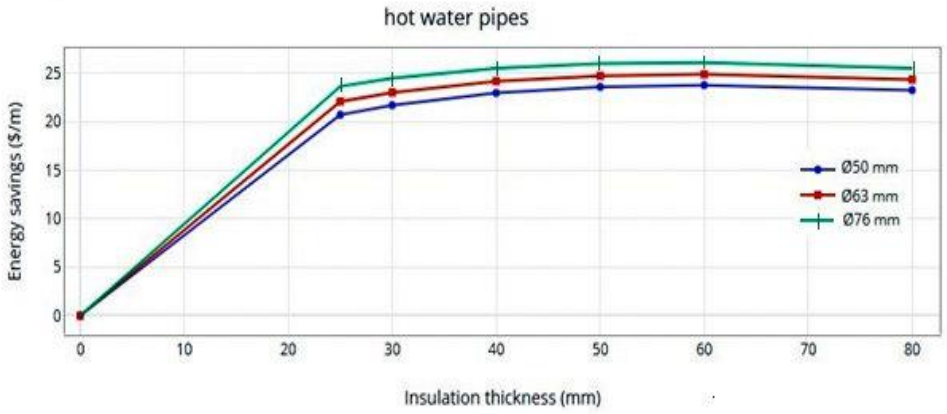

Figure 5. Energy savings of hot water pipes depending on various pipe diameters

Payback periods for supply and return pipes, hot water pipes, and circulation pipes have been respectively found as 1.59-0.06 years, 2.53-0.11 years, and 1.26-0.09 years.

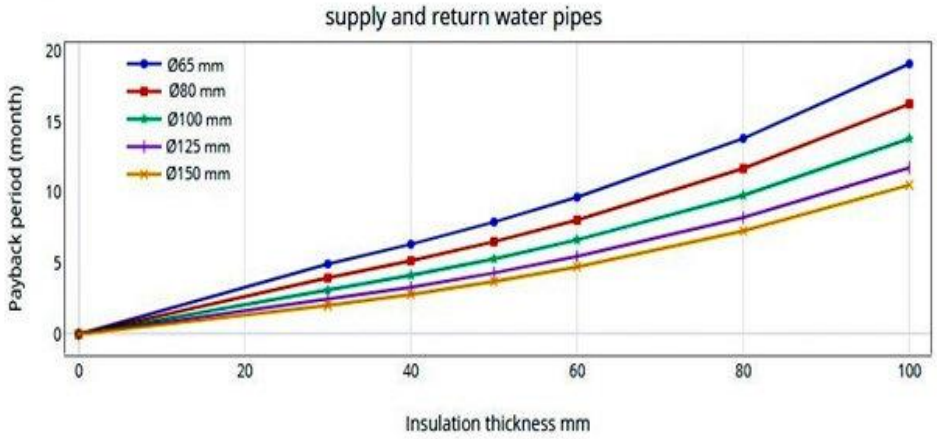

Figure 6. Changing of payback period according to different insulation thickness

4. CONCLUSIONS

The results of the study summarize as:

✓ According to the results, heat loss values from the pipes in the district heating network is as 46.48 kW, and 31.07 kW of this loss stems from supply and return pipes and 15.41 kW of this loss from hot water and circulation pipes.

✓ Annual heat loss value and heat loss ratio from all pipes in the network is respectively as 14.45×10^8 kJ and 5.44% considering all district heating system.

✓ Energy and fuel savings obtained by decreasing of heat loss thanks to insulation have been found for the different pipe diameters in the network used glass wool as insulation material according to the different insulation thicknesses.

✓ Optimum insulation thicknesses vary between 30-40 mm for all pipes and glass wool insulation material.

✓ While depending on different insulation thicknesses, the insulation costs of supply and return pipes (Ø150 mm-Ø20 mm) are changed between 11.78$/m-0.53$/m; the insulation costs of hot water pipes (Ø110mm-Ø25 mm) and circulation pipes (Ø76 mm-Ø20 mm) are between 4.94$/m-0.29$/m and 2.94$/m-0.27$/m.

✓ Energy savings are changed between 19.25$/m-102.127$/m for the supply and return water pipes, hot water, and circulation pipes by various pipe diameters during the economic life of 10 years.
✓ Payback periods vary between 2.53-0.06 years for all pipes.

REFERENCES

[1] A. Keçebaş, M. A. Alkan, M. Bayhan, Thermo-economic analysis of pipe insulation for district heating piping systems, *Applied Thermal Engineering*, **31**, 3929-3937, 2011.

[2] B. Rosti, A. Omidvar, N. Monghasemi, Optimal insulation thickness of common classic and modern exterior walls in different climate zones of Iran, *Journal of Building Engineering*, **27**, 100954, 2020.

[3] M. Kayfeci, Determination of energy saving and optimum insulation thicknesses of the heating piping systems for different insulation materials, *Energy and Buildings*, **69**, 278-284, 2014.

[4] A. Keçebaş, Determination of insulation thickness by means of exergy analysis in pipe insulation, *Energy Conversion and Management*, **58**, 76-83, 2012.

[5] A. Keçebaş, Determination of optimum insulation thickness in pipe for exergetic life cycle assessment, *Energy Conversion and Management*, **105**, 826-835, 2015.

[6] U. İlhan, Optimum insulation thickness for pipes in district heating systems, *Journal of Mechanical and Energy Engineering*, **42**, 225-232, 2018.

[7] A. R. Mazhar, S. Liu, A. Shukla, A state of art review on the district heating systems, *Renewable and Sustainable Energy Reviews*, **96**, 420-439, 2018.

[8] M. A. Sayegh, J. Danielewicz, T. Nannou, M. Miniewicz, P. Jadwiszczak, K. Piekarska, Trends of European research and development in district heating technologies, *Renewable and Sustainable Energy Reviews*, **68**, 1183-1192, 2017.

[9] P. Jie, Z. Tian, S. Yuan, N. Zhu, Modeling the dynamic characteristics of a district heating network, *Energy*, **39**, 126-134, 2012.

[10] I. del Hoyo Arce, S. H. Lopez, S. L. Perez, M. Rama, K. Klobut, J. A. Febres, Models for fast modeling of district heating and cooling networks, *Renewable and Sustainable Energy Reviews*, **82**, 1863-1873, 2018.

[11] J. F. Castro Flores, B. Lacarriere, J. NW. Chiu, V. Martin, Assessing the techno-economic impact of low-temperature subnets in conventional district heating networks, *Energy Procedia*, **116**, 260-272, 2017.

[12] Y. Başoğul, C. Demircan, A. Keçebaş, Determination of optimum insulation thickness for environmental impact reduction of pipe insulation, *Applied Thermal Engineering*, **101**, 121-130, 2016.

[13] L. Zhang, Z. Wang, X. Yang, L.Jin, Q. Zhang, W. Hu, Thermo-economic analysis for directly-buried pipes insulation of district heating piping systems, *Energy Procedia*, **105**, 3369-3376, 2017.

[14] K. Comakli, B. Yuksel, O. Comakli, Evaluation of energy and exergy losses in district heating network, *Applied Thermal Engineering*, **24**, 1009-1017, 2004.

[15] M. Terhan, K. Comakli, Design and economic analysis of a flue gas condenser to recover latent heat from exhaust flue gas, *Applied Thermal Engineering*, **100**, 1007-1015, 2016.

ENERGY MANAGEMENT

PARAMETRIC ANALYSIS OF A PLATE, FINNED AND CROSS FLOW HEAT EXCHANGER FOR HEAT RECOVERY IN BUILDINGS

Satılmış TEKİN, Göker TÜRKAKAR*,**
*Zonguldak Bülent Ecevit University, Department of Mechanical Engineering, Zonguldak/Turkey
Email: tukakar@beun.edu.tr
**Zonguldak Bülent Ecevit University, Department of Mechanical Engineering, Zonguldak/Turkey
Email: satilmistekin18@gmail.com

ABSTRACT

A plate-fin and cross-flow heat exchanger, HEX, is designed to recover the heat lost during the buildings' ventilation in winter. This study investigates the effects of the parameters such as the channel's width and height, outside air temperature, and the airflow rate on the heat exchanger's dimensions. The logarithmic mean temperature difference method (LMTD) was employed in the HEX design. The air requirement to ventilate a 100 m^2 house in wintertime was calculated by assuming four people live in the house. Based on this air requirement calculation, a parametric analysis was conducted. By fixing the hot and cold side inlet and outlet temperatures, the effect of channel width, height, and mass flow rate or the air on HEX length was investigated under pressure drop constraint (200 Pa). Moreover, for a fixed geometry creating a reasonable pressure drop value, the effect of outside air temperature on HEX's effectiveness was sought. The HEX's length in the present study was compared with the heat recovery devices with different fin geometry available in the literature for the same operating conditions and the main dimensions.

Keywords: Heat recovery device, heat recovery in buildings, air to air heat exchanger, plate finned heat exchanger, cross-flow heat exchanger.

Symbols

A	Heat transfer area (m^2)
C_p	Specific heat (J kg^{-1} K^{-1})
C_c	Cold fluid thermal capacity (W K^{-1})
C_{min}	Minimum thermal capacity (W K^{-1})
D_h	Hydraulic diameter (m)
F	Correction factor
f	Friction factor
h	Heat convection coefficient (W m^{-2} K^{-1})
k	Thermal conductivity (W m^{-1} K^{-1})
L	Fin height (m)
$\dot{m}$	Mass flow rate (kg s^{-1})
N	Number of fins
Nu	Nusselt number ($h\ D_h/k$)
PP	Pumping power (W)
Q	Heat transfer (W)
Re	Reynolds number ($V\ D_h/\nu$)
U	Overall heat transfer coefficient (W m^{-2} K^{-1})
V	Air velocity (m s^{-1})
W	Heat exchanger length and width (mm)
ΔP	Pressure drop (Pa)
η	Fin efficiency

$\dot{V}$	Volumetric flow rate ($m^3\ s^{-1}$)
ε	Effectiveness
ρ	Density ($kg\ m^{-3}$)

1. INTRODUCTION

In recent years, population growth has caused a rise in the need for housing. Therefore, energy demand for heating, ventilating and air conditioning, HVAC systems in buildings has also increased. 20% to 40% of total energy use in developed countries results from buildings' energy consumption [1]. To reduce this energy consumption in buildings, the recovery of waste heat has gained importance. Heat recovery devices are employed to recover energy from the exhaust air in the buildings. The heat recovery device is a heat exchanger. High-temperature fluid (exhaust gas) transfers its energy to low temperature (fresh) fluid. Heat recovery from hot air to clean cold air is provided in heat recovery ventilation systems in buildings. Heat recovery ventilation systems provide 65% -95% recovery of waste heat and improve energy efficiency in buildings significantly [2].

There are usually two different types of air-to-air heat recovery devices to recover heat in buildings. One can be classified as a rotary type heat recovery device and the other as plate heat exchangers. In the rotating type heat recovery device, hot air energy flowing from the upper section is stored in the rotary wheel. Cold air flows from the lower part, and it is heated by the energy stored in the rotary wheel. In this way, it recovers the thermal energy of the hot air. The efficiency of these devices is high; however, their use is limited in building applications because of the mixing of hot and cold air. In a plate type, heat exchanger, cold and hot air flow in cross or counter flow in channels separated by the plates.

Simonson and Besant [3] developed a numerical model for studying heat and humidity transfer of rotary type heat exchanger. Using the model, they designed the rotary type heat exchanger and examined the parameters affecting its performance. Zhang et al. [4] created a one-dimensional heat and mass transfer model to design and manufacture the wheel used in the rotary-type heat exchanger. The air passage channels of the wheel are honeycomb-shaped. In the mathematical model, the designed wheel was produced, and experimental work was performed. They compared their experimental and theoretical ones, and they concluded that these two results are in perfect agreement. To improve the rotary type heat exchanger's performance, they studied the effects of flow rate and wheel temperature on wheel speed.

One of the first examples of a plate heat recovery device belongs to Pescod [5]. They analyzed the performance of a plate heat recovery device that was insufficient for heat transfer. This heat recovery device was inadequate in terms of heat transfer. Sahan [6] studied problems arising during the use of air to air heat recovery (plate and cross-flow) exchangers. He emphasized that the heat recovery device should be used to reduce energy costs and advance the air quality of living spaces. Zhang et al. [7] designed a plate, cross-flow heat exchanger. They used different plate materials: paper, membrane, and modified membrane, to examine plates' moisture retention properties on heat exchanger performance. The best performing one was the modified membrane. They carried out experiments for different flow rates and different temperatures. Fernández-Seara et al. [8] designed a heat exchanger with triangular channels with polymer plates for houses' ventilation. They prepared a test assembly to examine the designed heat exchanger experimentally. The exhaust air inlet temperature and relative humidity were kept constant at 25 ˚C and 50%, respectively. The fresh air inlet temperature was kept constant at 5˚C. They found the polymer plate heat exchanger's heat transfer rate to be 672 W and thermal efficiency 80% (HEX effectiveness). They also conducted experiments to study the effect of inlet fresh (cold air) air temperature, exhaust air (hot air), relative humidity, and airflow velocity. Mardiana-Idayu and Riffat [9] designed a cross-flow, plate heat exchanger with a diamond shape. The heat and mass transfer surface of this heat recovery core comprises cellulose papers (pads) that allow both heat and moisture to be transferred. In this way, sensible and latent heat is intended to be recovered. They examined the designed heat exchanger under different operating conditions. The sensible heat recovery is reported to be close to 66%, and the latent energy efficiency was nearly 59% gained.

In this study, a plate, finned, cross-flow HEX is used to recover the buildings' thermal energy during the buildings' ventilation. HEX dimensions were determined for the need for ventilation (485 m^3/h) of a house (100 m^2, four people living). The effects of parameters such as mass flow rate, HEX channel width, channel height on overall HEX dimensions were examined. Heat exchange between the fluids was investigated for various outside fresh air temperatures.

2. DESIGN

2.1. Calculation of Ventilation Requirement

It is stated that the maximum air exchange coefficients should be 0.5 $m^3/(h.\ person)$ for the ventilation of the houses [10]. The maximum air requirement for a place with four people living, 100 m^2 floor area, and 2.75m ceiling height and to be ventilated in the winter months was calculated 550 m^3/h. The Ventilation requirement is accepted as 485 m^3/h. This value is in the range of volumetric flow rate interval specified in the manuals of the commercial heat recovery devices in the market [11,12].

2.2 Design Conditions and Operation Diagram

The Operating temperatures of the designed heat recovery device are presented in Table 1.

Table 1. Operating temperatures of heat recovery device

Operating temperature	**˚C**
Outlet air temperature, T_{h1}	25
Exhaust air temperature, T_{h2}	10
Fresh air temperature, T_{c1}	3
Inlet air temperature, T_{c2}	18

The operating diagram of the designed plate finned and cross-flow heat exchanger is illustrated in Figure 1.

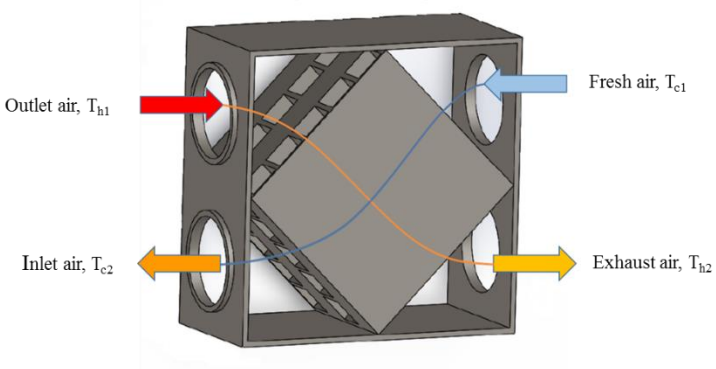

Figure 1. Operating diagram of heat recovery device

Air inlet and outlet ports on the HEX are illustrated in Figure 1. Hot and cold air flows through a cross-flow heat exchanger. Hot and cold fluids do not mix. The heat exchanger transfers the energy from the hot air to the cold air. In this way, the heat of the hot air is recovered. By using the plate, finned, and cross-flow heat exchanger, fresh and heated air is supplied to the building.

2.3 Heat Exchanger Shape and Dimensions

The designed plate finned and cross-flow heat exchanger is shown in Figure 2. Overall width and length of HEX are equal (both are symbolized as W).

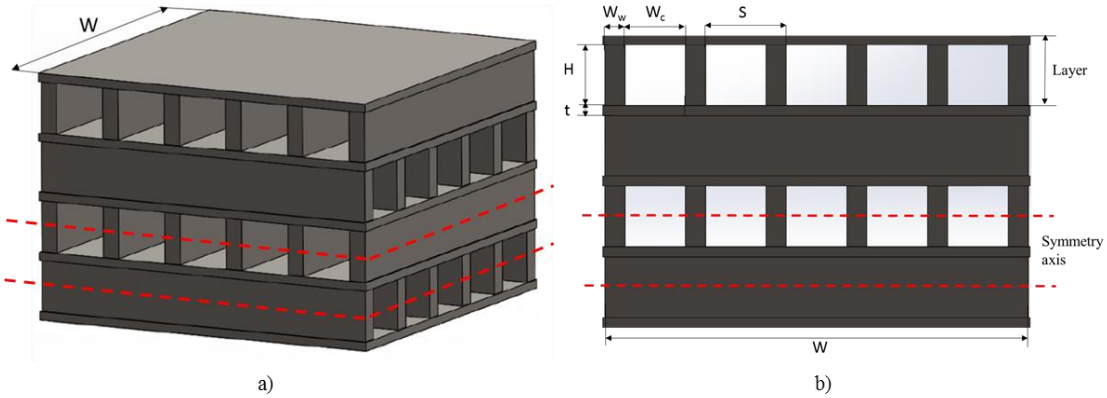

Figure 2. Designed heat exchanger a) Plate, finned and cross flow HEX b) HEX dimensions

HEX dimensions are provided in Table 2.

Table 2. Heat exchanger design dimensions

Parameters	Value
Plate thickness, t	0.5 mm
Fin thickness, W_w	1 mm
Channel width, W_c	2 mm
Channel height, H	5 mm
Number of layer (for hot side)	40, (80 in total)

The material used for heat exchanger design is steel with thermal conductivity (k_{steel}) 64 W m^{-1} K^{-1}. The region between the red dashed lines shown in Figure 2 is taken as the computational domain. As the red plane crosses the channel right into the middle, an adiabatic fin tip model is adopted. The layer indicated in Figure 2 is defined as the distance between two plates.

2.4 Fan Selection

Radial fans and plug fans are adopted in heat recovery devices. Plug fan is mainly used when a high mass flow rate is required. Since the need for ventilation is not high, a radial fan is preferred in this study. [13].

Pressure drop is a crucial parameter in the HEX design. The selected fan should meet the maximum pressure drop requirements. Therefore, the pressure drop in the heat exchanger and the maximum pressure drop that the fan can provide should be compared. The maximum pressure drop that ought not to be exceeded is defined as a design constraint. Pressure drop in plate heat exchangers is recommended to be between 100-200 Pa [14]. The design was made to ensure that the pressure drop does not exceed 200 Pa.

3. DESIGN CALCULATIONS

Some assumptions have been made to simplify the calculations,

- The HEX is thermally insulated against the environment, and the heat transfer is only from the hot fluid to the cold fluid.
- There is no axial heat conduction along the channel.
- Air properties are taken as constant. They are evaluated at the mean value of the inlet and the outlet temperatures.
- The length and width of HEX are identical.
- The flow in the channel is hydrodynamically and thermally fully developed.

3.1 Heat Transfer from Hot Fluid to Cold Fluid

Heat transfer between the fluids is calculated by Eq. 1 [15].

$$Q = \dot{m}\, C_p (T_{h1} - T_{h2}) \tag{1}$$

In equation (1), $\dot{m}$ symbolizes mass flow rate, C_p is specific heat. Thermophysical properties can be found by using thermophysical property tables of gases at atmospheric pressure [15]. As the heat transfer is known, the heat transfer area can be calculated using the Logarithmic Mean Temperature Difference method (LMTD) [15].

$$Q = U\, A\, \Delta T_{lm} \tag{2}$$

In equation (2), Q is heat transfer, U is overall heat transfer coefficient, A is the heat transfer area between two fluids. ΔT_{lm} is defined in Eq. 3 as $\Delta T_{lm} = \Delta T_{lm,cf}\, F$. ΔT_{lm} is logarithmic mean temperature difference, $\Delta T_{lm,cf}$ is logarithmic mean temperature difference calculated as counter flow, F is the correction factor [15]. In the first case, heat exchanger operating temperatures are constant. Therefore, the LMTD method has been adopted. Notwithstanding, an iterative ϵ-NTU method is preferred when examining the effect of fresh air (cold inlet, T_{c1}) temperature on heat transfer and inlet temperature (T_{c2}). Otherwise, the correction factor F must be defined for each case.

3.2 Calculation of Air Convection Coefficient

Air side convection coefficient is calculated by Eq. 3.

$$h = \frac{Nu\, k_{air}}{D_h} \tag{3}$$

In equation (3), k_{air} is air thermal conductivity, $D_h = 4A_C/P$ is the hydraulic diameter. Where A_c is the flow-channel cross-sectional area and P is the wetted perimeter. The type of flow is determined by the Reynolds number, $Re = \rho\, V\, D_h/\mu$. Nusselt numbers for four-side heated, laminar, and fully developed flow conditions are provided [16]. As it depends on the channel's aspect ratio, the whole table could not be presented here.

3.3 Calculation of Fin Efficiency

As the symmetry is used, the fin tip is considered as adiabatic. The fin efficiency definition is given in Eq. 4.

$$\eta_f = \frac{\tanh(mL)}{mL} \tag{4}$$

In equation (4), m is defined as $\sqrt{2\,h/k_{fin}W_w}$. L is fin height, and it is equal to H/2 for the present study. Overall fin efficiency is provided in Eq. 5.

$$\eta_0 = 1 - \frac{N\,A_f}{A_t}(1 - \eta_f) \tag{5}$$

In equation (5), A_f is defined as $2\,W\,L$, A_t is defines as $A_t = N\,A_f + A_b$, N is the number of the fin in the computational domain.

3.4 Calculation of Overall Heat Transfer Coefficient

Overall heat transfer coefficient is a combination of the thermal resistances. It is given in Eq. 6.

$$U = \left(\frac{1}{\eta_0\,h_{hot}} + \frac{A_t\,t}{k_{plate}W^2} + \frac{1}{\eta_0\,h_{cold}}\right)^{-1} \tag{6}$$

3.5 Calculation of Pressure Drop and Pumping Power

The pressure drop in the heat exchanger is calculated by Eq. 7 [16].

$$\Delta P = \frac{2\,f\,W\,\rho\,V^2}{D_h} \tag{7}$$

In equation (7), ρ is the air density, *f* is fanning friction factor. The fanning friction factor is calculated by Eq. 8 [16].

$$f.Re = 24(1 - 1.3553\alpha_c + 1.9467\alpha_c^2 - 1.7012\alpha_c^3 + 0.9564\alpha_c^4 - 0.2537\alpha_c^5 \tag{8}$$

Aspect ratio in equation (8), $\alpha = a/b$ is the ratio of the length of the short side to the long side of the channel. Pumping power is calculated by Eq. 9.

$$PP = \Delta P\,\dot{V} \tag{9}$$

In equation (9), PP is the pumping power, ΔP is the pressure drop and $\dot{V}$ is volumetric flow rate.

3.6 Calculation of Heat Exchanger Effectiveness

The heat exchanger's effectiveness is given in Eq. 10 [15].

$$\varepsilon = \frac{Q}{Q_{max}} = \frac{C_c(T_{c2} - T_{c1})}{C_{min}(T_{h1} - T_{c1})} \tag{10}$$

In equation (10), Q_{max} is the maximum heat transfer; C_c is the cold fluid's thermal capacity, C_{min} is the minimum thermal capacity value of the hot or cold fluid. The heat exchanger's effectiveness is calculated as 68% for the fixed inlet and outlet temperatures given in Table 1.

4. CALCULATION ALGORITHM

The computational algorithm is demonstrated in Figure 3.

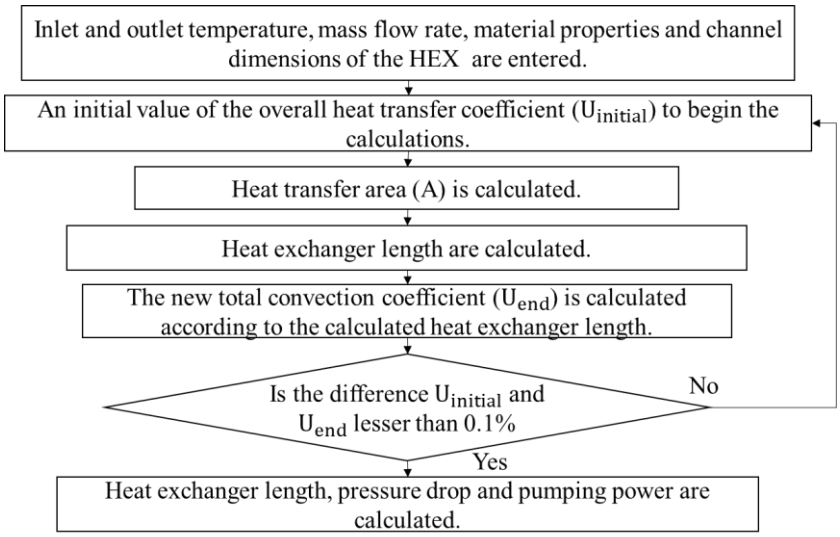

Figure 3. The computational algorithm for LMTD method

As the air inlet and outlet conditions are known, heat exchange and ΔT_{lm} can be calculated. However, since the HEX size is sought, the overall heat transfer coefficient, U, and the heat transfer surface area, A, are unknown at the beginning. Hence, an initial value for U is assigned. Based on this value, the heat transfer surface area is designated. The heat transfer coefficients, total thermal resistance, and the new overall heat transfer coefficient are identified using the surface area calculated based on the initial guess. Calculated U is compared with the initial guess. If the difference is higher than 0.1%, the iterative process is retained. If the convergence criterion is satisfied, the size of the heat exchanger is specified. As a result of the calculations, parameters, such as pressure drop, pumping power, HEX length are recorded. In the circumstances of the constant fluid inlet and outlet conditions, the LMTD method is employed (Fig. 4, Table 3). However, for the fixed dimensions of the HEX, fresh air temperature, T_{c1}, the effect on the heat transfer, and T_{c2} are investigated. In this case, as the fluid outlet temperature is not known, an iterative ϵ-NTU method is used (Fig. 5).

5. RESULTS

The developed algorithm is coded in MATLAB software. For the fixed fluid inlet/outlet temperatures and volumetric flow rate, the effect of channel height and width on the HEX length and the pressure drop is delved into (Fig. 4). Considering the results obtained in Fig 4, an overall HEX size satisfying pressure drop constraint is determined. After then, fresh air inlet temperature, T_{c1} effect on heat transfer, and inlet temperature, T_{c2} is practiced. Finally, for a fixed channel height, channel width's effect on total heat exchanger length/width (they are equal for all cases), pressure drop, and the pumping power is sought.

5.1 Calculation of the Heat Exchanger Length

For the volumetric flow rate value of 485 m^3/h, the effect of channel height and width on HEX length and pressure drop is examined. The number of layers (depicted in Fig. 2) used in the HEX is varied to keep the total HEX height

constant. For the channel heights of 3 mm, 4 mm, and 5 mm, the number of layers in the HEX varies as 65, 50, 40, respectively.

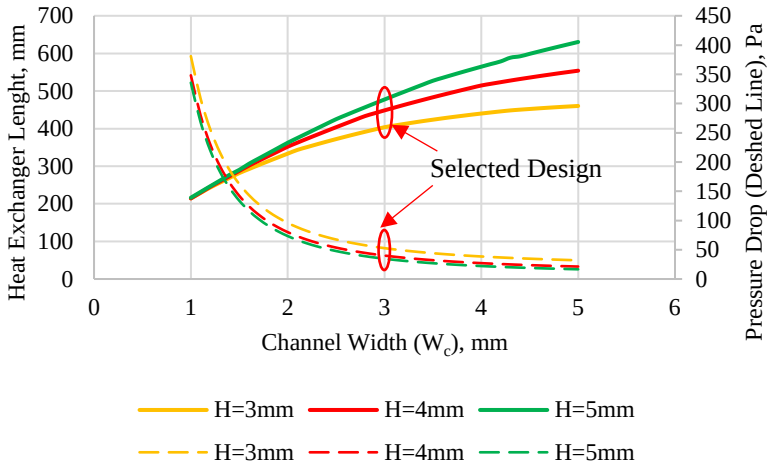

Figure 4. Change of heat exchanger length and pressure drop

Using the information given in Fig 4, the overall size of the HEX is specified. The Overall size of the HEX is selected by considering pressure drop constraint. Pressure drop exponentially decays with the increase of the channel width. Regarding this information, the channel width is chosen to be 3 mm. The use of 3 mm channel height results in the shortest HEX length; thus, 3 mm channel height is preferred. Chanel height variation has not resulted in significant deviations in the pressure drop. The heat exchanger dimensions for the selected channel height and width (3 mm×3 mm) are 420 x 404 x 404 mm (HEX Height x Width x Length). In this case, the pressure drop is 40.5 Pa. The pumping power required to meet the pressure drop has been calculated as 5.45W.

For the selected HEX dimensions (420 x 404x 404 mm), the effect of outdoor temperature (T_{c1}) on the inlet air temperature (T_{c2}) and heat transfer in the HEX is depicted in Figure 5.

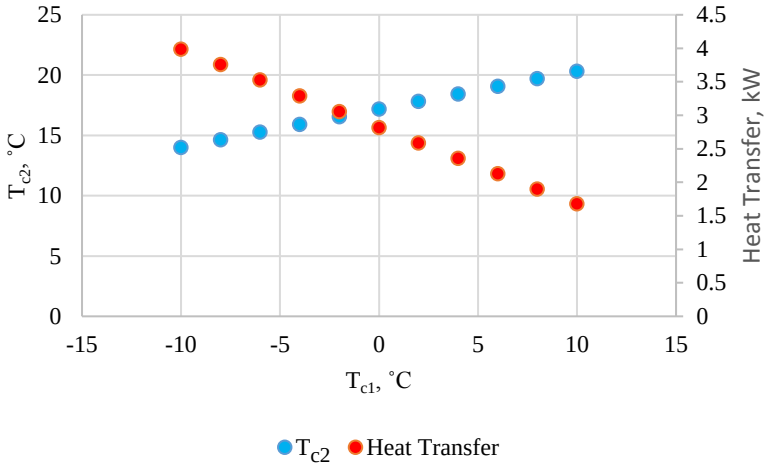

Figure 5. Change of inlet air temperature and heat transfer from the hot fluid to cold fluid ($\dot{V} = 485\ m^3/h$, ϵ-NTU method is used)

Outdoor temperature (T_{c1}) is varied between -10˚C with 10 ˚C. With the increment of outdoor temperature, the inlet air temperature, $T_{c2,}$ increased, but the heat transfers from the hot fluid to cold fluid decreased. The maximum heat transfer from the hot fluid to cold fluid is 3.99 kW, and the minimum heat transfer is 1.68 kW.

5.2 Effect of Flow Rate and Channel Width on Heat Exchanger Length

Table 3 indicates the change of heat exchanger length, pressure drop, pumping power, and heat transfer when the flow rate and channel width alter. In the calculations conducted in this part, the operating temperatures given in Table 1 and the dimensions provided in Table 2 are used. HEX dimensions were specified regarding the results of Figure 4 as 420 x 404 x 404 mm (HEX Height x Width x Length) for the selected channel height and width (3 mm×3 mm). In Table 3, the HEX length is sought for a fixed total HEX height (420mm) and channel height of 3 mm. The HEX length is calculated for various volumetric flow rates and channel widths.

Table 3. Heat exchanger length, pressure drop, and pumping power (total HEX height=420mm, H=3mm)

Volumetric Mass Flow, (m^3/h)	Heat Transfer (W)	Channel Width (mm)	Heat Exchanger Length (mm)	Pressure drop (Pa)	Pumping Power (W)
600	3021	1	240.5	415.3	69.22
		2	403	90.9	15.15
		3	531	42.9	7.15
		4	628.2	27.43	4.51
700	3541	1	259.8	484.5	94.21
		2	435.3	106.1	20.63
		3	573.6	50.1	9.74
		4	678.4	32.1	6.24
800	4047	1	277.7	553.7	123.04
		2	465.3	121.2	26.93
		3	613.2	57.2	12.71
		4	725.3	36.6	8.13

The heat exchanger length and pressure drop are pointed out. They are presented for four volumetric flow rates and four different channel heights. The heat exchanger's length has increased with the augmentation of the volumetric flow rate and the heat transfer rate. Pressure drop and pumping power decreased with increasing channel width, but the heat exchanger's length increased. Narrower channels yielded higher pressure drop and pumping powers. If the channel width value of 1 mm is chosen, the pressure drop exceeds the critical value of 200 Pa. Similarly, for the same channel width value, the required pumping power is much higher than other channel widths. Therefore, the channel width's minimum value needs to be picked as 2 mm regardless of the volumetric flow rate value.

5.3 Size Comparison of the Present Study with the Literature

Li et al. [17] designed a plate, triangular duct, cross-flow heat recovery device. Operating temperatures were T_{h1} = 35˚C and T_{c1} = 20 ˚C. The Pressure drop was 53 Pa. For these operating conditions, they calculated the heat exchanger dimensions as 462 x 185 x 185 mm. For the same operating temperatures, the heat transfer, and the same pressure drop values, overall heat exchanger size is detected for the channel shape and the algorithm used in the present study. Overall HEX dimensions are calculated as 462 x 134 x 134 mm. When compared to literature,

a smaller HEX is designed for the same operating conditions. It is found that a smaller HEX design is possible with the use of square ducts.

7. CONCLUSION

A plate, finned, and cross-flow heat exchanger is designed to recover the heat lost during the buildings' ventilation in the winter. The logarithmic Mean Temperature Difference method (LMTD) was used in the design. The air requirement for a house with four people living and a 100 m^2 floor area to be ventilated in the winter months was calculated (485 m^3/h). An iterative algorithm is developed in MATLAB software.

Selecting the heat exchanger channel height 3 mm and channel width 3 mm has been found suitable for pressure drop and ease of production accordingly. The heat exchanger dimensions for the determined channel dimensions were 420 x 404 x 404 mm. In this case, the pressure drop is 40.5 Pa, and pumping power is 5.45W. When the outdoor temperature increases, the inlet air temperature increases but the heat transfer from the hot fluid to the cold fluid decreases. The maximum heat transfer from the hot fluid to cold fluid is 3.99 kW, and the minimum heat transfer is 1.68 kW. If the channel width value of 1 mm is chosen, the pressure drop exceeds the critical value of 200 Pa for all volumetric flow rate values inspected in the study (600, 700, 800 m^3/h). The pumping power can be reduced by widening the channels. A mapping study is conducted so that one can decide on design parameter and dimensions for a house which needs 485 m^3/h ventilation.

REFERENCES

[1] Pérez-Lombard, L., Ortiz, J., Pout, C., A review on buildings energy consumption information, *Energy and Buildings*, 40(3), 394-398, 2013.

[2] Cuce, P. M., Riffat, S., A comprehensive review of heat recovery systems for building applications, *Renewable and Sustainable Energy Reviews*, 47, 665-682, 2015.

[3] Simonson, C. J., Besant, R.W., Heat and Moisture Transfer in Desiccant Coated Rotary Energy Exchangers: Part I. Numerical Model, *HVAC&R Research*, 3(4), 325-350, 1997.

[4] Zhang, X. J., Dai, Y. J., Wang, R. Z., A simulation study of heat and mass transfer in a honeycombed rotary desiccant dehumidifier, *Applied Thermal Engineering*, 23(8), 989-1003, 2003.

[5] Pescod, D., A heat exchanger for energy saving in an air conditioning plant, *ASHRAE Transaction*, 85(2), 238-51, 1979.

[6] Şahan, A. M., Isı Geri Kazanım eşanjörlerinin kullanım opsiyonları, *VI. Ulusal Tesisat Mühendisliği Kongresi Ve Sergisi*, 2003.

[7] Zhang, L. Z., Liang, C. H., Pei, L. X., Heat and moisture transfer in application scale parallel-plates enthalpy exchangers with novel membrane materials, *Journal of Membrane Science*, 325(2), 672-682, 2008.

[8] Fernández-Seara, J., Diz, R., Uhía, F. J., Dopazo, A., Ferro, J. M., Experimental analysis of an air-to-air heat recovery unit for balanced ventilation systems in residential buildings, *Energy Conversion and Management*, 52(1), 635–640, 2011.

[9] Mardiana-Idayu, A., Riffat S. B., An experimental study on the performance of enthalpy recovery system for building applications, *Energy and Buildings*, 43(9), 2533-2538, 2011.

[10] Bulgurcu, H., Lokal Isı-Enerji kazanımlı havalandırma cihazlarının tasarımı, *V. Ulusal Tesisat Mühendisliği Kongresi Ve Sergisi,* 2001.

[11] https://venco.com.tr

[12] http://www.ventas.com.tr

[13] https://elektromarketim.com.tr

[14] Şahan, A. M., HVAC Uygulamalarında ısı geri kazanımı, *IV. Ulusal Tesisat Mühendisliği Kongresi Ve Sergisi*, 1999.

[15] Incropera, F. P., DeWitt, D. P., Bergman, T. L., Lavine, A. S., Fundamentals of Heat and Mass Transfer 6th Edition, Fundamentals of Heat and Mass Transfer 6th Edition, (2007).

[16] Kandlikar, S., Garimella, S., Li, D., Colin, S., King, M. R., Heat Transfer and Fluid Flow in Minichannels and Microchannels, First edition, 2006.

[17] Lia, Z. X., Zhong, T. S., Niu, J. L., Xiao, F., Zhang L. Z., Conjugate heat and mass transfer in a total heat exchanger with cross-corrugated triangular ducts and one-step made asymmetric membranes, *International Journal of Heat and Mass Transfer*, 84, 390-400, 2015.

AN ORE ENRICHMENT PLANT, THE EFFECT OF OPERATION OPTIMIZATION OF OPERATORS ON PRODUCTION AND ENERGY EFFICIENCY

Ecem BULAT*, Cemalettin AYGÜN**
* Gümüşhane University, Department of Energy Systems Engineering, Gümüşhane/Turkey
Email: ecembulat@gmail.com
** Gümüşhane University, Department of Energy Systems Engineering, Gümüşhane/Turkey
Email: caygun@ktu.edu.tr

ABSTRACT

The Republic of Turkey has identified strategies for reducing external dependence on energy, increasing energy efficiency, and using energy resources more efficiently in public, private sector, industry, and housing within the framework of National Energy and Mining Policy.

With this study prepared based on national strategies, it aims to increase energy efficiency in the industry and to use mines and resources more efficiently. In this context, an Ore Enrichment Plant in the mining sector, enriched by the flotation method, was examined. The plant consists of crushing screening, grinding, flotation, dewatering stages.

In this study, the electric energy use per tone of the crushing and screening unit, which is the base of the flotation method mineral liberation first process, is aimed to decrease. It represents the first step that affects the other unit's efficiency and production quality. The operations process in the crushing screening unit and the machines used operate by operators.

The failures are identified which is based on operator mistakes both directly and implicitly, the effects of failure typical errors and analyses on energy efficiency are examined by Process Failure Mode and Effect Analysis which is a risk analysis method. In this method, the interaction of operators of machines and processes are taken into consideration, and the risk priority factors of the failures that affect efficiency are calculated and sorted.
By identifying failures that have a high-risk priority factor, the optimization work is done, and the increased rate of production and energy efficiency is indicated as charts and graphics that comprise controls are presented. The effect of an increase in energy efficiency in the energy consumption per tone is identified.

Keywords: Optimization, Efficiency, FMEA

1. INTRODUCTION

The energy issue is significantly important for Turkey and has been shaped in the framework of the policies under development and the strategies in progress. Turkey has lately assumed a critical mission both on national and international energy platforms and continues to strengthen its energy policies. The National Energy and Mining Policy was developed to this end, and the strategies introduced in this policy are designed to consolidate Turkey's position in global energy markets. These strategies are summarized under the headings of security of supply, indigenization of energy sources, and a foreseeable energy market (Table 1) [1].

Table 1. Strategies and Goals Of The National Energy And Mining Policy

	SECURITY OF SUPPLY	INDIGENIZATION	FORESEEABLE ENERGY MARKET
STRATEGIES	• To increase diversification of energy resources and supplier countries • To increase the capacity of natural gas and oil storage facilities • To increase the capacity to provide natural gas to the system • To strengthen the infrastructure of energy delivery • **To increase energy efficiency**	• To make progress in renewable energy through local production, R&D and YEKA • To contribute to the generation of electricity by using nuclear technology • To indigenize mining technology	•To improve the energy supply infrastructure • To restructure the institutions in the sector • To revive the energy markets • **To consolidate the mining market**
GOALS	• To achieve quality and sustainable energy by increasing security of supply • To reach 10 bcm natural gas and 5 mto storage capacity • To conduct oil and natural gas explorations in the Mediterranean and Black Seas • To provide natural gas services to all Turkish provinces • **To save 8.4 billion U.S. dollars from energy costs**	• To increase domestic energy production • To increase the share of renewable energy in total energy production by at least 30 percent • To increase the share of NPPs in electricity generation by at least 10 percent according to the forecasts for 2023 • **To decrease the imports in the mining sector through enrichment and the reuse of mines for their raw or intermediary materials.**	• To improve the infrastructure of natural gas storage facilities, oil pipelines, FSRU and LNG • To restructure TEİAŞ, BOTAŞ, TPAO and ETİMADEN for their integration into the energy market • To increase functionality of the Energy Exchange Istanbul (EXIST) • To improve the mining sector through the cooperation of the public and private sectors

Our country is within strategies and targets set on the scope of the National Energy and Mining Policy: In this study, which was prepared based on the objectives of using energy efficiently, strengthening the mining market, saving energy costs, and contributing to the reduction of imports in the sector by enriching the mines in the country, An Ore Enrichment Plant in the mining sector, where enrichment is done by flotation method, is discussed. In this context; It is aimed to reduce energy dependency, increase energy efficiency, use energy resources more efficiently in the public, private sector, industry, residences, and process mines and resources with high yield.

It is called rock ore, which is composed of one or more minerals with economic value and can be found in the industry by enriching it directly or as a result of some processes. Ore constitutes the raw material of metal production [2]. The ores which are enriched are listed in Figure 1.

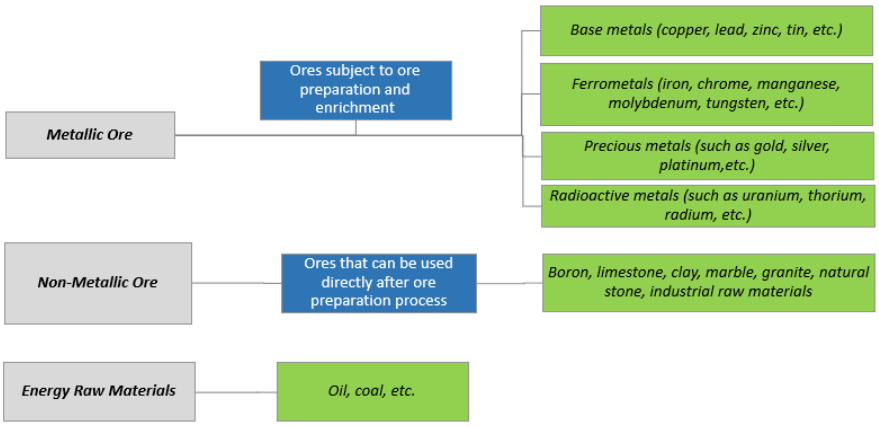

Figure 1. Ore Types and Energy Raw Materials.

Although raw ore [3] has an economic value as it is extracted, its value is further increased by the enrichment process. Ore enrichment facilities are designed according to the characteristics of the ore, and many methods are

available for enrichment [4].In this study, the flotation method, which is one of the enrichment processes based on the surface feature, seen in Table 2, is handled. A facility enriched with this method; consists of four main parts: Crushing, Screening, Grinding, Flotation, Dewatering. The general flow chart of mineral processing before enrichment is presented in Figure 2.

Table 2. Ore Enrichment Methods

Ore Enrichment Methods	Enrichment with Extraction	Manual Extraction
		Automatic (Optical)Sorting
	Enrichment by Classification by Size	Screens
		Hydrocylons
		Classifiers
	Enrichment with Gravite	Jigler
		Heavy Media Separators
		Spirals, Tables
		MGS,Falcon,Knelson
	Enrichment with Magnetic Separation	Low area Severe M.A.
		High area Severe M.A.
	Enrichment with Electrostatic Separation	Electrostatic Separator
		Tribostatic Separator
	Surface Enhancement	**Flotation**
		Agglomeration
		Floculation
		Amalgamization
	Chemical Enrichment	Leach
		Calcinulation
		Roasting
	Biological Enrichment	Microorganisms-With Bacteria

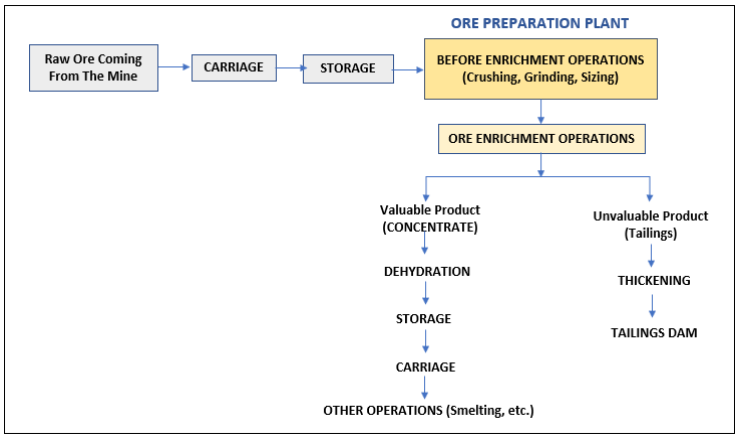

Figure 2. General Flow Chart of Mineral Processing Process.

1.1. Process Information

The first stage of mineral processing is the process of reducing the size of the raw ore and begins in the Crushing and Screening Unit. Raw ore is transferred from the stock area to the bunker and fed to the primary crusher via the vibrating feeder moving with the bunker. The ore, which is reduced in size in the primary crusher and sent to the vibrating screen via conveyor belts and sieved, is sent to the silo if it is suitable for the desired grain size. If the outside of the size range, it is sent to the secondary and tertiary crusher depending on the size range. In these crushers, the ores that come to the vibrating screen by being crushed are sieved again and this cycle continues as a closed circuit. The ore reduced to the desired grain size as a result of the crushing process is transferred to the silo. In the Crushing and Screening Unit, the process is operated by operators and can generally be summarized as above.

The ores with a reduced grain size that reach the silo are ground in the grinding unit to be released in a finer size (-0.2 +0.01 mm) and the milled ores are taken to the condenser tank for enrichment. The free mineral grains are processed here with various reagents, making the difference in surface properties between them clear. Thus, precious and valueless minerals are separated from each other by flotation based on their physicochemical property differences. [5-7].

The grinding unit is the unit with the highest energy requirement in ore enrichment plants. If the ore sizes coming to the grinding unit are larger than the desired size range; The ore cannot be ground by insufficient grinding and cannot give enough granular products and while more energy is used for grinding, in case of being small, it leads to low enrichment efficiency by grinding. For this reason, the production and efficiency of the size reduction process performed in the Crushing and Screening Unit will affect the efficiency of the Grinding unit and thus the efficiency of the flotation process.

In the ore enrichment plants, there is intense energy consumption in the process of the raw ore to the final product concentrate production. Due to today's competitive conditions and rising energy prices, an enterprise can use the energy consumed efficiently only by investing punctually and saving the technology as a result of the optimization and continuous control of the operating circumstances [8].

1.2. Adaptation of Failure Mode And Effects Analysis to Process

To sustain their existence, companies are carrying out quality improvement efforts to satisfy their customers and reduce their costs. One of the improvement studies in the literature is Failure Mode and Effect Analysis, FMEA. FMEA is a technique that systematically analyzes errors, producing both curative and preventive effects, thereby minimizing the cost of failures and increasing reliability. The purpose of FMEA is to ensure that appropriate measures are taken to identify potential errors related to the process during the planning and development phase, to determine, assess and prevent their importance. For this reason, FMEA has been one of the most accepted among the preventive quality assurance approaches that businesses have implemented to excel in competition [9]. In this context, Table 3 shows the first applications of FMEA.

Table 3. History of the FMEA

Application Date - Standard	Implementer	Applied Sector	Application Subject
9 November 1949, MIL - P - 1629	U.S Army	"Procedures for Performing a Failure Mode, Effects and Criticality Analysis"	Evaluation of system and equipment errors Errors are classified for personnel and equipment safety
Between 1960 – 1965	NASA	Aerospace Industry	Apollo Project (Moon travel programs)
Between 1970 - 1975, SMC 800-31	United States of America	Aircraft Industry	Today, the US armed forces are the military standard of MIL –STD 1629 A
1974, MIL-STD-1629	United States of America	Naval Forces	
Between 1972-1980	Ford Motor	Automotive Industry	Automobile design tool
1975	NEC (Nippon Electronic Company)	Electronic	Improving equipment reliability during the design of new systems
1988	Chrysler, Ford ve General Motors	Automotive Industry	Adopted as a general standard.

FMEA is a technique that became widespread recently. It has been used to prevent errors in various fields such as food, metal, marine vehicle manufacturing, software, nuclear designs, especially in the automotive sector [10-12].

As a result of the literature studies; It has been observed that the energy expenditure per unit production can be further reduced by carrying out the quality improvement efforts of the companies simultaneously with the activities aimed at increasing production and energy efficiency. As a result of reducing costs, their competitiveness will increase compared to their stakeholders in the sector.

When studies to increase production and energy efficiency begins, some situations may arise, such as the inability to access historical energy consumption data and to measure data. In this study, which was set out to solve these problems, make energy analysis in units, and estimate consumption, a risk analysis was made to determine energy consumption. Risk: an event from hazards is defined as a combination of the probability of occurrence and the degree of harm[13].

As a result of the literature studies, it has been found that the type of error and effects analysis method is suitable for the application of energy consumption risk analysis. For the application of the method, the Crushing Screening Unit, which is the first stage of the enrichment plant, was selected for the reasons described in section 2 process information section and it is aimed to reduce the kWh/ton value of the selected unit by optimizing the impact of direct and indirect operator-induced process failures on production and energy efficiency.

Today, four types of FMEA are used. The FMEA varieties focusing points and objectives are briefly described in Figure 3.

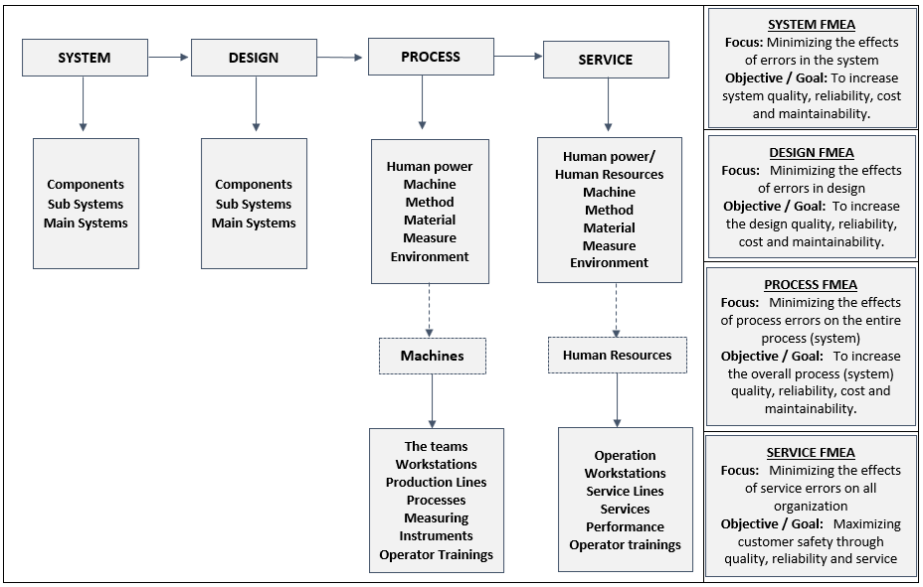

Figure 3. FMEA types[14].

Since there is no standard implementation process in Failure Mode and Effects Analysis, each enterprise has created and followed an implementation process according to its organizational structure and requests [14]. In this context, a standard was created for the unit under study, and Process FMEA, one of the FMEA varieties described in Figure 3, was applied.

At the stage of establishing this standard, current diagrams, breakdown, and production reports were examined from the existing data related to the unit, and since the energy consumption data required for energy optimization could not be reached, the "if there is no numerical data available" approach in Table 4 is followed.

Table 4. Selection criteria for methods to be used for evaluation in process FMEA [14]

If	Used	Selection
If statistical process control is applied in the process	Statistical data, reliability data, process capability, current distributions, mathematical models, simulation	Available data and / or process capability ratio (Cpk)
If the process is similar to other processes or historical data are available	Historical data and similar systems data, reliability data, process capability, current distributions, mathematical models, simulation	Current data and / or process capability ratio (Cpk)
If there is historical data on errors	Historical data, mathematical models, simulation, cumulative data and / or error rates based on reliability, design and real distributions	Current data and / or cumulative error numbers
If the process is new and / or there is no numerical data available	Team judgment	Subjective criteria, consensus on the team

By separating the process into sections, failures that could adversely affect production and energy efficiency were identified and FMEA steps in Figure 4 were applied. As a result of the process followed, the priorities of the failures were determined.

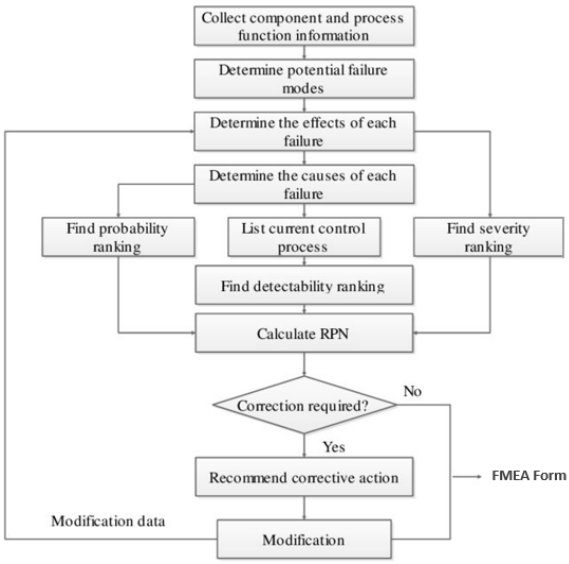

Figure 4. FMEA process [11].

1.2. Determination of Failures Priorities

In determining failure priorities: There are three auxiliary components: Emergence (E), Weight (W), Detection (D) [15]: Emergence of these components, frequency (probability) of error; The weight indicates the severity (impact) of the error; Detection shows the noticeability of the error before it reaches the next section. Controls to prevent or reduce the occurrence of error contribute to finding the degree of occurrence. The degree of emergence: can be reduced by measures such as plans, specifications, production methods, production flow methods, organization, changes in designs [14]. In the study, the analysis of the plant failure reports and production reports of the previous years helped to determine the type, effect, and causes of the errors.
There are many methods for determining the values of the above components. The usual method is the use of numerical scales (risk criteria table) [16]. Errors in the process sections are evaluated using a scale of 1-10 according to the risk criteria tables in Table 5.

Table 5. Risk criteria table[11]

RISK CRITERIA TABLE

Probability of Emergence	Rank	Probability of Failure (As working day)	Weight	Rank	Detection	Rank	Possibility to Detect (%)
Nearly impossible	1	<1:20.000	Nearly impossible	1	Extremely high	1	86-100
Low	2	1:20.000	Low	2		2	76-85
	3	1:10.000		3	Very high	3	66-75
Moderate	4	1:2.000	Moderate	4		4	56-65
	5	1:1.000		5		5	46-55
	6	1:200		6	Moderate	6	36-45
High	7	1:100	High	7		7	26-35
	8	1:20		8		8	16-25
Very high	9	1:10	Very high	9	Low	9	6-15
Extremely high	10	1:2	Extremely high	10	Nearly impossible	10	0-5

After determining the error degrees with risk criteria tables, risk priority numbers (RPN) are calculated.

1.3. Calculation of Risk Priority Number

In the calculation of RPN, two approaches, RPN = E x W x D with multiplication, and RPN = E + W + D with addition, can be mentioned. The commonly used approach in practice is to calculate RPN with multiplication

[16]. In this study, multiplication is used to calculate the risk priority number of errors. Decisions to take corrective action according to RPN values in FMEA applications are made according to the following criteria:
• If RPN <40, there is no need to take precautions.
• It is useful to take 40 ≤ RPN ≤ 100 measures.
• If RPN> 100, precautions must be taken.

In applications carried out in Renault, errors with RPN> 100 are those that carry the risk of corrective action. [9] Since values over 100 will carry the most risk, it gives the error to is handled first. One of the situations encountered with PRN in applications is that different errors have the same RPN value. If there are two or more errors with the same RPN value, the weight and then the high detection value should be considered first. The high weight error has priority because this value shows the effect of the error. Detection is more critical than its emergence value because what is involved here is that the error reaches the next section. Failures reaching the next section should be approached with more priority than frequent errors [14]. In the process for reducing the values of RPN: measures such as examining the job descriptions of the operators, reviewing the shift schemes and the reports on the shift they are responsible for, repeating vocational training, testing the level of knowledge and competence after production, and energy efficiency awareness studies, and predicting new risk priorities are calculated.

2. STUDIES

2.1. Application of Error Type and Effects Analysis to Process

In the studies in the literature, the risk priority number of errors in the process is calculated and new RPN values are revealed by optimizing the errors and each error has an improvement rate in itself. In the application study, the failures in the unit were divided into sections in the order of workflow and optimized after the measures described above were adapted to the process and the effect of the improvement rates of the failures in the sections on the system was found.

Within the scope of this study, risk analysis was performed to address the errors with RPN > 100, to determine the failure effects in situations without energy consumption data, and to predict the rate of improvement in production and energy efficiency. As a result of the risk analysis, it was aimed to reduce the errors with high RPN value by optimizing them with the measures taken, and to increase the production and energy efficiency by reducing the Crushing Screening Unit kWh / ton value.

2.2. Optimization of The Impact of Direct Operator-Induced Failures

In the first of the risk analysis conducted for this purpose: the effect of direct operator failures on production and energy efficiency has been examined and the risk priority numbers have been calculated based on Table 5 and presented in Table 6.

Table 6. Risk priority number of direct operator-induced failures

RISK PRIORITY NUMBER OF DIRECT OPERATOR INDUCED FAILURES				
Operator Related Failures	**Effect on Production and Energy Efficiency**			
	Emergence	Weight	Detection	RPN
Sleep	7	7	1	49
Nutrition	6	5	2	60
Lack of motivation	9	8	2	144
Age	3	2	7	42
Experience	9	7	1	63
Mission awareness	9	9	1	81
Shift order	7	10	1	70
Working in accordance with job description	9	9	2	162
Conscious and controlled use of machinery / equipment	9	10	2	180
Carrying out maintenance and checks at regular intervals	8	10	2	160
Keeping reports organized and attentive/Data logging	5	7	2	70
Information transfer to the next shift	7	7	2	98

Low Risk	**RPN** < 40	No need to take precautions
Moderate Risk	40 ≤ **RPN** ≤ 100	Precautions can be taken
High Risk	**RPN** > 100	Precautions must be taken

The risk analysis application is carried out by monitoring the approach if there is no quantitative data available in Table 4, based on the experience gained as a result of observing previous training for operators in different areas. By applying the measures to reduce the RPN values mentioned in the literature section, it has been demonstrated that the failures with high-risk priority numbers in Table 7 can optimize on average 25%. The effect of the improvement difference on the system is as seen in Figure 5.

Table 7. Number of risk priorities after optimization of direct operator-induced failures

EFFECT ON PRODUCTION AND ENERGY EFFICIENCY									
Operator Related Failures	BEFORE OPTIMIZATION				AFTER OPTIMIZATION				Difference
	Emergence	Weight	Detection	RPN	Emergence	Weight	Detection	RPN	
Lack of motivation	9	8	2	144	6	4	2	48	96
Working in accordance with job description	9	9	2	162	4	4	2	32	130
Conscious and controlled use of machinery / equipment	9	10	2	180	5	4	2	40	140
Carrying out maintenance and checks at regular intervals	8	10	2	160	5	5	2	50	110

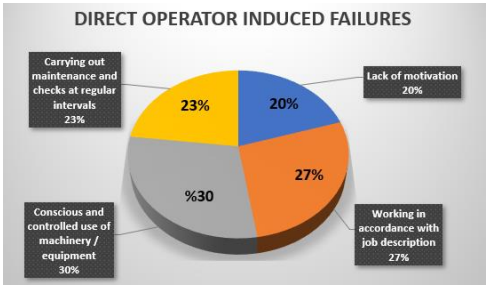

Figure 5. The impact of direct operator-induced failures on production and energy efficiency

2.3. Optimization of Operators' Impact on Machines

After optimizing the errors caused directly by the operator, risk analysis carries out to determine the effects of the operators on the machines on the production and energy efficiency.

In the second application within the study's scope: The risk priority numbers of the operators responsible for the operation of the process on the machines calculate. The leading equipment used by operators for this calculation; The bunker and feeder, primary crusher, secondary and tertiary crusher, vibrating screen, and others are discussed in five separate sections, respectively. By examining the unit fault records, the errors occurring within each section were determined by machine and operator. First of all, failures related to the bunker and the feeder section were determined and the risk priority numbers are presented in Table 8.

Table 8. Risk priority count of operator-induced failures in the bunker and feeder section

EFFECT ON PRODUCTION AND ENERGY EFFICIENCY								
BUNKER and FEEDER	Machine Related Failures				Operator Related Failures			
Failures	Emergence	Weight	Detection	RPN	Emergence	Weight	Detection	RPN
Bunker and sides wear	5	6	4	120	9	5	2	90
Blockage of the bunker	6	9	2	108	8	9	2	144
Vibrating feeder wear and clogging	5	7	3	105	6	7	3	126
Feeder grill opening	3	4	2	24	7	8	2	112
Speed drive / Frequency converter failure	2	10	1	20	10	9	1	90
Vibration motor malfunction (Vibromotor)	2	10	2	40	10	10	1	100
Belt change	5	5	1	25	6	6	2	72
Lubrication	5	4	4	80	6	5	3	90
Electrical fault / motor failure	2	10	1	20	4	8	2	64

Within the scope of the study, optimization of errors with high-risk priority numbers stated in Table 8 was followed by the approach, similar to the method described above, according to the approach if there is not

enough data in Table 4. It has been evaluated to consider the effects of operators on machines. The improvement difference is given in Table 9, and the percentages of the optimization envisaged in the section can be seen in Fig. 6.

Table 9. Number of risk priorities after optimization of operator-induced failures in the bunker and feeder section

EFFECT ON PRODUCTION AND ENERGY EFFICIENCY									
BUNKER and FEEDER	**BEFORE OPTIMIZATION**				**AFTER OPTIMIZATION**				**Difference**
Failures	Emergence	Weight	Detection	RPN	Emergence	Weight	Detection	RPN	
Blockage of the bunker	8	9	2	144	6	7	2	84	60
Vibrating feeder wear and clogging	6	7	3	126	4	6	3	72	54
Feeder grill opening	7	8	2	112	5	6	2	60	52

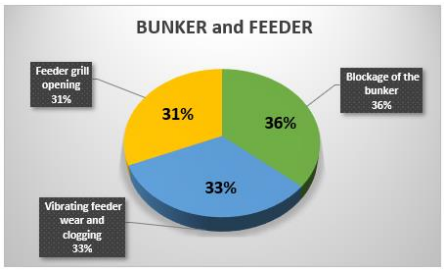

Figure 6. The impact of operator-induced failures in the bunker and the feeder section on production and energy efficiency

After the Bunker and Feeder section, risk priority numbers were calculated by applying similar operations for jaw(primary) crusher, secondary and tertiary crusher, and other departments respectively. The improvement rates predicted after optimization gives in Fig. 7, Fig. 8, Fig. 9, and Fig. 10.

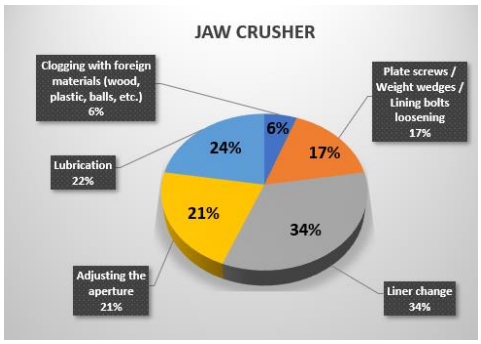

Figure 7. Jaw crusher section

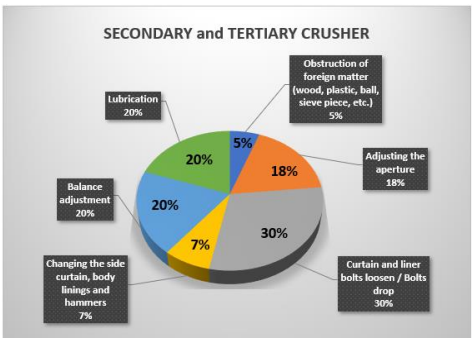

Figure 8. Secondary and tertiary section

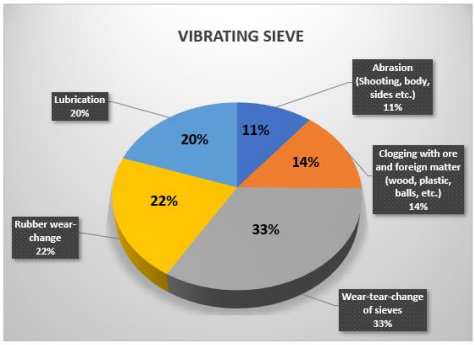

Figure 9. Vibrating sieve section

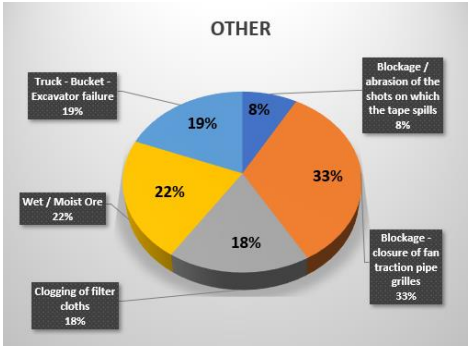

Figure 10. Other section

3. RESULTS AND DISCUSSION

When high-risk failures directly from the operator are examined, it is seen that the failures and their effects are related to each other. According to the optimization prediction, the improvement rate estimated to be an average of 25% in section 2.2 has affected both the probability, impact, noticeability RPN values of failures in this section and failures in section 2.3.

Due to the 20% improvement of the lack of motivation failure in Fig. 5, it is expected that the awareness and responsibility of operators in the work done by increasing the motivation to work will also increase. The operator, who is aware of the responsibility, will do his job labor of love and care and will be more willing to participate in in-house training. The operator, who fully fulfills his duties and responsibilities, will be more conscious in the use of machines and the operation of the unit and will regularly follow the maintenance and control periods. Therefore, it will be seen that the increase in the operator's work efficiency is reflected in production and energy efficiency.

When the impact of operators on machines was examined in Section 2.3, it was observed that this was directly related to operator-related failures and failures in section 2.3.

After optimizing the failures in Section 2.2, the operator who increases his work awareness, responsibility and attention will approach his work more sensitively and will be more experienced against the failures that may occur in the machines. With increased job tracking, they will be prepared in advance for any errors that may occur and early intervention can be made before growth. Thus, the time allocated to care will be used more effectively, as the necessary program for maintenance will be implemented in a timely period, and postures that may cause long-term postures will be avoided. In this way, the continuity of production will be ensured, the effect of errors, frequency, and differentiability of errors will decrease thanks to the routine maintenance and follow-up of the machines, and a good crusher operation and the RPN values will be reduced. Thereby, an increase in production and energy efficiency will be observed.

4. CONCLUSION

When the projected improvement rates of failures affecting production and energy efficiency are evaluated,

- In the first application; In Fig. 5 1, it is seen that the effect of direct operator related errors on production and energy efficiency is 25% on average.
- In the second application; According to the data obtained in Fig.6, Fig.7, Fig.8, Fig.9, and Fig.10, the effect of the operator on the sections can be improved by an average of 33% in the bunker and feeder section, in the jaw (primary) crusher, vibrating screen and other sections can 20%, secondary and In the tertiary crusher part, it was concluded that an average of 16% can be optimized.
- By turning the production and energy efficiency of processes and operators into a focal point, the kWh/ton value spent on the size reduction process will be reduced, while the machine's downtime due to failures will be reduced and unit efficiency will be increased. The efficiency increase in the relevant unit will also increase the efficiency of the subsequent units.
- As a result of the projected, applications can be made at the plant by taking measures to reduce the RPN values and the actual recovery rates can be compared. Thus, if there are missing points in the way of improving failures, measures are determined and reviewed. After improving operator related errors, machine-related failures can be examined and maintenance work and frequency can be reprogrammed.
- The potential percentage to be optimized by applying total quality management techniques by plant conditions and availability can be further increased.
- With the establishment of the ISO 50001, Energy Management System at the plant increased energy awareness of operators and increased productivity in production can be examined. Also, this system can be studied simultaneously with Quality Management Systems.

REFERENCES

[1] Karagöl, E., Kavaz, İ. & Özdemir B., National Energy and Mining Policy Of Turkey, *SETA*, No:35,**10**, July 2017.

[2] Erdemir F., Karadeniz Teknik Üniversitesi Mühendislik Fakültesi, Metalürji ve Malzeme Mühendisliği Bölümü, *Laboratuvar Föyü Cevher Hazırlama Deneyi*, 2016.

[3] Eti Maden, Maden Terimleri Sözlüğü.

[4] Hacıfazlıoğlu, H., *Cevher Zenginleştirme Yöntemlerine Giriş*, Bölüm 1, 2016-2017.

[5] Bentli, İ., Flotasyon ve Flotasyon Makineleri, Dumlupınar Üniversitesi Fen Bilimleri Enstitüsü Dergisi, **98**, Sayı 002, 97-110, 2001.

[6] Aytekin, Y., Yamık, A. & İpekoğlu, Ü., Cevher Hazırlama ve Zenginleştirmedeki Gelişmeler, *Akdeniz Üniversitesi İsparta Müh. Fak. Dergisi*, Maden Müh. Seksiyonu, S: 1, 1-13,1988.

[7] Wills. B.A., *Mineral Processing Technology 4th edition Pergamon Press*, New York, 584 p.,1988.

[8] Akbaş,B., Kaya D., Eyidoğan, M., Bir Otomobil Montaj Fabrikasının Enerji Tüketim Analizi ve Enerji Tasarrufu Potansiyelinin Değerlendirilmesi, *Mühendis ve Makina Dergisi*, **86**, cilt 59, sayı 691, 85-100, 2018.

[9] Sönmez, Y., Unğan, M., Hata Türü Etkileri Analizi ve Otomotiv Parçaları Üretiminde Bir Uygulama, *İşletme Bilimi Dergisi*, **5**(2): 217-245, 2017.

[10**]** Scipioni, A., Saccarola, G., Centazzo, A., & Arena F., FMEA Methodology Design, Implementation and Integration with HACCP System in a Food Company", *Food Control*, 13: 495–501, 2002.

[11] Pillay, A., Wang, J., Modified Failure Mode and Effects Analysis Using Approximate Reasoning, *Reliability Engineering and System Safety*, **79**: 69–85, 2003.

[12] Zalewski, J., Ehrenberger, W., Saglietti, F., Górski, J., Kornecki, A., "Safety of computer control systems: challenges and results in software development", *Annual Reviews in Control*, **27**: 23–37, 2003.

[13] TSE İş Sağlığı ve Güvenliğin Yönetim Sistemi Tetkikçi/Baş Tetkikçi Eğitim Notları, *Türk Standartları Enstitüsü*, 12-28, 2004.

[14] Stamatis, D. H., Failure mode and effects analysis – FMEA from theory to execution, *ASQC Quality Press*, Wisconsin, 28-34, 2003.

[15] Soysal, A., FMEA Seminer Notları, İstanbul, 7-27, 2002.

[16] Yılmaz, A. Hata türü ve Etki Analizi, Yüksek Lisans Tezi, *İTÜ Fen Bilimleri Enstitüsü*, İstanbul, 1-60 1997.

LEAD ACID BATTERIES FOR MICRO HYBRID ELECTRICAL VEHICLES – INFLUENCE OF DIFFERENT TYPE EXPANDERS ON THE PERFORMANCE OF THE NEGATIVE PLATES

Yakup ŞİRİN, Yıldırım EYDEMİR, Çağatay AYHAN, Enes DEMİRYÜREK, Emre KOÇ
Abdulkadir Özcan Otomotiv Lastik Sanayi ve Ticaret Anonim Şirketi, R&D Center, Cankırı, Turkey.
Email: yakup.sirin@akoaku.com

ABSTRACT

Battery performance of the start-stop vehicles whose production rate increasingly go on, which affects the CO_2 emission and fuel consumption directly. Lead batteries are used in start-stop and hybrid automotive applications to provide CO_2 savings and economic benefits to our society. During recharge process, however, a start-stop function is commonly compromised by low DCA and the formation of lead sulfate morphologies that inhibit proper dissolution and regeneration of the active material. The object of this study is to increase the profits of fuel consumption and CO_2 emission by maintaining the effectiveness of the battery performance in a lifetime. The innovative product manufactured by working on the start-stop feature of the battery will come into play in the developing technology and add value to our country by supplying it to the international automotive industry.
This study is aimed to increase the electrical performance of enhanced flooded batteries (EFB) by improving chemical properties and changing chemical composition (wt. %) of the negative electrodes. For that purpose, different types (EFB-1-2-3-4-5) of expanders were used as an additive in the negative paste. This study consists of three steps. In the first step, different types of EFB expander additives were characterized. In the second step, negative active materials (NAM) were prepared. In the last step, enhanced flooded batteries (12V 60Ah 520EN) were manufactured, and electrical performance tests were carried out in accordance with Turkish Standards Institute (TSI) 50342-1 and 50342-6 standards. The electrical test results of the experiments that include different types of additives were compared with a standard Ako company enhanced flooded batteries (EFB). Herewith, with the use of the EFB-1 in lead-acid battery, some properties have considerably enhanced, which are capacity, cold cranking ampere, internal resistance, charge acceptance, and life-cycle performance.

Keywords: Enhanced flooded battery (EFB), expander, negative active material (NAM).

1. INTRODUCTION

1.1. History of Lead Acid Battery

The battery is a chemical energy storage that converts chemical energy to electrical energy. The primary task in vehicles is to run the starter that gives the engine the first movement. Besides, in a state of problems with the charger, the air conditioner, heater, radio, a headlight is needed to operate such systems [1]. The main elements of the lead-acid battery were found place approximately over 100 years ago. Gaston Plante was the first to submit that a beneficial discharge current could be withdrawn from a double of lead plates (positive-negative plate) that had been submerged in sulfuric acid and subjected to a charging current [2].Lead-acid batteries form the basis of rechargeable battery systems. Lead-acid batteries' reliability, low cost, and life span for many years despite the developing technology of new battery systems are still the most preferred battery in the world as the most widely used system. On the other hand, the use of lead-acid batteries was limited to their very low capacity. In the late 1870s, there was an excessive need of new technologies for lead-acid production [3]. In 1881, Camille Fauré (1881) added red lead (II) oxide (Pb_3O_4) to the battery paste, water, and sulfuric acid within the lead positive plates. The positive paste was converted to active material with charging to form PbO_2 and Pb, so the specific energy of the lead-acid batteries was raised [3]. In 1882, Gladstone et al. brought into the open the reactions that occurred at the two electrodes during battery performance and reported double sulfate theory [4].

In 1883, Hermann Aron explored the charge and the discharge period of lead-acid batteries. At the same time, Aron also indicated a correlation between the discharge time and specific density of H_2SO_4 electrolyte [3].

1.2. Lead Acid Battery Components

Lead–acid battery composed of negative/positive electrodes, separators, connections, terminals, polypropylene case and lids, and sulfuric acid solution as an electrolyte. These compound types are shown in Figure 1.

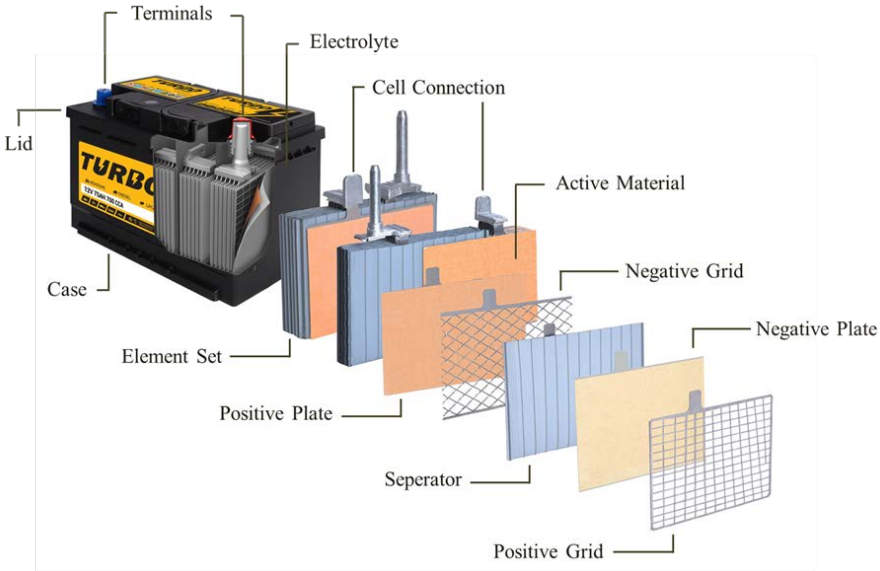

Figure 1. Standard lead-acid battery

The functions of the four basic components in the lead-acid battery;

1- The active material: It is a chemical mixture that is pasting on the grid's surface and transforms the grid into a plate. Namely, the negative and positive active materials are applied to the surface of the grids to form positive and negative electrodes in the battery.

2- Negative electrode: Before charging process, the negative electrode consists of metallic lead (Pb), lead oxide (PbO), and additives (carbon black, barium sulfate, lignin derivative, etc.) in the lead-acid battery. With the charging process, the negative electrode ingredients transform to metallic lead (Pb) and lead sulfate ($PbSO_4$) in the lead-acid battery.

3- Positive electrode: Before charging process, the positive electrode includes metallic lead (Pb), lead oxide (PbO) and red lead (II) oxide (Pb_3O_4) in the lead-acid battery. During charging process, the positive electrode constituents convert into the lead dioxide (PbO_2) in the lead-acid battery.

4- The electrolyte: Distilled water and sulfuric acid solution are mixed, which occurs electrolyte in the lead-acid battery. Sulfuric acid provides ionic charge transfer between the positive and negative electrodes.

1.3. Lead-Acid Battery Production Process

Lead-acid battery production is composed of many different processes, which are oxide manufacturing, strip/grid manufacturing, paste mixing, pasting, curing, assembly, formation, laboratory, and test processes [5].

1.4. Reaction of Lead Acid Battery

The charge and discharge reactions of lead-acid batteries for the positive and negative electrode respectively are as follow;

E_0 is the normal electrode potential for lead acid battery electrodes while the electrode is in a normal state.

$$\text{Positive Electrode;}\quad PbO_2 + 3H^+ + HSO_4^- + 2e^- \underset{\text{charge}}{\overset{\text{discharge}}{\rightleftharpoons}} PbSO_4 + 2H_2O \quad (E^0_{(+)}=+1{,}740\ \text{V})$$

$$\text{Negative Electrode;}\quad Pb + HSO_4^- \underset{\text{charge}}{\overset{\text{discharge}}{\rightleftharpoons}} PbSO_4 + H^+ + 2e^- \quad (E^0_{(+)}=-0{,}270\ \text{V})$$

$$\text{Total Reaction;}\quad PbO_2 + Pb + 2H^+ + HSO_4^- \underset{\text{charge}}{\overset{\text{discharge}}{\rightleftharpoons}} 2PbSO_4 + 2H_2O \quad (E^0_{(+)}=+2{,}010\ \text{V})$$

1.5. New Model Enhanced Flooded Lead Acid Batteries (EFB)

Vehicle emission legislations have been forcing the automotive industry universal to reduce its carbon emission [6]. Friendly to the earth, plug-in hybrid and fully electric vehicles enhance their popularity, so their sales volume is increasing, but due to nominal sales numbers, their impact on fleet emission degradation is limited. Fuel-efficient micro-hybrid vehicle sales are increasing too. According to market researches, total micro-hybrid vehicle sales will increase from 9 million in 2013 to 55 million in 2022 [7]. Standard lead-acid batteries are till now peerless for micro-hybrid vehicles as well as traditional vehicles due to their robust and safe design, low-cost raw materials, laborless and cost-optimized producing process, and already founded powerful recycling processes. Lead-acid battery engineered for a micro-hybrid vehicle should have add missions over a standard lead-acid battery engineered only for starting, lightening, and ignition (SLI) applications. A micro-hybrid vehicle battery must supply energy when the engine is in a neutral position. It can be charged at high current rates during brake energy regeneration and it also helps to increase acceleration of the engine through a generator.To achieve these new functions, some inventional developments have been adapted to lead-acid batteries. Newly, improved carbon additives have been applied to (NAM) negative active materials to increase the micro-cyclic and dynamic charge acceptance. Negative-positive grids have been designed to minimize voltage loss at high current rates without increasing the grid weight. High pore and low sinuous separators with low internal resistances have been-used in lead acid batteries to enhance their electrical performance, such as increased cyclic endurance and higher dynamic charge acceptance. These new type lead-acid batteries are named as EFB (enhanced flooded batteries). EFB can last much longer than that of common flooded lead-acid batteries (SLI) under the high electrical stress of micro-hybrid vehicles. In contrast to traditional vehicles, micro-hybrid vehicles use lead-acid batteries in a partial state of charge (SOC) to capture energy during regenerative braking [7]. In this study, the effects of EFB expander used in the negative active material on the battery performance were investigated. Thus, negative electrodes with five different brands of EFB expanders were used in lead-acid batteries (12 V 60 Ah 520 CCA (EN)) which were fabricated.

2. MATERIALS AND METHODS

2.1. Lead-Acid Battery Negative Active Material (NAM) Component

Lead (II) oxide and sulfuric acid as main materials, expanders (carbon black+lignosulfonate+barium sulfate), and also fiberglass as an additive were used in this study.

2.2. Plate Preparation and Battery Design (EFB Expander Materials Added to NAM)

The pre-prepared EFB additives have the similar active surface area and different particle size range from several microns. EFB-free negative active material was used for comparison.

2.3. Negative Paste Preparation and Characterization

Experimental groups of EFB additives doped to negative pastes are shown in Table 1. Paste without EFB was also prepared and used for assembling reference plates. The paste was made by mixing all chemicals for all studies. All the plates were cured and dried at 55-85 ˚C for 24 h. Before formation process, the samples of NAM and HRPSoC cycling were characterized by Brunauer–Emmett–Teller (BET) Surface Analyzer.

Table 1. Experimental groups of EFB expander additives to the negative plate

Signature	Composition	Concentration in NAM (wt.%)
EFB-1	EFB-1 brand expander	0,2
EFB-2	EFB-2 brand expander	0,2
EFB-3	EFB-3 brand expander	0,2
EFB-4	AKO-1 company expander	0,1
EFB-5	AKO-2 company expander	0,1

2.4. Lead-Acid Battery Design and Production

The influence of EFB expander additives on the performance of negative lead-acid battery plate was investigated in 12V 60 Ah 520 CCA (EN) lead-acid batteries.

2.5. Charging of the Produced Batteries

There is no difference between batteries except the EFB expander type in the paste of the negative plate. All the main differences are with respect to the EFB expander used in different brands.
In this study, batteries contain six positive and seven negative plates in each cell. This battery has 60 AH and 520 CCA (EN) features as standard. Batteries were charged with a constant current in the charging pools in the laboratory. The pool temperature is fixed at 35˚C.

2.6. After Charging: Open Circuit Voltage (OCV)/ Cold Cranking Ampere (CCA) Specification

OCV and CCA of the batteries were tested with the Midtronics device, which is accepted as the norm for all battery companies at the end of charging. OCV refers to the total voltage of the six cells of the battery value that should be 12,72 V and above after two hours. CCA value shows the battery's cold-cranking ampere. After two hours, 520 A and above are suitable. (EN: European Norm)

2.7. Capacity Test

The capacity (C_n) is 20 h capacity (C20-Ah) defined for the temperature of 25°C ± 2°C. Capacity test was implemented according to TS EN 50342-1.

The battery must be discharged with the current, which is kept constant at ± 1% of the rated value, until the voltage between the terminals drops to 10,50 V ± 0,05 V. This discharge time, t (h), should be recorded. The beginning of the discharge should be within the period of 1 hour to 5 hours from the end of the charge. The nominal 20 h capacity C_n is the electric charge (in Ah) that a battery can supply with a current: $I_n = C_n$ /20 h
C_e = t x I_n (Ah)

2.8. Cranking Performance Test

The cranking performance test was carried out according to TS EN 50342-1. The battery temperature should be brought to -18˚C ± 1˚C. The battery must be discharged with I_{cc} current. After 10 s discharge, the voltage U_f between the terminals should be recorded, and the current cut off. The Uf voltage should not be less than 7.50 V. The battery should then be discharged with a current of 0,6 I_{cc}. Discharge should be terminated when the battery voltage reaches 6V. Discharge time (t'_{6V}) up to 6V at 0,6 I_{cc} should be recorded in seconds.

2.9. Charge Acceptance Test

The battery should be discharged at a temperature of 25 °C ± 2 °C at a current I_0 (A) for 5 h where:

$I_0 = C_e/10h$

The value C_e should be taken as the maximum value C_e of the previous discharges. Within 10 min after the discharge, the battery should be placed in a cooling chamber with (forced) air circulation at a temperature of 0 °C ± 1 °C until the temperature of the middle cells is 0 °C ± 1 °C. It is generally accepted that the required temperature will be achieved after a minimum period of 15 h in the cooling chamber. At this temperature, the battery should be charged at a constant voltage of 14,40 V ± 0,05 V and I_{max} = 50 A for batteries having sizes defined in EN 50342-2 and I_{max} = 100 A for batteries having sizes defined in EN 50342-4. After 10 min, the charging current I_{ca} should be recorded. Requirements: $I_{ca} \geq 2\ I_0$

2.10. Micro-Cycle Test

According to TS EN 50342-6 standard, the batteries were taken to rest for 48 hours after being discharged for 3 hours at 25 ˚C + 2 ˚C in the first step with nominal discharge current (In). In the second step, the micro-cycle test was started. According to:

1. Take a rest for 10 seconds in standby mode
2. Charging 14V, 100A during $1+t_{DCH}$ (s)
3. Discharging 48A during t_{DCH} (s)
4. Discharging with high ampere during 1 sec.
5. Repeat the first 4 steps 100 times.
6. Take a rest for 12 hours in standby mode
7. Repeat the first 6 steps 80 times.

Thereby, 8000 cycles are completed.

3. RESULTS

3.1. EFB Expander Materials Specification

The pre-prepared EFB expander additives have the similar active surface area and different particle size range from several microns. EFB expander-free negative active material was used for comparison. The characteristics of EFB expander additives are shown in Table 2.

Table 2. Characteristics of EFB expander additives under investigation.

Characteristic	**Value**	**EFB-1**	**EFB-2**	**EFB-3**	**EFB-4**	**EFB-5**
BET Surface	m^2/g	250,45	180,36	32,41	26,45	24,83
Barium Sulphate	X kg	4X	6X	6X	6X	4X
Vanisperse	X kg	2X	2X	2X	2X	3X
Expanded Graphite	X kg	4X	2X	-	-	-
Carbon Black	X kg	-	-	2X	2X	3X
Ash	%	44,85	66,12	65,84	58,68	52,84
Iron (Fe)	ppm	0,003	0,004	0,003	0,006	0,008
Nickel (Ni)	ppm	0,005	0,005	0,006	0,008	0,004
Copper (Cu)	ppm	0,018	0,022	0,025	0,034	0,042
Manganese (Mn)	ppm	0,003	0,001	0,002	0,004	0,004

3.2. Charging Features

The current, voltage ampere-hour, and temperature graphs of the test batteries during the charging are as follows.

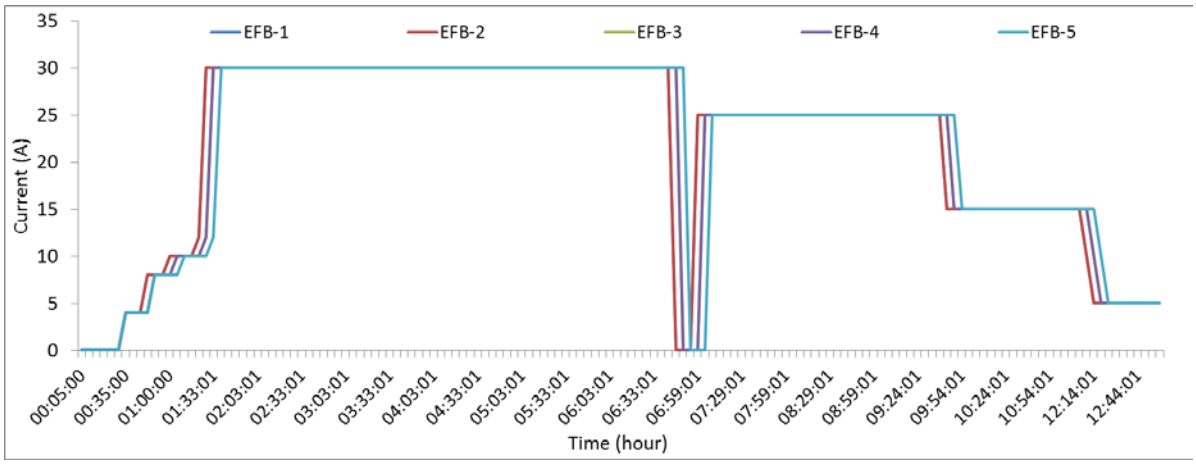

Figure 3. The current of the batteries during charging

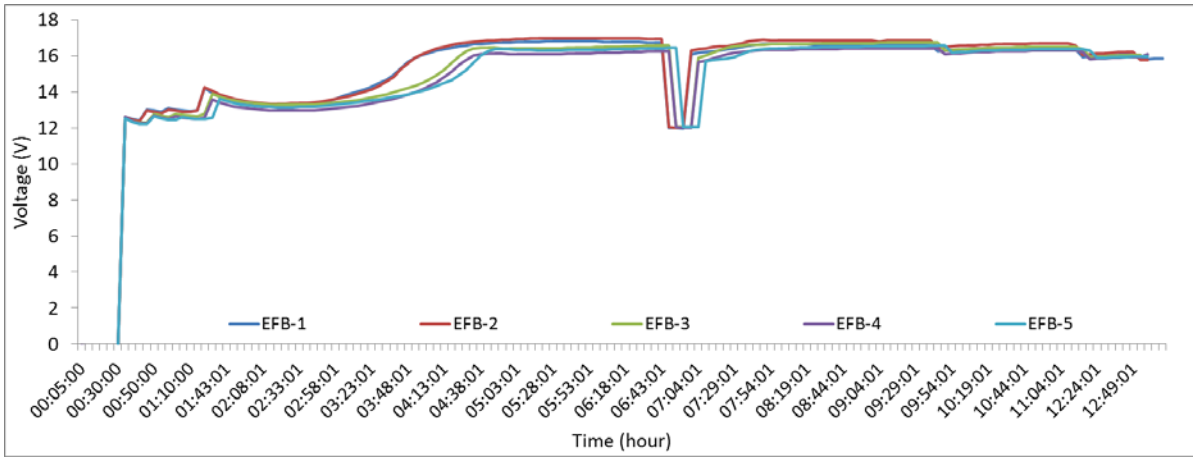

Figure 4. Voltage changes of the batteries during charging

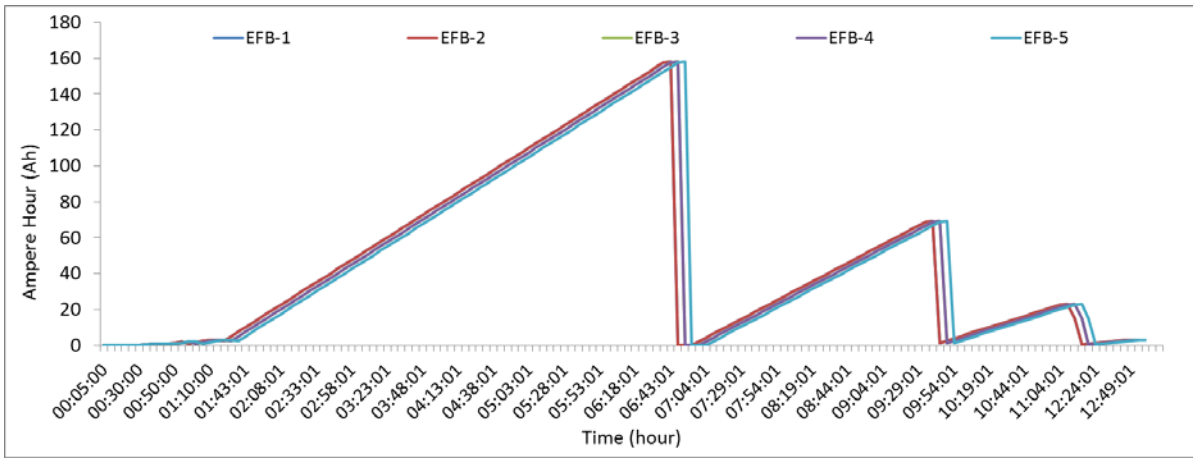

Figure 5. Total ampere-hours are given to the batteries during charging.

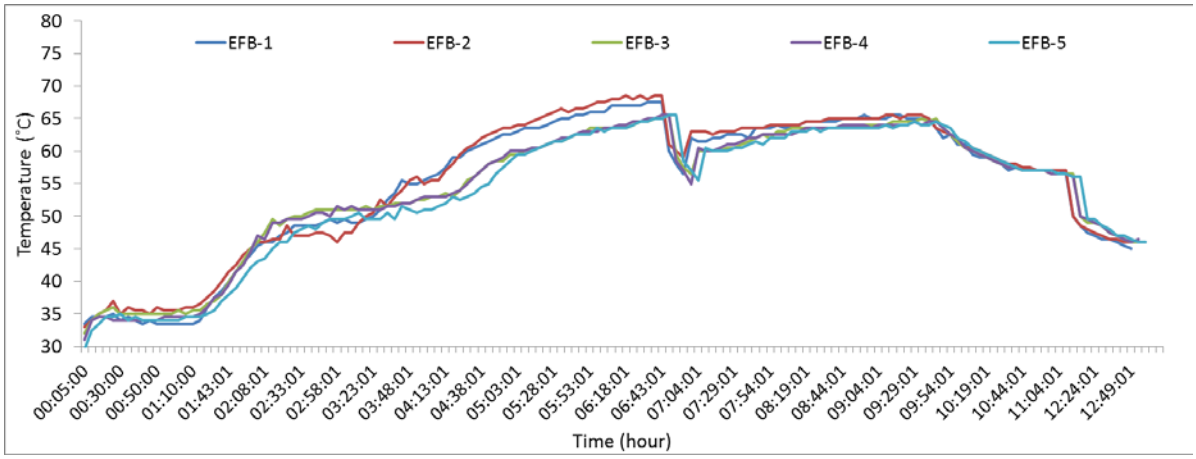

Figure 6. The internal temperature of the batteries while charging.

3.3. After Charging OCV and CCA Results

Electrical performance results (OCV, CCA) are given in Figure 7 and Figure 8, respectively.

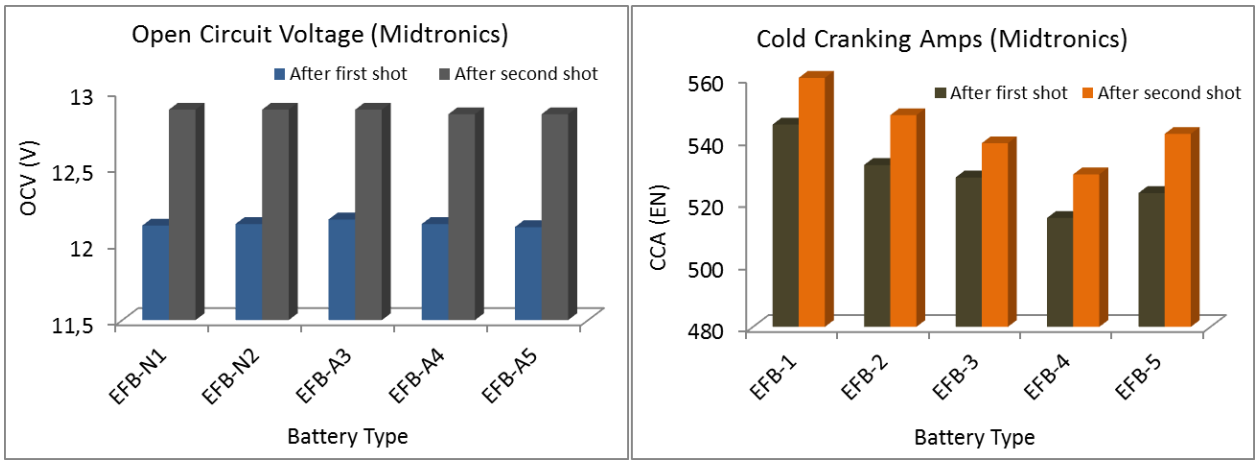

Figure 7. OCV and CCA graphic after charging.

3.4 Internal Resistance Test

Electrical performances results as an internal resistance of the batteries are shown in Figure 9.

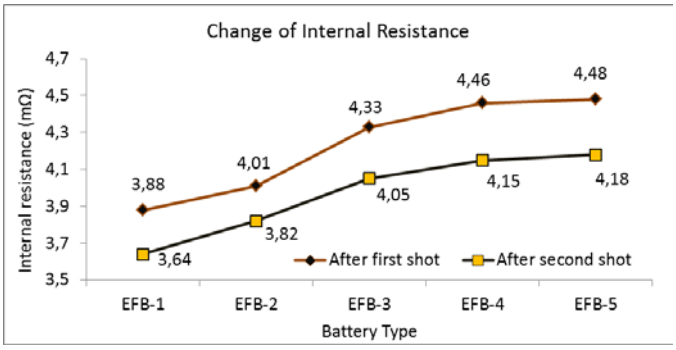

Figure 9. Internal resistance graphic after charging.

3.5. Capacity Test

Electrical performance result as a capacity of the batteries are given in Figure 10.

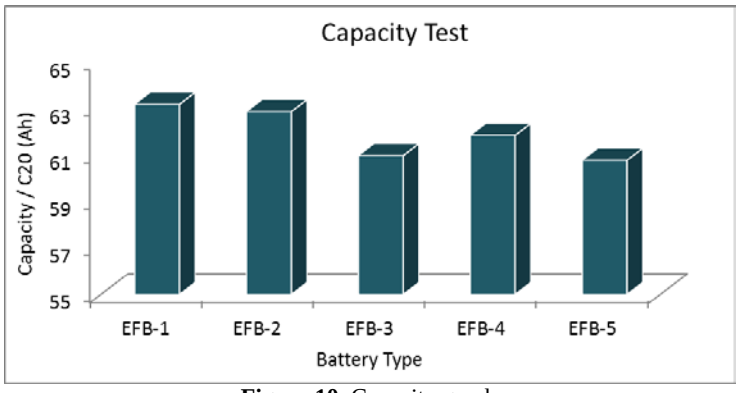

Figure 10. Capacity graph

3.6. Cranking Performance Test

Performance test results are given in Table 3.

Table 3. Cold-cranking ampere results

EFB Type	Current draw	U_f	After U_f voltage ≥ 7,5	t'_{6v}≥90s
EFB-1	520	10,4	7,77	124
EFB-2	520	10,4	7,72	122
EFB-3	520	10,1	7,72	123
EFB-4	520	10,3	7,70	123
EFB-5	520	10,4	7,74	120

3.7. Charge Acceptance Test

Charge acceptance test results of lead-acid batteries are shown in Figure 11.

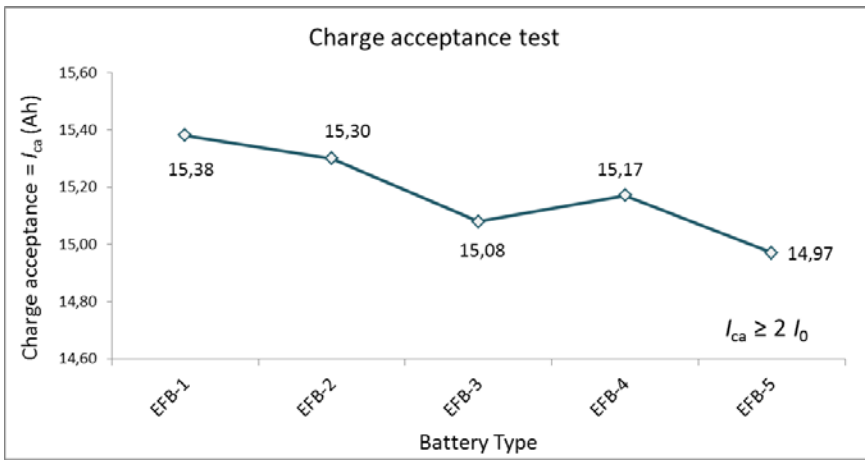

Figure 11. Charge acceptance test graph

3.8. Micro-Cycle Test

Cycle test result of lead-acid batteries are demonstrated in Figure 12.

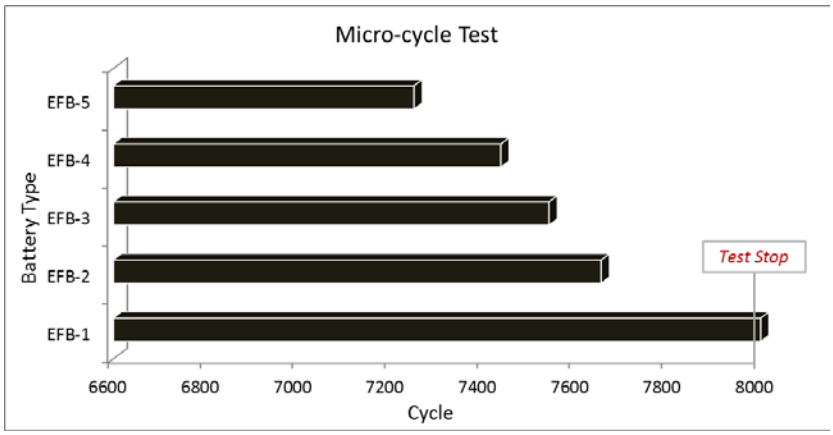

Figure 12. Micro-cycle test graph

4. RESULTS

As a result of this study, the EFB-1 battery achieved 30 units increase in CCA (A). Batteries containing EFB-1 increased 5% in capacity (Ah). Besides, batteries containing EFB-1 increased 38% in the cranking performance test. Also, batteries that contain the EFB-1 increased 25% in the charge acceptance test. Finally, battery cycle life is increased by 15% with the EFB-1 additive. Future research will be conducted in order to develop the electrical properties of batteries by using EFB expanders in more different types and proportions (wt. %) in paste recipe of negative active material.

ACKNOWLEDGEMENTS

We acknowledge to Abdulkadir Özcan Otomotiv A.Ş. board of directors for their financial and moral support.

REFERENCES

[1] Boden, D.P., Improved oxides for production of lead/acid battery plates, *Journal of power sources*, **73**(1), 56-59, 1998.

[2] Planté, G., Nouvelle pile secondaire d'une grande puissance, *Mallet-Bachelier, Comptes rendus de l'Académie des Sciences*, **50**(1), 640-642, 1860.

[3] Pavlov, D., Lead-acid batteries: science and technology, *Elsevier*, pp. 11-12, 2011.

[4] Gladstone, J. H., Tribe, A., The chemistry of the Plante and Faure accumulators, *Nature*, **25**, 221-223, 1882.

[5] Eydemir, Y., Strengthened battery design for start-stop vehicles, *Gazi University, Energy Systems Engineering, Ankara*, pp. 12-28, 2019.

[6] Albers, J., Meissner, E., & Shirazi, S., Lead-acid batteries in micro-hybrid vehicles, *Journal of Power Sources*, **196**(8), 3993-4002, 2011.

[7] Aksakal, C., & Sisman, A., On the compatibility of electric equivalent circuit models for enhanced flooded lead-acid batteries based on electrochemical impedance spectroscopy, *Energies*, **11**(1), 118, 2018.

EFFECT OF COLLECTION TANK LEVEL ON ENERGY CONSUMPTION OF LIFTING PUMPS IN DRINKING WATER DISTRIBUTION SYSTEMS

Ufuk SEKMEN*, Mehmet YILMAZ, Özgür ÖZDEMİR*, Ahmet İNCE***
*KASKİ General Directorate, Head of District Services, Kayseri/Turkey
Email: ufuks@kaski.gov.tr
**İnonu University, Department of Mechanical Engineering, Malatya/Turkey
Email: m.yilmaz@inonu.edu.tr
*KASKİ General Directorate, General Manager, Kayseri/Turkey
Email: ozgurozdemir@kaski.gov.tr
*KASKİ General Directorate, SCADA&Optimization Branch Manager, Kayseri/Turkey
Email: ahmeti@kaski.gov.tr

ABSTRACT

Submersible pumps and lifting pumps are among the indispensable elements of drinking water supply systems. The operational costs as well as the investment costs of this mechanical equipment, are of essential importance for the operating institutions. Most of the energy consumption costs, which have an essential place in the expenditure budgets of the water and sewerage administrations, arise from the pumps in the system. Therefore, the efficiency of this system's elements has a significant role in terms of energy costs for the water and sewage administrations responsible for supplying drinking water to the public in our country. Today, dependence on energy and increasing energy consumption necessitate measures to reduce costs on energy. Lifting pumps are pumps that pump water from a mid-level collection tank, where water is drawn from the wells by submersible pumps, to an upper feed tank. This study aimed to investigate the effect of collection tank level on the energy consumption of lifting pumps in drinking water distribution systems. For this purpose, an experimental setup consisting of a borehole, a collection tank, a lifting pump and a distribution tank was established in an independent laboratory in Kayseri. A SCADA system was integrated into the experimental system to monitor and evaluate energy consumption. The results showed that the pump efficiency increased with the tank level, thus reducing energy consumption.

Keywords: Drinking water supply, Lifting pump, Specific energy, Specific cost.

1. INTRODUCTION

Water will be a strategic resource in the future due to increasing threats, and that excessive water use and high loss rates have social, economic, cultural and political reasons, and the cost of water from the source to the tap should be an essential issue be addressed. The purpose of drinking water supply and distribution systems is to provide a population with water of satisfactory quality and sufficient quantity. The system consists of water intake structures, transmission lines, tanks, main pipes, primary and secondary distribution pipes, pressure boosting pumps, valves, fire hydrants, pressure breaker, stabilizer valves and subscriber connections [1].

Energy costs comprise the major component of the operating costs of water supply systems (WSS). The most considerable quantity of energy is usually consumed by water pumping stations. The overall operating cost associated with a particular pump station is dependent upon the following factors: the pumps, the distribution system, the pump drivers, and the governing energy rate schedule [2]. Water companies/administrations use a variety of water treatment and transport processes, which are high electricity consuming. It is estimated that means of water distribution absorb from 3% to 7% of electricity, worldwide [3-5]. According to Watergy [6], approximately 2% to 3% of the worldwide electricity consumption is used for pumping in WSS, while 80%–90% of this consumption is absorbed by motor-pump sets [7]. Copeland and Carter [8] states that 67% of energy consumption in WSS comes from tap water pumping, 14% from water treatment, 11% from raw water pumping, and 8% from in-plant water pumping (e.g. backwash water of filters). Accoding to Vilanova and Balestieri [3],

80-90% of electricity consumption, due to water distribution, comes from the running of pumping stations. The researchers mentioned here and many other researchers point out that pumping stations make a significant contribution to electricity consumption. Therefore, any efficiency improvement in the relevant processes is very important [5].

There are several methods that have a positive effect on on the reduction of energy consumption in WSS [4-21]. Coelho and Andrade-Campos [4] provides several strategies to improve the energy efficiency of the WSS. According to Zimoch and Bartkiewicz [5] the main improvements in energy efficiency can be achieved with: (a) implementation of control and monitoring systems SCADA (Supervisory Control and Data Acquisition), (b) installing higher efficiency pumps motors and drives, (c) generating energy in WSS using alternative energy sources. Feldman [10] states that the significant improvements in energy efficiency can be achieved using the following methods: (a) improvement of pumping stations and system design; (b) VSDs installations; (c) efficient operation of pumps; and (d) minimizing of water losses through pressure control. According to Luna et al. [11], in order to improve the efficiency of the water supply system operation, two optimization approaches are generally considered, namely optimization of the water levels in the storage tanks and optimization of the scheduling of the pumping operations. Both approaches may be relatively successful depending on the case study.

A slight increase in efficiency caused by pumping optimization may cause significant savings in electric energy and expenses [22]. Sarbu [7] presented several comparative studies of energy efficiency in water distribution systems considering distinct configurations of the networks and also considered implementing of the variable-speed pumps. The improving energy efficiency of water pumping is briefly reviewed by presenting a representative real case study. Four strategies are described to improve the energy efficiency of water pumping: using control systems to vary pump speed drive according to water demand, pumping to storage tanks, using intermediary pumping stations integrated into the network, and using elevated storage tanks floating on the system. He concluded that it is possible to achieve significant savings in operating costs. According to Grundfos, one of the world's largest pump manufacturers, for two-thirds of the currently operated pumps, energy savings of up to 60% are possible [23]. Nowak et al. [24] presented an optimization process and an extended decision support process for the design and operation of water supply systems, emphasizing the use of variable speed pumps. It was applied to a model of the water supply system at Worms, Germany. Different scenarios were compared using an optimization process that predicted energy savings of up to 18% annually. Georgescu and Georgescu [25] used a Honey Bees Mating Optimization Algorithm to optimize pump schedules for four pumping stations, three tanks and a constant level water source using a simplified model of the piping network. Case studies indicated that pumping energy savings vary widely depending on the circumstances, but overall savings of between 5 and 30% of current energy demand appeared achievable [26]. The more considerable savings will be mainly due to improving maintenance and closer matching of pumps to their duties. Energy efficiency gains from new pumping technology will probably be less than 5% since the technology is generally mature. However, more significant improvements should be feasible in submersible and borehole pumps where hydraulic and electrical configurations are more complex. The case studies and examples tend to focus on these two areas, but there is a broad range of activities worldwide, from leakage reduction to renewable energy [26]. Luna et al. [11] developed a hybrid genetic algorithm to optimize the pumping scheduling of a water supply network aiming to minimize the energy consumption and costs. They found that optimizing pump planning can improve energy efficiency by an average of 15% (maximum 25%) compared to actual operation. Table 1 presents energy-saving opportunities and viable potential in WSS.

Lifting pumps are pumps that pump water from a mid-level collection tank, where water is drawn from the wells by submersible pumps, to an upper feed tank. This study aims to investigate the effect of collection tank level on the energy consumption of lifting pumps in drinking water distribution systems. An experimental setup consisting of a borehole, a collection tank, a lifting pump and a distribution tank was established in an independent laboratory in Kayseri. A SCADA system was integrated into the experimental system to monitor and evaluate energy consumption. Energy consumption and energy cost characteristics are determined. Suggestions are made to reduce energy consumption and improve energy efficiency in drinking water distribution systems.

Table 1. Energy-saving opportunities and viable potential in WSS [27].

Energy-saving opportunities	Saving (%)
Pumps and Pumping (Common Potential Ranges)	5-30
Improving existing pumps	5-10
Improvement to new pumping technology	3-7
Maintenance improvement and closer matching of pumps to their duties (such as using VSDs)	Up to 30

2. MATERIAL AND METHOD

2.1. Experimental System

An experimental system was set up in an independent laboratory in Kayseri to examine the effect of collection tank level on energy consumption of lifting pumps in drinking water distribution systems. The experimental system is shown in Fig. 1. The experimental system consists of 3 main parts: Part A (see also Fig. 2), Part B (see also Fig. 3), and Part C. Part A consists of well (1), deep well pump (submersible pump) (2), power panel with frequency converter (3), level sensor (4), bullock check valve (5), manometer (6), output pressure sensor (7), sliding valve (8), promotional line (9), SCADA control panel (10), electromagnetic flowmeter (11) and line pressure sensor (12). The essential elements of Part B are: collection storage tank (1), inline centrifugal pump (2), power panel with frequency converter (3), SCADA control panel (4), bullock check valve (5), manometer (6), pressure sensor (7), sliding valve (8), vacuum meter (9), promotional line (10), and electromagnetic flowmeter (11). Part C consists of a 100 m^3 distribution storage tank. Fig. 4 shows a general view of the experimental setup.

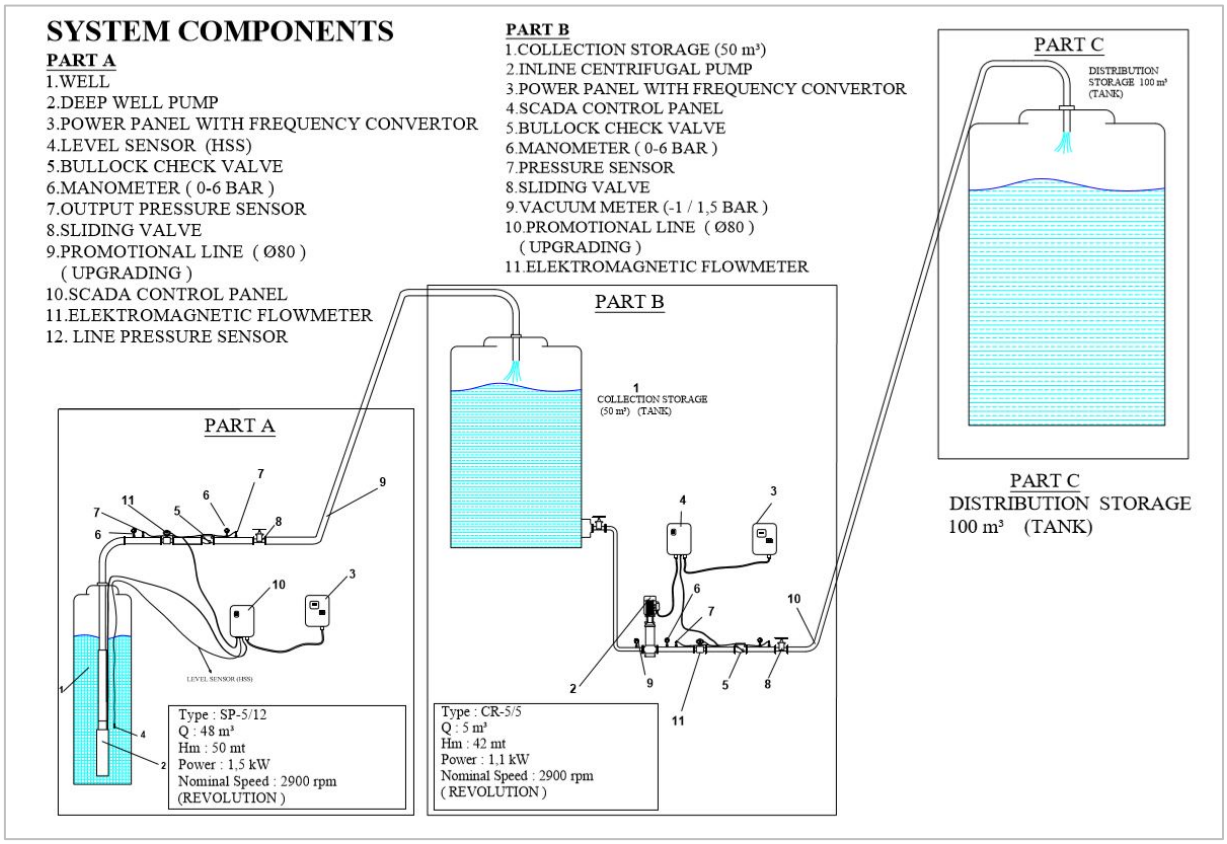

Figure 1. A schematic diagram of the experimental setup [28].

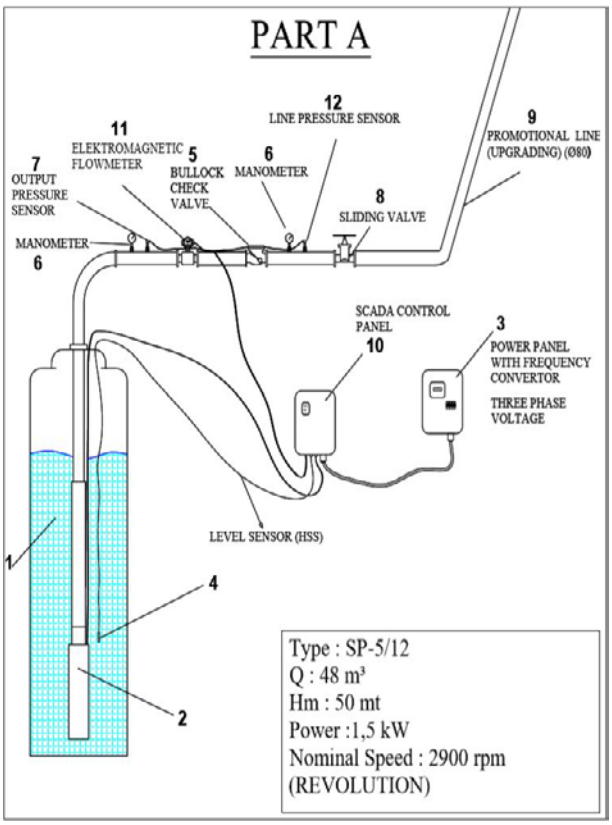

Figure 2. A schematic diagram of the experimental setup - Part A [28].

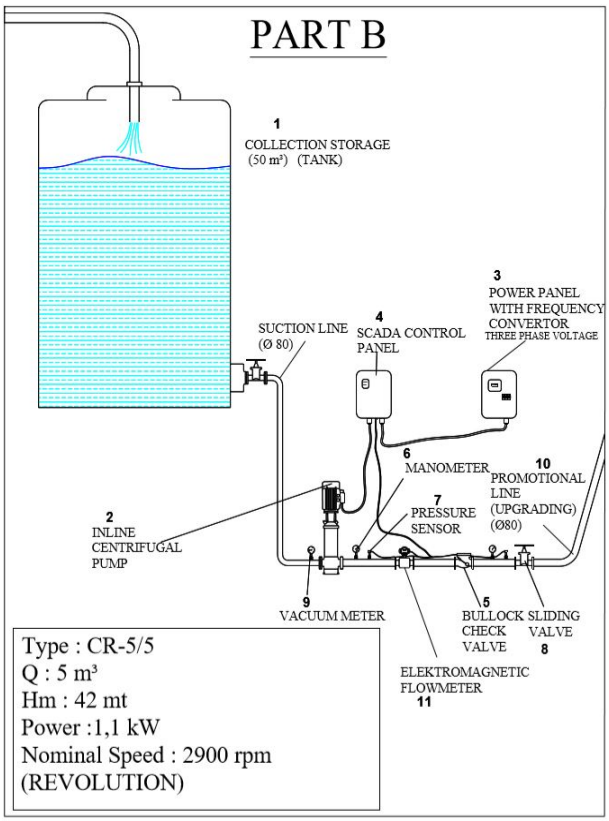

Figure 3. A schematic diagram of the experimental setup - Part B [28].

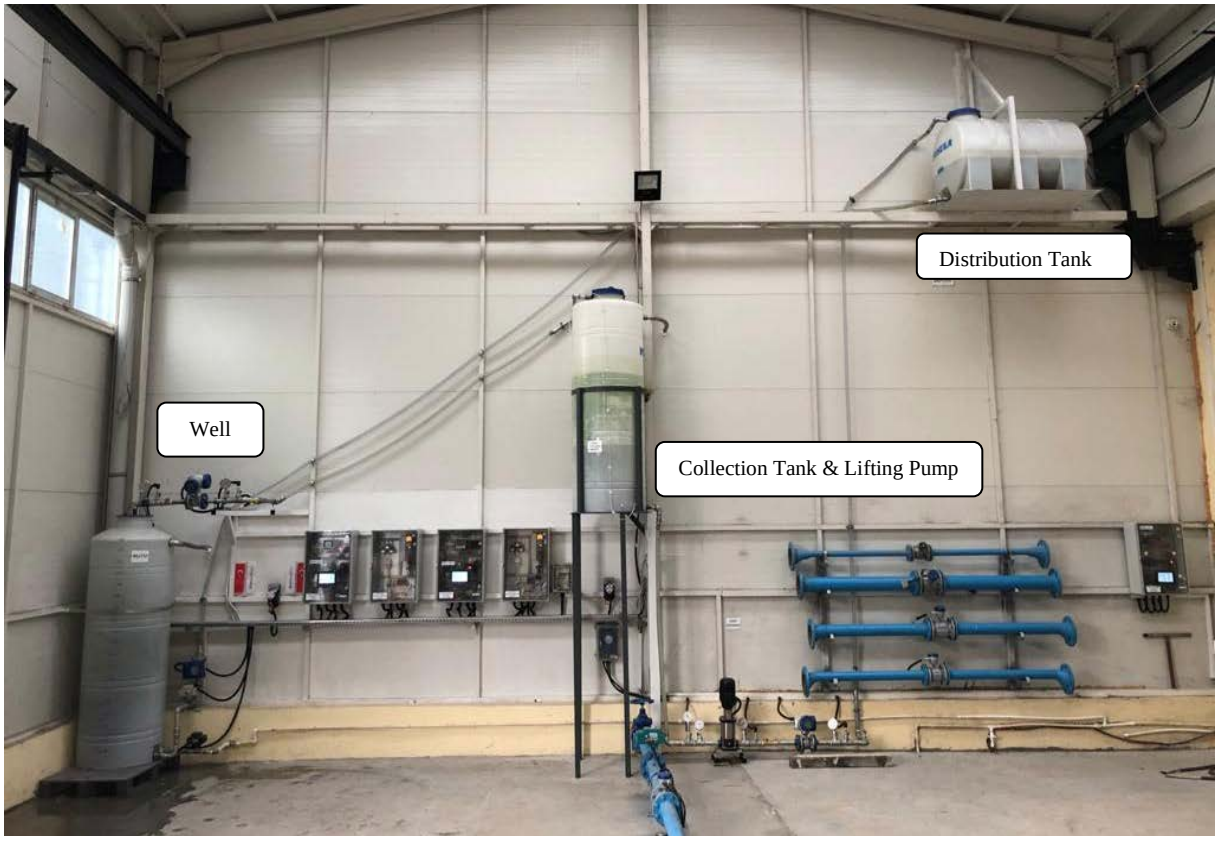

Figure 4. A general view of the experimental setup [28].

A SCADA system was integrated into the experimental system to monitor and evaluate energy consumption. Using the SCADA system, the instantaneous measurement values measured by the measuring devices were recorded. Using the measuring devices, the following data were taken:

(a) Well: water level, outlet flow rate, outlet pressure, line pressure, energy information (voltages, currents, power),
(b) Collection tank: inlet pressure, outlet pressure, outlet flow rate, energy information (voltages, currents, power),
(c) Distribution tank: water level, outlet flow rate.

Data was transferred from the system every 10 seconds via servers, and the received data were recorded. Using these data, characteristics of the well part, collection storage part and distribution storage part were evaluated. Energy consumption and cost characteristics were calculated.

2.2. Method

This study aimed to examine the effect of collection tank level on the energy consumption of lifting pumps in drinking water distribution systems. The experiments were carried out in an experimental system established in an independent laboratory in Kayseri. Five different levels of 40, 80, 120, 160 and 180 cm were used for the collecting tank. Measurements were taken for 2 hours for each level of the collection tank. Energy consumption and energy costs were analyzed at different collection tank levels, and savings were calculated.

The power absorbed by a pump in a water supply system P, in W, and the electricity consumption W, in kWh, can be calculated using the following equations [7, 24]:

$$P = \frac{\gamma Q H_p}{\eta} \quad (1)$$

$$W = PT_p \quad (2)$$

where γ is the specific weight of water, in N/m^3; Q is the pump discharge, in m^3/s; H_p is the pump head for the operating point, in m; η is the global efficiency of the pumping station; and T_p is the operation period, in h. The specific energy, E, is the energy that is used to generate 1 m^3 of drinking water.

3. RESULTS AND DISCUSSIONS

3.1. Results for System Established in an Independent Laboratory in Kayseri

This study was carried out to examine the effect of collection tank level on the energy consumption of lifting pumps in drinking water distribution systems. Experiments were carried out for five different levels of the collection tank: 40, 80, 120, 160 and 180 cm. The specific energy and specific cost were determined.

The effect of collection tank level on specific energy is shown in Fig. 5. While the collection tank level is 40 cm, the specific energy is 0.08129 kWh/m^3. When the tank level is 120 cm, the specific energy decreases to 0.07699 kWh/m^3; when the tank level is 180 cm, the specific energy decreases to 0.07257 kWh/m^3. These results show that the tank level has significant effects on specific energy. The regression equation that gives the relationship between the specific energy and the water level is given below:

$$E = 0.08427 - 0.00657h \quad (3)$$

where E is the specific energy, in kWh/m^3; h is the collection tank level, in m.

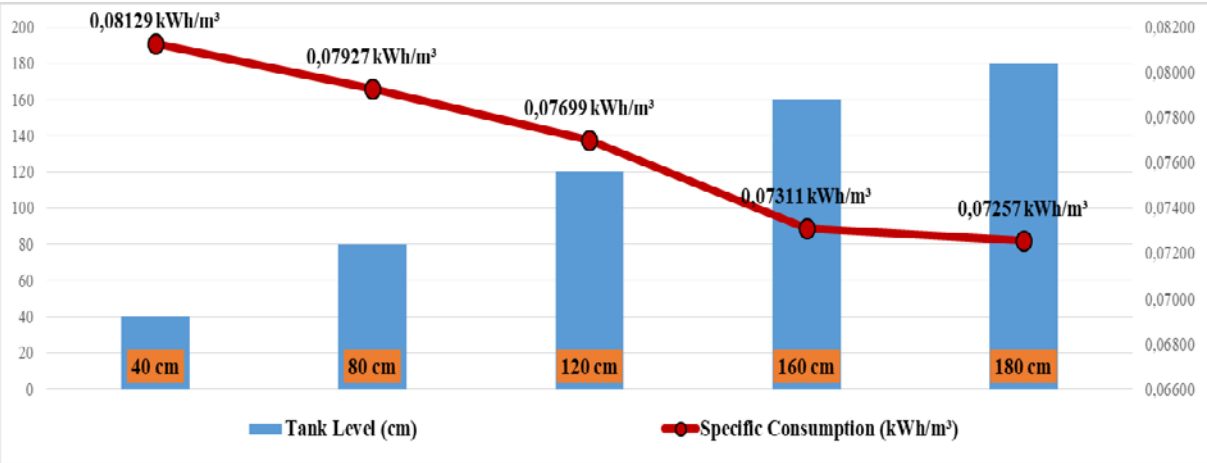

Figure 5. The effect of collection tank level on specific energy.

Fig. 6 shows the effect of collection tank level on the specific cost. While the collection tank level is 40 cm, the specific cost is 0.06016 TL/m^3. When the tank level is 120 cm, the specific cost decreases to 0.05697 TL/m^3; when the tank level is 180 cm, the specific cost decreases to 0.05370 TL/m^3. These results show that the tank level has significant effects on specific cost.

The effect of the tank level on both the specific energy and the specific cost is given in Fig. 7. The examination of the figure reveals that both specific energy and specific cost decrease with increasing tank level. Table 2 presents specific energy and specific cost savings when the water level in the collection tank increases. The minimum water level in the tank is taken as 40 cm. When the water level is increased to 80 cm, 2.48% saving in specific energy

occurs. When the water level is 120 cm, 160 cm and 180 cm, a specific energy savings of 5.29%, 10.06%, and 10.73% occurs, respectively, relative to the 40 cm water level. All these results show that with the increase in the water level, significant savings will be achieved in the energy consumed by the lifting pumps. These results reveal the importance of making the height of the collection tanks as high as possible when building collection tanks in water catchment areas. However, in this case, simulations involving all three essential elements (submersible pumps, collection tanks/lifting pumps and distribution tanks) must be made to determine the adequate saving amount of energy consumed by the pumping stations.

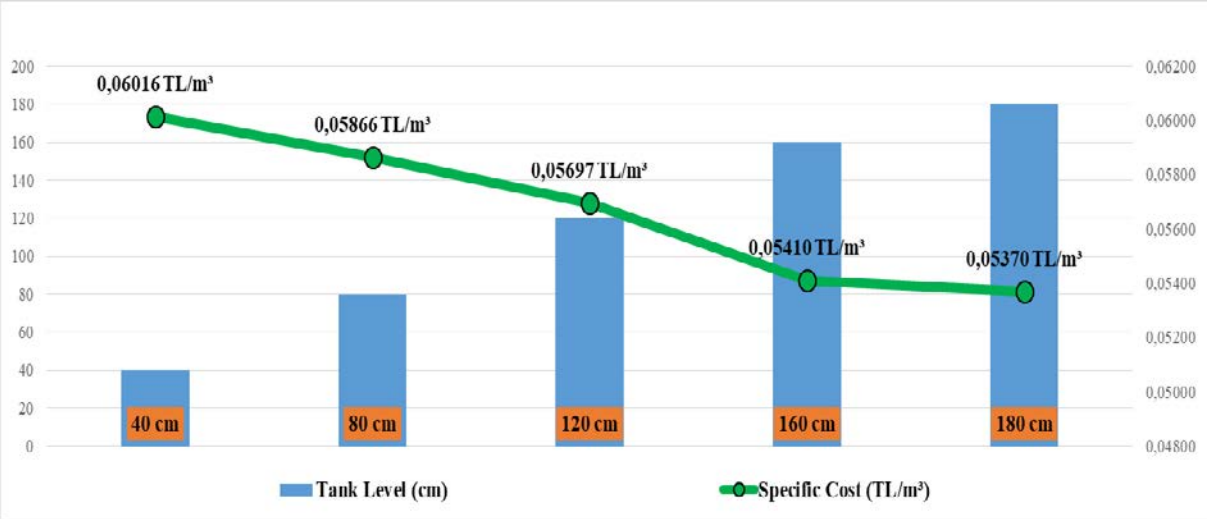

Figure 6. The effect of collection tank level on specific cost.

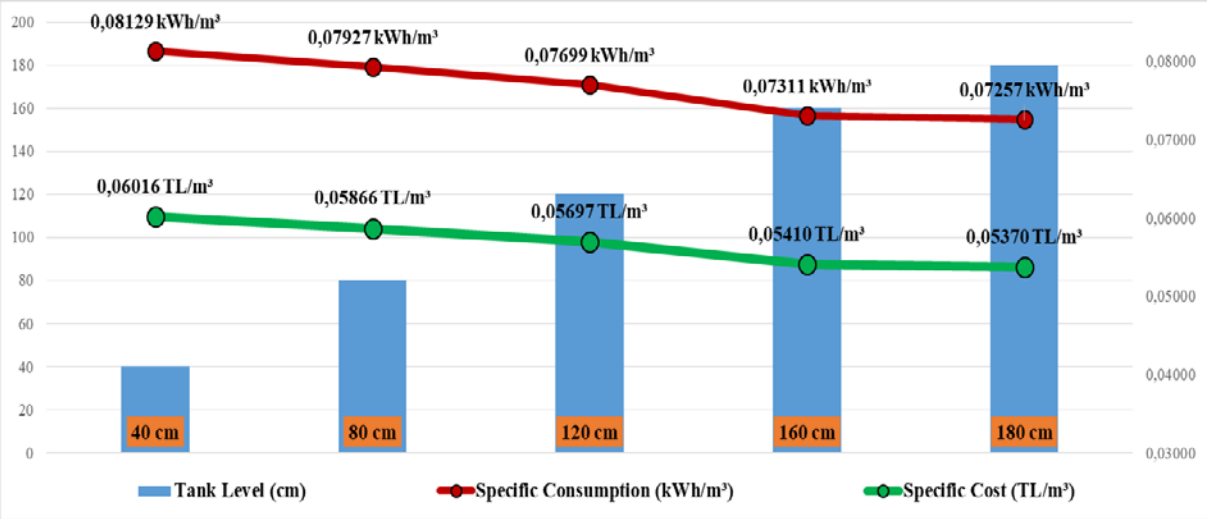

Figure 7. The effect of collection tank level on specific energy and specific cost.

Table 2. Comparison of the effect of the collection tank level on specific energy and specific cost.

Tank level (cm)	Specific energy (kWh/m³)	Specific cost (TL/m³)	Saving rate (%)	Total saving rate (%)
40	0.08129	0.06016	-	
80	0.07927	0.05866	2.48	2.48
120	0.07699	0.05697	2.88	5.29
160	0.07311	0.05410	5.04	10.06
180	0.07257	0.05370	0.74	10.73

3.2. Evaluation for Central Pumps Group of Kayseri Water and Sewerage Directorate (KASKİ)

In this study, a demo was created by simulating the well, collection tank/lifting pump and distribution tank, that are the essential elements of drinking water supply systems. The operating performances of the lifting pumps with the water level of the collection tank have been examined. It is observed that if the collection tank has 180 cm of water instead of 40 cm, the lifting pump saves approximately 10.73% energy.

There are 12 drinking water catchment areas in the Kayseri Water and Sewerage Directorate (KASKİ) responsibility in Kayseri city centre (Table 3). The annual water production and energy consumption in these catchment areas are given in Table 3 and Fig. 8. Fig. 8 is drawn using the amount of water produced and energy consumed by the KASKİ central group pumps between 01.01.2019 and 31.12.2019. These data were taken from the KASKİ SCADA system. As seen, 96 622 443 m^3 water is promoted annually in the city centre of Kayseri, and 21 720 354 kWh energy is consumed [29].

Table 3. Lifting stations water production and energy consumption in KASKİ for the city centre [29].

	Catchment area	Water production (m^3)	Energy consumption (kWh)
1	Beştepeler	15.859.770,00	3.715.705,00
2	Germiraltı	17.666.991,58	2.338.626,06
3	Karpuzatan	10.313.356,00	2.411.265,00
4	Keykubat	12.247.152,66	3.796.873,84
5	Mahrumlar	8.803.192,18	2.479.551,81
6	Dokuzpınar	5.657.216,00	819.042.00
7	Eğribucak	6.187.519,00	1.952.352,00
8	Gediris	3.394.392,00	756.182,00
9	Konaklar	6.303.890,00	607.356,00
10	İldem	3.606.256,00	999.024,00
11	Çaybağları	4.320.438,00	1.758.171,00
12	Talas	2.262.270,00	905.248,00
Total		**96.622.443,42**	**21.720.354,71**

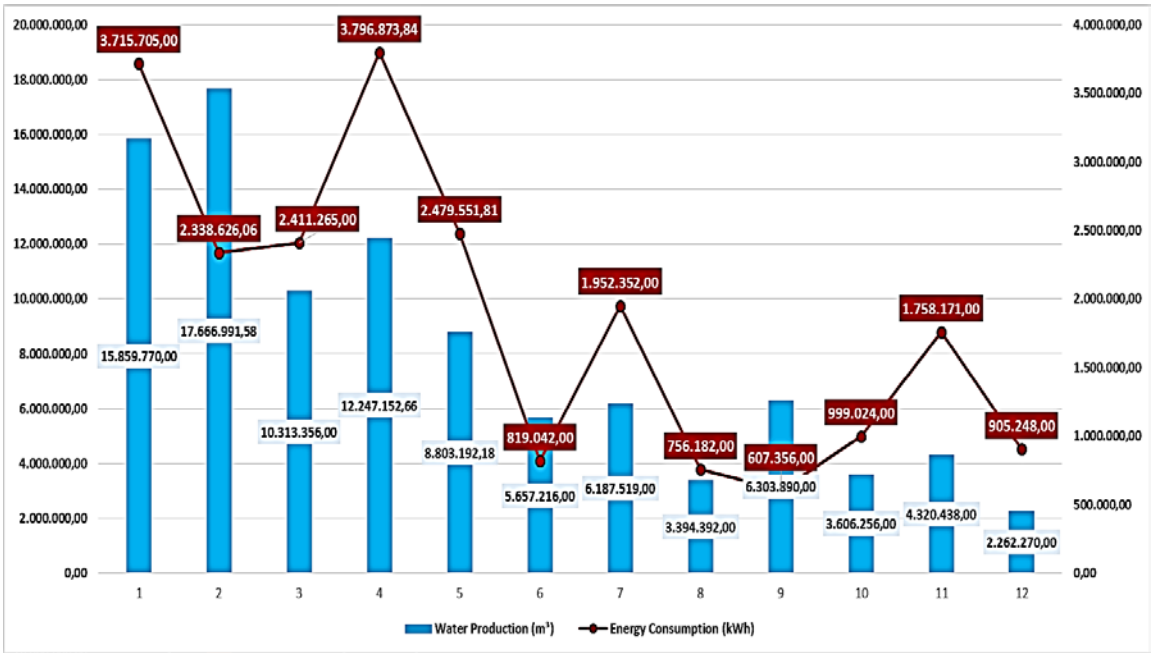

Figure 8. Lifting stations water production and energy consumption in KASKİ for the city centre [29].

Fig. 9 shows the Germiraltı drinking water catchment area, whose altitude is 1095 m. There are 18 deep wells in the Germiraltı catchment area, 16 of which are active. In the Germiraltı catchment area, the average static levels of drinking water wells, whose depths are around 200 meters, are 34 meters, and their dynamic levels are around 36 meters. The drinking water in the catchment area, at 1060 elevation underground, is promoted to the collection tank with a size of 9.5x15.50x3.40 m and a capacity of 500 m³ at 1095 elevation by submersible pumps. The drinking water collected here is promoted to distribution tanks at higher elevations by three centrifugal pumps. Technical features of the lifting pumps are given in Table 4.

Figure 9. Germiraltı catchment area [29].

Table 4. Technical specifications of the lifting pumps in the Germiraltı catchment area [29].

	Flow rate (m³/h)	Discharge head (m)	Revolutions per minute (rpm)	Power (kW)
Pump-1	1 080	34	1 500	132
Pump-2	400	101	1 500	200
Pump-3	100	90	2 900	37

As a result of the demonstration study, it is determined that the water level in the collection tank should be kept as high as possible to save energy. If an analogy is made to this result, it is concluded that the water level of the collection tank in the Germiraltı catchment area must be kept high in order to save energy. Due to the high water production and high energy cost in the the catchment area, significant financial savings will be achieved by keeping the water level in the collection tank high. On the other hand, since there are twelve submersible pumps feeding the collecting tank, it should be decided by making an optimization study which pumps to be used while filling the collecting tank. Our work on this subject continues.

4. CONCLUSION

In this study, the energy consumption behaviour of the lifting pumps used in drinking water supply systems was examined for different tank levels. Signifiant findings of this study are concluded as follows:

(a) The tank level has significant effects on specific energy. The specific energy of the lifting pump decreases with increasing tank level.
(b) The tank level has significant effects on specific cost. The specific cost of the lifting pump decreases with increasing tank level.
(c) The increase in the water level creates significant savings in the energy consumed by the lifting pumps. If the collection tank has 180 cm of water instead of 40 cm, the lifting pumps save approximately 10.73% of energy.
(d) In order to reduce the energy consumed by the lifting pumps, the height of the collection tanks in the catchment areas should be made as large as possible.
(e) The water levels in collection tanks built in the catchment areas should be kept as high as possible to reduce the energy consumed by the lifting pumps.
(f) Simulations involving all three essential elements (submersible pumps, collecting tanks/lifting pumps and distribution tanks) should be conducted to determine the actual amount of savings that can be made in the amount of energy consumed by pumping stations.
(g) Since many lifting pumps are used in water supply systems of provinces, significant energy savings can be achieved by sizing collection tanks appropriately and keeping the water level in the tanks high.
(h) Since the water production and energy consumption of the lifting stations in KASKİ for the city centre are very high, significant financial savings may be achieved by keeping the water level in the collection tanks high.

ACKNOWLEDGEMENTS

The authors would like to acknowledge ENVEST Energy and Water Technologies Ltd. Co. (Kayseri, TURKEY) for their support in the establishment of the experimental system and the integration of the SCADA system. The authors would also like to acknowledge KASKİ General Directorate for sharing the data regarding the catchment areas in the city centre.

REFERENCES

[1] Cabrera, E., Pardo, M. A. & Arregui, F. J., Measuring the Energy Efficiency of Water Utilities, Pipelines, *Climbing New Peaks to Infrastructure Reliability—Renew, Rehab, and Reinvest,* 669-680, 2010.

[2] Guyer, J. P., Introduction to Pumping Stations for Water Supply Systems, *Course No: C04-027,* NY-USA, 2012.

[3] Vilanova, M. R. N. & Balestieri, J. A. P., Energy and Hydraulic Efficiency in Conventional Water Supply Systems. *Renewable and Sustainable Energy Reviews* **30** (10), 701–714, 2014.

[4] Coelho, B. & Andrade-Campos, A., Efficiency Achievement in Water Supply Systems - A Review, *Renewable and Sustainable Energy Reviews,* **30**, 59–84, 2014.

[5] Zimoch, I. & Bartkiewicz, E., Optimization of Energy Cost in Water Supply System, *E3S Web of Conferences* **22**, 00204, ASEE17, 1-8, 2017.

[6] Watergy. 2009. Available online: http://www.watergy.net/-overview/why.php.

[7] Sarbu, I., A Study of Energy Optimisation of Urban Water Distribution Systems Using Potential Elements, *Water*, **8**, 593, 2016.

[8] Copeland, C. & Carter, N.T., Energy-Water Nexus: The Water Sector's Energy Use, *Congressional Research Service*, Washington DC-USA, 2-10, 2017.

[9] Pabi, S., Amarnath, A., Goldstein, R. & Reekie, L., Electricity Use and Management in the Municipal Water Supply and Wastewater Industries, *Electric Power Research Institute*, 1–194, 2013.

[10] Feldman, M., Aspects of Energy Efficiency in Water Supply Systems. *In Proceedings of the 5th IWA Water Loss Reduction Specialist Conference*, Cape Town-South Africa, 2009.

[11] Luna, T., Ribau, J., Figueiredo, D., Alves, R., Improving Energy Efficiency in Water Supply Systems with Pump Scheduling Optimization, *Journal of Cleaner Production*, **213**, 342-356, 2019.

[12] Bolognesia, A., Bragallia, C., Lenzi, C., Artina, S., Energy Efficiency Optimization in Water Distribution Systems, *Procedia Engineering*, **70**, 181-190, 2014.

[13] Ramos, H. M., Vieira, F. and Covas, D. I. C., Energy Efficiency in a Water Supply System: Energy Consumption and CO_2 Emission, *Water Science and Engineering*, **3**(3), 331–340, 2010.

[14] Vieira, F., Ramos, H.M., 2008. Hybrid Solution and Pump-Storage Optimization in Water Supply System Efficiency: A case study. *Energy Pol.* **36**, 4142-4148, 2008.

[15] Moreira, D.F., Ramos, H.M., 2013. Energy Cost Optimization in a Water Supply System Case Study, *J. Energy* 1-9, 2013.

[16] Cherchi, C., Badruzzaman, M., Gordon, M., Bunn, S., Jacangelo, J. G., Investigation of Cost and Energy Optimization of Drinking Water Distribution Systems, *Environ. Sci. Technol.*, **49**, 13724−13732, 2015.

[17] Senon, C., Badruzzaman, M., Contreras, A. J., Allen, M. S., Jacangelo, J. G. Drinking Water Pump Station Design and Operation for Energy Efficiency, *Water Research Foundation Report 4308, Water Research Foundation: Denver, CO*, 2015.

[18] Kurek, W., Ostfeld, A., Multi−Objective Optimization of Water Quality, Pumps Operation and Storage Sizing of Water Distribution Systems, *Journal of Environmental Management*, **115**, 189-197, 2012

[19] Cherchi, C., Badruzzaman, M., Oppenheimer, J., Bros, C. M.; Jacangelo, J. G., Energy and Water Quality Management Systems for Water Utility's Operations: A Review, *J. Environ. Manage*., **153**, 108−120, 2015.

[20] Al-Ani, D., Habibi, S., Optimal Operation of Water Pumping Stations. *WIT Transactions on Ecology and The Environment, Vol 178, Water and Society II* 185- 198, 2014.

[21] Sekmen, U., Yılmaz, M. & İmik, E., Derin Kuyulardan İçme Suyu Temininde Pompa Seçiminin Enerji Verimliliğine Etkisi, *ULIBTK'19 22th Congress of Thermal Sciences and Technology*, Kocaeli-Turkey, 2019.

[22] Giustolisi, O., Laucelli, D. & Berardi, L., Operational Optimization: Water Losses Versus Energy Costs. J. Hydr. Engng. **139**(4), 410–423. doi: 10.1061/(ASCE)HY.1943-7900.0000681, 2012.

[23] Energieeinsparung; Grundfos Pressetext: Erkrath, Germany, 2017.

[24] Nowak, D., Krieg, H., Bortz, M., Geil, C., Knapp, A., Roclawski, H. & Böhle, M., Decision Support for the Design and Operation of Variable Speed Pumps in Water Supply Systems, *Water* **10**, 734, 2018.

[25] Georgescu, S. C.; Georgescu, A. M. Application of HBMOA to Pumping Stations Scheduling for a Water Distribution Network with Multiple Tanks. *Procedia Eng.*, **70**, 715–723, 2014.

[26] Brandt, M.J., Middleton, R.A. & Wang, S., Energy Efficiency in the Water Industry: A Compendium of Best Practices and Case Studies - Global Report, *UKWIR Report* Ref. No. 10/CL/11/3, 2010.

[27] Liu, F., Ouedraogo, A., Manghee, S. & Danilenko, A., A Primer on Energy Efficiency for Municipal Water and Wastewater Utilities, *ESMAP Technical Report* 001/12, 2012.

[28] ENVEST Energy and Water Technologies Ltd. Co., Kayseri, TURKEY.

[29] KASKİ General Directorate, Kayseri, TURKEY.

SHIP ENERGY EFFICIENCY ANALYSING APPROACHES: A CASE STUDY

Onur YILMAZ*[1], Tayfun UYANIK*[2], Yasin ARSLANOĞLU*[3]
*İstanbul Technical University, Maritime Faculty, Marine Engineering Department, 34940, Tuzla, İstanbul,Turkey
Email: yilmazon@itu.edu.tr[1], uyanikt@itu.edu.tr[2], arslanoglu@itu.edu.tr[3]

ABSTRACT

Ship Energy efficiency has become an important concern for ship owners and all stakeholders in the maritime sector. With rising environmental awareness, the problem of reducing ship-borne pollution is becoming more and more important. For this purpose, it is crucial to maintain appropriate methods to sustain energy efficiency and reducing the emissions on marine vessels. These approaches include the construction of a low-resistance vessel, the use of effective propeller and shaft systems, the selection of an appropriate and efficient main engine and generator, and the use of alternative energy sources during the design process. During the operation of the vessel, methods such as routine maintenance work, the operation of the vessel through compliance with energy efficiency and emission regulations are essential.

In this study, the methods used to increase the energy efficiency of ships within the framework of the Energy Efficiency Design Index (EEDI), the Energy Efficiency Operational Indicator (EEOI) and the Ship Energy Efficiency Management Plan (SEEMP) employed to assess the energy efficiency of the ships were reviewed and evaluated. Applications to improve energy efficiency for different types of ships have been studied with the aid of these approaches. A case study showed that the methods which were examined contribute between 20% and 30% to improving the vessel's energy efficiency.

Keywords: Ship, energy efficiency, EEDI, SEEMP, EEOI

GLOBAL WARMING
AND
ENVIRONMENTAL POLLUTION

SUSTAINABLE PHYTOREMEDIATION WITH ENERGY CROPS IN TURKEY

Benginur BAŞTABAK*, Elif GÖDEKMERDAN*, Günnur KOÇAR*
* Ege University, Solar Energy Institute, Biomass Energy and Technology Center, İzmir/Turkey
Email: benginurbastabak@outlook.com, elifgodekmerdan@gmail.com, gkocer@gmail.com

ABSTRACT

Contamination of soil by toxic elements and compounds is a global issue. This problem is increasing day by day with anthropogenic effects. Conventional methods of soil decontamination possess disadvantages in the forms of environmental and financial burdens. Alternative solutions are being sought for cleaning contaminated areas. One of these is phytoremediation. Phytoremediation has considerable economic and environmental advantages. Our article focuses on the phytoremediation potential of energy crops that are cultivated for biomass production in Turkey. Energy crops are resistant to stress conditions and can provide high biomass yield in a short time. Also, they help restore the properties of contaminated soils due to their absorption mechanism of toxic substances. For phytoremediation to be carried out with energy plants in a sustainable manner, the obtained biomass must be evaluated in the energy production plants. In this context, Turkey was divided into regions both the energy crops cultivation and biomass energy production plants were examined. This approach ensures local and safe energy production by reducing dependence on external energy sources through economic and eco-friendly improvement.

Keywords: Energy crops, phytoremediation, biomass energy, soil contamination.

1. INTRODUCTION

Soil is one of the most essential sources for the continuity of life. Soil is becoming an organic and inorganic source directly to the living creatures on it. Some of the soil's nutritional composition results from primary minerals, secondary minerals in the rocks, Fe, Al, Mn oxides, and sometimes carbonates such as $CaCO_3$. The organic matter component of the soil comes from the mesofauna, colloidal humus formed by microorganisms, dead plant debris and, rotten products and microorganisms. Complex soil structure can often be disrupted by anthropogenic effects. With this deterioration, the lives of the living creatures that provide the nutrient source from the soil become risky.

There are various remediation techniques for the removal of organic and inorganic pollutants in the soil. These techniques are defined as isolation and immobilization technologies, mechanical separation technologies, pyrometallurgical technologies, electrokinetic technologies, biochemical technologies, electrokinetic technologies, biochemical technologies, liquid and in situ cleaning technologies, and phytoremediation methods. A large part of the mentioned techniques requires a significant amount of economic resources. Unlike other techniques, phytoremediation methods are stated to be cost-effective and sustainable. Phytoremediation is briefly the removal of pollutant factors from the soil by plant cultivation. With the phytoremediation methods, soil pollutants can be removed from the soil by nutrient absorption by plants.

Plant cultivation for biomass energy is not recommended in areas where limited agricultural resources and food-based agricultural production are maintained. However, if energy crops are grown in areas contaminated with organic and inorganic pollutants, it is possible to convert high amounts of biomass that need to be destroyed after phytoremediation into renewable energy. In this context, the possibilities of evaluating the biomass obtained after the phytoremediation process with the cultivation of energy crops in the contaminated areas were investigated.

1.1. Phytoremediation Methods for Contaminated Soils

Phytoextraction

Also known as phytoaccumulation. The plant takes the pollutant amount of metal in the soil with its roots and transmits it to the aboveground parts. These plants are called hyperaccumulators. Compared to other plants, they accumulate large amounts of metal. Plants can be selected according to environmental conditions and contaminant metal content in the soil. By one or more harvests, contaminant factors in the soil are removed. Harvested plants can be processed to cycle metals, or their incinerated ashes can be taken to the hazardous waste storage area [1-3].

Rhizofiltration

It is the adsorption of pollutant factors on plant roots. At first, plants to be used in this method are grown in water. It is planted with contaminated soil for a while and then planted in the contaminated area. In the harvest, the roots are collected. The burning or separation process is carried out [1,2].

Phytostabilization

Pollutants in soil and groundwater are absorbed by plant roots and collected in the roots or deposited in the root area. Using this process, the movement of the pollutant factor is reduced, preventing the transition to groundwater, the atmosphere, and the food chain. This technique is used for high metal concentrations in surface soils. Metal tolerant species can also prevent contamination where natural vegetation is destroyed by wind erosion [1,2].

Phytodegradation

It is also called phytotransformation. It is the breakdown of the pollutant factors by taking them through the metabolic process by plants. The pollutant decomposes, joins plant tissues, and is used as nutrients [1].

Rhizodegradation

It is also called enhanced rhizosphere biodegradation, phytostimulation, or plant-assisted bioremediation/degradation. Compared with phytodegradation, it is the breakdown of the pollutants in the soil in a slower process where the activity increases with the rhizodegradation. Some yeast, fungi, and bacteria consume organic matter for their nutritional and energy needs. These microorganisms can digest organic substances that are dangerous to humans and make them harmless using iodine degradation. The plant has essential functions such as loosening the soil, carrying water, and increasing the activity of natural substances and microorganisms secreted by the root [1].

Phytovolatilization

The plant takes the pollutant factor, and the form of the pollutant is changed and released into the atmosphere. Some of the pollutants fly into the atmosphere at relatively low concentrations, while some may remain in the leaves [1].

1.2. Biomass Energy Resources, Conversion Methods and Products

Biomass is organic materials that are not of fossil origin. The energy obtained by some methods from non-fossil materials can be defined as biomass energy. Biomass energy is considered as the most promising source in terms of meeting the energy need in the future because of providing energy security and reducing net carbon emission as it can be evaluated regionally. Biomass energy sources can be agricultural, industrial, or urban origin. As seen in **Figure 1**, one of the biomass energy sources, biochemical, chemical, thermochemical, and physochemical conversion methods, can produce gas, liquid, and solid fuel (biohydrogen, biogas, biodiesel, bioethanol, biomethanol, biochar, synthesis gas), Heat and electrical energy from these products can be obtained.

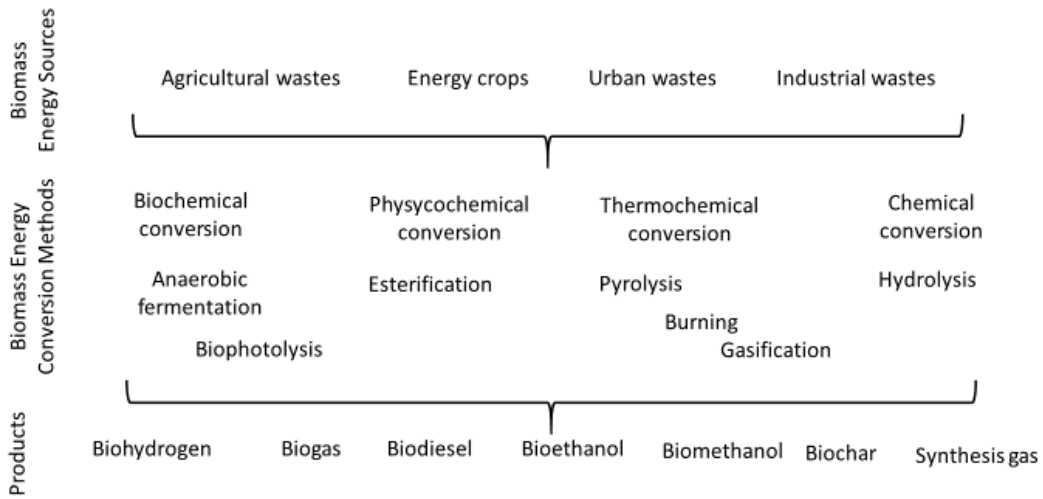

Figure 1. Biomass energy sources, conversion methods and products

2. MATERIAL AND METHODS

In this study, soil contamination was investigated in seven different climatic regions of Turkey. Soil pollution has been examined in terms of heavy metal and permanent organic compounds. In this context, researches made in terms of heavy metal and permanent organic compounds in the determined regions have been examined. Energy crops that can be used in phytoremediation according to pollution types and climate characteristics have been proposed.

3. RESULTS AND DISCUSSION

3.1. Sources of Soil Contamination in Turkey

Turkey is based between 26°–45° and 35°51′–42°06′ north latitude in the northern hemisphere. The total surface area is 777.971 km^2. There are seven geographical regions: Black Sea, Marmara, Aegean, Mediterranean, Central Anatolia, Eastern Anatolia, and South-Eastern Anatolia [4].

Figure 2. Climatic regions of Turkey

According to a TUIK (2013) [5] report, Turkey's population will reach 84.3 million by 2023. Especially with the increase in the city population, it is inevitable to experience large-scale environmental problems. Pollution of

soil in Turkey, as in other parts of the world since the beginning of the 20.century, has emerged with the mechanization of agriculture and rapid industrialization [6]. Soil contamination threatens both the natural ecosystem and the health of agricultural products. Sources of pollution are very diverse: urbanization due to demographic explosion and lousy land-use policies, industrial wastes, mining wastes and activity, urban wastes (wild storage), hazardous wastes (wild storage), excessive use of fertilizer, excessive pesticide use, livestock wastes, geothermal wastewaters, oil pollution, domestic wastewater (discharge without treatment), contaminated water resources and highways.

Marmara Region

There are 384 industrial establishments in more than 15 industrial groups in the Kocaeli, İzmit province. There is a hazardous waste and garbage incineration plant (İZAYDAŞ) with a capacity of 35,000 tonnes a year located at the city border [7]. The study of Özkul et al. (2008), took soil samples from 16 different regions. Cu, Zn, Ni, and Co contents of these samples were examined [7]. In some regions, heavy metal was found at the level of pollution. The primary pollutant sources are thought to be the exhaust, industrial waste, and solid waste incineration plants. It is also stated that the pollution is caused by the emission of the petrochemical, metal, chemical, cellulose, and paper-cardboard industries.

Polychlorinated Biphenyl (PCB) concentration was high in some of the soil samples taken from the Alikahya region of 2100 hectares, 10 kilometers from İzmit city center, in the east of Kocaeli province. Polycyclic aromatic hydrocarbon (PAH) concentration is above the limit values in all regions. It is thought that the reason for the high concentrations of may be due to waste incineration plants and industrial facilities depending on the prevailing wind directions [8].

PAHs in the soil of olive groves located in 7 different Bursa regions; concentrations, species distributions were examined and toxicity risk assessments were made. It has been determined that PAH pollution shows a large oscillation locally (2-2452 ng/g). The regions where the Σ12 PAH pollution in the soils is the least and the highest are the Mudanya Yörükali and Gemlik Campus regions, respectively and their concentrations are measured as 2 ng/g KM and 2452 ng/g. It is concluded that the industry, settlement, and traffic in these regions are exposed to high PAH contamination due to their high density. It is thought that the low level of PAH pollution in the Mudanya Yörükali region is because this region is a rural area away from pollutant sources [9].

Ni concentration above the limit values allowed in 55% of Iznik lake basin (Bursa). Irrigated agriculture is carried out in areas where crop production. The water of Iznik lake is used for irrigation. Sewage and wastewater from settlements around Iznik Lake are supplied to the lake. Also, manure and drug residues reach the lake with superficial washing and flow. All this explains the pollution in agricultural land [10].

In a study, an area including the district of Bandırma in Balıkesir province and its immediate surroundings was selected. Excessive amounts of Cr in phosphate fertilizers may be the most important source of this metal in soils. The average Cr concentration is 54-70 ppm and the critical value is 75-100 ppm for world surface soils. Cr concentrations measured in the region range between 169-395 mg/kg. The highest concentration of Cr was found in the region close to the production and storage area. Ni concentrations in the region range between 17-181 mg/kg. It exceeded the average world value of 30 mg/kg in all groups for copper (Cu). Cu concentrations range from 32 to 215 mg/kg. The highest Cu concentration was found in the region (215 mg/kg) near production and storage. Zinc (Zn) concentrations range from 48 to 263 mg/kg. The limit value for Cd is given as 3 mg/kg. In the research region, Cd concentrations vary between 3,5- 152 mg/kg. The highest concentration was obtained in the region near the production and storage area. Antimony (Sb) concentrations in the region range between 5-46 mg/kg. The world average for Sb is given as 1 mg/kg [11].

Ergene River collects the waters of the Ergene Basin, which has a drainage area of 10730 km² in Trakya, from east to west. An average of 80,000 m³ of wastewater is discharged daily to domestic and industrial origin to Çorlu Water and Ergene River [12]. The fact that the Ergene River contains high amounts of chlorine and sodium has caused serious accumulation of sodium and chlorine in the soil. This raises the problem of salinity and alkalinity. The high salinity rate has resulted in delayed germination and emergence, shortening of plant

height, and leaf and stem diameter reduction in crops cultivated in the area [13]. Another consequence of the Ergene River pollution is that it negatively affects the sales value of agricultural lands [14].

In the study of Adiloğlu and Sağlam (2015), the cobalt pollution in the agricultural areas on the highway edges of the Tekirdağ province was investigated [15]. For this purpose, 50 soil samples were taken from both sides of the road from agricultural lands on the roads within the provincial borders and extractable cobalt contents were determined. According to the research results, the cobalt content of the soil was found to be 0.008-0.587 mg kg^{-1}. When these findings are compared with the pollution limit values, cobalt pollution has been observed in the research areas. It is stated that this pollution is 52% for cobalt [15].

According to the study carried out in Çorlu district of Tekirdağ province, Zn, Cr, Cd, and Ni content was determined above the limit values specified in the Soil Pollution Control Regulation, especially in the soil samples collected from Türkgücü village, Çorlu stream and around Velimese Çerkezköy Organized Industrial Zone [16].

Aegean Region

In a study, Muğla-Yatağan Thermal Power Plant emissions on heavy metal scopes of agricultural and forest soils around the power plant were investigated. In soil samples, some soil properties such as Ni, Cd, Fe, Cu, Zn, Mn, S have been determined. It has been determined that the heavy metal and S content of the soils are not related to the distance to the power plant, but are mostly affected by the dominant wind direction. It has been determined that the heavy metal content of soil samples is related to soil pH. It was observed that the total Cd and S values were relatively higher than average values. It was determined that the extractable metal content of the soils were generally high in the south and southwest directions of the power plant. It has been determined that the amount of the heavy metal in plants is high. The amount of S taken on the needle leaves of pine trees is higher than other plants. Cu, Cd, Zn were found very high in sesame and carrot. It has been determined that these amounts are above the values allowed to be consumed for vegetables. The moss, which is considered a biological monitoring plant, has been found to have too high metal and S content [17].

Mediterranean Region

According to the report of the Ministry of Environment (2019), soil pollution caused mostly by industrial wastes in Adana, wild stored wastes in Antalya, mining wastes in Burdur, and excessive usage of fertilizer in Hatay [18]. Contamination factors are thought to be heavy metal and permanent organic compounds.

Central Anatolia Region

The area of Çayırhan Thermal Power Plant in Ankara is 5,032,000 m^2. It is stated that pH decreases in the dominant wind direction. The reason for this is thought to be an interaction with SO_2 emissions. Cd concentration in the dominant wind direction was above the limit value. S contamination is noteworthy throughout the region. It is thought that it may create a risky situation in the following periods [19].

Black Sea Region

In the study conducted by Candemir and Özdemir (2010), it was determined that a total of 957,900 ha of land assets in Samsun province, 51.92% of them were exposed to severe erosion, and the misuse and misuse of potential agricultural lands was 18% [20].

In a study conducted in Sinop Province, concentration levels of heavy metals such as Cr, Fe, Ni, Cu, Zn, As, and Pb were investigated in soil samples collected from 88 sampling points. Average concentrations of Cr, Fe, Ni, Cu, Zn, As, and Pb were found as 194.73, 39.848.57, 85.02, 43.19, 65.10, 5.66, and 17.01 mg/kg, respectively. The results showed that average concentrations of Cr, Ni, As, and Pb exceed the world crust average, excluding Fe, Cu, and As. The multivariate analysis results showed that Cr, Ni, Zn, As, and Pb levels in the studied area were significantly affected by anthropogenic inputs such as agricultural practices [21].

Eastern Anatolia Region

In the study by Kaptanoğlu and Bakır (2017), cadmium, nickel and copper amounts were measured in the soils [22]. It is thought that the soil samples of the Engil river pouring into Lake Van do not come to the extent of pollution, but if not paid attention, risky situations may arise. In this context, it is necessary to give importance to the treatment plants from industrial and domestic pollution. Soil pollution originating from industrial facilities is thought to occur in the soils around the organized industrial zone [23,24].

Southeast Anatolia Region

In Koca's (2019) study, the soils surrounding the thermal power plant located next to the Cizre-Silopi highway, is evaluated as a pollutant source, is located approximately 4.5-5 km west of the Silopi district center of Şırnak Province [25]. At the end of the study, it was observed that Cr and Ni values were high, especially in the soils having primary material such as serpentine in the region.

Al, As, Pb, Cr, Cu, Zn, Ni, Co, Mn, and Fe heavy metals were investigated in a study in Şanlıurfa, Harran Plain. Co, Cr, and Mn are 1.4 times higher and Ni is 3.1 times higher than the corresponding average values worldwide. It can be said that this pollution is formed by anthropogenic and natural sources, while arsenic pollution occurred by anthropogenic sources (agrochemicals). These findings show that agricultural chemicals were used intensively be used as a model for risks related to contamination in agricultural areas.

3.2. Phytoremediation With Energy Crops in Turkey

Corn, castor oil, camelina, canola, jatropha, wild artichoke, jojoba, mycanus, poplar, eucalyptus, cotton, sunflower, cane sugar, sugar beet, soybean, camel thorn, branched millet, kenaf, and millet are both energy crops. They are some of these crops that can be used in phytoremediation. These crops have high resistance to organic and inorganic soil pollutants. At the same time, heavy metals can collect permanent organic pollutants (POPs), PAH, and atrazine from the soil and accumulate them in their body. Many annual and perennial energy crops can also be used as a phytoremediation crops.

It is strictly not recommended for plants grown for phytoremediation in contaminated soils to enter the food cycle directly. Obtaining energy from the obtained biomass is a recommended practice because it is outside the food sector. For example, Jatropha (*Jatropha* L.) is a crop used in biodiesel production and can be grown in arid regions due to the low demand for fertilizers and water. It cannot be used as a foodstuff because it contains phorbol esters ($C_{20}H_{28}O_6$) toxic to animals and humans in the oil from this crop [26,27]. Jatropha, which is not valuable as a food raw material, is also able to absorb these substances by absorbing these substances and reduce the amount of toxic heavy metals and permanent organic compounds in the soil because it is tolerant of toxic metals in the soil and POPs [26,27]. Castor oil (*Ricinus communis*) is another crop that can be used as a biomass energy source. Castor oil seed oil is known as non-drying oil since it contains only double bonds in the fatty acid chain. Having a long shelf life and being resistant to high temperatures makes this plant attractive [28-30]. Cultivation of this crop in our country is not expected [31]. However, it is thought to be economically beneficial if it becomes widespread. Since the substance of resin in the castor oil crop seed is toxic to living things, it cannot be consumed as a nutrient. However, it seems advantageous to use as a biomass energy source after phytoremediation with its wide usage area.

The sunflower (*Helianthus annuus*) is considered a source of biomass and biochars as a source of energy due to its high oil content and lignocellulosic content [32]. At the same time, sunflower crops are used as food raw materials for human and animal nutrition. However, it can be used in phytoremediation because it is tolerant of toxic metals in the soil and POPs and can be used in soil cleaning by absorbing them. However, since the crop harvested from the contaminated area is inconvenient to use as a food raw material, it seems advantageous to evaluate the sunflower as a biomass energy source when the energy plant potential is evaluated.

It has been reported that the amount of energy obtained by the biomass energy conversion methods after the corn (*Zea mays*) plant was grown in contaminated land is 33,000-46,000 kW_h/ha. Also, in terms of CO_2 emissions,

21.000 kg/ha/year less emission occurs than a coal power plant. It is stated that Zn accumulation in the soil can be reduced by 0.4-0.7 mg/kg per year [33].

Werle et al. (2018) performed phytoremediation with *MiscanthusxGiganteus* and *Sida hermaphrodita* crops in contaminated soils in two separate regions [34]. It has been stated that the contaminated soil also affects the content of the cultivated energy plant and thus the application of the thermal transformation method [34]. In their study, Trinh et al. (2018) applied NPK fertilizer to the soil during the phytoremediation process [35]. It has been determined that the activation energy of plants grown in the soil where NPK fertilizer is applied has increased compared to control application during conversion to biomass energy. After the phytoremediation procedure performed with poplar (*Populus* L.) by Aghaalikhani et al. (2017), the plant residues were evaluated in the gasification process, and according to the obtained results, it was found that the heavy metal absorbed by the plant did not cause a significant problem in the gasification process and the observed effect was negligible [36].

When the Marmara region is examined in terms of soil pollution, it is seen that the most criticial pollution factors are heavy metal and permanent organic compounds due to intense industrial activity and urbanization. Considering the pollution factors and climate characteristics of the region, energy crops such as corn (*Zea mays*), castor oil plant (*Ricinus communis*), sunflower (*Helianthus annuus*), millet (*Sorghum bicolor*) are recommended. When the pollution factors in the Aegean region are examined, heavy metal pollution originating from the thermal power plant stands out, especially in the Muğla province. It is remarkable that the areas affected by the pollution are in the direction of the prevailing wind. In this context, heavy metal accumulator energy plants such as mischantus (*Mischantus* sp.), canola (*Brassica napus*), corn (*Zea mays*), wild artichoke (*Cynara cardunculus*) are recommended for these areas. When the soil pollution factors in the Mediterranean region are examined, heavy metal and PAHs accumulator energy crops such as jatropha (*Jatropha* L.), jojoba (*Simmondsia chinensis*), corn (*Zea mays*), wild artichoke (*Cynara cardunculus*), sesame (*Sesamum indicum*) are recommended for these areas. When the soil pollution factors in the Central Anatolia region are analyzed, excessive fertilizer usage, wild solid domestic wastes, industrial wastes and thermal power plants are encountered. From these sources, heavy metal and permanent organic compounds cause contamination. In the contaminated soils in this region, miscanthus (*Mischantus* sp.), sugar beet (*Beta vulgaris*) are recommended.

4. RESULTS

Soil contamination in Turkey is a problematic situation with potential long-term effects on environmental and human health. In this study, phytoremediation technologies with energy plants in soil contamination and current situation regarding the soil contamination in Turkey are reviewed. Some measures are taken in the country to prevent soil pollution. It is stated that, especially in Hatay and Erzurum provinces, efforts to combat erosion [18]. In the fight against erosion, energy plants suitable for the climate of the region will have an economic return and soil cleaning by minimizing the pollution factors. In Turkey, severe and very severe erosion is 61.3 million ha or 78.7 percent of the total area of the country; wind erosion is active on about 500 thousand ha [37]. The major areas with salt-affected soils in Turkey are Konya-Ereğli, Aksaray and Malatya plains of Central Anatolia, and the alluvial plains of lower Seyhan, Iğdır, Menemen, Bafra, Söke, Acıpayam and Salihli. The distribution of the salt-affected arable lands are 60 percent slightly saline, 19.6 percent saline, 0.4 percent alkali and 8 percent saline-alkali. Our findings suggest that there are also magnesium soils in Denizli-Acıpayam, potassium-nitrate-alkali soils in Nigde- Bor, Kayseri, and gypsiferous soils in Central Anatolia although sodium salts are the main components of the salt-affected soils. Compared to Turkey, intensive studies are carried out on growing energy plants in contaminated soils and obtaining energy from the biomass obtained through conversion methods in Europe. When phytoremediation and biomass energy are evaluated for our country, it is seen that there are few laboratory and pilot-scale studies on the subject. However, with more research on the applicability of the approach and regional integrated efforts, contaminated land rehabilitation and management in Turkey will accelerate the regional studies which are carried out by the research institutions. At same time, the policymakers will develop economic, environmental and social benefits in order to regain the contaminated areas based on these studies.

REFERENCES

[1] Chakravarty, P., Bauddh, K., Kumar, M. Phytoremediation: A Multidimensional and Ecologically Viable Practice for the Cleanup of Environmental Contaminants, K. Bauddh et al. (eds.), Phytoremediation Potential of Bioenergy Plants, 2017.

[2] Raskin, L., Smith, R. D. and Salt, D. E. Phytoremediation of metals: using plants to remove pollutants from the environment Abbreviation EDTA ethylenediaminetetraacetic acid. Current Opinion in Biotechnology, 8221–226. 1997.

[3] Ismail, S. Phytoremediation: A Green Technology. Approaches to Heavy Metal Tolerance in Plants, 69–87. 2012.

[4] Okumus, K., 2002. Turkey's Environment—A review and evaluation of Turkey's environment and its stakeholders. The Regional Environmental Center for Central and Eastern Europe.

[5] www.tuik.gov.tr

[6] Ceritli, I., 1997. Soil problem of Turkey. J. Ecol. 22, 4–8 (in Turkish).

[7] Özkul, C. 2008. İzmit (Kocaeli) Civarında Endüstrileşmenin Toprak Ağır Metal Derişimine Etkisi. Uygulamalı Yerbilimleri Sayı:2 (Ekim-Kasım 2008) 1-9.

[8] Çetindamar, D., Veli, S., Öztürk, T., Arslanbaş, D., Aslan Klavuz, S., Doğru Parmak, Ş., Doğan, E. Topraklarda PCB ve PAH'ların İncelenmesi: Alikahya Bölgesi /Politeknik Dergisi, Cilt 17, Sayı 3, 2014.

[9] Sanli, G.E.,Sivri, S.(2019).Farklı Toprak Kullanım Alanlarında Poliaromatik Hidrokarbon (PAH) Kirliliği: İlkbahar Mevsimi. DEUFMD, 21(63), 805-817.

[10] Meşeli, A. 2010. İznik Gölü Havzasında Çevre Sorunları. Dicle Üniversitesi Ziya Gökalp Eğitim Fakültesi Dergisi, 14, 134-148.

[11] Dartan, G., Toröz, İ. 2013. Güney Marmara Bölgesinde Tarım Topraklarında Ağır Metal Kirliliğinin Araştırılması. Marmara Üniversitesi, Fen Bilimleri Dergisi, 25 (1) (2013) 24-40.

[12] Ordu Sağlam, Ş. 2005. Ergene Havzasındaki Yüzeysel Su Kirlenmesinin Çevre Bilgi Sistemi Yardımıyla İzlenmesi ve Kontrol Yöntemlerinin Geliştirilmesi. Yıldız Teknik Üniversitesi, Fen Bilimleri Enstitüsü, Çevre Mühendisliği Anabilim Dalı, Doktora Tezi, s. 39, İstanbul.

[13] Sürek, H. 2003. Ergene Nehri Kirliliğinin Çeltik Tarımına Olan Etkisi, HASAD Aylık Gıda, Tarım ve Hayvancılık Dergisi, Yıl 18, Sayı 213, Mart 2003, s. 70-71, İstanbul.

[14] Kocaman, H., Koldere Akın, Y., Oğuzhan, A. 2011. Trakya'da Ergene Nehri Kirliliğinin Tarım Üretimine Olan Etkisi: Edirne Örneği. Karadeniz Fen Bilimleri Dergisi / The Black Sea Journal of Science ISSN: 1309-4726 FABA 2011 SYMPOSIUM SPECIAL ISSUES Yıl/Year:3 Cilt/Volume:2 Sayı/Number:5 Sayfa/Page 89-104.

[15] Adiloğlu, S., Sağlam, T.M. 2015. Karayolu Kenarlarındaki Tarım Arazilerindeki Topraklarda Ekstrakte Edilebilir Kobalt (Co) İçerikleri. AKU J. Sci. Eng. 15 (2015) 035403 (24-29) DOI: 10.5578/fmbd.9981

[16] Dökmeci, A.H., Çelik, S.Ö., Kaykıoğlu, G., Öngen, A. 2017. Tekirdağ'da Çorlu İlinde Endüstriyel Alanlardaki Toprakta Ağır Metal Kirliliğinin Çevresel ve İnsan Sağlığı Açısından Etkileri. J. BAUN Inst. Sci. Technol., 19(2), 256-263, (2017) DOI: 10.25092/baunfbed.342418

[17] Haktanır, K., Sözüdoğru, S., Karaca, A., Arcak, S., Çimen, F., Topçuoğlu, B., Türkmen, C., Yıldız, H. 2009. Muğla-Yatağan Termik Santrali Emisyonlarının Etkisinde Kalan Tarım ve Orman Topraklarının Kirlilik Veri Tabanının Oluşturulması ve Emisyonların Vejetasyona Etkilerinin Araştırılması, Ankara Üniversitesi Çevrebilimleri Dergisi, 1,1, 16, 1309-1107.

[18] Türkiye Çevre Sorunları ve Öncelikleri Değerlendirme Raporu (2017 verileriyle). 2019. Çevresel Etki Değerlendirmesi, İzin ve Denetim Genel Müdürlüğü Çevre Envanteri ve Bilgi Yönetimi Dairesi Başkanlığı. Ankara https://ced.csb.gov.tr/turkiye-cevre-sorunlari-ve-oncelikleri-raporu-i-82679

[19] Karaca, A., Türkmen, C., Arcak, S., Haktanır, K., Topçuoğlu, B., Yıldız, H. 2009. Çayırhan Termik Santralı emisyonlarının yöre topraklarının bazı ağır metal ve kükürt kapsamlarına etkilerinin belirlenmesi, Ankara Üniversitesi Çevrebilimleri Dergisi, 1,1, 16, 1309-1107, DOI: 10.1501/0005042.

[20] Candemir, F., Özdemir, N. 2010. Samsun ili arazi varlığı ve toprak sorunları. Anadolu J. Agric. Sci., 2010,25(3):223-229.

[21] Baltas, H., Sirin, M., Gökbayrak, E., Ozcelik, A.E., 2020. A case study on pollution and a human health risk assessment of heavy metals in agricultural soils around Sinop province, Turkey. Chemosphere 241. https://doi.org/10.1016/j.chemosphere.2019.125015.

[22] Kaptanoğlu, S., Bakır, A. 2017. Van Gölü'ne Dökülen Engil Çayı'nın Mansabındaki Su ve Toprak Örneklerinde, Ağır Metal Miktarlarının Mevsimsel Değişimlerinin İncelenmesi. Yüzüncü Yıl Üniversitesi Fen Bilimleri Enstitüsü Dergisi/ Journal of the Institute of Natural & Applied Sciences 22 (2): 102-109, 2017.

[23] Aydoğdu, B.İ. 2014. Yerel ve Bölgesel Düzeyde Çevre Kirliliği Sorunları: Elazığ İli Örneği. Fırat Üniversitesi Harput Araştırmaları Dergisi Cilt:I, Sayı: I, Elazığ.

[24] Elazığ İl Çevre Durum Raporu, 2011, T.C. Çevre ve Şehircilik Bakanlığı, Elazığ Çevre ve Şehircilik İl Müdürlüğü, Elazığ.

[25] Koca, Y.K. 2019. Termik Santralin Çevresel Kirletici Etkisinin Toprak Kirlilik Yönetmelikleri Çerçevesinde Değerlendirilmesi. KSU J. Agric Nat 22(Ek Sayı 1): 148-153, 2019. DOI:10.18016/ksutarimdoga.vi.533995

[26] Goel, G., Makkar, H. P. S., Francis, G. and Becker, K. Phorbol esters: Structure, biological activity, and toxicity in animals. International Journal of Toxicology, 26(4), 279–288. doi:10.1080/10915810701464641, 2007.

[27] Tan, T., Lu, J., Nie, K., Deng, L. and Wang, F. Erratum to Biodiesel production with immobilized lipase: A review [Biotechnology Advances, 2010, 28, 5, 628-34]. Biotechnology Advances, 28(6), 937. doi:10.1016/j.biotechadv.2010.07.007, 2010.

[28] Bauddh, K., Singh, K., Singh, B. and Singh, R. P. Ricinus communis: A robust plant for bio-energy and phytoremediation of toxic metals from contaminated soil. Ecological Engineering, 84, 640–652. doi:10.1016/j.ecoleng.2015.09.038, 2015.

[29] Ogunniyi, D.S. Castor oil: a vital industrial raw material. Biores. Technol. 97, 1086–1091, 2006.

[30] Conceicao, M.M., Candeia, R.A., Silva, F.C., Bezerra, A.F., Fernandes, V.J., Souza, A.G. Thermoanalytical characterization of castor oil biodiesel. Renew. Sustain. Energy Rev. 11, 964–975. 2007.

[31] Başalma, D. and Pashazadeh, M. Hintyağının (Ricinus communis L.) Önemi, Bitkisel Özellikleri ve Tarımı. Uludağ Üniversitesi Ziraat Fakültesi Dergisi, 25(2), 57–67. 2015.

[32] Hunce, S. Y., Clemente, R. and Bernal, M. P. . Energy production potential of phytoremediation plant biomass: Helianthus annuus and Silybum marianum. Industrial Crops and Products, 135(March), 206–216. doi:10.1016/j.indcrop.2019.04.029, 2019.

[33] Meers, E., Slycken, S. Van, Adriaensen, K., Ruttens, A., Vangronsveld, J., Laing, G. Du, … Tack, F. M. G. The use of bio-energy crops (Zea mays) for ' phytoattenuation ' of heavy metals on moderately contaminated soils: A field experiment. Chemosphere, 78(1), 35–41. doi:10.1016/j.chemosphere.2009.08.015, 2010.

[34] S., Tran, K. Q., Magdziarz, A., Sobek, S., Pogrzeba, M. ve Løvås, T. Energy crops for sustainable phytoremediation – Fuel characterization. Energy Procedia, 158(2018), 867–872. doi:10.1016/j.egypro.2019.01.223, 2019.

[35] Trinh, T. T., Werle, S., Tran, K. Q., Magdziarz, A., Sobek, S. ve Pogrzeba, M. Energy crops for sustainable phytoremediation-Thermal decomposition kinetics. Energy Procedia, 158, 873–878. doi:10.1016/j.egypro.2019.01.224, 2019.

[36] Aghaalikhani, A., Savuto, E., Di Carlo, A. ve Borello, D. Poplar from phytoremediation as a renewable energy source: Gasification properties and pollution analysis. Energy Procedia, 142, 924–931. doi:10.1016/j.egypro.2017.12.148, 2017.

[37] Status of the World's Soil Resources. Main Report. FAO.2015

GEOPOLYMER CEMENT PRODUCTION IN THE STRUGGLE TO GLOBAL WARMING

Sevgi Özen
Recep Tayyip Erdoğan University, Department of Geological Engineering, Rize/Turkey
Email: sevgi.ozen@erdogan.edu.tr

ABSTRACT

Concrete made from ordinary Portland cement is one of the most popular and widely used building materials. Manufacturing of OPC generates the chemical reactions that releases large amount of CO_2 into the atmosphere. Today, the world cement industry is responsible for approximately 1.35 billion tons of the total greenhouse gas emissions. Therefore, the efforts have been made to develop building materials alternative to OPC has increased greatly in recent years. To produce environmentally friendly concrete, geopolymers, as new types of cement, attract many researchers. In the production of geopolymer, there is no need for a process at high temperature as in Portland cement. In this way, CO_2 emissions and energy consumed are reduced, thus reducing production costs. Compared to OPC, geopolymers also have many technical advantages such as high compressive strength, high acid resistance, low shrinkage and low alkali silica reaction. Source materials for the synthesis of geopolymers have an important role in final properties of the geopolymers. Natural pozzolans, one of the starting materials for geopolymers, is readily available worldwide, yet its use is limited. The technology of making geopolymer cement using local pozzolanic materials from Bayburt tuff (Gümüşhane) and Pileki Stone (Rize) and the results of laboratory tests conducted is carried out in this study. In conclusion, Bayburt tuff and Pileki stone-based geopolymer cements show considerable mechanical development in terms of construction industry and also it is able to reduce the effects of global warming. In addition, it is found that Bayburt tuff is more reactive than Pileki stone.

Keywords: Geopolymer, Global warming, Environmental pollution, Bayburt tuff, Pileki Stone.

1. INTRODUCTION

The production of cement is one of the most significant industrial activities with respect to volume of CO_2 emissions. The production of ordinary Portland cement (OPC) contributes approximately 7% of greenhouse gas emissions [1]. Some of these CO_2 emissions from OPC production are resulting from calcination of limestone, while the other emissions are due to the usage of fossil fuel. China is one of the countries that has the worst cement production in the world at 826.9 million metric tons in 2019. In addition, CO2 emissions from cement production were determined for India, USA, Turkey and South Korea is 143.7 million metric tons, 41.3 million metric tons, 30.4 million metric tons, 22.6 million metric tons, respectively [1]. Furthermore, cement production is an energy intensive process, which represents approximately 30% of total production cost [2]. Electrical power consumption of a cement plant is approximately 120 kWh per ton of cement [2]. Besides, another problem facing today is the emission of pollutants which causes additional environmental pollution. Therefore, alternative binding materials have been searched in order to replace Portland cement in concrete. The geopolymer technology which is also named as green cement reserves a considerable promise in the construction industry as an alternative binding material to the OPC.

In 1978, Davidovits developed inorganic and amorphous polymeric material with excellent physical and mechanical properties, which has potential to replace OPC [3]. According to literature [4], geopolymer cement has the crucial potential to reduce greenhouse gas emissions nearly by 80%. Besides, geopolymers also have many technical advantages such as high compressive strength, high acid resistance, low shrinkage and low alkali silica reaction when compared to OPC. Geopolymers consist of three dimensional amorphous structure resulting from polymerization of alumina/silica-hydroxy species and oligomers in an alkaline environment [3]. The

mechanism of geopolymerization can be divided into three main stages, which involves deconstruction, polymerization and stabilization. As a result of these geopolymeric reactions, solid and stable materials are formed [3].

Starting materials for the synthesis of geopolymers have an important role in final properties of the geopolymers. Generally, any material rich in silica and alumina can be a source material for the synthesis of geopolymer binder. In literature, properties of fly ash-based geopolymers have been largely studied but less information is available for natural pozzolan-based geopolymers despite their low cost, readily availability and vast quantity worldwide. Therefore, further studies are needed to explore the possible utilization of natural pozzolan-based geopolymers. Furthermore, the main advantage of local raw materials like Bayburt Tuff and Pileki Stone is being economical because it is easy to reach and mine. Therefore, the present study is focused on improving the knowledge of the mechanical behavior of natural pozzolan based geopolymers. At the same time, the possible usage of natural pozzolanic materials (Bayburt tuff and Pileki Stone) are examined, which could contribute to the reduction of the effect of global warming. This study, therefore, examines the properties of natural pozzolan-based geopolymers by focusing on the compressive strength analysis.

2. MATERIALS AND EXPERIMENTAL METHODS

2.1 Materials

Bayburt tuff notated as BT was obtained from a natural zeolite deposit in Gümüşhane, Turkey and Pileki Stone notated as PS came from Rize, Turkey. The samples were crushed by a ball mill (MG171 Automatic Swing Mill) during a time period of 30 min. Sodium silicate (Na_2SiO_3) and sodium hydroxide (NaOH) was used as an alkaline activator. The Na_2SiO_3 solution has a composition by weight of 27.7% SiO_2, 9.8% Na_2O and 62.5% H_2O. The NaOH solution (12M) was obtained by dissolving NaOH pellets of 98% purity in distilled water.

2.2 Geopolymer Synthesis

The starting materials were mixed with NaOH solution for 3 min. Next, sodium silicate solution was added to the mixture and mixed for another 3 min. The sodium silicate /sodium hydroxide ratio of 2 and material/activator ratio of 2 were used. The mixture was then cast into 50 mm^3 molds and covered with a thin film to avoid moisture evaporation. The specimens were cured at 50°C for 7, 28 and 56 days.

2.3 Experimental Methods

The chemical composition of starting materials was determined using X-ray fluorescence (Rigaku, ZSX Primus II). The particle size distribution of the two samples was measured by laser diffraction using a Malvern Mastersizer 2000 laser diffractometer. The Blaine fineness was determined according to ASTM C204 standard method [5]. The mineralogical phases of raw materials were examined with X-ray diffraction (XRD) analysis by using Philips PW 1730 diffractometer with Ni-filtered, CuKα1 radiation, operating at 40 kV, 30 mA. The compressive strength testing was performed on a universal testing device (Utest 6410, load cell = 10 kN) at a loading rate of 6 Ns^{-1}. Samples were tested after 7, 28 and 56 days. All strength measurements were achieved from the average of three samples.

3. RESULTS AND DISCUSSION

3.1 Zeolite Characterization

The chemical composition of starting materials is shown in Table 1. The total SiO_2 and Al_2O_3 values of BT and PS are 84.33% and 66.14%, respectively, which could demonstrate a higher reactivity of BT than PS. On the other hand, all oxides values of PS are higher than BT except SiO_2 and K_2O values.

Table 1. Chemical composition of the raw materials

Chemical Compositions (%)	BT	PS
SiO_2	70.71	45.98
Al_2O_3	13.62	20.16
Fe_2O_3	1.21	8.53
CaO	3.15	6.57
MgO	1.09	3.74
K_2O	4.56	3.88
Na_2O	0.47	5.02
L.O.I	5.19	6.12
Total	100	100

The particle size distributions of Bayburt tuff (BT) and Pileki Stone (PS) are presented in Fig. 1. The Bayburt tuff (BT) particles are finer than Pileki Stone (PS) particles, which might designate higher reactivity of BT than PS. Blaine fineness of BT and PS samples are 5282 m^2/kg and 4829 m^2/kg, respectively, according to the particle size analysis.

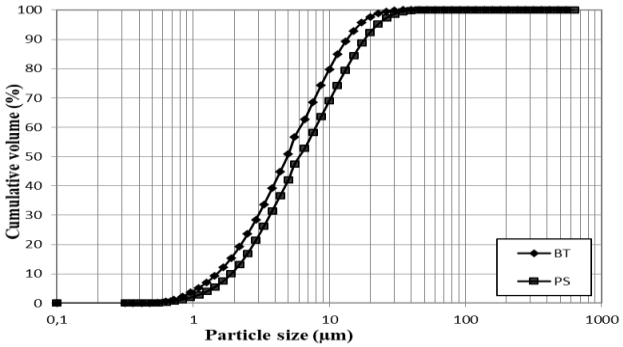

Figure 1. Grain size distributions of Bayburt tuff (BT) and Pileki Stone (PS).

XRD analysis was carried out to detect the phases present in the raw materials. According to the XRD pattern, clinoptilolite is the major phase (2θ of 9.96, 11.30, 22.52 with *d*-spacing values of 8.86, 7.82, 3.94 Å, respectively) for the Bayburt tuff (BT) sample. Quartz (2θ of 26.72, 20.91 with *d*-spacing values of 3.33 and 4.25 Å) and feldspar (2θ of 27.50 with *d*-spacing value of 3.24 Å) are also presented in the XRD pattern of BT (Figure 2).

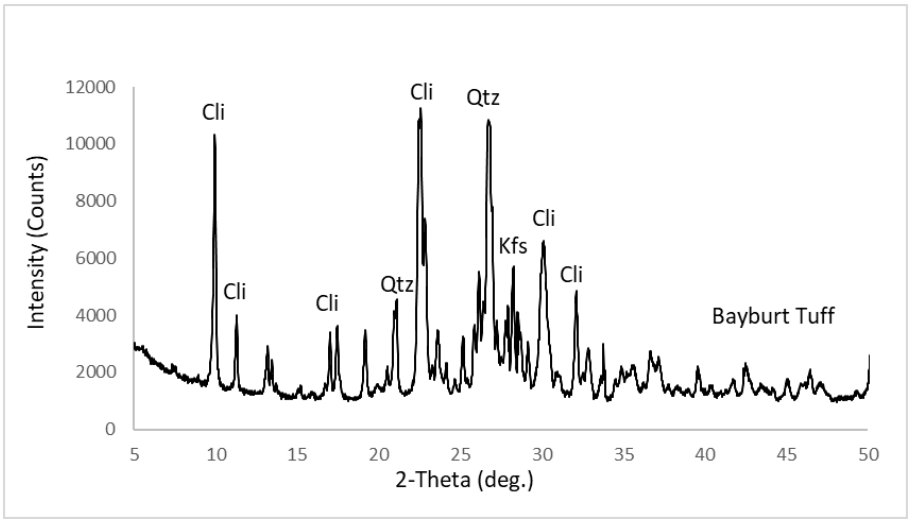

Figure 2. XRD pattern of Bayburt tuff (BT).

XRD analysis of PS, on the other hand, reveals the presence of analcime (2θ of 15.79, 25.92, 30.56 with *d*-spacing values of 5.60, 3.43, 2.92 Å), quartz (2θ of 26.77 with *d*-spacing value of 3.32 Å) and feldspar (2θ of 23.56, 26.77, 27.69 with *d*-spacing values of 3.77, 3.32, 3.21 Å).

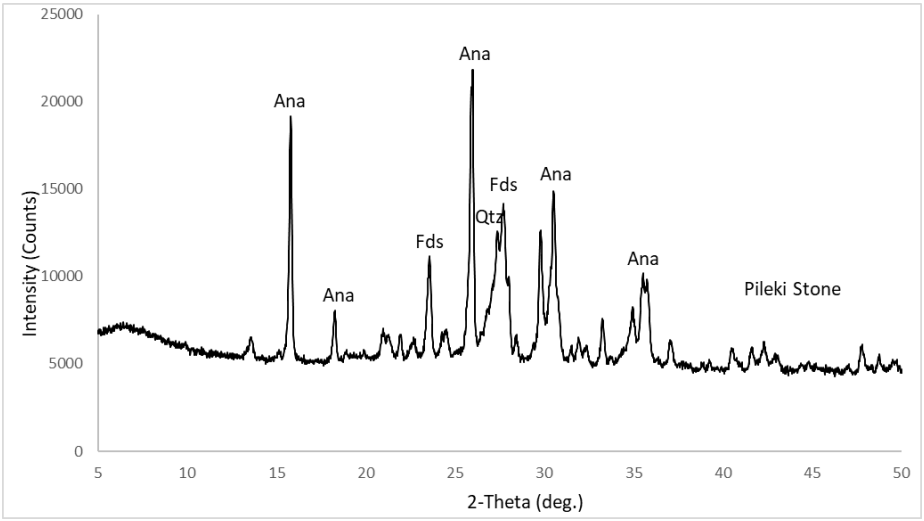

Figure 3. XRD pattern of Pileki Stone (PS).

3.2 Mechanical Properties

Depending on the raw materials used, the development of the compressive strengths differs. Bayburt tuff based geopolymer gives a higher compressive strength than Pileki Stone based geopolymer at all testing ages. The BT based geopolymer activated with Na_2SiO_3 and NaOH gains remarkably high compressive strength between 7 and 56 days. PS, on the other hand, leads after 28 days to little development of compressive strength. The difference in mechanical development is attributed to the nature of phases found in starting materials. Clinoptilolite phase found in Bayburt tuff might have an important role in geopolymeric reaction.

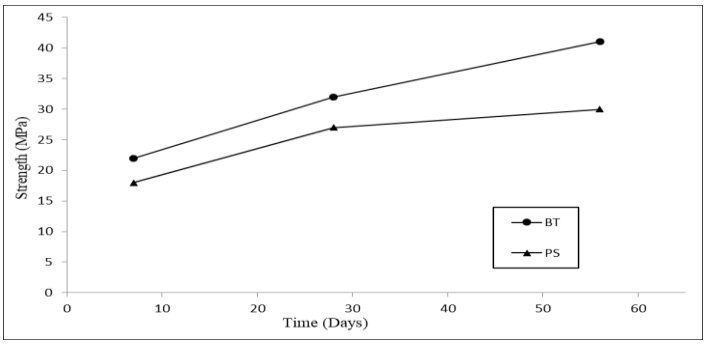

Figure 4. The compressive strengths of Bayburt tuff (BT) and Pileki Stone (PS) geopolymers at 7, 28 and 56 days.

3. CONCLUSIONS

In this study, geopolymer cement production in the struggle to Global warming and the possible usage of natural pozzolanic materials were studied. Based on the experimental analysis, the main conclusions can be drawn as; Bayburt tuff and Pileki stone-based geopolymer cements show considerable mechanical development in terms of construction industry and also it is able to reduce the effects of global warming. In addition, it is found that Bayburt tuff is more reactive than Pileki stone.

REFERENCES

[1] International Energy Agency World Business Council for Sustainable Develepment Cement Technology Roadmap 2009: Carbon Emissions Reductions up to 2050 (2009).

[2] Parmar, M., Solanki, D. & Vegada, B. Energy And Exergy Analysis Of Cement Rotary Kiln, *International Journal of Advance Engineering and Research Development*, **3**, 284-293, 2016.

[3] Davidovits, J., Geopolymers-inorganic polymeric new materials, *Journal of Thermal Analysis*, 37, 1633-1656, 1991.

[4] Tuner, L.K. & Collins, F.G. Carbon dioxide equivalent (CO2-e) emissions: a comparison between geopolymer and OPC cement concrete, *Construction and Building Materials*, 43, 125-130, 2013.

[5] American Society for Testing and Materials (ASTM) # C204-11e1, Standard Test Methods for Fineness of Hydraulic Cement by Air-Permeability Apparatus, ASTM International, West Conshohocken, PA, USA) 2011.

COMPARATIVE ENVIRONMENTAL SUSTAINABILITY OF TWO DIFFERENT SIZES OF WIND TURBINES

Burçin ATILGAN TÜRKMEN*
*Bilecik Seyh Edebali University, Department of Chemical Engineering, Bilecik/Turkey
Email: burcin.atilganturkmen@bilecik.edu.tr

ABSTRACT

Wind power is one of the cleanest electricity sources today; unlike fossil fuels, wind turbines do not release greenhouse gasses or pollutants when generating electricity. However, some environmental impacts associated with the construction of wind turbines need to be considered. The goal of the study is to compare the life cycle environmental impacts of electricity generation from 0.75 MW and 4.5 MW of onshore wind turbines. The assessment of environmental sustainability has been carried out using life cycle assessment. The scope of the study is from cradle to gate, comprising electricity generation as well as plant construction. Both fixed (tower and basement) and moving parts (rotor, nacelle, mechanics, cabling, and electronics) are considered for the construction of the turbines, considering the manufacturing of construction materials, transportation, and energy requirements for installation. The LCA study has been carried out following the guidelines in the ISO 14040/44 standards. The environmental impacts have been calculated according to the CML methodology. The results indicate that the impacts from the 4.5 MW turbine are higher than for the 0.75 MW turbine (by 43% - 82%). However, its TETP is 84% lower than for the small turbine. GWP and MAETP are the same for the turbines. The production of the wind turbine stage is the main contributor to the impacts for both turbines. Future research should extend the system boundaries including decommissioning of the wind turbines considered in this study.

Keywords: Energy systems, Wind turbines, Environmental sustainability

TÜRKİYE ŞARTLARİNDA FİTOREMEDİASYON TEKNİĞİNDE KULLANILAN VEYA KULLANILMA POTANSİYELİ OLAN BAZI BİTKİLER

Erkan YILMAZ*, Ömer KILIÇ*, Muhammad ZAFAR, Mushtaq AHMAD****
* Adıyaman University, Faculty of Pharmacy, Department of Basic Science of Pharmacy, Adıyaman/Turkey.
2 Department of Plant Sciences, Quaid-I-Azam University, Islamabad/Pakistan.
*Corresponding author Email: erkanyilmaz77@yahoo.com

ÖZET

Endüstriyel gelişme, artan dünya nüfusu ve kentsel yaşamın beraberinde getirdiği çevre kirliliği insan sağlığı başta olmak üzere doğal yaşamı tehdit etmekte ve ciddi çevresel problemlere sebep olmaktadır. Çevresel kirlilikten kaynaklanan olumsuzlukları azaltmak için bu kirleticilerin doğal ortamdan uzaklaştırılmalarına yönelik teknikler de gelişmektedir. Kirlenmiş alanların iyileştirilmesinde (remediasyon) kullanılan geleneksel mühendislik yöntemleri pahalı olduğu için bunun yerine düşük maliyetli ve çevre dostu olan fitoremediasyon tekniği üzerinde yoğunlaşılmıştır. Fitoremediasyon, bitkiler kullanılarak insan aktiviteleri sonucunda kirletilmiş toprak, su ve havanın temizlenmesi olarak tanımlanmakta olup, bu yöntem bitki ile iyileştirmeye odaklanan, doğanın dengesini bozmayan, yapılabilirliği yüksek, su, sediment ve topraklarda kirleticileri parçalamak, sabitlemek ve uzaklaştırmak suretiyle temizlemeyi hedeflemektedir. Fitoremediasyon yöntemi ile arıtılabilen kirletici grupları arasında ağır metaller, radyoaktif maddeler, klorlu çözücüler, petrollü hidrokarbonlar, poliklorlu bifeniller, polisiklik aromatik hidrokarbonlar, klorlu pestisitler, organofosforlu pestisitler, patlayıcılar, nutrientler ve yüzey aktif maddeler sayılabilir.

Fitoremediasyon tekniğinde çevresel kirleticileri absorbe eden, dokularında yüksek seviyelerde biriktiren (hiperakümülatör) ve fiziksel, kimyasal ve biyolojik süreçler aracılığıyla detoksifiye eden bitkilerin kullanımı tercih edilmektedir. Fitoremediasyon yöntemi ile klorlu pestisitler, organofosforlu pestisitler ve poliklorlu bifeniller topraktan temizlenebilmektedir. Fitoremediasyon yönteminin başarılı olması için, kirliliğin yoğunluğu, kirliliğe toleranslı ve biriktirici bitki seçimi, bitkinin gelişimi için uygun ortamın hazırlanması ve takibi, iyileşmenin oluşacağı sürenin planlanması dikkat edilecek hususlardandır.

Bu çalışma ile çevre kirliliği ile bundan kaynaklı olumsuzlukları azaltmak için güncel ve en avantajlı tekniklerden biri olan fitoremediasyon tekniği ile ilgili konular vurgulanarak bu teknikte kullanılan veya kullanılabilme potansiyeli olan bazı bitkilerin tanıtılması hedeflenerek ilgili literatüre katkılar sağlanması amaçlanmıştır.

Anahtar Kelimeler: Fitoremediasyon, hiperakümülatör, bitki, çevre kirliliği.

OCCUPATIONAL HEALTH AND SAFETY IN ENERGY SECTOR

RÜZGAR ENERJİ SANTRALLERİNDE İŞ SAĞLIĞI VE GÜVENLİĞİ

Süleyman ŞİMŞEK*,Funda DOĞAN**
*İstanbul Aydın University, Department of Mechanical Engineering, İstanbul /Turkey
Email: suleymansimsek@aydin.edu.tr
**İstanbul Aydın University, Department of Occupational Health and Safety, İstanbul/Turkey
Email: fundogan@gmail.com

ÖZET

Ekonomik kalkınmanın ve toplumsal gelişmenin ana kaynağı olan enerji her geçen gün gereksinimi ve önemi artan bir konu olmaktadır. Enerji ihtiyacının devamlı artması, aynı zamanda var olan kaynakların kısıtlı ve tükenebilir olması, bizleri alternatif enerji kaynaklarını bulma ve geliştirme yoluna sokmuştur. Temiz ve yenilenebilir enerji kaynaklarından biri olan rüzgâr enerjisi çok eski tarihlerden günümüze kadar kullanılmıştır. Günümüzde ise modern rüzgâr türbinleri ile rüzgâr enerjisi elektrik enerjisine dönüştürülerek kullanılmaktadır. Ülkelerin gelişmişlik seviyelerini belirleyen rüzgâr enerji sektörü, ülkemizde de son yıllarda ciddi bir ivme kazanarak büyümeye devam etmektedir. Ülkemizde ve dünyada rüzgâr enerjisi sektörü yenilenebilir enerji kaynakları arasında en hızlı gelişen çevre dostu enerji kaynaklarındandır. Bu nedenle yenilenebilir enerji kaynakları arasında rüzgâr enerjisi, dünyada birçok ülkenin tercih ettiği alternatif bir enerji türü olmaktadır. Birçok üretim sektöründe sıklıkla görülmeyen ağır hava şartlarındaki merkezi yerleşimlerden uzak çalışma alanlarında rüzgâr enerjisi sektörüne özel bir dizi riskler bulunmaktadır. Dolayısıyla, bu sektörde iş sağlığı ve güvenliği ile ilgili riskler genellikle diğer üretim sektörlerindeki risk faktörlerinden temel olarak farklılık göstermektedir. Yaşanmış ve yaşanacak olan iş kazalarının kaza türlerinin belirlenebilmesi ancak elde edilen veriler aracılığıyla analiz edilebilir ve mükemmel bir sonuca varılabilir. Bu çalışmada Türkiye'deki rüzgâr enerjisi santrallerinde meydana gelen yaralanmalı iş kazaları ve bunların nedenleri değerlendirilmiştir.

Anahtar Kelimeler: Rüzgâr Enerjisi, Rüzgâr Enerji Santrali, İş Sağlığı ve Güvenliği

POWER PLANTS
AND
POWER GENERATION

AUXILIARY POWER GENERATION DESIGN FOR POWER PLANTS WITH USING THERMOELECTRIC GENERATORS

Şükrü Kaan YENER*, Burak AKBOĞA , Barbaros ÇETİN*****
* İhsan Doğramacı Bilkent University, Department of Mechanical Engineering Ankara/Turkey
Email: kaanyener97@gmail.com
** İhsan Doğramacı Bilkent University,Department of Mechanical Engineering, Ankara/Turkey
Email: burakboga1996@gmail.com
***İhsan Doğramacı Bilkent University, Department of Mechanical Engineering Ankara/Turkey
Email: barbaros.cetin@bilkent.edu.tr

ABSTRACT

Today, power plants are one of the main sources of energy production. Since fossil fuels such as natural gas are used in energy production, it is important to increase efficiency in terms of environmental concerns. Power generation efficiency of a power plant is generally varies between 25% and 40%. The waste heat recovery systems exist in a way that heating of buildings and industrial steam generation. The following proceeding will introduce waste heat recovery system with using thermoelectric generators (TEG), the operation of which is based on, Seebeck Effect. Sample data is provided by BilEnerji Power Plant for the analysis part. Mathematical modelling of thermoelectric generators are presented. A vertical rectangle type heat exchanger is designed, optimized and analyzed in terms of pressure drop and heat transfer coefficients. In this proceeding, this case is analyzed with the software MATLAB. During analysis, heat transfer coefficients, Peltier effect, Reynolds number, and Nusselt number for different correlations are used and the efficiency of TEG's were tried to maximize with changing the parameters given. Finally, the proceeding propose to use more efficient TEGs to run the system and using fin in heat exchanger will increase total electrical power output of TEGs.

Keywords: Thermoelectric Generators (TEG), Waste Heat Recovery (WHR), Power Plant, Exhaust Heat Recovery (EHR)

1. INTRODUCTION

World energy consumption has been increasing in line with the development of technology and increment of population. Primary energy consumption increased by 50% between 1984-2004 [1]. Industries and researchers have been studying on new technologies which would enhance the efficiency of current power plants and renewable energy sources to reduce fossil fuel consumption. The waste heat utilization significantly affects the efficiency of power systems. Although there are various options for waste heat utilization, recent technological developments on semiconductors have opened the way to use Thermoelectric Generators (TEGs) in waste heat recovery [2]. Thermoelectric generators are devices that produces electrical potential based on temperature difference which phenomenon is called as Seebeck Effect. It is a direct conversion of thermal energy to electricity. In a thermoelectric device, multiple of p- and n-type couples connected in series. So, size can vary from a small computer chip to a couple of meters. Efficiency of commercially available TEGs starts at 1% and could go up to 10% [9]. Although, conversion efficiency is low, TEGs have some advantages:

- Solid state devices: There are no moving parts or fluids inside TEGs [14].
- Highly reliable: TEGs could produce electricity for many years. Since no maintenance required for many years, there is no maintenance cost and no interruption of operation [3].
- Quiet and non-vibrating operation conditions since it is a solid state device.
- A wide range of application area: It could be used for both productions of hundreds of kilowatts or microscale sensors.

- Direct conversion of energy [1].
- Waste heat recovery of power generation

Although power output to cost ratio is low and an obstacle for high power systems, in recent years many car manufacturers developed thermoelectric generator systems for exhaust gases. Nissan, BMW and Honda successfully integrated TEG systems to cars. GMZ Energy which produces TEG for Honda Accord has developed an advanced Thermoelectric generator which has a total power output around 1 kW consist of five thermoelectric with power output around 200W. This result is achieved by using half-Heusler type materials instead of BiTe. Moreover, GMZ's project costs are co-funded by US army [2]. US Department of Energy's, whose main goal is to reduce America's dependence of oil, emphasize the thermoelectric generators as one of the encouraged research topic [3]. Due to highly reliable characteristic, TEGs are used in space applications. NASA sent many exploration shuttle to space with TEGs. These are Pioneer, Curiosity, Voyager, Apollo [1].

Power plant waste heat utilization with TEGs is relatively rare application than automobile exhaust and space applications. In this proceeding, energy harvesting from a gas motor waste heat at a conventional power plant with thermoelectric generators are introduced. The temperature and mass flow rate data are taken from Bil-Energy power plant in Ankara, Turkey. Waste heat is already utilized at Bil-Energy as heating of water in waste heat driven heat exchangers which is employed for the heating of Bilkent University. Proposed energy harvesting serves as preheater for boiler while electricity is produced by TEGs from temperature difference between water and exhaust gas. Since efficiency of TEGs are around %5, rest of 95% of heat is rejected to water [13]. Exhaust gas enters the preheater around 450ºC and water enters around 40ºC. Preheater geometry is a double pipe heat exchanger which has thermoelectric generators in between inner walls as seen in Figure 1. Four identical preheaters are assumed to be operated with the same mass flow rates and heat convection parameters. Values given in Table 2 is the sum of four mass flow rates. A mathematical modelling is introduced to calculate the temperature profiles of TEGs surfaces and to predict output of TEGs. Heat transfer coefficients of tube and annulus side is calculated [6]. Nusselt number correlations according to dimensions of the heat exchanger are used to calculate heat transfer coefficients. Heat transfer coefficient affects to temperature distribution, efficiency and output power along the channel is discussed. Moreover, the effects of mass flow rates are discussed.

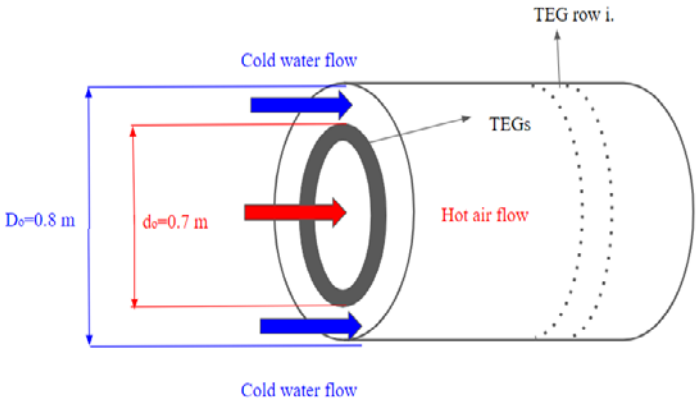

Fig. 1. Implementation case schematic representation

2.MATHEMATICAL MODEL

Thermoelectric generators consist of single P and N poles, arranged in specific patterns. The variation in dimension of TEGs are created with the P and N poles used in a thermoelectric generator. According to their size, a TEG can has 40, 70, and 128 P and N poles [11]. The thermoelectric analysis was calculated for a single P and N pole and was processed as 20 rows and 10 columns. The exit temperature calculated in one pole is accepted as the input temperature for the next pole and calculations are made over this cycle. While doing thermoelectric analysis, some assumptions are made as follows:

(1) The flow is steady state.
(2) The thermal resistance of copper is ignored as it is quite low.

(3) Air is treated as an ideal gas.
(4) Conduction and convection heat transfer in the ceramic part of TEG are ignored.
(5) Thermal contact resistance is ignored.
(6) Heat conduction is considered in one dimension which is perpendicular to flow direction.
(7) The thermal conductivity of the TEG is steady and constant.
(8) The reference TEG has 20 columns and 10 rows so it has 200 poles. All poles are considered to have same performance value with the calculated pole. The analysis is performed for the configuration given below [11].

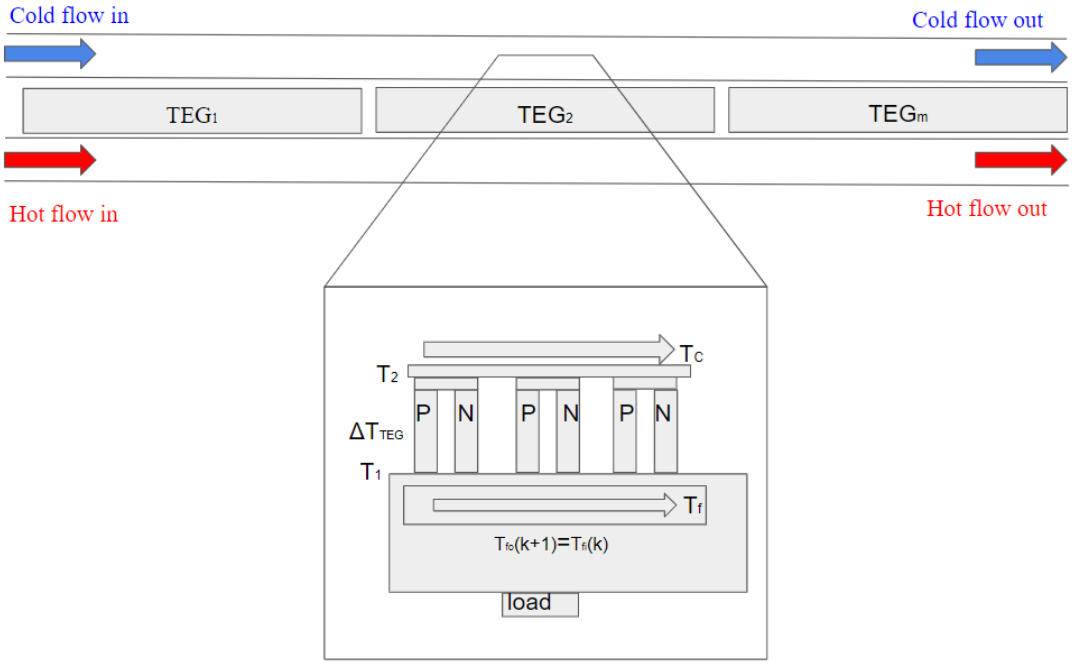

Fig. 2. A schematic diagram of the system

The absorbed and released heat in a TEG module can be modeled as follows:

$$q_1^n = h_1 A_1^n [-T_1^n + (T_{fi}^n + T_{fo}^n)/2] \quad (1)$$

$$q_2^n = h_2 A_2^n [T_2^n - (T_{co}^n + T_{ci}^n)/2] \quad (2)$$

where A_1^n and A_2^n are the heat exchange areas of the hot side and cold side in the j unit. $h_1$is the convective heat transfer coefficient of the hot side; $h_2$represents the convective heat transfer coefficient of the cold side. T_2^n and T_1^nrepresent the TEG side temperatures and $T_{fi}^n, T_{fo}^n$are hot air inlet and exit temperature values. In addition, T_{ci}^n, T_{co}^nrepresent the cold water inlet and exit temperature values.

The released and absorbed heat equations can also be modeled as:

$$q_1^n = \alpha I T_1^n + K^n (T_1^n - T_2^n) - I^2 R_1^n/2 \quad (3)$$

$$q_2^n = \alpha I T_2^n + K^n (T_1^n - T_2^n) - I^2 R_1^n/2 \quad (4)$$

where K^n is the thermal conductance of j unit; $R_1^n$is the electrical resistance of k unit of PN couple.
The combination of these equations, the following equations can be obtained:

$$h_1 A_1^n\,(T_{fo}^n - T_{fi}^n)/2 - T_1^k = \alpha I T_1^n + K(T_1^n - T_2^n) - I^2\,R_1^n/2 \quad (5)$$

$$h_2 A_2^n (T_2^n - (T_{ci}^n - T_{co}^n)/2)_{❑} = \alpha I T_2^n + K(T_1^n - T_2^n) - I^2\,R_1^n/2 \quad (6)$$

The temperature of hot gas and cold water must be changed after heat transfer in j unit, the equation can be used to consider this condition:

$$q_1^n = h_1 A_1^n(((T_{fo}^n - T_{fi}^n)/2) - T_1^n) = C_f M_f\,(Tfi^n - T_{fo}^n)/r \quad (7)$$

$$q_2^n = h_2 A_2^n (T_2^n - (T_{ci}^n - T_{co}^n)/2) = C_c M_c\,(Tco^n - T_{ci}^n)/r \quad (8)$$

where C is the specific heat capacity, and M is the mass flow rate.

As an assumption, all units are independent and load resistance is divided into the number of PN couples which is n. The current can be shown as:

$$I = U_n(R_2/m + R_1^n) \quad = \alpha\,(T_1^n - T_2^n)/(R_2/m + R_1^n) \quad (9)$$

where $R_2$is load resistance (external electric resistance), n is the total number of PN couples. It is seen that current is a function of T_2^n and T_1^n. Equations (5) -(9) creates a problem to solve because they are dependent equations. There is a need for iteration which is applied to current values. To solve this issue, the average value of current is considered and in the applicable ranges, the current is iterated.

The output power of a PN couple can be expressed as:

$$P^n = \alpha I T_1^n - \alpha I T_2^n - I^2 R_1^n \quad (10)$$

and the efficiency is:

$$\eta^n = k/q_1^n \quad (11)$$

The overall output power and efficiency can be written as:

$$P_{overall} = r\sum_{k-1}^{m} P^n \quad (12)$$

$$\eta_{overall} = \sum_{j-1}^{m} P^n / \sum_{j-1}^{m} q_1^n \quad (13)$$

The implementation cases are considered for a heat exchanger with parallel flow. Hot air and cold water are used to analyze the effect of TEGs in a heat exchanger. Total heat coefficient of air and is calculated with the given formula:

$$\mathrm{h} = Nu\;k/D_e \quad (14)$$

where Nu is the Nusselt number of air achieved with an appropriate correlation and k is the thermal conductivity of air [7]. For a concentric double pipe heat exchanger, $D_e$is calculated with the dimensions of heat exchanger:

$$D_e = 4\,A_c/P_h \quad \text{where } P_h = \pi d_0 \text{ and } A_c = \pi\,(D_o^2 - d_0^2)/4. \quad (15)$$

In addition, Reynolds number is used to determine which correlation will be chosen to calculate Nusselt number [12].

Table 1. Parameters of the TEG used in analysis

Parameters	**Values**
Seebeck Coefficient, α^n	$40 + 0.2T$ [μV/K]
Electrical Resistivity, ρ^n	1.04×10^{-5}[Ωm]
Thermal Conductivity, k^p, k^n	$1.5, 2.5[W/mK]$
Height, H	$0.005[m]$
Sectional Area , A_n	$0.01 \times 0.01[m^2]$
TEG Area, A_t	$0.15 \times 0.50[m^2]$
Convection Area ,A_c	$0.015 \times 0.025[m^2]$
Number of PN Junction of Each TEG	10×20
Number of TEG in Each Row	2

Table. 2. Implementation Case Parameters

Implementation Case Parameters	**Values**
Heat Exchanger Out Diameter, D_o	$0.86[m]$
Heat Exchanger Pipe Diameter, d_o	$0.64[m]$
Exhaust Air Inlet Temperature , T_f	450[℃]
Cooling Water Inlet Temperature, T_c	40[℃]
Convection Heat Transfer of Air, h_1	$200 - 2000[W/m^2\,K]$
Convection Heat Transfer of Water, h_2	$2000[W/m^2\,K]$
Exhaust Air Mass Flow Rate , m_f	$10[kg/s]$
Cooling Water Mass Flow Rate, m_c	$22[kg/s]$

3. RESULTS AND DISCUSSION

Parameters that used in proceeding are listed in Table 1 and taken from Wang et al [2]. Moreover, Table 2 list other parameters that are specific to this study such as inlet temperatures, mass flow rates and size of preheater energy production heat exchanger. Above 55ºC is desired for water outlet temperature is desired for heating process.

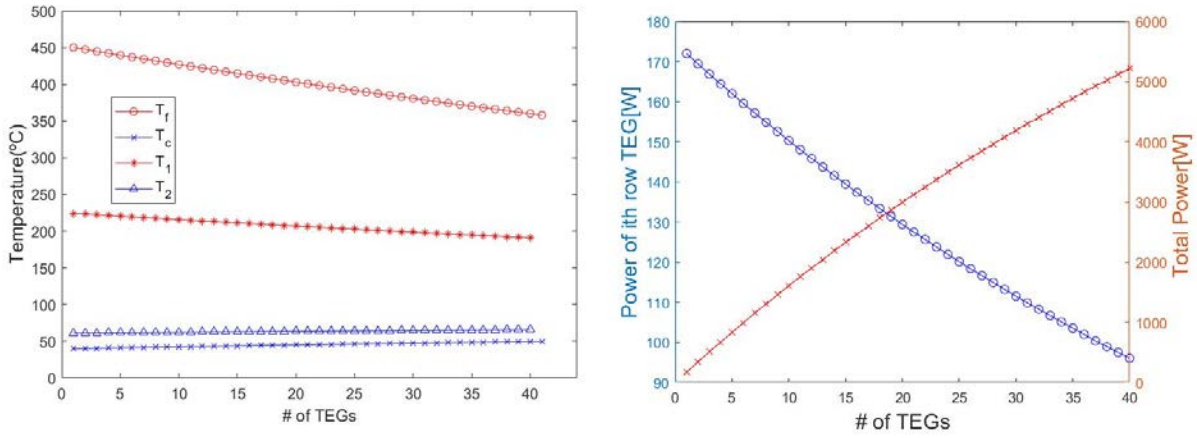

(A) **(B)**

Fig. 3. (A) Temperature distributions in the heat exchanger and TEG. **(B)** Total power produced and power for each row of TEG

Fig. 3A shows that results of temperature distributions with given parameters. Hot exhaust gases enter at 450 ºC and leaves system at 358ºC whereas cold water enters heat exchanger at 40ºC and leaves at 49. ºC. Moreover surface temperature of hot side starts from 224ºC and goes down until 190.8ºC whereas cold side of TEGs surface temperature starts from 61.2ºC and decreases until 65.7ºC.Fig. 3B shows that total power produced and power produced by each row of TEG's. Since one TEG has 0.5-meter-long, 40 corresponds to last TEG and 20 meter from the inlet. Total 5200 Watts of electrical energy is produced from 4 preheaters. As seen in figure, power produced of first TEG is nearly 2 times higher than last one due to reduced efficiency shown in Fig. 4 and reduced temperature difference between surfaces of TEGs.

Fig. 4 shows that efficiency of TEG efficiency for each row of preheater. Average efficiency is shown as dotted line and its value is 5.55%.

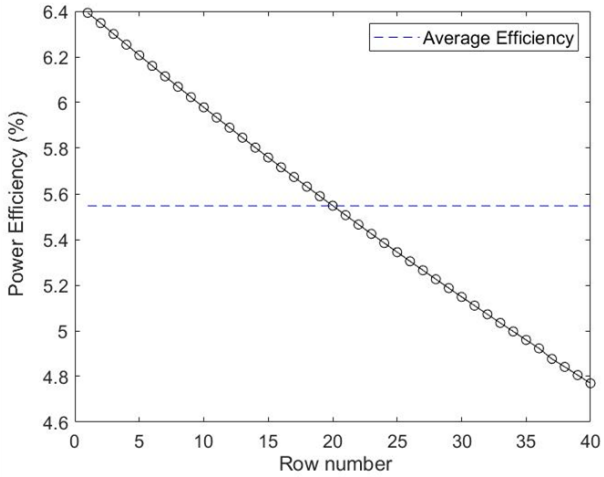

Fig. 4. Efficiency of TEG

Since water outlet temperature is under desired value which is 55ºC, an improvement is needed. To reach higher heat transfer, fins could be added to outer surface of tube. In current values, thermal resistance of annulus side is much dominant than tube side due to low heat transfer coefficient. To decrease thermal resistance of annulus side and increase the overall heat transfer, adding fins to surfaces could be a solution. In general fin effectiveness could reach up to 4 [10]. Fig. 5A shows effective exhaust heat transfer coefficient with fins and its effect to power output

at each row whereas Fig. 5B shows the total output power at that row of heat exchanger.

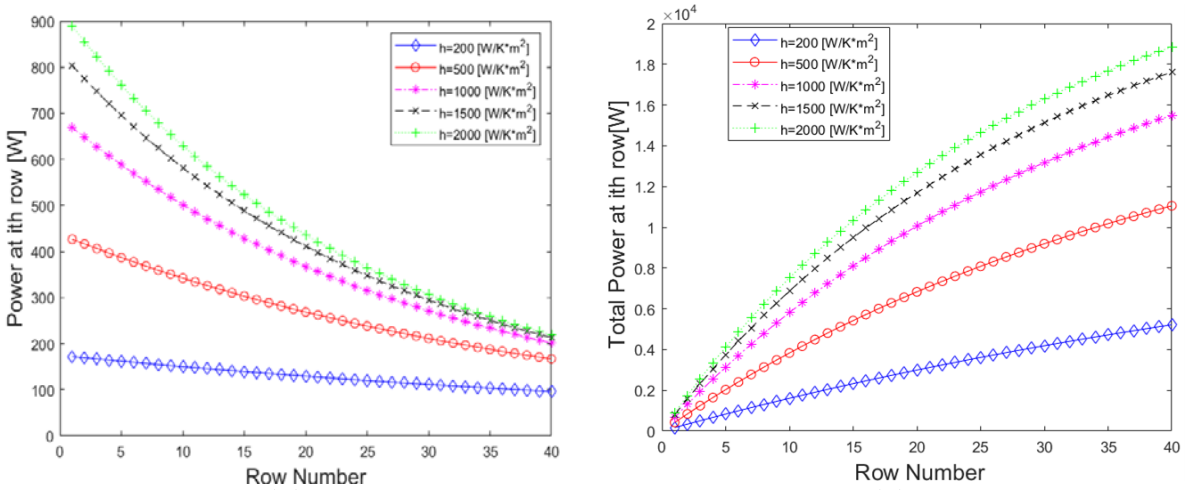

(A) **(B)**

Fig. 5. (A) Power values for different heat transfer coefficients. **(B)** Total power for different heat transfer coefficients

Nearly 20 kW electrical power is obtained when effective heat transfer coefficient of exhaust gas is 2000 W/m^{2}K and it is nearly equal to water side heat transfer coefficient. Since minimum 55ºC water outlet temperature is desired, temperatures are shown in Fig. 6A with effective heat transfer coefficient of 2000 W/m^{2}K. Exhaust gas leaves from preheater at 278ºC and 57ºC which is efficient. Hot side temperature of TEGs starts from 397.2 ºC and decreases until 256ºC. Cold side temperature of TEGs starts from 84.9ºC and decreases until 80.4ºC. The result of increased temperature difference is increasing of efficiency shown in Fig. 6B.

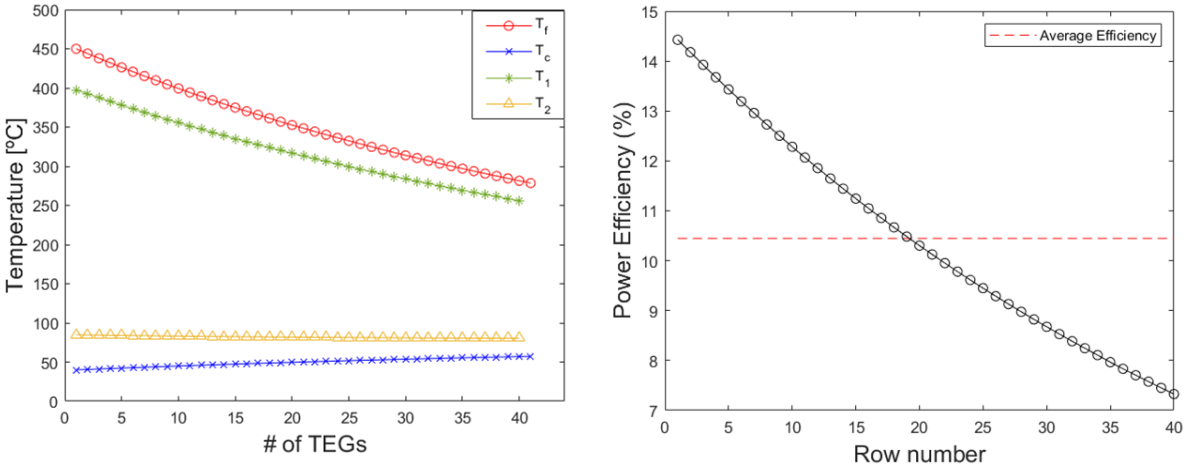

(A) **(B)**

Fig. 6. (A) Temperature values of exhaust gas(T_f),water (T_c), cold side(T_2) and hot side(T_1) of TEG for h = 2000$W/m^2\,K$ **(B)** Efficiency distribution for h=2000 $W/m^2\,K$

4. CONCLUSIONS AND FUTURE WORK

Based on Seebeck effect, a mathematical model of thermoelectric generators is presented in this proceeding. A theoretical energy harvesting from a conventional power plant waste heat is introduced. Main conclusions that could be obtained from this study are followings:

(1) Increased heat transfer coefficients to decrease total thermal resistance will result increase in both efficiency and output power. To increase annulus side (exhaust side) heat transfer coefficient a theoretical finned

surface is considered and increased overall heat transfer coefficient is reflected to proceeding by increased heat coefficient called effective heat transfer coefficient. Future work will consider finned surfaces and its effectiveness range.

(2) Better power output and water output temperatures could be obtained by geometry optimization. Since Nusselt Number and Reynold's Number is highly geometry dependent, a better geometry will result in higher and more efficient power output. Future work will consider geometry optimization.

(3) Output power is very low compared the overall capacity of gas motor in Bil-Energy (4200 kW). A thermoeconomic analysis is not considered in this proceeding. However, after geometry optimization of preheater, designing fins for the heat exchanger and considering full process scheme of Bil-Energy, a thermoeconomic analysis will be conducted.

(4) Material properties of PN junctions and sizes of Thermoelectric Generators are taken from Wang et al (2013) [2]. Since properties of PN junctions and size of TEG highly affect the power output and efficiency, in future work this relationship will be investigated and size of a TEG will be optimized.

REFERENCES

[1] Pérez-Lombard, Luis et al. "A Review On Buildings Energy Consumption Information". *Energy And Buildings*, vol 40, no. 3, 2008, pp. 394-398.

[2] Wang, Yuchao et al. "Theoretical Analysis Of A Thermoelectric Generator Using Exhaust Gas Of Vehicles As Heat Source". *Applied Energy*, vol 112, 2013, pp. 1171-1180. *Elsevier BV*,

[3] Amatya, R., and R. J. Ram. "Solar Thermoelectric Generator For Micropower Applications". *Journal Of Electronic Materials*, vol 39, no. 9, 2010, pp. 1735-1740.

[4] Sztekler, Karol et al. "The Thermoelectric Generators Use For Waste Heat Utilization From Conventional Power Plant". *E3S Web Of Conferences*, vol 14, 2017, p. 01032.

[5] Champier, Daniel. "Thermoelectric Generators: A Review Of Applications". *Energy Conversion And Management*, vol 140, 2017, pp. 167-181.

[6] Chen, Shuo, and Zhifeng Ren. "Recent Progress Of Half-Heusler For Moderate Temperature Thermoelectric Applications". *Materials Today*, vol 16, no. 10, 2013, pp. 387-395.

[7] Dirker, J., and J. P. Meyer. "Convection Heat Transfer in Concentric Annuli". *Experimental Heat Transfer*, vol 17, no. 1, 2004, pp. 19-29.

[8] Teffah, Khaled et al. "Modeling And Experimentation Of New Thermoelectric Cooler–Thermoelectric Generator Module". *Energies*, vol 11, no. 3, 2018, p. 576. *MDPI AG*,

[9] Zorbas, K. T., E. Hatzikraniotis, and K. M. Paraskevopoulos. "Power and efficiency calculation in commercial TEG and application in wasted heat recovery in automobile." *Proc. of 5th European Conference on Thermoelectrics*. Vol. 8. 2007.

[10] SlKKA, S., and M. IQBAL. "Temperature Distribution And Effectiveness Of A Two-Dimensional Radiating And Convecting Circular Fin". *AIAA Journal*, vol 8, no. 1, 1970, pp. 101-106.

[11]56X56 - Tecteg Power Generator.Com". *Tecteg Power Generator.Com*, 2020, https://tecteg.com/store-thermoelectric-power-module-selection-purchase/56x56/.

[12] Persoons, Tim et al. "A General Correlation For The Stagnation Point Nusselt Number Of An Axisymmetric Impinging Synthetic Jet". *International Journal Of Heat And Mass Transfer*, vol 54, no. 17-18, 2011, pp. 3900-3908.

[13] Hatzikraniotis, E. et al. "Efficiency Study Of A Commercial Thermoelectric Power Generator (TEG) Under Thermal Cycling". *Journal Of Electronic Materials*, vol 39, no. 9, 2009, pp. 2112-2116.

[14] LeBlanc, Saniya. "Thermoelectric Generators: Linking Material Properties And Systems Engineering For Waste Heat Recovery Applications". *Sustainable Materials And Technologies*, vol 1-2, 2014, pp. 26-35.

EXERGY

SECOND LAW ANALYSIS OF NOVEL FRACTAL STRUCTURE HEAT EXCHANGER

[*]Alperen Buğra ÇOLAK, [**] İsak KOTCİOĞLU, [***] Oğuz ARSLAN
[*]Bilecik Şeyh Edebali University, Vocational School, Bilecik/TURKEY
bugra.colak@bilecik.edu.tr
[**]Atatürk University, Department of Mechanical Engineering, Erzurum/TURKEY
ikotcioglu@atauni.edu.tr
[***]Bilecik Şeyh Edebali University, Department of Mechanical Engineering, Bilecik /TURKEY
oguz.arslan@bilecik.edu.tr

ABSTRACT

In this study, thermodynamic analysis of a fractal-like ducted heat exchanger is examined through performed experiment. The hydraulic diameters of the milled ducts on the heat exchanger used in this study ranged from 3.00 mm to 6.00 mm. The heat exchanger is formed by milling the 156 channels with three different hydraulic diameters, lengths and symmetrical shapes on circular aluminum plates and assembling the plates together. The heat exchanger is analyzed for two cases. In these cases, the average fluid temperature circulating in the cooling circuit of the system is above and below ambient temperature. Exergy loss and second law efficiency are calculated in case of heat exchanger that was developed in this experimental study. Also, the methods for improving the efficiency of this designed heat exchanger are investigated.

Keywords: Fractal Heat Exchanger, Energy Analysis, Exergy Analysis

1.INTRODUCTION

Heat exchangers are equipment that is widely benefited in all parts of the industry. It plays an essential role in energy-saving and prevention of global warming. Energy saving is one of the main targets of economy-related issues today and the future. The most effective method for reducing energy demand is to consume energy efficiently. As mentioned above, heat exchangers are extensively used in various fields of the industry, such as petrochemical, power engineering, heating ventilation and air conditioning. Therefore, the design of heat exchangers has significance regarding energy saving. The optimum energy consumption level has gained importance while the energy resources have decreased, and the energy cost has increased [1].

The first law of thermodynamics is related to the quantitative conservation of energy in different forms transferred between the system and its environment, also the energy stored in the system. The first law states that energy cannot be created and destroyed with regard to heat and work interactions. Then, the second law of thermodynamics is associated with energy quality [2].

Paisarn Naphon (2006) analyzed the second law analysis of a horizontal coaxial tube type of heat exchanger in his study. He used water as a working fluid in his experimental study. In his experiment, the flow rate was between 0.02 kg / s to 0.20 kg / s and the hot water inlet temperature was between 40-50 C, and cold water inlet temperature was between 15-20 C. Following these issues, the effects of fluid circulating in the heat exchanger such as heat transfer, entropy production and exergy loss are investigated in this study [3].

In our previous study, the first law of thermodynamics was also examined [4]. In this paper, the second law analysis of the experimental study is analyzed. Also, essential points that are emphasized in the newly developed heat exchanger design are examined.

2. MATERIAL AND METHOD

2.1. Structure of Heat Exchanger

The heat exchanger that used in this study consists of cylindrical section channels that have different length and diameter values opened by milling method to 12 mm thick aluminum plates. Water is utilized as a working fluid. It enters the heat exchanger in an axial direction and leaves the heat exchanger through the discharge points placed in the radial direction.

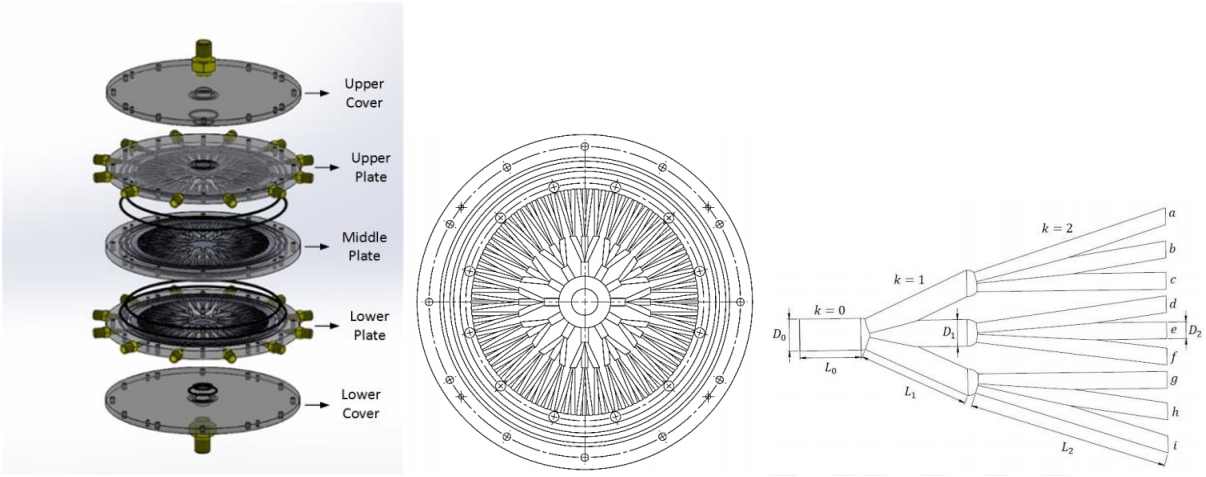

a) Heat Exchanger Structure b) Plate Structure c) Branch Structure

Figure 1. Parts of Heat Exchanger and Branching Detail [4, 5]

Details about the diameter and length of the ducts on the heat exchanger were given in Table 1 and Figure 1.

Table 1. Dimensions of Heat Exchanger [4, 5]

Branching Level (k)	Number of Arms in Branch	Hydraulic Diameter(D_h)	Branch Length (L_k)
0	12	6,00 mm	11,50 mm
1	36	5,00 mm	20,00 mm
2	108	3,17 mm	37,50 mm

The heat exchanger is created by combining five plates with the top and bottom covers. The outer covers provide mechanical support to the heat exchanger. Each plate has half of the channel with a cylindrical cross-section. First plate merges with the next plate, then forms a cylindrical cross-sectional structure.

2.2. Test System

The test system consists of test zone, heaters, radiators, water pumps, temperature, pressure and flow measurement equipment, electronic boards for data acquisition, compressed air system for cleaning the test system and other connection elements. In Figure 2 components of the test system were given. Components are categorized in numbers between 1 to 18; (1) Flowmeter (2) Test Zone (3) PT100 Temperature Transmitter (4) Expansion Tank (Heating Side) (5) Expansion Tank (Cooling Side) (6,19) Circulation Pump (7) Hydrometer (8) Pressure Gauge (9) Heating Tank (10) Cooling Radiator (11) Cooling Fan (12) Switchboard (13) Electronic System Panel (14) Pressure Transmitter (15) Bypass Valve (16) Filling Valve (17) Power Connection (18) Collector. [4,5]

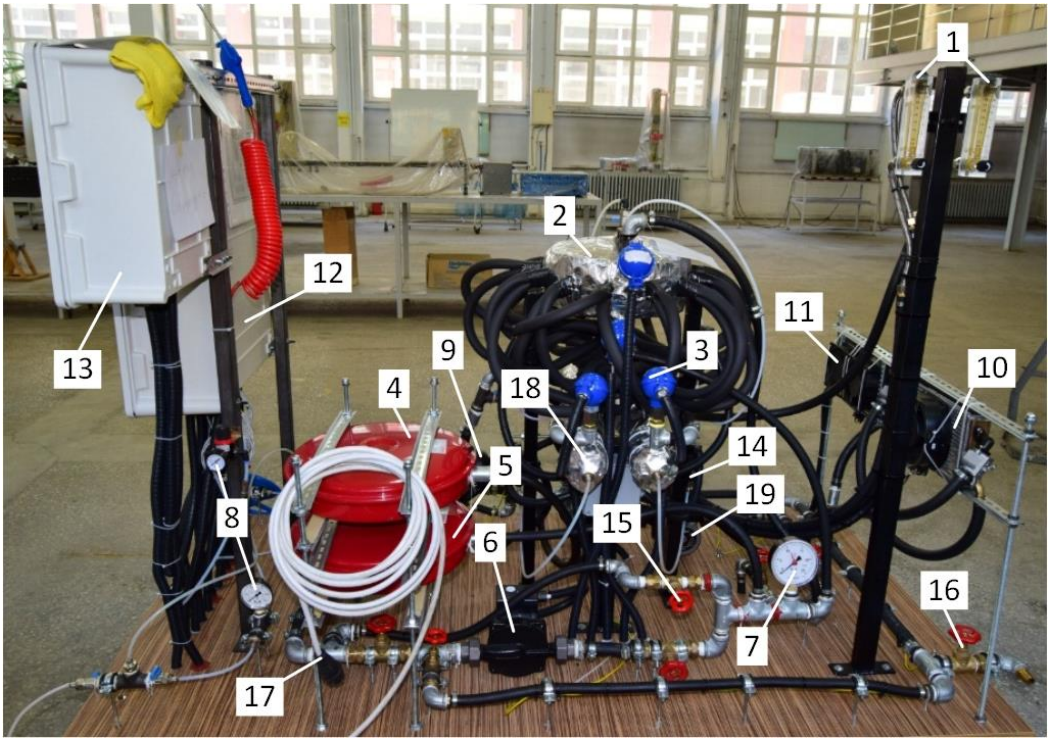

Figure 2. Components of the test system [4, 5]

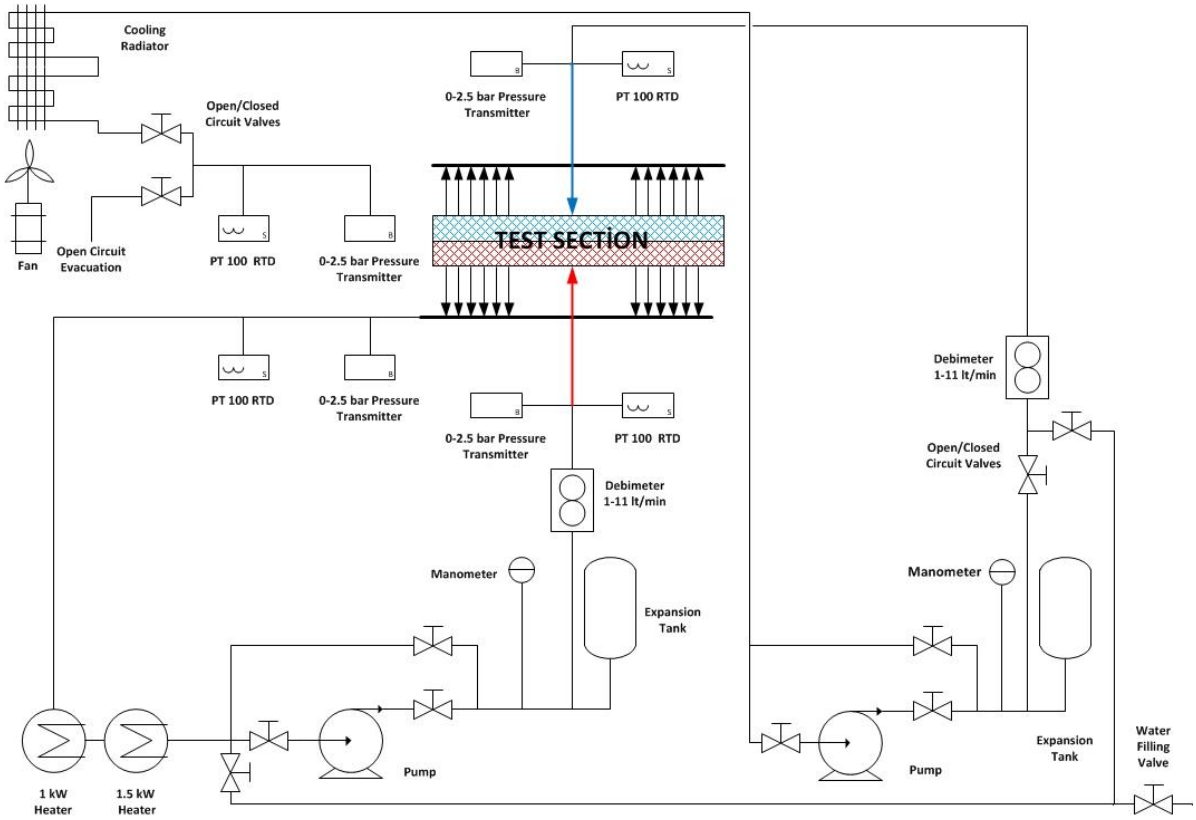

Figure 3. Schematic Diagram of Experiment System [4, 5]

The test system is operated in two different ways. The main difference between these ways is associated with the fluid circulating temperature in the cooled part of the test zone. In the first operation, the fluid circulates in the cooled section that caused the temperature to change in the fluid entering the cooled section as the temperature and flow rate of the heated fluid changed by the test system's radiators. In the second way operation, the fluid circulating in the cooled section is mains water, and the inlet temperature to the heat exchanger is constant.

The fluid circulating in the heating section is heated by using electricity. The controls related to temperature and system balance are made via computer, that is connected to the experimental system. Fluid flow adjustments were made using mechanical type float flowmeters which adjusted manually.

2.3. Mathematical Modeling

2.3.1. Energy Analysis

According to the thermodynamics' first law, the total energy entering the heat exchanger in the test zone. The total energy output from the heat exchanger and the energy produced in the heat exchanger gives the energy change in the test zone. In this case, the energy balance of the system is expressed by using equation 1[6].

$$\dot{E}_{in} - \dot{E}_{out} + \dot{E}_g = \frac{dE_{sistem}}{dt} \tag{1}$$

Since there is no heat generation in the test zone ($\dot{E}_g = 0$) calculations are made according to equation 2.

$$\left(\dot{E}_1 + \dot{E}_3\right) - \left(\dot{E}_2 + \dot{E}_4\right) + \dot{Q}_{loss} = 0 \tag{2}$$

In equation 2, the energy of the fluid entering the heating section $\dot{E}_1$, the energy of the fluid entering the cooling section $\dot{E}_3$, the energy of the fluid leaves the heating section $\dot{E}_2$, the energy of the fluid leaves the cooling section $\dot{E}_4$. $\dot{Q}_{loss}$ is the thermal loss in the test zone. The equation can be expressed as equation 3.

$$\left(\dot{m}_{hot}.h_{hot,in} + \dot{m}_{cold}.h_{cold,in}\right) - \left(\dot{m}_{hot}.h_{hot,out} + \dot{m}_{cold}.h_{cold,out}\right) + \dot{Q}_{loss} = 0 \tag{3}$$

$\dot{m}_{hot}$ and $\dot{m}_{cold}$ are the mass flow rates of the fluids circulating in the heating and cooling sections of the heat exchanger. The enthalpy of the fluid entering the $h_{hot,in}$ heating section, the enthalpy of the fluid entering the $h_{cold,in}$ cooling section, the enthalpy of the fluid leaving the $h_{hot,out}$ heating section is the enthalpy of the fluid leaving the $h_{cold,out}$ cooling section. Since the mass flows of the fluids circulating in the heating and cooling sections during the experiment are equal, the equation is expressed as equations 4 and 5.

$$\dot{m}_{hot} = \dot{m}_{cold} = \dot{m} \tag{4}$$

$$\dot{Q}_{loss} = \dot{m}\left[\left(h_{cold,out} + h_{hot,out}\right) - \left(h_{hot,in} + h_{cold,in}\right)\right] \tag{5}$$

Heat exchanger effectiveness is expressed as equation 6.

$$\varepsilon = \frac{\dot{Q}}{\dot{Q}_{max}} = \frac{\dot{m}\left(h_{cold,out} - h_{cold,in}\right)}{\dot{m}\left(h_{hot,out} - h_{cold,in}\right)} \tag{6}$$

2.3.2 Exergy Analysis

Exergy expresses the usability of the total energy in a system according to a reference temperature value. Exergy is the upper limit on the amount of work a system and it can do without violating thermodynamic laws. The system, that is in balance with its environment, is a system in a dead state [2].
The exergy balance of the heat exchanger can be expressed as equation 7.

$$\dot{E}x_{in} - \dot{E}x_{out} - \dot{E}x_d = \frac{dEx_{sis}}{dt} \tag{7}$$

In equation 7, $\dot{E}x_{in}$ exergy enters the system, $\dot{E}x_{out}$ leaves the system, $\dot{E}x_{d}$ is the exergy destruction**.** Physical exergy is calculated for each stream entering and leaving as follows and the system can be expressed as equation 8.

$$\dot{E}x^{Ph} = \dot{m}[(h - h_0) - T_0(s - s_0)] \tag{8}$$

In this case, the exergy balance in the heat exchanger is expressed as equation 9.

$$\dot{E}x_1^{Ph} + \dot{E}x_3^{Ph} - \dot{E}x_2^{Ph} - \dot{E}x_4^{Ph} - \dot{E}x^{Q} = \dot{E}x_d \tag{9}$$

In equation 9, $\dot{E}x_1^{Ph}$ physical exergy of the fluid entering the heating section, $\dot{E}x_3^{Ph}$ physical exergy of the fluid entering the cooling section, $\dot{E}x_2^{Ph}$ physical exergy of the fluid leaving to the heating section, $\dot{E}x_4^{Ph}$ is the physical exergy of the fluid leaving to the cooling section. $\dot{E}x^{Q}$ is the exergy caused by heat losses in the system. $\dot{E}x_d$ gives us exergy destruction in the system. $\dot{E}x^{Q}$ is expressed as equation 10.

$$\dot{E}x^{Q} = \left(1 - \frac{T_0}{T}\right)\dot{Q}_{loss} \tag{10}$$

The second law efficiency for the heat exchanger is calculated as equation 11.

$$\eta_{II} = 1 - \frac{Ex_d}{Ex_1^{Ph} + Ex_3^{Ph}} \tag{11}$$

3. RESULTS AND DISCUSSION

3.1. Results of Energy Analysis

Energy analysis results are given in Table 2. Temperature T1 is the temperature of the fluid entering to the heating section of the heat exchanger. Temperature T2 is the temperature of the fluid leaving to the heating section of the heat exchanger. Temperature T3 is the temperature of the fluid entering to the cooling section. Lastly, Temperature T4 is the temperature of the fluid leaving to the cooling section.

Table 2. Energy Analysis [4, 5]

Ölçüm No	m (kg/s)	T1 [C]	h1 (kJ/kg)	E_1 (kW)	T2 [C]	h2 (kJ/kg)	E_2 (kW)	T3 [C]	h3 (kJ/kg)	E_3 (kW)	T4 [C]	h4 (kJ/kg)	E_4 (kW)	Q (kW)	ε
1	0,066	44,80	187,60	12,38	37,49	157,04	10,365	10,84	45,54	3,01	17,82	74,79	4,94	-0,09	0,26
2	0,05775	44,61	186,81	10,79	37,04	155,16	8,9607	11,04	46,38	2,68	18,19	76,34	4,41	-0,10	0,28
3	0,0495	44,98	188,36	9,32	36,93	154,70	7,6578	11,10	46,63	2,31	18,70	78,47	3,88	-0,09	0,29
4	0,04125	45,00	188,44	7,77	36,35	152,28	6,2816	11,19	47,01	1,94	19,32	81,07	3,34	-0,09	0,32
5	0,033	44,65	186,98	6,17	35,58	149,06	4,9191	11,56	48,56	1,60	20,25	84,96	2,80	-0,05	0,36
6	0,066	39,81	166,74	11,00	33,66	141,04	9,3086	11,13	46,76	3,09	17,07	71,65	4,73	-0,05	0,26
7	0,05775	39,97	167,40	9,67	33,71	141,25	8,1571	11,24	47,22	2,73	17,13	71,90	4,15	-0,09	0,26
8	0,0495	40,06	167,78	8,31	33,21	139,16	6,8883	11,63	48,85	2,42	17,90	75,12	3,72	-0,12	0,29
9	0,04125	40,21	168,41	6,95	33,07	138,57	5,7161	11,95	50,20	2,07	18,92	79,39	3,27	-0,03	0,33
10	0,033	40,22	168,45	5,56	32,43	135,90	4,4846	12,32	51,75	1,71	19,91	83,54	2,76	-0,03	0,38
11	0,066	35,11	147,10	9,71	29,99	125,70	8,2961	10,78	45,29	2,99	15,82	66,42	4,38	-0,02	0,26
12	0,05775	35,11	147,10	8,50	29,66	124,32	7,1794	10,76	45,21	2,61	15,91	66,79	3,86	-0,07	0,27

13	0,0495	35,06	146,89	7,27	29,26	122,65	6,0709	10,82	45,46	2,25	15,99	67,13	3,32	-0,13	0,28
14	0,04125	35,19	147,43	6,08	29,12	122,06	5,035	11,23	47,18	1,95	16,99	71,31	2,94	-0,05	0,32
15	0,033	35,17	147,35	4,86	28,75	120,51	3,9769	11,29	47,43	1,57	16,85	70,73	2,33	-0,12	0,32
16	0,099	64,93	271,83	26,91	61,38	256,96	25,439	48,17	201,69	19,97	51,32	214,86	21,27	-0,17	0,24
17	0,0825	64,89	271,66	22,41	61,02	255,45	21,075	47,68	199,64	16,47	51,16	214,19	17,67	-0,14	0,26
18	0,066	64,99	272,08	17,96	60,34	252,60	16,672	45,95	192,41	12,70	50,00	209,34	13,82	-0,17	0,28
19	0,0495	65,08	272,46	13,49	59,48	249,00	12,326	44,27	185,39	9,18	49,21	206,04	10,20	-0,14	0,32
20	0,033	65,13	272,66	9,00	57,37	240,18	7,9258	41,32	173,05	5,71	47,42	198,56	6,55	-0,23	0,38
													0,00		
21	0,099	60,09	251,56	24,90	56,87	238,08	23,57	44,77	187,48	18,56	47,69	199,68	19,77	-0,13	0,24
22	0,0825	59,94	250,93	20,70	56,42	236,20	19,487	44,42	186,01	15,35	47,59	199,27	16,44	-0,12	0,26
23	0,066	59,78	250,26	16,52	55,55	232,56	15,349	42,87	179,53	11,85	46,42	194,38	12,83	-0,19	0,28
24	0,0495	60,09	251,56	12,45	55,25	231,31	11,45	41,61	174,26	8,63	45,91	192,24	9,52	-0,11	0,32
25	0,033	60,02	251,26	8,29	53,54	224,15	7,397	39,35	164,81	5,44	44,51	186,39	6,15	-0,18	0,36
26	0,099	54,75	229,21	22,69	51,86	217,12	21,495	40,94	171,46	16,97	43,37	181,62	17,98	-0,19	0,22
27	0,0825	55,00	230,26	19,00	51,88	217,21	17,919	40,75	170,67	14,08	43,45	181,96	15,01	-0,15	0,24
28	0,066	54,99	230,22	15,19	51,38	215,11	14,198	40,32	168,87	11,15	43,27	181,21	11,96	-0,18	0,27
29	0,0495	54,85	229,63	11,37	50,75	212,48	10,518	39,94	167,28	8,28	43,32	181,41	8,98	-0,15	0,31
30	0,033	54,73	229,13	7,56	49,41	206,87	6,8268	38,74	162,27	5,35	42,82	179,32	5,92	-0,17	0,38
31	0,099	50,28	210,51	20,84	48,21	201,86	19,984	41,24	172,72	17,10	42,99	180,03	17,82	-0,13	0,25
32	0,0825	50,28	210,51	17,37	47,87	200,44	16,536	40,40	169,20	13,96	42,40	177,57	14,65	-0,14	0,27
33	0,066	49,93	209,05	13,80	47,12	197,30	13,022	38,87	162,81	10,75	41,27	172,84	11,41	-0,11	0,29
34	0,0495	49,81	208,55	10,32	46,48	194,63	9,634	38,62	161,76	8,01	41,24	172,72	8,55	-0,15	0,33
35	0,033	49,94	209,09	6,90	45,31	189,74	6,2613	36,54	153,07	5,05	39,78	166,61	5,50	-0,19	0,37
36	0,099	45,22	189,36	18,75	43,27	181,21	17,939	36,06	151,07	14,96	37,71	157,96	15,64	-0,12	0,23
37	0,0825	45,22	189,36	15,62	43,06	180,33	14,877	35,80	149,98	12,37	37,54	157,25	12,97	-0,15	0,24
38	0,066	44,88	187,94	12,40	42,25	176,94	11,678	34,74	145,55	9,61	36,83	154,29	10,18	-0,15	0,28
39	0,0495	44,81	187,65	9,29	41,55	174,01	8,6136	33,31	139,58	6,91	35,84	150,15	7,43	-0,15	0,31
40	0,033	44,88	187,94	6,20	40,99	171,67	5,6651	33,14	138,87	4,58	35,91	150,44	4,96	-0,15	0,35

3.2. Results of Exergy Analysis

The second law efficiency (η_{II}) and exergy destruction ($\dot{E}x_d$) values are calculated from the data that is obtained at the end of the experimental study. The experiments are carried out in two groups. In the first group, the temperature of the fluid entering to the heated and cooled section of the heat exchanger is constant and the temperature of the fluid entering to the cooled section is lower than the ambient temperature. In the second group, the fluid entering the cooled section is cooled in a radiator. The temperature of the fluid entering to the cooling section varies based on the temperature and flow rate of the fluid entering the heating section.

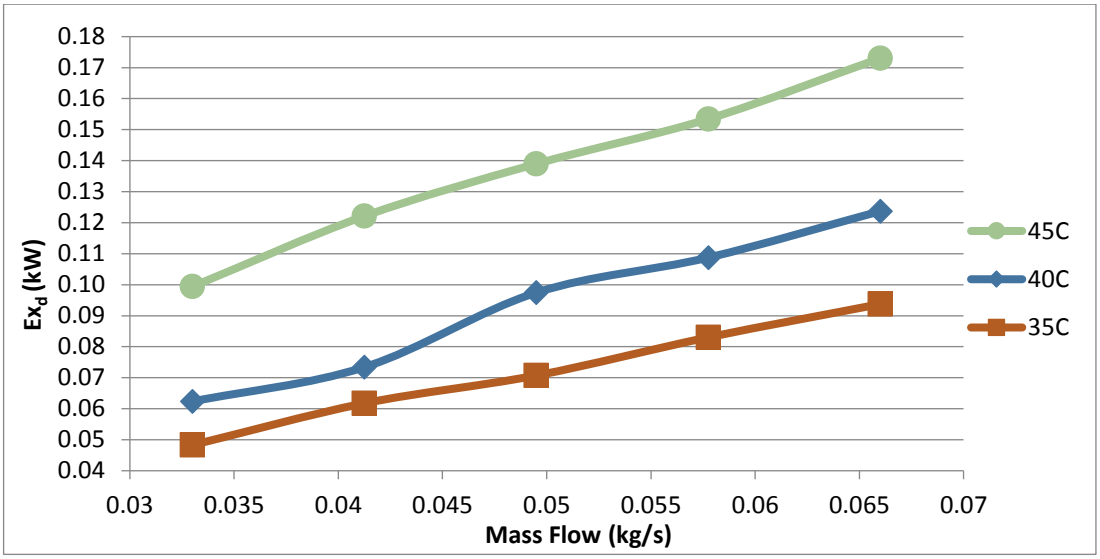

Figure 4. Exergy Destruction Rates vs. Mass Flow (T_1,T_3 constant)

As seen in Figure 4, the exergy destruction rate rises with the increase of inlet temperature (T1) of the heating section. Simultaneously, the exergy destruction rate increases with the increase of mass flow, due to the constant temperature of (T3).

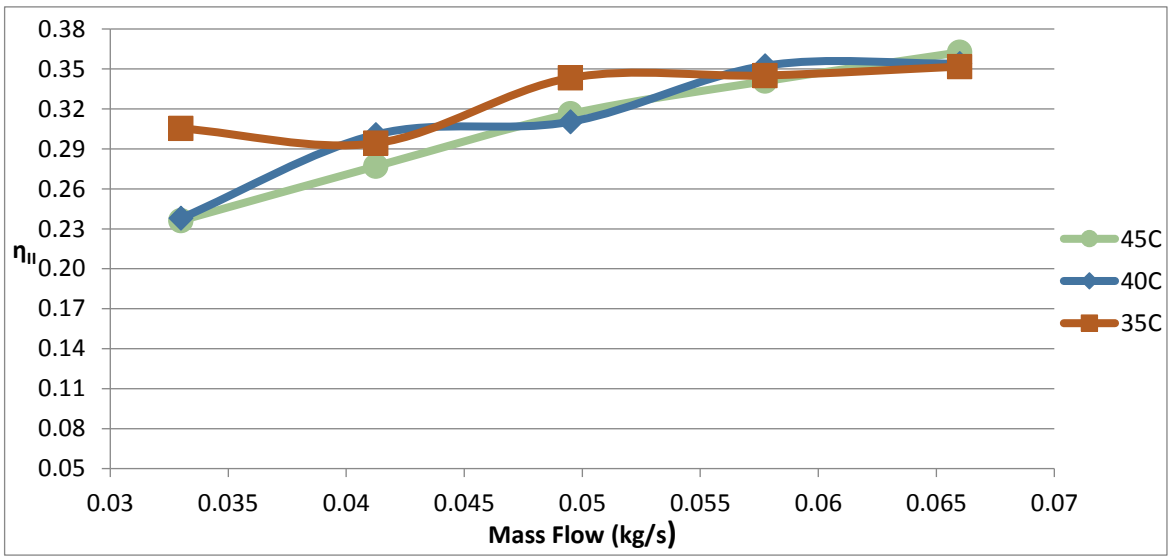

Figure 5. Second Law Efficiency vs. Mass Flow (T_1,T_3 constant)

As seen in Figure 5, regarding the determination of the second law efficiency, there is no significant effect on the fluid temperature in the heating section. Rise of the flow rate increases the heat transfer and second law efficiency. It is concluded that the reason for the usual low-level second law efficiency is that the heat exchanger plates are thick, and this reason is dominant to determine heat ratio transfer when the temperature differences are high.

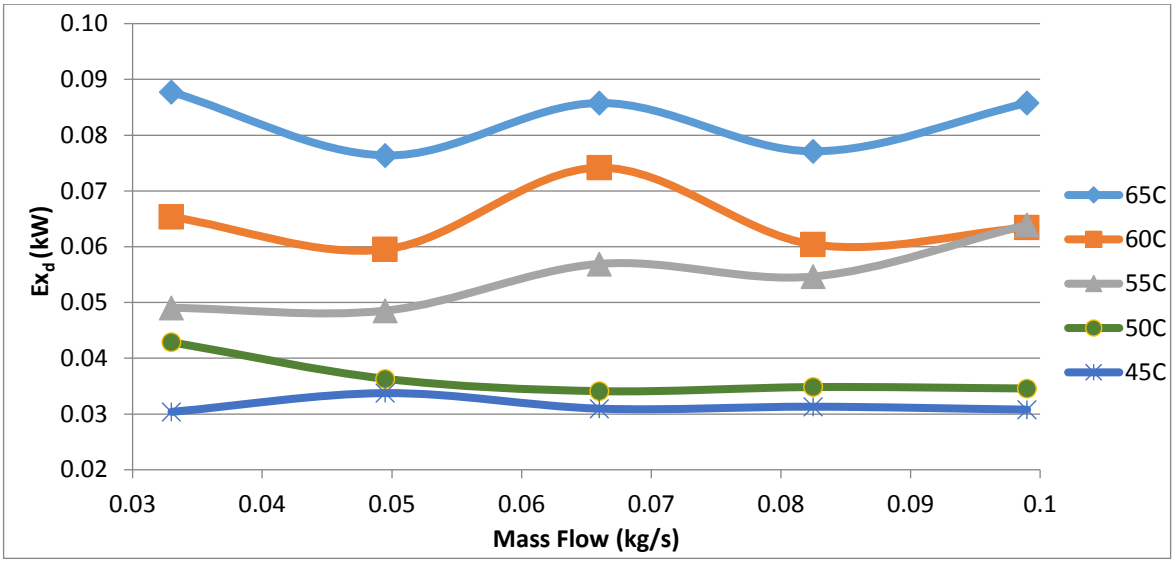

Figure 6. Exergy Destruction Rates vs. Mass Flow (T_1 constant, T_3 depend on T_1)

As seen in Figure 6, the exergy destruction rate increased with the rise of inlet temperature (T_1). It is observed that the increase in flow rate does not affect on exergy destruction at the same temperature. When the temperature increases, exergy destruction also increases. However it has been observed that there is no effect on exergy destruction since the flow rate also affects the fluid temperature entering the cooling section.

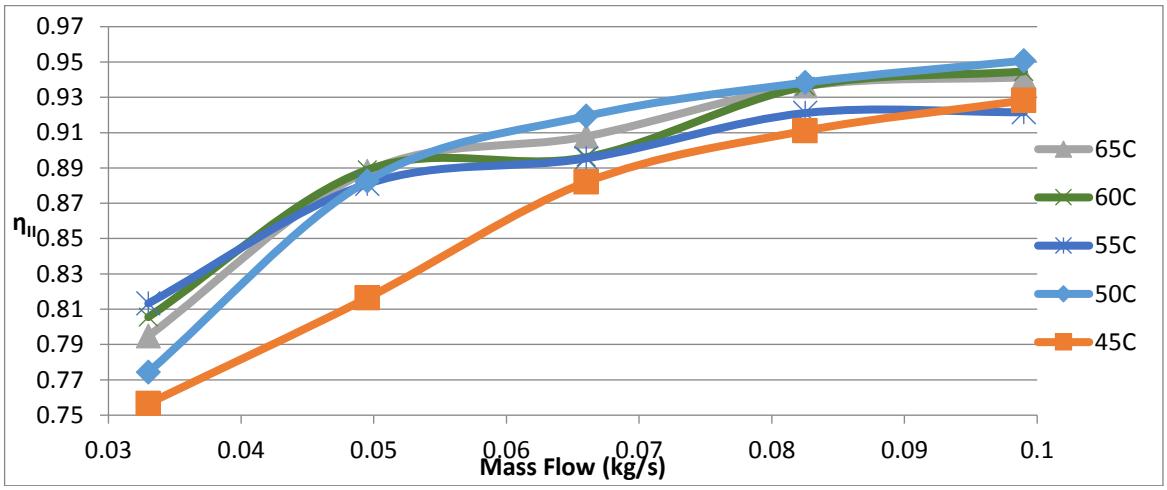

Figure 7. Second Law Efficiency vs. Mass Flow (T_1 constant, T_3 depend on T_1)

As seen in Figure 7, the temperature of the fluid in the heating section does not have a significant effect in determining the second law efficiency. Together with the increase in the flow rate, the amount of heat transfer and the efficiency of the second law increased. The second law efficiency is generally high because the fluid temperature circulating in the cooling section is close to the fluid temperature entering to the heating section. The low-temperature difference caused low exergy destruction and high second law efficiency.
The results in Figure 7 show that the low-temperature differences in heating and cooling sections are more dominant factors than heat exchanger plate thicknesses.

4. CONCLUSION

In this study, it is observed that excessive plate thickness significantly influences the results related to the heat transfer even if there is a right geometry obtained concerning the flow characteristics in this newly designed heat exchanger. It is observed that the designed heat exchanger is more effective on the second law analysis and exergy destruction, especially in low-temperature differences.

REFERENCES

[1] Manjunath K., Kaushik S.C. Second law thermodynamic study of heat exchangers: A review, *Renewable and Sustainable Energy Reviews*, 40, 348-374, 2014.

[2] Yunus A. Çengel, Termodinamik, Beşinci Baskı, İzmir Güven Kitabevi, İzmir, 2008.

[3] Naphon P., Second law analysis on the heat transfer of the horizontal concentric tube heat exchanger, *International Communications in Heat and Mass Transfer*, 33, 1029–1041, 2006.

[4] COLAK A.B., KOTCIOGLU I., NASIRI KHALAJI M. Tree Shaped in Channels Parallel and Counter Flow Through Heat Exchanger Heat Transfer and Flow Investigation of Characteristic. *Hittite Journal of Science and Engineering*,, 5 (Special Issue: Selected Papers from ULIBTK'17) 33-49, 2018.

[5] ÇOLAK A.B. Ağaç Şekilli Dal Kanallı Zıt ve Paralel Akışlı Isı Değiştiricisinin Isı Transferi ve Akış Karakteritiklerinin İncelenmesi. Yüksek Lisans Tezi, Atatürk Üniversitesi, Fen Bilimleri Enstitüsü, 2017.

[6] Yunus A. Çengel, Isı ve Kütle Transferi Pratik Bir Yaklaşım, Üçüncü Basım, İzmir Güven Kitabevi, İzmir, 2011.

NANOFLUIDS

MIXED CONVECTION IN A SQUARE CAVITY FILLED WITH HYBRID NANOFLUID

Birol ŞAHİN*
* Recep Tayyip Erdogan University, Department of Mechanical Engineering, Rize/Turkey
Email: birol.sahin@erdogan.edu.tr

ABSTRACT

Mixed convection in a square cavity heated from the left wall and cooled from the right wall is investigated numerically. The horizontal walls of the cavity are insulated. The heated wall of the cavity is moved upwards. The cavity is filled with a water-based hybrid nanofluid containing Ag-MgO nanoparticles. Three different nanoparticle volume fraction (0,1, and 2 %) and two different Richardson number (10^{-1} and 1) are investigated numerically for different Reynolds numbers. Differential equations are discretized over the SIMPLE algorithm and solved iteratively using the finite control volume method. Streamlines, isotherms, local and average Nusselt numbers for the heated wall are presented. It is determined that the heat transfer increase with increasing nanoparticle volume fraction. However, the change of the Richardson number and Reynolds number significantly affects the heat transfer much more than the nanoparticle volumetric fraction.

Keywords: Mixed convection, square cavity, hybrid nanofluid.

List of Symbols

c_p	specific heat (J/kg. K)
g	gravitational acceleration (m/s²)
H	height of the cavity
k	thermal conductivity (W/m.K)
L	length of the cavity
Nu	Nusselt number
$\overline{Nu}$	average Nusselt number
p, P	pressure, dimensionless pressure
Pr	Prandtl number, $Pr = \nu_{f/\alpha_f}$
Re	Reynolds number, $Re = v_o L/\nu_f$
Ri	Richardson number, $Ri = \mathrm{Gr}/Re^2$
T	temperature (K)
u, U	velocity component in x direction, dimensionless velocity component in X direction
v, V	velocity component in y direction, dimensionless velocity component in Y direction
x, X	horizontal coordinate, dimensionless horizontal coordinate
y, Y	vertical coordinate, dimensionless vertical coordinate

Greek Symbols

α	thermal diffusivity (m²/s)
β	thermal expansion coefficient (1/K)
ϕ	solid nanoparticle volume fraction
ψ	stream function
μ	dynamic viscosity (kg/m.s)
ν	kinematic viscosity (m²/s)

ρ	density (kg/m³)
θ	dimensionless temperature

Subscripts

l	left wall
f	main fluid
r	right wall
nf	nanofluid
p	nanoparticle

1. INTRODUCTION

Conventional heat transfer fluids such as air, water, ethylene glycol, oil, etc., have limited heat transfer conductivity. Therefore, some nanometer-sized particles are added to main fluid in order to increase the heat transfer. Generally, Ag, Al, Cu, TiO_2, Al_2O_3 nanoparticles are added to the main fluid in specific volumetric fractions. This fluid, called nanofluid, is used in many heat transfer applications today. Heat exchangers, cooling of automotive and electronic devices, crystal growth, and lubrication can be given as examples of these applications where especially natural and mixed convection occur. Moallemi and Jang [1] studied Prandtl number effects on mixed convection in a square cavity for different Reynolds and Grashof numbers. As a result of the study, a correlation was developed that gives the Nusselt number based on the dimensionless numbers. Basak et al. [2] studied mixed convection in a linearly heated square cavity for different dimensionless parameters. The first studies on nanofluids were done by Choi and Eastman [3] in the 1990s. As a result of the study, it was observed that the nanoscale particles added to the main fluid in specific proportions increase the heat transfer. After these years, studies on nanofluids have increased significantly due to the developing technology. Talebi et al. [4] numerically investigated mixed convection heat transfer in a square enclosure filled with Cu-water nanofluid when heated differentially at vertical walls while the horizontal walls are insulated very well. As a result of the study, it was found that increasing the solid particle concentration improves heat transfer significantly at fixed Reynolds number and Rayleigh number. Kahveci and Öğüt [5] studied mixed convection and fluid flow in a lid-driven square cavity heated from bottom partially and filled-with water-based nanofluids including Ag, Cu, CuO, Al_2O_3, and TiO_2 nanoparticles. They obtained that the heat transfer increased by between 21-37%. Mansour et al. [6] examined mixed convection heat transfer in a square cavity heated from partially at the bottom wall while the other walls cooled uniformly when filled with nanofluid containing different nanoparticles. It was found that increases nanoparticle volume fraction causes a decrease in fluid motion and fluid temperature. Increase in heater length causes increase in flow intensity and fluid temperature. Maximum Nusselt number occurred when Al_2O_3 nanoparticles added vice versa when using TiO_2 nanoparticles. Zeghbid and Bessaih [7] investigated numerically mixed convection heat transfer and entropy generation in a square cavity heated two heat sources mounted on each vertical wall at different locations when the cavity filled with water-based nanofluid. Increasing the Rayleigh number, Reynolds number, and volumetric fraction of nanoparticles decrease the total entropy generation. Esfe et al. [8] experimentally analyzed the effect of nanoparticle volume fraction on thermal conductivity and dynamic viscosity of water-based Ag–MgO hybrid nanofluid. They developed a correlation for the thermal conductivity and dynamic viscosity of the hybrid nanofluid based on the volumetric mixing ratio. Ma et al. [9] examined the effect of magnetic field on forced convection in a channel with active heaters and coolers when the Ag-MgO/water hybrid nanofluid was used in the channel. They used a correlation given by Esfe et al. [8] for thermal conductivity and dynamic viscosity of the hybrid nanofluid. At the end of the study, it was found that heat transfer increased with increasing nanoparticle volume fraction or decreasing Hartman number.

As can be seen from the previous studies, there has been no study in mixed convection for Ag-MgO / water hybrid nanofluid in the square cavities that heated left wall move upwards. The aim of this study is to observe the changes in mixed convection heat transfer parameters using the thermophysical properties obtained from experimental data for Ag-MgO water hybrid nanofluid. Thus, more accurate numerical analysis can be made with the results obtained according to the experimental data.

2. THEORETICAL STUDY

Mixed convection heat transfer in a square cavity filled with water-based hybrid nanofluid containing equal amounts of Ag (50%) and MgO (50%) nanoparticles is shown in Fig. 1 with thermal boundary conditions. The square cavity is heated from the left wall and cooled from the right wall while the horizontal walls are insulated. The heated left wall is assumed to slide from bottom to top with a constant speed of V_0. The length of the cavity (L) is equal to its height (H).

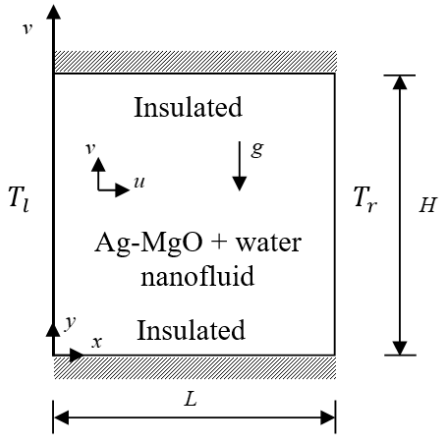

Figure 1. Schematic diagram of the square cavity and boundary conditions.

The main fluid of the hybrid nanofluid is water, and Prandtl number is taken as 6.2. It is assumed that the hybrid nanofluid is incompressible and Newtonian, and the thermal properties of the hybrid nanofluid are constant except for density. The thermophysical properties of the component of the hybrid nanofluid are given in Table 1.

Table 1. Thermophysical properties of the hybrid nanofluid [5, 10]

	Thermophysical property			
	c_p (J/kgK)	ρ (kg/m3)	k (W/mK)	$\beta x10^{-5}$ (1/K)
Water (H_2O)	4179	997.1	0.613	21
Ag	235	10500	429	1.89
MgO	1005	3585	52	1.37

The necessary equations for the solution of the problem in two dimensional are given below with Boussinesq approach:

$$\frac{\partial U}{\partial X}+\frac{\partial V}{\partial Y}=0 \quad (1)$$

$$U\frac{\partial U}{\partial X}+V\frac{\partial U}{\partial Y}=-\frac{\partial P}{\partial X}+\frac{1}{\mathrm{Re}}\frac{\nu_{nf}}{\nu_f}\left(\frac{\partial^2 U}{\partial X^2}+\frac{\partial^2 U}{\partial Y^2}\right) \quad (2)$$

$$U\frac{\partial V}{\partial X}+V\frac{\partial V}{\partial Y}=-\frac{\partial P}{\partial Y}+\frac{1}{\mathrm{Re}}\frac{\nu_{nf}}{\nu_f}\left(\frac{\partial^2 V}{\partial X^2}+\frac{\partial^2 V}{\partial Y^2}\right)+\frac{(\rho\beta)_{nf}}{\rho_{nf}\beta_f}Ri\theta \quad (3)$$

$$U\frac{\partial \theta}{\partial X}+V\frac{\partial \theta}{\partial Y}=\frac{\alpha_{nf}}{\alpha_f}\frac{1}{\mathrm{RePr}}\left(\frac{\partial^2 \theta}{\partial X^2}+\frac{\partial^2 \theta}{\partial Y^2}\right) \quad (4)$$

Non-dimensional parameters are given in single-phase fluid as follows

$$X=\frac{x}{L},\quad Y=\frac{y}{L},\quad U=\frac{uL}{\alpha_f},\quad V=\frac{vL}{\alpha_f},\quad \theta=\frac{T-T_c}{T_h-T_c},\quad P=\frac{pL^2}{\rho_{nf}{\alpha_f}^2} \quad (5)$$

The dimensionless numbers are Richardson number (Ri), Reynolds number (Re), and Prandtl number (Pr) introduced below:

$$Ri = \frac{Gr}{Re^2},\ Re = \frac{v_o L}{\nu_f},\ Pr = \frac{\nu_f}{\alpha_f} \quad (6)$$

The thermophysical properties of the hybrid nanofluid depending on the nanoparticle volume fraction (ϕ) are given by

$$\rho_{nf} = \{(1-\phi_2)\left[(1-\phi_1)\rho_f + \phi_1\rho_{p_1}\right]\} + \phi_2\rho_{p_2} \quad (7)$$

$$\left(\rho c_p\right)_{nf} = \{(1-\phi_2)\left[(1-\phi_1)\left(\rho c_p\right)_f + \phi_1\left(\rho c_p\right)_{p_1}\right]\} + \phi_2\left(\rho c_p\right)_{p_2} \quad (8)$$

$$(\rho\beta)_{nf} = \{(1-\phi_2)\left[(1-\phi_1)(\rho\beta)_f + \phi_1(\rho\beta)_{p_1}\right]\} + \phi_2(\rho\beta)_{p_2} \quad (9)$$

Thermal conductivity of nanofluid was given according to experimental data [8] as

$$k_{nf} = k_f\left(\frac{0.1747\times10^5+\phi_p}{0.1747\times10^5-0.1498\times10^6\phi_p+0.1117\times10^7\phi_p^2+0.1997\times10^8\phi_p^3}\right) \quad (10)$$

In addition, the dynamic viscosity of nanofluid was given according to the experimental data [8]

$$\mu_{nf} = \mu_f\left(1+32.795\phi_p-7214\phi_p^2+714600\phi_p^3-0.1941\times10^8\phi_p^4\right) \quad (11)$$

Thermal diffusivity and kinematic viscosity of the hybrid nanofluid

$$\alpha_{nf} = \frac{k_{nf}}{\left(\rho c_p\right)_{nf}} \quad (12)$$

$$\nu_{nf} = \frac{\mu_{nf}}{\rho_{nf}} \quad (13)$$

Boundary conditions of the analyzed problem are given below

On the left wall, U = 0 and V = V_0, $\theta = 1$
On the right wall, U = V = 0, $\theta = 0$
On the upper and bottom wall, U = V = 0, $\frac{\partial\theta}{\partial Y} = 0$
Local and average Nusselt number along the heated left wall are given as follows, respectively.

$$Nu_l = -\frac{k_{nf}}{k_f}\frac{\partial\theta}{\partial X}\Big|_{X=0} \qquad \overline{Nu_l} = \frac{1}{H}\int_0^H Nu_l dy \quad (14)$$

In the solution of Eq. 1-4, the finite control volume method was used according to the SIMPLE algorithm given by Patankar [11]. In order to obtain the grid-independent solution, six different grid structures (10x10, 30x30, 60x60, 90x90, 120x120 and 150x150) have been solved in a FORTRAN program. Since there is no significant change after the 90x90 grid structure, this grid structure is used in all solutions. To demonstrate the accuracy of the study, a comparison was made with the literature [1] for the square cavity heated from its lower wall and cooled from its moving upper wall. As seen in Fig. 2, it is determined that the obtained results are largely similar to each other.

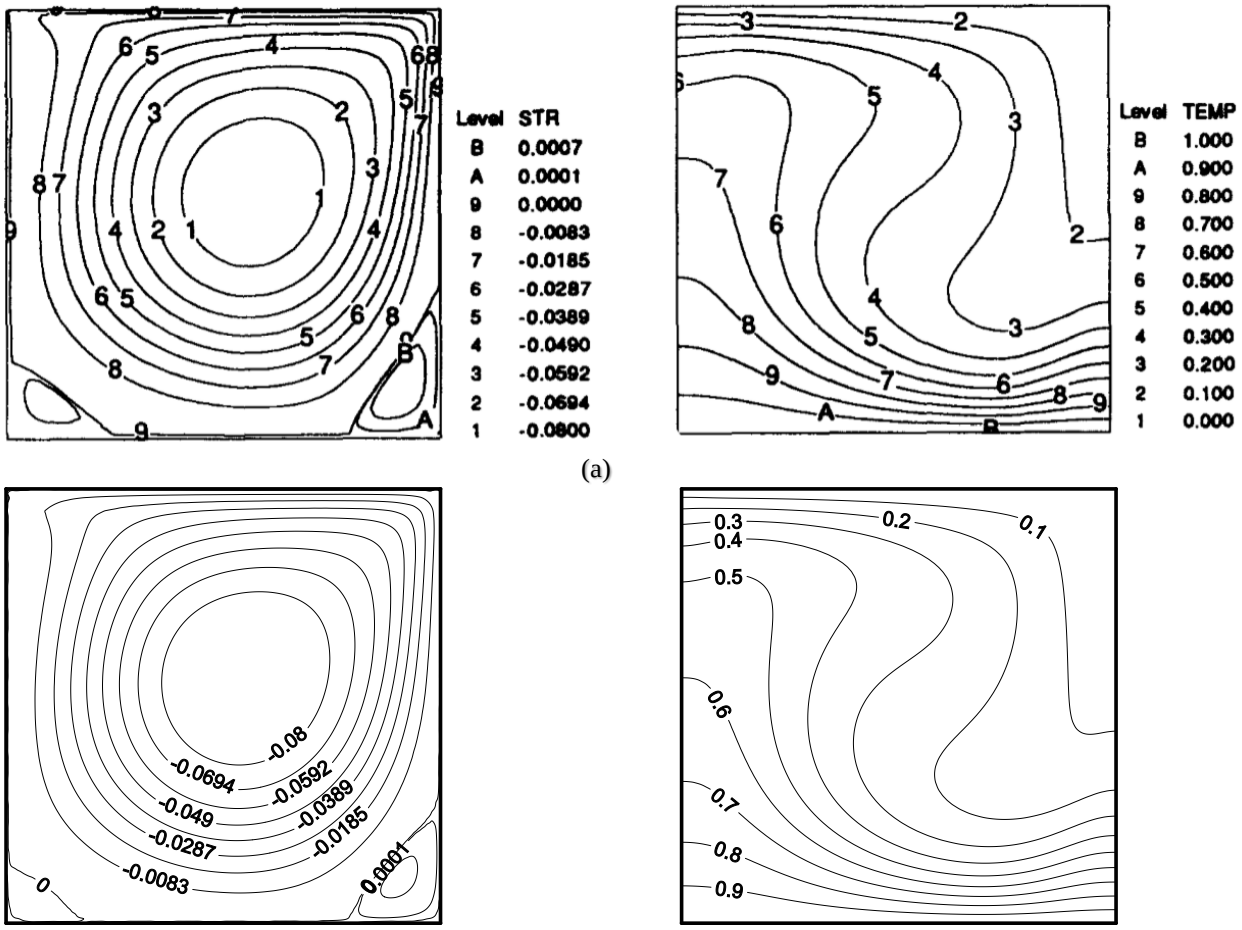

Figure 2. Comparison of the streamlines (left) and isotherms (right) in a differentially heated square cavity at Re=1000, Ri=0.01, and Pr=0.1 a.) Moallemi and Jang [1], b.) Present study.

3. RESULTS AND DISCUSSION

In this study, mixed convection in a square cavity filled with water-based Ag-MgO hybrid nanofluid is investigated numerically. The nanoparticle volume fraction is taken as 0, 0.01, and 0.02 and Richardson number 0.1, and 1, Reynolds number 100, and 1000. Streamlines and isotherms about the solutions are given in Fig. 3 for Re=100, and Fig. 4 for Re=1000. As seen in Fig. 3, the streamlines concentrated around a single cell, the center of which is slightly above the center of the moving left wall. According to the isotherm curves, it is seen that there are high temperatures in large part of the cavity and that they develop upward with the effect of the buoyancy force in the areas close to the moving left wall. The intensity of the flow increases with increasing Richardson number. The increase in the hybrid nanofluid volumetric fraction does not affect the streamlines and isotherm curves much.

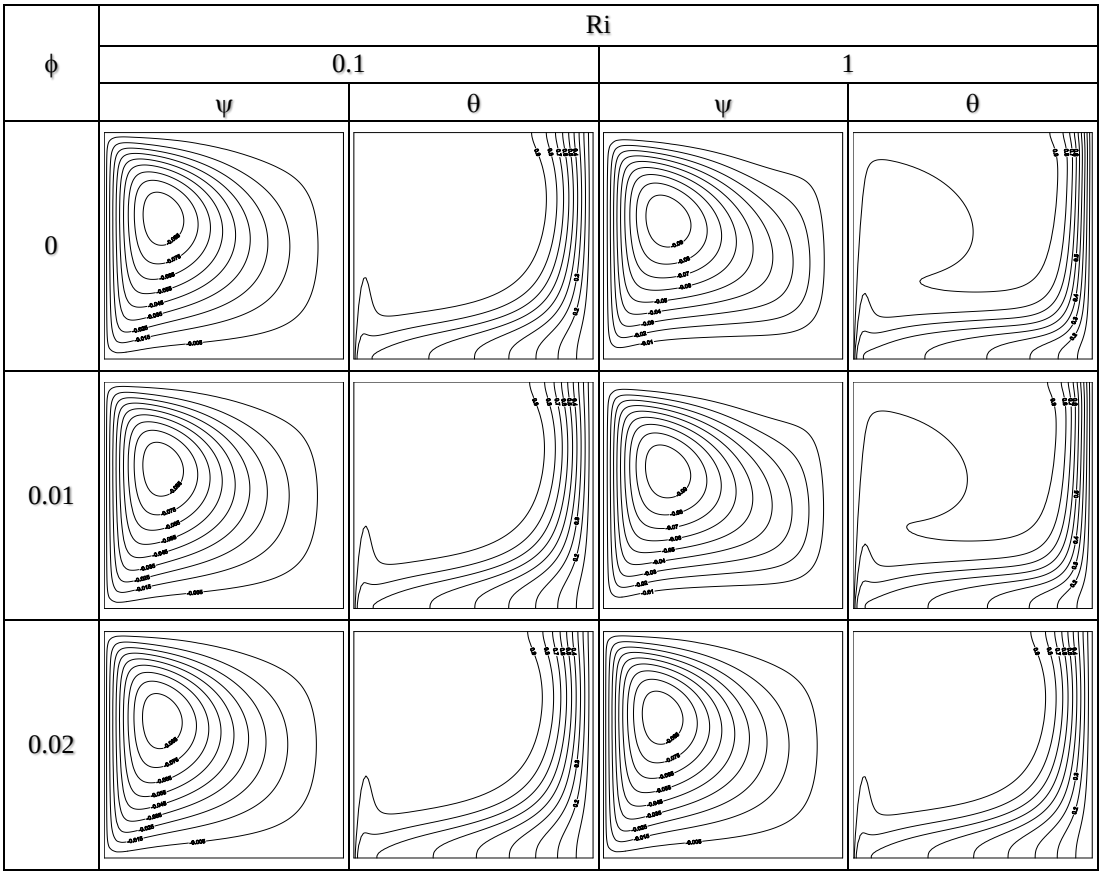

Figure 3. Streamlines and isotherms at Re=100.

In Fig. 4, it was determined that the streamlines developed around the center of the cavity, and their intensity increased slightly. The increase in the volumetric fraction of the nanoparticles slightly increases the flow intensity. Due to the moving left wall, high temperatures are observed in large part of the cavity, especially near the heated wall. With the increase of the volumetric fraction of Ag-MgO nanoparticles, high temperatures were determined except for the places near the right wall of the cavity. In the regions near the hot left wall, sudden increases in temperatures were detected.

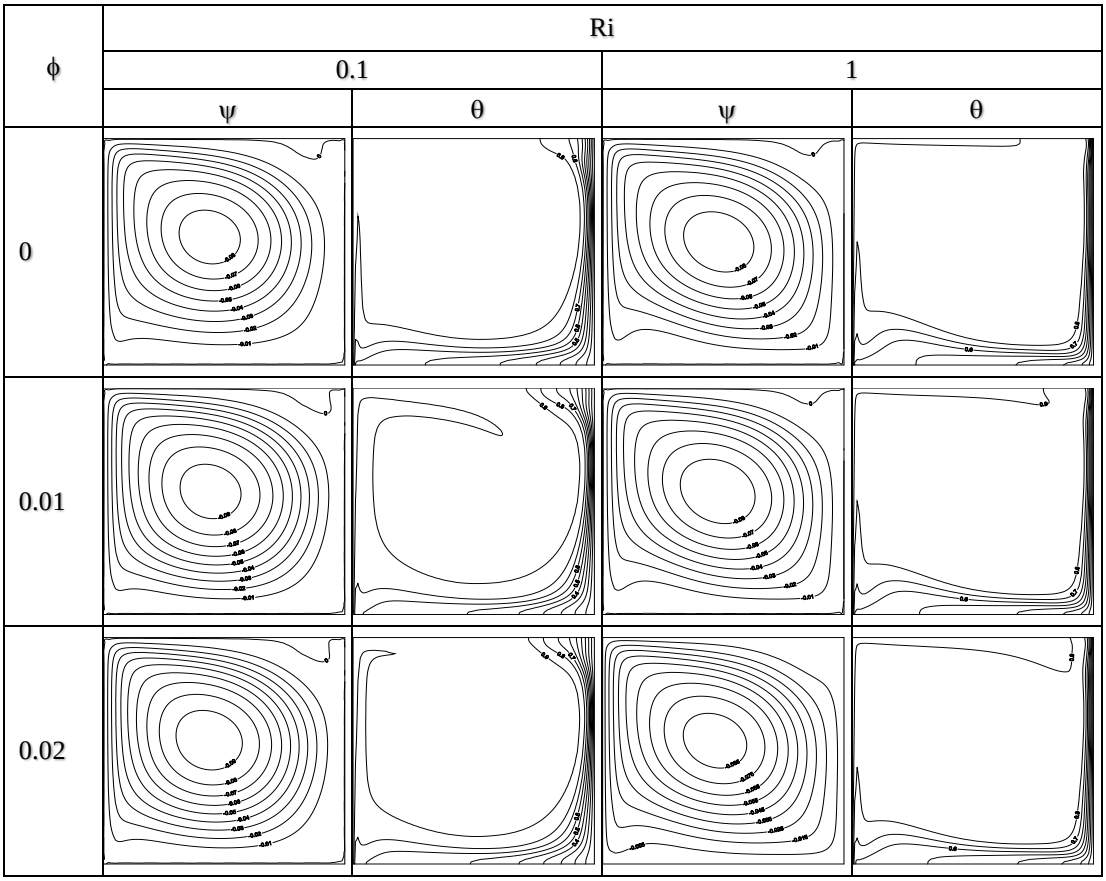

Figure 4. Streamlines and isotherms at Re=1000.

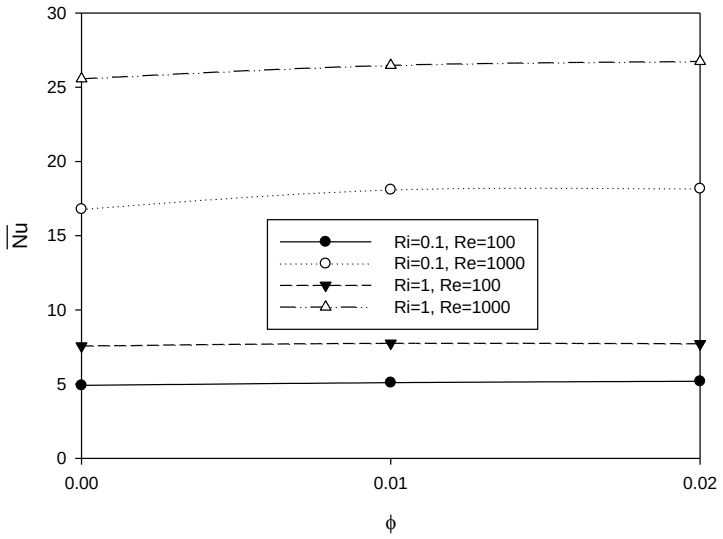

Fig. 5. Average Nusselt numbers on the left wall for different configurations.

As seen in Figure 5, where the average Nusselt numbers are given, a little increase in heat transfer was detected with the increase in the volumetric fraction of nanoparticles. With the increase in the Richardson number, a

significant increase in heat transfer was recorded. Also, the increase in the Reynolds number increases the heat transfer more than the Richardson number. The highest heat transfer values are seen at the highest Reynolds number and Richardson number, while the lowest values are seen in the opposite case.

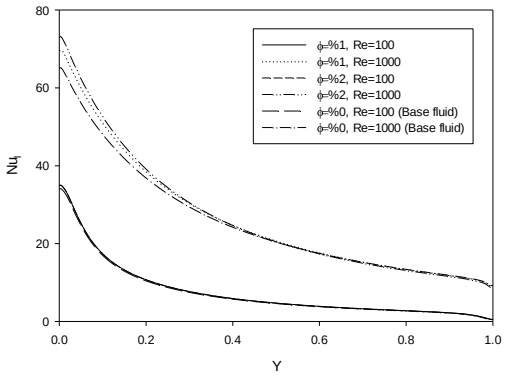

Fig. 6. Local Nusselt numbers on the left wall for different configurations (Ri=1).

Local Nusselt number variations of the heated left wall are given in Fig. 6 for Ri=1. As with the average Nusselt numbers, heat transfer increases with increasing Reynolds number and the volumetric fraction of nanoparticles. Due to the cold nanofluid accumulating in the lower parts of the enclosure, heat transfer occurs more in these regions but gradually decreases as the upper points are approached.

4. CONCLUSIONS

Mixed convection heat transfer in a two-dimensional lid-driven square enclosure filled with hybrid nanofluid heated differentially from vertical walls and insulated from horizontal walls are investigated numerically. Ag and MgO nanoparticle ratios in water-based hybrid nanofluid are equal to each other. The total nanoparticle volumetric fraction was taken as 0, 0.01, and 0.02. As a result of the study, the following results were obtained for water-based hybrid nanofluid containing Ag-MgO nanoparticles:

1. The change of the volumetric fraction in hybrid nanofluid does not affect the heat transfer much, while the change of the Richardson number and Reynolds number significantly affects the heat transfer.
2. The increase in the Richardson number also increases the heat transfer.
3. The increase in the Reynolds number increases the heat transfer more than the Richardson number.
4. High temperatures are observed in large part of the cavity near the heated left wall.

REFERENCES

[1] Moallemi, M. K., & Jang, K. S. Prandtl number effects on laminar mixed convection heat transfer in a lid-driven cavity. *International Journal of Heat and Mass Transfer*, 35(8), 1881-1892, 1992.

[2] Basak, T., Roy, S., Sharma, P. K., & Pop, I. Analysis of mixed convection flows within a square cavity with linearly heated side wall (s). *International Journal of Heat and Mass Transfer*, 52(9-10), 2224-2242, 2009.

[3] Choi, S. U. S., & Eastman, J. A. ASME International Mechanical Engineering Congress and Exposition. San Francisco, CA, 12-17, 1995.

[4] Talebi, F., Mahmoudi, A. H., & Shahi, M. Numerical study of mixed convection flows in a square lid-driven cavity utilizing nanofluid. *International Communications in Heat and Mass Transfer*, 37(1), 79-90, 2010.

[5] Kahveci, K., & Ogut, E. B. Mixed convection of water-based nanofluids in a lid-driven square enclosure with a heat source. *Heat Transfer Research*, 42(8), 2011.

[6] Mansour, M. A., Mohamed, R. A., Abd-Elaziz, M. M., & Ahmed, S. E. Numerical simulation of mixed convection flows in a square lid-driven cavity partially heated from below using nanofluid. *International Communications in Heat and Mass Transfer*, 37(10), 1504-1512, 2010.

[7] Zeghbid, I., & Bessaïh, R. Mixed convection and entropy generation in a square cavity using nanofluids. *Thermophysics and Aeromechanics*, 25(2), 245-256, 2018.

[8] Esfe, M. H., Arani, A. A. A., Rezaie, M., Yan, W. M., & Karimipour, A. Experimental determination of thermal conductivity and dynamic viscosity of Ag–MgO/water hybrid nanofluid. *International Communications in Heat and Mass Transfer*, 66, 189-195, 2015.

[9] Ma, Y., Mohebbi, R., Rashidi, M. M., & Yang, Z. MHD convective heat transfer of Ag-MgO/water hybrid nanofluid in a channel with active heaters and coolers. *International Journal of Heat and Mass Transfer*, 137, 714-726, 2019.

[10] Zhu, D., Jacobson, N. S., & Miller, R. A. Thermal-mechanical stability of single crystal oxide refractive concentrators for high-temperature solar thermal propulsion. *International Solar Energy Conference*, Lahaina, Maui, Hawaii, April 11–15, 1999.

[11] Patankar, S. V., Numerical Heat Transfer and Fluid Flow, McGraw Hill, New York, 1980.

POSTER PRESENTATIONS

Sensorless Flow Rate and Total Head Measurement of Centrifugal Pumps Operating with Variable Frequency Drive

Lecturer Erkan Karakaş, Prof. Dr. Yusuf Öner, Assoc. Prof. Dr. Selami Kesler

Pamukkale University, Department of Electrical Electronics Engineering, Denizli / Turkey

Abstract

Centrifugal pumps are widely used in industrial and HVAC applications. In many applications, centrifugal pumps are worked with variable frequency drive control to reduce energy consumption and regulate operational state. Some control systems need to use pump measurements to monitoring system variables and stability of control. Therefore, additional components needed such as sensors, circuity and cables which can increase system cost and complexity. In this study, a method of sensorless flow rate and total head measurement to regulate centrifugal pumps outlet are presented. Estimation of pump output values at different operating points and speeds has been realized using known pump characteristic curves and the affinity transformations. The sensorless algorithm can be easily applied to any centrifugal pump application to reduce the cost of the sensor.

Introduction

Pumping equipment is used in modern manufacturing systems as the major part of many industries. Pumping automation leads to improvement in machine performance [1]. Centrifugal pumps are widely used in industrial and municipal applications, and they are an important end-use application of electric energy. However, in many cases centrifugal pumps operate with a significantly lower energy efficiency than they could, which typically has an increasing effect on the pump energy consumption and the resulting energy costs [2]. Centrifugal pumps are often controlled by adjusting their rotational speed, which affects the resulting flow rate and output pressure of the pumped fluid. Typically, the speed control is realized with a frequency converter that allows the control of the rotational speed of an electric motor. Electric motor is controlled from a variable frequency drive (VFD) to use optimum electric energy where depends on system requirement. In some application VFD controller in pump system needs flow rate (Q) and total head (H) of fluid. Flow rate and total head is related to rotational speed (n) of pump according to affinity laws. Also consumed electric power (P) is related to motor speed. By taking measurements at constant working speeds and using affinity laws, the flow and total head at the working points can be estimated.

Methods and Material

The sensorless flow rate and total head estimation is realized by obtaining the characteristic of the pump and applying it to the similarity laws. PQ and HQ tables should be created to use the pump characteristics with the law of similarity. In order to determine the pump characteristic, pump input power, flow rate and head values must be obtained for all operating situations at a constant speed. Using the obtained pump characteristic data and affinity laws, H and Q values can be calculated at different pump speeds and operating points.

Affinity Laws:

According to the affinity laws two different flow, head and power values are related with speed.

$$\frac{Q_1}{Q_2}=\frac{n_1}{n_2} \qquad \frac{H_1}{H_2}=\left(\frac{n_1}{n_2}\right)^2 \qquad \frac{P_1}{P_2}=\left(\frac{n_1}{n_2}\right)^3$$

At a reference speed, Q and H values can be calculated by obtaining PQ and HQ tables and using affinity laws.

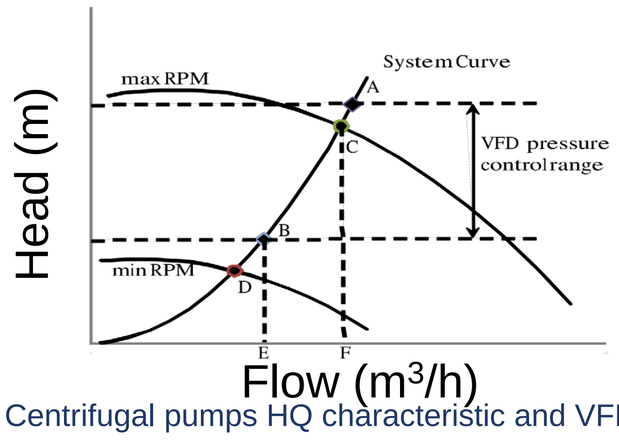

Figure 1: Centrifugal pumps HQ characteristic and VFD operation

If VFD control knows actual speed and power of motor, it can use these parameters to estimate power and flow values. In practice, motor input power will be used instead of pump power since motor input power measurement is simpler. The data that did not exist in the pump characteristic tables at the time of calculation were obtained by linear interpolation. Thus, operations can be performed with tables containing fewer elements.

The sensorless flow rate and total head measurement algorithm consist of the following steps:

1. Acquire motor input power (P_act) and actual motor speed (n_act).
2. Calculate reference power (P_ref) using affinity power law.
3. Find corresponding flow rate (Q_ref) from PQ table
4. Calculate actual flow (Q_act) using affinity law.
5. Find corresponding head (H_ref) from HQ table
6. Calculate actual total head (H_act) using affinity law.

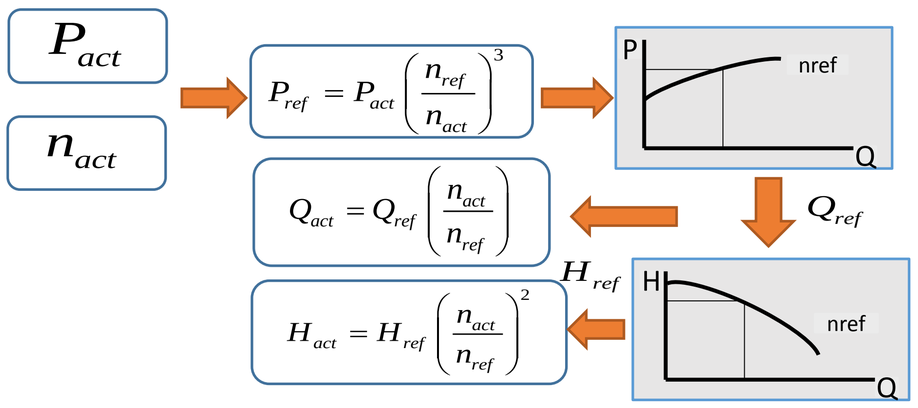

Figure 2: Sensorless H and Q estimation block diagram

Results

Flow and pressure sensors published in centrifugal pumps are difficult and expensive to apply. In a system with known pump characteristics, a sensorless detection can be realized by using the laws of similarity. With the proposed algorithm, in applications that do not require high accuracy, a reference value can be created for the VFD controller by estimating the flow rate and head and the pump can be operated in a more efficient control zone. Thus, while eliminating the cost of the sensor, the centrifugal pump can also be operated in an area where it consumes less energy.

References

Bakman, Ilja. "Implementation and testing the sensorless pressure measurement of centrifugal pumps." *13th International Symposium "Topical Problems in the Field of Electrical and Power Engineering." Doctoral School of Energy and Geotechnology II, Pärnu, Estonia*. 2013.

Ahonen, Tero. *Monitoring of centrifugal pump operation by a frequency converter*. Lappeenranta University of Technology, 2011.

WILO, A. G. Fundamental Principles of pump technology. *Wilo AG, Dortmund*, 2005.

https://www.gsengr.com/uploaded_files/Variable Frequency Drive Recommendations For Centrifugal Pumps.pdf

Author's Index

O. Kizilkan	391,613
E. Koc	495,503,514,592,730
C. Kocabiyik	122
E. Kocak	78,277
G. Kocar	574,679,754
E. Kosa	316
R. Kose	460,468,475
I. Kotcioglu	784
T. Koyun	543
B. Kul	92
I. Kurtbas	2,306
B. Markal	92,630
A. Mavi	201,208
D. Nehari	69
M. A. Omid	474
Y. Oner	429,804
S. Ozbektas	266
M. Ozbey	139
M. F. Ozbey	564
Z. Ozcan	403
F. Ozdemir	174
K. Ozdemir	19
O. Ozdemir	740
A. Ozdogan	436
S. Ozen	764
O. Ozenc	11
M. B. Ozerdem	223
F. Ozgen	327
E. Ozgirgin Yapici	78
S. Ozgul	574
S. Ozkan	627,628,655
I. Ozsevgin	122
B. Ozturk	532
E. Ozturk	555
A. Rahmanparast	33
O. B. Saban	603
M. Saglam	239,259
B. Sahin	794
M. E. Sahin	485
U.R. Sahin	11
Z. Sahin	658
M. Sarioglu	115
B. Sarper	239,259
U. Sekmen	740
O. F. Sel	162
D. S. Semerci	229
E. Sen	403
M. Sener	2,306
M. F. Serincan	524,603
I. Sezer	670
A. M. S. Shakir	152
S. Simsek	772
Y. Sirin	592,730
G. Soyturk	385,613
S. Sultana	626
B. Sungur	266
M. Tebbal	376
S. Tekin	708
M. Terhan	697
S. C. Toker	391,613
B. Topaloglu	266
A. Topcu	532
M. Toptas	335
O. E. Turgut	418
C. Turhan	564,583,687
G. Turkakar	637,708
B. A. Turkmen	769
H. Turkoglu	277
T. Uyanik	412,752
M. E. Vakhshouri	298
E. Yagci	249
O. F. Yalcin	532
T. Yavuz	229,503
M. Y. Yazici	259
S. K. Yener	774
A. Yildirim	50
K. Yildizli	555
E. Yilmaz	626,770
M. Yilmaz	335,740
O. Yilmaz	412,752
S. Yilmaz	383
O. O. Yolcan	460,468,475
Z. Yumurtaci	195
E. Yuzuak	627,628,655,656
M. Zafar	626,770
J. Zahoor	626
A. Zaim	647